

AD-A282 496

AERODYNAMIC DATA ACCURACY AND QUALITY: REQUIREMENTS AND
CAPABILITIES IN WIND TUNNEL TESTING(U) ADVISORY GROUP
FOR AEROSPACE RESEARCH AND DEVELOPMENT NEEDS
JUL 88 AGARD-CP-429

1/6-

UNCLASSIFIED

F/G 1/1

NL



MICROCOPY RESOLUTION TEST CHART
NATIONAL BUREAU OF STANDARDS-1963-A

FILE COPY

(1)

AGARD-CP-429

AGARD-CP-429

AD-A202 496

AGARD CONFERENCE PROCEEDINGS No.429

**Aerodynamic Data Accuracy and
Quality: Requirements and Capabilities
in Wind Tunnel Testing**

DISTRIBUTION STATEMENT A

Approved for public release;
Distribution Unlimited

DTIC
ELECTRONIC
S OCT 2 1968
D

ENTIRE CONTENTS AND AVAILABILITY
ON BACK COVER

\$8 1025 121

AGARD-CP-429

NORTH ATLANTIC TREATY ORGANIZATION
ADVISORY GROUP FOR AEROSPACE RESEARCH AND DEVELOPMENT
(ORGANISATION DU TRAITE DE L'ATLANTIQUE NORD)

AGARD Conference Proceedings No.429
AERODYNAMIC DATA ACCURACY AND QUALITY:
REQUIREMENTS AND CAPABILITIES IN WIND TUNNEL TESTING



Accession For	
NTIS CRA&I	<input checked="checked" type="checkbox"/>
DTIC TAB	<input type="checkbox"/>
Unannounced	<input type="checkbox"/>
Justification	
By	
Distribution/	
Availability Codes	
Dist	Avail and/or Special
A-1	

Papers presented and discussions held at the Symposium of the Fluid Dynamics Panel in Naples, Italy,
28 September—1 October 1987.

THE MISSION OF AGARD

According to its Charter, the mission of AGARD is to bring together the leading personalities of the NATO nations in the fields of science and technology relating to aerospace for the following purposes:

- Recommending effective ways for the member nations to use their research and development capabilities for the common benefit of the NATO community;
- Providing scientific and technical advice and assistance to the Military Committee in the field of aerospace research and development (with particular regard to its military application);
- Continuously stimulating advances in the aerospace sciences relevant to strengthening the common defence posture;
- Improving the co-operation among member nations in aerospace research and development;
- Exchange of scientific and technical information;
- Providing assistance to member nations for the purpose of increasing their scientific and technical potential;
- Rendering scientific and technical assistance, as requested, to other NATO bodies and to member nations in connection with research and development problems in the aerospace field.

The highest authority within AGARD is the National Delegates Board consisting of officially appointed senior representatives from each member nation. The mission of AGARD is carried out through the Panels which are composed of experts appointed by the National Delegates, the Consultant and Exchange Programme and the Aerospace Applications Studies Programme. The results of AGARD work are reported to the member nations and the NATO Authorities through the AGARD series of publications of which this is one.

Participation in AGARD activities is by invitation only and is normally limited to citizens of the NATO nations.

The content of this publication has been reproduced directly from material supplied by AGARD or the authors.

Published July 1988

Copyright © AGARD 1988
All Rights Reserved

ISBN 92-835-0469-0



*Printed by Specialised Printing Services Limited
40 Chigwell Lane, Loughton, Essex IG10 3TZ*

PREFACE

The wind tunnel continues to be the main instrument for providing experimental aerodynamic data to the aerospace industry and the aerodynamic researcher for the purpose of load and performance evaluation and for verification of theoretical results. In both cases it is imperative that the user has confidence in the quality of the results, which means that he must have information on what accuracy to attach to the data.

The quality of wind tunnel results depends upon both the accuracy of measurements and the imperfections provided by the wind tunnel environment. Great strides have been made in recent years on measurement accuracy and as a rule this need no longer be of much concern if properly attended to. However, imperfections provided by the wind tunnel environment are still with us and these are today the main sources affecting the quality and accuracy of aerodynamic data obtained in a wind tunnel.

These imperfections can be classified into two categories, those which are facility related (on-coming flow non-uniformities, unsteadiness and noise; wall and support interference; test repeatability; etc...) and those which are simulation related (Mach and Reynolds numbers; boundary layer simulation; model conformity; etc...).

Operators as well as users are continuously striving to reduce or eliminate imperfections in these various areas so as to improve the accuracy/quality of data.

It was the purpose of this symposium to try to define what accuracy has presently been achieved in modern facilities and to compare these achievements with the actual demands that the users may have in this matter.

The symposium consisted of seven sessions.

Session 1 took stock of the situation thanks to comparisons between results obtained in different wind-tunnels on models supposed to have similar shapes.

Session 2, in particular thanks to the experience of propulsion researchers, showed the benefit which can be derived from a systematic analysis of measured uncertainties.

Session 3 presented the state of the art in the field of drag measurement, which is of prime importance for transport aircraft performance evaluation.

Sessions 4 and 5 reported actions taken to enhance the data accuracy by properly accounting for facility imperfections and by improved simulation techniques.

Session 6 highlighted the progress which can be expected from the use of new testing techniques.

Session 7 allowed the wind tunnel users, including representatives from the Flight Mechanics Panel and from the Structures and Materials Panel to express their needs with regard to data accuracy.

Finally a round table discussion launched by the Symposium Technical Evaluator Mr L.Laster provided a forum where both operators and users from the Research Community as well as from the Aircraft Industry exchanged their views and had stimulating discussions.

B. MONNERIE
L. OHMAN

...

La soufflerie continue à être le moyen principal pour fournir des résultats expérimentaux à l'industrie aérospatiale et aux chercheurs aérodynamiciens en vue de la prévision des performances et des charges aérodynamiques et de la validation des résultats théoriques. Dans les deux cas il est impératif que l'utilisateur puisse avoir confiance dans la qualité des résultats, ce qui implique qu'il ait des informations sur la précision qui est attachée à ces résultats.

La qualité des résultats de soufflerie dépend à la fois de la précision des mesures et des imperfections de l'écoulement délivré par la soufflerie. De grands progrès ont été réalisés ces dernières années en matière de précision de mesure et de façon générale cela ne devrait plus poser beaucoup de problèmes si l'on procède de façon correcte. Cependant, les imperfections de l'écoulement délivré par la soufflerie sont toujours là et c'est principalement elles qui affectent la qualité et la précision des résultats aérodynamiques fournis par les souffleries.

Ces imperfections peuvent être classées en deux catégories, celles qui dépendent de l'installation (non uniformité, instabilités et bruit de l'écoulement incident; interférences de parois et de support; répétabilité des conditions d'essais; etc...) et celles qui sont relatives à la simulation qui est réalisée (nombres de Mach et de Reynolds, simulation de la couche limite, conformité de la maquette; etc...).

Les responsables d'installations aussi bien que les utilisateurs s'efforcent en permanence de réduire ou d'éliminer les imperfections dans ces différents domaines pour améliorer la précision et la qualité des résultats.

Ce symposium a été organisé pour essayer de définir quel niveau de précision était actuellement réalisé dans les installations modernes et pour comparer ces réalisations aux besoins réels que les utilisateurs peuvent avoir en cette matière.

Le symposium a comporté sept sessions.

La session 1 a permis de dresser un premier bilan de la situation grâce à des comparaisons de résultats obtenus dans différentes souffleries sur des maquettes censées avoir des formes semblables.

La session 2, en particulier grâce à l'expérience des motoristes, a montré le bénéfice qui peut être tiré d'une analyse systématique des incertitudes de mesure.

La session 3 a présenté l'état de l'art en matière de mesure de la trainée qui est une caractéristique d'importance capitale pour les avions de transport.

Les sessions 4 et 5 ont relaté des mesures qui ont été prises pour augmenter la précision des résultats en prenant en compte les imperfections de l'installation et en améliorant les techniques de simulation.

La session 6 a mis en évidence les progrès qui peuvent être espérés de l'utilisation d'un certain nombre de techniques d'essai nouvelles.

La session 7 a permis aux utilisateurs en particulier aux représentants des commissions de Mécanique du Vol et des Structures et Matériaux, d'exprimer leurs besoins en ce qui concerne la précision des résultats de soufflerie.

Enfin, une discussion de table ronde lancée par l'Evaluateur Technique du Symposium Monsieur L. Laster a donné l'occasion aux responsables d'installations et aux utilisateurs de la Recherche et de l'Industrie d'échanger leurs points de vue sur la question et d'avoir des discussions stimulantes.

B. MONNERIE
L. OHMAN

AGARD FLUID DYNAMICS PANEL

Chairman: Dipl. Ing. P.W.Sacher
Messerschmitt-Bölkow-Blohm-GmbH
LK 122
Postfach 80 11 60
D-8000 München 80
Federal Republic of Germany

Deputy Chairman: Mr D.H.Peckham
Superintendent AE1 Division
Royal Aircraft Establishment
R141 Building
Farnborough Hants GU14 6TD
UK

PROGRAMME COMMITTEE

M.l'Ing. en Chef B.Monnerie (Co-Chairman)
Chef de la Division d'Aerodynamique Appliquée
ONERA
B.P. 72
92322 Châtillon
France

Prof. J.J.Ginoux
Director
Von Kármán Institute for Fluid Dynamics
Chaussée de Waterloo 72
B-1640 Rhode-Saint Genèse
Belgium

M.C.Dujarric
ESA — Bâtiment Poincaré
18 Avenue Edouard Belin
31055 Toulouse Cedex
France

M.J.Leynaert
Directeur Adjoint des Grands Moyens d'Essais
ONERA
B.P. 72
92322 Châtillon
France

Prof. H.Hornung, Ph.D.
DFVLR
Institut für Experimentelle Strömungsmechanik
Bunsenstrasse 10
D-3400 Göttingen
Federal Republic of Germany

Prof. Dr G.Georgantopoulos
Hellenic Air Force Academy
Tatoi
Athens
Greece

Major Z.Gikas
Hellenic Air Force Tech. Res. Center
KETA
Terpsithea
16501 Glyfada
Greece

Prof. Dr L.G.Napolitano, Ph.D.
Chair of Aerodynamics
Faculty of Engineering, University of Naples
P. Le Tecchio 80
80125 Napoli
Italy

Mr L.H.Ohman (Co-Chairman)
Head, High Speed Aerodynamics Lab.
National Aeronautical Establishment
National Research Council — Montreal Rd
Ottawa, Ontario K1A 0R6
Canada

Prof. M.Onorato
Dipartimento di Ingegneria Aeronautica e
Politecnico di Torino
C. so Duca degli Abruzzi 24
10129 Torino
Italy

Ir J.P.Hartzuiker
Chief, Compressible Aerodynamics Dept.
National Aerospace Laboratory NLR
Anthony Fokkerweg 2
1059 CM Amsterdam
Netherlands

Prof. A.F.de O.Falcão
Pavilhão de Maquinas
Instituto Superior Técnico
1096 Lisboa Codex
Portugal

Prof. Dr C.Ciray
Aeronautical Eng. Department
Middle East Technical University
Inonu Bulvarı
Ankara
Turkey

Mr D.H.Peckham
Superintendent AE1 Division
Royal Aircraft Establishment
R141 Building
Farnborough, Hants GU14 6TD
United Kingdom

Mr A.Vint
W310E — British Aerospace PLC
Warton Aerodrome
Warton
Preston PR4 1AX
United Kingdom

Dr J.F.Campbell M/S 294
Transonic Aerodynamics Division
NASA Langley Research Center
Hampton
Virginia 23665
USA

Dr K.L.Kushman
Chief, Facility Technology Division
AEDC/DOTR
Arnold Air Force Station
Tennessee 37389
USA

PANEL EXECUTIVE

From Europe:

Mr M.C.Fischer
AGARD-OTAN
7 rue Ancelle
92200 Neuilly-sur Seine
France
Tel.(1)4738-5775 Telex 610176

From USA and Canada:

AGARD-NATO
APO New York 09777

CONTENTS

	Page
PREFACE	iii
FLUID DYNAMICS PANEL	v
(insert a doc page) →	Reference
SESSION I - WIND TUNNEL DATA COMPARISONS	
Chairman: M. Onorato	
A CRITICAL ASSESSMENT OF WIND TUNNEL RESULTS FOR THE NACA 0012 AIRFOIL by W.J. McCroskey	1
EXPERIMENTS ON THE DFVLR-F4 WING BODY CONFIGURATION IN SEVERAL EUROPEAN WIND TUNNELS by G. Redeker, R. Müller, P.R. Ashill, A. Elsenaar and V. Schmitt	2
COMPARISON OF THE RESULTS OF TESTS ON A300 AIRCRAFT IN THE RAE 5 METRE AND THE ONERA F1 WIND TUNNELS by C. Quemard and P.B. Earnshaw	3
ANALYTICAL AND EXPERIMENTAL METHODS USED TO RESOLVE THE AERODYNAMIC RESULTS OF TESTS CONDUCTED IN THREE TEST FACILITIES by R.D. Clark and H.J. Rosenstein	4
SESSION II - UNCERTAINTIES ANALYSIS	
Chairman: L.G. Napolitano	
HIERARCHY OF UNCERTAINTY SOURCES IN TRANSONIC WIND TUNNEL TESTING by J.M. Whorric and R.W. Hobbs	5
WIND TUNNEL PREDICTED AIR VEHICLE PERFORMANCE: A REVIEW OF LESSONS LEARNED by E.C. Rooney and R.F. Lauer, Jr	6
MEASUREMENT UNCERTAINTY OF THE AGARD/PEP UNIFORM ENGINE TEST PROGRAM by J.P.K. Vleght	7
AN OVERVIEW OF THE APPLICATION OF STANDARD MEASUREMENT UNCERTAINTY METHODOLOGY TO PROPULSION TESTING by J.W. Thompson, Jr., W.F. Kinzey and W.O. Boals, Jr	8
SESSION III - DRAG ACCURACY ACHIEVEMENTS	
Chairman: A. Vint	
THE ACCURATE MEASUREMENT OF DRAG IN THE 8R x 8R TUNNEL by M.N. Wood and D.S. Capps	9
ACCURATE DRAG ESTIMATION USING A SINGLE COMPONENT DRAG MODEL TECHNIQUE by A.M. Cassie	10
DEVELOPMENT OF TESTING TECHNIQUES IN A LARGE TRANSONIC WIND TUNNEL TO ACHIEVE A REQUIRED DRAG ACCURACY AND FLOW STANDARDS FOR MODERN CIVIL TRANSPORTS by E.C. Carter and K.C. Pallister	11
AMELIORATION DE LA PRECISION DE LA MESURE DE LA TRAINEE D'UN AVION DE TRANSPORT par C. Armand et C. Pujol	12

cont.)

Reference

SESSION IV - FACILITY PROBLEMS
Chairman: H. Hornung

FLOW UNSTEADINESS IN THREE LOW-SPEED WIND TUNNELS by U. Michel and E. Froebel	13
IMPACT OF NOZZLE DESIGN CONSTRAINTS ON TEST SECTION FLOW QUALITY by D. Van Every, S. Raimondo and G. M. Elfstrom	14
TRANSONIC WIND TUNNEL BOUNDARY INTERFERENCE - A CORRECTION PROCEDURE by R. C. Crites	15
THE USE OF COMPUTATIONAL FLUID DYNAMIC METHODS TO ASSESS THE EFFECTS OF MODEL SUPPORT SYSTEMS AND WORKING SECTION MODIFICATIONS ON THE FLOW AROUND WIND TUNNEL MODELS by D. R. Stanniland	16
ACCURACY OF VARIOUS WALL-CORRECTION METHODS FOR 3D SUBSONIC WIND-TUNNEL TESTING by R. A. Maarsingh, Th. E. Labrujère and J. Smith	17
WIND-TUNNEL - SIDEWALL - BOUNDARY-LAYER EFFECTS IN TRANSONIC AIRFOIL TESTING - SOME CORRECTABLE, BUT SOME NOT by F. T. Lynch and C. B. Johnson	18

SESSION V - SIMULATION PROBLEMS
Chairman: J. P. Hartzuiker

PHYSICAL ASPECTS OF VISCOUS SIMULATION AND ASSOCIATED RESEARCH REQUIREMENTS by E. Stanewsky	19
ON REYNOLDS NUMBER EFFECTS AND SIMULATION by A. Elsenaar	20
A PROPOSED BOUNDARY LAYER SIMULATION METHODOLOGY FOR WIND TUNNEL TESTING by E. Reshotko	21
EXPERIMENTS ON BOUNDARY LAYER TRANSITION TRIPPING AT LOW REYNOLDS NUMBERS by G. P. Russo	22
DES DIFFICULTES DE PREDICTION EN SOUFFLERIE LE TREMBLEMENT D'UN AVION CIVIL MODERNE - REMEDES PROPOSES par R. Destuynder, V. Schmitt, J. Berger et R. Barreau	23
ACCURACY REQUIREMENTS FOR HIGH-SPEED TESTS WITH ENGINE SIMULATION ON TRANSPORT AIRCRAFT MODELS IN THE NLR-HST by W. Burgsmüller, J. W. Kooi and K. W. Möller	24
ENGINE SIMULATOR TESTS: COMPARISON OF CALIBRATION AND WIND TUNNEL RESULTS by W. Baumert, B. Binder and W. Stäger	25

SESSION VI - PROGRESS IN TESTING TECHNIQUES; Requirements
Chairman: C. Dujarric

MESURE DES EFFORTS INSTANTANES SUR UNE MAQUETTE SOUMISE A DES VARIATIONS RAPIDES DE COMMANDE par J. P. Drevet et M. Robert	26
BALANCE ACCURACY AND REPEATABILITY AS A LIMITING PARAMETER IN AIRCRAFT DEVELOPMENT - FORCE MEASUREMENTS IN CONVENTIONAL AND CRYOGENIC WIND TUNNELS by B. Ewald	27

	Reference
CHACTERIZATION OF HYPERSONIC WIND TUNNEL FLOW FIELDS FOR IMPROVED DATA ACCURACY by A.H.Boudreau	28
PRECISION DES MESURES DE PORTANCE ET DE CENTRE DE POUSSEE DE GOUVERNES DE MISSILE par J.Perinelle et M.Ribadeau-Dumas	29
COMPUTERIZED THERMOGRAPHIC TECHNIQUE FOR THE DETECTION OF BOUNDARY LAYER SEPARATION by R.Monti and G.Zuppari	30
 <u>SESSION VII - REQUIREMENTS</u> Chairman: D.H.Peckham	
ACCURACY PROBLEMS IN WIND TUNNELS DURING TRANSPORT AIRCRAFT DEVELOPMENT by G.Krenz	31
REQUIREMENTS AND CAPABILITIES IN UNSTEADY WINDTUNNEL TESTING by R.G.den Boer, R.Houwink and R.J.Zwaan	32
SPECIFICATIONS PARTICULIERES CONCERNANT LES RESULTATS DES ESSAIS EN SOUFFLERIE POUR LA MECANIQUE DU VOL par M.Pianko	33
WIND TUNNEL REQUIREMENTS FOR COMPUTATIONAL FLUID DYNAMICS CODE VERIFICATION by J.G.Marvin	34
ROUND TABLE DISCUSSION	RTD

methods;

— topics: Wind tunnel tests, West Germany, Great Britain, France, Transonic airfoils; Wing body configurations; Wind tunnel models; Jet transport aircraft; Aerodynamics; Transonic wind tunnels; Measurement uncertainty; Aerodynamic drag estimates; Civil aviation; Unsteady flow; Jet engine nozzle design; Boundary interference; Wind tunnel walls; Computational fluid dynamics; Air flow corrections; Reynolds number; Boundary layer transition; Hypersonic wind tunnels; Flow fields; Computerized thermography; Boundary layer separation. (NATO-furnished; cdc) *

A CRITICAL ASSESSMENT OF WIND TUNNEL RESULTS FOR THE NACA 0012 AIRFOIL

W. J. McCroskey
U.S. Army Aeroflightdynamics Directorate (AVSCOM)
NASA Ames Research Center, N258-1
Moffett Field, California 94035, USA

ABSTRACT

A large body of experimental results, which were obtained in more than 40 wind tunnels on a single, well-known two-dimensional configuration, has been critically examined and correlated. An assessment of some of the possible sources of error has been made for each facility, and data which are suspect have been identified. It was found that no single experiment provided a complete set of reliable data, although one investigation stands out as superior in many respects. However, from the aggregate of data the representative properties of the NACA 0012 airfoil can be identified with reasonable confidence over wide ranges of Mach number, Reynolds number, and angles of attack. This synthesized information can now be used to assess and validate existing or future wind tunnel results and to evaluate advanced Computational Fluid Dynamics codes.

I. INTRODUCTION

Reliable determination and assessment of the accuracy of aerodynamic data generated in wind tunnels remains one of the most vexing problems in aeronautics. Aerodynamic results are seldom duplicated in different facilities to the level of accuracy that is required either for risk-free engineering development or for the true verification of theoretical and numerical methods. This shortcoming is particularly acute with regard to today's rapid proliferation of new Computational Fluid Dynamic (CFD) codes that lack adequate validation [1].

On the other hand, the NACA 0012 profile is one of the oldest and certainly the most tested of all airfoils; and it has been studied in dozens of separate wind tunnels over a period of more than 50 years. Although no single high-quality experiment spans the complete subsonic and transonic range of flow conditions, the combined results of this extensive testing should allow some conclusions to be drawn about wind-tunnel data accuracy and reliability, at least for two-dimensional (2-D) testing. This paper attempts to extract as much useful, quantitative information as possible from critical examinations and correlations of existing data from this single, well-known configuration, obtained in over 40 wind tunnels and over wide ranges of Mach number, Reynolds number, and angles of attack.

A preliminary comparison by the author [2] in 1982 of results from about a dozen widely-quoted investigations for the NACA 0012 airfoil revealed significant and unacceptable differences between wind tunnels, and subsequent examinations of more data sets merely compounded the confusion, as indicated in Figs. 1 and 2. Therefore, a major part of the present investigation was the development of a filtering process for screening the available data and classifying the experimental sources into broad categories of estimated reliability. This process is described in the next section. Detailed comparisons, correlations, and uncertainty estimates are discussed in subsequent sections, where the following results are considered:

1. Lift-curve slope versus Mach and Reynolds number
2. Minimum drag versus Mach and Reynolds number
3. Maximum lift-to-drag ratio versus Mach and Reynolds number
4. Maximum lift versus Mach and Reynolds number
5. Shock-wave position versus Reynolds number at $M = 0.8$

As this list indicates, the present study deals mostly with the integral quantities, lift and drag. Despite the large number of references available on this most popular of all airfoils, it was found that there is insufficient overlap in the experiments to make many meaningful, direct comparisons of more detailed quantities, such as pressure distributions, in the transonic regime. It is acknowledged that pitching moment is also a sensitive integral parameter that displays interesting transonic behavior, but C_m is not considered in this paper.

II. THE FILTERING AND ANALYSIS PROCESS

The main objective of this section is to combine the critical, relevant information that is available on airfoil testing and on airfoil aerodynamic behavior into a systematic screening, or "filtering," process that can be used to assess the quality of individual experimental sources of data. This process will then be used to classify each data set and to weigh the accuracy of those data against the quantitative or qualitative information that they can provide about the aerodynamic characteristics of the NACA 0012 airfoil.

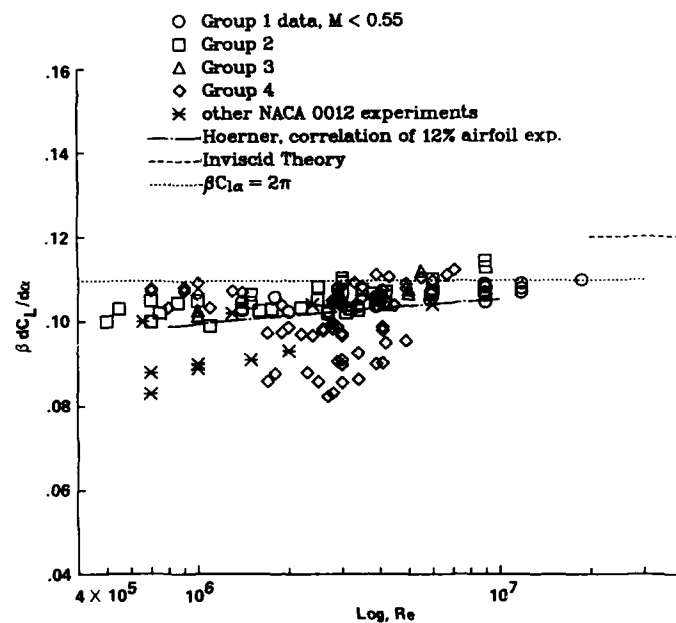


Fig. 1. Lift-curve slope at zero lift vs. Reynolds number; all data, $M < 0.55$. Legend explained in Tables 1-4, $\beta = \sqrt{1 - M^2}$

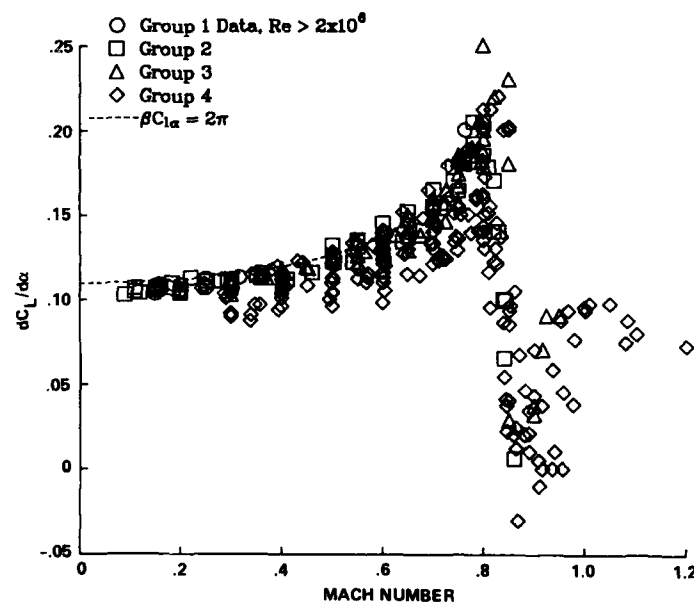


Fig. 2. Lift-curve slope vs. Mach number; all data. Legend explained in Tables 1-4.

A. Development of the Process

The critical information used in the development of the process is derived from four broad categories, as follows:

1. A very large collection of wind-tunnel data for the NACA 0012 which varies widely for many possible reasons.
2. A modest collection of "facts," i.e.,
 - a. well-established theories and similarity laws
 - b. generally-accepted empirical laws
 - c. recent advances in identifying, analyzing, and correcting for wind-tunnel wall effects.
3. A fuzzy collection of "folklore" about airfoil behavior, test techniques, and wind-tunnel characteristics.
4. Recent CFD results for a few standard airfoil cases in both simulated free-air conditions and combined airfoil/wind-tunnel installations.

This aggregate of information firmly establishes some important sources of wind-tunnel errors and certain properties of airfoils such as the NACA 0012. This knowledge can be summarized as follows: first, all four wind-tunnel walls generally interfere with the flow around the airfoil, and this phenomenon is generally more acute than for three-dimensional (3-D) bodies. The top and bottom walls particularly affect the effective angle of attack, the shape of the pressure distribution (and hence pitching-moment coefficient), and the shock-wave location, and to a lesser extent, lift, drag, and effective Mach number. Solid walls increase the effective α and Mach number, but these effects are considered to be easily correctable, at least in subsonic and mildly transonic flows. Slotted or porous walls lower the effective α ; attempts are often made to correct for this, but it is difficult.

Second, side-wall boundary layers have been shown to lower C_L , C_D , and the effective M , and to move the shock forward. Flow separation at the airfoil-wall juncture affects the shock location and reduces $C_{L_{max}}$. The effects can be reduced substantially by the application of suction on the side walls, and corrections can be applied if there is no separation in the corners.

Third, free-stream turbulence and boundary-layer trips increase C_D and often affect C_L , C_m , and shock location. Many airfoils, including the NACA 0012, may be particularly sensitive to Reynolds number variations if no trip is used; however, extreme care must be exercised in tripping the boundary layer to avoid causing excessive drag increments and erroneous changes in C_L and shock position. The effects of both trips and turbulence are difficult to quantify.

Concerning airfoil behavior, two important "facts" have been established about the behavior of lift and drag in subsonic flow at small angles of attack. At high Reynolds numbers, both C_D at zero lift and the quantity $\sqrt{1 - M^2} C_L$ are independent of M and are only weakly dependent upon Re . Unfortunately, most other aspects of airfoil characteristics are not as firmly established, and even these two quantities are not well defined in transonic flow. However, measurements of general trends and qualitative behavior are generally accepted, even if the absolute values of C_L , C_D , and C_m , for example, are uncertain.

To improve on this situation, the following filtering or screening process is proposed. First, an attempt will be made to identify the highest-quality experiments in which the aforementioned wind-tunnel problems were carefully controlled, corrected for, or otherwise ameliorated. Second, the results of these tests will be used to establish the quantitative, "factual," behavior of the critical parameters C_{D_0} and aC_L , where $\beta = \sqrt{1 - M^2}$, as functions of Re in the subsonic regime where they are essentially independent of M . This information comprises the filters that are necessary, although not sufficient, screening criteria for judging the credibility of the remaining data. Third, these filters will be used to help identify obviously erroneous aspects of all the data sets and to classify each experiment accordingly. Fourth, all the data will be critically examined outside the range of Mach and Reynolds numbers for which the filters were developed. Finally, a subjective extension of the fourth step will be made. The "folklore" correlations and other information referred to above, and established transonic similarity laws, will be used to combine selected NACA 0012 and other airfoil data in order to estimate the transonic properties of the NACA 0012 over a range of Mach numbers, $0.85 < M < 1.1$, for which virtually no reliable data exist.

B. Application of the Process

Table 1 lists and summarizes the experiments which clearly stand out as having been conducted with the utmost care and/or as most nearly eliminating the important sources of wind-tunnel errors. These sources are referred to throughout this paper as Group 1. It will be noted from Table 1 that, unfortunately, only one of the experiments extends slightly into the transonic regime, and that the turbulence level in that test was relatively high. Also, for the present purposes, it is unfortunate that the only data reported from that experiment were obtained with a boundary-layer trip, although some unpublished data were also obtained without a trip.

The results for $\alpha C_{L\alpha}$ from Group 1 are plotted versus Re in Fig. 3. It is clear that the results shown in this figure represent a major improvement over the large scatter in Fig. 1. A good fit of the lift-curve slope data in the limited range $2 \times 10^6 < Re < 2 \times 10^7$ is given by

$$\alpha C_{L\alpha} = 0.1025 + 0.00485 \log(Re/10^6) \quad \text{per degree} \quad (1)$$

with an rms standard error of 0.00024 and a maximum error of 0.0029 for the 30 points shown.

Similarly, the results for C_{d0} are plotted in Fig. 4. The meaning of the various groups is explained below. The drag data from Group 1 without a boundary-layer trip, i.e. the open circles, can be approximated well by

$$C_{d0} = 0.0044 + 0.018 Re^{-0.15} \quad (2)$$

with an rms standard error of 0.00005 and a maximum error of 0.0007 for the 36 points from Group 1. The data with a boundary layer trip show a greater sensitivity to Reynolds number. In accord with the approximate variation of fully turbulent skin friction with Reynolds number [3], a good fit to the Group 1 tripped data is given by

$$C_{d0} = 0.0017 + 0.91/(\log Re)^{2.58} \quad (3)$$

where the constant 0.0017 was chosen to optimize the curve fit shown in Fig. 4.

For reference, it is estimated that the individual values of $\alpha C_{L\alpha}$ and C_{d0} can be determined or calculated from the individual Group 1 data points to an overall precision of about ± 0.0005 and ± 0.0002 , respectively. It may be mentioned that Ref. 4 lists the desired accuracy of C_d from wind tunnels as 0.0005 for the assessment of configuration changes and 0.0001 for the validation of CFD codes.

The information in Eqns. 1-3 can now be used to assess the accuracy of the data from the remaining sources and to group the data into separate categories. After much deliberation, it was decided to define Group 2 as comprising those data which generally agree with both the lift and drag criteria expressed in Eqns. 1-3, to within ± 0.0040 for $\alpha C_{L\alpha}$ and to within ± 0.0010 for C_{d0} . These experiments are listed in Table 2. Foremost in this group is the experiment of C. D. Harris [5]. Although this experiment was carefully conducted and offered the advantage of a large aspect ratio, lift-interference corrections on the order of 15% are required for the angles of attack. These were a major concern initially, but in the subsequent discussions and figures it will become evident that these results are comparable in accuracy to those of Group 1.

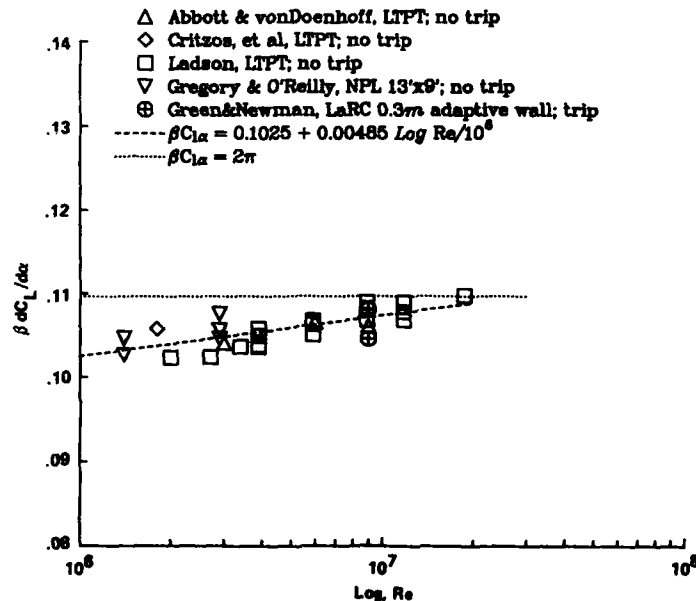


Fig. 3. Lift-curve slope at zero lift vs. Reynolds number; Group 1 data, $M < 0.55$. Expanded vertical scale.

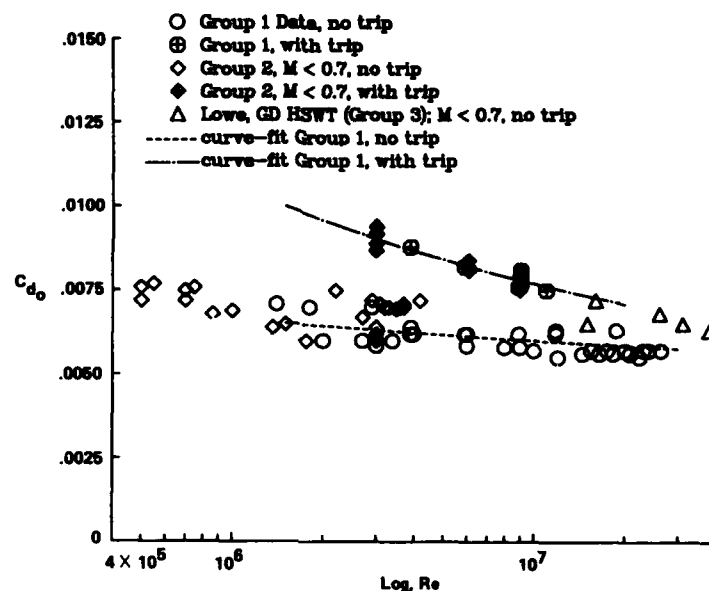


Fig. 4. Drag coefficient at zero lift vs. Reynolds number.

Several sources provide data that agree well with the Group 1 results for either αC_{L_0} or C_{d_0} , but not for both. In some cases, only one of these key quantities was measured. These are classified as Group 3 and are listed in Table 3. An example of this group is the essentially interference-free experiment of Vidal et al. [6], which provides good lift data, but which used a large trip that evidently produced excess drag.

A few sources provided data that generally satisfy the basic lift and/or drag criteria outlined above, but for which other major problems have been identified. In addition, a significant number of tests fail to satisfy either of these two criteria, but they do cover ranges of Mach number where even qualitative information is helpful. These sources are referred to as Group 4 and are briefly summarized in Table 4. Finally, still other sources were examined that failed to satisfy the criteria, and which did not appear to offer any significant additional information relevant to the present investigation. For information purposes these are listed in Table 5, but their results are not used in this paper.

III. RESULTS AND DISCUSSION

In this section, the results from Groups 1-4 and from the other sources alluded to Section II.A are used collectively to establish the primary characteristics of the NACA 0012 airfoil over a wide range of Mach number, Reynolds number, and angle of attack.

A. Lift-Curve Slope, $dC_L/d\alpha$

Figure 5 shows the data from Groups 1-3 for αC_{L_0} as a function of Reynolds number, for $M < 0.55$. Harris' results [5], at $Re = 3$ and 9×10^6 , are highlighted by solid symbols, and this convention will be followed in most of the remaining figures. The scatter in the Group 2 data is slightly greater than that of the Group 1 results, but the quantitative behavior of αC_{L_0} seems to be established now over the range of most wind-tunnel tests for aeronautical purposes.

The complex transonic behavior of C_{L_0} is illustrated in Fig. 6, where the relevant Group 3 data have been added. This figure clearly represents a major improvement over Fig. 2. For these conditions, the good agreement between Harris' results [5] and those of Green and Newman [7] constitute further validation of the former. The largest discrepancies that remain occur with the data from Vidal et al. [6] below $M = 0.8$, which seems to be mostly a Reynolds-number effect, and Sawyer [8], who reported large values at $M = 0.8$. It is unclear whether this is due to side-wall interference, or something else. But in all cases, the peak in C_{L_0} occurs at $M = 0.80 \pm 0.01$.

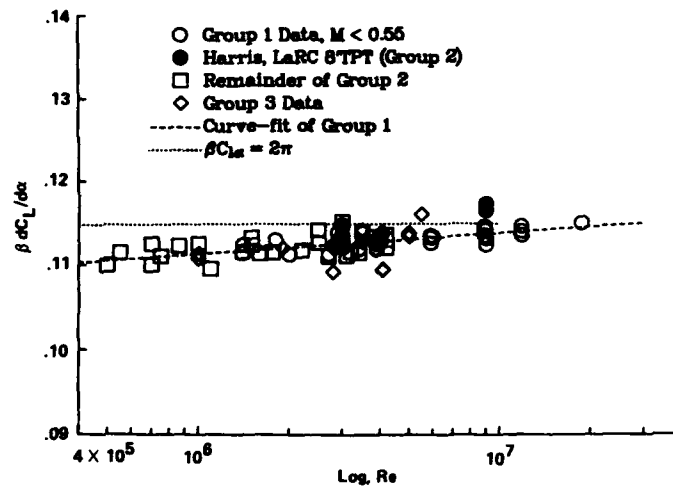


Fig. 5. Lift-curve slope vs. Reynolds number. Same scales as Fig. 1.

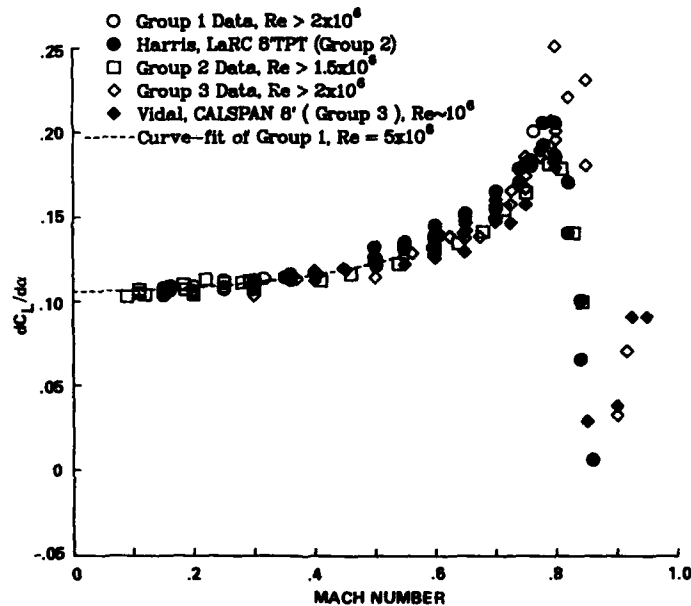


Fig. 6. Lift-curve slope vs. Mach number.

The data in Fig. 6 indicate rapid variations with Mach number in the narrow range $0.8 < M < 0.9$. Unfortunately, the Group 2 and 3 data are very sparse in this region, and are nonexistent above $M = 0.95$. Therefore, an attempt was made to extract selected additional information from the Group 4 data and from other sources, as discussed above. Three points are relevant here. First, in the transonic portion of Fig. 2, the results of Scheitel & Wagner [9] can be argued to be the most reliable of the Group 4 measurements, because side-wall suction was used and because their results are more nearly consistent with the Group 2 and 3 data where there is some overlap. Second, all of the supersonic data points of Group 4 are in good agreement with one another and with the similarity correlation given below which encompasses other symmetrical airfoils [10,11],

$$C_{L_{\alpha}} = 0.055[(\gamma + 1)M^2 t/c]^{-1/3} \pm 10\% \quad (4)$$

It must be noted that this simple relation is only valid in the low supersonic range, $0.1 < \bar{M} < 1$, where $\bar{M} = (M^2 - 1)/[(\gamma + 1)M^2 t/c]^{-1/3}$, and although it is based on transonic similarity, the thickness correlation breaks down for $\bar{M} < 1$ [10].

A third important aspect of Figs. 2 and 6 is the behavior around $M = 0.9$. There is a wide variation in the minimum value of $C_{L\alpha}$ and in the Mach number at which this occurs; and Refs. 9 and 12 of Group 4, and Ref. 13 of Group 5 reported negative values of $C_{L\alpha}$. This phenomenon was investigated briefly in Ref. 14, wherein Navier-Stokes calculations at $M = 0.88$ and $\alpha = 0.5^\circ$ produced a marginally-stable solution with $C_{L\alpha} = 0$. These calculations were repeated recently with a time-accurate code, and this time they produced an unsteady solution with periodic oscillations with an amplitude of $\Delta C_{L\alpha} = 0.1$ around a mean value of approximately zero. This behavior appears to be qualitatively the same as the transonic self-induced oscillations reported on a biconvex airfoil by Levy [15] and in several subsequent investigations. On the other hand, only "steady" results have been reported in the NACA 0012 experiments, and this unsteady behavior may have been overlooked. Furthermore, it is not known what effect the wind-tunnel walls may have. Considering these factors, it is the author's subjective opinion that the correct behavior for the mean value of $C_{L\alpha}$ is a minimum value somewhere between 0 and -0.05, occurring at $M = 0.88 \pm 0.02$. This area needs further investigation.

Figure 7 shows the collective, "filtered" information described above in the Mach number range from 0.6 to 1.2, including the author's judgement of the upper and lower bounds of the correct transonic lift characteristics of the NACA 0012 airfoil at moderate Reynolds numbers and small angles of attack. In summary, the most important points are the following:

1. In the subsonic range $M < 0.5$, $C_{L\alpha}$ is given by Eqn. 1 to within $\pm 2\%$.
2. The maximum value of $C_{L\alpha}$ is $0.21 \pm 5\%$ and it occurs at $M = 0.80 \pm 0.01$.
3. The minimum value of $C_{L\alpha}$ is -0.025 ± 0.025 and it occurs at $M = 0.88 \pm 0.02$.
4. A secondary maximum in $C_{L\alpha}$ occurs near $M = 1$, with a value of $0.09 \pm 10\%$.
5. In the low supersonic range $1.05 < M < 1.2$, $C_{L\alpha}$ is given by Eqn. 4 to within $\pm 10\%$.

These estimates represent the maximum precision that can be extracted from the existing information, and they represent what is probably the best absolute accuracy to which interference-free lift can be measured on airfoils in wind tunnels today for an arbitrary angle of attack.

B. Minimum Drag, C_{d0}

The baseline information for this fundamental quantity in subsonic flow was discussed earlier in connection with Fig. 4. Although the data from Groups 1 and 2 are self-consistent, the scatter in the results from Groups 3 and 4 (not shown), owing to free-stream turbulence, surface roughness and/or boundary layer trips, wall interference, and measurement errors, would almost totally mask the variation of drag with Reynolds number. Numerical results compiled by Holst [16] in his recent validation exercise for transonic viscous airfoil analyses, suggest that fully-turbulent C_{d0} lies between the values given by Eqns. 2 and 3, but this has not been validated adequately.

Another interesting situation is the transonic drag rise, Fig. 8, for which only a limited number of high-quality sources are available. Here the scatter is excessive, but below $M = 0.7$, each individual data set seems to be essentially independent of Mach number. This suggests subtracting out an average of the subsonic values for any given data set, as follows:

$$\Delta C_{d0} = C_{d0}(M) - \bar{C}_{d0}(M) \quad (5)$$

where \bar{C}_{d0} is the average of the measurements for $M < 0.7$.

The results of applying this procedure are shown in Fig. 9, which is an obvious improvement over Fig. 8. Remarkably, even the Group 3 data are in good agreement for ΔC_{d0} . The drag-divergent Mach number can now be estimated at $M_{dd} = 0.77 \pm 0.01$, with a small amount of drag creep for $M > 0.72$.

The behavior at higher transonic Mach numbers is much more difficult to establish. All of the data from Groups 1-4 are plotted in Fig. 10, along with estimates based on transonic similarity correlations of data from many other symmetrical airfoils [10,11,14,17-20]. These latter sources indicate that airfoil behavior in the low supersonic region is given by

$$C_{d0} = \bar{C}_{d0} + a(t/c)^{5/3}[(\gamma + 1)M^2]^{-1/2} \quad (6)$$

where a is a "constant" that varies from source to source, but which is bounded by about 4.0 and 5.6. The dashed line in Fig. 10 is for $a = 4.8$.

Data from Groups 1-4 do not extend beyond $M = 0.95$. Between $M = 0.8$ and 0.9 , where C_{d0} is rising rapidly, there is a large amount of scatter, and the uncertainty in the measurements is virtually impossible to assess. The solid lines represent the author's subjective judgement of the probable upper and

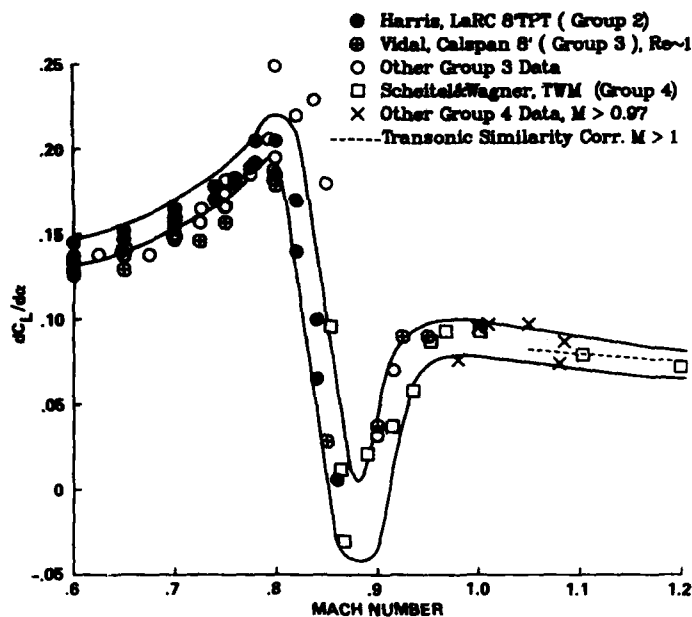


Fig. 7. Lift-curve slope vs. Mach number, including estimated upper and lower bounds.

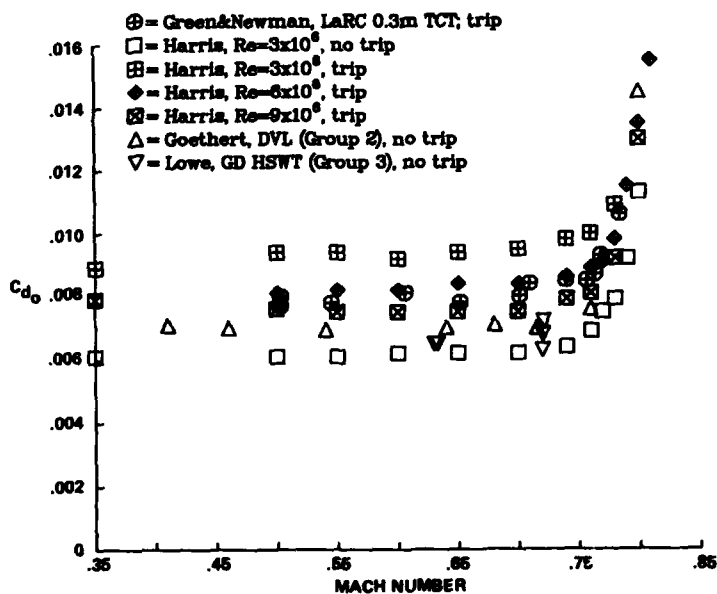


Fig. 8. Minimum drag vs. Mach number; $2 \times 10^6 < Re < 4 \times 10^7$.

lower bounds of the correct transonic drag characteristics for this airfoil. In brief, the most important points concerning minimum drag may be summarized as follows:

1. The subsonic behavior without a boundary layer trip is given by Eqn. 2 to within about ± 0.0003 in the range $10^6 < Re < 3 \times 10^7$.

2. The subsonic behavior with a fully-developed turbulent boundary layer over the entire airfoil is given approximately by Eqn. 3. The uncertainty is difficult to estimate from the available data, but the value ± 0.0005 is proposed.
3. The drag-divergence Mach number is between 0.76 and 0.78. Above M_{dd} , C_{d0} rises rapidly to a maximum value of $0.11 \pm 10\%$, which occurs between $M = 0.92$ and 0.98 .
4. In the low supersonic range $1.05 < M < 1.2$, C_{d0} is given by Eqn. 6 to within $\pm 10\%$. In this regime, both C_{d0} and $C_{L\alpha}$ vary as $M^{-2/3}$.

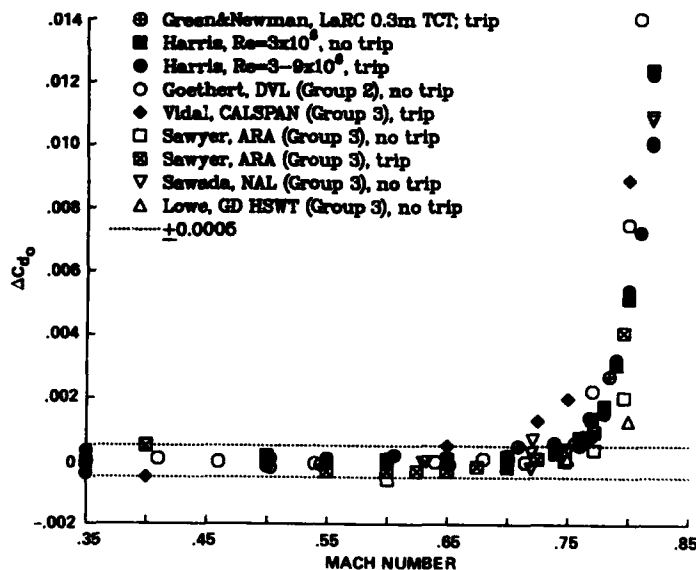


Fig. 9. Incremental drag vs. Mach number; Groups 1-3.

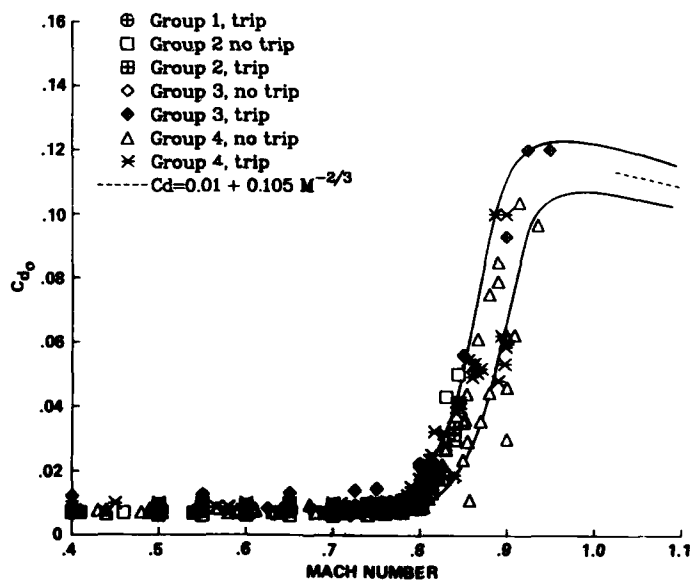


Fig. 10. Minimum drag vs. Mach number; all data, including estimated upper and lower bounds.

C. Maximum L/D Ratio

This quantity has important practical consequences for both fixed-wing aircraft and rotorcraft, and it also represents a rather different and sensitive check on wind-tunnel accuracy and flow quality. On the one hand, it compounds the uncertainty in both lift and drag, but does so under test conditions that are less severe than $C_{L_{max}}$, for example. On the other hand, errors in angle of attack or uncertainties in the α -corrections are not at issue here. Therefore, some experiments in which $C_{L_{\alpha}}$ is suspect may still provide useful information on $(L/D)_{max}$.

Reynolds-number effects on $(L/D)_{max}$ can be isolated for examination if the Mach number is less than about 0.5. This is illustrated in Fig. 11, which shows an increase in $(L/D)_{max}$ by about a factor of two between $Re = 10^6$ and 10^7 . In Fig. 11, the Group 1 results generally show the highest values of $(L/D)_{max}$, consistent with the overall high quality of these investigations. Several of the Group 2 experiments extend the Reynolds number range to lower values than those of Group 1. In addition, the Group 3 results and three sets of data from Group 4 are in fair agreement. Unfortunately, Harris [5] did not provide lift and drag polars for untripped conditions, but it is interesting to note that his results with a boundary-layer trip are in fair agreement with the other data shown. This was not the case for any other tripped data.

At higher Mach numbers the variations in $(L/D)_{max}$ with Mach and Reynolds number are almost impossible to separate from one another. As a compromise between the limitations of so few data available at a given Reynolds number and the large changes in $(L/D)_{max}$ with Re , Fig. 12 shows the available results for the narrow range $4 \times 10^6 < Re < 9 \times 10^6$. The data from Groups 3 and 4 are of interest here, because they are the only available results without a trip that extend into the transonic regime. However, they are suspicious because they lie significantly below the tripped data of Harris [5]. Additional transonic data would be particularly valuable to clarify the quantitative behavior of (L/D) .

D. Maximum Lift

Conventional wisdom holds that three-dimensional separated boundary-layer effects are almost impossible to control at the stall conditions, and there is some question as to whether true two-dimensional stall exists, even for extremely high aspect ratios. Parenthetically, the accurate prediction of $C_{L_{max}}$ for the NACA 0012 airfoil also remains one of the greatest challenges to CFD. Therefore, this quantity needs to be established experimentally.

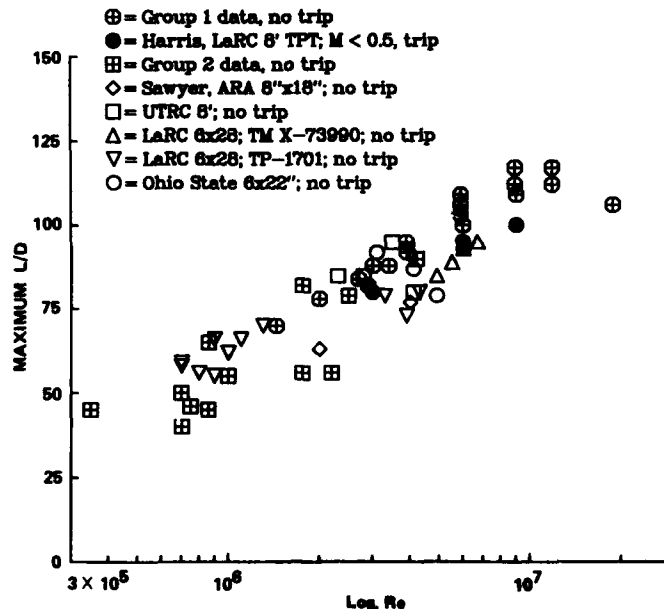


Fig. 11. Maximum lift-to-drag ratio vs. Reynolds number; $M < 0.5$.

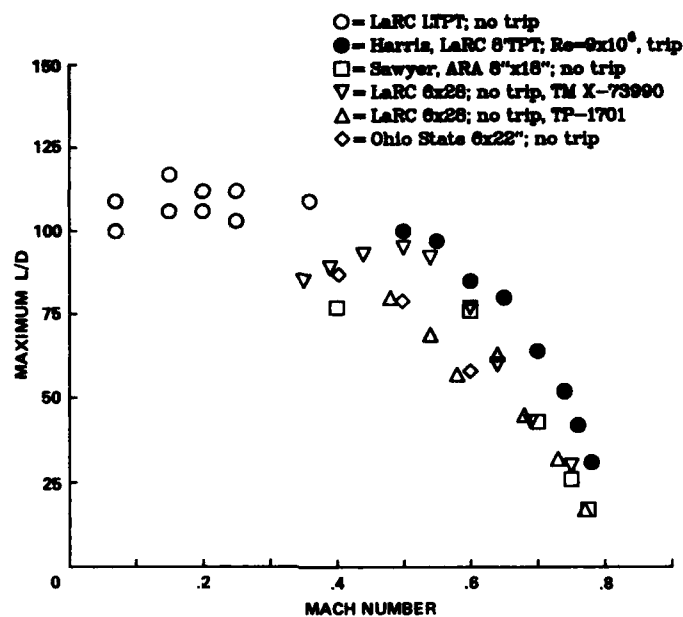


Fig. 12. Maximum lift-to-drag ratio vs. Mach number; $4 \times 10^6 < Re < 9 \times 10^6$.

Figure 13 shows the variation of $C_{L_{max}}$ vs Re for the available data from Groups 1 and 2, at Mach numbers less than 0.25. A monotonic increase in maximum lift with Reynolds number is evident. These particular results are surprisingly consistent, whereas the values from Groups 3 and 4 (not shown) were found to be significantly lower, in general. Also, it should be mentioned that the data shown at $Re < 10^6$ are somewhat higher than the values often quoted (e.g., Ref. 3), based on older sources.

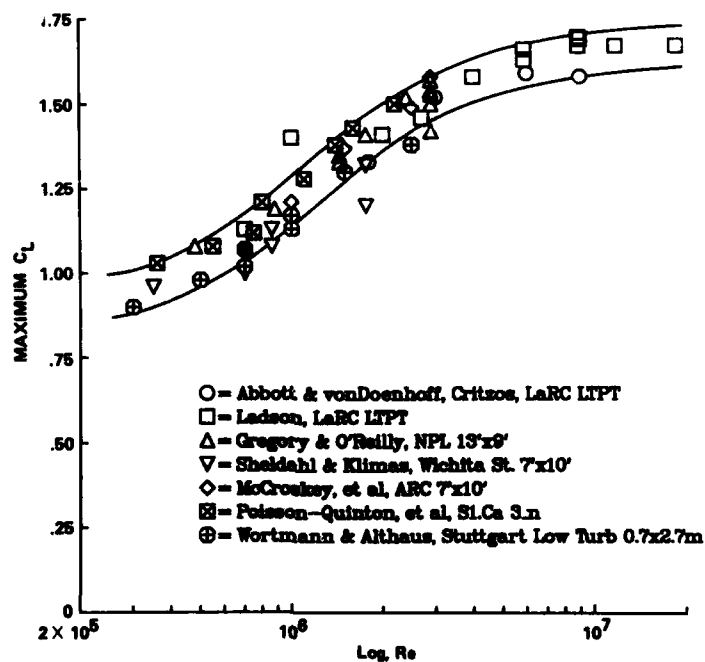


Fig. 13. Maximum lift vs. Reynolds number; Groups 1-2, no trip; $M < 0.25$.

The effect of Mach number on $C_{L_{max}}$ is shown in Fig. 14, for $Re > 2 \times 10^6$. The scatter below $M = 0.25$ seems to be partly due to Reynolds number and partly due to wind-tunnel wall effects. However, local transonic effects in the leading-edge region evidently play an increasingly dominant role in the stall process at $M = 0.25$ and above, where the maximum lift starts to monotonically decrease with increasing M . It is interesting to note that most of the Group 4 data are only slightly below the data from Groups 1-3 at $M > 0.4$, and the scatter in this regime is surprisingly small.

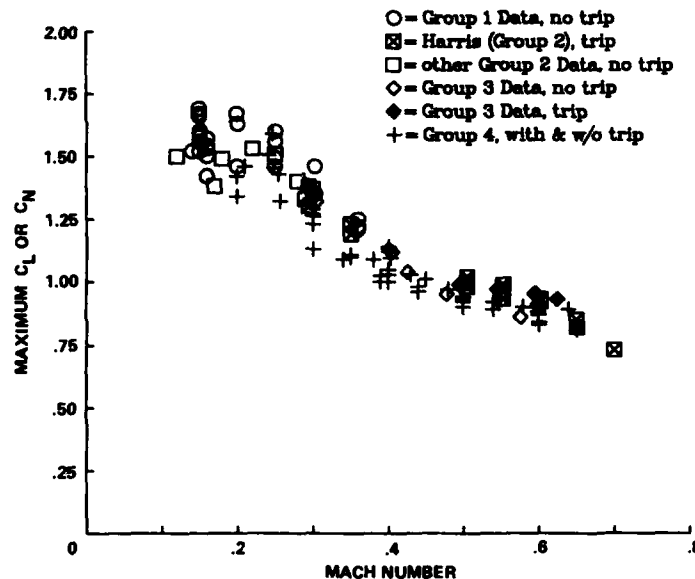


Fig. 14. Maximum lift vs. Mach number; all data, $2 \times 10^6 < Re < 10^7$.

E. Shock-Wave Position

As noted in the Introduction, there is so little overlap in the specific transonic test conditions of the myriad experiments, that most comparisons are necessarily limited to force and moment data. However, some interesting comparisons can be made of the measured shock-wave positions, as this quantity appears to be particularly sensitive to wall-interference effects and to errors in Mach number.

Data from 17 experiments at $M = 0.80$ and $\alpha = 0$ are plotted in Fig. 15, where X_s is defined as the approximate midpoint of the pressure rise across the shock wave. In this figure, the open diamond symbols represent data obtained at sufficiently-large aspect ratios that side-wall boundary layer effects should be minimal, and the solid diamond is a data point corrected by W. G. Sewall in a private communication using his theoretical analysis of side-wall effects [21]. (The principal effect is to increase the effective Mach number by about 0.01). The squares denote experiments in which the side-wall boundary layer was either removed or its effect corrected for. The circles represent the remaining sources, for which no particular attention appeared to be given to side-wall effects.

The grouping of the data in Fig. 15 is inspired by recent numerical analyses [22,23], which showed the tendency of three-dimensional viscous effects on airfoils in wind tunnels to move the shock wave forward of its two-dimensional position. This explanation is tempting for some of the data with unreasonably small values of X_s , but data from several other sources without side-wall treatment appear "normal." Neither does there seem to be any systematic effect of other factors, such as boundary-layer trips or the amount of tunnel slot or perforation openness. Although the majority of the results seem to lie between $X_s = 0.44$ and 0.48 , the overall scatter is disturbing, and the actual reason for it remains a mystery. Therefore, this is yet another area where the key experimental information that would be valuable for CFD code validation is not satisfactory.

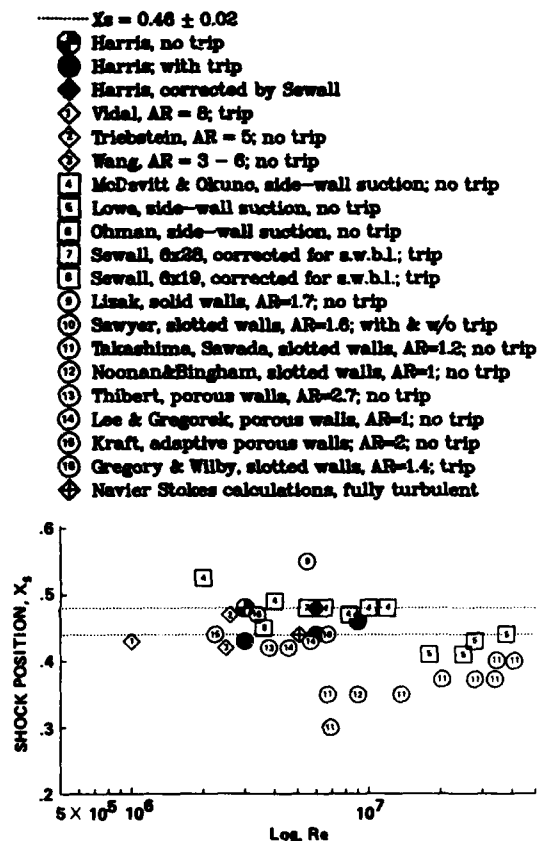


Fig. 15. Shock-wave position vs. Reynolds number at $M = 0.80$ and $\alpha = 0$; all data.

IV. SUMMARY AND CONCLUSIONS

Results from more than 40 two-dimensional wind-tunnel experiments have been critically examined and analyzed.* Sadly, the scatter in the total ensemble of data is unacceptable in the author's view, and it is not readily apparent which of these results are correct. It is clear, however, that the requirements for flow quality and data accuracy set forth in AGARD Advisory Report 184 [4] are seldom met in airfoil testing.

The results of this investigation also suggest that no single existing experiment is adequate either for defining the complete aerodynamic characteristics of the NACA 0012 airfoil, or for validating CFD codes.

Nevertheless, the aggregate of available data is extremely useful. A systematic screening process has been used to help define the relative merits of the various experiments and to filter considerable useful, quantitative information from the confusion. Correlations of key parameters with Mach and Reynolds number have also narrowed the uncertainty in the airfoil section characteristics to acceptable levels, and the judicious use of airfoil theory and numerical calculations permits extrapolations to be made into regimes where hard evidence is sparse. This combined information serves three important functions. First, it allows individual experiments to be critiqued with more confidence than heretofore; second, it allows the complete NACA 0012 airfoil characteristics to be estimated more precisely. Third, the synthesized results presented in the figures and equations can be used to establish the credibility of individual airfoil facilities.

On the basis of both completeness and accuracy, the experiment of Harris [5], chosen by Holst [16] in his recent validation exercise for viscous transonic airfoil analyses, emerges as the most satisfactory

*Tabulations of the data presented in this paper are available from the author upon written request.

single investigation of the conventional NACA airfoils to date. Harris' range of flow conditions is not nearly as complete as desired, and the accuracy of the data was not evident a priori, as lift-interference corrections on the order of 15% were proposed for the angles of attack. However, the present study indicates that Harris' estimates of this phenomenon are, in fact, adequate, at least for low angles of attack, and that most other major sources of errors were minimized. On the other hand, the author is persuaded by the arguments of Mr. W. G. Sewall [21] that some side-wall boundary-layer interference existed. Therefore, it is strongly recommended that this be corrected for before using Harris' data for CFD code validation.

As discussed in Section III, the values of lift-curve slope and minimum drag in subsonic flow can now be established with high confidence in the Reynolds number range $10^6 < Re < 3 \times 10^7$. The behavior of these key quantities can also be estimated throughout the transonic regime and up to low supersonic Mach numbers, but with rapidly-deteriorating confidence above $M = 0.8$. The issue of self-induced oscillations and the possibility of negative values of $C_{L\alpha}$ in the range $0.85 < M < 0.90$ need further investigation. A better definition of the behavior at and above $M = 1$ would be useful for CFD code validation.

The variations of $C_{L\alpha}$ with M and Re can now be specified with a moderate degree of confidence, and the data from most of the available sources are surprisingly consistent above $M = 0.4$. This conclusion appears to contradict folklore, conventional wisdom, and recent numerical studies of wall interference.

On the other hand, the behavior of the maximum lift-to-drag ratio and shock-wave position is not nearly as well defined, and both these quantities appear to be particularly sensitive to wind-tunnel wall effects and turbulence. Therefore, additional studies under carefully-controlled conditions are strongly recommended. It is also suggested that both of these quantities would be especially important criteria for CFD code validation, if they could be reliably established by well-documented experiments.

Finally, the results of this investigation indicate that measurements, corrections, and/or treatments for all four walls of the test section are essential for any reasonably-sized model under transonic flow conditions. Although results from some facilities appeared to suffer more than others from wall-interference effects, no facility that failed to address the potential problems on all four walls provided data that could be judged entirely satisfactory.

V. ACKNOWLEDGEMENTS

The author is extremely grateful to the many people who generously shared stimulating ideas and insights, background information, reference sources, and unpublished results during the course of this investigation. The manifold contributions of Messrs. Charles Ladson and William Sewall of NASA-Langley, including extensive unpublished data, were truly invaluable. Grateful acknowledgement is also extended to Dr. Terry Holst of NASA-Ames, Mr. Frank Harris of Bell Helicopter Textron, and Mr. Ray Prouty of McDonnell-Douglas Helicopters, for their helpful comments, suggestions, and unpublished information. Mr. Lars Ohman of the National Aeronautical Establishment and Messrs. B.F.L. Hammond and T.E.B. Bateman of the Aircraft Research Association, Ltd. provided Mach-number corrections and other useful information concerning their respective facilities. Also, Messrs. Lawrence Green, Clyde Gumbert, and Perry Newman of NASA-Langley, Herr O. Althaus of the Universität Stuttgart, Prof. Siegfried Wagner of Universität der Bundeswehr München, Mr. Kazuaki Takashima of the National Aerospace Laboratory, and Ms. Mary Berchak of Ohio State University kindly provided explanations and tabulations of unpublished data, and their generous assistance is deeply appreciated.

VI. REFERENCES

1. McCroskey, W. J. "Technical Evaluation Report on 'AGARD FDP Symposium on Applications of Computational Fluid Dynamics in Aeronautics,'" AGARD Advisory Report No. 240, 1986.
2. McCroskey, W. J. "Round Table Discussion on 'Wall Interference in Wind Tunnels,'" AGARD Conference Proceedings 335, May 1982.
3. Abbott, I. H., and von Doenhoff, A. E. Theory of Wing Sections, including a Summary of Airfoil Data, Dover Publications, New York, 1959, pp. 124-187.
4. Steinle, F., and Stanewsky, E. "Wind Tunnel Flow Quality and Data Accuracy Requirements," AGARD Advisory Report 184, 1982.
5. Harris, C. D. "Two-Dimensional Aerodynamic Characteristics of the NACA 0012 Airfoil in the Langley 8-Foot Transonic Pressure Tunnel," NASA TM 81927, April 1981.
6. Vidal, R. J., Catlin, P. A., and Chudyk, D. W. "Two-Dimensional Subsonic Experiments with an NACA 0012 Airfoil," Calspan Corporation Report No. RK-5070-A-3, 1973; also, Paper No. 11, AGARD Conference Proceedings CP-174, Oct. 1975.

7. Green, L. L., and Newman, P. A. "Transonic Wall Interference Assessment and Corrections for Airfoil Data from the 0.3m TCT Adaptive Wall Test Section," AIAA Paper 87-1431, 1987.
8. Sawyer, Mrs. J. "Results of Tests on Aerofoil M102/9 (NACA 0012) in the A.R.A. Two-Dimensional Tunnel," Aircraft Research Associates Model Test Note M102/9, 1979.
9. Scheitle, H. "Messreihen zur Bestimmung stationärer Profilbeiwerte der Profile NACA 0012, H1-Tb und H3-Tb," Inst. für Luftfahrttechnik und Leichtbau, Universität der Bundeswehr München Institutsbericht Nr. 87/2, 1987; also private communications from S. Wagner, 1987.
10. Ladson, C. L. "Two-Dimensional Airfoil Characteristics of Four NACA 6A-Series Airfoils at Transonic Mach Numbers up to 1.25," NACA RM L57F05, 1957.
11. McDevitt, J. B. "A Correlation by Means of the Transonic Similarity Rules of the Experimentally Determined Characteristics of a Series of Symmetrical and Cambered Wings of Rectangular Planform," NACA TR 1253, 1955.
12. Prouty, R. "Aerodynamics," Rotor & Wing International, Aug. 1984, pp. 17-22; also private communications 1982, 1984, and 1987.
13. Feldman, F. K. "Untersuchung von symmetrischen Tragflügelprofilen bei hohen Unterschallgeschwindigkeiten in einem geschlossenen Windkanal," Mitteilungen aus dem Institut für Aerodynamik, No. 14, A. G. Gebr. Leeman & Co., Zurich, 1948.
14. McCroskey, W. J., Baeder, J. D., and Bridgeman, J. O. "Calculation of Helicopter Airfoil Characteristics for High Tip-Speed Applications," J. American Helicopter Soc., Vol. 31, No. 2, pp 3-9, April 1986.
15. Levy, L. L., Jr. "Experimental and Computational Steady and Unsteady Transonic Flows about a Thick Airfoil," AIAA Journal, Vol. 16, No. 6, pp. 564-572, June 1978.
16. Holst, T. L. "Viscous Transonic Airfoil Workshop - Compendium of Results," AIAA Paper 87-1460, 1987.
17. Crane, H. L. and Adams, J. J. "Wing-Flow Investigation of the Characteristics of Seven Unswept, Untapered Airfoils of Aspect Ratio 8.0," NACA RM L51D24a, 1951.
18. Daley, B. M. and Dick, R. S. "Effect of Thickness, Camber, and Thickness Distribution on Airfoil Characteristics at Mach Numbers up to 1.0," NACA TN 3607, 1956.
19. Hoerner, S. F. Fluid-Dynamic Drag, published by the author, Midland Park, N.J., 1965, pp. 17-7 to 17-12.
20. Hoerner, S. F. and Borst, H. V. Fluid Dynamic Lift, published by Mrs. L. A. Hoerner, Brick Town, N.J., 1975, pp. 2-12 to 2-14.
21. Sewall, M. G. "Effects of Sidewall Boundary Layers in Two-Dimensional Subsonic and Transonic Wind Tunnels," AIAA Journal, Vol 20, No. 9, pp. 1253-1256, Sept. 1982; also private communications 1985, 1986, and 1987.
22. Obayashi, S. and Kuwahara, K. "Navier-Stokes Simulation of Side-Wall Effect of Two-Dimensional Transonic Wind Tunnel," AIAA Paper 87-037, 1987.
23. Obayashi, S. and Kuwahara, K. "Side-Wall Effect for a Wing at High Angle of Attack," AIAA Paper 87-1211, 1987.

Table 1. NACA 0012 - Summary of Experiments -- Group 1

SOURCE	MACH range	Re (10^6) range	TRIP ? Xt	TUNNEL CHAR.	REMARKS
1. Abbott et al.; Langley LTPT	0.07-0.15	0.7-26	yes & no "Std. R"	solid walls AR = 0.75-6 h/c = 1.9-15	linear wall corrections; very low turbulence; excessively thick trip; possible minor side-wall boundary-layer effects
data available: C_x , C_m , C_d , $(L/D)_{max}$, $C_{t_{max}}$					
2. Ladson; Langley LTPT	0.07-0.36	0.7-19	yes & no Xt=0.05	solid walls AR = 1.5 h/c = 3.8	linear wall corrections; very low turb. at low M; possible minor side-wall boundary-layer effects
data available: C_x , C_m , C_d , $(L/D)_{max}$, $C_{t_{max}}$					
3. Gregory and O'Reilly; NPL 13'x9'	0.08-0.16	1.4-3	yes & no varying	solid walls AR = 3.6 h/c = 5.2	linear wall corrections; with & w/o side-wall boundary-layer control
data available: C_x , C_m , C_d , i.e. C_p , $(L/D)_{max}$, $C_{t_{max}}$					
4. Green & Newman; Langley 0.3m TCT	0.5 - 0.8	9	yes Xt = 0.05	adaptive walls AR = 2 h/c = 2	four-wall corrections; moderate turb. level
data available: C_{x_α} , C_{d_0} (low α only)					

References for Table 1:

- 1a. I. H. Abbott and A. E. von Doenhoff: Theory of Wing Sections, 1959.
- 1b. A. E. von Doenhoff and F. T. Abbott, Jr.: NACA TN 1283, 1947.
- 1c. C. C. Critzos, H. H. Heyson, and R. W. Boswinkle, Jr.: NACA TN 3361, 1955.
2. C. L. Ladson: NASA-Langley, private communication.
3. M. Gregory and C. L. O'Reilly: NPL Aero Report 1308 (ARC 31 719), 1970.
4. L. L. Green and P. A. Newman: AIAA Paper 87-1431, 1987, and private communications.

Table 2 - Summary of Experiments -- Group 2

SOURCE	MACH range	Re (10^6) range	TRIP ? Xt	TUNNEL CHAR.	REMARKS
5. Harris; Langley 8' TPT	0.3 - 0.86	3 - 9	yes & no Xt=0.05	slotted walls AR = 3.4 h/c = 3.4	large α corrections; possible side-wall boundary effects on X_s & C_d
data available: C_n , C_m , C_d , C_p , $(L/D)_{max}$, X_s , limited $C_{L_{max}}$					
6. Goethert; DVL 2.7m W.T.	0.3 - 0.85	2 - 6	no	solid walls AR = 2.6 h/c = 5.4	wall and end-plate corrections; turbulence level $\approx 1\%$; some flow asymmetry
data available: C_x , C_m , C_d , C_p					
7. Sheldahl & Klimas Wichita St. 7'x10'	0.1-0.2	0.35-1.8	no	solid walls AR = 2.4-6 h/c = 5.6-15	linear wall corrections; some flow asymmetry; $0 < \alpha < 180$
data available: C_p , C_d , $(L/D)_{max}$, $C_{L_{max}}$					
8. McCroskey, et al Ames 7'x10' No.2	0.1-0.3	1 - 4	yes & no Xt = 0.01	solid walls AR = 3.5 h/c = 5	linear wall corrections; continuous dynamic data
data available: C_x , C_m , limited C_d , C_p , $(L/D)_{max}$					
9. Bevert; Poisson Quinton & Sievers; SI.Ca 3m	0.06-0.11	1.1-2.2	no	solid walls AR = 1.3 h/c = 4	linear wall corrections; $Tu < 0.2\%$
data available: C_x , C_m , C_d , C_p , $(L/D)_{max}$, $C_{L_{max}}$					
10. Wortmann & Althaus; Techn. Hochs. Stuttgart Lam. W.T.	0.07-0.17	0.3-2.5	no	solid walls AR = 1.5-3 h/c = 5.5-11	side-wall suction; very low turbulence early $C_{L_{\alpha}}$ suspect
data available: C_x , C_d , $(L/D)_{max}$, $C_{L_{max}}$					

References for Table 2:

5. C. D. Harris: NASA TM 81927, April 1981.
6. B. H. Goethert: NACA TM-1240, 1949; Nat. Res. Council (Canada) TT-27, TT-31, TT-38, 1947; RAE TN Aero 1684, 1945.
7. R. E. Sheldahl and P. C. Klimas: Sandia Nat. Labs Report SAND80-2114, 1981.
8. W. J. McCroskey, K. W. McAllister, L. W. Carr, and S. L. Pucci: NASA TM 84245, 1982.
- 9a. A. Bevert: ONERA Doc. 76/1157.AN, 1972.
- 9b. Ph. Poisson-Quinton and A. de Sievers: AGARD CP-22, Paper No. 4, 1967.
- 10a. F. X. Wortmann: AGARD CP-102, 1972.
- 10b. D. Althaus: Institut für Aerodyn. und Gasdynamik, Stuttgart, private communication, 1987.

Table 3 - Summary of Experiments -- Group 3

SOURCE	MACH range	Re (10 ⁶) range	TRIP ? Xt	TUNNEL CHAR.	REMARKS
11. Bernard-Guelle; ONERA R1.Ch	0.325	3.5	no(?)	solid walls AR = 0.67 h/c = 3.3	side-wall suction, careful study of side-wall effects
data available: limited C_x , C_m , C_d					
12. Sawyer; ARA 8"x18" Trans. W.T.	0.3 - 0.85	3 - 6	yes & no Xt=0.07	slotted walls AR = 1.6 h/c = 3.6	α , M, and curvature corrections; poss. side-wall boundary layer effects
data available: C_x , C_d , C_p , $C_{x_{max}}$, $(L/D)_{max}$, X_s					
13. Vidal et al., CALSPAN 8'	0.4 - 0.95	1	yes xt=0.1	porous walls AR = 8 h/c = 16	thick transition strips; slight flow angularity; minimum interference
data available: C_x , C_m , C_d , C_p , $(L/D)_{max}$, limited $C_{x_{max}}$, X_s					
14. McDevitt & Okuno; Ames Hi-Re Channel	0.72 - 0.8	2 - 12	no	solid walls AR = 2 h/c = 3	contoured walls, wall pressure meas.; side-wall suction; unsteady measurements
data available: C_{x_α} , C_p , X_s (low α only)					
15. Gumbert & Newman; Langley 0.3m TCT	0.7 - 0.8	3 - 9	yes & no Xt=0.05	slotted walls AR = 1.3 h/c = 4	α corrected; side-wall boundary-layer corrections
data available: C_{x_α} , C_{d_0} (low α only)					
16. Takashima, Sawada et al. NAL Transonic W.T.	0.6 - 0.8	4 - 39	no	slotted walls AR = 1.2 - 2 h/c = 4 - 6.7	wall pressure-rail meas.; poss. side-wall b.l. effect on shock position;
data available: C_x , C_d , C_p , X_s (low α only)					
17. Sewall; Langley 6" x 28" (revised)	0.3 - 0.83	4 - 9	yes & no Xt=0.08	slotted walls AR = 1 - 2 h/c = 4.7-9.3	α and side-wall b.l. corrections
data available: C_x , C_m , C_d , $C_{x_{max}}$, X_s					
18. Lowe General Dyn. Hi-Re 2D Test Sect, HSWT	0.63-0.82	15-38	no	perfor. walls AR = 1 h/c = 4	22% perforation, side-wall suction; uncertain α corr.
data available: C_x , C_d , C_p , X_s					
19. Jepson; Lizak; Carta; UTRC 8'	0.3 - 0.9	2 - 6	no	solid walls AR= 1.7-5.8 h/c=4.7-5.8	linear wall corrections; multiple entries; various models and end plates
data available: C_x , C_m , C_d , C_p , $(L/D)_{max}$, $C_{x_{max}}$, X_s					
20. Wang et al. Chinese Aero. Inst. Transonic W.T.	0.7 - 0.9	3(?)	yes Xt=0.06	perfor. walls AR= 3.2-6.4 h/c=2.6-5.2	porosity adjusted for min. interference
data available: limited C_x , C_p , X_s					

References for Table 3:

11. R. Bernard-Guelle: 12th Applied Aero. Colloq., ENSMA/CEAT (NASA TT-F-17255), 1975; also J. P. Chevallier: ONERA TP 1981-117, 1981.
12. Mrs. J. Sawyer: Aircraft Research Associates Model Test Note M102/9, 1979.
13. R. J. Vidal, P. A. Catlin, and D. W. Chadyk: Calspan Corporation Report No. RK-5070-A-3, 1973.
14. J. B. McDevitt and A.F. Okuno: NASA TP 2485, 1985.
15. C. R. Gumbert and P.A. Newman: AIAA paper No. 84-2151, 1984.
- 16a. H. Sawada, S. Sakakibara, M. Satou, and H. Kanda: NAL TR-829, 1984.

Table 3 - Concluded.

- 16b. K. Takashima: ICAS Paper 82-5.4.4, 1982.
 16c. K. Takashima: National Aerospace Lab, also private communications, 1985 and 1987.
 17. W. G. Sewall: NASA TM 81947, 1981, also private communications 1985, 1986, and 1987.
 18. W. H. Lowe: General Dynamics Report HST-TR-74-1, 1974.
 19a. W. D. Jepson: Sikorsky Report SER-50977, 1977.
 19b. A. O. St. Hilaire, et al: NASA CR-3092, NASA CR-145350, 1979.
 19c. W. H. Tanner: NASA CR-114, 1964.
 19d. A. A. Lizak: Army Trans. Res. Comm. Report 60-53, 1960.
 20. S. Wang, Y. Chen, X. Cui, and B. Lu: presentation to Sino-U.S. Joint Symposium on "Fundamental Experimental Aerodynamics," NASA-Langley, 1987.

Table 4 - Summary of Experiments -- Group 4

SOURCE	MACH range	Re (10^6) range	TRIP ? Xt	TUNNEL CHAR.	REMARKS
21. Sewall; LaRC 6"x19"	0.58 - 0.92	3 - 4	yes Xt=0.08	slotted walls AR = 1 h/c = 3.2	data corrected for thick side-wall boundary interference but not lift interference
data available: C_{n_0} , C_{d_0} , X_s					
22. Moonan & Bingham; Ladson; LaRC 6"x28"	0.35 - 1.0	1-10	yes & no Xt = 0.1	slotted walls AR = 1.0 h/c = 4.7	α corrected; side-wall b.l. effects on shock position and $C_{s_{max}}$
data available: C_n , C_m , C_d , C_p , $(L/D)_{max}$, $C_{s_{max}}$, X_s					
23. Ohman, et al; NAE 5' x 5' with 2D insert	0.5 - 0.93	17-43	no	porous walls AR = 1.3 h/c = 5	20% porosity; side-wall suction; data slightly asymmetric; Mach No. corrected herein
data available: C_{d_0} , C_p , X_s at $\alpha = 0$					
24. Thibert, et al; ONERA S3.Ma	0.3 - 0.83	1.9 - 4	no	porous walls AR = 2.7 h/c = 3.7	large wall corrections, but wall press. measured; thick side-wall b.l.
data available: C_x , C_d , C_p , X_s					
25. Scheitle & Wagner; TWT München Univ. Bundeswehr	0.36 - 1.6	3 - 10	no	slotted walls AR = 1.5 h/c = 3.4	suction on all four walls, variable with M to match other facilities; moderate turb. level
data available: C_{x_0} , $C_{d_{min}}$, $(L/D)_{max}$, $C_{s_{max}}$					
26. Jepson; NSROC 7'x10'	0.3 - 1.08	2 - 5	no	slotted walls AR = 7.5 h/c = 5.3	large lift interference
data available: C_x , C_m , C_d , $(L/D)_{max}$, $C_{s_{max}}$					
27. Lee, et al; Ohio State 6"x22" Trans. Airf. Facil.	0.2 - 1.06	2 - 12	no	porous walls AR = 0.5 - 2 h/c = 0.9-7.1	independent plenums for top and bottom walls
data available: C_x , C_m , C_d , $(L/D)_{max}$, $C_{s_{max}}$, X_s , limited C_p					
28. Prouty; LAC 15"x48"	0.34-0.96	3 - 7	no	slotted walls AR = 1.5 h/c = 4.6	large lift interference; poss. side-wall boundary layer effects; some flow asymmetry
data available: C_x , C_m , C_d , $(L/D)_{max}$, $C_{s_{max}}$					
29. Gregory & Wilby; NPL 36"x14"	0.3-0.85	1.7-3.8	yes Xt=0.02	slotted walls AR = 1.4 h/c = 3.6	probable wall effects on all data fairly large roughness
data available: C_x , C_m , C_d , C_p , $(L/D)_{max}$, $C_{s_{max}}$, X_s					

Table 4 - Concluded.

30. Kraft & Parker; AEDC I-T	0.8 - 0.9	2.2	no	adaptive walls AR = 2 h/c = 2	variable porosity and hole angle; no side-wall treatment
data available: C_p , X_s					
31. Triebstein; DFVLR 1m TWT	0.5 - 1.0	1 - 3	no	porous walls AR = 5 h/c = 5	no corrections applied; unsteady measurements
data available: X_s , C_p					
32. Ladson; LaRC 6"x19"	0.5 - 1.1	1.5 - 3	no	slotted walls AR = 1.5 h/c = 4.8	a corrected for lift interference but not side-wall boundary layer
data available: C_n , C_m , C_p , surface oil flow, schlieren					
33. Ladson; LaRC ATA 4"x19"	0.8 - 1.25	2.7	no	slotted walls AR = 1.0 h/c = 4.8	no corrections applied
data available: C_n					

References for Table 4:

21. W. G. Sewall: AIAA Journal, Vol 20, No. 9, pp 1253-1256, 1982; also private communications 1985, 1986, and 1987.
- 22a. K. W. Noonan and G. J. Bingham: NASA TM X-73990, 1977.
- 22b. K. W. Noonan and G. J. Bingham: NASA TP-1701, 1980.
23. J. Thibert, M. Grandjacques, and L. Ohman: AGARD AR-138, Ref. A1, 1979; also private communication from L. Ohman, 1987.
24. J. Thibert, M. Grandjacques, and L. Ohman: AGARD AR-138, Ref. A1, 1979.
- 25a. H. Scheitle: Inst. für Luftfahrttechnik und Leichtbau, Universität der Bundeswehr München Institutsbericht Nr. 87/2, 1987.
- 25b. S. Wagner: Universität der Bundeswehr München, private communications, 1987.
26. W. D. Jepson: Sikorsky Report SER-50977, 1977.
- 27a. J. D. Lee, G. M. Gregorek, and K. D. Korkan: AIAA Paper No. 78-1118, 1978.
- 27b. M. J. Berchak and G. M. Gregorek: Ohio State University, private communications, 1987.
28. R. Prouty: "Aerodynamics," Rotor & Wing International, Aug. 1984, pp. 17-22; also private communications 1982, 1984, and 1987.
29. N. Gregory and P. G. Wilby: ARC CP-1261 (NPL Aero Report 017), 1973.
30. E. M. Kraft and R. L. Parker, Jr.: AEDC Reports TR-79-51, 1979, TR-80-63, 1981.
31. H. Triebstein: J. Aircraft, Vol. 23, No. 3, pp. 213-219, 1986.
32. C. L. Ladson: NASA TD D-7182, 1973.
33. C. L. Ladson: NACA RM L57F05, 1957.

Table 5 - Experiments examined but not used -- Group 5

34. J. Stack and A. E. von Doenhoff: NACA Report 492, 1934 (NASA-Langley 11" HST; solid walls, severe blockage effects).
35. R. Jones and D. H. Williams: ARC R&M 1708, 1936 (MPL Compressed Air Tunnel; effects of surface roughness and Re on wings; $AR = 6$).
36. E. N. Jacobs and A. Sherman: NACA Report 586, 1937, and Report 669, 1939 (NASA-Langley VDT; $AR = 6$; high turbulence level).
37. H. J. Goett and W. K. Bullivant: NACA Report 647, 1938 (NASA-Langley 30'x60' Full-Scale WT; $AR = 6$; low turbulence).
38. J. V. Becker: NACA Wartime Report L-682, 1940 (NASA-Langley 8' HSMT; transition and skin-friction measurements at high Re).
39. A. E. von Doenhoff: NACA Wartime Report L-507, 1940 (NASA-Langley LTT; boundary-layer and minimum-drag measurements vs Re).
40. F. K. Feldman: Techn. Hochsch. Zurich Mitteilungen aus dem Institut fur Aerodynamik, No. 14, 1948 (Ackeret's High-Speed Wind Tunnel; transonic measurements on wings; $AR = 3.3$).
41. L. K. Loftin and H. A. Smith: NACA TN 1945, 1949 (NASA-Langley LTT; low lift values, not symmetrical for positive and negative angles of attack).
42. J. Stack and W. F. Lindsey: NACA Report 922, 1949 (NASA-Langley 24" HST; solid walls, variable AR).
43. L. K. Loftin: NACA TN-3241, 1954; P. J. Carpenter: NACA TN-4357, 1958; C. L. Ladson: NASA TD D-7182, 1972 (NASA-Langley LTPT using freon).
44. J. Ponteziere and R. Bernard-Guelle: L'Aero. et l'Astro. Vol. 32, 1971-8; (ONERA R1.Ch before side-wall studies).
45. A. G. Parker: AIAA Journal, Vol. 12, No. 12, pp. 1771-1773, 1974 (Texas A&M 7'x10'; large airfoil, comparison of open and closed test section).
46. N. Pollock and B. D. Fairlie: ARL Aero Report 148, 1977, and Aero Note 384, 1979 ARL Variable-Pressure WT with slotted and solid walls; large corrections, but pressures measured on solid walls).
47. K. W. McAlister, W. J. McCroskey, and L. W. Carr: NASA TP 1100, 1978 (NASA-Ames 7'x10' #2; large airfoil; unsteady measurements; with and without end plates).
48. F. W. Spaid, J. A. Dahlin, F. W. Roos, and L. S. Stivers: Supplement to NASA TM 81336, 1983; L. Stivers, NASA-Ames, private communications (NASA-Ames 2'x2' TWT; large lift interference; incomplete results available).
49. Q. Zhang: presentation to Sino-U.S. Joint Symposium on "Fundamental Experimental Aerodynamics," NASA-Langley, 1987 (Nanjing 0.6x0.6m HSMT; detailed study of alternative interference corrections).
50. R. J. Hansman and A. P. Craig: AIAA Paper 87-0259, 1987 (MIT 1'x1' LTWT; comparative study of the effects of trips and rain at low Re).

EXPERIMENTS ON THE DFVLR-F4 WING BODY CONFIGURATION IN SEVERAL EUROPEAN WINDTUNNELS

G. Redeker and R. Müller, DFVLR*
P.R. Ashill, RAE+
A. Elsenaar, NLR**
V. Schmitt, ONERA++

* Deutsche Forschungs- und Versuchsanstalt für Luft- und Raumfahrt e.V. (DFVLR)
Flughafen D-3300 Braunschweig

+ Royal Aircraft Establishment (RAE)
GB - Bedford MK41 6AE

** National Lucht-en Ruimtevaartlaboratorium (NLR)
Anthony Fokkerweg 2, NL-1059 CM Amsterdam

++ Office National d'Etudes et de Recherches Aérospatiales (ONERA)
29, Avenue de la Division Leclerc, F-92320 Chatillon

SUMMARY

Under the auspices of GARTEUR (Group for Aeronautical Research and Technology in Europe) an international research programme was carried out in order to improve design methods for three-dimensional configurations in transonic flow and to increase the confidence in windtunnel data. The selected configuration was the DFVLR-F4 wing-body combination incorporating a transonic wing of high aspect ratio and a fuselage of Airbus type.

This paper deals with the experimental part of the exercise, where the same model of the above mentioned configuration was tested in three European transonic windtunnels: HST of NLR, S2MA of ONERA and 8ft x 8ft of RAE. The tests followed an agreed test programme comprised force and moment measurements as well as measurements of pressure distribution on wing and fuselage. Selected test results from the three windtunnels will be compared, the main emphasis of the discussions being placed on the comparison of results from different windtunnels on physically the same model. The results show that the data of the three windtunnels are in reasonable agreement, although the severe accuracy requirements of industry for judging performance data from different windtunnels could not be met.

NOTATIONS

b	wing span	L	length of fuselage
$s = b/2$	wing semispan	D	diameter of fuselage
S	wing reference area	M	freestream Mach number
φ	leading edge sweep angle	α	angle of attack
		Re	Reynolds number based on c
φ_{25}	sweep angle of quarter chord line	C_L	lift coefficient
c	local wing chord	C_M	pitching moment coefficient with reference to N_{25}
\bar{c}	aerodynamic mean chord	C_D	drag coefficient
δ	relative local wing thickness	$C_{L_B}, C_{M_B}, C_{D_B}$	coefficients of fuselage alone
y	spanwise coordinate	$C_{L_W}, C_{M_W}, C_{D_W}$	coefficients of wing alone
$\eta = y/s$, ETA	dimensionless spanwise coordinate	C_n	local normal force coefficient
x/c	dimensionless chordwise coordinate, origin at the leading edge	C_m	local pitching moment coefficient
$A = b^2/S$	aspect ratio of wing	C_p	static pressure coefficient
λ	taper ratio		

1. INTRODUCTION

In the 1950 AGARD selected a number of calibration models in order to compare results of different transonic and supersonic windtunnels [1]. As these models hardly exhibit a similarity with transport aircraft a simple configuration of this type was proposed by

ONERA [2] in 1970. This model was chosen as calibration model and had been tested in various transonic windtunnels all over the world [3]. As the accuracy and quality requirements of the aircraft industry on windtunnel results have become more demanding in the recent years, mainly due to a severe competition in commercial aircraft production, the need for further investigations in this direction on a configuration more similar to a current subsonic transport aircraft was felt to be necessary.

Thus, in order to improve transonic design methods for three dimensional configurations and to increase confidence in windtunnel data, a cooperative aerodynamic research programme was initiated under the auspices of GARTEUR. In the Action Group AD(AG01) "Wing body aerodynamics at transonic speeds" a series of aerodynamic investigations on a wing body configuration had been proposed incorporating experimental investigations in the transonic windtunnels of NLR, ONERA and RAE, as well as computational studies with the best available computer codes for three-dimensional transonic flow.

The model chosen for this exercise was the DFVLR-F4 wing body configuration incorporating a supercritical wing of high aspect ratio and advanced design [4,5]. This paper summarizes the main results of the experimental part of the GARTEUR study.

The experimental investigations on the DFVLR-F4 wing body configuration were made in the transonic windtunnels NLR-HST [6], ONERA-S2MA [7] and RAE-8ft x 8ft [8] following an agreed test programme, and comprise force and moment measurements, surface pressure measurements on the wing as well as on the body contour and measurements for deriving buffet onset data from rms-values of wing root bending moment and wing root and tip accelerometer.

This paper compares selected test results from the three windtunnels. In the following section the DFVLR-F4 wing body configuration will be described, followed by a short description of the windtunnels and test arrangements used for this exercise. After the discussion of the test programme and presentation of the data selected for comparison, a detailed discussion of the comparison between the results will be presented. The main emphasis of the discussion is placed on the comparison of results from different windtunnels on nearly physically the same model rather than on the aerodynamic performance of the DFVLR-F4 wing body configuration.

2. EXPERIMENTAL ARRANGEMENT

2.1 Model Configuration

The model which was used for the exercise in the GARTEUR Action Group AD(AG01) is a wing-body configuration (DFVLR-F4) which was designed and built by DFVLR. It represents a typical configuration of a modern wide-body transonic transport of Airbus-type. Fig. 1 presents a general view of the model including the main dimensions.

The design Mach number of the wing is $M = 0.785$ at a lift coefficient of $c_L = 0.5$. The aim was to achieve at the design point a nearly shockfree pressure distribution on the upper surface combined with an elliptical spanwise lift distribution [5]. The wing section derives from that of the airfoil DFVLR-R4 [4]. The wing surfaces were generated by using a linear lofting procedure between four defining wing sections at $\eta = 0.126$ (wing root), $\eta = 0.4$ (kink at the trailing edge), $\eta = 0.7$ and $\eta = 1.0$ (wing tip).

The main geometrical data of the wing are as follows:

Aspect ratio:	A	=	9.5
Taper ratio:	λ	=	0.3
Leading edge sweep:	φ	=	27.1°
Sweep of quarter chord line	φ_{25}	=	25°
Wing thickness at root:	δ	=	0.15
outer wing:	δ	=	0.122
Wing span:	b	=	1.1754 m
Wing reference area:	S	=	0.1454 m ²
Aerodynamic mean chord:	\bar{c}	=	0.1412 m.

The shape of the fuselage of the model is shown in a sideview in Fig. 2. It is formed by a forebody including a cockpit, a cylindrical part containing the wing and an afterbody. The main dimensions of the fuselage are as follows:

Length of the fuselage:	L	=	1.192 m
Fuselage diameter of the cylindrical part:	D	=	0.14842 m

The location of the wing relative to the fuselage is indicated in Fig. 1.

2.2 Model Construction and Measuring Equipment

The windtunnel model comprises two wings and a fuselage which can be separated in the vertical plane of symmetry. These components are mounted on a central core which also contains the housing for the six-component force balance. The fuselage shells were manufactured from aluminium alloy whereas the wings are made of steel. Inside each wing there is a cavity either for pressure tubes or other equipment (see below) which is covered by a flush-fitting plate on the lower surface.

Concerning the measurement equipment the right wing is equipped with 252 pressure ports of 0.3 mm diameter at the seven spanwise stations $\eta = 0.185$, $\eta = 0.238$, $\eta = 0.331$, $\eta = 0.409$, $\eta = 0.512$, $\eta = 0.636$ and $\eta = 0.844$. Each station contains 36 pressure ports, 23 on the upper and 13 on the lower surface (cf. Fig. 3). The left wing was equipped by ONERA for unsteady measurements, that is a strain gauge near the wing root to record the wing root bending moment and two accelerometers to measure the normal acceleration at the wing root and near the wing tip.

The cylindrical part of the fuselage is provided with 44 pressure ports in the vertical plane of symmetry equally spaced on the upper and lower line of the fuselage (cf. Fig. 3).

3. TESTS IN THE DIFFERENT WINDTUNNELS

3.1 Windtunnels and Test Set-up

All three windtunnels used in this exercise are continuous running transonic facilities which are well-known in Europe. All test sections are located within a pressure shell and the windtunnels can be pressurized. Thus, Mach and Reynolds numbers can be varied independently of each other. Fig. 4 compares the cross-sections of the test sections of:

NLR - HST:	1.60 m x 2.00 m
ONERA - S2MA:	1.75 m x 1.77 m
RAE - 8ft x 8ft:	2.44 m x 2.44 m.

It is obvious that the cross-sectional area of the RAE-8ft x 8ft windtunnel is nearly twice of the area of the two others. All three windtunnels have different types of test section walls:

NLR-HST:	slotted top and bottom walls with 12% open area ratio, closed side walls
ONERA-S2MA:	perforated top and bottom walls with 6% porosity, closed side walls
RAE-8ft x 8ft:	closed walls

In all three windtunnels the model was mounted on a sting-support; but it was not possible to use the same sting in all facilities. As shown in Fig. 5 NLR-HST and ONERA-S2MA used a z-sting arrangement of nearly the same size. For this installation only minor model modifications concerning the cavity in the afterbody for the sting and the central core with the balance housing were necessary. In the case of the RAE-8ft x 8ft tests a central sting support had to be used. For this installation, a new afterbody and a different central core had to be manufactured, the latter change being necessary because of the different diameter of the balance used by RAE. Careful inspection of the two central cores ensured that the geometrical set-up of the models was the same in the various facilities.

3.2 Transition Fixing of the Boundary Layer on Wing and Fuselage

During all measurements reported here the model was equipped with transition strips on wing and fuselage. The location of the strips on the wing itself was a result of oilflow tests during the first test series in the NLR-HST windtunnel. Extensive discussions within the action group finally lead to the strip location shown in Fig. 6. This was a compromise between the need to fix transition upstream of the shock over a wide range of Mach numbers and the requirement for a number of test cases suitable for CFD assessment where the boundary layer was not separated at the trailing-edge crank.

On the upper surface the strip location varies linearly from 5% chord at the wing root to 15% chord at station 4, near the crank, maintaining this value to station 7 ($\eta = 0.844$) and then varying linearly to 5% chord at the wing tip. On the lower surface the strip is located at 25% of chord everywhere.

On the fuselage the strip is located 15 mm aft of the nose. All strips have a width of 2mm and were made from carborundum grits of different size.

On the fuselage the transition strip remains the same during all tests and was not replaced. It comprised from carborundum of grade K 150 (0.089 mm).

For the wing it was decided to optimize the grit sizes of the transition strip in each windtunnel, thus taking into account differences in flow quality and windtunnel noise. The optimization took place, separately for upper and lower surface, at $M = 0.78$ and $C_L = 0.6$ by determining the smallest grit size for the strips which produced turbulent boundary layers just aft of the strip.

In the NLR-HST and ONERA-S2MA windtunnels the effectiveness of the strips were checked using a sublimation technique, whereas in RAE-8ft x 8ft windtunnel a technique was used based on observations of the variation of drag with Reynolds number at a given lift coefficient.

Thus, the following grit sizes were used at $Re = 3 \cdot 10^6$:

	upper surface	lower surface
NLR-HST	K 180 (0.074 mm)	K 240 (0.053 mm)
ONERA-S2MA	K 220 (0.060 mm)	K 240 (0.053 mm)
RAE-8ft x 8ft	K 220 (0.060 mm)	K 180 (0.074 mm)

In order to ensure that the strips were applied in a consistent manner their application was supervised by the second author in all three windtunnels.

3.3 Test Programme

The windtunnel tests were carried out after an agreed test programme. The main Reynolds number for all tests was $Re = 3 \cdot 10^6$. Besides the optimization of the transition strips, force and pitching moment measurements for the complete model and the fuselage alone have been carried out for lift coefficients in the range of $0.1 < c_L < c_{Lmax}$ at Mach numbers $0.6 < M < 0.82$. At the same conditions unsteady measurements have been made with the aim of establishing the buffet-onset boundaries.

Pressure measurements on fuselage and wing have been carried out at various fixed lift coefficients of the complete model for a range of specified Mach numbers.

Furthermore a limited number of tests have been done at a lower Reynolds number of $Re = 1.5 \cdot 10^6$. In this paper only the results of $Re = 3 \cdot 10^6$ will be discussed.

3.4 Data Evaluation and Compilation of Results

Each establishment reduced the data to coefficient form after applying the usual corrections. These corrections differed from windtunnel to windtunnel and are briefly summarized here:

Correction applied to	NLR-HST	ONERA-S2MA	RAE-8ft x 8ft
<u>angle of attack</u>			
• sting and balance deflection due to aerodynamic loads	+	+	+
• upwash	+	+	+
• wall interference	- *)	+	+
<u>Mach number</u>			
• wall interference	- *)	+	+
<u>drag coefficient</u>			
• buoyancy drag	+ **)	+	-
• sting influence		+	-
• wall interference	- *)	+	+
• base pressure	-	-	+

*) tunnel to tunnel comparison indicated that wall interference is negligible small for this size of the model

***) from empty test section including sting and sting support

All data from the different windtunnels have been compiled for comparison purposes by DFVLR.

4. COMPARISON OF RESULTS

In the following sections only some selected results of the whole measurements will be presented to demonstrate the main conclusions of this exercise.

4.1 Force and Pitching Moment Measurements

The presentation of force and moment measurements is restricted to the Mach number $M = 0.75$ which demonstrates the main features of the comparison.

Fig. 7 shows the comparison of the curves c_L vers. α and c_L vers. c_M for the complete model. In general, the agreement is quite satisfactory for the c_L vers. α curves. Closer examination shows differences at low c_L -values, $c_L = 0.2$, where the angle of attack of the HST-measurements is approximately $\Delta\alpha = 0.1^\circ$ smaller than that of the S2MA or 8ft x 8ft measurements. This difference decreases with increasing lift coefficients and disappears at $c_L > 0.6$. A similar behaviour can also be observed at the other Mach numbers not shown here. In the region of higher lift coefficients - near c_{Lmax} - some discrepancies occur. Whereas HST and S2MA measurements show a reasonable agreement in this region, the c_L -values of the 8ft x 8ft measurements have their first break at a lift coefficient which is $\Delta c_L = 0.02$ lower than that of the other two windtunnels. The comparison of the pitching moment coefficients c_M vers. c_L shows in the whole region of lift coefficients significant differences, although the tendency with c_L is nearly the same for all three windtunnels. The most negative pitching moment coefficients are observed in the 8ft x 8ft-windtunnel, whereas the corresponding values measured in the HST and S2MA windtunnels are less negative and the differences are in the order of $\Delta c_M = 0.006$ and $\Delta c_M = 0.011$, respectively at $c_L = 0.5$. These deviations are partly due to the differences in the model mounting and will be explained later.

For the same Mach number $M = 0.75$ the drag polars are compared in Fig. 8. Between the different windtunnels a deviation of drag coefficients of $\Delta c_D = 0.0005$ can be found at minimum drag coefficient and of $\Delta c_D = 0.0008$ at a $c_L = 0.5$. These deviations decrease with increasing Mach numbers and vice-versa. The same situation is valid for the curves normal force coefficients c_Y vers. axial force coefficients c_T (not shown here). In order to understand the differences between the results from the different windtunnels, fuselage alone tests have been made. The model mounting is expected to exert most influence on the flow in the region of the afterbody, the effect diminishing rapidly with further distance upstream. Therefore first-order effects of the model mounting are eliminated by analysing wing-alone force coefficients established by subtracting the fuselage-alone results from those for the complete model at given angles of attack,

$$\text{e.g.: } c_{LW} = c_L - c_{LB}, \quad c_{DW} = c_D - c_{DB} \text{ and } c_{MW} = c_M - c_{MB}.$$

Looking at the wing lift coefficients c_{LW} vers. α curves at $M = 0.75$, Fig. 9, one can state that the differences in angles of attack have decreased and are in the region of unseparated flow $\Delta\alpha = 0.05^\circ$. The situation of the wing alone pitching moment coefficients is also illustrated in Fig. 9. Owing to the increasing nose-up pitching moment coefficient c_{MB} of the fuselage alone with increasing angles of attack, the tendency of the wing alone results is changed compared to the complete model results for the wing alone pitching moment decreasing with lift coefficient.

Significant differences occur between the results of the three windtunnels which are not fully understood in detail. Although the deviations are smaller than those for the complete model a surprising feature should be noted. Despite the fact that the model mounting in NLR-HST is more like that in ONERA-S2MA than that used in RAE-8ft x 8ft, the data from NLR-HST are in better agreement with those of RAE-8ft x 8ft.

If one analyses the drag polars presented in Fig. 10 one can state that the differences of the drag coefficients of the wing alone results have decreased in comparison with those of the complete model. At $c_L = 0.5$ for this case a difference of $\Delta c_{DW} = 0.0006$ can be found.

It should be noted here, that the differences shown in c_{LW} , c_{MW} or c_{DW} -values are higher than the theoretical accuracy of the measurements quoted by each establishment. This is especially true for the pitching moment coefficients.

The agreement of force and moment coefficients from the windtunnels of NLR-HST, ONERA-S2MA and RAE-8ft x 8ft is not sufficient to satisfy the requirements of the aircraft industry [9]. In order to compare and to judge different wing designs, tested in different windtunnels, the aircraft industry requires an accuracy of $\Delta c_D = 0.0005$ and of $\Delta c_M = 0.001$.

4.2 Comparison of Performance Boundaries

In this section the dragrise boundaries and the buffet onset boundaries of the complete model tests in the three windtunnels will be compared.

From the drag polars the dragrise Mach numbers have been evaluated. For constant lift coefficients $c_L = 0.3, 0.4, 0.5$ and 0.6 the drag coefficients of the complete model have been plotted vers. Mach number in Fig. 11. This figure again demonstrates that the drag coefficients from the three windtunnels can differ by a value of $\Delta c_D = 0.0010$. Despite these discrepancies the dragrise Mach numbers M_D , evaluated after $dc_D/dM = 0.1$ are nearly the same for the three windtunnels except for the value of $c_L = 0.5$ where the RAE-measurements indicate a somewhat lower dragrise Mach number in the order of $\Delta M = 0.008$. The same behaviour can be noticed if one evaluates the wing alone data. Although the differences in drag coefficients have decreased to $\Delta c_{DW} < 0.0006$ nearly the same dragrise Mach numbers as for the complete model results can be found.

The dragrise boundaries are presented in Fig. 12 as loci in the c_L - M plane. In the same figure the buffet onset boundaries are presented, which have been derived from the rms-values of the unsteady signal provided by the wing root accelerometer. For several constant Mach numbers the rms-values have been measured as a function of angle of attack.

The breakpoints of these curves are used to define the lift coefficients for buffet onset. The curves of the three windtunnels indicate that in the most interesting region of Mach numbers $0.75 < M < 0.8$ a reasonable agreement has been achieved. The difference in lift coefficients at $M = 0.75$ is in the order of $\Delta c_L = 0.02$, which increases with increasing Mach number. For $M > 0.8$ the results of ONERA-S2MA indicate a buffet-free region below a c_L -value of $c_L = 0.47$, whereas the measurements of NLR-HST and RAE-8ft x 8ft show a further decreasing buffet-free c_L -value with increasing Mach number. Buffet onset boundaries have also been derived from steady state force and moment measurements, where a certain deviation in coefficient after the first appearance of a breakpoint in the corresponding curve is used as criterion. Furthermore the rms-signals of the wingtip accelerometer and the wing root bending strain gauge have been used for determining buffet onset. The differences of all buffet onset boundaries derived using the various techniques in one windtunnel are in the same order of magnitude as shown in Fig. 12 for the various windtunnels.

4.3 Comparison of Pressure Measurements

Fig. 13 presents the comparison of the wing pressure distribution at the seven spanwise stations for $M = 0.75$, $Re = 3 \cdot 10^6$ and a lift coefficient of $c_L = 0.6$.

These conditions correspond to one of the three test cases chosen from the GARTEUR action group for computational purposes. The pressure coefficients presented in this figure are measured at $c_L = 0.6$ in the windtunnels of HST-NLR and ONERA-S2MA, whereas for the RAE-8ft x 8ft windtunnel the c_p -values shown are interpolated between values of lift coefficient in the neighbourhood of 0.6. In general, there is an excellent agreement between wing pressures on the lower surface and for the region of subsonic flow at the upper surface. Where there are differences they can be explained by pressure holes becoming blocked or damaged during the course of this exercise. In the region of supersonic flow the agreement is still reasonable although differences in shock wave position are evident on the outer part of the wing. At the outer wing station ($\eta = 0.409$) the shock wave positions of the NLR-HST results appear approximately $\Delta x/c = 0.03$ to 0.05 more upstream than those of the ONERA-S2MA results, which provide the most downstream shock locations. This effect results in a higher wing loading at the outer wing for the ONERA-S2MA experiments which will be discussed later.

Fig. 14 presents the pressure distributions for the same case at the cylindrical part of the fuselage. They are in good agreement.

From the wing pressure distributions given in Fig. 13 the local normal force coefficients c_n and the local pitching moment coefficients with respect to the local quarter chord line c_m have been evaluated and plotted in Fig. 15. Whereas the local pitching moment distribution vers. span from the three different windtunnels is in reasonable agreement, the normal force coefficients of the ONERA-S2MA results are somewhat higher in the outer part of the wing than those of NLR-HST and RAE-8ft x 8ft. This behaviour can also be observed at other cases not shown here. These discrepancies could not be explained by blocked or damaged pressure holes. Although the overall lift coefficient of the complete model should be the same the wing loading at the outer wing seems to be different in the various windtunnels. This effect could not be explained.

Despite these differences one can state that the measured pressure distributions are a quite useful datum-set of a modern transport aircraft configuration for assessment of computational methods.

5. CONCLUSIONS

In the framework of GARTEUR an European research programme has been carried out on a schematic configuration of a modern transport aircraft. In order to compare experimental results of the same model measured in the main transonic windtunnels in Europe the DFVLR-F4 wing-body configuration was tested in the NLR-HST, the ONERA-S2MA and the RAE-8ft x 8ft windtunnel. After an agreed test programme overall forces and moments, pressure distributions on wing and fuselage and buffet onset data have been measured. A comparison of selected results of the best available data for each windtunnel has been presented.

For the complete model this comparison reveals typical differences in the order of:

$$\begin{aligned} \Delta \alpha &< 0.1^\circ \\ \Delta c_D &< 0.0010 \\ \Delta c_M &< 0.015. \end{aligned}$$

Half of these differences can be explained from differences of the fuselage alone tests, indicating that model support and buoyancy effects are of some importance. Pressure distributions compare very well, although differences in shock position can be as large as 5% of local chord. Although the agreement is reasonable, the results do not meet, altogether the accuracy requirements of industry, stated as $\Delta c_D = 0.0005$ and $\Delta c_M = 0.001$. The situation is improved, at least for the drag coefficients, if one looks to the wing alone data. But at present, a comparison of various wing designs, tested in different windtunnels does not seem to be possible with sufficient accuracy.

Nevertheless, the present set data is quite useful as a datum-set for computational exercises on a modern transport aircraft configuration.

In order to avoid some of the shortcomings of the present exercise and in order to reduce the doubts arising from different experimental set-ups it is recommended for future comparison:

Use exactly the same model in all windtunnels including model support and instrumentation.

Preserve model state the same in all windtunnels (smoothness and cleanness of wing surfaces).

Intensify investigations on model support and wall interference effects.

REFERENCES

- [1] A review of measurements on AGARD calibration models.
AGARDOGRAPH 64, (1961).
- [2] Poisson-Quinton, Ph. Information in a roundtable discussion on ONERA calibration models.
AGARD CP-83, (1971)
- [3] Poisson-Quinton, Ph. Prevision des caractéristiques aérodynamiques d'un avion d'après la comparaison des résultats sur une maquette étalon dans diverses grandes souffleries transoniques.
Vaucheret, X.
AGARD CP-242, (1977).
- [4] Redeker, G. Design and experimental verification of two supercritical airfoils.
Müller, R.
DGLR-Paper 78-075, (1978). DGLR-Sym. "Transonic Configurations" Bad Harzburg, FRG, June 1978
- [5] Redeker, G. Design and experimental verification of a wing for a transport aircraft.
Müller, R.
Schmidt, N.
AGARD CP-285 (1980).
- [6] User's guide to the 1.6 x 2.0 m² high speed windtunnel HST of NLR.
- [7] Laverré, J. La soufflerie S2MA du centre d'essais aérodynamiques de Modane-Avrieux
Charpin, F.
ONERA NT 1983-5, (1983).
- [8] Taylor, C.R. Notes on the performance and operation of the 8ft x 8ft tunnel
RAE TM Aero 1546, (1974).
- [9] Windtunnel flow quality and data accuracy requirements.
AGARD-AR-184, (1982).

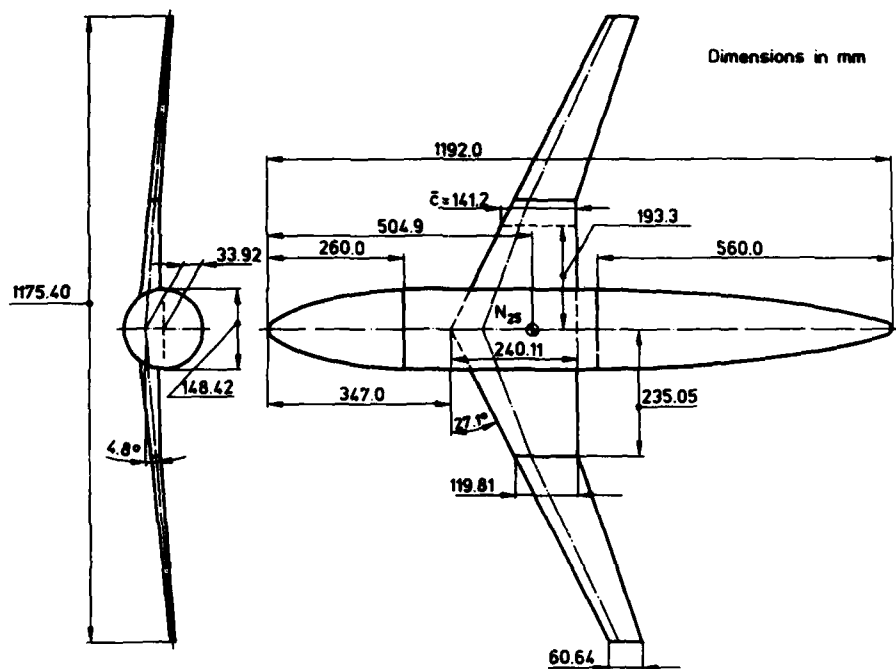
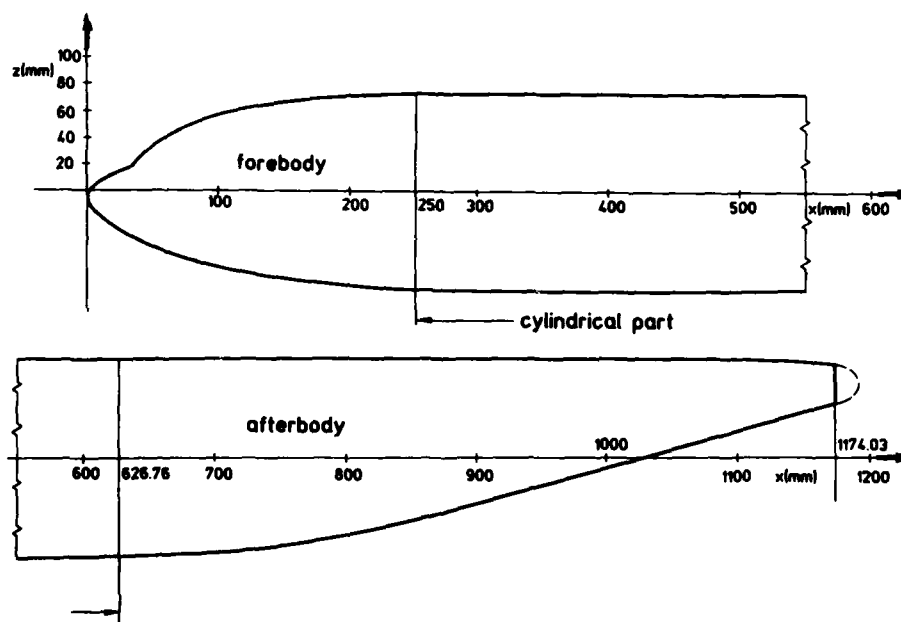


Fig. 1 General arrangement of DFVLR-F4 model



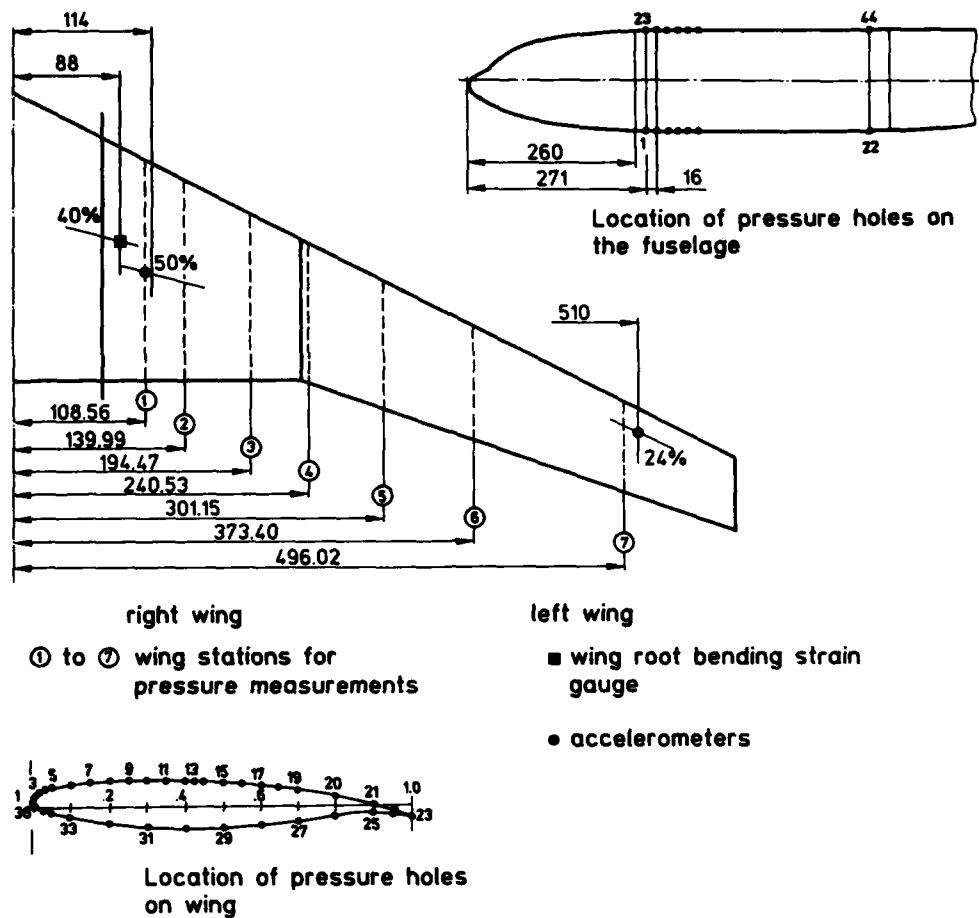


Fig. 3 Wing and fuselage equipment

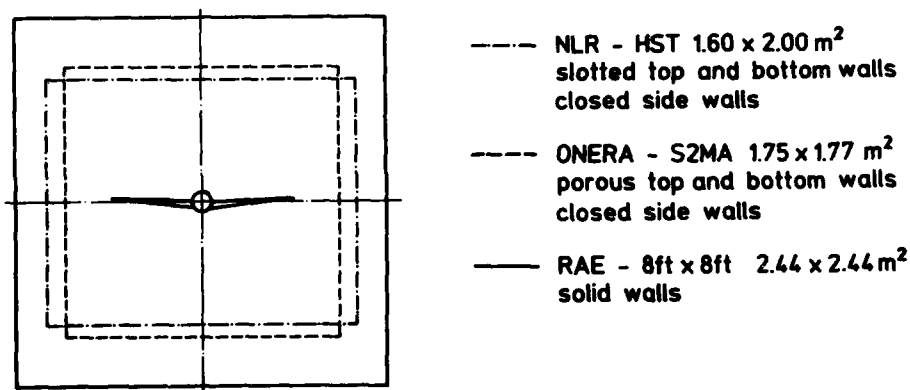


Fig. 4 Test section dimensions of the three wind tunnels

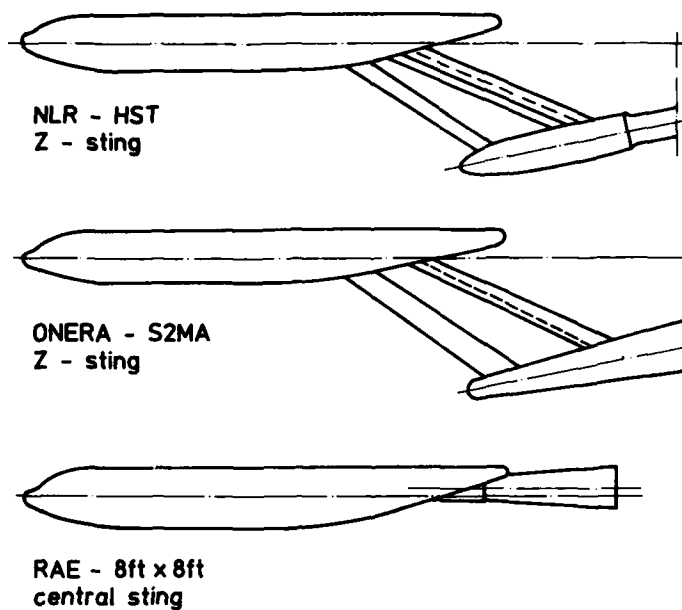


Fig. 5 Model support arrangements in the three wind tunnels

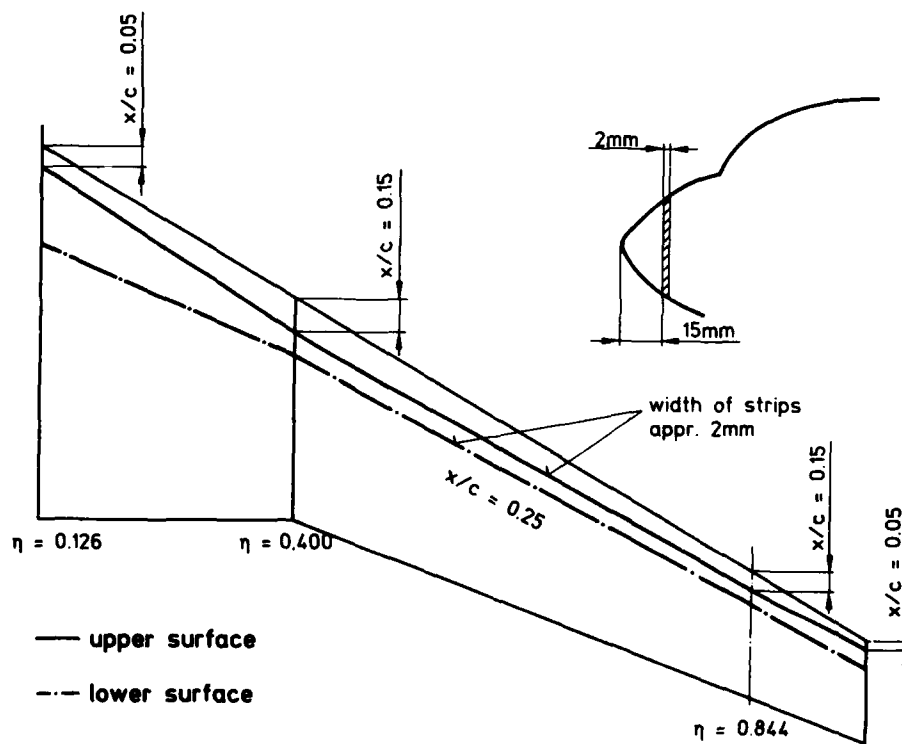


Fig. 6 Location of transition strips on wing and fuselage

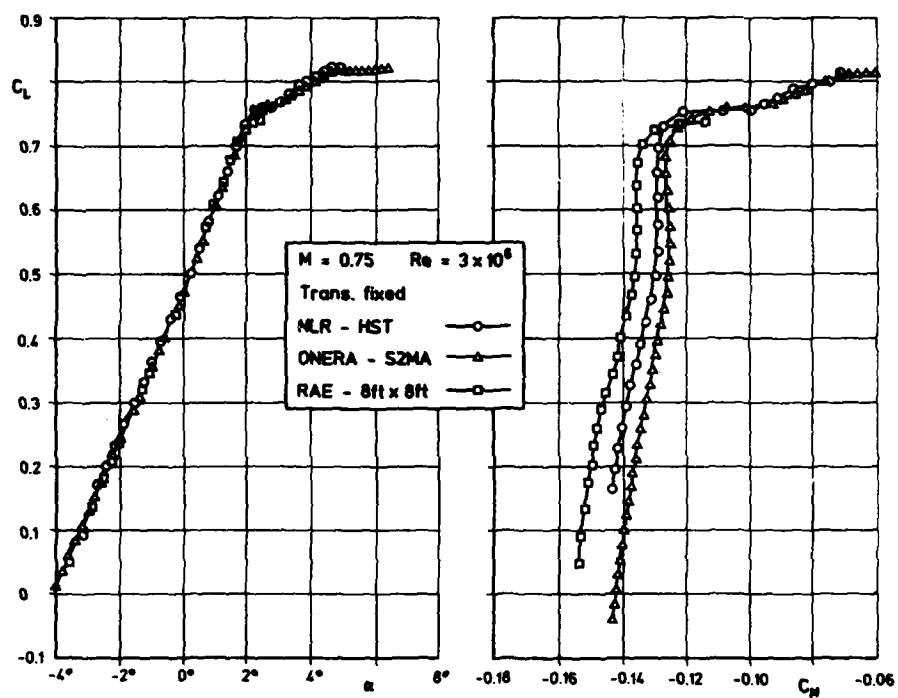


Fig. 7 Lift and pitching moment coefficients of complete model

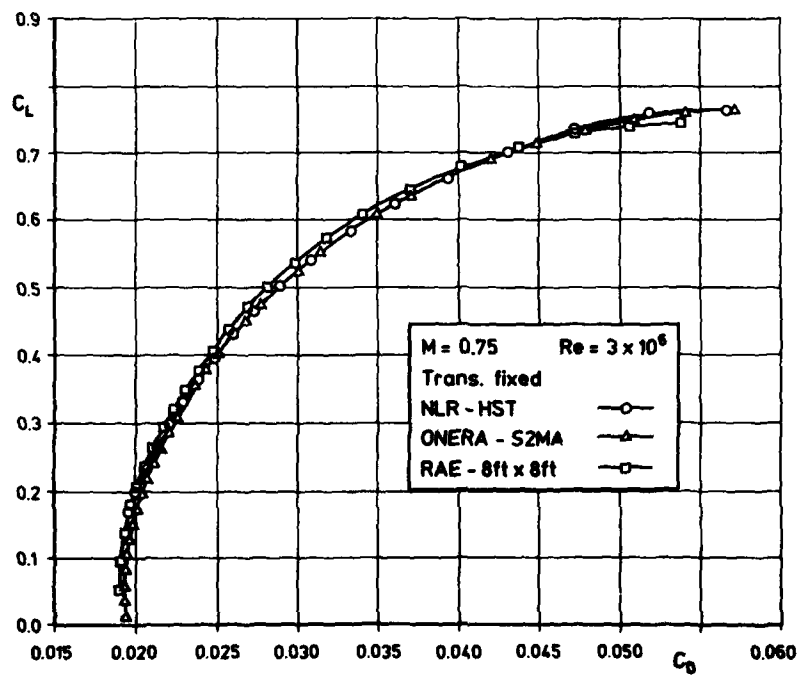


Fig. 8 Drag polars of complete model

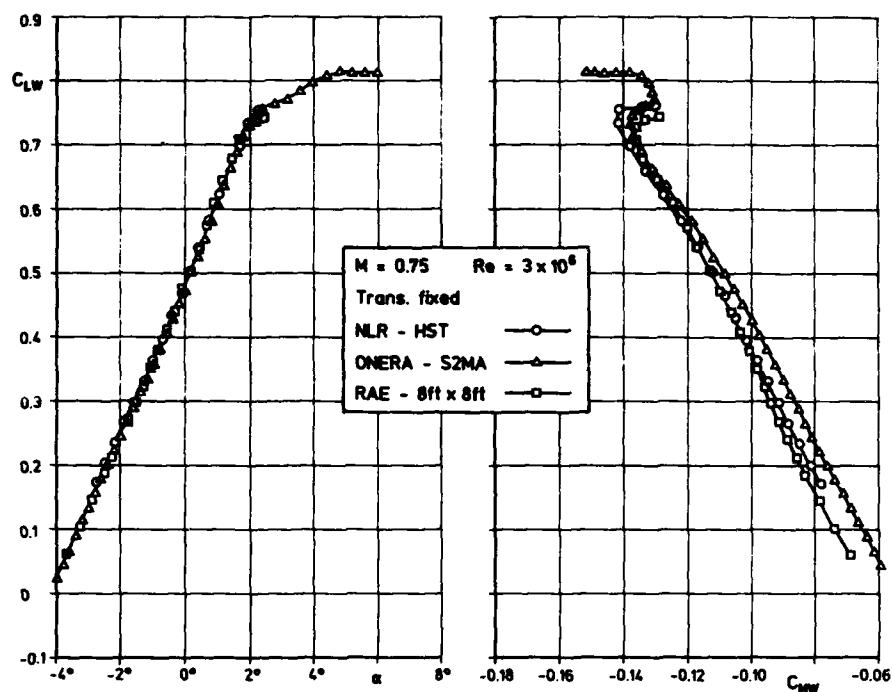


Fig. 9 Lift and pitching moment coefficients of wing alone

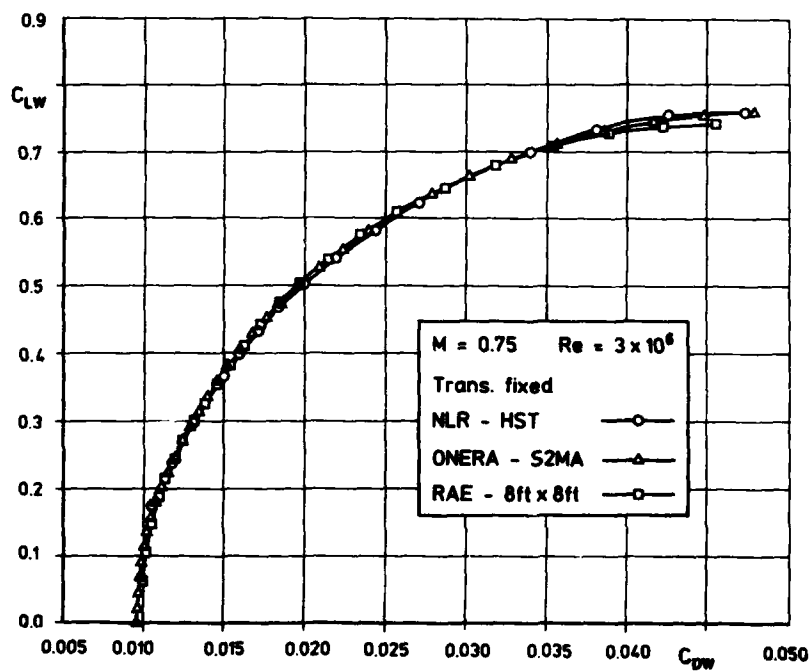


Fig. 10 Drag polars of wing alone

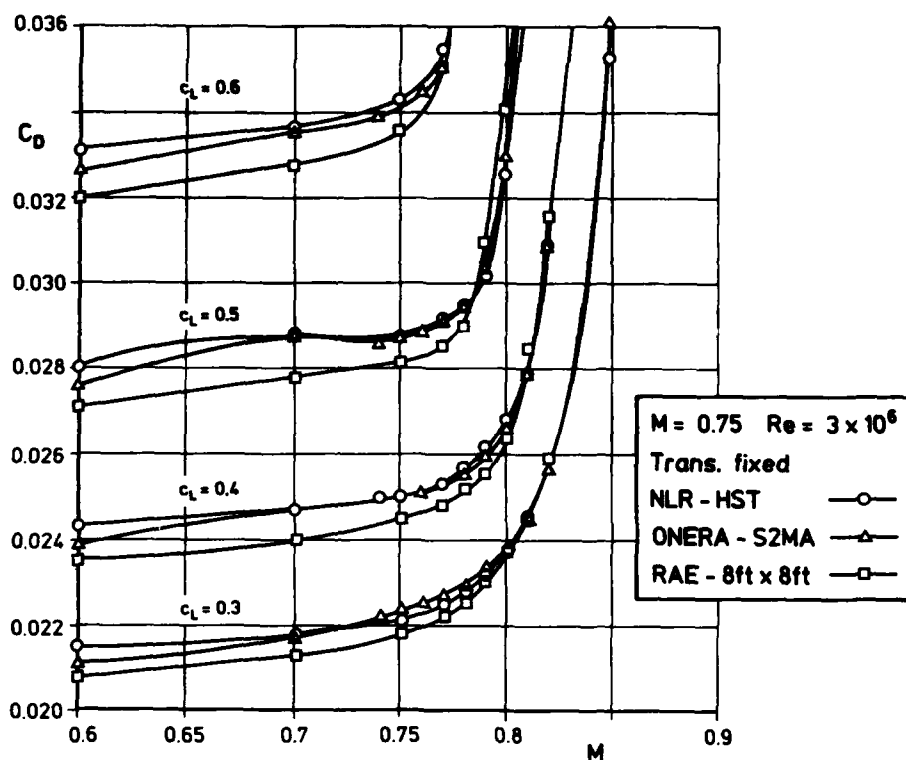


Fig. 11 Drag coefficients vers. Mach number at various constant lift coefficients

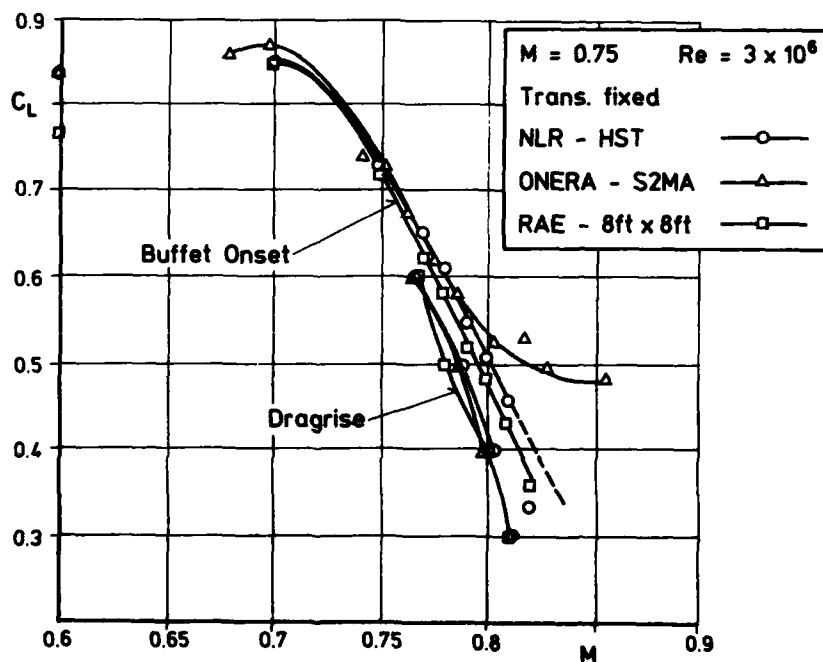


Fig. 12 Dragrise and buffet onset boundaries of complete model

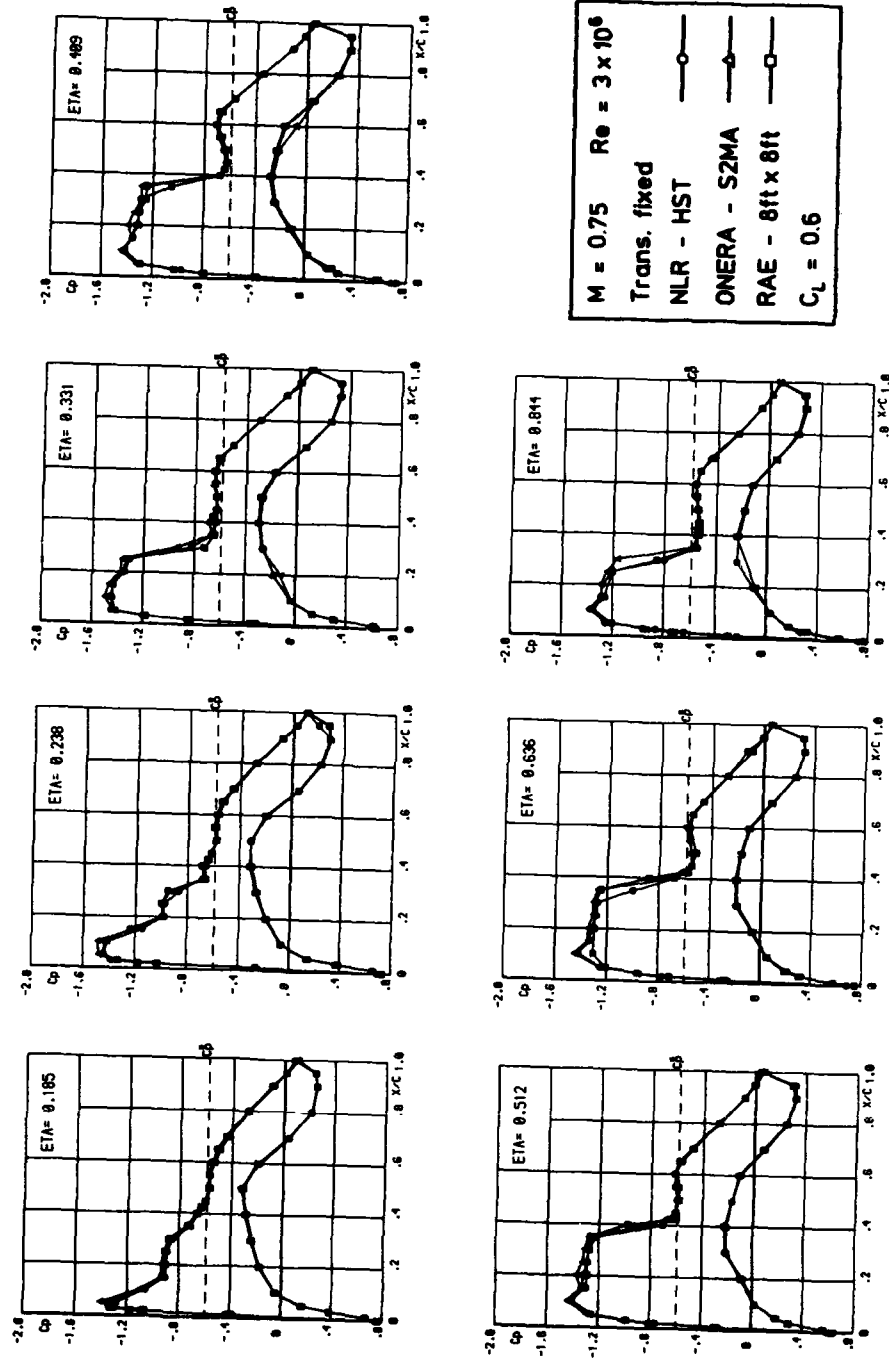


Fig. 13 Wing pressure distributions at seven spanwise stations

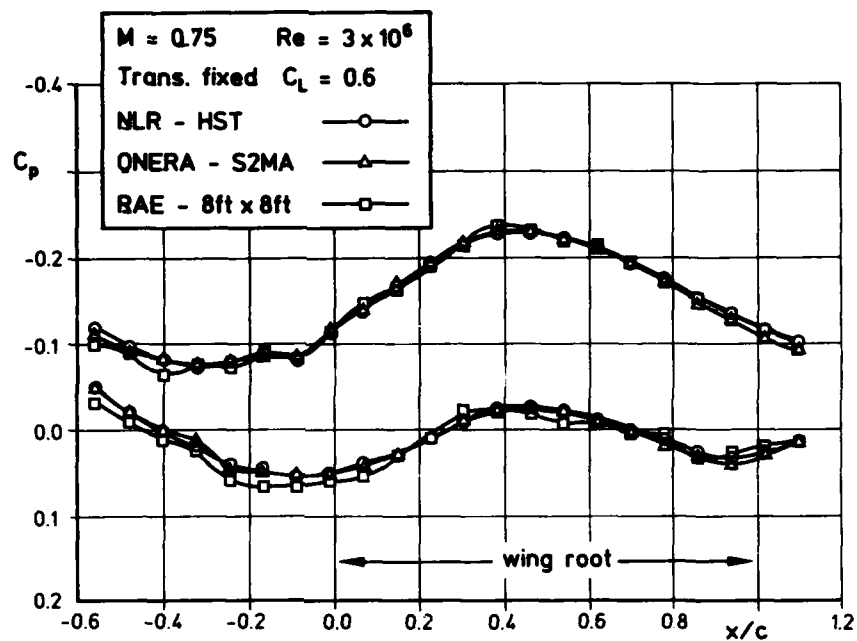


Fig. 14 Fuselage pressure distributions

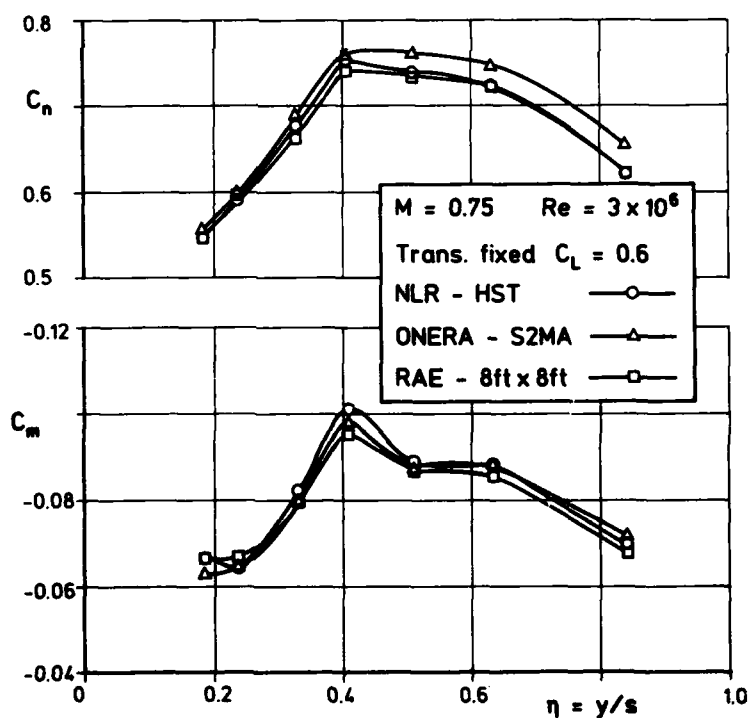


Fig. 15 Spanwise normal force and pitching moment coefficient distributions

COMPARISON OF THE RESULTS OF TESTS ON A300 AIRCRAFT IN THE RAE 5 METRE AND THE ONERA F1 WIND TUNNELS

by

C. QUEMARD

Office National d'Etudes et de Recherches Aéropatiales
BP 72 - 92322 Châtillon Cedex, France

P.B. EARNSHAW

Royal Aircraft Establishment, Aerodynamics Department
Farnborough Hants, Great-Britain

SUMMARY

Studies of the A300 Airbus aircraft have been carried out in the pressurised low-speed wind tunnels at RAE (5 metre) and ONERA F1. Initially comparison of the results obtained in the two facilities, with the same model mounted on an identical three-strut support, showed discrepancies which in the case of lift coefficient amounted to about 2.5%.

At the request of Airbus Industrie, and working within the framework of the Anglo-French Aeronautical Research Programme, AFARP, ONERA and RAE then began a systematic comparison of their measurement techniques together with the methods used in the reduction of the resulting data.

The production of uncorrected aerodynamic coefficients requires the measurement of loads by means, in this case, of underfloor balances and of the reference pressure. Checks were carried out on the balance calibrations confirming their accuracy after which an attempt was made in both establishments to assess and refine the accuracy of the reference pressure measurement. As a result of this exercise, corrections were applied to the measurements made in both wind tunnels which reduced but did not eliminate the differences between the two sets of results.

The data reduction relies on corrections to be applied for tunnel wall interference as well as that from the strut support system. Comparison of the calculation techniques used at the two tunnels showed some differences in the evaluation of certain terms resulting from wall constraint. Discussions have enabled agreement to be reached on defining a common basis for application of these corrections.

Support interference effects form the subject of a GARTEUR Action Group study and both wind tunnels have representatives who serve on this Action Group. As a result of this common interest, a large number of tests carried out at RAE together with calculations made by both organisations have now led to very similar corrections.

Taking account of all these modifications including the measurements of reference pressure as well as corrections for wall and support interference, the results on lift and drag on the A300 which have been provided by the two tunnels now show good agreement confirming the accuracy of the measurement techniques and the broad framework of the corrections.

1. INTRODUCTION

Check tests of the performance of aircraft from the Airbus series have been carried out in various major subsonic and transonic European wind tunnels. Among the low-speed tunnels, the RAE 5 metre and the ONERA F1 play an essential role since their pressurisation up to levels of three and four bars respectively allows a study of the effects of Reynolds number on the aerodynamic characteristics at constant Mach number and this permits a more reliable extrapolation to flight Reynolds numbers.

Both organisations have a common interest in demonstrating that their results are independent of the wind tunnel in which the tests were carried out. Evidently this interest is shared also by the aircraft manufacturers who might wish to plan test series in either tunnel.

It was within this context that a test was set up in 1981 by Aerospatiale in order to repeat in the F1 the same performance measurements of the A300B as had already been carried out at RAE. During their construction phases, the possible need to exchange models had already been foreseen. In particular, both tunnels have underfloor balances which are capable of mounting models by using what are essentially identical three-strut support systems. On its side, the 5 metre tunnel had constructed what might be regarded as a calibration model of the A300B aircraft early in the lifetime of the tunnel with a view to carry out an eventual programme of flight-tunnel comparisons. This model was made available to the F1 for their own test programme. This paper aims therefore to describe the methods of test at both ONERA and RAE, the results obtained, and the critical study of the test and data reduction techniques which has enabled good agreement to be achieved.

2. MODEL AND TEST

2.1. Wind tunnels

The ONERA F1 wind tunnel at Toulouse (Figure 1), and the RAE 5 metre wind tunnel at Farnborough (Figure 2), are the two major European pressurised low-speed facilities. They were designed to allow studies of Reynolds number effects on the aerodynamic characteristics of high-lift configurations used for landing and take-off.

The test section of the 5 metre is $5 \times 4.2 \text{ m}^2$ and that of the F1 is $4.5 \times 3.5 \text{ m}^2$. Maximum stagnation pressure is 4 bars in the F1 and 3 bars in the 5 metre. Consequently, the maximum Reynolds number calculated with a reference length of $0.1 \sqrt{\text{working section area}}$ is very similar in the two tunnels; it is achieved for Mach numbers between 0.2 and 0.3 corresponding to those for take-off and landing (Figure 3).

Civil aircraft models studied in the two tunnels typically have a span of around 3 metres, and a reference chord of around 0.4 m.

2.2. Support system

Several support systems are used in these low-speed tunnels in order to enable the desired model attitude to be achieved. Examples are shown in Figure 4.

Firstly, there is the classical sting support using a quadrant: several variants are available for the form of the sting including a cranked sting as shown in the photograph from the 5 metre and a blade sting shown in the F1. Then, there are strut supports, the simplest being the single strut shown here in the F1 where this is often used for studies of lateral characteristics, this support allowing simple application of both incidence and yaw.

Alternatively, as also shown in Figure 4, both tandem and three-strut mounting arrangements may be employed in which cases, in normal use, the struts are partially shielded from the airflow by guards attached to the test section floor in order to reduce the tare loads on the struts.

The three-strut mounting scheme which was in fact used for the comparative tests described here is shown in more detail in Figure 5 as used in the F1. Incidence variation is provided by varying the length of the rear strut and all three struts are carried on an underfloor balance which in the F1 is formed from a live plate supported from an earthed plate by six dynamometers (three vertical and three horizontal) each fitted with two strain gauge bridges.

The three support system is in fact a copy of that used at RAE although shortened both in the struts themselves and their wind shields to allow for the reduced height of the F1 working section.

In the case of the 5 metre, the underfloor balance is a six-component, self-balancing weighbeam type of balance which is considered to offer inherently higher accuracy and ability to resolve smaller increments of load in the presence of large tare loads than an internal strain gauge balance.

2.3. Model

The model used in the two test programmes is Model 121.2, a 1/13 scale model of the Airbus A300B. This model has a steel wing equipped with various high lift systems representative of those on the full-scale aircraft:

- at the leading edges, Krugers and slats
- at the trailing edges, flaps and all-speed ailerons.

The spoilers and air brakes were not used during the RAE / ONERA comparative tests, nor have there been any test with a horizontal tail.

The nacelles used were GE CF6.50 with short tailpipes, attached to the wing with M6 pylons.

Finally, the model could be equipped with a main undercarriage under the wings together with a forward tricycle undercarriage.

The various configurations of the slats and flaps studied in the two tunnels are as follows:

- landing 25/25 undercarriage both raised and lowered
- take-off 16/8 undercarriage raised
- take-off 16/0 undercarriage raised.

(the first number corresponds to slat angle and the second to the flap).

Since both facilities have the means to vary Reynolds number at constant Mach number, an ability which enables the results to be extrapolated to flight Reynolds numbers with better accuracy, lifting surfaces in most cases are tested without the use of transition fixing in order to avoid the problems of scaling the roughness element to suit the Reynolds number. This was so in this instance; there was therefore no question that differences between measurements in the tunnels could occur as a result of differences in application of a transition trip on the wing.

For each of the configurations tested, the sensitivity to Mach number and Reynolds number was indeed studied. The comparative tests between the F1 and the 5 metre were as follows:

F1	5 metre	Configuration	M	Re X 10 ⁴
155	10015, 13001	25/25 *UCD	0.20	6.6
40	13002	25/25	0.20	6.6
126	10028	16/0	0.30	6.6
116	10029, 13020	16/8	0.26	8.2
86	13014	16/8	0.24	6.6
88		16/8	0.24	7.6

where *UCD indicates a configuration including undercarriage and where the first two columns give the records allocated in the two facilities to the particular polars being compared.

Figure 6 shows the overall dimensions of the model and its position in the F1 and 5 metre test sections. Figure 7 shows a photograph of a typical configuration in the 5 metres.

2. DISCUSSION OF RESULTS

3.1. First comparisons

Figures 8 and 9 show the results obtained in both tunnels for two typical landing and take-off cases, other conditions being essentially the same.

The lift coefficient C_L obtained at RAE is systematically higher than that at F1 and the lift curve slope itself is also greater at RAE, the relative discrepancy being in the range 2.5 - 3.0 %.

The drag coefficient C_D at any particular C_L is lower at the RAE than at ONERA, the drag polars being more "open" at the RAE.

Finally, there is a slight difference in the position of the aerodynamic centre as deduced from the pitching moment curves.

These discrepancies were too large to ignore and required that an immediate inquiry was made into their origins. The Anglo-French cooperative group, AFARP1, was given the task of seeking the source of errors in either the measurements themselves or in their interpretation.

Now, an aerodynamic force coefficient is the ratio between the force measured on a balance and the product of the dynamic pressure $q_0 = 1/2 \rho V_0^2$ with the reference area S of the model:

$$C_F = \frac{F}{q_0 S}$$

The errors in the measurements themselves can therefore arise directly from the balance measurements and/or from the dynamic pressure. Less directly, interactions can arise through errors in the measurement of the model attitude relative to the approaching airflow whose direction of course defines the drag axis.

The coefficients are next corrected for the interference due to the presence of the walls on the one hand and of the supports on the other. These corrections are large and differences in the methods can contribute to discrepancies in the final results.

A systematic study was therefore mounted at both RAE and ONERA in order to:

- to detect possible errors in the measurement of both forces and reference pressure,
- to establish the differences in the methods of correction and if possible to converge on a common technique.

3.2. Review of measurements

Force measurement

An obvious cause of error in the measurement of forces would of course be to use a balance for which the calibration had changed slightly. Check calibrations were consequently carried out on both the F1 and 5 metre balances and established that the accuracy was better in both cases than 0.1%. This leads, at the maximum dynamic pressure for which comparative tests were carried out (13 kPa), to the following maximum errors on the coefficients in the F1:

$$\begin{aligned}\Delta C_L &= 0.01 \\ \Delta C_D &= 0.0010 \\ \Delta C_m &= 0.009.\end{aligned}$$

The repeatability of the measurements is better because it eliminates the systematic errors due to hysteresis which affect the accuracy. An example of the level of repeatability from the F1 in Figure 10.

In the 5 metre tunnel, the maximum errors in coefficient terms are rather less, reflecting the better match of the model to the balance and tunnel. Thus:

$$\begin{aligned}\Delta C_L &= 0.005 \\ \Delta C_D &= 0.0011 \\ \Delta C_m &= 0.0015.\end{aligned}$$

Checks on the calibrations of both of these balances have been carried out on both lift and drag axes using calibrated weights and pulleys. They showed no evidence of deviation outside of the expected limits on repeatability.

In conclusion, therefore, checks on the calibrations have shown no way in which the force measurements themselves could provide any systematic discrepancy.

Strut tares

Measurements made of both the lift and pitching moment must of course be corrected for the model weight. With this correction, the remaining forces are purely aerodynamic; these include the forces on the exposed parts of the support struts.

The strut tares are obtained in both tunnels by force measurements on the struts in isolation. Corrections to the coefficients, C_L , C_D and C_m , are then calculated and these subtracted from the total values.

Figure 11 shows the comparisons between the drag tares measured in the F1 and in the 5 metre. The agreement is excellent. Measurements in both wind tunnels suggest that it is advisable to correct C_L by 0.01; this correction was not taken into account at the F1. Consequently a correction $\Delta C_L = 0.01$ for F1 is included in the comparative tables of corrections arising from this comparison.

Reference pressure measurement

The reference pressure and speed are measured in the F1 by means of a pitot-static probe at the entrance to the test section.

The static pressure derived from this has been calibrated with respect to that existing on the tunnel centre line by means of an axial probe five metres in length. These measurements showed the existence of a slight streamwise pressure gradient; the static pressure from the reference pitot-static probe is then corrected for the discrepancy from the true static pressure at the quarter chord point.

This correction had been applied at the time of the A300B tests. However, it has been supposed at the time that the total pressure was uniform across the test section. In the course of this comparative study, checks were carried out which demonstrated that the total head distribution is somewhat "dished" across the test section. While the source of this variation is unconfirmed, a similar non-uniformity in the 5 metre tunnel is known to result from the losses induced by the screens in the non-uniform flow approaching the contraction. Neglect of this head loss leads to an overestimate of the dynamic pressure and thus to an underestimate of the coefficients by around 0.5%. Thus:

$$\frac{\Delta C_L}{C_L} = 0.005$$

which has to be added to the results in the F1.

After checking the static and total pressures, there remained the need to check that the measured references were not subject to interferences from the model flow field; that is to say that the reference pitot-static was effectively at infinity upstream. This check has been carried out in the F1 by comparing the usual reference pressures with those measured at 2.4 metres further upstream on the contraction wall, these latter being themselves calibrated with respect to the pressure on the test section centre line using the long axial probe.

The results were almost identical implying that the entry plane to the test section is indeed effectively at infinity upstream.

In the 5 metre tunnel, a standard elliptic nosed static probe, such as had been used satisfactorily for many years in low-speed wind tunnels at RAE, had been used to carry out the tunnel calibration. However, in the course of the comparative study, it transpired that at the higher Reynolds numbers per metres for which the tunnel had to be calibrated, boundary layer transition occurred over the sensing holes. The turbulent boundary layer gave rise to about 0.75% increase in pressure sensed and this led to an effective decrease in measured dynamic pressure. This effect is shown in Figure 12, where the function ϕ plotted is the ratio between the pressure drop in the contraction to that measured by the probe with suitable corrections applied to allow for compressibility. During earlier tests this step change had been translated into a smoothed gradual change over the tunnel operating range. At the typical test point considered later in section 4, the error relative to the new accurate calibration is 0.8% giving:

$$\frac{\Delta C_L}{C_L} = -0.008$$

Mean flow upwash

In both tunnels, the flow angularity had been measured by inverting calibration models. In the F1, tunnel geometry had not been changed, it was possible therefore to confirm that the zero value of the mean upwash was accurate.

Unfortunately, in the 5 metre tunnel where the mean upwash had been measured as -0.09° , the non-uniformity of upwash had been considered unsatisfactory and a high quality honeycomb had been installed before the comparative test programme had begun, reducing the mean upwash to zero. Although there seems no reason to question the earlier value, it is now no longer possible to confirm it. It should be pointed out however that in order to provide an accuracy on lift of 0.1% at $C_L = 2$, the upwash should be accurate to 0.02° while to provide an accuracy of 5 drag counts would demand an accuracy on upwash of 0.015° .

3.3 Review of corrections

Wall corrections

The results of the wind tunnel measurements have to be corrected for the interference generated by the test section walls and by the model support system.

Wall constraint corrections in subsonic flow comprise corrections to the approach velocity or blockage corrections and corrections to the upwash or incidence corrections. Figure 13 gives an example of the different corrections applied successively to a polar for the A300B in the F1.

Blockage corrections themselves comprise solid blockage, wake blockage and separation blockage. Expressions with varying degrees of sophistication lead to the following values for the solid blockage:

$$\frac{dV_0}{V_0} = 0.0045 \quad \text{at the 5 metre}$$

$$\frac{dV_0}{V_0} = 0.0056 \quad \text{at the F1}$$

These two values should roughly be inversely related to the relative cross-sections of the tunnels to the power 3/2. The residual error of around 0.1% is evidently not a major contribution to the discrepancies between the tests.

Incompressible calculations modelling the far field of the wake by means of a source lead to the equation:

$$\frac{dV_0}{V_0} = \frac{S}{4C} C_D$$

where S is the model reference area and C is the test section area. This equation was used in the two tunnels but, at the RAE, C_D was taken to represent the minimum profile drag whereas, at ONERA, the total drag was used. After some discussion, it was agreed that it would be more appropriate to choose the part of the drag corresponding to the difference between the total drag and the vortex drag, for conditions where there were no extensive areas of separation. Thus:

$$\frac{dV_0}{V_0} = \frac{S}{4C} \left(C_{Dc} - \frac{kC_L^2}{\pi A} \right)$$

where the subscript c indicates corrected results, A the aspect ratio and k is a calculated value for the induced drag factor.

The third term in the blockage correction takes account of the effective increase in model volume generated by the presence of regions of recirculating flow. Basically the same correction is used in the two tunnels and is based on that derived by Maskell. Given that this is by and large applied only in the immediate neighbourhood of the stall, there is even less likelihood of substantial differences arising from this source.

In addition to the blockage velocities, the presence of the walls also modifies the local upwash velocities, and consequently the effective incidence of the model.

Evidently the upwash velocity generated by the presence of the walls varies over the whole wing. It is convenient to interpret the effect of this interference field as an increment in incidence for the same lift coefficient. To achieve this, classical theory indicates that the upwash must be calculated at the 3/4 chord point of any streamwise section. The mean effect of the wing as a whole must then be suitably weighted for the value of the local chord at any spanwise position.

The early results from RAE were in fact corrected on the basis of the upwash calculated at the 1/4 chord line.

The values of the correction in the two cases are:

$$\begin{aligned} \Delta\alpha &= 0.502 C_L \quad \text{at } 1/4 \text{ chord} \\ \Delta\alpha &= 0.586 C_L \quad \text{at } 3/4 \text{ chord.} \end{aligned}$$

giving:

$$\Delta C_L = \left(\frac{dC_L}{d\alpha} \right) \Delta\alpha \approx 0.1 (0.586 - 0.502) C_L$$

and

$$\frac{\Delta C_L}{C_L} = 0.0084$$

which must be subtracted from the RAE results.

Finally, the application of this correction to incidence results in a rotation of the axes of the measured force. Thus:

$$\begin{aligned} C_L &= C'_L \cos \Delta\alpha - C'_D \sin \Delta\alpha \\ C_D &= C'_L \sin \Delta\alpha + C'_D \cos \Delta\alpha \end{aligned}$$

When applied at the F1, the term $C'_D \sin \Delta\alpha$ used to correct C_L was neglected. In fact this term is not negligible and should be subtracted from the F1 results. Thus, typically:

$$\Delta C_L = 0.009 \text{ at } C_L = 2$$

Strut corrections

In the absence of any information on the interference which the support system induces on the flow around the model, RAE began an experimental study of the support interference, while ONERA and Aérospatiale undertook a theoretical study of the flow about the support system.

Since the A300B model had been designed to permit support by both a three-strut rig and a tail-mounted sting support using an internal six-component strain-gauge balance, RAE assessed the effects of strut interference by mounting the model on an internal balance in the presence of the fairings from the strut support system, the strut tares themselves being measured in the absence of the model.

No attempt was made in the course of these tests to assess the near-field interference (largely of the wake of the strut tops with the flap flow) by including the strut heads on the model since, at the time when it was carrying out its experimental assessment of strut interference, RAE like ONERA was concurrently attempting to calculate the interference field of the support system; this was thought to be feasible only in the far field. In the presence only of the strut guards, however, interference simply of the far field was involved which enabled the results to be analysed using only the lift interference to establish the upwash and streamwash.

The effects of the strut interference as deduced from the experimental programme were interpreted as arising from modifications both to the mean streamwise velocity and to the mean incidence seen by the wing. Figure 18 shows the extent to which this simplified interpretation agrees with the experimental data as well as with the Aérospatiale calculations.

The main results from the Aérospatiale calculations using a panel method are presented in Figures 14 and 15.

The horizontal component of interference velocity is expressed in the form of a pressure coefficient C_p which, in compressible flow, is equivalent to the variation of dynamic pressure dq_0/q_0 . Figure 14 shows the variation of pressure along the length of the fuselage; in the first analysis of the A300B tests at the F1, a mean value of the dynamic pressure was chosen to correspond to that calculated for the mean 1/4 chord position, namely $dq_0/q_0 = 0.010$.

In a similar manner, the upwash velocity induced by the support system varies markedly both along the length of the model as shown in Figure 14 and along the span as shown in Figure 15 where the upwash is plotted as an increment in incidence. As for the blockage velocities, these results were analysed to provide a mean incidence calculated at 1/4 chord giving a value $\Delta\alpha = 0.22^\circ$.

These two corrections lead, at fixed incidence, to correction to C_L given by:

$$\Delta C_L = \frac{dC_L}{d\alpha} \Delta\alpha + C_L \frac{dq_0}{q_0}$$

Figure 16 shows the differences in corrections to C_L between the RAE experimental results and the theoretical results calculated specifically for the three-strut rig in the 5 metre test section. In addition to the curves, RAE's own calculated fit to the data is also given. At the time of these tests, this was equivalent to the single values for blockage and upwash velocities independent of lift. These values for ΔC_L used by RAE in its programme of data reduction are lower than those used at the F1 by about 0.01.

On the basis of this comparison then, it seems fair to conclude that the support corrections used in the two facilities were broadly similar at least so far as the lift is concerned and did not contribute substantially to the discrepancies found. However this is not true of drag which is rather more sensitive to the accuracy of the upwash angle than is the lift. In this case, as has been noted above, at the F1, the upwash was calculated at the 1/4 chord line rather than the 3/4 chord line resulting in an error of 0.09° leading in turn to a significant correction to the drag of:

$$\Delta C_D = C_L \sin 0.09^\circ = 31 \times 10^{-4} \text{ at } C_L = 2$$

This modification in upwash correction from 0.22° to 0.13° then gives substantially better agreement on the drag as shown in Figure 18. For consistency, a corresponding additional small correction has to be made also to lift:

$$\Delta C_L = 0.009.$$

Now a comparison of results from different facilities however relies on the application of a common standard of support corrections, not necessarily an accurate one. Consequently, the same form of correction using a single value for $\Delta\alpha$ and for dq_0/q_0 has been adopted in each tunnel.

$\Delta\alpha$	dq_0/q_0	WT
0.156	0.014	5 metre
0.130	0.010	F1

These values give rise to an improved collapse of the experimental results over those used initially. They result from a rather better choice of mean values and follow in part from a detailed study of support interference carried out by an Action Group Working within the framework of GARTeur. Despite the agreement however, it remains possible that significant common errors exist in the measurements since the near-field interference from the strut top has not been treated in this comparison.

4. TABLE OF CORRECTIONS - NEW COMPARISONS

A detailed study of the various sources of difference between the results of the tests on the A300B in the F1 and 5 metres wind tunnels leads, for lift, to the following balance sheet, in which points from polar 88 in the F1 and from 10064 for the 5 metre are considered. In each case, a C_L near to 2 has been chosen.

Source of correction	F1	5 metre
- corrections to balance loads	0	0
- corrections to support tares	- 0.01	0
- corrections to dynamic pressures	+ 0.01	- 0.016
- correction to wake blockage	+ 0.015	- 0.002
- correction to incidence 1	- 0.005	- 0.017
2	+ 0.009	0
	+ 0.019	- 0.035

In each column, a series of ΔC_L is listed which are either to be subtracted (-sign) or to be added (+ sign) to the C_L calculated when the first comparisons were made (Figure 8). From this table, the discrepancy is reduced by 0.054, or 2.7% local C_L from its original value of around 0.06 - 0.07.

Some differences between the curves for C_L shown in Figure 17.a) and b) remain but these are clearly less than 1% with the exception of the post-stall region.

The discrepancies in $[C_L - C_L^0] / IIA$ shown as a function of incidence in Figure 18 now appear to be around 5×10^{-4} except for the region approaching the stall and are typical of the normal level of accuracy of the measurements.

5. CONCLUSION

Some considerable effort has been spent at both ONERA and RAE to ensure that the quality of the measurements carried out in the F1 and 5 metre tunnels should be very high. The existence of differences between the two sets of what should have been identical, fully corrected data led therefore to an immediate effort to identify, and then remedy, the sources of these differences.

As a result of the present comparative programme, a series of modifications to the procedures both in using reference pressures and in applying corrections for wall and support interferences have been introduced. Following the modifications, the corrected lift and drag measurements on the A300B which have been produced in the two tunnels now show very good agreement, confirming the accuracy of the measurement technique and the broad framework of the corrections. Evidently, there remains the possibility of errors which are common to both series of measurements, among which may be some arising from interference between the top of the struts with the wing flow, since in this case both tunnels have used essentially the same correction technique.

It is relatively rare that the opportunity to carry out a direct comparison using the same model on the same support is possible in two different tunnels. In this case, it was possible due to the close contact between the two design teams throughout the construction phases of the two tunnels. However, even with this advantage of direct comparability of measurement, the effort involved in undertaking the detailed re-examination must not be underestimated. The check calibrations of the balances, and more importantly of the tunnels, the design of new probes, and step-by-step comparisons of the calculations and application of wall and support interference corrections have been time consuming but, as the results show, very rewarding.

With the benefit of hindsight, it might be felt that the changes which have now been shown to be necessary are obvious but in several of the cases involved here, they are applied to procedures or techniques which have been carried over from other wind tunnels where they have worked adequately, or at least have not been criticised in the past, and have consequently not demanded re-examination. In view of the present experience, it seems probable that such inadequacies may exist elsewhere but are likely to come to light only as a result of very exhaustive re-examination.



Fig. 1 — Aerial view of F1 wind tunnel.



Fig. 2 — Aerial view of 5 metre wind tunnel.

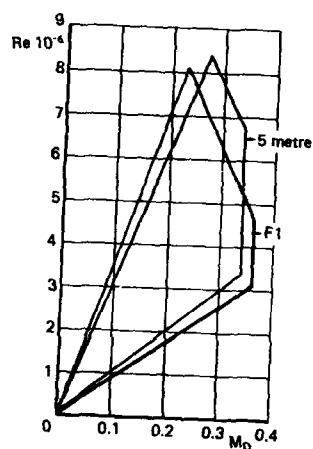


Fig. 3 — Performance envelope of 5 metre and F1
(Re based on $0.1 \sqrt{AREA}$ at $T = 15^\circ C$).

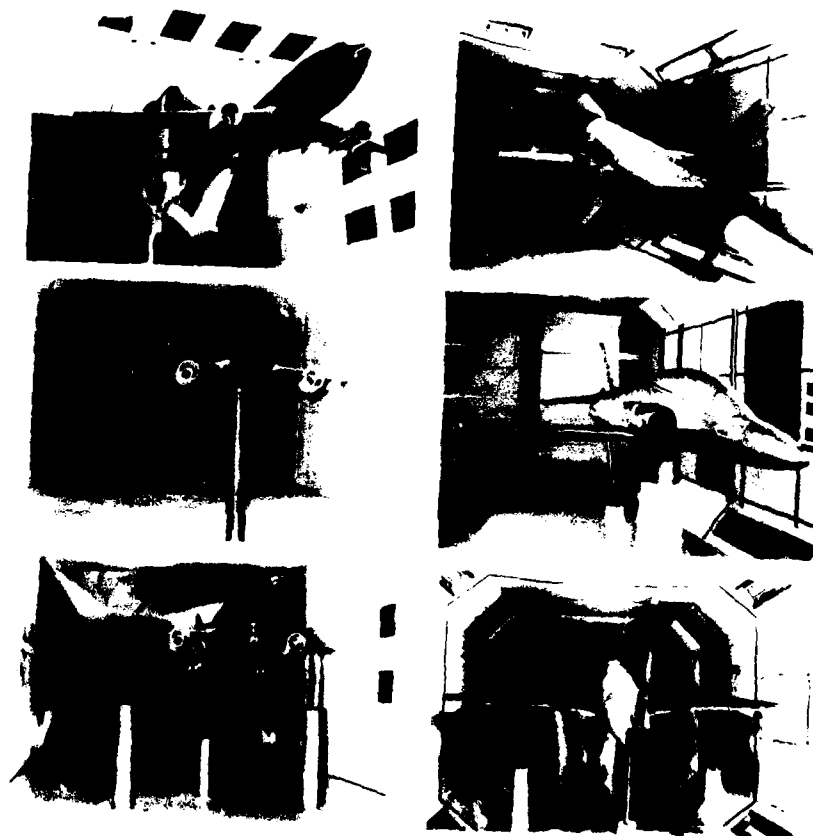


Fig. 4 — Some support options available in F1
and 5 metre wind tunnels.

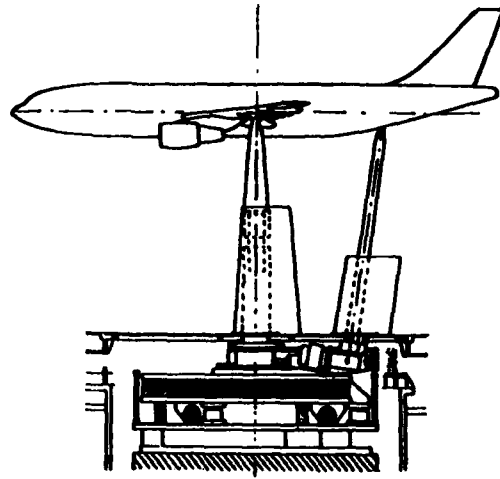


Fig. 5 - Model mounted on three-strut support system in F1.

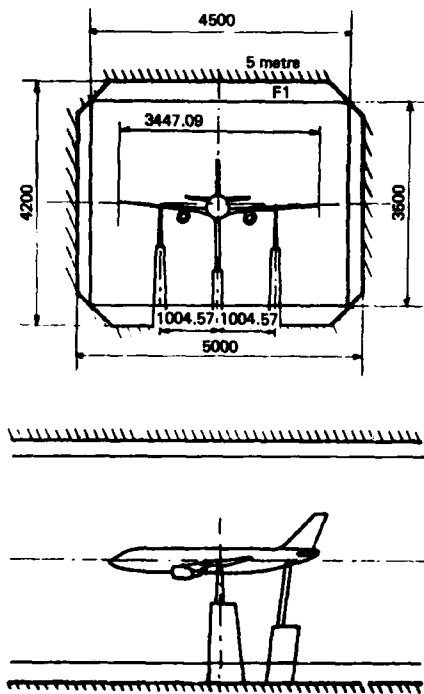


Fig. 6 - Position of model in F1 and 5 metre test section.

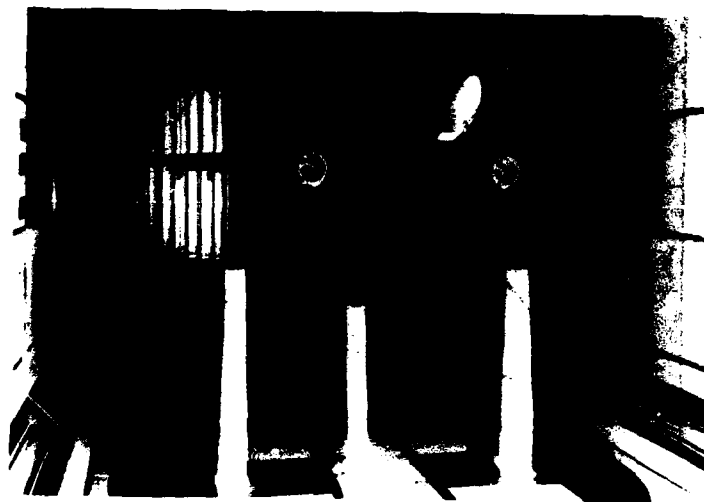


Fig. 7 - A300B model in 5 metre test section.

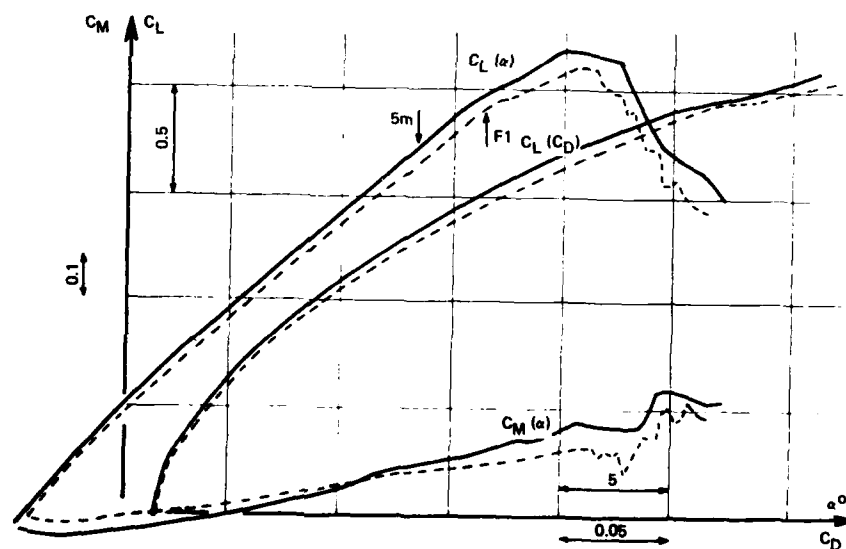


Fig. 8 - First comparative measurements on model in landing configuration.

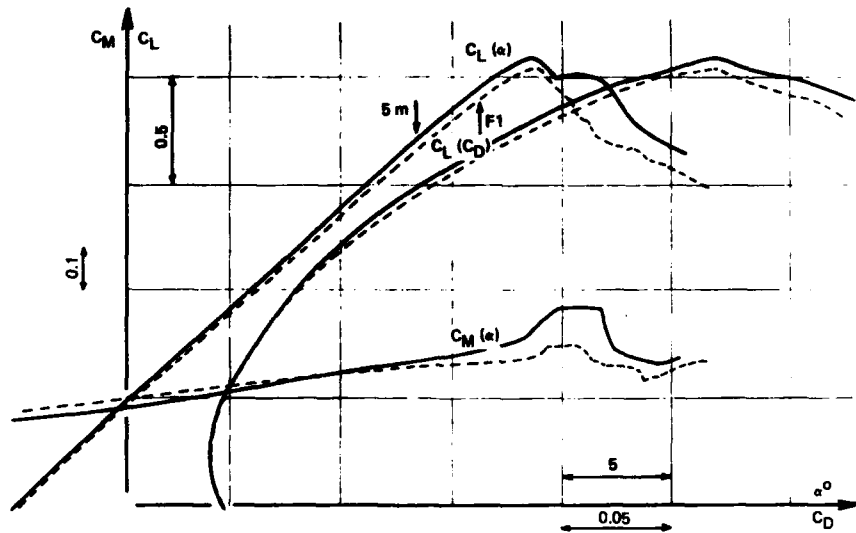


Fig. 9 - First comparative measurements on model in take-off configuration.

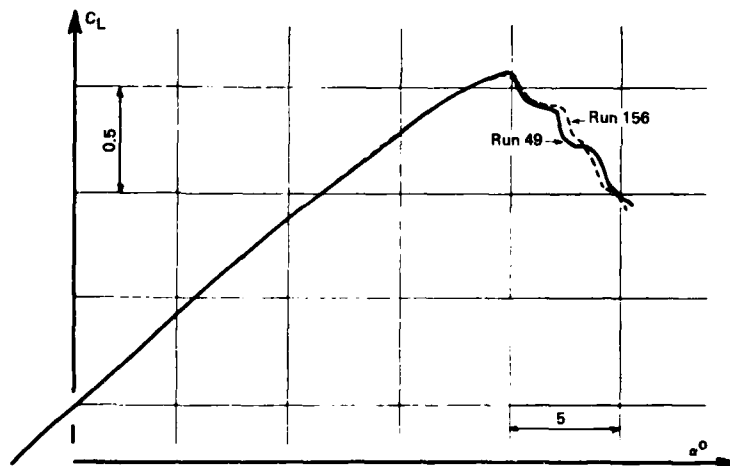


Fig. 10 - Repeatability of measurements in F_1 (landing configuration).

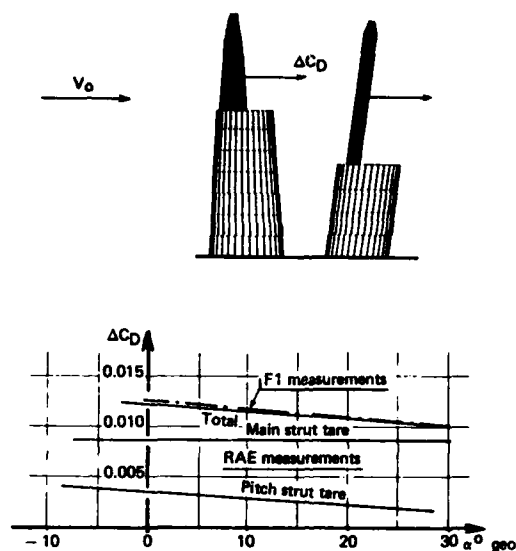


Fig. 11 - Drag tares for A300B strut system.

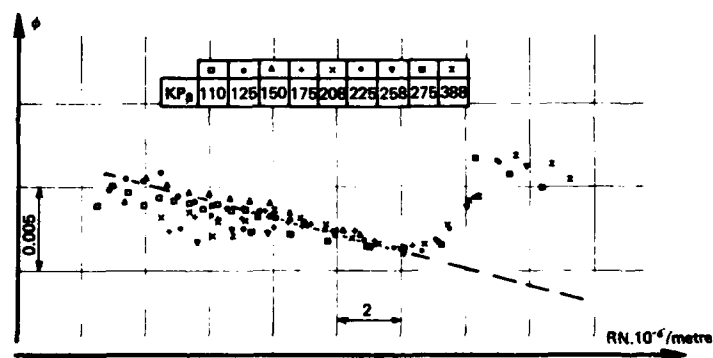


Fig. 12 - 5 metre wind tunnel calibration for augus. 1985.

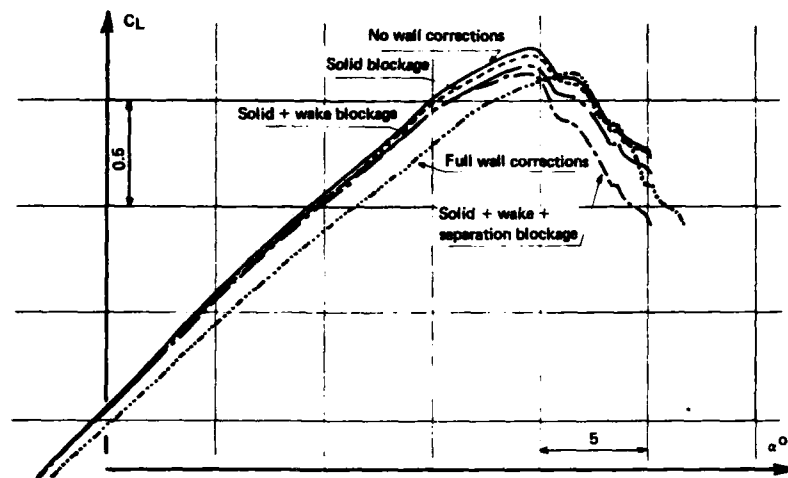


Fig. 13 - Successive applications of well corrections.

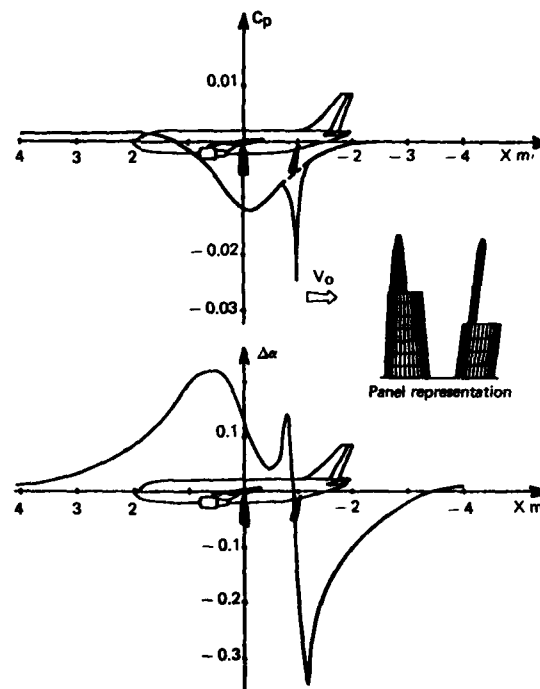


Fig. 14 - Variation of calculated pressure and upwash along model axis.

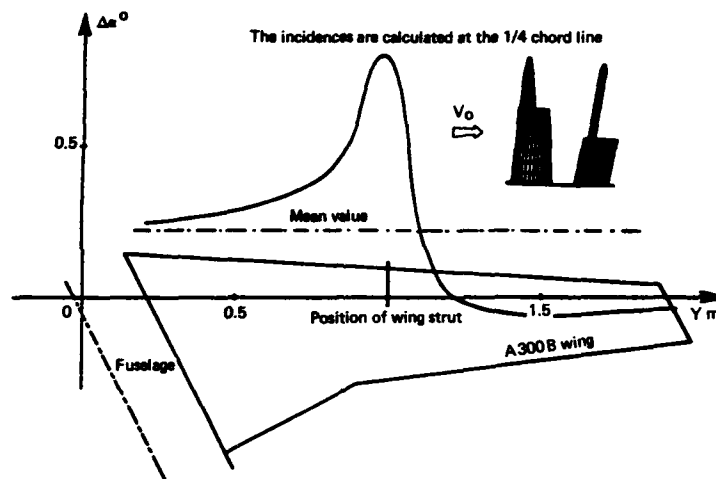


Fig. 15 — Local spanwise incidences on heavy duty struts.

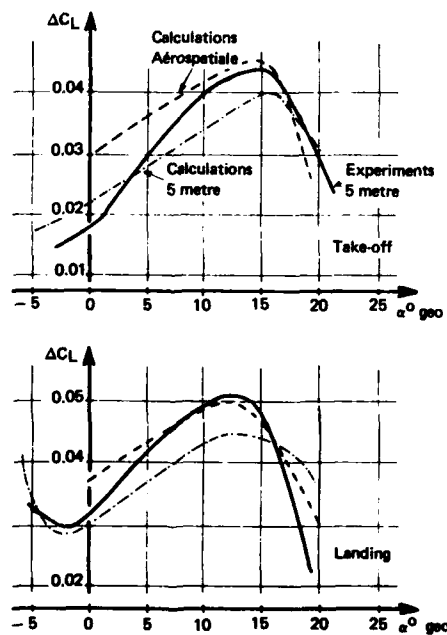


Fig. 16 — Lift correction due to strut interference.

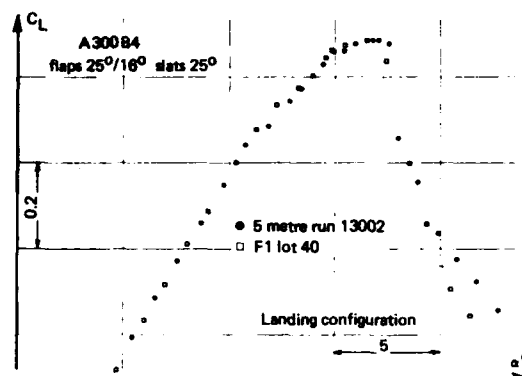


Fig. 17a — Comparison of finally corrected lift data.

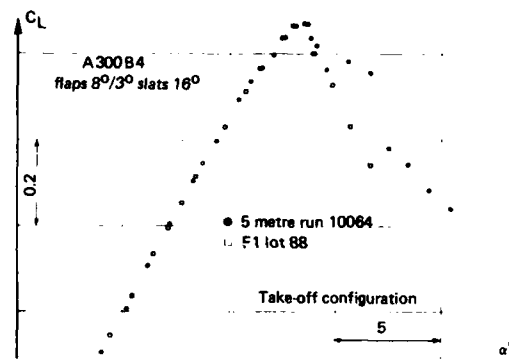


Fig. 17b — Comparison of finally corrected lift data.

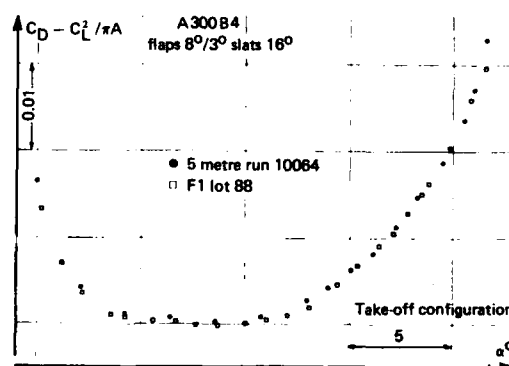


Fig. 18 — Comparison of finally corrected drag data.

ANALYTICAL AND EXPERIMENTAL METHODS USED TO
RESOLVE THE AERODYNAMIC RESULTS OF TESTS CONDUCTED
IN THREE TEST FACILITIES

Ross D. Clark
Manager Advanced Aircraft Aerodynamics
and

H. J. Rosenstein
Senior Manager Aerodynamics

BOEING VERTOL COMPANY
Philadelphia, Pennsylvania 19142
U.S.A.

1.0 ABSTRACT

This paper describes the work performed to fully understand and validate the V-22 Aerodynamic drag and stability data base developed through extensive wind tunnel testing. Early drag and stability aerodynamic testing showed differences in characteristics when comparing results from different test facilities. A joint Bell-Boeing/Navy plan involving a thorough understanding/refinement of test techniques, facility calibrations and application of computational methods resolved these issues and permitted validation of the data base.

2.0 NOTATION

c	Wing Chord ~ Ft
e	Oswald's Efficiency Factor
q	Dynamic Pressure ~ P.S.F.
C_{AF}	Axial Force Coefficient ~ $C_{AF} = A.F./q S$
C_D	Drag Coefficient ~ $C_D = D/q S$
C_L	Lift Coefficient ~ $C_L = L/q S$
$C_{L\alpha}$	Model Lift Curve Slope ~ 1/deg
C_{NF}	Normal Force Coefficient ~ $N.F./q S$
C_M	Pitching Moment referred to 25% Chord ~ $C_M = M/q S C$
C_p	Pressure Coefficient
N.P.	Aircraft Neutral Point ~ % Chord
S	Wing Reference Area ~ Ft ²

SUBSCRIPTS

Max	Maximum Lift
Min	Minimum Drag
O_L	Zero Lift
O	Pitching Moment at Zero Lift
REF	Coefficients referred to Baseline Values of Test No. 3

3.0 INTRODUCTION

The V-22 "Osprey" is a multiservice, multimission tilt rotor aircraft suitable for a wide variety of missions and uses advanced but mature technology in achieving this capability. It is designed to takeoff and land like a helicopter and fly like a turbo-prop airplane - reaching high speeds and high altitudes and possessing long range capabilities. Significant increases in performance are obtained with a short rolling takeoff using partially tilted nacelles. These unique flight characteristics are possible because the pilot can control the direction of the thrust vector by tilting the nacelles. The large wing tip mounted rotors can be tilted through more than 90 degrees, hence the name tilt rotor. An artists impression of the V-22 is shown in Figure 1. The aircraft is currently in full scale development with first flight scheduled for mid 1988. This program will reshape the rotary wing industry as we know it today.

In December 1981, the Defense Department identified the tilt rotor as a possible candidate to meet the Marine Corps' new aircraft needs and initiated the V-22 program (originally

called JVX). In June of 1982, a Joint Technology Assessment Group determined that the tilt rotor had potential to meet the needs of all four military branches and a memorandum of understanding was completed among the services by December. The missions identified included Marine medium assault transport, Navy/Air Force combat rescue, Army cargo and medical evacuation and Air Force special operations; all of which benefit from the tilt rotor's speed and range capability. The U. S. Navy is the executive service for this development. To respond to these requirements, a team consisting of Bell Helicopter Textron and Boeing Vertol was formed in April of 1982.

4.0 DEVELOPMENT SCHEDULE

In April of 1983, the V-22 development program was initiated by a preliminary design contract to the Bell-Boeing team. Figure 2 shows the overall program schedule. The basic program will produce 913 aircraft for the four services with additional applications already under consideration.

Boeing and Bell share the responsibility for the development of the V-22. Boeing is responsible for developing the empennage, overwing fairings, fuselage, flight controls and avionics integration. Bell is responsible for the wing, nacelles, transmissions, rotor and hub assemblies and integration of government furnished engines. Allison Division of General Motors is developing and supplying the engines. Grumman Aircraft will build the empennage and Lockheed, the wing trailing edge flaps. In addition, there is substantial other sub-contractor involvement in the program.

5.0 CONFIGURATION DESCRIPTION

Figure 3 shows the V-22's salient design features. Two 38 foot diameter gimbale rotor and transmission systems are mounted on each wing tip, powered by 6150 shaft horsepower Allison T406-AD-400 engines. The aircraft operates as a helicopter when taking off and landing vertically. Once airborne, the nacelles are rotated 90 degrees forward which converts the aircraft into a turboprop airplane. The rotors are synchronized by means of an interconnect shaft that runs through the wing between the nacelle mounted transmissions. This shaft also provides power transmission from one rotor system to the other in the event of engine failure. Auxiliary drives from a center wing gearbox provide power for hydraulics, oil cooler and electrical generators. An APU drives through the center gearbox for engine starting. The aircraft folds compactly for stowage aboard ship and uses an advanced digital fly-by-wire control system. It is constructed of composite materials and has crashworthy seating for 24 combat troops. The Osprey is capable of all weather instrument flight, day or night, and continuous operation in moderate icing conditions.

6.0 AERODYNAMIC DEVELOPMENT

An extensive wind tunnel test program was initiated to support the aerodynamic development of the V-22 configuration, establish the aerodynamic data base for flight test of the full scale development aircraft and reduce overall program risk. The program included drag models to be tested in both low speed and transonic tunnels, dynamic models, a large scale nacelle model, a spin model, a powered model for rotor/airframe interactions and a 2/3 scale rotor for hover rotor performance. Figure 4 shows the models used in the development. Over 8000 test hours were completed between June of 1983 through June of 1986 in both industry and government facilities. The major portion of the aerodynamic development of the V-22 was accomplished using a 0.15 scale force and moment model. This model was used to support configuration trade studies for the general lines of the fuselage, the empennage configuration, sponson shape, wing-body fairing and trailing edge flap geometry. It consists of an internal steel frame to which fiberglass body shells were mounted along with a removable wing, empennage, nacelles, and sponsons. Wing flaperons were remotely controllable to maximize testing efficiency. The model used an internal six component balance to measure forces and moments. It was tested three times in the Boeing Vertol 20 Ft x 20 Ft low speed tunnel (BVWT), once in the Boeing 8 Ft x 12 Ft transonic tunnel (BTWT) and once in the Arnold Engineering Development Center, 16T transonic wind tunnel (AEDC).

Initial configuration development tests were carried out in the Boeing Vertol low speed, 20 Ft x 20 Ft wind tunnel (Test No. 1), in September of 1983 to establish the basic configuration data base. This configuration is shown in Figure 5. The model used the Boeing "A" balance, and was mounted on a 3.0 inch diameter pre-bent sting which entered through the lower aft body. Provisions were made for an upper blade sting which entered the model through the top of the fuselage forward of the tail. These support stings were used to establish support system tare and interference corrections. Flow-through nacelles were designed to establish engine inlet spillage drag, with the flow controlled by plugs placed in the exhaust. Internal flow was measured by exhaust pressure rakes and used to establish the internal drag of the nacelle.

In February of 1984, the 0.15 model was tested (Test No. 2) in the Boeing 8 Ft x 12 Ft transonic tunnel to establish incremental high speed aerodynamic characteristics. The installation is shown in Figure 6, and in the photograph, Figure 7. The same configuration and balance used in Test No. 1 were used. The mounting system was modified to a lower blade type sting. No alternate support systems were used to establish support system tare and interference corrections.

In November of 1984, the model was updated, Figure 8, to represent the then current configuration for Test No. 3. This required the manufacture of new skins for the fuselage and sponsons, new empennage and new flow-through nacelles. The nacelles were precision cast aluminum and contained static and total pressure probes, mounted internally, just forward of the exhaust. Screens with various density mesh were inserted just aft of the inlet throat, to control the inlet conditions. The same sting support system as was used in earlier testing in the Boeing Vertol wind tunnel was used to mount the model.

The nacelle instrumentation was calibrated at the Boeing Flight Simulation Chamber on a balance mounted at the front of a pressure chamber which was evacuated to create flow through the nacelle. The measured forces were correlated with internal pressure and temperature instrumentation to establish the internal drag corrections during wind tunnel tests of the complete model.

The model tested in the Arnold Engineering Development Center (AEDC) 16T tunnel (Test No. 4) in February 1985, was the same model tested at Boeing Vertol during Test No. 3. The only modifications were the use of a larger capacity internal balance, Boeing "B", and swept, tapered support stings designed to adapt to the AEDC tunnel sector and to locate the model pitch and yaw reference centers at the centerline of the 16 Ft test section for both pitch and yaw runs. Both a lower swept support sting and a swept upper blade sting were used. The lower swept sting was the primary support, with the upper blade being used to establish support system tare and interference effects for the primary support system (Figure 9). Testing was conducted from Mach No. 0.2 to 0.75.

In March of 1986, the last test (Test No. 5) of the 0.15 scale model was made in the Boeing Vertol 20 Ft x 20 Ft low speed wind tunnel. Virtually the same model was tested as was used at AEDC for Test No. 4. Modifications were made to reflect minor changes in the fuselage and sponson lines. The wing, flap system and empennage were unchanged. The flow-through aluminum nacelles were new for this test reflecting a change to the exhaust exit area, and were recalibrated for internal drag at the Boeing Flight Simulation Chamber, prior to the test. The model is shown in Figure 10. For this test, a new support system sting adapter was made so that the swept support stings used at AEDC could be used, along with a straight sting more commonly used at Boeing Vertol.

The same large capacity, internal balance (Boeing "B") that was used at AEDC was used in this test. Extensive tare and interference effects for all three support systems, (upper swept blade, straight and lower swept stings) were determined on a model component by component basis, in a standard model build-up fashion. The support system configurations are shown in Figure 11.

7.0 PROBLEM STATEMENT AND PLAN FOR RESOLUTION

Throughout the aerodynamic testing, a policy was established where reference runs were made during the initial part of each test period to tie-in the current test configuration with the previously established data base. These were done to verify the data reduction program and tunnel corrections/calibrations.

When these tie-in runs were compared for Test No. 3 at BVWT and Test No. 4 at AEDC (Figures 12 and 13) at the same Mach and Reynold's numbers it was seen that the AEDC test results were greater in drag than the BVWT data base. $C_{d_{MIN}}$ was greater by 35 counts, C_L for $C_{d_{MIN}}$ was reduced as was overall span efficiency. Stability from the AEDC results as seen in Figure 13, was also increased. As a result of this comparison, all the results from the previous tests with the 0.15 scale model were reviewed and are summarized in Table 1. $C_{d_{MIN}}$ established in Test No. 1 was 83 counts less than Test No. 3, 123 counts less than the Test No. 2 that was not corrected for support system tare and interference (T&I's) and 118 counts less than the fully corrected value obtained during Test No. 4 at the AEDC tunnel. The 83 count difference between Test No. 1 and Test No. 3 was attributed to changed fuselage lines, wing/body fairing, enlarged sponsons and enlarged vertical tails. The difference between Test No. 4 and Test No. 3 data was not explainable by configuration differences since the same model was used for both tests. It should be noted that aerodynamic increments due to compressibility were similar at BTWT (Test No. 2) and AEDC (Test No. 4).

The differences in the results at BVWT (Test Nos. 1 & 3) were attributable to refinement

Table 1. Comparison of Initial Aerodynamic Characteristics at Model Scale

PARAMETER	TEST NO. 1 (BVWT)	TEST NO. 2 (BTWT)	TEST NO. 3 (BVWT)	TEST NO. 4 (AEDC)
LIFT $C_L/C_{L_{REF}}$.924	1.031	1.0	1.02
α_L	-2.0°	-2.25°	-1.50°	-1.20
$C_{L_{MAX}}/C_{L_{MAX_{REF}}}$.975	LIMITED BY G RANGE	1.0	1.0
DRAG $C_{D_{MIN}}/C_{D_{REF}}$.867	1.046	1.00	1.066
δ	.786	.827	.810	.8426
LONGITUDINAL STABILITY C_{M_0}	.145	.170	.190	.230
NP	55.5	54.5	51.7	55.67
T&I SUPPORT SYSTEM	Y'S	NO	YES	YES
BALANCE	A	A	A	B
FLOW-THROUGH NACELLE	WOOD PLUG AND PAKE	WOOD PLUG AND PAKE	METAL SCREEN FSC CALIB.	METAL SCREEN FSC CALIB.

PRELIMINARY
DESIGN
CONFIGURATION

EARLY
FSD
CONFIGURATION

FINAL
FSD
CONFIGURATION

of the general configuration. Data from BWWT (Test No. 2) was used for increments since no support system T&I data corrections were applied and the model was flown above the tunnel centerline to achieve increased angle of attack range.

The 35 count difference in the drag level between BVWT (Test No. 3) and AEDC (Test No. 4) were less easily explained. Since the same model was used in both tunnels, configuration differences were eliminated as the source of the drag increase. Extensive pretest balance calibrations on the Boeing "B" balance were carried out at AEDC, prior to the test with both a bare balance and with the model installed on the balance in the tunnel. The remaining sources for the discrepancy could be either with the application of the support system tares, the Boeing "A" balance used in all previous tests or with the tunnels themselves, either in the q measurement system or with a tunnel test section pressure gradient.

The rotation of the drag polar (Figure 12) could be effected by the flow-through nacelle correction, tunnel upflow, or the accuracy of the Boeing "A" balance. The stability change (Figure 13) could have been the result of inaccurate support system tares for the lower swept AEDC sting.

Early in 1985, the Bell/Boeing team, representatives of the test facilities and the Navy, met to review the results of the testing and test techniques and to plan an approach to resolve the differences in the data base. The plan for resolution involved calibration of the Boeing Vertol and AEDC tunnels, use of computational fluid dynamic (CFD) methods to correlate the tunnel calibration at Boeing Vertol, evaluation of wall effects at AEDC and a review of the test approach/technique for the next test scheduled for early 1986 (Test No. 5). For this test the Boeing "B", large capacity balance, the same as was used at AEDC, would be installed in the model. Since the nacelle was to be updated to the latest lines and exhaust area, it would be recalibrated in the Boeing flight simulation chamber. The Boeing Vertol straight support sting along with the AEDC lower swept sting and swept upper blade sting would be used to develop an extensive support system T&I data base to allow configuration component evaluation on all three support systems.

8.0 RESOLUTION

8.1 WIND TUNNEL CALIBRATIONS

The Boeing Vertol Low Speed Wind Tunnel is designed for V/STOL testing, and has a test section 20 Ft x 20 Ft x 45 Ft long. It has the capability for running in an open throat configuration, a solid wall or slotted wall configurations. Air is exchanged in the tunnel by variable outlet and inlet doors, fore and aft of the test section. For drag testing, the normal configuration is with the test section walls 12% slotted. Calibrations were made with a 17 ft. static pressure probe located on the tunnel centerline, with the tunnel in various configurations. Results are shown in Figure 14, where static pressure coefficients are plotted vs. tunnel axial station for the normal operating tunnel configuration, including the support system. For a well designed tunnel, the cross-sectional area should expand to account for test section boundary layer growth and support system solid blockage, so that the pressure gradient is near zero or calibrated with sufficient accuracy so that static pressure corrections can be applied to the test results. The tunnel configurations including test section, probe and support system were modeled using the VSAERO potential flow CFD program, (Ref 1 and 2) and the measured results were confirmed, (Ref. 3), and are shown in Figure 15. By using this analytical technique, it was possible to establish the incremental effects on the tunnel centerline pressure gradient of support system components such as: pitch-yaw adapters, tapered assembly collars, pitch-yaw encoders and auxiliary actuators mounted on the support system.

Using the static pressure gradients, both measured and calculated, an incremental drag correction was calculated for the primary model components. These increments are given in Table 2, for the three support systems used in Test No. 5. The incremental drag correction, ΔC_D , varies for the three support systems since each sting locates the model at a different longitudinal station in the tunnel and imposes a different pressure gradient over the length of the model. The AEDC 16T tunnel was calibrated for static pressure gradient and showed that the tunnel was adequately compensated for boundary layer growth and support system solid blockage. AEDC used Euler CFD codes to compute anticipated tunnel/model interference effects and correlated this with measured tunnel wall pressure distributions. This work is reported in Ref. 4.

Table 2. ΔC_D Due to Tunnel Static Pressure Gradient

PARAMETER	BVWT STRAIGHT STING	LOWER SWEEP AEDC STING	AEDC UPPER BLADE MOUNT
BASIC FUSELAGE	.00196	.00394	.00336
SPONSONS	.00050	.00092	.00080
VERTICAL TAILS	.00013	.00018	.00017
HORIZONTAL TAIL	.00016	.00021	.00020
WING AND WING CROWN FAIRING	.00055	.00111	.00094
NACELLES	.00022	.00037	.00032
ΔC_D STATIC PRESSURE GRADIENT (MEASURED)	.00352	.00673	.00579
ΔC_D STATIC PRESSURE GRADIENT - VSAERO (COMPUTED)	.00370	.0065	.0055

NOTES: SLOTTED TEST SECTION
RE-ENTRY DOORS CLOSED
ALL ANGLES OF ATTACK

8.2 MOUNTING SYSTEM/TARE AND INTERFERENCE

A major component of the plan to resolve the data differences was the establishment of the support system tare and interference corrections to be applied to the data. The approach was to establish T&I's for both support systems used in Test No. 4 at AEDC, along with the straight support used in the Boeing Vertol tunnel. These three systems are shown in Figure 11. Interference effects were established for all three systems in Test No. 5, on a component by component basis, as the model was built up from the body alone to the complete aircraft configuration.

Results of this investigation are given in Figure 16, for normal force, axial force and pitching moment for the complete aircraft. These results are compared to the results for the lower swept sting, as measured in Test No. 4 at AEDC. The correction for the AEDC lower swept sting exhibits the same variations and slope as a function of angle of attack in all parameters in both AEDC and Vertol tunnels. Only normal force exhibits a difference in sign, positive at AEDC and negative in BVWT. T&I corrections for lateral directional data were obtained in both tunnels and no major differences were evident when they were compared.

8.3 TEST TECHNIQUE

This section discusses those test techniques which could influence the drag polar rotation and stability differences shown in Figures 12 and 13.

The angularity of the tunnel flow in the test section influences the angle for zero lift and rotates the drag polar. During Test No. 5, the upflow was determined by comparison of pitch runs made with the complete model upright and inverted. The resulting drag polars are shown in Figure 17. Using these data, it was determined that the model induced an upflow of -18° over the referred C_L range of 0 to .6.

As described in section 7, the flow-through nacelles were modified between AEDC Test No. 4 and BVWT Test No. 5. Both nacelles were instrumented and calibrated for static and dynamic pressure and temperature at the exhaust plane of the nacelle. This instrumentation was used to correlate corrections for the nacelle internal forces to be applied to the tunnel data.

The corrections to lift and pitching moment are quite small; however, the correction to drag is significant and is shown in Figure 18. The drag correction at $\alpha = 0^\circ$ is 20 to 25 counts, increasing to 100 counts at $\alpha = 20^\circ$ for the revised lines and 135 counts for the original nacelle lines used during Test No. 4 at AEDC. The primary reason for the change in value in the Boeing Vertol Wind Tunnel is the reduced exit area of the revised nacelle. The variation in the drag with angle of attack results from the change in the nozzle exit conditions, due to increased tip vortex strength as lift on the wing increases with angle of attack. This parameter varied greatly as wing trailing edge flaps were deflected and appropriate corrections were made to the data as determined by the correlation of the instrumentation results and the flight simulation chamber calibration data base.

9.0 FINAL RESULTS

In March of 1986, Test No. 5 of the V-22 full scale development configuration was undertaken in the Boeing Vertol Tunnel. This test utilized the 0.15 scale model, and all of the test techniques and corrections described in section 8.0. Table 3 compares the results of Test No. 5 with Test No. 4. All the aerodynamic characteristics are quite similar, including the minimum drag which was the major discrepancy in the previous aerodynamic data base. The minimum drag is built up in Figure 22 at model scale for the three support systems used at AEDC and Boeing Vertol and compared to the results from AEDC. Tested results for each aircraft component are adjusted to account for shadow areas. Results from Test No. 5 for the lower straight sting and lower swept sting, are within three counts of the minimum drag obtained at AEDC during Test No. 4, and compare very well on a component by component basis. The drag breakdowns obtained in Test No. 5, with the model mounted on the upper blade support, compare well for all components with the exception of the empennage, which is 18 counts less than that for the other three support systems. This is a result of the blade affecting the flow over the aft fuselage and between the twin vertical tails and is not adequately accounted for in the support system tare and interference correction.

Table 3. Comparison of Final Aerodynamic Characteristics at Model Scale

PARAMETER	TEST NO. 4 (AEDC)	TEST NO. 5 (BVWT)
LIFT $C_L / C_{L_{REF}}$	1.02	1.01
α_{0L}	-1.20°	-1.30°
$C_{L_{MAX}} / C_{L_{MAX_{REF}}}$	1.0	1.05
DRAG $C_{D_{MIN}} / C_{D_{REF}}$	1.056	1.061
ϕ	.8428	.8849
LONGITUDINAL C_{M_0}	.230	.195
STABILITY NP	65.67	63.46
T&I SUPPORT SYSTEM	YES	YES
BALANCE	B	B
FLOW-THROUGH NACELLE	METAL SCREEN FSC CALIB.	METAL SCREEN FSC CALIB.

FINAL FSD CONFIGURATION

FINAL FSD CONFIGURATION

Figures 19 through 21 compare pitching moment, lift and drag from Test No. 5 and Test No. 4. For the complete aircraft, C_m vs. angle of attack, is in very close agreement. Stability as compared in Figure 19, shows the same level for all three support systems in Test No. 5, but slightly less than that obtained in AEDC (Test No. 4) on the lower swept sting. C_{m0} is slightly offset for each support system. The drag polars, compared in Figure 21, show the same minimum drag level, as shown in Figure 22 but the AEDC data shows slightly more induced drag above a referred C_L of 0.2.

10.0 CONCLUSIONS

Wind tunnel testing during a large development program will invariably be conducted in more than one test facility with more than one model, with the inevitable differences in the data obtained. In the past, data differences were often attributed to "tunnel" differences or "configuration" differences without any real explanation. This often led to an incomplete understanding of the data base which resulted in uncertainties as to the appropriate absolute levels or to erroneous increments. As the result of the extensive wind tunnel test program, the following conclusions are drawn:

- Pretest planning and careful design and calibration of the model, support systems, balances, and instrumentation combined with considerations of the installation in the selected wind tunnel will result in a consistent data base.
- Modern computational methods are an invaluable aid in understanding and reducing tunnel differences with the same model by permitting the assessment of the different mounting systems which may be used in various wind tunnels.
- It is desirable to perform T&I's on a component by component basis, as part of each test to track absolute differences and avoid later surprises.

11.0 REFERENCES

1. Maskew, B., "VSAERO User's Manual", NASA CR166-476, November 1982.
2. Maskew, B., "VSAERO Theory Document", Published as NASA CR 4023, November 1986.
3. Carlin, G. J., Jr., and Bevan, D., "Prediction of Subsonic Wind Tunnel Mounting System Interference Via a Lower Order Panel Method", AIAA Paper 86-1816-CP July 1986.
4. Donegan, T. L. and Lee, W. H. "Computation of Wall Interference Effects on the .15 Scale JVK Tilt Rotor Model", AEDC-TMR-85-P7, April 1985.

ACKNOWLEDGMENT

The authors would like to acknowledge the contribution to this paper of the Bell Boeing Technical Staff who planned and conducted the tests and analysis reported in this paper. In addition, special thanks to Ms. Jean Ferro and Mr. Ken Bartie for their efforts in preparing this paper for publication.



Figure 1. Artist's Impression of MV-22 Osprey

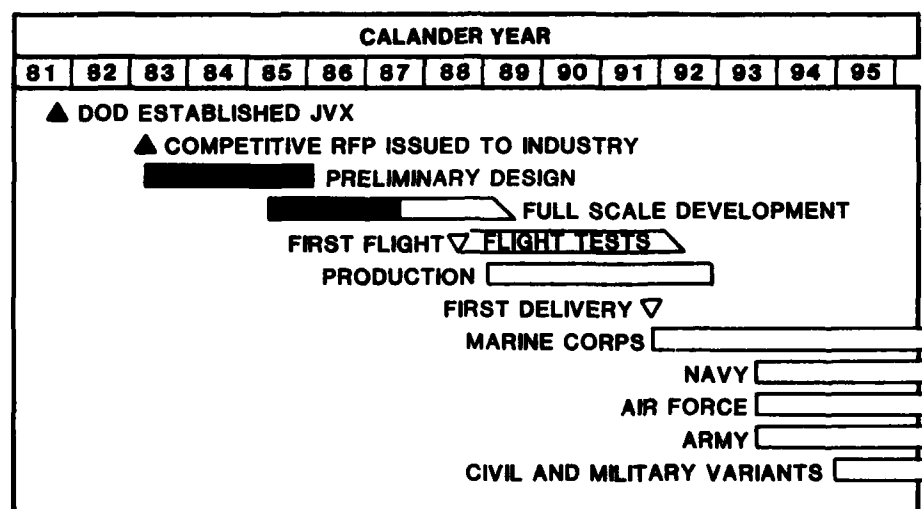


Figure 2. Overall Program Schedule

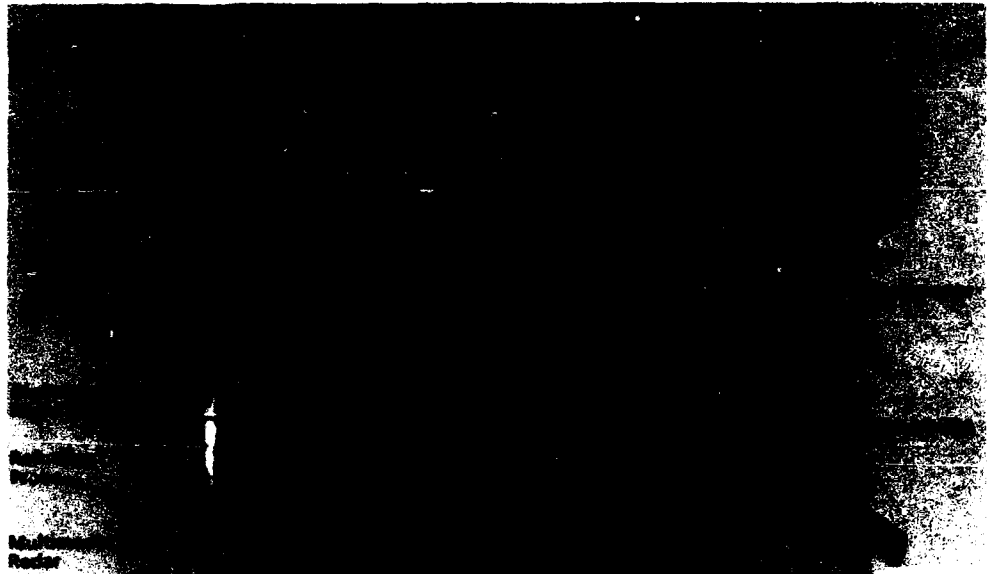


Figure 3. V-22 Characteristics

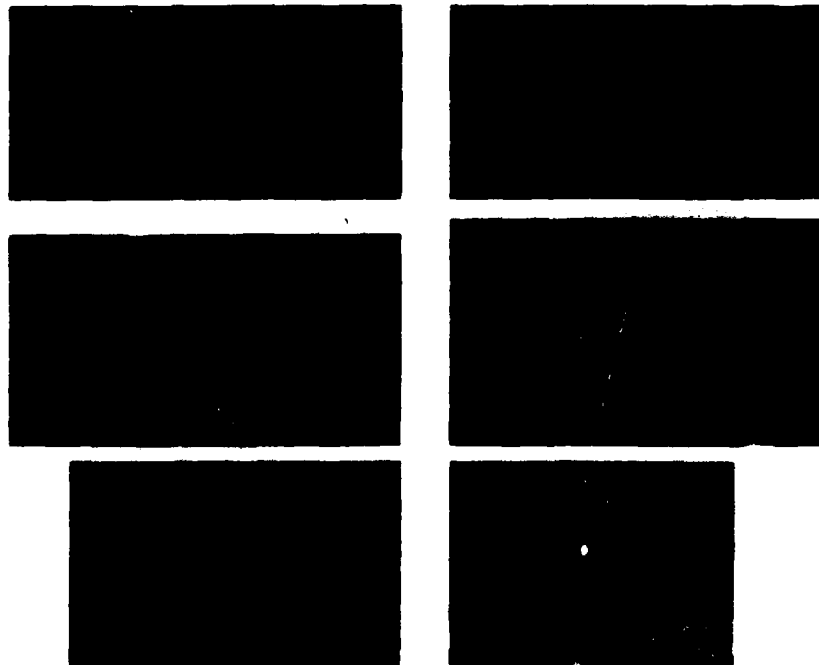


Figure 4. V-22 Modelling Activity



Figure 5. Initial 0.15 Scale Model Configuration In Boeing V/STOL Wind Tunnel (Test No. 1)

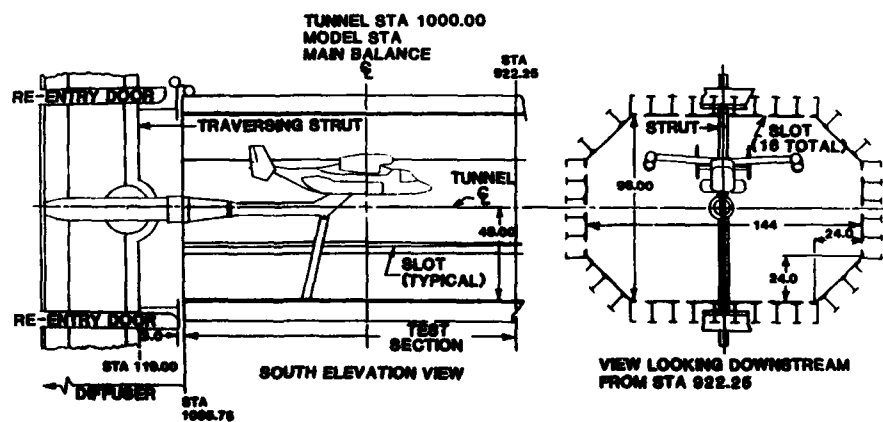


Figure 6. 0.15 Scale Model Installation in Boeing Transonic Wind Tunnel (Test No. 2)



Figure 7. 0.15 Scale Model Configuration in Boeing Transonic Wind Tunnel (Test No. 2)

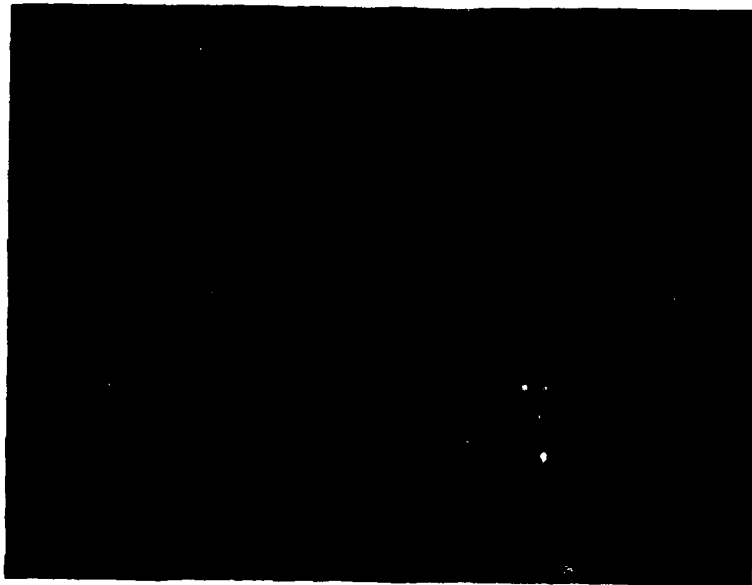


Figure 8. 0.15 Scale Model Configuration in Boeing V/STOL Wind Tunnel (Test No. 3)

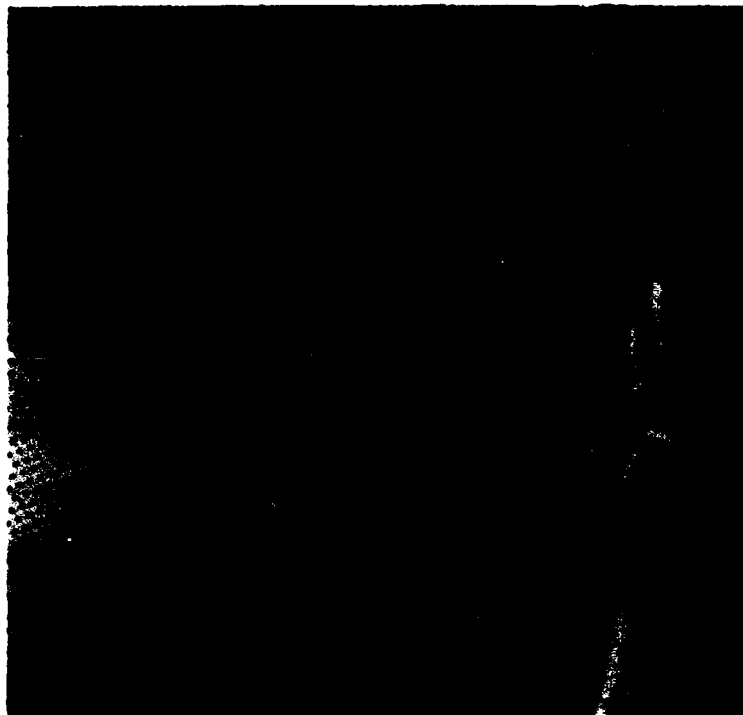


Figure 9. 0.15 Scale Model Configuration in Arnold Engineering Development Center 16T Wind Tunnel (Test No. 4)



Figure 10. 0.15 Scale Model Configuration in Boeing V/STOL Wind Tunnel (Test No. 5)

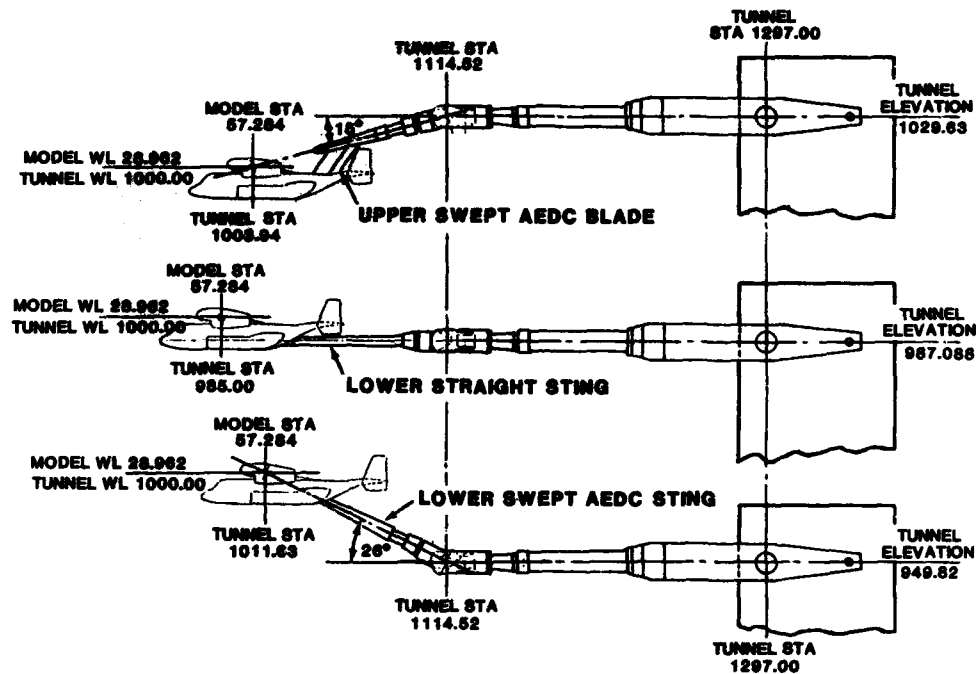


Figure 11. Support Systems for 0.15 Scale V-22 Drag Model for Test No. 5

NOTES: COMPLETE AIRCRAFT
 FLAPS 0°
 NACELLES 0°
 $MACH = .20, Re/Ft = 1.4 \times 10^6$
 LOWER 16° PRESENT STING FOR BVWT
 LOWER SWEPT STING FOR AEDC

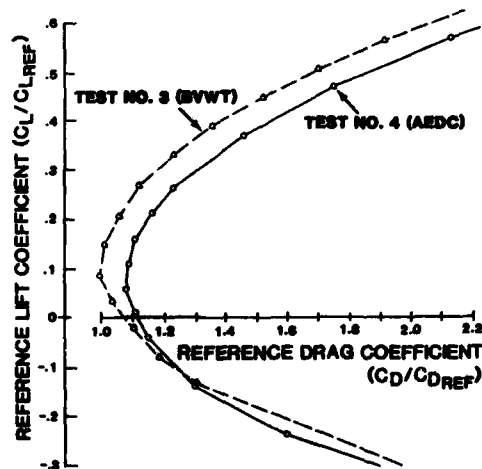


Figure 12. Comparison of Test No. 3 and Test No. 4 - Drag

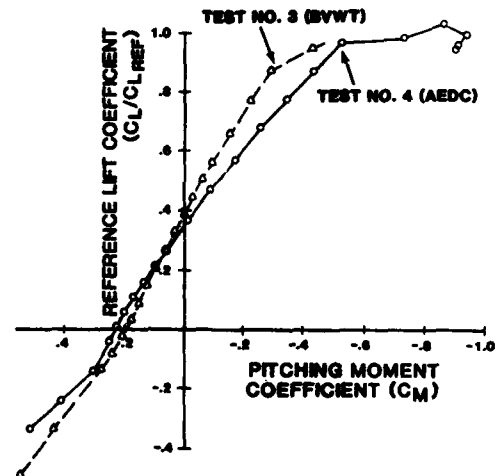


Figure 13. Comparison of Test No. 3 and Test No. 4 - Pitching Moment

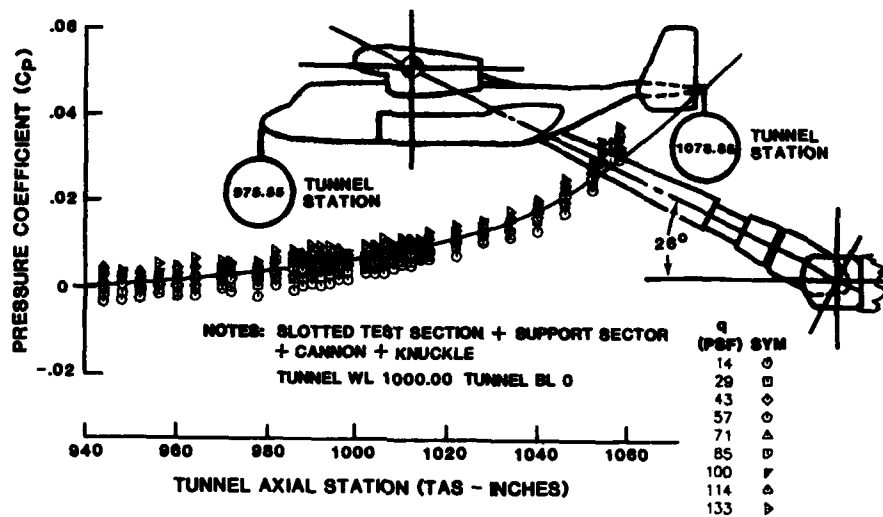


Figure 14. BVWT Horizontal Centerline Static Pressure Distribution

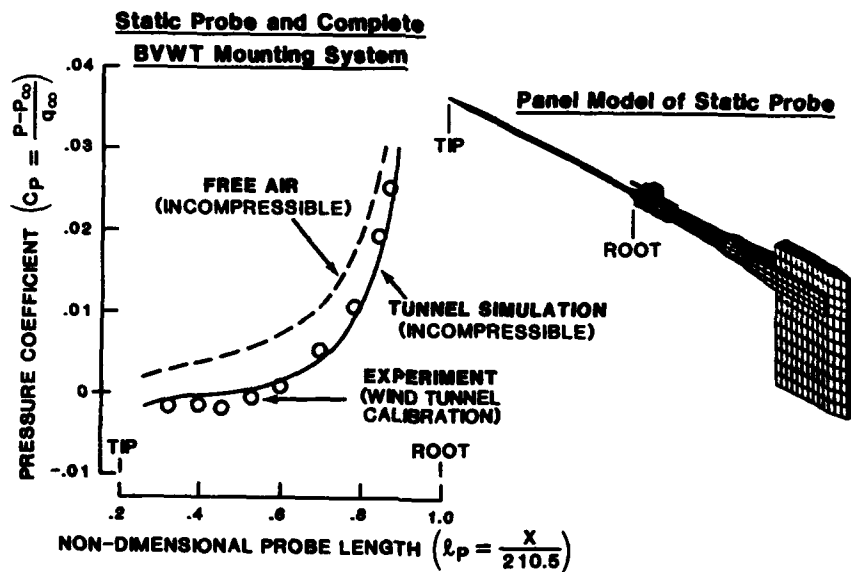


Figure 15. Comparison of Computed and Measured Pressure Distributions for Static Probe

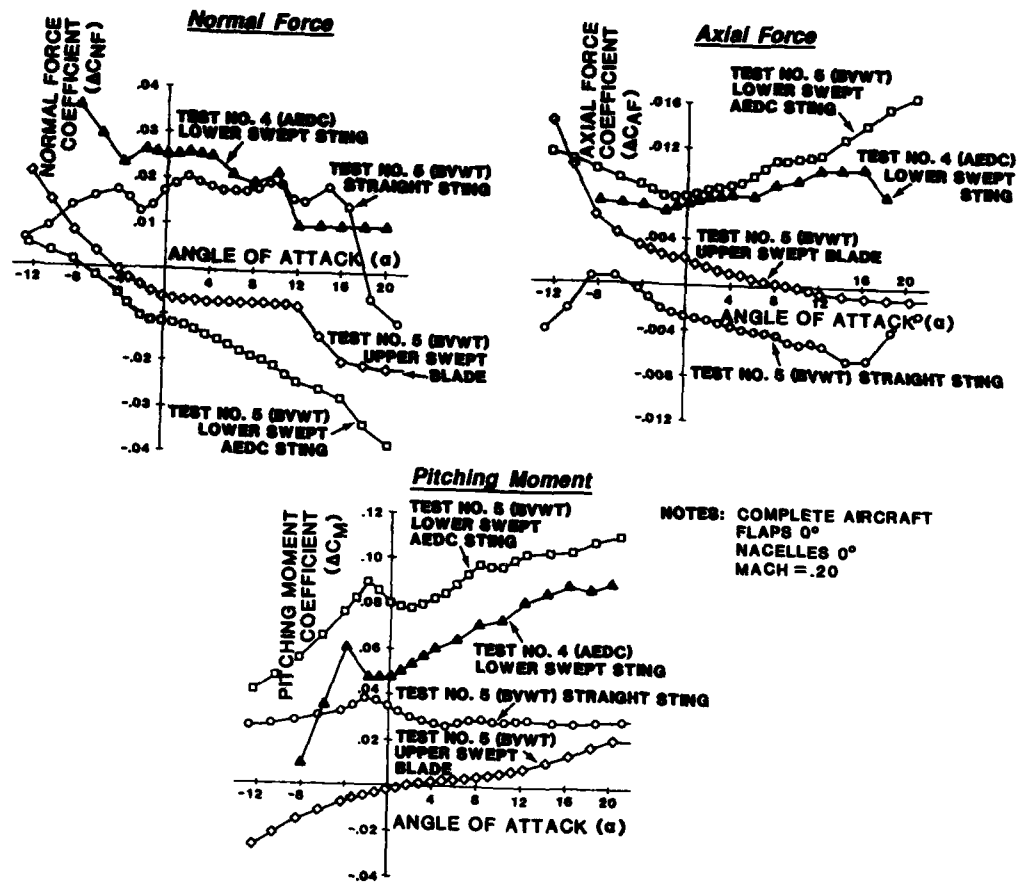


Figure 16. Test No. 5 Sting T&I Correction Coefficients

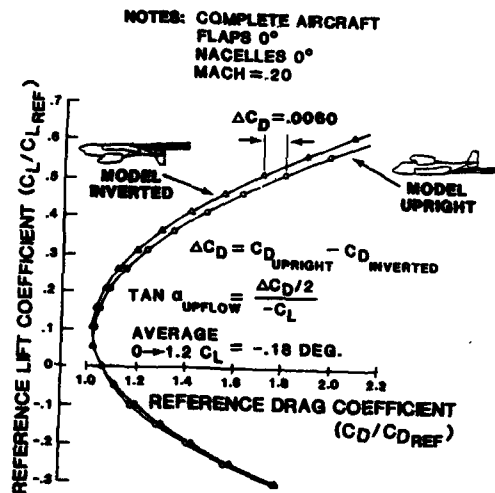


Figure 17. BVWT Tunnel Up-Flow

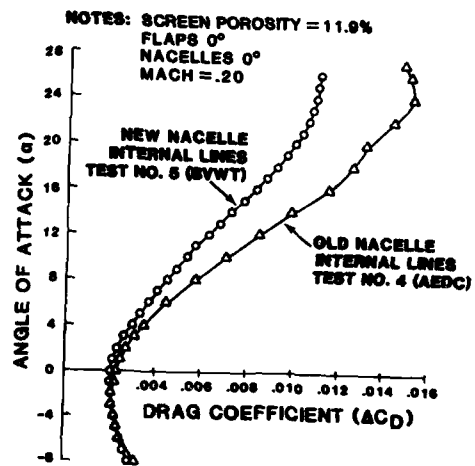


Figure 18. Drag Increment Due to Nacelle Internal Flow

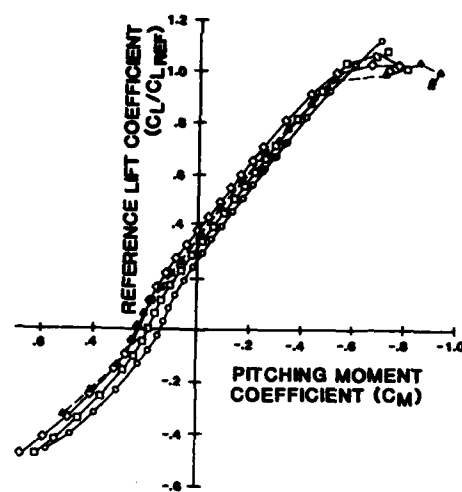


Figure 19. Comparison of Final Results - Stability

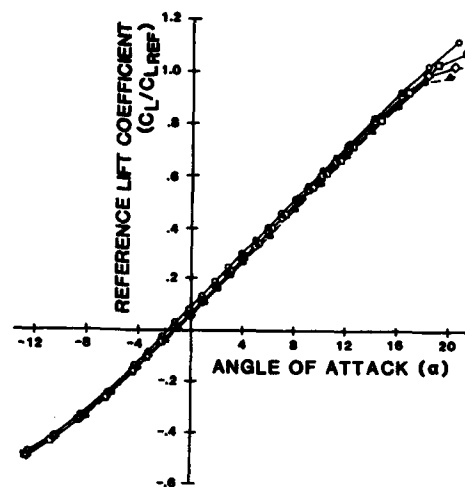


Figure 20. Comparison of Final Results - Lift

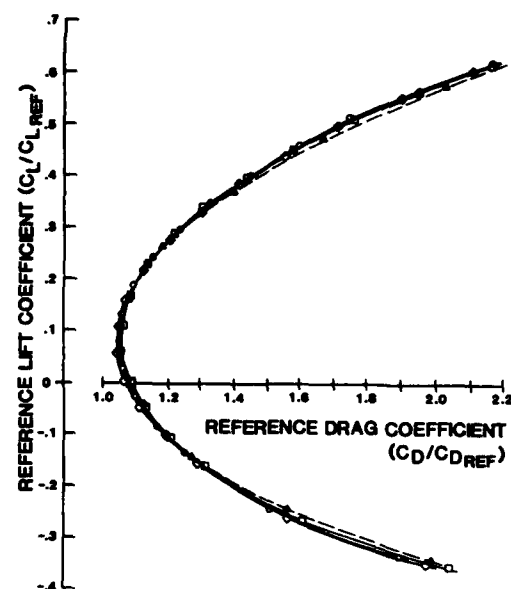


Figure 21. Comparison of Final Results - Drag

LEGEND AND NOTES FOR FIGURES 19, 20, AND 21

SYMBOL	MOUNTING SYSTEM
○	LOWER SWEPT TEST NO. 5 (BVWT)
□	LOWER STRAIGHT TEST NO. 5 (BVWT)
◇	UPPER BLADE TEST NO. 5 (BVWT)
▲	LOWER SWEPT TEST NO. 4 (AEDC)

NOTES: COMPLETE AIRCRAFT
FLAPS 0°
NACELLES 0°
MACH = .20
CG AT 25% M.A.C.
WL 150
DATA CORRECTED FOR T&I's AND
FLOW-THROUGH NACELLES

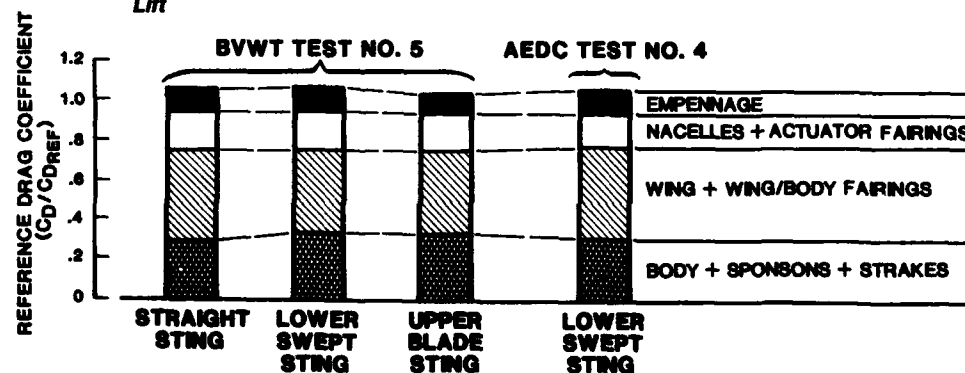


Figure 22. Component Drag Breakdown Comparison at Model Scale

HIERARCHY OF UNCERTAINTY SOURCES IN TRANSONIC WIND TUNNEL TESTING*

by
James M. Whorric, Section Head and Randy W. Hobbs, Project Engineer
16T/8 Aerodynamics Section, Propulsion Wind Tunnel Facility
Calspan Corporation/AEDC Division
Arnold Engineering Development Center
Arnold Air Force Station, Tennessee 37389-9998 USA

SUMMARY

A numerical perturbation technique was employed to compute the aerodynamic coefficient uncertainties attributable to uncertainty sources associated with transonic wind tunnel testing. A force accounting system which included data from an aerodynamic reference test, a nozzle afterbody test, and an inlet test was established to develop a system of equations by which to compute nominal flight values of lift, drag, and pitching-moment coefficient and also to perform the parameter perturbations necessary to compute the coefficient uncertainties. Uncertainty estimates included standard instrumentation uncertainties along with estimates of either influence coefficients or the uncertainties for such sources as wall interference, specific humidity, and viscous simulation which were based on combinations of CFD calculations and experimental data. Four cases were analyzed: (1) fighter subsonic cruise, (2) fighter transonic maneuver, (3) fighter supersonic cruise, and (4) transport cruise. An analysis of the perturbation results for these cases produced a hierarchy of uncertainty sources. The top five uncertainty sources were (1) strain-gage balance, (2) specific humidity, (3) wall interference, (4) test conditions, and (5) tunnel noise and turbulence. Angle-of-attack, model aeroelastic effects, internal duct flow, and exhaust jet temperature simulation were also identified as significant uncertainty sources in transonic wind tunnel testing.

NOTATION NOMENCLATURE

B	Elemental bias error
CFD	Computational fluid dynamics
C _X	Aerodynamic coefficient, X = L for lift, D for drag, and m for pitching moment
C _{X,EXT}	Aerodynamic coefficient from the aerodynamic reference model adjusted to full-scale flight conditions at a reference inlet and exhaust condition. Full-scale aeroelastic and protuberance effects are not included in the adjustments.
ΔC _{X,INLET}	Uncertainty in engine performance attributable to measurement or simulation uncertainties in the inlet test which is counted as thrust loss or drag.
ΔC _{X,NAB}	Aerodynamic coefficient increment from the NAB test that adjusts C _X from the reference exhaust condition to the required flight condition
FAS	Force accounting system
FT	Feet
IN	Inches
LB _f	Pound force
LB _m	Pound mass
M, MACH	Mach number
NAB	Nozzle afterbody
NPR	Nozzle pressure ratio
N _z	Load factor
PTR	Inlet total pressure recovery
RE	Tunnel unit Reynolds number, per foot
RE ₀	Momentum thickness Reynolds number at the location of the onset of transition
S	Elemental precision error
T	Static temperature
T _{DP}	Dew point temperature
T _T	Total temperature
U	Total uncertainty
X _{TR}	Location of transition onset
ALPHA, α	Angle of attack
δ*	Boundary-layer displacement thickness
τ	Tunnel free-stream turbulence level, percent of free-stream velocity

In the quest for guidance to prioritize data quality improvements at the Arnold Engineering Development Center (AEDC), a study was initiated by the AEDC Directorate of Technology to identify the sources of data uncertainties in AEDC transonic wind tunnel test data and to quantify the effects of those uncertainty sources. The objective of the study was to establish a hierarchy of the significant uncertainty sources to provide

*The research reported herein was performed by the Arnold Engineering Development Center (AEDC), Air Force Systems Command. Work and analysis for this research were done by personnel of Calspan Corporation/AEDC Division, operating contractor for the AEDC aerospace flight dynamics test facilities. Further reproduction is authorized to satisfy needs of the U. S. Government.

guidance for resource allocation to ensure that "high payoff" efforts were being worked and given top priority. The study was to include identification and quantification of uncertainty sources in the lift, drag, and pitching-moment coefficients of some typical test configurations from the AEDC Aerodynamic Wind Tunnel (4T) and the Propulsion Wind Tunnel (16T). A comparison of some of the characteristics of these two facilities is presented in Table 1. The uncertainties were quantified in terms of percent of flight coefficient values which would be predicted using data from an aerodynamic reference model test, a nozzle-afterbody (NAB) model test, and an inlet model test. Typical fighter and transport configurations were selected for analysis. The cases evaluated (Table 2) were a subsonic and supersonic cruise point and a transonic maneuver point for the fighter configuration and a cruise point for the transport configuration. All cases were evaluated for an altitude of 30,000 ft.

Table 1. Comparison of AEDC Transonic Wind Tunnels.

AEDC FACILITY	TEST SECTION SIZE, FT	SIDE WALL DESIGN	MACH NO. CAPABILITY
PROPULSION WIND TUNNEL 16T	16 X 16	FOUR WALLS PERFORATED WITH FIXED 6% OPEN POROSITY	0.06 TO 1.6
AERODYNAMIC WIND TUNNEL 4T	4 X 4	FOUR WALLS PERFORATED WITH VARIABLE 0 TO 10% OPEN POROSITY	0.2 TO 1.3, 1.6, 2.0

Table 2. Case Studies.

CASE	AIRCRAFT	MACH NUMBER	ALTITUDE FT	C_L	N_z	AEDC FACILITY
SUBSONIC CRUISE	FIGHTER	0.8	30,000	0.288	1.0	4T AND 16T
TRANSONIC TURN	FIGHTER	0.9	30,000	1.20	5.3	4T AND 16T
SUPERSONIC CRUISE	FIGHTER	1.5	30,000	0.078	1.0	16T
CRUISE	TRANSPORT	0.78	30,000	0.545	1.0	16T

The wind tunnel data base used in the analysis from the two facilities of interest (AEDC Tunnels 16T and 4T) was derived from models having a variation of model to tunnel blockage ratios from 0.11 to 0.91 percent. Furthermore, some of the models used artificial roughness to fix the boundary-layer transition point, and others had natural transition. A summary of the models, tunnels, blockage ratios, and viscous simulation techniques is presented in Table 3.

Table 3. Summary of Model-Tunnel Characteristics.

MODEL	MODEL TYPE	AEDC TUNNEL	MODEL TO TUNNEL BLOCKAGE RATIO %	VISCOUS SIMULATION TECHNIQUE
AERODYNAMIC REFERENCE	FIGHTER	16T	0.11	FIXED TRANSITION
AERODYNAMIC REFERENCE	FIGHTER	4T	0.36	FREE TRANSITION
NOZZLE AFTERBODY	FIGHTER	16T	0.56	FREE TRANSITION
AERODYNAMIC REFERENCE	TRANSPORT	16T	0.91	FREE TRANSITION

UNCERTAINTY ANALYSIS METHODOLOGY

The uncertainty analyses methodology used in this study is an adaptation of a method that was developed by the AEDC Engine Test Facility (ETF) for engine thrust uncertainty analysis (Ref. 1). ETF personnel calculated the influence of the error in each independent quantity on the engine thrust at specific flight conditions using a numerical perturbation technique on a specific set of equations which described the relationship between the dependent and the independent parameters in the calculation of the engine thrust. The technique involved calculating the engine thrust at a specific flight condition using measured or otherwise determined values of the independent parameters, and then each independent parameter is separately perturbed by its uncertainty value to determine its effect on the engine thrust.

Adapting this type of uncertainty analyses to the present study involved the following steps:

1. Identify the uncertainty sources associated with the three types of transonic wind tunnel tests.
2. Establish a specific set of equations via a force accounting system (FAS) by which the flight aerodynamic coefficient predictions could be made including terms to allow for evaluation of all uncertainty sources identified in Step No. 1.
3. Establish uncertainty values for all perturbation parameters.

4. Establish nominal values for all independent parameters for the cases being considered to compute nominal values of lift, drag, and pitching-moment coefficient for each case.
5. Perturb each independent parameter in the FAS separately by its estimated uncertainty value to get a perturbed value of the coefficients for each case considered.
6. The perturbed values of the coefficients are then subtracted from the nominal values to obtain the uncertainty in the nominal value attributable to the particular perturbation parameter uncertainty.

UNCERTAINTY SOURCES

The first task of the study was to identify and categorize the various sources of wind tunnel data uncertainty. Three main categories were established: (1) flow quality, (2) test technique and simulation, and (3) instrumentation. Specific sources of data uncertainty identified for each category and each type of wind tunnel test are shown in Figs. 1, 2, and 3. Flow quality sources included uncertainties associated with obtaining the tunnel Mach number calibration, i.e., calibration pipe orifice effects, specific humidity, and the parameters associated with the use of the calibration, such as total and plenum pressure, total temperature, and tunnel wall angle. In addition, sources associated with tunnel flow non-uniformity, such as longitudinal pressure gradients, flow angle, and noise and turbulence, were also identified as sources of uncertainty in the flow quality category. The flow quality uncertainty sources are present in all three types of wind tunnel tests. However, it can be seen in Figs. 1, 2, and 3 that the uncertainty sources associated with test technique and simulation vary significantly with the test type. The aerodynamic reference model test which provides an absolute value of the aerodynamic coefficients has the largest number of uncertainty sources. The adjustments that are applied to the basic coefficient measurements from this test are all sources of errors. The adjustments include static tares, base and cavity pressure, model-to-flight skin-friction extrapolation, support interference, and internal duct drag flow effects. Various physical parameters related to the model including moment transfer distances, reference areas and lengths, control surface angles, and aeroelastic effects are also sources of data uncertainty for the aerodynamic model test. Furthermore, in the transonic Mach number range, tunnel wall interference can be a significant source of data uncertainty along with the simulation of viscous effects such as the boundary-layer laminar to turbulent transition locus. Parameters producing uncertainties in the results obtained with fixed transition are trip placement, Mach number, and Reynolds numbers, whereas with free transition, error sources associated with the viscous simulation are tunnel noise and turbulence, Mach number, and Reynolds number.

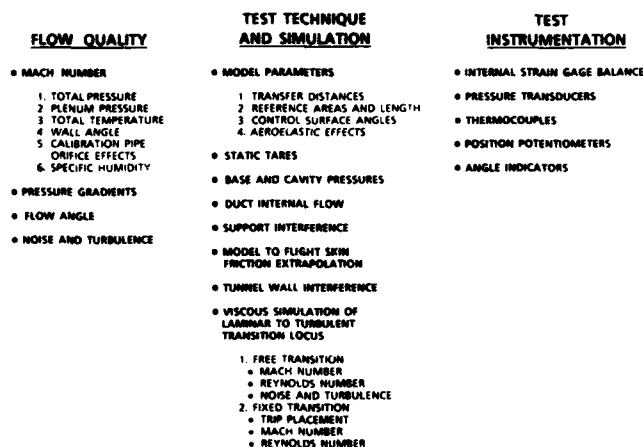


Fig. 1. Uncertainty Sources in Aerodynamic Reference Test Data.

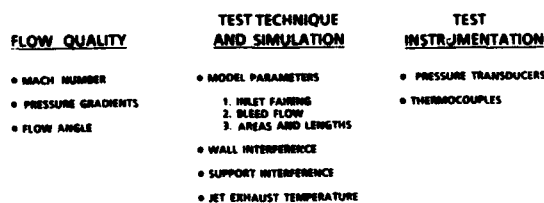


Fig. 2. Uncertainty Sources in NAB Pressure Test Data Increment.

FLOW QUALITY	TEST TECHNIQUE AND SIMULATION	TEST INSTRUMENTATION
• MACH NUMBER	• INLET BOUNDARY LAYER	• PRESSURE TRANSDUCERS
• PRESSURE GRADIENTS	• FLOW PLUG POSITION	• POSITION POTENTIOMETERS
• FLOW ANGLE		

Fig. 3. Uncertainty Sources in Inlet Performance Increment.

There are significantly fewer sources of data uncertainty associated with test technique and simulation in a nozzle afterbody (NAB) pressure test than in the reference aerodynamic test because the incremental method is used in acquiring the desired information; compare Figs. 1 and 2. The NAB test provides coefficient increments to be added to the adjusted aerodynamic reference test coefficients to adjust the data from the aerodynamic reference model nozzle pressure ratio (NPR) and the area ratio to those at the flight condition of interest. Pairing of the inlet along with the absence and/or the inaccurate simulation of bleed flows, as well as the uncertainty in integration areas, are sources of uncertainty in NAB testing associated with the model. Other NAB testing uncertainty sources are tunnel wall interference, model support interference, and improper simulation of jet exhaust temperatures.

In reviewing the possible test technique and simulation uncertainty sources associated with an inlet test where total pressure recovery and mass flow ratio are the primary parameters being measured, the uncertainty sources identified were improper inlet boundary-layer simulation and mass flow control via the positioning of a flow control plug.

Under the category of test instrumentation, the uncertainty sources identified were those associated with force, moment, pressure, temperature, position, and angle measurements.

FORCE ACCOUNTING SYSTEM

A force accounting system was established by which to formulate a specific set of equations with which to make the flight coefficient predictions. Such systems are typically set up by the aircraft manufacturers to account for all the corrections and/or adjustments to the wind tunnel data as well as all interacting forces that exist between the airframe aerodynamics and the propulsion system. Most force accounting systems separate the forces that are invariant with engine power from those that vary with engine power setting. The force accounting system used in this study is shown in Fig. 4. The aerodynamic reference test which uses a complete model with flow-through propulsion simulation with a fixed inlet and nozzle geometry provides an absolute value of aerodynamic coefficients, C_{XEXT} , at a reference mass flow ratio and nozzle and inlet geometry. The NAB test provides the data to adjust the aerodynamic reference test data from the reference condition to the flight condition of interest. Normally the inlet test provides data for accounting for inlet spillage effects, for determining loss of engine thrust through total-pressure recovery data and for assessing engine operating stability through inlet distortion index measurements. However, in the accounting system in this study, the inlet spillage effect is included in the aerodynamic reference test accounting, and

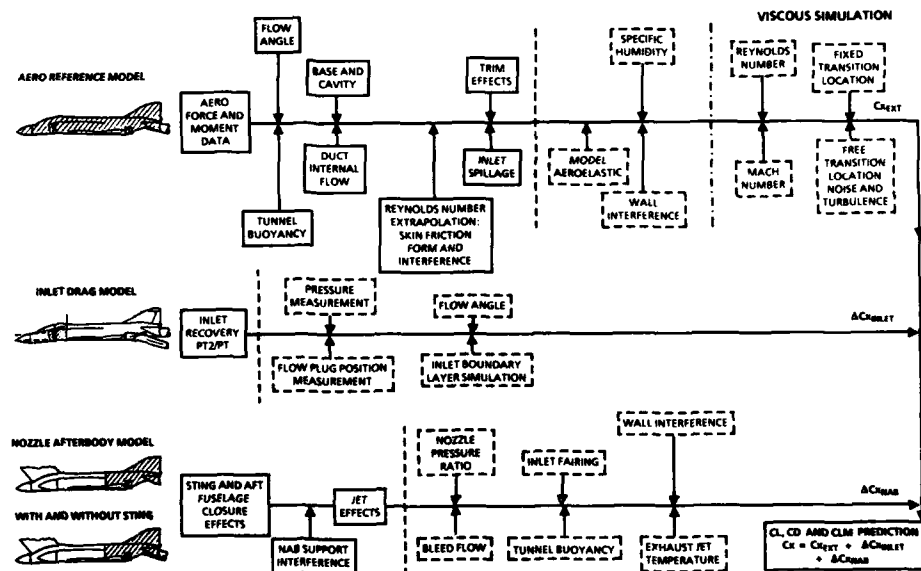


Fig. 4. Uncertainty Analysis Force Accounting System.

the inlet term ΔC_{XINLET} provides for accounting for uncertainties in the measured total pressure recovery (PTR) as losses in engine thrust, which is considered as additional drag. The coefficient prediction is obtained by adding the three terms:

$$C_X = C_{XEXT} + \Delta C_{XNAB} + \Delta C_{XINLET} \quad (1)$$

where $X = L$ for lift, D for drag, and m for pitching moment.

EQUATION SYSTEM DEVELOPMENT

In the force accounting system presented in Fig. 4, the adjustments and corrections to the wind tunnel data normally applied by the aircraft industry are shown in solid-line blocks. Those items shown with dashed-line blocks are not normally included in a standard force accounting system, but are treated as data uncertainties in this study. Specific analytic and/or empirical equations can be written for each of the terms in the solid-line boxes. Included in the current study are equations for calculating test conditions, uncorrected body and stability axes, base and cavity, and duct internal flow momentum loss aerodynamic coefficients. Trim and inlet spillage effects were included as surface fits of experimental data which also provided the capability of perturbing these effects by the angle of attack and control surface angle uncertainty. Tunnel flow angle and buoyancy effects were determined from experimental data at the conditions of interest and included as constants in the system of equations. The differences in skin-friction drag between the aerodynamic reference model and the full-scale vehicle is taken into account by subtracting the model skin-friction drag from the wind tunnel measured drag and adding in the full-scale vehicle skin-friction drag. The Prandtl-Schlichting empirical relationship from Ref. 2, which includes compressibility effects, was used for calculating turbulent flow skin-friction coefficients, and the Blasius equation (Ref. 3) was used for laminar flow skin-friction coefficients. The skin-friction drag for both the model and full-scale vehicle was calculated using the component buildup technique of Ref. 4 using empirically determined form and interference factors with the appropriate skin-friction coefficients and wetted areas. To get the true full-scale flight values, adjustments are also usually made for full-scale aeroelastic effects and for the effects of full-scale protuberances not simulated on scale models. However, these two effects were not included in the accounting system equations for the current study. Body and stability axes coefficient increments from the NAB test were computed using pressure integration equations. The NAB coefficient increment included accounting for the sting and aft fuselage deformation effects that are present in the aerodynamic reference test data. NAB support interference was included as a constant which was evaluated from experimental data.

Analytical and/or empirical relationships did not exist for the items in the dashed-line boxes in Fig. 4. The effects of many of these items were included as constant terms in the equations and estimated from experimental data. Included in those effects were the inlet fairing, bleed flow simulation, and specific humidity for the fighter configuration. Wall interference, model aeroelastic, tunnel noise and turbulence, and specific humidity effects for the transport configuration were also included as constant terms, but were evaluated using CFD techniques or a combination of CFD and experimental techniques. These techniques will be discussed in detail in the next section. The remaining terms, which include exhaust jet temperature, Reynolds number and Mach number effects in the viscous simulation, nozzle pressure ratio, transition strip placement, and inlet performance effects, were included in the system of equations by first estimating an influence coefficient or derivative, $\partial C_X / \partial Y$, where Y is the independent parameter of interest. It is recognized that Mach number and Reynolds numbers are not independent parameters, but $\partial C_X / \partial M$ and $\partial C_X / \partial Re$ are calculable and can be used, as indicated below in Eq. (2), to propagate errors in the independent parameters to the viscous effects. The influence coefficient estimates were accomplished using CFD and/or experimental data. The equation used to calculate the influence of uncertainty, ΔY , on coefficient C_X was

$$\Delta C_X = \frac{\partial C_X}{\partial Y} \Delta Y \quad (2)$$

For example, in the inlet accounting, estimates were made of the derivative $\partial C_D / \partial PTR$ by using engine performance data and an assumed aircraft drag to calculate the change in drag coefficient for a given change in total-pressure recovery, PTR. Then using the uncertainties in the PTR measurement attributable to the identified sources, an increment in drag coefficient was calculated using the equation

$$\Delta C_{DINLET} = \sum_Y \frac{\partial C_D}{\partial PTR} (\Delta PTR)_Y \quad (3)$$

where $Y =$ the particular uncertainty source.

UNCERTAINTY ESTIMATES

The estimates of the uncertainty in the perturbation parameters for the cases studied are presented in Table 4. Most of these parameters are the independent parameters in the system of equations. The majority of the uncertainties presented in this table are instrumentation uncertainties which contain systematic, non-random errors called bias (B) and random errors referred to as precision (S). The instrumentation uncertainties were calculated as

$$U = \pm (B + 2S) \quad (4)$$

For the balance uncertainties the bias and precision were calculated as follows from the calibration data:

$$\text{BIAS} = \frac{\sum_{i=1}^N (\text{RES})_i}{N} \quad (5)$$

and

$$\text{PRECISION} = \left[\frac{\sum_{i=1}^N (\text{RES} - \text{BIAS})^2}{N-1} \right]^{1/2} \quad (6)$$

where RES = APPLIED LOAD - CALCULATED LOAD and N = No. of measurements.

While the uncertainties calculated for the balances used in this study were made using the bias and precision values computed using equations 5 and 6, the current thinking at AEDC is that these equations probably do not compute the balance bias and precision properly and the methodology of determining these parameters are being re-evaluated.

Table 4. Perturbation Parameter Uncertainty Estimates.

PARAMETER GROUP	PERTURBATION PARAMETER	UNITS	FIGHTER CONFIGURATION						TRANSPORT
			SUBSONIC CRUISE		TRANSONIC MANUEVER		SUPER-SONIC CRUISE	CRUISE	
			16T	4T	16T	4T	16T	16T	
TEST CONDITIONS	TOTAL PRESSURE	PSF	1.26	1.29	1.25	1.29	1.25	1.29	
	PLENUM PRESSURE	PSF	1.21	1.22	1.19	1.20	1.14	1.28	
	TOTAL TEMPERATURE	°R	3.65	0.75	3.65	0.75	3.65	3.65	
	WALL ANGLE	DEG	0.015	---	0.015	---	0.015	0.015	
	ORIFICE EFFECTS	---	0.0078	0.0076	0.0090	0.0088	0.0178	0.0088	
MODEL ATTITUDE	PITCH SECTOR ANGLE	DEG	0.04	0.04	0.04	0.04	0.04	0.04	
	ROLL MECHANISM ANGLE	DEG	0.04	0.04	0.04	0.04	0.04	0.04	
BASE AND CAVITY EFFECTS	BASE AND/OR CAVITY PRESSURE	PSF	1.75	---	1.48	---	0.53	3.05	
DUCT INTERNAL FLOW MOMENTUM LOSS	CALIBRATED DUCT EXIT TOTAL PRESSURE	PSF	2.55	---	2.39	---	2.12	---	
	UNCALIBRATED DUCT EXIT TOTAL PRESSURE	PSF	6.3	---	6.3	---	6.3	---	
	DUCT EXIT STATIC PRESSURE	PSF	1.78	---	1.53	---	1.15	---	
	DUCT EXIT STATIC PRESSURE	PSF	1.78	---	1.53	---	1.15	---	
MODEL FORCES AND MOMENTS	BALANCE TEMPERATURE	°F	3.88	3.88	3.88	3.88	3.88	3.88	
	BALANCE VOLTAGE	VOLTS	0.017	0.011	0.017	0.011	0.017	0.017	
	BALANCE NORMAL FORCE	LB	4.1	1.4	4.1	1.4	4.1	33.9	
	BALANCE AXIAL FORCE	LB	0.9	0.6	0.9	0.6	0.9	5.5	
	BALANCE PITCHING MOMENT	IN-LB	14.0	4.1	14.0	4.1	14.0	182.2	
NAB INCREMENTS	NAB PRESSURE AT OPERATING CONDITION	PSF	2.0	---	2.0	---	2.0	---	
	NAB PRESSURE AT REFERENCE CONDITION	PSF	2.0	---	2.0	---	2.0	---	
	NAB JET NOZZLE PRESSURE RATIO	NONE	0.2	---	0.2	---	0.2	---	
	JET TEST TEMPERATURE	°R	10°	---	10°	---	10°	---	
	JET TEMP DIFFERENCE	°R	670	---	2200	---	2200	---	
INLET INCREMENT	TOTAL PRESSURE RECOVERY INSTRUMENTATION	---	0.001	---	0.001	---	0.001	---	
	TOTAL PRESSURE RECOVERY, FLOW PLUG POSITION	---	0.001	---	0.001	---	0.001	---	
	TOTAL PRESSURE RECOVERY, BOUNDARY LAYER SIM	---	0.002	---	0.002	---	0.002	---	
	TOTAL PRESSURE RECOVERY, FLOW ANGLE	---	0.0004	---	0.0004	---	0.0004	---	
MODEL GEOMETRY	CONTROL SURFACE ANGLE	DEG	0.1	0.1	0.1	0.1	0.1	0.1	
	LENGTHS	IN	0.010	0.010	0.010	0.010	0.010	0.010	
	AREAS	%	1.0	1.0	1.0	1.0	1.0	1.0	
VISCOUS SIMULATION FIXED TRANSITION	FIXED TRANSITION STRIP PLACEMENT	IN	0.1	N/A	0.1	N/A	0.1	N/A	

The test condition uncertainty attributable to calibration pipe orifice effects is given in terms of Mach number error. Uncertainty estimates have been made for duct internal flow momentum loss for both a calibrated and an uncalibrated duct. The uncalibrated duct calculation uses weighting factors combined with duct total-pressure measurements to calculate the duct mass flow. The uncertainties in the average total-pressure measurement for the uncalibrated duct were calculated using that same weighting methodology. NAB jet temperature uncertainty is listed as jet test temperature, which is the instrument uncertainty, and as jet temperature difference, which is the difference in temperature between the wind tunnel test and the flight operating condition.

The effect of the tunnel walls on the models is highly model-dependent and must be evaluated for each model tested. In general, no corrections are made to the model data to account for any wall effects; therefore, the wall interference effects are considered uncertainties in the data. The wall interference effects for the models and tunnels in this study were computed using the methodology described in Ref. 5. The procedure used to solve the wall interference problem involved the creation of a computational mesh for the tunnel and a wing-body representation of the model. A second larger mesh was created which exactly overlays the first and extended four tunnel heights for the free-air solutions. The Euler equations were used as the basis for the flow-solver portion of the computations. The wall interference is calculated by taking the difference between a free-air and tunnel flow-field solution. Some typical results from the wall interference calculations at Mach 0.8 are presented in Fig. 5.

Moisture in the flow field around a wind tunnel model can significantly affect the aerodynamic coefficient data. As local condensation occurs, heat is released into the flow field which alters the pressure and temperature distributions over the model. The effects of humidity are particularly significant at high transonic and supersonic Mach numbers at which shock locations can be altered by local condensation in the flow field. The CFD code HUMID/EULER described in Ref. 6 was used to calculate specific humidity effects at the nominal conditions of the cases studied. This code also uses the Euler equations and a two-dimensional model representation. Experimental data were available at Mach numbers of 0.9 and 1.2 for the fighter configuration, and those data were used to adjust the results of the computations for both the fighter and transport configurations. As with the wall interference, two points were required for each case in order to compute a coefficient increment. One point was tunnel air dry and one point was with the air at the specific humidity criteria for tunnel operation.

The humidity criteria used in the AEDC transonic wind tunnels is that the air dew-point temperature must be less than the free-stream static temperature at subsonic Mach numbers, and at supersonic Mach numbers the specific humidity must be less than 0.0015 $\text{LB}_m\text{H}_2\text{O}/\text{LB}_m\text{AIR}$. The results of the calculations for the transport configuration are shown in Fig. 6. The deltas used in the uncertainty analysis were the values extrapolated to the 4×10^6 unit Reynolds number humidity criteria line, which was the test condition at which the transport data base was acquired. Also shown in Fig. 6 is the tunnel humidity criteria line for 2.5×10^6 unit Reynolds number to show the sensitivity of the uncertainty to air density.

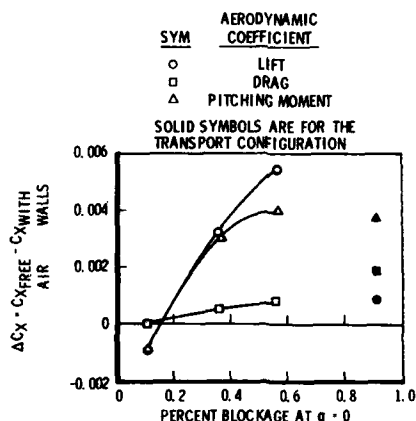


Fig. 5. Wall Interference Effects at Mach = 0.8.

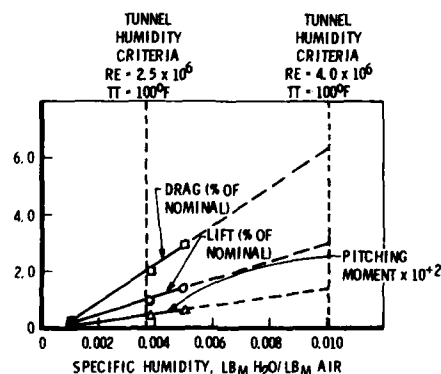


Fig. 6. Specific Humidity Results of HUMID/EULER 2D Calculation for Transport Configuration, Mach = 0.78.

The computation of uncertainties associated with the viscous simulation was accomplished using several CFD codes coupled with some empirical results. The methodology of the calculation is shown in Figs. 7 and 8. Initially the flow field is calculated using the FLO 27 flow solver described in Ref. 7 which solves the full potential equations. The pressure distributions from the initial calculation are input into the boundary-layer code of Ref. 8 to calculate the laminar boundary-layer profile to the start of transition. The code of Ref. 9 is used for the turbulent boundary-layer calculations. An intermittency function is used to mix the laminar and turbulent skin-friction coefficients over the transition region. Turbulent values are used to compute the displacement thickness distribution over the rest of the geometry. The onset of transition and the length of the transition region are specified from empirical data. The displacement thickness distributions are then input as modifications to the original geometry, and the calculation is repeated until the displacement thickness distribution no longer changes. The codes were used to calculate the influence coefficients, $\partial C_x / \partial \mu$, $\partial C_x / \partial M$, and $\partial C_x / \partial X_{TR}$, that were used in the accounting equations. They were also used to evaluate the uncertainty associated with tunnel noise and turbulence using the Ref. 10

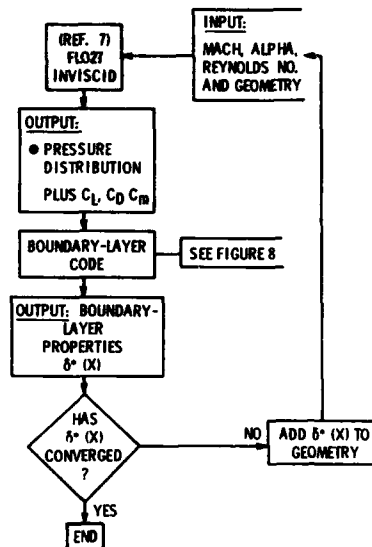


Fig. 7. Viscous Simulation Evaluation Code.

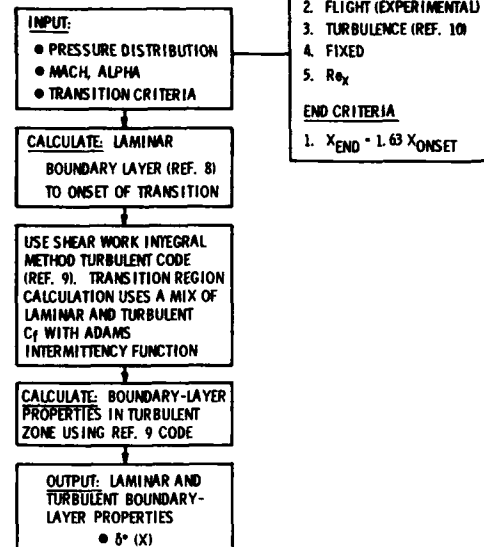


Fig. 8. Boundary-Layer Calculation Methodology.

equation

$$RE_0 = 190 + \exp(6.88 - 103\tau) \quad (7)$$

where τ = tunnel turbulence in percent of free-stream velocity. The code has the capability of computing the lift, drag, and pitching-moment coefficient for a given geometry and test condition as a function of turbulence. Typical drag coefficient results computed for the wing of the transport configuration are shown in Fig. 9. In order to get the coefficient uncertainty increment attributable to tunnel turbulence, one must first decide what the tunnel turbulence is and also what is an appropriate turbulence value for flight. Experimental data (see Fig. 10) were available for the two wind tunnels and also from a flight test

which provided the onset of transition criteria (RE_0) as a function of Mach number. The data were obtained with the same slender cone and are reported in Refs. 11 and 12. Using the data in Fig. 10 along with Eq. (7), one can ascertain the flight and tunnel turbulence values for the determination of the drag coefficient increment from the data in Fig. 9. At Mach 0.8 the 4T and 16T tunnel turbulence was 0.8 percent, whereas the flight value was about 0.6 percent. It is also interesting to note that while the drag of the transport configuration decreased as free-stream turbulence increased, the drag of the fighter configuration increased. The changes in the form drag with free-stream turbulence account for the difference in trends. The transport wing is a supercritical wing, and, as the data in Fig. 9 show, the form drag decreased more rapidly than the skin-friction drag increased as turbulence was increased. The fighter configuration wing is not supercritical, and the form drag changes were very small compared to the skin-friction changes with turbulence, resulting in an increase in total drag as turbulence increased.

The aerodynamic reference model geometry is designed to represent one flight condition and is generally treated as a rigid body. In the study reported herein, aeroelastic effects of the aero-reference fighter and transport models were computed to evaluate the error associated with that assumption. A finite-element model of the fighter and transport wing was developed, load distributions (see Fig. 11) were generated from experimental pressure distributions, and the wing twist distribution underloads were then calculated. Typical results of those calculations are shown in Fig. 12. The viscous simulation evaluation code (Fig. 7) was used to calculate the difference in the lift, drag, and pitching-moment coefficients between the two twist distributions. In some instances when the code would not run, the average value of the change in the twist distribution was treated as

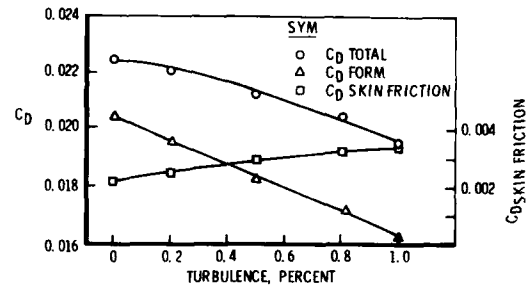


Fig. 9. Predicted C_D Versus Turbulence for Transport Wing, $M = 0.78$, $\alpha = 2.14^\circ$, $RE = 4.0 \times 10^6/FT$.

an angle-of-attack error, and the resulting error in the longitudinal aerodynamic coefficients was computed via the perturbation technique.

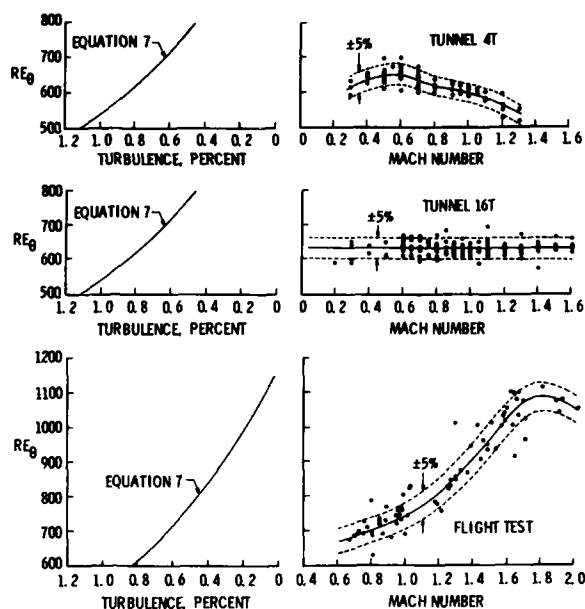


Fig. 10. Experimental Transition Onset-Turbulence Correlation.

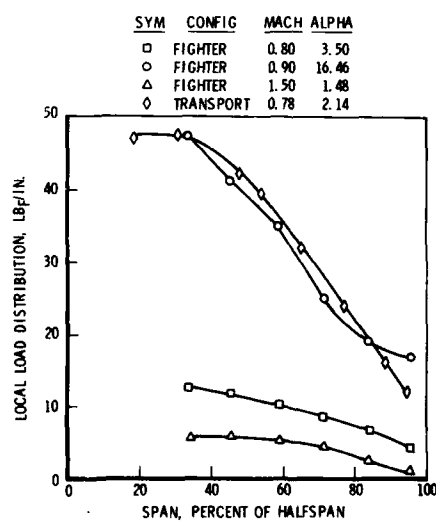


Fig. 11. Wing Load Distribution.

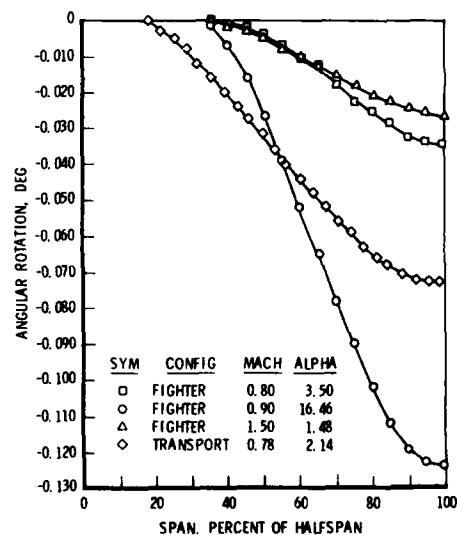


Fig. 12. Estimated Incremental Wing Twist.

STUDY RESULTS AND CONCLUSIONS

The uncertainties in the lift and drag coefficients associated with the various parameter uncertainties expressed in percent of the nominal coefficient value as well as a coefficient increment value are presented in Figs. 13 through 17. Since the cases studied represent trimmed flight conditions, the pitching-moment coefficient uncertainties are only presented as coefficient increments. Comparisons are made, where applicable, of coefficient uncertainties associated with the two AEDC transonic wind tunnels 16T and 4T. Parameters for which no results are presented produced smaller uncertainties than those which are presented.

The total uncertainties which were calculated by simply taking the square root of the sum of the squares of all the perturbation uncertainties are presented in Fig. 13. Included in this figure are accuracy requirements for the lift, drag, and pitching-moment coefficients for a transport configuration which were established by Steinle and Stanewsky in Ref. 13. It is obvious that the total uncertainties established in the current study are well outside of the Ref. 13 values.

An analysis of the detailed results presented in Figs. 14 through 17 resulted in the establishment of a hierarchy of uncertainty sources presented in Fig. 18. Heading the list are strain-gage balance measurements. Steinle and Stanewsky also identified force and moment measurements as the major contributor to wind tunnel data uncertainty. They recommended investigation into advanced calibration techniques taking into account temperature effects, non-linearities, and hysteresis characteristics. Obviously, this is an area that needs considerable emphasis.

The second item in the hierarchy of uncertainty source is specific humidity. This result was somewhat of a surprise, especially the drag error for the subsonic cruise fighter case. The specific-humidity criterion, i.e., $T - T_{pp} \leq 0$, for subsonic Mach numbers is obviously not stringent enough for a model with a wing that has no supercritical flow. Moreover, the transport configuration which has a supercritical airfoil would require a more stringent specific humidity criterion than the fighter. One could adopt the most restrictive specific-humidity criterion which is that the dewpoint temperature be below the static temperature corresponding to the highest Mach number of the flow over the model. Steinle and Stanewsky (Ref. 13) feel that is too restrictive and suggest a criterion, $T - T_{pp} \leq 3.6^\circ\text{F}$. From the results of this study it appears that more experimental work needs to be done to adequately define the tunnel specific-humidity criterion for models with supercritical airfoils. Moreover, the CFD code HUMID/EULER needs to be improved to provide the capability of predicting what an acceptable tunnel humidity is for various models.

REFERENCE 14 TRANSPORT CONFIGURATION ACCURACY REQUIREMENTS

INCREMENTAL MEASUREMENTS	ABSOLUTE MEASUREMENTS
$\Delta C_D = 0.0001$	0.0005
$\Delta C_L = 0.01$	0.01
$\Delta C_m = 0.001$	0.001
$\Delta \alpha = 0.01$	0.05
$\Delta \text{MACH NO.} = 0.001$	0.001

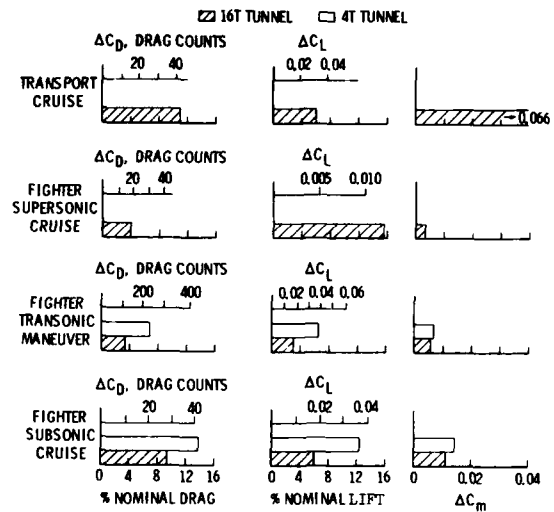


Fig. 13. Total Uncertainties.

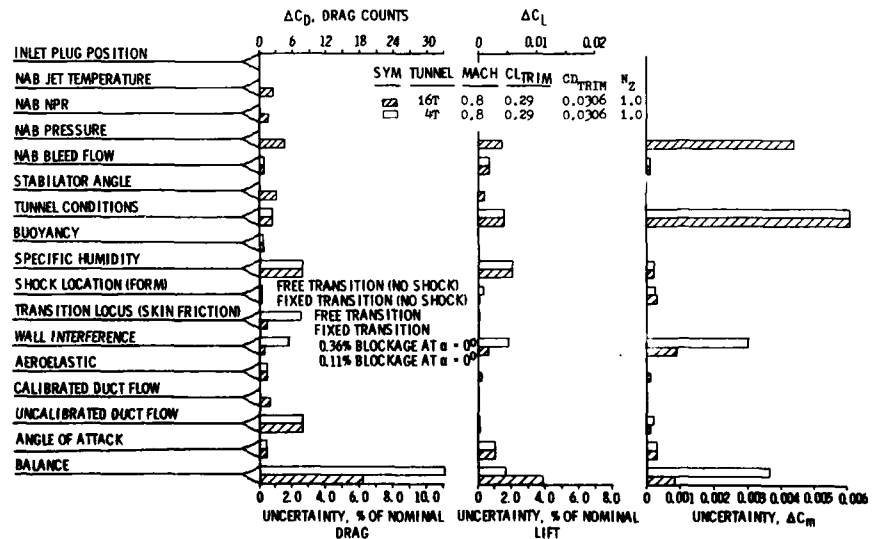


Fig. 14. Uncertainties, Fighter Subsonic Cruise Condition.

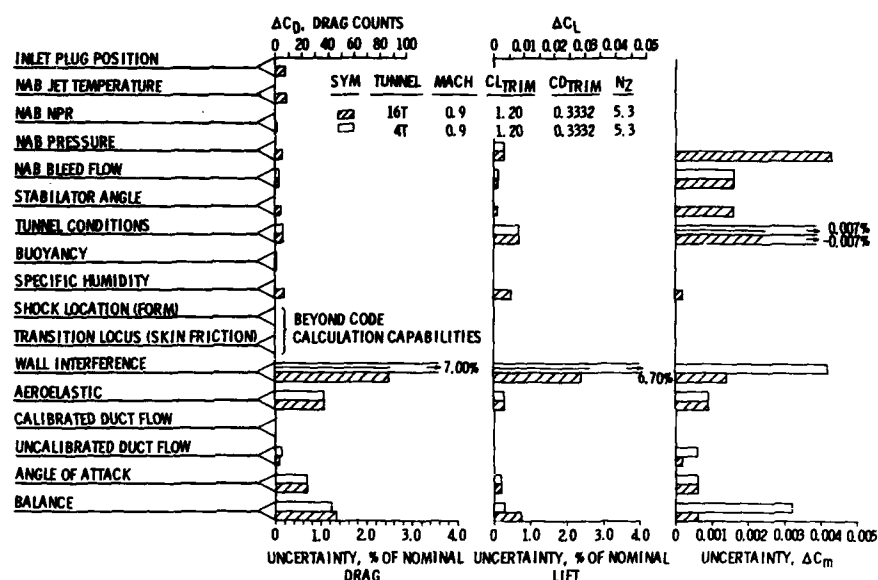


Fig. 15. Uncertainties, Fighter, 5.3 "G" Turn.

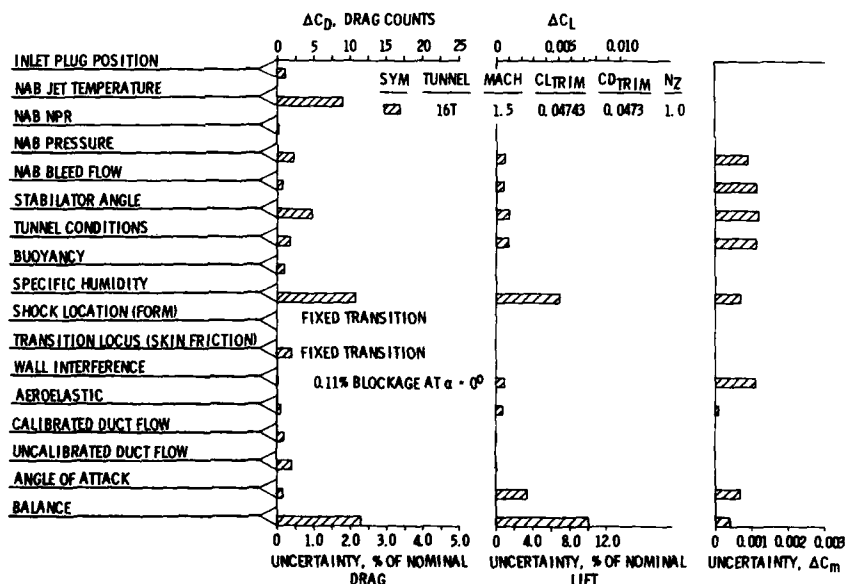


Fig. 16. Uncertainties, Fighter, Supersonic Cruise Condition.

Wall interference as number three in the uncertainty source hierarchy was no surprise. The perturbation analysis showed that wall interference effects were significant even with models with blockages as low as 0.36% of the test section area. Over the past several years, AEDC has developed the capability to make wall interference calculations with confidence and routinely evaluates such effects for models to be tested in their facilities. These results show the need to continue development of the "adaptive wall" wind tunnel and for pursuing other wall interference correction techniques as outlined in Ref. 5.

Uncertainties associated with establishing test conditions, which was fourth in the uncertainty source hierarchy, are primarily due to orifice effects associated with the centerline pipe static-pressure orifices that are used for the tunnel calibration. Secondary effects are the pressure transducer uncertainties for the total-pressure and plenum-pressure measurements.

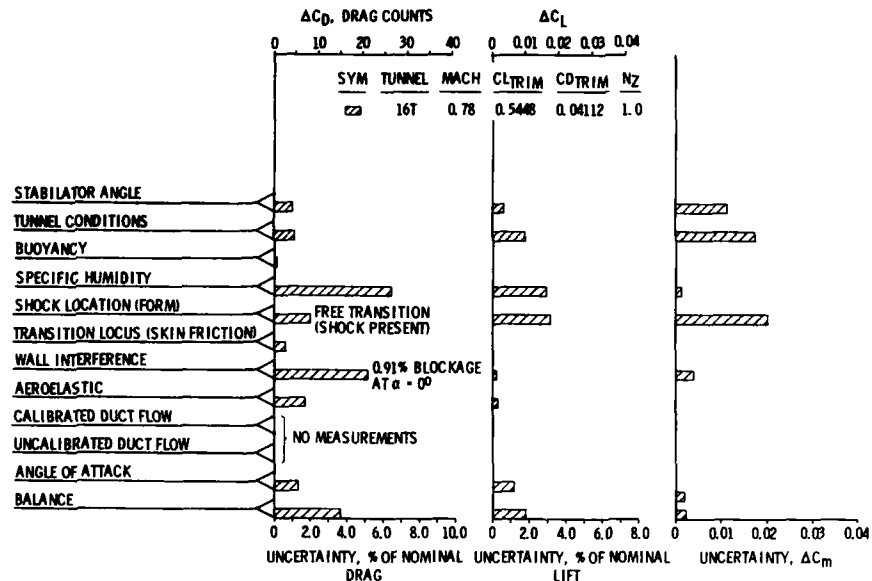


Fig. 17. Uncertainties, Transport Cruise Condition.

Tunnel noise and free-stream turbulence holds the fifth place in the uncertainty source hierarchy, but only for models which utilize natural laminar to turbulent boundary-layer transition. Proper viscous simulation with such models requires knowledge of the tunnel noise and free-stream turbulence or some method of characterizing those parameters with respect to flight. In laminar flow control experiments the knowledge of these parameters becomes even more important because of the dominance of external disturbances on the stability of laminar boundary layers.

The uncertainty in angle of attack placed sixth in the uncertainty source hierarchy; however, only a 0.04-deg uncertainty in the main sector angle was included in the coefficient uncertainty calculations. Other sources of angle-of-attack uncertainty include sting prebends and pre-roll angles, model-balance incidence angles, and sting balance deflection angles to name a few. If the uncertainties associated with the determination of these angles were included, then angle of attack would move up in the uncertainty source hierarchy. These results point out that the testing community needs to put some emphasis on improving angle-of-attack measurement accuracy.

The remaining items in the uncertainty hierarchy indicate that model aeroelastic effects should not be ignored. Moreover, determining the internal duct drag with an uncalibrated duct can produce significant errors in the drag coefficient determination. Furthermore, adjustments should be made to the NAB drag increments for the mismatch between the flight and model exhaust temperatures. This adjustment has been successfully accomplished for axisymmetric nozzles using an empirical technique described in Ref. 14. However, configurations with non-axisymmetric nozzles will require the development of an experimental data base to produce a correction technique.

CONCLUDING REMARKS

The objective of this study was to produce a hierarchy of uncertainty sources in transonic wind tunnel testing to ensure that the "high payoff" sources were being given proper priority and fiscal consideration. In summary, force and moment and angle-of-attack measurement are the dominant sources of data uncertainty in transonic wind tunnel testing and need to be given top priority for measurement uncertainty improvement by the testing community. Furthermore, specific humidity, wall interference, test conditions, and noise and turbulence can also produce significant data uncertainties, and special attention needs to be given to each of these parameters in order to produce the highest quality transonic wind tunnel data. Moreover, taking model aeroelastic effects into

1. STRAIN GAGE BALANCE
2. SPECIFIC HUMIDITY
3. WALL INTERFERENCE
4. TEST CONDITIONS
5. TUNNEL NOISE AND FREE-STREAM TURBULENCE (VISCOUS SIMULATION OF FREE TRANSITION)
6. ANGLE OF ATTACK
7. MODEL AEROELASTIC EFFECTS
8. UNCALIBRATED DUCT FLOW
9. NAB JET EXHAUST TEMPERATURE SIMULATION
10. NAB BLEED FLOW SIMULATION
11. NAB PRESSURE
12. INLET PLUG POSITION
13. CALIBRATED DUCT FLOW
14. CONTROL SURFACE ANGLE
15. NAB NOZZLE PRESSURE RATIO

Fig. 18. Hierarchy of Uncertainty Sources.

account and performing mass flow calibrations of flow through ducts of aerodynamic reference models will further improve data quality.

REFERENCES

1. Couch, B. O., Boals, W. O., and Bishop, B. M., ARO, Inc., "ALCM Preflight Test Thrust Uncertainty Analysis," AEDC-TR-81-2 (AD-A101443), July 1981.
2. Hoerner, S. F., Midland Park, N. J., Fluid-Dynamic Drag; Practical Information on Aerodynamic Drag and Hydrodynamic Resistance, Published by Author, 1965.
3. Blasius, H., "Boundary Layers in Fluids of Small Viscosity," Dissertation, Göttingen, FRG, 1907.
4. Covert, E. C. et al., Massachusetts Institute of Technology, "Thrust and Drag: Its Prediction and Verification," Progress in Astronautics and Aeronautics, Vol. 98, 1985.
5. Kraft, E. M. and Ritter, A., Calspan Corporation/AEDC Division, "Advances at AEDC in Treating Transonic Wind Tunnel Wall Interference," ICAS-86-1.6.1, September 1986.
6. Robinson, C. E. and Bauer, R. C., Sverdrup Technology, Inc., AEDC Group, "Estimating Water Vapor Condensation Effects for Transonic and Supersonic Flow Fields," AEDC-TR-85-63 (AD-A163146), December 1985.
7. Caughey, D. A., Cornell University, and Jameson, Anthony, New York University, "Numerical Calculation of Transonic Potential Flow about Wing-Fuselage Combinations," AIAA Paper No. 77-677, Albuquerque, New Mexico, June 1977.
8. Patankar, S. V. and Spalding, D. B., Heat and Mass Transfer in Boundary Layers, A General Calculation Procedure, Intertext, London, 2nd Edition, 1970.
9. Whitfield, D. L., ARO, Inc., "Integral Solution of Compressible Turbulent Boundary Layers Using Improved Velocity Profiles," AEDC-TR-78-42 (AD-A062946), December 1978.
10. Hall, D. J., Ministry of Defence (England), and Gibbings, J. C., Liverpool University (England), "Influence of Stream Turbulence and Pressure Gradient upon Boundary Layer Transition," J. Mechanical Engineering Science, Vol. 14, No. 2, April 1972.
11. Dougherty, N. Sam, Jr. and Fisher, David F., ARO, Inc., "Boundary-Layer Transition Correlation on a Slender Cone in Wind Tunnels and Flight for Indications of Flow Quality," AEDC-TR-81-26 (AD-A111328), February 1982.
12. Fisher, David F. and Dougherty, N. Sam, Jr., ARO, Inc., "In-Flight Transition Measurement on a 10° Cone at Mach Numbers from 0.5 to 2.0," NASA-TP-1971, June 1982.
13. Steinle, F., NASA, and Stanewsky, E., DFVLR-AVA, "Wind Tunnel Flow Quality and Data Accuracy Requirements," AGARD AR 184, November 1982.
14. Peters, W. L., Calspan Corporation/AEDC Division, "A Simulation Technique for Jet Temperature Effects on Nozzle-Afterbody Drag at Transonic Mach Numbers," AIAA Paper No. 85-1463, July 1985.

WIND TUNNEL PREDICTED AIR VEHICLE PERFORMANCE: A REVIEW OF LESSONS LEARNED

by

E. C. Rooney
Head, Aerodynamics and Flight Controls
Naval Air Systems Command
Washington, D.C., USA 20361-5300

R. F. Lauer, Jr.
Head, Propulsion Wind Tunnel Inlet Engine Section
Calspan Corp/AEDC Division
Arnold Air Force Base, TN, USA 37389-5000

SUMMARY

Air vehicle development programs continue to experience difficulty in predicting the performance of new aircraft configurations. Advances in the states-of-the-art in wind tunnel simulation techniques, flight performance measurements and Computational Fluid Dynamics have provided the basis for investigating the accuracy of the aerodynamic elements used in the performance prediction process. This paper reviews the force accounting procedures, model and wind tunnel simulation techniques and correction procedures, and full scale adjustments used to predict the performance of air vehicles. The "lessons learned" in this review should enhance the capability to predict aircraft performance for future air vehicle development programs.

SYMBOLS AND NOTATION

A	Geometric area	m	Mass flow
AEDC	Arnold Engineering Development Center	m/m_0	Inlet mass flow ratio
C_{AF}	Axial force coefficient	NPR	Nozzle pressure ratio
C_D	Drag coefficient, D/q_{REF}	P	Pressure
CFD	Computational Fluid Dynamics	PSF	Pounds per square ft
C_f	Skin friction drag coefficient	PWT	Propulsion Wind Tunnel (AEDC 16T)
CG	Center-of-gravity	q	Dynamic pressure
C_p	Pressure coefficient, $(P-P_0)/q_0$	Re	Reynolds number
D	Drag	S	Reference area
D_{AFS}	Airframe system drag	STA	Station
D_{REF}	Full scale adjusted WT drag	T	Temperature
F	Force	V	Velocity
FT, ft	Feet	WT	Wind tunnel
F_N	Net thrust	WL	Water line
F_{EX}	Excess thrust	α	Angle of attack
F_{IPF}	Installed net propulsive force	γ	Ratio of specific heats
log	Logarithm	Δ	Incremental quantity change
M	Mach number		

Subscripts:

E	Exit plane	MISC	Miscellaneous
EHX	Exhaust	∞	Remote at infinity
FS	Full scale	REF	Reference
INL	Inlet	Re	Reynolds number
INT	Internal	T	Total
MAX	Maximum	TRIM	TRIM (CG/thrust vector effects)
MIN	Minimum	WT	Wind tunnel

1. INTRODUCTION

The accuracy of air vehicle performance predictions is dependent on the quality of the aerodynamic, mass property and propulsion system information used in the prediction process. For most aircraft development programs, the aerodynamic elements are obtained from the conduct of scale model tests in wind tunnel facilities. For some wind tunnel aerodynamic investigations, a high degree of accuracy may not be required (e.g., those performed for parametric investigations or incremental configuration effects). For other programs, however, such as those to be used as the basis for contract requirements, the accuracy associated with the derivation of the aerodynamic elements must be thoroughly understood.

Air vehicle development programs requiring high levels of accuracy continue to experience discrepancies in data obtained with different scale models in the same wind tunnel, with the same model in different wind tunnels, and between prediction and that achieved in flight. The ability to isolate and correct the source of these differences has been enhanced in recent years through improvement in the states-of-the-art in wind tunnel model and facility simulation techniques, in application of Computational Fluid Dynamics (CFD), and in flight measurements (particularly in-flight thrust determination). Investigation has revealed that the major causes of these discrepancies are associated with:

- o The accounting process and approach used to isolate all required force elements during wind tunnel test programs, and proper combining of these forces at the full scale operating conditions.

- o Inadequate test techniques and procedures used to account for the effects, both internal and external, of model internal flow.
- o Lack of total understanding and accountability for the interference effects associated with wind tunnel model support systems.
- o Lack of accountability for the effects of wind tunnel wall interference on model measurements in the high subsonic and transonic Mach regimes.

Additional contributors to these differences may also include wind tunnel conditions, pressure gradient and flow angle; force balance uncertainty, model fidelity, accountability for Reynolds number effects, and jet exhaust temperature simulation.

This paper reviews and discusses wind tunnel capabilities, test techniques and procedures, uncertainty of results and "lessons learned" associated with the facility and simulation aspects of the wind tunnel development process for the critical aerodynamic drag parameter required for the accurate prediction of air vehicle performance. Areas of discussion include: (1) process employed for the derivation of full scale aerodynamic drag from wind tunnel tests, (2) need for and requirements of a force accounting system, (3) wind tunnel capabilities (flow field quality, model support systems and tunnel wall interference, (4) wind tunnel programs (simulation fidelity, internal flow measurement, propulsion interactions, and boundary layer simulation for Reynolds number effects).

Only the subsonic and transonic flight regimes are addressed herein. The supersonic flight regime is not addressed because of a lack of thorough documentation concerning error sources. However, the simulation and test technique principles are applicable to the supersonic flight regime.

2. WIND TUNNEL DRAG PREDICTION PROCESS

As illustrated in Fig. 1, the derivation of full scale aerodynamic drag (D_{REF} term in eq. (4)) from wind tunnel model tests is accomplished in a four-step process as follows:

Step 1. Model drag is determined at model operating conditions (m/m , NPR) and wind tunnel test conditions (M , Re , α). The accuracy of the model drag measurements at the model reference conditions (usually flow through inlet and exit conditions) is a function of the full scale configuration fidelity of the model, precision and resolution of the force balance measurements and quality of the wind tunnel flow conditions.

Step 2. Model drag measurements are corrected for the effects of wind tunnel and model items which are not representative of the full scale vehicle (e.g., support system, internal flow, wall interference, geometry distortion) and from model operating conditions to full scale reference operating conditions (reference conditions are discussed in Section 3) for inlet mass flow ratio and nozzle pressure ratio. These corrections are discussed in detail in Sections 4 and 5.

Step 3. The corrected model drag is adjusted from model scale to full scale to account for the effects of Reynolds number, Re , on vehicle skin friction drag. The Re drag adjustment is a function of surface boundary layer conditions (i.e., laminar or turbulent flow, and surface roughness). The usual Re adjustment is based on smooth flat plate turbulent boundary layer theory applied to each of the air vehicle components (body, wing, tails) at both the model test and full scale reference conditions. Various correlations of turbulent boundary layer data exist.^{1,2} One relationship for skin friction drag, for the fully turbulent, incompressible case, is given by Schlichting:

$$C_f(M=0) = \frac{.455}{(\log Re)^{2.58}} \quad (1)$$

Similarly, various correlations of the effect of compressibility on friction drag exist in the literature. The relationship defined by Frankl-Voishel is given by:

$$C_f/C_{f(M=0)} = \frac{(1 + \gamma - 1 M^2)^{-.467}}{2} \quad (2)$$

Because of normally low values of the model test Reynolds number and the low level of surface roughness on a typical model compared to the full scale vehicle, the model boundary layer must be "tripped" from potentially laminar to turbulent flow conditions (see Section 5.4). High levels of surface roughness on the full scale vehicle may result in non-achievement of the full Re beneficial drag reduction effect on some or all of the vehicle components, especially at the higher Reynolds numbers. This phenomenon is known as Re "cutoff". For the purpose of the drag prediction process, it is generally acceptable to assume that the full scale vehicle surface roughness can be controlled such that Re cutoff will not exist. This assumption should not be made if the levels of surface roughness anticipated for the flight vehicle are sufficiently high to precipitate Re cutoff. Accountability for surface roughness is discussed in detail in Ref. 1, Chapter II.

Variations on the smooth flat plate boundary layer theory discussed above have been employed in various aircraft development programs. These variations have included:

- o Empirical three-dimensional correction to account for the fact that aircraft components are comprised of curved versus flat surfaces.
- o Empirical correction for relating the drag associated with mutual interference between aircraft components (wing, body, tails) to Reynolds number.

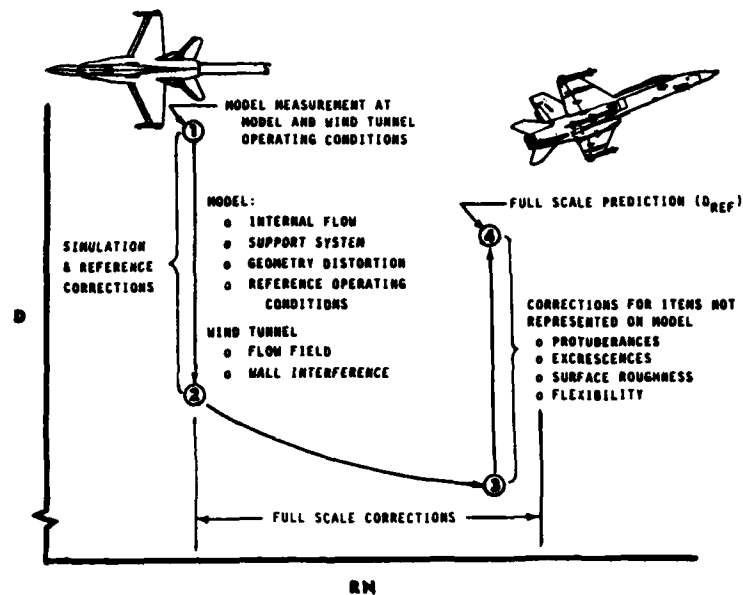


Fig. 1 Wind Tunnel to Flight Drag Prediction Process

- o Treatment of total drag (skin friction plus form or pressure drag) as a function of RN.
- o Combinations of the above.

Each of these modifications to the basic smooth flat plate skin friction boundary layer theory increases the magnitude of the incremental drag reduction from model test to full scale reference conditions. Flight measurements have validated only the basic flat plate turbulent boundary layer theory, except where RN cutoff is in evidence.^{3,4,5,6} Therefore, only this procedure should be employed in the wind tunnel based drag prediction process.

Step 4. The wind tunnel model drag adjusted to full scale RN in Step 3 is then corrected to vehicle full scale drag through accountability for those drag items that were not represented (or practical for representation) on the wind tunnel model, such as protuberances (e.g., antennae, air data sensors, scoops); excrescences (e.g., surface steps, gaps, mismatches and flush inlets and exhausts) and aeroelastic effects. Ref. 1 is generally the basis used for the protuberance and excrescence corrections. Aeroelastic corrections are not normally made to wind tunnel data but may be required for very large flexible aircraft configurations or if performance requirements exist at accelerated flight conditions. Analytic techniques are generally employed for flexibility corrections. At the performance prediction phase, however, a true accounting for these items is influenced by: (1) optimism in the manufacturing techniques to be employed to minimize excrescence drag, (2) optimism in the full scale vehicle protuberance requirements, and (3) fidelity of the prediction techniques in Ref. 1 and those used to account for vehicle flexibility.

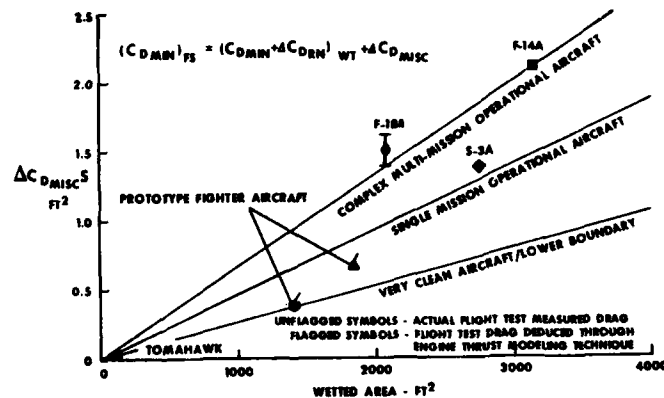


Fig. 2 Accountability for Drag Items Not Represented on Wind Tunnel Model

A separate check on the amount of drag associated with the estimate for these items is contained in Fig. 2 which was originally presented in Ref. 4 and is included here with an additional aircraft. This approach is based on historical tracking of resulting full scale air vehicle drag, as determined during the flight test documentation process, versus that determined at Step 3 in Fig. 1. The miscellaneous drag increment in Fig. 2 is an empirical approach to assessing those drag items associated with manufacturing tolerances, protuberances, excrescences, auxiliary equipment inlets and exhaust, leakage and cooling. The data in Fig. 2 indicates that the accountability for these items are functions of the vehicle size (wetted area), aerodynamic complexity, mission capability and stage of development (prototype or production aircraft). It should be recognized that the data in Fig. 2, in addition to accounting for items not represented on the model, could also contain residual errors from the wind tunnel aspects of the drag prediction process as discussed in Sections 4 and 5.

Subsequent discussion will address the details of force accounting systems and the wind tunnel aspects of the drag prediction process in Steps 1 and 2 of Fig. 1.

3. FORCE ACCOUNTING SYSTEMS

The discussion in this section is based on the Thrust-Drag methodology developed in Ref. 2, Chapter II. Fundamental to the success of accurate prediction of air vehicle performance is the selection of a force accounting or "bookkeeping" system, and supporting wind tunnel models and test procedures, tailored to the aerodynamic and propulsion system being evaluated. A well defined performance integration system is required to ensure that the various elements (i.e., inlet, exhaust, airframe, turbomachinery) of the airplane system are combined properly to yield an accurate prediction of overall system performance. Also, comparison of aircraft performance predictions with the results of the flight test documentation process requires an understanding of the elemental thrust and drag forces to validate the aircraft performance model and isolate the source of any aerodynamic or propulsion differences that may exist.

The need for a bookkeeping system in the wind tunnel based prediction phase of an aircraft development program arises largely from the inability to determine the performance of the complete airplane system, with simultaneous real inlet and exhaust operation, in a single test. The implicit assumption exists that the effect of the inlet, and exhaust nozzle can be measured separately and combined linearly. This is valid for the burried propulsion configuration, shown in Fig. 3, near the ideal angle of attack. The assumption may or may not be valid for some configurations and certain flight conditions. For the podded nacelle configuration, where the inlet and nozzle are aerodynamically close coupled, the assumption is rarely valid. For the latter configuration, use of a turbine powered engine simulator (illustrated in Fig. 4) or a separate CFD analysis may be required to accurately isolate the aerodynamic and propulsion force increments.

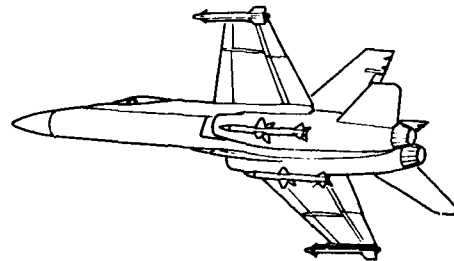


Fig. 3 Integrated (Burried) Propulsion System

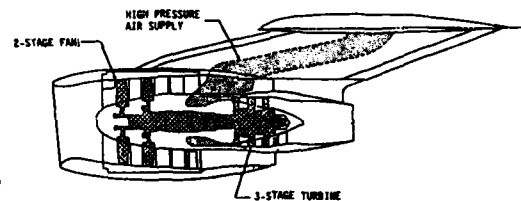


Fig. 4. Podded Nacelle Propulsion System with Turbine Powered Engine Simulator

The variety of actual and possible aerodynamic and propulsion system configurations makes it impractical to specify a single rigorous accounting system. The accounting system should, however, address the following characteristics:

- o Requirement for consistency. All forces must be accounted for once and only once.
- o The bookkeeping procedures should afford as much visibility as feasible to the performance of the elements of the airplane system.
- o Selection of reference conditions, although somewhat arbitrary, should provide for a way to correct the airplane drag polar to realistic inlet and exhaust system operating conditions.
- o The thrust-drag accounting methodology must be suitable and consistent for tracking of integrated propulsion/airframe performance throughout the aircraft development program.

Considering an aircraft in level flight, the simplified force equation applied in the flight direction takes the form:

$$F_{EX} = F_{IPF} - D_{AFS} \quad (3)$$

Additional forces included in the airframe system drag (D_{AFS}) and net propulsive force (F_{IPF}) terms account for defined or chosen reference full scale operating conditions and excursions from the reference full scale operating conditions. The breakout of the additional forces for a thrust-drag accounting system applicable to the fully integrated propulsion system illustrated in Fig. 3 is as follows:

$$F_{EX} = \underbrace{(F_N + \Delta F_{INL} + \Delta F_{EXH} + \Delta F_{TRIM})}_{F_{IFF}} - \underbrace{(\Delta D_{REF} + \Delta D_{INL} + \Delta D_{EXH} + \Delta D_{TRIM} + \Delta D_{RN})}_{D_{NFS}} \quad (4)$$

The incremental forces in Eq. 4 are not all inclusive but are characteristic of the kinds of items that must be included. Additional items, such as force increments due to inlet and exhaust of secondary airflow systems may be required.

The various elements of this accounting system are categorized relative to strictly defined reference and operating conditions (see Ref. 2, Chapter II for additional details) including aerodynamic (aero) reference, full scale geometry reference and full scale operating conditions. The establishment of full scale reference conditions requires selection of several variables, including inlet mass flow ratio, inlet geometry, nozzle pressure ratio, nozzle geometry, secondary airflows, and aircraft trim setting. Since these variables influence the installation drag, a fixed set of reference conditions must be identified.

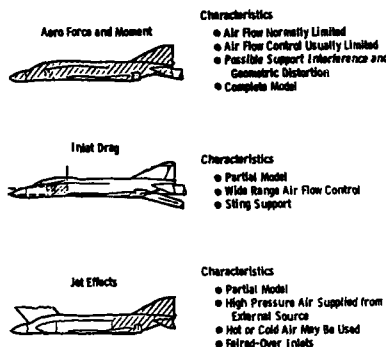


Fig. 5 Example Wind Tunnel Models

This accounting methodology must be supported by models and a wind tunnel test program designed to isolate the identified forces and force increments. Fig. 5 shows example wind tunnel models (including model characteristics) that would be required to isolate the aerodynamic forces and aerodynamic/propulsion force increments in Eq. (4).

The force elements identified in Eq. (4), although developed from wind tunnel model tests, are applicable to the full scale aircraft. A separate accounting system is required for the D_{NFS} term in Eq. (4) to correct the aerodynamic force and moment model measurements to the desired bookkeeping reference conditions, "real" aircraft geometry, and free air conditions (e.g., accountability for model support system, internal flow, geometry distortion and wall interference). The force terms F_N (installed engine net thrust) and ΔD_{RN} (drag associated with flight vehicle Reynolds number excursions from the full scale reference Reynolds number) in Eq. (4) are not germane to the subject matter of this paper and are not further discussed. The remaining elements of the force accounting system in Eq. (4) and corrections to the aerodynamic force and moment model measurements are discussed in subsequent Sections.

4. WIND TUNNEL CAPABILITIES

Traditionally, incremental data from wind tunnels have been considered to be quite valid. However, absolute data for total air vehicle configurations have been suspect because of flow quality and model/wind tunnel simulation uncertainties. These uncertainties and progress toward solutions in the 1983 timeframe, are discussed in Ref. 7. Recent advancements in instrumentation capabilities and increased understanding and attention to the details of the many elements of the wind tunnel process have enhanced confidence in the accuracy of absolute levels of wind tunnel data.

4.1 Flow Field Quality.

Instrumentation advances have made it possible to calibrate the wind tunnel with measurement uncertainties on the order of 0.0005 in Mach number from subsonic to low supersonic conditions and quote free-stream static pressure to an accuracy of one PSF.⁸ Total spatial angularity variations on the order of 0.1 degree are readily obtainable, even in large wind tunnels, and freestream turbulence levels now approach or equal those values obtainable in flight (e.g., in the AEDC Tunnel 16T, the root-mean-square value of stagnation pressure fluctuations is down a factor of three to five from the 0.5 percent of total pressure, typical of the timeframe of Ref. 9 and noted in Ref. 5 of this Symposium). Presuming that extreme care is taken to assure that the test section axial Mach number, or static pressure variations are minimal or non-existent, no buoyancy correction should be required as experienced in Ref. 10 and discussed in Ref. 4 of this Symposium.

Thus, the sources of continuing wind tunnel errors are the force and moment balances (discussed in Ref. 5 of this Symposium), model support system and tunnel wall interference and, unfortunately, test techniques employed in the wind tunnel process.

4.2 Model Support System Interference.

In many cases, the effects of the support system on model force and moment measurements are ignored because either they are assumed to be negligible or are judged as being too costly to evaluate.

AGARD-CP-242
REFERENCE 16, FIGURE 34

$R_{\text{REF}} = 12 \text{ ft}^2$

$C_D = 0.002$

$\Delta C_D = 0.0006$

C_D

0.001

0.6 0.7 0.8 0.9 1.0

M

FULL SCALE WIND TUNNEL

PLUG TEST

WALL INTERFERENCE

FULL SCALE WIND TUNNEL ADJUSTED FOR WALL INTERFERENCE USING THE TECHNIQUES OF REF. 12

● FULL SCALE WIND TUNNEL ADJUSTED FOR WALL INTERFERENCE USING THE TECHNIQUES OF REF. 12

experimentally. These assessments can lead to major problems in predicting vehicle performance as illustrated in Figs. 6 and 7. Fig. 6 shows three different mounting installations for the same wind tunnel model. The results of experimental isolation of the interference effects of each of these mounting systems are shown in Fig. 7. Also shown in Fig. 7 is the correction required for one of these mounting systems (AEDC Lower Sweep Sting) in a second wind tunnel facility. As can be seen, the variation in axial force interference correction among the three mounting systems is very large (100-200 drag counts depending on angle of attack). Equivalent variations in normal force and pitching moment were also observed as discussed in Ref. 4 of this Symposium.

When accounting for the effect of support systems experimentally, care must be taken in the design of the models and alternate support system to prevent flow interactions between the alternate and primary support system (e.g., for some configurations a wing tip mounting system may be required to isolate the effects of an aft mounted sting support system). Also, the increased blockage of the alternate support system could change wall interference effects in the transonic Mach regime. In this case, CFD may be required to isolate the secondary wall interference effects of the alternate support system. It should be noted that considerable success has been achieved in isolating support system interference through the use of CFD¹¹.

A major problem in wind tunnel to flight drag comparisons is the lack of correlation in drag divergence (or drag rise) in the transonic flight regime. Ref. 6 attributes this disparity, at least in part, to wall interference effects on wind tunnel models. Ref. 4 documents this problem showing three different drag rise characteristics for the same vehicle as evaluated from subscale, full scale and flight measurements, as shown in Fig. 8. Approaches which have been under evaluation to solve this problem include: (1) development of adaptive wall systems to eliminate the interference and (2) employment of wall interference assessment and correction techniques. Each of these approaches requires in-tunnel measurements and cannot be used to predict the effects of wall interference. Fig. 9 shows use of the prediction techniques of Ref. 12 in identifying extensive wall interference effects at the test blockage (ratio of vehicle cross sectional area to test section area) condition of approximately 8% which were correlatable with wind tunnel drag measurements having lower blockage values. Shown in Fig. 9 is the calculated distortion (incremental C_p variation) in model surface pressures as the difference between free air and that caused by the influence of the tunnel walls.

AD-A202 496

AERODYNAMIC DATA ACCURACY AND QUALITY: REQUIREMENTS AND
CAPABILITIES IN WIND TUNNEL TESTING (U) ADVISORY GROUP
FOR AEROSPACE RESEARCH AND DEVELOPMENT NEEDS

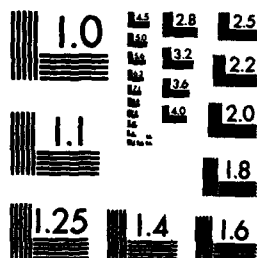
2/6

UNCLASSIFIED

JUL 88 AGARD-CP-429

P/G 1/1

NL



MICROCOPY RESOLUTION TEST CHART
NATIONAL BUREAU OF STANDARDS-1963-A

The magnitude and predominance of either the kinetic exit momentum or pressure force terms in Eq. 5 for duct drag determination are functions of the duct design (inlet/exit area ratio defining subcritical, critical or supercritical duct flow over the range of operating conditions to be evaluated) and the influence of the internal and external flow fields on the duct exit static pressure. It should be noted that the change in momentum from free-stream to exit conditions includes a change in direction from parallel to the wind axis to parallel to the body axis (assuming negligible exit inclination angle). Therefore, the effects on lift and pitching moment should be considered and evaluated, not arbitrarily ignored.

The free-stream conditions in Eq. (5) are determined from wind tunnel freestream measurements (V_∞ , P_∞ , and T_∞). Evaluation of the model internal drag, therefore, is dependent on model measurements of duct mass flow, m , duct exit velocity, V_e , and duct exit static pressure, P_e . This requires measurement of the average total and static pressures at relevant duct axial planes. Rake systems may be mounted internal to the duct and model or external at the nozzle exit plane. Models with internally mounted rakes also require measurement of the static pressure at the exit plane, while static pressure probes can be included on external rakes. Depending upon the configuration, externally mounted rakes can be attached to either the model itself or to the support system. For the case where the rake is attached to the model, the model force measurements are invalid. Therefore, two data runs are required - one for duct drag and a second, without the rake installed, for force and moment measurements. However, the pressure field of the rake can affect the exit momentum of the duct enough to be significant when the rake is removed. Therefore, it is recommended that internal duct exit static pressure measurements, in conjunction with rake installed total pressure data, be used to define duct mass flow and exit momentum when the force data (rake removed) is being obtained. For the case of the support system mounted rake, force data can be obtained with the rake attached. However, the rake installation must be accurately simulated when the support system interference is evaluated (discussed in Section 4.2). An additional problem that arises with the externally mounted rake system is that of alignment. As the model loading is varied with angle of attack, the rake is deflected relative to the model. Extreme care is required to assure correlation of the measured pressures with the duct exit geometry.

The above discussion is usually adequate for simple duct systems with relatively uniform flow. For these duct systems and especially for duct systems with distorted flow (which could be caused by separation, supersonic velocities or proximity of rake measurement probes to flow control devices), accurate determination of average duct conditions can be obtained by calibration of the duct system and instrumentation in a mass flow and thrust (if available) measurement facility to assess calibration factors for measured m , V_e and P_e .

Experience has shown that the best accuracy in internal flow and drag measurements is achieved, in descending order, by:

1. Mass flow and thrust (if possible) calibration of the duct and instrumentation systems.
2. Determination of mass flow and exit momentum with internally installed duct instrumentation.
3. Determination of exit total pressure recovery with externally mounted instrumentation rakes. Mass flow and exit momentum are obtained with this total pressure recovery and internally mounted exit static pressure measurement with the rake removed.
4. Determination of mass flow and exit momentum with external static and total pressure measurements.

5.3 Propulsion Interactions.

The force accounting system in Eq. (4) identified incremental forces that are a function of engine operating conditions. For this bookkeeping system, the throttle-dependent drags fall into three categories: inlet spillage drag, exhaust system or jet-effect drag and propulsion aspects of aircraft trim drag. These items are evaluated during wind tunnel programs employing various models as indicated in Fig. 5 and Section 5.1.

5.3.1 Inlet Spillage Drag

Throttle-dependent inlet spillage drag is defined as the change in aircraft drag resulting from the differences between the operating conditions and the operating reference condition inlet mass flow ratios. Spillage drag varies with inlet mass flow ratio as illustrated in Fig. 11. Drag of the aero-reference model inlet Fig. 11 (1) is included in the aero reference drag. The incremental drag between (1) and the full scale operating reference condition (2) represents the scale model to full scale drag correction ΔD_{INL} . Drag differences between engine operating conditions (3) and full scale engine reference conditions (2) are accounted for as throttle dependent inlet drag ΔF_{INL} to be included in the net propulsive force.

Inlet spillage drag is composed of two parts: (1) additive drag, which operates on the incoming air slipstream; and (2) lip suction force, which is due to the change in pressure caused by the mass flow change over the affected surface external to the inlet highlight area.

If the total surface area affected by inlet mass flow change can be defined, the additive and lip suction force elements can be determined separately with an inlet model incorporating extensive surface pressure instrumentation and inlet plane momentum instrumentation (total and static pressure). An alternative is to use the aerodynamic reference model or a specially designed inlet drag force model. For either of these cases, it is possible only to measure the total inlet spillage drag, or sum of the additive drag force and lip suction force. Whichever model approach is used, the data must be corrected for the internal flow momentum loss, as discussed in Section 5.2. If the aerodynamic reference model is used, it must be possible to vary the inlet mass flow by means of internal remote control valve(s) or by changing variable porosity "choke" plates or screens as indicated in Fig. 12. If internal rakes are used

for determining the inlet mass flow and exit momentum, care must be taken so that the choke plates or screens are not located such that they invalidate or adversely affect the rake measurements.

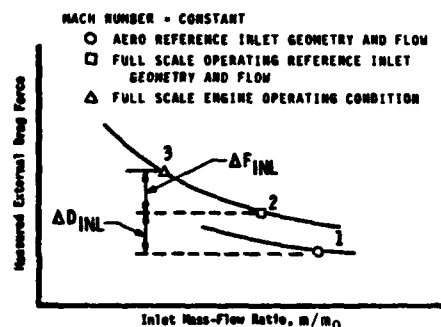


Fig. 11 Drag Force Variation with Inlet Mass Flow Ratio

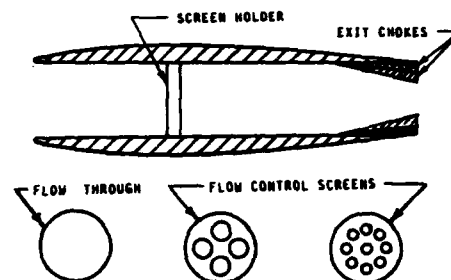


Fig. 12 Schematic of Model Flow Duct with Alternative Flow Control Devices

Mass flow variation through changing the model duct exit area (as shown in Fig. 12) is not recommended because the model base area is affected (which may add an additional error source in accounting for the base pressure-area correction) as well as the flow area (which requires a different rake installation if the exit total pressure or exit momentum is obtained with externally mounted rakes).

However the mass flow is varied, special care must be taken in order that the very slight change in duct exit nozzle pressure ratio, resulting from the flow rate changes, is well defined and does not cause a change in the model afterbody drag (Section 5.3.2) that might be confused with or considered to be inlet spillage drag. This can be a critical problem because, at flow through nozzle pressure ratios, the slope of afterbody drag as a function of nozzle ratio pressure is at a maximum value.

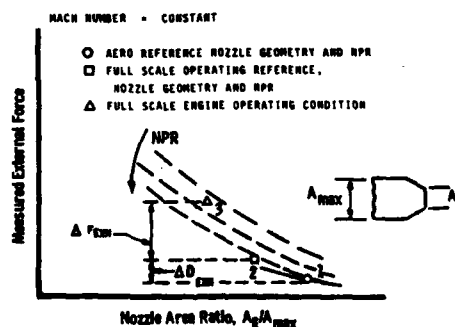


Fig. 13 Drag Force Variation with Nozzle Area and Nozzle Pressure Ratio

5.3.2 Exhaust System Drag.

Throttle-dependent exhaust system or jet-effects drag is defined as the change in aircraft drag resulting from the difference between the actual operating condition and the operating reference condition in terms of nozzle pressure ratio and area. For integral exhaust systems, nozzle pressure ratio can influence the afterbody pressure distribution and drag. Changing nozzle area alters the afterbody closure and pressure distribution, which in turn affects aircraft drag. Fig. 13 illustrates typical variations in aircraft drag with nozzle area and pressure ratio. Jet effects or powered model tests are conducted to evaluate throttle dependent exhaust system drag characteristics for accountability in Eq. (4). Drag of the aero-reference model nozzle in Fig. 13 (1) is included in the aero-reference drag. The incremental drag between (1) and the full scale operating reference condition (2) represent the scale model to full scale drag correction ΔD_{EXH} to be included in the full scale drag polar. Drag differences between engine operating conditions (3) and the full scale reference conditions (2) are accounted for as throttle-dependent exhaust system drag ΔF_{EXH} to be included in the net propulsive force.

The throttle-dependent exhaust system drag can be investigated for an integrated propulsion system (e.g., that shown in Fig. 3) using a blown afterbody model (as shown in Fig. 5) or a blown aircraft model. The term "blown" refers to the use of a high pressure external air source to vary nozzle pressure ratio. The airplane model inlets are usually faired over since the external rather than inlet airflow is exhausted. As with inlet procedure, either a model containing a force balance or one with extensive surface pressure instrumentation may be used to isolate the required force increments. Since the throttle-dependent drag is predominantly a pressure drag, no Reynolds number correction is usually required to relate scale model to full scale characteristics.

The high pressure air used to provide the nozzle pressure ratio to evaluate the jet interference is usually "cold" air. For some applications, especially afterburner operation, the exhaust gas temperature can have an appreciable effect on the jet interference drag. In this case, it may be advisable to either attempt simulation of the engine exhaust gas temperature levels or provide a correction to account for the difference.

5.3.3 Trim Drag

Trim drag is that drag associated with the change in control surface positions required for flight at the various full scale actual operating conditions throughout the vehicle flight envelope. Throttle-dependent trim drag is defined as the change in aircraft drag resulting from the difference in control surface positions required for trim at the actual operating condition and that required for trim at the full scale operating reference conditions in terms of inlet mass flow ratio and exhaust system NPR and area.

The variation of aircraft drag with control surface deflections is determined with the aerodynamic force and moment model through measurement of model drag and pitching moment while incrementally changing control surface positions. These data are the basis for determining the throttle-dependent trim force increments in Eq. (4) (ΔD_{trim} and ΔF_{trim}) through evaluation of any moment changes associated with determination of the throttle-dependent inlet spillage and the exhaust system forces discussed in Sections 5.3.1 and 5.3.2.

ΔD_{trim} is the external force increment due to the change in control surface position from that required for trim at the aerodynamic reference (usually aero model) conditions to the control surface position required for trim at the propulsion operating reference conditions and actual center-of-mass location. ΔF_{trim} is the throttle-dependent external force due to the change in control surface position from that required for trim at the reference inlet, exhaust and center-of-mass location to that control surface position required for trim at the actual inlet and exhaust operating conditions.

5.4 Boundary Layer Simulation

As stated previously, the normally low values of Reynolds number and surface roughness for subscale models results in non-representative boundary layer conditions (affecting skin friction drag and, potentially, flow separation) compared to the full scale vehicle.

Boundary layer modification to simulate full scale flow conditions (laminar to turbulent) or fix shock locations, is usually accomplished by installing boundary layer transition trips on the model surfaces. Transition trips normally consist of glass beads or carborundum grit embedded in an adhesive. The transition strips must be of sufficient height to affect boundary-layer transition without interfering with the model drag measurements. Requirements for grit sizing to meet these conditions are detailed in Refs. (14) and (15).

Location of the boundary-layer transition trips, particularly for the wing, is dependent on the flow conditions. For non-critical flow, the transition trips should be located downstream of the leading edge suction peak and maximize simulation of the full scale turbulent boundary layer flow conditions. For supercritical wings, boundary layer transition can affect the shock-wave location on the model and the presence and extent of shock-induced separation compared to the full scale vehicle. The technique used to minimize scale effects in shock-induced separated flow is to fix the boundary-layer transition point at the proper location on the wind tunnel model so that the boundary-layer on the model is simulated in the region of the separation. Reference (16) outlines procedures for location of the transition trips. The transition trip locations may be different on the upper and lower wing surfaces. If boundary-layer simulation is based on shock location considerations, an accounting must be made for the effect of laminar flow ahead of the transition trip location on skin friction drag. This adjustment can either be based on evaluation of the results of Reynolds number variation tests in the wind tunnel or the theory discussed in Section 2, Step 3.

Problems that have been encountered in wind tunnel programs relating to boundary-layer simulation include: (1) lack of accountability for the effects of laminar flow on skin friction drag when boundary-layer simulation was based on shock location, and (2) boundary-layer not tripped on full scale wind tunnel model. Reynolds number variations should be included in the wind tunnel test program to determine that turbulent flow exists or provide the basis for corrections if some flow is laminar (e.g., when transition is set to replicate shock locations). Model manufacturing procedures, even for full scale models, can result in partial laminar flow conditions on the model compared to turbulent boundary-layer conditions for the flight article (made using production manufacturing techniques and tolerances).

6. CONCLUDING REMARKS AND LESSONS LEARNED

The current state-of-the-art in wind tunnel facility and model simulation techniques and procedures is such that high quality results are achievable, at least in the subsonic and transonic flight regimes. Continued improvement in the fidelity of wind tunnel simulation is expected as CFD applications are refined, especially in the areas of accountability for the effects of model support systems and wind tunnel wall interference. Highly accurate results, such as those required for contract commitments, can be obtained with devotion of sufficient resources to ensure that the items discussed herein are rigorously followed. Unfortunately, attempts are continually made (usually because of perceived scheduling and/or monetary constraints) to compromise the fidelity of the simulation program. This invariably produces adverse results requiring additional resources to correct the problems resulting from these compromises.

Returning to Fig. 1, the overall lessons learned concerning the drag prediction process include:

- A force accounting system must be identified at the inception of a program. This system must be compatible with the aerodynamic and propulsion system being evaluated.

- o The scale model tests to support this accounting system must be conducted in a facility of known flow quality using proven test techniques and procedures designed to enhance the fidelity of the simulation.
- o Scaling of the wind tunnel results for the effects of Reynolds number on skin friction drag should be based only on flat plate turbulent boundary-layer theory.
- o Adjustment of the wind tunnel drag measurements for the effect of items not represented (or practical for representation) on the wind tunnel model should be realistic.

Specific lessons learned to ensure fidelity of the wind tunnel simulation include:

- o It is absolutely necessary to understand and account for the effects of model support systems.
- o The potential effects of wind tunnel wall interference should be defined and accounted for, if required.
- o The effects of model internal flow must be accurately isolated.
- o The effects of propulsion system interactions must be thoroughly evaluated.
- o Boundary-layer simulation must be thoroughly understood to provide the proper corrections to flight Reynolds number.

REFERENCES

1. Hoerner, S. F.; "Fluid-Dynamic Drag", Published by the Author, 1968.
2. Covert, E. E., et al; "Thrust and Drag: Its Prediction and Verification", Progress in Astronautics and Aeronautics, Vol. 98; AIAA, New York, 1985.
3. Rooney, E. C.; "Development of Techniques to Measure In-Flight Drag of a U.S. Navy Fighter Airplane and Correlation of Flight Measured Drag with Wind Tunnel Data", AGARD-CP-124 October, 1973.
4. Rooney, E. C.; Craig, R. E.; "Development of Techniques and Correlation of Results to Accurately Establish the Lift/Drag Characteristics of an Air Breathing Missile from Analytical Predictions, Sub-Scale and Full Scale Wind Tunnel Tests and Flight Tests", AGARD-CP-242, May 1978.
5. Craig, R. E.; Reich, R. J.; "Flight Test Aerodynamic Drag Characteristics Development and Assessment of In-Flight Propulsion Analysis Methods for the AGM-109 Cruise Missile"; AIAA Paper No. 81-1423, November 1981.
6. Saltzman, E. J. and Ayers, T. G.; "Review of Flight-to-Wind Tunnel Drag Correlation", J. Aircraft, Vol. 19 No.10, October 1982.
7. Elsenear, A.; "Technical Evaluation Report on the Fluid Dynamics Panel Symposium on Wind Tunnels and Testing Techniques", AGARD AR-193, May 1984.
8. Magnon, J. W.; et al; "Pressure Measurement for the Determination of Wind Tunnel Performance", ISA Paper No. 87-0206, May 1987.
9. Dougherty, M. S. Jr and Fisher, D. F.; "Boundary-Layer Transition Correlation on a Slender Cone in Wind Tunnels and Flight for Indications of Flow Quality", AEDC-TR-81-216, AD-A111328, February 1982.
10. Carlin, G. J. Jr and Bevan, D.; "Prediction of Subsonic Wind Tunnel Mounting System Interferences", J. Aircraft, Vol. 24 No. 5, May 1987.
11. Suhs, M. E.; "Computational Estimates of Strut Support Interference at Transonic Mach Numbers", AIAA Paper No. AIAA-85-5018, October 1985.
12. Donegan, T. L.; Benek, J. A. and Erickson, J. C. Jr; "Calculation of Transonic Wall Interference", AIAA Paper No. 87-1432, June 1987.
13. Peters, W. L.; "A Simulation technique for Jet Temperature Effect on Nozzle-Afterbody Drag at Transonic Mach Numbers" AIAA Paper 85-1463, July 1985.
14. Braslow, A. L.; and Knox, E. C.; "Simplified Method for Determination of Critical Height of Distributed Roughness Particles for Boundary-Layer Transition of Mach Numbers From 0 to 5", NACA TN 4363, 1958.
15. Braslow, A. L.; Hicks, R. M. and Harris, R. V. Jr; "Use of Grit-Type Boundary-Layer-Transition Trips on Wind-Tunnel Models", NASA TN D-3579, 1966.
16. Blackwell, J. A. Jr; "Preliminary Study of Effects of Reynolds Number and Boundary-Layer-Transition Location on Shock-Induced Separation", NASA TN D-5003, 1969.

MEASUREMENT UNCERTAINTY OF THE AGARD/PEP UNIFORM
ENGINE TEST PROGRAM

by

J.P.K. Vliegert
National Aerospace Laboratory NLR
Postbus 90502, 1006 BM Amsterdam,
The Netherlands

SUMMARY

In the AGARD/PEP Uniform Engine Test Program (UETP) two engines were tested in 8 facilities in 5 different countries to compare measuring practices and results. The underlying report gives an overview of the UETP with the emphasis on Uncertainty Assessment according to the method proposed by Dr. Abernethy, in which the total Uncertainty is split in a random error (scatter, precision) and a bias error or offset. The results show that the random error is small but that appreciable bias error exists between participants.

1. INTRODUCTION

The Uniform Engine Test Program was instigated in 1980 by the then Chairman of the Propulsion and Energetics Panel of AGARD, Prof. E.E. Covert, to compare engine performance as measured in different test cells. Similar programs have been executed comparing performance of a standard aeroplane or missile model in different wind tunnels. In the case to be presented the comparison is hindered by the fact that the test item does not necessarily stay the same throughout the testing period. To check for possible deterioration or alteration of the engine characteristics it was arranged for the engine to return to the first site for its last test, to try to eliminate possible site effects from the comparison.

An advantage of testing an engine as compared with a wind tunnel model is the fact that the results of different measurements are to some extent interdependent through thermodynamic relations, which can be used to check the results. On the other hand the configuration of a modern high pressure engine must vary considerably over its running range, which can introduce discrepancies due to - for instance - slight differences in the setting of the variable stator vanes. As a measuring program which covers this by testing at different settings would be prohibitively expensive, an older engine type was chosen with a minimum of variable configuration, i.e. only on/off intercompressor bleed valves, and the engine was tested only over the higher thrust range with the bleed valves closed.

To ensure the best possible comparability and to safeguard against failure, two engines were used with a reference instrumentation package, containing pitot/static probes for in- and outlet together with thermocouples to determine average flow conditions. Fig. 1) shows the different stations in the engine which were instrumented to some extent; more so than would be the case on a production engine test, but not as extensively as on a development engine. A General Test Plan (GTP; ref. 1) gives details of the instrumentation.

The probes and duplicated fuel flow meters travelled with the engines; each facility used its own transducers and recording system. Apart from the reference system each participant used its standard test cell instrumentation to determine flow conditions and engine performance, including separate fuel flow meters and a thrust stand.

An Altitude Test Facility consists of machinery to provide engine intake air at the total pressure and temperature representative of the desired flight conditions, while additional machinery maintains the cell pressure and therefore the exhaust back pressure at the value equal to the static pressure at flight altitude. The engine is usually run "connected" to the intake piping, i.e. not with a representative intake and not with outside flow apart from cell ventilation. Fig. 2) gives a typical test cell without the extensive installation required for air conditioning. Between engine and test cell is a sliding seal which does not transmit axial forces - or only known, small ones -; the thrust measured results from the impulse difference of the air mass flow through the engine in this arrangement. It is not necessarily equal to the in-flight thrust, but this value can be calculated from the measurements. In a "connected" test interference effects like pre-entry drag, intake efficiency and post-exit thrust cannot be evaluated.

2. TEST PROGRAM

The engines were tested at 10 conditions which exercised the ATF over a large part of its capability, i.e.

TABLE I
Test Conditions

P =	12	7.5	5.0	3.0	psia
	82.7	51.7	34.5	20.7	(KPa)
T =	253	268	288	308	K
PR =	1.00	1.06	1.30	1.70	-
	st	0.29	0.62	0.90	Ma

Not all combinations were tested, and in some cases a test was added at a condition as close to sea level static as the capability of the ATF allowed, so as to have a reference for a static test bed. Tests were done in 5 countries at 8 facilities, 4 of which were ATF

TABLE II
List of Participants (in order of testing)

		type
1) NASA Lewis Research Center Cleveland, Ohio, USA	(LeRC)	ATF
2) Arnold Engineering Development Center Arnold, Tennessee, USA	(AEDC)	ATF
3) National Research Center of Canada Ottawa, Ontario, Canada	(NRCC)	g_d level
4) Centre d'Essais des Propulseurs Saclay, France	(CEPr)	ATF
5)		and g_d level
6) Engine Overhaul Division Turkish Air Force Ankara, Turkey	(TuAF)	g_d level
7) Royal Aircraft Establishment formerly Natl Gas Turbine Est. Pyestock, Hampshire, UK	(RAEPy)	ATF
8) Naval Air Propulsion Center Trenton, New Jersey, USA	(NAPC)	open air

the engines were retested at NRCC and at LeRC

At each condition the engines were tested in 9 steps over the full thrust range with intercompressor bleed valves closed, which means successively setting up a number of values of high pressure spool RPM (N2), holding each point till conditions are stabilised, and then making a recording of all parameters. In the subject case stabilisation times of 2-3 mins were used to settle internal temperatures (and therefore blade tip- and labyrinth seal clearances), after which two recordings were made. During this stabilisation time engine output may change several percent. The interfacility comparison was made at the Target Value, which was approximately mid-range of the tests.

Each facility prepared a test plan based on the General Test Plan (ref. 1) with an a-priori estimate of the accuracy expected to be attained. Measuring results were validated within the facility and then reported to an evaluation team consisting of the facilities who had already tested and a number of experts comprising Working Group 15 of AGARD/PEP. Its results are reported in Ref. 2). The results of the Accuracy Assessment were analysed by a Sub-Group of WG 15. From its findings an AGARDograph has been prepared (ref. 3) of which the present report is an abstract. The interested reader will find a lot more detail in the References given.

3. UNCERTAINTY METHODOLOGY

3.1 Error types

The uncertainty analysis used is the method proposed by R.B. Abernethy and J.W. Thompson in the Handbook Uncertainty in Gas Turbine Measurement (Ref. 4). According to this method the total Uncertainty (U) can be split up in a random error (scatter (S), precision) and a bias (B) or offset, which is systematic but in first instance unknown -all known offsets are corrected for by calibration.

RAEPy used to work with the MIDAP classification (ref. 5) which in fact splits up the bias error in a day-to-day variation and a long term variation. By introducing the "Defined Measurement Process" (DMP) both models can be reconciled; any errors which vary in this process are classified as scatter, while a fixed error is bias. The latter can therefore only be found by comparing the results of several DMP's. This has the consequence that errors may change class according to the extent of the DMP. In first instance a result may be determined from a least squares curve fit of a number of tests, which constitute a DMP. Comparing a number of such results from different but comparable DMP's constitutes a new DMP in which a least some of original bias errors appear as scatter.

The above process serves to estimate part of the bias error; this assumes that mistakes and malfunctions (like leakage or defective instruments) have been eliminated. This can be done by careful control that the right calibrations have been used and comparing redundant instruments or measurements, e.g. reducing the engine parameters to standard sea level conditions for comparison. Other possibilities in this field are to calculate non-engine related parameters like the nozzle flow- or thrust coefficient. To facilitate evaluation of this the engine's original centerbody nozzle has been replaced by an extended conical nozzle with rake instrumentation (see ref. 1).

3.2 Error Evaluation

3.2.1 Prediction Synthesis

For error prediction by synthesis a complete, exhaustive list must be made of every possible error for all measurements that affect the end test result. These can be grouped in categories as follows (see fig. 3):

- 1) elemental errors in determination of the Basic Physical Parameters i.e. pressure, temperature, force, length and time or frequency. These can be subdivided in the following groups:
 - a) Calibration Hierarchy; i.e. relation to a standard
 - b) Data Acquisition due to outside influences on data transmission, transducer, signal conditioning and recording
 - c) Data Reduction, e.g. resolution and curve fit errors
 - d) Non-Instrument or Sensor System errors, for instance probe errors, Thrust Zero, pipe swirl in a fuel flow meter

- 2) Errors in the determination of the Input Parameters which define the effective values in the engine. This error is connected with the number of transducers used and possible pattern variation and can be closely related to 1d).

The total bias and precision can be determined by adding the elemental contributions. If these are unrelated the best estimate is by Root-Sum-Square (RSS) addition in each category. An overall estimate of the Uncertainty of a single test result can then be given by combining bias and precision error. Usually, however, precision is based on statistics of calibrations or of previous test results, while bias errors have an element of engineering judgement. Therefore it is not strictly correct to add both contributions into a single Uncertainty value with a statistical confidence level. Abernethy gives two values, with the following effective confidence levels, i.e.

$$U_{add} = B + t95.S \quad (\text{appr. 99\% coverage})$$

$$U_{rss} = \sqrt{B^2 + (t95.S)^2} \quad (\text{appr. 95\% coverage})$$

in which $t95 = 2$ for more than 30 degrees of freedom.

The engine Performance Parameters - the most important being Thrust, Specific Fuel Consumption and Air Flow - are related mathematically to the above named Input Parameters. To calculate the Uncertainty in such a Performance Parameter the Influence Coefficients must be determined, which can be done mathematically by perturbing the equation (given in Ref. 1) over a small range; e.g. 1 or 2%, of the Input Parameters. An example is given in Table III; the resulting bias and scatter can then again be found by RSS addition. As the way a Performance Parameter is determined depends to some extent on the installation, the Influence Parameters of the different facilities are not directly comparable.

There is one more source of error when the Target Point is determined from a curve fit at a certain value of a comparison parameter, if that parameter itself is subject to error. This Curve Slope Effect can be determined as $\Delta y = \Delta x \left(\frac{\partial y}{\partial x} - \frac{\partial x}{\partial x} \frac{dy}{dx} \right)$ where $\frac{\partial y}{\partial x}$ and $\frac{\partial x}{\partial x}$ are the Influence Coefficients of the Performance Parameters y and x , i.e. the partial derivatives due to variation of the Input Parameters x , and dy/dx is the curve slope. This latter value is particularly large when using high pressure spool RPM (N2); this is therefore not a very suitable comparison parameter.

3.2.2 Test Data Analysis

Prediction Synthesis is essential to find out if there are any weak links in the measurement chain and it is useful as a reference as to what discrepancies can be tolerated during testing and as an aid in trouble shooting. For supervising the test results a Test Data Analysis must be performed, preferably on-line as then the tests can be repeated or halted if required with a minimum of wasted effort.

Test Data Analysis can be a check on the variation of, or on outliers in specific parameters during a single test or it can encompass such a check on the end results of a number of tests, constituting a DMP. In the latter case it is possible to calculate the Random Error Limit of Curve Fit (RELCP, see ref. 6) which is a measure of the scatter within this DMP. The RELCP gives the limits on both sides of a fixed curve within which the true curve is expected to lie, within 95% probability.

As was discussed in 3.1 this scatter contains some of the bias errors of the constituting tests, but by no means all as a number of usually consecutive tests is not truly independent. Therefore bias errors remain which can be found by comparing end results of preferably different facilities, if these differ more than the RELCP values. Hopefully these differences will be within the predicted bias errors, otherwise the prediction must have missed an important source of bias error.

It is emphasized that an outlier must only be skipped after analysis if a good technical reason is found; the analysis may show up hidden faults in the instrumentation or in the set-up for the experiment.

4. INSTRUMENTATION AND CALIBRATION SYSTEMS

The different participants use systems for their facility measurements which differ in number and position of probes, in number of transducers and in cycle time. The reference probe system is the same for all, but in one case rake probes were manifold before recording. Most facilities use mechanical scanning for pressures, where a number of pressure lines are connected in sequence to a single transducer. In several cases relatively large volume high accuracy transducers were used, which require line pressure to be stabilised after switching, resulting in a relatively long cycle time (1 minute or more).

Some facilities had each pressure line connected to its own transducer - in one case even to two - and used electronic scanning. In that case the cycle time can be in the order of a few seconds, and several scans can be made in 20-30 seconds, which allows a check to be made on unsteadiness of instruments, engine and facility. During each dwell - i.e. the time a certain transducer is connected to the recorder system - a number of readings (n) can be made which exercises the signal conditioner and the analog-to-digital converter, reducing some of the errors with \sqrt{n} . The transducer error is not reduced because the transducer is not exercised. To prevent aliasing, the transducer signal must go through a low pass filter compatible with the reading frequency.

Calibration was generally done at least once a day using a separate calibration manifold, with reference values also measured by laboratory standards. An automatically calculated first or second order curve is then used for the tests that follow. NASA PSL-4 in the test of the returned engines could do this on command or automatically every 20 mins. With mechanical scanning some test points can be included in the scan to give a check on transducer reliability.

5. RESULTS OF THE ACCURACY ASSESSMENT

In first instance the estimated bias and scatter for the main Performance Parameters Thrust, SFC and Airflow were compared and found to vary considerably between participants. Therefore it was proposed to go into further detail in the estimation procedure. To this end the North American facilities put together an Error Audit which detailed items to be considered for each of the Basic Physical Parameters. An example is given in Table IV. The errors were to be evaluated at Target Point, for a low altitude case and for high altitude, where the measured values are smaller and in many cases the relative error larger.

Fig. 4, 5, 6 and 7 give the error values for the Physical Parameters. Different facilities tend to group their errors together differently and they do not agree which group is most significant. Partly this reflects real differences in the total instrumentation systems, but also modelling, i.e. accounting differences play an important role. A lot of discussion took place about this assessment and although full agreement could not be reached the final results were much closer than the initial values. Some critical items are mentioned underneath.

Stand Force constitutes the larger part of engine net thrust; the electrical calibration is highly reproducible, but the test stand zero is a critical item, especially at altitude.

Air Flow is in most cases measured by determining airspeed in a section of the intake tube; if this is taken too wide the speed is low which decreases accuracy, while a small section may give trouble due to boundary layer growth in the divergent section leading into the engine. Airflow is not directly a performance parameter but it is needed to correct the intake momentum drag to arrive at the true net thrust value.

Fuel Flow: in all but one case turbine type flow meters were used. Although the accuracy remains a constant percentage of the value measured over most of the range, this type of meter is sensitive to swirl in the pipes which can be induced by bends and it is doubtful whether introducing a straight end of piping and a flow straightener before and after the transducer suffices to remove this error in all cases.

Pressure error varies over the instrument measuring range. Different facilities used a constant percentage over a fraction of the range varying from 1/3 to 4/5. Below this range the absolute error is assumed constant, which means an increasing percentage error (see fig. 8).

Temperature bias error was generally taken to be 0.5 to 1 C, but no agreement existed about errors for thermocouples and resistance probes.

The final results for the accuracy of the Engine Performance parameters are given in fig. 9). This shows, despite the above discussed detail differences, that in most cases reasonable agreement exists, except that AEDC claims a lower error at altitude, and comes out with a somewhat higher error at low altitude. The precision- and bias errors are given separately for different altitudes. RAEPy has done an in-depth Post Test Analysis of their RELCP values (see fig. 10) and concludes that quite good agreement exists between predicted and observed values, but that random error is small relative to the possible bias. An example is given in fig. 11 for the thrust coefficient which shows that the envelope covering all conditions in one facility does not quite cover that of another facility, showing that bias errors do exist. In most cases there is no apparent systematic variation of the thrust coefficient with measuring condition within the facility.

6. CONCLUDING STATEMENTS

- 1) There is reasonable overall agreement in the second error assessment of the participating facilities, after extensive discussion and the setting up of an Error Audit.
- 2) There is no detail agreement about error sources. This may reflect real differences in instrumentation systems, but also the accounting differs, even within the Error Audit format.
- 3) The calibration error, which is usually given as a percentage of full scale output by the manufacturer, can be reduced appreciably and kept a constant percentage to a fraction of FSO by employing multiple calibrations during the test period and applying the results as the tests progress. Usually higher order than linear is employed.
- 4) Non-Instrumentation - or Sensor System - effects are difficult to quantify. They are a potent Source for bias errors which do not necessarily reduce with the value measured and therefore can have a large relative effect at altitude.
- 5) Post-test analysis shows the random error to be small relative to the possible bias error. This is shown up in the results by the fact that Random Error Limits of Curve Fit for different facilities often do not cover each other.
- 6) It is essential to check the test results in-house, first for errors and malfunctions, and secondly for consistency, reducing the measured values to non-dimensional parameters and calculating nozzle coefficients, which should not be engine-dependent.
- 7) There is a trend towards the use of multiple transducers with electronic scanning for transient testing, with mechanical scanning only being used for periodic on-line calibration.
- 8) This has been a most useful exercise in all its aspects, that is the actual testing, validation of the results, and the accuracy assessment. The less-experienced participants have obviously learned a lot, but also the big facilities have gained by exchanging engineering practices.

The author would like to thank all the members of WG15 for their generous assistance, without which this document could not have been prepared.

7. REFERENCES

- 1) AGARD-PEP Working Group 15 Uniform Engine Testing Program General Test Plan revised edition Dec. 1982
- 2) AGARD-PEP Working Group 15 Results of the Uniform Engine Testing Programme Issue no. 2, April 1987
P.F. Ashwood

- 3) AGARDograph 307 Investigation of Measuring Uncertainty within the UETP
AGARD-PEP sub WG15 preliminary issue spring 1987
J.P.K. Vlaghart
- 4) R.B. Abernethy Handbook Uncertainty in Gas Turbine Measurement
J.W. Thompson AEDC-TR-73-5
- 5) AGARDograph 237 Guide to In-Flight Thrust Measurement of Turbojets and Fan Engines
MIDAP Study Group Jan. 1979
- 6) J.C. Ascough A Test Code for Contract Performance Measurement
NGTE 78020 April 1978

BASIC MEASUREMENT (x1)	NOMINAL VALUE	BIAS LIMIT %	PRECISION INDEX %	INFLUENCE COEFFICIENT ($\partial x_i / \partial y$)				BIAS LIMIT ($b_i \pm \partial x_i$)				RESULT	PRECISION INDEX ($s_i \pm \partial x_i$)			
				SFC	FNR	WAFR	WFR	SFCR	FNR	WAFR	WFR		SFCR	FNR	WAFR	WFR
T2	289 K	0.42	0.17	-0.51	0.01	0.01	-0.5	0.21	0.00	0.00	0.21	0.09	0.00	0.00	0.00	0.09
P2	99.7 kPa	0.09	0.05	0.66	-1.64	0.46	-1.0	0.06	0.15	0.04	0.09	0.03	0.08	0.02	0.05	
PS1	93.6 kPa	0.10	0.05	0.10	-0.10	-	-	0.01	0.01	-	-	0.01	0.01	-	-	
	6.4 kPaA	0.67	0.07	-	-	-0.47	-	-	-	0.32	-	-	-	0.03	-	
PAMB	99.3 kPa	0.09	0.05	-0.47	0.47	-	-	0.04	0.04	-	-	0.02	0.02	-	-	
WF	680 g/s	0.26	0.08	1.0	0.01	-	1.0	0.26	0.00	-	0.26	0.08	0.00	-	0.08	
SG	0.78 g/kNs	0.28	-	1.0	0.01	-	1.0	0.28	0.00	-	0.28	-	-	-	-	
FS	29.8 kN	0.41	0.06	-0.98	1.0	-	-	0.40	0.40	-	-	0.06	0.06	-	-	
A2	0.54 m ²	0.09	-	-0.01	0.01	1.0	-	0.00	0.00	0.09	-	-	-	-	-	
A8	0.24 m ²	0.09	-	0.0	0.00	-	-	0.00	0.00	-	-	-	-	-	-	
TFUEL	290 K	0.25	0.17	-0.25	-	-	0.26	0.06	-	-	0.06	0.04	-	-	-	0.04
CD1	-	0.50	-	-	-	1.0	-	-	-	0.5	-	-	-	-	-	
Bias and Precision Root Sum Square Totals (%)								0.60	0.43	0.60	0.45	0.14	0.10	0.04	0.13	

Uncertainty % SFCR 0.88 WAFR 0.68
FNR 0.63 WFR 0.71

TABLE III NRCC BIAS AND PRECISION ESTIMATES FOR RESULTANT PERFORMANCE PARAMETERS

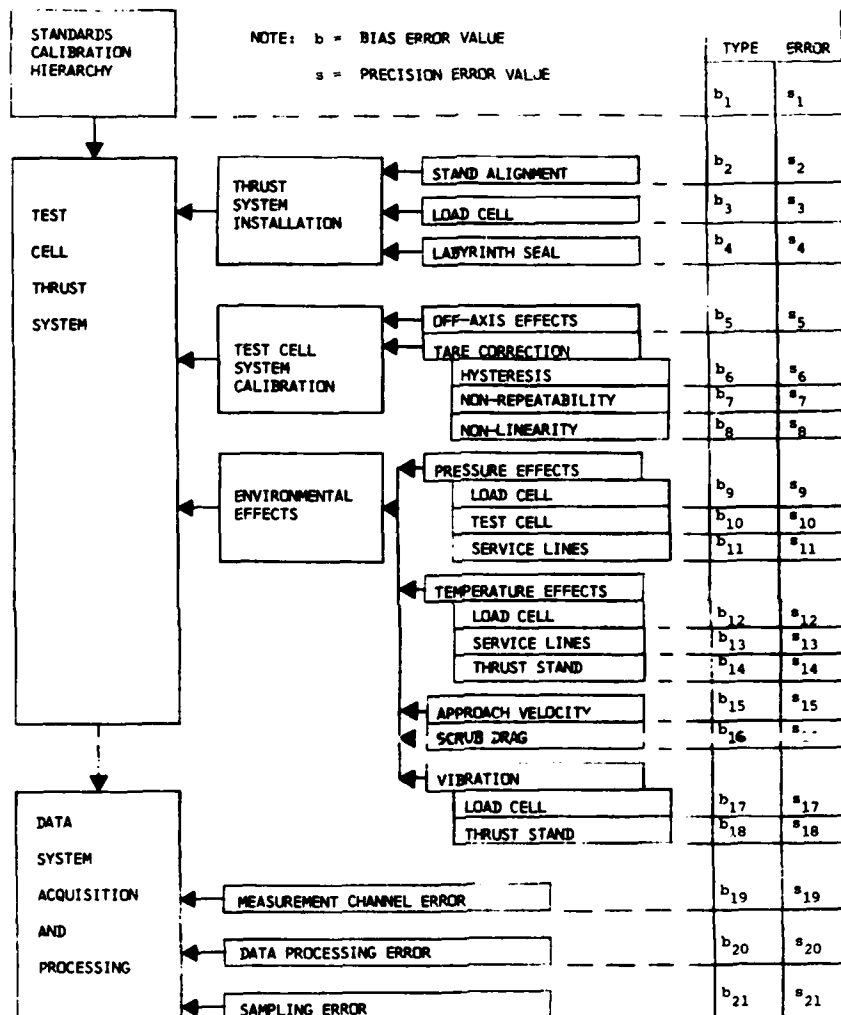


TABLE IV FORCE MEASUREMENT ERROR SOURCE DIAGRAM

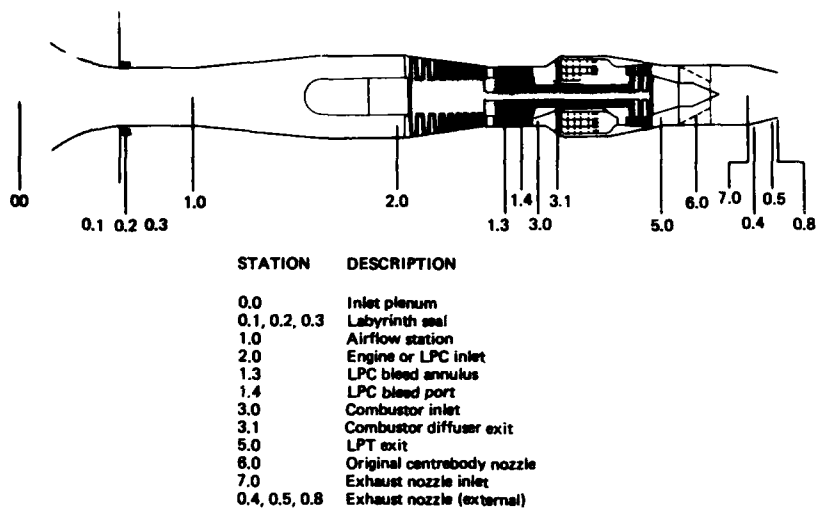


FIG 1 INSTRUMENTATION LOCATIONS

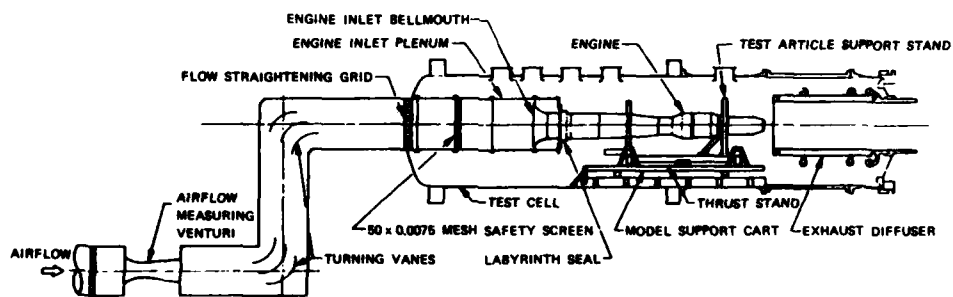


FIG 2 TYPICAL ENGINE INSTALLATION IN ALTITUDE TEST CELL

Figure 1 displays a series of bar charts arranged in a 5x10 grid. The rows represent different categories: NASA, AEDC, NRCC, RAE, and CEPy. The columns represent different groups: CAL, THRUST SYST. INST., TEST CELL SYST CAL, ENV. EFF'S, D.ACO, D.RED, and TOTAL R.S.S. Each chart shows the percentage distribution of various items (represented by numbered bars) for that category and group. The y-axis for each chart ranges from 0 to 1.5%.

The categories and their corresponding groups are:

- NASA:** CAL (1*), THRUST SYST. INST. (2, 3, 4), TEST CELL SYST CAL (6, 7, 8), ENV. EFF'S (9, 14), D.ACO (19), D.RED (20), TOTAL R.S.S. (8, 5).
- AEDC:** CAL (1*), THRUST SYST. INST. (2, 3, 4), TEST CELL SYST CAL (6, 7, 8), ENV. EFF'S (9, 14), D.ACO (19), D.RED (20), TOTAL R.S.S. (8, 5).
- NRCC:** CAL (1*), THRUST SYST. INST. (2, 3, 4), TEST CELL SYST CAL (6, 7, 8), ENV. EFF'S (9, 14), D.ACO (19), D.RED (20), TOTAL R.S.S. (8, 5).
- RAE:** CAL (1*), THRUST SYST. INST. (2, 3, 4), TEST CELL SYST CAL (6, 7, 8), ENV. EFF'S (9, 14), D.ACO (19), D.RED (20), TOTAL R.S.S. (8, 5).
- CEPy:** CAL (1*), THRUST SYST. INST. (2, 3, 4), TEST CELL SYST CAL (6, 7, 8), ENV. EFF'S (9, 14), D.ACO (19), D.RED (20), TOTAL R.S.S. (8, 5).

The CEPy row includes a double-headed arrow between columns 6 and 14, indicating a comparison or relationship between these two groups.

FIG 4 ERROR BUILD-UP FOR THRUST STAND

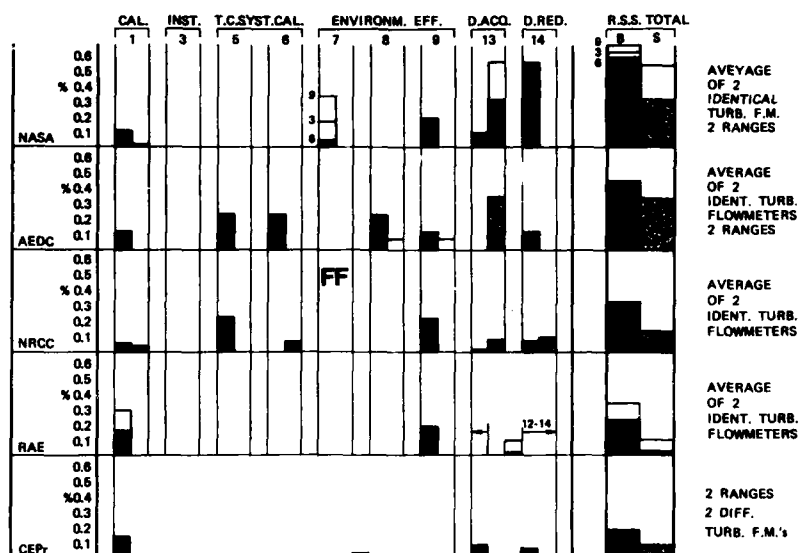


FIG 5 ERROR BUILD-UP FOR FUEL FLOW

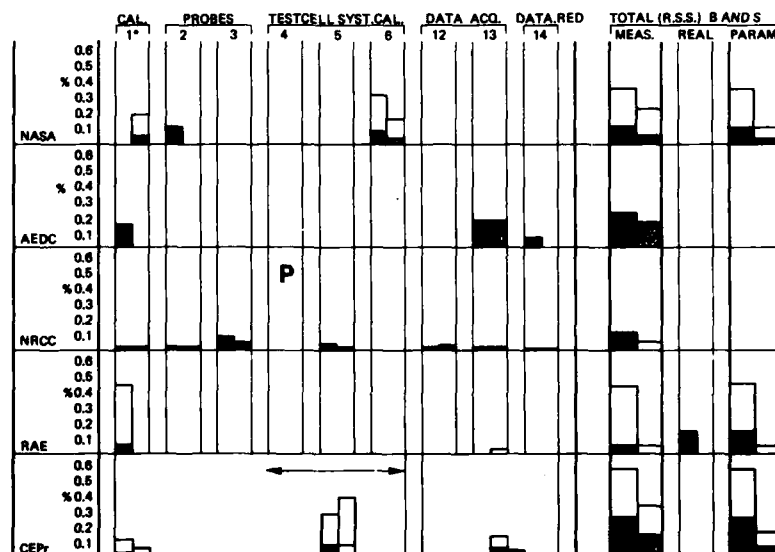


FIG 6 ERROR BUILD-UP FOR PRESSURE

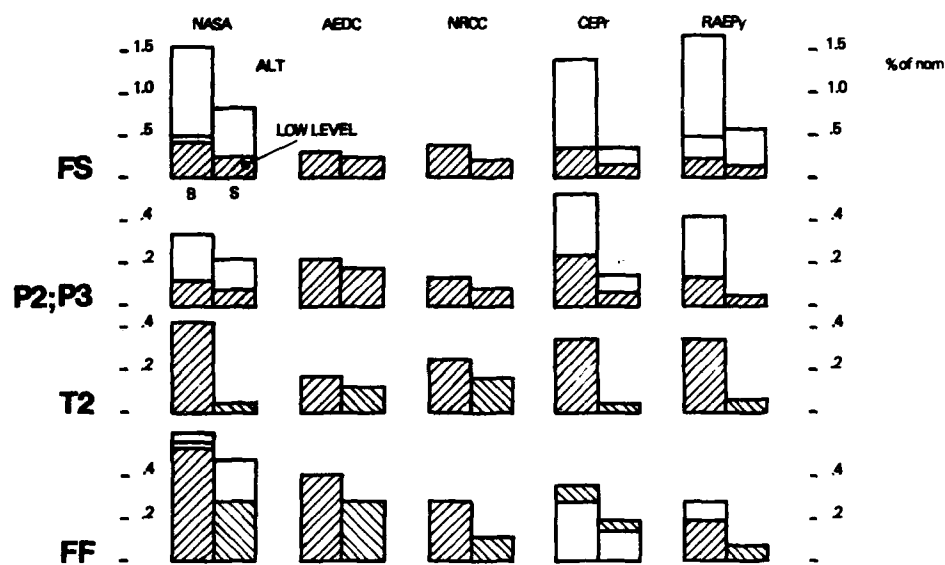


FIG 7 BIAS (B) AND PRECISION (S) ERRORS AT LOW FLT LEVEL (TC 3;6) AND ALT (TC 9)

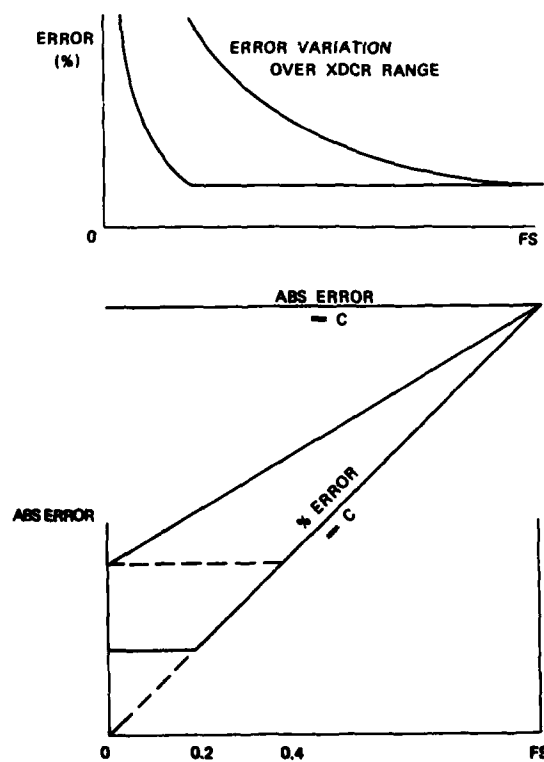


FIG 8 ERROR VARIATION OVER MEASURING RANGE

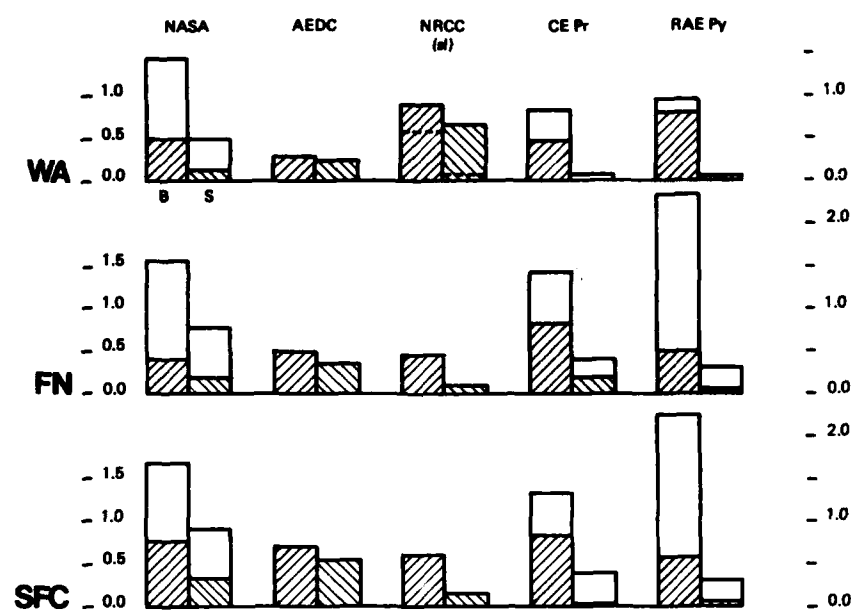


FIG 9 BIAS (B) AND PRECISION ERROR

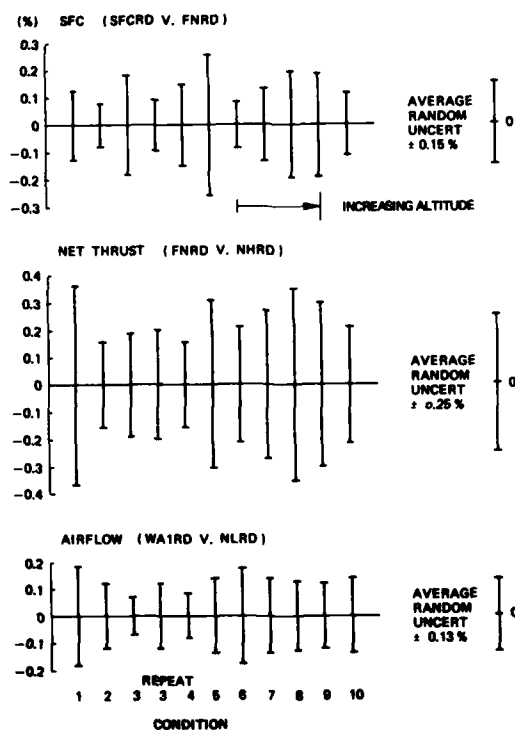


FIG 10 RANDOM ERROR LIMIT OF CURVE FIT FOR DIFFERENT TEST CONDITIONS

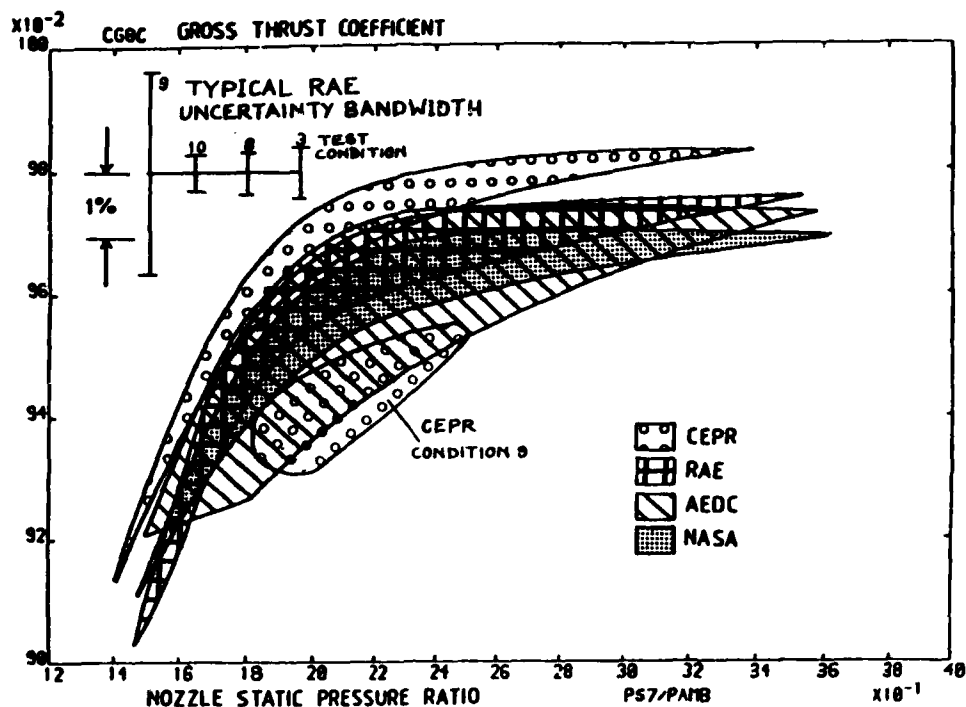


FIG 11 A COMPARISON OF THE GROSS THRUST COEFFICIENT ENVELOPE FOR ALL ALTITUDE TEST FACILITIES

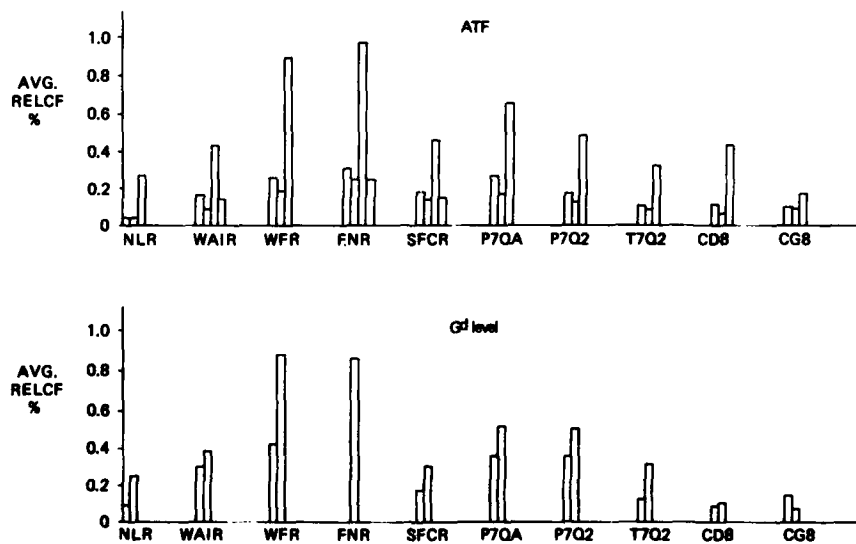


FIG 12 AVERAGE RANDOM ERROR LIMIT OF CURVE FIT FOR DIFFERENT FACILITIES

AN OVERVIEW OF THE APPLICATION OF STANDARD MEASUREMENT UNCERTAINTY METHODOLOGY TO PROPULSION TESTING*

by
J. W. Thompson, Jr.,
Director, Instrumentation and Controls
and
Dr. W. F. Kimzey,
Vice President and General Manager
W. O. Boals, Jr.
Senior Engineer
Sverdrup Technology, Inc., AEDC Group
Arnold Air Force Station, TN 37389-9998

SUMMARY

In the past several years, a standard measurement uncertainty methodology has been adopted by the SAE, ASME, AIAA, ISA, JANNAF, and ISO (draft status). This standard methodology has significantly improved the ability to resolve and understand measurement systems accuracies in the Engine Test Facility (ETF) at AEDC. This paper overviews the measurement accuracy assessment methodology and its development background. The procedural steps in making an uncertainty analysis are reviewed, and typical results of an analysis effort are illustrated by reviewing the elemental errors and uncertainties for state-of-the-art measurement systems used in simulated altitude tests of air-breathing engine propulsion systems. Typical elemental and combined uncertainties for measured values of pressure, force, flow, and temperature and uncertainties of propulsion system thrust and specific fuel consumption performance parameters are included.

LIST OF SYMBOLS

- B The estimate of the upper limit of the bias error, either B_x or B_y
 B_x The estimate of the upper limit of the bias error for an individual measurement obtained by root-sum-squaring the measurements elemental bias errors
 B_y The estimate of the upper limit of the bias error for a calculated performance parameter obtained by propagating the measured parameters B_x 's through the performance parameter equation
 n The number of independent random samples of the underlying normal distribution (sample size)
 S The engineering estimate of the population data set standard deviation σ , either S_x or S_y
 S_x The estimated standard deviation of an individual sample calculated from n samples [see Eq. (2.3)]
 \bar{S}_x The estimated standard deviation of the mean of n samples [see Eq. (2.4)]
 S_y The estimated standard deviation of a calculated performance parameter obtained by propagating the measured parameters S_x 's through the performance parameter equation
 \bar{S}_y The estimated standard deviation of the mean of n samples of the performance parameter
 t_{95} The 95th percentile point for the two-tailed student's "t" distribution; the t_{95} value is a function of the number of degrees of freedom used in calculating S
 U The uncertainty or largest expected error. Defined as
 Additive Model:
$$U_{ADD} = \pm \left(B + t_{95} \frac{S}{\sqrt{n}} \right)$$

 or
 Root-Sum-Square Model:
$$U_{RSS} = \pm \sqrt{B^2 + \frac{(t_{95}S)^2}{n}}$$

 X An individual measurement, sometimes called an observation or reading
 Y A calculated performance parameter

1.0 INTRODUCTION

In 1965, JANNAF, then called ICRPG (Interagency Chemical Rocket Propulsion Group), organized a Performance Standardization Committee to develop measurement uncertainty standards for the rocket engine industry. A survey of the industry showed that there were many different uncertainty assessment methods in use. The work of this committee, a rocket uncertainty methodology (Ref. 1), was published in 1968 and received widespread acceptance in the propulsion community. The successful application of the rocket methodology to gas turbines inspired the USAF Aeropropulsion Laboratory in 1973 to produce a similar handbook specifically treating the gas turbine measurement process. This document (Ref. 2) was given worldwide distribution by the USAF and was widely used within the aerospace industry. In 1980, the Instrument Society of America reprinted the USAF document as an ISA Handbook (Ref. 3). Many technical societies (SAE, Ref. 4; ASME, Refs. 5, 6, and 7; AIAA, Refs. 8 and 14; and ISO, Refs. 10 and 11) have adopted the uncertainty methodology and produced documents applying it to specific measurement processes.

*The research reported herein was performed by the Arnold Engineering Development Center (AEDC), Air Force Systems Command. Work and analysis for this research were done by personnel of Sverdrup Technology, Inc., AEDC Group, operating contractor for the AEDC propulsion test facilities. Further reproduction is authorized to satisfy needs of the U. S. Government.

The adopted uncertainty methodology fulfills a vital need for a standard method for estimating errors so comparisons of measurement systems between facilities can be made and the interpretation and understanding of error analysis can be unified. The methodology possesses many significant attributes including:

- a practical balance between engineering and statistics to deal with a complex subject that does not lend itself to a vigorous, scientifically correct answer for all situations. Monte Carlo simulation methods provided objective, comparative selection of the standard methodology features from the many possible alternatives;
- a systematic straightforward approach which is understandable and achievable with reasonable effort;
- an appealing approach to engineers because it is truly an aide in understanding, improving, and communicating measurement system performance;
- an evaluation of error sources independently so that the major error contributors can be identified and improvements made if justified; and
- a single number to describe the goodness of a test result with the easily understandable interpretation that the single number is the largest error reasonably expected.

Use of the uncertainty methodology since 1970 at the AEDC/ETF has been beneficial in improving propulsion measurement techniques and practices and in establishing and maintaining credibility in reporting propulsion system performance evaluations where buyer/seller relationships are involved. Use of the methodology provides a vital thread linking all phases of ETF propulsion test programs from the test program definition and planning phase through the testing phase, and through result analyses and reporting. In the pre-test phase, the predicted uncertainties are determined and the selected test measurement systems and test techniques are compared with the program uncertainty requirements.

The measurement systems and practices are selected to meet the program requirements while limiting resource expenditures. During testing, the measurement processes and test results are monitored and controlled to ensure that pre-test predictions are either valid or that adjustments to predicted uncertainties are made based on the actual performance of the measurement process. The larger error contributors identified in the pre-test analysis are given special monitoring attention during testing.

The post-test phase activities analyze the test results for consistency with pre-test error predictions and with actual measurement system performance information collected during testing, and with post-test instrumentation calibration results. The objective is to ensure that the reported uncertainties are in fact representative of the test results reported. Careful application of the uncertainty methodology provides the necessary information for monitoring and controlling each phase of the test program and thus ensuring that test program objectives are met.

The objective of this paper is to provide an overview of the basic principles of the adopted uncertainty methodology, an overview of procedural steps involved in performing an uncertainty analysis, and example results from uncertainty analyses of typical turbine engine test measurement and performance parameters. References are cited throughout the text to direct the reader to a more detailed treatment of the topics over-viewed. With the overview provided, it is hoped the reader would be able to structure a plan for assessing the error sources and error estimates for his particular measurement process.

2.0 MEASUREMENT UNCERTAINTY METHODOLOGY

A single number (some combination of bias and precision) is needed to express a reasonable limit for error. This single number, called uncertainty, U , must have a simple interpretation and be useful. It is impossible to define a single rigorous statistic because the bias is an upper limit involving judgment which has unknown characteristics. Any function of these two numbers must be a hybrid combination of an unknown quantity (bias) and a statistic (precision). However, the need for a single number to measure error is so great that the use of an arbitrary standard is warranted.

2.1 Uncertainty Model

Two models are in use. The additive model,

$$U_{ADD} = \pm \left(B + t_{95} \frac{S}{\sqrt{n}} \right) \quad (\text{see Note 1}) \quad (2.1)$$

NOTES:

1. In the rocket and turbine uncertainty handbooks (Ref. 1, 1969, and Ref. 2, 1973, respectively) the uncertainty model is written as $U = \pm (B + t_{95}S)$. In the more recent uncertainty documents using the same uncertainty methodology (Ref. 3, Dr. Abernethy's

and the root-sum-squares model,

$$U_{RSS} = \pm \sqrt{B^2 + \frac{(t_{95}S)^2}{n}} \quad (\text{see Note 2}) \quad (2.2)$$

where B is the bias error, S is the precision index, t_{95} is the 95th percentile point for the two-tailed student's "t" distribution whose value is a function of the degrees-of-freedom associated with the S estimate, and n is the sample size associated with the S estimate.

Either the U_{ADD} or the U_{RSS} option may be used, provided the following constraints are followed: (1) the random and systematic error components are separately propagated to the end test result, (2) the two error components are reported separately, and (3) the choice of uncertainty model used is stated. Under these constraints, the uncertainty, U , is the last calculation and may easily be redone, if desired. The estimated confidence level or coverage provided by the U_{ADD} model is 99 percent and the U_{RSS} model is 95 percent. Reference 4 provides comparisons of these two models based on Monte Carlo simulations.

The ETF uses the U_{ADD} model as illustrated in the examples.

A discussion of the B , S , and t_{95} error terms follows.

2.1.1 Precision Error

Random errors are encountered in repeated measurements and are the differences between the observed values and the average value of a very large sample. Repeated measurements at steady-state (constant) conditions are not expected to produce precisely the same data. There are numerous, small effects which may cause measurement variations. These variations tend to spread about an average value in the fashion of a normal distribution curve, Fig. 2.1. The curve is characterized by the standard deviation, σ .

The precision index, S , is the computed estimate of the standard deviation, σ , of the data and is calculated as follows:

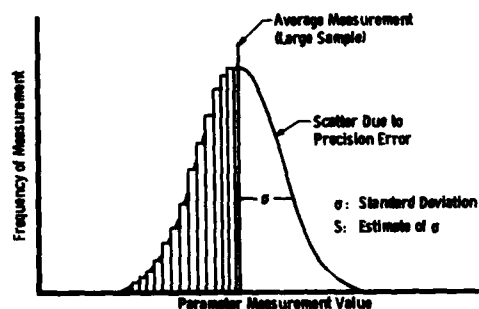


Fig. 2.1. Normal Distribution Curve Resulting from Typical Steady-State Data Measurement.

$$\text{Precision Index} = S_X = \sqrt{\frac{\sum_{k=1}^n (x_k - \bar{X})^2}{n-1}} \quad (2.3)$$

where

n = number of measurements

x_k = individual measurements

$$\bar{X} = \text{average value of individual measurements} = \frac{\sum_{k=1}^n x_k}{n}$$

The estimated precision index of the mean of the samples is calculated as

$$S_{\bar{X}} = \frac{S_X}{\sqrt{n}} \quad (2.4)$$

NOTES: (Continued)

AIAA Paper, 1985; Ref. 10, ISO (Draft), 1987; and Ref. 9, ANSI/ASME, 1985) the uncertainty model is written as $U = \pm (B + t_{95} \frac{S}{\sqrt{n}})$. Based on a thorough review of the documents and a discussion with Dr. Bob Abernethy, the intent of the earlier S notation was to be $S_{\bar{X}}$ which is $\frac{S}{\sqrt{n}}$ used in the more recent model notation for the estimated precision index. Therefore, proper application of the two model expressions yields the same results. The model expression using $\frac{S}{\sqrt{n}}$ is the preferred notation and is used throughout this document.

Care must always be exercised to ensure that all of the estimated terms in the uncertainty model are consistent with the measured and calculated results they represent.

2. To help achieve national and international consensus on the standard uncertainty methodology, the U_{RSS} model has been included with the historical U_{ADD} model methodology since about 1980 at the suggestion of the National Bureau of Standards (NBS). The error components are identical in both models.

2.1.2 Bias Error

The bias component is a fixed or systematic error, B , which remains unchanged for the duration of a test. In repeated measurements at steady-state (constant) test conditions, each measurement has the same bias magnitude. The relationship between bias, precision, and the true value of the measured quantity is depicted in Fig. 2.2. The magnitude of the bias cannot be determined unless the measurements can be compared with the true value, which is generally not feasible. Therefore, bias limits ($\pm B$) are estimated using applicable test information and engineering judgment. Note that an uncertainty analysis assumes a carefully controlled measurement process within which every known calibration correction has been made. Because the calibration corrections are not ideal, some small, fixed, systematic errors will remain. The bias limits are estimates of the largest possible remaining systematic error after all corrections have been made.

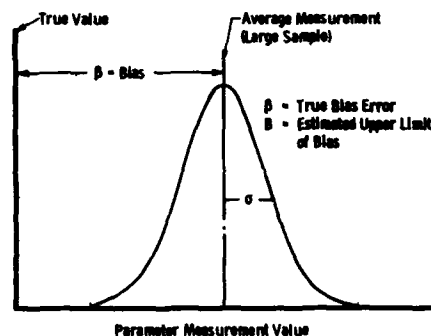


Fig. 2.2. Bias Error.

2.1.3 t_{95}

The t_{95} value is a function of the number of degrees-of-freedom, ν , used in calculating S . For small samples, t will be large, and for larger samples t will be smaller, approaching 1.96 as a lower limit. The use of the t inflates the limit U to reduce the risk of underestimating S when a small sample is used to calculate S . Since 30 degrees-of-freedom yield a t value of 2.04 and infinite degrees-of-freedom yield a t of 1.96, an arbitrary selection of $t = 2$ for values of from 30 to infinity is used.

In a sample, the number of degrees-of-freedom is the size of the sample. When a statistic is calculated from the sample, the degrees-of-freedom associated with the statistic are reduced by one for every estimated parameter used in calculating the statistic.

2.2 Uncertainty Interval

Figure 2.3 illustrates the U_{ADD} limits which provide an estimate of the largest error that may reasonably be expected for that measurement process. The probability that the "true" values lie within the uncertainty limits is known as the coverage.

A rigorous calculation of confidence level or coverage of the true value by the uncertainty interval is not possible. However, Monte Carlo simulations (Ref. 4) using various relative sizes of the bias and precision components indicates that the coverage of U_{ADD} is about 99 percent, whereas that of U_{RSS} is about 95 percent.

In the case of nonsymmetric uncertainty intervals where the bias is nonsymmetric, i.e., $B^+ \neq B^-$, see Ref. 2 for further discussion.

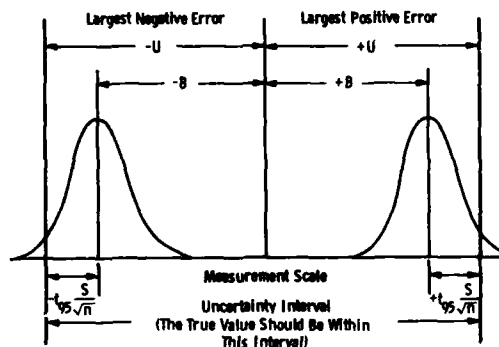


Fig. 2.3. Measurement Uncertainty Interval (Additive Model) Symmetrical Bias.

3.0 USING THE MEASUREMENT UNCERTAINTY METHODOLOGY

3.1 Getting Started

To get started, it is necessary to establish specific measurement uncertainty practices within your company's operation that meet the measurement uncertainty methodology guidelines. In the AEDC/ETF, a committee was convened, made up of members from each of the disciplines involved in the measurement activities: measurement installation, calibration, data acquisition, data processing, and analysis. The committee established measurement practices consistent with the uncertainty methodology. This includes instrument calibration practices, instrument installation requirements, error source identification and classification (i.e., precision or bias), measurement evaluation practices, and the measurement error evaluation procedures.

Provisions must also be made to continuously monitor the on-going test programs to ensure that the measurement uncertainty requirements are being met. This task primarily consists of reviewing test calibration data and taking random measurement samples, and evaluating measurement repeatability and bias errors while the test is being conducted. At the completion of the test, the final evaluation of the measurement uncertainty levels

achieved for the test must be made and the results reported. The findings from each test are used to establish a measurement uncertainty data base from which future pre-test predictions are made.

3.2 Steps in Performing Uncertainty Analysis

Uncertainty analysis activities for test programs can be logically divided into pre-test, test, and post-test phases. In the pre-test phase, the objective is to determine if the test techniques/measurement systems satisfy test program uncertainty requirements. The objective during the test phase is to ensure that a well-controlled measurement system exists throughout testing to produce valid results consistent with the pre-test uncertainty analysis. The post-test phase reviews the pre-test analysis in light of the actual test phase results and the post-test calibrations of the working standards, sensors/transducers, and test systems; adjusts the pre-test error estimates as required; and reports the test program uncertainty results. The analysis steps in each phase of the test program are discussed in the following paragraphs.

3.2.1 Pre-Test Phase

- a. Define the measurement process - The first step in any uncertainty analysis is to define the complete measurement process required to arrive at the desired result. Included will be the measurements and performance parameters including their uncertainty requirements. The performance parameter equations are defined identifying all measurements involved and the definition of each measurement process to be used, including calibrations of all instrumentation and installed systems.
- b. Identify all measurements to be analyzed - Analyze each performance parameter formula by which the final answer will be obtained to identify all the equation terms which must be investigated in the uncertainty analysis.
- c. Identify the elemental error sources for each measurement - For each measurement, make a list of the possible sources of elemental errors. To aid in identifying error sources and bookkeeping them, it is helpful to place the elemental error sources into the categories of calibration, data acquisition, data reduction, and installation/environment.
- d. Obtain an estimate of each elemental error - Obtain an estimate of each elemental error and initially classify as either a precision or bias error. Initially classify an error as a precision error if the estimate is derived by a statistical analysis of repeated measurements, and classify as a bias error if the estimate is from nonstatistical methods. Assessment of both precision and bias elemental errors may include analysis of information from the following:
 - measurement system end-to-end checks where known inputs are compared to the observed outputs,
 - calibration of test working standards and test sensors/transducers,
 - special tests performed on systems or components to help quantify errors,
 - analysis of redundant measurements, and
 - engineering judgment of the most knowledgeable persons about the error source being estimated.

For the most complete understanding of a measurement system's performance, first assess the elemental errors and then verify the results through end-to-end evaluations (applied loads tests). The elemental error assessment is beneficial in identifying the major error contributors and in directing attention to critical errors to control during installation and the test phase to achieve desired uncertainty results (Ref. 12).

The end-to-end evaluation is recommended as the preferred method of validating combined elemental or overall system performance errors. Care is required in making elemental error determinations since generally either interpretation of manufacturer's specifications is required (vendors are generally not yet using the Standard Uncertainty Methodology) and/or the judgment of the person most knowledgeable about the error sources is required. Special tests analogous to end-to-end evaluations are frequently used to help quantify elemental error values.

The final error estimates are generally a hybrid combination of end-to-end results with some additional elemental error values to allow for the fact that the end-to-end evaluations seldom account for all of the installation and test environmental effects, for example, aerodynamic tap error associated with a static pressure measurement.

An estimate of the upper limit of the systematic error, B, is more difficult to obtain than S. Caution should be exercised against the tendency to underestimate systematic errors especially when a subjective approach, like engineering judgment, is used. Underestimating bias errors is partly through human optimism and partly through overlooking the existence of some sources of systematic error. Even after applying all known corrections through the calibration process, some systematic errors will most likely remain and must be included in the error assessment.

Sometimes the physics of the measurement system is such that the systematic error may be nonsymmetrical. For example, hot thermocouples in the presence of colder walls, radiate and conduct thermal energy away from the sensor, resulting in a lower

temperature indication. Thus the bias error limits are of the form B+ and B- versus ±B. See Ref. 2 for a further treatment of nonsymmetrical bias limits.

- e. Calculate the measurement error components - Calculate the precision index S_X and the associated degrees-of-freedom and bias limit B for each measurement.

The measurement error component S_X is the root-sum-square of the elemental precision errors determined in Step d above:

$$S_X = \sqrt{\sum_{j=1} \sum_{i=1} S_{ij}^2}$$

where j defines the categories (1) calibration, (2) data acquisition, (3) data reduction, and (4) installation/test environmental, and i defines the sources within the categories.

Also calculate the degrees-of-freedom and the corresponding t_{95} value associated with the S_X .

In like manner, the measurement error component B_X is the root-sum-square of the elemental precision errors determined in Step d above:

$$B_X = \sqrt{\sum_{j=1} \sum_{i=1} B_{ij}^2}$$

where j and i definitions are the same as above.

- f. Propagate the measurement error components to the calculated parameter - Propagate the measurement error components through the function to the calculated performance parameters using either the Taylor Series (Ref. 2) or influence coefficient (Ref. 4) method. The Taylor Series expansion of the function provides the partial derivatives of the performance parameter with respect to the measurements. By inserting nominal measurement values and measurement precision and bias error components into the Taylor series expansion, the error components for the calculated parameter are obtained.

The influence coefficient method is convenient for determining the sensitivity of a result to a measured quantity (i.e., as the error propagated to the result due to unit error in the measurement). Finite increments may be used to evaluate the influence coefficient method with computer calculations:

$$\theta_i = \frac{\Delta R}{\Delta Y_i}$$

The result is calculated using Y_i to obtain R, and then recalculated using

$$(Y_i + \Delta Y) \text{ to obtain } (R + \Delta R).$$

Regardless of the method used, the measurement error components, S_X and B_X , are propagated separately to obtain the calculated parameter error components, S_Y and B_Y . Also, evaluate the degrees-of-freedom for the S_Y error component. If the degrees-of-freedom was ≥ 30 for all of the measurement S_X 's propagated, then the degrees-of-freedom for the calculated parameter S_Y will be ≥ 30 and a t_{95} value of 2 may be used. If degrees-of-freedom less than 30 was used for any measurement S_X 's propagated, then the Welch Satterthwaite formula must be used for evaluating the calculated parameter degrees-of-freedom (Ref. 2).

- g. Calculate the uncertainty of the performance parameter - Calculate the predicted uncertainty of the calculated parameter using the selected model U_{ADD} or U_{RSS} . If the predicted measurement and calculated performance parameter uncertainty estimates satisfy the test program objectives, then proceed with the test. If the uncertainty objectives are not satisfactory, then we must find a way to improve either the measurement systems, the calibration process, or the method for calculating the performance parameter before proceeding with the test.

The uncertainty statement is termed predictive at this stage of the uncertainty analysis process since unexpected influences or effects during testing may require inclusion of additional error terms or changes to the pre-test estimated errors. Care must be taken during the testing phase to ensure that these pre-test estimates are credible. The next section discusses the measures required to ensure that a controlled measurement process exists during testing.

3.2.2 Test Phase

A credible measurement uncertainty analysis requires a well-controlled measurement process in which there are no gross mistakes or errors. It also requires that correct calibrations have been applied. To ensure that a controlled measurement process exists, all measurement systems should be monitored during their installation, calibration, and pre-use periods. Assessment of the degree of control or closeness to pre-test estimate assumptions may include information from the following:

- comparison of specific calibration results for working standards, sensors/transducers, and installed systems with their respective calibration history and pre-test predictions,
- zero shifts in measurement systems from the beginning to the end of each test period,
- test condition and test article stability checks prior to and during each acquisition cycle,
- observed effects on measurement systems attributable to simulated altitude changes, changes in engine service systems pressure, and changes in environmental temperature and vibration,
- comparison of like test conditions from test period to test period during the test program,
- comparison of redundant measurements,
- comparison of related measurements or performance parameters,
- detection and elimination of outlier data values, and
- analysis of any special checks to ensure that large error contributing sources are properly controlled.

The availability of information from the above list will be dependent upon the specific test program, the measurement systems involved, and the ingenuity used in planning the conduct of the test program to acquire sufficient information to ensure that the total measurement process is in control, and that sufficient information exists so the post-test phase can confirm the pre-test analysis results or apply adjustments as needed so the final error report credibly represents the test results.

3.2.3 Post-Test Phase

The test program post-test phase consists of validating or adjusting as needed the pre-test uncertainty predictions to account for actual events/happenings throughout the test program, make final classification on measurement system errors based on the defined measurement process, and report the test data uncertainties.

- a. Adjust pre-test error estimates - Information to be analyzed in the post-test phase to validate or adjust pre-test error estimates would include the following:
 - analysis of information obtained during the test periods relating to how well the measurement process was in control or deviated from the pre-test error estimates,
 - results of post-test calibrations of working standards, sensors/transducers, and installed system, and
 - comparison and consistency checks of performance results.

Based on the results from the above information, the pre-test error estimates are adjusted as required.

- b. Final classification of pre-test error estimates - The final classification (Ref. 4) of the pre-test error estimates is based on the specific measurement objectives obtained from the defined measurement process in the pre-test phase. Most test programs have multiple measurement/performance parameter objectives which are satisfied with the same measurement systems. For example, one objective may be to measure the absolute level of a performance parameter, and the second objective may be to measure the difference in the same performance parameter before and after a test article component change. The uncertainty of the absolute performance parameter would include the precision and bias error sources, whereas the uncertainty of the difference in performance parameters before and after a component change would not include the bias error terms since they would be the same for the before and after test and would cancel out.

The uncertainty results then would be quite different from these two measurement objectives even though they both involved the same measurement systems. The classification of calibration precision errors (Ref. 4) will change if the measurement process is such that the precision errors manifest themselves as a bias error in the measured or calculated result. For example, if a particular measurement process involved many calibrations over a long period of time, the calibration process precision errors would cause variations in the measured values. Conversely, if only one calibration was involved, then the calibration precision error would manifest itself as a bias error in the measured value. Precision errors which are reclassified as a result of the defined measurement process should be marked with an asterisk (S*) (fossilized precision error) (Ref. 4) and treated as a bias error.

- c. Reporting of measurement uncertainty - The report should include all of the information necessary to describe and to allow for further propagation of measurement and test result uncertainties. This requires reporting the error components and applicable measurement or calculated parameter range for each measurement and calculated parameter.

The following error component and uncertainty information is required:

- S, the estimate of the precision index,
- ν , the degrees-of-freedom associated with each S,
- B, the estimated bias error, and
- U, the uncertainty limit including the model, U_{ADD} or U_{RSS} , used.

Each test facility should retain in their files the measurement system elemental error information for review as required to substantiate reported uncertainty results and for use in performing pre-test uncertainty analyses for future test programs.

4.0 EXAMPLE RESULTS FROM UNCERTAINTY ANALYSIS OF TYPICAL TURBINE TEST MEASUREMENT AND PERFORMANCE PARAMETERS

The AEDC/ETP simulated altitude test facilities use a variety of measurement systems in support of airbreathing engine and rocket motor performance testing. The same uncertainty methodology is used for evaluating measurement systems used in both types of testing. In this paper, examples from airbreathing engine testing are used.

Example error assessment results are provided for the measurements of aerodynamic pressure, temperature, airflow, fuel flow, and scale force. The error components from these measurements are then propagated to the calculated parameters, net thrust, and thrust-specific fuel consumption. The results are representative for steady-state testing of a nonafterburning, low-bypass turbofan engine. The examples use the U_{ADD} model which has been the practice of AEDC/ETP since 1970. The several turbine engine test configurations from which the examples are taken are described in Section 4.1 (Refs. 12 and 13). The specific examples are included in Sections 4.2 through 4.7. Each example gives a brief description of the measurement system, a table of the error sources and estimates grouped into the categories of calibration, data acquisition, data reduction, and installation/environment. A summary table gives the error components by category and the error components and uncertainty for the parameter.

The error components and uncertainty values are calculated from the error source audit table values, assuming that the defined measurement process is such that the calibration precision errors are not reclassified. In some cases, the calibration precision errors would become reclassified or fossilized as discussed in Section 3.2.3-b and, therefore, treated as a bias error.

The format of the error source audit table provides sufficient detail of the errors involved to easily reclassify/recombine them into error components consistent with the test objectives.

The airflow example in Section 4.4 uses the pressure (Section 4.2) and the temperature (Section 4.3) measurement error components along with the other required error sources, as shown in Table 4.4.1. The Table 4.4.1 error components are then propagated to the airflow parameter through the influence coefficient method, as illustrated.

Error calculations for net thrust and thrust-specific fuel consumption requires both the error components for all of the measurements involved and the influence coefficient for each measurement at the desired altitude/Mach number test condition, as illustrated.

Tables 4.7.1 and 4.7.3 are illustrative of the uncertainty information required in test reports, as discussed in Section 3.2.3-c.

4.1 General Test Configuration

The examples are from the so-called direct-connect test configuration. This configuration derives its name from the fact that the engine inlet is directly connected to a controlled air supply system. The engine exhaust exits into a separately controlled environment.

The direct-connect configuration provides the best opportunity for the measurement of the steady-state behavior of the axial component of thrust produced by a turbojet or turbofan engine. The essential features of the direct-connect configuration are shown in Fig. 4.1.1. Although there are a number of hardware options available to implement each of the key functions in a direct-connect test configuration, it is nevertheless essential that each of the functions represented by these specific hardware items identified in Fig. 4.1.1 be successfully implemented.

First, the flow of air through the engine must be known very precisely. The venturi shown in Fig. 4.1.1 represents one of the devices available to accomplish this measurement. After the flow rate of the air is determined, the temperature and pressure profiles entering the engine are made uniform by use of flow-straightening screens, a plenum chamber, and a bellmouth. The engine exhaust gases are removed from the cell through the exhaust collector. The simulated flight conditions are set by control valves upstream of the venturi to provide the desired temperature and pressure to the engine inlet and by control valves downstream of the exhaust collector to set the desired altitude ambient pressure in the test cell.

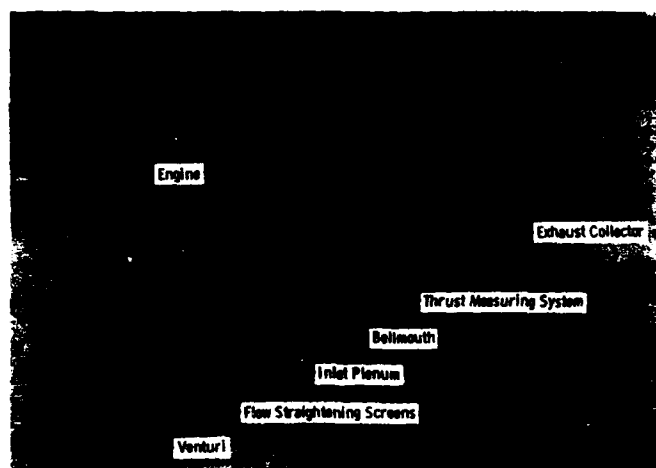


Fig. 4.1.1. Direct-Connect Engine Installation.

4.2 Aerodynamic Pressure Measurement

4.2.1 Measurement Process

The most common method of measuring aerodynamic steady-state pressures is with strain-gage pressure transducers calibrated in-place with a standard quartz pressure generator.

Normally the pressure measurement is made with a single transducer; however, for widely varying ranges of pressure in a program this may not be adequate. As alternatives, delta pressure transducers or multiple ranges of transducers might be used. Figure 4.2.1 shows a typical installation where several pressure probes are multiplexed onto one pressure transducer.

4.2.2 Error Source Audit

Typical steady-state elemental error sources and error estimates for a turbine engine test are tabulated in Table 4.2.1. Table 4.2.2 provides a summary of the errors of each group and the error components and uncertainty for the measurement using the U_{ADP} model.

Figure 4.2.1 shows a typical engine inlet thermocouple rake connected to an in-cell thermocouple reference unit.

4.3 Temperature Measurement

4.3.1 Measurement Process

Most temperature measurements are made with thermocouple probes. The most commonly used types of thermocouples at AEDC are Chromel®-Alumel® for temperatures in the higher range (100 to 1100°C) and copper-constantan for temperatures in the lower range (-40 to 260°C).

Thermocouple systems are calibrated by insertion of millivolts from a standard voltage source. The voltage to temperature conversions are accomplished with polynomial equations which approximate the National Bureau of Standards tables of the International Practical Temperature Scale (IPTS) for each thermocouple type.

Figure 4.3.1 shows a typical engine inlet thermocouple rake connected to an in-cell thermocouple reference unit.

4.3.2 Error Source Audit

Typical steady-state elemental error sources and error estimates for a turbine engine test are contained in Table 4.3.1. Table 4.3.2 provides a summary of the errors by group and the error components and uncertainty for the temperature measurements using the U_{ADP} model.

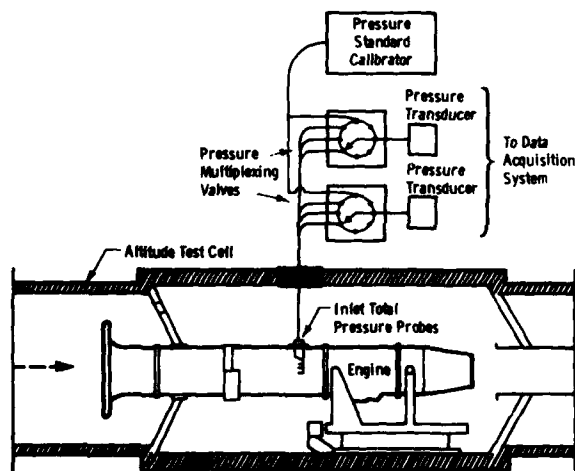


Fig. 4.2.1. Engine Inlet Aerodynamic Pressure Measurement.

Table 4.2.1. Aerodynamic Pressure Steady-State Elemental Error Source Audit.

Nonafterburning, Low-Bypass Turbopump Measurement Range 35 to 100 kPa			
Error Source	Precision Index		Bias Limit
	Percent of Reading	Degrees of Freedom	Percent of Reading
I. Calibration (Transfer Error)			
a. National Standard to Laboratory Standard	0.007	>30	0.02
b. Laboratory Standard to Working Standard	0.007	>30	0.02
c. Working Standard to Measurement System	0.013	>30	0.1
	$S_{cal} = \pm 0.016$	$df_{cal} > 30$	$B_{cal} = \pm 0.104$
II. Installation/Environment			
a. Thermal Effects	Negligible		0.05
b. Probe Effects	Negligible		Negligible
	$S_{I/E} = 0$		$B_{I/E} = \pm 0.05$
III. Data Acquisition			
a. Excitation Voltage	0.027	>30	0.04
b. Signal Conditioning	0.05	>30	0.073
c. Analog-to-Digital Conversion	0.05	>30	0.053
	$S_{DA} = \pm 0.07$	$df_{DA} > 30$	$B_{DA} = \pm 0.099$
IV. Data Processing			
a. Computer Resolution	Negligible		Negligible
b. Curve Fitting	Negligible		Negligible
	$S_{DP} = 0$		$B_{DP} = 0$
	$S_{total} = \pm 0.07$	$df_{total} > 30$	$B_{total} = \pm 0.15$

Table 4.2.2. Aerodynamic Pressure Steady-State Error Source Audit Summary.

Error Source	Precision Index		Bias Limit
	Percent of Reading	Degrees of Freedom	Percent of Reading
Calibration Transfer Error	± 0.016	>30	± 0.104
Installation/Environment	± 0		± 0.05
Data Acquisition	± 0.07	>30	± 0.099
Data Processing	± 0		± 0

Error Components: $S_{total} = \sqrt{\sum S_i^2} = \pm 0.07$ $B_{total} = \sqrt{\sum B_i^2} = \pm 0.15$

Uncertainty: $U_{ADD} = \pm [(0.151) + 2(0.07)] = \pm 0.29$ percent

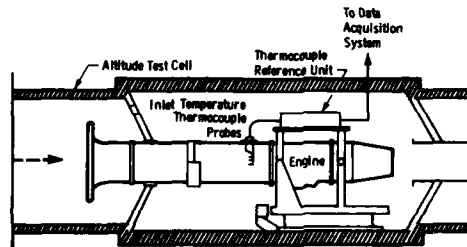


Fig. 4.3.1 Engine Inlet Temperature Measurement.

Table 4.3.1. Temperature, Steady-State Elemental Error Source Audit.

Nonafterburning, Low-Bypass Turbopump Measurement Range 233 to 336°K			
Error Source	Precision Index		Bias Limit
	Percent of Reading	Degrees of Freedom	Percent of Reading
I. Calibration (Transfer Error)			
a. National Standard to Laboratory Standard	0.0002	>30	0.0002
b. Laboratory Standard to Working Standard	0.0002	>30	0.0018
c. Working Standard to Measurement System	0.0018	>30	0.185
	$S_{cal} = \pm 0.0018$	$df_{cal} > 30$	$B_{cal} = \pm 0.185$
II. Installation/Environment			
a. Conduction Effects	Negligible		0.052
b. Radiation	Negligible		Negligible
c. Recovery Factor	0.02	>30	0.0075
	$S_{I/E} = \pm 0.02$	$df_{I/E} > 30$	$B_{I/E} = \pm 0.053$
III. Data Acquisition			
a. Reference Function	0.057	>30	0.09
b. Electrical Simulation	0.0013	>30	0.0017
c. Signal Conditioning	0.006	>30	0.057
d. Analog-to-Digital Conversion	0.017	>30	0.013
	$S_{DA} = \pm 0.056$	$df_{DA} > 30$	$B_{DA} = \pm 0.1$
IV. Data Processing			
a. Computer Resolution	Negligible		Negligible
b. Curve Fitting	Negligible		Negligible
	$S_{DP} = 0$		$B_{DP} = \pm 0.07$
	$S_{total} = \pm 0.06$	$df_{total} > 30$	$B_{total} = \pm 0.22$

Table 4.3.2. Temperature (T/C) Steady-State Error Source Audit Summary.

Error Source	Precision Index		Bias Limit
	Percent of Reading	Degrees of Freedom	Percent of Reading
Calibration Transfer Error	± 0.0018	>30	± 0.185
Installation/Environment	± 0.02	>30	± 0.053
Data Acquisition	± 0.056	>30	± 0.1
Data Processing	± 0		± 0.07

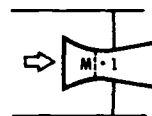
Error Components: $S_{total} = \sqrt{\sum S_i^2} = \pm 0.06$ $B_{total} = \sqrt{\sum B_i^2} = \pm 0.22$

Uncertainty: $U_{ADD} = \pm [(0.221) + 2(0.06)] = \pm 0.34$ percent

4.4 Airflow Measurement

4.4.1 Measurement Process

Airflow rate measurements for gas turbine engines are generally made with a critical flow (sonic) venturi (illustrated in Fig. 4.4.1) and shown in the test configuration in Fig. 4.1.1. Critical flow venturis are designed to operate with sonic flow at the nozzle throat plane and, as such, do not require a measurement of the flow-field velocity. The variables involved in the calculation of engine airflow are also shown in Fig. 4.4.1.



Mass Flow Equation

$$W_A = \rho C_D P_t A_{\text{throat}}$$

where C_D is a theoretically determined discharge coefficient which accounts for both viscous and inertial effects.

Fig. 4.4.1. Isolated Critical Flow Venturi.

4.4.2 Error Source Audit

The steady-state elemental error sources and error estimates for each of the airflow equation terms are tabulated in Table 4.4.1. Table 4.4.2 gives an error summary for each equation term. Also, the influence coefficients are defined and the resulting airflow measurement error components and uncertainty are presented in Table 4.4.3.

Table 4.4.1. Airflow Steady-State Elemental Source Audit.

Nonafterburning, Low-Bypass Turbofan Airflow Measurement Range 20 to 100 kg/sec			
Error Source	Precision Index		Bias Limit
	Percent of Reading	Degrees of Freedom	Percent of Reading
I. Total Pressure (Same as Engine Inlet Total Pressure, Fig. 4.2.1)	0.07	>30	0.147
II. Total Temperature (Same as Engine Inlet Total Temperature, Fig. 4.3.1)	0.06	>30	0.22
III. Venturi Throat Area a. Calibration Transfer b. Instrument Error	0 0 $S_{\text{area}} = 0$		0.03 0.04 $B_{\text{area}} = \pm 0.05$
IV. Venturi Discharge Coefficient a. Viscous Boundary Layer b. Inertial Profile	0 0 $S_{CD} = 0$		0.07 0.07 $B_{CD} = \pm 0.10$

Table 4.4.2. Airflow Steady-State Error Source Audit Summary.

Error Source	Precision Index		Bias Limit
	Percent of Reading	Degrees of Freedom	Percent of Reading
Total Pressure	0.07	>30	0.15
Total Temperature	0.06	>30	0.22
Venturi Throat Area	0		0.05
Venturi Discharge Coefficient	0		0.10

Table 4.4.3. Influence Coefficient Matrix for Airflow.

Independent Parameter	Influence Coefficient, $\frac{\partial W_A}{\partial (\cdot)} \cdot \frac{(\cdot)}{W_A}$	
	Altitude - Sea Level Mach No. = 0	Altitude - 30,000 ft Mach No. = 0.9
Total Pressure	1.0	1.0
Total Temperature	-0.5	-0.5
Venturi Throat Area	1.0	1.0
Venturi Discharge Coefficient	1.0	1.0

Error Components: $S_{WA} = \pm 0.076$ percent $B_{WA} = \pm 0.22$ percent

Uncertainty: $U_{ADD} = \pm 0.22 + 2.0(0.76) = 0.37$ percent

*The partial differential value of airflow with respect to the independent parameter times the ratio of the independent parameter to airflow with all other parameters held constant.

4.5 Fuel-Flow Measurement

4.5.1 Measurement Process

The most common method of measuring engine fuel flows is with calibrated turbine-type flowmeters which produce an output signal whose frequency is proportional to the volume flow rate through the meter. Turbine meters are calibrated by flowing a measured volume

of fluid through the meter and recording the total number of turbine meter cycles (pulses) generated.

At AEDC, to minimize the uncertainty of the fuel-flow measurements, up to three ranges of flowmeters are used to cover the engines total fuel-flow operating range. A typical engine fuel-flow installation, along with the variables required to calculate fuel flow, is shown in Fig. 4.5.1.

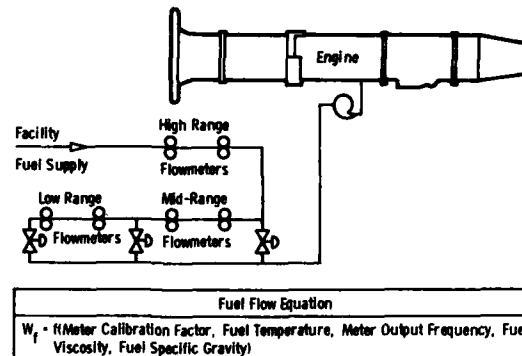


Fig. 4.5.1. Fuel-Flow Measurement System.

4.5.2 Error Source Audit

The steady-state elemental error sources and error estimates are shown in Table 4.5.1. Table 4.5.2 provides a summary of the errors by group and the error components and uncertainty for the fuel-flow measurement using the U_{ADD} model.

Table 4.5.1 Fuel-Flow Steady-State Elemental Error Source Audit.

Nonafterburning, Low-Bypass Turbofan Measurement Range 600 to 1500 g/sec			
Error Source	Precision Index		Bias Limit
	Percent of Reading	Degrees of Freedom	Percent of Reading
I. Calibration (Transfer Error)			
a. National Standard to Laboratory Standard	0.005	>30	0.007
b. Laboratory Standard to Working Standard	0.011	>30	0.01
c. Working Standard to Measurement System	0.10	>30	0.005
	$S_{cal} = \pm 0.101$	$df_{cal} > 30$	$B_{cal} = \pm 0.013$
II. Installation/Environment			
a. Flowmeter Orientation	Negligible		Negligible
b. Plumbing Configuration	0.01	>30	Negligible
c. Thermal Effects	Negligible		0.01
d. Specific Gravity	0.05	>30	0.10
e. Viscosity	0.026	>30	0.05
	$S_{1/E} = \pm 0.057$	$df_{1/E} > 30$	$B_{1/E} = \pm 0.11$
III. Data Acquisition			
a. Electrical Simulation	0.002	>30	0.001
b. Signal Conditioning	0.15	>30	0.21
c. Analog-to-Digital Conversion	0.02	>30	0.01
	$S_{DA} = \pm 0.15$	$df_{DA} > 30$	$B_{DA} = \pm 0.21$
IV. Data Processing			
a. Computer Resolution	Negligible		Negligible
b. Curve Fitting	Negligible		0.05
	$S_{DP} = 0$		$B_{DP} = \pm 0.05$
	$S_{total} = \pm 0.19$	$df_{total} > 30$	$B_{total} = \pm 0.24$

Table 4.5.2. Fuel-Flow Steady-State Error Source Audit Summary.

Error Source	Precision Index		Bias Limit
	Percent of Reading	Degrees of Freedom	Percent of Reading
Calibration Transfer Error	± 0.101	>30	± 0.013
Installation/Environment	± 0.057	>30	± 0.11
Data Acquisition	± 0.15	>30	± 0.21
Data Processing	± 0		± 0.05

Error Components: $S_{total} = \sqrt{\sum S_i^2} = \pm 0.19$ $B_{total} = \sqrt{\sum B_i^2} = \pm 0.24$

Uncertainty: $U_{ADD} = \pm [(0.24) + (2)(0.19)] = \pm 0.62$ percent

4.6 Scale-Force Measurement

4.6.1 Measurement Process

The essential characteristic of the scale-force measurement method is that the engine is installed so that it may be handled as a free body, and the net forces acting around the free body provide a measurement of the engine gross thrust. The scale-force measurement method requires the use of a thrust stand which attaches directly to the engine

mounting hardware. The essential functions of a thrust stand are shown schematically in Fig. 4.6.1.a.

In the altitude test cell configuration, the engine thrust stand measures only a portion of the axial forces present on the metric engine free body. The total forces acting on the free body for a planar nozzle engine, the simplest of the engine arrangements, are shown in Fig. 4.6.1.b. The gross thrust, F_G , is the sum of the momentum and pressure area terms at the engine inlet and the scale force measured from the engine thrust stand.

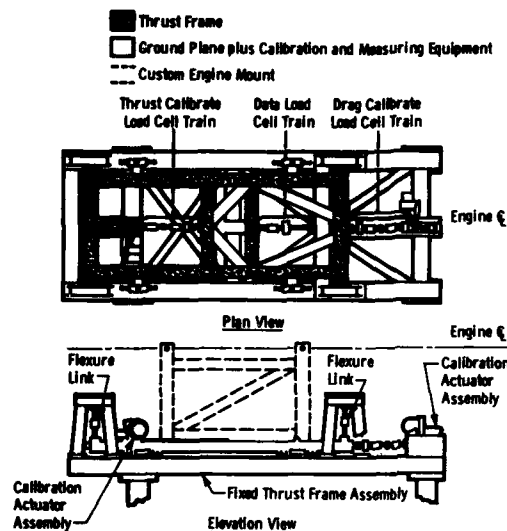


Fig. 4.6.1.a. Thrust Stand Schematic.

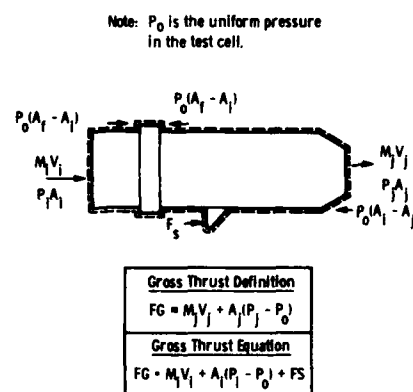


Fig. 4.6.1.b. Total Forces Acting on the Free Body for a Planar Nozzle Engine.

4.6.2 Error Source Audit

An example error audit for a nonafterburning, low-bypass turbofan engine test is contained in Table 4.6.1, which identifies and quantifies the individual error sources. Table 4.6.2 shows a summary of the errors by group to show the relative influence of each group. The scale-force error components and uncertainty using the U_{ADD} model is also shown.

4.7 Net Thrust and Thrust-Specific Fuel Consumption

The net thrust is determined from the engine gross thrust (shown in Fig. 4.6.1.b) by subtracting the ram drag. Ram drag is the product of airflow and flight velocity.

$$\text{Net Thrust} = \text{Gross Thrust} - (\text{Airflow} \times \text{Flight Velocity})$$

The specific fuel consumption is

$$\text{Thrust Specific Fuel Consumption} = \text{Fuel Flow/Net Thrust}$$

The final error results from each of the measurement systems are propagated to obtain the total measurement uncertainty for the overall engine performance parameters. These measurement error results are shown in Table 4.7.1.

Table 4.7.2 provides the sensitivity of turbine engine net thrust to each of the independent error sources. As would be expected, the measurement uncertainty is strongly influenced by the engine cycle and engine operating conditions of altitude, Mach number, and power setting. The sensitivity is expressed in terms of the influence coefficient,

$$\frac{\partial FN}{\partial (\text{Independent Variable})} \cdot \frac{\text{Independent Variable}}{FN}$$

For example, for a one-percent change in scale force, the net thrust will change 0.87 percent at sea-level conditions. The influence coefficients are combined with the precision and bias error components to obtain the net thrust uncertainty presented in Table 4.7.3.

Table 4.6.1. Scale-Force Steady-State Elemental Error Source Audit.

Nonafterburning, Low-Bypass Turbofan Measurement Range 15K to 50K N			
Error Source	Precision Index		Bias Limit
	Percent of Reading	Degrees of Freedom	Percent of Reading
I. Calibration (Transfer Error)			
a. National Standard to Laboratory Standard	0.027	>30	0.023
b. Laboratory Standard to Working Standard	0.009	>30	0.027
c. Working Standard to Measurement System	0.056	>30	0.10
	$S_{cal} = \pm 0.073$	$df_{cal} > 30$	$B_{cal} = \pm 0.106$
II. Installation/Environment			
a. Load Cell Ambient Pressure	0.023	>30	0.04
b. Tare Loads	0.047	>30	0.073
c. Centerline Loading	0.025	>30	0.047
d. Thermal Effects	0.047	15	0.079
e. Cell Cooling Air	0.007	>30	0.007
f. Labyrinth Seal Misalignment	0.002	12	0.02
	$S_{I/E} = \pm 0.076$	$df_{I/E} > 30$	$B_{I/E} = \pm 0.127$
III. Data Acquisition			
a. Excitation Voltage	0.011	>30	0.011
b. Electrical Simulation	0.011	>30	0.011
c. Signal Conditioning	0.013	>30	Negligible
d. Analog-to-Digital Conversion	Negligible	>30	Negligible
	$S_{DA} = \pm 0.02$	$df_{DA} > 30$	$B_{DA} = \pm 0.016$
IV. Data Processing			
a. Computer Resolution	Negligible		Negligible
b. Curve Fitting	Negligible		Negligible
	$S_{DP} = 0$		$B_{DP} = 0$
	$S_{total} = \pm 0.125$	$df_{total} > 30$	$B_{total} = \pm 0.167$

Table 4.6.2. Scale-Force Steady-State Error Source Audit Summary.

Error Source	Precision Index		Bias Limit
	Percent of Reading	Degrees of Freedom	Percent of Reading
Calibration Transfer Error	± 0.073	>30	± 0.106
Installation/Environment	± 0.076	>30	± 0.127
Data Acquisition	± 0.02	>30	± 0.016
Data Processing	± 0	>30	± 0

Error Components: $S_{total} = \sqrt{S_{cal}^2 + S_{I/E}^2} = \pm 0.12$ $B_{total} = \sqrt{B_{cal}^2 + B_{I/E}^2} = \pm 0.17$

Uncertainty: $U_{ADD} = \pm [(0.17) + 2(0.12)] = \pm 0.41$ percent

Table 4.7.1. Steady-State Measurement Uncertainty Estimates (Nonafterburning, Low-Bypass Turbofan).

Parameter	Range	Precision Index (S)		Bias Limit (B)		Uncertainty U_{ADD}
		Percent of Reading	Degrees of Freedom	Percent of Reading	Percent of Reading	Percent of Reading
Flow Total Pressure	35 to 100 KPA	± 0.07	>30	± 0.15		± 0.25
Flow Total Temperature	233 to 338°K	± 0.06	>30	± 0.22		± 0.34
Scale Force	15K to 50K N	± 0.12	>30	± 0.17		± 0.41
Fuel Flow	0.6 to 1.5 kg/sec	± 0.19	>30	± 0.24		± 0.42
Airflow	20 to 100 kg/sec	± 0.076	>30	± 0.22		± 0.37

Table 4.7.2. Influence Coefficient Matrix for Net Thrust (Nonafterburning, Low-Bypass Turbofan at Military Power).

Independent Parameter	Influence Coefficient, $\frac{\partial FN}{\partial I} \cdot \frac{I}{FN}$	
	Altitude - Sea Level Mach No. = 0	Altitude = 30,000 ft Mach No. = 0.9
Scale Force	0.87	0.76
Engine Inlet Total Pressure	1.30	1.08
Engine Inlet Total Temperature	0.07	0.19
Lab Seal Static Pressure	-0.03	-0.04
Test Cell Ambient Pressure	-1.41	-0.95
Venturi Inlet Total Pressure	0.14	-0.37
Venturi Inlet Total Temperature	-0.07	0.18

* The partial differential value of net thrust with respect to the independent parameter times the ratio of the independent parameter to net thrust with all other parameters held constant.

Table 4.7.3. Steady-State Engine Performance Parameter Uncertainty Estimates (Nonafterburning, Low-Bypass Turbofan).

Flight Conditions		Engine Power Setting	Net Thrust				Specific Fuel Consumption			
			Precision		Bias		Precision		Bias	
			Percent of Value	Degrees of Freedom	Percent of Value	Percent of Value	Percent of Value	Degrees of Freedom	Percent of Value	Percent of Value
Mach Number	Altitude, ft									
Static	Sea Level	Military	0.17	>30	0.31	0.65	0.26	>30	0.40	0.91
0.9	30K	Military	0.13	>30	0.25	0.49	0.23	>30	0.34	0.80

5.0 CONCLUDING REMARKS

This paper reviews a standard measurement uncertainty methodology, its development background, and national and international acceptance. The general procedural steps in applying the methodology to measurement processes were reviewed, and examples illustrating results of uncertainty analysis from typical turbine testing measurement systems showing both error source audits and uncertainties from the AEDC/ETP were provided.

Implementation of the uncertainty methodology provides (1) a systematic way to evaluate and report measurement uncertainties, (2) a basis for a detailed understanding of measurement systems performance such that system improvement planning can be based on cost versus benefit analysis, (3) information to enable the selecting and tailoring of measurement systems and practices to meet test program requirements, and (4) a basis for comparison of test results between test facilities.

Future efforts should be directed toward total national and international acceptance and implementation of the described methodology by the propulsion testing industries, instrumentation manufacturers, and others related to the testing industry. The propulsion testing industries should continue to explore ways to improve estimating and validating bias errors through cooperative efforts.

REFERENCES

1. Abernethy, R. B., Pratt and Whitney Aircraft, et al., "ICRPG Handbook for Estimating the Uncertainty in Measurements Made with Liquid Propellant Rocket Engine Systems," JANNAF (formerly ICRPG) Performance Standardization Working Group Report CPIA No. 180 (AD851 127), April 1969.
2. Abernethy, R. B., Pratt and Whitney Aircraft, and Thompson, Jr., J. W., ARO, Inc., "Handbook Uncertainty in Gas Turbine Measurements," AEDC-TR-73-5 (AD-755356), February 1973.
3. Abernethy, R. B., Pratt and Whitney Aircraft, et al., "Uncertainty in Gas Turbine Measurements," Revised 1980 Edition, ISA I-483-3.
4. "Uncertainty of In-Flight Thrust Determination," SAE AIR 1678, 1985.
5. ANSI/ASME MFC-2M, "Measurement Uncertainty for Fluid Flow in Closed Conduits," 1983.
6. Abernethy, R. B., Benedict, R. P., and Dowdell, R. B., Pratt and Whitney Aircraft, "ASME Measurement Uncertainty," ASME Paper 83-WA/FM-3.
7. ANSI/ASME PTC 19.1, "Measurement Uncertainty," Performance Test Codes Supplement, 1985.
8. Abernethy, R. B. and Ringhiser, Barbara, United Technologies Corp., "The History and Statistical Development of the New ASME-SAE-AIAA-ISO Measurement Uncertainty Methodology," AIAA Paper 85-1403, July 8, 1985.
9. AIAA Thrust-Drag Editorial Board, chaired by Dr. E. E. Covert, Director MIT, "Measure and Prediction of Thrust and Drag from Transports to Fighters," 1985.
10. "Fluid Flow Measurement Uncertainty," Draft, Revision of ISO/DIS 5168 for International Organization for Standardization Committee, ISO TC30 SC9.
11. ISO 5168, "Measurement of Fluid Flow--Estimation of Uncertainty of a Flow-Rate Measurement," 1976.
12. Smith, R. E., Jr. and Wehofer, S., Sverdrup Technology, Inc., AEDC Group, "Uncertainty of Turbine Engine Performance Measurements in Altitude Ground Test Facilities," Published in *Proceedings of the 29th International Instrumentation Symposium*, Volume 29, 1983.
13. Smith, R. E., Jr. and Wehofer, S., Sverdrup Technology, Inc., AEDC Group, "From Measurement Uncertainty to Measurement Communications, Credibility, and Cost Control in Propulsion Ground Test Facilities," ASME Paper, Published in *Journal Fluids Engineering*, Volume 107, No. 2, June 1985.
14. Book, *Thrust and Drag: Its Prediction and Verification*, Associate Editors, Eugene E. Covert, MIT, William F. Kimzey, Sverdrup Technology, Inc., C. R. James, Vought Aircraft Co. (Retired), G. K. Richey, Air Force Wright Aeronautical Laboratory, and E. C. Rooney, U. S. Navy, AIAA Progress in Aeronautics and Astronautics Series, Martin Summerfield, Editor-in-Chief, 1984.

ACKNOWLEDGMENTS

The authors would like to gratefully acknowledge S. Wehofer, W. A. Turrentine, Jr., and T. R. Ward for their help with the examples and reviews of the paper.

THE ACCURATE MEASUREMENT OF DRAG IN THE 8 FT X 8 FT TUNNEL

by

M. N. Wood and D. S. Capps
 Royal Aircraft Establishment
 Bedford MK41 6AE UK

SUMMARY

The techniques currently adopted in the 8ft x 8ft Wind Tunnel at RAE Bedford for the accurate measurement of drag are described in detail. Data are presented from three series of tests on a model of the A 310 aircraft and these demonstrate the level of accuracy which can be achieved.

LIST OF SYMBOLS

C_A' residual coefficient of axial force (body axes)
 C_D coefficient of drag
 C_D' residual coefficient of drag
 C_L coefficient of lift
 C_N coefficient of normal force (body axes)
 C_N' residual coefficient of normal force (body axes)
 M Mach number corrected for blockage effects
 ΔM increment in Mach number due to model blockage
 α incidence
 ϕ roll angle

1 INTRODUCTION

The accurate, repeatable measurement of drag presents the wind tunnel engineer with one of his more difficult problems. In particular, measurement of the drag of a subsonic civil transport model at cruise conditions to the accuracy required for project evaluation provides a most severe test of quality for the tunnel environment, instrumentation and experimental procedures. Cruise conditions for such a model represent a drag coefficient of approximately 0.03 at a lift coefficient of 0.5. Thus the achievement of an accuracy of one drag count (ie 0.0001 on C_D) requires the direction of the resultant aerodynamic force on the model to be defined to an accuracy of 0.01°, which presents a daunting challenge.

The RAE has a long history of involvement in drag measurement for research and military and civil projects, and the techniques currently employed in the 8 ft x 8 ft Wind Tunnel are essentially the same as those developed over 20 years ago and described in Ref 1. In the intervening years the instrumentation and data acquisition system have been transformed and there have been some refinements in technique but both the strain gauge balance design developed in the 1960's and the basic philosophy have stood the test of time.

This Paper describes the process by which drag data is produced for British Aerospace in support of the various Airbus projects. Before it can be used directly for project evaluation the data must be corrected for support sting interference, wake buoyancy effects, model distortion, transition trip drag, tail plane trim drag, propulsion effects etc, but these are topics in their own right, some of which are discussed in Ref 1. It seemed appropriate in this Paper to concentrate on a detailed discussion of the problems involved in generating the basic drag data which form the essential starting point for these additional corrections. Some of the problems and techniques adopted are specific to the environment of the 8 ft x 8 ft Tunnel and the equipment which is available but it is hoped that the overall picture will be informative.

Data from tests on a model of the A 310 configuration are presented. This particular model has been tested on three separate occasions over a period of four years, involving two different strain gauge balances, and the data should offer a fair picture of the accuracy and repeatability which is possible with sufficient care and attention to detail.

2 DESCRIPTION OF THE WIND TUNNEL

The 8 ft x 8 ft Wind Tunnel is a conventional, pressurised, continuous flow tunnel (Fig 1) which has several unusual features. The number of compressor stages can be varied, with a permanently installed low pressure section (originally with four stages but

now with only two) for subsonic testing, and a removable six stage high pressure section which is inserted for testing at supersonic speeds. The roof and floor of the test section and nozzle consist of long flexible plates which can be continuously adjusted to generate the required supersonic flow. The diffuser has movable sidewalls which are adjusted to improve pressure recovery at supersonic speeds. They can also be used to generate a sonic throat immediately downstream of the test section for control of subsonic Mach number above Mach 0.4 and incremental steps of 0.001 in Mach number can be readily achieved. At subsonic speeds, the sonic throat also inhibits the upstream transmission of aerodynamic noise generated in the diffuser, resulting in a quiet flow in the test section. The flow quality is further enhanced by the presence of a horizontal tube cooler upstream of the settling chamber. This consists of over 57000 tubes 5 m long and 30 mm internal diameter and acts as an extremely efficient honeycomb.

The tunnel has good control of stagnation pressure, temperature and humidity down to a frost point of -40°C , and the operating range of the tunnel (Fig 2) offers a useful variation in Reynolds number, particularly at subsonic speeds. Sting mounted models are firmly supported from an extremely stiff quadrant giving precise and repeatable control of model attitude.

In summary, the design of the tunnel and the control of flow parameters provide an excellent environment for high quality aerodynamic testing.

3 THE BALANCE AND INSTRUMENTATION

Details of the strain gauge balances used for Airbus testing are presented in Fig 3. The balances, manufactured from maraging steel, are 76.2 mm (3 inches) in diameter and are designed for a maximum normal force of 17.8 kN (4000 lb). At each end of the balance there is a taper joint of 16° included angle and great care is taken with the assembly of these joints when rigging the model to minimise the effects of joint slip. This cannot be completely eliminated and the effects need to be measured as part of the experimental technique described later.

The balance bridges are thermally compensated for zero shift but not for variations in Young's Modulus. The effects of possible thermal gradients along the balance are minimised by the use of dual element gauges and by careful positioning of the bridges. Temperatures are monitored at several points on the balance during wind tunnel testing. The basic calibrations over the design load range are carried out at room temperature and the partial calibrations described in section 5 are made at more representative temperatures to define the sensitivity of each individual balance channel for use in the data reduction process. Experience over many years has established that the balance design is basically sound and that the calibration can be adequately defined over the complete load range by means of simple first and second order interactions.

The balance signals, in the ± 10 mV range, are passed through individual 1000:1 fixed gain amplifiers and low pass filters which are usually set to 1 Hz for accurate drag measurement. The unfiltered signals are also monitored to provide a continuous check on the dynamic behaviour of the model. The filtered signals are multiplexed through a 16 bit analogue to digital converter scanning at 70 KHz. Several samples of data are taken at each test condition, inspected for noise and then averaged. Electrical noise is minimal and the resolution is more than adequate; typically one drag count represents about 25 adc counts for the data presented in this Paper. The amplifiers can be calibrated at any time during a test as can the adc using a 16 bit binary voltage source.

Quadrant attitude is monitored by an absolute encoder having a resolution of 0.001° and calibrations have established that the simple rack and pinion drive is extremely linear with no discernible hysteresis. The sturdy construction of the support system ensures that the attitude of the quadrant is unaffected by aerodynamic load. Deflections under load of the sting and balance are calculated using calibration data generated during the test series as explained in section 5. An inclinometer can be mounted in the model as an additional check on incidence but this is not essential to the technique.

The various reference pressures which are required for the data processing are measured by individual self-balancing capsule manometers (Ref 2). Although these manometers, with large internal reservoirs, have a slow response, they have a very stable zero and calibration and have proved extremely reliable for over 30 years. The manometers recording stagnation pressure have a resolution of 0.01 inch of mercury (0.34 mbar) representing 0.016% of set pressure at high Reynolds number. Those recording the various wall hole pressures have a resolution of 0.005 inch, (0.17 mbar) 0.024% of dynamic pressure at cruise Mach number.

4 A 310 MODEL INSTALLATION

The A 310 was represented by a model of approximately 1:26 scale with a wing span of 1.67 m (5.48 ft) and an overall length of 1.75 m (5.74 ft). The tailplane and nacelles were not represented for the particular tests discussed in this Paper. Transition bands, comprising a sparse distribution of appropriately sized glass beads retained by a thin film of epoxy adhesive, were applied to all surfaces. The mass of the model varied over the three series of tests, averaging 158 kg (348 lb).

The model was supported on a 76.2 mm (3 inch) diameter sting (Fig 4) which positioned the balance centre 185 mm (7.3 inches) upstream of the centre of rotation of the quadrant. The forward attachment block was designed to incline the fuselage datum 3° nose

down relative to the sting/balance axis. The cylindrical cavity in the rear fuselage, to provide clearance for sting/balance deflections, had a diameter of 95.2 mm (3.75 inches).

5 TEST PROCEDURES

All drag measurements on Airbus models follow well established test procedures. Prior to the main test runs a short 'warm-up' run is carried out in which the tunnel is operated at representative test conditions and the model is taken through the full anticipated range of aerodynamic loads. This short preliminary run brings the model, balance and tunnel up to a reasonable working temperature and level of dryness, as well as exercising the balance and the various joints in the support system.

Balance measurements are taken before each run at several angles of pitch and roll to determine the weight of the model and the 'zero gravity' zero for each balance channel. The model weight is a significant proportion of the subsequent aerodynamic loads and a detailed inspection of the pre-run data provides a check of some of the parameters being used for the data reduction.

During a test run, drag polars are generated at a range of Mach numbers close to cruise, generally at one fixed Reynolds number which for the A 310 was 6.2×10^6 based on aerodynamic mean chord. Measurements are made with the model at roll angles of 0° and 180° , the data being used subsequently to confirm or re-determine some of the parameters used in the analysis, as explained in section 6.

An unfortunate feature of the 8 ft x 8 ft Tunnel is that up to 75 minutes can elapse between taking the initial balance zeros and achieving the first set of test conditions. This is due partly to the need to synchronise the main compressor drive motor with the power supply and partly to the slow charging rate currently available. During this period it is possible for the balance zeros to drift slightly so, after the main drag polars have been completed, a small amount of data is repeated at each Mach number and then the tunnel is stopped and brought back to atmospheric pressure as quickly as possible, generally in less than ten minutes. Data taken before and after the run are inspected and the repeat wind-on data is compared with the main drag polars to confirm that the indicated drifts during the run are within acceptable limits.

In each test series a run is carried out to confirm that boundary layer transition has been adequately fixed at the test Reynolds number, without being over fixed. Visual techniques have not, up to now, proved successful in the 8 ft x 8 ft Tunnel and the method currently in use is to measure the drag at a fixed Mach number over a range of Reynolds number and to compare the data with theoretical estimates.

Finally, before the model/sting assembly is disconnected from the quadrant, a series of dead loads, combinations of normal force, axial force and pitching moment covering the range experienced during the tests, are applied to the model which is supported in an inverted position. These loads provide a check of the primary sensitivities of the balance channels and of the more significant interactions onto axial force. In addition, the angular deflection under load is measured between the quadrant and the model datum, including the small but significant internal deflection between the model datum and the 'live' end of the balance.

At each loading the quadrant is adjusted to maintain the fuselage datum at a fixed attitude, generally horizontal but 3° nose up for the particular A 310 configuration because of the model/balance angle. Indicated balance loads and quadrant attitude are recorded. When the loadings are complete additional measurements are made to determine certain angles which are required for the data reduction. They include the pitch angle which would exist, under zero gravitational force, between the roll axis and the fuselage datum and between the balance and the roll axis. The significance of the various measurements is discussed in the next section.

This calibration process is time consuming and it would clearly be far simpler to use a standard calibration for the balance and an inclinometer to determine the attitude of the model. To adopt such a technique would involve ignoring the possibility that the balance primary sensitivities and interactions, as well as the internal model deflections, may depend on the particular installation, whereas experience in the 8 ft x 8 ft Wind Tunnel has shown that drag accuracy is lost if these factors are ignored.

6 DERIVATION OF PARAMETERS FOR DATA REDUCTION

Each balance has a well defined calibration consisting of primary sensitivities together with matrices of first and second order interactions referred to axes aligned with the 'live' end of the balance. An instrumentation fault is suspected if any primary sensitivity indicated by the in-stream calibration differs from the standard value by more than 0.25%. A further check on the primary sensitivities of the normal and axial force channels can be obtained by comparing known values of model weight with those derived from the balance data taken before each test run.

For convenience, and to avoid the need to determine separately the flexibility of the model/balance connection under applied normal force and pitching moment, the balance interactions are re-defined so as to refer to axes which are fixed in the model and aligned with the forward end of the balance at zero load. In particular this can require appreciable changes to be made to the interactions onto axial force from (Normal force) and (Normal force) x (Pitching moment).

The total deflection of the sting/balance/model assembly can be as high as 1.2° at the test conditions appropriate to cruise. The response to load is linear except for small differences between data for increasing and decreasing load, due to slight hysteresis in the slip of the various joints in the support system.

The data from the in-stream calibration is processed using the derived balance parameters together with the measured angles and flexibilities. The analysis should confirm that the model was at zero incidence with zero applied drag force throughout the calibration and there is some scope for fine tuning of the various parameters to improve the collapse of the data. The analysis of the aerodynamic data from the main tests, particularly comparisons between measurements made at roll angles of 0° and 180° may suggest the need for further small alterations to the processing parameters, as discussed in the next section. The final choice of parameters, which is individual to the particular test series, is based on an overall assessment of the available data.

Turning now to the tunnel airflow parameters, Ref 3 describes in detail the method adopted for calibrating the solid-walled test section and for determining the dynamic pressure at the model, corrected for the effects of blockage. Figs 5 and 6 shows the variation with Mach number of the theoretical increase in Mach number due to blockage at the model reference point and the residual variation over the planform of the model at Mach 0.78. The same linear theory can also be used to estimate the changes in static pressure at selected positions on the roof and floor of the test section adjacent to the model. Comparison between the estimated changes at the wall and those actually measured during the tests generates a correction to the estimated blockage effect at the position of the model.

The mean cross-flow at the model is determined by comparing the variation of lift with incidence measured with the model mounted at roll angles of 0° and 180° . A downwash angle of approximately 0.03° is indicated, which is relatively independent of Mach number and Reynolds number.

7 ANALYSIS OF THE A 310 DATA

Three series of tests were performed on the A 310 model, in 1983 using the 3 inch 'O' balance and in 1986 and 1987 on the 3 inch 'Q' balance. The model was assembled to nominally the same aerodynamic standard for each test series with the same position and quality of transition bands. Because of practical difficulties experienced during the first two series, there was some uncertainty about the derivation of some of the parameters required for the analysis of the data. Additional hardware was manufactured for the 1987 tests and a comprehensive in-stream calibration was carried out, which had not previously been possible with this particular model. The data was analysed in accordance with the process outlined in section 6.

Fig 7 presents a comparison of data obtained in 1987 at Mach numbers of 0.78 and 0.8 at high Reynolds number for the model mounted at roll angles of 0° and 180° . In an attempt to improve the presentation of the data and to highlight the discrepancies and experimental scatter, the aerodynamic coefficients have been modified by the removal of a linear variation of normal force with incidence in Fig 7a, a parabolic variation of axial force with normal force in Fig 7b, and a lift dependent drag term in Fig 7c.

Collapse of the normal force data confirms that the sting support system, at zero indicated pitch angle, is correctly aligned with the mean flow direction. There is a small uncertainty in the determination of cross flow angle because of the experimental scatter evident in Fig 7a. The computation of drag is sensitive to angular error, so axial force, for which the computation does not involve flow angle, is inspected. The collapse of the data shown in Fig 7b confirms the choice of the various parameters used in the data reduction, and collapse of the drag data then provides further confirmation of the correct determination of cross flow angle. The derivation of the parameters for the data reduction was straightforward for this particular test series and the collapse of the data was very satisfactory. This is not always the case and the analysis can become a protracted process of adjusting the many parameters within prescribed tolerance limits to provide the best collapse of the data from the aerodynamic tests and the in-stream balance calibration.

The accompanying Table quantifies the main corrections which must be applied to the axial force measurements at a typical condition, $C_L = 0.475$ at Mach 0.78. (Axial force indicated by the balance is negative because of the 3° balance/model angle.) At zero roll angle the values of the corrections have been obtained by interpolation as no data is available at exactly this condition.

	$\phi = 0^\circ$	$\phi = 180^\circ$
Indicated axial force (Newtons)	-62.4	-266.1
Correction for first order balance interactions	-89.7	-124.7
Correction for second order balance interactions	+24.9	+46.4
Correction for model weight	-109.0	+110.5
Correction for sting cavity pressure	+41.8	+38.9
Corrected axial force (Newtons)	-194.4	-195.0
(1 drag count = 1.9 Newtons)		

The difference in load indicated by the axial force channel at roll angles of 0° and 180° is equivalent to more than 100 drag counts. The magnitudes of the balance interactions are different for the two conditions because of the asymmetric manner in which the gravitational loads contribute to the total loads. The removal of the component of model weight is the most significant correction, largely because of the 3° balance/model angle for this particular configuration, and highlights the need for accurate determination of the weight of the model and the total angular deflection. The different corrections for sting cavity pressure arise because the sting is in a different position in the cavity in the two cases due to the deflection of the sting and balance under gravitational load. This difference is unimportant however because it has been established during measurements of sting interference that although movement of the sting in the cavity does cause appreciable variations in the internal pressure, it does not affect the net external drag force.

Comparative data from the three series of tests are presented, again in modified form, in Fig 8. The apparent discrepancy in Fig 8a between the data collected in 1983 and the later tests is equivalent to an error in incidence of approximately 0.02° . As the data for roll angles of 0° and 180° collapse satisfactorily, this implies that the balance/model angle of 3° was underestimated for the 1983 tests. This error would reduce the computed axial force coefficient by 0.00017 at a lift coefficient of 0.5 and there is a suggestion of such an error in the data presented in Fig 8b. On the other hand the computation of drag would be unaffected and indeed the repeatability of the drag data across the three series of tests is very reassuring.

It was pointed out earlier in the section that the calibration procedures were not entirely satisfactory for the early test series resulting in small uncertainties in the definition of some of the parameters, particularly the angles which have such a significant effect on the data reduction. Despite these small discrepancies it is felt that the repeatability of the data across the three series of tests is acceptable, particularly when it is appreciated that two different strain gauge balances were involved and that the repeatable assembly of a wind tunnel model can never be guaranteed absolutely.

8 CONCLUDING REMARKS

It would be wrong to suggest that the level of accuracy demonstrated in this Paper can be achieved automatically for all test series. The conditions for each test are different in detail, particularly the angles and deflections which have such an important influence on the determination of drag. Care and vigilance are required in applying the experimental techniques and analysing the data, and the techniques are constantly being reviewed. An integral sting/balance is currently being manufactured which will eliminate the sting/balance joint and improve the rigidity and repeatability of the model attachment, and there is some scope for improvement in model design to minimise the internal deflections under load.

It is hoped that these improvements will reduce the need for some of the comprehensive calibration procedures which are currently found to be necessary but it is anticipated that the generation of accurate drag data will continue to present a significant technical challenge.

REFERENCES

- 1 C. R. Taylor, J. R. Hall, R. W. Hayward. Super VC 10 cruise drag - a wind-tunnel investigation. Part 1 Experimental techniques. ARC Current Paper No 1125 1970.
- 2 G. F. Midwood, R. W. Hayward. An automatic self-balancing capsule manometer. ARC Current Paper No 231 1955.
- 3 D. Isaacs. Calibration of the RAE Bedford 8 ft x 8 ft Wind Tunnel at subsonic speeds, including a discussion of the corrections applied to the measured pressure distribution to allow for the direct and blockage effects due to the calibration probe shape. ARC R&M 3583 1968.



Fig. 1 The 8ft x 8ft Wind Tunnel

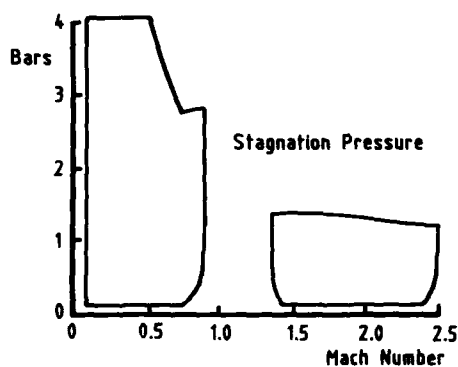
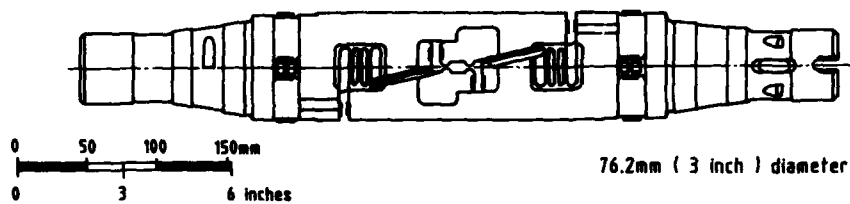


Fig. 2 Performance Envelope



Maximum Design Loads					
Normal Force	17.8 KN	4000 lbs	Side Force	4.18 KN	940 lbs
Axial Force	2.22 KN	500 lbs	Yawing Moment	0.73 KNm	535 lb.ft
Pitching Moment	2.26 KNm	1670 lb.ft	Rolling Moment	0.73 KNm	535 lb.ft

Fig. 3 RAE Strain Gauge Balance

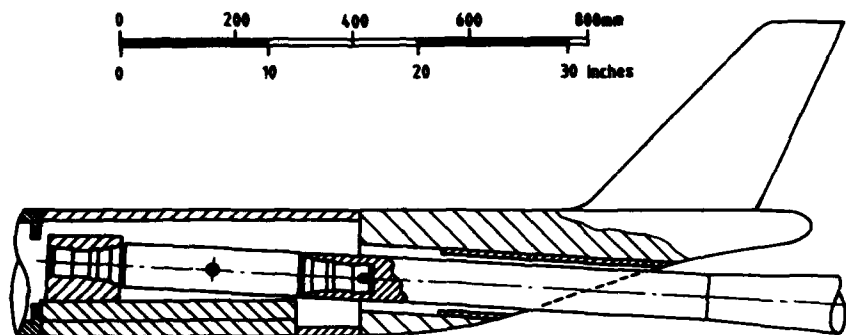


Fig. 4 Arrangement of A310 model on sting and balance

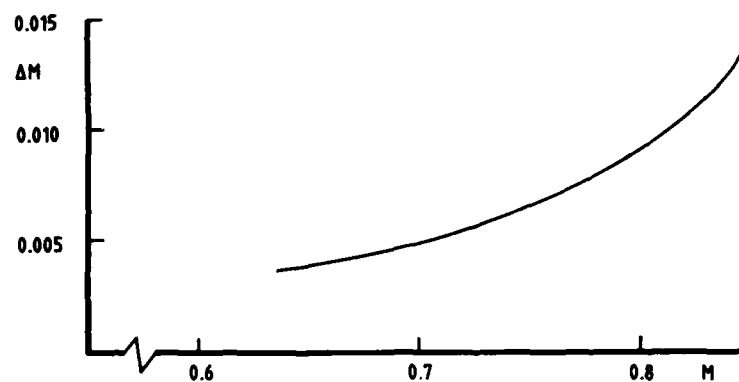


Fig. 5 Increase in Mach number due to blockage at the A310 model reference point

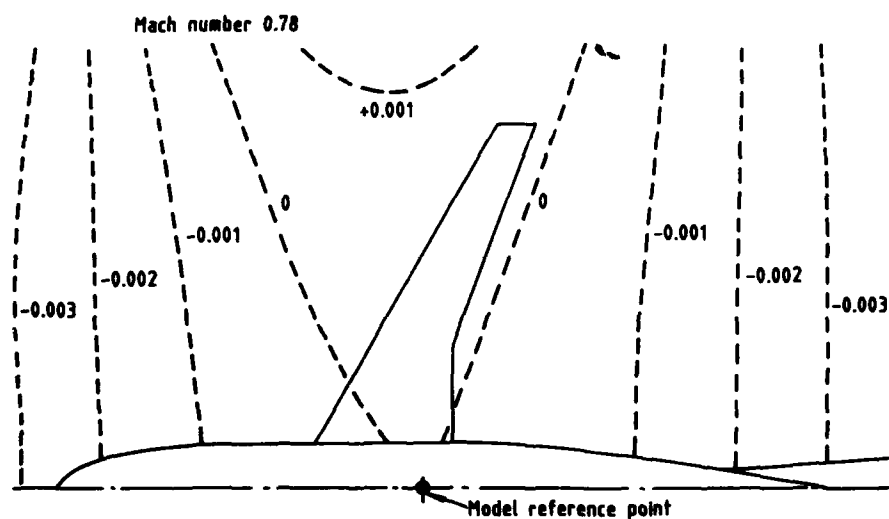


Fig. 6 Residual variation in Mach number due to blockage

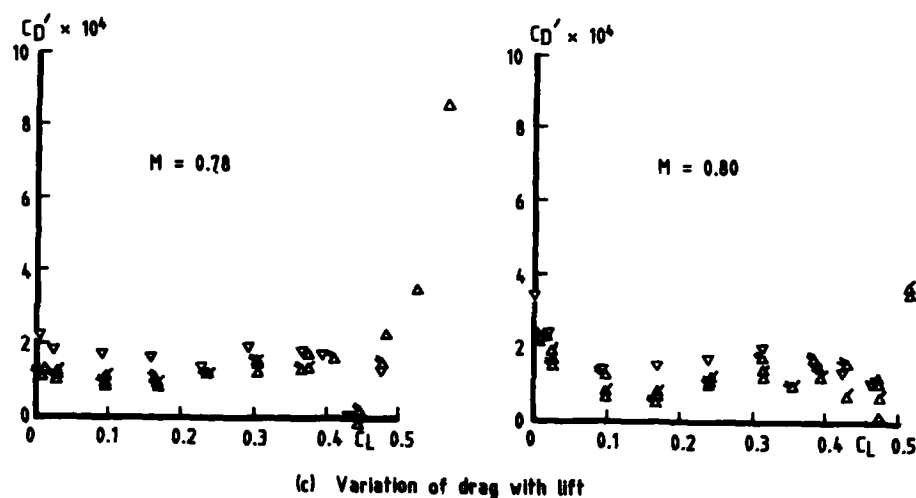
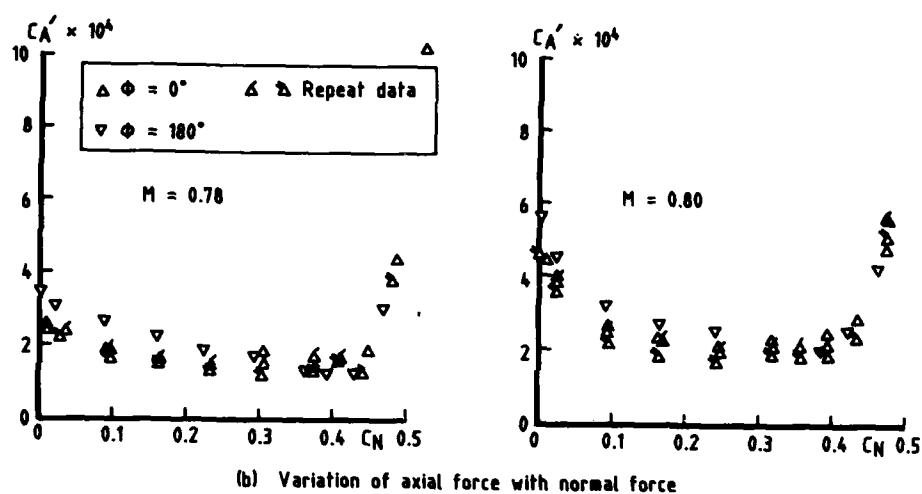
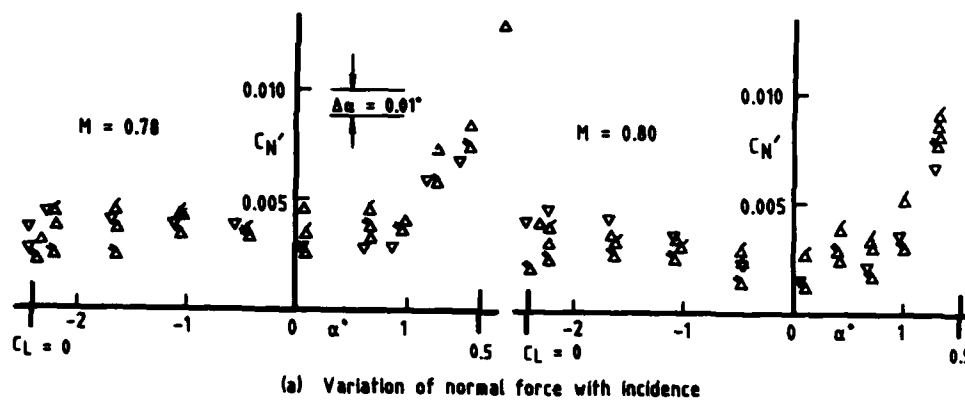


Fig. 7 Comparison of 1987 test data at zero and 180° of roll

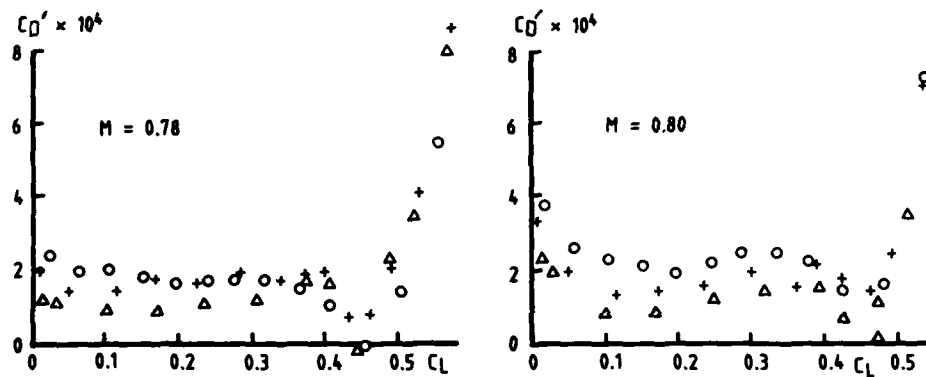
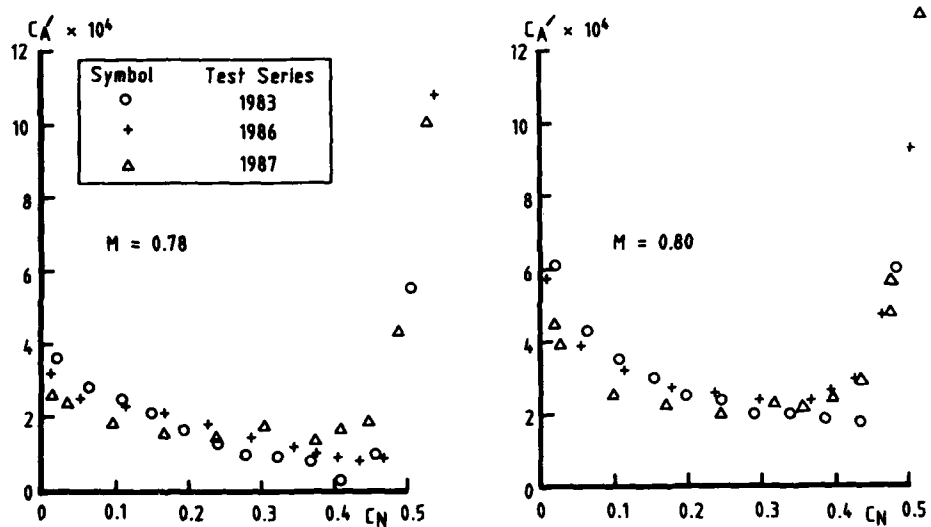
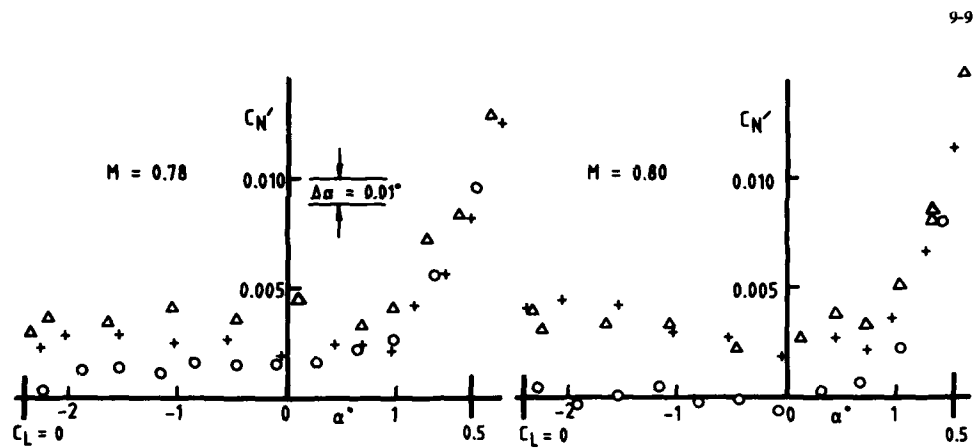


Fig. 8 Comparison of data from three test series

ACCURATE DRAG ESTIMATION USING A SINGLE COMPONENT DRAG MODEL TECHNIQUE

by
A.M. Cassie
Senior Wind Tunnel Engineer
1.2m High Speed Wind Tunnel
British Aerospace PLC
Warton Unit
Preston PR4 1AX
UK

SUMMARY

This paper covers the design, development and operation of an advanced afterbody drag rig at the High Speed Wind Tunnel, Warton.

The rig has been extensively used over a 16 year period for minimisation of modern combat aircraft afterbody drag. Accurate incremental drag data is produced by measurement of the axial force on a fully representative metric afterbody section.

A full description of the rig is given along with techniques for data correction and presentation of typical data.

LIST OF SYMBOLS

A	Area	bal	Uncorrected balance output
Cd	Drag coefficient	c1	Balance cavity
Cp	Pressure coefficient	c2	Seal cavity
D	Afterbody axial force	c3	Port annulus cavity
dB	Decibels	c4	Starboard annulus cavity
f	Frequency	c5	Bearing block cavity
HSWT	High Speed Wind Tunnel	c6	Afterbody rear cavity
JPR	Jet Pressure Ratio	jp1	Upstream jetpipe external area
M	Mach number	jp2	Downstream jetpipe external area
P	Pressure	noz	Nozzle exit external area
P _∞	Tunnel static pressure	s1-s6	Outer seal frame areas
q	Tunnel dynamic pressure	seal	Inner seal frame area
S	Cd reference area	sh1	Shroud forward internal area
T	Thrust	sh2	Shroud exit internal area
(T-D)	Thrust-Drag	tp	"Trouser-piece" maximum area

Subscripts:

bb1	Bearing block frontal area
bb2	Bearing block void area

1. INTRODUCTION

It is well appreciated that the afterbody drag of a twin jet combat aircraft can amount to over 30% of the total aircraft zero lift drag. There is, therefore, considerable scope for drag minimisation if a suitable wind tunnel rig is available during early project design. Prior to 1969 little direct measurement of afterbody drag had been possible in the U.K. Available afterbody test rigs were of the "Thrust - Drag" type requiring very accurate calculation or calibration of nozzle thrust and then not always giving acceptable accuracy of the small drag difference. Rigs of this type are still widely used (see Refs. 1-5). The alternative method of calculating afterbody drag from pressure measurements is only adequate and convenient for simple single nozzle configurations with a minimum of separated flow.

The need arose at the start of development of MRCA (later Tornado) for better measurement of afterbody forces. In 1969, therefore, design and build of an advanced drag data rig was undertaken at Warton. The rig was to have the following capabilities:

- (i) Measurement of afterbody axial force, independently of thrust, side force and normal force loadings, with maximum accuracy and repeatability.
- (ii) Simulation of a jet efflux with controllable and repeatable pressure ratio.
- (iii) Measurement of jet thrust, independently of afterbody axial force, side force and normal force loadings.
- (iv) Minimum support structure interference on the metric portion of the rig.
- (v) Measurement of internal static pressures for thrust and drag correction purposes.
- (vi) Measurement of external static pressures for diagnostic purposes.
- (vii) Measurement of jet air supply mass flow and jetpipe static pressures for the accurate calculation of jet pressure ratio.

(viii) Ease of afterbody and detail configuration changes.

(ix) Ability to be operated in the supersonic working section of the Warton 1.2m High Speed Wind Tunnel over a Mach number range of 1.4 to 2.5.

The requirement resulted in the design and manufacture of a twin sting, model-cart mounted afterbody drag rig which was first used for testing in 1971. The rig was subsequently modified in 1977 to reduce interference on planned research afterbodies and is now operated over a Mach number range of 0.4 to 2.0 giving highly accurate and repeatable afterbody axial force data.

During design integration of engines and airframe, there is often a possible trade-off between installed thrust and afterbody drag. For a fighter configuration with an interceptor role, thrust-minus-drag is extremely important. The cost effectiveness of increasing thrust by using more sophisticated nozzles, compared with designing for minimum afterbody drag, is difficult to evaluate unless model measurements can be obtained at an early stage.

At transonic and supersonic speeds, measurements from rear sting mounted overall forces and component loads models have many limitations when used in drag synthesis. Afterbodies may be necessarily distorted to accommodate the sting, flow-through intake duct outlets and metric/non-metric clearance. This applies particularly to the Warton 1.2m HSWT which, being a high Reynolds number tunnel, requires stronger, and hence larger, stings in order to withstand the increased loads. Afterbody distortion is also an unfortunate consequence of the increasingly compact afterbody designs for today's fighter aircraft.

Corrections for sting interference and the absence or incomplete simulation of jet interaction with external flow are not very amenable to theoretical treatment. However, direct afterbody force measurements can now be made on a rig able to mount simulated single sting mounted afterbodies and realistic afterbodies with representative jet flow. This offers the possibility of applying incremental drag corrections to six-component model measurements.

2. RIG DESCRIPTION

2.1 CURRENT CONFIGURATION

The Warton afterbody drag rig in its present configuration (figures 1 and 2) is able to mount accurate twin jet combat aircraft afterbody representations at a scale of around 1/20. The rig can be broken down into four major components which are described below.

The rig support structure has been developed to eliminate reflected support shock wave interference on the metric afterbody section at transonic and supersonic speeds and to give a minimum and constant pressure field interference at subsonic speeds. This enables accurate incremental drag measurements to be made without recourse to pressure field corrections. High pressure air, power supplies, signal wiring and pneumatic tubing are fed to the wing tips via hollow side struts spanned by a cross-yoke arrangement. This assembly is bolted to the tunnel structure (figure 3). The support structure is designed to give minimum blockage area whilst retaining sufficient strength for operation up to Mach 2.0.

The wings and forebody are the non-metric part of the model. The forebody is configured to be representative of a twin engined fighter type with faired intakes. The nose cone, canopy and spine can be easily changed to represent different designs. The wings, which support the forebody and attach at the wingtips to the side strut supports, are of a NACA symmetrical section with a constant leading edge sweep of 57.3° and a constant t/c ratio of 7%. The wings are ducted to carry the high pressure air supply into the main fuselage section and also carry electrical wiring and pressure tubing into the model. The whole wing/centre fuselage (figure 4) is an integral unit manufactured in eight sections and electron beam welded together for maximum strength. Each wing consists of a leading edge, centre section and trailing edge and the centre fuselage (including wing root) is made up of two symmetric halves. The material for this assembly is Maraging steel with an Ultimate Tensile Strength of 1800 N/sq.mm. For representation of delta-wing configurations "stub-wing" fairings are fitted to the trailing edge of the inboard wing. A corresponding wing root section is included on the metric afterbody with a metric/non-metric gap maintained between this and the stub wing.

Figures 5 and 6 illustrate the design and assembly of the thrust system. The non-metric flow entry blocks contain floating inner high pressure chambers which are constrained to move only in an axial direction by bearings on the attached jetpipes. The chambers are sealed from the model internal cavity by metal bellows. Air flows through to the exit nozzles via "jetpipe" sections and a "trouser-piece" section which alters the jet centreline to that required. The air ducts contain anti-swirl devices and perforated plates which ensure a "flat" total pressure distribution with minimum boundary layer thickness.

In order to minimise the cross sectional area of air ducts through the wing the air supply is maintained at high pressure until it enters the thrust system. However, the supply pressure then needs to be reduced to a sensible level, this is a difficult task in such a small volume. The two sets of perforated plates reduce supply total pressure by a factor of up to 5 giving maximum typical achievable jet total pressures for dry and reheat

nozzles of 1020 and 485 kPa respectively.

The thrust assembly is attached at the forward end to the thrust balance via an axial flexure arrangement.

Figures 7 and 8 illustrate the drag balance system and the assembly of the afterbody. The afterbody is built around a bushed block which runs on bearings on the hardened jetpipes. Attached to the bearing block at the forward end is a seal frame which blends in profile with the forebody and houses a double PTFE seal to prevent external pressure leakage into the afterbody cavity. The seal provides a low friction sliding joint between the forebody and afterbody. In a "zero-load" condition the seal gap is approximately 0.2 mm.

The remainder of the afterbody is attached to the rear of the bearing block and usually consists of upper and lower main afterbody sections, fin, final boat-tail section and nozzle shrouds. Various attachments may be available for a particular configuration such as upper and lower gully fillers, parachute and sensor housings, internozzle fairings, airbrakes and actuator fairings, missiles, vortex generators, etc.

The metric afterbody is attached to the drag balance via upper and lower links running forward through the thrust system; flexures are incorporated in the forward end of the drag links.

External pressures on the afterbody, boat-tail and shrouds and internal cavity pressures are fed forward to the Scanivalve via PVC tubing in the afterbody and nickel tubing across the centre fuselage section.

2.2 RIG DEVELOPMENTS TO PRESENT DATE

Initially the rig was of short span and was intended for operation in the Mach number range 1.4 to 2.5 only. Subsequently it was operated subsonically (up to $M = 0.95$) with acceptable wing/forebody/support interference. Operation was restricted to the above Mach number ranges due to unacceptable reflected shock interference in the transonic and low supersonic regions.

Pressure to provide accurate data in the transonic range led to a major re-design of the rig. The modifications required to eliminate shock interference had the added benefit of significantly reducing the subsonic support interference. The main features of the re-design were:

- (i) Doubling the rig span to eliminate side support shock wave interference on the longest envisaged afterbody. This also had the effect of producing a constant and greatly reduced wing/forebody/support pressure field in the afterbody region.
- (ii) Provision of shorter side support fairings suitable for use at all Mach numbers including operation in the ARA 2.7x2.4m transonic tunnel. These fairings were designed to avoid support shock wave impingement on the afterbody and retain constant subsonic support interference.
- (iii) Reduction of the possibility of JPR dependent subsonic interference because of the increase in afterbody/cross-yoke longitudinal separation as a result of doubling rig span.

The pressure field interference of the modified rig was predicted using a subsonic panel program. The program had been validated for the original support configuration by excellent agreement with data taken from a pressure plotted parallel afterbody.

The program predicted subsonic interference for the new rig to be zero at $M = 0.6$ and $0.0003 \Delta C_d$ at $M = 0.9$ (C_d based on maximum fuselage cross sectional area). Such interference is seen as negligible in the prime use of the rig for afterbody development and for measurement of increments only in overall aircraft drag synthesis.

As a result of increasing the rig span, supersonic starting loads in the HSWT were increased. It was therefore necessary to restrict operation to $M = 2.0$.

The original rig was model cart mounted in the HSWT, but following the modifications it is now bolted to the tunnel structure for additional strength.

2.3 RIG INSTRUMENTATION

Afterbody axial force, thrust and thrust-drag are measured by means of a modular 3-component strain gauge balance assembly mounted in the centre-fuselage section of the rig (figure 9). The assembly is attached to the non-metric part of the rig at the thrust-minus-drag module. Overloading of the balances is avoided by closure of the clearances between the modules at maximum load. The modular construction of the assembly facilitates the changing of a balance range, if necessary. Figure 10 shows typical thrust and thrust-minus-drag balance data.

Internal and external steady pressures are measured by means of an 'S' type Scanivalve mounted in the forebody of the model (figure 11). Pressures are sampled at a rate of 25 ports per second giving an average seven datapoints per 25 second run in the HSWT. Figures 12, 13 and 14 show typical pressure data gathered by the Scanivalve.

Requests for unsteady or dynamic pressure measurement are becoming increasingly common. This data is used to analyse aerodynamic effects such as fin buffet or nozzle shroud pressure loading due to twin jet interaction (screech). For this purpose, miniature transducers are mounted in the model at the location in question. Figure 15 shows typical unsteady pressure data after Power Spectral Density Analysis.

In order to provide accurately calculated values of Jet Pressure Ratio, the total mass flow rate of the model air supply system is measured external to the tunnel using an orifice plate system. Jetpipe static pressures are measured using transducers mounted in the afterbody.

2.4 TUNNEL FACILITIES

The 1.2m HSWT at Warton is an intermittent blowdown facility operating from 4000 kPa storage pressure and discharging to atmosphere. Supersonic and transonic working sections lie in tandem. The closed wall supersonic section covers a Mach number range 1.4 to 4.0 set by top and bottom flexible plate walls. The perforated wall transonic section has a Mach number range of 0.4 to 1.2, working section and plenum pressures are controlled by varying second throat and diffuser settings. Models or rigs can be mounted on either of two model carts plus a half-model cart. Access to the tunnel is through one opening side wall in the transonic section. A supply line has been provided for cold air jet blowing models, this is fed from storage vessels separate to the main tunnel air supply but also at 4000 kPa maximum storage pressure.

The afterbody drag rig has also been successfully used in the 2.7 x 2.4m transonic tunnel at ARA, Bedford. This is a continuous running, closed circuit facility providing Mach numbers up to $M = 1.35$. The support sting mounted from a full span blade will accept the afterbody drag rig on a standard 4 inch taper joint. There is an adequate air supply and pressure control system to provide cold air jet simulation.

2.5 RIG OPERATION

The normal test variable for a run is jet pressure ratio. This is varied by rapid response valve via control hardware. The air supply controller is pre-set with up to eight total pressure demands calibrated to achieve the required JPR's. The controller is stepped via a discrete output from the model control software. Each JPR datapoint has a duration of roughly 3.5 seconds, including settling time, to allow a full Scanivalve scan. Data is recorded when steady conditions are reached.

Because of increasing demand for more comprehensive coverage of afterbody external pressures, current practice is to do separate "drag" and "pressure" runs for each configuration. This is solely because an excess of pneumatic tubing inside the afterbody and bridging the metric/non-metric break may cause hysteresis and inaccurate drag balance output due to friction between the tubing and metric components of the rig. A minimum number of pressures are measured for drag runs. These must include six internal cavity pressures and up to six metric/non-metric seal gap pressures for corrections to the balance output (figure 16). Up to eight internozzle base and shroud base pressures may be measured for diagnostic purposes (figure 17). For pressure runs up to 18 shroud and 21 afterbody surface pressures may be measured. Unsteady pressure transducers are also only installed for pressure runs.

Oil flow visualisation runs may also be requested. For these a single jet pressure ratio is maintained for a run of about 10 seconds duration (figure 18). Schlieren flow visualisation is a standard output for all supersonic runs (figure 19).

2.6 FUTURE DEVELOPMENTS

There are a number of future projects outlined for the rig. Some of these require further development of the rig which will increase its versatility and the quality and volume of data output per run.

The HSWT is developing ZOC electronic pressure scanning equipment operation to replace the use of electro-mechanical Scanivalves (figure 20). The use of this equipment will mean faster data acquisition and hence more JPR datapoints per run. Pressure data will also be more accurate and it may be possible to re-combine drag and pressure runs due to a large reduction in tubing/wiring crossing the metric/non-metric break.

The use of ambient temperature air for jet simulation obviously does not ideally reproduce the effect of a hot jet exhaust. A proposal for hot jet simulation is being examined and a scheme for the installation of liquid hydrogen burners in the rig has been produced.

Testing of re-usable space vehicle afterbody configurations is proposed which will lead to the development of a multi-nozzle rig.

The feasibility of limited incidence variation for transonic testing is being investigated. This would be most desirable for a multi-nozzle space vehicle configuration with large base area and subsequent high drag sensitivity to angle of attack variation.

3. CALIBRATIONS AND CORRECTIONS

3.1 BALANCE CALIBRATIONS

It is crucial to the production of highly accurate and repeatable force data from the rig that calibrations of the strain gauge balances can be performed with the model fully rigged. Therefore, simple techniques have been developed which allow the application of calibration loads to the metric thrust and afterbody axial force systems with the model fully assembled and installed in the tunnel.

Drag calibrations are repeated during a test phase after any model configuration change likely to have disturbed the internal layout of pressure tubing, wiring, etc. Data from a drag calibration is checked for unacceptable hysteresis or large deviations from the mean calibration slopes. If necessary, model rigging is rechecked and the calibration repeated.

3.2 INTERNAL PRESSURE CORRECTION BOOK-KEEPING

Variation in internal cavity pressures during a run inevitably causes a variation of the balance outputs. Variation of seal gap pressure (external to the seal) has a similar effect. These errors are accounted for by monitoring internal cavity and seal gap pressures. Force corrections are calculated due to these pressures acting on relevant areas. Thrust and drag corrections are derived; both corrections are applied to the thrust-minus-drag balance output. Figure 21 shows typical drag correction data.

Corrections are calculated and applied as follows:

(i) DRAG

Corrected Drag:

$$D = D_{bal} + \Delta D$$

Total drag correction:

$$\Delta D = \Delta D_1 + \Delta D_2 + \Delta D_3$$

Seal pressure correction:

$$\Delta D_1 = -I(2.A_{sn}.(P_{sn}-P_{\infty})) \text{ where } n = 1 \text{ to } 6$$

Internal cavity pressure correction:

$$\Delta D_2 = \Delta D_{21} + \Delta D_{22} + \Delta D_{23}$$

$$\Delta D_{21} = -(A_{seal} - A_{bb1}).(P_{c2} - P_{\infty})$$

$$\Delta D_{22} = (A_{bb2} - A_{bb1}).(P_{c5} - P_{\infty})$$

$$\Delta D_{23} = -(A_{bb2} - A_{sh1}).\left[\frac{P_{c5} + P_{c6}}{2} - P_{\infty}\right]$$

Nozzle/shroud annulus pressure correction:

$$\Delta D_3 = -(A_{sh1} - A_{sh2}).\left[\frac{P_{c3} + P_{c4}}{2} - P_{\infty}\right]$$

(ii) THRUST

Corrected Thrust:

$$T = T_{bal} + \Delta T$$

Total thrust correction:

$$\Delta T = \Delta T_1 + \Delta T_2 + \Delta T_3 + \Delta T_4$$

$$\Delta T_1 = A_{jp1}.(P_{c1} - P_{\infty})$$

$$\Delta T_2 = (A_{tp} - A_{jp1}).(P_{c5} - P_{\infty})$$

$$\Delta T_3 = -(A_{tp} - A_{jp2}).(P_{c6} - P_{\infty})$$

$$\Delta T_4 = -(A_{jp2} - A_{noz}).\left[\frac{P_{c3} + P_{c4}}{2} - P_{\infty}\right]$$

(iii) THRUST-DRAG

Corrected thrust-drag:

$$(T-D) = (T-D)_{bal} + \Delta T - \Delta D$$

Note: All pressures are referenced to tunnel ambient static. The assumption is made that in an ideal situation P_{∞} would act on every surface of the model.

4. DATA QUALITY

The Marton afterbody drag rig has consistently achieved "jet on" axial force repeatability tolerances of ± 0.0005 Cd short term and ± 0.0010 Cd long term (figures 22 and 23), where Cd is based on maximum fuselage cross-sectional area. These figures represent a maximum error in measured force of $\pm 1.0\%$ at $M = 1.6$. "Jet off" results generally show a larger random scatter believed to be due to larger amplitude base pressure fluctuations which occur when the stabilising influence of the jet is removed.

Possible sources of error and their quantitative effects on incremental axial force measurement are as follows:

(a) Hysteresis

Calibration of the balance and bearings alone shows negligible hysteresis. However, when a model is fully rigged, the addition of the seal and pressure plotting tubes bridging the metric split produces an average error due to hysteresis equivalent to ± 0.0008 Cd. Operation in a blowdown tunnel with its impulsive starting loads is likely to reduce the effect of hysteresis compared to that measured from a static calibration, this is reflected in the short term ("in phase") repeatability margin of ± 0.0005 Cd. Much of the long term repeatability margin of ± 0.0010 Cd can probably be accounted for by variation in the rigging of pressure tubes between test phases.

(b) Temperature Effects

Cooling due to air expansion through the perforated plates could cause balance drift due to heat conduction from the balance through the thrust link. This effect is negligible in a blowdown tunnel due to the short run duration.

(c) Leakage

For a rig with a metric/non-metric split there exists the possibility of leakage through the internal cavity driven by the pressure differential between the split station and the nozzle/shroud base annulus. Adequate monitoring of internal cavity pressures allows corrections for internal pressure variation to be applied to the balance data. The ability to maintain very small nozzle/shroud annular clearances, due to axial bearing support, is very important. It ensures that the cavity acts as a reservoir of stable pressure, despite fluctuating base pressures, and measurement of annulus pressure gives an extremely sensitive indication of any internal leakage. The split seal on the rig is very effective and errors due to seal leakage are negligible.

(d) Pressure Measurements

The limit of accuracy of pressure measurement is set by the sampling error possible when the output signal from the Scanivalve transducer, filtered down to 40 Hz, is digitised. Every effort is made to eliminate pneumatic errors by minimising tube lengths and thoroughly leak checking and response checking during model rigging. The use of reference pressures on the Scanivalve gives an effective zero reading for each datapoint and an additional reference line allows calibration of the Scanivalve in-situ.

The internal cavity pressures have been measured within a tolerance of ± 0.001 Cp corresponding to a possible internal correction error of ± 0.0005 Cd. The annulus pressures have been measured within a tolerance of ± 0.002 Cp, correction error ± 0.0003 Cd. Base and external surface pressure coefficients have a sampling error range of ± 0.003 Cp, showing the benefit of small clearances in stabilising the cavity pressure. The remaining pressure correction is that external to the seal at the split station. The sampling error scatter for those pressures is ± 0.002 Cp, equivalent to a possible correction error of ± 0.0004 Cd.

Summarising measurement accuracies which contribute to repeatability we have:

$$\text{HYSTERESIS} + \text{CAVITY Cp} + \text{ANNULUS Cp} + \text{SEAL GAP Cp} = \text{TOTAL ERROR}$$

The overall accuracy due to the above factors is given by:

$$\pm \sqrt{(0.0008^2 + 0.0005^2 + 0.0003^2 + 0.0004^2)} = \pm 0.0011 \text{ Cd}$$

This compares very well with the observed long term repeatability.

5. DRAG SYNTHESIS FOR THE AIRCRAFT

The derivation of a drag dataset for assessing aircraft performance is commonly based on wind tunnel model data. Supersonic zero-lift drag in particular requires measurements from a representative model since even modern day computational methods cannot give absolute drag levels with certainty.

Basic airframe zero-lift drag is generally measured using a sting mounted model without jet simulation. To accommodate the sting and also intake flow out of the base of the model some distortion of the afterbody of the model is necessary. In consequence the

effect of the distortion needs to be determined. A representation of the distorted afterbody is tested on the afterbody rig to provide an increment to a chosen jet pressure ratio reference condition for a representative afterbody model with jets (figure 24).

A schematic of the book-keeping adopted is shown in figure 25. It can be seen that afterbody model measurements are used to provide:

- (i) An increment to reference conditions for the drag account.
- (ii) The effect of jet conditions for incorporation in the engine account; engine thrust being debited for engine throttle-dependent intake drag and afterbody force.

In addition a Time Marching Euler method of computation is used in drag synthesis to account for minor configuration changes between the aircraft definition and the model tested. The method uses panelled afterbody simulations, taking account of separated regions, (figure 26) and provides a correction for the boat-tail drag difference. Base drag differences are corrected by applying wind tunnel model base pressure data to defined areas (figure 27).

6. CONCLUSIONS

- (i) An advanced afterbody drag rig has been developed which is able to provide very accurate incremental drag measurements from fully representative afterbodies with jet simulation.
- (ii) The rig has an excellent long term repeatability record, repeat data is consistently within a tolerance of ± 0.001 Cd (based on maximum fuselage cross-sectional area).
- (iii) Data from the rig is used both in afterbody development during early project design and for full aircraft drag synthesis as corrections applied to measurements from sting mounted forces and moments models.
- (iv) The versatility of the rig has been demonstrated, comprehensive coverage of afterbody surface and base pressure measurement is possible including unsteady pressures for buffet and shroud loading investigations.
- (v) Future developments of the rig will increase its versatility and further improve data quality and throughput.
- (vi) The rig is an extremely useful aid to modern combat aircraft design and has already more than proved its worth in terms of greatly reducing the amount of flight testing necessary to perfect an afterbody configuration.

7. REFERENCES

1. Capone, F.J. Aeropropulsive Characteristics at Mach numbers up to 2.2 of Axisymmetric and Nonaxisymmetric Nozzles Installed on an F-18 Model. NASA TP 2044 August 1982
2. Capone, F.J. Aeropropulsive Characteristics of Twin Nonaxisymmetric Vectoring Nozzles Installed with Forward-Swept and Aft-Swept Wings. NASA TP 1778 March 1981
3. Chesters, C.M. & Pozniak, O.M. The Design and Development of a Rig for Measuring the Installed Performance of Twin Nozzle Afterbodies. ARA Memo No. 150 September 1969
4. Goldsmith, E.L. & Carter, E.C. A Review of Methods Used for the Representation of Engine Flows in High Speed Wind Tunnel Testing. RAE Tech. Report 72012 April 1972
5. Pozniak, O.M. The Technique of Thrust and Afterbody Drag Measurement - A Bibliography with Extracts and Notes. ARA Report No. 45 July 1977
6. Watson, A. The Design and Development of an Afterbody Drag Rig. BAe Warton AXM 85 March 1975
7. Watson, A. A Modified Support Structure for R32 Afterbody Drag Rig. BAe Warton AXM 97 October 1978

10-8

- | | | | |
|-----|---------------|---|---------------|
| 8. | Watson, A. | Summary of Supersonic Afterbody Drag Measurements on a Series of Wind Tunnel Model Configurations Terminating at the Jet Exit.
BAe Warton AXR 38 | March 1978 |
| 9. | Vint, A. | R32 Afterbody Rig Improvement.
BAe Warton Ae 385 | December 1977 |
| 10. | Leyland, D.C. | Lessons from Tornado Afterbody Development.
AGARD CP 339 Paper No. 8 | October 1982 |

8. ACKNOWLEDGEMENTS

The author would like to acknowledge the assistance of the following persons in preparation of this paper.

Mr. D. C. Leyland for section 5.

Mr. A. R. Whitaker for submission of the original abstract.

Mr. A. Watson and Mr. G. Lawson for their extensive experience of the rig.

This work has been carried out with the support of the Procurement Executive, Ministry of Defence.



FIGURE 1 THE WARTON AFTERBODY DRAG RIG

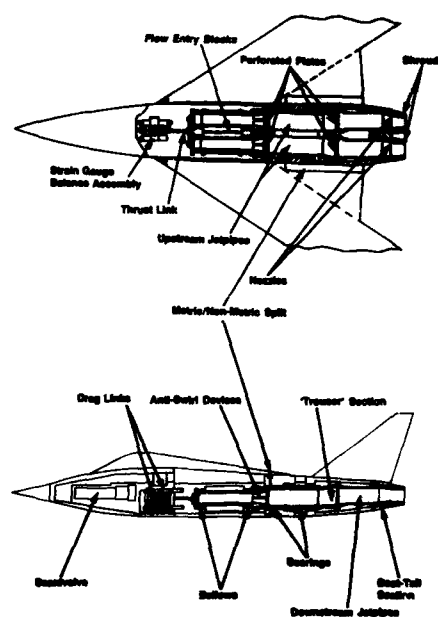


FIGURE 2 GENERAL ARRANGEMENT OF AN AFTERBODY DRAG MODEL

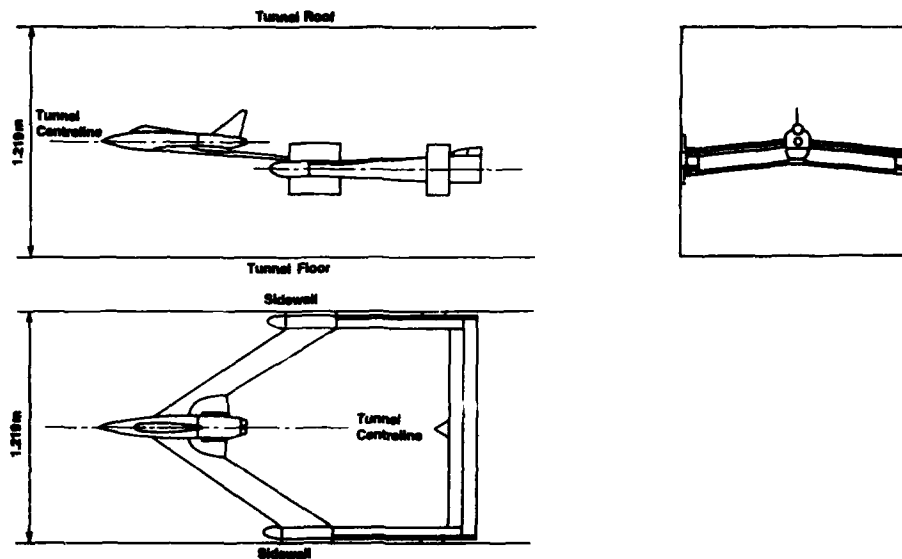


FIGURE 3 INSTALLATION OF THE AFTERBODY DRAG RIG IN THE WARTON 1.2m HIGH SPEED WIND TUNNEL (TRANSONIC WORKING SECTION)

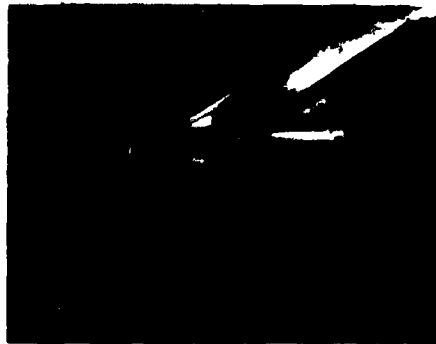


FIGURE 4 NON-METRIC WING/CENTRE FUSELAGE ASSEMBLY

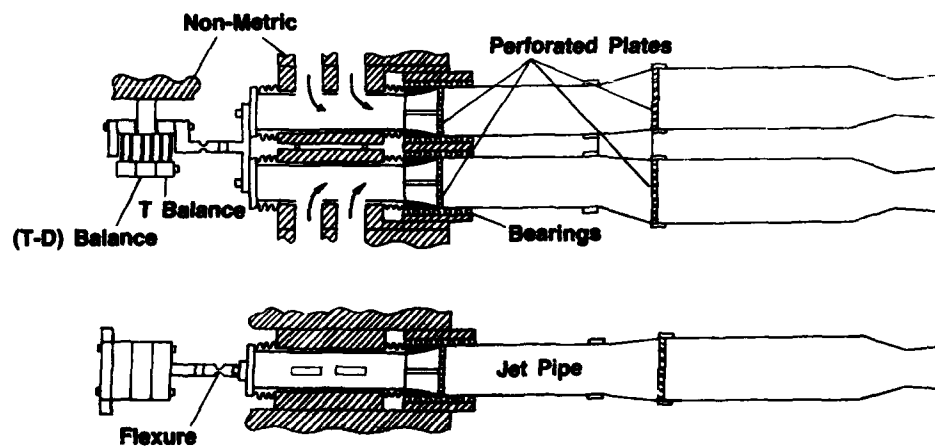


FIGURE 5 DESIGN OF THE METRIC THRUST SYSTEM

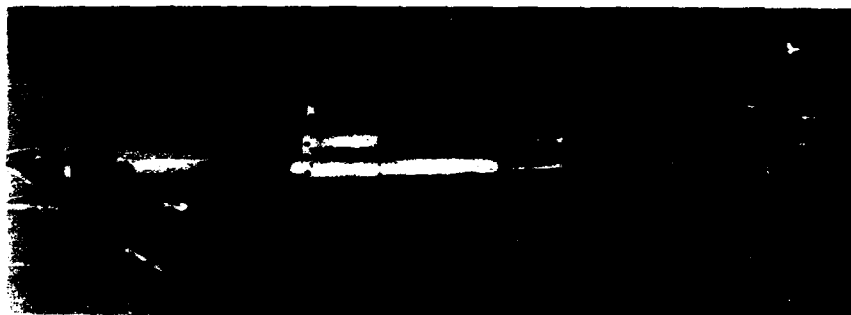


FIGURE 6 THE THRUST SYSTEM

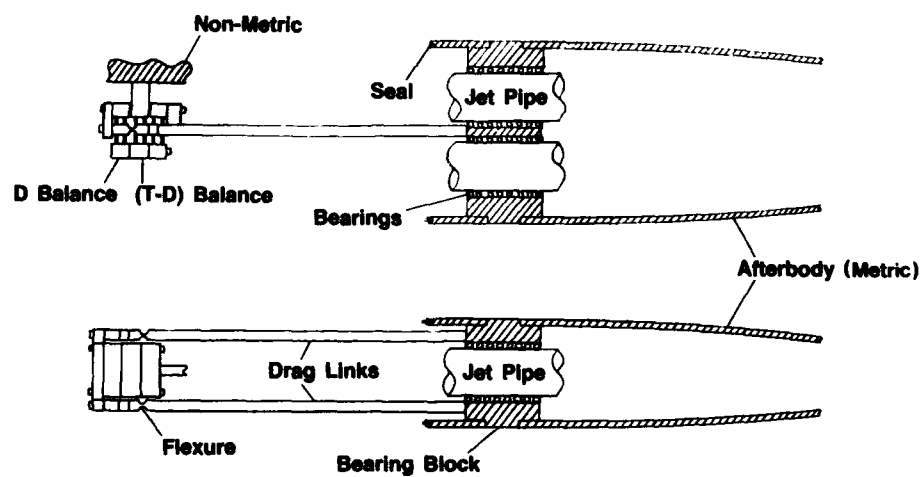


FIGURE 7 DESIGN OF THE METRIC AFTERBODY AXIAL FORCE SYSTEM

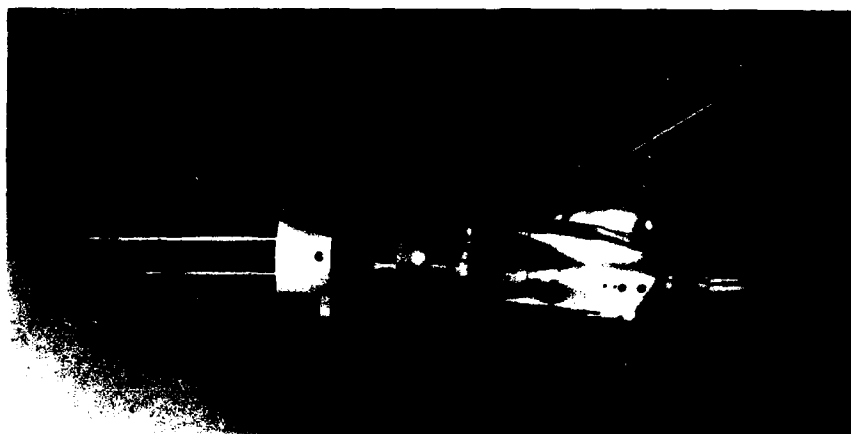


FIGURE 8 THE AFTERBODY AXIAL FORCE SYSTEM

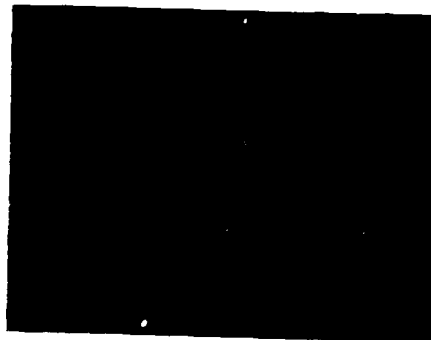


FIGURE 9 THREE-COMPONENT STRAIN GAUGE ASSEMBLY

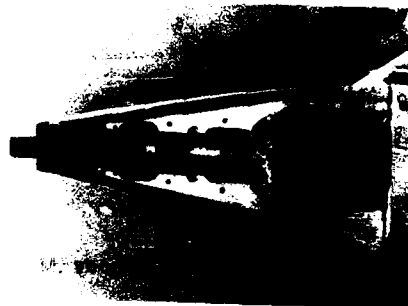


FIGURE 11 SCANIVALVE MOUNTED IN FOREBODY

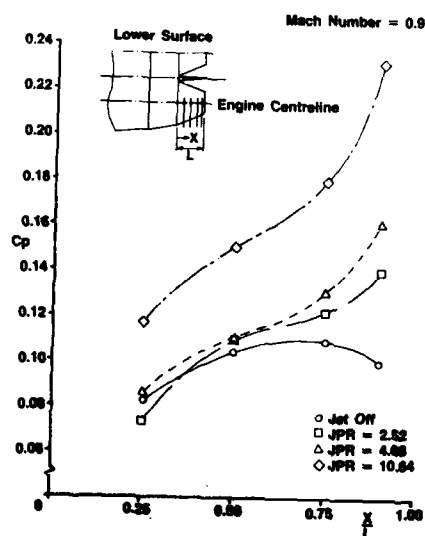


FIGURE 13 SHROUD SURFACE PRESSURE DATA

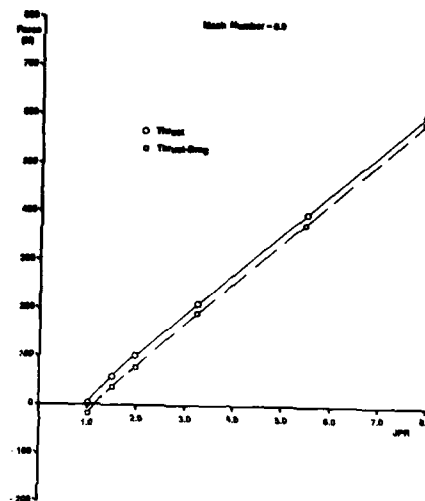


FIGURE 10 THRUST AND THRUST-MINUS-DRAG DATA

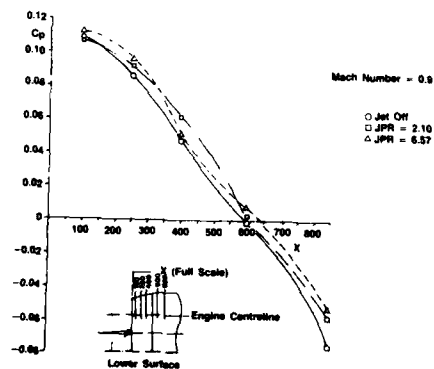


FIGURE 12 AFTERBODY SURFACE PRESSURE DATA

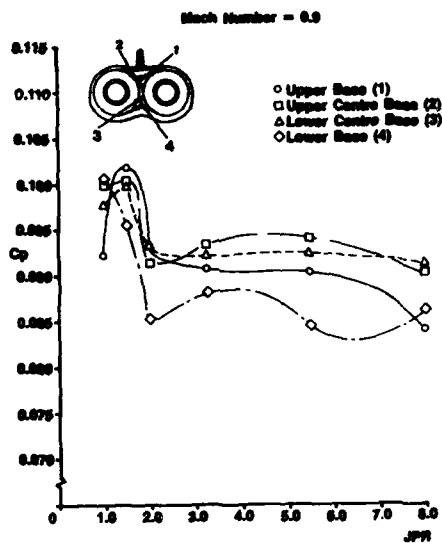


FIGURE 14 BASE PRESSURE DATA

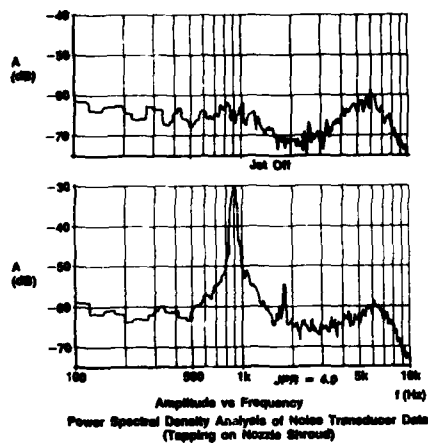


FIGURE 15 UNSTEADY PRESSURE DATA

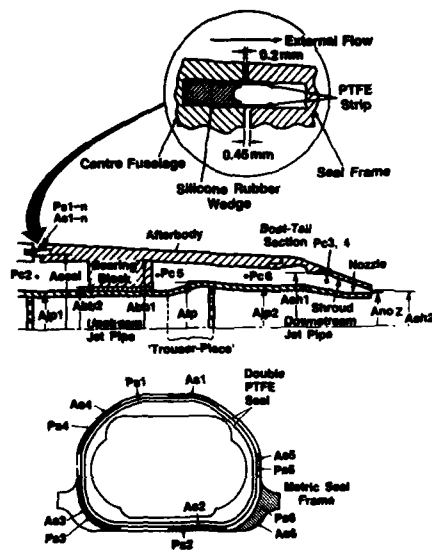


FIGURE 16 LOCATION OF PRESSURES AND AREAS FOR FORCE MEASUREMENT CORRECTION

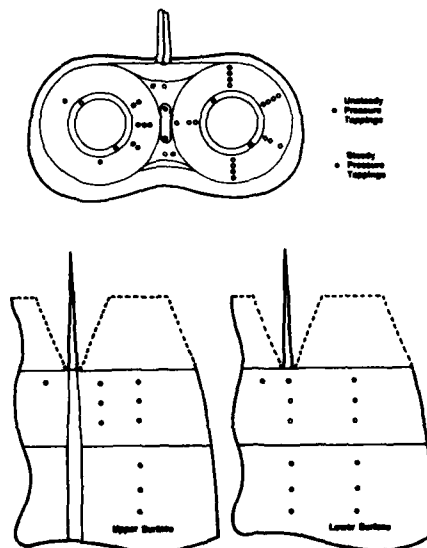


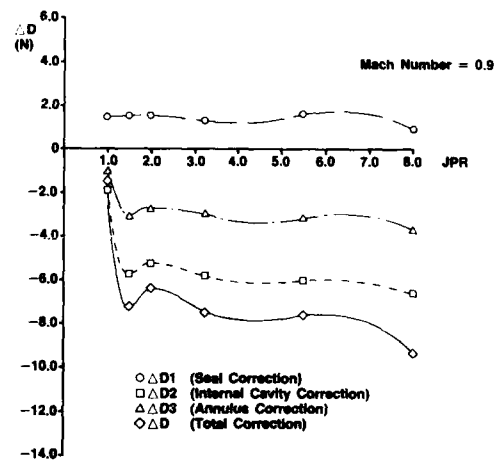
FIGURE 17 LOCATION OF AFTERBODY PRESSURE TAPPINGS

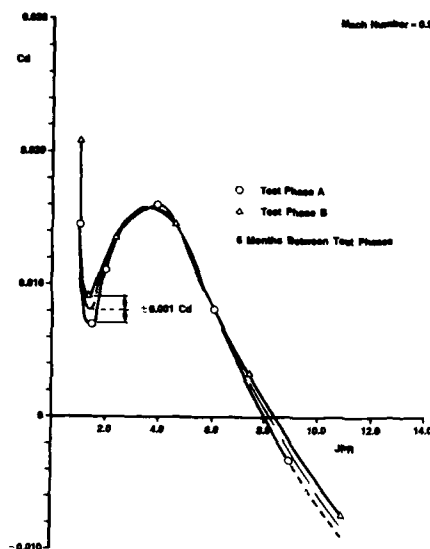


FIGURE 18 OIL FLOW VISUALISATION



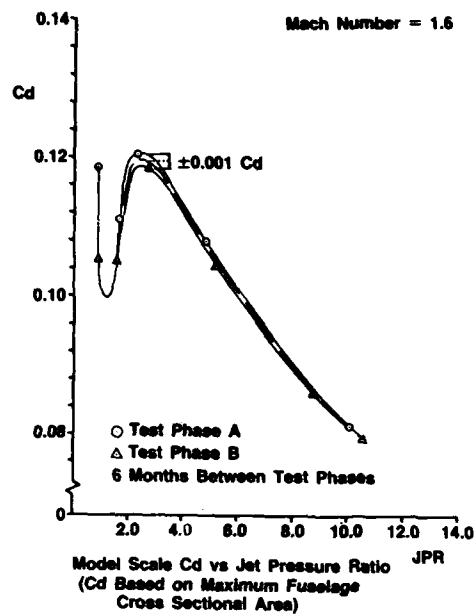
FIGURE 19 SCHLIEREN FLOW VISUALISATION

FIGURE 20 ZOC PRESSURE SCANNING
MODULESFIGURE 21 AFTERBODY AXIAL
FORCE CORRECTIONS



Model Scale Cd vs Jet Pressure Ratio
(Cd Based on Maximum Fuselage Cross Sectional Area)

FIGURE 22 LONG TERM AFTERBODY AXIAL FORCE REPEATABILITY (SUBSONIC)



Model Scale Cd vs Jet Pressure Ratio JPR
(Cd Based on Maximum Fuselage Cross Sectional Area)

FIGURE 23 LONG TERM AFTERBODY AXIAL FORCE REPEATABILITY (SUPERSONIC)

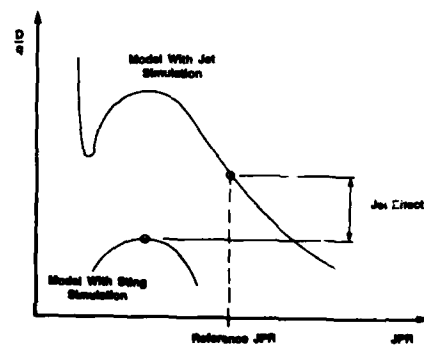


FIGURE 24 DERIVATION OF THE JET EFFECT INCREMENT USED IN DRAG SYNTHESIS

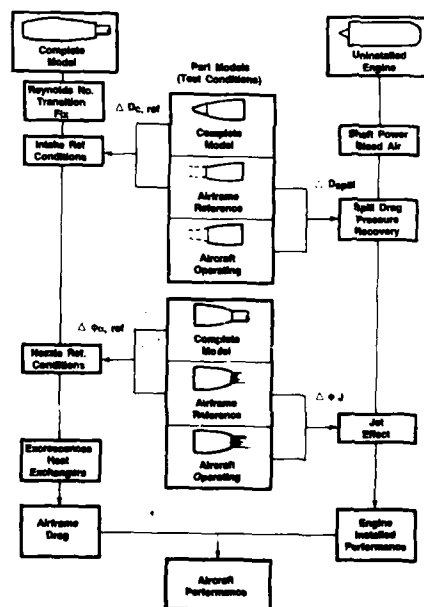
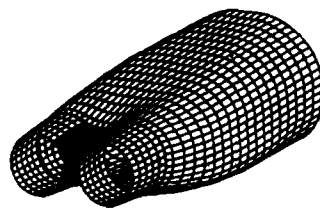
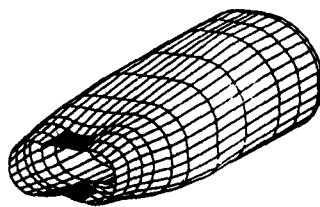


FIGURE 25 WIND TUNNEL MODEL DRAG ANALYSIS AND AIRCRAFT PERFORMANCE SYNTHESIS



■ Internozzle and Centre Base Separated Flow Region

Numerical Aircraft Geometry



■ Approximation to Attached Flow Path

Numerical Model Geometry

FIGURE 26 DISTORTION OF GEOMETRY FOR DRAG SYNTHESIS USING A TIME MARCHING EULER PROGRAM

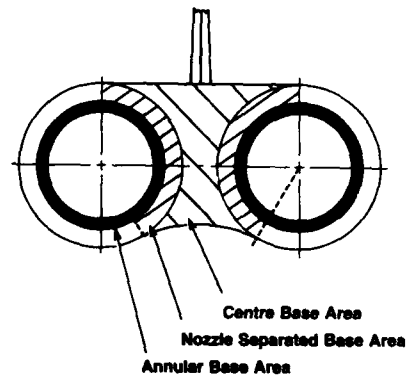


FIGURE 27 BASE AREA DEFINITIONS FOR DRAG SYNTHESIS

DEVELOPMENT OF TESTING TECHNIQUES IN A LARGE TRANSONIC WIND TUNNEL TO ACHIEVE
A REQUIRED DRAG ACCURACY AND FLOW STANDARDS FOR MODERN CIVIL TRANSPORTS

by

R.C.Carter and K.C.Pallister
Aircraft Research Association Ltd.
Manton Lane, Bedford UK

SUMMARY

This paper uses experience and results obtained over recent years in the ARA 9' x 6' transonic wind tunnel to address the questions of measurement and flow quality, data accuracy and achieved performance. The discussions relate primarily to experience with civil transports for which accurate drag prediction and efficient drag reduction through reliable experimental techniques is of major importance. The quality of results is studied via the definition of the problem areas, the correction methods and analysis of dynamics of the flow and the associated measurements. Techniques specific to a large development transonic tunnel are discussed in detail with a constant awareness of the cost and efficiency in relation to the required accuracy and repeatability standards.

1 INTRODUCTION

The requirements of the civil aircraft transport industry present some of the most stringent demands on accuracy and reliability of wind tunnel data. Aircraft developments in the past 7 years have concentrated on refinements to maximise the performance of designs within what superficially appears to be a very similar family of shapes. The large step jumps in configurations seen in early airliner developments have tended to stabilise into conventional wing body arrangements with wing mounted nacelles, with the concentration on optimisation of the total configuration to give an aerodynamically refined product. Whilst this situation is currently being changed by the introduction of the open rotor concept the work described in this paper has been based on the need for reliable experiments to recognise and confirm the existence of very small increments of performance.

The major advances in configuration performance have mainly been derived from wing aerodynamics. Improvements in design targets and design methods have together shown improvements in wing/body aerodynamic efficiencies of the order of 17% over the past 10 years. The inevitable but necessary excrecences that grow on the optimised wing body configuration must be accounted into the production aircraft performance. These, to a large extent, are difficult to account in present theoretical methods, and so, the wind tunnel, whilst being challenged by CFD for the definition of optimum shapes at specific design points, remains a vital adjunct to the assessment of viscous, vortical and separated flows on real wings with pylons, engine flows, flap track fairings and wing tip fences.

The purpose of this paper is to describe how the large ARA transonic wind tunnel has been adapted through operating and testing techniques to meet the stringent accuracy requirements of civil transports.

Consideration will be given to the need for model shape accuracy to meet the design pressure distributions and the need for large models. Flow quality of the empty tunnel stream must be within the limits of significance of calculation and experimental methods. Flow description in the presence of the model interference must be known and support interference must be capable of evaluation. In this accurately-defined flow environment, performance of measuring systems are examined along with the stability of the airstream and methods for accommodating model induced instabilities of the test flow.

Techniques of tunnel operation to minimise flow instabilities and speed fluctuations are discussed and the effects of taking data during the continuous traverse mode.

In addition to tunnel flow quality, the stabilising of the body and wing viscous flow is discussed and the use of transition fixing and detection methods and techniques.

As a means to increasing model scale and Reynolds number the use of the half model technique is discussed as a technique for providing incremental data particularly in relation to engine flow representations and powered models. The relationship between half model and complete model test conditions will be discussed and the effect of large half models on flow instability.

The theme of the paper is the continuous attention to detail that is necessary to achieve the high quality demanded of modern wind tunnels even for relative accuracy measurements. Absolute accuracy, which can only be validated in relation to flight test accuracy is only briefly mentioned.

2 THE DRAG MEASUREMENT PROBLEM

Fig. 1 illustrates typical drag polars which can be considered to be the ultimate objective of a wind tunnel drag measurement campaign. Such tests are conducted using full span scaled civil transport type models in the ARA 2.74m x 2.44m transonic wind tunnel. A typical model (1.70m wing span) supported on a 53.34mm diameter single sting is illustrated in Fig. 2. A relatively large number of intermediate model configurations between the clean wing and the fully complete model layouts depicted in Fig. 1 are usually investigated to quantify the drag associated with the installation of many aircraft items such as nacelles and pylons, flap track fairings, tip devices, variable camber etc. Fig. 3 shows typical incremental drag characteristics associated with a number of these items. Considerable use is also made of a twin sting method of model support, shown in Fig. 4, to examine the drag characteristics of different rear fuselage and empennage designs. The twin sting support system is also used to quantify single sting interference effects. Thus Fig. 1 and 3 immediately indicate that drag measurement testing can be considered to have two related aims;

- (i) the establishment of the absolute model drag, and
- (ii) the establishment of incremental drag characteristics.

At conditions of practical interest ($M = 0.82$, $C_L = 0.45$, say) the magnitude of the components which constitute the total measured model drag may be typically

(a) fuselage skin friction C_D	0.0072
(b) fuselage form drag C_D	0.0005
(c) wing skin friction C_D	0.0059
(d) wing form drag C_D	0.0017
(e) wing vortex drag C_D	0.0075
(f) wing wave drag C_D	0.0035

Total clean wing drag (without empennage) = 0.0263

- (g) each additional individual model item
 $\Delta C_D = 0$ to ± 0.00050 (say)
 eg. flap track fairings, tip devices etc.

The measurement of model drag by an internal strain gauge balance gives the total drag and hence the individual "theoretical" components listed in (a)-(f) above cannot be isolated directly by balance measurements alone. These data, however, give a good indication of the magnitude of the drag constituents and it is clearly the way in which these each vary with lift coefficient and Mach number which ultimately leads to the measured shape of the polar.

The incremental drag of each individual model item, (g) above, including mutual interference drag, is obtained from two model configurations using the simple expression;

$$\Delta C_D (\text{item}) = C_D \text{ of model with item} - C_D \text{ of model without item}$$

(M, C_L = constant say)

although this is fundamentally an inaccurate method, in that relatively small drag changes are

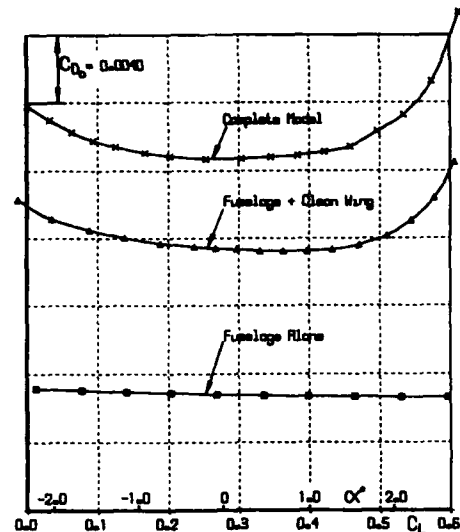


Figure 1. Typical Model Drag Polars.

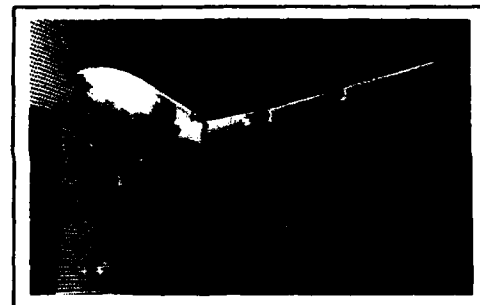


Figure 2. Typical Full span civil transport model supported on a single sting.

calculated as the difference between two large measurements, it is probably the only way of obtaining the required drag increments which are usually dominated by mutual interference effects. The major reasons for incremental drag measurement testing are not only to measure the installed characteristics, of say a given wing tip device, but also to ascertain which of a number of variations and modifications to the geometry of, for example the tip device, give the optimum installed drag characteristics.

Thus it is the prediction of the total aircraft drag at full scale conditions which leads to the absolute model drag accuracy measurement requirement specified in Reference 1 of 0.0005 in C_D and the incremental requirement which leads to the 0.0001 accuracy in ΔC_D . It should also be noted that for diagnostic reasons the aerodynamic designer demands these levels of accuracy not just close to the design flight conditions but also over a sizable M, C_L envelope. Interpreted from the wind tunnel engineers viewpoint, the

Note:

The parameter $C_{D0} = C_D - C_L^2/w \times \text{Aspect Ratio}$ is frequently used by ARA when presenting drag data and should not be confused with the drag at $C_L = 0$.

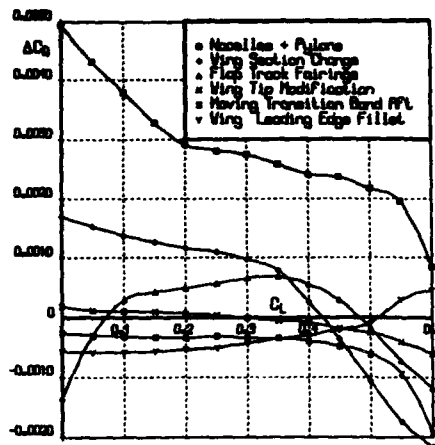


Figure 3. Typical Drag Increments.



Figure 4. Typical Full span civil transport model supported on the twin sting rig.

absolute drag measurement requirement means that at the very least, each time the same model is tested in the wind tunnel the drag coefficient measurements must repeat to within 0.0005. In order to achieve the incremental drag target accuracy, exercises usually have to be conducted within a given test series, (i.e. the model has to remain in the wind tunnel for all the tests) whilst the required increments are being obtained.

When Reference 1 was written, one practical situation which leads to an absolute accuracy measurement requirement of closer to 0.0001 in C_D was not considered. In practice it is sometimes necessary to compare model characteristics obtained from different test series which may have been undertaken many months apart. Such a case may arise if the characteristics of a new wing design are to be compared with those of an earlier design already tested. If all the model components are still available then, at the expense of repeat testing, "back to back" tests may be performed (but possibly still involving two entries into the wind tunnel). If the new wing is physically the old model wing irreversibly modified then "back to back" tests cannot be performed and an inter-test series comparison has to be relied upon.

Based on the above discussion ARA aim to measure model drag to better than ± 0.00005 in C_D to achieve the incremental drag requirement of 0.0001 and to repeat inter-test series drag characteristics on an identical model configuration to within ± 0.0001 in C_D . This has been found to be a very demanding objective.

Although each transonic wind tunnel facility involved in measuring the drag of civil transport aircraft models have common accuracy goals, the way in which these targets are achieved depends enormously on the particular characteristics of each facility. The techniques used by ARA have evolved over the last thirty years but it is probably only in the last decade that drag accuracies close to those now demanded have been regularly achieved. It has been principally the demand for good quality drag data on models of such aircraft as the BAe 125, BAe 146, A300B, A310, A320 and currently the A330/ A340 European Airbus that has stimulated the relentless search at ARA for improved accuracy.

3 SOURCES OF ERROR

3.1 Transition Fixing

All wind tunnel establishments have their own views on the most appropriate boundary layer fix techniques applicable to their tunnel. The ideal approach requires a combination of preliminary tests covering detailed pressure plotting, with a range of roughness band transition fixes and associated sublimation and oil flow tests, and theoretical calculations of pressure distributions and boundary layer for both model and full scale conditions. This work over a range of M , C_L and full scale and test Reynolds numbers would currently impose an unacceptable time delay and cost on most schedules. In lieu of theoretical calculations over the range of possible model transition positions it is more common to optimise experimentally to achieve model surface flows that simulate the calculated full scale flow conditions e.g. specific boundary layer parameters, Ref 3, at the foot of the shock or at the trailing edge. A forward fix is desirable for drag definition for part of the C_L range as long as it is compatible with the leading edge suction peaks and supercritical flow development on both surfaces. At M/C_L outside this range an aft transition fix may be possible to produce the same shock position and separation pattern as predicted for full scale. Care must be taken to keep the aft transition band sufficiently far forward of the shock (say 15%) to ensure no influence on the shock strength and position and on the rate of its forward movement at higher C_L . The analysis of these flows, in the absence of detailed pressure plotting can be done with the help of oil flows for shock and separation detection and acenaphthene sublimation techniques for boundary layer state.

For the ARA tunnel which is basically limited to near atmospheric stagnation pressure, Reynolds number sweeps cannot be used and so the requirement of viscous flow simulation by controlled transition position is normal practice, with particular concentration on the correct representation of viscous interaction at the foot of the shock to give the correct development of separations either at the foot or at the trailing edge.

Preliminary work requires an initial transition free oil flow test to determine the most optimistic aft shock positions at the critical design point eg cruise M/C_L or buffet M/C_L . The state of the boundary layer is also determined from sublimation tests. An aft band position is

defined as being in a laminar boundary layer at a position 18% forward of the shock at its forwardmost design condition. The minimum band height to achieve a turbulent fix is determined to minimize the chance of overfix to an unrepresentative turbulent boundary layer and to minimize the band form drag. ABA technique is to use glass bead Ballotini of uniform size with a maximum band width of 1mm, very sparsely applied so that individual turbulence wedges can be detected behind the band. Transition is detected by sublimation of acenaphthene crystals on the wing surface which are not applied ahead of the band. Experience indicates that sublimate ahead of and in the roughness will reduce the effectiveness of the band leading to a tendency to use a too-large band with overfix for normal test conditions where sublimate is not present. The initial transition-free oil flow and sublimate tests will indicate the areas of laminar flow that can exist ahead of a band and also the possibility of early transition occurring due to the presence of a weak root shock across the wing upper surface.

This approach requires painstaking effort both in the testing stages and the analysis. It is however much easier on the civil configuration with limited design points and operating envelope than the transonic high performance fighter with its wide range of wing flow conditions, shock interactions and separated flows. The regions of validity of results for aft band tests must be carefully considered, as steps and jumps in drag results may well indicate interactions between the shock movement and the band. Equal care must also be taken on the lower surface of modern heavily rear loaded wing sections at lower C_L .

There is strong need for a methodology spelling out guide lines and warnings related to this

very important subject and the report of the W009 on Wind Tunnel Boundary Layer Simulation and Control, Ref.2, is expected to fill this need.

3.2 Corrections for tunnel wall interference effects

Routine corrections are applied to measured data based on semi-empirical correlations of a range of experimental and theoretical data. Early correlations of tunnel results covered the full range of subsonic transonic and supersonic operation. Only comments related to subsonic operation are made here. For these purposes a typical transport aircraft configuration has been used as a calibration model. This is illustrated in Fig.5.

This layout in the tunnel indicates the high degree of flow uniformity in the region of the model which is an area of very non-uniform porosity. It was anticipated that theoretical methods of wall constraint correction applied to walls of uniform porosity would not be applicable in this case and empirical factors related to the basic theory might be obtained.

The basis of the determination of the empirical relationship has been a comparative series of tests in a solid wall version of the tunnel and in the porous wall. Standard closed wall corrections Ref.4 have been applied for Mach numbers up to $M = 0.88$ at which speed the solid wall blockage corrections were considered to be coming close to the limits of the theory at a ΔM correction of 0.025. For the porous tunnel of uniform porosity, theoretical calculations indicated that the blockage should be of the order of -0.25 of the solid wall blockage correction (or 0.5 of an open wall correction).

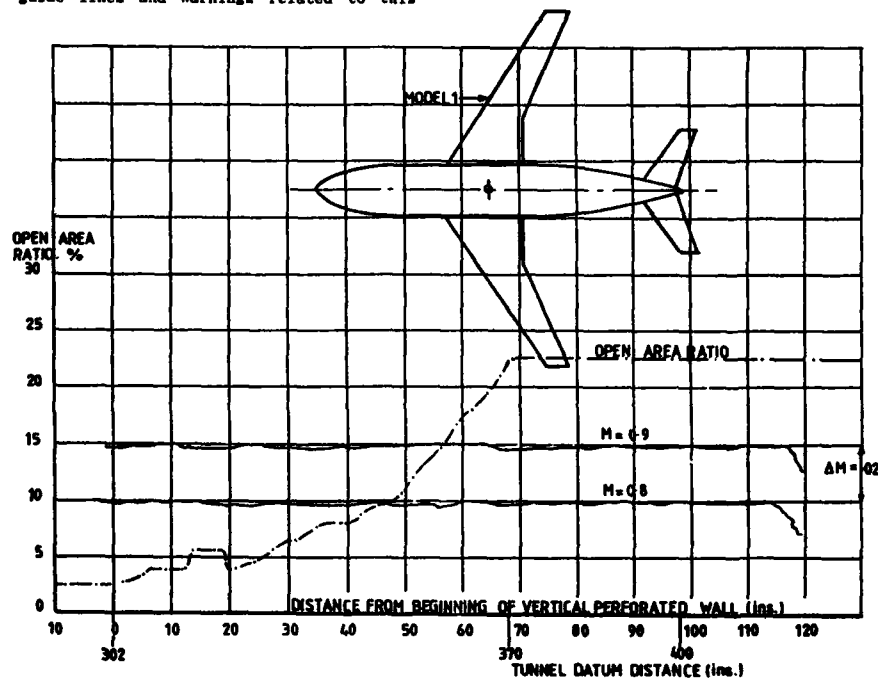


Figure 5 ABA 8' x 9' Tunnel perforated wall porosity distribution, Flow distribution and calibration model

To check this, the wing trailing edge pressures, being representative measurements in the region of the centre of the model where the blockage corrections are assumed to apply, are compared for the porous and closed wall conditions. This is a particularly sensitive method of checking local Mach number because the trailing edge C_p is near to zero and reasonably independent of C_L and Mach number, near minimum drag. Consequently any deviation of the trailing edge pressure coefficient from the 'true' closed tunnel value arises from the use of an incorrect static pressure P_0 which in turn arises from the use of an incorrect Mach number at the model. At $M = 0.8$ a $C_{p_{TE}}$ error gives a ΔM error of $0.5\Delta C_p$.

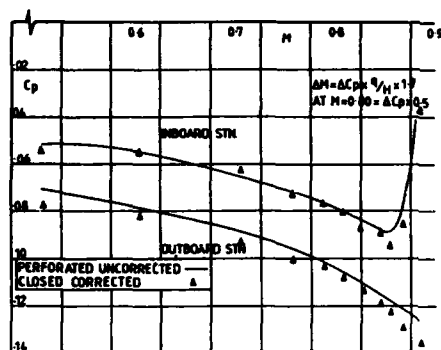


Figure.6 Use of trailing edge pressure to indicate tunnel blockage

Fig.6 shows the correspondence of two trailing edge pressure stations between the porous and closed wall results. These indicate close agreement up to the point where the closed wall results become dubious and where the wing trailing edge pressure becomes sensitive anyway. For Mach numbers up to 0.86 the porous tunnel

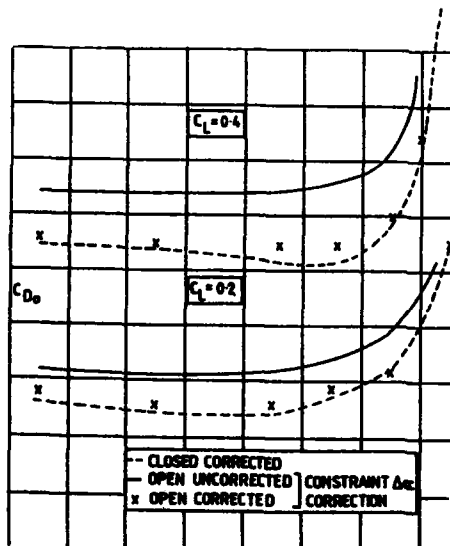


Figure.7 Drag correction due to constraint

blockage correction to M is seen to be less than 0.003. Thus no M correction is used for civil transport work up to $M = 0.86$.

Comparative results of lift have indicated a need for a simple α correction of the conventional form which is a linear function of C_L up to 0.7 and independent of M . The value of the empirical factor from the experimental data corresponds very closely with the expected 0.5 of a full open tunnel value.

Tunnel interference on drag, albeit at the correct stream Mach number is automatically corrected for the wall constraint effect by the α correction but can also be influenced by empty tunnel buoyancy and axial variation of blockage. Typical calibration model results are shown in Fig. 7 which illustrate the major correction effect of Δx wall but shows the presence of a small further correction needed to bring results in line with corrected closed tunnel data at the higher values of M . The simple blockage theory for both open and closed tunnels predicts zero blockage axial force correction over a closed body, the theory for infinite porous walls does indicate existence of a buoyancy gradient. These typical results are indicated in Fig. 8.

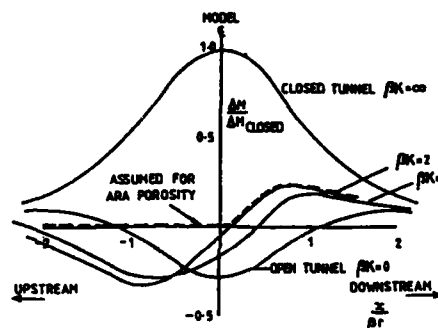


Figure.8 Blockage buoyancy correction

Comparison of pressures on the fore and aft body of the calibration model indicate in the ARA tunnel, with its rapidly changing porosity, that a blockage buoyancy correction of the order of 0.5 the theoretical estimate for a 22% uniform porosity would be applicable. A correction of this magnitude is usually applied to measured balance axial force the magnitude being a strong function of M and only of small significance for $M < 0.8$. Typical corrections are about 5 drag counts at $M = 0.85$ and are assumed invariant with C_L . Such a correction is of course consistent through any comparative tests and has no effect on comparative increments.

Half Models

Correction procedures for half models follow those of the complete model on the basis of modified factors from the standard theory. Corrections are applied for tests as appropriate to a reflection plate half model in a tunnel of modified aspect ratio. Also incorporated in this Δx correction (f_{WEC}) is the effect of lift on the half fuselage spacer, the tunnel flow boundary layer and the probable deviation of the flow from a true reflection plane. The typical correction is of the order of an increase in lift curve slope of about 1%. In practice of course, for the purpose of this paper, the half model

results are used almost entirely for comparative and incremental data and the magnitude of the correction is adjusted to the complete model datum by changes to α_0 and $\partial C_D / \partial \alpha$ to maintain

similar polar shapes.

4 THE DRAG METHODS USED AT ARA AND THE PROBLEMS ENCOUNTERED

The need for absolute and incremental drag accuracy basically imposes the same demands and both objectives generally benefit from any improvements in technique. Drag is obtained from internal strain gauge balance measurements using the simple expression

$$C_D = C_N \sin \alpha + C_A \cos \alpha$$

and the quality of the C_N , C_A and α parameters depends upon;

- the performance of balances, pressure transducers, "incidence meters" and the data acquisition kit,
- model geometric fidelity and the sensible use of boundary layer manipulation by the use of roughness bands,
- time averaged Mach number and Reynolds number deviation
- the effect of the low frequency flow unsteadiness,
- the consequences of flow temperature variations,
- the accuracy of flow direction and model attitude measurement,
- the quality of support interference, base pressure and any internal flow corrections, and
- the skills of the people involved together with the techniques employed.

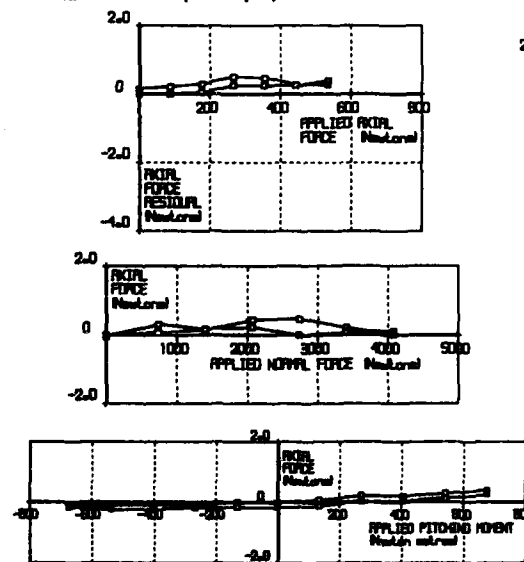


Figure 9. Results from a check balance loading showing acceptable axial force residuals.

It is by maximising the performance of some of these items and minimising the errors in others that high quality wind tunnel drag measurements are obtained.

4.1 Balances and instrumentation

ARA uses 6 component 57.15mm diameter balances supported on 53.34mm diameter flared single stings for virtually all full span model drag tests. These balances are calibrated in a dedicated calibration room using dead weight loads. The full balance matrix consists of 6 direct sensitivities, 30 first order and 126 second order interaction terms (although some terms are zero). Such balances, used for civil drag work, are checked at least once a year by applying axial forces, normal forces and pitching moments. For this design of balance typical axial and normal force sensitivities are 0.22 and 1.20 Newtons per microvolt respectively. From the aspect of accurate drag measurement the most important terms result from the interaction of applied normal force and pitching moment on the axial force bridge output. Fig.9 shows the axial force residuals obtained from a check loading on a balance which is currently used for A330/A340 model testing. The magnitude of these errors was considered to be satisfactory. The residuals from a recent check loading on another 57.15mm diameter balance showed slight axial force hysteresis, see Fig.10, for this and other reasons this balance

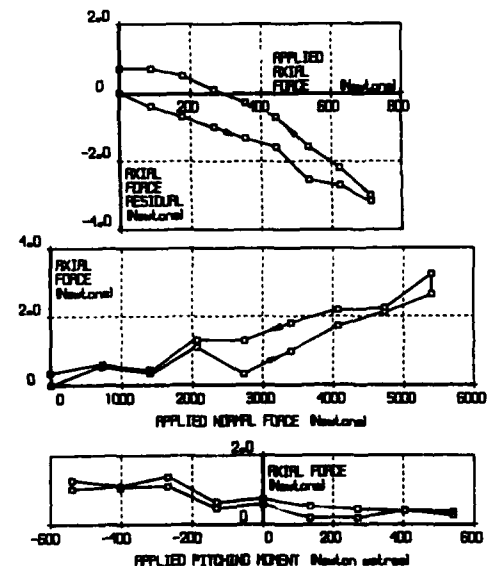


Figure 10. Results from a check balance loading showing unacceptable axial force residuals.

is in the process of being regauged. All ARA balances have the bridges thermally latched, which in practical terms totally eliminates any effects of a uniform temperature change on the balance sensitivity. However, bridge zeros are sensitive to any significant thermal gradients across the balance and these effects have to be minimised by adopting appropriate test techniques as described later in section 5.5.

The data acquisition kit has 16 bit recording, that is $\pm 32,768$ counts full scale. Each kit count is M microvolt, hence a recording

resolution of ± 4 microvolt gives axial and normal force resolutions of ± 0.11 and ± 0.60 Newtons respectively. For a typical q of 8000 Newtons this gives C_A and C_N resolution of ± 0.000013 and ± 0.00008 respectively. Each of the amplifier modules incorporates a filter which for drag work has no DC cut off, a 3dB cut off frequency of 0.5 Hz and attenuation at high frequencies of 18dB per octave. It follows that all high frequency noise is filtered out before the recording stage. All the amplifiers have matched response characteristics and the 64 channels (to be increased to 154 by the end of 1987) on the data logger are currently sampled by a single ADC in a total time of 0.004 seconds. (During the current update programme the data logger system will be changed to have 1 ADC per 22 channels).

Three samples of each amplifier output are digitised but only the median value is recorded on disc. Each bridge is energised by a precise controlled 5 volt DC supply and an accurate fraction of this is fed onto each amplifier at the start and end of every run. This reference voltage is used to provide a correction for every reading to allow for any changes in the supply voltage or amplifier gain.

Working section total head and static (plenum) pressures are measured by Ruska type DDE5000 pressure gauges (0-2.5bar) which have a specified accuracy of ± 0.04 mb. The reading of these gauges is matched (in the data reduction process) to the output from a Druck DPI140 precision barometer at the start of every run. This barometer has a specified accuracy of ± 0.15 mb. Thus the possible maximum errors in q and Mach number derived from these gauges are typically $\pm 0.02\%$ and ± 0.00010 respectively.

Base pressure corrections, associated with the presence of the single sting, are measured using ± 345 millibar Druck type PDCR22 differential pressure transducers. These have a specified accuracy of 0.06% full scale which when converted to a drag coefficient with a typical value of base area to wing reference area of 0.015 gives a possible error in C_D of 0.00001.

The primary source of model attitude measurement is the Sunstrand QA900 accelerometer, usually referred to at ARA as an "incidence meter". When a precision load resistance of 10K ohms is used these instruments have a resolution of 0.0011' per μ microvolt and a zero stability of $\pm 0.0005'$ over a 30°C temperature range. With some extra filtering these instruments operate reasonably satisfactory even when light model motions are encountered near buffet onset conditions (where the need for fine drag accuracy is no longer a major consideration).

4.2 Model Geometric Fidelity

There is clearly no point in going to extreme lengths to accurately measure the drag of a model if the scaled geometric shape of the model is incorrect. Geometric errors usually arise from two sources;

- (i) manufacturing inaccuracies,
- (ii) poor model preparation.

Fig.11, shows an example of manufacturing errors due to distortion of the high grade steel which occurred during the numerically controlled machining process in the manufacture of this particular civil model wing. The wing had, at this stage, been fully completed except for final polishing. Fig.11(a) shows the manufacturing errors aft of the leading edge region for an inboard wing station of 242 mm chord length. It

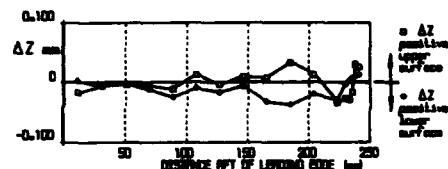


Figure 11(a). Wing manufacturing errors close to root. Acceptable

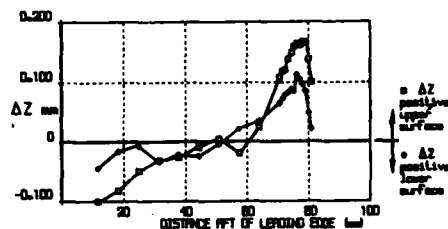


Figure 11(b). Wing manufacturing errors close to tip. Unacceptable

can be seen that the manufacture is not perfect but the geometry is everywhere within ± 0.04 mm and there are no erroneous rapid changes in surface curvature. This section was accepted as being satisfactory. An outboard section, however, shown in figure 11(b) has both a twist error (of approximately -0.16°) and has a "hook" at the trailing edge of about 0.10mm. The twist error would clearly affect the spanwise loading and hence the vortex drag. Fig.12 shows that geometric errors near the trailing edge can increase or decrease the drag depending on the C_L value. (Such drag changes are, however, very sensitive to the configuration design). For the example shown, where about half the wing had a local mean error before rectification of about 0.10mm at the trailing edge, the error in model drag would have been about $\Delta C_D = -0.0001$ at $C_L = 0.6$. However, at $C_L = 0.4$ the error would have only been approximately $\Delta C_D = 0.00002$. By the use of electro depositing techniques the distorted wing was locally built up on the lower surface and further hand worked on both surfaces until the errors were as shown in Fig.13. These errors were now considered acceptable. It follows that the need to manufacture models to achieve a faithful scaled representation can be both time consuming and expensive.

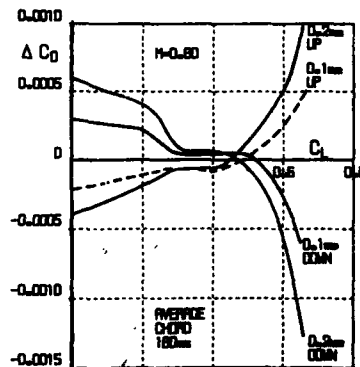


Figure 12. Typical drag errors due to errors in wing trailing edge geometry occurring over last 5% of chord.



Figure 13 Wing manufacturing errors close to tip following some rectification. (just acceptable)

Maintaining high standards of model preparation can often be a difficult task. Both skill, dedication and patience are needed. It is also important to know what is and what is not acceptable. It can, for example, be calculated that the drag of 350 wing static pressure holes 0.50mm diameter is negligibly small ($\Delta C_D = 0.000003$) whilst the drag of a 500 mm length of forward facing step (eg a poor joint round a fuselage) of 0.125mm height is unacceptably large ($\Delta C_D = 0.00008$). Figs. 14 and 15 show two examples of how model imperfections can influence drag accuracy. During a short Mach number traverse (figure 14) a piece filler material 14mm diameter and approximately 3 mm thick which filled a datum hole on the wing lower surface lifted during the run up to $M = 0.78$ and remained protruding until one data point was taken at $M = 0.82$, it then left the model to leave a circular recess for the remainder of the test run, which included increase in the Mach number to 0.84 and then a reduction back in stages to $M = 0.78$. Comparing these results with those from a further repeat test which was conducted when the model had been repaired shows that the protruding filler induced a drag error of about $\Delta C_D = 0.00015$ whilst the recess caused a somewhat smaller error of $\Delta C_D = 0.00005$.

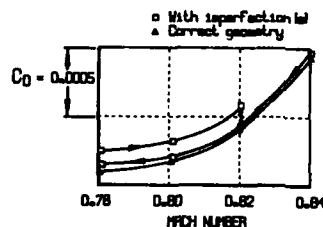


Figure 14. Effect of typical model imperfection.

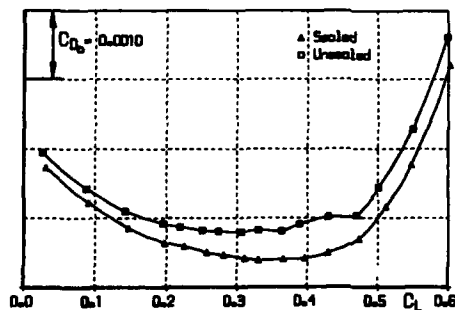


Figure 15. Effect of a leak path (into the fuselage) at the wing upper surface/fuselage junction. $M = 0.78$.

The second example illustrated in Fig. 15 shows the effect of a plastic wing root fairing located in the junction between the fuselage and wing upper surface cracking and lifting slightly during the test. The fairing did not break but in lifting it allowed a leak path between the inside of the fuselage and the inboard wing upper surface pressure field. (The reason for the erroneous drag in this example was particularly difficult to diagnose because when visually inspected at the end of the run the fairing had resettled in its correct position. It was only by inspection of both base pressure measured inside the model and the inner wing upper surface pressure distributions that the leak was detected and its location identified). This specific example shows that all non representative leak paths must be sealed. In this case errors of $\Delta C_D = 0.0004$ were introduced.

4.3 Mach number and Reynolds number deviations

Mach number is usually held constant in the ARA transonic wind tunnel to approximately $\Delta M = \pm 0.001$ about a mean during the execution of a polar by servo control of the fan inlet guide vane trailing edge flaps from a p/H signal. Accurate drag data are however of interest at conditions above the start of the compressibility drag rise where $dC_D/dM=0$ and hence a deviation of $\Delta M = \pm 0.001$ can introduce some scatter into the drag data. This is allowed for at ARA by post test data processing where dC_D/dM is calculated for every data point by curve fitting the test data set. Fig. 16(a) shows the typical deviations in Mach number experienced during a polar and Fig. 16(b) illustrates that the corresponding calculated errors in C_D are of order 0.0002. A part of the measured polar is compared with the corrected data in Fig. 16(c). The corrected polar results are now in a form where they can easily be interpolated to give C_D values at specified values of C_L and used in the derivation of drag increments.

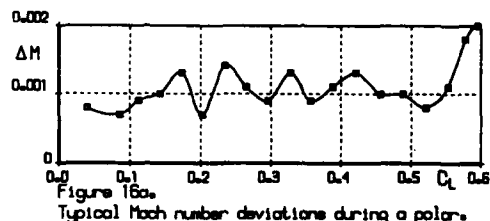


Figure 16a. Typical Mach number deviations during a polar.

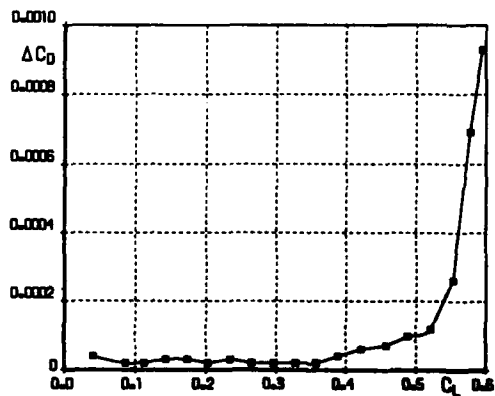


Figure 16b. Errors in C_D due to Mach number deviations.

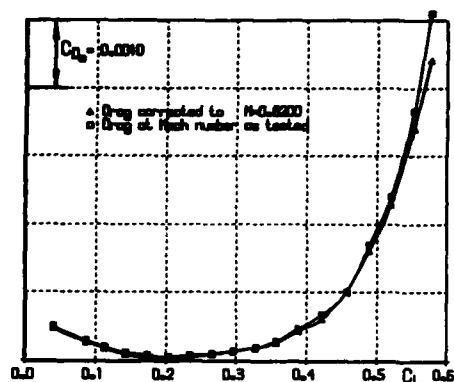


Figure 16c.
Typical effect of post test Mach number smoothing on drag data.

The ARA transonic wind tunnel is usually operated at close to atmospheric stagnation pressure (although it does have the limited capability of being operated from approximately 0.8 to 1.2 atmospheres) and hence there is a Reynolds number variation with Mach number. The facility also has very limited means of controlling the air temperature which also affects the Reynolds number variation. It is currently common practice to remove the variations in measured drag due to systematic or random variations in Reynolds number during the data reduction process by using the calculated drag variation with

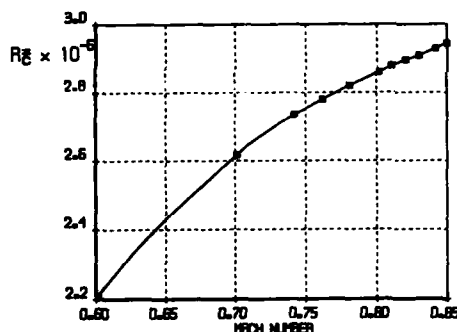


Figure 17. Typical variation of test Reynolds number with test Mach number. $M = 1$ bar.

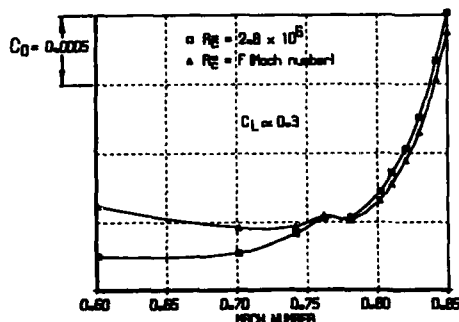


Figure 18. Typical effect of varying R_E on drag rise characteristics.

Reynolds number in the form $dC_D/d \log R_E$. Thus every drag data point is corrected to a constant Reynolds number of say $R_E = 2.8 \times 10^6$. Fig. 17 shows a typical variation of test Reynolds number with test Mach number and the effect of correcting the drag to a constant Reynolds number is illustrated in Fig. 18. The accuracy of this procedure depends on the closeness of the estimated and actual model drag variation with Reynolds number and also on the difference between the test and reference Reynolds number. Fig. 19 shows the measured drag variation with Reynolds number (obtained by testing from $M = 0.8$ to 1.2 bars) of an A330 Airbus layout. The slope of this variation is closely approximated by $dC_D/d \log R_E = -0.0059$, compared with a theoretical estimate of $dC_D/d \log R_E = -0.0065$. For the example considered this can lead to $\Delta C_D = -0.00001$ incremental drag errors and an absolute drag error of -0.00006 in C_D is possible at $M = 0.60$. It should be noted, that this method deliberately only gives a first order allowance for Reynolds number effects. In particular no attempt is made to adjust the drag data for the detailed effects that changes in Reynolds number can have on the supercritical flow development.

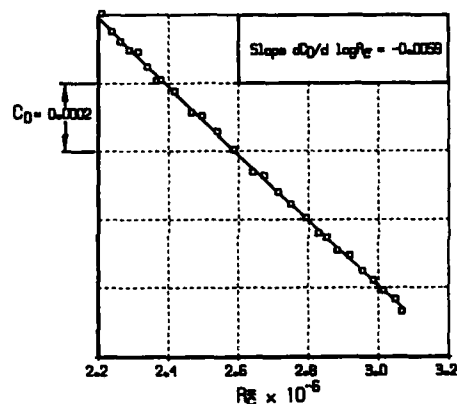


Figure 19. Typical drag variation with Reynolds number. $M = 0.80$ $C_L = 0.30$

4.4 The effect of low frequency flow unsteadiness

Although the working section flow is accurately maintained at the time averaged test Mach number, the ARA transonic wind tunnel working section flow oscillates at low frequencies with significant content at 0.25 Hz and 0.5 Hz. Fig. 33 (which is discussed later in Section 6.3) presents a typical 30 second record of the working section Mach number to illustrate this phenomena and the corresponding C_D record shows that when reduced to coefficient form the model drag is not perfectly constant. (These data have been electrically filtered as described in section 5.1). To overcome this problem, 48 point data samples are recorded over a period of between 4.8 and 6 seconds and the results averaged. The amplitude of the drag oscillations varies with test condition as depicted in Fig. 20. However, the simple averaging process produces C_D values which generally repeat to within ± 0.00001 .

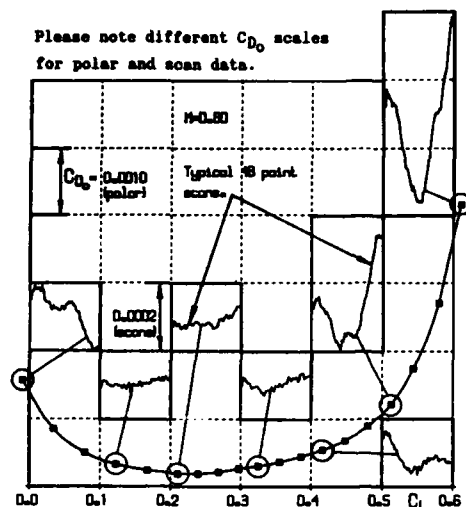


Figure 20. Typical drag variations during 48 point scans which are averaged to give each polar point.

4.5 The effect of flow temperature variations

The effect of temperature variations through the mechanism of Reynolds number effects were discussed in section 4.3. Unfortunately, however, changes in flow temperature often induce a temperature gradient across the strain gauge balance which in turn introduces what can be interpreted as a spurious zero axial bridge output. After a typical one hour run (9 polars) it is possible that the axial force balance zeros may have drifted by up to the equivalent of $C_D = \pm 0.0003$ based on a $q = 25,000$ Newtons/m² (due to the effects discussed above). Such a drift is clearly unacceptable. To overcome this problem ARA uses the technique of matching the level of the drag polars to a datum measured during a short, separate " C_{D0} run" (or "Mach number traverse"). " C_{D0} runs" are conducted in the shortest possible time when steady conditions are judged to prevail in the wind tunnel (ie when both spatial and temporal temperature gradients are insignificantly small). For these runs the model is set at a moderate incidence where both dC_{D0}/dC_L and dC_{D0}/dM are small and the tunnel Mach number is quickly changed in steps through the desired test range, multiple readings being taken at each test Mach number. Adoption of this technique gives minimal instrumentation drifts but if a substantial drift did occur (ie giving $C_D > 0.00005$) the data would be discarded and a run repeated. It has been found in practice that during a normal run most of the axial force drifts tend to occur in the early part of the run and greater consistency of data is achieved if the post-run instrumentation zeros are used to establish the datum level. These drag data are thus, to first order, effectively corrected for even the smallest axial force balance drifts. For a 1 hour run of typically 9 polars and a zero drift of up to $C_D = 0.0003$, if it is (pessimistically) assumed the drifting occurred at a constant rate then the drift from the start to the end of any one polar would be of order $C_D = 0.00003$, this is considered acceptable for the definition of the polar shape.

4.6 The Effect of Working Section Flow Direction and Model Attitude Measurement

Using the simple expression for C_D given in section 4.1 it can easily be seen that for $C_D = 0.5$ and a drag accuracy of $C_D = 0.0001$, α has to be known to an accuracy of 0.01° . This requirement is difficult to achieve. (It should be stressed that in the current context α is the inclination of the balance axial force calibration axis to the mean free stream direction).

Model attitude usually consists of the sum of two terms

- (i) the model angle relative to the horizontal, and
- (ii) the angle of the mean working section flow to the horizontal

Working section flow angle is derived by matching lift curves measured with the model both erect and inverted. Typical values for the ARA transonic wind tunnel measured during two test campaigns conducted 6 months apart are presented in Fig.21. The floor of the working section is nominally horizontal whilst the roof has a slope of nominally 0.3° to allow for the boundary layer displacement surface growth on all four working section walls. Thus the geometric norm for the working section centreline flow against which the measured values should be compared is 0.15° . The measured upwash is normally within 0.05° of this theoretical value. The objective for accurate drag work is that the flow angle be known to a high degree of precision.

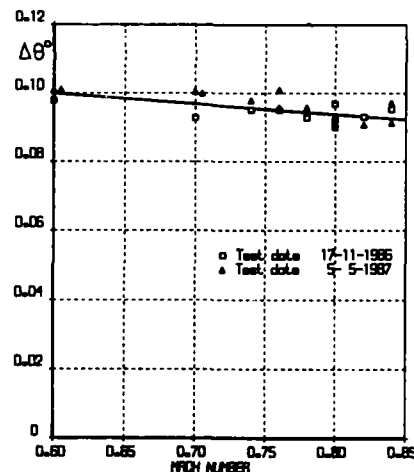


Figure 21. Typical variation of working section flow angle with Mach number.

The combination of scatter and repeatability in flow angle measurements presented in Fig.21 is about $\pm 0.004^\circ$. This is considered to be just acceptable. Of all the items which can possibly affect the working section flow angle it is known that the cleanliness state of the smoothing screen in the settling chamber has the largest single effect. The level (but not the variation with Mach number) of the working section flow angle can and does vary with time. This effect, is however, deliberately minimised by weekly cleaning of the lower part of the smoothing screen. The flow angle is carefully monitored and frequently checked.

Experience has shown that the use of good quality "incidence meters" is an effective method of measuring incidence and ARA relies on these heavily. It is essential that they have both a very stable sensitivity and electrical zero. If either of these were to drift significantly, the effects on accurate drag measurement would be catastrophic. The electrical zero and sensitivity of these instruments are obtained by calibration using a granite surface table and a set of cast iron wedges of known angle. Calibrations performed immediately before and after every test series are undertaken to maintain the quality of attitude measurement; these checks, however, always give the same results. Incidence meters are rigidly fixed to a model component as near as possible to the front part of the balance thus minimising the number of model joints between the meter and balance where minute hysteresis could occur.

The old method of calculating model attitude (now discarded) from a knowledge of the loads on the model and the elastic deflection characteristics of the support carts, sting and balance is only retained as a backup system. There is ample evidence to indicate that this system regularly gave errors of order 0.02° and could also have been responsible for an additional flow angle error of order 0.02°.

4.7 Support Interference

ARA has for many years favoured the simple, circular single sting support system shown in Fig.2 for drag testing on full span models on civil transport aircraft. This however, is not to the total exclusion of all other layouts, a lower blade configuration having been used on some occasions. For some model configurations the fin entry system may have certain attractions but ARA has, as yet, no experience with this method of support. The corrections associated with the presence of a single sting and the clearance bore in the rear fuselage are obtained by supporting the model on twin stings, as shown in Fig.4, and measuring the forces on the rear fuselage with and without a simulation of the central sting. Corrections to lift and pitching moment are usually very small and are insensitive to Mach number and incidence. Correction to drag can, however, be substantial. Typical drag corrections are illustrated in Fig.22. These results are relatively insensitive to Mach number but vary almost linearly with incidence. Fig.23 illustrates schematically the model layout adopted for measurement of sting interference. The method relies on the fundamental assumption that the presence of the sting has sensibly no

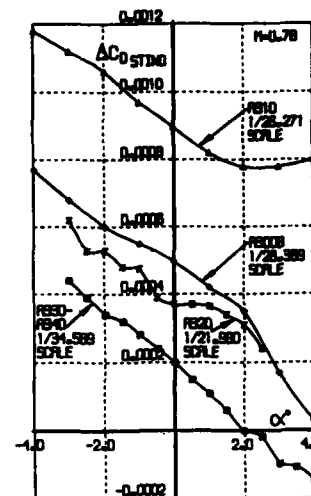


Figure 22. Typical sting corrections for Airbus models.

effect forward of the split in the fuselage. The balance measures the forces on the rear fuselage with the dummy sting in position (as shown) and with the dummy sting removed and the bore replaced by the correct rear fuselage geometry. The difference between the two sets of balance readings gives the sting interference. However, before the balance readings are subtracted they have to be corrected for the pressure force acting on the internal fuselage surfaces aft of the split and, (for the dummy-sting on case,) for the pressure force acting on the seal plate, see Fig.23. The accurate determination of these pressure forces is vital. This can be appreciated by examining the magnitude of their different contributions. A typical model rear fuselage (without empennage) may have the following forces acting in the drag direction,

- (i) force on external wetted surface
 $C_D = 0.0022$
- (ii) pressure force on fuselage internal surface $C_D = 0.0015$
- (iii) external pressure force on seal plate
 $C_D = -0.0016$ is base pressure (dummy sting installed)

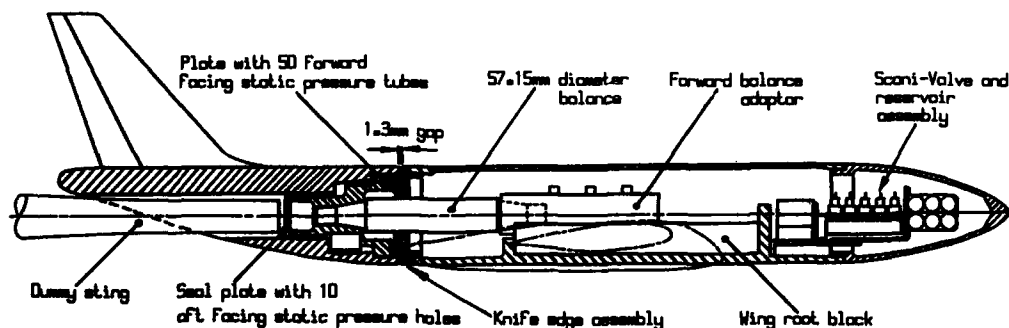


Figure 23. Details of balanced rear fuselage to obtain single sting corrections.

Thus the unwanted pressure forces are each of similar magnitude to the actual rear fuselage drag. These forces are obtained by measuring approximately 50 pressures inside the fuselage and about 10 pressures on the seal plate. The most accurately available differential pressure transducers are used to measure the pressures with plenum pressure used as reference. Since these pressures have small low frequency components (which are effectively filtered out of the balance output) the effective pressure is obtained by matching the response characteristics on both sides of the pressure transducers diaphragm.

The twin sting support system itself is not interference free and induces its own pressure field. Based on calculations by a panel method this field may subject a rear fuselage to a buoyancy force of order $\Delta C_D = -0.0004$. Fortunately, a pressure field of this magnitude has an insignificant effect on the isolation of the single sting support interference (principally because the sting interference is obtained by differencing). Under aerodynamic loading the whole twin sting support rig, the model wings and the fuselage balance all deflect. To compensate for the resultant movement of the rear fuselage relative to the simulated dummy sting, which experiences very small deflection, the forward part of the dummy sting, is moved by a small integral actuator. This device has been utilised to explore the sensitivity of the rear fuselage drag to the vertical position of the simulated sting. (This is a practical requirement, for in the single sting support case the sting will take up different vertical positions in the rear fuselage bore as the aerodynamic loads cause different amounts of relative deflection). Fig.24 shows the very useful result that the rear fuselage drag (and hence the sting corrections) are insensitive to

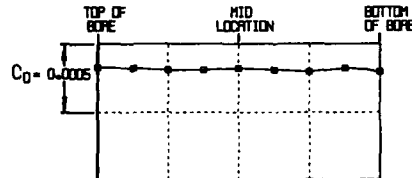


Figure 24. Fuselage drag variation with vertical location of single sting support.

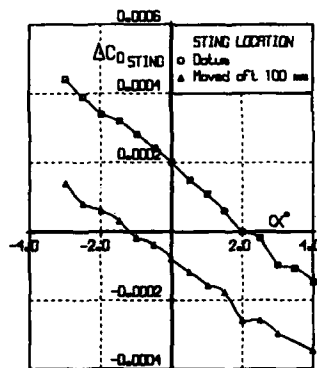


Figure 25. Effect of sting fore and aft location on drag corrections.

sting vertical position. This is not the case for sting fore and aft position. Fig.25 shows that moving the sting by 100mm relative to the rear fuselage changed the sting interference by $\Delta C_D = 0.0003$.

5 ENGINE FLOW REPRESENTATION

Whilst much of the previous discussion has been related to the accurate determination of wing-body data, the engine installation is a major area of drag improvements or deficits. The basic position of the engine is dictated by various design aspects which may well be unrelated to optimisation of cruise performance. Certain guidelines have become known as good design practice but there is always interest in optimising these guidelines for the specific application in hand. Variations of particular interest are nacelle toe and pitch, fore and aft position, pylon height, width, and leading edge fairings, all of which are influenced by 2/4 engine configurations, by-pass ratio, and local wing pressure distribution.

The pattern of testing evolved has been dictated by the assumption that inlet and exhaust engine flow conditions will automatically have an effect on the engine installation drag increment and the installation drag interference. Through flow nacelles (TFN) are used to provide a standard datum wing + body + nacelle configuration for tests of the complete model. Internal axial force is normally obtained by calculation of the losses in the internal streamtube between upstream and downstream infinity using internal pressure distributions for boundary layer calculations. Data reduction programmes based on boundary layer theory are part of the standard data reduction system. These automatically make the small adjustment for variations with incidence and sideslip as seen by the internal pressures, with corresponding changes in mass flow and internal drag. Data is computed via an off-axis application of internal axial force which increments on the balance data and is subsequently computed in the correct axes systems. Complete model data derived this way will normally have correct external nacelle cowl lines but reduced inlet mass flow and incorrect exhaust representation. Results typical of this basic complete model test representation showing the variation of nacelle installed drag with C_L are given in Fig.3.

To complement this complete model data, a more exact engine representation is obtained with tests on a half model. In these tests, at the larger scale of the half model, it is possible to represent more precisely the details of the engine installation and, in particular, the exhaust flow. For the complete model, it is extremely difficult to represent the correct engine exhaust flow conditions whilst making force balance measurements because of the difficulty of conducting the high pressure air needed for the simulator across an internal balance in the model. It is much easier, and provides more accurate results, if the exhaust flow work is done on a half model, mounted on a half model underfloor balance, across which it is more easy to conduct the high pressure air without interference. A large part of the engine installation test work at ARA is conducted on a sensitive strain gauge underfloor balance, designed with the appropriate capacity for typical civil half models with a flexible duct across the live balance elements. Calibration of the balance with this duct as integral part, using small pressure interaction terms, enables test data to be basically discriminated to 0.1

drag counts in the presence of a 0.5 C_L . In order to represent both inlet and exhaust flows simultaneously, a turbine powered simulator is used, giving correct fan flow exhaust representation of high by-pass engines in both pressure and temperature rise. The inlet flow is nominally deficient by the inverse of the by-pass ratio and this is compensated by the use of a modified inlet cowl shape which provides the correct pressure distribution on the cowl at the reduced inlet mass flow (typically about 12% A/A_0). The core exhaust flow is cold and has proportionally higher mass flow than the hot core of the real engine but it is considered that the correct fan flow which shrouds the core will well represent the true fan and core exhaust flows. Engine power variations are simulated by changes in simulator RPM but only a limited range is used in practice because of the spillage drag changes which will take place at the same time. Major power effects are determined from comparison of full power TPS and zero power TFN builds with the same mass flow ratio. A typical result is shown in Fig. 26. Complementary with these tests are

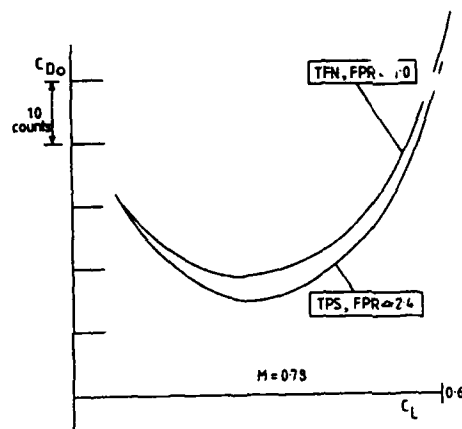


Figure 26 Effects of fan pressure ratio (FPR) at the same inlet mass flow

datum through-flow-nacelle tests to relate back to the complete model tests. Comparative test conditions between complete and half models require consideration, as it is well known that crossflow tunnel boundary layer effects on the half model fuselage present flows unrepresentative of complete model conditions. For this reason, comparative test conditions are based on local and spanwise lift distributions derived from the model pressure distributions in conjunction with the half model force balance overall lift values. Related drags are then based on derived values of incidence α from the corresponding complete model wing lift applied to the half model. The half model of course may be tested with or without a metric half fuselage and there are conflicting arguments why one method should be preferred to the other. It was original ARA practice to use a non-metric fuselage, on the arguments that the unrepresentative fuselage loads did not confuse the relationship between half and complete models. This philosophy however later gave way under the mechanical problems of providing an effective non-interfering wing root seal and the aerodynamic considerations that engine/nacelle interference on the fuselage was not measured on a non-metric fuselage. A fundamental basis of the ARA half model test philosophy with

through-flow nacelles TFN, and turbine powered simulators TPS, is the need and ability to be able to calibrate the internal drag of the former and the gross thrust and mass coefficients of the latter to a required high standard of accuracy, ie at least 0.5% in drag or 0.2% in gross thrust. Details of these techniques are comprehensively covered in Refs 5 and 6.

As a further complementary part of the test sequence, special tests are also made of the isolated nacelle, either TFN or TPS, to determine the isolated drag for comparison with theoretical estimates and for comparison with the installation increments from tests with and without nacelles installed Fig. 27a.

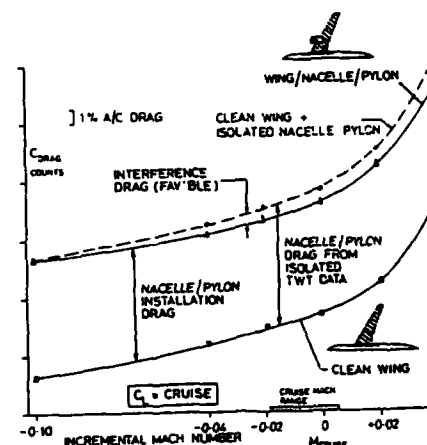


Figure 27a Half model tests showing favourable interference

In addition to overall performance data, incremental results associated with the

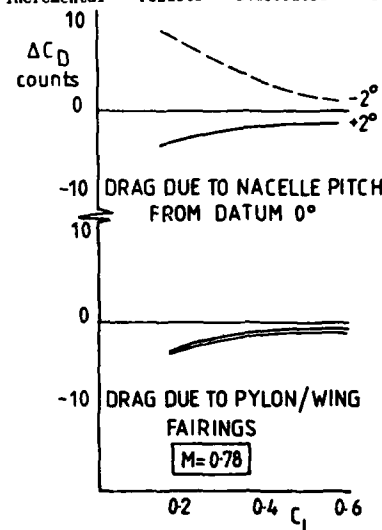


Figure 27b Typical nacelle installation increments and discrimination

optimisation of the installation are the most reliable. Changes in fairings, pylon shaping and nacelle position can be quantified in incremental drag terms to a confidence level of $\pm 4\%$ drag count Fig.27b as long as all the contributory error factors - Section 3 - are meticulously observed from test to test. In particular, because effective free stream flow angle is such an important parameter in drag definition, it is essential that datum repeats, from which α may be defined to 0.01° accuracy, must be spaced throughout a sequence.

5 CONTINUOUS TRAVERSE DATA

In addition to demands for ever-increasing accuracy there is inevitably a demand for reducing test costs. To meet this, the use of continuous α traverse testing has been studied on the basis that it should improve productivity whilst maintaining the required accuracy.

There is no doubt that results obtained from the filtered force data system at low rates of α (0.25 degrees/sec) provides more than adequate accuracy on all components other than drag. Drag of course is derived from body axis measurements of normal force and axial force and in order to minimise the effects of inaccuracy in the measurements of the less sensitive normal force component of the balance, balances are, where possible, aligned with the wind axes near the cruise attitude. In this condition the behaviour of the axial force need only be analysed.

At the start of testing in the continuous mode in 1981, it was established that twice the rate of data acquisition could be achieved with an α of 0.25°/sec and 6 data points per second. This produced results of the form Fig.28. These showed a very reasonable standard of agreement for C_L , C_m and C_D (RMS wing root buffet) Fig.28a. The drag results Fig.28b however showed some minor variations in drag level compared with the steady-state point data. Repeats using pause-traverse polars showed much smaller differences and the basic shape of the polars was much smoother. As the α results looked potentially acceptable there did appear to be good reason to study the drag repeatability by analysing various factors which might contribute to these small apparent errors.

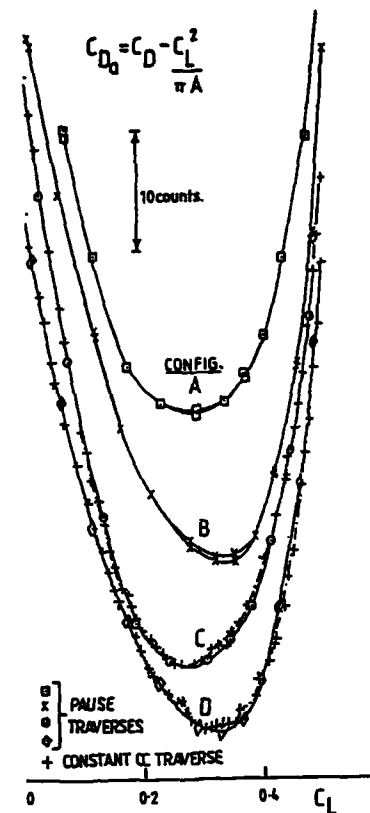


Figure.28b Drag, comparison of continuous traverse and pause data

6.1 Mach Number Fine Control

Prior to the introduction of continuous traverse

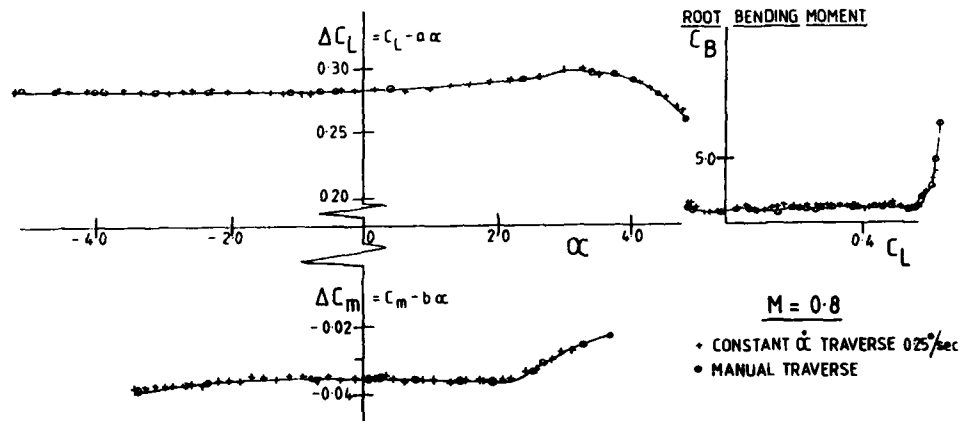


Figure.28a Lift and pitch, comparison of continuous traverse and pause data

testing, tunnel subsonic fine speed control was by servo operation of a plenum chamber air bleed circuit from the low speed leg of the tunnel

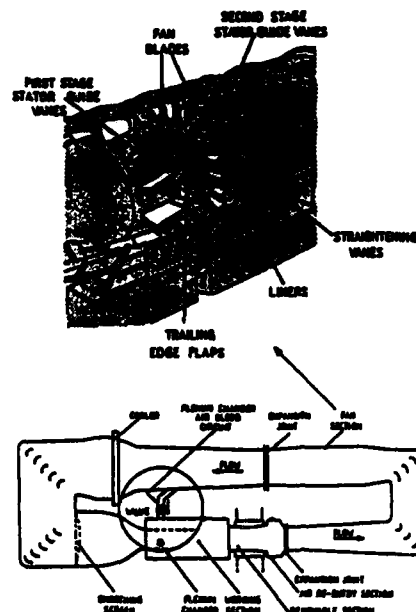


Figure.29 Details of tunnel speed controls

(Fig.29). The air flow through this circuit was controlled by a servo operated valve the position of which was controlled to maintain constant plenum pressure throughout an incidence traverse (actually it controlled P/H). The position of this bypass valve was continuously monitored by

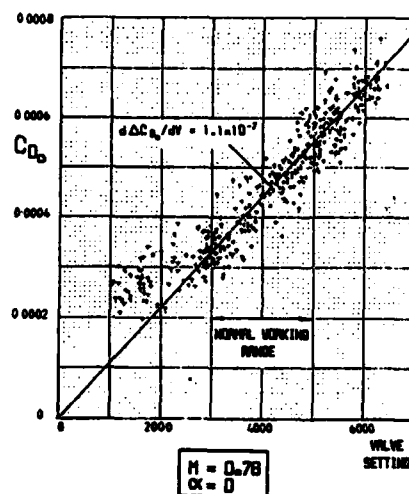


Figure.30 Variation of CDo with automatic speed control valve setting

the tunnel driver and if the valve moved outside its acceptable working range a coarser speed control by the fan stator flaps was used manually to bring the valve position back into normal working range. The valve speed control was very responsive and was a great improvement on the lags associated with the old system which used stator flap alone, the valve however but had the slight disadvantage of introducing a small working section buoyancy pressure term which in turn influenced model drag Fig.30.

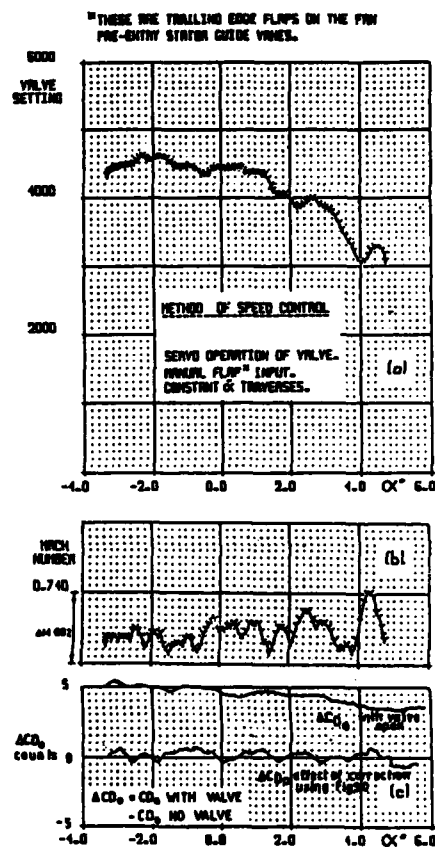


Figure.31 variation of valve setting and Mach number during manual and constant α incidence traverses

Fig.31 shows typical valve setting and Mach number histories for an incidence traverse from -4° to +5°, performed using the combination of servo valve and manual stator flaps. Mach number was maintained constant within ± 0.001 of the mean M and the valve movements only introduced a total C_D change of about 1.8 drag counts due to buoyancy. This buoyancy term introduced by valve movement was corrected automatically in the data reduction via the slope given in Fig.30 to an accuracy of ± 0.3 counts.

6.2 An Improved Control for Fine Mesh Number

The original method described above had two disadvantages.

- (a) the valve circuit introduced a buoyancy correction to drag (which was much larger on half models)
- (b) the tunnel driver was still in the manual loop and had to anticipate rates of increase of stator flap to compensate rates of movement of the valve due to α .

To overcome these deficiencies the rate of movement of the fan stator flaps was increased fourfold to provide a more responsive stator flap servo system which might permit elimination of the valve.

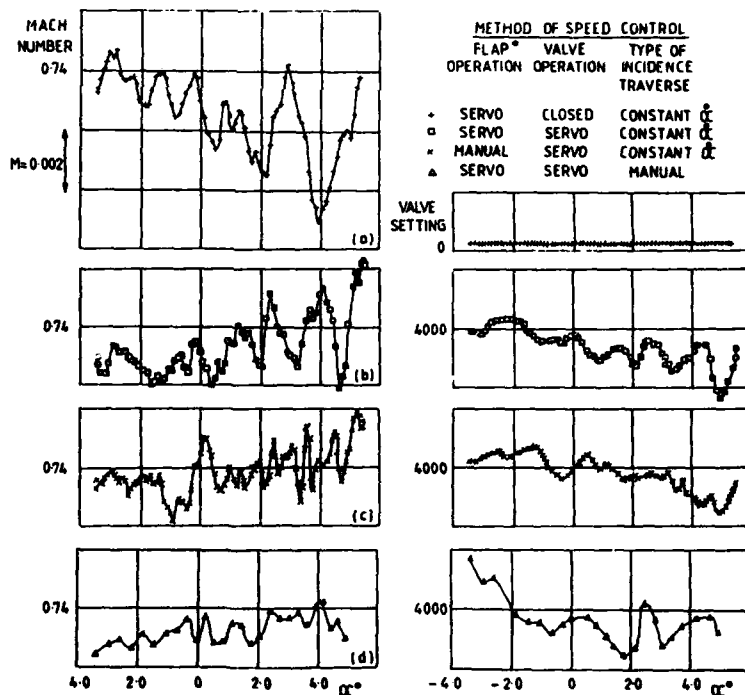
The results in Fig.32a-d show that this mode of control with flaps and no valve was still too slow for the test condition of $M = 0.74$ and would have been much worse at high M where the model drag (i.e. tunnel losses) were larger and more rapidly changing.

The next stage was to revert to an automatic version of the original control system utilising servo control of both stator flaps and valve movement. The valve effectively controlled the Mach number but the flaps now also responded with the aim of minimising the valve movement. The results Fig.32b show that the absolute Mach number control was no better than ± 0.002 but the associated valve movements were minimized with consequent reduction in buoyancy drag correction. Since neither of these two methods controls the Mach number to the required accuracy of ± 0.001 the current control method for α traverses is

servo valve with manual stator flap (but using the higher rate of movement) Fig.32c. For manual setting of a move/pause polar the valve and flap servo control is quite satisfactory see Fig.32d. The corresponding valve movement shown on the right of Fig.32 would, if uncorrected, give a drag buoyancy of 1.2 counts. For tests however where datum and increment drag accuracies of the highest order are required it is standard practice to obtain data in the pitch/pause mode with the use of the servo valve and its associated buoyancy correction.

6.3 Working Section Flow Unsteadiness

At an early stage it was apparent that continuous traverse data was essentially single point record data which although heavily filtered to remove the higher frequency (> 1 Hz) content would still be subject to time variations at lower frequency. Data taken in the move-pause mode would contain multi point data inputs which are computer-averaged to give a mean result. Thus continuous traverse data must inevitably provide random point selection of the varying signals and must as a result be less accurate than the averaged data. In studies of surface pressure fluctuations and tunnel plenum chamber pressure fluctuations on tests with an axisymmetric body it was found that the oscillations were sensibly identical and the amplitude of the oscillations in recorded drag data were, for body alone tests, very small i.e. about 0.15 drag counts. To pursue this investigation further the effects of working section flow unsteadiness on a wing body



* THESE ARE TRAILING EDGE FLAPS ON THE FAN PRE-ENTRY STATOR GUIDE VANES. SPEED OF FLAP MOVEMENT INCREASE 4x FOR THESE TESTS.

Figure 32 Effect of various modes of speed control servo on mach number and valve position

configuration have been examined by recording data in a 30 second period at a rate of 4 points per second. The results shown in Fig.33 were obtained at $M = 0.8$ over a range of C_L variations from 0.2 to 0.5. Fig.33 shows that not only did the tunnel plenum pressure oscillate but the model pitched with an amplitude of about $\pm 0.01^\circ$. At the stronger fluctuating conditions corresponding to higher C_L the traces clearly show that the flow pressure unsteadiness and model bounce were inter-related. Correction for the inertial bounce effect on α did reduce the amplitude of the C_L and C_D fluctuations but a significant force relationship to pressure fluctuation was retained. The results in Fig.33 show that the amplitude of the C_D and C_L oscillations were very small at $C_L = 0.2$ but at $C_L = 0.5$ the drag oscillations increased to ± 0.5 drag counts.

At both of these C_L test conditions at $M = 0.8$ the main frequency was about 0.25 Hz with plenum pressure amplitudes doubled from ± 0.7 mb at low C_L to ± 1.4 mb at $C_L = 0.5$. The body pressure were found to fluctuate in phase with the plenum

and with an amplitude close to that of the plenum. These results indicate that a time averaged force or pressure result taken over a period of about 4 seconds should encompass all the very low frequency variations to give a reasonable mean value. For steady state move-pause data it is practice, particularly where scanivalve pressure data is being recorded, to take a force sample for every scanivalve port which gives 48 force data points over a sample period of 4.8 seconds. Fig.33 indicates that comparison of single point data with the time averaged data gives a possible scatter of the former of:

$$C_L = 0.2 \quad C_D \pm 0.2 \text{ drag counts, } C_L \pm 0.0015$$

$$C_L = 0.5 \quad C_D \pm 0.7 \text{ drag counts, } C_L \pm 0.003$$

It is seen that a continuous traverse mode of force data recording on a complete model at typical cruise levels of lift will not be satisfactory for incremental drag discrimination between two configurations. Traverse data will however be just acceptable for absolute drag

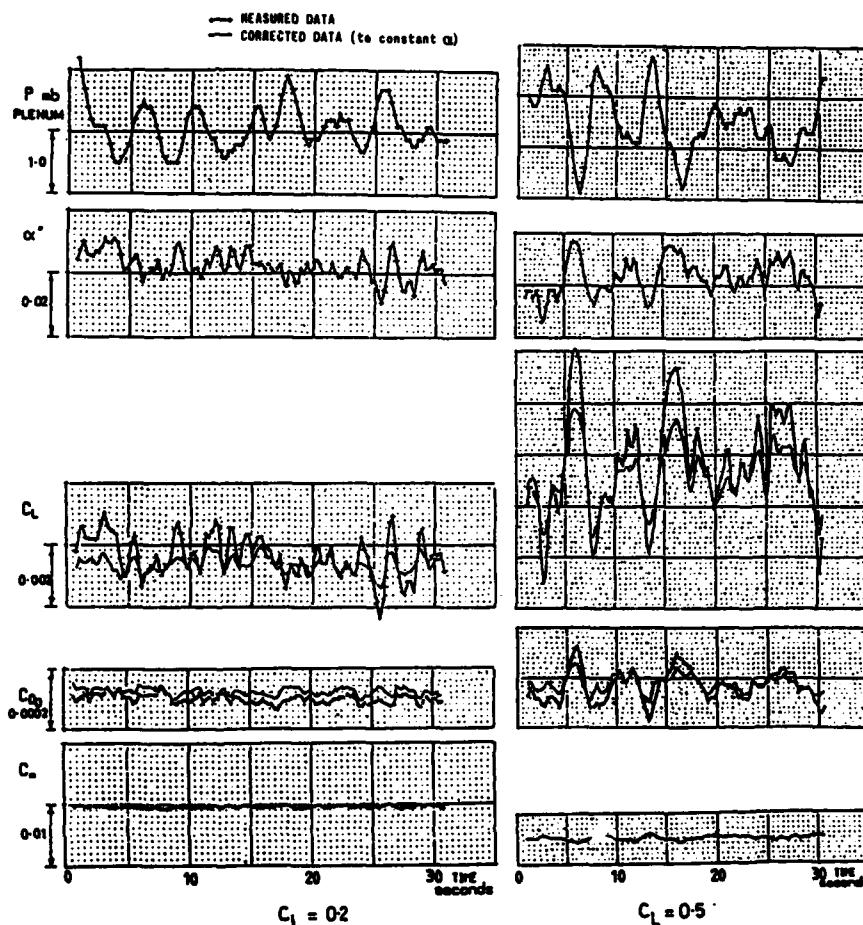


Figure 33 Time variant data records of pressures and forces on a complete model of a civil aircraft. $M=0.8$

definition or series to series comparison. It can however be argued that a polar defined by a multitude of points from a continuous traverse may well provide significantly enhanced drag accuracy after data smoothing.

6.4 Half Model Testing

For modern advance civil wing configurations Reynolds number effects are large enough to require development testing to be done on as large a model as possible. In addition, as mentioned in section 5, for development of wing mounted engine configurations with engine simulators it is more practical to mount a half model carrying simulators on a floor or wall mounted half-model balance. The consequent model scale is normally about 40% greater in linear dimensions with the lift generated on the half wing being equal to that on the wing of the complete model. As a result the distance of the tunnel wall opposite the lifting surface of the half wing is non-dimensionally the same as that of the complete model, whilst carrying twice the lift. As a consequence it was not surprising to find that the amplitude of the fluctuations on the working section and plenum pressures was considerably greater for the half model. Examples of typical fluctuations in force and pressure data are shown in Fig.34. A direct relationship has been shown between the tunnel plenum pressure fluctuations (or M indicated) and the pressures measured on the surface of the half body and the axial force on the balance, which effectively remains unfiltered at these very low frequencies. The C_p fluctuation levels shown in Fig.34 are about half the original

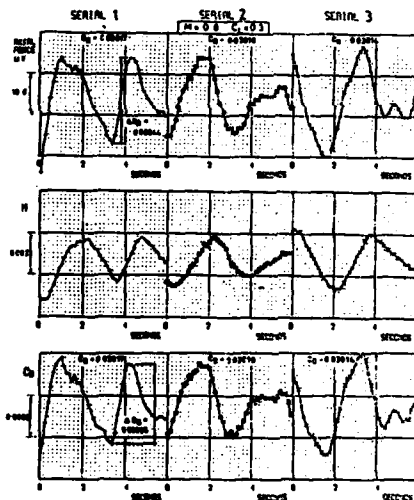


Figure 34 Instabilities with half models.
Details of data samples constituting
3 CD points at fixed α .

magnitude as it was found that these fluctuations were related to a strong separation of the tunnel flow in the WS corner on the wall opposite the lifting surface which responded well to the addition of vortex generators. As a result of the large amplitude of these low frequency fluctuations it is impossible to use continuous traverse data. All data is now taken in the 48

point averaging mode and from Fig.34 it is seen that the value of the averaged axial force for the three repeat cases studied is consistent to better than 0.5 counts. For tests where the Mach number is beyond the drag rise, account must also be taken of the computed M for each of the 48 points to select only those points which are within ± 0.0005 in ΔM of the nominal M , the drag for these points are then averaged to give the value at the nominal M . Attention to this type of detail is essential if the apparent randomness of data is to be understood and reduced.

7 QUALITY OF DRAG RESULTS

Fig.35 shows the standard of drag measurement repeatability achieved in the ARA transonic facility a few years ago. The inter-test series repeatability obtained on nominally the same model configuration tested during three campaigns gave a total uncertainty in C_D of about 0.0006. (The model was totally disassembled between each of these tests). Fig. 36 shows that the shapes of drag polars (matched to the same drag level at $C_L = 0.295$) could differ, within a given test run, by up to 0.0001 in C_D . These standards just met the requirements specified in reference 1 but certainly did not meet the further requirement discussed in section 2. It was against this background that concerted efforts were made to gradually improve all the constituents which

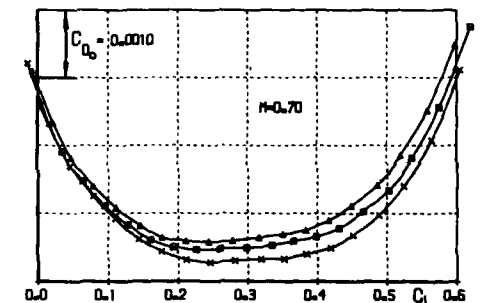


Figure 35. Old standard of inter-test series repeatability. Single sting tests.

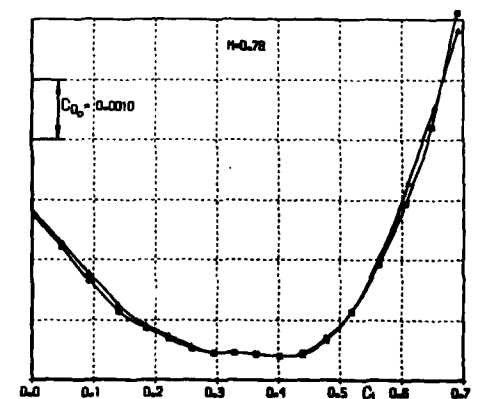


Figure 36. Old standard of polar shape repeatability measured in the same test run. Single sting tests.

affected the quality of drag data. Fig. 37 shows the current quality of typical inter-test series drag results which may be compared with the earlier standards illustrated in Fig. 35. Inter-test series repeatability is now close to $C_D \pm 0.0001$ about a mean. Differences in the shape of repeat drag polars performed during the same test run, Fig. 38, are now so small that the two polars are indistinguishable.

In the past it was not common practice at ARA to investigate the quality of drag measurements by undertaking extensive repeat testing and hence examples which predate those given in Fig. 35 (say of 10 years ago) cannot be presented. Even now, "back to back" testing is uncommon and statistics on inter-test series repeatability are often difficult to obtain. The reasons for this, however, are quite understandable in an industrial facility. For as a civil aircraft model passes through the development phase the model often starts each successive series of tests embodying the geometric changes evolved during the previous tests.

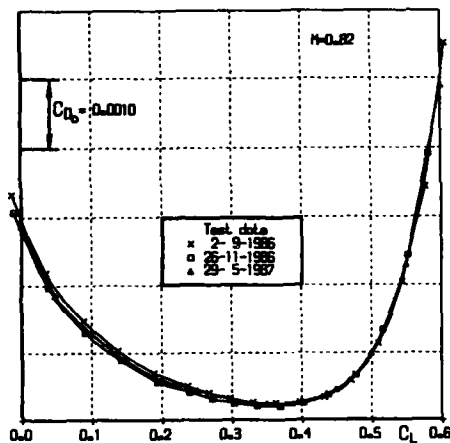


Figure 37. Current standard of inter-test series repeatability. Single sting tests.

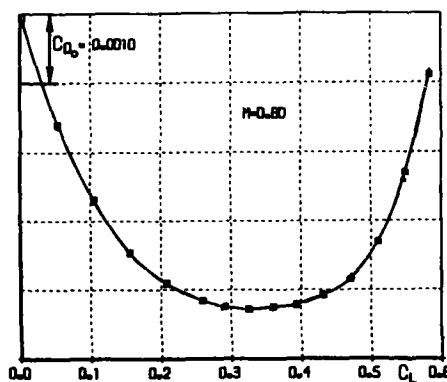


Figure 38. Current standard of polar shape repeatability measured in some test runs. Single sting tests.

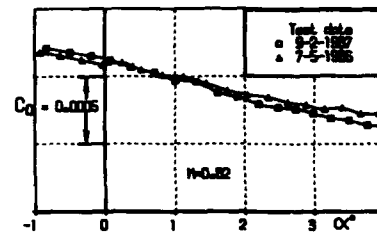


Figure 39. Current standard of inter-test series drag repeatability. Twin sting tests.

It can be seen that even with the current standard of intertest series repeatability ($C_D \pm 0.0001$) it is still essential to establish a drag datum level within a given test series when fine drag increments are a primary test objective.

The current standard of inter-test series drag repeatability obtained from model tests conducted using the twin sting support system is illustrated in Fig. 39 to be within $C_D \pm 0.0001$ about a mean. When it is remembered that these results are derived after the application of very large corrections to remove the fuselage internal pressure force from the balance readings it is quite remarkable that such a standard is achieved.

Whilst inter-test series drag quality is not demonstrated on a regular basis, the repeatability within a given test series is now determined routinely. It is common practice to:

- (i) repeat at least 1 polar, and
- (ii) repeat each " C_{D0} run"

for every configuration.

This effectively means that the drag level of each polar is measured at least twice and the shape of approximately 1 in 5 polars is also checked. Sample results from both single and twin sting exercises are presented in Figs. 38, and 40 to 42. Drag repeatability measurements are now consistently achieved within:

polar shape $C_D \pm 0.00002$

polar level $C_D \pm 0.00003$

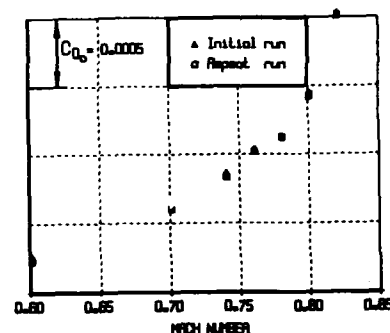


Figure 40. Current standard of drag level repeatability. Single sting tests.

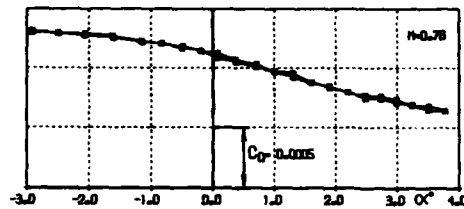


Figure 41. Current standard of polar shape repeatability measured in some test runs. Twin sting tests.

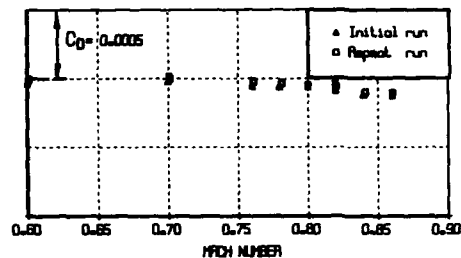


Figure 42. Current standard of drag level repeatability. Twin sting tests.

Although these standards are now well established, repeatability measurements still form an integral part of any test series. Such measurements are necessary to help indicate if errors have occurred within the tests and demonstrate that high standards are being maintained which in turn justifies the credibility of the results obtained.

8 REFERENCES

1. F.Steinle and E.Stanewsky. Wind tunnel flow quality and data accuracy requirements AGARD Report AR-184. 1982.
2. AGARD Report of WG 09 (to publish). Wind Tunnel Boundary Layer Simulation and Control.
3. A.B.Haines. Scale effect in transonic flow. RAE 27th Lanchester Memorial Lecture May 1987.
4. H.C.Garner, W.E.A.Acum, E.W.E.Rogers, E.C.Maskell. Subsonic wind tunnel wall corrections. AGARDOGRAPH 109 (1966).
5. A.E.Harris, E.C.Carter. Wind tunnel test and analysis techniques using powered simulators for civil nacelle installation drag assessment. AGARD CP-301. 1981
6. A.E.Harris, K.C.Paliwal. Civil turbofan propulsion system integration studies using powered testing techniques at ARA Bedford. AIAA Paper 84-0593.

AMÉLIORATION DE LA PRÉCISION DE LA MESURE DE LA TRAÎNÉE D'UN AVION DE TRANSPORT

par

C. ARMAND
ONERA

Centre d'Essais de Modane-Avrieux
B.P. n° 25, 73500 Modane, France

et

C. FUJOL
AEROSPATIALE Toulouse
B.P. n° 3153, 31060 Toulouse Cedex 03, France

RÉSUMÉ

La prévision des performances d'un futur avion de transport nécessite une précision de la mesure du coefficient de traînée du "point" (1.10^{-4}).

L'exposé présente les résultats obtenus dans ce domaine dans les souffleries SIMA et S2MA du Centre d'essais de l'ONERA, à Modane-Avrieux. Les méthodes utilisées pour obtenir la qualité cherchée ne présentent pas de nouveauté de fond, mais toutes ont été mises en oeuvre de façon très soignée en multipliant les redondances et les comparaisons. L'exposé présente aussi des exemples des méthodes employées pour corriger les résultats des effets de parois et de support.

INTRODUCTION

L'un des objectifs que se fixent les expérimentateurs en soufflerie est de mesurer le coefficient de traînée d'une maquette d'avion de transport de type AIRBUS (figure 1) avec la précision absolue de 1.10^{-4} , aux conditions de la croisière (référence 1). Le coefficient de traînée à mesurer dans ces conditions étant de l'ordre de 350.10^{-4} , la précision relative est de l'ordre de 0,3 %. Cette précision doit permettre d'identifier de façon assurée des écarts de traînée entre différentes configurations de l'ordre de 1 % de la traînée, soit environ 3.10^{-4} , et de faire mieux, si possible.



Fig. 1

COÛT D'EXPLOITATION

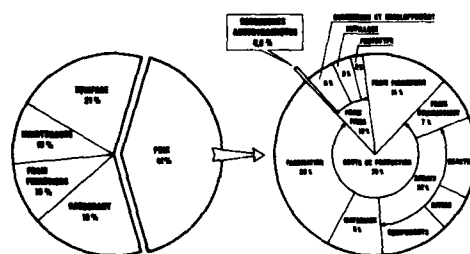


Fig. 2

A quoi correspond cette exigence de précision dans le cadre du développement d'un nouvel avion de la famille AIRBUS ? La figure 2 présente dans sa partie gauche les composantes essentielles du coût d'exploitation direct d'un avion de transport moderne, et, à droite, les éléments constitutifs du prix de l'avion tirés de la référence 2. Le prix du carburant entre pour 18 % dans le coût d'exploitation direct alors que l'ensemble des recherches aérodynamiques ne représente que 0,5 % du prix, soit 0,2 % du total, la part des essais en soufflerie ne formant qu'une partie de ces deux millièmes. Un gain de 1 % sur la traînée, donc sur le carburant, conduit à une économie de 0,2 % sur le coût d'exploitation direct et couvre le financement de l'ensemble des recherches aérodynamiques.

ques. Il est donc particulièrement intéressant d'investir dans ce domaine. L'évolution du prix du carburant peut modifier ces ordres de grandeur mais ne change pas fondamentalement l'intérêt économique d'une réduction de la traînée, d'autant que cette réduction présente aussi des avantages en matière de distances franchissables et de charges utiles. On remarquera à cette occasion que l'influence du prix des essais en soufflerie sur le coût direct d'exploitation d'un avion de transport est presque négligeable.

C'est pour répondre à ce besoin que la Direction des Grands Moyens d'Essais de l'ONERA a développé les méthodes et les moyens liés à la mesure précise de la traînée des avions de transport. Ce développement a été conduit en collaboration avec les constructeurs concernés, l'AÉROSPATIALE et MBB, et a donné les fidélités de l'ordre de grandeur voulu pour les essais industriels effectués dans les souffleries SIMA et S2MA du Centre de Modane-Avrieux. Ces résultats ont été présentés dans la référence 3, et le présent document reprend ces éléments en leur apportant un complément d'informations.

La précision absolue du 10^{-4} , doit être comprise au sens habituel des calculs d'erreur, c'est-à-dire comme une évaluation de l'écart maximum entre la mesure réelle et une hypothétique mesure parfaite qui serait effectuée dans les mêmes conditions. Cette précision ne peut être évaluée pratiquement qu'en multipliant les mesures et en analysant leur dispersion. Cette dispersion qualifie la fidélité des mesures et c'est elle qui est donnée comme une évaluation de la précision en considérant que le premier des objectifs à atteindre est d'être capable de retrouver les mêmes résultats dans des conditions identiques. Une fidélité des mesures au niveau de précision requis est d'ailleurs suffisante pour identifier les écarts cherchés entre configurations. La justesse des mesures ne pourrait être globalement évaluée qu'en se référant à d'autres mesures de qualité au moins égale effectuées par ailleurs. De telles mesures ne sont pas disponibles pour SIMA qui n'a pas d'équivalent, et elles sont rarement disponibles parce que les essais effectués dans différentes installations correspondent généralement à des phases successives du développement du projet et font que les comparaisons sont difficiles à organiser. L'expérimentateur ne peut donc assurer la justesse des mesures et leur validité qu'en choisissant des appareils de mesures précis, en les vérifiant constamment et en utilisant des redondances chaque fois que la mesure d'un paramètre est possible par plusieurs moyens de mesure différents.

Définir la précision absolue avec laquelle les caractéristiques en vol seront prévues à partir des essais en soufflerie est un tout autre problème. La transposition au vol est effectuée en deux étapes. La première consiste à corriger les résultats d'essai des termes parasites propres à la soufflerie pour évaluer les résultats qui seraient obtenus sur la même maquette, dans les mêmes conditions aérodynamiques, mais en champ libre et sans support. Les corrections de ce type usuellement appliquées à SIMA et S2MA seront présentées dans la suite, mais l'évaluation de leur justesse est très difficile à obtenir. La deuxième étape, qui est une transposition prenant en compte les différences de géométrie et de conditions aérodynamiques entre la maquette en champ libre et l'avion en vol, ne sera évoquée qu'au niveau des contrôles des déformations des maquettes en essai.

1 - ESSAIS DANS SIMA

La soufflerie SIMA est une soufflerie continue atmosphérique dont les veines d'essai de 8 mètres de diamètre permettent d'essayer des maquettes d'avion de transport d'environ 4 mètres d'envergure jusqu'à des nombres de Mach de 0,90.

1.1 - Fidélité à SIMA

La figure 3 présente un exemple de recouplement obtenu au sein d'une rotation à SIMA ; elle montre l'évolution des caractéristiques longitudinales de la maquette au cours d'une variation continue de l'incidence effectuée dans les mêmes conditions aérodynamiques en début et en fin de rotation. Les résultats sont obtenus par interpolation des données brutes à nombre de Mach et C_z fixés. Les écarts sont trop petits pour pouvoir être observés à l'échelle habituelle de ces tracés et des agrandissements locaux sont nécessaires pour les mettre en évidence. Dans ce cas, l'écart en C_x à C_z 0,5 est de $0,3 \cdot 10^{-4}$, c'est-à-dire à l'intérieur de la fourchette de dispersion à tenir.

S1. POLAIRES DE RECOUPEMENT

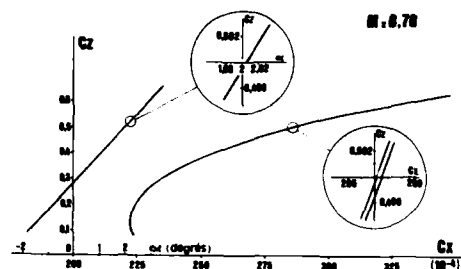


Fig. 3

La comparaison des résultats successivement obtenus est facilitée en calculant la traînée moyenne à portance donnée, puis les écarts algébriques par rapport à la moyenne. Les figures 4, 5 et 6 présentent des exemples de ces comparaisons au sein d'une rotation (figure 4), entre rotations d'une même campagne (figure 5) et entre campagnes (figure 6). La figure 7 regroupe des éléments statistiques pour ces trois types de comparaisons.

S1. RECOUPEMENT DANS UNE ROTATION

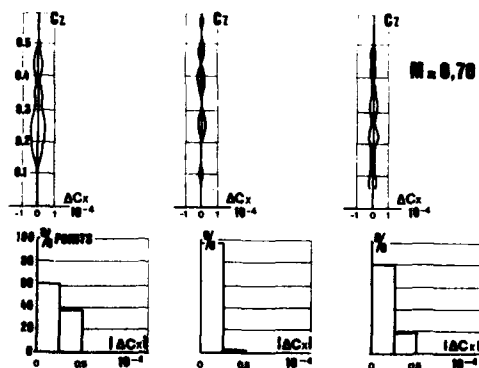


Fig. 4

Chaque graphique de la figure 4 présente un recouplement à $M = 0,70$ dans une rotation. Sur chaque diagramme les écarts algébriques en traînée par rapport à la moyenne (abscisse) sont pointés en fonction de la portance (ordonnée). Les histogrammes associés aux graphiques donnent les distributions des valeurs absolues des écarts. Les points pris en compte pour établir ces histogrammes sont obtenus par interpolations des données brutes (voir 1.2.8) et leur nombre dans le domaine de variation observé est choisi par l'expérimentateur. Le pourcentage des points dans une fourchette d'écart qualifie la part de la courbe représentative dans ce domaine. Les cas présentés sont représentatifs de ce qui est généralement observé : les écarts entre portées comparables de début et de fin d'une même rotation ne dépassent pas 1.10^{-4} , soit $\pm 0,5.10^{-4}$ par rapport à la moyenne. Ces courbes représentatives des écarts et ces histogrammes sont systématiquement produits à la fin de chaque rotation, ce qui permet à l'expérimentateur de juger aussitôt la validité de l'expérience en cours. Sur la figure 7, l'histogramme de gauche regroupe tous les histogrammes obtenus de cette façon pour les 24 rotations d'un même essai. Dans 91 % des cas, les écarts par rapport à la moyenne sont inférieurs à $0,5.10^{-4}$ et ils ne dépassent 1.10^{-4} que pour 0,5 % des cas. Les écarts les plus forts ont été observés au cours d'une rotation après laquelle il avait été constaté que des orifices à la surface de la maquette n'étaient plus obturés avec la même qualité qu'avant le démarrage. Ce défaut avait été estimé suffisamment peu important pour que les résultats soient conservés ; l'histogramme général en porte néanmoins la trace. Les rotations pour lesquelles des défauts sont clairement identifiés ne sont pas incluses dans ces statistiques comme ne faisant pas partie de la même population. La disponibilité de cet histogramme général permet de juger immédiatement si la dispersion observée lors d'une rotation est normale ou non, et, dans le cas où elle ne l'est pas, l'expérimentateur engage une expertise pour identifier l'origine de l'anomalie.

S1. RECOUPEMENT ENTRE ROTATIONS

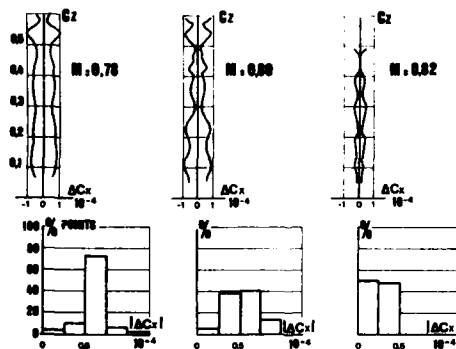


Fig. 5

Ces comparaisons systématiques effectuées à un nombre de Mach modéré (0,70) qualifient essentiellement la fidélité du dispositif expérimental dans des conditions où les phénomènes transsoniques ne jouent pas de rôle significatif. La fidélité effectivement obtenue aux conditions de la croisière est illustrée par la figure 5. Les graphiques présentent les écarts algébriques en fonction de la portance (ordonnée) entre deux rotations différentes effectuées en début et fin d'une même campagne, sur une configuration donnée,

pour trois nombres de Mach de 0,78 à 0,82. Les histogrammes associés à chacun des graphiques donnent la distribution des écarts par rapport à la moyenne. Ces écarts ne dépassent 1.10^{-4} que très exceptionnellement et sont inférieurs à $0,75.10^{-4}$ dans 93 % des cas. Sur la figure 7, l'histogramme du centre présente l'ensemble des écarts constatés entre début et fin d'une campagne d'essai pour huit nombres de Mach compris entre 0,60 et 0,84. Les mesures de traînée sont dans une fourchette de $\pm 0,75.10^{-4}$ dans 90 % des cas. Une amélioration de la précision pourrait être obtenue en augmentant le nombre des mesures et des rotations, mais les constructeurs concernés n'ont pas jugé nécessaire d'augmenter la taille du prélèvement, les précisions tenues donnant satisfaction.

S1. RECOUPEMENT ENTRE CAMPAGNES

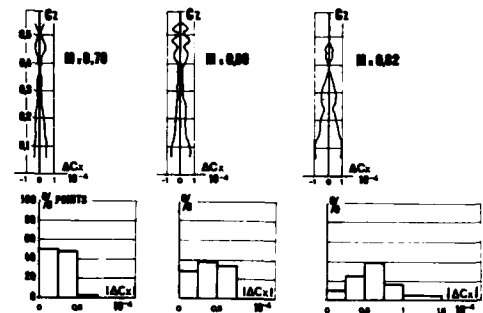


Fig. 6

La figure 6 présente enfin une comparaison entre deux campagnes d'essai séparées par un intervalle de six mois pendant lequel la maquette et le montage ont été entièrement démontés puis remontés. Le système de représentation est le même que pour les figures précédentes. Aux nombres de Mach 0,78 et 0,80, tous les écarts de traînée sont inférieurs à $0,75.10^{-4}$ et, au nombre de Mach 0,82, les écarts ne dépassent 1.10^{-4} que dans 10 % des cas. Sur la figure 7, l'histogramme de droite présente l'ensemble des écarts entre ces campagnes regroupés pour sept nombres de Mach entre 0,60 et 0,84. Tous les écarts sont inférieurs à $1,5.10^{-4}$ et, dans 80 % des cas, ils sont inférieurs à 1.10^{-4} .

S1. RECOUPEMENTS. HISTOGRAMMES D'ENSEMBLE

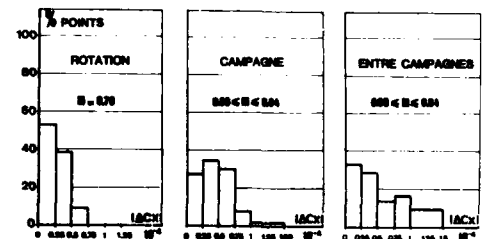


Fig. 7

Les histogrammes de la figure 7 permettent de comparer des dispersions au sein d'une rotation, entre rotations d'une même campagne, entre campagne pour un grand nombre de prélèvements. Les écarts sont tous inférieurs à $1,5.10^{-4}$, mais la distribution des écarts devient plus plate quand la durée d'observation augmente et que le nombre de facteurs perturbateurs augmente.

L'ensemble de ces résultats présente les fidélités à court terme et à long terme. Elles sont considérées comme satisfaisantes par les demandeurs d'essais. Quelques essais ont présenté des fidélités meilleures mais ils ne sont pas assez nombreux pour être considérés aujourd'hui (1987) comme constituant la norme et ne sont pas présentés ici.

1.2 - Dispositif expérimental

Comment cette fidélité est-elle obtenue ?

Les moyens employés sont ceux habituellement utilisés au Centre de Modane-Avrieux pour les essais de pesée, mais tout le processus expérimental a été repensé de façon à incorporer les meilleurs appareils et les meilleures méthodes disponibles. Il n'y a donc pas de nouveauté de fond, mais un simple changement de degré dans le niveau général de la qualité. Ce changement de niveau ne peut être obtenu qu'en organisant spécialement les essais et en consacrant du temps à de très nombreux contrôles. Il en résulte une augmentation des durées et des prix qui limite le perfectionnement du processus expérimental et réserve son utilisation aux expériences où la connaissance très précise de la traînée est un objectif prioritaire.

1.2.1 - Méthode

Le processus expérimental comporte toutes les étapes de l'expérience, depuis sa conception jusqu'à la fourniture des résultats définitifs. Tous les éléments qui le composent conditionnent la qualité du résultat final et doivent être utilisés au mieux. La défaillance d'un seul compromet le tout. Il est donc important que, dès le départ, l'objectif de qualité soit explicitement exprimé et communiqué à tous les participants avec, si possible, les valeurs chiffrées qui doivent être tenues. Cette orientation initiale est nécessaire car, dans des essais où de nombreuses équipes collaborent sur des intervalles de temps qui peuvent couvrir des mois et des années, l'objectif doit être également perçu par tous. La réussite dépend d'une définition explicite de l'objectif puis d'une bonne coopération de toutes les équipes. L'une des conséquences de cette façon de procéder est qu'il faut accepter d'écarter les mesures complémentaires dont la réalisation pourrait compromettre l'obtention du résultat principal.

1.2.2 - Maquettes

Les figures 8, 9 et 10 présentent des maquettes caractéristiques pour SIMA. Il s'agit de



Fig. 8 - SIMA. A310 sur dard droit



Fig. 9 - SIMA. A310 sur dard en lame de sabre

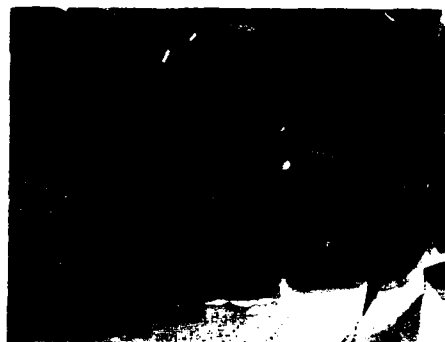


Fig. 10 - SIMA. A310 sur dard dérive

maquettes de l'A 310 au 1/14 de l'AEROSPATIALE (figures 8 et 9) et au 1/9,5 de MBB (figure 10). Ces échelles permettent une bonne représentation de la géométrie de l'avion, y compris des détails qu'il serait difficile de reproduire sur des maquettes plus petites. Une maquette de l'A 310 au 1/38 utilisée à S2MA a aussi été essayée à SIMA dans le but de définir les effets de parois à S2MA ; ce point sera abordé au chapitre 2.

L'AEROSPATIALE et MBB, en accord avec l'ONERA, portent une grande attention à la conception et la réalisation des maquettes pour obtenir que leur géométrie soit bien définie et fidèle dans les conditions de l'essai. Les précautions prises sont très nombreuses et on en donnera ici quelques exemples. Les maquettes sont d'abord calculées pour que, sous les charges en essai, leur forme soit celle de l'avion dans les conditions à simuler. Un contrôle expérimental de la flexion du bord de fuite et de la torsion du bout d'aile a été effectué à l'occasion d'essais exploratoires (voir le paragraphe 1.2.13). Les éléments qui les composent sont robustes et en nombre aussi réduit que possible pour limiter les causes d'incertitude sur les formes. Une bonne solution est d'avoir un caisson central à la forme du fuselage, fixé directement sur la balance et recevant la voilure, les pointes avant et arrière (figure 11). Les liaisons mécaniques sont soignées pour assurer une bonne rigidité et une bonne fidélité lors des montages et démontages successifs. Les raccordements entre éléments qui affectent la surface mouillée sont réalisés de préférence dans des zones de géométrie simple pour faciliter les réalisations et les contrôles. Les éléments de la maquette sont assemblés avec des joints ou des produits assurant l'étanchéité des liaisons de façon à éliminer les écoulements parasites. En cours d'essai, les expé-

rimentateurs s'efforcent de n'employer que des méthodes cohérentes avec les précautions initiales. Les géométries réalisées à la pâte à modeler et les étanchéités par rubans adhésifs ne peuvent être employées dans des essais où la fidélité des formes et des écoulements est essentielle.

STRUCTURE DE LA MAQUETTE

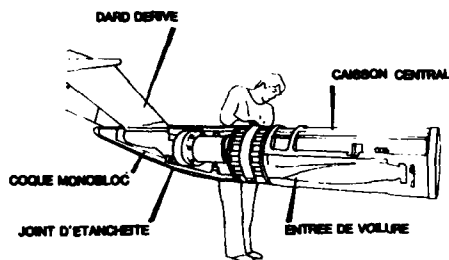


Fig. 11

1.2.3 - Montages

La figure 12 présente trois types de montage utilisés à SIMA. La maquette de l'A 310 au

S1. MONTAGES

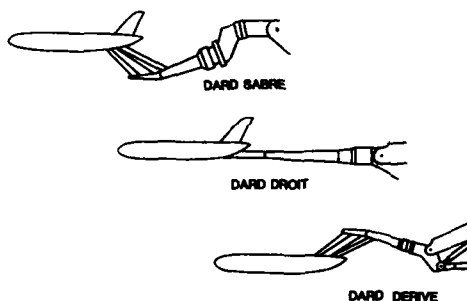


Fig. 12

1/14 de l'AÉROSPATIALE a été montée sur un dard droit (figure 8) et sur un dard en lame de sabre (figure 9) au cours d'une même campagne. Le montage sur dard droit comportait une balance interne de grande sensibilité en traînée mais dont la capacité en portance était limitée, montage spécialement choisi pour donner une bonne précision en traînée à la croisière. Le deuxième montage associait un dard sabre et une balance interne de forte capacité pour permettre des essais au tremblement. Ce double montage évite de soumettre une balance très sensible en traînée aux charges dynamiques induites par le tremblement qui risqueraient de la détériorer. Cet exemple illustre une volonté commune à l'AÉROSPATIALE et à l'ONERA de choisir les montages qui donnent les meilleures garanties de réussite dans les domaines où ils seront employés. La figure 10 donne un autre exemple de montage choisi pour garantir la bonne qualité des mesures de traînée. La maquette MBB est tenue par un dard dorsal dont la lame prend la place de la dérivation de l'avion. Le dard pénètre dans une partie du fuselage où les pressions varient peu, ce qui minimise les interactions. Les interactions résiduelles ont peu d'influence sur la force axiale puisque leur projection sur l'axe est sensiblement nulle et ces effets sont encore réduits par un

dispositif d'étanchéité entre la lame et le fuselage. Enfin le dard lui-même, placé au-dessus de la maquette, perturbe moins le champ de pression de la pointe arrière. Ce montage a donné satisfaction à SIMA et un dispositif analogue a été réalisé pour la soufflerie S2MA et a été mis en œuvre au début 1987 au cours d'essais pour l'AÉROSPATIALE.

1.2.4 - Balances

La réussite des essais dépend fortement de la qualité des balances. Les essais de mesures précises de la traînée bénéficient des progrès réalisés dans ce domaine par les spécialistes de la dynamométrie au sein de la Direction des Grands Moyens d'Essais de l'ONERA. Là aussi, on ne peut donner que quelques exemples. Tous les ponts de jauge des balances sont compensés thermiquement en zéro et sensibilité et la balance dans son ensemble est conçue et équipée pour minimiser les effets des gradients thermiques. Les effets thermomécaniques résiduels sont pris en compte en équipant les lames de découplage entre parties pesées et non pesées de la balance de ponts de jauges qui mesurent les efforts internes et dont les signaux sont traités par la matrice de la balance. L'ensemble de ces dispositifs est éprouvé et ajusté lors des tarages qui comportent une simulation aussi proche que possible des conditions thermiques qui seront rencontrées en essai. Ces précautions sont indispensables à SIMA où, comme on le verra plus loin, les essais sont effectués à des températures pouvant aller jusqu'à 60°C. Les tarages sous efforts sont effectués sur un banc dont les grandes dimensions, la structure rigide et les équipements de mesure donnent de très bonnes conditions d'étalonnage. Les matrices d'étalonnage prennent en compte toutes les interactions en force et moment, linéaires et carrées. Enfin, dans la mesure du possible, les balances sont réalisées en double pour que, en cas de défaillance de l'une d'elles, il soit possible de continuer l'essai avec la balance jumelle. Il est important de souligner que la balance, qui joue un rôle essentiel, ne peut pas être contrôlée sur le site en cours d'expérience, du moins avec le niveau de qualité requis. La validité des résultats dépend donc fortement de la qualité des réalisations et des tarages. En cours d'essai le bon fonctionnement de la balance est régulièrement vérifié en s'assurant qu'avant et après chaque rotation, dans des conditions identiques, la balance fournit bien les mêmes signaux (voir 1.2.6). Le contrôle de son bon fonctionnement est aussi vérifié en effectuant périodiquement la même expérience (poisiers de recouplement) et en contrôlant l'homogénéité des résultats.

1.2.5 - Incidence

La mesure des efforts est effectuée avec une balance interne liée à la maquette, donc dans son système d'axes, et la traînée est définie dans les axes liés à la direction du vent. Le changement de trièdre doit être effectué avec une précision cohérente avec la précision cherchée. Pour une précision requise de 1.10^{-4} sur le coefficient de traînée et un coefficient de portance de 0,4 à la croisière, la précision sur l'incidence doit être meilleure que 1,4 centième de degré, en supposant toutes les autres erreurs nulles. C'est une précision difficile à obtenir et à tenir au cours d'essais très longs. Une simplification admise est de considérer que les mesures effectuées sont comparatives et que, pourvu que l'ascendance de veine ne varie pas, la mesure de l'assiette de la maquette suffit à qualifier l'incidence. L'expérience justifie cette hypothèse. Mais, dans les cas où la connaissance de l'incidence elle-même est nécessaire, il faut effectuer des mesures de

l'ascendance de veine à partir de pesées de la maquette à l'endroit et à l'envers.

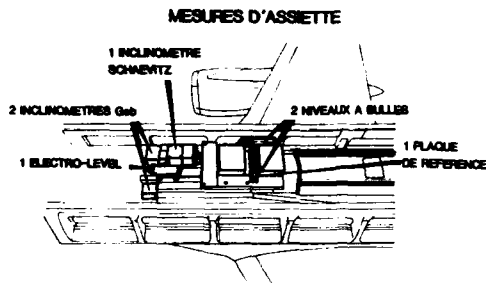


Fig. 13

La figure 13 présente l'équipement interne d'une maquette avec les différents dispositifs et appareils de mesure de l'incidence. Le premier des dispositifs est une surface d'appui usinée dans la structure et destinée à recevoir les appareils d'étalonnage. Cette surface permet de définir la référence horizontale de la maquette et son calage en roulis. Deux niveaux à bulle de précision sont associés à cette surface ; une fenêtre transparente ménagée dans la paroi de la maquette permet de les observer lors des arrêts et de s'assurer que la maquette est bien placée dans l'attitude angulaire pour laquelle les mesures de référence doivent être effectuées. Un niveau à bulle à sortie électrique est utilisé pour repérer la valeur nulle de l'assiette à l'arrêt et en cours de rotation. La résolution de ce niveau est très élevée, de l'ordre de trois dix millièmes de degré. Le repérage de l'assiette nulle en cours de rotation est utilisé pour contrôler le zéro des capteurs d'incidence. Les expérimentateurs prévoient d'utiliser un deuxième niveau électrique calé à une assiette donnée pour vérifier en cours d'essai une autre incidence de la maquette et ainsi contrôler la sensibilité des appareils de mesure. Enfin la mesure de l'incidence elle-même est assurée par trois capteurs pendulaires : deux inclinomètres Geb, conçus et fabriqués par l'ONERA, et un inclinomètre Schaevitz. Ces appareils repèrent l'angle de leur axe avec la direction de la pesanteur. Dans les deux cas, une masselotte est suspendue par une lame qui fléchit lorsque la direction de la pesanteur n'est pas dans son plan. Dans les inclinomètres Geb, un pont de jauge fixé sur la lame mesure les contraintes induites par la flexion. L'inclinomètre Schaevitz utilise un dispositif d'asservissement qui agit sur la position de la masselotte pour que la flexion de la lame reste nulle et c'est l'intensité dans le circuit d'asservissement qui est mesurée. Les deux types de capteurs fournissent des tensions dont l'assiette est déduite par des étalonnages. La résolution de ces appareils est de trois millièmes de degré pour les inclinomètres Geb et un millième de degré pour l'inclinomètre Schaevitz. L'équipement de cette maquette n'est pas exceptionnel et il arrive que des maquettes comportent des capteurs angulaires supplémentaires mis à l'épreuve pour essayer d'améliorer la précision. En fait, l'objectif de cet équipement très complet est de disposer de redondances dans tout le domaine d'essai, lors des essais et des contrôles sans vent.

1.2.6 - Contrôles de la balance et des mesures d'incidence

La balance et le système de mesure de l'assiette sont contrôlés tout au long des essais. Chaque rotation est précédée d'une "balade sans vent", variation continue de l'incidence à la même

vitesse qu'en cours d'essai et pendant laquelle toutes les mesures d'assiette et de force sont effectuées. Les efforts aérodynamiques sont calculés comme s'il s'agissait d'un essai, mais, si la balance et les capteurs d'assiette sont correctement réglés, ces efforts devraient évidemment être trouvés nuls dans tout le domaine. Ce résultat idéal ne peut être obtenu et des valeurs résiduelles apparaissent qui ont pour origine la résolution et le bruit de fond des appareils et de la chaîne de mesure. Il est alors nécessaire de vérifier que ces résidus ne dépassent pas un seuil fixé, généralement choisi pour être équivalent à une incertitude en incidence inférieure au centième de degré. Ce résultat est régulièrement obtenu lors des essais.

Les balades en incidence sont aussi utilisées pour comparer entre elles les mesures d'incidences effectuées par les inclinomètres. Les écarts entre les différentes mesures ne dépassent pas le centième de degré en général, ce qui est satisfaisant. De tels contrôles sont évidemment effectués tout au long de l'essai pendant les rotations elles-mêmes. Toute anomalie conduit à effectuer des contrôles supplémentaires et, si nécessaire, à interrompre l'essai pour corriger les défauts. Ces contrôles permanents sont indispensables pour garantir le même niveau de qualité sur un intervalle de temps parfois très long, de plusieurs semaines, voire plusieurs mois quand il s'agit de campagnes successives. Le rôle de l'expérimentateur est de les effectuer systématiquement, sans défaillance. Il est aidé en cela par l'utilisation de l'ordinateur.

1.2.7 - Références soufflerie

Les paramètres de référence de la soufflerie, nombre de Mach, pression et température d'arrêt, pression cinétique, sont systématiquement mesurées avec des moyens redondants. La confiance dans la validité des mesures de référence est établie sur une comparaison systématique des différentes mesures.

La commande de la soufflerie est réalisée par un automate qui règle soit le nombre de Mach, soit le régime des ventilateurs, c'est-à-dire la puissance. Cet automate donne des réglages très répétitifs d'une fois sur l'autre et cette propriété est utilisée par les expérimentateurs pour réaliser des cycles de balayage du nombre de Mach fidèles au cours des rotations.

1.2.8 - Acquisition et traitement des données

Les essais sont effectués en variation continue de l'incidence à nombre de Mach donné. La vitesse de variation de l'incidence est de l'ordre de $0,2^\circ/s$, soit environ 40 s pour explorer une polaire entre -3° et $+5^\circ$ d'incidence. La figure 14 présente des polaires brutes $C_x(C_z)$ obtenues aux nombres de Mach nominaux 0,70, 0,80 et 0,90 (le nombre de Mach porté sur la planche est celui mesuré au premier point de la polaire). Les courbes représentatives montrent des perturbations en traînée d'autant plus fortes que le nombre de Mach est plus élevé. Ces perturbations ont pour origine essentielle les fluctuations du nombre de Mach pendant le temps d'exploration de la polaire. Elles ont pour origines secondaires les fluctuations d'incidence liées aux oscillations de la maquette et aux fluctuations possibles de l'ascendance de veine ainsi que le bruit de fond de la chaîne de mesure.

RESULTATS BRUTS

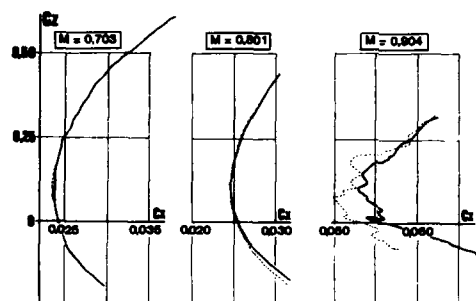


Fig. 14

RESULTATS INTERPOLES

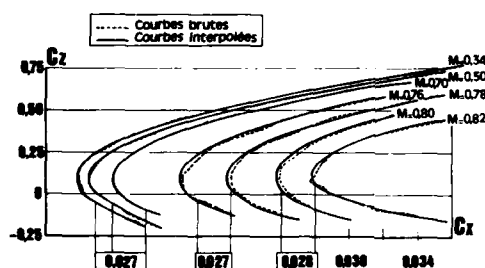


Fig. 15

L'expérience montre qu'il est possible de définir les polaires à un nombre de Mach donné par interpolation entre toutes les données disponibles. C'est la méthode généralement employée et qui donne les meilleurs résultats pourvu que les conditions suivantes soient réunies :

- les coefficients aérodynamiques ne dépendent que des paramètres mesurés, nombre de Mach et incidence. C'est le cas dans les essais à SIMA ;
- les moyens de mesure donnent des informations en phase, c'est-à-dire que les valeurs instantanées de toutes les grandeurs mesurées sont synchrones. Cette propriété est physiquement vraie dans la soufflerie SIMA car les fluctuations sont relativement lentes. Les expérimentateurs doivent néanmoins veiller à régler les filtrages pour que le dispositif de mesure n'altère pas cette propriété ;
- le nombre de points de mesure doit être suffisamment élevé et leur distribution adaptée au domaine de Mach-incidence à explorer. Ces conditions conduisent à ajouter des nombres de Mach aux programmes des essais : par exemple, pour un programme d'essai comportant onze nombres de Mach, seize seront effectivement réalisés.

1.2.9 - Conduite des essais

Les essais sont conduits pour fournir un échantillon de mesures bien constitué en vue des interpolations. Il faut pour cela prendre des précautions expérimentales dont ce paragraphe donne un exemple.

L'accroissement de l'incidence produit une augmentation de la traînée et de la puissance absorbée en veine et, si la puissance de la soufflerie reste constante, il en résultera une dimi-

nution de la vitesse, c'est-à-dire du nombre de Mach. L'automate de réglage de la soufflerie pourrait être utilisé pour contrer cette dérive et maintenir le nombre de Mach constant, mais il est alors constaté que le fonctionnement de cet asservissement induit lui-même des fluctuations du nombre de Mach qui perturbent les évolutions des coefficients aérodynamiques. Les expérimentateurs ont donc choisi d'utiliser l'automate pour maintenir constant le régime des ventilateurs, c'est-à-dire la puissance de la soufflerie, pendant l'exécution d'une polaire. Il en résulte des dérives régulières du nombre de Mach pour lesquelles l'interpolation ne pose pas de problème. Les polaires seront plus nombreuses aux nombres de Mach voisins du coude de traînée, pour fournir plus d'informations dans cette zone. Les valeurs des nombres de Mach à portance nulle sont réglées pour être toutes les mêmes au cours de toutes les rotations de façon à obtenir une distribution fidèle ; il en résulte aussi la possibilité de comparer directement les résultats bruts issus de différentes rotations.

L'interpolation appliquée aux données obtenues dans ces conditions donne des courbes régulières dont la figure 15 présente des exemples.

1.2.10 - Hygrométrie

Le refroidissement de SIMA est assuré par un échange d'air avec l'extérieur et les résultats peuvent être affectés par la teneur en eau de l'atmosphère d'une façon d'autant plus importante que les phénomènes transsoniques sont plus intenses et que la maquette est plus grande. La figure 16 présente des répartitions de coefficient de pression sur le profil d'une voilure mesurées trois fois dans les mêmes conditions aérodynamiques. Les cas A et B pour lesquels les tempéra-

HYGROMETRIE

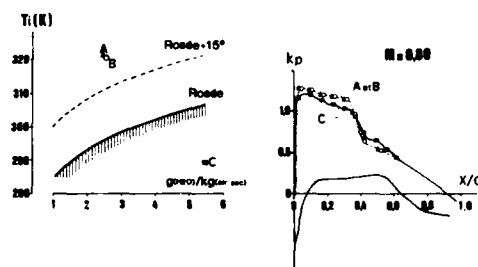


Fig. 16

res génératrices (T_i) et les teneurs en eau sont très voisines, donnent des répartitions de pression presque identiques. Dans le cas C où la teneur en eau est plus forte et la température génératrice plus faible, les mesures sont effectuées dans des conditions où la condensation pourrait se produire et la répartition de pression obtenue est nettement différente. Pour éviter l'apparition de ces phénomènes, il faut réunir des conditions hygrométriques et thermiques dans la veine telles que la condensation ne puisse pas se produire. Comme il n'est pas possible d'agir sur la teneur en eau, SIMA étant une soufflerie atmosphérique, les expérimentateurs agissent sur la température et maintiennent les températures statiques en veine à 15° au-dessus des températures de rosée en veine. Cette marge de 15° a été ajustée expérimentalement et doit être respectée d'autant plus strictement que les teneurs en eau sont plus élevées.

1.2.11 - Effets thermiques

Dans les essais à SIMA, les températures extrêmes sont de -5 à $+60^\circ\text{C}$, ce qui a pour conséquence de placer tous les instruments de mesure dans des conditions thermiques différentes. Les températures les plus basses sont relevées en conditions hivernales, lors des mesures de référence avant essai et les températures les plus élevées résultent d'un fonctionnement prolongé à forte puissance. L'échauffement à partir des températures les plus basses pourrait produire une dérive des signaux des capteurs et des conditions thermiques à la surface de la maquette nuisibles à la qualité. Pour limiter ces effets les essais proprement dits sont systématiquement précédés d'une rotation de chauffe. Tous les capteurs sont protégés contre les effets thermiques dans la mesure du possible, soit par leur conception même (balance), soit en les montant dans des enceintes thermostatisées (capteurs d'incidence). Les essais sont conduits de façon à suivre le même cycle thermique dans les mêmes délais. La figure 17 en donne l'illustration. Elle présente l'échauffement de la soufflerie en fonction du nombre de Mach pour une ouverture fixée des entrées d'air de la soufflerie et regroupe sur un même graphique $T_i(M)$ les cycles thermiques de rotations successives.

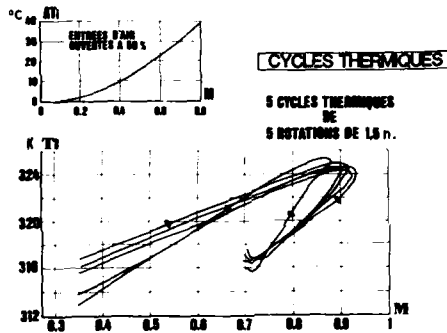


Fig. 17

1.2.12 - Frottement

La dispersion des nombres de Reynolds à nombre de Mach donné provoquée par des variations de la température ou de la pression génératrice induit des variations du C_x de frottement. Les graphiques en bas de la figure 18 donnent les ordres de grandeur des variations du C_x de frottement pour une maquette de l'Airbus au 1/9,5 en fonction de la température génératrice (T_i) et de la pression génératrice (P_i). Les graphiques, dans la partie supérieure de la figure 18, présentent les polaires avant et après correction de frottement.

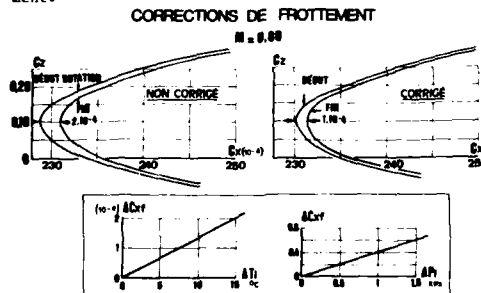


Fig. 18

D'autre part, les changements de nombre de Mach sont réalisés de façon à faire varier lentement la température pour qu'au moment de la mesure la maquette soit en équilibre thermique avec l'écoulement. Il a été vérifié expérimentalement que, si cette précaution n'est pas prise, le C_x en est affecté.

1.2.13 - Savoir-faire

Aux méthodes qui viennent d'être décrites s'ajoutent un grand nombre de procédés qui ne sont pas détaillés ici pour limiter l'exposé et qui couvrent les domaines du déclenchement et du contrôle de la transition, la vérification de la géométrie de la maquette, la mesure des répartitions de pression internes, les détections des contacts accidentels entre parties pesées et non pesées, le contrôle quotidien des chaînes de mesure, le filtrage, l'acquisition et le traitement des signaux, etc. Pour obtenir la qualité voulue il faut que toutes ces méthodes soient mises en oeuvre en parallèle, avec de grandes précautions, pendant toute la durée des essais, sans défaillance, la moindre inattention produisant une diminution de la qualité. La réussite dépend donc fortement du savoir-faire des expérimentateurs chargés des essais dans les équipes de constructeurs comme dans celles de l'ONERA.

1.2.14 - Méthodes complémentaires

L'amélioration de la précision de mesure du coefficient de traînée entraîne la nécessité d'améliorer d'autres techniques expérimentales. On en donnera deux exemples :

1 - La géométrie des voilures doit être connue avec une précision cohérente avec celle des résultats obtenus, ce qui a conduit à développer des méthodes de mesures de déformation des maquettes sous charge en cours d'essai. La figure 19 en présente un exemple tiré de la référence 4. Une

MESURE DES DEFORMATIONS

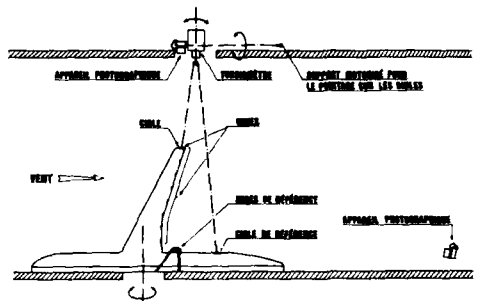


Fig. 19

demi-maquette est montée au plancher d'une veine d'essai de SIMA. Les mesures de déformations portent sur la torsion du bout d'aile et la flexion du bord de fuite. La mesure de la torsion est effectuée par un torsiomètre optique. Cet appareil émet un faisceau de lumière polarisée, dont le plan de polarisation peut être réglé. Ce faisceau est pointé sur des cibles elles-mêmes polarisées et qui réfléchissent une lumière dont l'intensité dépend de l'angle des plans de polarisation. La lumière réfléchie est captée par le torsiomètre qui ajuste son plan de polarisation pour que la lumière réfléchie soit minimum. La mesure de l'orientation du plan de polarisation du torsiomètre donne donc l'orientation de la cible visée. Dans cette expérience deux cibles sont fixées, l'une sur le fuselage, et l'autre en bout d'aile. Le

torsionmètre, monté sur un support motorisé, est successivement pointé sur les deux, d'abord à l'arrêt, puis dans les conditions aérodynamiques où la mesure doit être effectuée et l'exploitation de ces mesures fournit la déformation en torsion du bout d'aile. Par ailleurs, des mires de référence fixées sur un support au plancher et des mires au bout d'aile sont photographiées par un appareil placé au plafond et permettent d'effectuer une autre mesure de la torsion.

La déformation en flexion du bord de fuite de l'aile est déduite de photographies de mires de référence et de mires fixées sur le bord de fuite par un appareil à l'aval de la maquette.

L'ensemble de ces mesures est utilisé pour vérifier la validité des déformations sous charge calculées.

2 - Une connaissance précise des petites différences de traînée entre des configurations a rendu nécessaire de rendre plus précis les relevés des distributions de pression sur les voilures qui, pour être comparatifs, doivent être effectués exactement dans les mêmes conditions. Pour cela, les commutateurs de pression mécaniques ont été remplacés par des commutateurs de pression électroniques PSI, qui permettent de faire des mesures quasiment synchrones sur toutes les prises de pression, et le prélèvement est réalisé lorsque le nombre de Mach diffère du nombre de Mach nominal de moins de 0,001. Les commutateurs sont d'abord préparés pour effectuer une mesure. Le nombre de Mach est prélevé une fois par seconde et, par exemple, pour un relevé à Mach 0,800, lorsque sa valeur est comprise entre 0,799 et 0,801, dix prélèvements successifs sont effectués en 0,33 seconde. Les répartitions de pression relevées par ce procédé donnent des distributions remarquablement fidèles d'un prélèvement à l'autre, ce qui permet les comparaisons entre configurations.

1.3 - Résultats corrigés

Les corrections apportées aux résultats bruts concernent essentiellement la prise en compte des champs de pression de la veine, les effets de parois et de support.

1.3.1 - Champ de la veine

Le champ de la veine est mesuré par une sonde qui donne la répartition de pression statique sur l'axe de la soufflerie pour un nombre de Mach affiché à la prise de référence (figure 21). Ces répartitions sont utilisées pour définir deux corrections :

- une correction de nombre de Mach, pour tenir compte de l'écart entre mesures effectuées à la prise de référence et au point de référence de la maquette ;
- une correction de traînée liée au fait que la pression statique le long de l'axe de la veine n'est pas parfaitement uniforme. La variation de la pression statique induit sur chaque élément de volume de la maquette une poussée localement assimilable à une poussée d'Archimède, c'est-à-dire proportionnelle au volume mouillé et au gradient de pression le long de l'axe. La somme de ces poussées élémentaires est calculée à partir de la distribution des volumes de la maquette ou loi des aires et de la répartition des pressions relevées. La correction de C_x à ajouter aux coefficients de traînée bruts pour obtenir les résultats corrigés, est de l'ordre de $4 \cdot 10^{-4}$.

1.3.2 - Effets de parois

Les effets de paroi sont évalués par un calcul ajusté en fonction de relevés expérimentaux. La maquette et son champ sont représentés par les singularités de l'incompressible, avec une extension pour tenir compte de la compressibilité (référence 5) : 10 à 20 doublets pour représenter le volume de la maquette, une source dont l'intensité dépend de la traînée pour le sillage, 5 nappes tourbillonnaires pour la portance. Les tourbillons peuvent être ajustés pour tenir compte de la flèche de la voilure et de la répartition de portance en envergure.

Les parois sont prises en compte par une méthode assimilable à celles des images étendue pour tenir compte de la porosité des parois. Cette porosité, supposée uniforme, entre dans le calcul par un coefficient qui lie les vitesses de traversée de la paroi aux perturbations de pression locales, coefficient qui ne peut être actuellement déterminé qu'à partir d'expériences. Une même série d'essais est d'abord effectuée en veine habituelle, avec quatre fentes ouvertes (1, 2, 3, 4 sur la figure 22), puis dans la même veine rendue artificiellement étanche, c'est-à-dire de porosité nulle (fentes fermées). Le coefficient de porosité de la veine est ajusté pour que les résultats corrigés issus de ces deux essais soient les mêmes. Une expérience est également effectuée avec huit fentes ouvertes.

EFFETS DE PAROIS

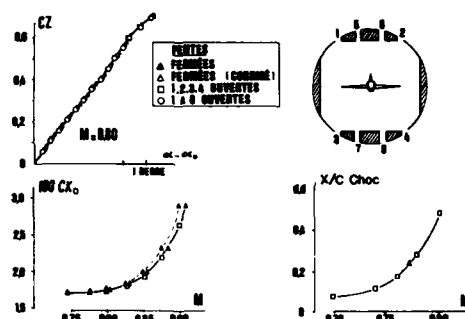


Fig. 20

La figure 20 présente la comparaison de mesures globales (pesées) et locales (position du choc d'extrados tirée de pressions pariétales) pour une maquette de l'AEROSPATIALE dont l'envergure et la longueur sont proches de 3 mètres. On peut constater que, pour ce cas d'essai, la veine à quatre fentes longitudinales est pratiquement exempte de corrections.

1.3.3 - Effets de supports

Les supports produisent des effets locaux très importants dans la zone où le support pénètre dans la maquette. Ces effets ne sont pas accessibles au calcul et n'ont pas été évalués expérimentalement à SIMA. Les expérimentateurs essayent donc de les minimiser lors du choix des montages. C'est la raison pour laquelle en particulier, les dards dérivés ont été développés.

Les effets des supports assimilables à des effets en champ lointain sont évalués par le calcul à partir de représentations par des singularités, comme pour les effets de parois (références 5 et 6). Ces calculs donnent des corrections de nombre de Mach, de traînée et d'ascendance de l'écoulement.

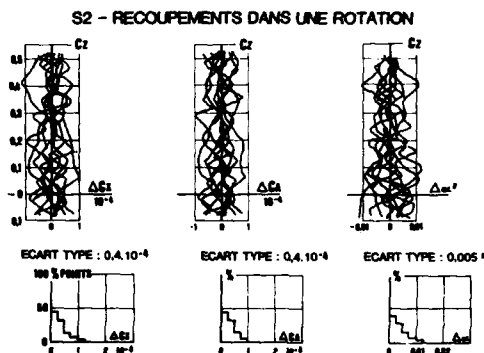
2 - ESSAIS A SZMA

La soufflerie SZMA est une soufflerie continue pressurisée, équipée d'une veine transsonique de 1,77 m de haut sur 1,75 m de large, à nombre de Mach variable de 0,2 à 1,3 et d'une veine supersonique de 1,93 m de haut sur 1,75 m de large, à nombre de Mach variable de 1,5 à 3,1, à parois verticales pleines, plafond et plancher perforés à porosité réglable.

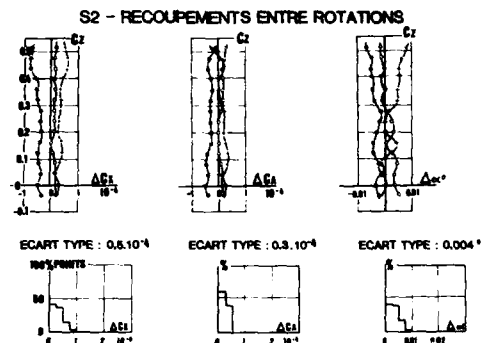
2.1 - Fidélité à SZMA

Des essais d'une maquette de l'Airbus A310 au 1/38 ont été effectués à SZMA en plusieurs campagnes pour mettre au point les méthodes donnant la précision requise. Ces essais ayant donné satisfaction, un essai industriel a été effectué au début 1987 sur l'A310 au 1/38 et une nouvelle maquette de l'AEROSPATIALE. Ce sont les résultats issus de cet essai qui sont présentés ici.

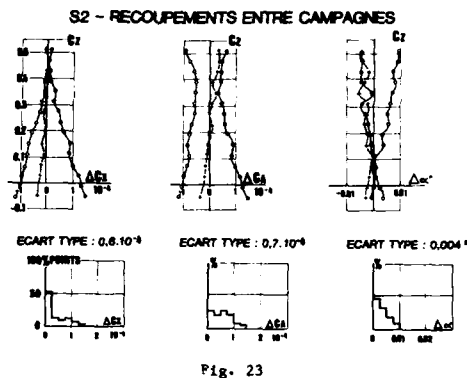
La figure 21 présente des recouvrements au sein d'une rotation, la figure 22 des recouvrements entre campagnes avec démontage de la maquette entre les campagnes. Le nombre de Mach est 0,80 dans tous les cas. Les dispersions en C_x , C_A et incidence sont pointées (abscisse) en fonction de la portance (ordonnée). Les courbes représentent la dispersion par rapport à la moyenne de tous les résultats comparés.



Au cours d'une même rotation, des groupes de trois polaires successives sont effectués au nombre de Mach 0,80 en début, au milieu et en fin de rotation, soit neuf polaires au total. Les résultats de chaque polaire sont définis par interpolation linéaire sur le nombre de Mach et la portance. Le graphique, à gauche sur la figure 21 présente la dispersion en traînée. 98 % des mesures sont dans un intervalle de $\pm 1.10^{-4}$ et l'écart type des dispersions est de $0.4.10^{-4}$. La dispersion en incidence est qualifiée par un écart type de l'ordre de 0,5 centième de degré. L'ensemble des dispersions présente un caractère aléatoire qui indique que le système de mesure est utilisé à sa limite de résolution.



La figure 22 présente des recouvrements entre trois rotations d'une même campagne. Les écarts en C_x par rapport à la moyenne sont tous inférieurs à 1.10^{-4} . La comparaison des figures 21 et 22 fait apparaître une dispersion plus faible sur trois polaires dans trois rotations différentes que sur neuf polaires dans une même rotation. Les différences de dispersion ne semblent donc liées qu'à la taille de l'échantillon, ce qui indique une bonne stabilité des moyens de mesure d'une rotation à l'autre.



La figure 23 présente des recouvrements entre trois campagnes avec démontage et remontage de la maquette entre campagnes. Les plus grands écarts entraînés atteignent $1,5.10^{-4}$ et 87 % des écarts sont inférieurs à 1.10^{-4} . Les écarts constatés peuvent avoir pour origine de petits défauts géométriques liés aux démontages et remontages successifs.

L'ensemble de ces résultats est considéré comme satisfaisant pour les essais à réaliser.

2.2 - Dispositif expérimental

Les méthodes et les moyens utilisés à SZMA sont de même nature qu'à SIMA. Mais les essais à SZMA présentent des particularités dont on donnera quelques exemples.

2.2.1 - Montages

Les figures 24, 25 et 26 présentent les montages utilisés à SZMA pour les pesées d'avions de transport. Chaque montage est employé pour garantir la qualité dans un domaine d'essai particulier. Le montage sur lame de sabre est utilisé pour les essais d'étude du tremblement. Le dard

droit (figure 25) convient pour les essais d'étude des performances incluant des mesures en dérapage. Le dard dérive (figure 26), utilisé depuis le début 1987, est adapté aux mesures fines des caractéristiques longitudinales. Son principe et sa géométrie ont été choisis pour minimiser les interactions au niveau de la partie arrière de la maquette (voir le paragraphe 2.3.1).

S2. MONTAGES

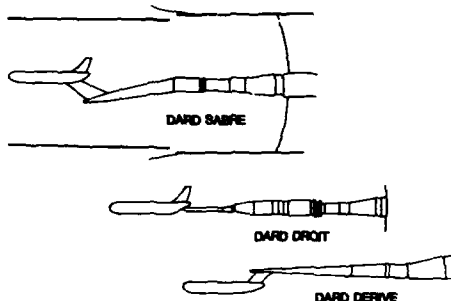


Fig. 24

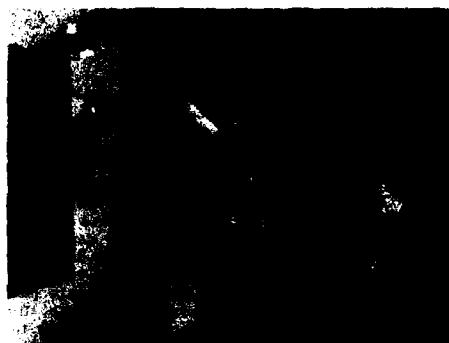


Fig. 25 - S2MA. A310 au 1/38 sur dard droit



Fig. 26 - S2MA. A310 au 1/38 sur dard dérive

2.2.2 - Porosité des parois

Les essais sont effectués dans la veine transsonique dont les parois verticales sont guidées et dont le plancher et le plafond sont à porosité réglable (figure 27). La porosité est réglée en faisant glisser des plaques (tiroirs) dont les perforations obturent de façon variable les

perforations des parois. Lorsque les tiroirs laissent entièrement ouvertes les perforations (positions à 100 % d'ouverture) la porosité des parois définie par la surface des orifices rapportée à celle des quatre parois est de 6 %. Les tiroirs entièrement fermés laissent une porosité résiduelle liée à l'imperfection de l'étanchéité et voisine de 1,6 %. Toutes les positions intermédiaires peuvent être obtenues. Jusqu'au début des années 80 les essais ont été effectués avec les tiroirs ouverts à 100 %. L'analyse des résultats obtenus montrait des instabilités des coefficients aérodynamiques qui limitaient les améliorations de la précision. Il aurait été possible d'éliminer ces fluctuations par une augmentation de la taille des échantillons et un traitement des données approprié, mais cette façon de procéder ne pouvait donner satisfaction qu'en augmentant fortement le nombre des prélèvements, donc la durée des essais. Il a été préféré de chercher l'origine des fluctuations pour tenter de l'éliminer. L'analyse des résultats disponibles montrait une relation entre porosité de la veine et fluctuations et c'est dans ce domaine que les expérimentateurs ont engagé leur action.

S2. EFFET DE LA POROSITE

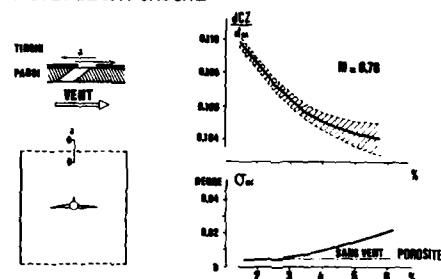


Fig. 27

Des mesures en paliers stabilisés de plusieurs minutes ont été effectuées pour différentes porosités de la veine, pendant lesquels les fluctuations des coefficients aérodynamiques ont été observées. Il a été vérifié que les fluctuations de C_x ne dépendaient, en première approximation, que des fluctuations de l'incidence, c'est-à-dire de l'ascendance de veine, l'assiette étant constante. Le graphique en bas à droite sur la figure 29 présente l'évolution de l'écart moyen quadratique des fluctuations d'ascendance en fonction de la porosité au nombre de Mach 0,78. Cet écart moyen quadratique décroît avec la porosité des parois et devient voisin de celui induit par le bruit de fond du dispositif de mesure pour une porosité de 2,9 % correspondant à une position des tiroirs dite à 55 %. Les effets d'une fermeture plus complète des tiroirs ne sont pas décelables, les fluctuations résiduelles étant du même ordre de grandeur ou inférieures au bruit de fond des mesures. L'analyse de ces fluctuations montre qu'elles ont pour origine des variations de l'ascendance de veine, elles-mêmes induites par des instabilités de l'écoulement dans les perforations des parois. Ces problèmes ne sont pas particuliers à la soufflerie S2MA et se rencontrent dans d'autres souffleries comparables.

Les gradients de portance tirés des mêmes essais sont portés sur le graphique en haut à droite. L'ensemble des résultats forme un nuage (zone hachurée) dont la hauteur caractérise la dispersion induite par les fluctuations de l'ascendance de veine. La diminution de la porosité réduit la dispersion et augmente le gradient de portance moyen. Cette augmentation du gradient a pour origine les effets de parois qui varient avec la fermeture des tiroirs.

Sur la base de ces observations, le choix s'est porté sur la veine avec les tiroirs à 55 % pour les essais où des mesures comparatives de traînée doivent être effectuées avec la meilleure fidélité possible. On verra au paragraphe 2.3.2 que ce réglage offre aussi des avantages en matière de corrections de parois.

2.3 - Résultats corrigés

2.3.1 - Effets de support

Les champs de perturbations liés au support ont fait l'objet de nombreux travaux menés en accord par l'AEROSPATIALE et l'ONERA. La figure 28 en donne un exemple ; elle présente les champs de perturbations en déviation verticale et coefficient de pression du dard à lame de sabre de S2MA. Dans ce cas, l'intégration des perturbations de pression sur le fuselage donne une correction du coefficient de traînée jugée trop élevée.

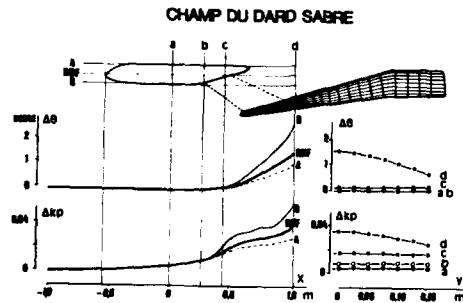


Fig. 28

S2 - CHAMP DU DARD DERIVE CALCULS AS/CALCULS ONERA

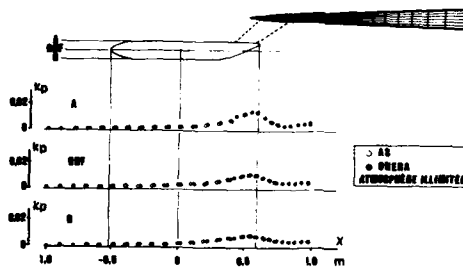


Fig. 29

L'AEROSPATIALE et l'ONERA ont étudié conjointement un nouveau dard adapté à S2MA et inspiré du dard dérive de SIMA. La figure 29 présente un élément de ces études. Le champ de perturbations du cône du dard dérive a été calculé en atmosphère infinie par l'AEROSPATIALE avec une méthode de panneaux et par l'ONERA avec une méthode de singularités. L'accord des deux méthodes est satisfaisant. Le même accord est constaté pour les déviations verticales de l'écoulement (non présentées ici).

La figure 30 présente un contrôle expérimental de la validité des calculs préliminaires. L'ONERA a calculé le champ de perturbation de pression de la partie conique du dard dérive en présence des parois perforées de S2MA, avec les tiroirs réglés à 55 %. Le calcul a été effectué pour plusieurs valeurs de Q , coefficient de perméabilité des parois. Une expérience réalisée par

S2. CHAMP DU DARD DERIVE EXPERIENCE/CALCULS ONERA

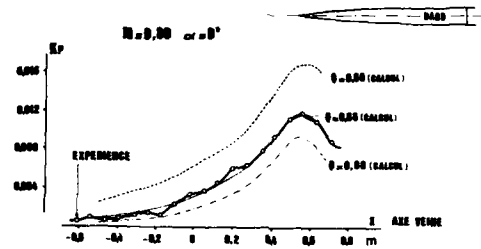


Fig. 30

ailleurs est présentée au paragraphe suivant, conduisant à retenir la valeur $Q = 0,65$ pour les tiroirs à 55 %. Le cône du dard dérive a été réalisé et son champ a été mesuré dans la veine de S2MA. L'accord entre l'expérience et le calcul est tout à fait satisfaisant. Il valide le calcul et la valeur $Q = 0,65$.

Le dard dérive réalisé à la suite de ces calculs et expériences est présenté par les figures 24 et 26.

2.3.2 - Effets de parois

Les effets de parois sont calculés à S2MA selon les mêmes principes qu'à SIMA et leur validité dépend de la connaissance de la perméabilité des parois. Cette perméabilité a été déterminée à S2MA à partir de pesées en veine guidée et en veine perméable, mais aussi par des pesées comparatives de la même maquette dans les souffleries SIMA et S2MA. La figure 31, qui présente les dimensions d'une maquette de S2MA et des deux souffleries, met en évidence que les effets de parois dans SIMA peuvent être considérés comme très faibles et que les essais dans cette soufflerie peuvent être utilisés comme essais de référence. Les corrections de parois seront ajustées pour que les résultats corrigés soient ceux obtenus dans SIMA.

PESEE D'UNE MEME MAQUETTE A S1 ET S2

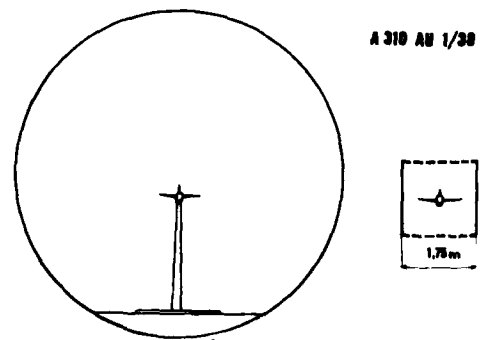


Fig. 31

Cette méthode est satisfaisante dans son principe, mais sa mise en oeuvre pratique est difficile, car les essais doivent être conduits avec la meilleure précision possible pour ne pas attribuer aux effets de parois des différences qui pourraient avoir une autre origine : différence d'ascendance de veine ou de champs de pression parasites par exemple. Les mesures doivent être effectuées avec la même maquette, la même transi-

tion, les mêmes nombres de Reynolds. La ligne de dards employée à S2MA doit rester associée à la maquette et l'ensemble transporté d'une soufflerie à l'autre sans démontage, avec les mêmes capteurs à l'intérieur de la maquette.



Fig. 32 - S1MA. A310 au 1/38 sur dard droit de S2MA

Cette expérience a été réalisée de façon satisfaisante en 1986. La maquette de l'A 310 au 1/38 montée sur un dard droit à S2MA (figure 25) a été transportée à S1MA (figure 32). Les différences de géométrie de support à S1MA et S2MA ont été prises en compte par des expériences (relevés de champs de pression) et des calculs. L'AEROSPATIALE a calculé les perturbations d'incidence induites par le support de S1MA (figure 33), pour deux incidences de la maquette : +2 et -2 degrés. Ces perturbations sont prises en compte dans l'exploitation des résultats, en particulier dans la détermination de l'ascendance de veine par retournement de la maquette.

S1. CHAMP DU SUPPORT. CALCUL.

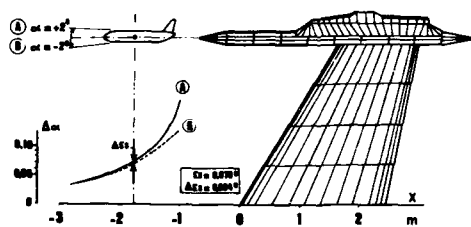


Fig. 33

La figure 34 présente les gradients de portance obtenus à S1MA et à S2MA en veine à 55 % aux nombres de Reynolds de S1MA (1,7 million) et aux nombres de Reynolds usuels de S2MA (3 millions). Le graphique de droite est un agrandissement qui montre les écarts en incidence de ces trois résultats par rapport à leur moyenne en fonction de la portance. Les écarts résiduels doivent être attribués aux résolutions de mesure.

Dans ces conditions et pour ces maquettes, la veine de S2MA avec tiroirs à 55 % donne des gradients de portance pratiquement exempts d'effets de parois. Ces résultats conduisent à retenir une valeur du coefficient de perméabilité des parois de 0,65, valeur cohérente avec les observations sur le champ du dard dérive présentées au paragraphe précédent.

CZ(omega) A S1 ET S2 DEFINITION DE LA POROSITE DE S2 M:0,80

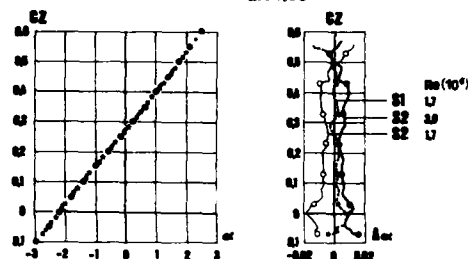


Fig. 34

3 - CONCLUSION

Les résultats satisfaisants qui viennent d'être présentés ne doivent pas laisser croire que les problèmes de mesure précise de la traînée des avions de transport sont considérés comme définitivement résolus au Centre de Modane-Avrieux.

En matière de fidélité, à côté des perfectionnements apportés aux appareils et aux méthodes actuelles, il faut aussi mettre à l'épreuve des solutions nouvelles. On en donnera un exemple. Lorsque les expérimentateurs constatent des différences entre des résultats obtenus dans des conditions réputées identiques, il leur faut déterminer l'origine des différences et, en particulier, savoir si le défaut provient du dispositif de mesure ou d'une infidélité des conditions aérodynamiques. Les expérimentateurs souhaitent donc que la maquette elle-même soit équipée de moyens de mesure permettant de vérifier la fidélité des conditions aérodynamiques à son niveau : prises de pression anémométriques pour donner un nombre de Mach de référence sur la maquette, pressions le long du fuselage pour le contrôle du champ de pression longitudinal, pressions différentielles de bord d'attaque donnant les incidences aérodynamiques locales.

Dans le domaine des corrections de parois et de support, il est généralement difficile d'apporter la preuve de la justesse des corrections effectuées. Les essais comparatifs d'une même maquette dans S1MA et S2MA ou la comparaison des champs du dard dérive calculés et mesurés sont des exemples de méthodes complémentaires qui permettent de vérifier la validité des corrections.

Les meilleures précisions ne sont encore obtenues qu'en poussant toutes les méthodes expérimentales au mieux de leurs possibilités. Les conditions à réunir pour garantir la qualité des essais sont très nombreuses et, pour réussir, aucun détail ne peut être négligé. Le maintien du meilleur niveau de qualité ne peut être garanti qu'au prix d'un effort d'attention permanent et d'une étroite coopération avec les demandeurs d'essais.

C'est en oeuvrant dans cet esprit que la confiance a pu être acquise en la possibilité de comparer des traînées à 1 point près ($1 \cdot 10^{-4}$ de Cx), même à des intervalles de temps éloignés.

Références

- 1 - J. LEYNAERT
Synthèse d'exposés recueillis au Symposium FDP de Casme, septembre 1983.
20ème Colloque d'Aérodynamique Appliquée. AAAF - Toulouse 1983.
- 2 - B. EWALD
Integriertes Flügel - antriebsystem für verkehrsflugzeuge (Optimisation de l'ensemble propulsion - voilure sur avion de transport).
22ème séminaire DMPT de Garmisch-Partenkirchen. 8 et 9 octobre 1980.
- 3 - C. ARMAND, P. HUGOUVIEUX, R. SELVAGGINI
Progrès récents dans la mesure en soufflerie du coefficient de traînée de maquettes d'avions de transport.
23ème Colloque d'Aérodynamique Appliquée. Aussois. Novembre 1986
- 4 - F. CHARPIN, C. ARMAND, R. SELVAGGINI
Mesure des déformations des maquettes en soufflerie.
63ème Meeting AGARD "the structures and materials panel"
Athènes - Octobre 1986.
- 5 - CHEVALLIER, X. VAUCHERET
Effets de parois en soufflerie
20e AAAF - Toulouse 1983.
- 6 - M. YERMIA
Calcul des caractéristiques d'empennage dans le champ tourbillonnaire d'une voilure. 9e AAAF - Saint-Cyr 1977.
- 7 - M. YERMIA
Calcul du souffle moyen d'une hélice et de son influence sur les performances d'un avion.
19e AAAF - Marseille 1982.

FLOW UNSTEADINESS IN THREE LOW-SPEED WIND TUNNELS

by

U. Michel and E. Proebel
 Deutsche Forschungs- und Versuchsanstalt für Luft- und Raumfahrt e.V. (DFVLR)
 Abteilung Turbulenzforschung
 Müller-Breslau-Str. 8
 D-1000 Berlin 12
 Federal Republic of Germany

SUMMARY

This paper discusses the velocity unsteadiness in six test sections of three low speed wind tunnels. Large differences of the root-mean-square velocity or turbulence levels are observed in these tunnels. It is shown that these differences can be explained with the two independent contributions to the velocity unsteadiness in a wind tunnel: (i) vorticity which is convected into the test section from upstream, and (ii) pressure waves which have many origins but the important ones for low speed tunnels are the free shear layers of open test sections and slotted wall test sections. It is further shown that the turbulence level is not sufficient to describe the effect of velocity unsteadiness on the quality of data measured in a wind tunnel and it is demonstrated with the example of boundary layer transition that the distribution of the fluctuating energy in the frequency domain is more important.

NOMENCLATURE

a	sound speed
A	cross sectional area of test section
C_p	fluctuating pressure coefficient, $C_p = \bar{p}/((\rho/2)U^2)$
D	equivalent diameter of test section, $D^2 = 4A/\pi$
f	frequency
Re	Reynolds number, $Re = fD/a$
L	typical model dimension, e.g. wing span
M	Mach number, $M = U/a$
M'	fluctuating part of M
M'_v	contribution of vorticity to M'
M'_p	contribution of entropy to M'
M'_p	contribution of pressure to M'
p	(static) pressure
p'	fluctuating part of p
\bar{p}	root-mean-square value of p'
\hat{p}	peak value for the amplitude of p'
Re	Reynolds number, $Re = U D/\nu$
St	Strouhal number, $St = f D/U$
St_L	Strouhal number based on model length L , $St = f L/U$
T	(static) temperature
T'	fluctuating part of T
T'_e	contribution of entropy to T'
T'_p	contribution of pressure to T'
u	velocity component in the x-direction
u'	fluctuating part of u
u'_v	contribution of vorticity to u'
u'_p	contribution of pressure to u'
\bar{u}	root-mean-square value of u'
$\Delta \bar{u}^2/\Delta f$	power-spectral density of u'
U	mean of u
v	velocity component in the y-direction
v'	fluctuating part of v
\bar{v}	root-mean-square value of v'
$\Delta \bar{v}^2/\Delta f$	power-spectral density of v'
V	mean of v
w	velocity component in the z-direction
w'	fluctuating part of w
\bar{w}	root-mean-square value of w'
$\Delta \bar{w}^2/\Delta f$	power-spectral density of w'
W	mean of w
x	coordinate in the mean-flow direction
y	coordinate in the horizontal transversal direction
z	coordinate in the vertical transversal direction

1. INTRODUCTION

Flow unsteadiness in wind tunnels is one of the factors that contribute to the precision and quality of data obtained in wind-tunnel experiments. The Abteilung Turbulenzforschung (Turbulence Research Section) of DFVLR in Berlin has carried out hot-wire and microphone measurements in various European tunnels to investigate their flow unsteadiness. This paper discusses the velocity unsteadiness in six test sections of three tunnels.

The three tunnels concerned are outlined in figure 1. Most of the data presented here were measured in the NWB, a low speed tunnel of DFVLR in Braunschweig (Germany) with an open or a closed 3.25 m x 2.8 m test section. The walls of the closed test section are equipped with slots whose open area can be

varied between 0 % and 12 %. The nozzle contraction ratio is 5.6 and the maximum air speeds are 70 m/s for the open and 90 m/s for the closed test section. The tunnel has a conventional design with a fan in the return leg. The four corners are equipped with turning vanes. A honeycomb flow straightener and three screens are installed in the settling chamber.

Figure 1: Wind tunnels investigated.

NWB: 3.25 m x 2.8 m low speed tunnel, DFVLR Braunschweig, Germany

NWG: 3 m x 3 m low speed tunnel, DFVLR Göttingen, Germany

DNW: 8 m x 6 m low speed tunnel, German-Dutch Wind Tunnel, Marknesse, The Netherlands

The experimental results of the open test section are compared with corresponding data of the NWG, a 3 m x 3 m low speed tunnel of DFVLR in Göttingen (Germany) which has a nozzle contraction ratio of 5.4 and a maximum air speed of 66 m/s. Two 180 degree turns indicate an unconventional design for the circuit of this tunnel. The diffusers of the circuit are combined with the turns. Rows of staggered vanes are installed to inhibit flow separation. The return leg with the fan is circular while the two turns and the settling chamber are rectangular. The settling chamber is very long and equipped with honeycomb flow straightener and three screens.

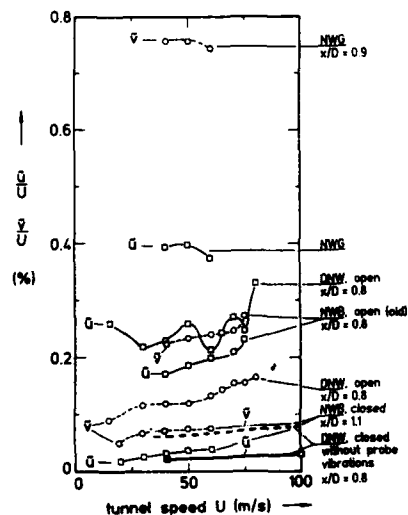
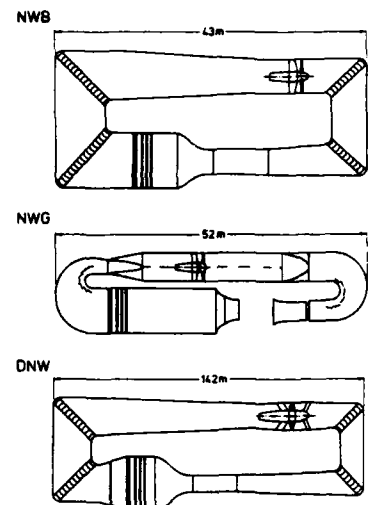
The results of the NWB are also compared with data of the open and the closed 8 m x 6 m open test sections of the DNW, the German Dutch Wind Tunnel in Marknesse (the Netherlands). The nozzle contraction ratio of these test sections is 9.0 and the maximum air speed is about 85 m/s for the open test section and 117 m/s for the closed test section. The tunnel can also be equipped with two other closed test sections with cross sections of 6 m x 6 m and 9.5 m x 9.5 m, but their flow unsteadiness was not studied. Several design features aim at a good flow quality including a low turbulence level: (i) A wide angle diffuser with screen at the entrance of the settling chamber permits a large nozzle contraction ratio. (ii) The diffuser angles in the rest of the circuit are small. (iii) The heat exchanger in the settling chamber has long flow channels for good heat transfer but also for the elimination of streamwise vorticity through viscous forces. (iv) It was not possible to manufacture the screens in the settling chamber in one piece. However, much care was applied in the soldering process of the seams to avoid irregularities of the screen as far as possible.

2. TURBULENCE LEVELS OF THE THREE TUNNELS

The velocity unsteadiness in wind tunnels is generally described in terms of "turbulence levels" \bar{u}/U , \bar{v}/U , and \bar{w}/U , where \bar{u} , \bar{v} , and \bar{w} are the root-mean-square values of the three components of the fluctuating velocity in the x, y, and z-directions, respectively, and U is the tunnel speed. The data reported here are measured with hot-wire anemometers using x-wire probes.

The anemometers (DFVLR) are equipped with polynomial linearizers which yield output voltages proportional to the velocity. A turbulence-level meter (DFVLR) is used to evaluate the two velocity components u and v (or u and w, depending on the orientation of the x-wire), to separate the fluctuating portions from the mean, to evaluate the mean velocities U and V, and the turbulence levels \bar{u}/U and \bar{v}/U . The averaging times and the cut-off frequencies of the high-pass and low-pass filters can be set to suitable values. Generally the filter settings 0.1 Hz and 10 kHz are used for these turbulence measurements. The turbulence-level meter also

Figure 2: Turbulence levels \bar{u}/U (squares) and \bar{v}/U (circles) in the studied test sections. The levels in the closed test section of the DNW are estimated from measurements that include spurious signals. Note the factor of about ten for the ratio between the turbulence levels of the NWG and the closed test sections of the DNW or NWB.



outputs the fluctuations u' and v' for realtime frequency analysis in signal analysers. The latest version of the equipment is interfaced to a computer which makes it possible to adjust the lineariser constants to changed mean values of the temperature and the pressure in the flow. All settings of the equipment and the integrated results can be read by the computer. In addition, the orientation of the x-wire probe can be changed through computer control.

Figure 2 contains some results for the turbulence levels \bar{u}/U and \bar{v}/U from the three tunnels. The level \bar{u}/U of the longitudinal velocity fluctuations is seen to cover a range of values between 0.025 % for the DNW at about 40 m/s and 0.4 % for the NWG. The turbulence level \bar{v}/U of the horizontal transversal velocity fluctuations covers a similar range between 0.06 % for the DNW and 0.75 % for the NWG. The lowest values in the cross section of a typical model position for tunnel speeds of about 60 m/s are listed in the following table.

	NWB			NWG	DNW	
test section	open	closed	slotted	open	open	closed
contraction ratio	5.6			5.4	9.0	
lowest \bar{u}/U	0.19 %	0.04 %	0.05 %	0.38 %	0.22 %	0.03 %
lowest \bar{v}/U	0.21 %	0.08 %	0.10 %	0.75 %	0.12 %	0.075 %
corresponding \bar{v}/\bar{u}	1.1	2.0	2.0	2.0	0.6	2.5

The ratio \bar{v}/\bar{u} is much smaller than one in the center of the open test section of the DNW. It is almost equal to one in the open test section of the NWB while it is much larger than one in the NWG and the closed or slotted wall test sections. The origin of these differences will be studied later.

3. THREE CONTRIBUTIONS TO FLOW UNSTEADINESS

It was shown by Kovácsnay [1] in a linearized treatment of the flow equations that the flow unsteadiness in the empty test section of a wind tunnel can be described by three independent fundamental contributions: vorticity, entropy, and pressure fluctuations. All other fluctuating flow quantities in a tunnel can be expressed in terms of two or all three fundamental contributions. Examples for dependent fluctuations are velocity fluctuations. The velocity fluctuations u' in the mean flow direction x are given by

$$u' = u'_v + u'_p, \quad (1)$$

where u'_v is the contribution of the vorticity field and u'_p is the contribution of the pressure field. Temperature fluctuations T' are created by entropy and pressure fluctuations,

$$T' = T'_s + T'_p, \quad (2)$$

and Mach number fluctuations M' are created by all three basic contributions,

$$M' = M'_v + M'_s + M'_p. \quad (3)$$

Vorticity and entropy fluctuations are convected with the tunnel flow. The propagation velocity U_p of these disturbances is equal to the tunnel speed U . It was shown in reference 2 that pressure fluctuations are governed by a convective wave equation and that the component U_p of the propagation velocity of the pressure waves in the mean flow direction can have any value between zero and infinity, except a small range around the tunnel speed U which must be excluded for this linearized treatment.

Propagation velocities U_p proportional to the tunnel speed U are observed for pressure waves in the near fields of free shear layers or boundary layers. In these cases, U_p is close to the propagation speed of the disturbances in the shear layer. Plane sound waves propagate with a speed $U_p = U + a$, where a is the sound speed. Large values for $|U_p - U|$ can be observed for sound waves that propagate with an angle relative to the mean flow direction. The component $|U_p - U|$ in the flow direction becomes infinite for sound waves that propagate perpendicular to the mean flow direction. This is the case for the cut-on frequencies of higher order duct modes of sound.

Only velocity fluctuations are discussed in this paper. They are described by eq. (1) and equivalent equations for the two transversal velocity components. The velocity fluctuations u'_v in the x -direction (mean flow direction) due to vorticity depend on the two vorticity components in the y -direction (horizontal transversal) and z -direction (vertical transversal). The velocity fluctuations u'_p in the x -direction due to pressure waves depend on the propagation velocity of the pressure waves. According to ref. 2 we have for $U_p \neq U$

$$u'_p = p' / (\rho(U_p - U)). \quad (4)$$

This result indicates that the effectiveness of a pressure wave in generating velocity fluctuations in the mean flow direction of a wind tunnel depends very much on the difference $U_p - U$ between the component U_p of the wave propagation velocity in the x -direction and the tunnel speed U . For the rms-values \bar{u}_p of u'_p and \bar{p} of p' we obtain the relation

$$\bar{u}_p / U = C_p U / (2|U_p - U|), \quad (5)$$

where $C_p = \bar{p}/((\rho/2)U^2)$ is the fluctuating pressure coefficient. Eq. (5) shows that large normalized velocity fluctuations \bar{u}_p/U due to pressure waves require one or both of the following two conditions to be satisfied: (i) large values of the pressure coefficient C_p or, (ii) large values of $U/|U_p - U|$. For plane sound waves we obtain

$$\bar{u}_p/U = C_p(M) M/2, \quad (6)$$

where $M = U/a$ is the Mach number of the tunnel. M is small in low speed tunnels. In addition, $C_p(M)$ due to plane waves is generally small for small Mach numbers. Therefore, the contribution of plane sound waves to the velocity fluctuation level in low speed tunnels is generally negligible.

The case is different for pressure waves that propagate with $U_p = \alpha U$, where $\alpha = 0.6 \dots 0.8$. For this case we obtain from eq. (5)

$$\bar{u}_p/U = C_p \beta, \quad (7)$$

where $\beta = 1.25$ for $\alpha = 0.6$ and $\beta = 2.5$ for $\alpha = 0.8$. It will be seen that this contribution is not negligible in low speed tunnels in positions sufficiently close to shear layers.

4. DIFFERENTIATION OF FLOW UNSTEADINESS IN THE FREQUENCY DOMAIN

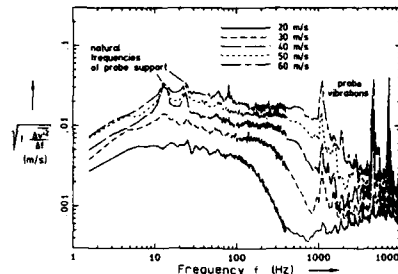
The description of flow unsteadiness in terms of turbulence levels \bar{u}/U , \bar{v}/U , and \bar{w}/U is not sufficient when the effect on the quality of wind tunnel results is concerned. E.g., boundary layer transition is influenced by fluctuations at rather high frequencies, buffet onset by medium frequencies, and measurements of static forces and moments by rather low frequencies (see e.g. Hartsuiker [3]). It will be shown later that tunnels with identical turbulence levels can yield completely different experimental results because their frequency spectra are different.

Figure 3: Frequency spectra for the v' -velocity fluctuations in closed test section of NWB for tunnel speeds between $U = 20$ m/s and $U = 60$ m/s. $x = 3.72$ m, $y = -0.04$ m, $z = 0$ m.

Figure 3 presents the frequency spectra of the v' -fluctuations in the closed test section of the NWB for different tunnel speeds U . The frequency is plotted logarithmically on the horizontal axis. This has the advantage of a good resolution of the spectra at low frequencies. The mean square value $\bar{\phi}^2$ of a spectrum is given by the integrals $\int (\Delta \phi^2 / \Delta f) df = \int (f \Delta \phi^2 / \Delta f) df / f = \int (f \Delta \phi^2 / \Delta f) d \ln f$. The first integral is convenient for a linear frequency axis where a frequency interval Δf has a constant length. The last integral is convenient for a logarithmic frequency axis because $d \ln f$ has a constant length on the axis in this case. Consequently, the power-spectral density $\Delta \phi^2 / \Delta f$ times the frequency f is plotted on the vertical axis in this paper. In addition, a logarithmic scale is used. The square root is used for axis labeling, because the square root of $(f \Delta \phi^2 / \Delta f)$ is proportional to the velocity fluctuations v' . Equal spectral density levels at different frequencies in figure 3 indicate equal importance of this part of the spectrum with respect to the root-mean-square value $\bar{\phi}$ of the fluctuations v' . Each spectrum in this figure is a combination of two spectra, the first one covers the frequency range from 1.6 Hz to 400 Hz, the second one the range up to 12.8 kHz. A combination of three or more spectra is necessary for a better resolution at low frequencies.

Figure 3 also illustrates the problem of hot-wire anemometry in low-turbulence flows: spurious peaks appear in the spectra. The peaks visible at low frequencies are caused by vibrations of the probe strut with its natural frequencies. The peaks at higher frequencies are caused by natural frequencies of the probe holder, probe, or sensor wires. The effect of small vibrations on the turbulence level can be demonstrated with an example. A vibration with an rms amplitude of $1 \mu\text{m}$ and a frequency of 4 kHz simulates an rms velocity fluctuation of $\bar{u} = 0.025$ m/s, or a turbulence level $\bar{u}/U = 0.05\%$ for $U = 50$ m/s. Such a contribution can dominate the indicated turbulence level of low-turbulence tunnels. Therefore, the turbulence levels of low turbulence tunnels can only be determined by cleaning the frequency spectra from apparent spurious contributions and integrating the spectra to yield the turbulence levels. All levels reported here are processed in this way. Only the \bar{v}/U data for the closed test section of the DNW in figure 2 are estimates deduced from values that include probe vibrations. Broadband contributions from forced vibrations of the probe cannot be distinguished from real velocity fluctuations and, consequently, are included in the turbulence levels reported here. The origin of the spectral levels at high frequencies is not known. It may be the noise floor of the electronic equipment which depends on the wind speed in the case of a hot-wire anemometer and cannot be checked in the no-flow condition.

It can be seen in figure 3 that higher wind speeds increase the spectral levels in the NWB and also increase the cut-off frequencies for the decay of the spectral level at high frequencies. A decay can also be observed for low frequencies. The cut-off frequency for the decay of the spectral density of v' at low frequencies is almost independent of tunnel speed, because it is primarily a function of the lateral dimension of the test section and the sound speed.



5. TEST SECTIONS THAT ARE DOMINATED BY VORTICITY

The spectra of figure 3 for the NWB are replotted in a non-dimensional form in figure 4, using the tunnel speed U and an equivalent diameter D for normalization. D is defined by $D^2 = 4A/\pi$, where A is the cross-sectional area of the test section. The normalized frequency $St = fD/U$ is called Strouhal number. Additional non-dimensional parameters of this problem are the Reynolds number $Re = UD/\nu$, the Mach number $M = U/a$, and the Helmholtz number $He = fD/a = MSt$. The most prominent influence of these parameters is a rise of the cut-off Strouhal number for the decay of the spectrum at high Strouhal numbers from a value of $St = 20$ to a value of about $St = 30$ which may indicate a Reynolds number influence. The cut-off at low Strouhal numbers is shifted to lower Strouhal numbers with increasing tunnel speed. This is a consequence of the dependence of the v' - and w' -fluctuations on tunnel dimension and sound speed described in the previous paragraph and can be expressed as a Helmholtz number dependence. The cut-off Helmholtz number is about $He = fD/a = 0.1$.

Figure 4: Normalized version of figure 3. Normalized frequency spectra for the v' -velocity fluctuations in closed test section of NWB for tunnel speeds between $U = 20$ m/s and $U = 60$ m/s. $x = 3.72$ m, $y = -0.04$ m, $z = 0$ m.

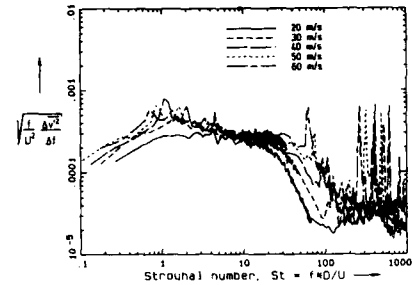
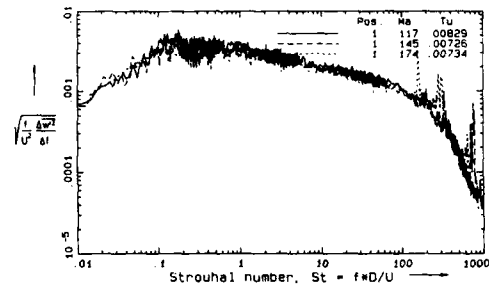


Figure 5 is a similar plot for the w' -fluctuations in the NWG. The normalized spectra are almost independent of tunnel speed for this tunnel. The Helmholtz number influence on the cut-off at low frequencies is replaced by a Strouhal number influence because the NWG is a free jet tunnel which has no walls that constrain the large transversal fluctuations at low frequencies. The cut-off Strouhal number has a value of $St = 0.1$. The Reynolds number influence at the high Strouhal number end of the spectra in the NWB has disappeared in the NWG. Note the large range of 5 decades of the Strouhal number axis. Two of the spectra are combined from four spectra with differing frequency ranges which yields a very good Strouhal number resolution at low Strouhal numbers. The third spectrum is a combination of three spectra.

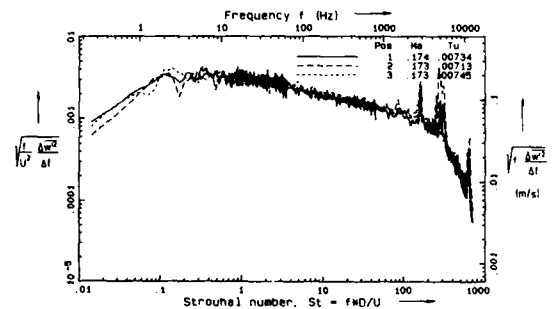
Figure 5: Normalized frequency spectra for w' -velocity fluctuations in NWG for different tunnel speeds, $U = 40$ m/s, 50 m/s, 60 m/s. $x = 1.0$ m, $y = z = 0$ m.



The spectra of figures 4 and 5 are dominated by vorticity fluctuations. A typical property of vorticity fluctuations in the test sections of wind tunnels is that their decay with increasing distance from the nozzle is negligible. This is demonstrated in figure 6 which shows w' -spectra on the center line of the NWG for $U = 60$ m/s for three distances, 1 m, 2 m, and 3 m from the nozzle.

A second property of vorticity is that the turbulence levels \bar{v}/U and \bar{w}/U for the velocity fluctuations perpendicular to the mean flow direction are larger than \bar{u}/U for the longitudinal fluctuations. This is obvious in the Strouhal number range $0.3 < St < 100$ of figure 7 for the velocity fluctuations in the closed test section of the NWB. The spectral levels tend to become equal for Strouhal numbers above 100 which indicates isotropic turbulence. The v' -fluctuations at small Strouhal numbers are larger than the w' -fluctuations because the dimension of the test section in the y -direction (3.25 m) is larger than in the z -direction (2.8 m).

Figure 6: Normalized frequency spectra for w' -velocity fluctuations in NWG for different axial positions $x = 1$ m, 2 m, and 3 m. $y = z = 0$ m. $U = 40$ m/s.

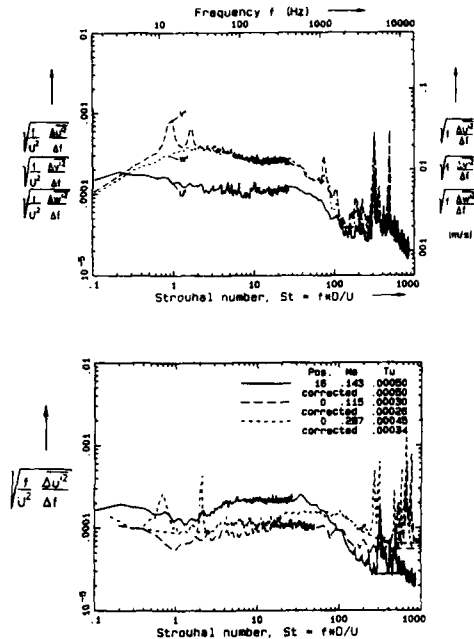


A third property of vorticity is that its propagation speed is equal to the tunnel speed. This was verified in the NWB with a tandem-wire hot-wire probe. Two normal wires were separated in the flow direction by $\Delta x = 20$ mm ($\Delta x = 10$ mm is now used for improved coherence). A lateral separation of about $\Delta y = 2$ mm was used to keep the second wire out of the wake of the first one. The phase velocity can be computed from the phase spectrum as a function of frequency and was found to be identical to the tunnel speed.

Figure 7: Comparison of normalized u' -, v' -, and w' -spectra in closed test section of NWB. $U = 50$ m/s, $x = 3.7$ m, $y = -0.04$ m, $z = 0$ m.

Figure 8 is a comparison between a normalized u' -spectrum of the NWB for $U = 50$ m/s with two corresponding spectra of the DNW for $U = 40$ m/s and $U = 100$ m/s. The DNW has smaller normalized levels for Strouhal numbers $St < 70$. A ratio of about 2.5 between the spectral levels of NWB and DNW would correspond to the different nozzle contraction ratios of both tunnels. This figure also illustrates the effect of cutting off the spurious peaks. The integrated turbulence levels are reported in the upper right corner of the figure. The turbulence level of the corrected spectra is seen to be identical to the uncorrected one in the case of the NWB. The turbulence level of the DNW for $U = 40$ m/s is reduced from $\bar{u}/U = 0.030$ % to 0.026 % and the turbulence level of the DNW for $U = 100$ m/s is reduced from $\bar{u}/U = 0.045$ % to 0.034 %.

Figure 8: Comparison of normalized u' -spectra:
 (—): NWB, $U = 50$ m/s, $x = 3.7$ m,
 $y = 0.04$ m, $z = 0$ m,
 (---): DNW, $U = 40$ m/s, $x = 6.5$ m,
 $y = z = 0$ m,
 (.....): DNW, $U = 100$ m/s, $x = 6.5$ m,
 $y = z = 0$ m.



6. INFLUENCE OF IMPERFECTIONS OF FLOW STRAIGHTENER AND SCREENS ON VORTICITY IN TEST SECTION

The turbulence levels \bar{u}/U , \bar{v}/U , and \bar{w}/U in the closed test section of the NWB as a function of position y are plotted in figure 9. The integration was performed between the Strouhal numbers 0.1 and 1000 which corresponds to frequencies $f = 1.5$ Hz and 15 kHz in the case $U = 50$ m/s and $D = 3.4$ m. All peaks in the frequency spectra were eliminated before the integration was carried out. The lowest turbulence levels of the tunnel are observed for $y = -0.2$ m. Narrow regions with higher turbulence levels are apparent close to the center line of the tunnel and at intervals of about $\Delta y = 0.54$ m. Their width is only about 0.1 m. These regions of increased turbulence can be related to the positions of the support structure of the honeycomb flow straightener in the settling chamber which has six elements in the y -direction. It is surprising that the three screens behind the flow straightener are not sufficient to eliminate the flow disturbance due to these structures. Also notable in figure 9 is a gradual rise of turbulence when the position approaches the wall.

Figure 9: Influence of lateral position y on turbulence levels \bar{u}/U , \bar{v}/U , and \bar{w}/U in the closed test section of the NWB, $x = 3.7$ m, $z = 0$ m, $U = 50$ m/s. Note the peaks at $y = -0.04$ m and -0.57 m which are traces of the wakes of the support structure of the honeycombs.

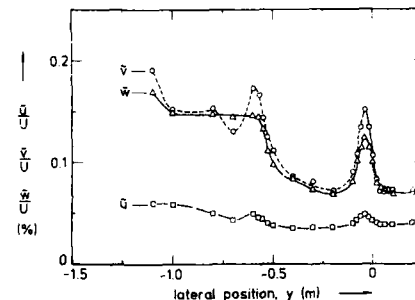


Figure 10 serves to demonstrate the causes of the change of turbulence level with position y . The v' -spectra in the NWB are compared for a tunnel speed $U = 50$ m/s for the positions $y = -0.04$ m, $y = -0.2$ m, and $y = -0.8$ m. It can be seen that the large rms-value at $y = -0.04$ m is caused by a broad-band contribution with a maximum at a Strouhal number around $St = 5$ or a frequency of about 70 Hz. The width of the wake responsible for this contribution can be estimated as follows. The Strouhal number $St_w = f W/U$ of the dominant frequency in the wake behind a two-dimensional blunt body with a width W is given by $St = 0.15$, approximately. If we consider that the flow speed in the settling chamber is $U = 9$ m/s we obtain a wake width of $W = 0.15 U/f = 0.02$ m which is a very reasonable value.

The spectrum at $y = -0.8$ m indicates a gradually increasing contribution for low Strouhal numbers. The spectral levels are almost identical with those in position $y = -0.2$ m for Strouhal numbers $St > 40$. The difference between the two spectra rises with decreasing Strouhal number. The largest difference is at the lowest Strouhal number of the plot, $St = 0.1$, where the factor between the plot, $St = 0.1$, where the factor between the two spectra is almost 4. The gradual change of the spectral level with Strouhal number indicates vorticity as origin of the fluctuations. A contribution from pressure fluctuations due to shear layers has a different spectral behavior as we shall see in the next section.

4D-A202 496

AERODYNAMIC DATA ACCURACY AND QUALITY: REQUIREMENTS AND
CAPABILITIES IN WIND TUNNEL TESTING (U) ADVISORY GROUP
FOR AEROSPACE RESEARCH AND DEVELOPMENT NEWLY

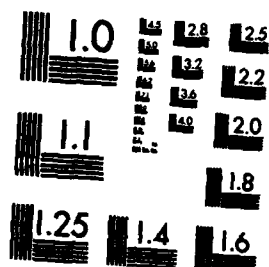
3/6

UNCLASSIFIED

JUL 88 AGARD-CP-429

F/G 1/1

NL



MICROCOPY RESOLUTION TEST CHART
NATIONAL BUREAU OF STANDARDS-1963-A

Figure 10: Normalized v' -velocity spectra in the closed test section of the NWB, $U = 50$ m/s, $x = 3.7$ m, $z = 0$ m.

- (—): in wake of honeycomb support structure, $y = -0.04$ m,
 (---): in position of lowest turbulence level, $y = -0.2$ m,
 (.....): closer to the wall, $y = -0.8$ m.

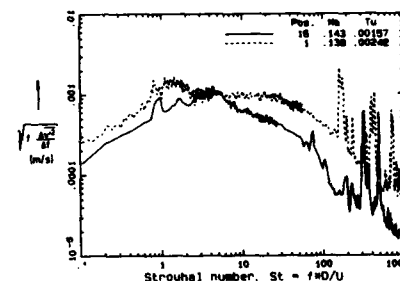
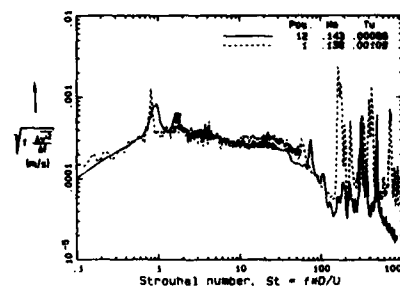
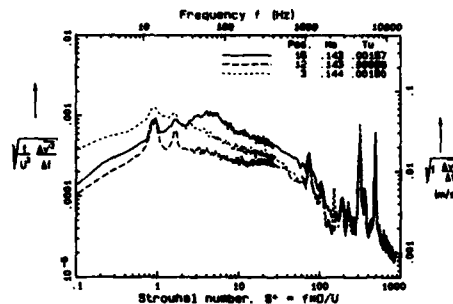
The last two screens in the settling chamber of the NWB were recently replaced and the influence of this change on the turbulence level was studied. The original screens were made from two pieces which were carefully soldered together. A seam in the vertical center line of the screen was visible but it was very surprising that its effect was measurable in the total pressure (communication by E. Otto, DFVLR Braunschweig) and in the turbulence level of the test section. The new screens have the same nominal dimensions but are woven in one piece. It can be seen from Figure 11 that the v' -spectra are almost unchanged in the area of minimum turbulence at $y = -0.2$ m or -0.27 m. The most prominent change is a considerable reduction of the influence from probe vibrations. Figure 12 is the corresponding plot for the tunnel center. The gain through elimination of the screen seams is clearly visible and has reduced the turbulence level from $\bar{v}/U = 0.24$ % to 0.16 %.

Figure 11: Normalized v' -velocity spectra in the closed test section of the NWB, before and after change of screen, $x = 3.7$ m, $z = 0$ m, y -position with low \bar{v}/U level.

- (—): new screen, $y = -0.2$ m, $U = 50$ m/s,
 (.....): old screen, $y = -0.27$ m, $U = 48$ m/s.

Figure 12: Normalized v' -velocity spectra in the closed test section of the NWB, before and after change of screen, $x = 3.7$ m, $z = 0$ m, in the wake of the honeycomb support structure and the seam of the old screen.

- (—): new screen without seam,
 $y = -0.04$ m, $U = 50$ m/s,
 (.....): old screen with seam,
 $y = -0.05$ m, $U = 48$ m/s.



7. SHEAR LAYER PRESSURE FIELD OF OPEN AND SLOTTED WALL TEST SECTIONS

The free shear layer between the flow and the test hall of an open test section contains large vortices which are convected downstream with a convection speed of about 0.6 times the tunnel speed. The vorticity distribution in the shear layer induces a non vortical fluctuating pressure field in the "potential core" of the free jet as well as outside the free jet. This fluctuating flow field propagates with approximately the speed of the large vortices. The influence on the turbulence level can best be studied with a tunnel with interchangeable test sections. The NWB and DNW are such tunnels.

Figure 13 is a comparison of two corresponding spectra from the open and the closed test sections of the NWB in the center of the test section. These spectra were measured with the old screen and, therefore, include the turbulence of the screen seam and the wake turbulence of the honeycomb support. The influence of the free shear layer is clearly visible for Strouhal numbers $St < 2$. Narrow peaks in the Strouhal number range $0.2 < St < 0.7$ indicate a feedback between acoustic resonance of the tunnel circuit and the generation of large vortices at the nozzle lip. The level of these peaks may change considerably with tunnel speed because the pumping power for the resonance depends on the phase between the arrival time of large vortices at the collector and the resonant wave. Vortex generators (Safford wings) are installed at the end of the nozzle of the NWB to inhibit the triggering of large vortices and to reduce coherence within the large vortices that hit the collector. Otherwise the peaks in the spectrum would have been even larger.

Figure 13: u' -spectra of open and closed test section in the NWB. Note shear layer induced hump for $St < 1$ and the almost identical spectral levels for $St > 2$ which are generated by vorticity.

A similar comparison for the DNW is presented in figure 14. The shear layer induced hump is much more prominent in this figure. The spacing between the narrow peaks is smaller than in figure 13 because the resonant frequencies of the tunnel are more closely spaced due to the relative large length of the circuit. The turbulence level of the open test section is 0.18 %. The integral over the spectrum of the closed test section yields 0.030 %. Also included is a corrected spectrum in which the peaks at high Strouhal numbers are removed. The integral over this spectrum yields a level of 0.026 %. The ratio of the turbulence levels of both test sections is 7. It is interesting to note that the vorticity level in the closed test section is higher than in the open test section in both figures 13 and 14. The reason for this is not known.

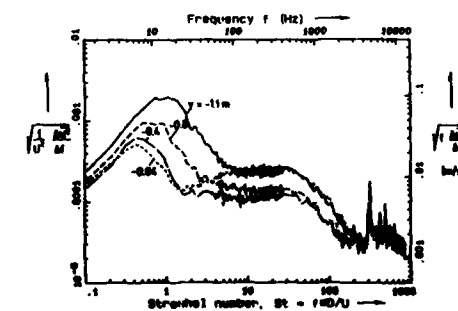
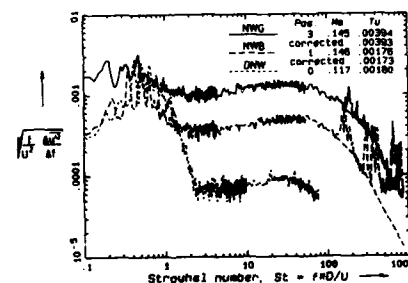
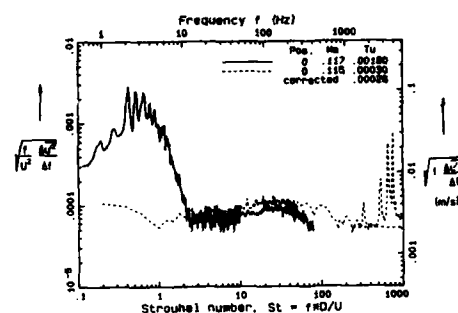
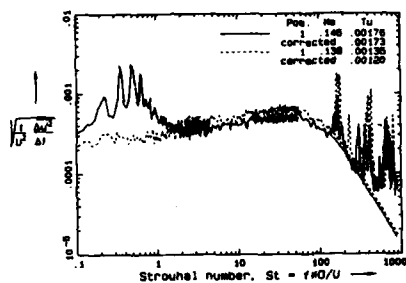
Figure 14: u' -spectra of open and closed test section in the DNW. Note that the shear layer induced hump for $St < 2$ is much more dominant than in figure 13 for the NWB because the vorticity induced spectral level for $St > 2$ is lower.

The open test sections of the three tunnels NWG, NWB (old screen), and DNW are compared in figure 15. The vorticity level is different in all three spectra. The typical contribution of the shear layer is almost identical. It is barely visible in the NWG because its vorticity level is so high. Characteristic for the steep fall-off of the pressure contribution for Strouhal numbers $St > 1$. The turbulence level \bar{u}/U of all three test sections is almost identical because it is dominated by the contribution of the pressure field at low Strouhal numbers. The peak frequency of this contribution is a function of normalised nozzle distance x/D . The peak level depends also on x/D as is shown in ref. 4.

Figure 15: u' -spectra of open test sections in NWG (—), NWB (---), and DNW (.....). Note that the shear layer induced humps are almost identical in all three tunnels.

Figure 16 demonstrates that a similar, though weaker, contribution at small Strouhal numbers can be observed in the slotted wall test section of the NWB. The slots were fully opened to 12 % of the total wall area. The hump at low Strouhal numbers is large for small distances from the wall and small for positions in the center. The decay is faster for higher Strouhal numbers as was predicted in ref. 2. The influence of the honeycomb strut wake can be seen in the vorticity region of the spectra for $y = -1.1$ m and $y = -0.04$ m. The turbulence levels \bar{u}/U are dominated by the spectral contributions at low Strouhal numbers and are almost independent of the vorticity level like in the case of the open test section.

Figure 16: u' -spectra for different y -positions in slotted wall test section of NWB. Note that slot shear layers also induce a hump for small Strouhal numbers similar to open test section (fig.13).

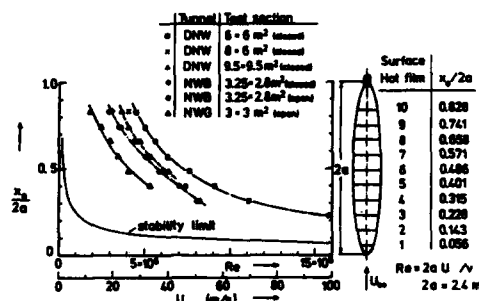


8. INFLUENCE OF VELOCITY UNSTEADINESS ON BOUNDARY LAYER TRANSITION

Experiments on the boundary layer transition on a prolate spheroid were carried out by Kreplin et al. [5,6] in six test sections of the three tunnels NWB, NWG, and DNW. The transition results were correlated by Meier et al. [7] with turbulence data. The principal results shall be reported here.

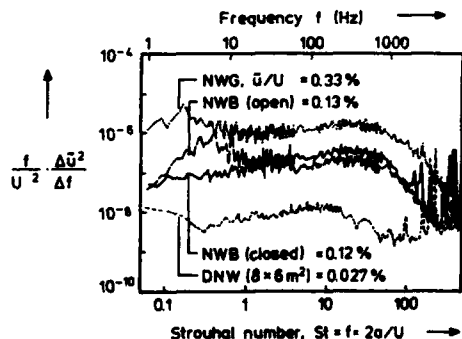
The spheroid with a length of $2a = 2.4$ m is shown on the right side of figure 17. Surface hot films were mounted in the ten indicated stations $x_0/(2a)$ to monitor the onset of laminar-turbulent boundary-layer transition. The position $x_0/(2a)$ of transition onset is plotted on the left side of figure 17 as a function of Reynolds number $Re = 2a U/\nu$. It can be seen that tunnel and test section are important parameters for the curves.

Figure 17: Position of transition onset $x_0/2a$ in boundary layer of prolate spheroid as a function of Reynolds number. Note that transition Reynolds number $Re = 2a U/\nu$ for a fixed station $x_0/2a$ (a horizontal line has to be followed in the plot) depends on tunnel and test section.



The u' -velocity spectra of the tunnels are plotted in figure 18 for a comparison with the transition data. The equivalent tunnel diameter D for the normalization of the frequency is now replaced by the length $2a$ of the spheroid. The spectral level in the NWB is rather high because the measurements were carried out in the center of the test section before the screen was replaced (see sec. 6). A comparison of the transition Reynolds number with the spectra reveals that it can be correlated with the spectral level $(\bar{u}^2/U^2)(\Delta \bar{u}^2/\Delta f)$ in the Strouhal number range $10 < St = 2a f/U < 100$. The lower this value the higher is the transition Reynolds number on a given station on the spheroid. It may be mentioned that such a correlation is not possible with the pressure spectra. The most convincing comparison is for the open and closed test section of the NWB. The turbulence level \bar{u}/U is higher in the open test section, yet the transition occurs at equal or slightly higher Reynolds numbers which corresponds with an equal or a slightly lower spectral level in the mentioned Strouhal number range.

Figure 18: Normalized u' -spectra in NWG, open and closed test section of NWB (old screen), and closed test section of DNW. The Strouhal number is normalized with the length $2a$ of the spheroid. The spectral level in the Strouhal number range $10 < St < 100$ correlates with the Reynolds number for transition onset.



No transition tests were carried out in the open test section of the DNW. However, it can be concluded from the corresponding frequency spectra that the transition Reynolds numbers will be almost identical in the open and the closed test sections despite a ratio of about seven between the turbulence levels.

9. INFLUENCE OF VELOCITY UNSTEADINESS ON THE MEASUREMENT OF STATIC FORCES AND MOMENTS

The measurement of static forces and moments is impaired by fluctuations at small frequencies because of their large scale. Velocity fluctuations may be considered to yield a quasi steady response of a model for frequencies $f < f_1$. The limiting frequency f_1 may be defined by a Strouhal number $St_1 = f_1 L/U < 2$, where L is a typical length of the model. This definition implies that frequencies that correspond to a wave length $\lambda = U/f < L/2$ can be neglected with respect to the static forces and moments. The corresponding tunnel Strouhal number is given by $St = St_1(D/L)$, where D/L is typically in the order of 3 for an aircraft if L is its wingspan.

With these values we conclude that the tunnel Strouhal number range $St < 6$ is important for the measurement of forces and moments. An inspection of the spectra in figures 4 through 8 and 10 through 12 indicates that about half the fluctuating energy in test sections that are dominated by vorticity is contained in this Strouhal number range. Almost all energy is contained below $St = 6$ in the open test sections of NWB and DNW. The situation gets even worse if a small model is tested in a large wind tunnel. Sometimes a model is tested in various tunnels with different test-section sizes to investigate the wall interference. One has to consider in these cases that the influence of velocity fluctuations on the measurements of static forces and moments will rise with tunnel size D due to its influence on the limiting tunnel Strouhal number.

The effect of lateral velocity fluctuations on the flow angle fluctuations shall be estimated now for a tunnel with a closed test section. A typical turbulence level for such a test section is $\bar{u}/U = 0.1$ % cor-

ponding to an energy level $(\bar{w}/U)^2 = 10^{-6}$. If we assume that one half of this energy comes from fluctuations below $St = 6$ we obtain a turbulence level of $\bar{w}/U = 0.0007$ for the quasi steady fluctuations. A crest factor of 3 would yield a maximum of $\bar{w}/U = 0.0056$ for the low frequency amplitude of w' . This corresponds to a maximum amplitude for the large scale angle of attack fluctuations of $\hat{\alpha} = (\bar{w}/U)(180 \text{ deg}/\pi) = 0.32 \text{ deg}$ or a total bandwidth for the angle of attack of $\Delta\alpha = 0.64 \text{ degrees}$. This is a considerable fluctuation which requires averaging of the readings, and limits the productivity of a tunnel. The situation is worse for open test sections or for test sections with slotted walls in which the velocity fluctuations at low frequencies are even larger.

10. CONCLUSIONS

The velocity unsteadiness in wind tunnels is created by contributions from vorticity that is convected into the test section and by pressure waves. Large differences of the velocity unsteadiness were observed in the three tunnels and six different test sections studied in this paper. The reason for these differences are differing contributions from vorticity and pressure fluctuations. The vorticity contribution to the turbulence level \bar{u}/U of the longitudinal velocity fluctuations varies between about 0.03 % for the DNW, 0.04 % for the NWB, and 0.4 % for the NWG. The difference between DNW and NWB can be explained with different nose contraction ratios. The probable origin of the large vorticity level of the NWG are large flow separations in the "diffuser turns" of the circuit (see fig.1).

A surprising finding is that the wake behind the support structure of the honeycomb flow straightener of the NWB contributes considerably to the vorticity fluctuations in the test section despite the presence of three screens. A similar influence was detected in the test section of the NWB from the wake of the screen seam. Therefore, screens woven in one piece should be used for low turbulence tunnels and the flow straightener should not generate wakes.

The pressure contribution to the velocity unsteadiness is small in the two closed test sections of NWB and DNW, but it is large in all three open test sections and in the slotted wall test section of NWB. The contribution from the free shear layers of an open test section in a position $x/D = 0.8$, $y/D = z/D = 0$ is in the order of $\bar{u}/U = 0.16$ %. This level depends on the position and on a feedback between shear layer vortices and tunnel resonances which is typical for open test sections.

Contributions from vorticity and pressure fluctuations are distributed differently in the frequency domain. Vorticity is distributed over a large frequency range whereas pressure waves dominate the low frequency range if they are noticeable. It is demonstrated that the boundary layer transition depends on the velocity fluctuations at high frequencies which are dominated by vorticity. A low vorticity level is necessary if tests shall be carried out that depend on laminar turbulent transition.

Fluctuations at small frequencies influence the force measurements in a tunnel because they have a very large scale. A tunnel with closed test section generates quasi steady angle of attack fluctuations with peaks of ± 0.2 degrees, typically. This fluctuation restricts the precision of force measurements unless a certain integration time is applied.

11. REFERENCES

1. Kovácsnay, L.S.G.: Turbulence in supersonic flow. *J. Aeronaut.Sci.* 20, 657-674 and 682 (1963).
2. Michel, U. and Froebel, E.: Definition, sources, and lowest possible levels of wind-tunnel turbulence. In: *Wind tunnels and testing techniques*, AGARD Conf.Proc.No. 348, 1984.
3. Hartsuiker, J.P.; Pugh, P.G.; Lorenz-Meyer, W.; Passo, G.E.: On the flow quality necessary for the large European high-Reynolds-number transonic windtunnel LEET. AGARD-R-644, 1976.
4. Michel, U. and Froebel, E.: Lower limit for the velocity fluctuation level in wind tunnels. To appear in *Experiments in Fluids* 5, (1987).
5. Kreplin, E.-P., Meier, H.U., and Baumgarten, D.: Wall shear stress measurements on a prolate spheroid at zero incidence in the DFVLR Low Speed Wind Tunnels NWG and NWB. DFVLR, IB 223-87 A01, 1986.
6. Kreplin, E.-P., Meier, H.U., Marcker, E., and Landhäuser, A.: Wall shear stress measurements on a prolate spheroid at zero incidence in the DNW Wind Tunnel. DFVLR-Mitt. 85-06, 1986.
7. Meier, H.U., Michel, U., and Kreplin, E.-P.: The influence of wind tunnel turbulence on the boundary layer transition. In: *Perspectives in Turbulence Studies*, Editors: H.U.Meier and P.Bradshaw, 26-46, Springer-Verlag Berlin Heidelberg New York London Paris Tokio, 1986.

IMPACT OF NOZZLE DESIGN CONSTRAINTS ON TEST SECTION FLOW QUALITY

by
D. Van Every, S. Raimondo and G.M. Elfstrom
DSMA International Inc.
Toronto, Canada
L4V 1V8

SUMMARY

A procedure is described which allows the design of relatively short adjustable nozzles without resorting to the assumption of radial flow upstream of the nozzle inflection point. This design procedure is used to generate a number of fully flexible nozzle designs for a design Mach number of 1.4. Flexible nozzle parameters such as pressure loading, number of actuators and nozzle length are varied in order that the influence of these parameters on test section flow quality may be evaluated. The influence of nozzle actuator setting accuracy is also estimated. The parametric study shows that high flow quality can be achieved for the shortest nozzle considered. The examination of jack setting errors shows that for well designed nozzles, jack setting error will be a significant source of test section flow non-uniformities.

LIST OF SYMBOLS

C - matrix coefficients which relate plate wall angles
 dS_i - the arc length between i and $i+1$ attachment points
 E - Young's modulus
 H - nozzle exit half height
 I - second moment of area per unit width
 K - matrix of attachment point curvatures
 K_i - plate curvature at attachment point i
 L - length of nozzle from throat to nozzle exit
 M - Mach number
 NAP - number of attachment points
 NWP - number of wall points at which the aerodynamic contour is specified
 P_0 - test section total pressure
 P_i - the differential pressure at attachment point i
 AP - matrix of pressure coefficients calculated from equation (5)
 R - radius of curvature
 R_t - radius of curvature at the nozzle throat
 S - arc length coordinate measured from the nozzle exit
 S_i - the arc length at the inflection point
 t - plate thickness
 V - y component of velocity
 y_t - throat half height
 θ - local wall angle
 θ_t - the wall angle at the nozzle exit
 θ_i - the wall angle at the inflection point
 σ_M - the standard deviation of the Mach number distribution on centre line for the test rhombus

1. INTRODUCTION

The nozzle section for a supersonic wind tunnel is a critical component which has a direct effect on the test section flow quality. Inadequate design of this component can lead to unacceptable Mach number and flow angle non-uniformities. Even with the best design procedures, the nozzle will generate some nonuniformities in the test section due to the physical compromises required in design and construction. The goal of any design procedure is to minimize the effect of the compromises required by the physical constraints.

Any nozzle design procedure can logically be divided into two tasks. The first task is to determine the ideal aerodynamic contour for the nozzle. This contour, if constructed, would yield a nozzle which gives perfect flow uniformity. The second task is matching the aerodynamic contour to a contour which can be realistically built to this aerodynamic contour. The nature of the matching process depends on the type of nozzle to be built (e.g. fully-flexible, semi-flexible, solid block).

The most commonly used approach to the problem of determining the ideal aerodynamic contour for a two-dimensional nozzle has been to assume that the flow from the throat of the nozzle to the inflection point can be approximated by a radial source flow (e.g. References 1,2,3 and 4). The remainder of the contour is then usually determined by employing some form of the method of characteristics. These design methods usually impose the constraint that the slope, curvature, and rate of change of curvature be continuous functions for the complete length of the contour. Regardless of the type of nozzle finally chosen to approximate the aerodynamic contour, these constraints will permit the best matching between the actual physical nozzle shape and the ideal contour. For example, a continuous flexible plate nozzle cannot accommodate discontinuities in curvature, and discontinuities in curvature slope are only possible at positions where actuators are attached to the plate. Therefore, in order to achieve the highest quality nozzle over a range of Mach numbers, when actuator locations are not known a priori,

it is best to have continuous slope, curvature, and rate of change of curvature. These requirements lead to the concept of a partial cancellation region for two-dimensional nozzles. In this region Mach "waves" are reflected at part strength from the wall. The rate at which the flow is turned at the wall is more gradual than is necessary in order to cancel the wave, thus permitting a smooth curvature distribution. These concepts for the solution of the nozzle flow field are illustrated in Figure 1a.

There are many possible approaches to the second task in the design process - the matching of the physical nozzle to the aerodynamic contour. Test section flow non-uniformities will arise from slope mismatches between the final shape achieved and the ideal aerodynamic contour. Successful matching procedures will in some way minimize the slope errors. Desai and Jain have developed a least-squares matching procedure which minimizes the slope error at attachment points only. (Reference 5). An elaborate numerical optimization procedure has also been developed by Varner. This procedure requires the calculation of the nozzle exit flow uniformity for many iterations in order to optimize nozzle parameters such as actuator number and position (see Reference 6).

The approach to aerodynamic contour design described above yields relatively long nozzles. This long length arises because a region of full partial cancellation is included and also because moderate throat curvatures are used. Throat curvatures must not be too severe in order that the radial flow assumption is not violated.

In this paper a method is presented which permits the design of shorter high quality nozzles than would be possible using the traditional design approach. The development of this method was stimulated by the requirement to retrofit an existing transonic facility, which has a semi-flexible nozzle, with a fully-flexible nozzle. Both present and near-future test requirements will place heavy emphasis on the transonic speed regime and therefore this paper will focus on nozzle design for the upper transonic (or lower supersonic) Mach numbers. The physical constraints that are important in the design of a nozzle will be discussed and the effect of these constraints on test section flow quality will be explored.

2. NOZZLE DESIGN CONSTRAINTS

The method presented here for the calculation of the aerodynamic contour can be matched to any type of construction for the physical nozzle (e.g. solid nozzle blocks, semi-flexible nozzle, fully-flexible nozzle). However only a fully-flexible configuration will be explored. The physical parameters which will affect nozzle shape and the closeness of the match to the aerodynamic contour are:

- The length available for the nozzle
- The number of actuators
- The number of attachment points
- The plate stiffness

The plate used to form the contoured walls of the nozzle will take up the shape of an elastic beam between attachment points. This shape can never match a given aerodynamic shape perfectly and this mismatch will cause Mach number and flow angle non-uniformities at the nozzle exit. The shape of this plate is set by the actuators and the end conditions. Two downstream end conditions are normally employed: a built-in end or one that is hinged. The hinge angle would be set by an actuator designated for that purpose. The upstream end condition is usually a hinged slider. A typical fully flexible nozzle design is shown in Figure 2. Note, that to minimize interaction with the throat region, the hinged slider should be placed well upstream, into a region of effectively incompressible flow, without local flow separation.

The actuators may be attached to the plate through a single pin attachment or through a two point attachment known as a whiffle-tree. Only single pin attachments will be considered here and thus the number of attachment points and the number of actuators will be equal.

As the length of the plate is increased and the number of actuators is increased for a given Mach number and test section size, the match to the aerodynamic contour will improve and therefore test section flow quality will improve. However, the cost of the nozzle will also increase, so the final object of any nozzle design exercise will always be to produce a nozzle with the minimum costs that meet the flow quality requirement. This then translates to a nozzle with minimum length and the minimum number of actuators and attachment points.

There are also practical aspects of nozzle construction which must be considered when specifying flow quality and designing the nozzle. There will be a finite achievable actuator setting accuracy and in some instances this may be the limiting constraint which finally determines the flow uniformity achievable. Other factors which may be very difficult to control include temperature effects on the structure and deformation of the plate in the cross-stream direction.

3. NOZZLE DESIGN METHOD

3.1 Aerodynamic Contour

As described above, many methods that have been used in the past to calculate an aerodynamic contour depend upon the assumption of radial flow from the throat to the inflection point. This assumption will most probably be valid if the contour is gradual and the throat curvature is small. If the nozzle is to be made short, thus requiring higher throat curvatures, the radial flow assumption may not provide an adequately accurate starting point for the solution of the supersonic flowfield downstream of the nozzle inflection point. Because of this concern, it was decided to use the simple small perturbation solution of the transonic flow in the throat region developed by Sauer (Reference 7). Although it has been shown that this solution is unrealistic for a small throat radius of curvature ($R_e/Y_c < 2.0$, Reference 8), this solution should be adequately accurate for the curvatures which are

practical for a flexible plate nozzle. Curvature will typically be limited by plate stresses: In the present study the smallest throat radius of curvature is about 3.34 throat half heights.

This solution to the transonic flow problem is used to determine the flow field in the throat region. The shape of the nozzle wall between the throat and inflection point is specified as a design input. Any smooth shape could be used as long as variation of the wall angle at the inflection point is possible. Only fully-flexible nozzles are considered here and thus a wall shape which can be perfectly matched by a flexible plate was chosen for this portion of the wall. The appropriate shape is that of a cubic spline curve. A single spline is used between throat and inflection point. For this initial curve the throat radius of curvature, the arc length between the throat and the inflection point and the wall angle at the inflection point are very simply related. This relationship is

$$S_1 = 2R_c \theta_1 \quad (1)$$

To determine the aerodynamic contour, either the arc length or the throat curvature will be fixed. The other two parameters are varied until the required nozzle Mach number is achieved. For the design point contours the throat radius of curvature would normally be fixed at the minimum possible, determined by flexible plate stresses. This will give the shortest S_1 for that contour. For the off design Mach numbers the arc length (S_1) would be selected to coincide with actuator spacings in such a way that off-design Mach number flow quality is optimized.

The method of characteristics algorithm given by Zuckrow (Reference 8) is used to solve the nozzle flow field from nozzle throat to inflection point. The shortest nozzle will be that for which there is no partial cancellation region. This will result in a discontinuity in curvature which in turn will produce nozzle exit non-uniformities when the flexible plate is matched to the aerodynamic contour. These non-uniformities may be within the specified flow quality and this could be a valid design approach. For the case with no partial cancellation, the nozzle exit Mach number will be achieved on the nozzle centre line at the end of the initial expansion region. (Point b in Figure 1b). The spline curve arc length and inflection point angle - these two parameters are not independent - are iterated on until the design Mach number is achieved. At each iteration the throat flow field and supersonic flow field is recalculated.

For the case where a region of partial cancellation is desired, the Mach number at point b will be less than the nozzle exit Mach number, and the centre line Mach number will continue to increase until point d is reached. In this case it is the Mach number at point d which is iterated on in order to determine the wall angle at the inflection point. The method of characteristics solution is carried forward to characteristic cd every iteration. The wall contour between points a and c is determined from a specified rate of change of wall curvature. The rate of change of curvature for the spline (throat to point a) is a constant and the rate of change of curvature for the partial cancellation region is specified as some fraction of the curvature slope for the spline. The wall contour in this region is then calculated at each point where a characteristic intercepts the wall by integrating the specified curvature distribution.

The wall contour in the full cancellation region is then determined by carrying the method of characteristics forward to the end of the nozzle and applying the equation of continuity to find the wall coordinates.

This approach to the design of the aerodynamic contour will give a discontinuity in curvature slope at the end of the partial cancellation region. The method also provides a high degree of flexibility in specifying the throat to inflection point contour. For a fully flexible nozzle the highest flow quality will be achieved if an actuator is attached to the plate at the point where the curvature slope discontinuity occurs. Because of the flexibility in the design procedure it is possible to achieve this for a family of contours that would be set using the same flexible nozzle.

This design method has been developed with the design of fully flexible nozzles in mind, however, the same method could readily be used for the design of other types of nozzles. The use of Sauer's solution for the transonic flow limits the throat radius for curvature to $R_c/Y_c > 2.0$. However, if smaller radii of curvature are desired a higher order throat solution could readily be incorporated into the design method (e.g. References 9 and 10).

3.2 Boundary Layer Growth

Once the inviscid aerodynamic contour has been determined, it is necessary to determine the nozzle boundary layer growth and correct the nozzle shape for the effects of boundary layer growth. The most common practice is to add 1 or 2 displacement thicknesses (δ^*) to the y coordinate. The addition of $2\delta^*$ compensates for the boundary layer growth on the side walls of the nozzle and the contoured walls. Correcting for the displacement effects of the boundary layer ensures that the design Mach number is achieved but does not necessarily ensure that the flow quality objectives are not compromised by the effects of boundary layer growth.

Very few attempts have been made to develop a boundary layer correction procedure which ensures that no additional flow disturbances are introduced by the correction procedure. Using the displacement thickness does not account for the manner in which the inviscid main flow interacts with the shear layer. Tucker (Reference 11) derived a theoretical reflection thickness (with many simplifying assumptions) but was unable to determine if this was superior to using δ^* to correct the contour. This particular aspect of nozzle design requires further investigation.

The effect of the boundary layer correction procedure used is, however, likely very small, as the correction should not change the aerodynamic contour curvature distribution significantly. It was decided here to correct the contours using $2\delta^*$.

3.3 Matching the Aerodynamic Contour to the Flexible Plate

Although the flexible plate for a fully flexible nozzle will extend upstream past the nozzle throat to form part of the contraction that feeds the supersonic nozzle, it is only the supersonic portion of the contour that will have a significant effect on nozzle exit flow quality. For throat radii of curvature appropriate for fully flexible nozzles, the shape of the sonic line will depend primarily on the throat radius of curvature. All that is required of the subsonic portion is that it fairs into the fixed contraction and that the subsonic contour match the supersonic contour at the throat. The subsonic contour should of course accelerate the flow smoothly and not cause any flow separations. Provided these criteria are achieved, changes in the subsonic contour will not affect the supersonic flow field.

Therefore, in order to ensure good flow quality, it is preferable to use a matching procedure which only considers that part of the flexible nozzle between the throat and the nozzle exit. The least-squares matching procedure described in Reference 5 has been extended to provide a more optimized match. This procedure is an analytical procedure which minimizes, in the least squares sense, the slope mismatch errors at all of the contour points determined during aerodynamic contour design.

The flexible plate is approximated as a simple beam with the actuators attached through pin connections. It is assumed that the actuators act normal to the plate everywhere and that moments are only transmitted to the plate at the nozzle exit (i.e. a built-in end condition). Only the region from just upstream of the throat to the nozzle exit is input into the matching process. After matching is completed, the subsonic actuators will be set so that a smooth contour results and the throat curvatures and displacement determined during the match is maintained. The curvature distribution for the plate will be piece-wise linear as a function of the arc length provided the change in plate angle is small between attachment points and the pressure loads are negligible. The plate angle at any point may be expressed as a function of the curvatures at the attachment point by integrating the as yet unknown piece-wise linear curvature distribution.

$$\Theta(S) = \frac{K_{i+1}}{2} \frac{(S - S_i)}{ds_i} + \frac{K_i}{2} (ds_i + ds_{i-1} - (S_{i+1} - S)^2/ds_i) + \sum_{n=2}^{n=i-1} K_n \frac{(ds_n - ds_{n-1})}{2} + \frac{K_1 ds_1}{2} + \Theta_E \quad (2)$$

Some of the nomenclature used in the above equation is illustrated in Figure 3. Equation (2) may be written for each of the discrete arc lengths determined for the aerodynamic contour. The right hand side of equation (2) may then be set equal to the required wall angles from the aerodynamic contour. The attachment point locations (S_i) have been specified, only the attachment point curvatures are unknowns in equation (2). In practice there will be many more calculated points on the aerodynamic contour than there are attachment points and therefore an overdetermined set of equations will have been formed.

Equation (2) may be written conveniently in matrix form,

$$[C]_{NMP \times NMP} \times [K]_{NMP \times 1} = [R]_{NMP \times 1} \quad (3)$$

$$\text{Where } [R] = [\Theta] - \Theta_E$$

This overdetermined set of equations may be solved in the least squares sense to minimize the difference between the aerodynamic wall angles and the plate angles. The result is,

$$[K] = [C]^T [C]^{-1} [C]^T [R] \quad (4)$$

Once the attachment point curvatures have been calculated it is a straightforward task to integrate the plate curvature distribution to determine flexible plate coordinates.

The effect of pressure loads on the plate shape may also be included in the least squares optimization of plate shape. This is easily done if the pressure distribution is approximated as linear between attachment points. Applying the conditions of static equilibrium to a section of the plate gives the following expression for plate wall angle between the i and $i+1$ attachment points.

$$\Theta(S) = K_1(S - S_i) + \frac{(K_{i+1} - K_i)(S - S_i)^2}{2ds_i} + A_1(S - S_i)^2 + B_1(S - S_i)^3 + C_1(S - S_i)^4 + \Theta_i \quad (5)$$

$$\text{where: } A_1 = \frac{(2P_i + P_{i+1}) ds_i}{12EI}$$

$$B_1 = -\frac{P_i}{6EI}$$

$$C_1 = -\frac{(P_{i+1} - P_i)}{24Eids_i}$$

In these equations P_i is the pressure at the attachment point locations determined from the aerodynamic contour calculation. Combining equations (5) and (2), rearranging, and writing in matrix form gives,

$$[C] \times [K] = [R] - [\Delta P] \quad (6)$$

In this equation the ΔP matrix is known for the aerodynamic contour wall points and the coefficients of this matrix may be determined from equation (5). Equation (6) is identical to equation (3) except that the right hand side has been modified by the effect of the pressure distribution. This overdetermined set of equations may be solved in the least squares sense as described above.

4. EFFECT OF NOZZLE PARAMETER VARIATION ON FLOW QUALITY

The quality of a nozzle can be assessed by solving the flowfield for the final nozzle shape. The method used here to solve the nozzle flowfield is similar to the analysis used in design. Sauer's small perturbation solution is applied to start the method of characteristics solution for the supersonic flow. Viscous effects could be included in the analysis by calculating the boundary layer for the applied pressure field and inviscid flow. The contour would be adjusted by the displacement thickness and the inviscid flow determined for the new shape. The core solution and boundary layer solution would be repeated until the solutions converge. However, this is only a second order effect comparable with other influences heretofore ignored (e.g. sidewall flow interactions). Thus, all such viscous-inviscid flow interactions are not considered in the present analysis.

A design study was conducted using the design and analysis procedure described above in order to evaluate the effects that varying such design parameters as nozzle length, number of actuators and pressure loads might have on test section flow quality. A Mach number of 1.4 was selected for the design point for the nozzle. Aerodynamic contours were developed for the throat radii of curvature given in Table 1. This table also shows the nozzle lengths that resulted from these choices of throat curvature. The partial cancellation region was determined as described in Section 3.0. For all of these contours the rate of change of curvature was kept constant from the nozzle throat to the end of the partial cancellation region. It would be possible to produce shorter nozzles by reducing or eliminating the region of partial cancellation. However, particularly for the high throat curvature nozzles, the reduction in length will be small and the match between aerodynamic contour and the flexible plate will be worse.

TABLE 1: Aerodynamic Contour Lengths

R_t/H	L/H
3.0	2.31
4.0	2.56
5.0	2.97
10.0	3.5
15.0	4.14
20.0	4.53
25.0	5.12

The curvature distributions for these contours are plotted in Figure 4 and the contours are plotted in Figure 5. The extent of the partial cancellation region is indicated on the curvature plots by the extent of linear curvature downstream of the inflection point. Note that for the short nozzle the partial cancellation region is very short, yet there are no discontinuities in curvature. These design contours were used to generate a number of different flexible nozzle designs for which actuator placement and number were varied.

4.1 Effect of Nozzle Length

The effect of nozzle length on flow quality was examined by matching the aerodynamic contour to the flexible plate using three actuators. These three actuators were placed at what was thought to be optimum positions for each contour. These positions were at the nozzle throat, the end of the partial cancellation region and midway between the end of the partial cancellation region and the end of the nozzle. In order to isolate effects, pressure loads were not included in the matching or in the analysis. Flow quality was estimated by calculating the standard deviation of the Mach number distribution over the centre line of the test rhombus (see Figure 1b) using the predicted Mach number distribution for the achieved plate shape.

The results of this analysis are shown in Figure 6. As would be expected the Mach number deviations decrease with increasing nozzle length. The plot also shows that the achievable Mach number deviations approach asymptotically a value of about a $\sigma_p = 0.0002$. There is little to be gained by increasing nozzle lengths to more than 4.0 test section half heights.

4.2 Effect of Number of Actuators

Nozzle lengths of $L/H=2.56$ and $L/H=4.14$ were selected for the purpose of examining the effect of actuator number. The placement of actuators was determined by examining the curvature distributions for the aerodynamic contour and choosing locations which would allow the piecewise linear curvature distribution of the plate to best approximate the curvature distribution for the aerodynamic contour. The placement of actuators used for the $L/H=2.56$ contour is summarized in Figure 7.

The standard deviation of the test section Mach number distribution for these two contours are plotted in Figure 8. This figure shows that even for the shortest nozzles high flow quality can be achieved given sufficient control of flexible plate shape.

It is also apparent that given a longer contour there is little benefit to increasing the number of actuators. This is only true of course if there is no pressure load effect. Pressure loads may require additional attachments in order to adequately support the plate.

4.3 Effect of Pressure Loads

The effect of pressure loads for a given nozzle with a given actuator distribution may be combined with plate stiffness into a single parameter. The matching process was used for a number of plate stiffnesses and the pressure distribution generated during aerodynamic contour design. This would give the optimum actuator extension for each condition. The results of the analysis are presented in Figure 9.

It was found that an additional actuator should be placed between the nozzle throat and the end of the partial cancellation region. Although these actuators were not required for the cases with no pressure loads, it was found that the long unsupported span in this region gave unreasonable deflections when pressures were applied.

The different slopes for the long and short nozzles seen in Figure 9 are largely a function of actuator spacing. The more closely actuators are positioned, the less will be the effect of changing plate stiffness or pressure loads.

4.4 Optimum Nozzle

The selection of an optimum configuration requires the consideration of flow quality achieved and nozzle cost. For longer nozzles actuator spacing will be determined by the effect of pressure loads. The number of actuators required to reduce pressure effects to tolerable levels could be far in excess of that required to achieve a good match without air loads. The analytical study presented above shows that the shortest nozzle with about six actuators should give the best compromise. Provided pressure loads are not too high (e.g. $h=0.8$ m, $t=0.015$ m, $P_0=3$ bars) a σ_M of about 0.001, from matching error, should be achievable.

The curvature distribution for the flexible plate and aerodynamic contours are compared for no pressure loads in Figure 10 and matching errors are shown in Figure 11. The Mach number distribution on test section centre line for this case is shown in Figure 12. The curvature comparison is repeated for pressure loads corresponding to $P_0=6$ bars, $h=0.8$ m, and $t=0.015$ m in Figure 13. A high pressure loading has been used in this case to show more clearly the effect pressure loading has on the plate curvature distribution.

The analysis used in this paper is an ideal inviscid, two dimensional analysis. There are many factors not considered in the analysis which will affect the flow uniformity that can be achieved with a given nozzle design. These factors will include:

- Actuator positioning accuracy
- Temperature differences causing elastic deformation of the structure
- Three dimensional flow effects
- Distortion of the plate in the cross-stream direction (anticlastic deflection)

Some of these effects are very difficult or impossible to model mathematically. For a properly designed facility, three dimensional flow effects on flow quality should be negligible compared with the other factors. Except for testing at cryogenic temperatures, the temperature effects should also be small. The effect of anticlastic deflection of the plate is very difficult to estimate and no attempt is made to do so here. This distortion can be minimized through proper mechanical design but it could still have a significant impact on test section flow quality. Actuator positioning accuracy is amenable to analysis and will be considered in the next section.

The test of a model in the upper transonic speed range will in general be carried out using a ventilated-wall transonic test section which is in tandem with a supersonic nozzle. These walls will cause flow perturbations which are usually greater than those resulting from a well-designed nozzle. Thus care should be taken when specifying flow uniformity requirements for a supersonic nozzle in the upper transonic speed range -- in many cases the requirements can be relaxed, without adversely affecting the flowfield in the vicinity of the model so that the cost of the nozzle is not needlessly driven up.

5. ACTUATOR POSITIONING ACCURACY

The ability to position adjustable nozzle actuators with a high degree of accuracy is as important in determining final nozzle exit flow quality as any other aspect of design or construction. An estimate of positioning requirements may be obtained from small perturbation theory. Small changes in test section Mach number can be related to small changes in wall angle by the following equation:

$$\Delta M = \frac{M(1 + \frac{\gamma-1}{2} M^2)}{\sqrt{M^2 - 1}} \Delta \theta \quad (7)$$

The top and bottom wall actuators for a flexible plate design will normally be linked together mechanically. Therefore the top and bottom wall actuators should produce the same setting error.

For this case

$$\Delta\theta = \frac{2M(1 + \frac{\gamma-1}{2} M^2)}{\sqrt{M^2 - 1}} \Delta\theta \quad (8)$$

The order of magnitude of change in wall angle at a given point resulting from miss-setting an actuator can be estimated from the rotation of the chord line between two attachment points. This together with equation (8) was used to generate Figure 14. In this figure ΔS_1 is the spacing between actuators and ΔY_1 is the error in actuator setting. The implied tolerance on actuator setting accuracy from this figure is quite severe. For example for maximum deviations in test section Mach number of 0.001, $M=1.4$, $\Delta S_1=400$ mm, an actuator setting accuracy of 0.1 mm is required.

Setting accuracies greater than 0.1 mm are very difficult to achieve even for the most massive and complex design of actuator. An actuator spacing of 400 mm or less would be typical for a flexible nozzle test section of 1.5 metres in height. Therefore a minimum test section flow perturbation of the order $M=0.001$ can be expected, from actuator setting errors alone, for this size of facility. As a given nozzle design is scaled, the requirements for setting accuracy will scale as well and thus for very large facilities actuator setting accuracy may not be a critical consideration.

As actuator spacing is decreased the effect of miss-setting actuators on nozzle exit flow non-uniformities increases. However decreased actuator spacing gives improved theoretical control of plate shape and thus improved predicted flow quality. There will be some optimum spacing which maximizes flow quality when all of the influences on flow quality are considered.

6. CONCLUSIONS

The techniques presented in this paper permit the design of relatively short adjustable nozzles that give high flow quality. Through proper design it is possible to reduce test section flow non-uniformities arising from design constraints to very low levels. For moderate pressure loadings, values of ϵ_M of less than 0.001 should be achievable from the (theoretical) matching standpoint.

There are many potential sources of test section flow non-uniformities other than those inherent in the design. These sources can generate flow disturbances which are larger than the flow non-uniformities that arise from the mismatching which always occurs between the aerodynamic design contour and the design flexible plate contour. A dominant source of flow non-uniformity is the miss-setting of nozzle jacks. An estimate of the effects of setting errors has been made and these are unlikely to be smaller than $\Delta M=0.001$.

REFERENCES

1. J.C. Sivealls, "Analytic Determination of Two Dimensional Supersonic Nozzle Contours Having Continuous Curvature", AEDC-TR-SC-11, July 1956.
2. J.T. Kenny and L.M. Webb, "A Summary of the Techniques of Variable Mach Number Supersonic Wind Tunnel Nozzle Design", AGARDograph 3, October 1954.
3. H.N. Riise, "Flexible Plate Nozzle Design for Two-Dimensional Supersonic Wind Tunnels", JPL Report No. 20-74, June 9, 1954.
4. M.O. Varner, W.E. Summers, and M.W. Davis, "A Review of Two-Dimensional Nozzle Design Techniques" AIAA-82-0609, AIAA 12th Aerodynamic Testing Conference, Williamsburg, Virginia, March 22-24, 1982.
5. S.S. Desai and R.K. Jain "A Method of Curvature Matching for Two-Dimensional Flexible Plate Wind-Tunnel Nozzles", AIAA Journal, Vol. 8, No. 11, pgs. 2105-2106, November 1970.
6. M.O. Varner, "Application of Optimization Principles to Flexible Wall Nozzle Design - A Case Study", AIAA 86-0775, AIAA 14th Aerodynamic Testing Conference, West Palm Beach, Florida, March 5-7.
7. R. Sauer, "General Characteristics of the Flow Through Nozzles at Near Critical Speeds", NACA Tech. Memo 1147, June 1947.
8. M.J. Zucrow and J.D. Hoffman, "Volume II Gas Dynamics", Wiley, 1977.
9. I.M. Hall, "Transonic Flow in Two-Dimensional and Axially-Symmetric Nozzles", Quart. Journal, Mech. and Applied Math., Vol. XV, Pt. 4, 1962.
10. J.R. Kliegel and J.N. Levine, "Transonic Flow in Two Dimensional and Axially-Symmetric Nozzles", AIAA Journal, Vol. 7, No. 7, July 1969, pp. 1375-1378.
11. M. Tucker, "Approximate Turbulent Boundary-Layer Development in Plane Compressible Flow Along Thermally Insulated Surfaces with Application to Supersonic-Tunnel Contour Correction", NACA Technical Note 2045, March 1950.

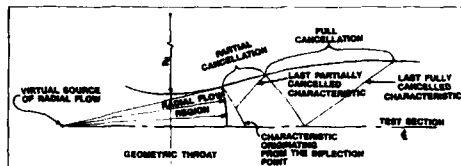


Figure 1a: Nozzle flowfield schematic - with radial flow.

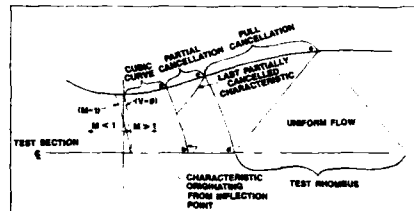


Figure 1b: Nozzle flowfield schematic - with throat solution.

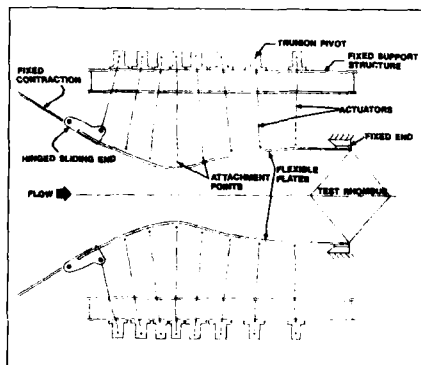


Figure 2: Flexible nozzle construction.

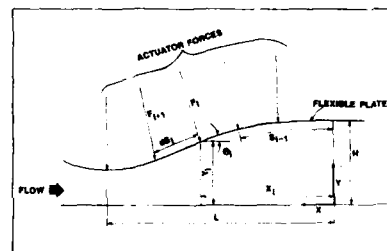


Figure 3: Flexible plate matching nomenclature.

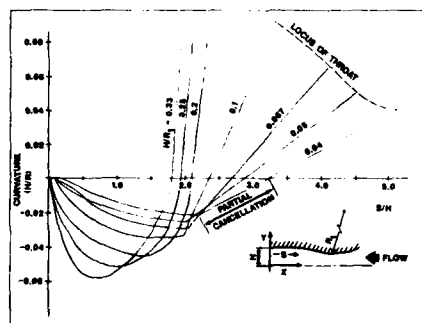


Figure 4: Aerodynamic contour curvature distributions, M=1.4

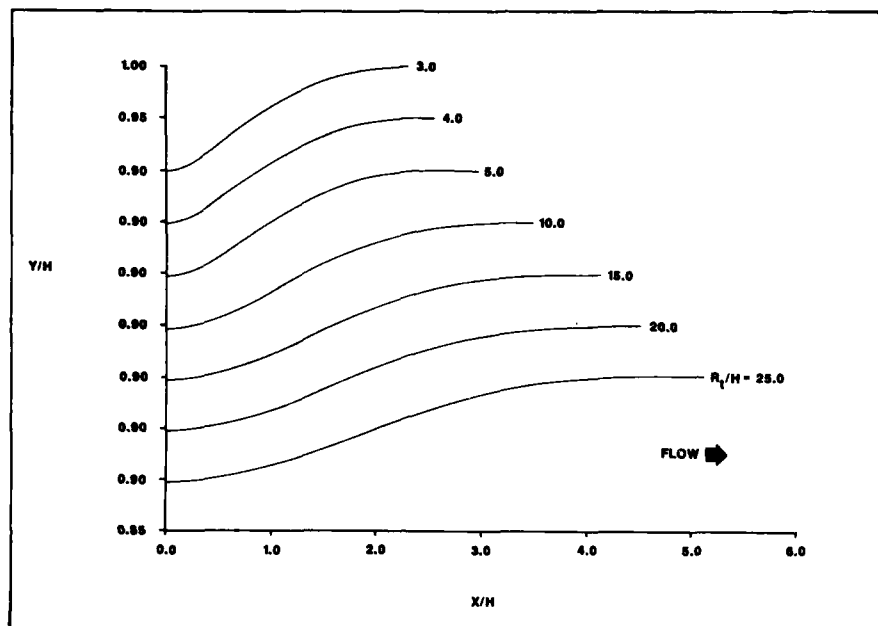
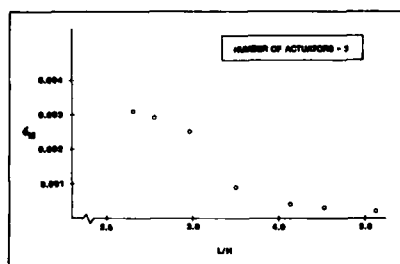
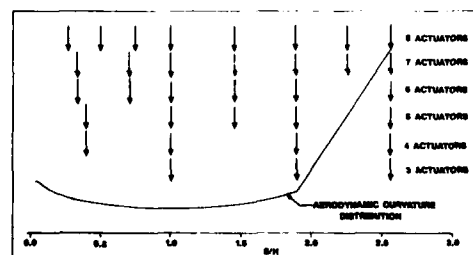
Figure 5: Aerodynamic contours, $M = 14$.

Figure 6: Effect of nozzle length variation on test section flow uniformity.

Figure 7: Schematic of actuator placement for the actuator study, $\frac{L}{H} = 2.56$.

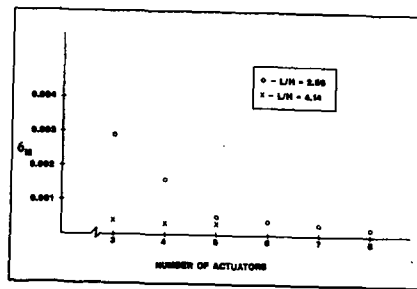


Figure 8: Effect of number of actuators on test section flow uniformity.

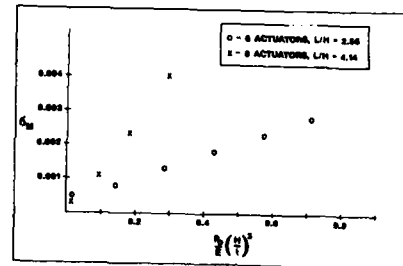


Figure 9: Variation of test section flow uniformity with plate stiffness and pressure load.

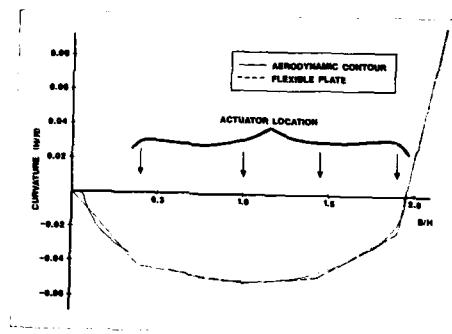


Figure 10: Comparison of curvature distribution for no pressure load, $\frac{L}{H} = 2.56$, Number of actuators = 5.

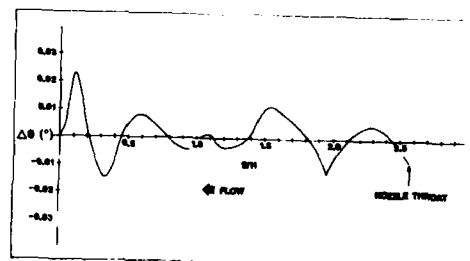


Figure 11: Matching errors for $\frac{L}{H} = 2.56$, 5 actuators and no pressure load.

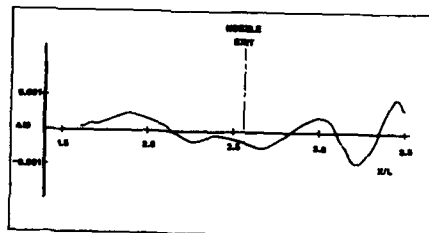


Figure 12: Mach number distribution on the test section centerline, $\frac{x}{L} = 2.56$, 5 actuators, no pressure loads.

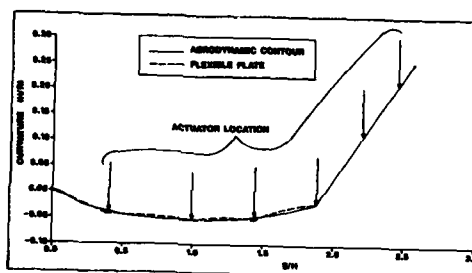


Figure 13: Curvature distribution for high pressure loading, $\frac{P_0}{E} \left[\frac{H}{t} \right]^3 = 0.44$.

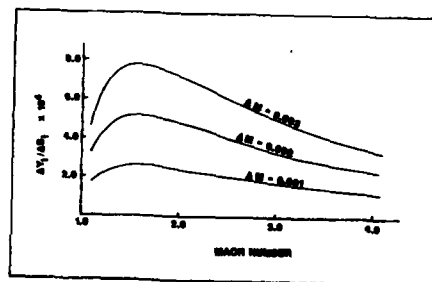


Figure 14: Mach number disturbance as a function of actuator setting error.

TRANSONIC WIND TUNNEL BOUNDARY INTERFERENCE A CORRECTION PROCEDURE

by

R. C. Crites
Aerodynamics and Propulsion Laboratories
McDonnell Aircraft Co.
Box 516, St. Louis, Missouri
United States of America

SUMMARY

An ongoing effort to develop a transonic wind tunnel boundary correction procedure is reported. The goal is a boundary correction procedure applicable to ventilated test sections from subsonic through transonic Mach numbers. "Boundary correction" is distinguished from "wall correction". Boundary corrections contain wall corrections, but also contain model support, and other tunnel dependent corrections. The approach taken uses CFD (Computational Fluid Dynamics) with measured boundary conditions to provide corrections at a few points in the test envelope. Conventional similarity principles and regression techniques are used to extend these corrections over the full test range. To provide experimental data needed for development and validation, a wind tunnel test program was initiated. A set of four wing-body models were built. Model size was varied while maintaining precise geometric similarity. The three smallest models were tested from Mach 0.5 to 1.2 in a small (1 ft. x 1 ft. cross-section) transonic tunnel. Preliminary testing of the two largest models was accomplished in a larger (4 ft. x 4 ft. cross-section) tunnel. Extensive boundary pressure data were measured in both tunnels. Typical results of these tests are reviewed, and the need for additional experimental effort identified. The computational effort is in progress. Status, interim results, and future plans are discussed.

1. INTRODUCTION

No generally accepted or proven method is available to correct transonic wind tunnel data for boundary interference effects. However, recent advances in CFD, computer technology, and wind tunnel instrumentation, imply that development of such a correction method is a practical goal. Accordingly, considerable innovative research effort has been expended by others to achieve this goal. No attempt will be made to detail the status of these efforts. Overviews of current issues and approaches are given by Kraft¹, Newman², and Binion³. Instead, a simplified discussion of the general nature of wind tunnel boundary interference will be given as background to the development effort discussed in the following sections.

Wind tunnel boundary corrections may be approached from two different points of view. First, the presence of the model causes a constriction in the tunnel, which alters the local velocity. Therefore the forces on the model correspond to a different velocity than indicated by the tunnel calibration. In addition, the presence of the walls distort the natural streamline development, changing the upwash. Therefore the forces on the model correspond to a different angle-of-attack than indicated in the tunnel. Most correction schemes approach the problem from this general perspective. They attempt to find Mach number and angle-of-attack corrections.

For models of practical size in small ventilated transonic wind tunnels, interference effects vary over the surface of the model. Effective or average values must be used for the Mach number and angle-of-attack corrections. Even though a Mach number/angle-of-attack combination is found that gives the same net forces as measured in the wind tunnel, the detailed pressure distribution is different. This implies a loss of geometric similarity. That is, the corrections obtained are for a slightly different model. For a wing in a strong interference field the effect is similar to a change in camber. Since there is always some gradient in the vicinity of the model, there is always some error in the correction. In many cases the error may be negligible, but in other cases the correction scheme fails completely and the data is said to be uncorrectable.

The other point of view focuses on the forces. At the test Mach number and angle of attack, the tunnel boundaries cause distortions in the natural (free-flight) flow field. These distortions are reflected in the forces developed on the model. To correct the data, it is necessary to estimate the incremental change in forces that would result from removing these distortions; i.e. simulating free flight.

The benefit of the force correction approach is that, in principle, it inherently accounts for interference gradients. Geometric similarity is maintained and there are no uncorrectable cases. In practice, the incremental change in model forces result from an incremental change in pressure distribution. Since boundary layer development depends on pressure distribution, incremental changes in forces can alter the viscous effects. In some cases the increment in boundary layer development may be negligible. In other cases the change in boundary layer development cannot be ignored. Where interference effects are strong, the correction procedure will have to account for viscous effects on the model.

Although the force correction approach poses a serious challenge in terms of modeling incremental viscous effects, we believe that it offers the greater potential for future development. Furthermore, this approach may be necessary for the development of valid corrections in small fixed wall tunnels with large interference gradients. Therefore, force correction is the orientation of the current work.

The tunnel walls are responsible for some, but not all of the interference. The model support system, plenum bypass, and Mach control system can all contribute. The model support introduces blockage like gradients in the vicinity of the model. The plenum bypass and reentry control can also produce three-dimensional gradients in the presence of a lifting model that are not seen during tunnel calibration. Finally, depending on Mach control technique, the model can interfere with the tunnel calibration, producing a bias error that is a function of the forces on the model. A general boundary interference correction procedure should account for all significant contributions to the deviation between free flight and wind tunnel test conditions.

As previously noted, such a correction procedure does not currently exist. However, we believe that the needed theoretical, computational, and experimental tools are available, and that a sustained effort will result in such a correction procedure. The following sections discuss our initial efforts toward this goal.

2. BASIC APPROACH

Our basic approach is illustrated in Figure 1. The upper left of this figure represents the model mounted in the wind tunnel. Tunnel wall pressures are measured over the full length of the test section. The forces on the model, L , are also recorded. The far-field assumption is made; i.e. the pressure signature at the wall is insensitive fine detail on the model. This permits considerable simplification in the mathematical simulation of the model. The mathematical simulation of the tunnel includes a significant length of nozzle upstream of the test section, the test section with model support hardware, and a significant length of diffuser downstream of the test section. This corresponds to the lower left of Figure 1.

The measured boundary conditions (on the walls) are imposed, and the forces on the simulated model are computed. The computed lift and pitching moment are compared with the measured values. If they do not agree reasonably well, the simulation of the model is adjusted. When the calculated lift and pitching moment agree with measured values, and the measured wall boundary conditions are duplicated, it is judged that the simulation is a valid representation of conditions in the wind tunnel. The next step (lower right of Figure 1) is to run the same calculations with tunnel walls and model support removed. The results correspond to the free-flight case. The incremental difference between the solution in the tunnel and in free flight is applied as a correction to the wind tunnel data. This approach is similar to that of Rizk and Murman⁴, except that they seek an incremental correction to Mach number and angle-of-attack.

CFD methods alone are too costly to provide practical correction of all the data. However, they can be used to provide solutions for a few points bracketing the test range. Conventional similarity relations and regression methods can be used to transfer these solutions to the rest of the test envelope. In this way, CFD is used to calibrate the interference effects for a particular model/tunnel configuration. These calibrations are combined into an interference correction data base. This data base includes model, model support, and tunnel characteristics. It also includes selected wall pressure data.

It seems reasonable that the demand for CFD solutions will decrease as the data base grows. Eventually the data base itself would suffice to provide interference corrections for the vast majority of testing. CFD solutions would only be required when a model did not match any of the configurations contained in the data base.

This point of view leads to a two phase development plan. As illustrated in Figure 2, Phase I is the development of the computational procedures needed to obtain boundary interference corrections. Once corrected and uncorrected data are available in sufficient quantity, a Phase II effort will be required to establish the corrections data base, and the empirical methods to be used with it. Ultimately a given tunnel will be able to apply this data base to obtain accurate boundary interference corrections during normal data reduction with no significant loss of data throughput.

3. WIND TUNNEL TESTS

Regardless of the computational scheme, measured boundary conditions are required. Furthermore, experimental verification of the computed corrections are essential before such corrections can be applied with confidence. Therefore an extensive experimental effort was required before the computational development could progress.

The procedure used to obtain experimental boundary interference data is illustrated in Figure 3. If geometrically similar models of different scale are tested in the same tunnel, the boundary interference effects will cause a lack of correlation in the aerodynamic force and moment data. A model with a blockage of 0.5% is expected to have very small - perhaps insignificant - interference. A model with a blockage of 1.5% is typical of the model size often used in small transonic tunnels. A model with 3.0% blockage is expected to show large interference effects. Any procedure which adequately corrects for these interference effects should collapse the data.

Collapsing the data from a set of geometrically similar models verifies that the method corrects the data to a common flow condition. It does not prove that this flow condition corresponds to free flight. A facility dependent common bias could still be present in the data. A much stronger verification of validity would be obtained by running a set of similar models in at least two wind tunnels that are of different size, and use different Mach control methods.

A series of wind tunnel tests were planned. The objective was to obtain data needed to facilitate the Phase I development, and to provide experimental verification of computed corrections. Tests were scheduled in the TWT (Transonic Wind Tunnel) and the PSWT (Polysonic Wind Tunnel) - McDonnell Aircraft Company facilities.

The TWT transonic test section is 36 inches long and has a cross section of 12 x 12 inches. The walls are 22.5 % porous with normal holes of 0.125 in. diameter and a thickness of 0.125 inches. Model pitch motion is provided by a parallelogram strut arrangement located in the diffuser inlet.

The PSWT transonic test section is 108 in. in length. It has a 48 x 48 in. cross section. The walls in this facility are also 22.5 % porous. This porosity is attained with .375 in. diameter holes which are normal to the surface. The wall is 0.75 in. thick. Model pitch motion is provided by a hydraulically driven sector system.

Both facilities are blowdown to atmosphere type. Run time is limited by available air storage. In the smaller facility, TWT, it can be extended to 20 minutes. In the PSWT, run time is usually limited to 1 minute or less (depending on Mach number and operational mode).

These two facilities provide an adequate test of the correction procedure. The PSWT is 16 times larger than the TWT in cross sectional area. Also, the operational modes are considerably different. The TWT has a passive plenum. Mach number is controlled by varying the area of the second throat. In the PSWT, the area of the second throat is not changed during a run. Mach number is controlled by varying suction on the plenum. The differences are great enough to allow an investigation of the effect of operational mode on boundary interference.

3.1 TWT TEST - HARDWARE

Initial tests were conducted in the smaller, more economical, TWT facility. A set of three simple wing-body models were fabricated for the TWT test. Figure 4 is a sketch of these models showing the relative sizes. These sizes were chosen to produce about 0.5%, 1.5%, and 3.0% blockage in the TWT. All models have cylindrical fuselages and conical noses. The wings are simple flat plates with biconvex leading and trailing edges. Leading edge sweep is 30 degrees and trailing edges are straight for all models. Every effort was made to insure that precise geometric similarity was maintained between models.

To measure the flow boundary, a set of 12 static pressure rails were fabricated. The design of these rails is shown in Figure 5. The pressure taps are located outside the wall boundary layer. The rails extend the full length of the test section (36 inches), and have 24 taps per rail. In the vicinity of the model the tap spacing is 1.0 inch. At the front and rear of the test section the spacing increases so that pressure is measured within 1.0 inch of the entrance and the exit of the test section. The upstream ends of the rails are tapered to provide a gradual increase in rail blockage. As shown in Figure 6, three rails were installed on each of the four test section walls. To remove rail blockage effects, the wind tunnel was recalibrated with the rails in place.

3.2 TWT TEST - TYPICAL RESULTS

The TWT test was conducted at Mach numbers of 0.5, 0.6, 0.7, 0.8, 0.9, 1.1, and 1.2. At each of these Mach numbers baseline data were taken with the tunnel empty. Recorded data included pressures from the 12 static rails, 12 model surface pressures, model base and cavity pressures, 16 plenum pressures, and the force and moment data.

Figure 7 is a photograph of the installation of the smallest model (tunnel open). Figure 8 is a photograph of the same model with the tunnel closed. Note the 12 static pressure rails used to measure the boundary pressure in the test section. Wall pressure signatures were found to be very repeatable. Figure 9 is a direct comparison of unsmoothed ceiling pressures for two different runs. This kind of repeatability is typical of all the rails. The run to run repeatability in pressure coefficient varied from about .0015 to .0002, depending on how well Mach number and angle-of-attack were repeated.

Figure 10 is a plot of the ceiling centerline pressure distribution for all three models. The rails clearly resolve the difference in pressure signature imposed by the different models. Similar differences are seen in the side wall and floor data. It is interesting that even the smallest model (0.5% blockage) is detected by the rail pressures.

Figure 11 is a comparison of centerline floor and ceiling pressure distribution. In the test section inlet, both floor and ceiling reflect freestream pressure. The presence of the model is clearly seen at about 8 inches into the test section. Both floor and ceiling show increasing pressure coefficients. At 14 inches, the floor and ceiling

pressures are still equal, but the level has increased significantly. Moving back over the model, the ceiling pressure drops due to lift induced circulation.

Blockage effects produce pressure perturbations of the same sign on the floor and ceiling. Circulation produces perturbations of opposite sign. Therefore blockage and circulation effects can be separated by looking at the sum and difference of the floor and ceiling rail data. This is illustrated in Figure 12 for the medium sized model (1.5% blockage) at Mach 0.7. The top figure is for an angle-of-attack of 0 degrees (insignificant lift), and the bottom figure is for 8 degrees angle-of-attack. The sum (floor + ceiling), which is driven by blockage, clearly reveals the presence of the model in either case. At 8 degrees, the excursions are slightly higher, otherwise the pattern is unchanged by pitching the model. The difference (floor - ceiling), which is driven by lift, is negligible at 0 degrees, but very pronounced at 8 degrees. The rail pressures (in addition to the measured forces and a suitable wall flow model) implicitly define the flow in the tunnel.

The rail data showed a surprising two-dimensionality. Typical results are shown in Figure 13. Each plot in the figure shows the distribution of pressure around a sectional cut through the test section. The darkened symbol marks the north ceiling rail. Moving to the right (increasing distance from the north wall) the next data point is the ceiling centerline rail. Continuing to the right, is the south ceiling rail. Next comes the three south wall rails (top to bottom). The plot then moves back to the left (toward the north wall), the symbols marking the floor rails. The sectional cut is completed at the extreme left of the plot with the north wall rails (bottom to top). In other words, each plot corresponds to the pressure across the ceiling, down the south wall, back across the floor and up the north wall.

At 5.0 inches into the test section the pressure is uniform on all four walls. Moving downstream, the blockage effect causes a uniform pressure rise. The sectional cut at 14 inches shows this condition. By 18 inches the circulation effect is felt and the ceiling pressure begins to fall. By 23 inches (which is close to the location of the effective center of pressure for the model wing) the effect is maximum. The circulation effect continues throughout the remainder of the test section. At 35 inches the pattern becomes distorted due to the presence of the strut, and the approaching expansion into the diffuser.

This relatively well behaved nearly two-dimensional pressure boundary is characteristic of all models so long as the shock waves do not reach the wall. Figure 14 shows the pressure boundary at 23 inches for the small model (0.5% blockage, 0.27 span to tunnel width ratio). The bounded area of the curve is less because of smaller lift, but otherwise it resembles the biggest model (3.0% blockage, 0.6 span to tunnel width ratio). The degree of similarity in wall pressure signature for different sized models supports the far-field assumption.

When shocks are present at the wall, this well behaved pressure boundary no longer exists. Figure 15 shows the pressure boundary at two locations in the test section only 3 inches apart. The boundary changes in a distinctly three-dimensional fashion in that 3 inches. So long as shock waves do not reach the wall, the 12 rails with pressure taps on 1.0 inch centers provide adequate measurement density. When shocks are present, a closer measurement interval may be desirable.

The nature of the boundary pressures above Mach 1.0 is further illustrated in Figures 16 and 17. Figure 16 shows the ceiling centerline pressure distribution for all three models. When allowance for the different model lengths is made, a high degree of similarity is revealed. Figure 17 is a plot of all three ceiling rails for the 0.5% blockage model. The abrupt discontinuous nature of these wall signatures will introduce severe demands on the simulation of the tunnel boundary.

3.3 PSWT TEST - HARDWARE

The largest of the TWT models was reamed to fit a 1.5 inch internal balance, and became the smallest model for the PSWT set. A larger model of the same geometric family was fabricated for use in the PSWT. It's size was limited by maximum balance load capacity to 1.8% blockage. A sting sleeve was fabricated to maintain the same model base to sting area ratio as the small model. Figure 18 is a photograph of the PSWT model with sting sleeve installed. This model has a wing span of 21.6 inches and a length of 33.75 inches.

The 12 static rails used in the TWT proved very effective for measuring the pressure boundary. However, a dozen rails standing above the boundary layer is undesirable for regular testing. Therefore we decided to investigate a less intrusive scheme for measuring the wall pressure data. A set of 4 static rails were installed - one on the centerline of each wall. Pressure taps were located 1.125 inches above the wall. This is less than a fourth of the mean boundary layer thickness. The additional blockage is negligible. Since the computational work in progress assumes symmetry about the X-Z plane (below Mach 1.0), it was decided to add additional pressure instrumentation to the south half of the test section.

This was done by inserting rows of corks into the holes in the porous wall (parallel to the rails), and adding a pressure tap to each cork. As shown in Figure 19, 4 rows of cork taps were added such that the south half of the tunnel was instrumented in a similar fashion to the TWT. In addition, not shown in the figure, 4 rings of cork taps were

added in the vicinity of the model. Each ring consisted of 16 pressure taps running from the ceiling rail to the south wall, down the wall and back to the floor rail.

3.4 PRELIMINARY TEST RESULTS

Preliminary testing indicated that this instrumentation scheme was inadequate. Spatial resolution was acceptable for the south half of the tunnel but excessive scatter was present in the wall data. Apparently the surface pressure at the wall is subject to edge tones and other turbulent local effects caused by flow through the holes. Although data acquisition time satisfied the criteria of Muhlstein and Coe⁶ for model pressures, it failed to do so for wall pressures.

Improved boundary instrumentation concepts are currently being studied. It may be possible to reduce local turbulence at flush mounted wall taps by blocking adjacent holes in the porous wall. Extended sampling periods and enhanced digital filtering methods are also being investigated. When the wall pressures can be measured with the required precision, the interference testing will begin. As previously discussed, high quality data from at least two different tunnels are essential for the development and verification of the correction procedure.

4. COMPUTATIONAL DEVELOPMENT

The degree of computational sophistication required to accurately describe the flow depends upon the flow conditions. Cost may increase exponentially with the degree of sophistication. Therefore it is important to use the least sophisticated methods consistent with accuracy requirements.

As pointed out by Newman and Kemp⁸, when comparing 2-D and 3-D flows, there is a transonic relief effect in 3-D flow which compresses the Mach range of nonlinear effects. Ashill⁷ assumes that the transformed small perturbation equation governs in the far field until local sonic flow reaches the walls. It seems likely, however, that once strong transonic flow is established over the model, more sophisticated methods will be needed.

Very near Mach 1.0 it will be necessary to use a more sophisticated approach. Vatsa⁹ describes an interesting explicit multistage Runge-Kutta approach to solve the 3-D TLNS (Thin-Layer Navier-Stokes) equations. It might be thought that this method, or one like it, could be used to compute the wind tunnel boundary interference corrections for the strongly transonic cases. Such an extension would be a formidable task.

Vatsa used a computational mesh with over 400,000 grid points to compute the flow over half a wing (X-Z symmetry). In a highly optimized and vectorized form it took 3000 iterations to converge. On the NASA/Langley VPS-32 computer system it took about 1.6×10^{-5} CPU seconds per grid point per iteration, or over 5 hours of computer time. The TWT test results indicate that a rough value of about 3,300,000 grid points would be required for boundary interference calculations. At the same convergence rate, it is estimated that it would take over 90 hours of CPU time per correction point - not really a viable option. This does not decrease the value of the advances in CFD made by Vatsa and others. It simply points out that with existing computer systems we are strongly motivated to seek alternate approaches.

Hounjet⁵ reports that these considerations prompted an investigation into integral equation methods. This investigation led to the development of a transonic shock-capturing panel code. Panel codes are very economical compared to 3-D FDM solutions, but they are inviscid. It may be possible to combine a shock-capturing panel method with a boundary layer solver. Altstatt¹⁰ reports the experimental verification of a boundary layer code that is applicable to a flow with shock wave/boundary layer interaction of the type occurring on airfoils in transonic flow. It may also be possible to make corrections to the surface pressures for nonlinearity and vorticity. Dillenius¹¹ reports such corrections applied to panel method studies in missile aerodynamics. This development would also be formidable, but offers the possibility of obtaining 3-D solutions with current computer technology at reasonable cost.

4.1 PANEL METHOD APPROACH

We elected to begin our computational effort in that portion of the Mach range limited to subcritical flow. In this range the linearized theory should be valid for typical models at small angle-of-attack (no massive separation). The choice of methods under these conditions is relatively easy. Panel methods are easy to apply and have recently been used for simulating wind tunnels.^{12,13,14} Strang¹⁵, in a comparison of four well known and proven panel codes, found MCAERO to be very robust, and less costly to run than the other higher order code being considered (PAN AIR). Therefore MCAERO was selected as the computational tool for the subsonic range.

Figure 20 shows typical paneling of the TWT tunnel with the 3% blockage model installed. Paneling density has been reduced, wakes removed, and nozzle and diffuser sections omitted for clarity. Figure 21 shows the free flight case - the same model with the walls and model support removed. Again, wakes have been removed for clarity. Boundary conditions are those for free flight. The differences in the computed force coefficients represent the desired interference correction.

4.2 WALL FLOW MODEL

There is no problem in generating free flight solutions with MCAERO. Figure 22 illustrates both the fidelity of the panel method and the nature of the boundary interference in the TWT facility. The data curve is centerline floor and ceiling rail data. The MCAERO curve is the computed pressure distribution in free flight at the position of the rails. The difference between these two curves is the result of interference.

Generating tunnel solutions with MCAERO can be a problem. Wall pressures are measured. However, MCAERO requires normal velocity as a boundary condition. Obtaining normal velocity components from pressure measured at a single elevation above the wall is not a well posed problem. If the wall pressures were measured with static pipes, as suggested by Nenni¹⁸ the problem might be reduced, or even removed for subsonic flows.

In order to generate appropriate boundary conditions additional information is needed. The problem is illustrated in Figure 23. Wall pressure distributions are measured. A wall flow model is assumed. This model relates the pressure drop across the wall to the mass flow through the wall, and to the normal velocity distribution at the boundary layer edge (or flow angle). Using this normal velocity distribution, a computational run is made. If the computed forces on the model do not match the measured forces in the tunnel, then the simulation of the model must be trimmed, and another run is made. When the forces do match, then the computed pressures at the rails are compared to the measured pressures. If these don't match, then the assumed wall flow model is corrected, and the process repeated. The wall flow model is adjusted iteratively until the computed pressure distribution matches the measured distribution. Each change in wall flow model changes the computed model forces. The problem is doubly iterative.

There are a number of ways of expediting the selection of a wall flow model and dramatically speeding up the convergence rate. The key to this is realizing that the wall flow is a highly nonlinear viscous phenomena. Jacocks¹⁷ determined the relationship between flow angle and wall mass flow for 60 degree slanted holes in the presence of typical pressure gradients expected in the wind tunnel. Erickson¹⁸ derived a model for boundary layer development on a porous wall, and computed flow angle versus wall cross flow. Chan¹⁹ obtained a relationship between flow angle and wall flow for a 20.5% porous wall with 0.5 inch diameter holes. Inger²⁰ used an integral method to derive a relationship for the growth of laminar displacement thickness in the presence of blowing. Flow angle versus normal flow can be deduced from his results.

The independent results of Jacocks, Erickson, Chan, and Inger are shown in Figure 24. There are several conclusions that can be drawn from these results. First, when there is no flow through the wall there is a small positive flow angle. This corresponds to the growth of the boundary layer displacement thickness with no cross flow (equivalent to a solid wall). For suction ($V_w/U_e < 0$) the flow angle is directly proportional to wall flow. For blowing ($V_w/U_e > 0$) the flow angle increases much more rapidly than the wall flow. This fluid dynamic amplification effect is due to the accelerated growth of the displacement thickness in the presence of blowing. The fact that the implied wall characteristics from such diverse approaches agree as well as they do, implies the existence of a very robust relationship between wall flow and flow angle (or normal velocity at the edge of the boundary layer).

This relationship can be expressed as a polynomial in wall flow. Furthermore, the actual wall flow is proportional to the square root of the pressure drop across the wall. For a passive plenum, such as the TWT, the plenum pressure is very uniform and can be assumed constant. Wall flow is then inversely proportional to the square root of the pressure coefficient.

In this case required boundary condition can be expressed as a polynomial in the square root of the pressure coefficient. The coefficients of this polynomial can be empirically determined on a wall by wall basis. For tunnels with active plenum pumping, such as the PSWT, the wall characteristic must be determined at several stations. This is necessary because the active pumping creates significant pressure gradients in the plenum. The calibration of the wall flow relationship is time consuming and requires considerable experimental effort. However, the wall characteristic is governed by local flow phenomena and does not have to be repeated for each new wind tunnel model.

An interesting alternate approach to the whole problem avoids the necessity of dealing with the wall flow. This approach is based on the concept that a stream tube exists just above the boundary layer which (for given starting conditions) is implicit in the pressure data. Since the local velocity is everywhere tangent (by definition) to this stream tube, a solid boundary can be substituted for the stream tube. Instead of computing wall flow and flow angle, the problem now is to deform the stream tube boundary so that the computed wall pressures match the measured pressures. This can be done by calculating the derivatives of the perturbation potential with respect to geometric changes and using an inverse technique to solve for the geometry that generates the specified pressure distribution.

This approach allows excellent replication of the measured wall pressures. However, the previous approach has distinct advantages. For one, it will detect the occurrence of massive separation or error in simulation of the model geometry. Once major separations occur, the pressure field generated by the simulation (even after adjustment to obtain the correct lift) will not match the computed wall pressures. This is a signal that

something is wrong. If the "stream tube" approach is used, a solution will be forced - an erroneous one. In this regard we feel that no solution is better than the wrong solution.

Another advantage is that the wall flow approach allows the possibility of extending the range of application to high angle-of-attack, or the testing of bluff bodies with massive separation. If the wall flows can be calculated with confidence from the measured wall pressures, then the deviation between computed and measured wall pressure is due to error in simulating the model. Since flow angle is determined from the wall flow, and pressure is measured, two parameters are known at the computational interface. As discussed by Lo¹¹, under these conditions it is possible to compute the effective shape of the model. Lo's work was 2-D, but in principle an inverse technique could be developed to yield incremental modification of the model and wake geometry to obtain an equivalent body which produces both the correct forces and the correct pressure field.

Regardless of the method used to set the wall boundary condition, it is essential that the process be approached with great attention to detail. Figure 25 shows the deviation between computed and measured ceiling pressure when continuity of mass is violated. The integration of transformed normal velocity over all wall panels did not equal zero. Figure 26 demonstrates the accuracy that can be achieved when the boundary conditions are correct.

4.2 LIFT CORRECTION

Figure 27 shows the lack of correlation between the three similar models in the TWT. As expected, the larger models (stronger interference) show depressed lift curve slopes. There is a significant deviation between the 0.5% model and the 1.5% model. We expected to see at least the same or larger increment between the 1.5% model and the 3.0% model. As seen in the Figure, this did not happen. The 3.0 % model did show an increase in interference, but the increment was much smaller. As the model size increases, the interference increment decreases. It is as if the porous wall produces a relief effect.

Computed lift corrections seem to confirm the effect. Figure 28 is typical of the results obtained. The 0.5% model lift is changed very little. The 1.5% model data seems to be over-corrected somewhat. The 3% data is brought into fairly good agreement with the 0.5% data. These corrections account for small changes in the tunnel calibration caused by the model, but they do not account for boundary layer growth on the model. This is believed to be responsible for some of the deviation remaining. As a result, our current effort is toward coupling MCAERO to a proper boundary layer solver.

5. CONCLUSIONS

The experimental data verifies that -

1. The pressure perturbations at the wall are highly repeatable.
2. Different models impose distinguishable pressure signatures at the wall.
3. The far field assumption is valid. Imposed perturbations are sensitive to reference area, blockage, etc., but not to fine detail on the model.
4. The effects of boundary interference on the three models are clearly distinguishable in the model force and moment data.
5. Below Mach 1.0, the wall pressure perturbations show a high degree of two-dimensionality. This two-dimensionality is lost between Mach 1.0 and 1.2.

The computational effort indicates that -

1. Force correction, as opposed to Mach number and angle-of-attack correction, is a valid approach with potential advantages for application to small fixed wall tunnels.
2. Boundary interference corrections should include not only wall effects, but also model support effects. It should also account for the interference of the model on the tunnel - subtle changes in tunnel calibration due to the presence of the model.
3. For subcritical Mach numbers, proven panel methods are an excellent computational vehicle for simulating the wind tunnel and computing interference effects.
4. Developing an accurate wall flow model is essential for proper treatment of the wall boundary conditions.

Future plans call for additional wind tunnel testing and a continuous development effort. There appears to be no major obstacle to bringing these methods to operational status for subcritical Mach numbers. Extension into weak transonic flow is promising. We plan to investigate various alternative computational approaches, including corrected transonic panel methods. Development of suitable computational methods will be the pacing task for extension of these correction procedures into high transonic flow.

REFERENCES

1. Kraft, E.M. "An Overview of Approaches and Issues for Wall Interference Assessment/Correction" NASA CP 2319, Jan. 1983, pp.3-20.
2. Newman, P.A. "Wall Interference Theories" NTF Research Symposium, Langley Research Center, Dec. 1983, pp. 7-1 - 7-11.
3. Binion, T.W.Jr. "Technical Evaluation Report on Fluid Dynamics Panel Specialists' Meeting on Wall Interference in Wind Tunnels" AGARD-AR-190, Mar. 1983.
4. Risk, M.H. and Murman, E.M. "Wind Tunnel Wall Interference Corrections for Aircraft Models in the Transonic Regime" Journal of Aircraft, Vol.21, No.1, Jan 1984, pp.54-61.
5. Muhlstein, L. and Coe, C.F. "Integration Time Required to Extract Accurate Data from Transonic Wind Tunnel Tests" Journal of Aircraft, Vol.16, No.9, Dec. 1979, pp.620-625.
6. Newman, P.A. and Kemp, W.B., Jr. "Wall-Interference Effects: Status Review and Planned Experiments in NTF High Reynolds Number Research - 1980." NASA CP 2183, pp.123-141.
7. Ashill, P.R. "Development in UK of a Method for Calculating Tunnel Wall Corrections from Flow Measurements" NASA CP 2319, pp.259-271.
8. Vatsa, V.N. "Accurate Numerical Solutions for Transonic Viscous Flow over Finite Wings" Journal of Aircraft, Vol 24, No.6, June 1987, pp.377-385.
9. Hounjet, M.H. "Calculation of Unsteady Transonic Flows with Shocks by Field Panel Method" AIAA Journal, Vol.20, No.6, June 1982, pp.857-859.
10. Altstatt, M.C. "An Experimental and Analytic Investigation of a Transonic Shock-Wave/Boundary-Layer Interaction" AEDC-TR-77-47, May 1977.
11. Dillenius, M.F.E. "Aerodynamic Predictions Using Supersonic Paneling Methods Accounting for Vorticity and Nonlinear Compressibility Effects" AIAA-86-0569, Jan. 1986, Reno, Nevada.
12. Morfy, M. and Digney, J.R. "Doublet-Panel Method for Half-Model Wind Tunnel Corrections" Journal of Aircraft, Vol.24, No.5, May 1987, pp.322-327.
13. Lee, K.D. "Numerical Simulation of the Wind Tunnel Environment by a Panel Method" AIAA Journal, Vol.19, No.4, April 1981, pp.470-475.
14. Carlin, G.J., Jr. and Bevon, D. "Prediction of Subsonic Wind Tunnel Mounting System Interference" Journal of Aircraft, Vol.24, No.5, May 1987, pp.317-321.
15. Strang, W.Z.; Berdahl, C.H.; Nutley, E.L.; Murn, A.J. "Evaluation of Four Panel Aerodynamic Prediction Methods (MCAERO, Pan Air, Quadpan, and VSAERO)" AIAA-P-85-4092, Oct. 1985, Colorado Springs.
16. Nenni, J.P.; Erickson, J.C., Jr.; Wittliff, C.E. "Measurement of Small Normal Velocity Components in Subsonic Flows by Use of a Static Pipe" AIAA Journal, Vol.20, No.8, Aug.1982, pp.1077-1083.
17. Jacocks, J.L. "Aerodynamic Characteristics of Perforated Walls for Transonic Wind Tunnels" AEDC-TR-77-61, June 1977.
18. Erickson, J.C., Jr. and Homics, G.F. "Numerical Simulations of a Segmented-Plenum, Perforated, Adaptive-Wall Wind Tunnel" AIAA Journal Vol.20, No.5, May 1982, pp.612-623.
19. Chan, Y.Y. "Wall Boundary-Layer Effects in Transonic Wind Tunnels" AGARD-CP-335, May 1982, pp.7-1 - 7-15.
20. Inger, G.R. "Laminar Boundary-Layer Solutions with Strong Blowing" AIAA Journal, Vol.5, No.9, Sept.1967, pp.1677-1679.
21. Lo, C.F. "Determination of Equivalent Model Geometry for Tunnel Wall Interference Assessment/Correction" NASA CP 2319, Jan. 1983, pp.335-342.

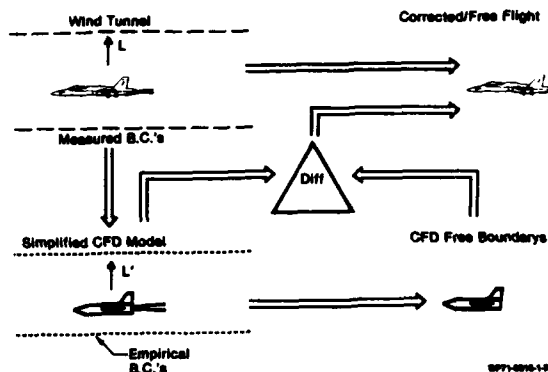


Figure 1. Phase I Correction Procedure

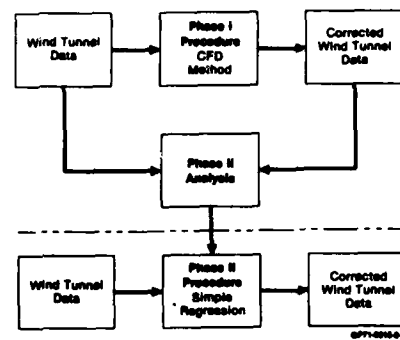


Figure 2. Two Phase Boundary Interference Correction Scheme

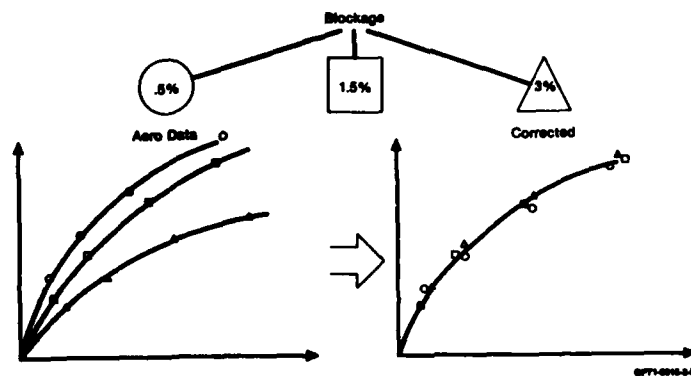


Figure 3. Wind Tunnel Test Approach

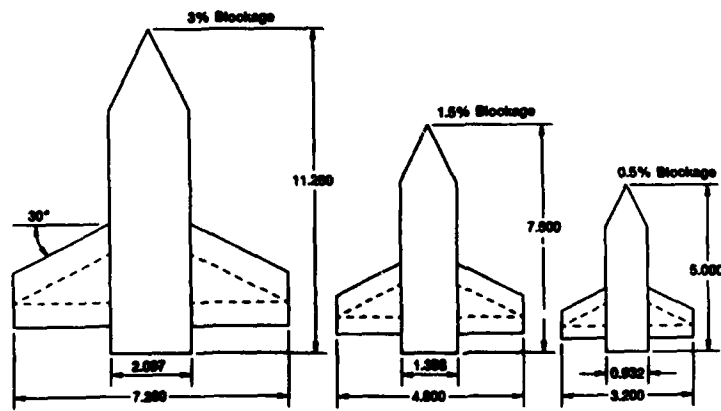


Figure 4. TWT Interference Model Design

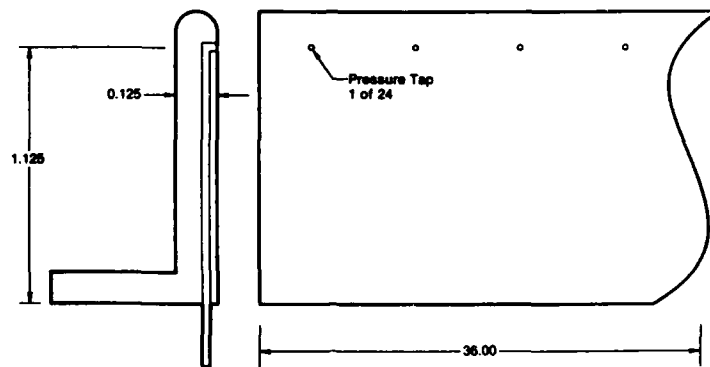


Figure 5. Static Rail Design

GP71-0015-6-R

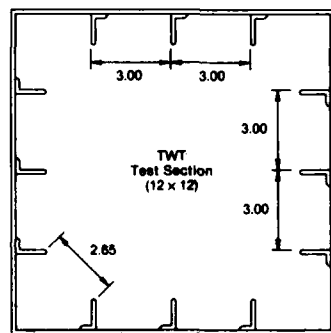


Figure 6. Rail Location

GP71-0015-4-R

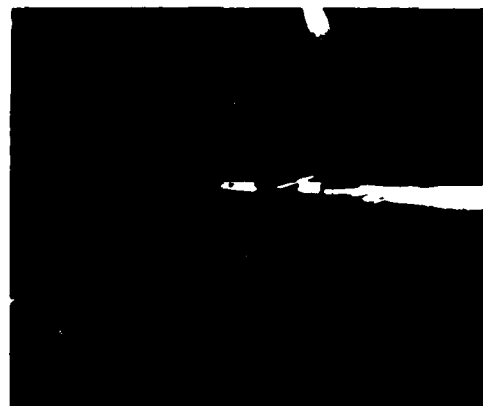


Figure 7. 0.5% Blockage Model Installation

GP71-0015-27-R

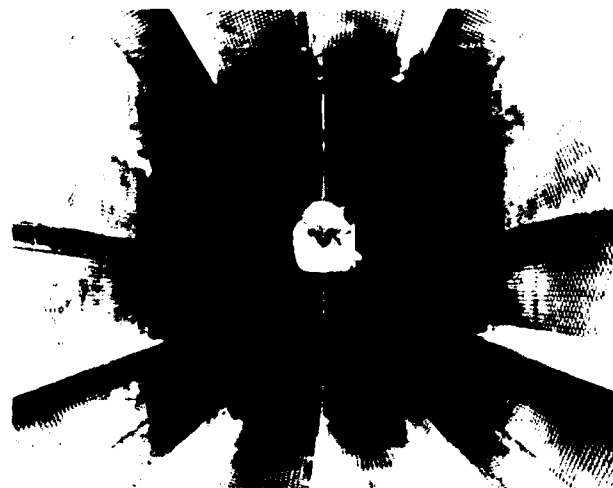


Figure 8. 0.5% Blockage Model in TWT Test Section

GP71-0015-25-R

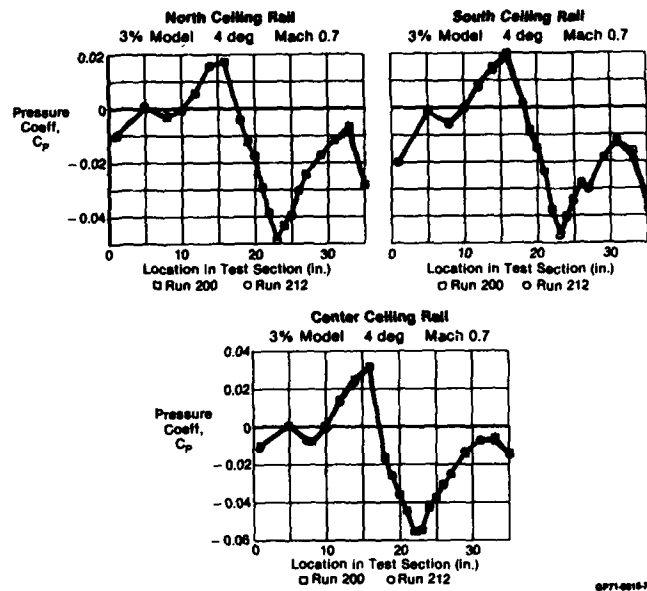


Figure 9. Rail Pressure Repeatability

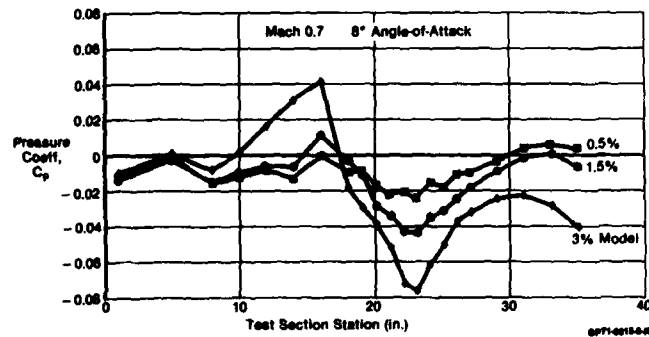


Figure 10. Centerline Ceiling Pressure Signatures

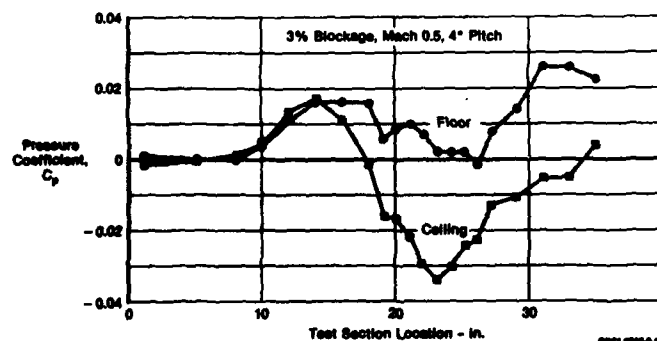


Figure 11. Typical Floor and Ceiling Pressure

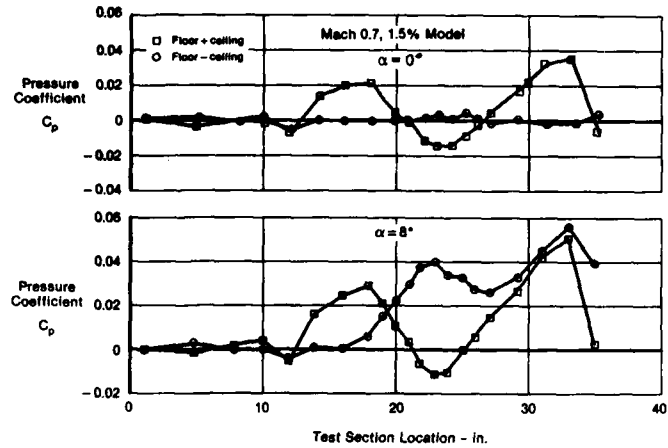
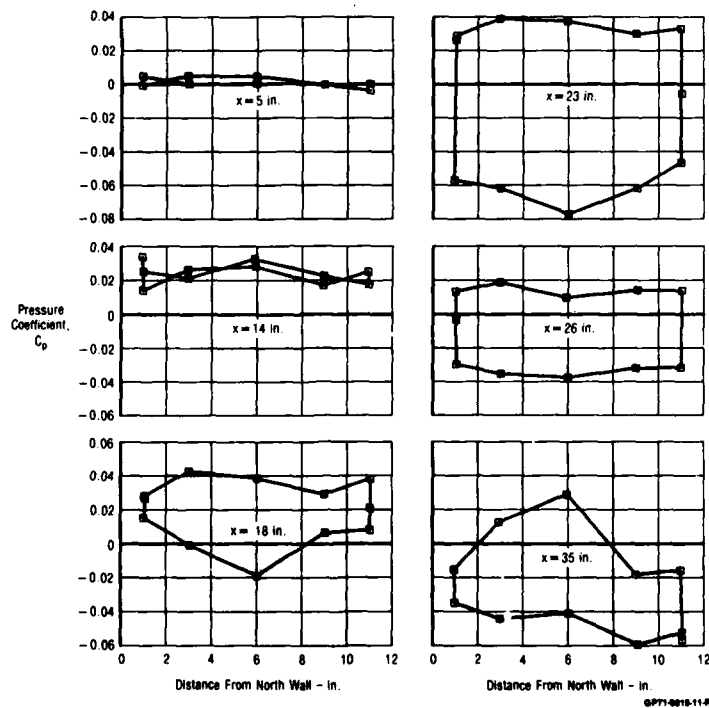


Figure 12. Separation of Blockage and Circulation

GP71-0015-10-R

Figure 13. Pressure Boundary at Specific Section Cuts
3% Model $\alpha = 8^\circ$ Mach 0.7

GP71-0015-11-R

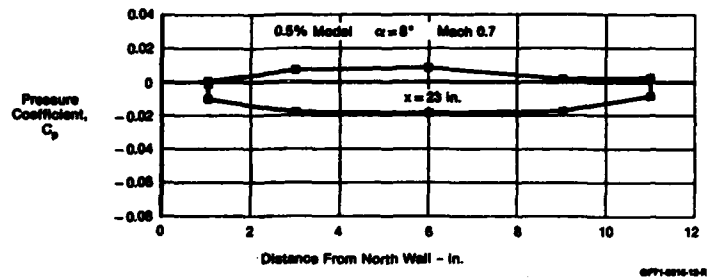


Figure 14. Small Model Pressure Boundary

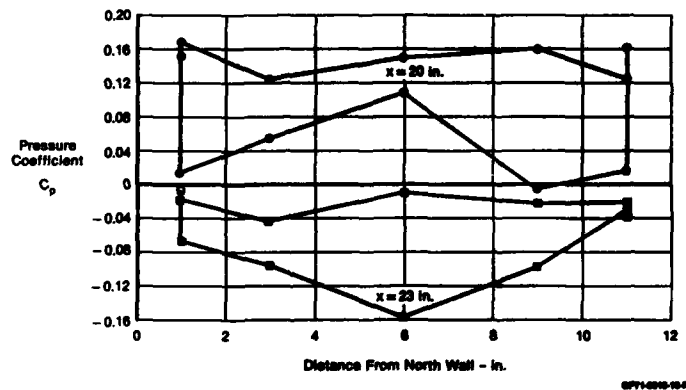


Figure 15. Mach 1.2 Pressure Boundary

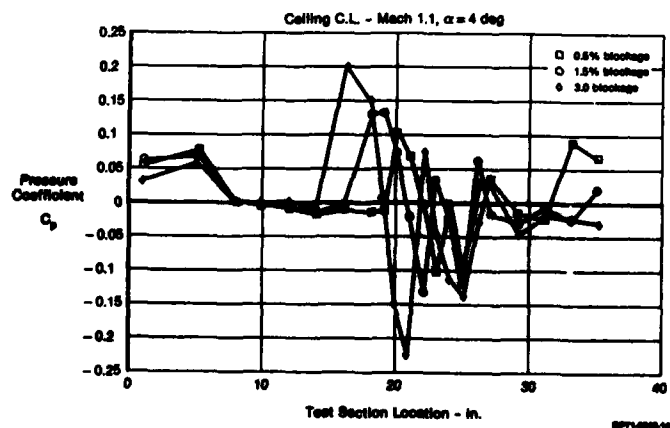


Figure 16. Three Models at Mach 1.1

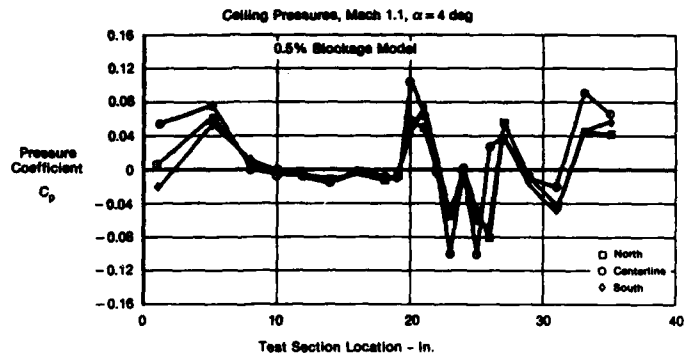


Figure 17. Ceiling Pressures at Mach 1.1

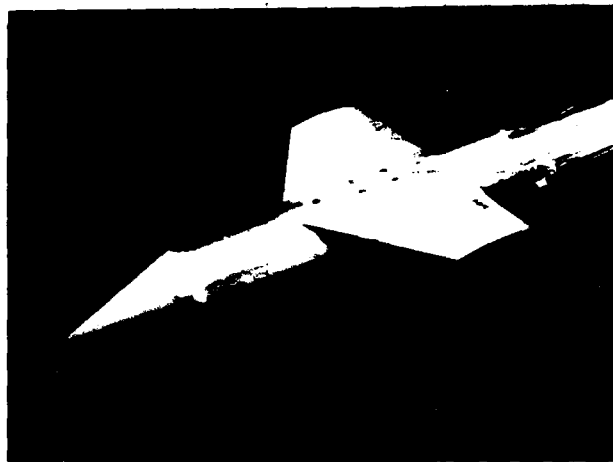


Figure 18. PSWT 1.5% Blockage Model

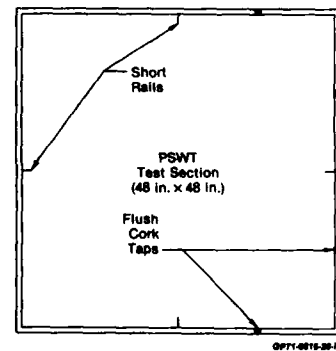


Figure 19. PSWT Pressure Instrumentation

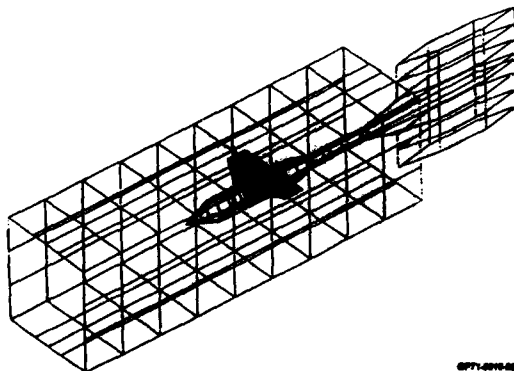


Figure 20. Wind Tunnel/Model Simulation

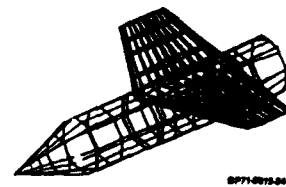


Figure 21. Free Flight Simulation

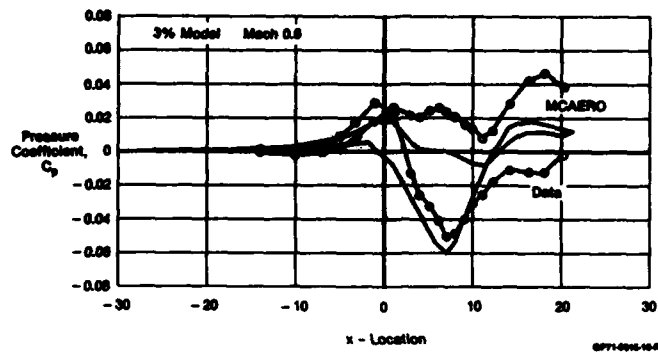


Figure 22. Free Flight and Tunnel Pressures

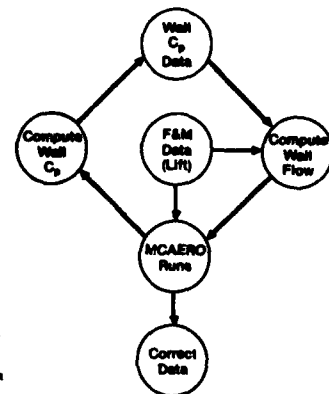


Figure 23. Wall Flow Boundary Problem

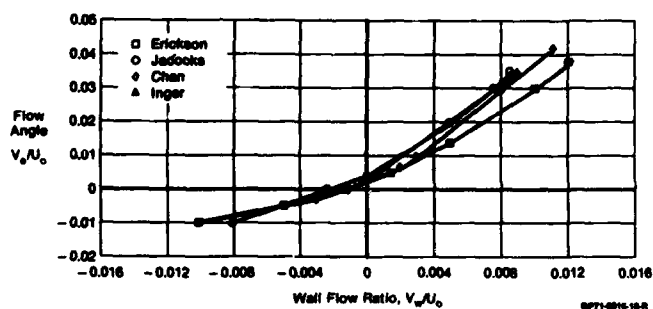


Figure 24. Flow Angle as a Function of Wall Cross-Flow

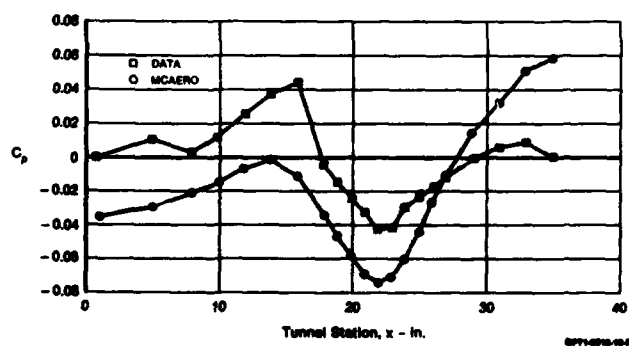


Figure 25. Result of Incorrect Wall Boundary Condition

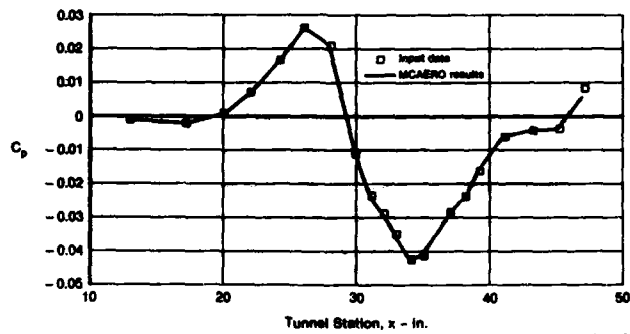


Figure 26. Result of Proper Wall Boundary Condition

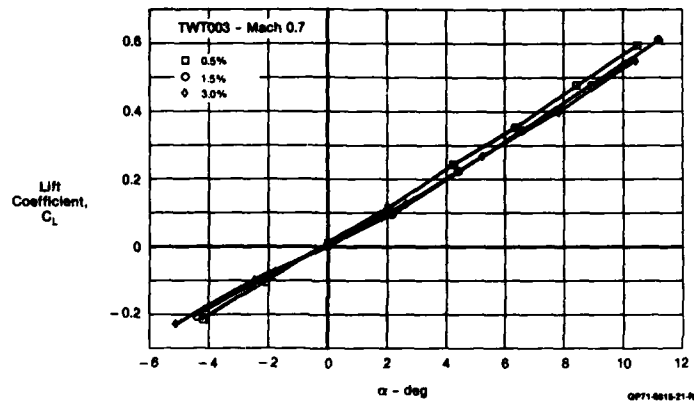


Figure 27. Uncorrected Lift Data

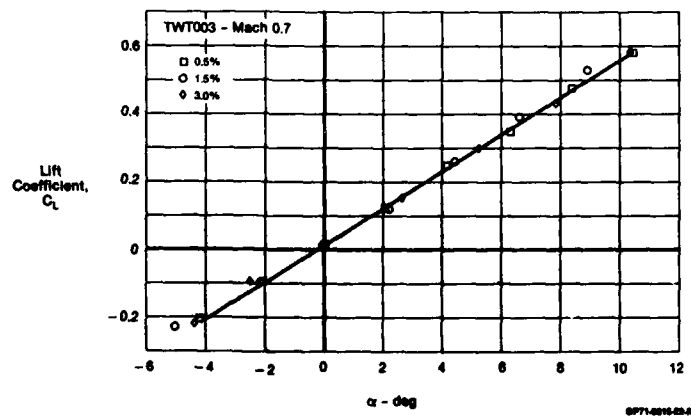


Figure 28. Corrected Lift Data

**THE USE OF COMPUTATIONAL FLUID DYNAMIC METHODS
TO ASSESS THE EFFECTS OF MODEL SUPPORT SYSTEMS
AND WORKING SECTION MODIFICATIONS ON THE FLOW
AROUND WIND TUNNEL MODELS**

D R Stanniland
Aircraft Research Association Limited
Bedford, England

SUMMARY

The continuing development of computer codes and power means that computational fluid dynamic methods can now be used, in conjunction with experimental techniques, to provide a more thorough understanding of measured flow phenomena. This paper demonstrates the use of various programs to evaluate the magnitude of the interference due to model support and flow measurement installations and to guide the design of an acoustic liner for the ARA Transonic Wind Tunnel. Various simplifications are necessary to permit the representation of the complex geometry within the constraints imposed by the programs, and hence, care is needed in using the computed results. Within this limitation, the methods can provide a valuable aid to the interpretation of experimental results and to guide the design of wind tunnel installations. The paper describes calculations using various theoretical methods, carried out in support of tests on five different wind tunnel installations.

Notation

C_D	Configuration drag coefficient
C_p	Pressure coefficient
ΔC_p	Incremental pressure coefficient due to rig interference
d	Acoustic liner depth
M	Free stream Mach number
M_L	Local Mach number
M_{MAX}	Maximum Mach number measured on the tunnel centreline in the throat of the acoustic liner
M_{340}	Mach number on the tunnel centreline measured at tunnel station $X = 340$ in
ΔM	Incremental Mach number due to rig interference
X	Axial distance along the tunnel
Y	Spanwise distance from the tunnel centreline
α	Incidence angle of onset flow
β	Sideslip angle of onset flow

1 Introduction

Development of computer based calculation methods has now reached a stage where their integration with wind tunnel based experimental techniques has become very important. It is unlikely that the theoretical methods will become sufficiently reliable to supersede the wind tunnel in the foreseeable future, particularly for a complex configuration such as a fully laden military aircraft where the grids necessary to define the fully separated flow around installations such as a multiple store carrier or an array of vortex generators defy imagination. Equally, it would be foolish to assume that experimental results cannot benefit from the application of computational techniques, even for configurations where the complexity of geometry requires gross simplifications to be made.

In order to carry out any computational fluid dynamic calculations, it is necessary to make a variety of assumptions. Implicit in any existing computational method are a number of approximations to the time-dependent Navier-Stokes equations so that they can be solved numerically. In addition, the geometry of the configurations must be represented in a numerically precise manner in order to provide a surface boundary condition, which is then satisfied at a number of discrete points. When applied to wind tunnel installations, assumptions must be made about the far field conditions which will generally not be precisely defined. However, in spite of these assumptions, it is possible to make use of the computational methods to guide the interpretation of experimental results.

The purpose of this paper is to describe a range of applications in which theoretical methods have been used to enhance the experimental results in an attempt to reduce the magnitude of the experimental error. Inevitably, this requires the use of either computationally 'simple' methods applied to complex configurations, or more complex methods applied to geometrically simple representations of the problem. The methods used will be described briefly, with particular reference to their limitations for the required applications. Five wind tunnel installations will then be considered, indicating some of the benefits which can be obtained from the use of computational fluid dynamic methods.

2 Description of the Theoretical Methods Used

The computational methods currently available and under development can be divided into two broad categories. Firstly, there are methods which are aimed at particular problems which consequently have geometry specifications appropriate to the configuration under consideration. These use state of the art solutions of the more precise approximations to the Navier-Stokes equations, with configuration specific grids. Examples of these are the wing/body/pylon/nacelle code of Forsey¹, the wing/fuselage/fin and tailplane method of Baker and Jameson² and the Multiblock technique of Weatherill et al³, applicable to complex aircraft geometries. The second group of methods is capable of handling more general complex configurations, for which it is only necessary to define the surface geometry. These include the panel methods^{4,5}, and their transonic development, the field integral methods⁶. These programs solve the simpler approximations to the flow equations, but have the advantage of being able to represent a variety of complex, mutually interfering components without the need to resort to extensive grid development for each application.

When considering the application of theoretical methods to wind tunnel rig interference calculations, the panel methods can be more readily applied to the complex configurations under consideration. However, it is occasionally possible to simplify the problem so that the more advanced methods can be used to consider a particular aspect in detail. These applications, requiring gross assumptions which apply the methods well beyond their normal limits, can nevertheless provide valuable guidance in the assessment of wind tunnel installations. It is therefore worth describing here the programs which have been used, and their various limitations:

SPARV⁴ (Source Patch and Ring Vortex). This is a panel method developed at BAe (Brough), applicable to subcritical flow, but using a compressibility correction to extend the method up to high subsonic speeds. In fact, we carry out calculations for cases where small regions of supercritical flow are present, accepting the fact that the flow will be computed incorrectly, but using the results to indicate areas which require careful consideration. A large number of mutually interfering components can be represented by source or doublet distributions at the centroids of the panels. This implies that the boundary conditions are only applied for these specific points and consequently, one must ensure an accurate representation of the geometry to avoid leakage through the surface. However, this must be balanced by the limited number of panels which are permitted by computer run times and disc storage. We find that 2000 panels are adequate for most calculations, particularly when it is possible to use the symmetry of the configuration to halve the number of panels required. On occasions, it may be necessary to simplify the geometry under consideration. In fact, it would not be reasonable to represent configurations precisely where one would expect areas of separated flow. In these cases, a simplified geometry will provide a more accurate representation of the external flow. Although the program has a viscous option, this is unlikely to provide a reliable solution for this class of configuration, and the simplified geometry is normally defined by an experienced user of the method.

ARA Solid Body Programs. Two programs are considered for configurations which can be represented by a single solid body. A method due to Baker⁷ solves the Full Potential Equation for axisymmetric shapes. Obviously, this has a limited application, but has proved useful and does permit the definition of discontinuities with a closely defined grid in the region of the discontinuity, which proved valuable for one of the applications I shall be describing. A generalised solid body program due to Weatherill and Shaw⁸, solves the Euler equations for a 3D body set at incidence and sideslip. This permits calculations with moderate supersonic onset Mach numbers, but it can prove difficult to specify a grid for a configuration, particularly in regions of discontinuities where the surface fitting techniques can introduce unsmoothness in the geometry specification, with consequent unsmoothness in the pressure distributions. In fact, one must be particularly careful to ensure a fully converged solution with Euler methods, which seem to be prone to computing unsteady pressures in regions of where the geometry appears to be accurately specified.

ARA Cowl Program⁹. This method solves the Full Potential Equation for generalised inlet shapes. In its present application, it has been used to design the lip of an acoustic liner for the ARA Transonic Wind Tunnel. Obviously, this did not permit the representation of the adjacent tunnel wall, but this could be allowed for to some extent by using the mass flow ratio in the calculation to define the upstream stream tube capture area.

Apart from the codes specified here, there are a variety of methods in use for comparison with the experimental results. To some extent, it is the steady improvement in these codes which drives the demand for increasing experimental accuracy and, on some occasions, highlights the need for more careful experimental techniques. One method which appears to offer prospects for future assessment of wind tunnel data, notably from the point of view of wind tunnel interference, is the Multiblock approach³ in which the field grid is broken down into a large number of blocks. Obviously, this would permit the representation of the wind tunnel wall as an outer boundary, with an imposed boundary condition to match measured wall conditions, whilst readily permitting an extension to free stream conditions for a direct calculation of the flow without interference. However, although this method already exists as a working tool, it requires development to create the appropriate topologies for wind tunnel applications, and at present, remains one of the methods against which wind tunnel results are compared.

Having mentioned some of the problems involved in using the theoretical methods, one must emphasise the attractions of the methods. Primarily, they permit detailed analysis of the complete flow field without the need for intrusive instrumentation. Secondly, they permit the assessment of small changes to the configuration without the need for design, manufacture and further testing with the inevitable expense and increased timescale which this involves.

3 Application of Theoretical Methods to Wind Tunnel Investigations

In order to demonstrate some of the applications of theoretical methods, a series of five examples will be described here. The aim here is not to describe the results in detail, but rather to show how the methods are used in an attempt to enhance the understanding of the wind tunnel results. Obviously, before we can use any of these methods with confidence, it is necessary to demonstrate the reliability of the calculations. This is developed by computing results for existing configurations, particularly those which appear anomalous, to give a sounder understanding of the flow measurements. Although there will not always be a precise comparison between theory and experiment, we can establish a level of confidence in the methods so that they can be integrated into test requirements where measured data are not available.

3.1 Isolated Nacelle Rig

The ARA isolated nacelle rig¹⁰, shown in Fig 1, is used to measure the internal performance and spillage drag of engine inlet cowls for subsonic transport aircraft. Internal mass flow is controlled by independent suction and the flow quality is measured at the engine face using rakes. Externally, cowl surface pressures are measured and the spillage drag is obtained from the momentum loss measured by an array of 5 pitot/static rakes which rotate through 36°. The full 360° field, is obtained by assuming symmetry in the vertical plane. Corrections to the measured data were developed during the commissioning

of the rig by comparison with a smaller scale (0.2% blockage) installation. However, during the course of some production testing in 1983, a single cowl was tested with the standard 5 arm drag rake and with a 12 arm rake, mounted at the crest of the cowl, intended to measure the forebody drag alone. The results from this comparison showed a large discrepancy between the forebody pressure distributions measured on the two configurations (Fig 2), indicating a significant inconsistency between the two tests. Full details of the extensive experimental and theoretical investigation have been presented by Carter and Hirst¹¹. For present purposes, it is sufficient to consider the contribution of the theoretical methods to the calculation of the interference due to the nacelle rig.

For these calculations, the SPARV method was used to represent the model support strut, the drag rake arms, the boundary layer rakes and the centre body, using a total of 1450 panels. No attempt was made to model the inlet; instead, the centre body was extended forward as a parallel body so that disturbances in the vicinity of the cowl could be attributed directly to the interference from the rig. Similarly, no attempt could be made to allow for the tunnel walls which have 22% open area perforations, since these could not be adequately allowed for in these calculations. Consequently, it is not possible to compute model blockage using this method. The SPARV panelling of this configuration is shown in Fig 3, with the computed body surface Mach numbers shown in Fig 4. It is apparent that the 12 arm rake has such a large effect on the forebody Mach numbers, both in terms of a deficit and a gradient along the surface, that the results can be considered uncorrectable. The standard 5 arm rake has a smaller, but still significant effect on the surface Mach numbers and even the taper of the centre body without rakes results in a Mach number reduction of the order 0.003, with an associated gradient in the vicinity of the cowl.

The effect of the drag rakes on the Mach number in the plane of the rake measurement is shown as a computed distribution in Fig 5, with the associated distribution in local Mach number along the rake arm in Fig 6. The comparison with the experimentally measured values shown here lends some confidence to the calculations, although there is a suggestion that the actual effects may be slightly greater than the values calculated, particularly near the surface of the body.

3.2 Isolated Store Drag

The ARA store drag rig (Fig 7) is used to measure the 'isolated' drag of detailed representations of externally carried stores, providing a data bank of drag measurements as a basis for installed drag prediction methods. The stores are mounted from a long support tube with a live or earthed pylon. Comparison between free flight data and rig measurements of the drag of a MK 10 bomb had led to the development of an empirical correction method which used pressure measurements on the upper surface of the support tube to allow for a buoyancy effect. However, it seemed likely that a significant proportion of the drag difference could be due to close interference between the pylon and the store. The SPARV panel method was therefore used to compare the flow around an isolated store with the full rig installation in order to consider this effect.

The isolated store drag rig was modelled using 1400 panels, as shown in Fig 8. No attempt was made to represent the tunnel walls in this calculation. In order to establish a level of confidence in the close interference effects, and to confirm that this was the dominant effect, comparisons were made between local Mach numbers measured on the top of the support tube and those computed by SPARV. The results, shown in Fig 9, confirm that these results are predicted well, even at $M = 0.9$, when the local Mach number on the support tube approaches unity and there would obviously be embedded regions of supersonic flow in the vicinity of the pylon.

Although it is possible to predict pressure distributions adequately using theoretical methods, it is, of course, a vastly different proposition to attempt to integrate the pressures in the axial direction to compute drag. Not surprisingly, the integrated drag from the SPARV results was significantly in error, and could not be used on an absolute basis. However, the incremental difference due to the presence of the rig did prove to be more reasonable, and this was used to correct the measured drag obtained from the rig. The resulting corrected drag is compared in Fig 11 with the drag measurements from sting mounted tests and with the empirically corrected results. It should be noted here that a small difference in drag levels between the sting mounted and rig mounted tests would be expected because of differences in the detailed representation of excrescences. This increment would be expected to remain constant with Mach number over the range shown and hence, the correction derived from the SPARV calculations can be considered a very encouraging result.

3.3 The Twin Sting Model Support

The twin sting rig is used in the ARA Transonic Wind Tunnel to support civil aircraft models, with one sting connected to the lower surface of each wing. This permits the accurate representation of the rear fuselage and empennage and hence, detailed changes in the afterbody can be investigated. However, the absolute drag measured on a balanced rear fuselage is sensitive to very small levels of rig interference; for example, a mean C_D of 0.001 over the rear fuselage can amount to an error in C_D of 0.0001 for a configuration where the fuselage cross sectional area is 1/10 of the wing area, which is typical of some wide bodied jets. The panel method SPARV has therefore been used to investigate the forward pressure field and flow angles due to the rig interference. This investigation considered the effect of alternative sting positions and designs, together with detailed contributions from each of the components of the rig.

The twin sting rig (shown in Fig 12) was modelled using 1142 panels to represent the central boss, yoke plate and sting. No attempt was made to allow for the tunnel walls, which are unlikely to have a major effect on the increments considered here. More significantly, no attempt was made to represent the parent aircraft, and consequently, the calculated influence of the leading edge of the stings assumes a free air condition and ignores the interference with the wing lower surface. Since the calculations are carried out at small incidences, this is not likely to have a major effect on the incremental differences which have been obtained, although we would ideally consider a representative aircraft shape and carry out calculations with and without the support rig present. However, this would require a very large number of panels, which was not feasible for this particular investigation.

The computed effect of the twin sting rig on the pressures in the vicinity of the model is shown in Fig 13, as contours of incremental C_p . A typical configuration afterbody position is superimposed on the field, but not included in the calculation. It is apparent that the incremental pressures on the afterbody are sufficient to cause a significant error in the absolute afterbody drag levels for this rig arrangement, although incremental differences between configurations are unlikely to be affected. The contribution of the three component parts of the twin sting rig to the incremental pressures is shown in Fig 14. This shows that the dominant component at zero incidence is the centre boss of the rig which is used to support the twin sting rig on the model cart. The additional effect of the yoke plate and the stings contributes approximately 30% of the mean pressure change over the afterbody.

3.4 Sting Taper and Model Surface Unsmoothness

A check calibration of the ARA Transonic Wind Tunnel has recently been carried out using a long centreline probe, supported far upstream ahead of the flexible supersonic nozzle, to measure the centreline Mach number distributions. In order to expedite the installation of the probe, it was adapted to fit into a complete model roll unit using a tapered sting (Fig 15), rather than the original installation which replaced the roll unit in the model cart. This had the additional advantage of calibrating the tunnel in the presence of the complete model support system and indicating the forward influence of the sting and roll unit taper on the centreline Mach numbers. However, we also required to measure the position of the fall-off in tunnel Mach number in order to define the rearward limit of the working section. Consequently, it was necessary to compute the effect of the tapered sting and roll unit on the surface pressures in order to identify where the measured results deviated from this distribution.

Since there was no requirement to represent the tunnel walls in this exercise, the methods of Baker⁷ and Weatherill and Shaw⁸ could be used, treating the probe, tapered sting and roll unit as a body of revolution. Although this seems a trivial task, a variety of problems were encountered before satisfactory computed results were achieved. Firstly, the very high fineness ratio of the probe led to an unacceptably coarse grid in the region of interest. It was therefore necessary to close the forebody arbitrarily, reducing the overall length but ensuring that it was sufficiently far upstream for the influence of the nose to be small for a reasonable distance upstream of the tapered sting. Secondly, the Euler code required the body to be defined as a continuous surface. It proved impossible to define the discontinuities on the tapered sting in this way without inducing oscillations in the surface geometry, and it became necessary to write a specific grid generation program for this application of the method. Finally, the Euler code was found to produce unsmooth Mach number distributions, even for numerically smooth geometry. This was partly due to the degree of convergence, and a large number of iterations were used to minimise this contribution. Additionally, there appears to be a spurious entropy in the solution which fails to converge. This was sufficiently large for the theoretical results to be unusable at subsonic speeds. Supersonically, where the order of accuracy of the measured flow is significantly lower, the results could be used with some caution, particularly since the contribution from the sting can be taken to be zero everywhere upstream of the taper, which covers the working section for all models which are likely to be tested at supersonic speeds.

The computed effects of the tapered sting are compared with the measured pressures on the calibration probe in Fig 16, and it is apparent that the theoretical methods are providing a satisfactory prediction of the taper effect in spite of the problems encountered in using the programs. Comparison between theory (Baker) and experiment at subsonic speeds shows that the aft end of the working section can be identified as tunnel station 415. Supersonically, there is no obvious fall off in tunnel Mach number over the range of measured pressures. However, there are small disturbances in the local Mach number over the length of the working section. These can be traced back to changes in the tunnel wall geometry; for example, the walls have graduated perforations to optimise the flow distributions at transonic Mach numbers and the position at which the perforated walls reach maximum ventilation can be identified as a small disturbance which cuts the centreline probe in the vicinity of the sting taper.

The problems in defining a smooth surface geometry for the Euler calculations led to some consideration of the effect of machining accuracy on the measured pressures. Measurements of the probe diameter over a 20 inch length showed a small variation which was within the manufacturing tolerance, but could be identified as a wave in the local surface. Calculations using Baker's Full Potential code, shown in Fig 17, indicated that the effect of this wave was significant in terms of the required accuracy of the pressure measurements. However, the program assumed an axisymmetric distribution of the machining inaccuracy, which was obviously inappropriate. Therefore, it was not possible to match the pressure tapping signatures which had been identified and corrected by experimental means. In order to assess this effect theoretically, it would be necessary to ensure a precise three-dimensional surface geometry with a surface grid which is sufficiently fine to identify the variations in curvature. This is well beyond any theoretical code which is currently available. However, it does highlight a difference between theory and experiment which could apply to any test application. Generally, these small differences in surface definition are not significant for attached flow conditions, but the advent of more advanced theoretical codes which attempt to handle separated conditions will need to identify details which can trigger the separated flow.

3.5 Acoustic Liner Design and Flow Uniformity

An acoustic liner is currently under development for use in the ARA Transonic Wind Tunnel (Fig 18), aimed at providing an acoustically quiet environment for propeller noise testing. Apart from the obvious need to meet the necessary acoustic standard, there are several requirements on the aerodynamic standard of the liner to ensure satisfactory results. The specific constraints which need to be met include:

- a uniform Mach number distribution within 0.01 of the required value, extending forward to tunnel station 330 in up to $M = 0.85$,
- a Mach number at the location of the propeller disc which is within 0.005 of the required value up to $M = 0.85$,

- a Microphone Traversing Rig (MTR) which is sufficiently strong to locate the microphones to within 0.1 in of the specified position in the tunnel. The implication of this is that a large body will be moving fore and aft on tracks in an effectively solid wall tunnel and it is necessary to ensure that the above Mach number criteria are satisfied for all positions of the rig.

These constraints can be translated into aerodynamic design requirements thus:

- design a liner lip which will accelerate the flow up to a constant working section Mach number without the risk of choking in the throat for Mach numbers up to $M = 0.85$,
- investigate the interference between the model support system and the liner walls to ensure that the flow remains within the specified tolerances in the working section and that there is no risk of choking around the model support,
- investigate the effect of the MTR on the Mach number distribution in the working section for its full range of movement.

3.5.1 Lip design

The leading edge of the liner is positioned at tunnel station 280 in, with the lip extending back to station 304 in. Initially, a simple blunted ogive lip section was chosen, relying on the change in liner cross sectional area to accelerate the flow smoothly up to a uniform Mach number in the working section. However, tests in a 1/12 scale representation of the transonic tunnel fitted with a model of the liner suggested that the constant Mach number would not be achieved by the required tunnel station. This led to an aerodynamic redesign of the liner lip section shape in an attempt to extend the working section of the liner further forward.

Details of the liner lip arrangement in the tunnel are shown in Fig 19a, and it is apparent that the geometry cannot, and should not, be modelled precisely for the theoretical calculations. The boundary layer bleed control plate is adjustable at this stage to permit the optimisation of the bleed gap. This will, of course, be replaced by a splitter plate when the design is finalised. The boundary layer bleed is terminated by a structural frame with a smaller bleed behind the liner into the perforated tunnel wall section. The best theoretical approximation to this arrangement is to attempt to match an upstream flow, giving the correct Mach number in the basic tunnel section, with a downstream flow appropriate to the working section of the liner. The details of the flow in the vicinity of the lip can then be satisfied by ensuring a representative stagnation streamline, with the correct internal liner lip shape.

Two theoretical methods were considered in the design of the liner lip. Firstly, the SPARV program was used, representing the tunnel as an inverted body (that is, a body with inward pointing normals). In this case, the configuration is treated as a throttled tube with the Mach number at upstream infinity adjusted to give the correct Mach number in the working section of the liner. For these calculations, the 'stagnation streamline' was approximated by a fairing between the upstream tunnel section and the liner lip (Fig 19b). Although the results were used as a positive guide to the lip design, these calculations were primarily used to show whether this was an appropriate representation of the tunnel for rig interference calculations. Secondly, the ARA cowl program was used to investigate alternative detailed specifications of the inlet lip shape. In this case, the liner was treated as a rectangular cowl with a field grid which gave an accurate specification of the lip shape (Fig 19c). Since no representation of the upstream tunnel walls was possible, the mass flow ratio was specified to ensure the correct stream tube cross sectional area far upstream. The program was then allowed to compute its own stagnation streamline, which appeared to give a satisfactory flow calculation.

Although the theoretical representations of the liner lip do not represent an accurate geometric specification of the liner, it is felt that they provide the most appropriate aerodynamic solution within the constraints imposed by the programs. The Mach number distributions for the simple lip design are compared with the 1/12 scale model tests in Fig 20. Unfortunately, the test results did not achieve the required free stream Mach number, but it is apparent that the cowl program provides a good indication of the acceleration of the flow due to the liner lip (bearing in mind that a given increment in working section Mach number will be achieved by a much smaller change in upstream Mach number). The SPARV results are a little disappointing in that they do not provide as good an indication of the acceleration into the liner. This is thought to be due to the very coarse panelling in the vicinity of the lip, resulting in a significant leakage through the tunnel walls. However, the results do appear to be a positive indication of the character of the flow development and are considered a satisfactory basis for the rig interference calculations where alternative methods are not applicable.

In redesigning the liner lip, the fundamental requirement is obviously to increase the bluntness of the section without generating sufficiently high local Mach numbers to cause the flow to choke in the throat. The Mach number distributions calculated for three lip designs are shown in Fig 21. Lip 1, the blunted ogive design, has comparatively low surface Mach numbers but, of course, has a delayed rise to a uniform working section flow. Lip 2, which uses a blunted ogive with a higher bluntness ratio, accelerates the flow more rapidly to a uniform level, but creates undesirably high velocities on the lip surface, which could lead to the flow becoming choked. Finally, lip 3, which uses a super-elliptic shape (ie an equation of the form $(x/a)^n + (y/b)^n = 1$), with a modified leading edge, reduces the suction peak whilst maintaining the improved acceleration to a constant working section Mach number.

The acoustic liner has now undergone testing in the ARA Transonic Wind Tunnel, using the Lip 3 design. No pressures are available on the lip itself, but measurements on the centreline calibration probe (Fig 21) indicate that there are no problems with the lip design. In fact, the results shown in Fig 22 show that stable Mach number distributions can be obtained in the liner up to $M_{2.40} = 0.9$. Beyond this value, a very small change in upstream Mach number results in the flow in the liner becoming choked, although this effect would be expected based upon area ratio considerations. However, the results show that the liner lip remains well behaved beyond the design requirement of $M = 0.85$.

3.5.2 Investigation of Working Section Modifications

The propellers tested in the acoustic liner will use one of two alternative model support systems. The first, which is a comparatively minor modification to the standard complete model support system, using a high pressure air supply to power the propeller, is not thought likely to cause significant interference. The second is a larger installation, designed to house two electric motors driving contra-rotating propellers. This is likely to have a more serious effect on the tunnel flow and therefore SPARV calculations were carried out to investigate the magnitude of the flow disturbance due to this model support, and to consider possible modifications to the liner walls to permit some compensation for this effect.

The acoustic liner and tunnel walls were modelled using 900 panels as shown in Fig 23. No attempt was made to represent the shape of the basic tunnel nozzle upstream or the diffuser downstream since these would be unlikely to have any effect on the interference between the model support and the liner representation. A further 900 panels were required to represent the model support body, including a long, parallel forward extension used to provide an indication of the magnitude of the rig interference in the vicinity of the propeller.

Calculations were carried out using SPARV in its inviscid mode. In this case, it would have been very desirable to compute the development of the boundary layer on the walls of the liner. However, these are made from perforated plate to ensure the effectiveness of the acoustic foam layer behind the walls, and the viscous module would not be appropriate for this type of surface. Consequently, an allowance for the boundary layer development was made empirically in addition to the computed wall interference calculations.

The effect of the large centre body on the Mach number distribution in a liner with parallel walls is shown in Fig 24a. Obviously, the main problem derives from the forward influence of the model support system which creates a pressure field extending upstream to the vicinity of the propeller plane. Further downstream, the flow accelerates around the model support and there is a risk of the flow becoming choked in this region before the required working section Mach number is achieved. In an attempt to alleviate these problems, modifications to the liner walls were considered. An example of the effect of a contoured surface is shown in Fig 24b, where the waisting of the liner is chosen to match the cross sectional area of the centre body. The Mach number distributions show that this has an excessive effect on the tunnel flow. Certainly, the velocities in the vicinity of the centre body are significantly reduced. However, the forward pressure field extends further upstream, into the working section of the liner. This is particularly apparent with the Mach number distributions in the plane of the propeller, shown in Fig 25, where there is an increase in the velocity near the walls due to the contoured surface, and a greater reduction near the centreline due to the forward pressure field of the centre body.

It is apparent from the results shown in Figs 24, 25 that significant changes in the flow field can be achieved by small modifications to the liner walls. In particular, the optimum design of the liner is obtained by a small divergence from the parallel walls shown in Fig 24a, rather than the major reshaping of Fig 24b. Results from the calculations permit these design changes to be investigated simply, enabling a balance to be obtained between the uniformity of the working section Mach number distribution and minimising the high velocities in the vicinity of the support body.

3.5.3 Investigation of the Microphone Traversing Rig

It has already been noted that the microphone position error requirements demand a structurally solid rig. In fact, the resulting MTR cross sectional area distribution gives a blockage in excess of 0.5% and, inevitably, this has a significant effect on the flow in the working section of the tunnel. In particular, the fore and aft movement of the rig means that an allowance must be made for the position of the rig in computing the tunnel Mach number.

The photograph of the MTR (Fig 26) makes it apparent that it cannot be represented accurately using a reasonable number of panels in the SPARV program. Two approximations to the rig have been considered to investigate its influence on the tunnel flow. Firstly, a body of revolution was used, matching the cross sectional area distribution of the MTR plus an assumed wake downstream of the body and legs of the rig. Secondly, the rig was represented slightly more accurately by treating the body as a body of revolution and the legs as thick 'lifting' surfaces. Again, a linear wake was assumed behind both the body and the legs of the rig.

Since the MTR is in close proximity to the walls of the liner, it was thought to be important to minimise the leakage through the walls for these calculations. Therefore, the liner working section was treated as a parallel tube, extending less far upstream and downstream than the representation used earlier and hence, permitting a denser panelling. The resulting modelling of the rig installed in the working section is shown in Fig 27, using a total of 1988 panels to represent the complete configuration.

The computed Mach number distributions on the tunnel port and starboard walls are shown in Fig 28. Comparison with the experimental measurements, shown as a band covering a wide range of propeller power settings, highlights some of the problems which can occur in using theoretical methods. It is apparent that there is a serious error in the calculations with the full MTR representation, whereas the equivalent body of revolution provides a sensible approximation to the effect of the rig on the tunnel flow. Consideration of the Mach number distribution at tunnel station 350 in shown in Fig 29, emphasises the reason for the difference between the two calculations. When the MTR legs are represented, the program predicts extremely high velocities between the legs, close to the body. This means that the velocities elsewhere in the field are significantly lower, in order to conserve mass flow. Obviously, this Mach number distribution is infeasible, and the program is being used beyond its range of applicability. However, the results can be interpreted as suggesting that this region could be a source of problems and that careful consideration should be given to the detailed design of the installation.

4 Conclusions

The aim of this paper was to demonstrate a variety of applications in which computational methods can assist in the design of wind tunnel rigs and in the interpretation of the measured results. It is concluded that:

- It is necessary to make various assumptions in using theoretical methods, both in the form of simplifications of the flow equations and the geometric representation of complex configurations.
- Care must be taken to ensure that geometric simplifications retain the aerodynamic characteristics of the problem to be solved. This may involve different representations of a given component for different applications.
- Theoretical calculations can provide valuable assistance in the design of wind tunnel rigs, ensuring an acceptable flow quality in the working section of the tunnel.
- The calculations can aid the interpretation of measured results, particularly when anomalous behaviour is found in the experiments.
- The calculations can provide results which permit the correction of experimental data and hence, improve the quality of the measurements.
- It is not anticipated that the theoretical methods will supersede the wind tunnel in the foreseeable future. However, it is important that theoretical and experimental techniques should become closely integrated so that the quality of predicted data can be improved.

References

- 1 Forsey, C R, An extension of a transonic wing/body code to include underwing pylon/nacelle effects, 1983, AIAA-83-1805.
- 2 Baker, T J, Mesh generation by a sequence of transformations, Journal of Applied Numerical Mathematics, Vol 2, No 6, 1986, pp 515-528.
- 3 Weatherill, N P, Shaw, J A, Forsey, C R, Rose, K E, A discussion of a mesh generation technique applicable to complex geometries, 1986, AGARD-CP-412, Paper 2.
- 4 Petrie, J A H, Description of the subcritical panel method SPARV, including first order viscous effects and wake relaxation, 1982, BAe Brough Note No YAD 3457.
- 5 Snyder, L D, Erickson, L L, Pan Air prediction of NASA Ames 12-foot pressure wind tunnel interference on a fighter configuration, 1984, AIAA-84-0219.
- 6 Sinclair, P M, A 3-dimensional field integral method for the calculation of transonic flow around complex configurations, Aeronautical Journal (to be published).
- 7 Baker, T J, Ogle, Mrs F A, A computer program to compute transonic flow over an axisymmetric solid body, 1977, ARA Memo 197.
- 8 Weatherill, N P, Shaw, J A, The simulation of inviscid flow around military forebody geometries using the Euler equations, 1987, ARA Memo 269.
- 9 Peace, A J, The calculation of transonic potential flow around inlet configurations, 1984, ARA Report 81.
- 10 Carter, E C, Pavitt, M, The operation and performance of the ARA cowl inlet test rig, 1976, ARA Memo 181.
- 11 Carter, E C, Hirst, W, Application of experimental and theoretical methods to validate results obtained on an isolated inlet cowl wind tunnel test rig, 1985, AIAA-85-5019.

Acknowledgements

The author would like to thank his colleagues at ARA for their assistance in the preparation of this paper. In particular, Mr A Baxendale provided the results for the Twin Sting Rig and Mr R Bryson provided the results for the Isolated Store Drag Rig. Work on the Isolated Store Drag Rig was carried out with the support of the Procurement Executive, Ministry of Defence.



FIG 1 PHOTOGRAPH OF THE ISOLATED NACELLE RIG
IN THE A.R.A. TRANSONIC WIND TUNNEL

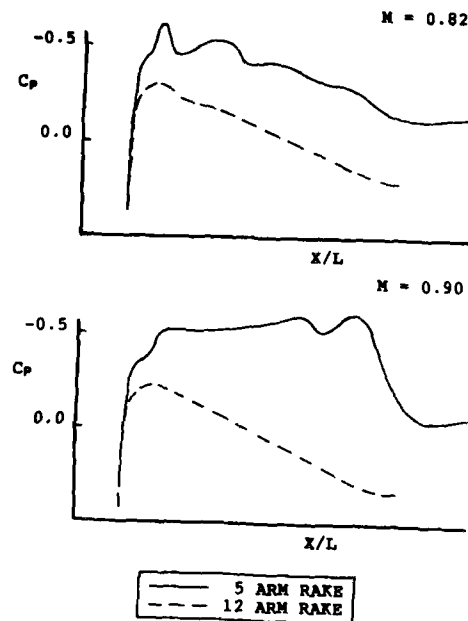


FIG 2 COWL FOREBODY SURFACE PRESSURES
WITH 5 AND 12 ARM RAKES

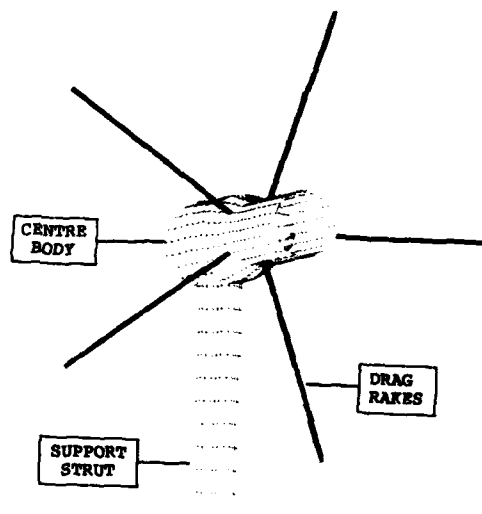


FIG 3 PANELLING OF THE ISOLATED NACELLE RIG
USED FOR SPARV CALCULATIONS

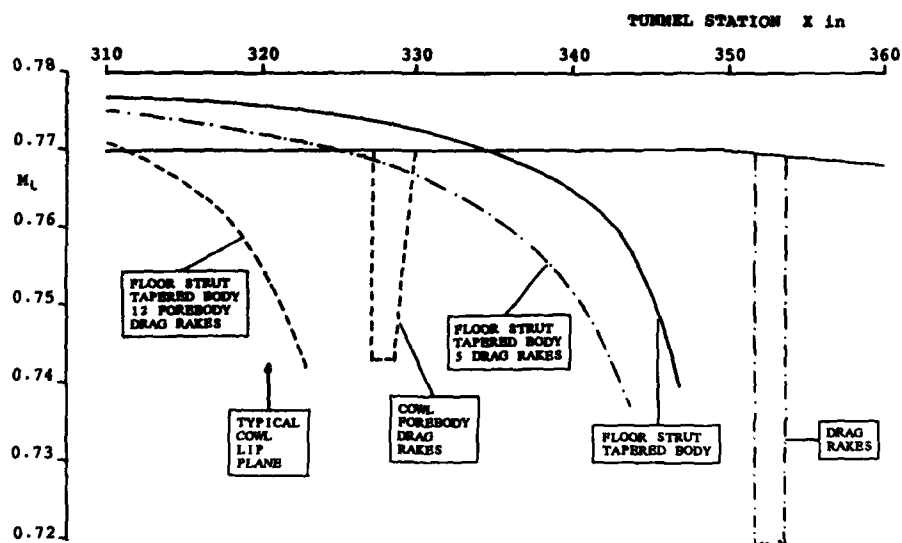


FIG 4 EFFECT OF BODY TAPER AND DRAG RAKES ON FOREBODY SURFACE MACH NUMBERS

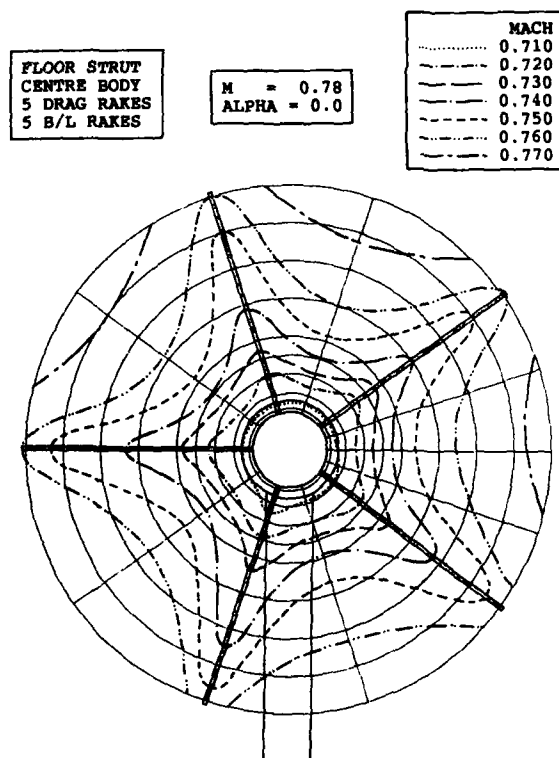


FIG 5 CALCULATED MACH NUMBER CONTOURS IN THE PLANE OF THE DRAG RAKES

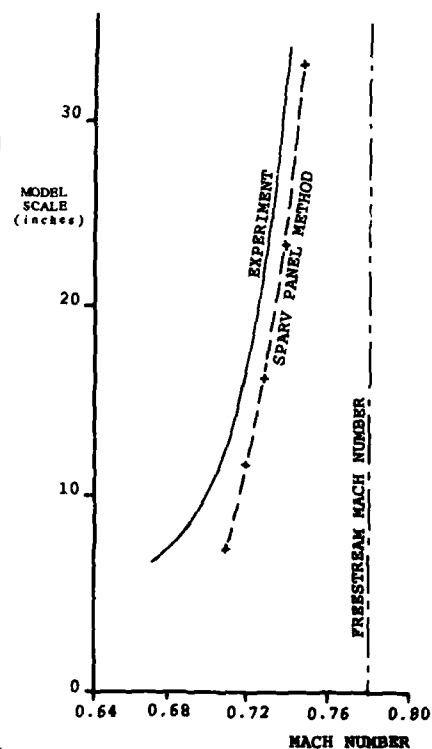


FIG 6 RAKE LOCAL MACH NUMBERS

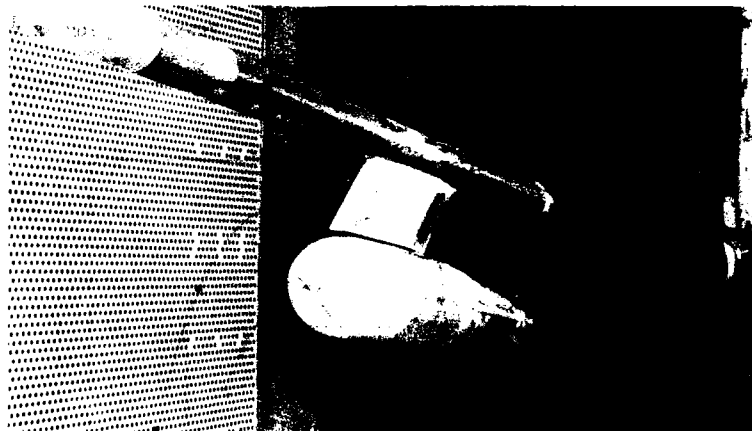


FIG 7 540 LB BOMB INSTALLED ON THE ISOLATED STORE DRAG RIG

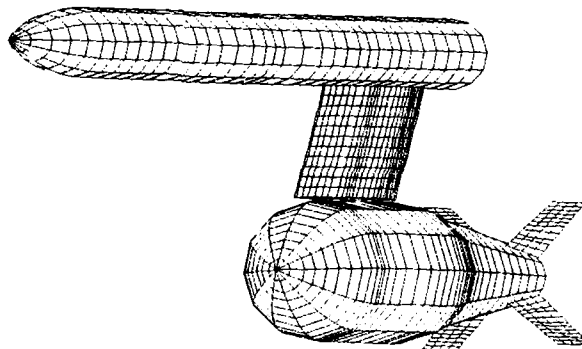


FIG 8 SPARV PANELLING OF THE ISOLATED STORE DRAG INSTALLATION

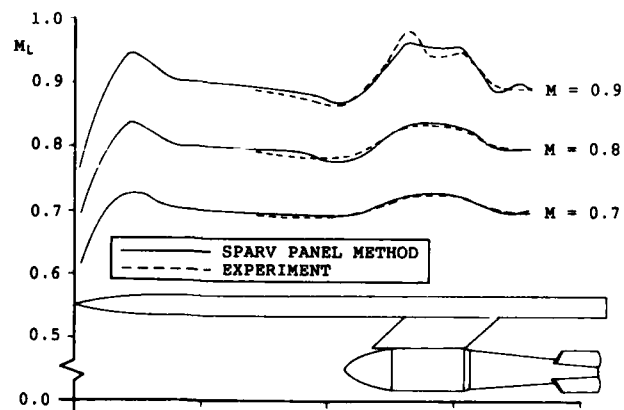


FIG 9 COMPARISON BETWEEN THEORETICAL AND EXPERIMENTAL MACH NUMBER DISTRIBUTIONS ALONG THE TOP OF THE SUPPORT TUBE

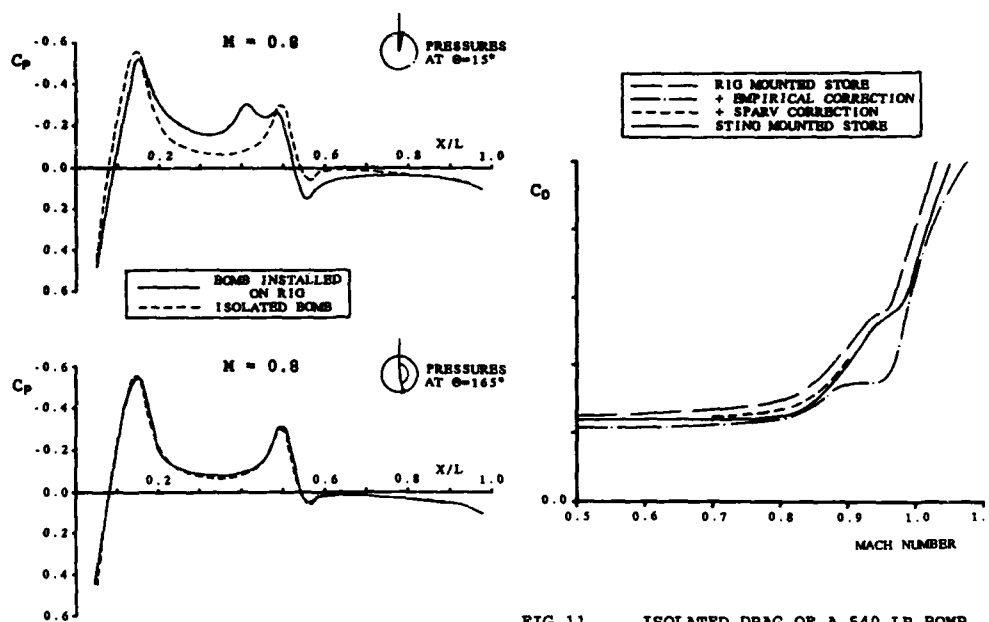


FIG 10 EFFECT OF THE 'ISOLATED' RIG ON THE BOMB SURFACE PRESSURE DISTRIBUTIONS



FIG 12 PHOTOGRAPH OF THE TWIN STING RIG INSTALLED IN THE ARA TWT

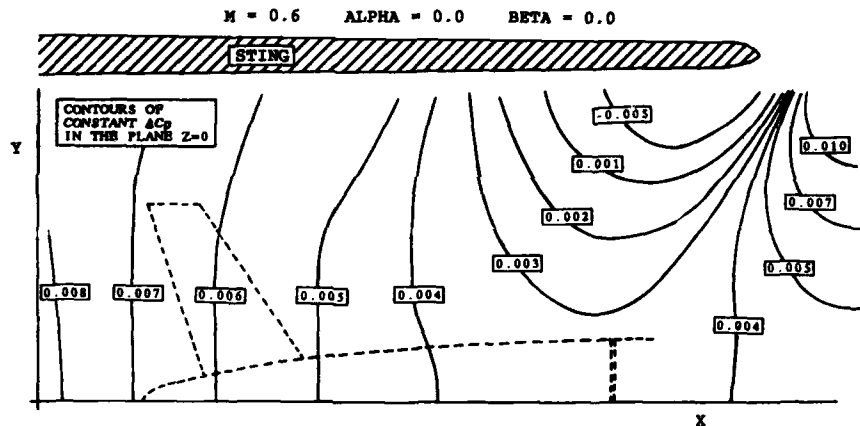


FIG 13 PRESSURE FIELD DUE TO THE TWIN STING RIG IN THE VICINITY OF A TYPICAL MODEL AFTERBODY

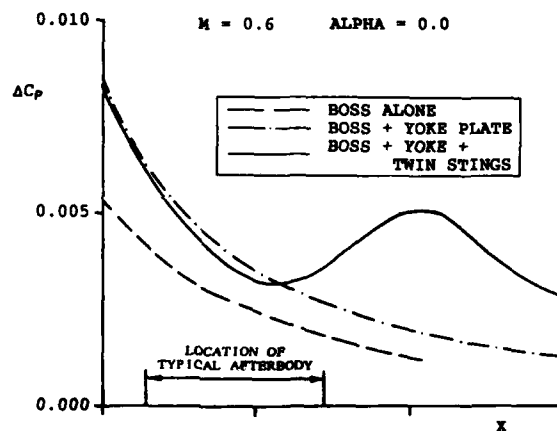


FIG 14 AXIAL PRESSURE DISTRIBUTION DUE TO THE COMPONENTS OF THE TWIN STING RIG

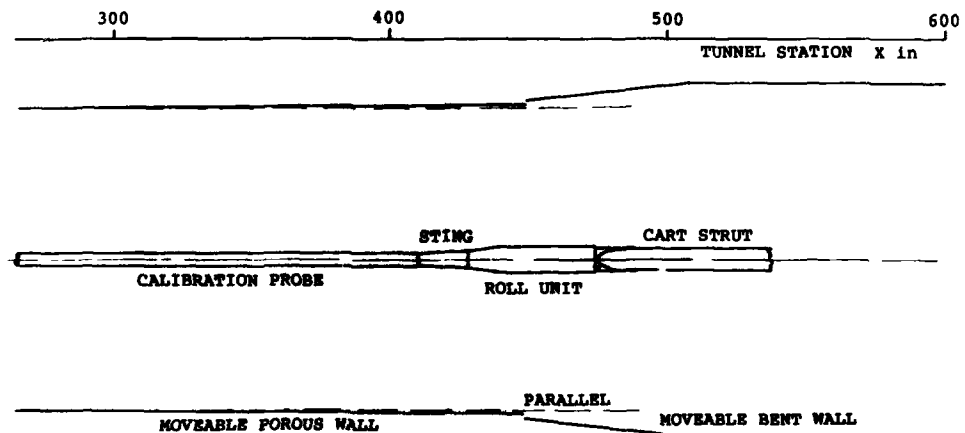


FIG 15 PLAN VIEW OF WORKING SECTION SHOWING CALIBRATION PROBE SUPPORT SYSTEM

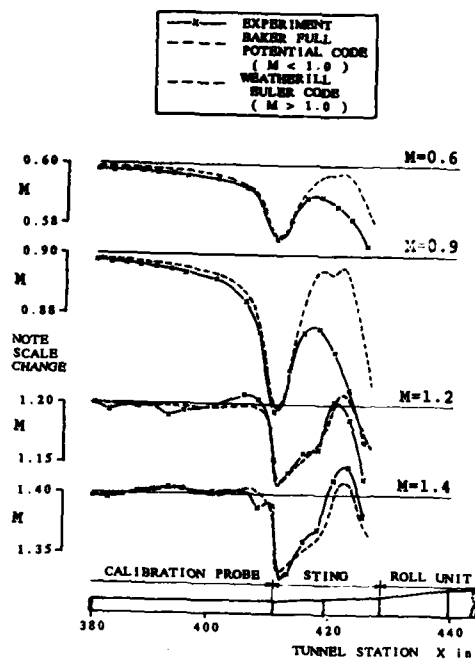


FIG 16 EFFECT OF THE TAPERED STING AND ROLL UNIT ON THE CENTERLINE MACH NUMBER DISTRIBUTIONS

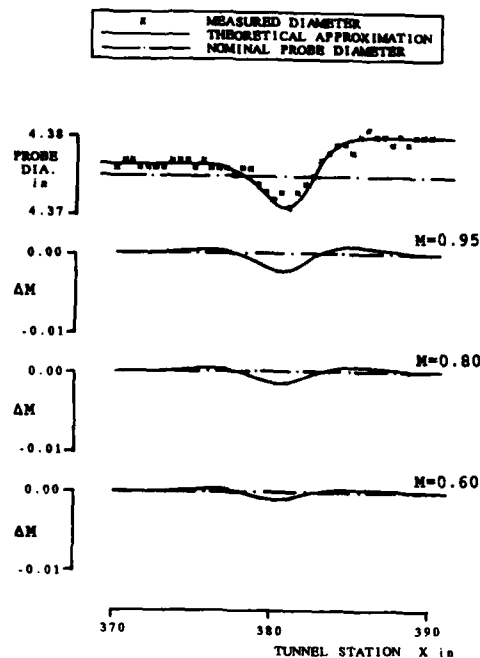


FIG 17 MACH NUMBER SIGNATURE OF CALIBRATION PROBE DUE TO MANUFACTURING TOLERANCE

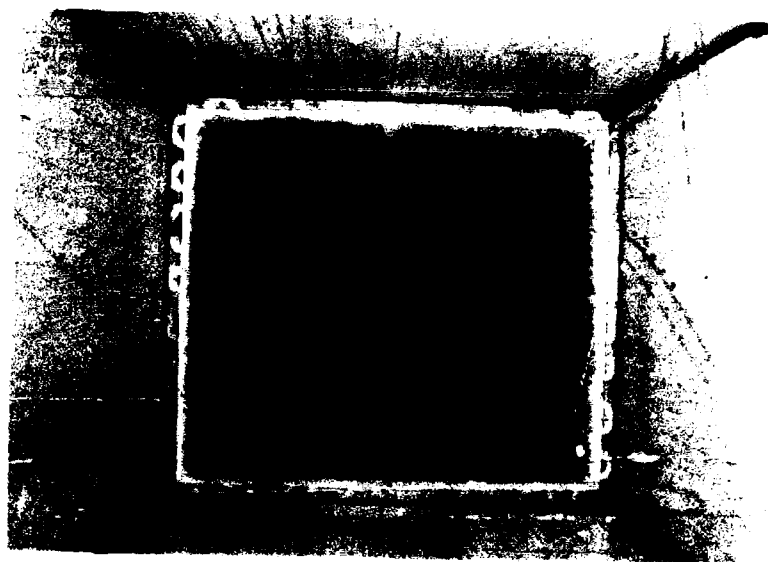


FIG 18 ACOUSTIC LINER INSTALLED IN THE ARA TRANSONIC WIND TUNNEL

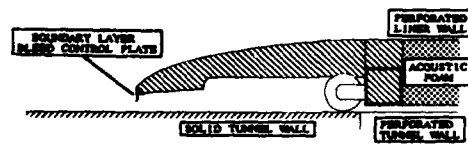


FIG 19a LINER INSTALLED IN THE TUNNEL

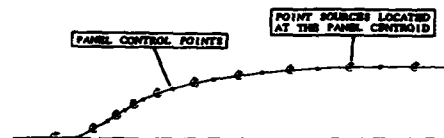


FIG 19b REPRESENTATION IN THE SPARV PROGRAM

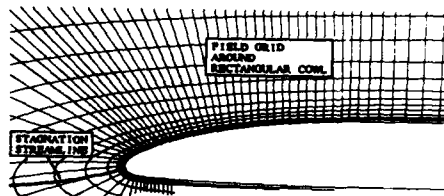


FIG 19c REPRESENTATION IN THE COWL PROGRAM

FIG 19 DETAILS OF LINER LIP AND ITS THEORETICAL APPROXIMATIONS

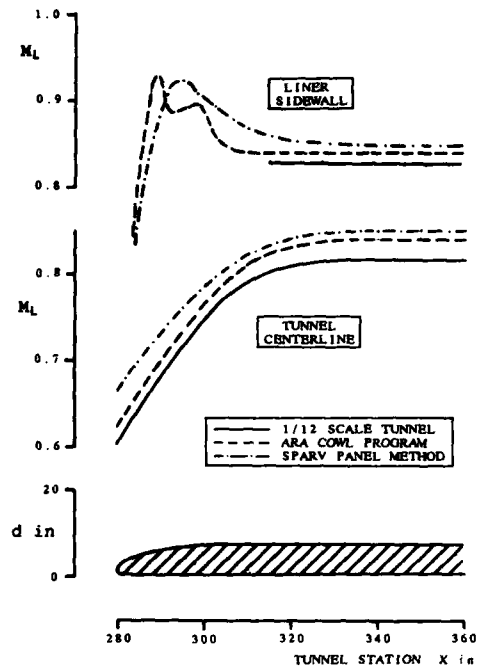


FIG 20 LIP 1 MACH NUMBER DISTRIBUTIONS

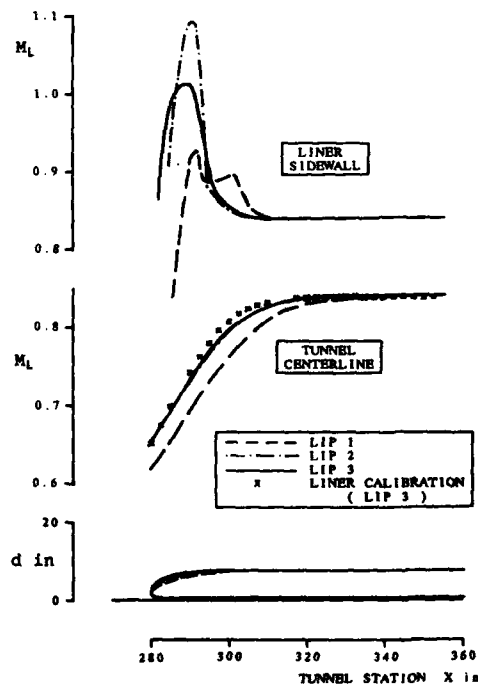


FIG 21 DESIGN OF THE INLET LIP FOR THE ACOUSTIC LINER

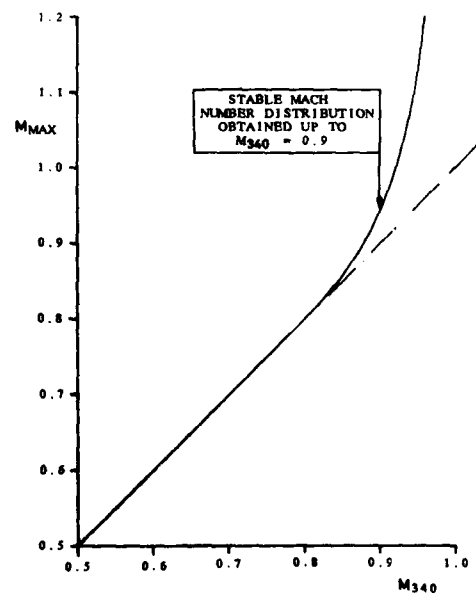


FIG 22 MAXIMUM MACH NUMBER IN LINER WORKING SECTION

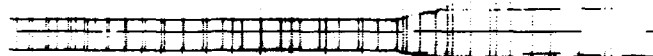


FIG 23 PANELLING OF LARGE MODEL SUPPORT BODY
IN LINER WORKING SECTION

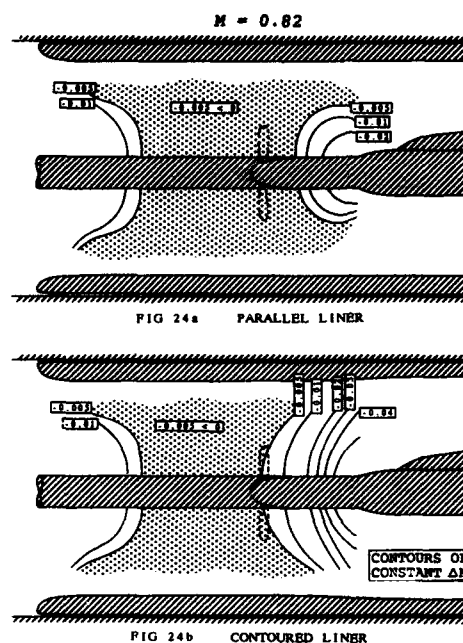


FIG 24 MACH NUMBER DISTRIBUTION IN THE
LINER WORKING SECTION

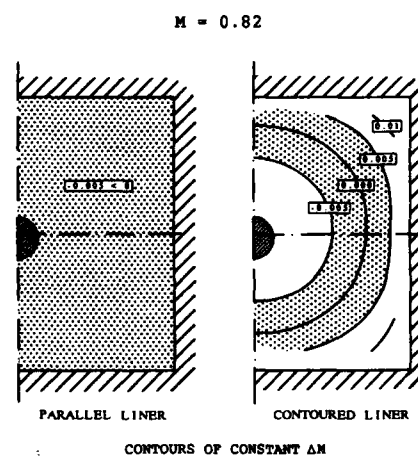


FIG 25 MACH NUMBER DISTRIBUTIONS IN
THE PLANE OF THE PROPELLER



FIG 26 PHOTOGRAPH OF THE MICROPHONE TRAVERSING
RIG INSTALLED IN THE ARA TRANSONIC WIND TUNNEL

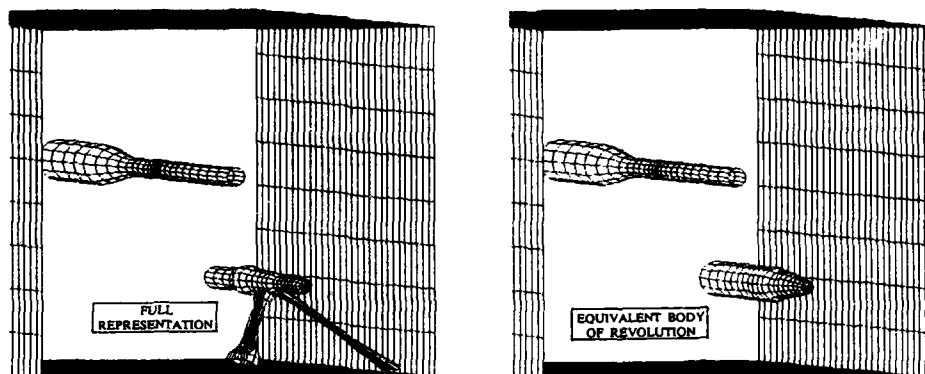


FIG 27 ALTERNATIVE REPRESENTATIONS OF THE M.T.R.

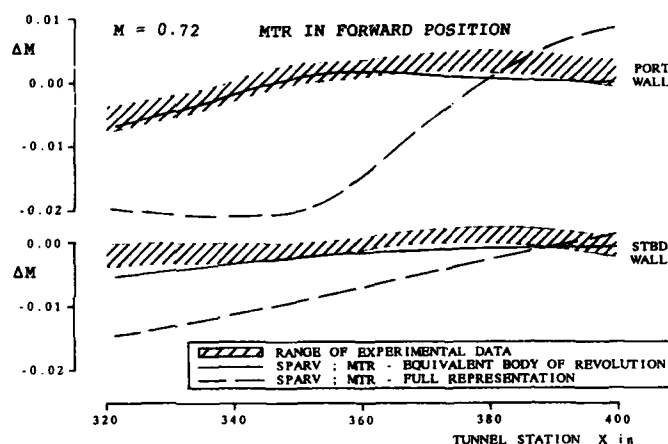


FIG 28 EFFECT OF MICROPHONE TRAVERSING RIG ON TUNNEL WALL MACH NUMBER DISTRIBUTIONS

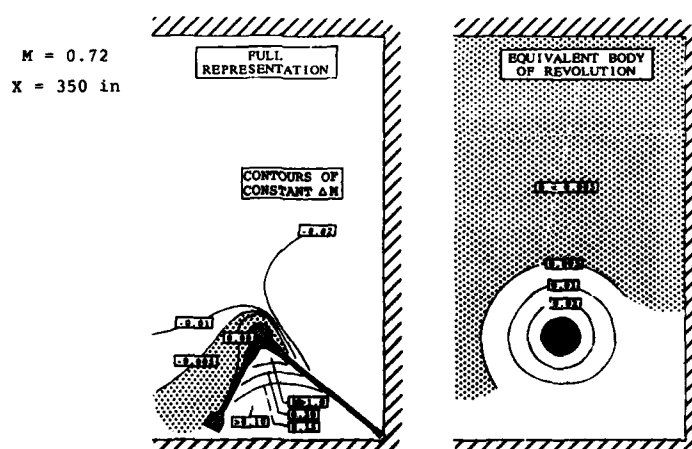


FIG 29 INCREMENTAL MACH NUMBER DISTRIBUTIONS DUE TO THE M.T.R.

ACCURACY OF VARIOUS WALL-CORRECTION METHODS FOR 3D SUBSONIC WIND-TUNNEL TESTING

by
R.A. Mearsingh, Th.R. Labrujère and J. Smith
National Aerospace Laboratory NLR
Anthony Fokkerweg 2
1059 CM Amsterdam
The Netherlands

SUMMARY

On the basis of wind-tunnel measurements on a (simple, unpowered, but complete) transport aircraft model in a small and a very large solid-wall test section the accuracy of four measured-boundary-condition (MBC) methods, as well as two classical methods, was analysed at low-speed conditions. Large reductions in the amount of in situ measured data are shown to be possible, yet yielding results which match almost with those of calculations using multiples of input data. Classical methods need not be abandoned at once in low-speed solid-wall testing. Higher priority should be given to the well-known interpretation problem: the determination of the actual model reaction upon the wall-induced flow field.

SYMBOLS

ALPHA	model (wing) incidence, corrected for wall interference	(deg)
B	breadth of test section	(m)
CD, CL	model force coefficients, corrected for wall interference	
CDT, CLT	uncorrected (test) values of CD and CL	
CM	pitching-moment coefficient (corrected)	
DA	difference in ALPHA between a corrected and a LST lift curve at the same value of CL	(deg)
DAL	model-incidence correction	(deg)
DCD	=DCDB+DCDI, total correction on CD	
DCDB	correction on CD due to (horizontal) buoyancy	
DCDI	correction on CD due to lift (upwash) interference at wing	
DCL	correction on CL due to incremental lift interference at horizontal tail	
DCM	=DCMC+DCMH, total correction on CM	
DCMC	correction on CM due to streamline curvature at wing	
DCMH	correction on CM due to incremental lift interference at horizontal tail	
DD, DM	difference in CD, CM resp., between a corrected curve CL vs CD, CL vs CM resp., and a corresponding LST curve at the same CL	
EFS	non-dimensionalized mean value of total correction on tunnel speed	
FW, FWB		
FWE, FWEH	notations for model configurations (see Fig. 1)	
H	height of test section	(m)
LST, MT	notations for large (LST 3x2.25) and small (MT 0.8x0.6) tunnel facility	
SF	cross-sectional area of model	(m ²)
S	model reference (wing) area	(m ²)
SW	semi-span of wing	(m)

1 INTRODUCTION

Wall interference is a well-known factor that degrades the accuracy and reliability of wind-tunnel data. Therefore, a large effort has been spent during the last decade to improve existing wall-interference assessment and correction methods. This effort resulted, among other things, in the by now well-known measured-boundary-condition (MBC) methods.

The most promising of these methods, theoretically at least, is of the so-called Cauchy-type, a "two-component" method which allows the calculation of the wall-induced perturbation velocity field throughout the test section, provided that all velocity components are known (i.e. measured) at the outer boundary (the tunnel walls). This method does not require any formulation of the model perturbation-flow field (the model representation). The only assumption is that irrotational subsonic flow prevails in the main part of the test section.

The basic idea is due to Ashill, et al., who applied it especially to solid-wall tunnels [1, 2]. At NLR this principle has been worked out further a few years ago. This resulted in a general method [3], from which several computer codes were developed characterized by various ways of reducing practical difficulties, i.e. measuring problems and/or long computing times. In order to evaluate these methods in a real wind-tunnel environment, a special experimental investigation was executed on a simple, unpowered low-speed aircraft model. The basic data were obtained in a solid-wall test section for which the model was fairly large, ensuring a sufficient amount of wall interference. In addition, the same model and its support system were tested in a much larger solid-wall test section, to obtain (almost) interference-free data.

The main question to be answered in the present paper is how the accuracy of the wall corrections is influenced by the measuring and/or computational efforts to be spent in producing them. To this end, the various wall-correction methods were applied to the basic data and the results were compared with the interference-free reference data.

2 EXPERIMENTS

2.1 Model and instrumentation

The main characteristics of the model and the two test sections are summarized in figure 1 and 2. The model was as simple as possible: a cylindrical fuselage, a rectangular wing provided with removable full-span flaps, and a removable horizontal tail. Thus, four different configurations could be selected. Because of the very low test Reynolds number (about 3×10^5 , based on wing chord) the wing-flap combination was designed carefully, in order to achieve a reasonably high lift ($CL_{max} \sim 2$).

The model dimensions were rather large (span-to-width ratio $y \sim .75$) relative to the small $0.8 \times 0.6 \text{ m}^2$ wind tunnel (MT), and very small relative to the large $3 \times 2.25 \text{ m}^2$ tunnel (LST). This is illustrated by including the orders of magnitude of the respective wall corrections in the table in figure 2. The model support (tail sting and strut) was identical in both test sections, apart from a necessary extension beam in the LST.

Model forces were measured by means of an internally mounted .75" Task (6-component strain gauge) balance, with ranges 600 N (normal force), 110 N (axial force) and 12 Nm (pitching moment), and an accuracy of about $\pm .1 \%$, $\pm .2 \%$ and $\pm .1 \%$ FSO respectively. The balance centre and moment reference point were located at the half-chord station of the wing. Model pressures were measured at one station on the wing, on the fuselage and inside the sting cavity (Fig. 3a), by means of a 3 psi Druck differential pressure transducer, having an accuracy of about $\pm .1 \%$ FSO, i.e. $\pm 40 \text{ Pa}$, corresponding with a $\Delta C_p \sim .02$ at the typical dynamic pressure of 2200 Pa. The pressures were scanned mechanically by means of a Scanivalve, mounted inside the fuselage as well. Forces measured simultaneously with model pressures were used only to monitor the tests. The proper force data were obtained with the pressure-measuring hardware removed.

The small test section was provided with 11 streamwise strips with 22 static-pressure holes each, distributed over the starboard half of the cross-sectional perimeter, complemented by 2 strips in the two corners (Fig. 3b). Only spanwise symmetrical conditions were considered. Thus, a rather dense grid of static-pressure stations was created. These pressures were measured by means of .5 psi and .75 psi Druck differential pressure transducers (accuracy $\sim \pm .2 \%$ FSO, or better).

All tests were performed with natural boundary-layer transition. The majority of the tests was carried out while varying incidence at constant Reynolds number (about 3×10^5 , based on wing chord). Some additional tests were performed with variable velocity, in order to assess the Reynolds-number sensitivity of the data.

2.2 Data reduction

The model data were subjected to the usual corrections (empty-tunnel calibration, model weight, sting deflection, etc.). Also the wall-pressure data were corrected by subtracting the corresponding empty-tunnel data therefrom. The term "empty tunnel" should be understood as a situation without model, but with model support. Force and pressure data are presented in the usual coefficient form, using dynamic pressure and wing area and chord as reference quantities. The correction for flow angularity was determined in the usual way, i.e. from a comparison of the force data obtained with "normal" and "inverted" model attitude. Herewith a support-interference effect on the pitching moment in both test sections was found, albeit not of the same magnitude. Also this effect has been taken into account in the form of a correction on CM. The small test-section data are to be considered as "uncorrected data", however, in terms of wall interference.

The LST results were corrected, in a conventional (classical) way, for the (very small) wall interference in the large test section, thus creating the best possible interference-free reference data.

2.3 Quality of experimental data

From repeated runs at a Reynolds number of about 3×10^5 the following figures were established for the repeatability in the small test section (MT).

QUANTITY	REPEATABILITY		
	BEST	WORST	MEAN
LIFT (CLT)	$\pm .0010$	$\pm .0080$	$\pm .0040$
DRAG (CDT)	$\pm .0003$	$\pm .0010$	$\pm .0005$
P.MOM (CMT)	$\pm .0010$	$\pm .0080$	$\pm .0030$

It may be noted, that lift and drag coefficients could be reproduced within some permills of their maximum measured values. This corresponds with about one permill of the respective ranges of the balance at worst. The pitching moments are clearly less satisfactory, showing a scatter of some percents of the maximum measured value or several permills of the range of the balance.

LST results were similar for lift and drag but somewhat better for the pitching moment.

Model- and wall-pressure coefficients could generally be reproduced, within about $\pm .0025$, corresponding

with about one permill of the transducer range values (.5 psi and .75 psi) for the wall pressures, and even better for the model pressures. Incidence setting was accurate to within a few hundredths of a degree.

3 WALL-INTERFERENCE ASSESSMENT AND CORRECTION METHODS

The several methods, presently applied to spanwise-symmetric conditions only, differ only with respect to the assessment of the interference velocity field. The interpretation of these interference velocities in terms of corrections to the measured data are similar for all methods. The assessment part of the methods will be characterized here briefly; more details are given in the final report [11].

The method referred to as WIN3D is a MBC method based on velocity-vector distributions, known on a control surface enclosing the model [3].

They are calculated, by means of a finite-difference technique, from measured wall-pressure and normal-velocity distributions, the latter of which is identically zero in the present (solid-wall) case. All WIN3D results have been calculated using all wall-pressure data (13 pressure strips). These calculations take roughly 20 sec. on a CDC Cyber 180/855, thus excluding the possibility of on-line operation. In addition, the amount of wall pressures used is hardly attractive for routine testing. Nevertheless, WIN3D may be considered as the "most sophisticated" method.

The results labeled "WIN3D4L" were also obtained by means of the computer program WIN3D, however, using a very limited set of wall data, viz. only strips 1, 5, 7 and 11 (Fig. 3b), and an interpolation of C_p along the perimeter of each test-section cross section. Even then, the computing time is too long for on-line calculations. However, it is intended to show the accuracy attainable with a "minimum" amount of measured wall pressures which seems practicable for routine testing, if only combined with a post-processing stage.

The method WIN3QT uses the same limited set of wall data as WIN3D4L. In addition, computing time is reduced so much that on-line processing on a local computer (such as a HP1000) is feasible. This is realized by omitting the finite-difference calculation and using approximate velocity-pressure relations instead.

WIN3MOV is a MBC method of a different type. It relies on measured wall pressures, instead of velocity vectors, in combination with a "model representation", using a Fourier-series interpolation as proposed by Mokry [4]. It uses pressure data from strips 1, 6 and 11 only (Fig. 3b), but can presently not be used in on-line fashion because of its (time consuming) "panel-method" formulation. It is less versatile than WIN3D and WIN3QT and will not be used for solid-wall test sections. It is of interest, however, for ventilated-wall tunnels until the problem of measuring wall-velocity vectors will be solved.

The "classical" correction method is basically the method of images. The version labeled CLASO (acronym for classical old) was until recently standard for NLR solid-wall tunnels and is based on small-model assumptions [5, 6 and 10]. The other, called CLASN (classical new), is more sophisticated and has been derived for relatively large, but conventional, low-speed transport aircraft models, combining ideas from relatively recent references [6-9].

4 ANALYSIS

4.1 Relative importance of corrections

The relative importance of the several terms constituting the correction of a lift vs. incidence curve is illustrated in figure 4. It is seen, that the blockage correction and the tail-plane interference correction on C_L , though not insignificant, are of minor importance relative to the strongly predominant incidence correction (DAL).

A similar exercise with the lift-drag polar (Fig. 5) also shows a strongly predominant term, i.e. the induced-drag correction (DCDI). In case of the pitching moment (Fig. 6), the correction term connected with the horizontal tail plane (DCMH) predominates.

Although these results, obtained with the most sophisticated method WIN3D, apply specifically to the present model, it seems reasonable to state, that the strong predominance of the "lift-interference" correction terms, acting on both the wing and (local) tail angle of incidence, is typical for low-speed tests on conventional transport aircraft models. Therefore, these terms will be analysed in detail.

4.2 Principal lift-interference corrections

Typical for the principal lift-interference correction quantities DAL, DCDI and DCMH are simple relationships with measured (uncorrected) lift:

$$DAL \div CLT, DCDI \div (CLT)^2, DCMH \div CLT.$$

Comparisons of the quantities DAL/CLT , $DCDI/(CLT)^2$ and $DCMH/CLT$, calculated by means of the various methods for the complete model (FWM), are illustrated in figure 7, 8, and 9, respectively. In contrast with classical methods, all MBC methods yield corrections with small or larger variations around a mean value, seemingly resulting from inaccuracies which may be larger at smaller lift coefficients.

Assuming that the WIN3D results are the most accurate ones, it is remarkable in figure 7 that the older classical (CLASO) angle-of-attack correction seems to show better agreement than the newer one (CLASH). The opposite is true, however, for the pitching-moment correction due-to- tail (Fig. 9), the CLASO result showing a largely overestimated tail-plane interference. This can be attributed to the fact that CLASO only roughly approximates the upwash at the tail, whereas the other methods actually calculate this local value.

Remarkable harmony between the classical methods is to be seen in figure 8, where both tend to overestimate the induced-drag correction.

As for the MBC methods, a close agreement between WIN3D and WIN3D4L is found generally, whereas the less allied methods WIN3QT and WIN3MOV often show deviations of the same order of magnitude as the classical ones.

Effects of the model configuration (not shown here), on the main lift-interference quantities could not be found to a significant extent, as distinct from blockage where a significant configuration effect (due to flap deflection) was found.

In view of the minor importance of blockage in conventional low-speed tests (i.e. at not-too-high incidence or lift, with small or no flow separation), it may be concluded that overall configuration effects will generally remain within bounds in low-speed tests.

This may be important for wind-tunnel investigations where only differences between various configurations are sought. Any wall-interference effect that is common to the various configurations will, of course, not appear in the increments.

4.3 Comparison with interference-free data

The present analysis concentrates upon the principal aerodynamic characteristics, in their globally corrected form, i.e. the curves CL vs incidence, CL vs CD and CL vs CM. Other issues, e.g. Reynolds sensitivity, exercises with model pressures, etc., are included in the final report [11].

Results to be discussed here are summarized in figure 10-12. For all four model configurations the upper part (a) shows corrected curves (for WIN3D only) compared with the corresponding LST curves, whereas the lower part (b) shows the remaining discrepancies between corrected and LST curves for both WIN3D and the other methods.

The latter diagrams have been constructed from curves similar to the former by subtracting LST values of incidence (ALPHA), drag (CD) and pitching moment (CM) respectively, from corrected values at the same discrete values of the ordinate CL. In this way a complete survey is shown of the qualities of all correction methods.

At first sight, the agreement between corrected and LST curves (Fig. 10a, 11a and 12a) often seems acceptable, considering that the corrections are quite large (Fig. 4-6). Nevertheless, especially in CD and CM, sometimes discrepancies can be found which exceed 10 % of the correction itself.

As a general trend to be seen in figure 10b, 11b and 12b it may be noticed, that these curves for one same configuration always show a close affinity, in that a common sequence of peaks and dips is present. Obviously, this stems from typical differences between the basic (uncorrected) MT curves and LST curves, rather than from the various correction methods.

Further, an undercorrection, i.e. a negative value of DA, DD and DM, is much in evidence, often showing a negative mean slope, i.e. an increasing undercorrection with increasing CL. The fact that this slope is mostly present in all methods, albeit not with the same magnitude, may indicate that this feature is caused by possible imperfections in the interpretation of the wall-induced flow field in terms of corrections rather than in its calculation. Typical differences between the various methods, observed earlier with respect to the principal lift-interference corrections (Fig. 7-9), are also found in figure 10b, 11b and 12b, of course.

The discrepancies in lift vs incidence curves (Fig. 10b), especially for the model configurations without flap (FW and FWH), remain roughly within a band of ± 1 deg., whereas for configurations with flap (FWF and FWPH) a clear tendency to undercorrection occurs for all methods except CLASH. Apparently, a negative slope is the rule rather than the exception.

A remarkable feature is that, especially for the complete model (FWPH), CLASH and to some extent also WIN3MOV seem to be superior to the other methods, including WIN3D. The methods CLASH and WIN3MOV are also conspicuous in showing no clear slope.

The tendency of CLASH and WIN3QT to give too large angle-of-attack corrections (Fig. 7) can be found here only to some extent for configurations without flap. Another important point to be mentioned once more is that results from WIN3D4L, i.e. the method with a minimum input of measured wall pressures, differ hardly from those using all wall data (WIN3D). This feature holds also for the CD and CM curves to be discussed subsequently.

The results for the lift vs drag curves (Fig. 11) have much in common with the previous ones.

A striking issue is a much more clear difference between configurations without flap and those with flap. In the former cases (FW and FWH) the discrepancies in CD are about within experimental error, apart from very small and very large values of CL and except for CLASH and CLASO at FWH, whereas the latter configurations (FWF and FWPH) are undercorrected by some tens of counts in CD.

The smaller discrepancies found with the classical methods for configurations with flap, as well as the overcorrections for configurations without flap, may be attributed to the relatively large induced-drag corrections of these methods found earlier (Fig. 8).

In the pitching-moment curves (Fig. 12) large differences in the discrepancies between configurations with and without horizontal tail are found.

For tailless configurations (FW and FWH) very little difference between the correction methods can be established; all methods yield corrections which amount to only one half of the difference between the (uncorrected) MT and LST results. Presumably, this is caused by a streamline-curvature effect on the fuselage: an incremental upwash at the rear of the fuselage induced by the walls, which is not, and can hardly be, accounted for in any existing correction method.

In the results of the tail-on configurations, especially FWH, many features can be traced back directly to those of the correction term DCM (Fig. 9): a close agreement between WIN3D, WIN3D4L and CLASH, a large overcorrection for CLASH and intermediate results for WIN3QT and WIN3NOV. Merely the large dip in the discrepancy curves for configuration FWH at intermediate values of CL is rather strange and difficult to explain. Apart from this peculiarity, which stems from the basic (uncorrected) NT results rather than from the wall-correction methods, also these curves show the trends mentioned.

5 CONCLUDING REMARKS

The differences between the various sets of corrected data can be attributed to the mutual differences in the mathematical formulations of the respective methods. This is supported by earlier numerical evaluations [3, 11], from which it was concluded also, that a) the MHC methods as considered here are versatile tools for calculating the wall-induced velocity field in any case where the underlying assumptions of subsonic irrotational flow are met, and that b) with respect to the accuracy of this assessment the most sophisticated method WIN3D is superior to all other MHC methods considered here.

The differences between the various sets of corrected data on the one hand and the interference-free LST data on the other, all show similar trends. Therefore, it is evident that these discrepancies must be related to imperfections in the correction procedure (which was identical for all methods but CLASH) used to "translate" the wall-interference velocities into meaningful corrections.

An important result is, that a classical method like CLASH seems comparable with WIN3D. It must be stressed, that this may only be the case for relatively simple models, since CLASH requires a (potential-flow) simulation of the model flow. On the other hand, it may be expected that WIN3D will uphold a same confidence level for more complex models as a classical method for simple models.

Very important, from a practical point of view, is the good correspondence between WIN3D and WIN3D4L, indicating that the quantitative demands on in situ measured wall data can be reduced considerably.

Further improvements of wall-correction methods probably should be pursued, not necessarily by improving the assessment methods, but by upgrading the correction procedures. This will be even more urgent in cases of more complex low-speed model flows (jets, propellers, rotors, etc). Alternatively, the correctability of the data should be improved, e.g. by means of adaptive walls.

6 REFERENCES

1. Ashill, P.R. and Weeks, D.J.: A method for determining wall-interference corrections in solid-wall tunnels from measurements of static pressure at the walls, AGARD-CP-335 (1982), Paper 1
2. Ashill, P.R. and Keating, R.F.A.: Calculation of tunnel wall interference from wall-pressure measurements, RAE Technical Report 85086 (1985)
3. Labrujère, Th. E.: Correction for wall interference by means of a measured-boundary-condition method, NLR TR 84114 U (1984)
4. Mokry, M.: Subsonic wall-interference corrections for finite length test sections using boundary pressure measurements, AGARD-CP-335 (1982), Paper 10
5. Fankhurst, R.C. and Holder, D.W.: Wind-tunnel technique, Pitman & Sons, London (1948)
6. Garner, H.C. et al.: Subsonic wind-tunnel wall corrections, AGARDograph 109 (1966)
7. Schleicher, M.: Über den Einfluss des Anstellwinkels auf die Verdrängungs-korrektur bei Windkanal-Messungen, Eidg. Flugzeugwerk Emmen, Bericht FO-1221 (1976)
8. Maskell, E.C.: A theory of the blockage effect on bluff bodies and stalled wings in a closed wind-tunnel, RAE Report No. Aero 2683 (1963)
9. Vayssière, J. -Ch.: Correction de blocage dans les essais en soufflerie. Effets des décollements, AGARD-CP-102 (1972)
10. Theodoresen, T.: The theory of wind-tunnel interference, NACA Rep. 410 (1931)
11. Labrujère, Th. E., Maarsingh, R.A. and Smith, J.: Optimisation and evaluation of various measured-boundary-condition methods for 3D subsonic tunnel-wall interference, Final report, to be published

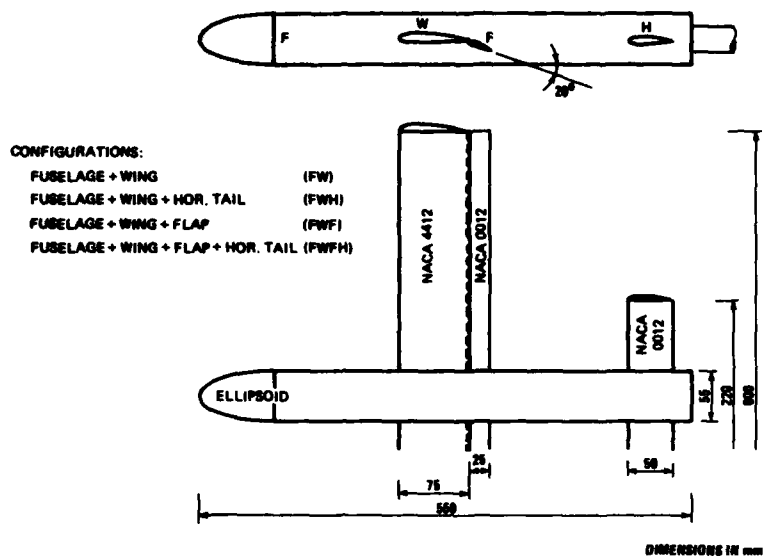
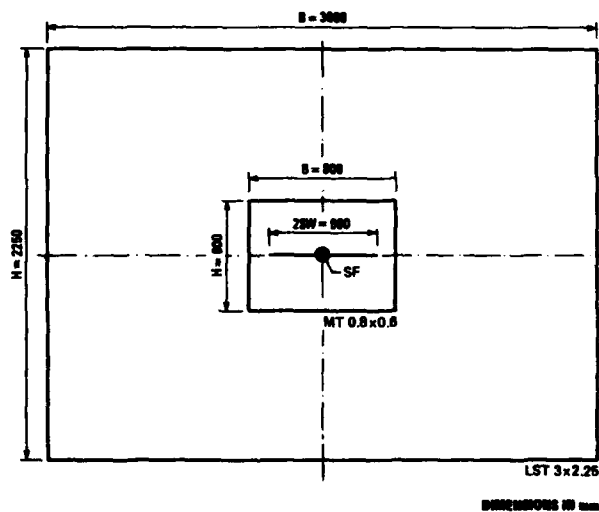
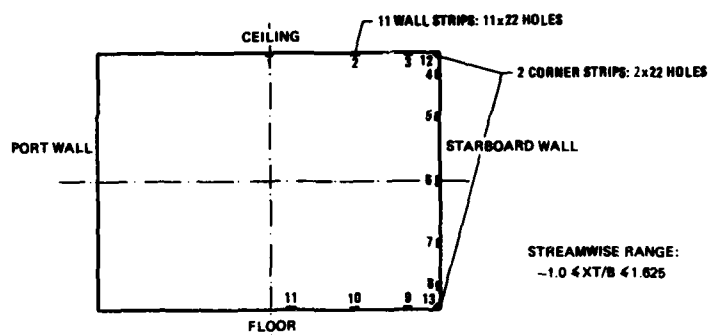


Fig. 1 Subsonic wall-interference model (SWIM)

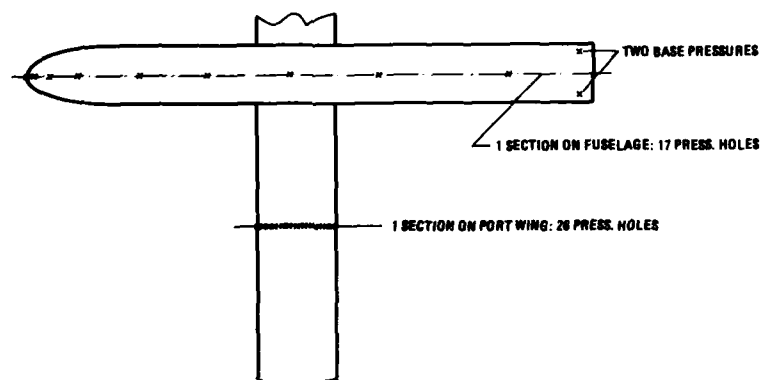


TUNNEL FACILITY	RELATIVE MODEL DIMENSIONS			ORDER OF MAGNITUDE OF WALL CORRECTIONS					
	$2B/H$	B/H	$SF/B.H$	EP	DAL/CL	$DALN-DAL/CL$	DCI/CL	DCB/CL^2	DCM/CL
MT 0.8x0.8	0.75	0.004	0.010	<0.01	0.05°	0.3°	-0.01	0.01	0.02
LST 3x2.25	0.20	0.007	0.0012	<0.0002	0.05°	0.007°	-0.0002	0.0006	0.0004

Fig. 2 Model/tunnel characteristics



b) PRESSURE STATIONS ON TUNNEL WALLS MT 0.8x0.6



w) PRESSURE STATIONS ON MODEL

Fig. 3 Number and positions of static-pressure holes on model and on strips mounted on wind-tunnel walls of the (small) MT 0.8x0.6

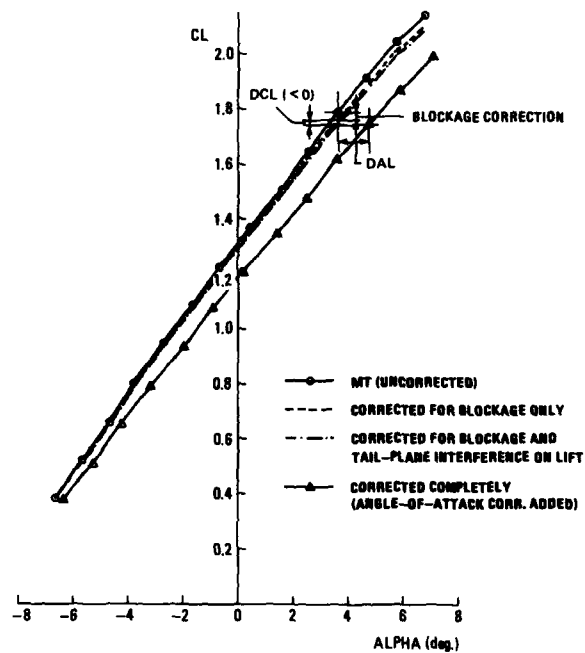


Fig. 4 Step-by-step correction of lift curve by means of WIN3D

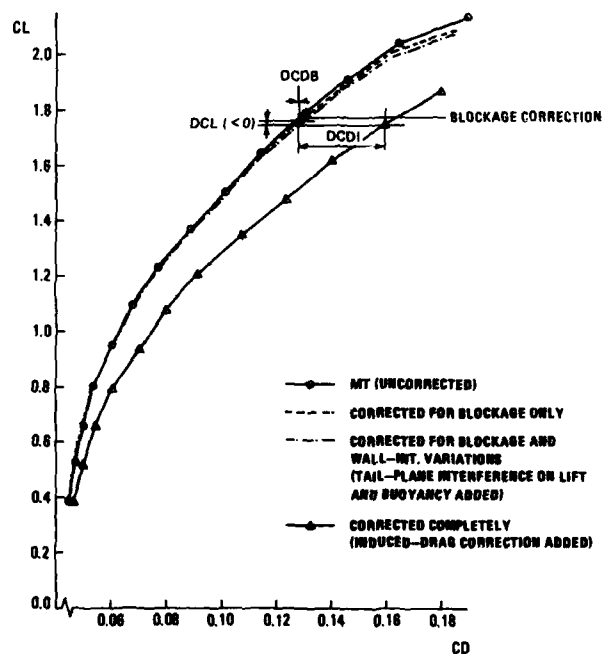


Fig. 5 Step-by-step correction of CL vs. CD curve by means of WIN3D

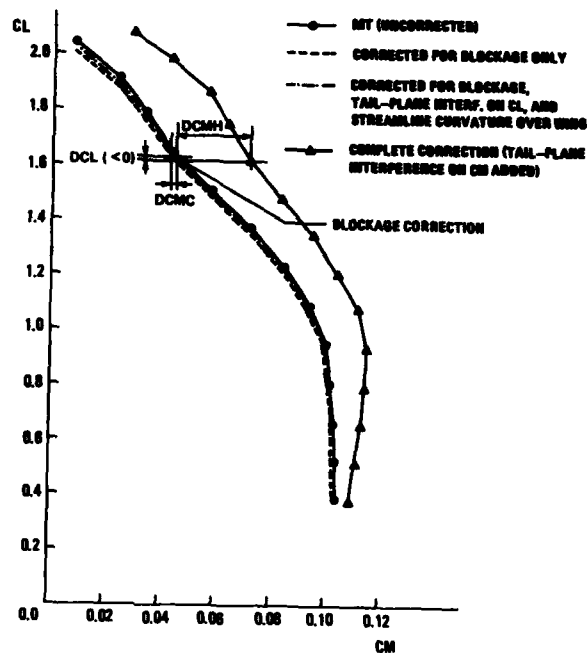


Fig. 6 Step-by-step correction of CL vs. CM curve by means of WIN3D

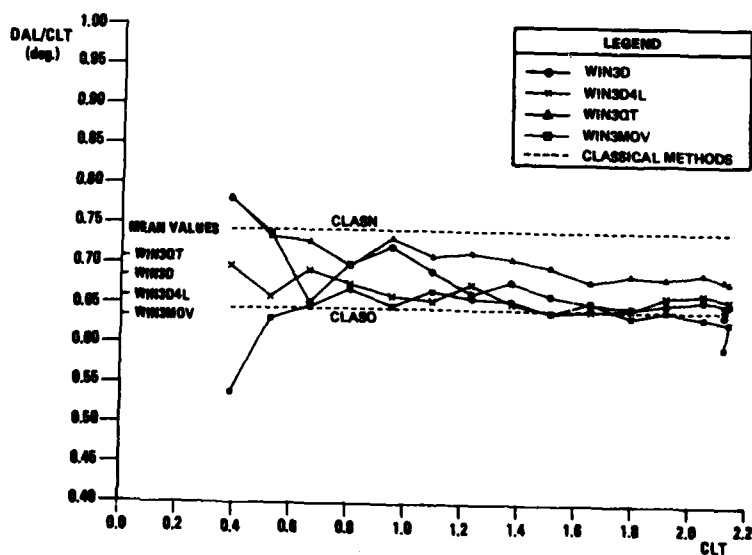


Fig. 7 Angle-of-attack correction acc. to HEC methods; complete model (FWFM) in NT

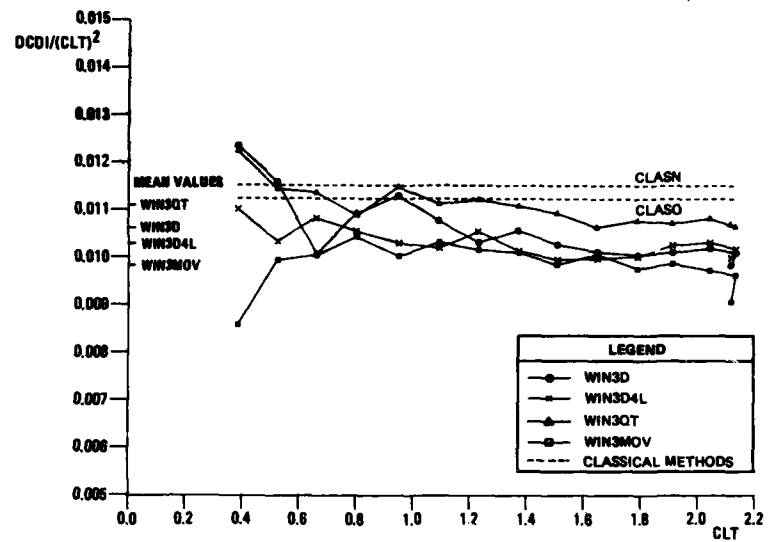


Fig. 8 Induced-drag correction acc. to MBC methods; complete model (FWFH) in NT

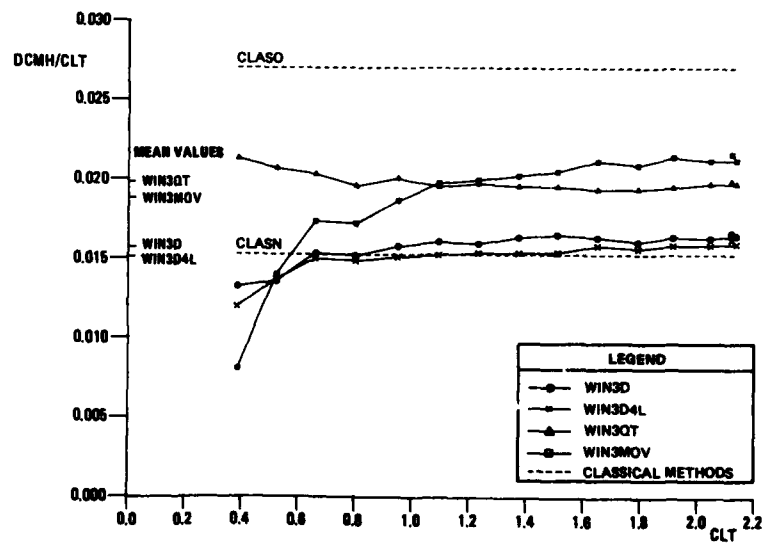
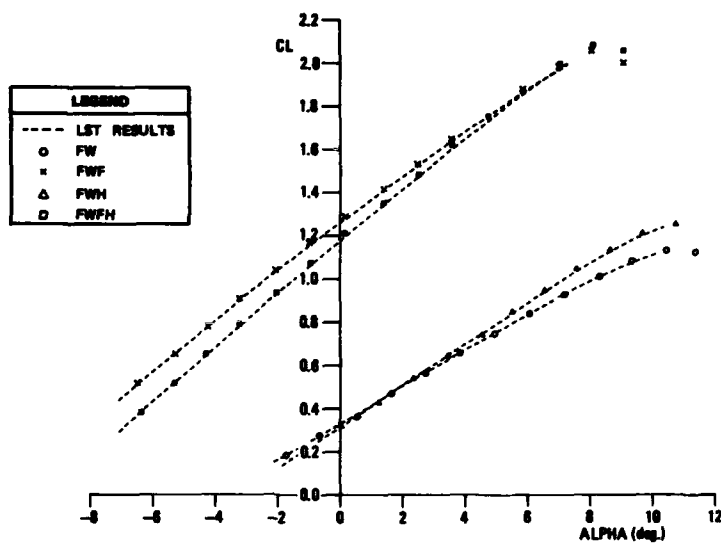
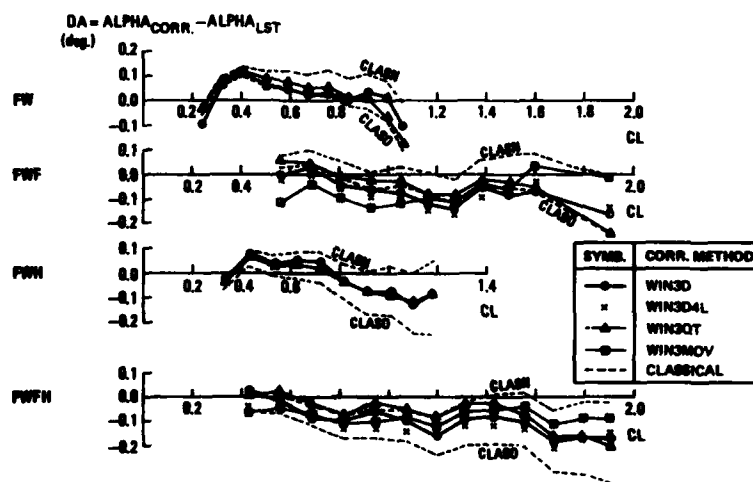


Fig. 9 Pitching-moment correction acc. to MBC methods; complete model (FWFH) in NT

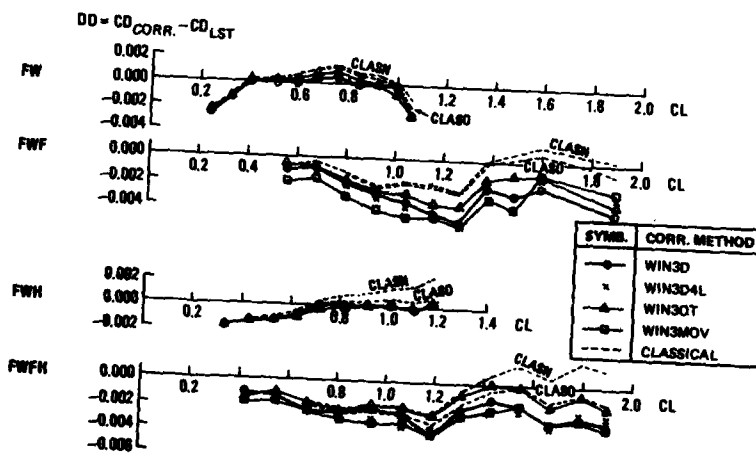
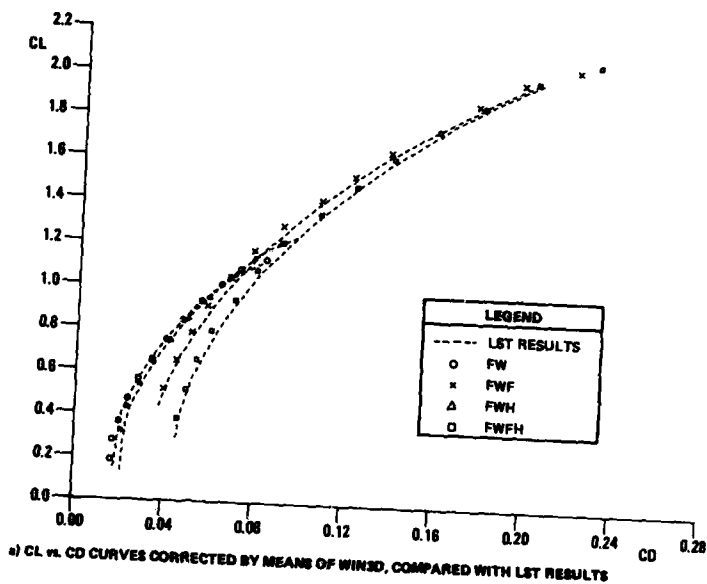


a) LIFT CURVES CORRECTED BY MEANS OF WINSD, COMPARED WITH LST RESULTS



b) DISCREPANCIES IN CORRECTED LIFT CURVES

Fig. 10 Corrected lift curves compared with LST results



b) DISCREPANCIES IN CORRECTED CL vs. CD CURVES

Fig. 11 Corrected CL vs. CD curves compared with LST results

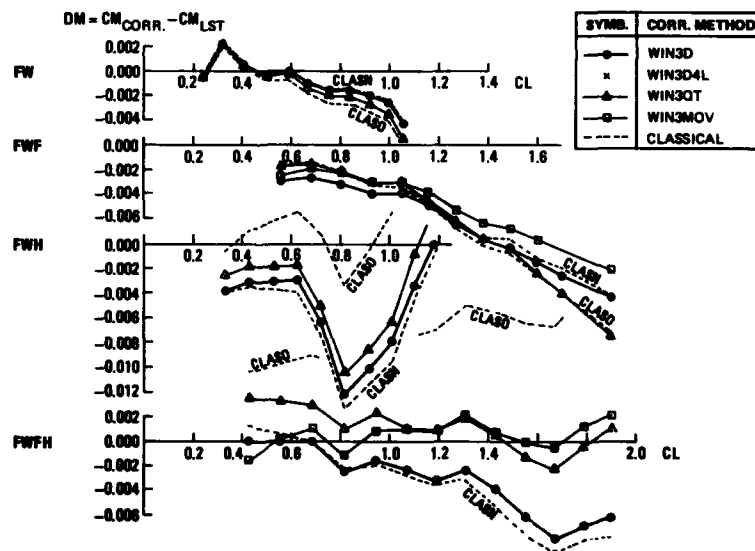
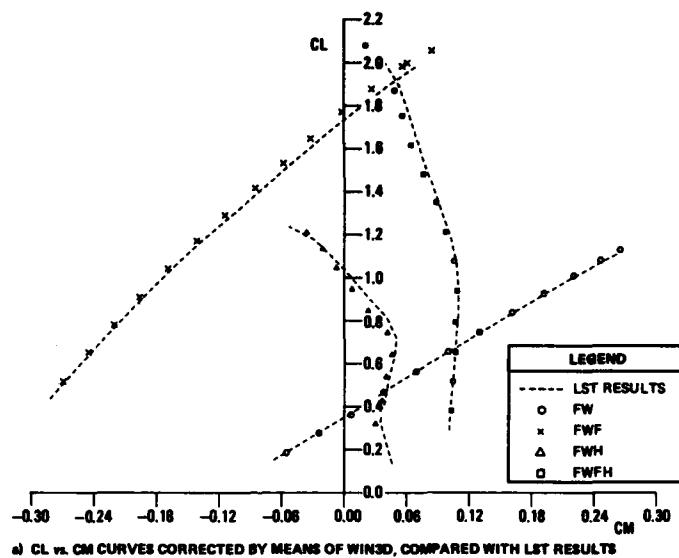


Fig. 12 Corrected CL vs. CM curves compared with LST results

WIND-TUNNEL - SIDEWALL - BOUNDARY-LAYER EFFECTS IN TRANSONIC AIRFOIL TESTING - SOME CORRECTABLE, BUT SOME NOT

by

F.T. Lynch, Technology Program Manager
Douglas Aircraft Company, McDonnell Douglas Corporation
3855 Lakewood Boulevard
Long Beach, CA 90846, USA

and

C.B. Johnson, Senior Aerospace Engineer
Transonic Aerodynamics Division
NASA Langley Research Center
Hampton, VA 23665-5225, USA

SUMMARY

The need to correct transonic airfoil wind-tunnel-test data for the influence of the tunnel sidewall boundary layers, in addition to the well accepted corrections for the restraining effect of the top and bottom walls, is addressed. A systematic experimental/analytical investigation has been carried out in order to evaluate sidewall-boundary-layer effects on transonic airfoil characteristics, and to validate proposed corrections and the limit to their application. This investigation involved testing of modern airfoil configurations in two different transonic airfoil test facilities, the 15 x 60-inch two-dimensional insert of the National Aeronautical Establishment (NAE) 5-foot tunnel in Ottawa, Canada, and the two-dimensional test section of the NASA Langley 0.3-Meter Transonic Cryogenic Tunnel (0.3-m TCT). Results presented include effects of variations in sidewall-boundary-layer bleed in both facilities, different sidewall-boundary-layer correction procedures, tunnel-to-tunnel comparisons of corrected results, and flow conditions with and without separation.

Analysis of these results, which show the effects of applying sidewall-boundary-layer corrections to drag polars, compressibility drag, shockwave location, and definition of buffet onset boundaries, lead to the conclusion that the application of sidewall-boundary-layer corrections of the type recommended by Murthy or Barnwell-Sewall is appropriate and necessary if meaningful comparisons of predicted versus experimental results are to be obtained at attached flow conditions. They are also necessary if the 2-D test results are to be correctly applied to 3-D wing designs. However, it is also shown that available sidewall boundary-layer correction methods are not appropriate for conditions when flow separation exists on the airfoil (or sidewall) such as occurs when approaching buffet onset and maximum lift.

Some important facilities-related lessons were also learned from this investigation. One significant observation is that providing sidewall boundary-layer bleed does not appear to provide any obvious advantage in obtaining more accurate transonic airfoil data at conditions when the flow on the model (and sidewall) is attached if appropriate sidewall boundary-layer corrections are used. In contrast, it is shown that sidewall boundary-layer bleed can be effective in maintaining 2-D flow on the model at separated flow conditions if the bleed is applied around the model, but upstream boundary-layer removal is not nearly as effective, if at all. It is also possible that increased airfoil chord lengths at a given chord Reynolds number are beneficial in delaying the onset of sidewall boundary-layer separation. Finally, tunnel flow quality is shown to be an important ingredient for any tunnel-to-tunnel comparison of test data, leading to the (perhaps obvious) recommendation that comparable tunnel flow quality should be a firm prerequisite for any planned tunnel-to-tunnel comparison studies.

1. INTRODUCTION

Two-dimensional transonic airfoil test results are used in two major ways in the development of three-dimensional wing designs in the transport aircraft industry today. First, the experimental development of effective low-drag transonic airfoil designs forms the foundation for any successful 3-D wing design. Secondly, transonic airfoil test results play a very important role in the development and validation of transonic airfoil computational methods that are usually the forerunner of any successful 3-D CFD transonic wing design method. Achieving reliable and accurate transonic airfoil test results is critical for both purposes. The correct effective test flow conditions must be known if the translation of 2-D airfoil test results to 3-D wing designs is to result in the proper performance at specified design conditions, and also if the results are not to contribute to the development of misleading CFD design codes.

Determination of correction techniques to account for the restraining effect of the top and bottom walls in wind tunnel facilities used for transonic airfoil testing has received much attention because of its accepted importance, but also because it is a well confined/defined problem amenable to analysis. Consequently, some very good procedures have been developed that are routinely used today. Similarly, much attention has also been devoted to means to minimize the effects of the top and bottom walls via either specially designed slots or adaptive walls. There is, however, another correction just as fundamental as the top and bottom wall correction that needs to be addressed and accounted for, and that is the effect of changes to the tunnel sidewall boundary-layer

thickness caused by the presence of the airfoil model. It has been clearly demonstrated that sidewall boundary-layer separation can significantly alter the apparent lift and drag characteristics of transonic airfoils. For this reason, most modern transonic airfoil test facilities utilize some type of sidewall boundary-layer control in an attempt to minimize these effects. However, even in the absence of any separation, the change in the sidewall boundary-layer thickness along the chord above and below the model leads to variations in the width of the flow passage that change the effective test Mach number.

The objective of this paper is to demonstrate, by using many examples, the legitimacy and effectiveness of applying corrections to account for sidewall boundary-layer effects in transonic airfoil testing, and also to highlight the conditions for which these corrections are appropriate and those for which they are not. Test results obtained from two modern transonic airfoil test facilities are utilized together with comparative predictions from state-of-the-art computational methods to accomplish this.

2. TEST FACILITIES EMPLOYED

Transonic airfoil test results from two modern test facilities, both capable of achieving quite high unit (and chord) Reynolds numbers, are used in this study of sidewall boundary-layer effects and correction procedures. These two facilities are the 15 x 60-inch two-dimensional insert in the National Aeronautical Establishment (NAE) 5-foot tunnel in Ottawa, Canada,² and the two-dimensional test section of the NASA Langley 0.3-Meter Transonic Cryogenic Tunnel (0.3-m TCT)^{3,4}. Descriptions of the pertinent features of these two facilities and the associated model installations follow:

NAE Two-Dimensional Facility - The NAE 5-foot tunnel is a blowdown type capable of operating at stagnation pressures up to 12 atmospheres. With the two-dimensional inserts installed, a 15 x 60-inch flow passage is provided for transonic airfoil testing. Test section top and bottom walls are perforated with a porosity of 20.5 percent, but are covered with a stainless steel gauze to suppress the edgetone noise which reduces the actual geometric porosity of the floor and ceiling to 7.9 percent. The sidewalls of the 2-D insert are solid except for 24 x 18-inch boundary-layer suction plates where the airfoil models are mounted (see Figure 1). These porous suction plates are made of compression-welded multilayer woven wire sheet, referred to as "Rigimesh." This suction system for sidewall boundary-layer control is regulated in order to maintain the required 2-D flow (where possible), and is operated in a passive manner, i.e., is bled to atmosphere. The suction values V_0/V_∞ used for results reported in this study ranged from a little more than 0.5 percent to a little less than 1 percent, leading to a sidewall boundary-layer-thickness ratio (δ^*/b) of 0.019 at typical airfoil drag-divergence conditions.

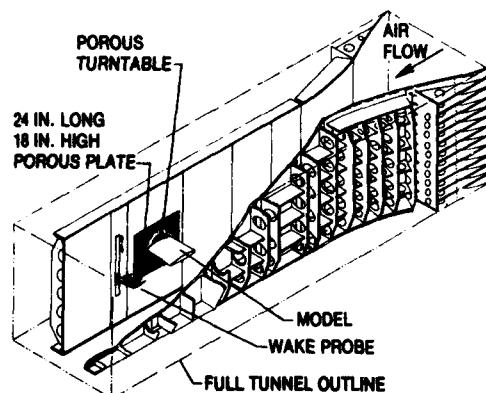


Figure 1. NAE 5-Foot Transonic Blowdown Tunnel With 15- by 60-Inch Insert and Sidewall Suction Boundary Layer Removal

Ten-inch-chord airfoil models are typically used in this facility, and they are supported on two 3-component balances which rotate with the model. Airfoil lift data are also obtained from the integration of a very dense distribution of static pressures on or near the model centerline, and drag data are, in addition, derived from wake survey measurements made 1.5 chord lengths downstream of the airfoil trailing edge.

Floor and ceiling static tubes, each mounted midway between the sidewalls, are used for measuring the wall pressures required for wall correction routines. Each tube has 40 longitudinally distributed orifices, starting nearly eight chord lengths upstream from the airfoil leading edge and extending four chord lengths downstream from the airfoil trailing edge. The tunnel Mach number control system consisting of two translating chokes installed in the diffuser second throat allows the desired Mach number (corrected for wall interference) to be constant during a specified α -step program.

Measurements and testing experience have shown that the freestream flow disturbance levels in this facility are quite low at the test Reynolds numbers used in this investigation, i.e., up to 15 million based on airfoil chord. Transition location measurements made by Fancher⁵ utilizing an advanced hot-film method showed that natural transition (in the absence of any adverse pressure gradient) occurred at the 33-percent chord location on the airfoil chord, clearly indicative of a very low freestream disturbance level.

NASA Langley 0.3-m TCT Airfoil Facility - This facility is a continuous flow fan-driven transonic tunnel which uses cryogenic nitrogen as a test gas. It is capable of operating at Mach numbers up to about 0.9. The stagnation pressure and temperature can be varied from about 1.2 to about 6.0 atm and from 144°R to 576°R, respectively. This unique

operational envelope allows airfoils to be tested at flight equivalent Reynolds numbers. Under steady operating conditions, the heat of compression imparted to the test gas by the fan is removed by automatic injection of liquid nitrogen into the tunnel circuit, and the stagnation pressure is maintained by the automatic control of the gaseous nitrogen exhaust. The two-dimensional test section insert for this tunnel has a cross section of 8 by 24 in., and is enclosed in a rectangular plenum chamber. The top and bottom walls of this insert have two longitudinal slots each, with a total open area of 5 percent. These slots were designed using Barnwell's low blockage criteria⁶.

A sidewall boundary-layer removal system upstream of the airfoil model is provided which can be operated in either the passive or the active mode⁴. A pair of 6 in. wide perforated plates having a nominal porosity of about 10 percent are fitted flush on both the sidewalls upstream of the model location, as illustrated in the top view photograph of the test section with the top of the plenum chamber and the slotted wall removed (see Figure 2).

In both the passive and active mode of operation, the amount of boundary-layer mass flow removed from the two sidewall boundary layers is independently controlled by digital valves on the discharge side of each sidewall. In the passive mode, which was used for the testing discussed in this investigation, the discharge from each wall is exhausted directly to the atmosphere. Consequently, the maximum rate at which mass can be removed in the passive mode is limited to the rate at which liquid nitrogen is being injected into the tunnel in order to maintain steady operating conditions. At higher Mach numbers where the heat of compression is large, the liquid nitrogen injection rate is higher and correspondingly higher removal rates can be obtained. Removal rates of up to 1.5 percent were used for the results reported on in this study, resulting in a reduction of the sidewall-boundary-layer-thickness ratio ($2\delta^*/b$) from 0.018 to 0.012 at typical airfoil drag-divergence conditions. For tests with sidewall boundary-layer removal, the upstream reference Mach number is increased to compensate for the decrease in Mach number at the model station due to sidewall boundary-layer removal.

Six-inch-chord airfoil models are typically used in this facility, and the required aerodynamic data are obtained from the pressure distributions around the airfoil model, the definition of the wake defect, and the corresponding angle of attack. The pressures on the airfoil model, measured by individual transducers connected to the tubing from each orifice, are integrated to obtain the lift characteristics, while the drag characteristics are obtained from wake survey measurements made 1.2 chord lengths downstream of the airfoil trailing edge. Wake survey measurements are obtained at five spanwise stations (centerline to $y(b/2) = 0.75$) to permit a qualitative assessment of the two-dimensionality of the flow in the region of the wake.

Floor and ceiling static pressure orifices, located midway between the sidewalls (and slots) are used to measure the wall pressures required for wall correction routines. These orifices are spaced about 2 in. apart, and extend from about 4 chord lengths upstream from the airfoil leading edge to about 3 chord lengths downstream from the trailing edge. Unlike the NAE control system, these floor and ceiling pressures are not used to set a constant (corrected for wall interference) Mach number during a specified α -step program.

Measurements and testing experience at a chord Reynolds number of about 15×10^6 have both indicated that the freestream flow disturbance levels in this facility are most likely much higher than those present in the NAE airfoil test facility at the same conditions. Hot-wire measurements⁷ have shown that the normalized velocity fluctuations in the settling chamber downstream of the screens typically range from about 2.0 to 3.0 percent. Correspondingly, airfoil drag measurements obtained at chord Reynolds numbers of 15×10^6 show no differences between data obtained with no transition fixing and data obtained with transition fixed at 5-percent chord, thereby indicating that the elevated disturbance levels in this facility cause transition to occur very near the leading edge. Unfortunately, no absolute tunnel-to-tunnel comparison of disturbance levels between the NAE and 0.3-m TCT facilities is possible at this time because of the lack of comparable data for the NAE tunnel. Based on Johnson's results⁸, which showed an extremely wide range of normalized velocity fluctuations in the 0.3-m TCT when four different techniques were used to establish flow quality, it is concluded that any meaningful quantitative tunnel-to-tunnel comparison of flow quality must be based on measurements of velocity, density, and total temperature fluctuations in both facilities using an identical technique and identical instrumentation.

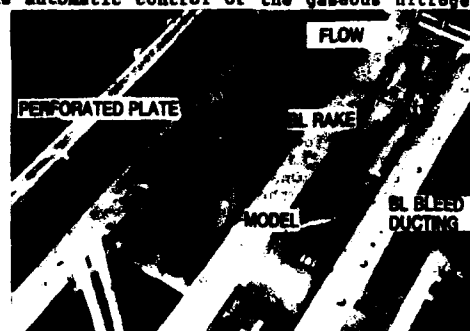


Figure 2. Two-Dimensional Test Section of the 0.3-m TCT with Perforated Plates for Boundary-Layer Removal

3. AIRFOIL MODEL CONFIGURATION

The same airfoil shape was used in both facilities for the results reported in this study. It was an aft-loaded "supercritical-type" airfoil with a cusped trailing edge. The model used in the NAE facility had a 10-inch chord, with a corresponding aspect ratio of 1.5, while the one used in the 0.3-m TCT had a chord of 6 inches, and a corresponding aspect ratio of 1.32.

4. WALL INTERFERENCE CORRECTION METHODS

The influence which the walls of "two-dimensional" transonic airfoil test facilities exert on the flow about an airfoil model at transonic conditions has been studied extensively for at least the last fifteen years. Two types of effects and corrections have been explored. One is the primarily inviscid effect caused by the top and bottom walls which results in the displacement of the streamlines near the walls away from the free-air positions. The other interference effect is that caused by the interaction of the airfoil pressure field with the sidewall boundary layers. Both sidewall boundary-layer separation and changes in thickness contribute to this interference source, but only the attached-sidewall-boundary-layer interaction with the model pressure field is amenable to analysis. Methods which are used to account for each type of interference, and, in particular, those used in this study, are discussed in this section.

Top and Bottom Wall Corrections - Three general types of correction methods are available today to account for the displacement of the streamlines caused by the presence of the floor and ceiling in transonic airfoil testing. First, there are the classical theoretical methods that analytically simulate the nonlinear transonic flow by using theoretical boundary conditions on both the airfoil model and the tunnel floor and ceiling walls. Typical methods of this type include those based on transonic small disturbance theory, like the initial method developed by Murman⁹, and those based on solutions of the transonic full potential equations, like the procedure developed by Shmilovich and Caughey¹⁰. While these methods are interesting in that they provide "a priori" estimates of the wall corrections, and they were the first transonic correction methods developed, they are rarely used anymore. They do not lend themselves to routine application for production type test programs where there may be thousands of test points, and furthermore, their accuracy is definitely subject to question since they are only as accurate as the theoretical models employed, and a practical accurate theoretical modeling of ventilated wall flow characteristics is beyond the current state-of-the-art capability.

The other two types of wall correction methods available overcome the requirement to theoretically model the wall flow characteristics by using the measured static pressure distribution on the tunnel walls as a boundary condition. Simplest, and most popular, of these methods are those that utilize the subsonic linear theory of wall corrections and apply it to the transonic range on the premise that the farfields of the subsonic and the transonic flows are very similar. An obvious requirement for the application of these methods is that the test section walls must be operated at subcritical flow conditions, even though local regions of supercritical flow may exist on the tested airfoil. These methods assume the tunnel flow is a superposition of a model-induced flowfield, a wall-induced flowfield, and the tunnel onset flow. Typical of these methods, which are largely based on the principles set forth by Capeller, Chevallier and Bouniol¹¹, is the procedure developed by Mokry and Ohman¹² that is used in a production mode in the NAE transonic airfoil test facility. In this NAE procedure, the wall boundary-condition measurements are combined with a singularity modeling of the airfoil which covers lift, volume, drag and pitching moments. Although this method is based on subsonic compressible flow analysis, Chan¹³ has shown by using an asymptotic transonic small disturbance analysis that the derived corrections to angle of attack and freestream Mach number are correct to the first order.

The third, and more complex, type of wall correction method utilizes the measured pressure distributions on the test airfoil together with the measured interface (wall) pressure distributions to compute an equivalent body including viscous effects by solving the so-called "inverse" problem. This equivalent body is then used to calculate its pressure distribution in unrestrained flow, iterating on Mach number and angle of attack until a model pressure distribution is achieved which "matches" the measured one. The best known method of this type is TWINTAN¹⁴, developed by Kemp, which is a nonlinear top and bottom wall correction method. TWINTAN, used for some time in the NASA Langley 0.3-m TCT airfoil facility, utilizes three separate solutions of an extended transonic small disturbance equation in order to obtain corrections to the tunnel Mach number, and angle of attack, as well as the wall-induced perturbation field. In addition, when the TWINTAN solution indicates a significant lack of convergence between the measured and computed airfoil pressure distributions, the results may provide an indication that the test condition produces a wall interference that is too large and hence the data is no longer useful or valid.

Sidewall-Boundary-Layer Corrections - The first known method proposed to address the interaction of the attached sidewall boundary layer with the airfoil model pressure field was developed by Preston¹⁵, who calculated an effective angle of incidence from an approximate modeling of the trailing vorticity assumed to have been shed due to a loss of lift in the boundary layer. Limited success was achieved with this method, but not enough to maintain interest. Thirty-five years later, spurred on by the experimental results obtained by Bernard-Guelle¹ which showed the effects of sidewall boundary-layer thickness on airfoil lift at both subsonic and transonic conditions, Barnwell^{16,17}

developed a method to account for the effect of changes in the attached sidewall-boundary-layer thickness due to the airfoil induced pressure field at subsonic conditions (see Figure 3). He related an equivalent Mach number change to the average displacement thickness on the sidewalls by use of the Prandtl-Glauert similarity rule. The use of this technique was demonstrated to correlate well with the Reference 1 experimentally observed variations in airfoil performance with changing sidewall boundary-layer thickness at subsonic conditions.

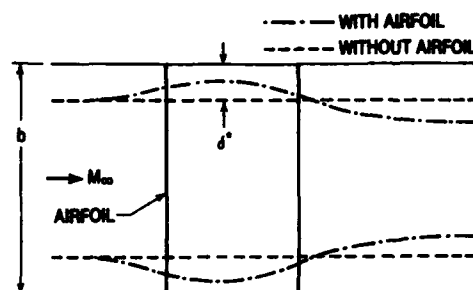


Figure 3. Typical Sidewall Boundary-Layer Growth About a Lifting Airfoil in a Two-Dimensional Wind Tunnel

number is approximately $2\delta^*/b$, which is the fraction of the tunnel occupied by the two sidewall boundary-layer displacement thicknesses. Pressure and force coefficients are correspondingly transformed by multiplying the tunnel values by $\bar{\beta}/\sqrt{1 - M_{test}^2}$.

Following the Barnwell-Sewall sidewall correction, a new small-disturbance method was developed by Murthy²⁰ to account for the change in the effective freestream Mach number due to changes in the attached sidewall boundary layer. This method is based primarily on the change in the area of the flow passage rather than on assuming the presence of significant spanwise velocities across the width of the tunnel as done in the Barnwell-Sewall method. For comparison of wind-tunnel measurements with theoretical predictions, the recommended corrections are as follows:

- Mach Number $M_{corr} = M_{test}/(1 + k)^{1/2}$
- Pressure Coef. $C_{p,corr} = C_{p,test}(1 + k)^{1/2}$
- Normal Force $C_{n,corr} = C_{n,test}(1 + k)^{1/2}$

where

$$k = (2 + 1/H - M_{test}^2)(2\delta^*/b)$$

The results of this approach show a continuing increase in the magnitude of the correction from incompressible to transonic speeds. At test Mach numbers near 1.0, the difference between these corrections and those of Barnwell-Sewall are not significant, although in the Mach number range of interest for this investigation, the Murthy-proposed correction to freestream Mach number is about 20 percent less than that predicted by the Barnwell-Sewall correction.

Murthy²¹ has recently proposed a modification to the method of reference 20 to account for airfoil aspect ratio effects, which is most important when the width of the tunnel is much larger than the airfoil chord. The linear cross-flow assumption of the basic Barnwell-Sewall method has been replaced with a wavy wall flow model. A very recent study conducted at NASA Langley by Green and Newman²² concluded that this method should be used in all future four-wall corrections. However, this latest method was not used for the four-wall corrections presented in this paper since the aspect ratios for the two models were nearly the same (i.e., 1.5 and 1.33 for NAE and 0.3-m TCT, respectively) and, most importantly, the differences between the two methods were not significant at these aspect ratios.

Combined Four-Wall Interference Assessment - Two types of procedures are employed for combining the corrections for the sidewall boundary layer and the top and bottom wall interference²³. One is a sequential application of the two types of corrections, while the other is a unified procedure that recognizes the combined effects of the two corrections as a unified wall-induced perturbation field. For the results presented in this paper, the sequential procedure has been used for all of the test results. The unified procedure is generally used for wall corrections in the Langley 0.3-m TCT facility, but the sequential procedure was used on the data presented in this paper so that the separate effects of the floor and ceiling corrections could be obtained.

Sewall¹⁸ subsequently extended the Barnwell method to transonic conditions by showing that the similarity of compressibility and sidewall boundary-layer effects results in a modified form of the von Karman transonic similarity rule. In this resultant Barnwell-Sewall method¹⁹, an equivalent Mach number for an ideal two-dimensional tunnel with no sidewall boundary layer ($\delta^* = 0$) is defined as

$$M_{corr} = M_{test}(1 - M_{corr}^2)^{3/4} / \bar{\beta}^{3/2}$$

where

$$\bar{\beta} = \sqrt{1 - M_{test}^2 + 2 \frac{\delta^*}{b} (2 + \frac{1}{H} - M_{test}^2)}$$

For tunnel Mach numbers between 0.7 and 0.9, and shape factors (H) ranging between 1.4 and 1.6, the correction to the Mach number is approximately $2\delta^*/b$, which is the fraction of the tunnel occupied by the two sidewall boundary-layer displacement thicknesses. Pressure and force coefficients are correspondingly transformed by multiplying the tunnel values by $\bar{\beta}/\sqrt{1 - M_{test}^2}$.

Adcock and Kemp²³ have compared results using the regular sequential procedure to results obtained using a reverse sequential procedure. In the regular sequential procedure, the similarity sidewall corrections are applied as an input to the floor and ceiling corrections, which in turn yields the four-wall corrections. In the reverse sequential procedure, the floor and ceiling corrections are made first, and then the similarity sidewall corrections are applied to the output from the floor and ceiling corrections. Results from the comparison of these two procedures were the same, indicating the principal of superposition is an acceptable means of substituting the Murthy²⁰ sidewall correction for the Barnwell-Sewall correction from the results of the TWINTM4 code developed by Kemp²⁴. All of the 0.3-m TCT data presented in this paper was first corrected using TWINTM4 in a regular sequential mode, which used the Barnwell-Sewall sidewall similarity correction, and then the Barnwell-Sewall correction was replaced by the Murthy sidewall correction.

A somewhat automated version of Kemp's TWINTM4 code²⁴ has been developed by Gumbert and Newman^{25,26} for processing data through the various steps in the 0.3-m TCT procedure. In TWINTM4, the corrected Mach number and angle of attack are obtained from the minimization of the mean square difference between the surface velocity over the airfoil in the tunnel and that over the same shape airfoil at the same lift in free air. This differs from TWINTAN where the Mach number correction is determined from the local wall-induced velocity perturbation at a user-specified match point location. TWINTM4 does not use a match point.

5. TRANSONIC AIRFOIL CFD CODES EMPLOYED

One means by which insight into the legitimacy and effectiveness of applying corrections for sidewall-boundary-layer effects in transonic airfoil testing can be obtained is by comparing corrected test results with the corresponding predictions of computational methods which have some known distinguishing characteristics. Two widely used transonic airfoil methods, both based on finite-difference solutions of the transonic full potential equations, are used in this study for that purpose. They are the nonconservative version of the Bauer, Garabedian and Korn (BGK) method²⁷ referred to as Program H, and the fully-conservative GRUMFOIL code developed by Melnik et al.²⁸ for airfoils with cusped trailing edges. Brief descriptions of these two airfoil analysis codes follow:

BGK Program H - The inviscid portion of this method²⁷ is based on a numerical solution of the full potential equations by mixed flow relaxation techniques in the "circle plane." Mass is not conserved across shock waves in this nonconservative method, although a mass-flux correction is applied to the drag computation. This lack of mass conservation leads to solutions in which the pressure rise across the shock is less than the theoretical value. Viscous effects are simulated by boundary-layer displacement additions to the airfoil surface, and the wake is modeled as a constant thickness extension of the airfoil. The turbulent boundary-layer method utilized is the integral method of Nash and MacDonald²⁹. An iterative solution of the coupled inviscid and boundary-layer solutions is used. Viscous profile drag is computed by using a compressible Squire-Young drag formula applied to the computed trailing-edge boundary-layer quantities. The grid size used is 160 x 28.

GRUMFOIL (NCM-9) - In this version²⁸, the inviscid flow is calculated by Jameson's "O" mesh multigrid scheme using rotated differences, and is fully conservative. The boundary-layer solution employs Carter's semi-inverse scheme³⁰. An extension of Thwaites' integral method is used for the laminar run and a revised form of Green's lag entrainment method³¹, modified for the inverse calculation, is used for the turbulent flow on the airfoil and into the wake. A complete set of matching conditions couple the inviscid and viscous flowfields encompassing displacement effects on the airfoil and in the wake, wake curvature effects, and the strong interactions at the shock wave and at the trailing edge. The solution used for the trailing-edge boundary-layer interactions is based on a formal asymptotic analysis for airfoils with cusped trailing edges, and hence it is strictly applicable only to airfoils with small included trailing-edge angles. Total drag is determined from an integration of the pressure and skin-friction over the airfoil surface, while profile drag is assessed from the wake momentum thickness far downstream. The fine grid size employed in this version of the code is 160 x 32.

Identifying Characteristics - A most useful parameter for assessing the accuracy of the corrected test conditions is the chordwise location of the shockwave on the upper surface of the airfoil. It is not uncommon for the shock wave on the upper surface of an aft-loaded airfoil to move as much as 10-percent chord for a 0.01 change in the freestream Mach number. Further, many studies^{32,33} have shown that the accuracy of the computed shock wave location is very closely interrelated with the accuracy of the predicted static pressure rise through the shock-wave/boundary-layer interaction region. Very simply, if the predicted shock pressure rise is too small, like it is with a nonconservative method, then the predicted shock location should be too far forward. Conversely, if the predicted pressure rise is too great, like it is with an inviscid fully conservative method, then the predicted shock location should be too far aft. In order to establish a database for use in evaluating the accuracy of predicted static pressure jump conditions for Program H and GRUMFOIL, an extensive correlation of experimentally observed jump conditions was assembled using measurements obtained in the NAE facility for seven different airfoil designs. These airfoils were all heavily instrumented with static pressures in the region of the shock wave, where a spacing of one-percent chord was used. The correlation obtained at a chord Reynolds number of 14.5×10^6 is shown in Figure 4 where it is compared to the jump conditions associated with an isentropic

shock, the Rankine-Hugoniot relations, the maximum stream deflection, and a sonic post-shock Mach number. The data correlation presented is independent of airfoil type, as expected, since the pressure jump across the shock interaction region is a local phenomenon. Also, since it is a local phenomenon, the correlation should be independent of any wall interference effects.

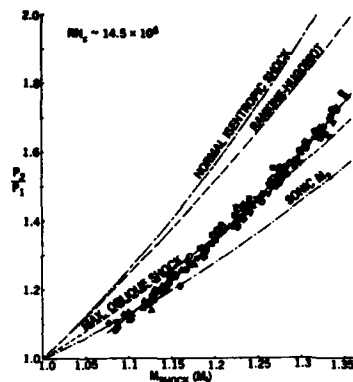


Figure 4. Static-Pressure Rise Through Shock Wave Interaction

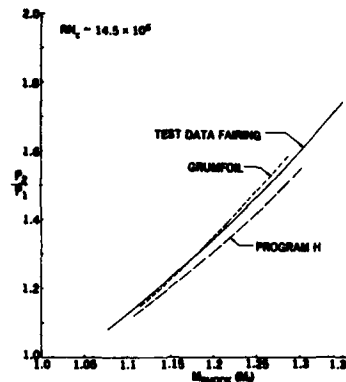


Figure 5. Predicted Versus Experimental Shock Pressure Jump

Predictions of the shock pressure jump from Program H and GRUMFOIL are compared to the fairing through the experimental database in Figure 5. Program H predictions are well below the test data, while the GRUMFOIL simulation of the shock-wave/boundary-layer interaction yields a pressure jump quite close to the test data fairing, but does tend to slightly underpredict the jump at low shock strengths, and slightly overpredict the jump for shock Mach numbers above 1.2. Consequently, it should be expected that if the corrections applied to the wind tunnel test results are appropriate, then the measured shock locations should, in general, always be aft of the Program H predictions, aft of the GRUMFOIL predictions at low shock strengths, but then forward of the GRUMFOIL predictions at higher shock strengths.

There are also other features of both Program H and GRUMFOIL that would preclude a perfect correlation with test data unless by coincidence. Such factors, which, if accounted for, could influence the predicted shock location and other characteristics are the neglect of total pressure losses through the shock, and the turbulence generation and amplification caused by the shock-wave interaction^{34,35} that would influence the boundary-layer growth through and downstream of the shock. However, the use of either method in these correlations should provide a consistent basis for comparison and evaluation.

6. CORRECTED TEST RESULTS VERSUS COMPARABLE PREDICTIONS

Five case studies have been selected to demonstrate the legitimacy and effectiveness of applying corrections to account for attached sidewall-boundary-layer effects in transonic airfoil testing, while a sixth example is used to illustrate the lack of applicability of such corrections for flow conditions when the sidewall boundary layer is separated. The first three studies of uncorrected and corrected test results versus comparative predictions utilize data obtained for aft-loaded airfoils in the NAE two-dimensional airfoil test facility. Both shockwave location and transonic drag characteristics are studied. The next two case studies are based on data obtained for one of the same airfoil designs in the NASA Langley 0.3-m TCT airfoil facility. These test results permit a direct tunnel-to-tunnel comparison of corrected test results for shock location and drag rise characteristics. The last case study is a comparison of the indicated buffet-onset boundaries measured in both tunnels for this same airfoil, a condition where the sidewall boundary layers would clearly be separated. All of the experimental results and predictions presented herein are at a chord Reynolds number of either 14.5×10^6 (NAE) or 15×10^6 (Langley), and with transition fixed in NAE at the 5-percent chord point on both upper and lower surfaces using 0.0016-inch diameter glass beads. Transition was not fixed for the 0.3-m TCT results presented herein because natural transition occurred very close to the leading edge. Studies of comparable results obtained at both higher ($25\text{--}30 \times 10^6$) and lower (6×10^6) Reynolds numbers in both facilities support the trends and conclusions obtained at the intermediate Reynolds numbers.

Case Study No. 1 - In this study, data obtained in the NAE facility on a representative aft-loaded airfoil both with and without sidewall boundary-layer bleed are examined to show how the application of appropriate sidewall boundary-layer corrections resolves apparent inconsistencies in relative shockwave locations. The effect of including sidewall boundary-layer corrections on the correlation of GRUMFOIL-predicted and measured

shock locations (defined where the local Mach number is 1.1) for this airfoil at attached flow conditions is illustrated in Figure 6. First, when only the inviscid floor and ceiling corrections based on measured boundary-pressure distributions¹² are applied, it can be seen that the measured shock locations are well forward of the GRUMFOIL predictions, but most importantly, the two sets of data appear to be inconsistent. It can also be seen that the measured shock location moves aft when sidewall suction is applied, suggesting the existence of a higher effective "freestream" Mach number (even though the tunnel had been calibrated for both situations). Next, the result of applying the Barnwell subsonic method^{16,17} to account for sidewall boundary-layer effects in addition to the floor and ceiling corrections is demonstrated. It can be seen that although application of this method greatly reduces the inconsistency between the two sets of data, it does appear to overcorrect for the sidewall boundary-layer influence. This result is also of interest since an initial evaluation of the effectiveness of applying sidewall boundary-layer corrections to airfoil data taken at transonic conditions in NAE was based on the application of this method, and led to a rather negative conclusion that needs to be put in proper perspective. Finally, the effects of applying the Barnwell-Sewall^{18,19} and Murthy²⁰ transonic corrections for sidewall boundary-layer influence in addition to the floor and ceiling corrections was investigated. Results obtained with the Murthy correction applied are shown in Figure 6c. Although not shown, the results obtained with the Barnwell-Sewall correction applied are very similar, with predicted shock locations within about 1-percent chord of the Murthy-predicted values. The correlations obtained with the GRUMFOIL predictions using either the Murthy or Barnwell-Sewall corrections are basically consistent with the GRUMFOIL shock pressure jump comparison shown in Figure 5, i.e., at conditions where the predicted jump is too high, the predicted shock tends to be aft of the experimental location, and vice-versa. Also, the apparent inconsistency between the two sets of data is greatly reduced when these corrections are utilized.

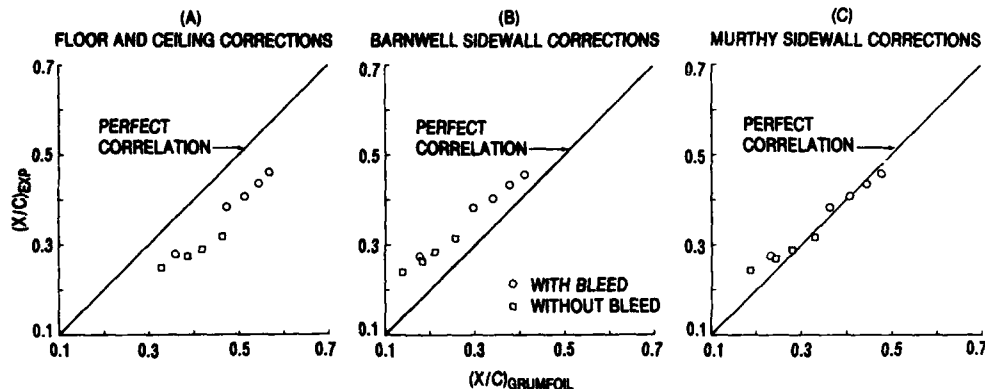


Figure 6. Effect of Wind Tunnel Sidewall Boundary-Layer Corrections on Correlation of NAE 15-by-60-in. Versus Predicted Shock Location

Another verification of the effectiveness and legitimacy of applying the Murthy and Barnwell-Sewall corrections is provided by examining the comparisons of the GRUMFOIL-predicted and measured static pressure distributions on the forward lower surface of this same airfoil with the various corrections applied (see Figure 7). Since the predictions for this region on the airfoil are not strongly influenced by any possible inadequacies in the transonic or viscous flow techniques, the measured and predicted pressures in this area should agree very closely if the tunnel corrections used are appropriate. It is seen from Figure 7 that this agreement is not good when only the floor and ceiling corrections are used, and is not good when the Barnwell subsonic sidewall correction is added, but the agreement is excellent when either the Barnwell-Sewall or Murthy corrections are used in conjunction with the floor and ceiling corrections. Since the Barnwell-Sewall and Murthy corrections yield quite similar results, all of the ensuing case studies addressing the effectiveness and applicability of sidewall boundary-layer corrections make use of the Murthy correction for convenience sake.

Case Study No. 2 - This investigation, which is an expansion of the first study, is a much more comprehensive evaluation of the effectiveness and legitimacy of applying sidewall boundary-layer corrections for attached flow conditions as evidenced by correlations of predicted and measured shock locations. The airfoil configuration used for this survey is very similar to that used in the first study, and is the same configuration tested in the NASA Langley 0.3-M TCT airfoil facility, the results from which are used in case studies 4, 5 and 6 involving tunnel-to-tunnel comparisons. Results from this case study, which involves correlations of both GRUMFOIL and BGR Program H predicted shock locations with NAE-measured locations, are presented in Figure 8. Correlations are shown first with no wall corrections applied, then with the inviscid floor and ceiling corrections based on measured boundary-pressure distributions applied, and finally with the sidewall boundary-layer corrections recommended by Murthy added to the floor and ceiling corrections. One observation that can be made from these shock location correlations is that

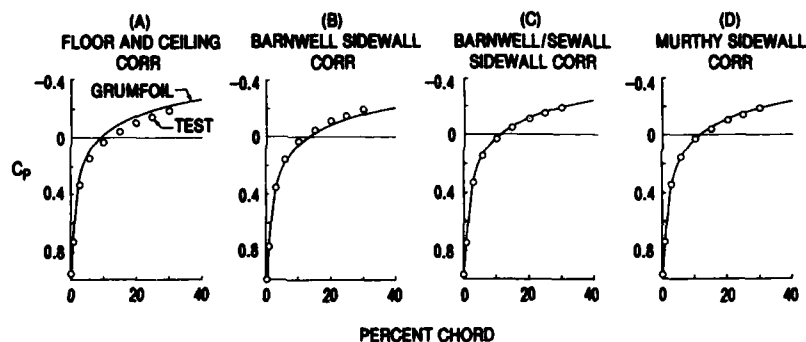


Figure 7. Effect of Wind Tunnel Sidewall Boundary-Layer Corrections on Correlation of NAE 15- by 60-in. Versus Predicted Lower Surface Pressures

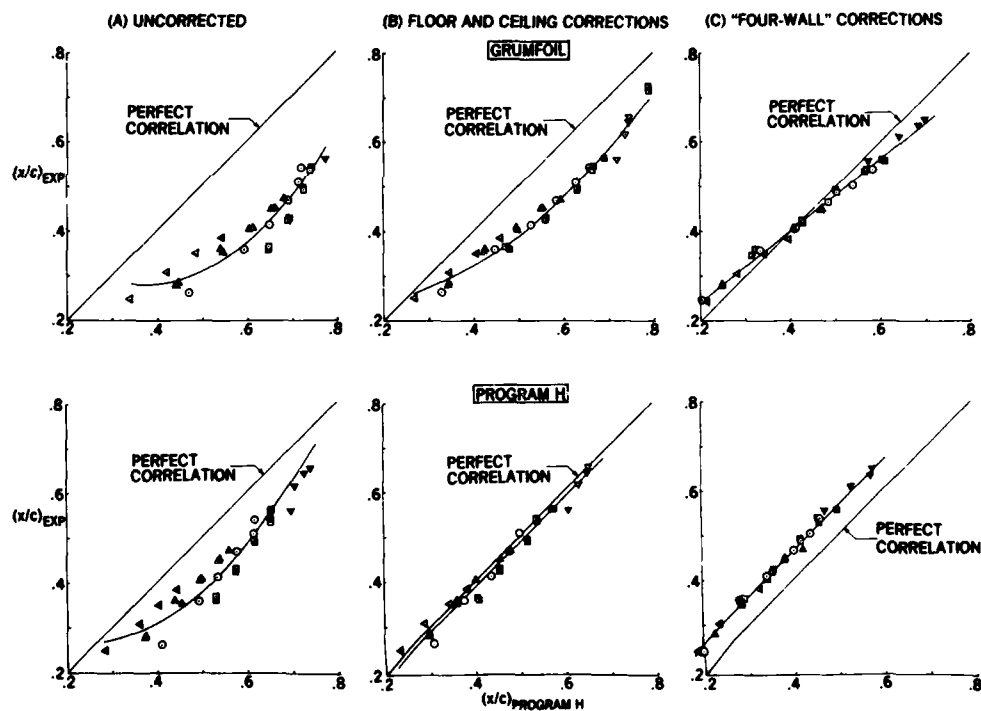


Figure 8. Effect of Wind Tunnel Wall Corrections on Correlation of Experimental Versus Predicted Shock Location

the data scatter with both GRUMFOIL and Program H correlations is progressively reduced as the wall corrections are sequentially applied, being smaller when both types of wall corrections are applied. Secondly, the GRUMFOIL correlation obtained with both wall corrections applied is very consistent with the GRUMFOIL shock pressure jump comparison, i.e., at conditions where the predicted jump is too high, the predicted shock is aft of the experimental location. Conversely, at conditions where the predicted jump is low compared to the empirical correlations, then the predicted shock is forward of the experimental location. Then, with regard to the Program H correlations, although the correlation is (coincidentally) best when only the floor and ceiling corrections are applied, the results obtained when both corrections are applied is consistent with the nonconservative formulation of Program H, i.e., the predicted shocks are forward of the

corresponding experimental values. The too-far-forward shock location predicted with Program H is also consistent with the overly pessimistic boundary-layer growth calculation procedure employed in Program H, which by itself would also cause the predicted shock location to be too far forward. On the basis of these correlations, it is concluded that the application of sidewall boundary-layer corrections of the type recommended by Murthy or Barnwell-Sewall are appropriate and necessary if meaningful comparisons of predicted versus experimental results are to be obtained, and also if the 2-D test results are to be correctly applied to 3-D wing designs.

Case Study No. 3 - This case study, utilizing test results obtained on another aft-loaded airfoil configuration in the NAE facility, illustrates how the application of sidewall boundary-layer corrections impacts the interpretation of predicted versus measured transonic drag characteristics. In this study, the predicted effects of an airfoil modification intended to reduce drag at high lift coefficients based on GRUMFOIL are compared to the measured test results with and without sidewall boundary-layer corrections applied. First, the comparison of the predicted and measured drag polars for the baseline airfoil and the modification, with only the floor and ceiling corrections applied, is shown in the upper half of Figure 9. It can be seen that important features of the measured improvement provided by the airfoil modification are not captured by the corresponding GRUMFOIL predictions in this case. The measured improvement in the early drag-rise region is clearly not represented by the predictions based on GRUMFOIL, and the magnitude of the improved lifting capability is obviously not properly represented. However, when the Murthy sidewall boundary-layer corrections are applied in addition to the floor and ceiling corrections, the corresponding comparisons of predicted and measured drag polars shown in the lower half of Figure 9 are in much closer agreement. The essence of the measured performance improvement provided by the airfoil modification is

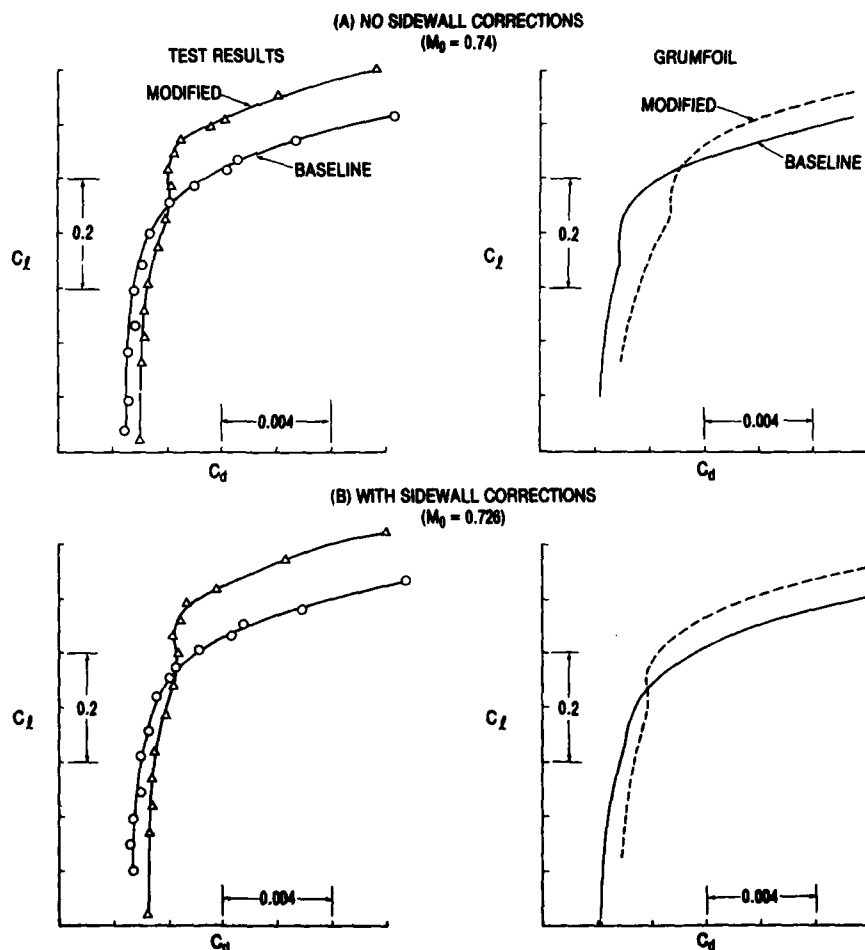


Figure 9. Effect of Sidewall Corrections on Transonic Drag Polars

now captured with the predictions based on GRUMFOIL. The improved correlation occurs primarily because the presumed test Mach number is reduced by about 0.014 when the side-wall corrections are applied.

Case Study No. 4 - As a follow up to the case 2 study of the effects of applying wall corrections on the correlation of predicted versus measured shock locations for an aft-loaded airfoil tested in NAE, a very analogous study has been carried out based on the results obtained from tests of the same airfoil design in the NASA Langley 0.3-m TCT airfoil facility. These two sets of results thereby permit a direct tunnel-to-tunnel comparison of the effectiveness of the current state-of-the-art wall corrections employed. Before examining the 0.3-m results, and comparing them to the corresponding ones from NAE, it is instructive to make note of some of the disparities that existed between the two studies as follows:

- Differences in model/tunnel geometries
 - Sidewall boundary-layer bleed is located upstream of airfoil in 0.3-m TCT, but surrounds model in NAE.
 - Tunnel floor and ceiling are perforated at NAE, whereas 0.3-m TCT employs low-interference slots.
 - Tunnel height/model chord ratio is 6 at NAE versus 4 at the 0.3-m.
- Differences in wall correction methods and techniques
 - Floor and ceiling corrections at NAE are based on linear theory that uses measured boundary conditions, followed by a sequential application of the Murthy²⁰ sidewall boundary-layer correction.
 - Floor and ceiling corrections at the 0.3-m TCT are also based on measured boundary conditions, but do not rely on linear theory.
 - The Barnwell-Sewall sidewall correction was used in the 0.3-m TCT four-wall correction method utilizing the sequential method procedure.
 - The four-wall corrections for the 0.3-m TCT with the Murthy sidewall correction have been obtained by using superposition, i.e. subtracting out the Barnwell-Sewall sidewall correction and adding in the Murthy²⁰ correction.
- Differences in tunnel flow quality
 - Freestream disturbance levels in the NAE facility at a chord Reynolds number of 15×10^6 are probably much lower than those existing in the 0.3-m TCT, and unsteadiness in Mach number existed through a typical angle-of-attack sweep in the 0.3-m TCT.
- Differences in test and analysis procedures
 - Only test results with sidewall boundary-layer bleed operating were obtained in Case Study No. 2 at NAE, while results with sidewall boundary-layer bleed both on and off were obtained at the 0.3-m TCT.
 - Only the GRUMFOIL program was used for the 0.3-m correlation of predicted versus measured shock locations since the NAE study showed the Program H predictions were not as reliable.

If the state-of-the-art wall correction methods employed in both facilities are adequate, and thereby account for the model/tunnel differences, then the only difference to be concerned about causing a discrepancy in the comparison of the final four-wall corrected results is the difference in tunnel flow quality.

Results of this case study, which is concerned with the correlation of GRUMFOIL-predicted versus 0.3-m TCT-measured shock locations, are presented in Figure 10. The correlation is shown first with no wall corrections applied, then with the TWINTN4 floor

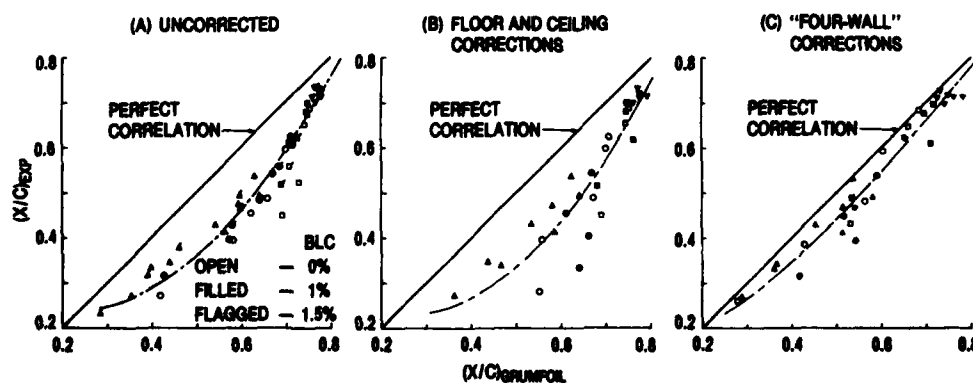


Figure 10. Effect of Wind Tunnel Wall Corrections on Correlation of 0.3m TCT Versus Predicted Shock Location

and ceiling corrections only applied, and then finally with the four-wall corrections applied. The four-wall correction used has been adjusted to include the Murthy-type correction to be consistent with the NAE results. Several differences from the corresponding NAE correlation are apparent. First, the effect of the floor and ceiling corrections is much smaller, a testimony to the effectiveness of the Barnwell slot design in the 0.3-m TCT. However, the correlation scatter is increased significantly, particularly near midchord, when the floor and ceiling corrections are applied. This phenomenon is undoubtedly caused by the relatively high level of unsteadiness present in this initial configuration of the 0.3-m TCT. This has been verified by viewing video tapes of the shock motion which were obtained by using a form of real-time Moiré interferometry developed at NASA Langley³⁶. This system makes use of the interaction of holographic grids to generate an interference fringe pattern, and a density perturbation in the flow, such as a shock wave, is easily detected as a local shift in the fringe pattern. Shock movements of 10 to 15 percent chord were typically observed near midchord, but smaller movements were seen when the shock was further aft, both of which correspond well with the correlation scatter seen in Figure 10. The other noticeable difference from the corresponding NAE correlation is the somewhat different form of the correlation obtained when the four-wall corrections are applied. While the correlation is certainly much improved over that obtained when only the floor and ceiling corrections were used, and is in reasonably good agreement with the NAE correlation for shock locations aft of midchord, the 0.3-m TCT measured shock location are about 5-percent chord forward of those observed in NAE at flow conditions where the predicted shock location is forward of midchord. As such, the 0.3-m TCT correlation is no longer consistent with the GRUMFOIL shock pressure jump deviation for these weaker, more forward shocks. While it is possible that some of this difference could be attributable to the differences, or inaccuracies, in the wall correction methods employed in both facilities, it is also very plausible that this difference could be largely attributable to the apparent higher free-stream disturbance levels that were present in the version of the 0.3-m TCT with an 8 by 24 in. test section. It is suggested that this increased freestream turbulence level would result in an increased rate of boundary-layer growth on the airfoil which, in turn, would cause the shock to be more forward, i.e., such as occurs with the thicker boundary-layer present at lower Reynolds numbers. Although there is some ambiguity involved in the interpretation of the corrected test results for this intended tunnel-to-tunnel comparison due to the flow quality problem, the shock-location correlations obtained with the final four-wall corrected results do agree fairly well, certainly better than the results not corrected for sidewall boundary-layer effects. It is also of interest to note the effect that the 0.3-m TCT sidewall boundary-layer bleed system, located upstream of the model, has on the data correlation. It can be seen from Figure 10 that the final correlation with the four-wall corrections applied is, in fact, poorer with the bleed system operating. There is no immediate explanation for this trend.

Case Study No. 5 - In this final case study involving flow conditions where the sidewall boundary layers are attached, the compressibility-drag characteristics measured in NAE and the 0.3-m TCT for the same airfoil configuration used in cases 2 and 4 are compared with each other and with GRUMFOIL predictions to further evaluate the effectiveness and legitimacy of applying sidewall boundary-layer corrections. The two sets of test results, together with the corresponding GRUMFOIL predictions, are presented in Figure 11, first with no corrections applied, then with the respective floor and ceiling corrections applied, and finally with the Murthy²⁰ sidewall boundary-layer correction included in addition. Before any corrections are applied, the two sets of data are not in agreement with each other or with the GRUMFOIL predictions in the critical steeper drag-rise region. When the respective floor and ceiling corrections are applied, it can be seen that the two sets of data are in better agreement, but they still do not correspond to the GRUMFOIL predictions in the drag-rise region. However, when the Murthy sidewall boundary-layer correction is added (to the floor and ceiling corrections), the measured drag-rise characteristics from both tunnels agree much better with the predicted results. To corroborate these findings, the measured and predicted airfoil pressure distributions were examined, and indeed, the measured and predicted pressure distributions (i.e., shock strength and associated wave drag, which dominates the steep part of the drag rise) did not closely match each other until the sidewall boundary-layer correction was applied. These results further substantiate the position that application of sidewall boundary-layer corrections of the type recommended by Murthy or Barnwell-Sewall is appropriate and necessary when the sidewall boundary-layer is attached if experimental results are to be correctly interpreted.

Case Study No. 6 - The derivations (and applications) of the Barnwell, Barnwell-Sewall, and Murthy sidewall boundary-layer correction procedures are based on having attached boundary layers on the tunnel sidewalls, and there are important performance conditions involving unseparated flows (i.e. at typical cruising conditions or when defining the drag rise characteristics) where use of these corrections is necessary to properly interpret transonic airfoil test results. However, there are also important performance conditions involving separated flows (like the buffet boundary) where it is equally important to correctly interpret the test results. In fact, the buffet boundary can at times be nearly as important a performance parameter as drag³⁷. In this case study, the indicated buffet onset boundaries (defined by trailing-edge pressure divergence), from both the NAE and 0.3-m TCT tests of the airfoil configuration used in the previous studies, are used to demonstrate that use of sidewall boundary-layer corrections at these separated-flow conditions is not meaningful. These results also provide some insight into the relative importance of boundary-layer bleed amount and location of the sidewall boundary-layer removal on the definition of the buffet-onset boundary when there is likely separation of the sidewall boundary layer.

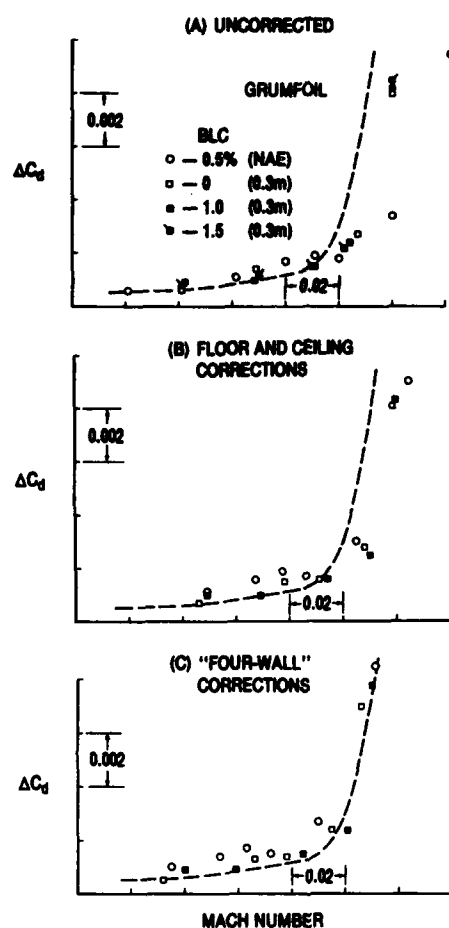


Figure 11. Effect of Wind Tunnel Wall Corrections on Compressibility Drag Characteristics

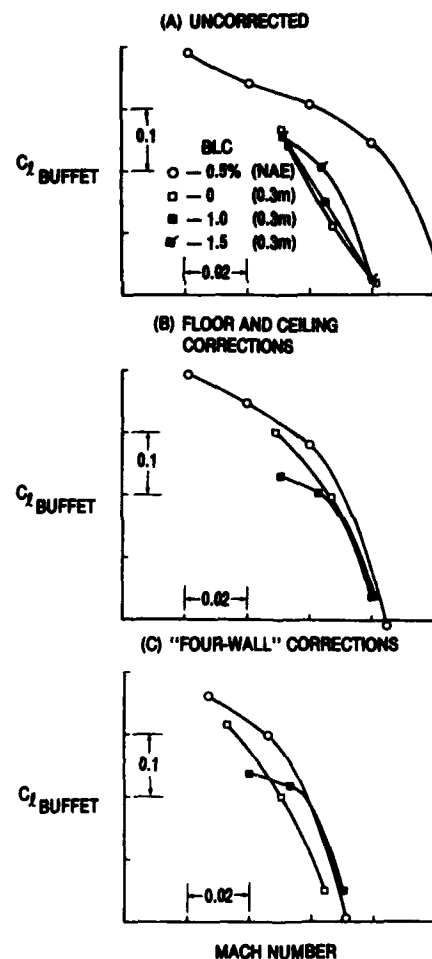


Figure 12. Effect of Wind Tunnel Wall Corrections on Indicated Buffet Onset

The buffet boundaries indicated from both the NAE and 0.3-m TCT tests are shown in Figure 12. Comparisons of the two sets of data are shown first with no wall corrections applied, then with the respective floor and ceiling corrections applied, and finally, with the Murthy²⁰ sidewall boundary-layer correction included in addition. There is a large disparity between the NAE results and the corresponding 0.3-m TCT results when no wall corrections are applied, but that disparity is significantly reduced with the application of the respective floor and ceiling corrections. As expected, the application of the Murthy sidewall boundary-layer correction to data with model-induced sidewall boundary-layer separation present does not provide any additional improvement in the tunnel-to-tunnel comparison, or even in the comparisons of the 0.3-m TCT data obtained with and without sidewall boundary-layer bleed.

With regard to the effectiveness of the different sidewall bleed arrangements, it can be seen from the data comparison with floor and ceiling corrections applied that the NAE suction arrangement, which effectively surrounds the model, appears to be more effective than the 0.3-m TCT upstream boundary-layer removal concept in reducing the adverse effect of the sidewall boundary layer. Furthermore, the comparison of the 0.3-m TCT data with and without sidewall boundary-layer bleed, which indicates a poorer buffet boundary when the bleed system is on, casts additional doubts on the usefulness of the upstream boundary-layer removal concept for test conditions with a separated sidewall boundary layer.

One other possible explanation for some of the differences in indicated buffet-onset boundaries obtained in the two different tunnels could be related to the differences in airfoil model chord, i.e., 10 inches in NAE versus 6 inches in the 0.3-m TCT. Murthy, Johnson, et al.³⁸ presented results for two different airfoil chord lengths in the

0.3-m TCT at the same chord Reynolds numbers that indicated that the compression of the airfoil pressure gradients on the sidewall boundary layer with the smaller model led to an earlier separation of the sidewall boundary layer.

7. CONCLUSIONS

A systematic experimental/computational investigation has been carried out to establish the legitimacy and effectiveness of applying corrections to account for sidewall boundary-layer effects in transonic airfoil testing, and also to highlight the conditions for which these corrections are appropriate and those for which they are not. Several examples have been presented to show the results of applying these corrections on drag polars, compressibility drag, shock-wave location, and definition of buffet onset boundaries. Areas covered have encompassed conditions with and without flow separations, situations with and without sidewall bleed, tests of the same airfoil configuration in two different tunnels, and different types of sidewall bleed. Analysis of the results from this investigation has led to the following conclusions:

1. The application of sidewall boundary-layer corrections of the type recommended by Murthy or Barnwell-Sewall is appropriate and necessary if meaningful comparisons of predicted versus experimental results at attached flow conditions are to be obtained, and also if the 2-D test results are to be correctly applied to 3-D wing designs.
2. Available sidewall boundary-layer correction methods, which assume attached flow, are not appropriate when flow separation exists on the airfoil (and sidewall) such as occurs when approaching buffet onset and maximum lift.
3. Incorporation of sidewall boundary-layer bleed does not appear to provide any obvious advantage in obtaining more accurate transonic airfoil data at conditions when the flow on the model (and sidewall) is attached if sidewall boundary-layer corrections are used.
4. Based on indicated buffet-onset results, boundary-layer bleed can be effective in maintaining 2-D flow on the airfoil at separated flow conditions, but only if the bleed is applied around the model. Upstream boundary-layer removal does not appear to help this situation. Increased airfoil chord lengths at a given chord Reynolds number may well be beneficial in delaying the onset of sidewall boundary-layer separation.
5. If tunnel-to-tunnel comparisons for specific airfoil configurations are to be undertaken to further validate the accuracy of current four-wall correction techniques, then comparable tunnel flow quality is an important prerequisite if ambiguous results are to be avoided.

REFERENCES

1. Bernard-Guelle, René, "Influence of Wind Tunnel Boundary Layers on Two-Dimensional Transonic Tests," NASA TT F-17, 255, 1976.
2. Ohman, L.H. and Brown, D., "The NAE High Reynolds Number 15" x 60" Two-Dimensional Test Facility: Description, Operating Experiences and Some Representative Results," AIAA Paper No. 71-293, 1971.
3. Kilgore, R.A., "Design Features and Operational Characteristics of the Langley 0.3-Meter Transonic Cryogenic Tunnel," NASA TN D-8304, 1976.
4. Johnson, C.B., Murthy, A.V. and Ray, E.J., "A Description of the Active and Passive Sidewall-Boundary-Layer Removal Systems of the 0.3-Meter Transonic Cryogenic Tunnel," NASA TM-87764, 1986.
5. Fancher, M.F., "Aspects of Cryogenic Wind Tunnel Testing Technology at Douglas," AIAA Paper No. 82-0606, 1982.
6. Barnwell, R.W., "Design and Performance Evaluation of Slotted Walls for Two Dimensional Wind Tunnels," NASA TM-78648, 1978.
7. Johnson, C.B. and Stainback, P.C., "Dynamic Measurement of Total Temperature, Pressure, and Velocity in the Langley 0.3-Meter Transonic Cryogenic Tunnel," NASA TP-2589, 1986.
8. Johnson, C.B., Johnson, W.G., Jr. and Stainback, P.C., "A Summary of Reynolds Number Effects on Some Recent Tests in the Langley 0.3-Meter Transonic Cryogenic Tunnel," SAE Paper No. 861765, 1986.
9. Murman, E.M., "Computation of Wall Effects in Ventilated Transonic Wind Tunnels," AIAA Paper No. 72-1007, 1972.
10. Shmilovich, A. and Caughey, D.A., "On Transonic flow Computations About Airfoils and Bodies of Revolution in Free Air and in Wind Tunnels," in Proc. of 11th IMACS World Congress on System Simulation and Scientific Computation, Aug. 1985.

11. Capelier, C., Chevallier, J.P. and Bouniol, F., "Nouvelle méthode de correction des effets de parois en courant plan," *La Recherche Aérospatiale* No. 1978-1, pp. 1-11, 1978.
12. Mokry, M. and Ohman, L.H., "Application of the Fast Fourier Transform to Two-Dimensional Wind Tunnel Wall Interference," *Journal of Aircraft*, Vol. 17, June 1980, pp. 402-408.
13. Chan, Y.Y., "A Singular Perturbation Analysis of Two-Dimensional Wind Tunnel Interferences," *ZAMP*, Vol. 31, No. 5, 1980.
14. Kemp, W.B., Jr., "TWINTAM: A Program for Transonic Wall Interference Assessment in Two-Dimensional Wind Tunnels," NASA TM-81819, 1980.
15. Preston, J.H., "The Interference on a Wing Spanning a Closed Tunnel, Arising from the Boundary Layers on the Sidewalls, with Special Reference to the Design of Two-Dimensional Tunnels," *NPL R&M* 1924, 1944.
16. Barnwell, R.W., "A Similarity Rule for Compressibility and Sidewall Boundary-Layer Effects in Two-Dimensional Wind Tunnels," *AIAA Paper* No. 79-0108, 1979.
17. Barnwell, R.W., "Similarity Rule for Compressibility and Sidewall Boundary-Layer Effects in Two-Dimensional Wind Tunnels," *AIAA Journal*, Vol. 18, No. 9, Sept. 1980, pp. 1149-1151.
18. Sewall, W.G., "The Effects of Sidewall Boundary Layers on Two-Dimensional Subsonic and Transonic Wind Tunnels," *AIAA Journal*, Vol. 20, No. 9, Sept. 1982, pp. 1253-1256.
19. Barnwell, R.W. and Sewall, W.G., "Similarity Rules for Effects of Sidewall Boundary Layer in Two-Dimensional Wind Tunnels," *AGARD CP-335*, 1982.
20. Murthy, A.V., "Corrections for Attached Sidewall Boundary-Layer Effects in Two-Dimensional Airfoil Testing," *NASA CR-3873*, 1985.
21. Murthy, A.V., "Effect of Aspect Ratio on Sidewall Boundary-Layer Influence in Two-Dimensional Airfoil Testing," *AIAA Paper* No. 87-0295, 1987.
22. Green, L.L. and Newman, P.A., "Transonic Wall Interference Assessment and Corrections for Airfoil Data from the 0.3-Meter TCT Adaptive Wall Test Section," *AIAA Paper* No. 87-1431, 1987.
23. Kemp, W.B. and Adcock, J.B., "Combined Four-Wall Interference Assessment in Two-Dimensional Airfoil Tests," *AIAA Paper* No. 82-0586, 1982.
24. Kemp, W.B., "TWINTN4: A Program for Transonic Four-Wall Interference Assessment in Two-Dimensional Wind Tunnels," *NASA CR-3777*, 1984.
25. Gumbert, C.R., Newman, P.A., Kemp, W.B. and Adcock, J.B., "Adaptation of a Four-Wall Interference Assessment/Correction Procedure for Airfoil Tests in the 0.3-m TCT," *NASA CP-2319*, 1984.
26. Gumbert, C.R. and Newman, P.A., "Validation of a Wall-Interference Assessment/Correction Procedure for Airfoil Tests in the Langley 0.3-Meter Transonic Cryogenic Tunnel," *AIAA Paper* No. 84-2151, 1984.
27. Bauer, F., Garabedian, P., Korn, D. and Jameson, A., "Supercritical Wing Sections II," *Lecture Notes in Economics and Mathematical Systems*, Vol. 108, Springer-Verlag, 1975.
28. Melnik, R.E., Mead, H.R. and Jameson, A., "A Multigrid Method for the Computation of Viscid/Inviscid Interaction on Airfoils," *AIAA Paper* No. 83-0234, 1983.
29. Nash, J.F. and Macdonald, A.G.J., "The Calculation of Momentum Thickness in a Turbulent Boundary Layer at Mach Numbers Up to Unity," *ARC CP* No. 963, 1967.
30. Carter, J.E., "A New Boundary-Layer Inviscid Interaction Technique for Separated Flow," *AIAA Paper* No. 79-1450, July 1979.
31. Green, J.E., Weeks, D.J. and Brooman, J.W.F., "Prediction of Turbulent Boundary Layers and Wakes in Compressible Flow by a Lag-Entrainment Method," *RAE-TR-72231*, 1973.
32. Collyer, M.R., "An Extension of the Method of Garabedian and Korn for the Calculation of Transonic Flow Past an Aerofoil to Include the Effect of a Boundary Layer and Wake," *British ARC, R&M* No. 3328, 1978.
33. Collyer, M.R. and Lock, R.C., "Prediction of Viscous Effects in Steady Transonic Flow Past an Aerofoil," *Aeronautical Quarterly*, Vol. XXX, Aug. 1979.
34. Delery, J.M., "Investigation of Strong Shock Turbulent Boundary-Layer Interaction in 2-D Transonic Flows with Emphasis on Turbulence," *AIAA Paper* 81-1245, 1981.

35. Zang, T.A., Hussaini, M.Y. and Bushnell, D.M., "Numerical Computations of Turbulence Amplification in Shock-Wave Interactions," AIAA Paper No. 82-0293, 1982.
36. Long, S.A.T., Spencer, R.C. and Robinson, D.M., "A Simplified Holographic-Interferometry Technique for Real-Time Flow Visualization and Analysis," NASA TN D-7421, 1974.
37. Lynch, F.T., "Commercial Transports - Aerodynamic Design for Cruise Performance Efficiency," in Transonic Aerodynamics (D. Nixon, Ed.), Progress in Astronautics and Aeronautics, Vol. 81, 1982.
38. Murthy, A.V., Johnson, C.B., Ray, E.J. and Stanewsky, E., "Investigation of Sidewall Boundary-Layer Removal Effects on Two Different Chord Airfoil Models in the Langley 0.3-Meter Transonic Cryogenic Tunnel," AIAA Paper No. 84-0598, 1984.

ACKNOWLEDGMENTS

The authors wish to acknowledge the substantial contributions of their colleagues at Douglas Aircraft Company and NASA Langley Research Center to the work reported in this paper. P. A. Wilcox and M. H. Bui at Douglas contributed much of the analysis for the six case studies, while C. R. Gumbert, P. A. Newman and A. S. Hill at NASA Langley provided the various wall corrections applied to the test data obtained in the 0.3-m TCT.

PHYSICAL ASPECTS OF VISCOUS SIMULATION AND ASSOCIATED RESEARCH REQUIREMENTS

(A summary report of the AGARD WG 09 Research Committee)

by

E. Stanewsky

Institut für Experimentelle Strömungsmechanik
Deutsche Forschungs- und Versuchsanstalt für
Luft- und Raumfahrt e.V.
D-3400 Göttingen, F.R.G.

INTRODUCTION

It seems reasonable to consider, before giving a summary of the results of the study of the Research Committee, the basic idea and meaning of viscous simulation and boundary layer control as applied to wind tunnel testing, although this is well known to most aerodynamicists involved in the design and development of transonic flight vehicles and the associated wind tunnel testing. For that purpose Figure 1 shows in two opposite plots the dependence of the lift coefficient for a transonic airfoil at a given freestream Mach number on the Reynolds number for a fixed transition location and on the transition location at a constant Reynolds number [1]. Common to both plots is the data point, marked by the octagonal symbol, at a Reynolds number of $Re = 2.4 \times 10^6$ and transition fixed at 7 percent chord. One observes in the right-hand plot that changing the Reynolds number between 2.4×10^6 and 31×10^6 results in a change in lift coefficient from about $C_L = 0.55$ to $C_L = 0.70$, i.e., a change by almost 30 percent. Considering now the left-hand plot, it is seen that varying the transition location between 7 and 50 percent chord causes about the same change in lift coefficient. Obviously there exists an equivalence between changing Reynolds number and transition location. There must, therefore, be some viscous parameter or parameters that dominate certain critical flow phenomena - to be specified later - and, as a consequence, the global flow development on the transonic airfoil considered.

Simulation procedures based on manipulating the transition location have, to various degrees, been applied for some time [2]. These procedures have, however, generally not been based on a sound understanding of the underlying physics of the flow since the dominating viscous and outer inviscid flow parameters that

govern certain critical flow phenomena - and that must, therefore, be duplicated at prominent locations on a given aerodynamic surface - are largely unknown. These deficiencies led to the formation of the Research Committee within the AGARD Working Group 09 "Boundary Layer Simulation and Control in Wind Tunnels" with the following objectives:

- Review of the physics associated with the simulation of high Reynolds number flow and, in particular, identification of viscous and outer inviscid flow parameters that dominate viscous/inviscid interactions sensitive to changes in the Reynolds number, hence crucial to the simulation process.
- Definition of research needed to improve the understanding of the flow physics associated with viscous simulation including research needed to identify and account for wind tunnel environmental effects.
- Definition of experiments and/or CFD exercises needed to establish the sensitivity of relevant flow phenomena or flow developments to viscous effects.

The Research Committee comprised the following members:

Prof. C. Ciray, Turkey
Mr. A.G.T. Croas, U.K.*
Prof. J.L. van Ingen, The Netherlands
Dr. E.M. Kraft, U.S.A.
Dr. R. Michel, France
Mr. J.D. Peterson, U.S.A.*
Dr. E. Stanewsky, F.R.G.
Dr. J. Szodruch, F.R.G.*

The gentlemen marked by an asterisk joined the Research Committee after completion of their assignment in the Review Commit-

tee. The final report of the Research Committee covers the following subjects in detail, always in the light of viscous simulation:

- Boundary layer development and transition
- Non-equilibrium boundary layers
- Shock boundary layer interaction
- Classical separation, trailing edge flow and buffet
- Vortex flows
- Environmental effects on the boundary layer development and transition
- Boundary layer manipulation

The present paper will present in some detail selected results pertaining to these subjects and summarize our findings with respect to the dominant viscous and outer inviscid flow parameters and most urgently needed research.

CRITICAL FLOW PHENOMENA

One can quite easily imagine that certain local flow phenomena that either affect the boundary layer development or are strongly influenced by changes in the condition of the boundary layer may largely contribute to the observed differences between low Reynolds number wind tunnel and full-scale flight results. These flow phenomena were termed "critical" by the Research Committee and I would like to demonstrate why critical by close examination of Figure 2 [1]. Plotted are, for a given freestream Mach number, the displacement thicknesses upstream of the shock on the upper surface of a transonic airfoil, immediately downstream of the shock and at the trailing edge, respectively, as function of the shock-upstream Mach number, i.e., in essence shock strength, varied by changing the angle of attack. The airfoil chord locations considered are indicated in the inset to the figure. The most important parameter of the graph in the present context of viscous simulation is the initial displacement thickness, i.e., the displacement thickness upstream of the shock, which was, for instance, varied by changing the location of the transition strip from 7 % chord, marked by circles, to 30 % chord, represented by triangles. One observes that this shift in transition location causes only a small difference in the displacement thickness upstream of the shock. Going through the shock, this difference increases markedly; a quite spectacular further increase occurs between shock and trailing edge due to the strong sustained adverse pressure gradients prevailing in that region. The change in lift coefficient, depicted in Fig. 1, is directly proportional to the change in displacement thickness at the trailing edge. Coming back to the criticalness, one sees that shock boundary layer interaction, trailing edge flow and classical trailing edge separation - whose occurrence is here indicated by the steep increase in the trailing edge displacement thickness at a shock-upstream Mach number

of about $M_1 = 1.33$ - are critical in the present sense since small initial differences in the boundary layer properties, exemplified by the displacement thickness, are changed considerably by the shock and rear adverse pressure gradients, which, in turn, results in a noticeable effect on the development of trailing edge separation.

Critical flow phenomena in the sense just described were identified by the Research Committee; they are summarized in Figure 3 and include, as already indicated,

- shock boundary layer interaction with the boundary layer, dependent on shock strength, either attached or separated,
- trailing edge flow in general and classical sustained adverse pressure gradient induced separation, where such separation may occur, as shown, in the trailing edge region of an airfoil or wing but also close to the leading edge, for instance, in form of a laminar separation bubble, and
- vortex flows - of course closely associated with separation - including the formation of wing and body vortices, shock vortex interaction and vortex breakdown.

There is a second group of critical phenomena which primarily affect the boundary layer development without having a direct influence on the outer flow - as do the strong viscous/inviscid interactions just considered. These phenomena are critical since the implementation of any viscous simulation process requires the understanding and predictability of the boundary layer development as it occurs naturally on a given aerodynamic surface - such as in flight - or as it evolves, for instance, under the influence of the wind tunnel environment or by boundary layer manipulation. The Research Committee considered, accordingly, relevant aspects of the wind tunnel environment, i.e., the effect of noise, turbulence, temperature spots and model irregularities on the boundary layer development including transition, and - most important in the present context - boundary layer manipulation techniques including conventional and advanced tripping devices, boundary layer suction and surface cooling.

We will now consider, as mentioned above, in some detail selected results of the Research Committee report pertaining to the critical phenomena.

SHOCK BOUNDARY LAYER INTERACTION

The importance of shock boundary layer interaction to the overall flow development, at least for transport aircraft configurations, was already pointed out. Shock boundary layer interaction comprises three main elements whose correct full-

scale simulation must be ensured in the low Reynolds number wind tunnel tests: the upstream influence, defined in Figure 4a and denoted L^* , the onset of shock-induced or incipient separation, defined as the condition where the wall shear stress just touches "zero" with increasing shock strength, Figure 4b, and the extent of the shock-induced separation bubble indicated by the region of negative wall shear stress, L_b , in the right-hand side diagram of Fig. 4b. Note, that instead of the wall shear stress, the shape parameter of the boundary layer $H_{32} = \delta^*/\delta$ can, as shown in this figure, be utilized to determine the onset and extent of separation [1] [3].

The upstream influence, which rules the interactive pressure gradient imposed on the boundary layer, hence determines the condition of the boundary layer leaving the interaction region, was found to be for a turbulent boundary layer solely dependent on the viscous parameter (δ_1^*/c) ($H_{11}-1$), where δ_1^* and H_{11} are the displacement thickness and the incompressible shape factor, respectively, immediately upstream of the shock.

Incipient separation was found to be rather insensitive to viscous effects and it is believed that duplicating the parameter dominating the upstream influence in the low Reynolds number wind tunnel tests will result in the correct simulation of full-scale shock boundary layer interaction up to separation.

We shall discuss now, in somewhat more detail, the development of the shock-induced separation bubble with increasing shock-upstream Mach number, M_1 , i.e., increasing shock strength. The discussion is based on a correlation of results obtained on two transonic airfoils in extensive surface pressure and boundary layer measurements [1].

The shock-induced bubble extent, normalized by the momentum thickness upstream of the shock, θ_1 , is shown in Figure 5 dependent on the shock-upstream Mach number, M_1 , and the condition of the incoming turbulent boundary layer, the latter varied by changing the Reynolds number and the transition location. One observes, first of all, that both airfoils - to be distinguished by the open and half-filled symbols, respectively - exhibit similar bubble developments with increasing M_1 , here varied by increasing angle of attack: The separation onset, or incipient separation, indicated by "zero" bubble extent, occurs for all viscous conditions considered close to a shock upstream Mach number of $M_1 = 1.30$. This confirms a fair number of experimental and theoretical results, all indicating that incipient separation, as already outlined, is rather independent of viscous effects [4] [5]. With increasing shock-upstream Mach number, an essentially linear downstream spreading of the bubble takes place which continues

to the so-called bubble blow-up [6], unfortunately not captured in the present tests. More important in the present context, one can recognize two distinct sets of curves: the lower one was obtained for a transition location of 30 % chord, i.e., a relatively thin boundary layer upstream of the shock, the upper one for a transition location of 7 % chord and a correspondingly thicker initial boundary layer. The thinner boundary layer clearly results in a slower progression in the development of the shock-induced separation bubble and, as a consequence, in a delay in the total breakdown of the flow.

In an attempt to correlate the results of the bubble extent and to identify the major influence parameters, a correlation parameter was derived empirically consisting of the shock-upstream Mach number in the form ($M_1 - 1.3$) - to account for the dominant influence of this Mach number and the insensitivity of incipient separation to viscous effects - and the initial momentum thickness normalized by the average upper surface contour radius between shock and trailing edge, R , Figure 6. The latter is primarily considered as a measure of the rear adverse pressure gradients which are different for the two airfoils considered. One sees that the correlation derived provides a rather satisfactory alignment of the experimental results which suggests that the dominant viscous parameter governing the bubble development is the momentum thickness upstream of the shock. It may - cautiously - be concluded from these results that duplicating the full-scale momentum thickness, normalized, of course, by the appropriate chord length, will provide a bubble development closely similar to the full-scale one.

The present data confirm results of a much more extensive investigation on airfoils and wings conducted over a wide Reynolds number range by Fulker and Ashill, who correlated the bubble extent, L_b/θ_1 , with the local Reynolds number based on the momentum thickness, $R\theta_1$, and the shock-upstream Mach number [6]. They have shown that for a three-dimensional wing duplicating the full-scale bubble extent in the low Reynolds number wind tunnel tests, i.e., essentially duplicating θ_1 , will result in the complete duplication of the full-scale three-dimensional pressure distribution. This is demonstrated in Figure 7 for the outboard region of a three-dimensional wing in the following way: Assumed as full-scale condition is a chord Reynolds number of $Re_c = 30 \times 10^6$ at a freestream Mach number of $M_\infty = 0.780$ and a lift coefficient of $C_L = 0.70$. According to the correlation of Fulker and Ashill, the bubble extent corresponding to this condition can be duplicated either by locating a transition trip (transition) at 15 % chord and testing at a Reynolds number of $Re_c = 13 \times 10^6$ or, alternatively, by locating a transition trip at 30 % chord and testing at a Reynolds number of

$Re_\delta = 5 \times 10^4$. The good agreement between the pressure distributions for these conditions, evident in Fig. 7, can be seen as confirmation of the dominant character of the initial momentum thickness but also as proof for the validity of the present approach to simulating the full-scale flow development in the presence of shock-induced separation.

CLASSICAL SEPARATION AND TRAILING EDGE FLOW

Considering classical separation, induced by sustained adverse pressure gradients, one can, within the context of viscous simulation, identify two critical locations: the leading edge, where the natural state of the boundary layer may, even at full-scale conditions, be laminar and the trailing edge region, where, for all practical situations, a turbulent boundary layer prevails. Treating turbulent boundary layer separation - we shall restrict ourselves here to that state of the boundary layer - one could proceed similar to the treatment of shock boundary layer interaction, identifying some dominant viscous parameter, say, at the location of the onset of the rear adverse pressure gradient, whose full-scale value must be duplicated in the low Reynolds number wind tunnel test. The Research Committee felt, however, that it is, in the case of classical separation, not necessary to rely on simple separation criteria - although helpful in identifying dominant viscous parameters - but employ Computational Fluid Dynamics (CFD) to determine the boundary layer development leading to separation, starting with some initial condition given, for instance, downstream of the shock boundary layer interaction region.

Applying CFD to determine the separation location, one must use certain indicators - "zero" skin friction would be the natural one but it is frequently not available and difficult to measure - that identify the location of separation on the aerodynamic surface considered. As an (alternative) indicator, one may, for instance, use a shape factor correlation such as the one depicted in Figure 8 where the shape parameter of the boundary layer is plotted in the form $(H-1)/H$ as function of the ratio of the displacement thickness to the boundary layer thickness [7] [8]. The two curves in the figure represent the relation between these viscous parameters for Coles' wall-wake description of the turbulent boundary layer profile, denoted W-W, and the Sandborn-Kline correlation for incipient "detachment", denoted I-D. The wall-wake correlation gives separation, i.e., $C_f = 0$, at $A = 0.5$ and a shape factor of $H = 4$, which is the value for equilibrium flow. The Sandborn-Kline correlation intersects the wall-wake curve in a region where the experimentally observed separation points are centered; the experimental data points show, however, a large amount of scatter around the intersection, with shape parameters rang-

ing from $H = 2.2$ to values above three. Assuming that the data scatter is not only due to experimental inaccuracies, one may conclude that the Sandborn-Kline correlation is not sufficient for the prediction of the boundary layer condition at separation for viscous simulation purposes. This is mainly due to the fact that this correlation - as do many others - draws too heavily on equilibrium flows and its related wall-wake velocity description. In order to make further progress, the departure of the boundary layer from equilibrium as it occurs, for instance, in strong adverse pressure gradients must be accounted for.

A promising step in this direction has been undertaken by Cross in revising Coles' law of the wall-wake to cope with the departure from equilibrium [9]. First, it was found to be necessary to reappraise the way, pressure gradient was included in the wall-wake description. Here, it was suggested by Coleman [10] to make the wake exponent χ in the expression for the velocity profile u/U_δ a variable. Cross showed subsequently that χ could be related to the departure from equilibrium flow conditions by considering the difference between the streamwise pressure gradient parameter $(\theta/U_\delta) (dU_\delta/dx)$ of the actual flow and the equivalent equilibrium flow, denoted τ_r [9]. This relation is shown in the inset to Figure 9. One observes that for equilibrium flow, i.e., $\tau_r = 0$, the Coles value of the wake exponent, $\chi = 2$, is obtained, while for a departure from equilibrium a strong deviation from this value is indicated. Note, that this relation also holds for three-dimensional flows.

At separation the law of the wall vanishes - together with the Reynolds number dependence - and the value of the shape parameter is determined solely by the degree of non-equilibrium flow distortion represented by the wake exponent. The relation between the shape parameter and the wake exponent at separation is shown in the main part of Fig. 9. For equilibrium flow, $\tau_r = 0 \rightarrow \chi = 2$, the shape parameter at separation corresponds, as already seen, to the Coles value $H = 4$, while H at separation is reduced significantly as the relative pressure gradient parameter, τ_r , is decreased. This is in agreement with experimental observations and may explain the apparent scatter of the results in the previous figure.

Unfortunately, not many results detailed enough to assess the quality of the present approach - here, most of all, experimental velocity profiles for comparison with the corresponding wall-wake profiles are needed - are available. Cross applied, therefore, boundary layer calculations, employing an entrainment integral method in conjunction with the boundary layer profiles described by his revised version of the wall-wake law to shock boundary layer interaction considering the shock simply as a very strong adverse pressure gradient [9]. Figure 10 shows as an

example of these calculations the distribution of the skin friction coefficient together with the pressure distribution [11] used as input to the boundary layer calculations. One observes from the comparison with experiment that the computed response of the boundary layer to the shock is correctly predicted so that one can expect the separation correlation of Fig. 9 to be valid, even for rather strong adverse pressure gradient flows. However, much more detailed experiments, including velocity profile measurements, are needed for the final validation of the approach to separation prediction just described.

VORTEX FLOW

Considering vortex flow, Dr. Kraft of the Research Committee concluded in his review that, in the large, research has not been performed to address the issues of sub-scale simulation of vortical flows so that the most pressing need is here a systematic scaling law analyses to be performed for the vortical flows of interest. Still, one may argue that for the correct simulation of the vortical flow development, it seems, first of all, important to duplicate the full-scale separation line and avoid the secondary separation if it is not present at full-scale conditions. This is likely to ensure, at least, the correct vortex trajectory. Concerning separation lines, guidance as to critical viscous parameters may, of course, be obtained from the discussion of shock boundary layer interaction and classical separation. The proper type of the boundary layer at separation, i.e., laminar, transitional or turbulent, must, of course, also be ensured.

Considering the different types of vortical flows listed in Fig. 3, one can separate these flows into the ones sensitive to viscous changes, i.e., Reynolds number, and insensitive. To the first category belong vortices off bodies and round leading edge wings, to the second category vortices off sharp leading edge wings and vortex breakdown and shock/vortex interaction; for the latter viscous simulation is not a major issue. Examples for the two categories are presented in Figure 11, where the angle of streamwise incidence for the formation of spiral vortices is shown as dependent on sweep, wing thickness, i.e., essentially leading edge radius, and Reynolds number [12]. One observes that, for a given sweep angle, a spiral vortex develops off the sharp leading edge wing at very low incidences and that the onset of vortex formation is completely independent of Reynolds number. For the round leading edge wing, a strong Reynolds number dependence of the onset of vortex formation exists, which means that here is a need for viscous simulation.

Another type of vortical flow development, essentially inviscid in nature, is, as mentioned above, shock vortex interaction. This is demonstrated in Figure 12 where

the breakdown limit for shock/vortex interaction is depicted as function of the initial rate of swirl, i.e., the ratio of the maximum tangential velocity to the axial velocity upstream of the shock, defined in the left-hand part of the figure, and the (uniform) shock upstream Mach number representing the pressure jump across the shock [13]. The limiting curve indicates that the initial rate of swirl has to be decreased with increasing shock strength if vortex breakdown is to be avoided. Insensitivity to viscous effects is derived from the fact that there is excellent agreement between the experimental results shown and inviscid calculations based on a numerical solution of the Euler equations. These results are supported by data for less severe sustained adverse pressure gradients which have shown that vortex breakdown is essentially dominated by geometric conditions of the wing and the external pressure gradient.

BOUNDARY LAYER DEVELOPMENT AND MANIPULATION

Regular Boundary Layer Development and Environmental Effects

Looking at the boundary layer development - the laminar development, transition and the turbulent development - one may distinguish between the regular or classical development, the evolution of the boundary layer under the influence of the wind tunnel environment and the development influenced by boundary layer manipulation. Concerning the classical boundary layer and here first the laminar boundary layer development, it was judged by Dr. Michel of the Research Committee that its theoretical treatment is "well in hand". For equilibrium turbulent boundary layers, it was indicated by the same source that the numerical codes available today are able to predict the boundary layer development, at least for incompressible flow, up to separation. For compressible flows, turbulence modelling is, for certain conditions - remember we are considering equilibrium boundary layers - still insufficient. These conditions include the presence of wall curvature and a non-adiabatic wall temperature distribution.

I want to demonstrate the importance of the correct assessment of non-adiabatic wall conditions by considering its influence on shock boundary layer interaction, Figure 13. It should be noted that the discussion may also be taken as a demonstration of a possible boundary layer manipulation technique but also as a potential unwanted model related environmental effect in the case of cryogenic wind tunnel testing. The results shown in the present figure were obtained by Inger, Lynch and Fancher [14] employing a modified version of Inger's shock boundary layer interaction solution [15] which operates with four independent input parameters - as indicated in the figure -

namely, the shock upstream Mach number, the local Reynolds number based on displacement thickness, the incompressible shape factor and the wall to boundary layer edge temperature ratio, T_w/T_e . Depicted are the upstream and downstream chordwise spread of the shock associated pressure rise, denoted L_u and L_p , respectively, as function of the wall temperature, both quantities referenced to adiabatic conditions. Considering first the pair of curves restricted to the lower part of the right-hand diagram, denoted H_{11} fixed, one observes that the influence of heat transfer on shock boundary layer interaction is rather small if heat transfer occurs only "localized", i.e., confined to the interaction region. The curves labelled T_w -effect, i.e., wall temperature effect, on H_{11} included represent a condition where the cumulative influence of a non-adiabatic wall temperature distribution upstream of the shock on H_{11} , i.e., the incompressible shape factor immediately upstream of the shock, is taken into account. Here, a large dependence of the chordwise spread of the pressure increase due to the shock on the deviation from adiabatic wall conditions is evident. This shows that in a viscous simulation process, wall cooling is a rather powerful tool to control shock boundary layer interaction and that, accordingly, an accurate prediction of the non-adiabatic boundary layer development is necessary. The results confirm, furthermore, that the shape factor H_{11} is one of the dominant viscous parameters in scaling the shock related upstream influence.

Boundary layer transition still carries a great number of open questions and much more research is needed in the experimental as well as the theoretical domain. Our knowledge concerning, for instance, the influence of noise, freestream turbulence and surface roughness on three-dimensional transition - as it occurs on a swept wing, say, where cross-flow instability may be dominant - is totally insufficient. In briefly touching transition, I would like to consider, therefore, the derivation of a criterion for three-dimensional transition again combining a demonstration of, what was termed, the regular boundary layer development with the one affected by the environment.

In their - actually well known - treatment of cross-flow instability, Coustols and Arnal tried to take advantage of results given by laminar stability theory by applying them to three-dimensional boundary layers [16]. In doing so, they consider, at a given streamwise location, the stability properties of different velocity profiles, U_e , which are projections of the actual profile into various directions ϵ , as indicated in the left-hand part of Figure 14, starting with the cross-flow profile $\epsilon = 0$. Stability calculations for these profiles revealed the existence of one most unstable direction, here designated as ϵ_{min} . Based on these consider-

ations and the various - but few - experimental data available for swept wings, a cross-flow instability transition criterion was established relating, as shown in the right-hand part of the figure, the Reynolds number based on the displacement thickness, formed with the profile in the direction $\epsilon = \epsilon_{min}$ at transition, to the streamwise shape factor H_1 and the freestream turbulence level Tu . One observes that the present approach to the prediction of transition due to cross-flow instability provides a rather good description of the experimental results. With regard to the transition Reynolds number, as defined here, it is seen that this Reynolds number increases - at the lower turbulence levels very rapidly - with increasing shape parameter and with decreasing turbulence level, the latter being for transition due to longitudinal instability a well-documented fact. One of the particular merits of the effort conveyed here, is, of course, the qualitative assessment of the influence of the wind tunnel environment on transition due to cross-flow instability. As mentioned above, much more research is required in this area.

Using the criteria for the various possible modes of transition as outlined, for instance, by Dr. Michel in the Research Committee report, i.e., criteria for transition due to leading edge contamination and streamwise and cross-flow instability, a parametric study was carried out by ONERA/CERT in order to show the combined effect of pressure gradient, sweep angle and Reynolds number on transition [17]. A representative result is shown in Figure 15 based on the pressure distribution depicted in the upper right-hand corner of the figure for the angle of incidence of $\alpha = 1^\circ$. One observes that transition due to longitudinal instability progresses only slowly upstream with increasing Reynolds number. Once cross-flow instability commences to dominate the flow development, a very rapid upstream movement of the transition point takes place with Reynolds number which is due to the strong negative pressure gradients attendant over the initial 40 percent of the chord. At the upper end of the Reynolds number range considered, leading edge contamination results in the boundary layer being completely turbulent over all of the wing. Note, that the pace of the transition point movement is rather strongly affected by the sweep angle.

Boundary Layer Manipulation

Concerning boundary layer manipulation, already briefly addressed in the preceding section, one may distinguish between manipulation devices that promote or delay transition in a desired fashion and devices that predominantly affect the development of the turbulent boundary layer - these devices are, of course, sometimes identical. In the first category, boundary layer tripping is the most

widely applied and perhaps easiest boundary layer manipulation technique to use, although limited in its range of application by the attendant model pressure distribution. A frequent question associated with boundary layer tripping is related to the boundary layer properties downstream of a given tripping device in comparison to the properties of a boundary layer having gone through natural transition, especially with respect to the velocity profile and the turbulence structure. Because of the wide utilization of tripping and the consequences to viscous simulation, should strong deviations in the subsequent boundary layer development from a naturally transitioned boundary layer occur, I want to address this issue here as the only further one concerning manipulation.

Figure 16 shows the measured velocity distributions in the boundary layer downstream of a tripping device, consisting of 0.015 inch disks, compared with the classical law of the wall and logarithmic velocity profiles for a turbulent boundary layer. The data were obtained at AEDC on a 7-degree cone at a freestream Mach number of $M_\infty = 0.60$ [18]. It is seen in Fig. 16a that immediately behind the trip - the trip was located at 16 inches - the velocity profile is representative of a transitional profile following, however, predominantly a laminar characteristic. Further downstream, the mean velocity distribution turns into a fully developed turbulent profile, as indicated in Fig. 16b.

The Reynolds shear stress distribution in the fully transitioned boundary layer downstream of the disk trips reflects correspondingly, as indicated in Figure 17, the same behavior as a naturally transitioned turbulent boundary layer, the latter marked by the circles. It should be noted that natural transition occurred here between 18 and 20 inches while the tripping device, as mentioned above, was located at 16 inches. From the results depicted in Figs. 16 and 17 one may conclude that distributed three-dimensional tripping elements, such as the disks considered, produce, at least in the absence of pressure gradients, the same type of boundary layer as natural transition. Investigations like the present one are also needed for realistic configurations with pressure gradients.

SUMMARY OF FUTURE RESEARCH REQUIREMENTS AND CONCLUSION

In the preceding section only a very few results of the study of the Research Committee were given in some more detail, the purpose of it having been, in essence, a demonstration of the approach the Research Committee has taken and of the type of results to be expected in the full committee report. In concluding I want to summarize relevant findings of the Research Committee placing emphasis on research most urgently needed (also see Figure 18).

Shock boundary layer interaction: Shock boundary layer interaction, one of the most important critical flow phenomena in the present context, comprises three main elements whose viscous simulation in low Reynolds number wind tunnel tests must be ensured:

- The upstream influence, which rules the interactive pressure gradient imposed on the boundary layer, was found to be only dependent on the viscous parameter $\delta_1^+(H_{11}-1)$, where δ_1^+ and H_{11} are the displacement thickness and the incompressible shape factor, respectively, immediately upstream of the shock,
- incipient separation, found to be rather insensitive to viscous effects, hence not problematic to viscous simulation, and
- the development of the shock-induced separation bubble with increasing shock-upstream Mach number (shock strength), found to be mainly dependent on the momentum thickness immediately upstream of the shock.

The full-scale values of the viscous parameters indicated above must be duplicated in the low Reynolds number wind tunnel tests for the correct simulation of full-scale shock boundary layer interaction. There remain, however, within the present context, several unresolved issues which require further experimental and theoretical research effort:

- The results, summarized above, are partly based on a rather limited number of experiments so that, especially in three-dimensional flow, well designed experiments must be carried out on realistic configurations to confirm the dominance of the viscous parameters identified above.
- Although there is some positive evidence, it must be conclusively determined how closely the boundary layer parameters at the downstream face of the shock boundary layer interaction region (e.g., δ^* , θ , H) correspond to the ones for the (higher) Reynolds number to be simulated.
- Partly as a consequence thereof, one must investigate whether the simulation of the high Reynolds number trailing edge flow behavior is ensured - or what degree of approximation can be achieved - if the shock boundary layer interaction is simulated correctly. Proper simulation of the trailing edge flow conditions is, of course, required to obtain in airfoil or wing flow the correct full-scale shock location and strength.

There are some more - but not as pressing - open issues related to shock boundary layer interaction, such as, for instance, the effect of turbulence amplification and generation due to the interaction on

trailing edge flow, for details of which the reader is referred to the committee report. (This holds, naturally, for all topics considered in this section.)

Classical separation and trailing edge flow: It was indicated above that, concerning classical separation within the present context, two critical locations where such separations may occur could be identified: the leading edge region where the incoming boundary layer may be laminar and the trailing edge region where, for all practical applications, a turbulent boundary layer prevails. Laminar separation bubbles with transition within the separated region, likely - but not exclusively - to be present in low Reynolds number wind tunnel tests for peaky-type pressure distributions, may have a large effect on the turbulence structure at and downstream of reattachment, hence on the subsequent turbulent boundary layer development. Adequate turbulence models in a sufficiently general form still have to be developed for this type of flow and suitable experiments must be devised to achieve this goal.

The parameters governing classical turbulent boundary layer separation are the shape factor H and the relative pressure gradient parameter w_r , the latter accounting for the degree of deviation of the boundary layer profile development from equilibrium conditions. Here, most of all, a further improvement of theoretical methods for the prediction of the two- and three-dimensional boundary layer development leading to separation is needed together with the establishment of accurate shape parameter correlations, especially for three-dimensional flows. Generally, it was concluded that

- an improvement of turbulence modeling is required for all situations where a strong interaction between the outer inviscid flow and the boundary layer occurs and that
- theoretical methods are increasingly becoming available which, though initially developed largely from the consideration of simpler flows, aim to treat very complex flows involving separation, large normal pressure gradients and shock waves. These methods require for validation and improvement thorough experiments which provide a full description of the incoming boundary layer giving all relevant flow parameters and boundary conditions, such as skin friction, velocity profiles, pressure gradient parameter, skin friction lines in three-dimensional flow and so on.

The simulation of the trailing edge flow development - attached or separated - on the upper and lower surfaces of an airfoil or wing should be such that the correct circulation is obtained. Important parameters to be considered here are the momentum loss, the displacement thickness,

the shape factor and the turbulence structure. How closely these parameters must be duplicated to simulate full-scale flow - or whether it is sufficient to just avoid separation, should it not occur at full-scale conditions - is not known and requires additional experimental and theoretical studies (also see the simulation of shock boundary layer interaction).

Vortex flow: For the correct simulation of the vortical flow development it seems, first of all, important to duplicate the full-scale primary separation line. Here, guidance concerning critical viscous parameters may be obtained from the discussion of shock boundary layer interaction and classical separation. The proper type of boundary layer at separation, i.e., laminar, transitional or turbulent, must, furthermore, be ensured. Basically, it was found in the review of the present subject, however, that, in the large, research has not been performed to address the issues of subscale simulation of vortical flows. To alleviate this deficiency, the following research is needed:

- A systematic scaling law analysis must be performed on vortical flows of interest. Appropriate length scales and physical phenomena must be identified as a guide to proper subscale simulation. The scaling laws determined must be evaluated against the full-scale flow development.
- Systematic studies of the influence of boundary layer tripping on vortex separation are needed. Specific objectives are to determine the influence of the state and condition of the incoming boundary layer, as altered by tripping and tripping techniques, on symmetrical and asymmetrical vortex shedding on forebodies, reattachment and secondary vortex formation on sharp leading edge wings, shock-induced vortices on sharp edged wings with supersonic leading edges and primary vortex separation on round leading edge wings.
- Vortex breakdown was found to be dominated mainly by geometric conditions on the wing and the external pressure gradient. Here, one last conclusive experiment needs to be performed to confirm the independence of vortex breakdown (and similarly shock/vortex interaction) on Reynolds number.

It is strongly urged that in all experimental research, body surface pressures, surface skin friction lines, surface streamline visualization, vortex trajectory visualization and vortex core velocities be obtained. These multiple pieces of information are necessary to understand the detailed behavior of the flow. It is also recommended that - as in the case of all critical flow phenomena - CFD be used to gain further understanding of vortical flow features.

Boundary layer development, environment and manipulation: Concerning the laminar boundary layer development, it is reasonable to state that its theoretical treatment for weak interactions with the outer flow field is, for all relevant configurations, "well in hand". For classical equilibrium turbulent boundary layers, it is reasonable to assume that the numerical codes available today are able to predict the boundary layer development, at least for incompressible flow, up to separation. For compressible boundary layers, turbulence modelling is, for certain conditions, still insufficient: More systematic experimental and theoretical studies must be conducted in order to obtain fundamental data on the structure of turbulence, especially at non-adiabatic wall conditions and in the presence of streamwise wall curvature. Also much needed is fundamental research on turbulent boundary layers at high Reynolds numbers for which cryogenic wind tunnels now provide an excellent tool.

Boundary layer transition still carries a great number of open questions and research is needed in the experimental as well as the theoretical domain. Needs for experimental studies are particularly pressing in three-dimensional flow:

- Transition criteria have been established based on but a few experimental data. These criteria must be verified in experiments where the main influence parameters are systematically varied.
- Knowledge concerning the influence of noise, freestream turbulence and surface roughness on three-dimensional transition is totally insufficient.
- Transition criteria must be established for realistic transonic configurations where pressure gradients play an essential role. Here, research is especially needed on the effect of wall temperature on transition since the influence of wall temperature is highly dependent on the attendant pressure gradients.

Concerning (stability) theory, it is judged that the amplification method (e^N) is the most promising approach to transition prediction in the present domain of interest, provided all effective parameters - such as freestream turbulence and noise - are properly accounted for.

It was found that, although a wide body of information is available in certain areas, environmental effects have generally not been studied in a systematic and well organized manner. Major deficiencies in that regard, hence research needs, are especially seen in the following areas:

- The influence of external turbulence on characteristics of the turbulent boundary layer has mainly been studied for zero-pressure gradient flows;

flows with non-zero-pressure gradients still require more detailed experimental and theoretical attention, especially with regard to the relation between pressure gradient and the mixing length of the external flow and its influence on the characteristics of the turbulent boundary layer. Also needed are more detailed studies of the effect of turbulence scale on the boundary layer development.

- The effect of external turbulence on certain flow phenomena, such as, for instance, shock boundary layer interaction and trailing edge separation, has not been sufficiently investigated. There is, however, some evidence that fairly high turbulence levels, usually not found in contemporary wind tunnels, seem to be needed before any effect on such flow phenomena is felt.
- The information on the influence of wind tunnel acoustical disturbances is not well defined beyond the cut-off turbulence intensity of 0.3 %, yet the noise spectrum characteristics are critical for the transition location. Here, well designed experiments where the influence of the various disturbance sources can be separated are required.

In order to better understand the way certain environmental disturbances act on the boundary layer characteristics (receptivity), improved theoretical methods must be devised.

It is obvious that, left to its own development, the boundary layer on a model in sub-scale simulation may have little resemblance, in general, to the boundary layer on the full-scale vehicle. Consequently it is inevitable that some sort of boundary layer manipulation will have to be performed. For the simulation process it is most important, of course, that the viscous parameters that must be controlled on the model are known for each fundamental test requirement. Boundary layer manipulation techniques must then be developed that produce the desired control of the relevant parameters; primary "manipulators" are here boundary layer tripping, boundary layer suction and surface cooling. Research must, most of all, be performed

- to explore the effectiveness of boundary layer manipulation devices for families of favorable and adverse pressure gradients and to develop correlations that define the boundary layer parameters, such as H_1 , δ^*/c , θ/c , that will occur downstream of a specific manipulation device, and, furthermore,
- to determine the flow structure in a transitioned boundary layer downstream of a cross-flow instability or

leading edge contamination induced transition in order to evaluate the adequacy of conventional tripping in simulating other than streamwise instability transition.

Finally, non-intrusive boundary layer measurement techniques must be improved and developed to the point of practical application since the identification of the transition location and the determination of the magnitude of dominant viscous parameters is an integral part of boundary layer manipulation. In addition, the use of CFD to infer viscous parameters that cannot be easily measured should be explored.

REFERENCES

- [1] Stanewsky, E., "Interaction between the Outer Inviscid Flow and the Boundary Layer on Transonic Airfoils", Dissertation, TU-Berlin (D 83), 1981 (also Z. Flugwiss. Weltraumforsch. 7, 1983, Heft 4, pp. 242-252).
- [2] Burgmüller, W., "Transition Fixing in High Speed Tests for Civil Aircraft Wing Development", DFVLR-Mitt. 84-17, 1984, pp. 55-79.
- [3] Walz, A., "Strömungs- und Temperaturgrenzschichten", Verlag G. Braun, Karlsruhe, 1966.
- [4] Delery, J., Marvin, J.G., "Turbulent Shock Wave Boundary Layer Interaction", AGARDograph No. 280, 1985.
- [5] Inger, G.R., Deane, A., "Transonic Shock Interaction with a Tangentially-injected Turbulent Boundary Layer", AIAA 22nd Aerospace Sciences Meeting, Paper No. 84-0094, Jan. 1984.
- [6] Fulker, J.L., Ashill, P.R., "A Model of the Flow over Swept Wings with Shock Induced Separation", Paper presented at the IUTAM Symposium on Turbulent Shear Layer / Shock Wave Interactions, Palais-seau, France, Sept. 9-12, 1985 (also Springer-Verlag, Berlin, Heidelberg, 1986).
- [7] Kline, S.J., "Contribution to a Round Table Discussion", in AGARD CP-291 Computation of Viscous-Inviscid Interactions, 1980.
- [8] Kline, S.J., Bardina, J.G., Strawn, R.C., "Correlation of the Detachment of Two-dimensional Turbulent Boundary Layers", AIAA Journal, Vol. 21, No. 1, January 1983, pp. 68-73.
- [9] Cross, A.G.T., "Boundary Layer Calculations Using a Three Parameter Velocity Profile", BAe Brough Report No. YAD 3428, December 1980.
- [10] Coleman, W.S., "Mean Field Development of an Incompressible Fluid in Turbulent Shear near a Wall", BAe Brough Report, unpublished, Feb. 1974.
- [11] Cook, P.H., McDonald, M.A., Firmin, M.C.P., "Aerofoil RAE 2822 - Pressure Distributions, and Boundary Layer and Wake Measurements", RAE TM 1725, Sept. 1977.
- [12] Poll, D.I.A., "On the Generation and Subsequent Development of Spiral Vortex Flow over a Swept-back Wing", in AGARD CP-342, April 1983.
- [13] Miller, D.S., Wood, R.M., "Leeside Flows over Delta Wings at Supersonic Speeds", AIAA Journal of Aircraft, Vol. 21, No. 9, Sept. 1984, pp. 680-686.
- [14] Inger, G.R., Lynch, F.T., Fancher, M.F., "Theoretical and Experimental Study of Non-adiabatic Transonic Shock / Boundary Layer Interactions", AIAA Journal, Vol. 23, No. 10, Oct. 1985, pp. 1476-1482.
- [15] Inger, G.R., "Application of a Shock-Turbulent Boundary Layer Interaction Theory in Transonic Flow Field Analysis", AIAA Progress in Astronautics and Aeronautics, Vol. 81, Transonic Aerodynamics, AIAA, New York, 1982, pp. 621-636.
- [16] Michel, R., Arnal, D., Coustols, E., "Stability Calculations and Transition Criteria in Two- and Three-dimensional Boundary Layers", 2nd IUTAM-Symposium on Laminar-Turbulent-Transition, Springer-Verlag, 1984.
- [17] Michel, R., Arnal, D., Coustols, E., Juillen, J.C., "Experimental and Theoretical Studies of Boundary Layer Transition on a Swept Infinite Wing", 2nd IUTAM-Symposium on Laminar-Turbulent-Transition, Springer-Verlag, 1984.
- [18] Sinclair D.W., Strike, W.T. Jr., "Boundary Layer Transition-Trip Study at Subsonic and Transonic Speeds in AEDC Tunnels A and 47", unpublished internal AEDC report, 1986.

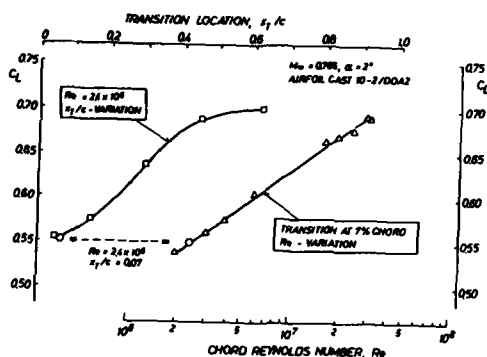


Figure 1: Apparent equivalence of change in Reynolds number and transition location, Ref. [1]

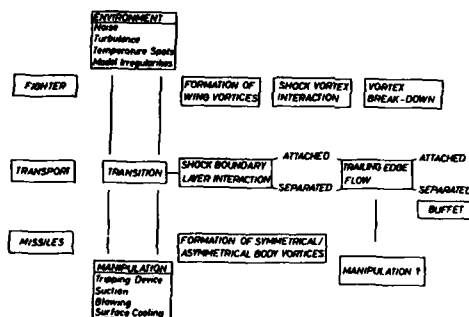


Figure 3: Critical flow phenomena

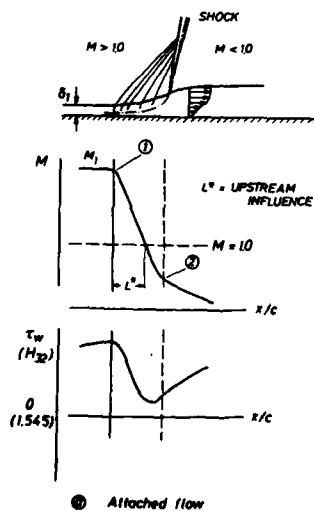


Figure 4: Definition of main features of shock boundary layer interaction

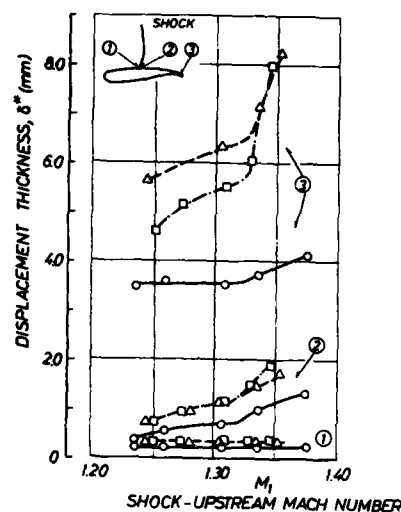
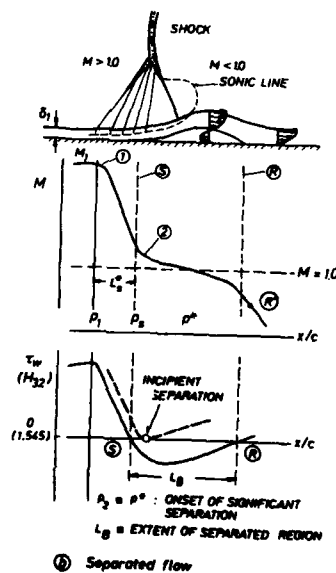


Figure 2: Effect of shock and rear adverse pressure gradients on differences in the initial displacement thickness, Ref. [1]

o $Re = 1.95 \times 10^6$
 Transition at 30% chord
 Δ $Re = 1.95 \times 10^6$
 Transition at 7% chord
 □ $Re = 3.5 \times 10^6$
 Transition at 7% chord
 Airfoil CAST 10-2/DOA2



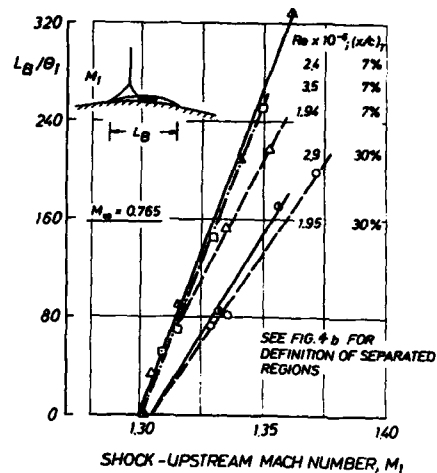


Figure 5: Effect of shock - upstream Mach number and initial boundary layer condition on the extent of the shock-induced separation bubble, Ref. [1]
Open symbols: Airfoil CAST 7/DOA1
Half-filled symbols: Airfoil CAST 10-2/DOA2

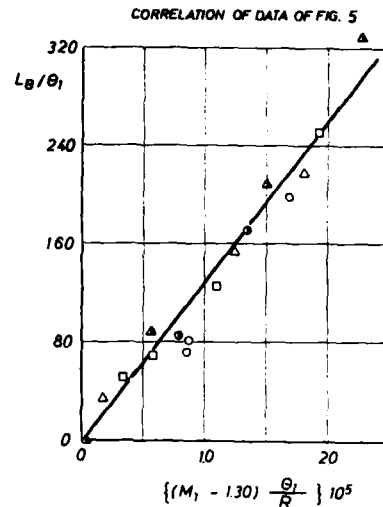


Figure 6: Correlation of the extent of the shock-induced separation bubble, Ref. [1]
Note: Symbols denote conditions as in Fig. 5

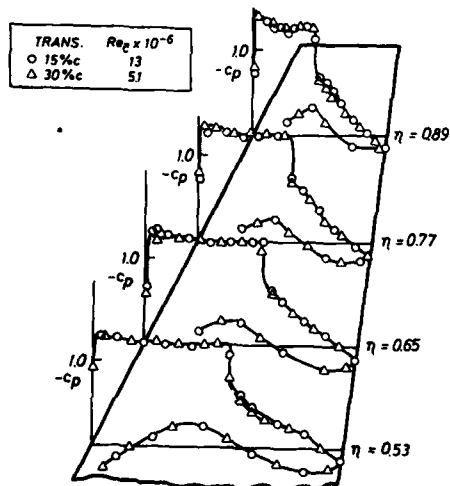


Figure 7: Independent simulation of full-scale pressure distributions for a three-dimensional wing at $M_\infty=0.780$ and $c_L=0.70$, Ref. [6]

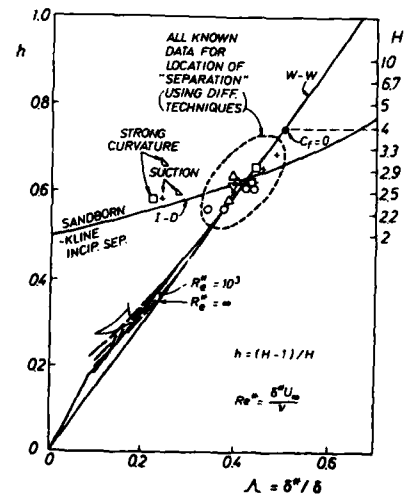


Figure 8: Shape factor correlation for "classical" separation, Ref. [7] [8]

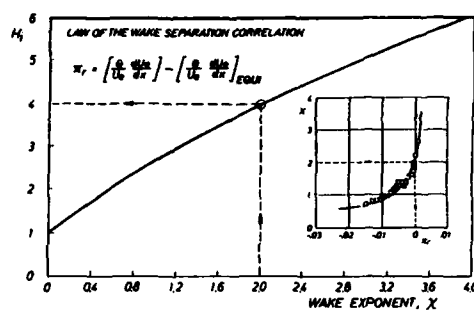


Figure 9: Separation correlation accounting for non-equilibrium effects, Ref. [9]

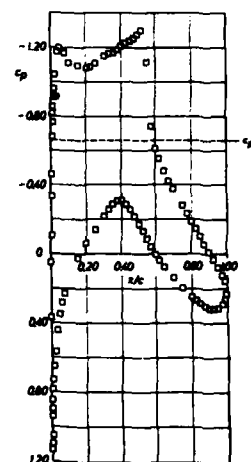


Figure 10: Boundary layer computation based on non-equilibrium wall-wake velocity profiles - comparison with experimental results, Ref. [11]
 $M_\infty = 0.730$, $\alpha = 3.19^\circ$, $Re = 6.5 \times 10^6$

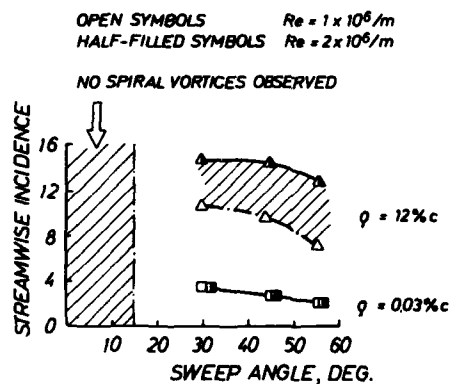
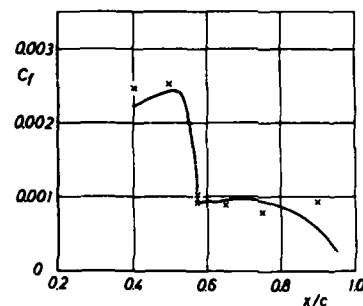


Figure 11: Influence of sweep, thickness and Reynolds number on the formation of a spiral vortex on a swept wing, Ref. [12]

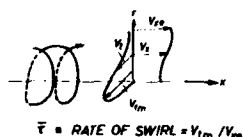
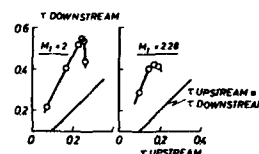
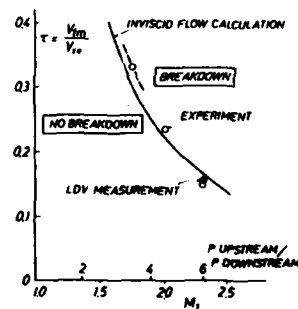


Figure 12: Vortex breakdown limit for shock/vortex interaction, Ref [13]



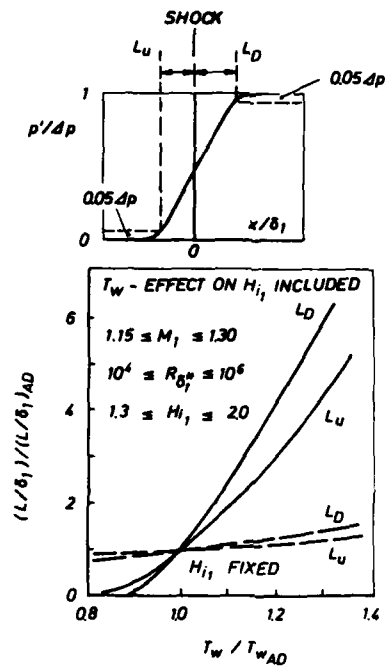


Figure 13: Effect of non-adiabatic wall conditions on shock boundary layer interaction, Ref. [14]

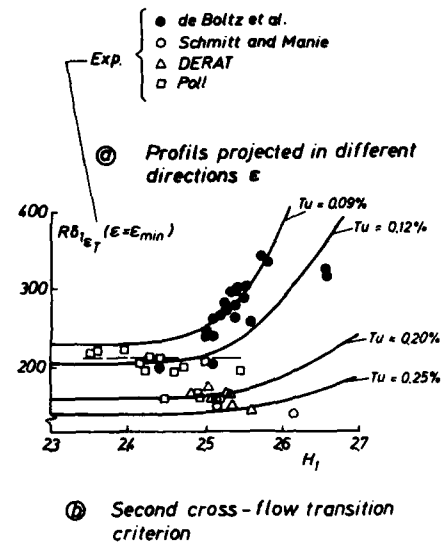
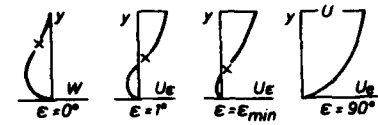


Figure 14: Cross-flow transition criterion according to Coustols and Arnal, Ref. [16]

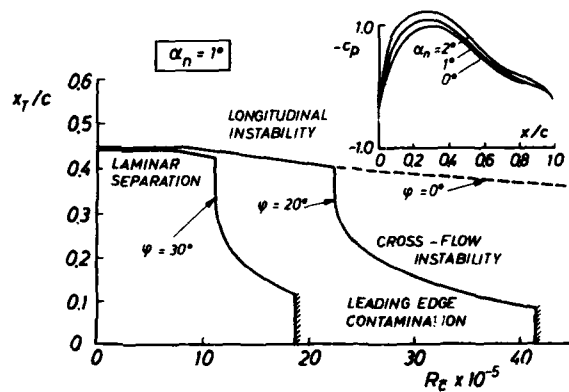
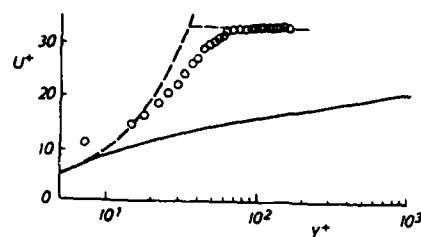
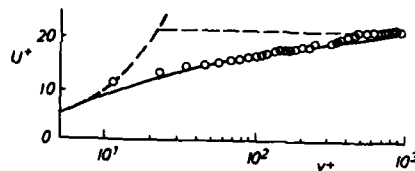


Figure 15: Application of transition criteria to an infinitely swept wing upper surface pressure distribution, Ref. [17]



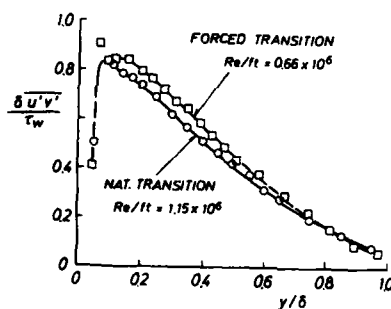
Ⓐ $x_s = 17.5$ inches



Ⓑ $x_s = 31$ inches

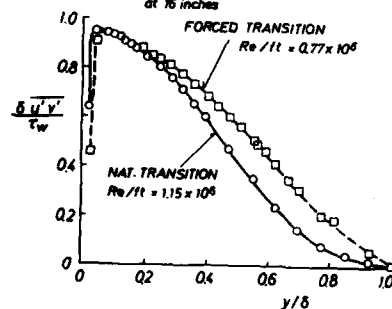
Figure 16: Velocity profiles downstream of a 0.015-inch disk tripping device at $M_\infty=0.60$, Ref. [18]

NOTE: See Fig. 41b



Ⓐ $x_s = 22$ inches

NOTE: Nat. transition occurred between 18 and 25 inches; trip was located at 16 inches



Ⓑ $x_s = 35$ inches

Figure 17: Shear stress distribution through the boundary layer downstream of a 0.015-inch disk tripping device at $M_\infty=0.60$, Ref. [18]

FLOW PHENOMENON	DOMINANT PARAMETERS	NEEDED FUTURE RESEARCH
SBLI⁺ - Upstream influence - Incipient separation - Separation bubble	$[\delta_1^*/c][H_{i1}-1]$ H_{i1}, M_1 θ_1, M_1	- Verification of dominant parameters especially in 3-D flows - Boundary layer parameters downstream of SBLI region in relation to full-scale flow - Is additional manipulation of trailing edge flow required? - Importance of turbulence generation/amplification to trailing edge flow - Improve theory
CLASSICAL SEPARATION/TRAILING EDGE FLOW (also see non-equilibrium boundary layers)	H_i, π_r δ^*, θ	- Improvement of theoretical methods to account for non-equilibrium effects in 2-D/3-D flows. Establish shape factor/pressure gradient parameter correlation for 3-D flows - Improve turbulence modelling for flows with transition occurring in laminar separation bubbles - Improve turbulence modelling for strong viscous/inviscid interactions
VORTEX FLOW	For primary separation line see SBLI and CLASSICAL SEPARATION	- Conduct scaling law analysis for vortical flows. Identify appropriate length scales - Determine the effect of tripping (state and condition of incoming boundary layer) on vortical flows of interest
BOUNDARY LAYER DEVELOPMENT - Equilibrium turbulent boundary layer - Transition (also see environment) - Non-equilibrium boundary layers (also see classical separation)		- Turbulence modelling in the presence of $T_w/T_{wAD} \neq 1$ and curvature - Fundamental research at high Reynolds numbers - Verify transition criteria - Influence of noise, turbulence and surface roughness on 3-D transition - Establish transition criteria for realistic transonic configurations. Effect of T_w/T_{wAD} for $dp/dx \neq 0$ - Provide experiments with a complete description of the incoming boundary layer (velocity profiles, wall shear stress, etc.)
ENVIRONMENT (also see transition)		- Influence of external turbulence on turbulent boundary layer for $dp/dx \neq 0$ - Effect of turbulence scale on turbulent boundary layer development - Effect of turbulence on certain flow phenomena (SBLI, classical separation) - Influence of noise on transition at $Tu > 0.3$ - Improve develop/theory
MANIPULATION		- Effectiveness of boundary layer manipulation devices for $dp/dx \neq 0$. Define boundary layer parameters (H_i, δ^*, θ , turbulence structure) downstream of specific manipulation devices - Boundary layer structure downstream of cross-flow instability transition in comparison to tripped boundary layer - Improve non-intrusive boundary layer measurement techniques - General: Find an inexpensive device that is easy to install, remotely controllable, does not disturb the flow and also measures the boundary layer condition upstream of "critical" flow phenomena

⁺SBLI = Shock boundary layer interaction.

δ^*, θ, H_i = Displacement thickness, momentum thickness, incompressible shape factor.

π_r = Relative pressure gradient parameter (see Fig. 9).

T_w = Wall temperature.

Subscripts: 1 = upstream of shock AD = Adiabatic wall conditions

Figure 18: Summary of results and major research requirements.

ON REYNOLDS NUMBER EFFECTS AND SIMULATION

Report of the Review Committee

of

AGARD Working Group 09

"Wind Tunnel Boundary Layer Simulation and Control"

by

A. Elsenaar

National Aerospace Laboratory NLR
Anthony Fokkerweg 2, 1059 CM Amsterdam
The Netherlands

1. INTRODUCTION

The change in flow development with Reynolds number, commonly referred to as the Reynolds number effect, has both attracted and annoyed the aerodynamic community for some time now. It annoys the aerodynamic designer who has to predict from sub-scale wind tunnel tests the aircraft performance. A misjudgment of the magnitude of the Reynolds number effect may lead to an over- or underestimation of flight performance resulting in economic loss. In the worst case a costly redesign is required during the period of flight testing. The question of Reynolds number effects attracts the aerodynamicist because of its very fundamental nature: a thorough understanding of viscous flow phenomena and their interactions with the inviscid flow field is required to explain Reynolds number effects.

As long as routine wind tunnel testing at the actual flight Reynolds number is not possible, other ways must be found to close the experimental Reynolds number gap. Basically, Reynolds number effects originate from a Reynolds number dependency of a viscous shear layer close to the body surface and its interaction with the outer inviscid flow field. If the boundary layer can be manipulated in the wind tunnel such that its development at flight Reynolds numbers is closely approximated, the inviscid flow senses the proper boundary condition and the overall flow development will then be very similar. With this in mind the AGARD Fluid Dynamics Panel formed in 1984 Working Group 09 "Wind Tunnel Boundary Layer Simulation and Control". The working group has split their activities into three committees: Review, Research and Methodology. This paper only reports the findings of the Review Committee. Use is also made of information collected by the present author as part of a contribution to an AGARDograph on Reynolds number effects. The basic questions that will be addressed in this paper are: "What do we know at present about Reynolds number effects?" and "What has been done in the past to ease the Reynolds number problem?"

2. SOME FUNDAMENTAL ASPECTS

Excellent reviews on Reynolds number effects can be found in two AGARD publications by Hall (ref. 1) and Green (ref. 2) both published in 1971. Some of the more fundamental aspects will be recalled here. Prandtl was the first to make a basic distinction between an inviscid outer flow and a usually thin viscous layer close to the surface. These two flow regions interact with each other. At high Reynolds numbers the typical scale of the thickness of the viscous layer is small compared with the typical length scale of the body in streamwise direction. The two flow fields can then be formally decoupled. The development of the viscous shear layer is governed by an externally imposed pressure distribution (that follows from the inviscid flow), subject to an initial condition (e.g. at a stagnation point) and a no-slip condition on the body surface. This viscous flow can be described by the boundary layer equations, a thin layer approximation of the full Navier Stokes equations. The Reynolds number is explicitly present in these equations. The thickness of the viscous layer varies typically as $Re^{-1/2}$. For turbulent boundary layers the Reynolds number dependency is more implicit and, for wall-bounded flows, hidden in the near-wall formulation of the turbulence model (as reflected in the "law of the wall"). Its thickness varies typically as $Re^{-1/5}$. Turbulent free shear layers are only Reynolds number dependent insofar as their initial conditions are affected by Reynolds number. The subsequent development of the free shear layer is basically Reynolds number independent (ref. 3).

The effect of the shear layer development on the external flow field can be expressed as a displacement effect or an effective outflow on the body surface or along a dividing streamline. As a result the external flow field is modified. When the boundary layer closely follows the body surface, the basic structure of the external flow is not changed by this interaction. One speaks of "weak interaction". However, when the viscous shear layer breaks away from the surface ("massive separation") the external flow field is drastically changed and so are the aerodynamic characteristics. The viscous and inviscid flow field can then only be treated simultaneously ("strong interaction"). The occurrence of flow separation marks an important point in the flow development and depends on the viscous flow development upstream of the separation point.

With this in mind a distinction can be made between direct and indirect Reynolds number effects. The direct Reynolds number effects are the effects of Reynolds number on the viscous shear layer development for a fixed ("frozen") pressure distribution. They can be studied as isolated phenomena. Typical examples are the effects of Reynolds number on boundary layer transition, boundary layer displacement thickness and skin-friction, (incipient) separation and shock wave boundary layer interaction. Some of these effects can be discontinuous like a sudden movement of a transition point, the break-down of a vortex or the burst of a laminar separation bubble. All airfoils experience one or more direct Reynolds number effects but it will depend on the pressure distribution and the Reynolds number range which effects actually occur. Indirect Reynolds number effects are defined here as the change in pressure distribution due to the direct Reynolds number effects. Typical examples are the change in shock strength and position or a variation in trailing edge pressure due to a Reynolds number increase. The magnitude of the indirect Reynolds number effect will depend on the sensitivity of the external flow to a change in the viscous boundary condition. Flow separation will generally cause a large variation in pressure distribution (see e.g. fig. 10 and 12 to be discussed later). But it is also well known that some supercritical airfoils are very sensitive to small disturbances near the design condition (see e.g. fig. 21). Small direct Reynolds number effects might then cause large changes in pressure distribution. Direct and indirect Reynolds number effects are indicated schematically in fig. 1. In the next sections this distinction will be used frequently as a logical frame work for the discussion of Reynolds number effects. In these sections arguments will be presented in support of the tentative table added to figure 1 that indicates which of the two effects is dominant for a particular aerodynamic characteristic.

3. EARLY EVIDENCE OF REYNOLDS NUMBER EFFECTS: THE IMPORTANCE OF BOUNDARY LAYER FIXATION.

The importance of Reynolds number as the basic scaling parameter in viscous flow has been recognized from the beginning of theoretical aerodynamics. This was also reflected in the experimental facilities that were constructed before the second world war, like the NACA "Variable Density Wind Tunnel" and "Low Turbulence Pressure Tunnel". Experiments in these facilities revealed a favourable effect of Reynolds number on maximum lift. This is not unexpected. At low Mach numbers and high lift conditions the pressure peak near the leading edge ensures a turbulent boundary layer development. The separation of this turbulent boundary layer will be delayed at higher Reynolds numbers, resulting in a favourable Reynolds number effect. With the advancement of transonic flight this simple view became somewhat obscured. In wind tunnel tests at transonic flow conditions a decrease rather than an increase in maximum lift was observed with increasing Reynolds number. In figure 2 and 3 more recent examples are given that show a similar behaviour. These results (of a supercritical airfoil) indicate at Mach = .6 a still very weak Reynolds number dependence whereas a strong adverse effect is found at Mach = .75. In one of the early wind tunnel studies on Reynolds number effects (ref. 4) a significant change in pressure distribution was observed when the Reynolds number was increased (fig. 4). These pressure distributions are characterized by a region of supercritical flow with a favourable pressure gradient terminated by a shock wave. At a low Reynolds number the boundary layer will be laminar but when the Reynolds number is increased the transition point will move towards the leading edge. The observed Reynolds number effect on the pressure distribution appeared to be related to a fundamental difference between laminar and turbulent shock wave boundary layer interaction as noted already by Ackeret et al in 1946 (ref. 5). It was argued at that time that transition fixing at low Reynolds numbers should make the pressure distribution more comparable with flight. The problem of shock wave boundary layer interaction was discussed further by Pearcey and Holder in 1954 (ref. 6). A sudden drop in trailing edge pressure was noted for shock Mach numbers between 1.22 and 1.24 and it was argued that this was related to shock-induced boundary layer separation. Scale effect was not specifically addressed although it was mentioned in a footnote that for a proper comparison with flight "the tunnel tests should, of course, be made with transition fixed". The case for transition fixing was discussed in more detail by Haines, Holder and Pearcey, also in 1954, who stated that "the major scale effects at high subsonic and transonic speeds arise from differences between the conditions under which the laminar and the turbulent boundary layer separate and how they behave after separation" (ref. 7).

The message of the 50's that artificial boundary layer fixation significantly affects the pressure distribution, has been confirmed since then numerous times. As was noted before, part of this effect is due to a fundamental difference in the interaction of a shock wave with either a laminar or a turbulent boundary layer. Since in the laminar boundary layer the sonic line is further away from the surface, the upstream interaction of the shock can extend over a much larger distance, resulting in a wider compression fan that weakens the shock strength locally. This is reflected in the pressure distributions as shown in figure 4a. A second, equally important effect is the smaller displacement thickness of a laminar boundary layer as compared with a turbulent one. This difference is particularly important in the trailing edge region of an airfoil since this defines the "viscous" Kutta condition and hence the overall circulation. Because of the large influence of the overall circulation on the shock strength and its position a large effect of transition fixation can be expected on the pressure distribution. The effect will be particularly severe for modern airfoils with substantial aft-loading as is the case for the airfoil shown in figure 5.

When the Reynolds number is increased, the natural transition position moves upstream and this causes large, discontinuous changes in the aerodynamic coefficients that are absent when the boundary layer is tripped artificially (fig. 6). Transition point variations can also be initiated by a change in pressure distribution with incidence or Mach number, resulting in peculiar bends in the CL_α and CL_{Ca} curves (fig. 7, 8). These variations are strongly felt in the drag, since the drag of a laminar boundary layer is appreciably less than the drag of a turbulent boundary layer. This combination of a direct (viscous drag) and an indirect (shock-wave strength) Reynolds number effect is most pronounced in the compressibility drag (fig. 9). These examples show that without boundary layer fixation qualitatively misleading results can be obtained.

It is good practice, especially for drag evaluation, to test a baseline configuration with forward fixation. Nevertheless free transition tests are sometimes favoured with the argument that the pressure distribution and notably the pitching moment, will be more similar to flight in view of the thinner laminar boundary layers at the low tunnel Reynolds number. This might be true in some specific cases, but the favourable effect of a laminar shock wave boundary layer interaction and the irregular effects due to transition point movements impose serious restrictions. There is, however, a potential problem with forward fixation. The thicker turbulent boundary layer can separate at the trailing edge at the low tunnel Reynolds number. This effect was noted already by Gamble (ref. 4) in 1951. He suggested a more aft fixation location in that case (see fig. 4b), a technique that appears to be the main item of the AGARD Working Group 09.

4. CONCERN IN THE SIXTIES: TYPE "A" AND "B" SEPARATION

In 1966 a NASA report (ref. 8) written by Loving was published that showed large differences in pressure distribution between wind tunnel and flight for the C-141 aircraft (fig. 10). Loving wrote: "the purpose of the discussion is to caution experimenters concerning the use of wind-tunnel results in predicting flight loads and moments when supercritical separated flow is present". Figure 10 is most likely the most referenced figure in publications on Reynolds number effects. Test engineers at that time had done their homework as discussed in the previous section and wind tunnel tests were made with fixed transition. But obviously, this was not sufficient to ensure similarity with flight. In a publication by Pearcey, Osborne and Haines in 1968 (ref. 9), a physical model was postulated that explained the phenomenon in more detail. The transonic flow on airfoils as used up to the mid-fifties was dominated by a strong shock wave with separation rapidly developing from shock to trailing edge with increasing incidence or Mach number. They classified this type of flow as class "A" separation (see fig. 11) and considered it to be weakly Reynolds number dependent in view of the dominant effect of the shock. However, the combination of a more controlled shock wave development and significantly more aft-loading as applied in modern airfoil designs could provoke "classical" (low speed) trailing edge separation even before the shock became important. Also, from low speed experience, trailing edge separation was known to be Reynolds number dependent. They noted "It is not surprising, therefore, to find these sensitivities carried over

into flows in which rear separation and the local effects of the shock interact with one another, nor indeed to find them amplified by the interaction". They named this class "B" separation (fig. 11).

The C-141 case was considered to be a good example of class "B" separation. Note that the effect of Reynolds number on the pressure distribution is somewhat similar to the effect of boundary layer fixation (as shown in fig. 5). In both cases the important phenomenon is the development of the boundary layer close to the trailing edge and its influence on the overall circulation. This effect will be more pronounced when large adverse pressure gradients are present near the trailing edge as is the case for most modern airfoils. One should, however, be cautious in interpreting figure 10 as the typical example of a strong Reynolds number effect. Loving himself wrote at that time "that the results disclosed herein should not come as a surprise; they are merely additional evidence of the problem associated with separating flows". This point can be further illustrated with figure 12 where the variation in pressure distribution with Reynolds number is presented for a particular airfoil just prior to and beyond maximum lift. Note the large difference in sensitivity to Reynolds number! The large change in pressure distribution merely reflects a shift in the separation boundary with Reynolds number (see fig. 3 for the corresponding lift curves). Therefore, the Reynolds number sensitivity of this type of flow should not be expressed as a change in pressure distribution, but as the variation of the separation boundary itself as a function of Reynolds number. This has been illustrated in figure 13 for a number of airfoils, including the one shown in figure 12.

The publication by Pearcy, Osborne and Haines started a vast number of studies of Reynolds number effects on separation. Significant progress has been made since then in the understanding of turbulent shock-wave boundary layer interaction. (ref. 10). Empirical relations were established to relate incipient separation or the extent of the separation bubble to local parameters. The more recent work of Fulker and Ashill (ref. 11) is an outstanding example in this respect. They relate the bubble length to the local momentum thickness of the boundary layer ahead of the shock and the shock strength. Their empirical relation, replotted in a different way in figure 14, indicates a very weak dependence on the local Reynolds number. Unfortunately, progress has been much more limited with respect to the understanding of the boundary layer development aft of the shock bubble and up to (near) separation at the trailing edge. Progress has been hampered by the fact that in order to calculate this flow, a proper mathematical treatment of the viscous/inviscid interaction is essential. Only the more recently developed calculation methods can handle the strong viscous/inviscid interaction (see e.g. ref. 12).

So unfortunately some aspects of the interaction between shock induced and rear separation are still very much uncertain. It has been argued that at a sufficiently high Reynolds number the separation will go from class "B" to class "A". However, Fulker and Ashill showed in ref. 11 that flow break-down (separation from shock to trailing edge) is determined by the growth of the shock bubble up to a critical point on the airfoil contour. Since only local parameters appear in the empirical relation for the bubble length, their model does not allow for a direct interaction between shock induced and trailing edge separation. Their relation in fact represents the more universal direct Reynolds number effect on the onset of separation from shock to trailing edge. But the indirect Reynolds number effect on shock strength, most likely to be airfoil dependent, contributes as well. Nevertheless, there is to the author's knowledge, no clear experimental evidence of a significant change in trend of maximum lift or buffet boundary with Reynolds number caused by a change from class "B" to class "A" separation (see also figure 13).

Are there ways to simulate the Reynolds number influence on the separation boundary in the wind tunnel? Figure 15 shows an example of how maximum lift can be increased with aft fixation in a way similar to the effect of Reynolds number. But the important question what transition location is required to simulate a particular Reynolds number is still unanswered. Fulker and Ashill suggest that their correlation (fig. 14) can be used to determine the transition strip location such that the same bubble length relative to the airfoil chord is obtained in the wind tunnel as in flight. But this is only valid when the shock strength, that enters their correlation in a sensitive way, is taken into account as well and this will depend on the trailing edge conditions. There appears to be a fundamental problem here that will be discussed further in the next section. Sometimes the most aft fixation location (say 10 % ahead of the shock) is taken to be the most representative one for flight conditions. Also vortex generators can be used in the wind tunnel (ref. 13 and 14) to delay flow break-down in a way somewhat similar to an increase in Reynolds number (or the effect of aft-fixation) as illustrated in figure 16. The pressure distribution will still be Reynolds number dependent in the case of massive separation from shock to trailing edge. For these conditions Cahill and Connor (ref. 15) and Cahill and Kahn (ref. 16) have proposed a procedure to reconstruct the high Reynolds number pressure distribution from low Reynolds number wind tunnel tests (fig. 17). The procedure is based on a correlation between trailing edge pressure, shock location and a viscous flow parameter (that combines shock strength and local skin friction). The numbers in this correlation are derived from low Reynolds number wind tunnel tests of that particular configuration. A more universal correlation is subsequently used to express the Reynolds number influence. The technique is mainly applied for load prediction.

5. A CLOSER LOOK: THE DRAG ISSUE

Concern about the Reynolds number sensitivity of modern supercritical airfoils in the late sixties initiated two different lines of action. It was argued that high Reynolds number facilities were urgently needed. In 1971 an AGARD conference was organized in Göttingen on "Facilities and Techniques for Aerodynamic Testing at Transonic Speed and High Reynolds Number" (ref. 17). Plans were developed to build such a facility (ref. 18, 19) leading to the construction of NTF in the USA and the design of ETW in Europe. But at the same time existing facilities were used to study Reynolds number effects in a systematic way (ref. 14, 20 - 24). Initially one was concerned from a fundamental point of view with shock wave boundary layer interaction and its effect on flow separation as exemplified by the work of Stanewsky and Little (ref. 25), Green (ref. 26) and Osborne and Pearcy (ref. 27). Later the attention was also directed towards (nominally) attached flow conditions. It was again Haines who noted in 1976 (ref. 28) that "uncertainties (due to Reynolds number effects) not only affect the flow separation characteristics but also the drag in conditions where the flow was attached". The argument was even carried one step further by Haines in 1979 (ref. 29) stating that the optimization of aircraft design is greatly hampered by the Reynolds number gap of present day wind tunnels: "a significant increase in design lift can be achieved when the design can be optimized for the flight Reynolds number" (see fig. 18). An excellent study of Reynolds number effects on compressibility drag was made by Blackwell of Lockheed (ref. 14, 24) in the seventies. He studied a number of airfoils with varying thickness. In general, the variations in pressure distribution appeared to be rather small for attached flow conditions, though more pronounced for the thicker airfoils. This was also

reflected in the variation of drag creep with Reynolds number (fig. 19). The thicker airfoils show a larger Reynolds number effect on compressibility drag. Similar studies made by the present author are fully in line with these results. In the figures 20 to 23 Reynolds number effects on the pressure distribution are presented for two supercritical airfoils, a rather extreme 16% thick airfoil (airfoil "A") and a more conservative design of 12% thickness (airfoil "B"). It has been attempted to make the comparison at constant lift. The most important effect that can be observed when the Reynolds number is increased is a gain of lift over the rear part of the airfoil. This is caused by a larger effective camber due to the thinner boundary layers over the aft part of the airfoil. At constant lift, the increase in lift over the rear of the airfoil is compensated by a decreasing lift on the forward part of the airfoil realized by a lower incidence. Hence, the overall effect of a Reynolds number increase at constant lift is a decrease in angle of attack and a shift in load from the front to the rear of the airfoil as also reflected by an important change in pitching moment (fig. 6, 8). At constant lift, the shock can move upstream (fig. 20), downstream (fig. 23) or not at all (fig. 22). This apparently inconsistent movement is the result of two opposing trends: with increasing Reynolds number a downstream movement of the shock due to a better pressure recovery over the rear of the airfoil resulting from the thinner boundary layer and an upstream movement of the shock due to the reduced incidence to keep the lift constant. Figure 21 finally shows a very special case: a change from a single to a double shock system. However, it is well known that supercritical airfoils close to the design condition exhibit a similar change in pressure distribution with small variations in Mach number and/or incidence. Irrespective of the shock wave movement, the shock strength appears to decrease with an increase in Reynolds number. Since the wave drag is very much dependent on the shock Mach number (see ref. 12) a decrease in shock strength will be reflected in improved compressibility drag characteristics. This is a nice example of an indirect Reynolds number effect that will depend on the particular airfoil characteristics: the effect will be especially large when the boundary layer is close to or beyond separation at the trailing edge as is the case for airfoil "A" (fig. 22, 23). Of course, the separation of the boundary layer near the trailing edge will have a direct effect on the drag as well, also reflected in the drag creep development. The combination of the direct Reynolds number effect on drag due to separation and the indirect Reynolds number effect on the shock wave strength explains the large differences in drag creep development between the two airfoils (fig. 24). In these examples only one aspect of the Reynolds number effect on drag has been revealed but other phenomena can be important as well. A typical example was presented by Haines in ref. 28 and reproduced in figure 25. It has been suggested that the thinner boundary layer at the highest Reynolds number favours the development of a second expansion (because the local effective surface curvature is increased) resulting in a double shock system with a detrimental effect on drag. (N.B. In the final publication of this paper it was remarked that some of these results are erroneous; see also figure 25). Note that the development of the pressure distribution is somewhat similar to the one presented in figure 21. Separation in the rear loading region on the lower surface is another potential problem area that might effect drag in a Reynolds number dependent way. The variation of the drag rise boundary with Reynolds number is also of great practical interest. This variation is closely coupled to the indirect Reynolds number effect on the shock wave strength and position and consequently, likely to be airfoil dependent (see also fig. 19 and 24).

Is it possible to derive high Reynolds number drag values from low Reynolds number wind tunnel tests? When the indirect Reynolds number effect is small (a small change in pressure distribution), the direct Reynolds number effect on the viscous drag can conveniently be estimated from classical form factor methods or from boundary layer calculations using the measured pressure distribution. The problem arises when the pressure distribution changes significantly with Reynolds number, most often in combination with a (limited) trailing edge separation. In that case boundary layer manipulation through aft-fixation as mentioned before might help here as well to simulate the correct high Reynolds number pressure distribution. But what criterion should be used to simulate a particular Reynolds number? As a first step one would like to duplicate the trailing edge conditions as was advocated by Blackwell in 1968 (ref. 30). Figure 26, taken from his paper, indicates that the pressure distribution is indeed very well simulated in this way. Figures 27 and 28 show two other examples where the trailing edge conditions are almost similar for the low Reynolds number case (with aft-fixation) and the high Reynolds number case (with full turbulent boundary layer development). However, duplication of the trailing edge condition does not necessarily mean that details of the so important shock-wave boundary layer interaction are similar as well. Even when the indirect Reynolds number effect on the shock strength is well represented, the boundary layer thickness ahead of the shock will be very different. The problem is illustrated by the figures 29 and 30. In figure 29 a very simple flat plate calculation is used to define the simulated Reynolds number such that the momentum thickness at the trailing edge is used as the matching criterion. In figure 30 similar results for a typical case are presented where the momentum thickness ahead of the shock is used as the relevant matching criterion. Note that the difference in simulated Reynolds number can be as large as a factor of 10, especially when the trip is located close to the shock. The question where the transition strip should be located to simulate the flight Reynolds number is in many cases an academic one. In practice, the variation of shock position with lift or Mach number severely limits the aft fixation position. It is possible, however, to use different trip positions for various parts of the flight regime as indicated in figure 31 taken from ref. 31.

It is not unexpected that it is very difficult to match the boundary layer development over the important regions of the airfoil with one single parameter: the location of the transition strip. A better local correspondence in the viscous boundary condition appears to be only possible with a more continuous manipulation of the boundary layer along the airfoil contour. This is possible, in principle, by boundary layer suction as proposed by Green (ref. 26). Another possibility is a modification of the airfoil contour such that the effective body contour (the sum of the geometry and the displacement thickness) is identical for wind tunnel and flight. In principle, this can only be achieved for one particular pressure distribution. Although both approaches merit more detailed studies, they are not easy to realize and have, as yet, not been applied for routine wind tunnel testing. The matter will be left to the Research Committee of WG 09 . . . !

6. REYNOLDS NUMBER EFFECTS ON OTHER CONFIGURATIONS

Over the years Reynolds number effects on supercritical airfoils with a well developed region of supersonic flow terminated by a shock, have got very much attention. This type of flow is typically encountered on high aspect ratio wings of transport type aircraft. Although three-dimensional effects cause some complications, the aft fixation technique can still be used to assess Reynolds number effects, provided that the

AD-A202 496

AERODYNAMIC DATA ACCURACY AND QUALITY: REQUIREMENTS AND 4/6
CAPABILITIES IN WIND TUNNEL TESTING(U) ADVISORY GROUP
FOR AEROSPACE RESEARCH AND DEVELOPMENT NEWLLY

UNCLASSIFIED

JUL 88 AGARD-CP-429

F/G 1/1

NL



MICROCOPY RESOLUTION TEST CHART
NATIONAL BUREAU OF STANDARDS-1963-A

boundary layer is still laminar between leading edge and shock. (For further discussions see ref. 1, 11, 24, 30 and 32). It is normally assumed that the natural transition location for a swept wing at flight conditions is at the leading edge. But it is less evident for the low Reynolds number in the wind tunnel that the boundary layer is always laminar. The natural transition location depends critically on Reynolds number, leading edge sweep and pressure distribution. In fact, the Reynolds number effect on transition is very complicated for swept wings. There are at least four different mechanisms, each one Reynolds number dependent, that determine if the boundary layer is laminar or turbulent as illustrated in figure 32 taken from ref. 33. Fortunately, for moderate sweep angles as found on transport-type aircraft, the natural boundary layer is usually laminar in the wind tunnel, so that the aft-fixation technique might be used.

At lower free stream Mach numbers and higher incidences the shocks move forward closer to the leading edge. For these conditions the aft-fixation technique can not be used anymore and one can only choose between forward fixation and natural transition. At still lower Mach numbers, the shock disappears and only a pressure peak remains. Hence, separation in the leading edge region can be pressure gradient or shock induced, depending on the Mach number. The problem is further aggravated by a very distinct difference in behaviour of the laminar or turbulent boundary layer separation just aft of the pressure peak or at the shock. Figure 33 (ref. 27) is an illustration of the effect of fixation in the nose region. It appears that Reynolds number effects for these conditions are not very well understood (see also ref. 23).

The flow in the leading edge region is even more important for delta wings with a rounded leading edge at high angle of attack. Boundary layer separation in the leading edge region determines the onset of the formation of the primary vortex. Large variations in pressure distribution have been observed in this case (fig. 34 from ref. 34). However, this does not necessarily indicate a large Reynolds number sensitivity. The situation is somewhat similar to the onset of flow break down as discussed in section 4. Reynolds number sensitivity should be judged from a graph that depicts the incidence at vortex formation as a function of Reynolds number. The large difference in pressure distribution only indicates an almost discontinuous change from attached to separated flow conditions (ref. 35).

After the formation of the primary vortex, the state of the boundary layer (laminar or turbulent) is of considerable importance for the formation and the effect of the secondary separation underneath the primary vortex (fig. 35). The laminar boundary layer is much more susceptible to separation and will therefore start at a more inboard position as compared with the turbulent separation. This causes a severe distortion of the pressure peak underneath the primary vortex. With a turbulent boundary layer separation, the inviscid (high Reynolds number?) pressure distribution as calculated is much better approximated. When laminar flow exists at tunnel Reynolds numbers, artificial fixation can be applied to more closely approximate the high Reynolds number case (see ref. 36, 37).

Vortex break down is another viscous flow phenomenon that might be affected by Reynolds number. However, figure 36 (ref. 38) does not suggest a systematic trend with Reynolds number. This is not unexpected since the development of a turbulent free shear layer is independent of Reynolds number (see section 2) apart from an effect on its initial conditions at separation. Since the pressure gradient along the vortex core is very important for vortex break down, indirect Reynolds number effects can not be ruled out. They can be caused by a change in pressure distribution due to variations in boundary layer displacement thickness and the location of primary and secondary separation.

An interesting area is formed by the Reynolds number effects on slender bodies. Afterbody drag is of great practical significance for turbofan engines of transport type aircraft and for fighter and missile configurations. Figure 37 taken from ref. 39 indicates a substantial effect of Reynolds number on afterbody drag. Flow separations at lower Reynolds numbers appear to be of importance here. This topic merits a much more detailed discussion, also in view of the fact that afterbody drag is highly sensitive to buoyancy effects introduced by the wind tunnel walls (calibration, wall interference effects). See also section 7. The problem of afterbody drag has some similarity with the effects of flow separation on drag in the trailing edge region of an airfoil as discussed before. Similar methods (e.g. aft fixation) might be used here as well to simulate more closely the high Reynolds number boundary layer development.

Vortex formation in the nose region of slender bodies is another very important area. The problem is to some extent similar to the vortex formation on a rounded leading edge of a delta wing. But the phenomena are far more complicated on slender bodies since it appears from theoretical calculations that multiple, stable solutions with respect to the spatial distribution of vortices (symmetric and asymmetric) are possible here. Secondary effects, like the wind tunnel environment or model imperfections can then be decisive in the selection of one particular flow pattern. The problem is emanant from large, irregular variations in side force (fig. 38 from ref. 42). There is no doubt that the state of the boundary layer, either laminar or turbulent, is of considerable importance as well (fig. 39). Sometimes helical trip wires are used to influence the vortex formation (see fig. 40 from ref. 43) but it is not quite clear to what extent this trip simulates high Reynolds number behaviour. It is not unlikely that the trip itself initiates a particular flow pattern. If this is the case it might be possible to design the forebody geometrically such that a stable vortex formation will be favoured and this might ease the sensitivity, also due to Reynolds number, of this kind of flow.

Finally, the flow on the complicated shapes of modern combat aircraft configurations at high angle of attack combines almost all of the phenomena described before. In a contribution to the working group, Cross summarized the existing practice as follows: "For combat aircraft at high incidence the uncertainty in scale effects is such that corrections of wind tunnel results to full scale is often not attempted". At transonic flow conditions and moderate angle of attack a supersonic region terminated by a shock might be formed on the wing surface, somewhat similar to the case of a two-dimensional airfoil as discussed before. The aft-fixation technique might then be used. Figure 41 taken from ref. 44 shows a typical example how the pressure distribution can be affected by moving the transition strip further aft. In this case one should especially be concerned with the very significant three-dimensional variations, e.g. the change on local sweep angle of the outboard shock. It is unlikely that manipulation of the boundary layer by various transition locations will yield the free flight aerodynamic behaviour over the entire flight envelope. The best one can achieve is a better qualitative impression of flow conditions where viscous effects are important. A basic understanding of the origins and effects of boundary layer transition and separation is a first but essential step.

7. PSEUDO REYNOLDS NUMBER EFFECTS

At the round table discussion of the Fluid Dynamics Specialist Meeting on "Wall Interference in Wind Tunnels" in London in 1982 (ref. 45) Mc.Croskey showed a slide with the title "Reynolds number effects - Model or facility?" (fig. 42). This figure, indicating large variations in the measured lift curve slope of the NACA 0012 airfoil, is a good illustration that experimental results are liable to experimental error and/or unwanted or even unknown influences of the wind tunnel environment. These effects may vary well change in magnitude with the tunnel pressure (the tunnel unit Reynolds number) or model scale. Hence, what is measured as a function of Reynolds number does not necessarily reflect the true Reynolds number effect of the particular aerodynamic configuration.

Mc.Croskey was not the first to realize this problem as will be illustrated with some typical examples in this section. A very early case can be found in ref. 46 published in 1955 and reproduced here as figure 43. It shows the variation in pressure distribution for a supercritical flow condition due to a change in flow quality of the wind tunnel. Note that the variation in pressure distribution is somewhat similar to the one shown in figure 4a. The obvious explanation is that the improved flow quality caused a rearward movement of the transition point resulting in a laminar instead of a turbulent shock wave boundary layer interaction. As was discussed already in section 3 this will have a significant effect on the pressure distribution. The relation between tunnel environment and transition location appeared to be a hot item in the sixties in connection with the so called "unit Reynolds number effect". The problem was more or less settled by Dougherty and Fisher in 1980 (ref. 47). They were able to correlate transition Reynolds numbers on the 10 degree AEDC cone in various wind tunnels and in flight with aerodynamic noise (fig. 44). Their correlation still shows appreciable scatter and it is likely that other wind tunnel environmental effects will be of importance as well. A very strong effect on transition location results from non-adiabatic wall conditions as illustrated in fig. 45 also from ref. 47. Although the transition cone data have been corrected to account for this, the effect is such that one has to worry about it, especially for cryogenic tunnels where temperature equilibrium might present a problem (see also ref. 48). It is well known that wind tunnel turbulence and model roughness effects have a significant influence on the transition location (see e.g. fig. 46 from ref. 49). As was discussed before, the state of the boundary layer, either laminar or turbulent, plays a very important role in Reynolds number effects, not only for shock wave boundary layer interaction but also for drag assessment and the flow development in the leading edge region of a wing. For that reason one should know the particular characteristics of a wind tunnel with respect to the natural transition. In view of possible uncertainties in the natural transition location it is often required to fix the boundary layer artificially. The transition strip size should be carefully selected. Since the critical roughness height scales with $Re^{-3/4}$ it is mandatory to adapt the strip size to Reynolds number. When a Reynolds sweep is made it is not sufficient to select the largest strip size that ensures transition over the full range of tested Reynolds numbers. Over-fixation can give misleading results for drag, as indicated in figure 47 (ref. 50) and also for the shock wave development (e.g. see ref. 28).

Conflicting results in drag tests on the AGARD Nozzle Afterbody in the seventies gave rise to the so called "Reynolds number paradox" (fig. 48). Aulehla and Besigh (ref. 40) were the first to note that this effect could largely be explained from a Reynolds number effect on the tunnel calibration. Forniak (ref. 41) has written a comprehensive review on this problem.

The Reynolds number effect on tunnel calibration can easily be taken into account. A much more serious problem is the Reynolds number effect on wall interference. Figure 49, reproduced from ref. 52, illustrates the problem very well. In this study, one airfoil (but with different chord length) was tested in a number of wind tunnels. Very large variations in Reynolds number trends were observed for maximum lift and drag rise Mach number. However, if the maximum lift at the drag rise Mach number is replotted as a function of Reynolds number a very consistent trend is obtained. It is likely that the original discrepancy is caused by a wall interference effect on Mach number. For a model of low aspect ratio the interaction of the pressure distribution on the model with the side wall boundary layer development can be a problem. This effect is likely to be Reynolds number dependent. Although corrections for this effect have been attempted (see e.g. ref. 53), it is advisable to do two-dimensional test with a sufficiently high aspect ratio (at least 2). It is less clear if the interference effects from the top and bottom walls are Reynolds number dependent. There is some evidence that this is the case for porous walls (e.g. see ref. 54). In any case, the more recently developed wall interference correction methods that are based on measured wall pressures appear to be capable to calculate wall corrections with sufficient accuracy for two-dimensional tests (ref. 55). The application of one of these methods (ref. 56) to two-dimensional measurements in the high speed tunnel HST of NLR indicated that the Reynolds number effect on wall interference was small for this slotted test section (fig. 50).

These few examples illustrate that for the assessment of Reynolds number effects high quality data are essential. It is to be expected that some of the experimental evidence of the past on Reynolds number effects is partly obscured by pseudo Reynolds number effects due to the wind tunnel environment. Fortunately the advancements in measuring techniques and wall interference correction methods increase the confidence in measured Reynolds number effects significantly.

8. FINAL REMARKS

In this review a distinction has been made between direct Reynolds number effects (the change in viscous flow development for a fixed pressure distribution) and indirect Reynolds number effects (a change in pressure distribution due to the direct Reynolds number effect). Indirect Reynolds number effects appear to be dependent on the type of flow. They can have a significant effect on lift and pitching moment, shock wave drag and the buffet boundary. Most of these effects can be clearly identified and related to a particular direct Reynolds number effect.

Many direct Reynolds number effects (e.g. the variation of skin friction drag with Reynolds number) are reasonably well understood and extrapolation to flight appears to be possible as long as the resulting effects on the pressure distribution (the indirect Reynolds number effects) are small. This is, however, certainly not the case with the change from laminar to turbulent shock wave boundary layer interaction and with the effects of turbulent boundary layer separation. Boundary layer fixation can be used in the wind tunnel to ensure turbulent boundary layer development, but a forward trip position increases the risk of shock induced or trailing edge separation, not present in flight. This will have a large effect on the pressure distribution. In principle boundary layer manipulation can be used to approximate more closely the boundary layer in flight. In practice, only the "aft-fixation" technique has been applied success-

fully. Obviously, the application of this technique is limited to conditions where the natural transition location is sufficiently aft in the wind tunnel. Moreover, the question which Reynolds number is actually simulated is still very much open.

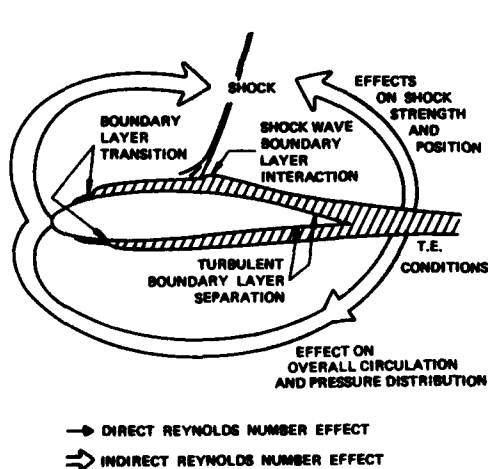
ACKNOWLEDGEMENTS

The author is very much indebted to his colleagues in the Review Committee: C. Armand, A.G.T. Cross, J. Peterson, J.L. Potter, G.P. Russo and J. Szodrach. Their work is at the basis of this contribution although this is only partly reflected in this paper. Further discussions in the working group and the study of the present author of Reynolds number effects on two-dimensional airfoils and transport type configurations (as part of a proposed AGARDograph) have influenced the authors thinking on Reynolds number effects considerable since the first (concept) publication of the report of the Review Committee. The many stimulating discussions with Barry Haines, Travis Binion and Egon Stanewsky have contributed very much to the somewhat different approach as reflected in the present paper.

REFERENCES

1. Hall, M.G., Scale effects in flows over swept wings. AGARD CP No. 83-71 (1971).
2. Green, J.E., Some aspects of viscous-inviscid interactions at transonic speeds and their dependence on Reynolds number. AGARD CP No. 83-71 (1971).
3. Townsend, A.A., The structure of turbulent shear flow, Cambridge University Press, 1956.
4. Gamble, H.E., Some effects of Reynolds number on a cambered wing at high subsonic Mach number. RAE Report No. Aero 2423 ARC 14, 448, May 1951.
5. Ackeret, J., Feldmann, F., Rott, W., Investigations of compression shocks and boundary layers layers in fast moving gases. Institut für Aerodynamik E.T.M. Zürich, Report No. 10 (1946).
6. Pearcey, H.N., Holder, D.W., Examples of the effect of shock-induced boundary-layer separation in transonic flight. ARC Technical Report, R & M No. 3510, 1954 (re-issued 1967).
7. Haines, A.B., Holder, D.W., Pearcey, H.N., Scale effects at high subsonic and transonic speeds, and methods for fixing boundary layer transition in model experiments. ARC Technical Report R & M No. 3012, Sept. 1954 (re-issued 1957 (?)).
8. Loving, D.L., Wind tunnel flight correlation of shock induced separated flow. NASA TN D-3580, 1966.
9. Pearcey, H.N., Osborne, J., Haines, A.B., The interaction between local effects at the shock and rear separation - A source of significant scale effects in wind-tunnel tests on aerofoils and wings. AGARD CP 35, Sept. 1968, paper 11.
10. Delery, J., Marvin, J.G., Turbulent shock wave boundary layer interaction, AGARDograph No. 280, 1985.
11. Fulker, J.L., Ashill, P.R., A model of the flow over swept wings with shock induced separation, IUTAM Symposium, Palaiseau, France, 1985.
12. Lock, R.C., Prediction of viscous and wave drag at high subsonic speeds by viscous-inviscid interaction techniques. AGARD VKI Special Course "Aircraft drag prediction and reduction", May 1985.
13. Han, S.O.T.H., Hartuik, J.P., On the effect of variation of transition position and of vortex generators on the high-speed stall characteristics of a swept-wing transport aircraft model. NLR TR 74008 U (1974).
14. Blackwell Jr., J.A., Scale effects on supercritical airfoils. Proc. of the XI Congress of ICAS, Lisbon, Portugal, 10-16 Sept. 1978, Vol. 1, paper No. B3, pp. 370-383.
15. Cahill, J.F., Connor, P.C., Correlation of data related to shock induced trailing edge separation and extrapolation to flight Reynolds number. NASA CR 3178 (1979).
16. Khan, M.H.S., Cahill, J.F., New considerations on scale extrapolation of wing pressure distributions affected by transonic shock induced separation. NASA Contractor Report 166426 (March 1983).
17. Facilities and techniques for aerodynamic testing at transonic speed and high Reynolds number, AGARD CP No. 83-71 (1971).
18. The high Reynolds number tunnel - A national need - Description and justification. AEDC - Feb. 1972.
19. Laib Group, The Need for large wind-tunnels in Europe, AGARD AR No. 60 (1972).
20. Cahill, J.F., Simulation of full-scale flight aerodynamic characteristics by tests in existing transonic wind tunnels. AGARD CP No. 83, April 1971, paper 20.
21. Miss, Browne, G.C., Bateman, T.E.B., Pavitt, M., Haines, A.B., A comparison of wing pressure distributions measured in flight and on a wind tunnel model of the Super VC-10. ARC R & M 3707 (1972).
22. Blackerby, W.T., Cahill, J.F., High Reynolds number tests of a C141A aircraft semi-span model to investigate shock-induced separation. NASA CR 2604 (1975).
23. Weeks, D.J., An investigation of scale effects on the transonic flow over swept wings. Part 1 ARC R & M 3842 (1976). Part 2 ARC R & M 3842 (1977).
24. Blackwell Jr., J.A., Scale effects on advanced aircraft wing designs. Proc. of the Lockheed-Georgia Company Viscous Flow Symposium, "Reviews in viscous flow" LG77 ER 0044 (June 1976).
25. Stanewsky, E., Little, B.H., Studies of separation and reattachment in transonic flow. Journal of Aircraft, Vol. 8, No. 12, Dec. 1971, pp. 952-958.
26. Green, J.E., Some aspects of viscous-inviscid interactions at transonic speeds and their dependence on Reynolds number. AGARD CP No. 83, April 1971, paper 2.
27. Osborne, J., Pearcey, H.N., A type of stall with leading edge transonic flow and rear separation. AGARD CP No. 83-71 (1971).
28. Haines, A.B., Further evidence and thoughts on scale effects at high subsonic speeds. AGARD CP No. 174, March 1976, paper 43.
29. Haines, A.B., Review of post-1974 evidence on scale effects at high subsonic speeds. ARA Memo No. 218 (1979).
30. Blackwell, J.A., Effect of Reynolds number and boundary layer transition location on shock induced separation. AGARD CP 35, Sept. 1968, paper 20.
31. Haines, A.B., ARA Memo No. 243, November 1982.
32. Kleemann, A., Experience with transition fixation in the high speed regime at NLR. NLR Memorandum AC-83-0390 (1983). (Also in ref. 50).
33. Hall, M.G., Treadgold, D.A., Difficulties in predicting boundary-layer transition on swept wings. RAE Technical Memorandum Aero 1465, ARC 35160 (1972).
34. McKinney, L.W., Beals, D.D., High Reynolds number research - 1980. NASA Conference Publication 2183.

35. Lamer, J.E., In-flight and wind tunnel leading edge vortex study on the F-106B airplane. NASA Conf. Publ. 2416 (1983).
36. Peaks, D.J., Tobak, M., Three dimensional interactions and vortical flow with emphasis on high speeds. NASA TM 81169 (1980).
37. Stahl, W.H., Aerodynamics of low aspect ratio wings. AGARD-LS-98 (1979).
38. Erickson, G.E., unpublished paper; see also AIAA 80-1423 (1980).
39. From ref. 41; data credited to Wilcox, F.A., Chamberlin, R. AGARD CP-150 (1975).
40. Anlehn, F., Benigh, G., Fore- and afterbody flow field interaction with considerations of Reynolds number effects. AGARD CP 150, paper 12, Sept. 1974.
41. Fomiat, O.M., A review of the effect of Reynolds number on afterbody drag. ARA Report 56 (1980).
42. Lament, F.J., Pressures around an inclined ogive cylinder with laminar, transitional, or turbulent separation. AIAA Journal 20, Nov. 1982.
43. Rao, D.M., Vortical flow management for improved configuration aerodynamics - recent experiences. AGARD CP 342 (1983).
44. Unpublished results, communicated by A.G.T. Cross in "Report of the Review Committee" (1986).
45. Wall interference in wind tunnels, Fluid Dynamics Panel Specialist Meeting, London, May 1982. AGARD CP No. 335.
46. Holder, D.W., Pearcy, H.E., Gadd, G.E., The interaction between shock waves and boundary layers. ARC Technical Report C.P. No. 180 (1955).
47. Dougherty, N.S., Fisher, D.F., Boundary layer transition on a 10-degree cone: wind tunnel/flight data correlation. AIAA-80-0154 (1980).
48. Lynch, F.T. et al, Nonequilibrium model wall effects on transonic airfoil performance in a cryogenic windtunnel. AGARD CP 348, paper 14 (1983).
49. Lachman, G.V. (ed.), Boundary layer and flow control, Volume 2, pp. 637-681 (1961).
50. Grenzschichtsteuerung durch transition fixierung. DFVLR-Mitt 84-17.
51. Galigher, L.L., Jackson, F.M., Robinson, C.E., Description of the AGARD nozzle afterbody experiments conducted by the Arnold Engineering Development Center. AGARD-AG-208, October 1975.
52. Stanewsky, E. et al, High Reynolds number tests on the CAST 10-2/DOA 2 transonic airfoil at ambient and cryogenic temperature conditions. AGARD CP No. 348, paper 10 (1983).
53. Barnwell, R.W., Similarity rule for sidewall boundary-layer effect in two-dimensional wind tunnels. AIAA Journal, Sept. 1980.
54. Cahn, Y.Y., Wall boundary-layer effects in transonic wind tunnels. AGARD CP No. 335, paper 7 (1982).
55. Mokry, M., Chan, Y.Y., Jones, D.J., Two-dimensional wind tunnel wall interference. AGARDograph No. 281 (1983).
56. Smith, J., A method for determining 2D wall interference on an aerofoil from measured pressure distributions near the walls and on the model. NLR TR 81016 U (1981).



DOMINANT RE-NUMBER EFFECT		
CHARACTERISTIC	DIRECT	INDIRECT
LIFT AND PITCHING MOMENT		X
VISCOUS DRAG	X	
WAVE DRAG		X
DRAG DIVERGENCE		X
BOUNDARY LAYER SEPARATION	X	
BUFFET BOUNDARY	X	X

Fig. 1 Direct and indirect Reynolds number effects

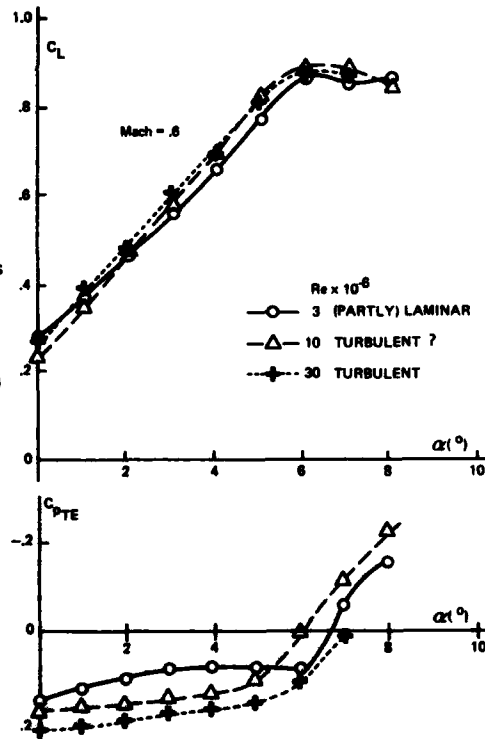


Fig. 2 Reynolds number effect on lift and trailing edge pressure development, free transition, Mach = 0.8

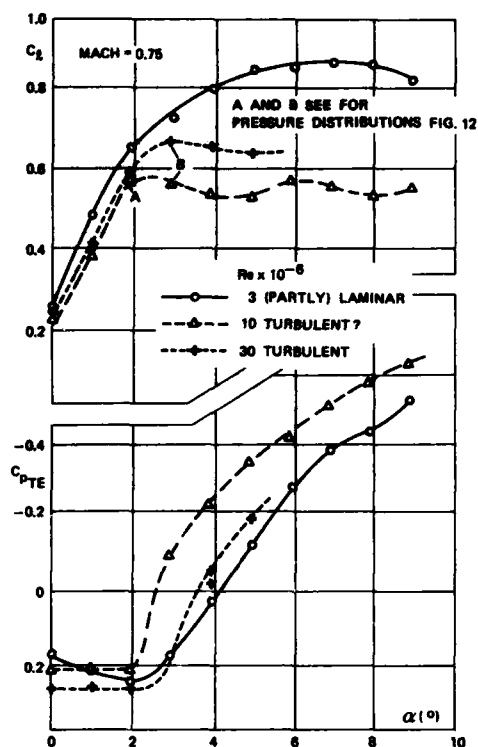


Fig. 3 Reynolds number effect on lift and trailing edge pressure development, free transition, Mach = .75

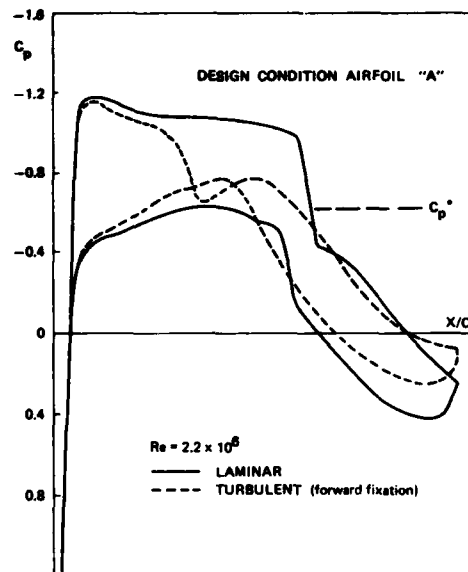


Fig. 5 Effect of boundary layer fixation on pressure distribution (from ref. 32)

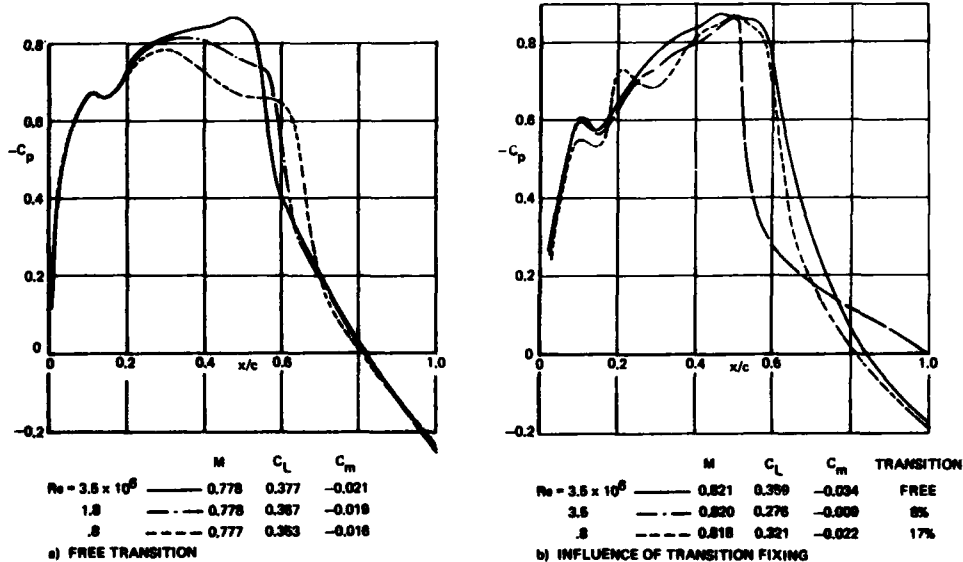


Fig. 4 Examples of early Reynolds number effects on pressure distribution (from ref. 4)

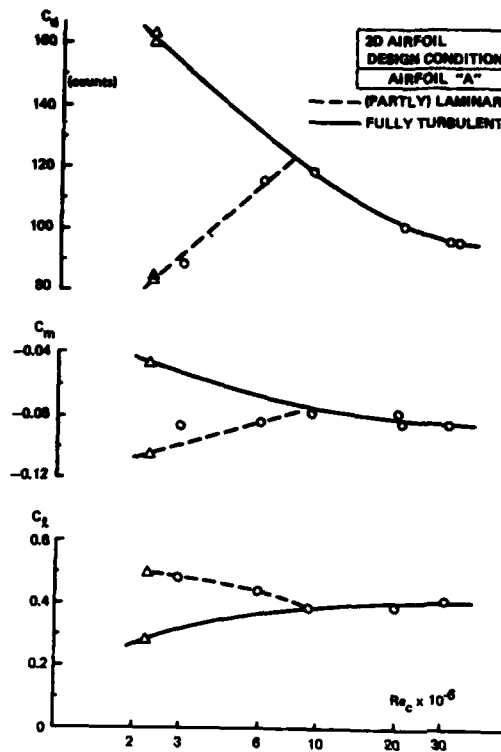


Fig. 6 Reynolds number effects at constant incidence on drag, pitching moment and lift with laminar and turbulent boundary layer development (ref. 32)

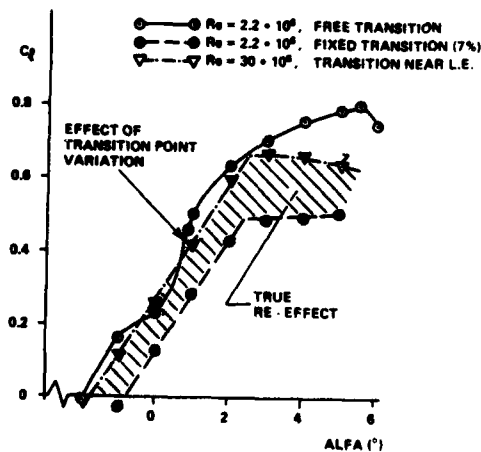


Fig. 7 Effect of Reynolds number and transition point variation on lift curve (ref. 32)

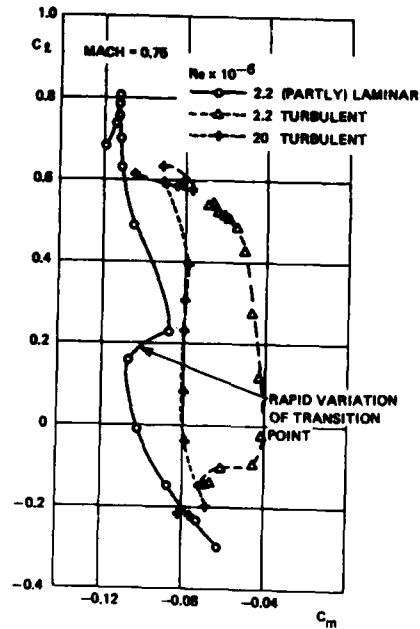


Fig. 8 Effect of Reynolds number and transition point variation on pitching moment

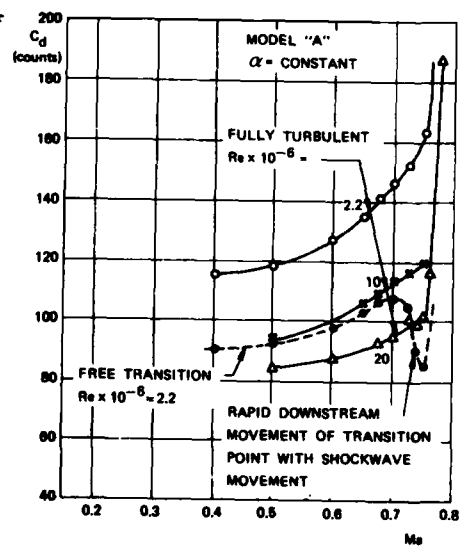


Fig. 9 Effect of Reynolds number and transition point variation on compressibility drag

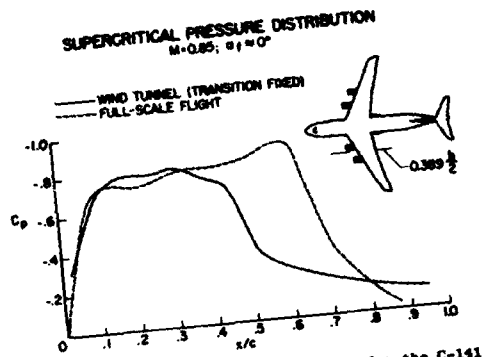


Fig. 10 Wind tunnel/Flight comparison for the C-141 (ref. 8)

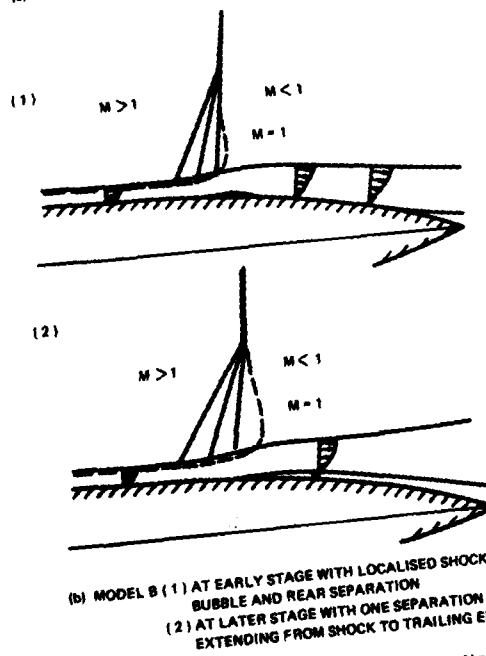
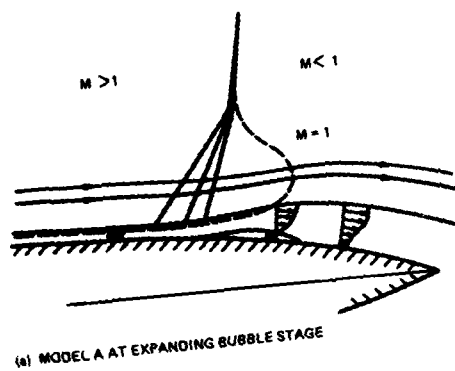


Fig. 11 Class "A" and "B" separation according to Pearcy, Osborn and Haines (ref. 8)

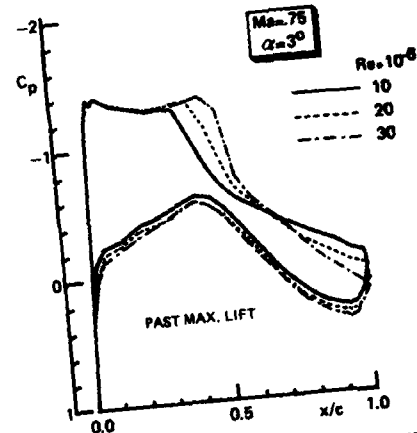
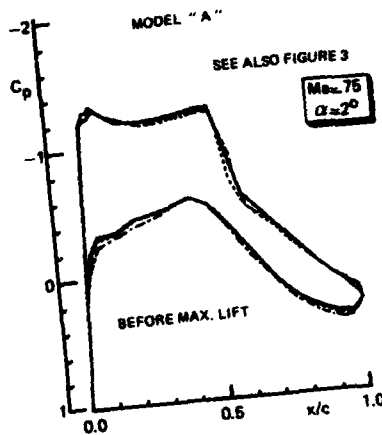


Fig. 12 Reynolds number effect on pressure distribution before and past maximum lift (ref. 32)

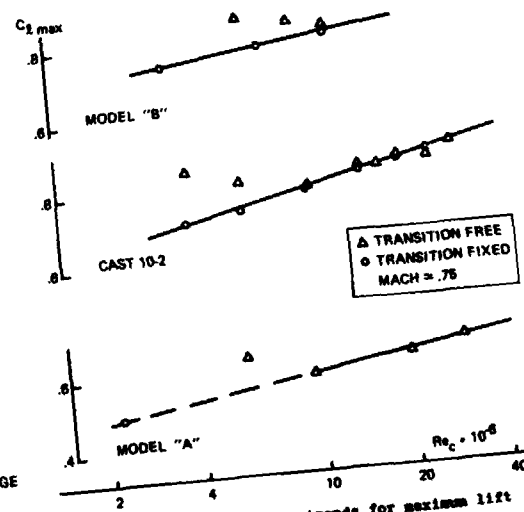


Fig. 13 Reynolds number trends for maximum lift

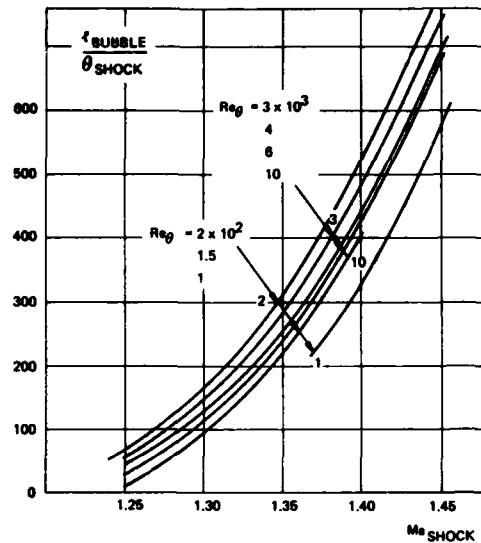
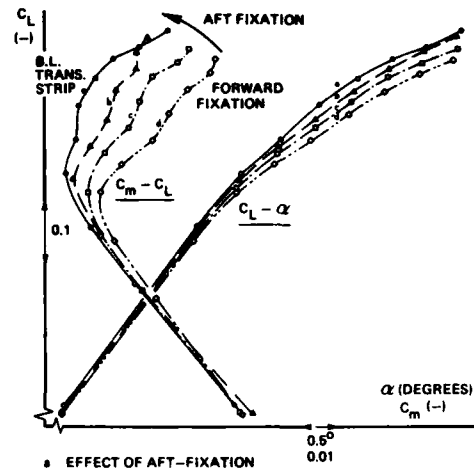


Fig. 14 Shock-bubble correlation (replotted results of ref. 11)



--- WITHOUT VORTEX GENERATORS
— WITH VORTEX GENERATORS

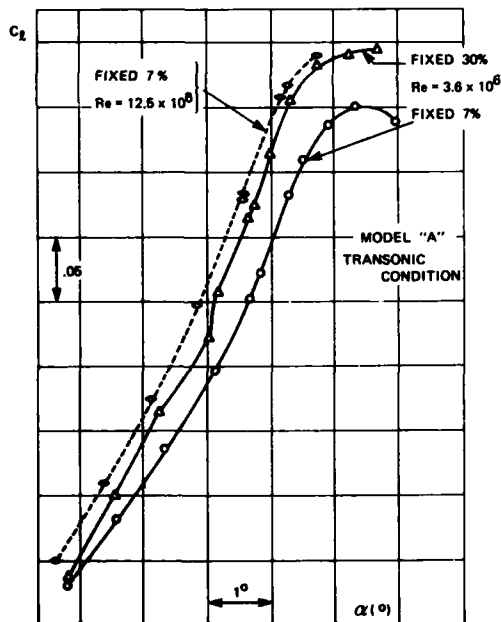


Fig. 15 Simulation of maximum lift development with aft-fixation

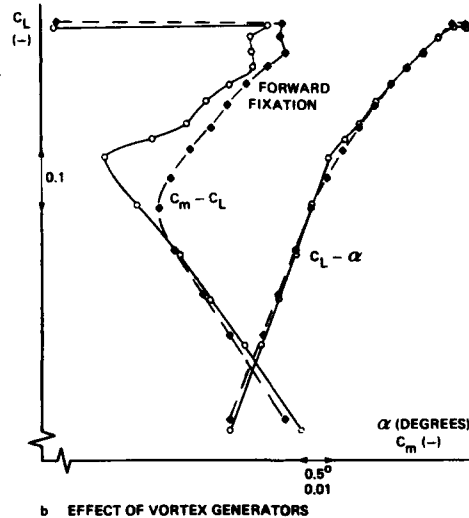


Fig. 16 Example of boundary layer manipulation by aft-fixation and vortex generators on transport-type wing (ref. 13)

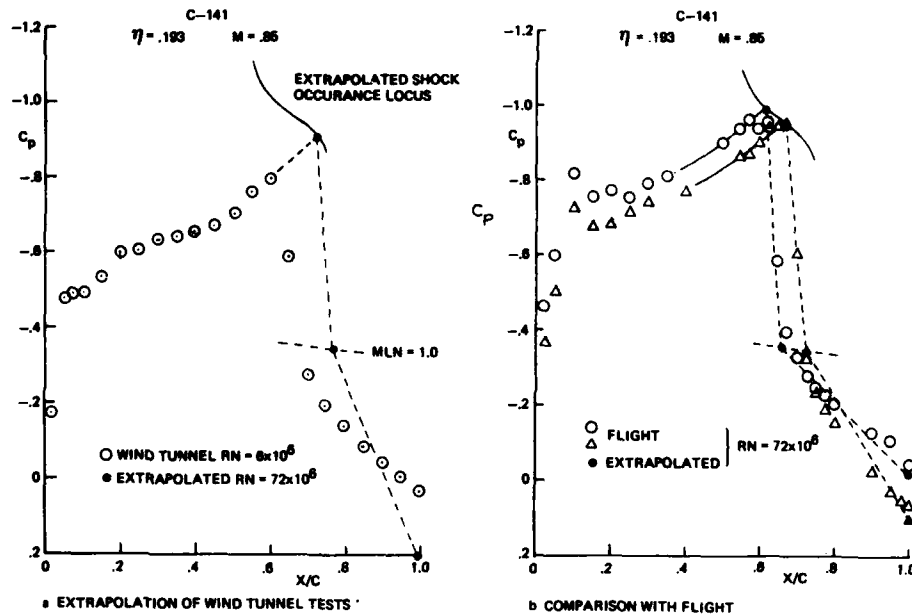


Fig. 17 Example of Reynolds number extrapolation of a pressure distribution (ref. 15)

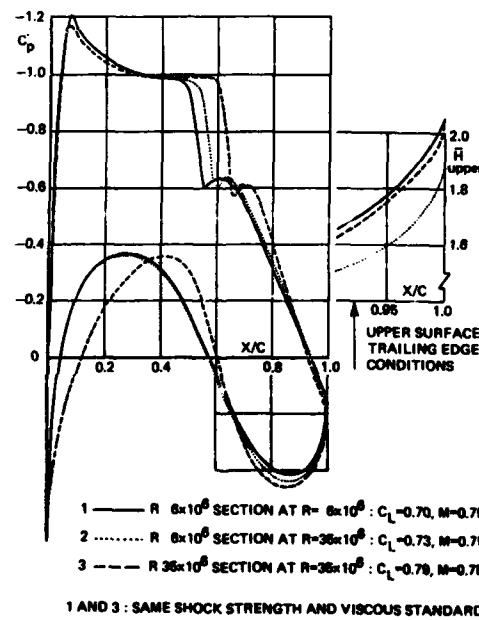


Fig. 18 Improvement in aerodynamic efficiency through high Reynolds number design (ref. 29)

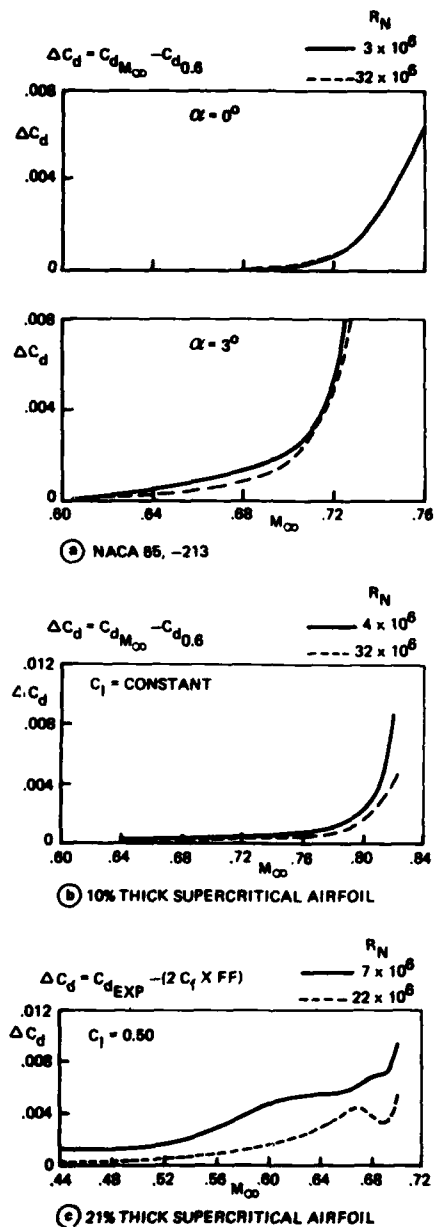


Fig. 19 Reynolds number effect on compressibility drag for three different airfoils (ref. 14)

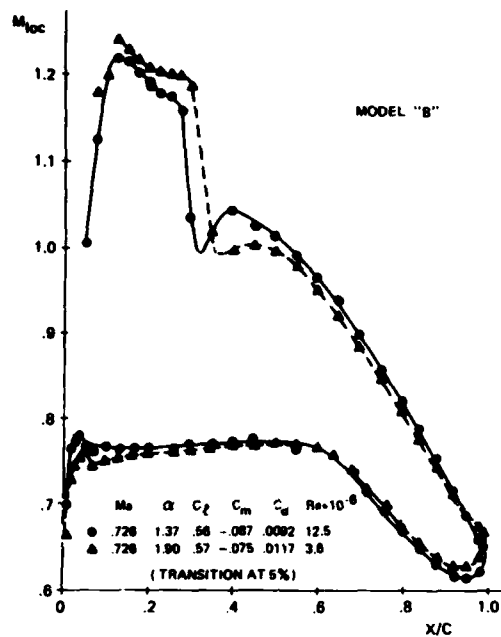


Fig. 20 Reynolds number effect on pressure distribution - example of upstream shock displacement

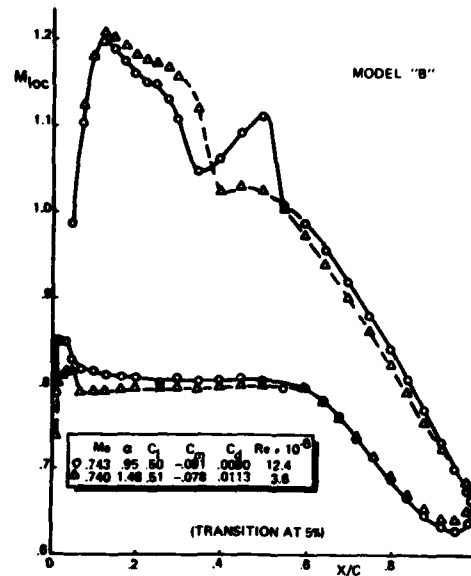


Fig. 21 Reynolds number effect on pressure distribution - example of change from single to double shock system

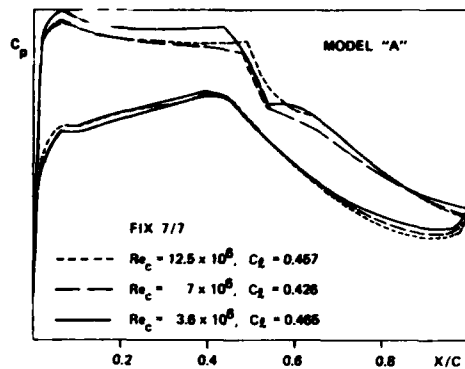


Fig. 22 Reynolds number effect on pressure distribution - example of almost stationary shock

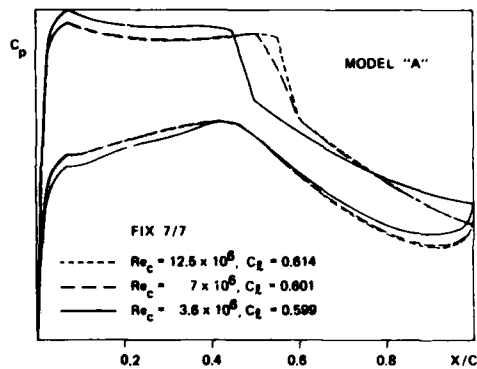


Fig. 23 Reynolds number effect on pressure distribution - example of downstream shock displacement

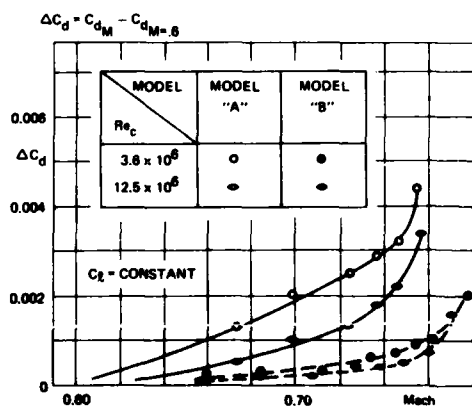
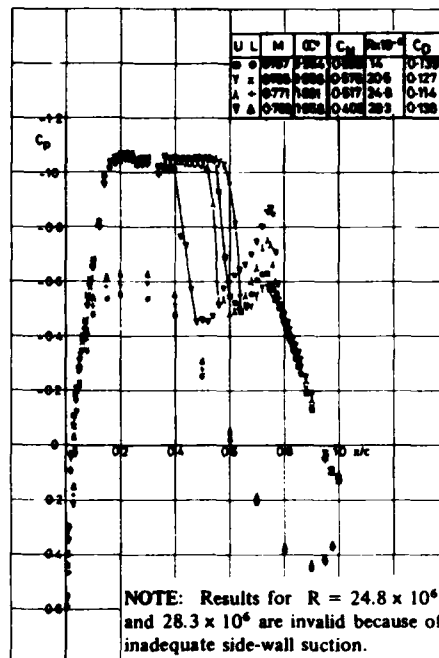
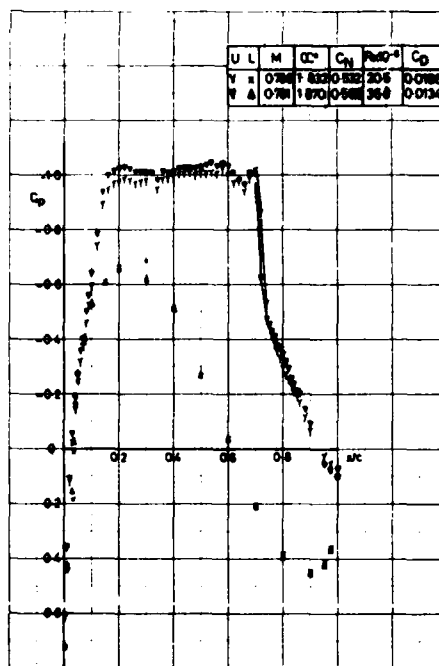


Fig. 24 Reynolds number effect on compressibility drag for model A and B (figs. 20 - 23)



⑤ BEFORE DRAGRISE



⑤ AFTER DRAG RISE

Fig. 25 Example of Reynolds number effect on second expansion behind the shock (ref. 28)

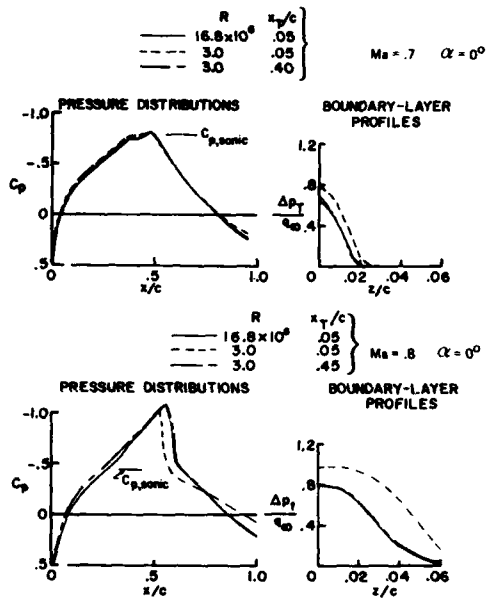


Fig. 26 Simulation of high Reynolds number pressure distribution with aft-fixation (ref. 30)

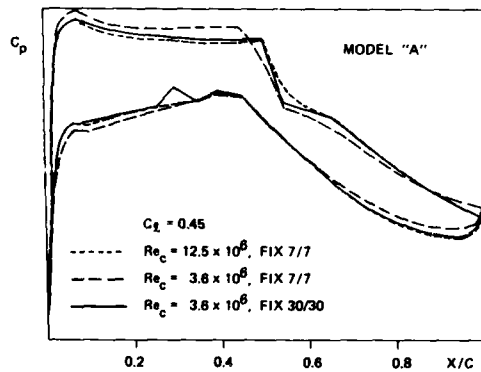


Fig. 27 Simulation of high Reynolds number pressure distribution with aft-fixation

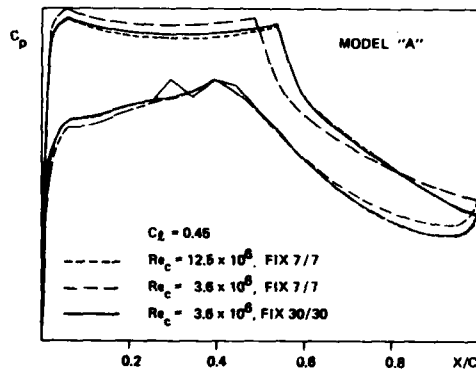


Fig. 28 Simulation of high Reynolds number pressure distribution with aft-fixation

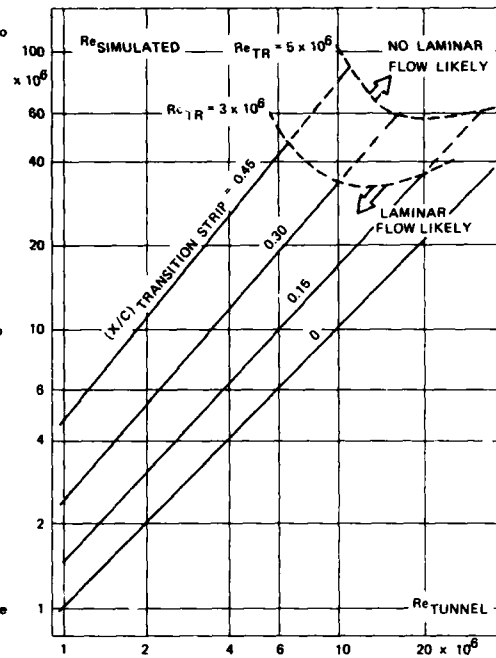


Fig. 29 Simple "flat-plate simulation criterion" : matching of trailing edge conditions

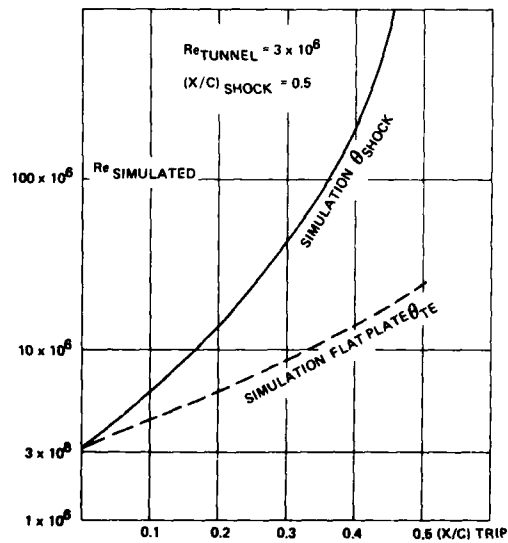
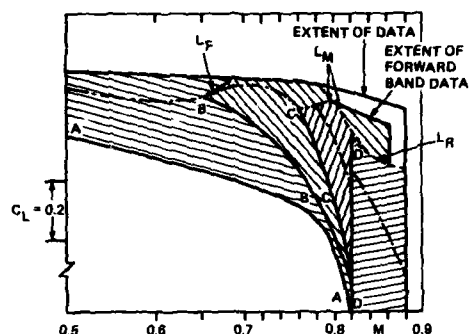
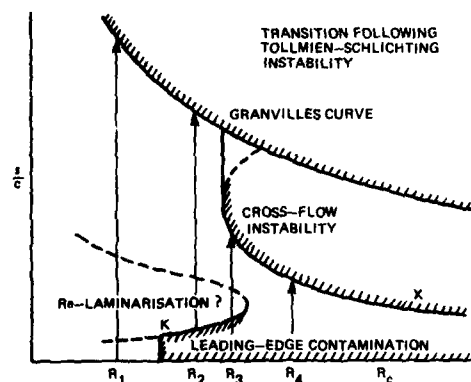


Fig. 30 Simple "flat-plate simulation criterion" : matching of conditions at shock location



- AA : LIMIT OF COMPLETELY SUBCRITICAL FLOW
- SHOCK UPSTREAM OF FORWARD BAND BUT FORWARD BAND DATA RECOMMENDED
- SHOCK AFT OF FORWARD BAND* FORWARD BAND DATA RECOMMENDED
- SHOCK AFT OF MID BAND* MID BAND DATA RECOMMENDED
- SHOCK AFT OF REAR BAND* REAR BAND DATA RECOMMENDED
- BOUNDARIES FOR TRAILING-EDGE PRESSURE DIVERGENCE
N.B. SHOCKS MOVING AFT BELOW AND FORWARD ABOVE THESE BOUNDARIES
- L_M, L_R : BOUNDARIES DEFINING UPPER LIMIT OF VALIDITY OF RESPECTIVELY FORWARD, MID AND REAR BAND DATA
- * : STRICTLY, SUFFICIENTLY FAR AFT TO AVOID ANY LOCAL INTERFERENCE BETWEEN ROUGHNESS BAND AND THE SHOCK STRENGTH AND POSITION

Fig. 31 Typical recommended boundary layer strip positions for the aft-fixation technique in the lift-Mach number plane (ref. 31)



- AT R_1 TRANSITION FOLLOWS FROM TOLLMIE-SCHLICHTING INSTABILITY
- AT R_2 LEADING-EDGE CONTAMINATION, FOLLOWED POSSIBLY BY RE-LAMINARISATION AND THEN TRANSITION THROUGH TOLLMIE-SCHLICHTING INSTABILITY
- AT R_3 LEADING-EDGE CONTAMINATION, FOLLOWED POSSIBLY BY RE-LAMINARISATION AND THEN TRANSITION THROUGH CROSS-FLOW INSTABILITY
- AT R_4 TRANSITION FOLLOWS FROM CROSS-FLOW INSTABILITY IF LEADING-EDGE CONTAMINATION WERE ABSENT

Fig. 32 Example of various transition types for swept leading edge (ref. 33)

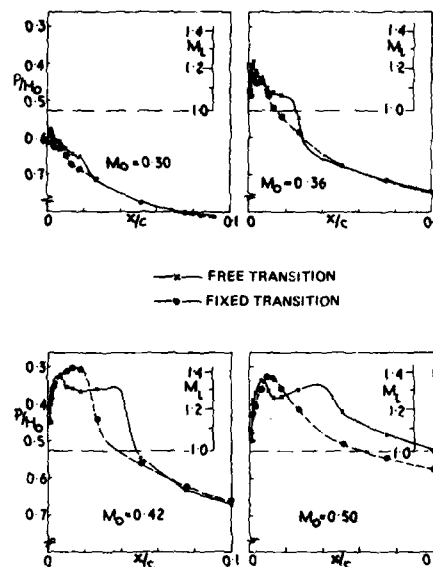


Fig. 33 Example of Reynolds number effects on pressure distribution in leading edge region for intermediate Mach numbers (ref. 27)

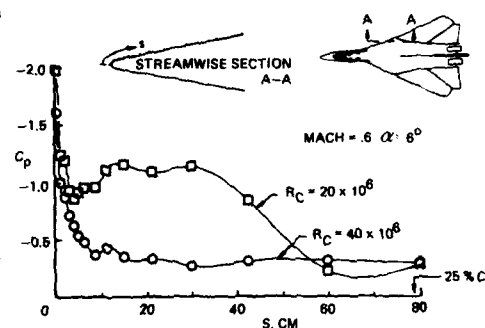


Fig. 34 Example of Reynolds number influence on vortex formation for delta wing configuration (ref. 34)

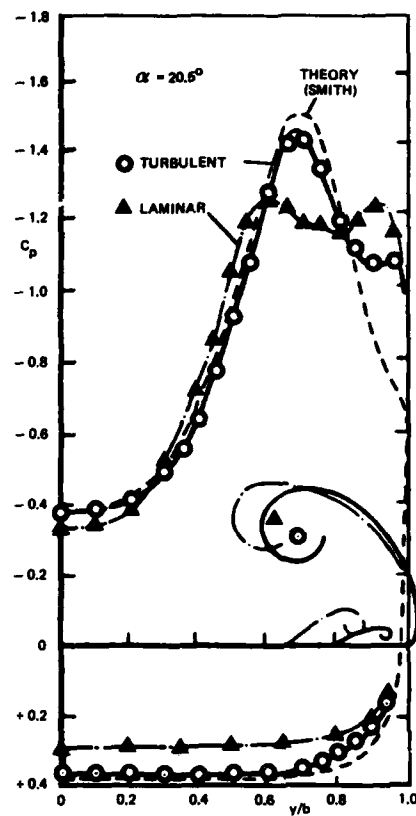


Fig. 35 Example of the effect on pressure distribution of laminar and turbulent secondary separation on a delta wing (ref. 36)

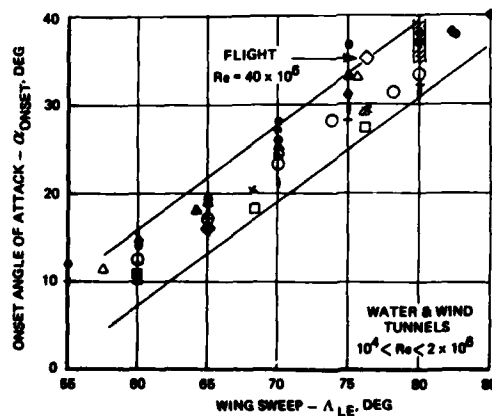


Fig. 36 Reynolds number effect on angle of attack for vortex break-down (ref. 38)

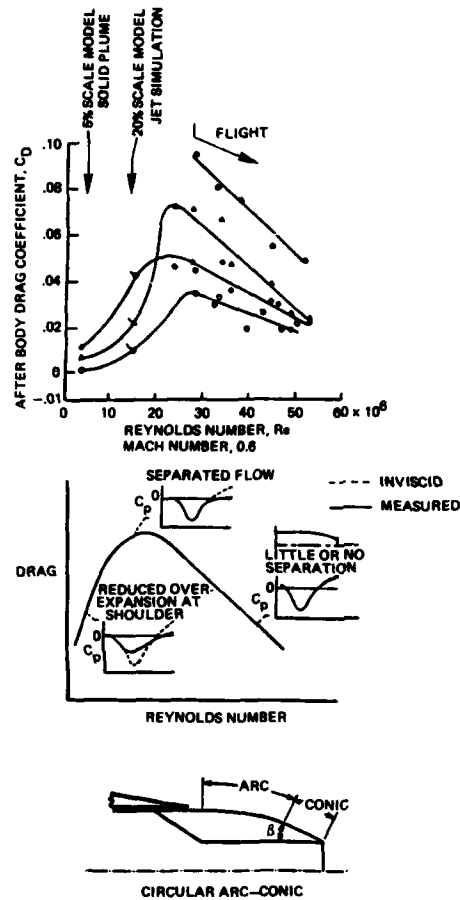


Fig. 37 Reynolds number effect on afterbody drag (ref. 39)

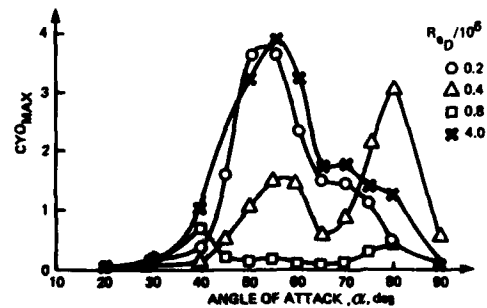


Fig. 38 Reynolds number effect on maximum side force for an ogive body (ref. 42)

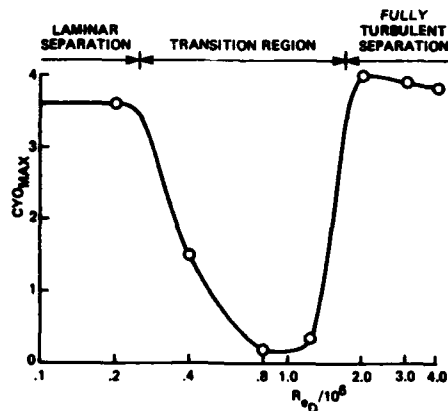


Fig. 39 Effect of the state of the boundary layer on maximum side force for an ogive body (ref. 42)

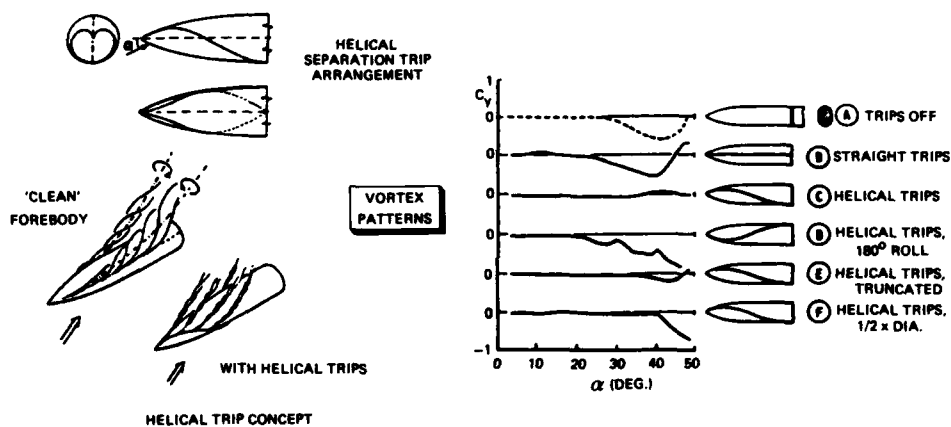


Fig. 40 Example of the use of helical trip wires for ogive bodies (ref. 43)

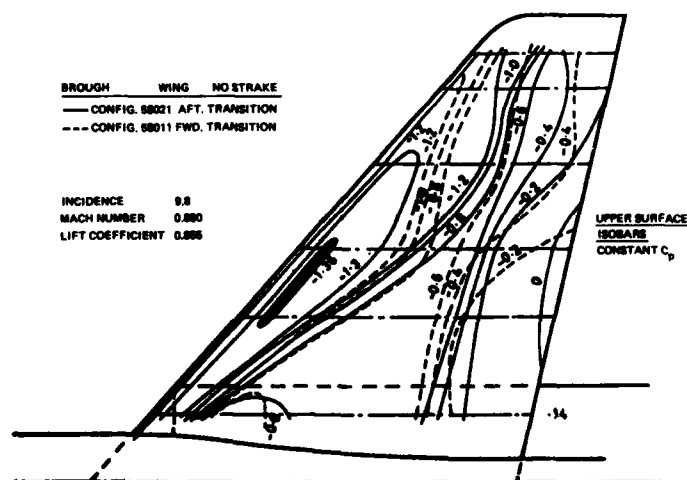


Fig. 41 Effect of transition strip location on shock position for a fighter configuration near buffet onset (ref. 44)

REYNOLDS NO. EFFECTS — MODEL OR FACILITY? (McCroskey)
LIFT CURVE SLOPE — NACA 0012

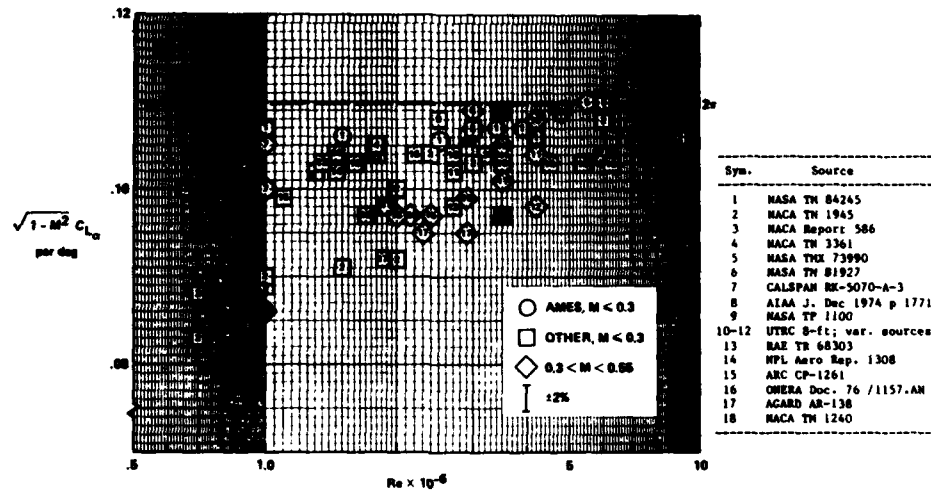


Fig. 42 Lift-curve slope as a function of Reynolds number for various wind tunnel tests (ref. 45)

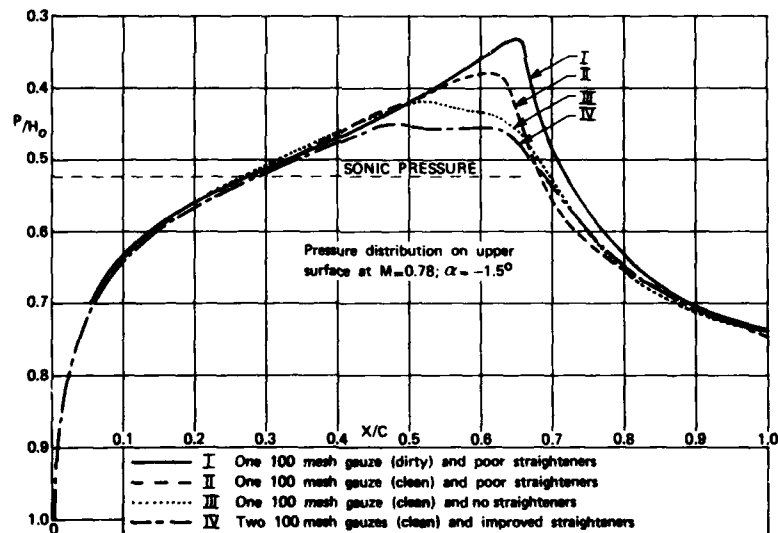


Fig. 43 Early example of the effect of flow quality on a supercritical 1 pressure distribution (ref. 46)

Sym	Tunnel	Sym	Tunnel
○	AEDC Tunnel 16T	□	NASA Ames 12 PT
△	AEDC Tunnel 16T (Walls Taped)	▽	RAE Bedford 8 x 8 SWT
▲	AEDC Tunnel 4T	■	NASA Langley 16 TT
⋈	AEDC Tunnel 4T (Walls with Tape or Screen)	△	NASA Langley 16 TDT*
▽	ONERA 6 x 6 S-2 Modane	●	NASA Langley 8 TPT
▽	NASA Ames 11 TWT	●	NSRDC 7 x 10 T
▽	NASA Ames 11 TWT (Walls Taped)	△	NASA Langley 4 SPT
△	NASA Ames 14 TWT	◇	RAE Bedford 3 x 4 HSST
⋈	NASA Ames 14 TWT (Walls Taped)	□	NASA Ames 9 x 7 SWT
○	Calspan 8 TWT	△	NASA Langley 4 SUPWT (TS No. 1)
○	ARA, Ltd. Bedford 9 x 8	○	Flight Data, Fig. 18

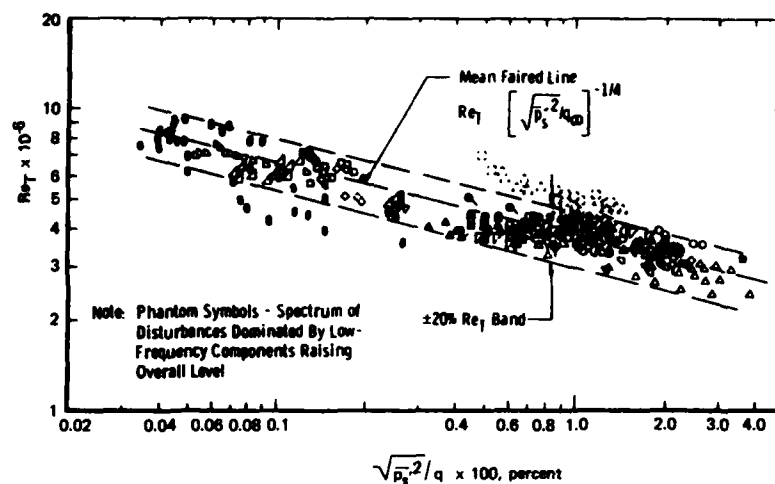


Fig. 44 Correlation of transition Reynolds numbers with pressure fluctuation levels on 10° ARDC cone (ref. 47)

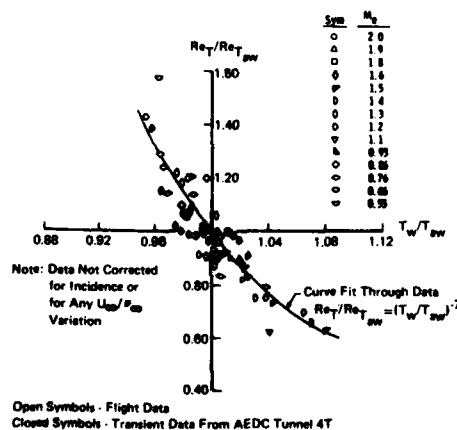


Fig. 45 Effect of temperature non-equilibrium on transition location (ref. 47)

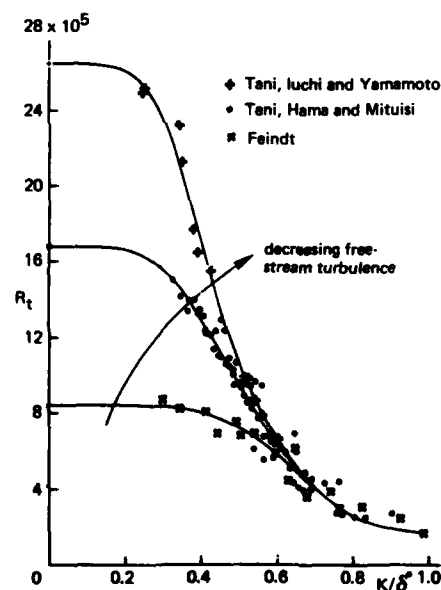


Fig. 46 Effect of tunnel turbulence and roughness height on transition Reynolds number (ref. 49)

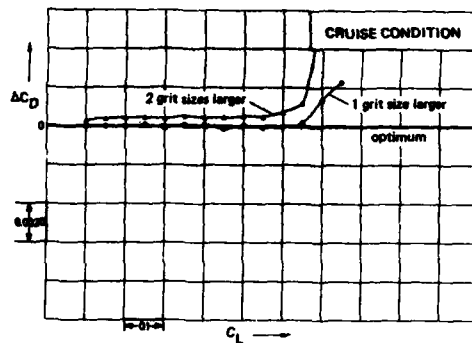


Fig. 47 Effect of over-fixation on drag for transport-type configuration (ref. 50)

SYM	SPONSOR	Re VARIED BY	EFFECT ON
A	LEWIS	SCALE	NOZZLE
B		DENSITY	
C	AFFDL	DENSITY	AIRFRAME
D			NOZZLE
E	LANGLEY	DENSITY TEMP SCALE	NOZZLE

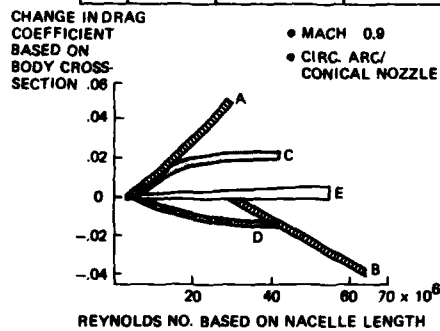
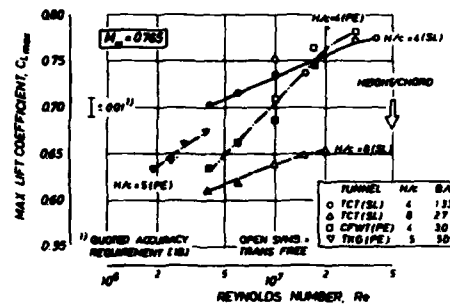
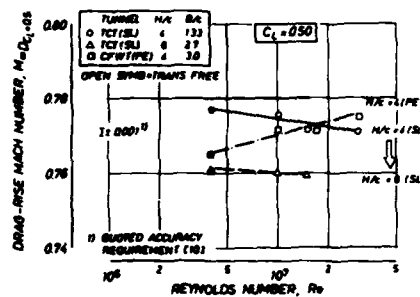


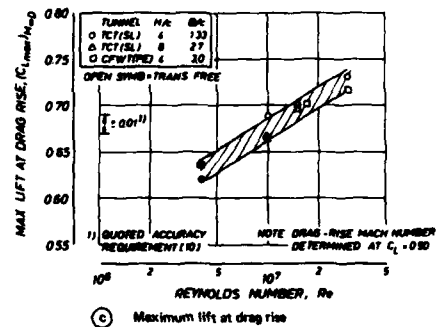
Fig. 48 The "Reynolds number paradox" for afterbody drag (ref. 41)



(a) Variation of maximum lift with Reynolds number



(b) Variation of drag rise boundary



(c) Maximum lift at drag rise

Fig. 49 Comparison of maximum lift and drag rise Mach number for various two-dimensional tests (ref. 83)

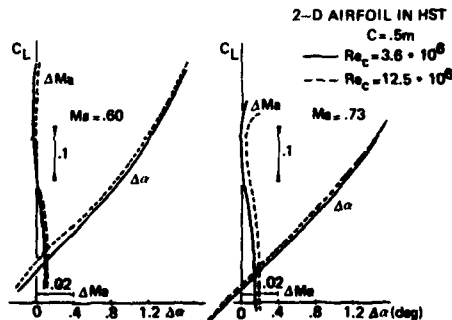


Fig. 50 Effect of Reynolds number on measured wall interference (wall pressure method) for the NLR slotted wall High Speed Tunnel

A PROPOSED BOUNDARY LAYER SIMULATION METHODOLOGY FOR WIND TUNNEL TESTING

Eli Reshotko*

Case Western Reserve University
Cleveland, Ohio 44106
U.S.A.

SUMMARY

While wind tunnels have now been used for about a century to obtain performance data for vehicles to be used in atmospheric flight, there are still numerous uncertainties and ambiguities in the interpretation of the data and in reliably extrapolating them to flight conditions. These issues have been recently addressed by the AGARD Fluid Dynamics Panel Working Group 09. This paper is a report of Committee 2 of the working group - that committee having undertaken the development of a boundary layer simulation/extrapolation methodology.

1. INTRODUCTION

The simulation problem in wind tunnels can be divided into two parts - far field and near field. The first of these recognizes the finiteness of the wind tunnel as compared to the infinity of the flight domain. Techniques have been proposed for assessing the blockage and interference effects due to the finite dimensions of the wind tunnel. More recently, such attention has been given to the adaptive wind tunnel. The near field simulation is referred to as viscous or boundary-layer simulation since it involves adjusting the boundary layer conditions on a model in such a way that the results can be reliably corrected to flight Reynolds numbers. This is usually done by some form of boundary layer tripping since transition locations in flight are likely to occur at smaller fractions of chord or fuselage length than in the wind tunnel.

The full report of the committee whose contents are shown in Table I, will appear as Chapter 3 of the report of Working Group 09. That report presents the rationale of a simulation methodology, describes the experimental, computational and empirical procedures that are needed to implement such methodologies, and finally develops detailed methodologies for the three cases of transport-type configurations, combat aircraft configurations and slender bodies or missile shapes. It is of course to be recognized that the methodologies, trips and scaling procedures would be different for each of the flight regimes - subsonic, transonic, supersonic and hypersonic. The emphasis in the activity of the working group is decidedly on the transonic regime. The present paper outlines the general framework of a simulation methodology and is based principally on Section 3.2.1 of the committee report. The authors of that section are A.B. Haines and A. Eisenbar.

2. DEVELOPING A SIMULATION SYSTEM

A simulation methodology is the underlying rationale for relating wind tunnel results to flight conditions. Such methodologies are not unique, and are in some ways dependent on the phenomenon being simulated. A methodology once chosen, will require the application of boundary layer controls or trips to implement the simulation. The methodology may dictate multiple tests, each with a different trip location. Finally, the wind tunnel results must be analyzed and extrapolated to the conditions of the full scale vehicle in flight. This is accomplished within the dictates of the simulation methodology using computational fluid dynamics (CFD) techniques or well based empiricism. The extrapolability of the test results is an important issue.

2.1. Organizing Concept

The organizing concept underlying any of the methodologies is the correct simulation of each of the flow regimes that might be identified in a lift coefficient (or angle-of-attack) vs. Mach number map for the configuration to be tested. These regimes are defined by the various shock-boundary layer interactions or separations or combinations thereof that might appear. For transport-type configurations there is more or less a single generic map such as that shown in Figure 1. For combat aircraft configurations there are a number of different cases that have to be considered depending on sweep angle, thickness ratio of the wing, leading edge shape, etc., making the situation a bit more complex. In all cases, the attempt is to duplicate the flight pressure distribution as closely as possible in the wind tunnel so that the principle extrapolation will be with respect to Reynolds number. This requires careful attention to reproducing shock locations and the character of the shock-wave boundary-layer interactions through tripping.

* Chairman, Committee on Simulation/Extrapolation Methodology, AGARD/FDP Working Group 09. The other members of the committee are C. Armand, Y.Y. Chan, A. Eisenbar, A.B. Haines, J.L. Potter and G.P. Russo.

It must be emphasized that there is far more to a simulation methodology than deciding whether, how and where to fix transition. Action is required before, during and after the actual tunnel tests. CFD codes should be used ahead of the tests to gain an early idea of the nature of the flow over the model to be tested and of where and how this flow is likely to be subject to uncertain scale effects. This knowledge will help to define the detail of how to control the boundary layer over the model in the tunnel tests. The experimental program should then include an in-depth study of the viscous effects, the aim being to reduce the uncertainties in the final phase after the tests when the data have to be extrapolated to full scale conditions. On the assumption that the maximum tunnel test Reynolds number is less than the full scale value, it should be recognized that some extrapolation of the data will probably always be required. Only on rare occasions will it be possible to find a test technique that will provide a complete simulation of the full scale viscous flow in all its important respects.

2.2. Types of Scale Effect

The simulation methodology has to address two types of scale effect:

- (i) "Direct" Reynolds number (or viscous) effects arising as a result of changes in the boundary layer (and wake) development for a fixed or "frozen" pressure distribution. Examples of "direct" effects range from the well known variation of skin friction with Reynolds number for a given transition position to complex issues such as changes in the length of a shock induced separation bubble for a given pressure rise through the shock.
- (ii) "Indirect" Reynolds number (or viscous) effects associated with changes in pressure distribution resulting from changes with Reynolds number in the boundary layer and wake development. As an example of an "indirect" effect, one can note that changes in boundary layer displacement thickness with Reynolds number can lead to changes in supercritical flow development and hence, in shock position and shock strength. Hence, a change in wave drag with Reynolds number at a given C_L or incidence can appear as an "indirect" viscous effect.

Strictly, this distinction (i,ii) between "direct" and "indirect" scale effect is merely a convenient artifice to simplify the discussion of the effects. It is an artificial distinction because, in practice, the two types of effect are always coupled. When the flow is subcritical and fully attached, one can often safely ignore this coupling because the indirect effects will be relatively small but when shock waves are present and even more when there is a tendency for the flow to separate, this coupling can be very important. In CFD terms, "strong coupling" implies that the flow has to be calculated by a method capable of allowing for strong as well as merely weak interactions between the inner (viscous) and outer (inviscid) flow fields. At the present time, (1987), such methods are only in the early stages of development and even when they have been developed in the future, it is possible that they will still be too costly and time-consuming to use in routine applications of a simulation methodology. Hence, the boundaries marking the appearance of flow phenomena giving rise to strong interactions are of particular significance in the context of a simulation methodology. While the interactions are weak, one can rely on CFD predictions that can be applied in practice as a guide to the extrapolation from model to full scale but where the interactions are strong, measured trends will have to form the basis for the extrapolation. The aim for a good simulation methodology must be to bring these boundaries, if possible, within the range of the tests.

2.3. Experimental Approach

The approach adopted for the in-depth study of the viscous effects is the central feature of the simulation methodology. Broadly, there are two possible approaches:

- (i) Reynolds number sweeps in which the model is tested over a range of Reynolds number with transition fixed at a position, probably near the leading edge, that is close to where it is forecast to occur in flight at full scale Reynolds numbers,
- (ii) With manipulation of the boundary layer to produce a viscous flow behavior closer to that forecast to occur at full scale Reynolds numbers. In practice, at the present time (1987), this implies using the aft-fixing technique in which the boundary layer is allowed to remain laminar over the forward part of the surface and transition is then tripped at a position further aft than in flight. In other words, this approach will typically involve a sweep through a range of transition positions.

Whenever possible, both these approaches should be practiced; this will give added confidence in the final extrapolation. Table II summarises the relative merits of the two approaches.

The first approach, ie Reynolds number sweeps, can strictly only be practiced in a variable pressure (or temperature) tunnel. The available test Reynolds number can be further extended by testing a complementary half model to a different scale, typically 1.4 to 1.8 x the scale of the basic complete model. One would not expect to be able to create a single curve of say C_D against Reynolds number at a given C_L directly from the measured results for the two models but by overlapping the test Reynolds number ranges for the two models, the trends through the half model data can be used as a basis for extrapolating the results for the complete model up to the maximum test Reynolds number for the half model. Even when the tests are being made in an atmospheric tunnel, tests on a complementary half model can still be helpful in establishing trends with Reynolds number but since there is then no overlap in the data, great care has to be taken in interpreting the comparison in view of the inherent doubts about the absolute accuracy of half model data. Clearly, the case for exploiting the second approach, ie manipulating the boundary layer by aft-fixing, will be greater if the tests are being made in an atmospheric tunnel.

2.4. Simulation Criteria

Turning now to the choice of simulation criterion, this may be regarded as the vital crux issue in the definition of the whole methodology. There is no clear consensus as to what to choose and probably, there is no single criterion that will serve for all test programs. The correct choice will always depend on the objectives of the particular test program and it will probably always be prudent to interpret the data on the basis of more than one criterion. In view of the widely different capabilities of likely potential users of the methodologies, it may be helpful to put forward several possible criteria to different levels of refinement:

- (a) a zero-level criterion: easy to apply, not dependent on the particular configuration under test.
- (b) a first order criterion representing the overall integrated scale effect on the pressure distribution or more probably, some leading feature of the pressure distribution, such as shock position or shock strength. Use of such criteria tends to minimize indirect scale effects.
- (c) a second order criterion based on the local viscous effects in some particularly sensitive local region. These tend to promote a more refined consideration of indirect scale effects.

Considering these ideas in more detail:

2.4.1. The zero-level criterion

At this level, the proposal is to use a simple 'flat plate simulation criterion' provided in Figure 2. This criterion is based on the requirement that the dimensionless boundary layer momentum thickness (θ/c) at the trailing edge of a flat plate is the same for the tunnel test Reynolds number and aft transition location and for the effective Reynolds number and transition at the leading edge (clearly, a different criterion would have to be used for any application in which extensive laminar flow was expected in flight). This criterion provides a very crude drag simulation. Figure 2 has been derived using simple incompressible boundary layer relations to provide a zero-order approximation to the direct scale effect. It is clearly simple to apply in converting test Reynolds number with aft transition to effective Reynolds number, but it knows nothing about any of the details of the flow. It is only of use in converting the Reynolds number and hopefully, in defining whether full simulation is possible in the test range of Reynolds numbers and transition positions. It will play no part in the extrapolation procedure beyond the effective Reynolds number (if this extrapolation is required) or in the assessment of Rcrit. Perhaps surprisingly, however, present evidence suggests that this simple criterion (due to Elsenaar) is remarkably good as a guide to the conversion from the model test Reynolds number (with aft transition) to an effective Reynolds number (see Section 2.5).

2.4.2. First-order simulation criterion

'First order' in this context implies that the criterion is chosen in an attempt to represent the overall viscous effects on the complete pressure distribution rather than a specific local viscous effect. In the future, it may become possible to use a manipulation technique, eg distributed suction, surface cooling, or changes in the model shape, that will produce the full scale pressure distribution in the model tests, but at the present time, as noted earlier, the only tool that is generally available is the aft-fixing technique which clearly is not capable of achieving this ideal objective. Rather, the aim must be to reproduce those features of the pressure distribution that have most impact on the aerodynamic characteristics, eg features such as shock strength and shock position. Kraft in his contribution to another section of the Working Group 09 report states: "unequivocally, the highest priority for a proper simulation in a transonic wind tunnel test is that the model scale test must reproduce the full scale location of the shock wave".

Shock position must therefore be a leading candidate for a first-order simulation criterion. This is not a surprising conclusion as most of the early examples (Refs. 1, 2) of serious scale effect were associated with significant differences in shock position between model and full scale.

In some instances where there is little change in shock position with Reynolds number, shock strength may be a better simulation criterion than shock position. Experience suggests that it may always show a decrease with Reynolds number at a given C_L .

Shock position and/or shock strength are naturally appropriate criteria only when the flow is supercritical. When the flow is subcritical, eg on the wing lower surface, the most obvious advance from the zero-order criterion is to use the calculated non-dimensional momentum thickness at the wing trailing edge as the criterion. In this way, allowance is made for the effects of the pressure distribution on the overall viscous effect.

This list of shock position, shock strength and non-dimensional momentum thickness at the trailing edge is by no means exhaustive of the criteria that might be suggested. For example, the non-dimensional boundary layer displacement thickness at 0.90c is another parameter in regular use (Ref. 3). Even if full simulation in terms of one or more of the parameters is achieved, some extrapolation will still be needed. The virtue of using shock position and shock strength as the criteria are that the subsequent extrapolation has merely to cope with the direct effects; adequate simulation of the indirect effects has already been obtained.

2.4.3. Second-order local simulation criteria

There are situations when the gross scale effect is apparently an indirect effect. This arises because the indirect effect, eg a change in shock position, has been magnified by an interaction with a direct effect such as a change with Reynolds number in the separation characteristics.

A list of local simulation criteria related to the direct scale effects is listed below (the first has already been mentioned under 2.4.2).

- (i) The non-dimensional momentum thickness at the trailing-edge relevant for the conversion of drag data.
- (ii) The non-dimensional length, L_{sep}/c , of the shock-induced separation bubble expressed as a function of either the boundary layer momentum thickness (Ref. 4) or displacement thickness and shape factor (Ref. 5) immediately ahead of the shock.
- (iii) The parameter, $(\delta^*/c)(S_{11} - 1)$, proposed by Stanewsky as a means of correlating the shock upstream influence, and possibly relevant also to the state of the boundary layer approaching the trailing edge and also possibly to the development of the shock-induced separation bubble.

One final comment about the terminology. A second order criterion should not be regarded as a refinement of a first order criterion. A second order criterion attempts to match some detailed feature of the pressure distribution thought to be relevant to a particular direct scale effect, whereas a first order criterion attempts to match the model and full scale pressure distributions in an average sense and thus, when applied successfully, should largely eliminate the indirect scale effects, leaving the test engineer with the problem of estimating all the direct effects. In practice, one should choose the criterion that appears to be most relevant in the context of the aims of the particular test program and one should attempt to obtain the closest approach to full simulation in respect of this criterion. In any event, the test data will likely have to be extrapolated to full scale to allow for the probable lack of full simulation.

2.5. Extrapolability of wind tunnel results

In order to discuss the extrapolability of wind tunnel data to flight Reynolds numbers, it is at this point necessary to define some terms that will be used in assessing a number of simulation scenarios. These are:

(a) Effective Reynolds Number (R_{eff})

The effective Reynolds number is the Reynolds number for the full scale vehicle under flight conditions that has the same simulation criterion as the wind tunnel model.

A simple example can be given with the aid of the zero order simulation criterion of Figure 2. Based on an equivalent θ/c at the trailing edge, a flat plate model of length Reynolds number of 4×10^6 with a transition trip at $0.45c$ has an R_{eff} of about 20×10^6 .

Generally, the required conversion between Reynolds number and transition position is obtained from CFD calculations, ideally for the 3D wing-body combination but realistically at the very least, for an equivalent two-dimensional aerofoil, and depends on what simulation criterion is chosen as a basis for the conversion.

(b) Critical Reynolds number (R_{crit})

R_{crit} is the Reynolds number at which there is a change in the simulation parameter from low Reynolds number behavior to high Reynolds number behavior (see Figure 3).

The differences between low and high Reynolds number behaviors may be due to a change in the dominant transition mechanism between the two regimes, a change in leading edge separation behavior with Reynolds number, or else, a change in the character of trailing edge separation with Reynolds number. Often the change is not as abrupt as shown in the sketch and some judgment is required in identifying R_{crit} .

(c) x_T^*

x_T^* is the transition location that duplicates on the model the flight value of the simulation criterion.

An example might be the transition location that places $(x/c)_{shock}$ at the location expected on the flight vehicle.

2.5.1. Simulation scenarios

Five possible simulation scenarios are shown in Figs 4-8, each of successively more questionable extrapolability. Although the simulation criterion is not specified, these diagrams have been drawn with dimensionless shock location in mind. These scenarios are described in turn:

(1) Fig 4: $R_{crit} < R_{flight} < \text{maximum test } R_{eff}$

This is the simplest case: the results suggest that no rear separation or other strong viscous-inviscid interactions will be present in flight and it has proved possible to test with a transition position (x_T^*) that should give, in terms of the chosen simulation criterion, full simulation of the flight behavior: no extrapolation required.

(2) Fig 5: $R_{flight} < R_{crit} < \text{maximum test } R_{eff}$

This is really a subdivision of case 1 but interpretation of the data is more uncertain. On paper, the conclusion is the same as for case 1, ie full simulation of flight has been achieved in the tests and no extrapolation is necessary. However, this conclusion rests critically on whether one can trust the CFD codes/separation criteria in forecasting that the flow separations observed under test conditions are equivalent to those for the flight conditions.

(3) Fig 6: $R_{crit} < \text{maximum test } R_{eff} < R_{flight}$

Some extrapolation required - from maximum test R_{eff} to R_{flight} but this should be manageable on the basis of the trends from CFD calculations including merely weak viscous/inviscid interactions.

(4) Fig 7: Maximum test $R_{eff} < R_{crit} < R_{flight}$

Real uncertainty is now creeping in: the extrapolation from maximum test R_{eff} to a forecast R_{crit} has to be on the basis of an extrapolation of the measured trends and then, from R_{crit} to R_{flight} on the basis of the trends in CFD calculations. It should be noted that R_{crit} cannot and must not be derived as the values of R at which the extrapolation of the measured data intersects the CFD predictions. This would be tantamount to saying that theory is capable of forecasting the flight results and there is no need for the tunnel tests. R_{crit} must be obtained by use of available empirical relations and techniques or by intelligent extrapolation of the measured trends, and then the CFD codes must be used merely to establish the trends between R_{crit} and R_{flight} .

(5) Fig 8: Maximum test $R_{eff} < R_{flight} < R_{crit}$

This is really a subdivision of case 4 but the extrapolation is even more uncertain because neither the measured nor calculated results will be capable of giving any precise guidance as to the quantitative consequences of the fact that a rear separation (etc) is still expected to be present in flight.

It must be stressed that Figs 4-8 are only diagrammatic and simplified. The real situation could be much more complicated. Some general points should be noted:

- (i) The pictures have been drawn on the basis that a discontinuous change in the direction of the trend with Reynolds number occurs at R_{crit} ; in real life, it is much more likely that the change in direction occurs gently and smoothly over a range of Reynolds number.
- (ii) The pictures imply that the changes with R that occur beyond R_{crit} are linear and monotonic. This is not necessarily true and the later discussion, for example about the possible use of shock position as a simulation criterion, will contain evidence that the variation of shock position with Reynolds number can be in either direction and one can envisage results for a given aerofoil in which the shock can move forward or rearward with changes of Reynolds number above R_{crit} , the direction being a function of Reynolds number.
- (iii) The range of transition positions available to the test engineer will be subject to various limitations, eg
 - (a) the ability to maintain laminar flow back to the desired transition position. This will depend on the tunnel turbulence, acoustic noise spectrum and the pressure distribution over the wing surface.
 - (b) the need to ensure a turbulent boundary layer/shock interaction.
 - (c) the need to avoid any local interaction between the transition trip and the flow near the shock.
 - (d) the need to minimise, as far as possible, any significant disturbance to the supercritical flow development over the forward part of the surface.

Limitations (b,c) dictate that the furthest aft acceptable transition position in the tunnel tests will be at least 0.10c and probably 0.15c ahead of the position of the shock.
- (iv) The chosen simulation criterion is used for both the variable plotted up the ordinate scale and for the conversion of the model test Reynolds number into an effective Reynolds number; however, the value of R_{crit} is not necessarily related to the chosen simulation criterion as this criterion may have no relevance to the flow phenomenon creating strong viscous/inviscid interaction at Reynolds number below R_{crit} .
- (v) There is no reason in principle why a given set of model test data should not be in one scenario for one simulation criterion and in a different scenario for another criterion. Experience is lacking as to whether this situation is liable to occur often in practice and whether, if so, it leads to serious problems in knowing how to extrapolate. If this situation arises, it would reinforce the early message that to be successful in applying the methodology, one must understand the nature of the flow over the configurations being tested.

2.6 Use of Reynolds number sweeps

The discussion in section 2.5 has concentrated on the boundary layer manipulation approach. However, when the tests are being made in a variable pressure tunnel, there is an additional degree of freedom that can be exploited to enhance confidence in the final result. The five possible scenarios, as discussed in section 2.5.1, still apply but, as noted in Figures 4-8, the maximum effective Reynolds number is now simply the maximum true Reynolds number for a particular model configuration provided that the Reynolds number sweep is performed with a transition position similar to that forecast for flight at full scale Reynolds number. As noted on the figures, half models can and should be used to exploit the tunnel capabilities to the full, but it is important to preserve an overlap in test Reynolds number between the half model and complete model tests. This is because the half model test should not be expected to provide absolute data but should be viewed as a dedicated experiment with a specific aim of investigating detailed Reynolds number effects.

In many variable pressure tunnels, it is possible to change the Reynolds number by a factor of about 2.5 for a given model and then, by use of the half model, to obtain a further increase by a factor of between 1.5 and 2, according to the configuration geometry and Mach number range of the particular tests. In other words, a Reynolds number sweep over a range of between 4:1 or 5:1 should be possible but this may still be somewhat less than could be achieved in R_{eff} in favorable cases by use of the boundary layer manipulation approach. One might find that the results are in scenario 3 with aft fixing or scenario 4 with a Reynolds number sweep but the significance of this point could be offset by the fact that some of the uncertainties of being in scenario 4 would be less important with a Reynolds number sweep where the data are being plotted against true test Reynolds number rather than a somewhat problematic effective Reynolds number. Also, in practice, the boundary layer manipulation approach is subject to various limitations, particularly when applied to the moderate or small aspect ratio wings of combat aircraft. The weak and strong points of the two techniques are summarized in Table II. It may of course be useful to use both approaches because, if one can establish that the trends in relation to true Reynolds number in the Reynolds number sweep and effective Reynolds number in the transition sweep are the same, it will obviously greatly increase confidence in the interpretation of the test data.

3. STEPS IN THE FULL SIMULATION METHODOLOGY

The discussion has now reached the point where the important concepts in the above philosophy can be assembled into a full methodology. The steps in the recommended general methodology can be set out briefly as follows:

A. BEFORE THE TESTS

STEP 1: Collection of Relevant Information - Planning

Ahead of the tests, learn about the tunnel, the model and the test objectives. Identify the important design/operating conditions. In the references below to CFD calculations, it is assumed that at the design/operating conditions for which these calculations are made, the flow is either completely attached or only includes local separations near the leading edge or trailing edge or at the foot of the shock up to the point when these separations develop in a dramatic fashion. Conditions beyond buffet onset are therefore excluded even though the flow under such conditions is of major concern in tests on a combat aircraft.

STEP 2: Preparatory Calculations

Ahead of the tests, apply CFD codes allowing for weak viscous-inviscid interactions to learn as soon as possible about the flow over the model to be tested and whether and how this flow is likely to be subject to significant scale effects of either the direct (change in boundary layer development) type. These calculations are made for the design/operating conditions identified in Step 1.

Ahead of the tests, apply the zero-order simulation criterion (see Section 2.4.1 and Fig. 2) to gain a first idea of whether it is likely to be possible to find a transition position in the model tests that will simulate the full scale behavior.

Finally, ahead of the tests, calculate the values of R_{crit} below which a strong viscous-inviscid interaction such as a rear separation or a laminar separation near the leading edge is predicted to occur with the forecast transition position for flight at full scale Reynolds number.

B. DURING THE TESTS

STEP 3: Initial Datum Tests

Start the tests with a general coverage of the whole test envelope to find whether the results are critically dependent on the state of the boundary layer, eg test with both transition fixed and free or with two alternative transition positions.

STEP 4: In-Depth Study of Viscous Effects

Include in the tests an in-depth study of the viscous effect either by undertaking Reynolds number sweeps (in a variable density tunnel) or by manipulating the boundary layer, eg by a sweep through a range of transition position (in an atmospheric tunnel). Wherever possible, both approaches should be practiced. Also, whenever possible, extend the Reynolds number sweep to higher Reynolds numbers

by testing a complementary half model, the tests on the complete and half model being arranged to overlap in a certain range of Reynolds number. The boundary layer manipulation approach is employed for two reasons:

- (i) to simulate, as far as possible, the full scale viscous flow behavior in the model tests,
- (ii) to include, if possible, R_{crit} in the test range of effective Reynolds number.

C. AFTER THE TESTS

STEP 5: Consolidation of Data; Establishment of Measured Trends

After the tests, take the results from the Reynolds number sweeps and plot appropriate parameters, eg shock position, shock strength, C_p etc at a given C_L against Reynolds number. Plot both the measured and computed results. Comparison of the measured and predicted trends will provide a check on the predicted values of R_{crit} and may lead to revised estimates of R_{crit} . If the tests (including the tests on any complementary half model have extended to beyond R_{flight} , the results are directly applicable to full scale conditions; if, as is more likely in general, the tests do not extend up to R_{flight} , the results have to be extrapolated by extending the measured trends to R_{crit} and then following the computed trends from R_{crit} to R_{flight} , care being taken to remember that it is unlikely that any sharp discontinuous change in the slope of the trends occurs at R_{crit} .

After the tests, the measured results from tests using the boundary layer manipulation approach should be plotted against an effective Reynolds number defined as the Reynolds number that would be needed if transition were fixed at the position for flight at full scale Reynolds number to produce the viscous flow behavior obtained in the model test with aft transition. The conversion to an effective Reynolds number should be based on either the zero-order simulation criterion (see Section 2.4.1 and Fig 2) or whatever first order or second order criteria that appear to be particularly relevant to the test objectives.

Compare the measured trends against effective Reynolds number in results such as shock position, shock strength, C_p and C_{pg} . These characteristics are chosen because they are particularly sensitive to the extra viscous effects which occur below R_{crit} . This comparison between measured and predicted trends provides a check on the estimates of R_{crit} .

Use the graphs produced above to identify which is the relevant scenario of the five discussed in Section 2.5.1 (see Figures 4-8). Remember to check on the basis of more than one simulation criterion.

STEP 6: Extrapolation to Full Scale

Implement the extrapolation procedure for the appropriate scenario as described in Section 2.5.1. The procedures as described may appear laborious but remember that the full procedure will probably only be followed to provide the best possible extrapolation for the important design/operating conditions identified in Step 1.

The procedure as described above is set out in much more detail in the separate methodologies for transport aircraft, combat aircraft and missile shapes in the full Working Group 09 report. It will be realized that in order to introduce the philosophy in a reasonably clear manner, various gross simplifications have been made in the outline above. Phrases such as 'testing with a certain transition position' suggest that the test configuration is merely a two-dimensional aerofoil. However, to extend the methodology to the high aspect ratio wing of a subsonic transport is not difficult. For the lower aspect ratio wing of a combat aircraft there has to be much more emphasis on the complex flow patterns that can be encountered but the same philosophy can still be followed in principle. In all cases, the recipe for success is:

- (a) Understand the nature of the flow over the test configuration.
- (b) Cover as wide a range of Reynolds number or effective Reynolds number as possible.
- (c) Be guided by past experience but do not necessarily repeat what one did with the previous design. It all depends on whether the flow is precisely the same; even if the two designs come from the same family, this is unlikely to be true, eg both the maximum effective Reynolds number and R_{crit} could be different and the results for the two wings could be in different scenarios.
- (d) Unless one is absolutely sure, avoid short cuts and simplifications.
- (e) Do not assume any results! Minor alterations in configuration can yield significantly different aerodynamics.

4. CONCLUDING REMARK

The present paper outlines the rationale underlying the simulation methodologies developed by AGARD FDP Working Group 09. It is a first step in the attempt to codify and systematize the best of our simulation capabilities to date and to provide the framework for further improvements. Such methodologies and their successors will be an essential component of the sophisticated wind tunnel

testing and evaluation procedures to which we aspire. The fact that these methodologies are now written down makes them available to the larger wind tunnel testing community and should lead to an overall improved confidence in the test results for the increasingly complex configurations that we seek to evaluate.

REFERENCES

1. Loving, D.L.: Wind Tunnel Flight Correlation of Shock Induced Separated Flow. NASA TN D-3580, 1966
2. Cahill, J.P.: Simulation of Full Scale Flight Aerodynamic Characteristics by Tests in Existing Transonic Wind Tunnels. AGARD CP 83, Paper 20, April 1971
3. Boppe, C.N.: Future Requirements of Wind Tunnels for CFD Code Verification. AIAA 86-753, March 1986
4. Fulker, J.L. and Ashill, P.R.: A Model of the Flow over Swept Wings with Shock Induced Separation. RAE TR 83088, 1983
5. Stanawsky, E.: Interaction Between the Outer Inviscid Flow and the Boundary Layer on Transonic Airfoils. Dissertation, TU-Berlin (D83), 1981. (Also Z. Flugwiss. Weltraumforsch. 7, 1983, Heft 4, pp. 242-252)

Table I. Report Contents

3.1	Introduction	E. Reshotko
3.2	General Framework	
3.2.1	An Outline of the Methodology	A.B. Haines A. Elsenaar
3.2.2	Experimental tools - tunnel and model requirements	A.B. Haines
3.2.3	Computational tools for simulation methodologies	Y.Y. Chan
3.2.4	Empirical tools	A. Elsenaar
3.3	Applications	
3.3.1	Transport-type Configurations	A.B. Haines A. Elsenaar
3.3.2	Comba. aircraft	A.B. Haines
3.3.3	Slender bodies	J.L. Potter
3.4	Conclusions	E. Reshotko

Table II. RELATIVE MERITS OF MANIPULATION (BY AFT FIXATION) AND REYNOLDS NUMBER SWEEPS

SIMULATION BY B L MANIPULATION	EXTRAPOLATION FROM REYNOLDS NUMBER SWEEPS
1a APPLICABLE FOR ALL WIND TUNNELS (PROVIDED $Re_c > 2 \times 10^6$ & PROBABLY $< 12 \times 10^6$)	1b APPLICABLE ONLY FOR VARIABLE DENSITY TUNNELS
2a MAY BY-PASS 'CRITICAL EVENTS', eg DISAPPEARANCE AT Re_{crit} OF REAR SEPARATIONS FORECAST NOT TO OCCUR AT FLIGHT REYNOLDS NUMBER; UNDER CERTAIN CONDITIONS (SEE 3a) POSSIBLE TO MATCH FLIGHT PRESSURE DISTRIBUTIONS; ONLY LIMITED EXTRAPOLATION (eg FOR DRAG) REQUIRED	2b THEORY IS REQUIRED TO PREDICT 'CRITICAL EVENTS' IN REYNOLDS NUMBER RANGE BEYOND TUNNEL CAPABILITIES AND TO PREDICT TRENDS AFTER THE CRITICAL EVENT
3a A REGION OF LAMINAR FLOW AHEAD OF THE SHOCK REQUIRED; THEREFORE ONLY APPLICABLE FOR CERTAIN REGIONS IN C_L - M PLANE	3b CONTINUOUS INFORMATION IN C_L - M NUMBER PLANE
4a UNCERTAINTY INTRODUCED BY VALIDITY OF THE SIMULATION CRITERION; MAXIMUM SIMULATED REYNOLDS NUMBER DEPENDS ON CHOICE OF CRITERION AND PRESSURE DISTRIBUTION, HENCE, C_L AND M	4b EXTRAPOLATION ERROR DEPENDS ON TUNNEL REYNOLDS NUMBER RANGE RELATIVE TO FLIGHT REYNOLDS NUMBER AND ON WHETHER 'CRITICAL EVENTS' OCCUR OUTSIDE TEST RANGE
5a THREE-DIMENSIONAL EFFECTS COULD CAUSE DIFFICULTIES NEAR ROOT AND TIP	5b THREE-DIMENSIONAL EFFECTS DO NOT REPRESENT AN ADDITIONAL PROBLEM BUT COULD ACCENTUATE DIFFICULTY OF 2b
6a REQUIRES A NUMBER OF TUNNEL RUNS WITH VARIABLE TRANSITION STRIP SIZE AND LOCATION; SHOCK WAVE POSITION MUST BE MONITORED RELATIVE TO STRIP LOCATION TO AVOID SPURIOUS EFFECTS IN REGIONS WITH SUPERSONIC FLOW	6b REQUIRES A NUMBER OF TUNNEL RUNS TO ADAPT TRANSITION STRIP SIZE TO REYNOLDS NUMBER; SPURIOUS TRANSITION STRIP EFFECTS RESTRICTED TO LEADING EDGE REGION BUT MIGHT STILL BE SIGNIFICANT

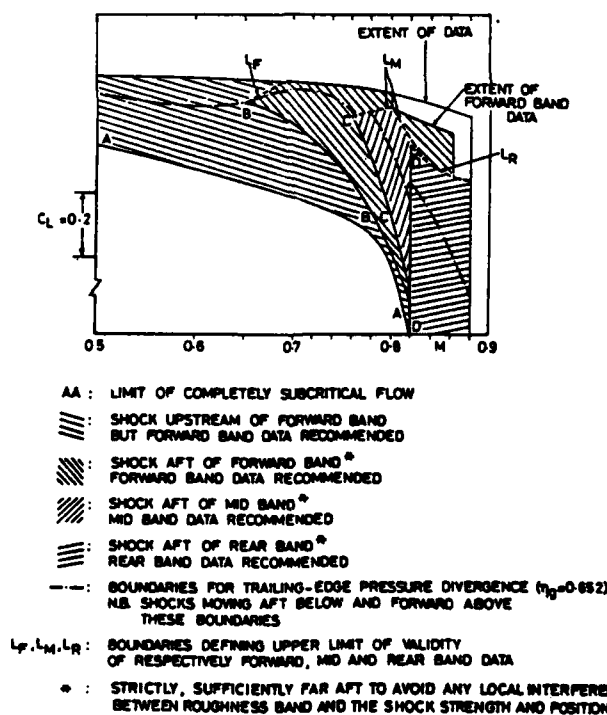


Fig. 1: C_L vs. Mach number map for transport type configurations.
Regions of validity of data with different roughness bands
on a wing upper surface.

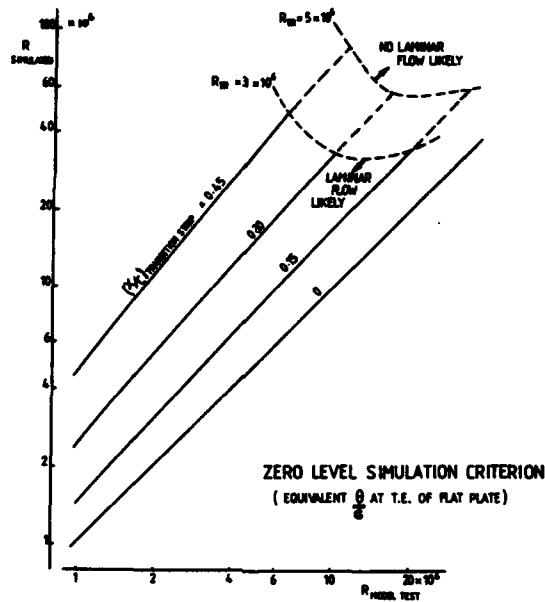
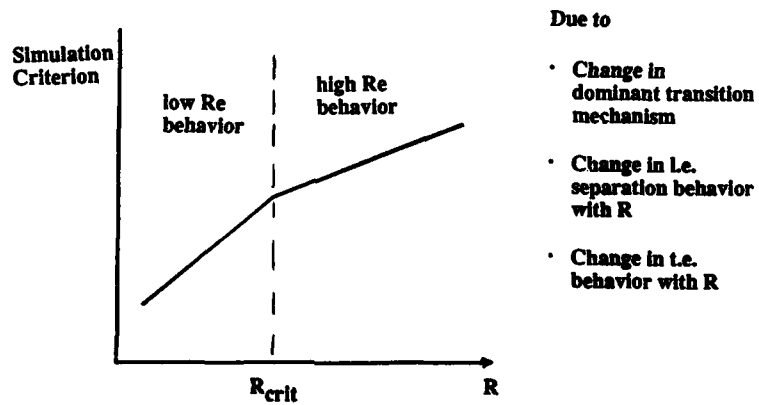


Fig. 2: Zero level simulation criterion

Fig. 3: Distinction between low Reynolds number behavior and high Reynolds number behavior; R_{crit}

$$R_{crit} < \max R_{eff} < R_{flight}$$

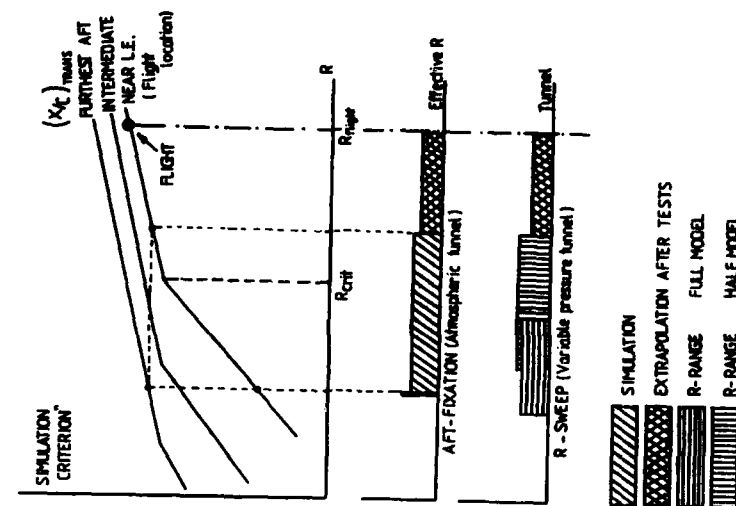


Fig. 6: Simulation scenario 3

$$R_{flight} < R_{crit} < \max R_{eff}$$

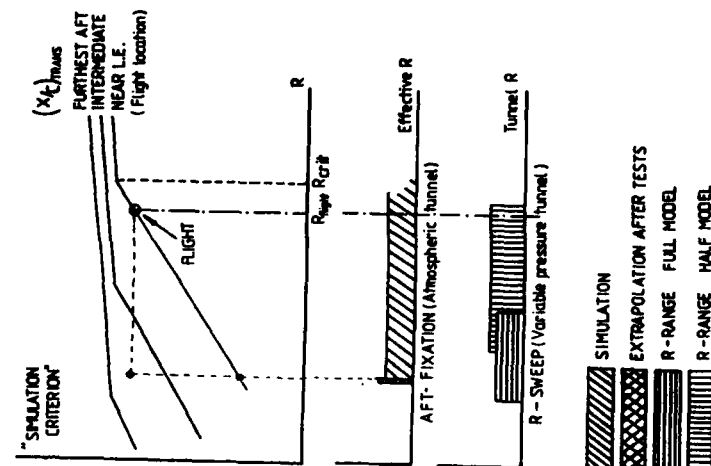


Fig. 5: Simulation scenario 2

$$R_{crit} < R_{flight} < \max R_{eff}$$

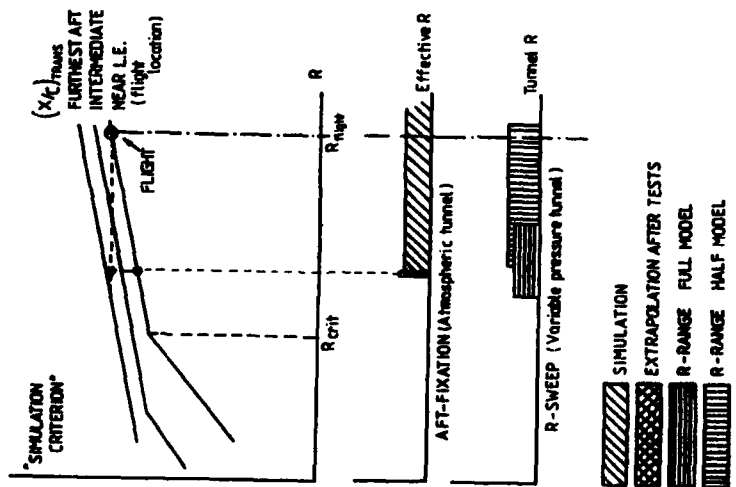


Fig. 4: Simulation scenario 1

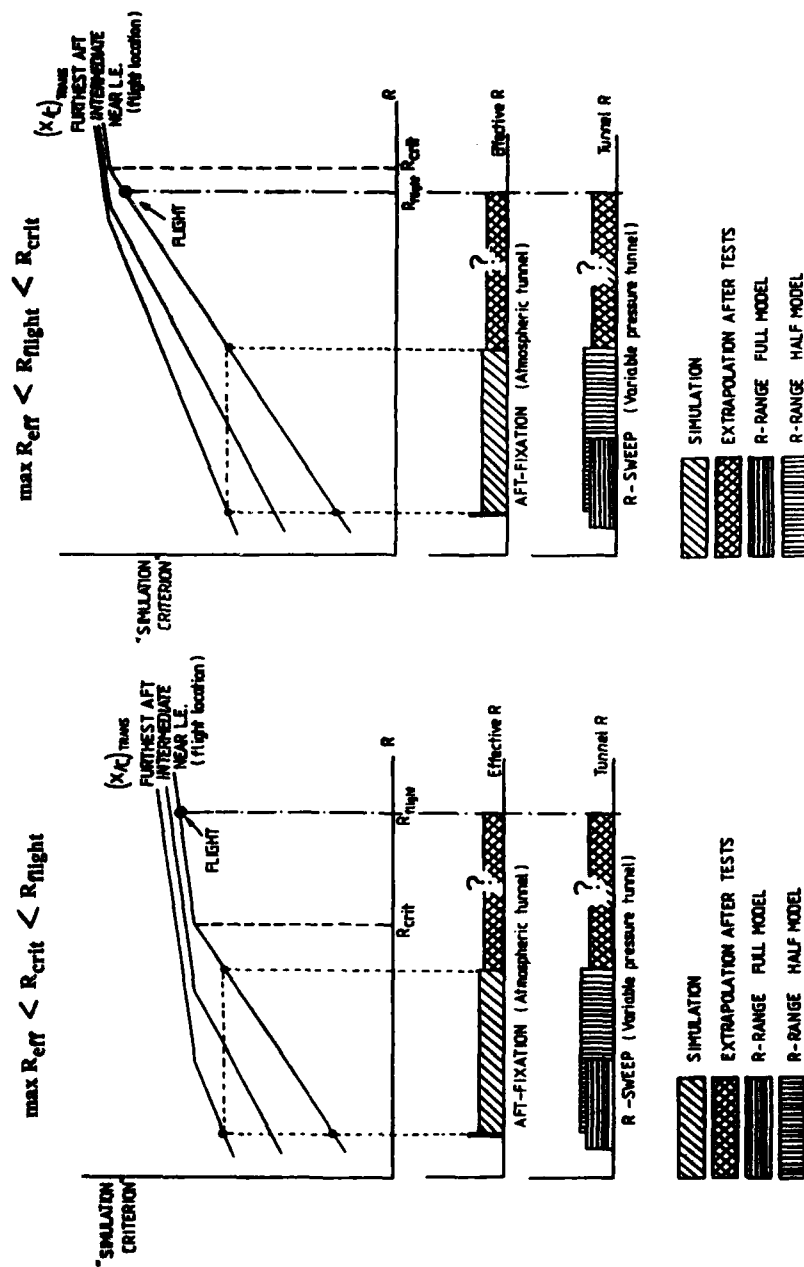


Fig. 8 Simulation scenario 6

Fig. 7: Simulation scenario 4

EXPERIMENTS ON BOUNDARY LAYER TRANSITION TRIPPING AT LOW REYNOLDS NUMBERS

by
Giuseppe P. Russo
Institute of Aerodynamics "Umberto Nobile"
University of Naples
Faculty of Engineering
Piazzale Tecchio, 80
80125, Naples
Italy

SUMMARY

In the present work a systematical experimental investigation has been undertaken with the aim of obtaining sound results on the effectiveness of distributed roughnesses in tripping transition on a flat plate at low Reynolds numbers. A 2.5 mm band of double stick scotch tape dusted with sparse carborundum grains has been used as a tripping element at various speeds, ranging from 11 to 17 m/s. Transition location has been detected by streamwise traversing, at a fixed height from the flat plate, both a pitot tube and a hot-wire probe; also relevant velocity profiles in the boundary layer have been measured. When needed surface flow visualization has been used to confirm the transition position. A good correlation has been found, in terms of the critical roughness Reynolds number needed to fix transition at the roughness, with the results found in the open literature.

LIST OF SYMBOLS

d = roughness diameter
 k = roughness height
 M = Mach number
 q = dynamic pressure
 $R = U_e L / \nu$ Reynolds number based on free-stream conditions and reference length $L(X, d, \delta^*, \theta)$
 $R_k = u_k k / \nu_k$ roughness Reynolds number based on roughness height and velocity and kinematic viscosity at top of roughness
 U = free-stream velocity
 u = local streamwise component of velocity inside the boundary layer
 V = dc output of a hot wire anemometer
 X = distance from leading edge
 δ = boundary layer thickness
 δ^* = displacement thickness
 θ = momentum thickness
 ν = coefficient of kinematic viscosity

Subscripts

cr = critical conditions
 k = referred to roughness
 T = transition

INTRODUCTION

Flight at the low Reynolds numbers typical of ultralight aircrafts, gliders and remotely piloted vehicles is strongly influenced by formation and bursting of laminar bubbles, leading edge stall and so on; since few practical theoretical methods exist taking full account of these phenomena extensive wind tunnel tests are usually required to predict the flight performances of a given wing.

Correct simulation in wind tunnel tests of these complex aerodynamic patterns, due to the even lower Reynolds number obtainable on a reduced scale model, often requires some kind of artificial boundary layer tripping in order to reproduce the exact transition location experienced in flight or, alternatively, to control the boundary layer scale at a desired location.

Furthermore, in free flight location of laminar to turbulent transition, laminar separation and subsequent turbulent reattachment, leading edge and trailing edge separations are all affected by the presence of wing contamination arising from manufacturing processes and/or natural accumulation (joints, rivets, warping, insects, ice etc.) acting as two-dimensional or three-dimensional or distributed roughnesses. These surface roughnesses by modifying the aerodynamic field may cause detrimental alterations in the performances of the wing. It is thus mandatory to test these effects in a wind tunnel.

Unfortunately trying to influence a boundary layer at very low Reynolds number is quite difficult as has been frequently put in evidence in the literature on the subject of transition tripping. Klebanoff, Schubauer and Tidstrom in their classical work published in 1955 (Ref.1) found that a lower limit exists for Reynolds number below which it is not possible to trip transition with a two-dimensional trip.

In 1966 Braslow, Hicks and Harris (Ref.2) found that for length Reynolds number, R_L , less than 10^5 it was more difficult to trip transition and a much higher roughness Reynolds number, R_{kz} , was needed with respect to the value of 600 they had found as an average from hundreds of experimental data on three-dimensional roughness elements.

Also in a recent work by Bloch and Mueller (Ref.3) difficulties have been encountered in attempts to affect the boundary layer behaviour in tests performed at chord Reynolds numbers ranging from 80000 to 200000. The authors found that roughness height prediction methods to fix transition location in this range of Reynolds numbers are insufficient.

There are therefore sufficient motivations to justify a direct experience in this field that is furthermore strongly dependent on many environmental parameters: wind tunnel turbulence, difficulties in reproducing with a good confidence the tripping device, wind tunnel noise etc.

BOUNDARY LAYER TRIPPING

The problem is to find a tripping device of minimum dimensions producing effective transition at the trip location without modifying appreciably the potential flow nor giving rise to prohibitive parasite drag; the procedure must furthermore be easily reproducible to warrant reliable results; the device should not be damaged by prolonged tests and lastly should be easily removable giving back unaltered conditions of the surface.

Boundary layer tripping devices, which are solid or fluid obstacles put inside the boundary layer to increase local turbulence and provoke premature transition, may be classified (Fig.1) as two-dimensional (cylindrical) devices (spanwise wires, ridges and grooves), three-dimensional (point-like) obstacles (cylinders or air jets normal to the surface of the model) and distributed roughness strips (ballotini or carborundum grains). Two-dimensional and three-dimensional obstacles essentially differ in the mechanism of producing instability in the laminar boundary layer (Ref.4): two-dimensional obstacles produce spanwise vortices while three-dimensional obstacles produce streamwise horseshoe vortices (Fig.2).

Two-dimensional trips thus induce in the laminar boundary layer an instability of the Tollmien-Schlichting type; this instability may produce, at a downstream location, transition to a turbulent pattern. As the diameter of a two-dimensional trip is increased the point of transition, X_{tr} , moves progressively upstream from the point of natural transition, X_n , towards the position of the trip, X_t (Fig.3). A frequently used characteristic parameter is the ratio between trip diameter and displacement thickness, the transition point reaching a position close behind the trip when this ratio is of the order of magnitude one.

Klebanoff and coworkers (Ref.1) found that when the length Reynolds number, R_L , is lower than 90000 it is not possible to trip transition and showed that the corresponding value of the Reynolds number based on the displacement thickness, $R_{\delta^*} = 520$, was in good agreement with the critical value found from a Blasius distribution for stability against small disturbances.

An empirical law for the determination of the relative position of transition point and trip in terms of the height of a two-dimensional roughness element has been given by Dryden (Ref.5). A corresponding critical Reynolds number, based on trip diameter and free stream flow conditions, $R_{kz} = U d / \nu$ equal to 700 has been calculated by Winter and coworkers (Ref.6) as a result of a correlation of many experimental data in the range of subsonic speeds up to $M=0.9$. At supersonic speeds the critical value increases exponentially with Mach number. Kramer (Ref.7) found a Reynolds number $R_{kz}=900$ for a fully effective trip but stated that also in this case a minimum distance remains between the position of the transition point and the position of the wire such that the difference between the corresponding Reynolds numbers is:

$$R_{kz} - R_{kz}^* = 2 \cdot 10^4.$$

Three-dimensional trips with accompanying horseshoe vortices produce regions of turbulent flow behind them that spread laterally downstream; transition across the whole span is achieved when the regions of turbulence formed downstream of the excrescences unite. This delay in the formation of a uniformly turbulent layer precludes the use of the technique if it is required to fix transition very close to the leading edge. In some cases the method has advantages in that the effect of the excrescences is believed to be quite independent of the direction of the flow in the boundary layer (3-D flows).

Several methods are available for constructing the excrescences: one is to insert short lengths of wire protruding from the surface of the model, a variant is the use of

small discs or spherical particles glued or soldered on the surface of the model. Care must be taken in achieving the desired type of trip since a spanwise row of obstacles with too narrow gaps and/or a too small height/diameter ratio will behave more as a two-dimensional than as a three-dimensional trip.

The experimental data collected by Braslow (Ref.8) for three-dimensional roughnesses show that for an effective trip the critical value of the roughness Reynolds number, based on the velocity at the height of the roughness and the height of the roughness, $R_{k,cr} = u_{\infty} k / \nu$, is a function of the ratio between the diameter, d , and the height, k , of the roughness. For $d/k=1$ the roughness Reynolds number is in the range 500 to 900 and is practically independent of Mach number at low speed.

A distributed roughness trip can be obtained coating a narrow band of the model surface with a minimum thickness of an adhesive (epoxy resin or lacquer) and dusting it with carborundum, sand or ballotini of known average grain size. Ballotini and carborundum grains are the most used roughness materials as ballotini can be graded down to quite small diameters with a small variation in particle size and carborundum is readily available and shows superior effectiveness in provoking transition due to the resulting sharp and irregular surface of the strip.

Again care must be taken in achieving the desired type of trip since a strip of distributed roughness will act as a rough-surface two-dimensional trip if particle distribution is too dense and as a lot of random three-dimensional obstacles if particles are sparse. Since the concept of "sparse" distribution is quite vague the need is felt to compare the quality of the obtained strip with some standard test specimens of proved effectiveness in order to warrant a good repeatability of the strips in different tests or in the case of replacement of a damaged strip.

Provided that the roughness be sparsely distributed, transition moves very close to the roughness when the critical roughness Reynolds number, $R_{k,cr}$, is attained. Experimental investigations have determined that this critical value is, as an average, equal to 600 (Ref.2). This value is constant, except at the low values of the length Reynolds number, R_L , at subsonic speeds. At low values of R_L , less than 10^5 , resulting from either a decrease in tunnel unit Reynolds number or a decrease in the distance of the roughness band from the leading edge, the value of $R_{k,cr}$ increases up to 1300. The value of $R_{k,cr}$ remains constant up to approximately $M=2$, thereafter it begins to increase.

As can be seen from the previously reported experimental results given in literature only an order of magnitude correlation is possible since minimum size of the trip is difficult to predict with sufficient accuracy and is a function of Reynolds and Mach numbers. Thus, if the minimum trip is to be used, preliminary experiments are required to determine its size and, furthermore, the size should be changed as the conditions of the experiment are modified.

Using trips one grit more than the minimum (overfixing) is believed to be a good practice to be sure on trip effectiveness in producing premature transition. Overfixing produces only small drag increases, on the contrary a trip slightly smaller than needed (underfixing) could provoke a rearward displacement of the transition point giving rise to strong variations in drag.

To overcome the difficulty of selecting the minimum useful size of the disturbance, which is a function of the particular experiment, a technique is sometimes used in which the size of the disturbance can be varied simply during the experiment from outside the tunnel. A row of holes is drilled across the span, and the disturbance is created by allowing a small quantity of air to flow from these into the boundary layer. This is probably the most elegant way of producing transition since the size of disturbance can be varied by controlling the air flow. It is, however, of limited application to general models on account of the pipework involved.

Due to low cost and effectiveness a carborundum band obtained by dusting a double-stick scotch tape has been chosen as a tripping device in the present work. A sparse distribution (about 40%) has been preferred since for most of the values of the Reynolds number attained in the tests transition could not be tripped by a two-dimensional roughness.

Experimental results obtained by Michel and Arnal with a "dense" carborundum trip are reported in Ref.9. No transition tripping was obtained for Reynolds numbers based on momentum thickness less than 200.

TRANSITION DETECTION

In order to control the effectiveness of a transition fixing device in the whole envelope of test conditions (angle of attack, Mach number etc.) reliable methods are required to check that a true turbulent boundary layer has been generated at the desired location.

It is possible to detect transition by measuring thermofluid-dynamic quantities inside the boundary layer; the inception of turbulence is inferred from theoretically

well-known features such as the shape of the velocity profile, the thickening of the boundary layer, the increase of the turbulence level and of the acoustic noise.

Velocity profiles at different chordwise stations can be measured with a single Pitot tube traversing the boundary layer normally to the model surface or, alternatively, with a rake of Pitot tubes. The procedure, relying on point measurements, is time consuming; furthermore the presence of the Pitot tube may alter the behaviour of the boundary layer.

A simpler procedure consists in measuring the total head in the proximity of the surface with a Preston tube. Transition is detected by a chordwise exploration of the boundary layer: the transition point is characterized by a sudden increase of the total head. Alternatively a total head exploration can be made at a distance from the wall slightly smaller than the expected turbulent boundary layer thickness; in this case a sudden decrease of the total head will indicate transition.

The onset of a high level of turbulence, typical of transition, can be directly measured with a fast response anemometer such as a hot-wire or a Laser-Doppler anemometer. Both anemometers give point measurements and are therefore most suited for the exploration of two-dimensional models; both require sophisticated electronic circuitries and data reduction procedures.

An alternative approach is the detection of increased acoustic noise in the zone of transition using surface stethoscopes or piezoelectric gauges.

Transition can also be detected by surface flow visualization methods based on the increase of mass, momentum and energy diffusions taking place at the model surface once transition to turbulent boundary layer has been achieved. The most used technique is surface flow visualization with oil flow or with sublimating or evaporating substances. Not broadly used in industrial practice, but nevertheless promising in a laboratory environment, are measurements of temperature recovery factor with thermocouples, hot films, liquid crystals and thermography.

The use of non volatile liquid films is based on the principle that the film moves in the direction of the surface shear stress on the model. It is of most value in showing the presence of any separation region or in indicating the surface streamlines. Also transition can be seen as the surface shear in a turbulent region may be sufficient to remove the liquid there, whilst it remains in a laminar region. Alternatively, during the time before the liquid is swept away from a turbulent region, it is sometimes possible to see a difference in the wave pattern on the surface of the liquid there, compared with a laminar region: the wavelength in the laminar region being larger than that in the turbulent region.

The viscosity of the liquid must be chosen according to tunnel speed and test duration. For low speeds wind tunnels the most suitable liquids, in ascending order of viscosity, are: kerosene, light Diesel oil, light transformer oil. In order to obtain a better contrast a pigment is added: white pigments, as titanium dioxide or china clay, on black models; a black powder (lampblack) on light models; fluorescent pigments, to be observed with ultraviolet light, irrespective of model colour. An additive, as oleic acid with titanium dioxide, is usually used to control the size of paint flocs.

If the surface of the model is alternatively coated with a thin film of a volatile liquid or a sublimable solid the turbulent region, due to its higher rate of mass diffusion, causes a higher rate of evaporation or sublimation. The disappearance of the liquid or solid film can be rendered visible with some appropriate artifice.

The volatile liquid film technique is frequently used when a quick indication of transition is required in the course of a wind tunnel test. A volatile oil is wiped on the surface, the film evaporates more quickly in the turbulent region. The indication is clearer on a matt black surface.

In the china-clay method, the model is permanently coated with white china-clay which is sprayed with a liquid having the same index of refraction of the solid particles; the coating appears transparent when moist and the white surface reappears after evaporation.

Alternatively a solution of a sublimating solid in a highly volatile liquid is sprayed onto the model. Indication of the state of the boundary layer is then shown by the different rates of sublimation of the solid deposit in different flow regimes. This technique is particularly indicated in tests at high speed.

A more comprehensive review of transition tripping and detection can be found in the Report of the AGARD Working Group 09 (Ref.10).

EXPERIMENTAL RESULTS

Tests have been performed on a flat plate 50 cm long having a 30 degrees wedge at the leading edge and a black matt surface for visualization purposes. The plate was at the exit section of a small open circuit, open test-section wind tunnel (Fig.4). Wind

tunnel speed can be varied from 0 to 20 m/s by acting on the variable rpm dc electrical motor powering the fan.

The average critical Reynolds number measured on the plate between 10 and 18 m/s is:

$$R_{cr} = 3.3 \times 10^5$$

The roughness element was a 2.5 mm wide, 0.1 mm thick band of double-stick scotch tape dusted with carborundum (grit number 24). The total nominal height of the trip was therefore $0.84 \pm 0.1 = 0.94$ mm. A sparse distribution of carborundum grains (about 40%) was selected to avoid a two-dimensional like behaviour of the trip given the low length Reynolds numbers obtainable at low speed and in the proximity of the leading edge.

Tests have been performed at six different speeds from 11.59 to 17.39 m/s (Table 1); starting from few cm from the plate leading edge the tripping band was moved in a streamwise direction with steps of one cm and its effectiveness tested until a position was reached where transition was no more moved from its natural position. In all tests transition, when tripped, was at the roughness location.

Transition has been detected using five different methods:

1) Surface flow visualization.

Oil flow did not give completely satisfactory results since a clean turbulent region was never achieved; only a different wave pattern in laminar and turbulent zones could be observed (see Fig.5).

Better results have been obtained with the evaporation technique: kerosene evaporated completely in few minutes in the turbulent region leaving the laminar region wetted (Fig.6).

Since visualization, that is a powerful method for the understanding of complicated flow regions (3-D configurations, separation, vortices etc.), is much less interesting when a very simple and predictable pattern is expected, as is the case of flow on a flat plate, it was discarded in favour of the following methods which are able to give also quantitative results.

2) Velocity profiles in the boundary layer have been measured at various locations along the plate using a pitot tube made from an hypodermic tube bent at right angle; transition can be detected both by the profile assuming the shape typical for a turbulent boundary layer (1/7 power law) and by the increased thickness of the boundary layer (Fig.7).

3) A streamwise pitot traverse has been made at a height of 2.5 mm, higher than the maximum expected laminar boundary layer thickness; the decrease in total head indicating that the pitot tube is in a turbulent boundary layer.

4) A similar procedure has been followed with a hot wire probe; in this case a sudden decrease in the output voltage V (mean value) corresponding to a similar decrease in local velocity is an indication of transition.

5) At the same time the output of the hot wire anemometer has been read on a rms voltmeter the incipient transition being detected by a marked increase in the level of turbulence.

Since the last three methods gave similar results (Fig.8) only the pitot tube streamwise traverse was used extensively to detect transition being simpler and less exposed to accidental failures than the expensive and delicate hot wire probes.

Only when a deeper insight in the behaviour of the mechanism of transition was required velocity profiles were measured at every cm in the streamwise direction. From Fig.9 it can be seen that using a tripping height in excess of the minimum required to provoke premature transition gives rise to an overthickening of the boundary layer. The resulting increase in the momentum thickness (Fig.10) is a measure of the roughness additional drag.

As a result of the tests a correlation is presented in Fig.11 among the Reynolds number based on the momentum thickness, R_{θ} , the ratio k/δ^* , between roughness height and displacement thickness, and the roughness location X_r . The correlation allows the determination of the minimum size of the roughness effective in tripping premature transition. It must be remarked that a "sparse" distribution of carborundum grains is still effective for R_{θ} well below the value of 200 found as a lower limit for a "dense" strip by Michel and Alhal.

In Fig.12 the values of the minimum critical roughness Reynolds number $R_{k,cr}$ found in the present work are showed to be consistent with the results reported in the classical work of Braslow and coworkers (Ref.2).

REFERENCES

1. Klebanoff P.S., Schubauer G.B., Tidstrom K.D.: "Measurements of the Effect of Two-Dimensional and Three-Dimensional Roughness Elements on Boundary-Layer Transition", J.A.S., November 1955, p.803-804
2. Braslow A.L., Hicks R.M., Harris R.V.jr: "Use of Grit-Type Boundary-Layer Transition Trips on Wind-Tunnel Models", NASA TN D-3579, September 1966.
3. Bloch D.R., Mueller T.J.: "Effects of Distributed Grit Roughness on Separation and Transition on an Airfoil at Low Reynolds Numbers", AIAA 4th Applied Aerodynamics Conference, San Diego, California, June 9-11, 1986- AIAA CP865, p.152-161
4. Sedney R.: "A Survey of the Effects of Small Protuberances on Boundary-Layer Flows", AIAA J., vol.11, n.6, June 1973, p.782-792.
5. Dryden H.L.: "Review of Published Data on the Effect of Roughness on Transition from Laminar to Turbulent Flow", J.A.S., 20, p.477-482, 1953.
6. Winter K.G., Scott-Wilson J.B., Davies P.V.: "Methods of Determination and of Fixing Boundary Layer Transition on Wind Tunnel Models at Supersonic Speeds", AGARD Memorandum AG 17/P7, Sixth Meeting of the Wind Tunnel and Model Testing Panel, Paris, France, 2-6 November 1954, p.167-191.
7. Kramer K.: "Über die Wirkung von Stolperdrahten auf den Grenzschichtumschlag", ZFW 9, p.20-27, 1961.
8. Braslow A.L.: "Review of the Effect of Distributed Surface Roughness on Boundary-Layer Transition", AGARD R-254, April 1960.
9. Michel R., Arnal D.: "Investigation of the Conditions for Tripping Transition with Roughness Elements and their Influence on Boundary Layer Development", Grenzschichtsteuerung durch Transitionsfixierung, DFVLR-Mitt.84-17, p.103-113
10. Russo G.P.: "Techniques for Boundary Layer Tripping and Control", Report of the AGARD FDP WG/09 on "Wind Tunnel Boundary Layer Simulation and Control"- To be published.

ACKNOWLEDGEMENTS

This work has been sponsored by the Italian Ministry of Education (M.P.I.60%) and by the National Research Council (C.N.R.)

TABLE I

U_e	X_k	k/δ^*k	$R_{\theta k}$	U_e	X_k	k/δ^*k	$R_{\theta k}$
(m/s)	(mm)			(m/s)	(mm)		
				16.39	40	2.77	134
11.59	30	2.69	98		50	2.48	150
	40	2.33	109		60	2.29	165
	50	2.09	127		70	2.10	180
					80	1.97	191
12.96	30	2.85	104		90	1.87	203
	40	2.47	117		100	1.77	217
	50	2.21	135		110	1.67	227
	60	2.01	147		120	1.60	237
	70	1.87	157		130	1.54	243
					140	1.48	251
14.20	40	2.58	123		150	1.43	258
	50	2.33	140		160	1.39	268
	60	2.13	157		170	1.35	279
	70	1.95	170		180	1.31	289
	80	1.83	179				
	90	1.72	188	17.39	40	2.86	139
	100	1.63	197		50	2.56	153
15.34	40	2.68	126		60	2.33	170
	50	2.40	145		70	2.16	186
	60	2.22	161		80	2.03	197
	70	2.04	175		90	1.91	209
	80	1.92	185		100	1.81	222
	90	1.78	194		110	1.72	232
	100	1.71	205		120	1.65	243
	110	1.62	217		130	1.59	251
	120	1.54	224		140	1.53	263
	130	1.49	234		150	1.48	274
	140	1.43	241		160	1.43	279
					170	1.39	285
					180	1.34	296
					190	1.31	304

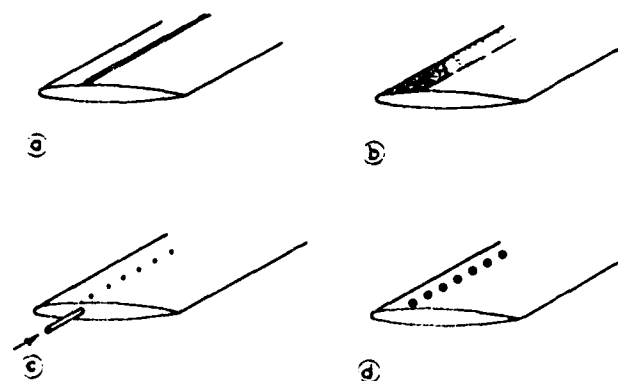
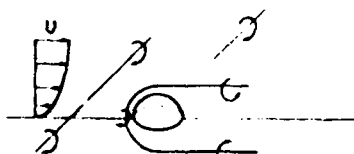


Fig.1-Some types of transition tripping devices:
 a) wire b) distributed roughness
 c) air injection d) isolated excrescences



(a) 2-D protuberance



(b) 3-D protuberance

Fig.2-Sketch showing the behaviour of vortex lines
 for 2-D and 3-D trips (Ref.4).

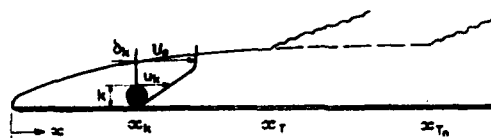


Fig.3-Sketch showing the mechanism of boundary layer transition tripping.

x_T =abscissa of tripped transition

x_{T_0} =abscissa of natural transition

x_k =trip location

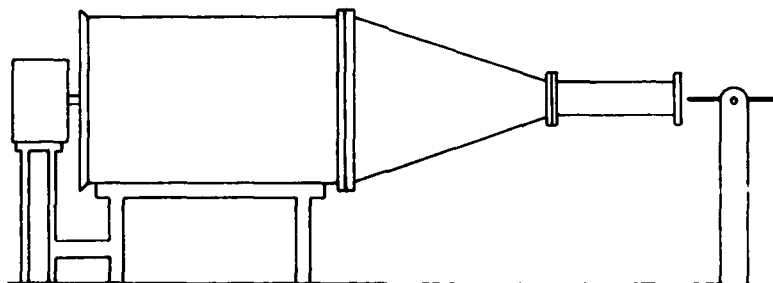


Fig.4-The flat plate positioned at the exit of the open test section, open circuit wind tunnel.

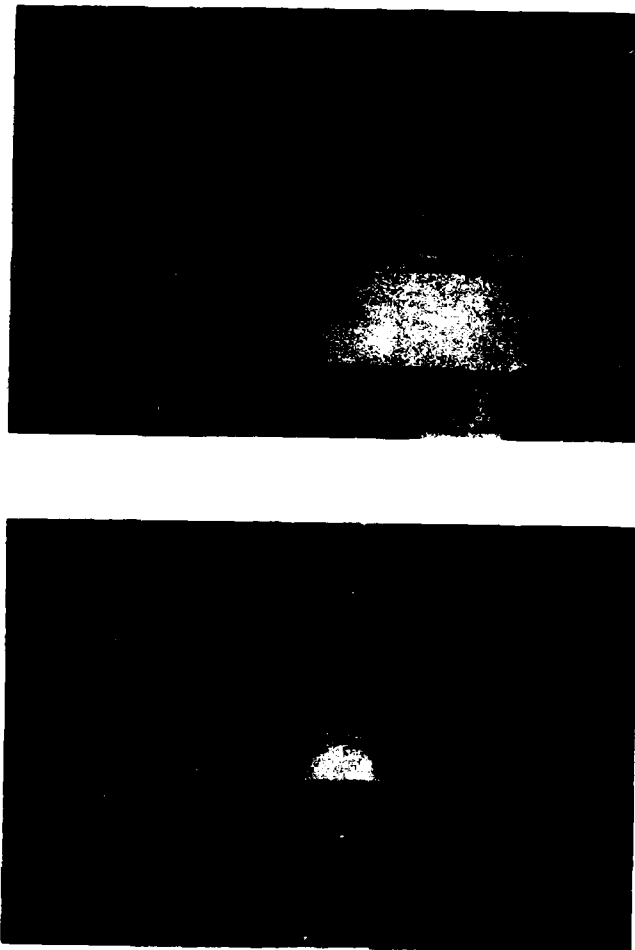


Fig.5-Detection of natural transition with the oil-flow method
(diesel oil+linseed oil+titanium dioxide).
 $U_e=17.39\text{m/s}$; $X_{To}=30\text{cm}$; $R_{Cr}=3.3 \times 10^5$



Fig.6-Detection of natural transition with an evaporating liquid (kerosene).
(same conditions as in Fig.5).

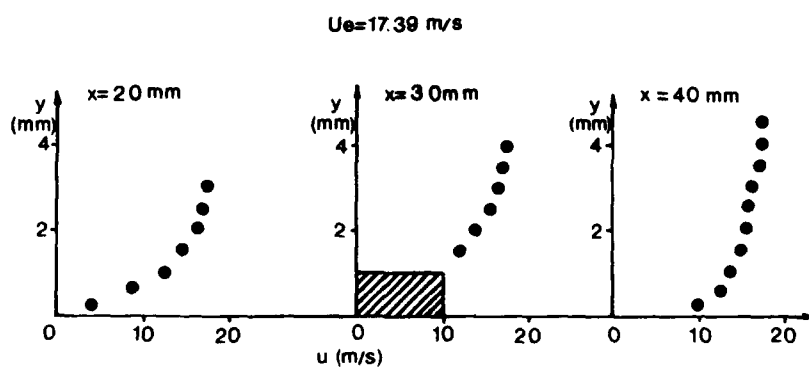


Fig.7-Velocity profiles measured upstream, on and downstream of the trip.

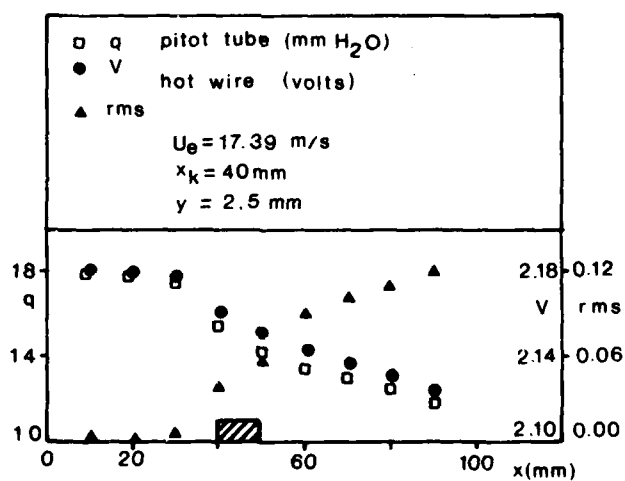


Fig.8-Transition detected by a pitot tube and a hot wire probe streamwise traverse at constant height.

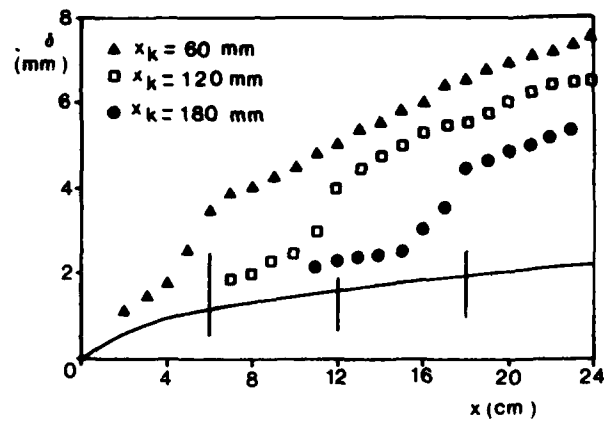


Fig.9-Boundary layer thickness profiles for three different transition locations. Vertical lines indicate trip position.
— laminar calculation

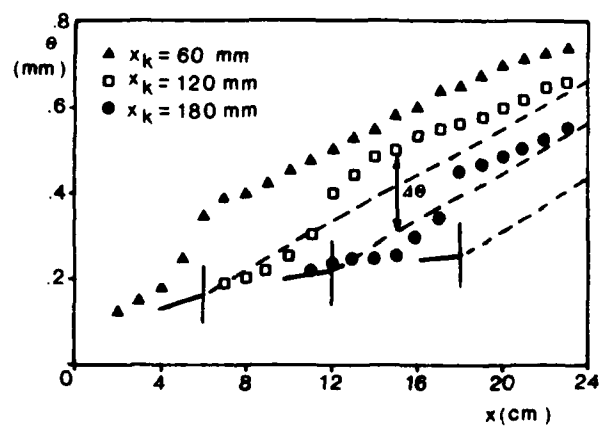


Fig.10-Momentum thickness profiles for the same cases as in Fig.9
— laminar calculation
--- turbulent calculation

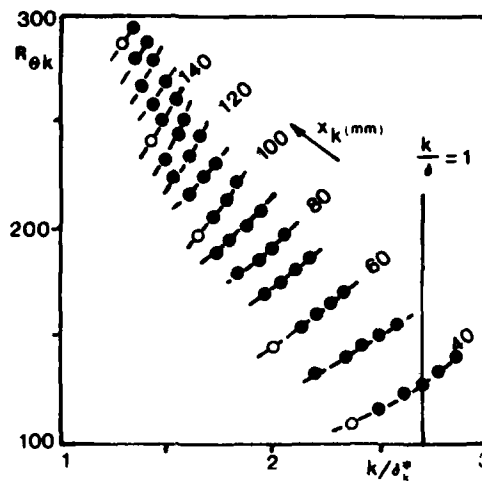


Fig.11-Reynolds number referred to the momentum thickness as a function of the ratio between trip height and displacement thickness. Full symbols refer to tripped transition.

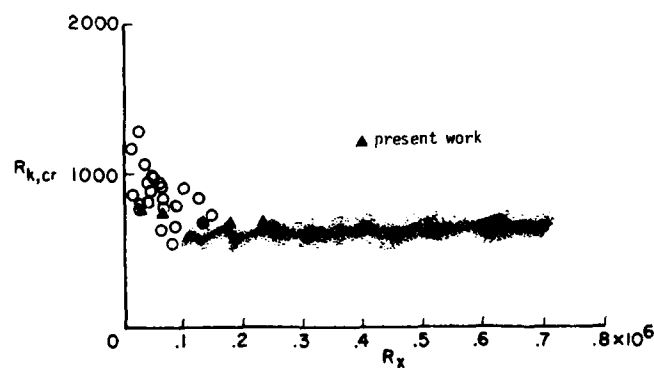


Fig.12-Effects of the length Reynolds number or the critical roughness Reynolds number.

DES DIFFICULTES DE PREDIRE EN SOUFFLERIE LE TREMBLEMENT D'UN AVION CIVIL MODERNE REMEDES PROPOSES

par

R.Destuynder — ONERA Châtillon
V.Schmitt — ONERA Châtillon
J.Berger — Aerospatiale Toulouse
R.Barreau — Aerospatiale Toulouse
Route de Bayonne, B.P. 3153
F31060 Toulouse Cedex 03, France

RESUME

La prévision de l'apparition du tremblement sur un avion de transport constitue un problème qui est, en dépit de progrès réalisés récemment dans la compréhension du phénomène, encore assez mal maîtrisé. Inaccessible actuellement, à une approche purement théorique, cette prévision est essentiellement basée sur des essais en soufflerie.

Après une revue des méthodes expérimentales couramment utilisées pour la détermination du tremblement sur maquette et une description succincte des techniques de transposition au vol, on met en évidence les problèmes de simulation qui affectent ces méthodes. La suite de la communication est consacrée à la discussion d'un certain nombre d'améliorations des maquettes et de la méthodologie expérimentale dont la mise en oeuvre doit aboutir à des prévisions plus fiables du tremblement sur les avions de transport.

SUMMARY

The prediction of transport aircraft buffet response still remains a challenge despite recent progress in understanding of the phenomenon. This prediction is up to now inaccessible to a purely theoretical approach and so is mainly based on wind tunnel investigations.

After a review of experimental methods currently used to determine model buffeting and a short description of full scale application techniques, the simulation problems that appear are presented. The next point deals with a number of improvements concerning models and experimental methodology with the final objective to provide more reliable buffeting predictions on large transport aircrafts.

NOTATIONS

$(A + Bi)$	Matrice complexe de forces aérodynamiques instationnaires
E	Module d'élasticité
$F(\omega)$	Force généralisée
I	Inertie
K	Facteur de similitude
L	Longueur de référence
M	Nombre de Mach
M	Massa
M^t	Moment
S	Surface de référence
Z	Altitude de vol
C_z	Coefficient de portance
f	Fréquence
g	Accélération de la pesanteur
q	$= 0.5 \rho v^2$ pression dynamique ; coordonnée généralisée
t	Temps
v	Longueur de référence
Λ	Facteur d'échelle
Ω	Pulsation complexe
α	Incidence ; amortissement
ϵ	Vrillage de l'aile induit sous charge
\ddot{x}	Accélération
μ	Massa généralisée
σ	Contrainte de cisaillement
ω	Pulsation

INDICES

a	Avion
c	Croisière
e	Extrémité de l'aile
m	Maquette
0	Terme sans vent

1. INTRODUCTION

L'importance d'une connaissance précise de l'entrée en tremblement d'un avion civil n'est plus à souligner. Un très grand nombre d'auteurs se sont attaqués au problème avec comme objectif d'étendre les résultats obtenus en soufflerie au domaine de vol de l'avion (1, 2, 3).

Cette connaissance du tremblement permet en effet de caractériser le domaine de vol de l'avion admissible à partir de la fonction $C_x = f(\text{Mach})$.

Jusqu'à présent les calculs aérodynamiques s'avèrent impuissants à déterminer avec précision les zones de décollement sur une voilure en transsonique ainsi que leur développement avec l'incidence. Les forces de décollement et leur répartition en envergure, forces qui donnent naissance aux vibrations de l'avion sur ses modes propres, sont encore plus difficiles à appréhender.

Le seul recours pour faire une prévision s'avère être des essais en soufflerie afin de fournir des valeurs applicables à un avion. Beaucoup de méthodes existent qui donnent lieu à des critères différents en vol et en soufflerie. Ces méthodes ne font que rarement appel à une connaissance précise des forces de décollement (4, 5, 6) qui représentent le seul critère utilisable pour calculer sur un avion la réponse de la structure en tous points dans la mesure où une base modale, représentative de l'avion, existe.

Dans une première partie on s'efforcera de montrer les difficultés et les inconvénients inhérents aux méthodes actuelles qui sont davantage dus à des problèmes de simulation en soufflerie qu'à des problèmes de mesure.

Dans une deuxième partie on présentera des méthodes nouvelles permettant de se rapprocher des valeurs de tremblement sur avion au moyen de maquettes plus représentatives et en tenant compte des difficultés dues aux souffleries (nombre de Reynolds, bruit de fond, conditions limites d'encastrement).

2. METHODES USUELLES DE DETECTION
DU TREMBLEMENT SUR MAQUETTE

Le tremblement est la réponse d'une structure à une excitation aérodynamique due à des zones de décollement en présence ou non de chocs.

Il est donc indispensable de considérer que le tremblement est un problème particulier pour chaque maquette et qu'il s'agit d'un phénomène non seulement aérodynamique mais aussi élastique.

De ce fait les méthodes de détection de tremblement sont multiples ; principalement on peut distinguer entre méthodes globales ou locales, stationnaires ou instationnaires.

Les décollements peuvent être mis en évidence par les méthodes globales suivantes :

- La visualisation de l'écoulement pariétal sur l'aile au moyen de fils fluorescents (fig. 1) ou de dépôts d'enduit visqueux (fig. 2a et 2b).
- Les courbes de portance globale $C_x = f(\alpha)$ mesurées par balance avec interprétation de la variation de la pente au début du décollement (fig. 3a) ou la mesure du moment de flexion (ou de torsion) à la cassure de l'aile en fonction de l'incidence (fig. 3b).

L'apparition des décollements peut aussi être détectée à partir de mesures locales ; dans ce domaine on peut citer :

- Les pressions statiques mesurées en particulier au bord de fuite de l'aile qui permettent de caractériser le décollement sur la voilure (fig. 4) à partir de la divergence des $K_{p_{eff}}$. Les figures 5a et 5b illustrent pour ce même cas la répercussion du décollement naissant sur la position de l'onde de choc.
- La mesure de pressions instationnaires dans le plan des fréquences, dans la zone décollée, soit sous forme de valeurs RMS (fig. 6) ou de densités spectrales de puissance DSP (fig. 7a et 7b).

Les décollements décelés par les méthodes qui viennent d'être décrites peuvent donner naissance à un phénomène de tremblement que l'on détecte essentiellement par les mesures suivantes :

- La mesure du moment de flexion instationnaire par une jauge de contrainte à la cassure de l'aile (fig. 8) qui se compare en stationnaire à la figure 3b.

- La mesure de la valeur RMS des signaux délivrés par des accéléromètres (fig. 9).

- Les mesures instationnaires peuvent, comme les accéléromètres par exemple, fournir le mode qui entre en vibration sous l'action des forces de décollement. L'amplitude de la réponse, fréquence par fréquence, fournit une indication supplémentaire sur l'intensité du phénomène comme le montre la figure 10.

A partir de toutes ces mesures stationnaires et instationnaires il faut définir et sélectionner un ou plusieurs critères caractérisant le début du tremblement et en déduire le C_z maximum en fonction du nombre de Mach ; parmi les plus souvent utilisés on peut citer :

- la prise en compte d'un accroissement $\Delta\alpha$ de 0,1 ou 0,2 degré au delà de la cassure de la courbe $C_z = f(\alpha)$ à Mach constant voir (figure 3a).

- La cassure de la courbe $\sigma_{rms} = f(\alpha)$ ou $\bar{\sigma}_{rms} = f(\alpha)$ d'un pont de jauge ou d'un accéléromètre en se fixant soit une contrainte maximum soit un niveau d'accélération à ne pas dépasser en un point donné.

Ce critère peut porter soit sur une bande de fréquence s'il s'agit d'une valeur RMS prise dans le domaine temporel soit sur un mode propre pris dans le plan des fréquences.

3. DIFFICULTES DE LA TRANSCRIPTION DES RESULTATS DU TREMBLEMENT OBTENUS EN SOUFFLERIE A UN AVION EN VOL

A partir d'un coefficient de portance d'apparition du tremblement $C_{z_{at}}$ ainsi déterminé en soufflerie la transposition au vol se fait habituellement par l'intermédiaire d'un avion de référence.

En vol un critère classique, au moins pour les avions civils de grand allongement, consiste à prendre une limite d'accélération de $\pm 0,2 g$, mesurée au siège pilote. Ce critère dépend essentiellement des modes propres de la structure ; le couplage entre les modes de la voilure et les modes propres du fuselage peut être différent d'un avion à l'autre et le siège pilote peut dans certains cas répondre très faiblement au tremblement.

Le tableau suivant illustre la nature du couplage entre la voilure et le siège pilote, en précisant les déplacements modaux, pour quelques modes à basse fréquence de la structure d'un avion moderne.

DEPLACEMENTS MODAUX

Modes		Bout d'aile	Siège pilote
flexion aile	2,11 Hz	7,0	0,5
pendule moteur	2,28 Hz	6,5	0,2
tangage moteur	3,76 Hz	0,5	3,0
2 noeuds fuselage	4,8 Hz	5,0	1,0
coplanaire aile	5,55 Hz	4,0	0,0

De ce tableau on peut conclure à l'incohérence entre les critères choisis en soufflerie (critères qui généralement ne tiennent compte que de l'aérodynamique) et en vol (critère tenant compte à la fois de l'aérodynamique et des caractéristiques modales de la structure). En effet, la figure 11 montre que même si l'essai en soufflerie permettait de prévoir correctement les résultats en vol correspondant au même critère $\Delta\alpha = 0,1^\circ$, l'écart par rapport au C_z démontré en vol reste considérable.

Par ailleurs la simulation du tremblement en soufflerie est affectée actuellement par les options et les limitations suivantes :

- Les maquettes utilisées sont du type semi-rigide et ne sont pas spécialement étudiées pour réaliser des conditions de tremblement. Il en résulte entre autre que les déformations statiques de ces maquettes (déformations en vrillage qui caractérisent et la position des chocs et les limites de décollement derrière ces chocs) ne sont pas représentatives des déformées de l'avion en transsonique.

La figure 12 représente l'évolution du vrillage ϵ_a en extrémité d'aile en fonction du coefficient de portance sur une maquette en acier d'une part et pour l'avion d'autre part. Des écarts importants sont mis en évidence pour les C_z élevés. La conséquence d'une telle variation de la déformation élastique sur la répartition des charges en envergure est considérable comme le montrent des calculs transsoniques stationnaires (fig. 13).

- La connaissance de l'apparition du tremblement est insuffisante pour apprécier les efforts instationnaires et leur répartition en envergure sur l'aile (distribution de force nécessaire pour calculer la réponse d'un avion dont on connaît les modes propres).

- Les effets de la turbulence de la soufflerie perturbent les réponses dynamiques des différents capteurs que ce soient des accéléromètres par exemple figure 14, des capteurs de pressions, ou tout autre et doivent être pris en compte dans l'appréciation des forces de tremblement.

- Le nombre de Reynolds est le plus souvent insuffisant pour caractériser correctement le décollement.

4. METHODES EN DEVELOPPEMENT POUR AMELIORER LA PREVISION DU TRAVAILLEMENT SUR AVION DE TRANSPORT CIVIL MODERNE A PARTIR D'ESSAIS EN SOUFFLERIE

4.1 - Conception d'une maquette de similitude statique -

Devant les difficultés qui s'opposent toujours à la fabrication de maquettes d'avions de transport respectant à la fois la similitude statique et dynamique et supportant les charges aux nombres de Reynolds les plus élevés une solution différente a été envisagée. En effet, dans une première étape on a essayé de calculer une maquette de soufflerie qui, par exemple pour un nombre de Mach donné (le point de croisière du domaine de vol) aurait, compte tenu du facteur d'échelle Λ , la même déformation que l'avion en tout point et donc le même dévissage sous charge (l'hypothèse étant que la déformation le long des cordes reste une droite ce qui est correct pour une aile caisson du type des avions de transport modernes de grand allongement).

Ce qui se traduit par :

$$(1) \quad \frac{\delta_m}{\delta_a} = \Lambda = \frac{(\rho_{m,g} + q_m S_m C_{z_m}) L_m^3 E_a I_a K_a}{(\rho_{a,g} + q_a S_a C_{z_a}) L_a^3 E_m I_m K_m}$$

$E_m / E_a = 1$ si le caisson maquette est homothétique de celui de l'avion avec le même axe élastique.

Sur une demi-maquette $\rho_{m,g}$ reste petit devant $q_m S_m C_{z_m}$, en effet q_m diminue comme le cube de l'échelle alors que S_m ne diminue que comme le carré de l'échelle (les grandeurs q_m et C_{z_m} étant données).

On déduit de (1) :

$$\Lambda = \frac{q_m}{q_a} \frac{E_a I_a}{E_m I_m} \Lambda^5$$

C'est à dire en utilisant les mêmes modules d'élasticité $E_m = E_a$ pour la maquette et pour l'avion :

$$(2) \quad \frac{I_a}{I_m} = \frac{q_a}{q_m \Lambda^4}$$

q_a et q_m caractérisent respectivement la pression dynamique pour l'avion et pour le point de soufflerie correspondant.

On peut noter que si la soufflerie est à pression génératrice variable le rapport (q_a / q_m) peut être maintenu constant et la similitude de déformation peut être respectée dans une large plage du domaine de vol à altitude constante. Dans tous les cas la similitude de déformation est valable pour toutes les valeurs de Λ pour un nombre de Mach et (q_m / q_a) fixé.

L'exemple suivant calculé pour la soufflerie S1 de l'ONERA (8m de diamètre, pression génératrice constante de 0.9 bar) montre la souplesse du procédé.

Λ étant fixé on a choisi trois points du domaine de vol avec $q_m / q_a = 2.77$:

Maquette Avion			
M	q_m (Pa)	q_a (Pa)	Z_a (Pieds)
0.7	22225.	9034.	35361.
0.78	25644.	9242.	37000.
0.84	28005.	10110.	38157.

Si on n'avait pas adapté l'altitude de vol entre Mach 0,70 et Mach 0,84 l'erreur sur (q_m / q_a) aurait été de l'ordre de 15 % (en effectuant un vol à C_{z_m} constant).

On peut aussi constater que le rapport (δ_m / δ_a) = Λ entraîne

$$\frac{\sigma_m}{\sigma_a} = \frac{M_m^t (I_a / v_a)}{(I_m / v_m) M_a^t} = \frac{q_m}{q_a} \frac{E_a I_a}{E_m I_m} \Lambda^4$$

ce qui donne à partir de (1) et (2) : (3) (σ_m / σ_a) = 1

Avec σ contrainte statique sous un moment M^t . v_a et v_m étant des longueurs de référence.

On constate l'égalité des contraintes dues aux charges statiques sur l'avion et sur maquette.

Une telle maquette qui respectera les déformations statiques de l'avion, en ayant en particulier le même dévissage en fonction de l'envergure n'aura pas les mêmes modes propres que l'avion ; étant plus légère que l'avion elle aura des fréquences propres beaucoup plus élevées, ce qui est un avantage puisque dans le domaine des fréquences réduites de l'avion il n'y aura que la réponse aux forces dues aux décollements et à la turbulence de la soufflerie.

Enfin, pour que le respect des déformations statiques soit complet il est nécessaire de respecter la position de l'axe élastique du caisson voilure et d'avoir en outre des conditions limites à l'encastrement qui soient représentatives de l'encastrement de l'aile avion sur le fuselage. L'étude d'un avant projet d'une telle maquette a montré sa faisabilité.

Bien entendu, durant les essais en soufflerie il sera nécessaire d'effectuer, par exemple à l'aide de cibles laser, la mesure de la déformation de la maquette au moins le long du bord d'attaque et du bord de fuite pour une aile caisson du type grand allongement, ceci afin de vérifier que les distributions de charges statiques donnent bien naissance à la déformation calculée.

Ce même type de maquette permet par ailleurs, d'améliorer avant tremblement, les comparaisons théorie-essais en ce qui concerne les coefficients globaux ou locaux, mesurés par balance ou par système scanivalve.

Par ailleurs elle pourrait aussi servir pour des études de contrôle de tremblement qui ont déjà été abordées à l'ONERA (7).

4.2 - Calcul des forces instationnaires dues aux décollements -

Suivant des techniques d'ores et déjà mises en oeuvre (8, 9, 10) on tentera ensuite de déterminer les forces instationnaires dues aux décollements par la mesure du champ de pressions instationnaires.

Les maquettes complètes ou les demi-maquettes montées à la paroi, réalisées à grande échelle pour être utilisées dans la soufflerie S1 de l'ONERA, peuvent être équipées d'un grand nombre de prises de pression mesurant simultanément les pressions stationnaires et instationnaires (par exemple fig. 15, 400 capteurs répartis sur 15 cordes en envergure).

Des sondeurs moyennateurs, travaillant dans le domaine temporel et portant sur chaque corde, permettent de déterminer à l'aide d'une pondération prédéterminée, la distribution de portance et de moment en valeurs efficaces. La transformée de Fourier complexe de ces quantités prenant une des cordes comme référence de phase, donne fréquence par fréquence le point d'application, le module et la phase relative des torques aérodynamiques instationnaires.

A titre d'exemple la figure 16 montre pour trois sections et un nombre de Mach donné l'évolution des forces de décollement par tranches dans le plan des fréquences en fonction de l'incidence de l'aile.

On en déduit (fig. 17) des forces généralisées de l'aile complète (ici pour le mode de flexion).

Dans le cas d'une aile semi-rigide le vecteur réponse des forces aérodynamiques instationnaires comprend en soufflerie trois composantes. La première provient de l'excitation de la maquette par la turbulence naturelle de la soufflerie (ce vecteur parasite est très atténué en général en vol), la seconde composante est visible sur les fréquences propres de la maquette et correspond à la réponse en pression induite par les mouvements de la maquette dus au tremblement, la troisième composante enfin, qui constitue le second membre des équations de l'aéroélasticité, existe sans mouvement de l'aile et correspond aux forces de décollement.

Par l'évolution des forces généralisées d'une incidence à l'autre la figure 17 illustre ces trois quantités. Le premier terme peut être considéré comme constant et indépendant de l'incidence tandis que le deuxième et le troisième terme existent théoriquement dès qu'il y a décollement.

Il est alors nécessaire de rechercher une fonction de lissage permettant de caractériser les seules forces de décollement que représente en général une fonction monotone (fig. 18).

Sur cette figure on peut noter que la fonction de lissage s'établit très vite et reste ensuite identique à elle-même. Dans l'exemple choisi une moyenne temporelle de six secondes a suffi pour définir, dans un large domaine de fréquences, la force de décollement.

Ce paramètre de la durée des moyennes est important dans la mesure où une comparaison avec les résultats d'essais en vol est effectuée. En effet, le pilote ne peut faire des pénétrations en tremblement à Mach, C_x et altitude constants que dans les manœuvres en virage donc avec facteur de charge. Il est difficile dans ces conditions de pouvoir faire des mesures stabilisées sur un temps long.

Tandis que la figure 19a compare les courbes de lissage entre elles (fonctions du 3^{ème} ordre), la figure 19b précise l'erreur quadratique moyenne montrant que très vite l'erreur sur la détermination de la force est inférieure à 10 %. Ces derniers résultats ont été obtenus sur une maquette d'avion de combat. A titre d'exemple la figure 20 montre la distribution de la force généralisée d'un mode de flexion en envergure. L'aile était divisée en six tranches correspondant à six cordes de mesure des pressions instationnaires. On peut remarquer que la zone de décollement est concentrée à 70 % de l'envergure. Cependant, il faut noter que le comportement d'un avion civil de transport au tremblement, dans le cas de décollement derrière un choc en transsonique, est très différent d'un avion de combat. Toutefois, sur cette maquette d'avion de combat dont on connaissait la base des modes propres et le résultat des mesures d'accélération en différents points de la structure, servant de cas test, on a calculé à partir de la distribution des forces complexes de décollement la réponse de la structure en un point sur deux modes ; la mesure d'accélération a été faite en bout d'aile.

Le tableau suivant résume les résultats obtenus à $M = 0.8$ et $\alpha = 10^\circ, 5$:

	Configuration 1		Configuration 2	
	exp	cal	exp	cal
Mode 1	5.1	4.9	2.6	2.45
Mode 2	8.0	11.3	12.3	12.8

Les configurations 1 et 2 correspondent à des conditions limites à l'emplanture différentes et donc à des fréquences et modes différents.

4.3 - Influence du nombre de Reynolds, en particulier sur les décollements -

Plusieurs études entreprises dans différents pays ont tenté de montrer l'influence du nombre de Reynolds sur les conditions de décollement. On peut citer :

- Des études en souffleries cryogéniques qui présentent l'avantage de travailler à $q = 1/2 \rho v^2$ constant quel que soit le nombre de Reynolds mais avec l'inconvénient de n'utiliser jusqu'à ce jour que des maquettes de faibles dimensions ce qui limite considérablement leur équipement.
- Des études faites dans des souffleries à grande pression génératrice dans lesquelles malheureusement les paramètres de pression dynamique associés à la déformation statique et de nombre de Reynolds sont difficiles à dissocier (excepté en bidimensionnel avec des maquettes que l'on peut considérer comme rigide (1)).
- Des études sur des grandes maquettes de 3 à 4 mètres de demi-envergure utilisées en transsonique par exemple dans la soufflerie S1 de l'ONERA (7) qui seules permettront la mise en oeuvre des mesures discutées au chapitre précédent.

Au travers de toutes ces études, il s'avère en particulier, que l'aspect instationnaire n'est pas souvent pris en compte. Des recherches dans ce domaine, y compris lors des essais en vol, paraissent indispensables pour l'avenir (12). Du point de vue stationnaire, il semble possible de simuler certains paramètres de couches limites sur l'avion, par exemple au bord de fuite, par un positionnement de la transition déterminé à partir de calculs couplés que l'on effectue respectivement dans les conditions de vol et de soufflerie.

4.4 - Principe de la transposition soufflerie vol -

A partir des mesures effectuées sur la maquette aérodynamiquement semblable la transposition au vol pourrait être réalisée de la façon suivante :

- A) Calcul des modes propres de l'avion ou détermination par un essai de vibration au sol des premiers modes structuraux (y compris leurs amortissements).
- B) A partir de ces modes propres on peut calculer, dans les équations de l'aéroélasticité, les forces aérodynamiques généralisées s'exerçant sur la structure, c'est-à-dire les quantités $A + Bi$.

$$(4) \quad (-\mu\Omega^2 + 2\mu\alpha\Omega_j + \mu\Omega_0^2 + (\pi\rho V^2/2)(A+Bi))q = F(\omega)$$

Le calcul peut se faire par une méthode de doublets corrigée par tranches à partir d'essais en soufflerie tenant compte des déformations statiques de la maquette sous charge. Dans le début du tremblement une correction non linéaire établie à partir de la mesure de C_x en fonction de α , fournit $dC_x / d\alpha$ et $dC_m / d\alpha$. Ces valeurs diminuent avec l'incidence croissante ; il en est de même des valeurs des pressions induites par le mouvement de l'aile.

- C) La troisième partie consiste à introduire dans le second membre de l'équation (4) les forces de décollement $F(\omega)$ sous forme de forces généralisées en partant des modes de l'avion et des valeurs de soufflerie déterminées par tranches. Ce calcul permet pour toute fréquence d'un mode propre d'obtenir en tout point de la structure sa réponse dynamique. En particulier, elle permettra en outre d'améliorer le critère qui limitera l'incidence maximum en fonction du nombre de Mach.

5. CONCLUSION

Les essais de tremblement en soufflerie sur des maquettes d'avion de transport peuvent et doivent être modifiés si on veut améliorer les comparaisons entre les résultats d'essais en soufflerie et en vol.

Les problèmes posés par les essais en soufflerie dans le tremblement (nombre de Reynolds, déformation des maquettes non contrôlée, bruit de fond important donnant des décalages de π dans les forces instationnaires, non connaissance des forces de décollement en particulier de leur distribution complexe en envergure) peuvent se résoudre au moins partiellement dans l'avenir.

Ces améliorations passent par le choix d'une soufflerie de grande dimension, de maquettes représentatives des déformations statiques de l'avion et d'un équipement de mesures de pressions stationnaires et instationnaires simultanées au moins par corde.

Moyennant ces améliorations il semble que de meilleures prévisions concernant la détermination du tremblement en vol soient réalisables dans un avenir proche, mais au prix d'un effort de recherche important qui ne peut pas être limité au seul domaine de la soufflerie et qui implique également des mesures en vol appropriées à l'analyse détaillée du phénomène.

- REFERENCES -

- (1) D.G. MAREY
Prediction of the severity of buffeting.
AGARD LS 94, VKI, RHODE SAINT GEORGES, 1978.
- (2) H. FORSCHING
Aeroelastic buffeting prediction techniques, a general review.
DFVLR FB 81-15, 1981.
- (3) G.F. BUTLER, J.G. JONES
The prediction of buffeting response in flight from wind tunnel measurements on models of conventional construction.
THE AERONAUTICAL JOURNAL, Vol 88, N°677, 1984.
- (4) H. JONN
Critical review of the methods to predict the buffet capability of aircraft.
AGARD R N°623, 1974.
- (5) A.M. CUNNINGHAM, P.G. WANER, D.B. BENEPE, D.W. RIDDLE
Development and evaluation of a new method for predicting aircraft buffet response.
AIAA 75-69, 1975.
- (6) A.M. CUNNINGHAM, D.B. BENEPE, D.WATTS, P.G. WANER
A method for predicting full scale buffet response with rigid wind tunnel model fluctuating pressure DATA.
Vol 1 : Prediction method development and assessment.
NASA C.R. 3035, 1978.
- (7) R. DESTUYNDER
Active control of the buffeting response on a large modern civil airplane configuration in wind tunnel.
C.P. of the second international symposium on aerelasticity and structural dynamics, Aachen 1985.
- (8) D.W. RIDDLE
Wind tunnel investigation of surface pressure fluctuations associated with aircraft buffet.
AIAA 75-67, 1975.
- (9) F.W. ROOS
The buffeting pressure field of a high aspect ratio swept wing.
AIAA 85-1609, 1985.
- (10) B. BENOIT, I. LEGRAIN
Buffeting prediction for transport aircraft application based on unsteady pressure measurements.
AIAA 87-2356 CP, 1987.
- (11) J.B. McDEVITT, A.F. OKOMO
Static and dynamic pressure measurements, on the MACA 0012 airfoil in the AMES high Reynolds number facility.
NASA TP 2465, 1985.
- (12) C.F. COE, A.M. CUNNINGHAM
Predictions of F-111 TACT aircraft buffet response and correlations of fluctuating pressures measured on aluminum and steel models and the aircraft.
NASA C.R. 4069, 1987.

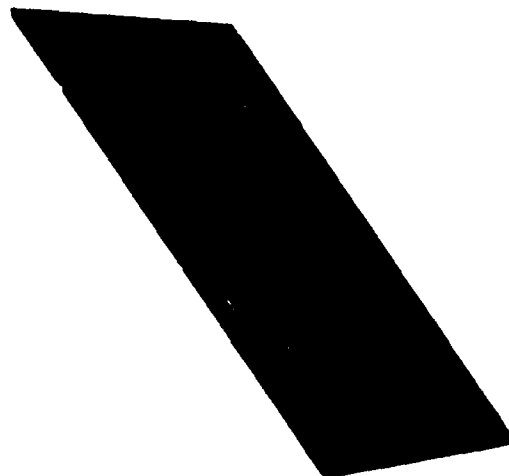


Fig. 1 — Visualisation de l'écoulement parétal par fils fluorescents avec décollement sur l'aile externe derrière un choc.



a) avant apperition de décollement



b) avec décollement de bord de fuite

Fig. 2 — Visualisation de l'écoulement parétal par enduit visqueux en transsonique.

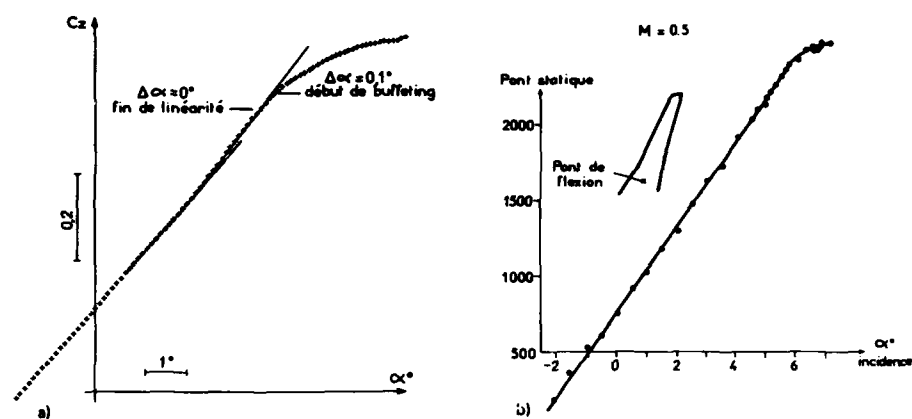


Fig. 3 - Effet des décroissements :
a) sur l'évolution du coefficient de portance, b) sur l'évolution du signal d'un pont de jauges statique.

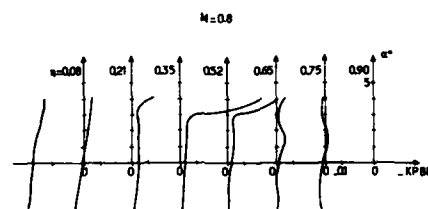


Fig. 4 - Détection des décroissements par la divergence du coefficient de pression au bord de fuite K_{pBF} .

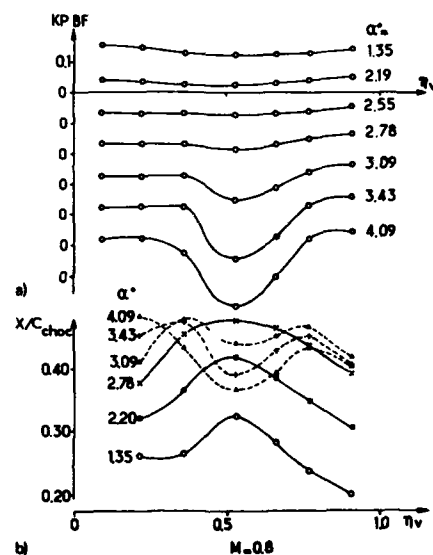


Fig. 5 - Influence d'un décroissement local
a) sur les K_{pBF} , b) sur la position du choc.

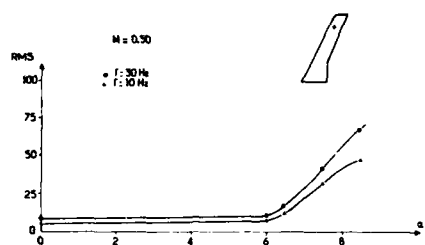


Fig. 6 - Divergence des valeurs RMS en bande étroite d'une pression instationnaire à l'apparition d'un décollement.

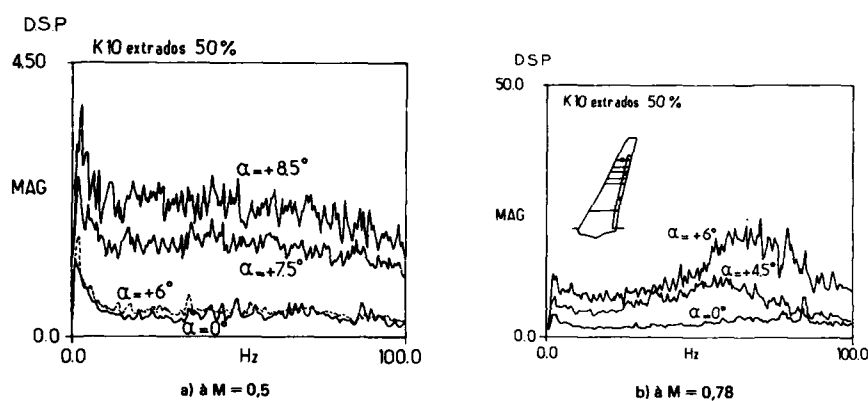


Fig. 7 - Densités spectrales de puissance d'une pression instationnaire pour plusieurs incidences.

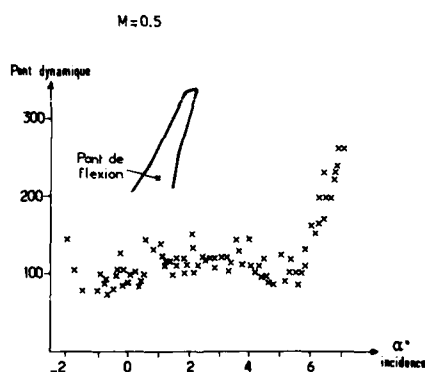


Fig. 8 - Détection du tremblement par les valeurs RMS d'un pont de jauge dynamique.

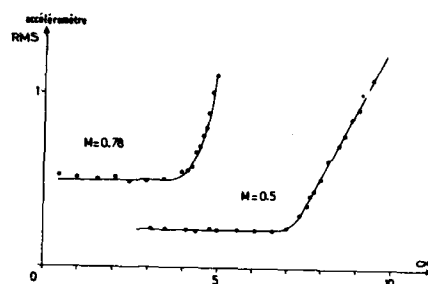


Fig. 9 — Réponses de structure par les valeurs RMS d'un accéléromètre en fonction de l'incidence.

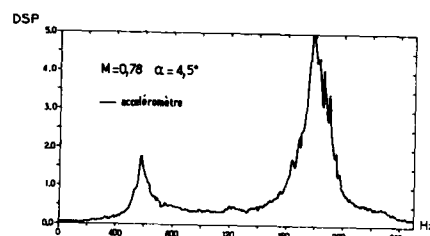


Fig. 10 — Densités spectrales de puissance d'un accéléromètre

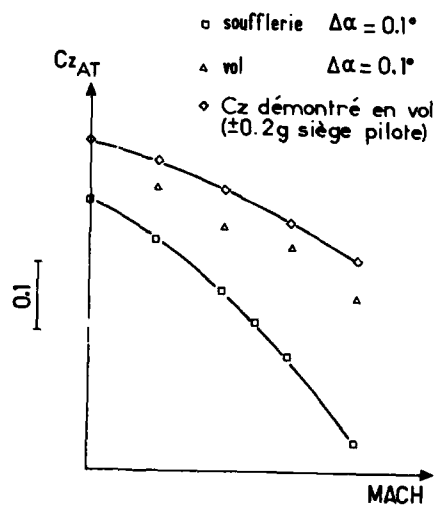


Fig. 11 — Coefficient de portance à l'apparition du tremblement en fonction du nombre de Mach en soufflerie et en vol.

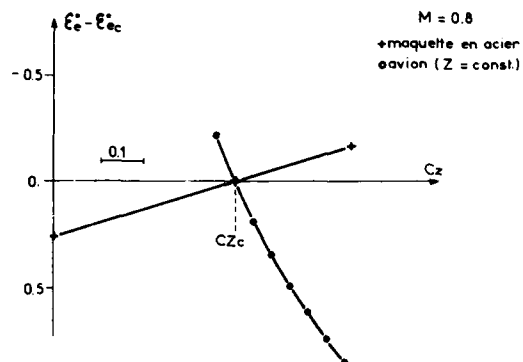


Fig. 12 — Variation du vrillage en extrémité d'aile en fonction de l'incidence sur maquette et sur avion.

Fig. 13 — Influence de la déformation aérodynamique sur la répartition des charges en envergure.

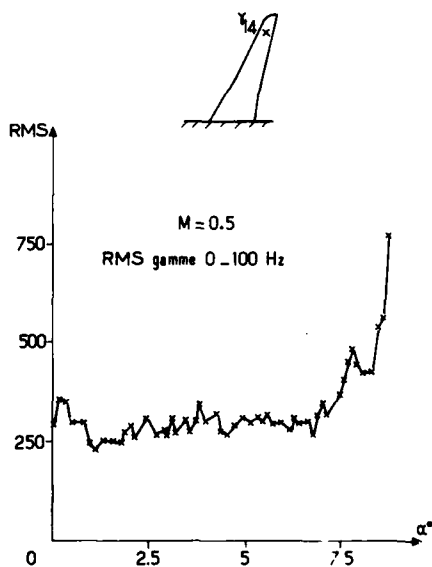
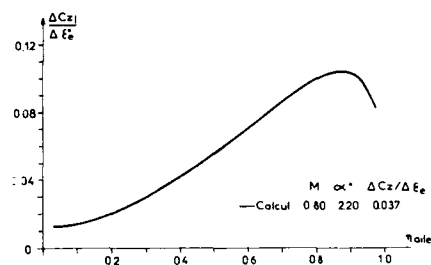
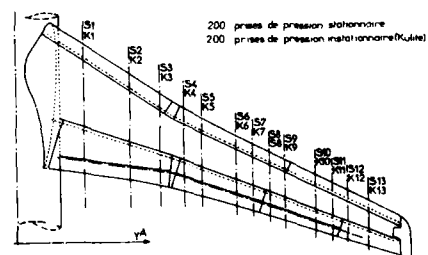


Fig. 14 — Effet de la turbulence de la soufflerie sur la réponse de la maquette mesurée par un accéléromètre.

Fig. 15 — Equipement d'une aile en prises de pression pour mesures stationnaires et instationnaires.



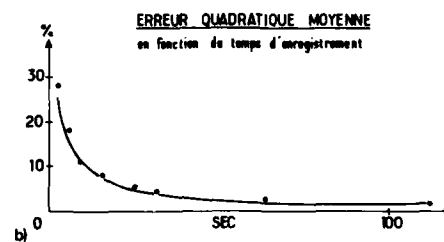
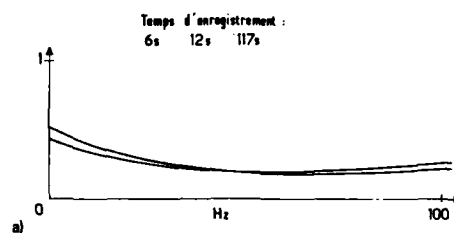
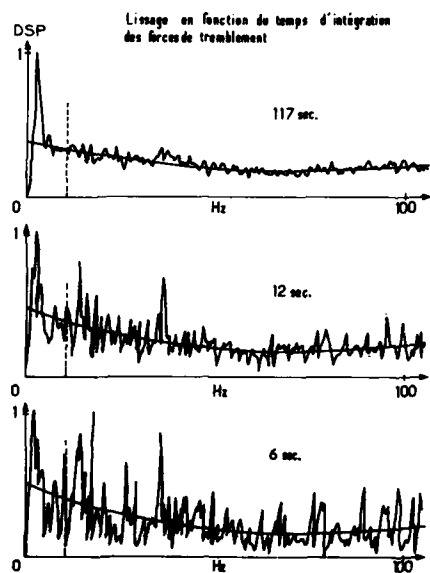
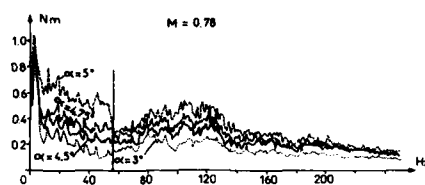
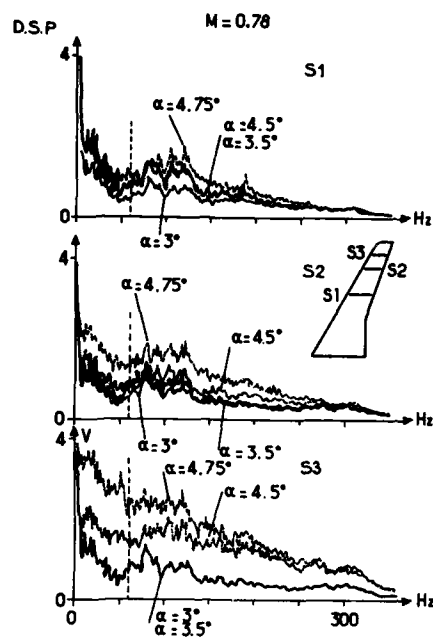


Fig. 19 - Analyse des fonctions de lissage.
a) comparaison pour plusieurs temps de mesure
b) erreur quadratique moyenne.

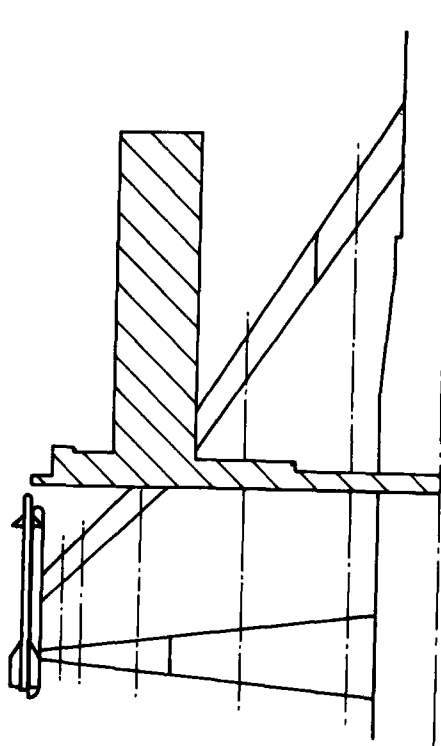


Fig. 20 — Répartition en envergure de la force généralisée
par section pour le premier mode de flexion.

ACCURACY REQUIREMENTS FOR HIGH-SPEED
TEST WITH ENGINE SIMULATION ON
TRANSPORT AIRCRAFT MODELS IN THE NLR-HST

W. Burgenmüller
Messerschmitt-Bölkow-Blom GmbH
Civil Transport Aircraft Division
Bremen, Federal Republic of Germany

J.W. Kooi
National Aerospace Laboratory NLR
Postbus 153
8300 AD Emmeloord
The Netherlands

K.W. Müller
National Aerospace Laboratory NLR
Postbus 90502
1006 BM Amsterdam
The Netherlands

SUMMARY

Air-driven turbo-powered simulators, so-called TPS units, are being used in wind tunnel testing to simulate the engine flow for an aircraft model. These simulators provide substantial improvement in testing as compared to simple through-flow nacelles used earlier.

In order to fully explore the improvement potential in aerodynamic simulation it is mandatory to assure a high level of accuracy or in case of increment testing a good repeatability because the effects of engine interference drag are of the order of a few counts. For increment testing a repeatability of at least ± 1 drag count must be achieved.

The paper describes the efforts made to demonstrate that this repeatability can be achieved in the NLR high speed wind tunnel HST for a half model with a wing-mounted TPS engine. The test was performed in a joint program of NLR and MBB-UT, where MBB delivered the model and TPS unit with engine cowlings, while NLR was responsible for engine calibration, wind tunnel instrumentation and the test.

To obtain the desired quality of the final test results the investigation was subdivided into several steps. These steps and the technical problems and questions encountered will be described in detail.

NOMENCLATURE

A_n	engine flow area at station n	F_N	engine net thrust
C_{DB}	bellmouth discharge coefficient	F_n	engine thrust at station n
C_{DC}	cubic nozzle discharge coefficient	\dot{m}_n	engine mass flow at station n
C_{Dn}	engine discharge coefficient at station n	p_o	tunnel free stream static pressure
C_{VB}	bellmouth velocity coefficient	p_{to}	tunnel total pressure
C_{VC}	cubic nozzle velocity coefficient	p_{tn}	engine total pressure at station n
C_{Vn}	engine velocity coefficient at station n	v_o	tunnel free stream velocity
F_E	engine ram drag force	v_{ni}	engine ideal velocity at station n
F_G	engine gross thrust	For engine station definitions see FIG. 17	

1. INTRODUCTION

Increasing competition between aircraft manufacturers steadily forces the experimental aerodynamicists - like the other development teams - to improve the accuracy and quality of their test results. The main goal of these improvements is first to minimize the financial and technical risk for the aircraft manufacturers, i.e. to minimize the gap between predicted overall performances and those measured during the later flight test period. Second, a steady improvement of global and detail testing techniques is necessary in order to give a better understanding of local flow effects. And, last not least, it is necessary to deliver high-quality results as input for the further development of computational fluid dynamics codes.

To indicate the importance of a decrease in the margin between predicted and realized performances, it should be mentioned, that for a modern Airbus-type aircraft a reduction in cruise drag of 1 percent corresponds with a reduction in fuel consumption dependent on block length between 200 and 800 kg per flight or about 0.2 percent DOC improvement.

Due to this, today's high-speed wind tunnel tests are aiming at an overall repeatability of about ± 1 drag count which corresponds with about 0.7 percent DOC in case of an Airbus type aircraft. This repeatability is necessary especially for the investigation of the effects of small modifications.

An important area of interest and the subject of this paper is the wing/pylon/engine interference. Investigations into this highly three-dimensional flow-problem require an accurate representation of the jet-flow of the engines, since its effects (jet-interference) are not negligible. The magnitude of jet-interference is highly dependent not only on the size and location of the engine relative to the wing, but also on the combination of wing profile and engine/pylon design. So, in order to make reliable performance predictions for a new aircraft and to enhance the understanding of these complex flow-phenomena, models with active engine-flow simulation necessitating sophisticated test techniques are required. The importance of these techniques probably will increase in the next future, when new engine developments like ducted and unducted propfans will mature for the application on new aircraft types.

In order to be prepared for these new applications as well as for improving existing aircraft, a joint test program of MBB-UT and NLR was performed, concentrating on interference effects in the high-speed flight regime of a transport aircraft. For these tests, a half model of a transport aircraft with turbo-powered engine simulator (TPS) was made available by MBB, while NLR was responsible for engine calibration in their model engine calibration facility and the tests in the NLR-HST transonic wind tunnel.

Main purpose of the tests was to show that test set-up and evaluation techniques are able to produce results with an overall repeatability of about ± 1 drag count. Thereafter in addition some preliminary investigations of small configuration changes were made.

2. TEST APPROACH

The main purpose of the present HST test was to show that the jet interference drag generated by a TPS on a half-model representing an Airbus type of aircraft could be defined with a repeatability of ± 1 count. To reach this high level of repeatability a step by step procedure was chosen to validate the main test elements used for model installation and instrumentation. This step by step procedure was followed both in the Model Engine Calibration Facility (ECF) where the TPS thrust had to be calibrated as well as in the HST where the half-model was tested wind-on. Additionally in both facilities a cubic nozzle reference test was executed giving the possibility to compare the ECF and HST results at $M = 0$. A review of the test approach contains the following items:

- In-situ "calibration" of the fully equipped ECF balance (fully equipped means that all wiring, oil supply line and low-reaction air supply line were present).
- Test of a cubic nozzle in the ECF.
- Calibration of the ECF bellmouth for mass flow metering in combination with an ECF balance check.
- Calibration of the TPS in the ECF.
- Complete calibration of the bare wind tunnel balance and a check on the effects of the additional wiring and the low-reaction air supply system.
- In-situ "calibration" of the HST fully equipped balance.
- Cubic nozzle test in the HST.
- Wind tunnel test on complete half-model.
- Repeat of the in-situ balance "calibration".

3. TEST FACILITIES

3.1 The Model Engine Calibration Facility

The TPS was calibrated in the NLR Model Engine Calibration Facility (ECF) (Ref. 1). The purpose of the calibration is to link the TPS internal instrumentation readings to its gross thrust under the conditions where the internal flow of the TPS matches the conditions in the wind tunnel. This internal flow matching is achieved by creating a pressure difference between the TPS inlet and exhaust plane equal to the wind tunnel engine ram drag pressure, i.e. the wind tunnel Mach number is statically simulated.

A schematic view of the ECF is shown in Fig. 1. The design of the facility is comparable to the Boeing (Ref. 2) and ARA (Ref. 3) facilities. The tank in which the TPS exhausts and which can be evacuated to create the desired pressure has a diameter of 3 meter and a length of 6 meter. The TPS/pylon combination is mounted on a substructure which itself is installed inside the central bellows. This bellows forms a flexible and airtight seal between the metric substructure and the non-metric earth frame. Three load cells measure the axial force, the side force and the yaw moment acting on the substructure. The accuracy of the balance is 0.2 percent of the measured value.

The pressure difference over the bellows frontal area exerts a load on the substructure. This force is compensated for by two additional bellows placed between the substructure and the earth frame. The two compensation bellows have together the same frontal area as the central bellows.

The drive air for the TPS turbine is supplied by a compressor plant which can continuously deliver 9 kg/sec dry air (dew-point 210 K at 1 bar) at a pressure of 90 bar. A control valve reduces the pressure to the level needed for the required rpm. The quality of the control valve was such that for the TPS used in the present investigation which has a maximum rotational speed of 45000 rpm, a rpm stability of ± 25 rpm could be obtained. Downstream of the control valve a heat exchanger heats the air to the required temperature, which was for this test selected to be about equal to the HST wind tunnel stagnation temperature (300 K). The heat exchanger is followed by the mass flow metering station consisting of a flow straightener, a temperature/pressure probe and a sonic venturi all designed according to the recommendations of Ref. 4. The non-metric supply line was connected to the metric line on the substructure via a six degree of freedom low-reaction airline bridge (Fig. 2) using three flexible pipe connectors (FPC). Each FPC has two angular degrees of freedom obtained by a single ply metal bellows caged in a Cardan link. Experience has shown that this type of arrangement limits the interaction and hysteresis to a very low level and that the residual effects of pressure and temperature variation can easily be corrected for.

The fan air is coming from outdoors and enters the inlet of the tank via mufflers and a pair of gauzes.

The total tank flow is measured by a bank of 9 sonic venturis located at the downstream end of the tank. The throat areas of the venturis form a binary series. To make the flow sufficiently uniform a perforated break-up basket is placed halfway the tank followed by four full mesh screens. Three annular mesh screens placed between the TPS exhaust plane and the break-up basket reduce the recirculation due to jet entrainment on the outside of the TPS nacelle to a very low level.

Metering the mass flow with the tank venturi bank has the disadvantage that during a calibration run the tank pressure increases with increasing rpm.

Therefore calibration results have to be interpolated to obtain constant tank pressure i.e. constant Mach number calibrations. This process can become rather annoying due to nonlinearity effects (Ref. 3) and will undoubtedly lead to a loss of accuracy. A way to circumvent this problem is to open all the tank venturis and to utilize for the mass flow measurements the bellmouth already attached to the TPS intake for inlet flow conditioning. Then the equivalent Mach number is controlled by the amount of suction with an accuracy of ± 0.002 . An additional advantage of the use of the bellmouth is a reduction of the time required for the calibration since the opening and closing of the venturis is very time consuming.

3.2 Wind Tunnel

The NLR High Speed Wind Tunnel HST used for the half-model test is a variable pressure transonic wind tunnel with test section dimensions of 1.6×2.0 meter (Ref. 5). The test section upper and lower wall have 6 slots each resulting in an open area ratio of 12 percent per wall. In the present test the tunnel stagnation pressure was slightly above ambient pressure as a result of the venting of the TPS drive air by simply opening a valve in the tunnel settling chamber.

The TPS drive air was supplied from a 600 m³ 40 bar storage vessel. The air dew-point was kept at 223 K (measured at 1 bar). The drive air pressure was regulated by a control valve making it possible to keep the rpm of the TPS during the measurement of a datapoint within 50 rpm of the selected value. The drive air was fed through a heat exchanger where the air was heated to tunnel stagnation temperature. This prevents heat flow from the supply lines to the balance. Mass flow metering was accomplished through the same sonic venturi as used in the ECF but now located in the wind tunnel supply line.

4. MODELS

4.1 Cubic Nozzle

The purpose of the cubic nozzle was to validate the ECF and HST instrumentation and to make a comparison between both facilities. The model is in principle a blown nacelle (Fig. 3). The nozzle geometry is conform with the design used by Boeing (Ref. 6). The nozzle dimensions were chosen such that the mass flow range matches the TPS mass flow range. A throttle plate positioned in front of the nozzle was designed to make the pressure level in the supply line equal to the level during the HST TPS-tests. This was done to have almost identical airline bridge conditions during nozzle and TPS-tests.

The nozzle instrumentation consisted of 7 total pressure probes and 5 thermocouples.

4.2 Nacelle With Turbo Powered Simulator

The model nacelle was equipped with a TDI 441 TPS having a fan diameter of 127 mm (5 inch). The core and fan duct instrumentation of the TPS consisted of total temperature and total pressure probe rakes, see Fig. 4. Experience has shown that during testing notwithstanding precautions, one of them being the use of a purge system, some probes may become blocked or leaky. The cause of this frequent malfunction of TPS instrumentation is due to the aggressive nature of the oil used for lubricating the bearings. With an redundant amount of probes (Fig. 4), missing one or two probes does not effect the accuracy provided that all results including those of the calibration are reprocessed without the faulty probe(s) or that some appropriate estimate for the missing values is made.

Apart from the rake assemblies the TPS instrumentation included thermocouples for bearing temperature monitoring, an acceleration pick-up for vibration monitoring and an rpm-transducer.

The TPS cowlings were, with the exception of the core plug and the core exhaust duct, made of aluminium. The core exhaust duct and the core plug were made of a material with a very low thermal conductivity (Tufnol) in order to prevent condensation and ice build up on trailing edge of the core exhaust duct due to the low turbine temperature and the humidity in the fan air.

4.3 Half-model

The aircraft model selected for this investigation was a 1 : 16 scale half-model of the Airbus type. A photograph of the model mounted in the NLR High Speed Wind Tunnel HST is shown in Fig. 5 and a sketch of the model with its main dimensions is given in Fig. 6. The model was attached to a 5-component strain gauge balance, with the following range:

K1 normal force	: 20000 N
K2 axial force	: 2000 N
K3 pitching moment	: 1500 Nm
K5 yawing moment	: 1700 Nm
K6 rolling moment	: 7000 Nm

The balance was situated inside the rotating inner barrel of the test section sidewall model support (Fig. 7). The angle of incidence of the model is set by rotating the inner barrel. The reproducibility of the angle of attack is 0.01 degree. The inner barrel carries an end plate, the turntable, flush with the side wall of the test section. A rubber seal was placed between the metric part of the balance and the turntable to prevent air leakage to the plenum. A so-called boundary layer plate is attached to the turntable. This plate is non-metric and has the same contour as the half-model fuselage centre-line contour. It compensates for the boundary layer on the side wall of the test section and accommodates a labyrinth seal. This seal was applied around the entire fuselage circumference.

The nose and rear end section of the half-model fuselage were equipped with a row of pressure taps, see Fig. 6. The purpose of these pressure taps was to get information about possible buoyancy effects due to jet interference on the fuselage.

For air supply to the model use was made of a six degree of freedom low-reaction airling bridge. The non-metric part of the airline bridge was attached to the inner barrel of the side wall model support. The design of the airline bridge was identical to the one used at the ECF.

5. MODEL ENGINE CALIBRATION FACILITY TESTS

5.1 Cubic nozzle

A static thrust calibration of the cubic nozzle was performed in the ECF keeping the tank pressure close to ambient conditions. The results of the calibration are shown in Fig. 8 and 9 together with the HST and Ref. 6 results. In the HST test the same venturi, instrumentation and transducers were used. For a further discussion of the results see section 6.

5.2 TPS

5.2.1 Bellmouth

In general the accuracy of bellmouth mass-flow metering (see section 2.2.1) is less than that of sonic venturi. This holds particularly for low mass-flow rates where the pressure difference between the inlet and the measuring station becomes small and measuring errors become significant. However, NLR experience has shown that by combining bellmouth and venturi results the bellmouth accuracy limitations can be relieved. The procedure followed is to determine first the bellmouth discharge coefficient (C_{pg}) without the TPS over the expected mass flow range using the venturi bank as the standard (Fig. 10). The coefficient C_{pg} was calculated from the static pressure distribution in the cylindrical part of the bellmouth and the ambient total pressure and temperature. The solid line in Fig. 10 is the curve-fit used in the data reduction program. The kink in the data is assumed to be caused by changes in the position of the boundary layer transition in the bellmouth as discussed further on in this chapter.

Next during the calibration runs with the TPS installed the accuracy of the bellmouth mass-flow metering is checked versus the choked tank venturis at the TPS maximum mass-flow. Moreover, to achieve the required accuracy, a correction has to be made for the changes in the humidity of the fan air. Then in general the difference between the two methods is less than 0.2 percent. Also at the lowest mass-flow a number of checks are made with the venturi bank. This mass-flow inaccuracy dominates the overall accuracy of the TPS force calibration in terms of C_v .

A second aspect of the use of the bellmouth is its influence on the force measurements. Common practice was followed here to neglect this effect in the C_v calculation. This introduces a bias error and in the following discussion an attempt will be made to estimate along different lines the magnitude of this bias error.

The forces acting on the bellmouth can be split into pressure- and friction-forces. Of these the friction-force represents a loss working in the direction against the pressure-forces and in principle has to be accounted for. This becomes clear when one thinks of a TPS calibrated twice, once with a very short bellmouth and once with a very long bellmouth. The difference in bellmouth length will result in different friction-forces and thus in different calibration results.

A first estimate of the friction-forces was made by calculating the boundary layer based on the measured pressure distribution and using the method of Ref. 7. Because the boundary layer transition was unknown the calculation was done twice, once with the transition calculated by the program and once with the transition fixed at the suction peak. The calculated transition point lays almost at the end of the bellmouth. For the calculated transition the friction-force is 1.5 N and for the fixed transition 2.6 N. The calculated friction force can be cast in the form of C_{VB} , where:

$$C_{VB} = \frac{X_{G1} - X_G \text{ friction}}{X_{G1}}$$

The calculated C_{VB} -values are indicated in Fig. 11 by the cross symbols.

The second C_{VB} estimate stems from the measured C_{DB} . In Ref. 8 it was shown that the nozzle C_{VB} are both related to the boundary layer characteristics. The C_{VB} -results calculated from the measured C_{DB} are shown in Fig. 11 by the two lines. The upper line gives the result for a laminar boundary layer and the lower line the results for the turbulent boundary layer. The kink in the lines corresponds with the kink in the C_{DB} -line shown in Fig. 10. As stated before the position of the transition point is unknown.

A third estimate comes from direct balance measurements of the bellmouth. The C_{VB} is measured force divided by ideal thrust. The results are given in Fig. 11 by the circles.

The results from the three methods agree, given the uncertainty in transition location, reasonably well. The conclusion to be drawn from this is that the friction-force is at maximum about 1.2 percent of the bellmouth ideal thrust which at maximum fan mass-flow corresponds to 233 N. At this condition the TPS produces 482 N thrust and the bias error in the calibration is therefore 0.5 percent.

Although application of this correction looks straight forward, there is a complication. During the calibration part of the inlet is replaced by the bellmouth. In the wind tunnel the inlet part is mounted again and in fact the friction-force on this part reduces the bellmouth bias error. An estimate of this reduction is difficult to give.

5.2.2 TPS-calibration

To evaluate the engine interference drag the thrust developed by the TPS has to be subtracted from the wind tunnel model forces measured by the balance. For the thrust calculation it is necessary to know the TPS nozzle velocity-coefficients C_{V18} , C_{V18} and the discharge coefficient C_{D18} as a function of the nozzle pressure ratio (NPR) or the fan mass-flow \dot{m}_{18} versus the rpm both corrected to ISA sea level conditions (for engine station numbering see Fig. 17). The coefficients were measured for the wind tunnel Mach numbers in the ECF over a range of rpm's covering the range between flow through and the cruise power setting. The C_{V18} -coefficient cannot be measured in the ECF and must be obtained from a separate isolated nozzle test. This coefficient is normally provided by the manufacturer. In the present investigation C_{V18} was set unity.

Typical examples of the C_{V18} and \dot{m}_{18} measured at equivalent Mach numbers of 0.70, 0.78, 0.80 and 0.82 respectively are shown in Fig. 12 and 13. The fan nozzle velocity coefficient C_{V18} is defined as:

$$C_{V18} = \frac{F_{18}}{\dot{m}_{18} \cdot v_{181}}$$

in which the fan thrust F_{18} is the difference between the engine gross thrust F_G measured by the ECF balance, minus the calculated core thrust:

$$F_{18} = F_G - \dot{m}_{18} \cdot v_{181}$$

The ideal velocities are calculated from the rake total pressures and temperatures assuming ideal expansion to ambient conditions.

The C_{V18} and \dot{m}_{18} results for the four Mach numbers (see Fig. 12 and 13) show with the exception of the lowest Mach number and high NPR hardly any Mach number dependence. A number of datapoints was repeated and based on these points and prior experience in the low Mach number range (Ref. 9) the repeatability in C_{V18} is estimated to be better than 0.4 percent (see Fig. 12) and for C_{D18} better than 0.2 percent.

During the calibration test an anomaly in the long term repeatability was observed. This anomaly was most pronounced in the fan discharge coefficient as shown in Fig. 14 where results from three test runs at an equivalent Mach number of 0.82 are given. Two of the three runs fall well within the 0.2 percent scatter band but the results of the third run deviate. The explanation for this is that due to the accumulation of dust on the fan blades the performance of the fan degraded. It was not until a number of runs with an unexpected bad reproducibility were made that the dust accumulation was discovered. After the blades were carefully cleaned and the filtration of the fan air coming from outdoors was drastically improved no further pollution problems were encountered. For each Mach number a fourth degree polynomial was curve fitted through the \dot{m}_{18} as a function of the rpm-reduced, the C_{D18} and the C_{V18} as a function of the NPR. These polynomials were used in the wind tunnel data processing. A further set of data used in the wind tunnel are the total pressure and temperature distributions measured by the fan and core rakes. The shape of these distributions during the wind tunnel and calibration test should be equal. Any change makes the applicability of the calibrations questionable. An example of the fan exit pressure distribution is given in Fig. 15. Moreover a good reproducibility during calibration as well as during the wind tunnel test requires that the TPS is in thermal equilibrium. This was monitored by tracing the output of one of the rake thermocouples as a function of time.

6. WIND TUNNEL TEST

6.1 Balance calibration

Prior to the tunnel mounting the half-model balance was extensively calibrated in the Calibration Room in the following configurations:

- The clean balance, without wiring for model instrumentation and low-reaction air supply, to determine the standard calibration coefficients under single and combined forces and moments.
- The balance equipped with wiring for instrumentation and tubing for the TPS lubrication system between the metric and the non-metric part. The influence of the wiring and tubes proved to be negligible.
- The balance equipped with the low-reaction supply system pressurized at various levels (1-40 Bar). This resulted in a small pressure dependent influence on the axial force (less than 1 N) and pitching moment (less than 1 Nm). These effects were accounted for in the data reduction of the wind tunnel test.

Next the balance was mounted on the side wall model support of the HST test section and a "calibration" in-situ was executed. With a special rig axial forces of ± 2000 N could be applied by means of dead weights. Moreover normal forces of ± 10000 N were applied in combination with the axial force by cable pull measured by a load cell. This led to some essential improvements:

- The adjustment of the FPC element was improved.
- An axial force correction due to the deformation of the rubber seal (see Fig. 7) between model adapter and turntable was necessary.

After introduction of these improvements the accuracy in axial force (K_2) of the balance equipped in its final configuration proved to be better than:

$$\pm 0.4 \text{ N if } -200 \leq K_2 \leq 200 \text{ N}$$

$$\pm 1.0 \text{ N if } -2000 \leq K_2 \leq 2000 \text{ N}$$

This corresponds at $M = 0.8$ to ± 0.3 respectively ± 0.8 drag counts for the indicated K_2 ranges.

After completion of the half-model test in the wind tunnel the in-situ "calibration" was repeated with the same accuracy results.

6.2 Cubic nozzle test

The next step in the validation of the test set-up was done by means of a cubic nozzle test at $M=0$. The cubic nozzle (see Fig. 3) was mounted on the balance/model adapter and connected to the air supply system thus enabling to check:

- The validation of the balance calibration and the low-reaction air supply system influence under flow through condition (including temperature variations of the supply air).
- The wind tunnel instrumentation, data acquisition and data reduction as far as the forces and moments measurement is concerned.

The results of the cubic nozzle test expressed in the velocity coefficient C_{Vc} and the discharge coefficient C_{Dc} are presented as a function of the nozzle pressure ratio NPR in Fig. 8 and 9. Also presented in these figures are results from the same nozzle tested in the ECF and results from Ref. 6 for similar nozzles. A systematic difference between HST and the ECF of 0.003 is found for C_{Vc} and of 0.005 for C_{Dc} . When the differences in C_{Vc} are related to the tangential force coefficient of the half-model this means an error of 0.2 - 0.5 drag counts depending on NPR thus about 0.3 counts in interference drag. The differences between the HST results and the mean value given in Ref. 6 are for C_{Vc} about 0.005 and for C_{Dc} about 0.004. When the balance accuracy is taken into consideration (0.4 N) then it is clear that better C_{Vc} agreement hardly can be expected. Although the C_{Vc} datapoints lay nearly on the scatter band given in Ref. 6, the reason for the systematic difference between the ECF and HST values requires further experimental investigation of the mass-flow metering system. This should include a direct comparison of the two mass-flow metering stations and, to check the absolute accuracy, a primary calibration of one of the stations. Moreover the limited instrumentation of the cubic nozzle (only 7 pressure and 5 temperature probes) together with a non-optimized flow straightener in front of the pressure/temperature rakes might contribute to this effect. Nevertheless the cubic nozzle tests showed that the test set-up and instrumentation (wind-off condition) was sufficiently reliable to determine the jet interference drag to the required accuracy level.

6.3 Half-model test

After completion of the cubic nozzle test the half-model with TPS-nacelle was installed without any changes on the already prepared and checked balance and air supply system. The used half-model technique fully conformed with the standard MNR method described in Ref. 10. The main features of the method are:

- Boundary layer plate between half-model and test section side wall, sealed with labyrinth.
- Body-alone correction on normal force, axial force and pitching moment coefficients.

- Empirical wall interference corrections.

With respect to the instrumentation and data handling the following remarks are made:

- The pressure transducers used for the measurements of mass-flow and TPS/nacelle pressure were the same as those used during the calibration of the TPS in the ECF. Also in the HST and ECF the same venturi was used for turbine (score) mass-flow measurements.
- For all wind tunnel and TPS/nacelle pressure measurements the same reference pressure was used (P-barometric).
- All tunnel and TPS/nacelle temperatures were measured by chromel/alumel thermocouples with the same reference (273.15 K).
- All tunnel and mass-flow pressure measurements were checked by a back-up (measuring the same value independently a second time).
- The single measured tunnel, venturi and reference pressures, the balance components and the rpm were read out continuously (48* per datapoint). All scanned pressures and temperatures (TPS/nacelle) were read several times per datapoint. In the data reduction the arithmetic means were used for further processing.
- On the nose and tail of the fuselage 20 pressures were measured to obtain information on buoyancy effects due to TPS power-setting.
- On the tunnel wall (slats), above and below the nacelle pressures were measured to signal possible changes in wall interference effects due to TPS power-setting.

The test procedure comprised incidence polars for the following conditions:

0.700	<= M	<= 0.820	(stability +/- 0.002)
$4.5 \cdot 10^6$	<= RE	<= $5.0 \cdot 10^6$	(stability p_0 +/- 100 Pa)
1.00	<= FNPR	<= 1.60	(stability rpm +/- 50)
-0.50	<= α	<= 3.00	(accuracy +/- 0.01 degree)

The change in the measured pressure distribution on the fuselage showed that the influence of TPS power setting on the fuselage pressure drag coefficient is less than 0.2 drag counts. Since the slat pressures on the tunnel upper and lower walls were independent of the TPS power setting, the influence of the power setting on the wall interference is assumed to be negligible.

7. RESULTS

The main parameters, used for the investigation of engine interference effects (Fig. 16) are

- installation drag, which is generally the difference between the model with and without nacelle/pylon and
- jet interference drag, which is the difference between the model with and without engine flow simulation.

Jet interference drag, which is often defined as the difference between a model with jet simulation and one with a conventional through flow nacelle (TFN). This allows to do the major part of tests in an aircraft development program on models with a simple TFN and to evaluate the jet interference increments only from some special tests.

7.1 Thrust calculation

Because the TPS is mounted directly to the model and hence to the balance, it is necessary to subtract the actual thrust from the overall balance forces in order to get the required aerodynamic loads. Net thrust is calculated as follows (Fig. 17):

$$\begin{aligned}
 F_N &= F_G - F_E && \text{with} \\
 F_G &= F_{18} + F_8 && \text{or} \\
 F_G &= \dot{m}_{18} \cdot v_{18i} \cdot C_{V18} + \dot{m}_8 \cdot v_{8i} \cdot C_{V8} && \text{and} \\
 F_E &= \dot{m}_{18} \cdot v_8
 \end{aligned}$$

F_E is acting along the axis of the tunnel flow and F_{18} , F_8 are acting along engine axis.

The values for C_{V18} and \dot{m}_{18} are obtained from the calibration, \dot{m}_8 is measured in the drive air line, v_{18i} and v_{8i} are calculated from pressures and temperatures measured on the rakes behind fan and turbine and C_{V8} is equal one (see chapter 5.2.2).

7.2 TPS versus IFN

For the investigation described here, the TPS was not only used to simulate an engine with jet flow corresponding to cruise condition, but also for the simulation of a through flow nacelle. The IFN-condition was defined such that $p_{t5}/p_{t0} = 1$, resulting in $v_{t5} = v_0$. This definition is based on the assumption that the main difference between a IFN and a real engine is due to the jet effects between wing and nacelle. To drive the TPS at the IFN-condition a small amount of drive air was required. As the first tests showed, the primary nozzle pressure ratio (p_{t5}/p_0) was below one for this condition at low angles of attack, so that it was not possible to calculate the turbine nozzle exit velocity from this ratio and hence no turbine thrust. The reason for this effect is the influence of the flowfield under the wing which also affects the static pressure behind the turbine for this subcritical flow condition (Fig. 18). The tests showed an increasing pressure p_{t5} with increasing incidence, so that for angles around cruise condition the turbine thrust calculation posed no problems.

As these variations in the static pressure field below the wing are the same for a test with a conventional IFN the only problem for the TPS-test was to find a way to calculate the true core nozzle exit velocity in order to come to a result which can be compared with a IFN-test.

To overcome the problem, the following solution was found:

Using p_{t5} , T_{t5} , A_5 as measured behind the turbine resp. in the drive air line plus the core nozzle exit area A_8 , it is possible to calculate the core nozzle exit Mach number by iteration of the following equation:

$$\frac{A_8}{p_{t5}} \cdot \frac{\sqrt{T_{t5}}}{A_5} = \left(1 + \frac{k-1}{2} \cdot M_8^2\right)^{-3} \cdot M_8 \cdot \sqrt{\frac{k}{R}}$$

The nozzle exit values for temperature and static pressure are calculated from

$$T_8 = \left(1 + \frac{k-1}{2} \cdot M_8^2\right)^{-1} \cdot T_{t5} \text{ and}$$

$$p_8 = \left(1 + \frac{k-1}{2} \cdot M_8^2\right)^{\frac{k}{1-k}} \cdot p_{t5}$$

$$\text{With } a_8 = \sqrt{k \cdot R \cdot T_8}$$

and

$$v_8 = M_8 \cdot a_8$$

the core thrust is

$$F_8 = A_8 \cdot v_8 + A_8 \cdot (p_8 - p_0).$$

The application of these equations for the TPS running at IFN-condition is shown on Fig. 19 together with the result obtained using the conventional procedure. The agreement between the two methods is very good for all cases with $p_8 \geq p_0$, while for $p_8 < p_0$ only the way described above produces acceptable results. So, this latter method was applied for all TPS-conditions without posing problems.

7.3 Repeatability

The most important question during the first TPS-tests in the NLR-HST covered the repeatability of the drag measurements. For this purpose runs with the TPS at IFN and cruise power-setting were repeated several times including such procedures as tunnel stops, tests at the beginning and the end of a longer run as well as longer time intervals between tests (weekend). As can be seen from Fig. 20, all results were within or close to the required scatter band of ± 1 drag count. This is valid for the IFN as well as for the cruise-condition. To realize such high-quality results in combination with a running TPS, a permanent control of all parameters needed for thrust calculation is necessary, i.e. all pressures and temperatures measured by the rakes behind fan and turbine as well as the drive-air massflow must be compared with their corresponding calibration values. If this would not be done, just the blockage of a single pressure port (out of 30 in the fan and 16 in the turbine) could be sufficient to produce an error in the thrust calculation of ≥ 0.3 percent, which in turn is already equivalent to the 1 drag count, the good for the overall repeatability of the test results. From this it can be concluded that each single parameter required for thrust calculation should have a repeatability of ± 0.1 percent or even better.

7.4 Use of TPS-technique

As mentioned above, the TPS-technique generally can be used to investigate

- jet interferences for one configuration or
- effects due to configuration changes for one single engine power-setting.

To investigate the jet interference, some tests with the TPS running at IFN-respectively cruise-condition were done for different Mach-nos. One of these typical results is shown on Fig. 21. As can be seen from this figure, the interference drag variation due to small RPM-variations around the cruise-condition was quite small and well within the scatter band of ± 1 drag count.

An example for the investigation of configuration changes in relation which different engine power-settings is shown on Fig. 22. This test was done in connection with the question whether drag variations due to small flap setting changes in the so called variable camber concept (V.C.) can be affected by engine power-effects or how reliable are IFN-tests in this respect. As can be seen from the diagram, the results were not influenced by power-setting or, in other words, no further corrections had to be applied to the corresponding IFN-tests.

8. CONCLUSIONS

In the HST drag force measurements have been accomplished on a halfmodel equipped with a TPS nacelle representing an Airbus type of aircraft.

The test results show that the jet interference due to power setting of the TPS ($1.0 < NPR < 1.6$) could be measured with a repeatability of ± 1 drag count. This result was reached by application of a test approach including several checks during calibration and wind-on tests in the ECF and HST respectively. In particular, the cubic nozzle-tests as a reference between ECF and HST for the assessment of data accuracy and as a final overall check of the facility instrumentation, data acquisition and data reduction proved to be very valuable.

However, the improvement of some details in the test procedure is still possible and will be pursued. Based on the recent MBB/NLR experience special attention should be given to the determination of bellmouth friction-forces during calibrations in the ECF.

Furtheron, the value of the cubic nozzle tests as an overall check can be enhanced with improved nozzle instrumentation.

Finally, possible improvements in the mass flow measuring system will be considered.

9. ACKNOWLEDGEMENT

This work was partly supported by the German Ministry of Research and Technology (BMFT).

10. REFERENCES

- [1] Doornbos, G. The NLR Calibration Facility for Model Engines, Description and Validation; NLR TR 840711, 1984
- [2] Fromm, E.H. The Boeing Simulation Chamber for Static Calibrations of Engine Simulators; Meeting of Subsonic Aerodynamic Testing Association, May 1976
- [3] Harris, A.E.
Carter, E.C. Wind Tunnel Test and Analysis Technique Using Powered Simulators for Civil Nacelle Installation Drag Assessment; AGARD CP-301, 1981
- [4] Hillbrath, H.S. Flow: It's Measurement and Control in Science and Industry, Proc. of the 2nd Symposium St. Louis, March 26th, 1981, Vol-2, pp. 407-420
- [5] NLR User's Guide to the $1.6 \times 2.0 \text{ m}^2$ High Speed Wind Tunnel
- [6] Fromm, E.H.
Floor, P. Boeing Cubic Nozzle Tests
Private Communication
- [7] Lindhout, J.P.F.,
Moek, G. Boer, E.,
Berg, B. van d A Method for the Calculation of 3D Boundary Layers on Practical Wing Configurations; Journal of Fluids Eng., Vol 103, March 1981, also NLR MP 79003 U
- [8] Reimer, R.M. Determination of ASME Nozzle Flow Coefficients by Thrust Measurement; Journal of Basic Engineering, pp 1058-1062. Trans. of the ASME, December 1965
- [9] Eckert, D.,
Ditshuizen, J.C.A van
Munnikema, B.,
Burgemüller, W. Low Speed Engine Simulation on a Large Scale Transport Aircraft Model in the DNW; ICAS-paper 84-2.10.4, 1984
- [10] Soeren, S.J.
Elsener, A. Half-Model Testing in the NLR High Speed Tunnel HST: Its Technique and Application; NLR MP 83036 U, 1983

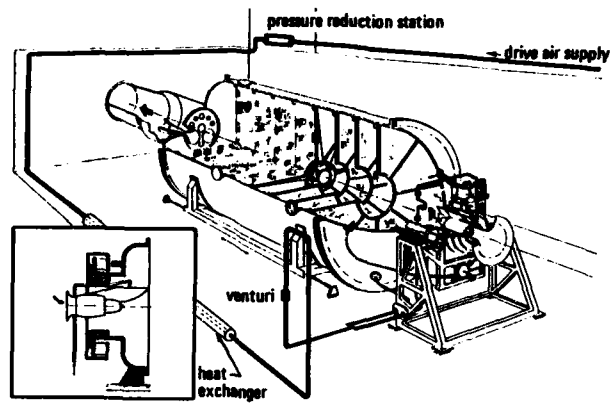


Fig. 1 Schematic view of the NLR model Engine Calibration Facility (ECF)

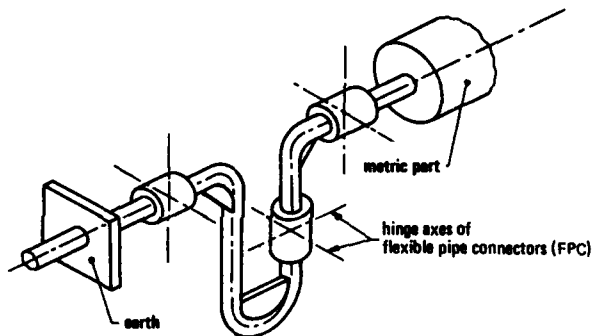


Fig. 2 Low-reaction air line bridge

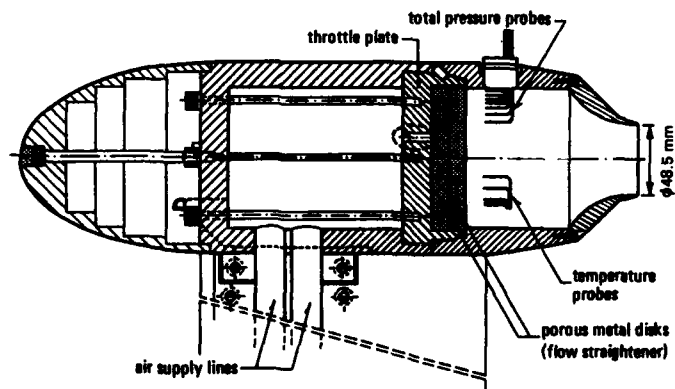


Fig. 3 Cubic nozzle

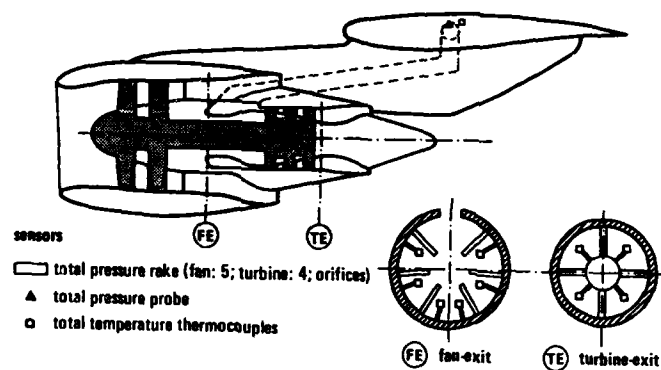


Fig. 4 Instrumentation of TPS



Fig. 5 Half-model mounted in HST

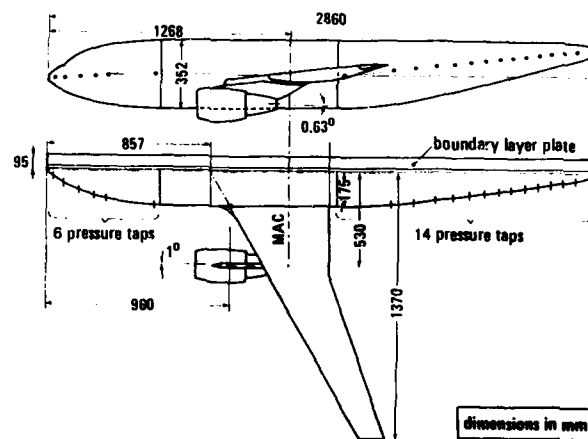


Fig. 6 Main dimensions of half-model

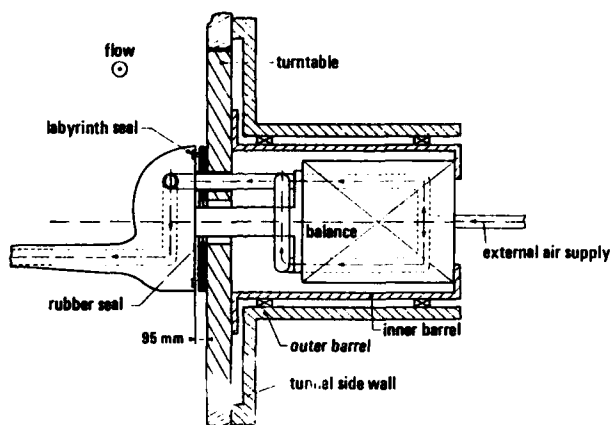


Fig. 7 Cross section of half-model and balance mounted in HST

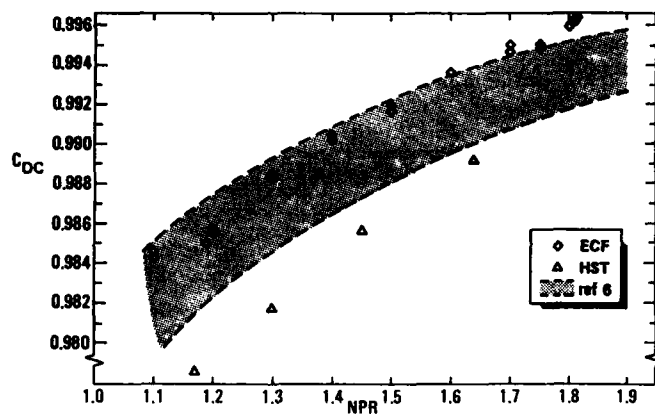


Fig. 8 Discharge coefficient of cubic nozzle versus nozzle pressure ratio

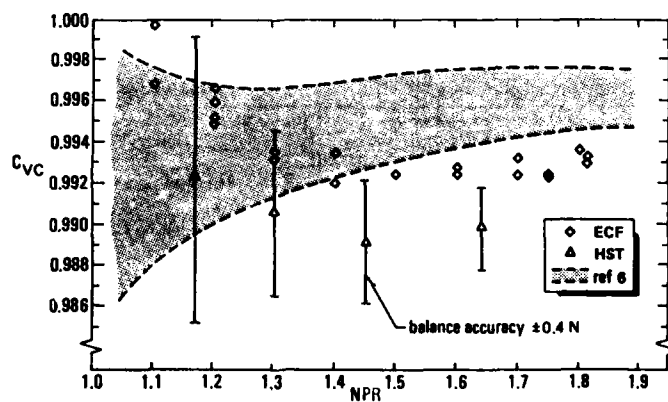


Fig. 9 Velocity coefficient of cubic nozzle versus nozzle pressure ratio

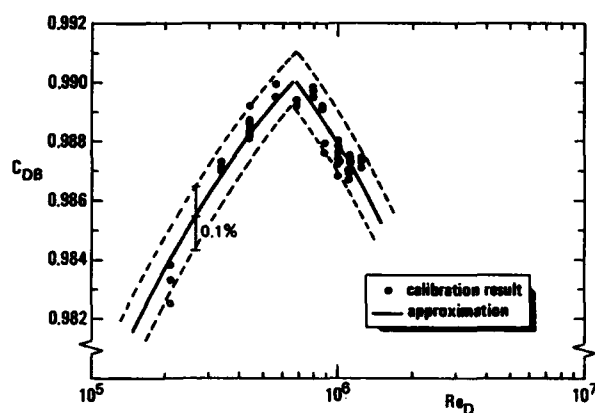
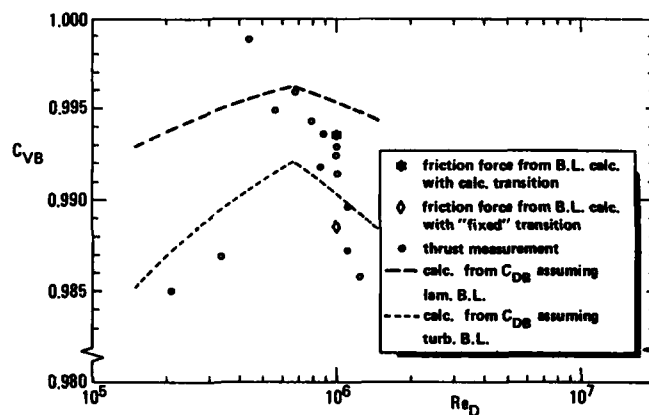
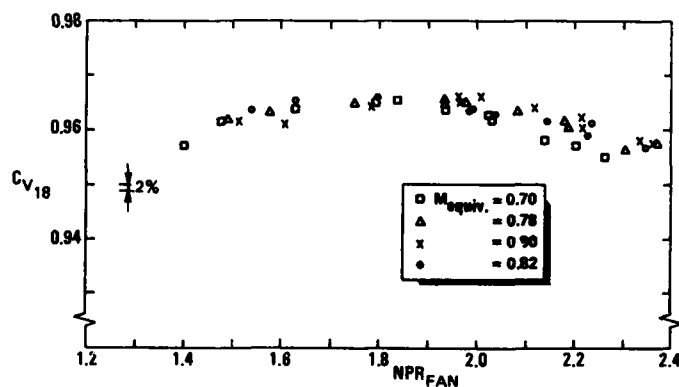
Fig. 10 ECF Bellmouth discharge coefficient versus Re_D Fig. 11 ECF Bellmouth velocity coefficient versus Re_D 

Fig. 12 TPS velocity coefficient of fan nozzle versus nozzle pressure ratio

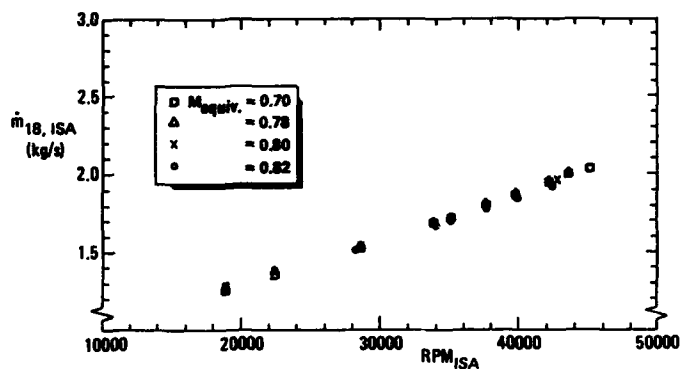


Fig. 13 TPS corrected fan mass flow versus corrected RPM

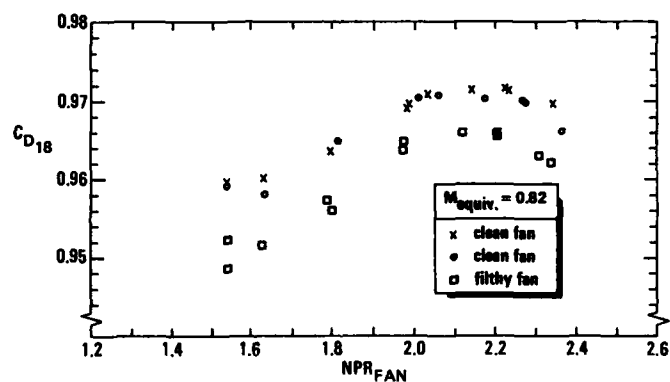


Fig. 14 TPS fan discharge coefficient versus nozzle pressure ratio

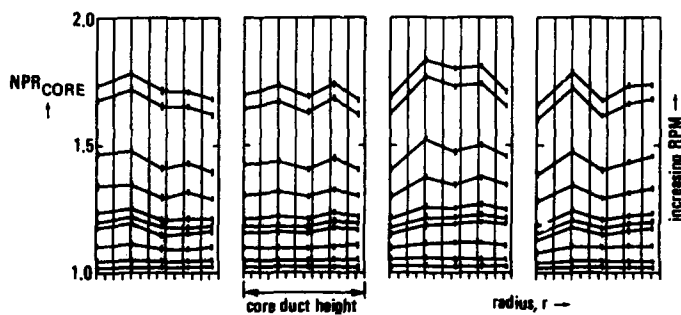


Fig. 15 TPS core duct total pressure distribution at four circumferential locations

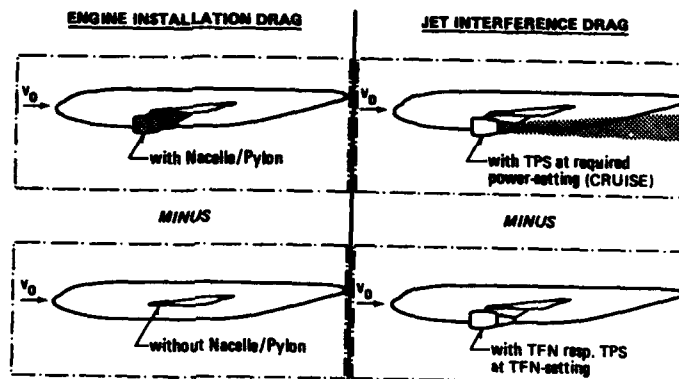
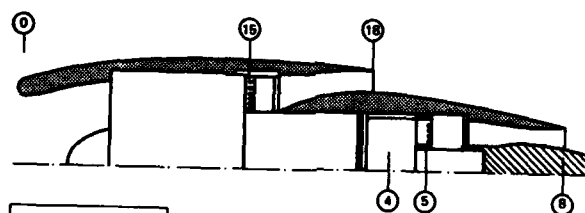


Fig. 16 Interference drag definitions



- 0 - ambient
- 4 - turbine entry
- 5 - exit turbine
- 6 - exit core nozzle
- 15 - exit compressor
- 18 - exit fan nozzle

Fig. 17 Location of thermodynamic stations

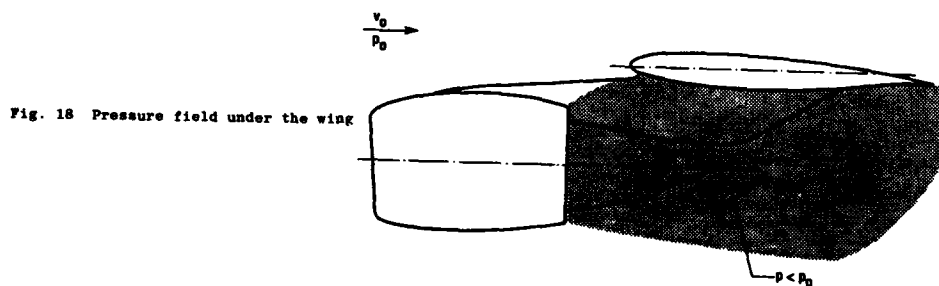
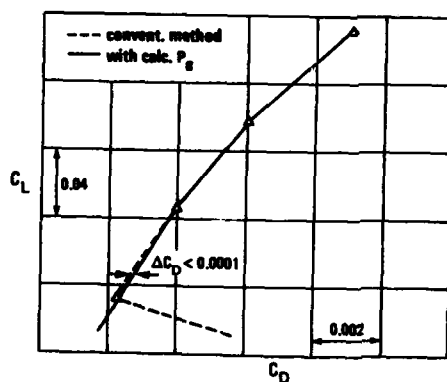


Fig. 18 Pressure field under the wing

Fig. 19 TFN-thrust calculation conventional
resp. with calculated P_8

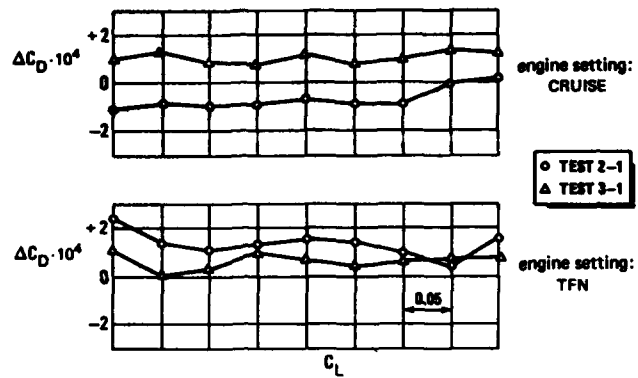


Fig. 20 Repeatability of test results

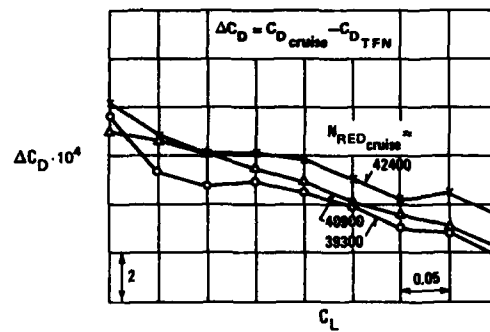
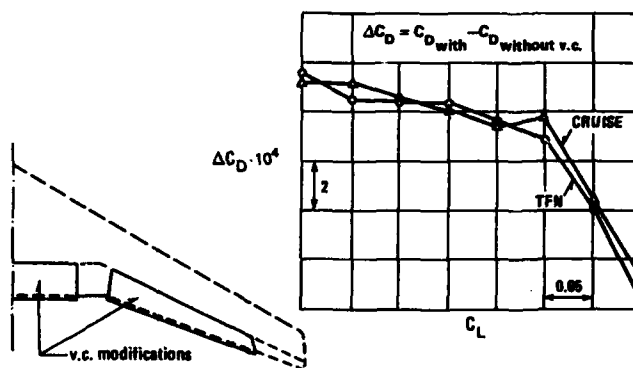
Fig. 21 Jet interference drag at M_{CRUISE} 

Fig. 22 Influence of power setting on configuration changes

**Engine Simulator Tests:
Comparison of Calibration and Wind Tunnel Results
by
M. Baumert, B. Binder, M. Stäger**

Deutsche Forschungs- und Versuchsanstalt für Luft- und Raumfahrt e.V.
Hauptabteilung Windkanäle
Bunsenstrasse 10, D-3400 Göttingen, West-Germany

Summary

A Turbine Powered Simulator (TPS 441) has been tested with a bellmouth inlet in the calibration tank and with a flight inlet in the low speed wind tunnel at DFVLR Göttingen.

Local Machnumber distribution shows good agreement in both facilities. The Pitot pressure distribution behind the fan however is different. This is probably due to the different inlet configurations. The nozzle coefficients obtained in the calibration tank are used to calculate the thrust of the simulator in the wind tunnel. The comparison with the thrust measured in the wind tunnel shows that additional corrections have to be applied when evaluating wind tunnel measurements with TPS.

List of Symbols

Ma		Machnumber
NRED		reduced rotating speed, $NRED = n/45000 \cdot \sqrt{288.15/T_0}$
PHI		perimeter angle, starting at the pylon
F-PR		fan pressure ratio, $F-PR = P_{t15}/P_{t0}$
F-NPR		fan nozzle pressure ratio, $FN-PR = P_{t15}/P_{18}$
CD		discharge coefficient, $CD = \dot{m}/\dot{m}_{id}$
CV		velocity coefficient, $CV = V/V_{id}$
CT		thrust coefficient, $CT = CV \cdot CD$
T	K	absolute temperature
F	N	thrust
\dot{m}	kg/s	mass flow
Subscripts		
0		free stream conditions
5		behind turbine
8		exit of primary flow
15		behind fan
18		exit of secondary flow
id		ideal conditions
t		total

1. Introduction

Interferences between engine and airframe may cause considerable reductions in flight performance of an aircraft. In order to get more information on these effects, DFVLR has created a test program on engine interference problems with a Turbine Powered Simulator (TPS) and a half-model of a transport aircraft. This program consists of three steps (fig.1).

Step 1:

The use of TPS in wind tunnel testing presumes careful calibration of the simulator. The calibrations are performed in a calibration tank (fig.2) which simulates the wind tunnel Machnumber by impressing an equivalent pressure ratio between inlet and exit of the TPS and sucking the mass flow through the TPS into a vacuum vessel. This tank has been described at the AGARD FDP Symposium at Ceame in 1983 (ref.1).

Step 2:

The calibration is checked by performing measurements with the TPS mounted on a single strut in the low speed wind tunnel of DFVLR Göttingen (fig.3, ref.2).

Step 3:

Measurements are conducted with the TPS, mounted on a half-model in the low speed wind tunnel.

These steps will give us more information about the installation interference especially at which parts of the engine or airframe these interferences occur. Step 1 and Step 2 have been performed. This paper presents some comparisons between the measurements in the calibration tank and the wind tunnel.

2. Test setup

The calibration tank (fig.2) is equipped with a balance to measure the thrust of the engine. The intake air is taken at ambient conditions from the laboratory, the exit flow is sucked into a vacuum vessel via 7 sonic venturi nozzles to measure the exit mass flow. The turbine drive air is measured by another sonic nozzle before entering the setup.

The TPS is mounted on the inner ring of the balance (fig.4). The fan cowl is sealed in the front plate of the tank by using a labyrinth. To provide undisturbed flow to the simulator a bellmouth inlet is used.

In the low speed wind tunnel the TPS is mounted on a half-model balance (fig.4). The strut with airsupply as well as the balance are inside a windshield, so only the aerodynamic forces on the TPS including the pylon are measured.

Two measuring planes inside the TPS are installed behind the fan (plane 15) and behind the turbine (plane 5), see fig.5. Each plane consists of total pressure rakes, temperature probes and static pressure holes at the wall. Additionally there are static pressure holes in the inlet, on the core cowl and on the plug. In the wind tunnel there are also static pressure tapings on the fan cowl. The pressures are measured with four Scanivalves with appropriate pressure transducers.

The first TPS calibration in the calibration tank has shown some imperfections of the measuring technique which have been corrected in the meantime:

- The control unit for the compressed air supply has been improved to get a faster and more steady control of the rotating speed of the TPS.
- The Scanivalve system which does not measure the total pressure survey at the same time was exchanged by a fast low level pressure scanner with a serial polling rate of 20 kHz.
- A real time data reduction has been installed, so errors can be detected earlier than before.

These improvements have been tested with other model engines in the meantime.

3. Results

The static pressure measurements are reduced to local Machnumbers (fig.6). For the fan and turbine exit flow the Machnumbers are calculated with the area-averaged total pressures measured with the rakes. There is a good agreement between calibration tank and wind tunnel measurements. In the case of wind tunnel test the local Machnumber distribution at the nose contour of the nacelle shows for the inner surface an overexpansion up to $Ma = 0.73$ followed by a sudden recompression. It is not possible to decide whether separation is induced by this recompression. In front of the fan the Machnumber is about 0.5 in both facilities. In the fan nozzle the flow is accelerated from Machnumbers of about 0.4 up to exit Machnumbers of 0.9. The exit Machnumber of the primary nozzle is about 0.7.

Most important for us is the total pressure survey behind the fan. The averaged value of this survey is used to calculate the nozzle coefficients which are the link between calibration and wind tunnel test. These total pressure distributions however differ quite a lot between calibration tank and wind tunnel. In fig.7 the measured total pressures are plotted versus the perimeter angle for different radial positions of the probes, while the lowest curve of each diagram is the static pressure at the casing. There are plots for the simulated Machnumber 0 (left) and 0.17 (right) measured in the calibration tank (top) and the wind tunnel (bottom). In the calibration tank the total pressure profile is more uniform than in the wind tunnel. The level of total pressures close to the casing is lower and close to the hub is higher for the wind tunnel test results than for the calibration tank values, while the static pressures measured at the casing agree very well for both tests. Probably the bellmouth inlet which was used in the calibration tank provides a much more uniform inlet flow than the inlet used in the wind tunnel. The angle of incidence however has no influence on the total pressure profile behind the fan (fig.8) in the wind tunnel measurement.

Although the total pressure profile behind the fan is quite different between calibration tank and wind tunnel the area-averaged value of the total pressure in plane 15 is quite the same when plotted versus the rotational speed (fig.9). There is no influence of the simulated Machnumber on the fan pressure ratio $F-PR$, defined as the average total pressure behind the fan divided by the total pressure P_0 in front of the engine. Fig.10 shows the difference of averaged total temperatures behind and in front of the fan versus the fan pressure ratio. The total temperature in plane 15 and the total pressure P_{15} allow us to calculate ideal exit conditions in plane 18, by assuming an isentropic expansion in the nozzle to the pressure in the calibration tank.

The fan mass flow is obtained by subtracting the turbine mass flow measured by a sonic nozzle from the total mass flow, measured at the exit of the calibration tank (fig.11). We see that fan mass flow increases with simulated Machnumber for low rotating speeds. When approaching choking conditions of the nozzle the influence of simulated Machnumber decreases. In the same way the gross thrust of the TPS increases with simulated Machnumber (fig.12). The gross thrust is the total exit momentum of fan and turbine nozzles. We obtain it by correcting the balance force with the force due to the pressure difference between tank and laboratory. The fan thrust is evaluated by subtracting the thrust of the turbine from the gross thrust. The turbine thrust is calculated from the measured mass flow, the total conditions measured in plane 5 and a velocity coefficient CV for the turbine nozzle given by the manufacturer. The real exit conditions are calculated with the measured fan mass flow and thrust in the calibration tank.

Dividing the real mass flow by the ideal mass flow we obtain the discharge coefficient CD of the fan nozzle. In the same way we get the velocity coefficient CV by dividing the real velocity (obtained from real thrust and mass flow) by the ideal velocity. The thrust coefficient CT is the product of both (fig.13). When we look to these coefficients we find quite a scatter for nozzle pressure ratios higher than 1.3. Looking to the unreduced data and cross-checking different results we assume some leakage effects in the Scanivalve system which we used to measure the total pressure surveys. In spite of these uncertainties we used a linear approach of CD and CT to calculate the fan thrust from the ideal fan nozzle exit conditions (plane 18) of the TPS for the wind tunnel test.

The total pressure and temperature measurement in plane 15 and plane 5 allow us to calculate the efficiency of fan and turbine (fig.14). These efficiencies were only calculated to cross-check the measured data. We did not make corrections for the boundary layer when averaging the total pressures and we did not take account of the recovery factor of the temperature probes. Therefore the efficiencies calculated for the fan are a little to high and for the turbine to low. The calculation of the efficiency is very sensitive to the accuracy of the temperatures. The scatter of the data lies within the reproducibility of our temperature probes. At high turbine pressure ratios the temperature in plane 5 is lower than the dew-point of the compressed air, in these cases the temperature probe heads probably were effected by condensation and icing.

To compare the force measurements of calibration tank and wind tunnel the mass flow of the fan for the wind tunnel test was calculated using the discharge coefficient obtained in the calibration tank. The exit velocity of the fan nozzle was calculated with the velocity coefficient obtained in the calibration tank and the exit velocity of the turbine nozzle was calculated with the given velocity coefficient. With these values the exit-momentum of fan and turbine nozzles and the inlet-momentum of the fan were calculated (ref.4). Fig.15 shows these forces and all in all the calculated net thrust of the TPS. In fig.16 the calculated net thrust is compared with the measured thrust in the wind tunnel. Probably the difference (fig.17) is mainly due to the losses caused by the nacelle inlet. Of smaller influence may be the change of exit conditions by the wind tunnel flow around the nacelle compared to the calibration tank. An additional correction factor evaluated from the data plotted in fig.17 will help us to calculate the thrust for the wind tunnel test with the half-model.

4. Resumes

The comparison of calibration tank and wind tunnel test results shows good agreement of the static pressures at the walls of the engine. The total pressure distribution in the fan exit plane however is apparently strong influenced by the inlet. Additional corrections obtained in the wind tunnel test with an isolated model engine are necessary to calculate the thrust of the TPS when mounted on the half-model. These test are now in preparation (fig.18) and will give us more information. Beside this measurements with another nacelle geometry are planned and theoretical calculations of the nacelle inlet flow will be done for comparison.

5. References

- 1 Binder, B.
Melzer, E.
Wulf, R. The New Calibration Tank for Engine Simulators
at DFVLR Göttingen.
AGARD-CP-348, 1983, pp. 28
- 2 Baumert, W. The Low-speed Wind Tunnels of DFVLR,
Calibration, Measuring Technique.
DFVLR Report IB 157-74 A 11, 1974
- 3 Burgenüller, W. Grundlagen zur Triebwerksimulation mittels TPS
im Windkanal.
BMFT ZKP-LFK 7911 Ergebnisbericht Nr. 5
VFW Bremen, 1980
- 4 Decher, R.
Gillette, W.B.
Tegeler, D.C. Nacelle-Airframe Integration: Model Testing
for Nacelle Simulation and Measurement Accuracy
AGARD-CP-174, 1975, pp. 26

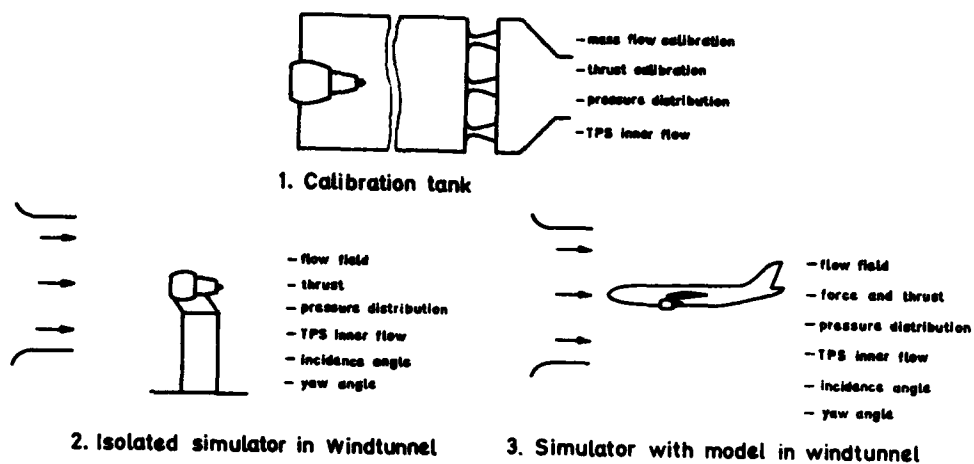


Fig.1: Steps in Simulator Testing

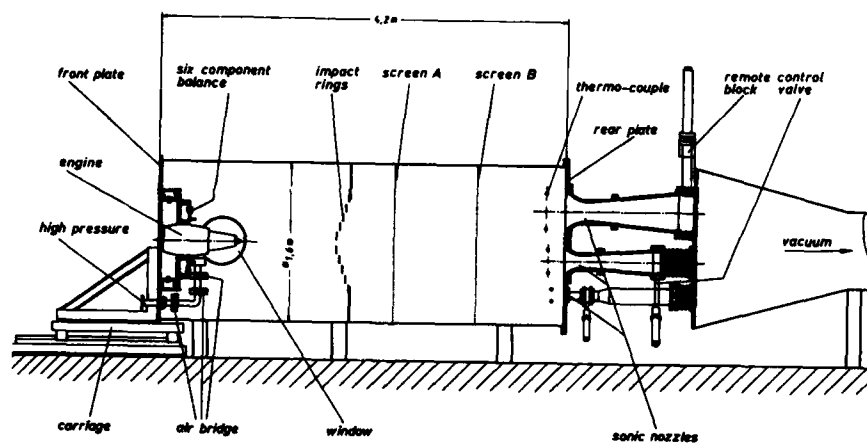


Fig.2: Calibration Tank (ETG)

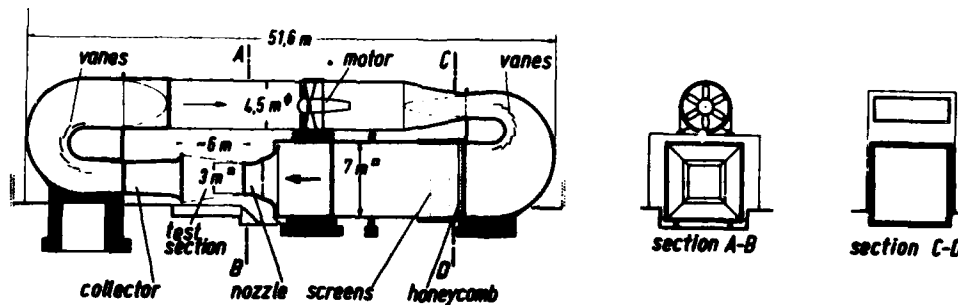
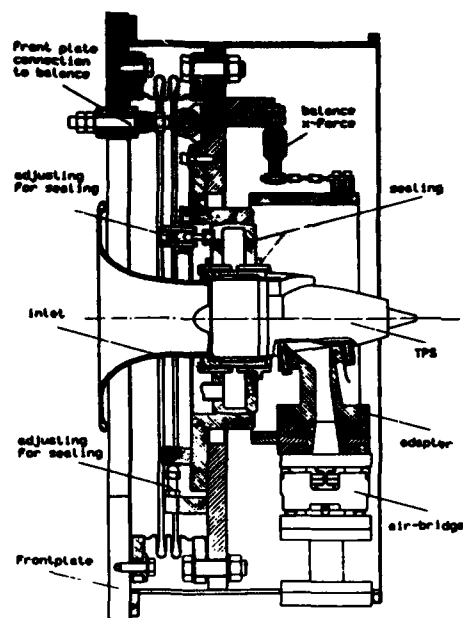
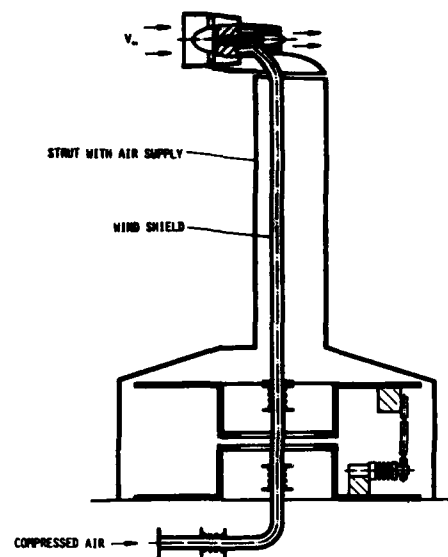


Fig.3: Low Speed Wind Tunnel (NW6)



Calibration Tank



Low Speed Wind Tunnel

Fig.4: TPS-Installation

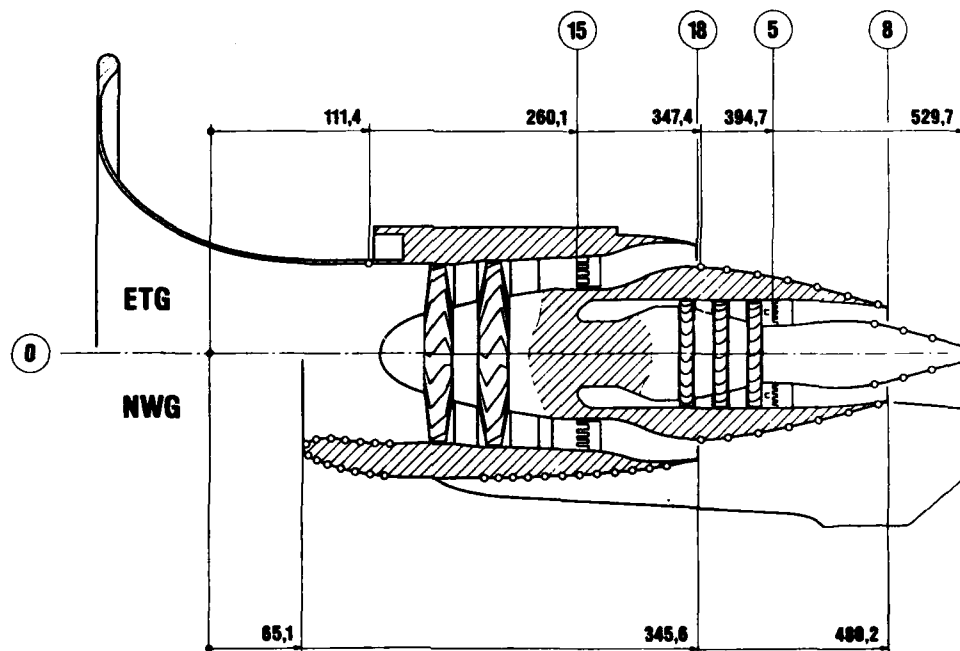


Fig.5: TPS-Instrumentation

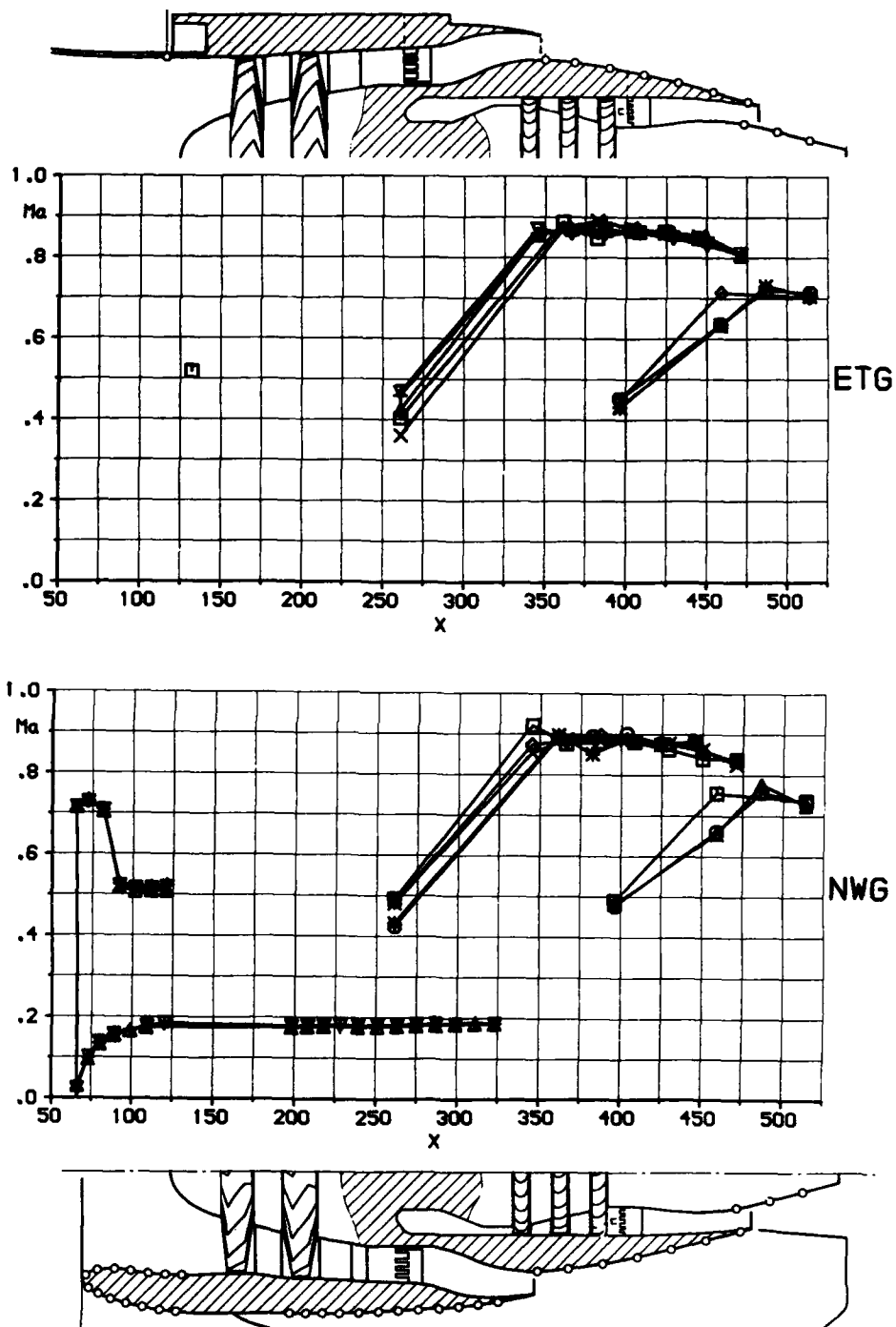


Fig.6: Local Machnumber at Different Angular Positions, NRED = 1, Ma = 0.17

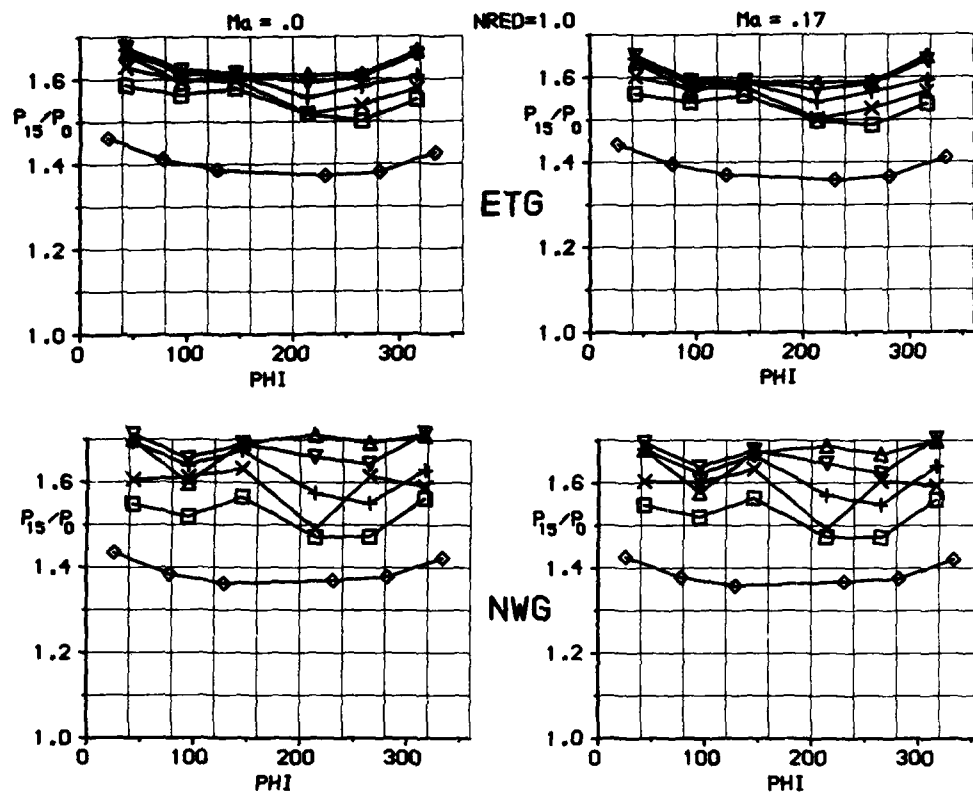


Fig.7: Total and Static Pressure Behind Fan in Calibration Tank (Top) and Low Speed Wind Tunnel (Bottom)

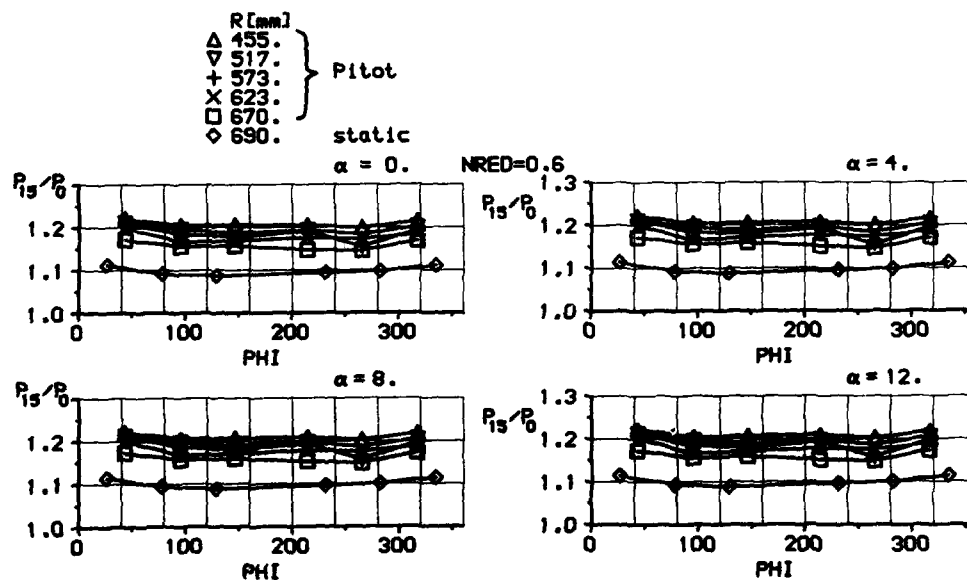


Fig.8: Total and Static Pressure Behind Fan, at Different Angles of Incidence

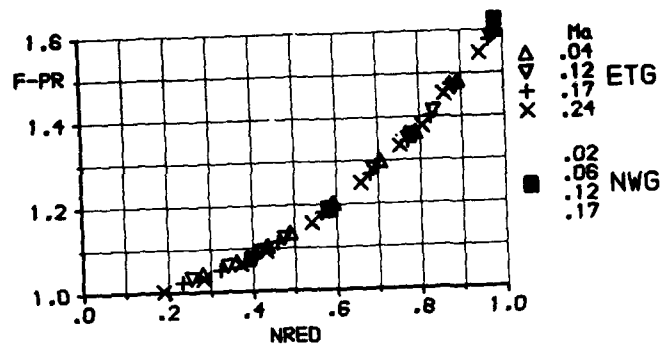


Fig. 9: Fan Pressure Ratio

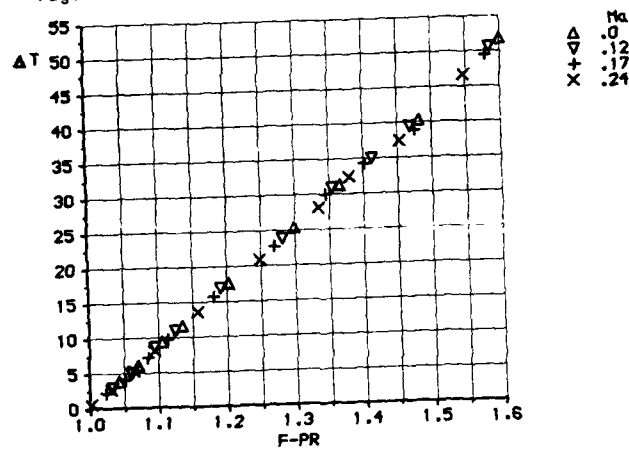


Fig. 10: Fan Temperature Rise

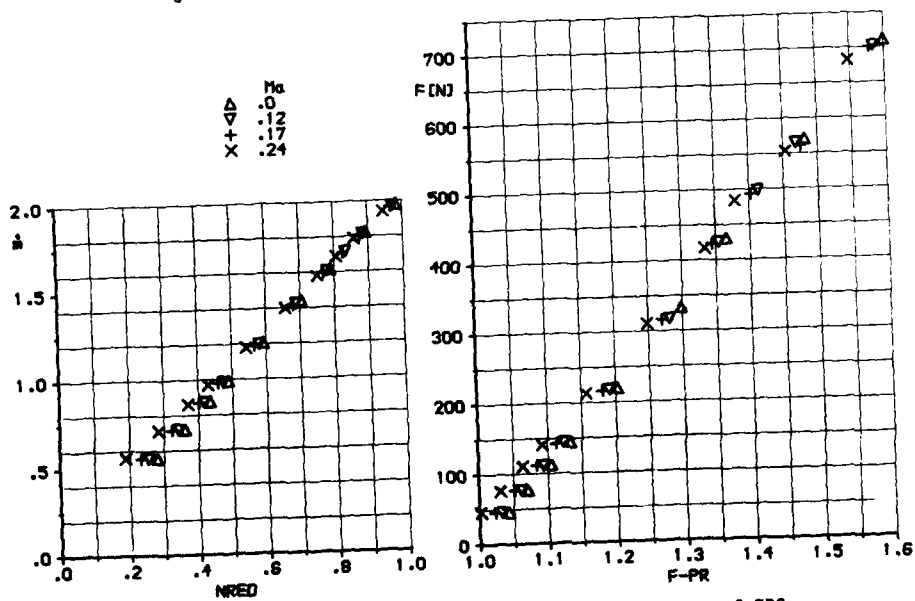


Fig. 11: Fan Massflow

Fig. 12: Gross Thrust of TPS

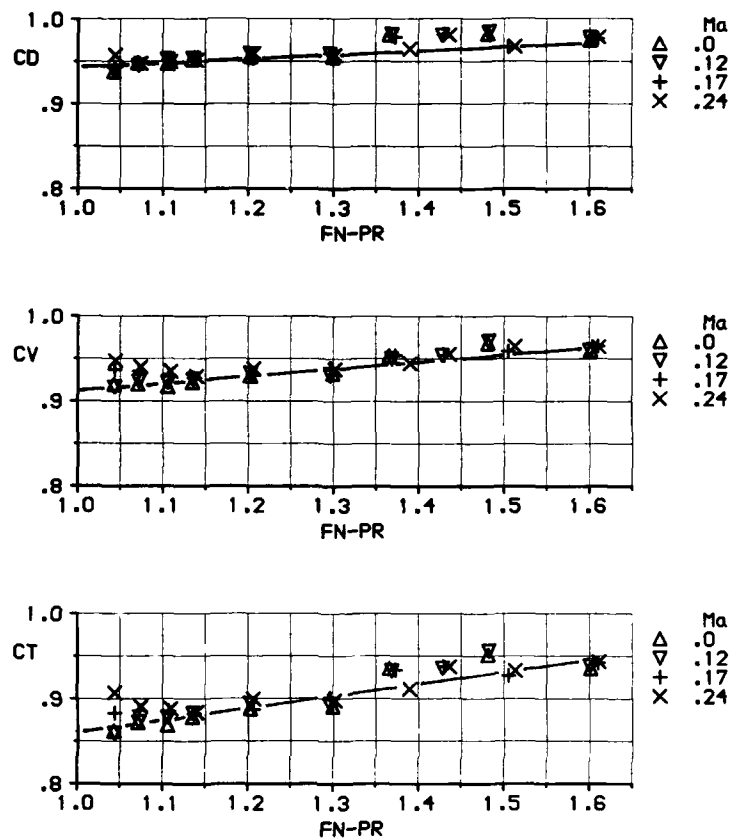


Fig.13: Coefficients of Fan Nozzle

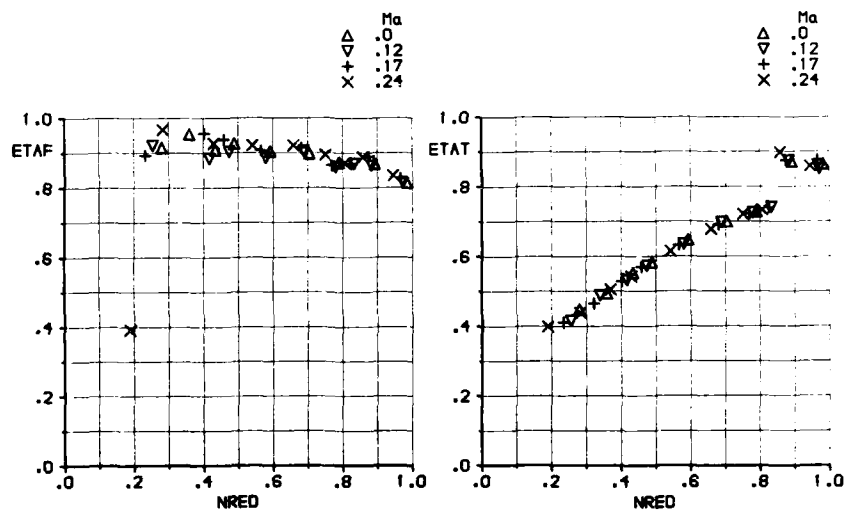


Fig.14: Efficiency of Fan and Turbine

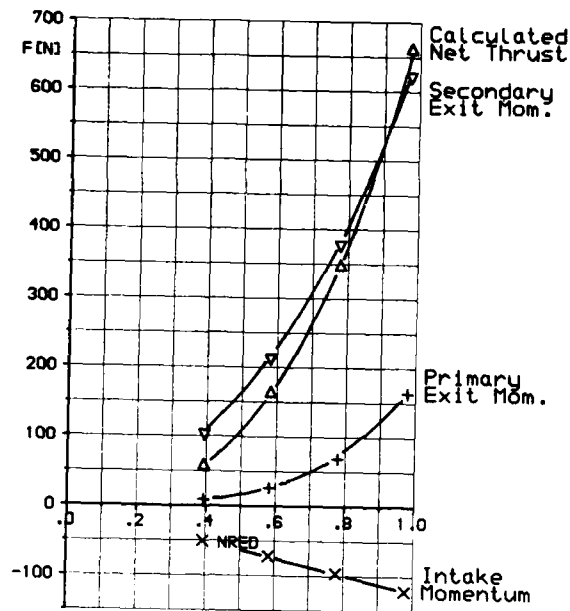


Fig. 15: Calculated Thrust of TPS

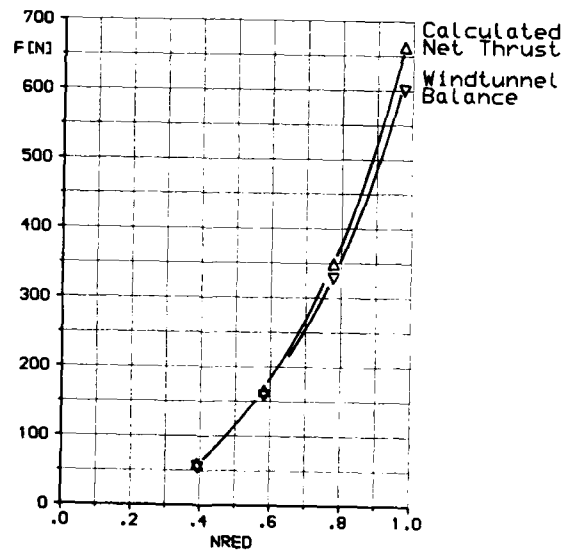


Fig. 16: Calculated and Measured Net Thrust of TPS

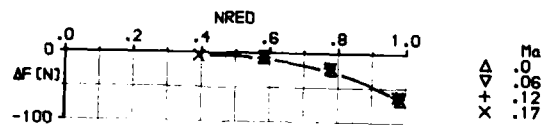


Fig. 17: Difference of Calculated and Measured Thrust

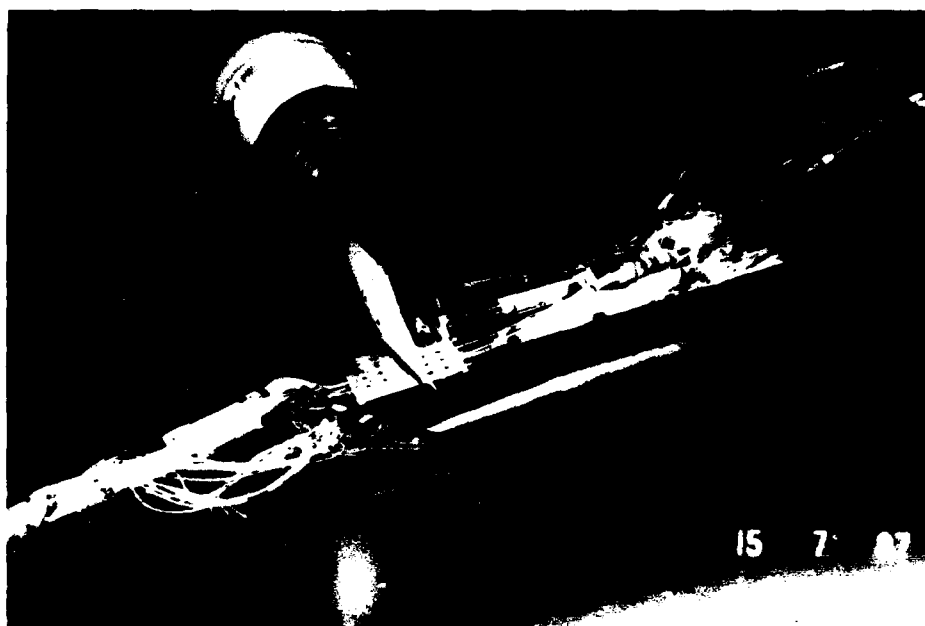


Fig.18: TPS 441 Mounted on Halfmodel Wing

MESURE DES EFFORTS INSTANTANES SUR UNE MAQUETTE SOUMISE A DES VARIATIONS RAPIDES DE COMMANDE

par

J.P.Drevet
ONERA

Centre d'Essais de Modane-Avrieux
B.P. No.25, 73500 Modane, France

et

M.Robert
Aérospatiale, Annexe de Gatines
91370 Verrières le Buisson, France

RESUME

Un nouveau type d'essai industriel est réalisé depuis plusieurs années à la Direction des Grands Moyens d'Essais de l'ONERA. Il s'agit de mesurer les efforts instantanés qui s'exercent sur une maquette en soufflerie lorsqu'elle est soumise à des variations rapides de commande. La méthode consiste à retrancher les efforts d'inertie des efforts globaux mesurés par une balance à jauges extensométriques.

Une maquette de l'AEROSPATIALE a été essayée dans ces conditions en décembre 1984 dans la veine supersonique de S2MA. Ce document présente la phase préparatoire de cet essai et montre les allures des efforts obtenus pendant un tir sans vent.

ABSTRACT

For many years, the Large Facilities Department of ONERA has carried out a new type of industrial test concerning the instantaneous force measurement on a model in a wind-tunnel when it is controlled by quick variations of the parameters. With this method the inertial forces are subtracted from gross-forces measured by a five component strain-gage balance.

An Aérospatiale model has been tested under the conditions in december 1984 in the supersonic test-section of the S2MA wind-tunnel. The preliminary part of the test and the trends of force components obtained during a control by nozzle jets without wind are presented in this paper.

1 - INTRODUCTION

Ce document décrit la phase préparatoire d'un essai dont le but est de mesurer en soufflerie les efforts instantanés qui s'exercent sur une maquette soumise aux variations rapides de commande d'un système de pilotage par jets latéraux.

D'une manière générale, la mesure des efforts en soufflerie fait toujours intervenir un support élastique sur lequel est fixée la maquette. Ce support est constitué par une ligne de dards terminée par une balance.

Les efforts alternés exercés sur la maquette entraînent des oscillations de la ligne de dards. La balance supporte alors, non seulement les efforts aérodynamiques et les efforts de pilotage appliqués à la maquette, mais aussi les efforts d'inertie qui résultent des mouvements de celle-ci.

Pour accéder aux efforts instantanés qui s'exercent sur la maquette, il faut donc retrancher les efforts d'inertie des efforts globaux mesurés par la balance. Les efforts d'inertie sont calculés à partir de la mesure des accélérations et de la connaissance du tenseur d'inertie de la maquette.

Pendant la phase préparatoire d'un tel essai, il faut évidemment définir les conditions de l'expérience, l'instrumentation, la chaîne de mesure et les codes de calcul nécessaires à l'exploitation mais il faut surtout vérifier que la méthode proposée permettra d'atteindre les objectifs fixés. Pour cela, des travaux préliminaires sont effectués ; ils permettent d'une part, de définir la plage de fréquence dans laquelle les mesures sont satisfaisantes et d'autre part, de s'assurer que le montage peut supporter les efforts périodiques auxquels il sera soumis.

Le domaine de validité d'une telle expérience dépend directement de la maquette. Ce document présente la préparation d'une maquette de l'AEROSPATIALE qui sera ensuite essayée dans la veine supersonique de la soufflerie S2MA avec son système de pilotage en fonctionnement dynamique. Ce système utilise un générateur à poudre.

La phase préparatoire se termine par un tir sans vent démontrant la faisabilité de l'essai.

2 - CONDITIONS D'ESSAIS

2.1 - But des essais

Le but de ces essais est de mesurer en soufflerie les efforts instantanés qui s'exercent sur la maquette pendant le fonctionnement du générateur de force dans des conditions qui se rapprochent le plus possible de celles d'un tir réel.

La précision souhaitée pour la mesure de la force développée par le générateur est de l'ordre de 10 %.

2.2 - Moyens d'essais

L'essai a lieu dans la veine supersonique de la soufflerie S2MA à une pression génératrice de 1,7 bar (voir figure 1).

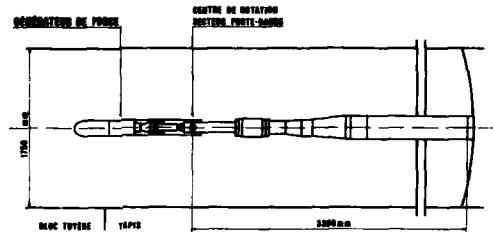


Fig. 1 - Montage de la maquette dans S2MA.

Les paramètres de l'essai sont :

- l'incidence variable de 0° à 10°,
- l'angle de roulis variable de 0° à 45°,
- les ordres du générateur de force correspondant à une manoeuvre en tangage et (ou) en lacet, ou à une absence de manoeuvre.

Les deux premiers paramètres, réglés avant l'essai, sont maintenus constants pendant la durée du tir.

2.3 - Description succincte de la maquette (voir fig.2)

La maquette représente extérieurement le missile à l'échelle 1. La portion cylindrique du fuselage en amont des voilures est raccourcie, pour éviter tout risque de perturbation de l'écoulement sur la partie arrière par l'onde de choc d'ogive réfléchiée par les parois.

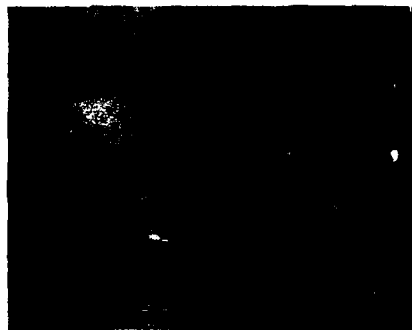


Fig. 2 - Vue de la maquette dans la veine supersonique de S2MA.

Elle comprend trois parties :

- la partie arrière sur laquelle se fixent la voilure et les gouvernes ; cette partie supporte aussi la fixation de la maquette sur la ligne de dards,
- la partie centrale qui constitue l'ensemble générateur,
- la partie avant dans laquelle se trouve le dispositif d'alimentation de la commande du commutateur.

Le générateur de force se compose lui-même :

- d'un générateur haute pression,
- d'une chambre basse pression où les gaz sont détendus ; cette chambre correspond à l'adaptation du générateur pour les essais en soufflerie de manière à respecter le taux de détente des tuyères,
- d'un commutateur répartissant les gaz détendus entre quatre tuyères disposées radialement à 90° les unes par rapport aux autres, suivant les quatre configurations représentées (fig.3) :

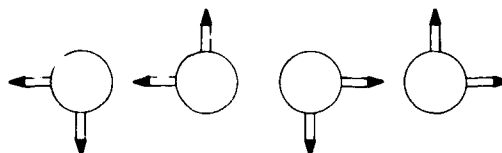


Fig.3 - Configurations d'éjection des gaz.

La commutation d'une configuration à l'autre s'effectue en moins de 10 ms.

Pendant le fonctionnement du générateur, un train de sollicitations représentatives du pilotage est commandé sur chacun des deux plans des tuyères ; un exemple est donné figure 4.

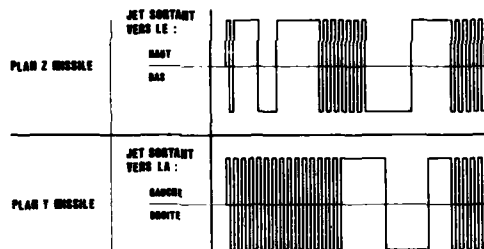


Fig.4 - Commande des tuyères.

3 - INSTRUMENTATION ET CHAÎNE DE MESURE

3.1 - Instrumentation

La définition technologique des équipements mécaniques et électromécaniques de la maquette n'est pas abordée, seul l'aspect mesure est développé.

3.1.1 - Balance

Pour cet essai la traînée du missile n'est pas demandée ; une balance cinq composantes est réalisée sans pont de X afin que la raideur du montage soit la plus importante possible. Cette balance est un barreau d'acier de 92 mm de diamètre sur lequel sont taillées des méplats recevant les jauges de contrainte. Elle a une capacité de ± 73500 N en effort de dérive et de portance ; ± 13500 Nm pour les moments de lacet et de tangage et de ± 2500 Nm en roulis. Avec une alimentation des ponts de jauges de 8V et une amplification des signaux de mesure de 1000 les coefficients de sensibilité sont de 2,8 N/mV pour les efforts et de 0,4 Nm/mV pour les moments.

3.1.2. Accéléromètres

L'exploitation des mesures repose sur l'hypothèse de vibrations de faibles amplitudes (de l'ordre de $\pm 0,5^\circ$) et d'une rigidité absolue de la maquette. Dans ce cas, six accéléromètres monodirectionnels suffisent à déterminer les six accélérations nécessaires aux calculs des efforts d'inertie.

Les accéléromètres sont positionnés deux par deux au voisinage du centre de gravité de la partie passée. La distance entre deux accéléromètres est de 310 mm en tangage et en lacet et de 150 mm en roulis (voir fig.5)

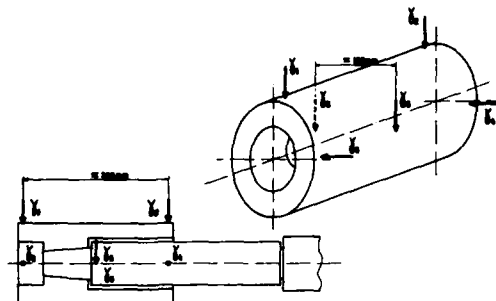


Fig. 5 - Position des accéléromètres.

Le choix du type d'accéléromètre est fait principalement à partir de ses caractéristiques dimensionnelles et de sa sensibilité ; ce choix s'est porté sur un capteur piézorésistif ayant une sensibilité de $0,25 \text{ mV} / (\text{m/s}^2)$ et une bande passante de 0 à 1200 Hz.

3.1.3 - Autres capteurs

Plusieurs grandeurs sont aussi mesurées pour analyser le fonctionnement du générateur. Il s'agit :

- de la pression de la chambre basse pression,
- des pressions mesurées en sortie de tuyère,
- des ordres de commande.

Pression chambre

L'allure de l'effort développé par le générateur dépend directement du niveau de la pression de la chambre et de son évolution. Un capteur mesure cette pression.

Pressions tuyères

Un capteur de pression instationnaire est monté à la sortie de chaque tuyère. Cette mesure est un contrôle de la bonne exécution de la commande ; elle permet aussi de vérifier que le jet a eu le temps de s'établir.

Ordres de commande

Les ordres de commande du commutateur sont numérisés. La comparaison de ces ordres avec les signaux des capteurs de pression des tuyères permet de déterminer les temps de commutation.

3.2 - Chaînes de mesure et acquisition

Une chaîne de mesure classique permet de mesurer les valeurs moyennes des paramètres nécessaires à la conduite de l'essai (références soufflerie, valeurs moyennes des efforts, ...) Les différentes mesures sont filtrées par un filtre passe-bas calé à 1 Hz et numérisées à raison de deux points par seconde.

Une chaîne de mesure dynamique (voir fig.6) est mise en oeuvre spécialement pour ces essais. Elle permet d'acquérir 25 signaux qui sont les signaux des ponts de la balance, des accéléromètres, des capteurs de pression (tuyères, chambre basse-pression) et des organes de commande (courants de commande, mise à feu ...). Elle se différencie de la précédente par la fréquence de coupure des filtres passe-bas qui sont calés à 100 Hz sur les voies de mesure utilisées pour le dépouillement des efforts et à 1000 Hz pour les autres voies (courants de commande, pressions dans les tuyères ...) et aussi par la fréquence d'échantillonnage qui est de 1000 Hz par voie. Il faut noter que les signaux des accéléromètres passent par un étage de préamplification puis sont filtrés avant d'être amplifiés pour obtenir le gain désiré, ceci afin d'éviter des saturations. Un magnétophone analogique est associé à cette chaîne ; il permet d'enregistrer 14 voies de mesure avec une bande passante allant de 0 à 1000 Hz.

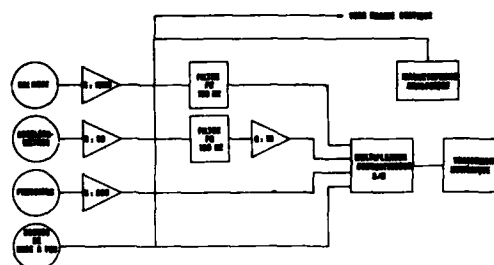


Fig 6 - Chaîne de mesure dynamique.

4 - MISE EN EQUATIONS

4.1 - Hypothèses

Le modèle mathématique retenu pour la mise en équations est fondé sur les hypothèses suivantes :

- la maquette est un solide indéformable,
- les repères balance et maquette ont leurs axes parallèles,
- la maquette admet une symétrie de révolution d'ordre 4.

4.2 - Notations

Le trièdre de référence est donné fig.7

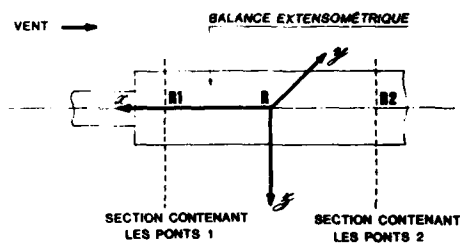


Fig. 7 - Trièdre de référence.

Notations	Désignations	Unités
R ou C.R.B	Centre de référence balance	
R_1, R_2	Centre des ponts (1) et (2) de la balance	
ΔX	Distance entre les ponts 1 et 2	m
$M_{1,2}$	Masse située à l'amont de la section 1,2	kg
$Cd_{G1,2}$	Centre de gravité de la masse $M_{1,2}$	
$XG_{1,2}$	Abscisse du centre de gravité dans le trièdre ($R_{1,2} \ x, y, z$)	m
$TG_{1,2}$	Tenseur d'inertie exprimé en $Cd_{G1,2}$ $TG_1 = \begin{bmatrix} A & 0 & 0 \\ 0 & B_1 & 0 \\ 0 & 0 & B_1 \end{bmatrix}$ $TG_2 = \begin{bmatrix} A & 0 & 0 \\ 0 & B_2 & 0 \\ 0 & 0 & B_2 \end{bmatrix}$	m^2kg
$\vec{T}_{G1,2}$	Accélération absolue du centre de gravité $Cd_{G1,2}$ (projection dans un repère lié à la balance : $\vec{V}_{G1,2}$ $\vec{Z}_{G1,2}$)	m/s^2
$\vec{\Omega}(p, q, r)$	Vecteur de rotation instantanée de la maquette (projections dans le repère maquette)	rad/s
$\delta_1 \ 1 \leq i \leq 6$	Désignation des accéléromètres	
YB	Composantes du torseur s'exerçant sur le dard (sans indice	N
ZB		N
LB	au centre balance R, avec indice aux sections correspon-	Nm
MB ou MB _{1,2}	dantes 1 ou 2)	Nm
NB ou NB _{1,2}		Nm
YA	Composantes du torseur s'exerçant sur la maquette (propul-	N
ZA	sion + aérodynamique) même remarque que ci-dessus	N
LA		Nm
MA ou MA _{1,2}		Nm
NA ou NA _{1,2}		Nm
TETA (Θ)	Variation d'attitude de la maquette dans le plan vertical	rad
$\theta_{1, 2, 3}$	Coordonnées généralisées	rad
$\omega_{1, 2, 3}$	Pulsation propre des 3 premiers modes	rad/s
$\alpha_{1, 2, 3}$	Amortissement réduit des 3 premiers modes	%/..
$\mu_{1, 2, 3}$	Masse généralisée des 3 premiers modes	m^2kg
$d_{1, 2, 3}$	Distance centre de référence balance R - centre de de rotation du mode	m
Δt	période d'échantillonnage	s
ZEX	Effort d'excitation appliqué à la maquette pendant	N
YEX	les essais de vibrations	N
LXEX	Moment d'excitation appliqué à la maquette pendant les	Nm
MYEX	essais de vibrations	Nm
NEX		Nm
SMB _{1, 2}	Signal du pont de tangage de la section 1,2	mV
SG _i	Signal de l'accéléromètre i	
tm	temps de montée des signaux trapézoïdaux	ms

Un point placé au dessus de la variable indique la dérivée première de cette variable par rapport au temps, un double point indique la dérivée seconde.

4.3 - Equations

Les équations sont des équations de moment obtenues en exprimant le théorème du moment cinétique au droit des sections 1 et 2 où sont collés les ponts de jauges de la balance.

Considérons la section 1 par exemple.

$$\frac{d}{dt} \{ I_{G1} \dot{\Omega} \} = \sum \text{moment des forces extérieures} = \vec{R_1 G_1} \wedge M_1 \cdot \vec{T_{G_1}}$$

Le terme $\vec{R_1 G_1} \wedge M_1 \cdot \vec{T_{G_1}}$ provient du fait que le centre de gravité de la partie pesée n'est pas confondu avec R_1 .

Les moments des forces extérieures sont :

- les moments dus aux forces de propulsion et aux forces aérodynamiques MA_1 , NA_1 ; ce sont les moments cherchés.

- les moments représentant l'action du dard sur la maquette - MB_1 et $-NB_1$; ces moments sont mesurés grâce aux ponts de jauges collés en 1. Ces moments sont calculés à partir d'une matrice déduite d'un étalonnage statique.

Remarque

Le dépouillement de la partie fluctuante du signal de chaque pont de la balance est fait par rapport à la valeur moyenne du signal de ce pont mesurée juste avant le tir. La pesanteur n'intervient pas dans les équations.

Les équations sont les suivantes :

- au droit de la section 1

$$MA_1 = B_1 \cdot \dot{q} + r \cdot p \cdot (A - B_1) + X_{G1} \cdot M_1 \cdot \ddot{z}_{G1} + MB_1$$

$$NA_1 = B_1 \cdot \dot{r} + p \cdot q \cdot (B_1 - A) - X_{G1} \cdot M_1 \cdot \ddot{y}_{G1} + NB_1$$

- au droit de la section 2

$$MA_2 = B_2 \cdot \dot{q} + r \cdot p \cdot (A - B_2) + X_{G2} \cdot M_2 \cdot \ddot{z}_{G2} + MB_2$$

$$NA_2 = B_2 \cdot \dot{r} + p \cdot q \cdot (B_2 - A) - X_{G2} \cdot M_2 \cdot \ddot{y}_{G2} + NB_2$$

$$LA = A \cdot \dot{p} + LB$$

Les efforts et moments (aérodynamique + propulsion) qui s'appliquent sur la maquette au centre de référence balance sont alors :

$$YA = \frac{NA_2 - NA_1}{\Delta X} \quad ZA = \frac{MA_2 - MA_1}{\Delta X}$$

$$MA = \frac{MA_1 + MA_2}{2} \quad NA = \frac{NA_1 + NA_2}{2}$$

Ce torseur sera comparé au torseur correspondant à l'action de la maquette sur le dard ; il se calcule d'une manière semblable à partir des moments mesurés par la balance :

$$YB = \frac{NB_2 - NB_1}{\Delta X}$$

Les termes tels que $r \cdot p \cdot (A - B_1)$ et $p \cdot q \cdot (B_1 - A)$ sont négligeables dans l'hypothèse des petits mouvements ; cette hypothèse est vérifiée a posteriori.

4.4 - Mesure des accélérations

Les accéléromètres sont montés sur une pièce très rigide appelée pièce intermédiaire fixée elle-même sur la balance (voir fig.5). Soit M le point où est placé l'accéléromètre : G_1 M (a_1 , b_1 , c_1)

Exprimeons l'accélération au point M :

$$\vec{\Gamma}_M \begin{vmatrix} Y_{G1} + a_1 \cdot (p \cdot q + r) - b_1 \cdot (r^2 + q^2) + c_1 \cdot (qr - p) \\ Z_{G1} + a_1 \cdot (p \cdot q - q) + b_1 \cdot (qr + p) - c_1 \cdot (p^2 + q^2) \end{vmatrix}$$

L'hypothèse des petits mouvements nous permet de négliger les termes p^2 , q^2 , r^2 , pq ... devant les termes p , q et r .

Prenons l'exemple de la mesure \ddot{Z}_{G1} et \dot{q} . Deux accéléromètres n°1 et 2 sont fixés sur la pièce intermédiaire avec leur axe sensible orienté selon z . Soient z_1 et z_2 , les accélérations mesurées par les accéléromètres 1 et 2 :

$$\Gamma_{z1} = \ddot{Z}_{G1} - a_1 \cdot \dot{q} \quad ; \quad \Gamma_{z2} = \ddot{Z}_{G1} - a_2 \cdot \dot{q}$$

Les accélérations angulaires et linéaires sont calculées à partir de ces deux relations :

$$\dot{q} = \frac{\Gamma_{z1} - \Gamma_{z2}}{a_2 - a_1}$$

$$\ddot{Z}_{G1} = \frac{\Gamma_{z1} + \Gamma_{z2}}{2} + \frac{a_1 + a_2}{2} \cdot \dot{q}$$

4.5 - Calcul de l'attitude instantanée de la maquette

Le torseur Y_A, Z_A, L_A, M_A, N_A correspond à la partie fluctuante des efforts qui s'exercent sur la maquette.

$$\begin{bmatrix} Y_A \\ L_A \\ N_A \end{bmatrix} = \begin{bmatrix} \text{Effet net du propulseur} \end{bmatrix} + \begin{bmatrix} \Delta \text{aéro dû aux mouvements} \\ \text{de la maquette} \end{bmatrix}$$

La partie [Effet net du propulseur] correspond aux efforts de propulsion et aux efforts aérodynamiques induits par la présence des jets.

La partie [$\Delta \text{aéro} \dots$] correspond aux efforts aérodynamiques induits par les mouvements de la maquette pendant le tir. Les efforts aérodynamiques qui en découlent doivent être retranchés du torseur $[Y_A, \dots, N_A]$ de manière à obtenir l'effet net du propulseur. Pour cela, il faut déterminer les variations d'attitude de la maquette (θ) dans le plan vertical, (ψ) dans le plan horizontal. Ces variations sont calculées à partir d'une représentation modale de la ligne de dards avec la maquette et du torseur aérodynamique $[Y_A, \dots, N_A]$. Le mouvement de la structure réelle est décrit dans le plan vertical et dans le plan horizontal par la superposition des trois premiers modes propres.

Dans le plan vertical, il vient :

$$\ddot{\theta}_1 + 2\alpha_1 \omega_1 \dot{\theta}_1 + \omega_1^2 \cdot \theta_1 = (M_A - Z_A \cdot d_1) / \mu_1$$

$$\ddot{\theta}_2 + 2\alpha_2 \omega_2 \dot{\theta}_2 + \omega_2^2 \cdot \theta_2 = (M_A - Z_A \cdot d_2) / \mu_2$$

$$\ddot{\theta}_3 + 2\alpha_3 \omega_3 \dot{\theta}_3 + \omega_3^2 \cdot \theta_3 = (M_A - Z_A \cdot d_3) / \mu_3$$

L'algorithme d'intégration de ces équations est le suivant :

$$\theta_1(n+1) = \frac{1}{\frac{1}{\Delta t^2} + \frac{\alpha_1 \omega_1}{\Delta t}} [(M_A(n) - Z_A(n) \cdot d_1) / \mu_1 - \omega_1^2 \theta_1(n) + \frac{\alpha_1 \omega_1}{\Delta t} \cdot \theta_1(n-1) - (\theta_1(n-1) - 2\theta_1(n)) / \Delta t^2]$$

La variation d'attitude dans le plan vertical est alors :

$$\theta = \theta_1 + \theta_2 + \theta_3$$

Le calcul de la variation instantanée d'attitude dans le plan horizontal est analogue.

5 - PRESENTATION DES TRAVAUX PRELIMINAIRES

Pour ces travaux le dispositif d'essai est accroché à un plot fixé lui-même sur un massif de béton. Il comprend la maquette inerte et la ligne de dards qui sera effectivement utilisée au cours des essais dans la soufflerie et la chaîne de mesure instationnaire.

Ces travaux ont un triple but, ils doivent permettre :

- d'identifier dynamiquement le montage,
- de valider la méthode de dépouillement et définir la fonction de transfert du dispositif de mesure,
- de vérifier la tenue du montage en excitant celui-ci avec une force sinusoïdale dont l'amplitude et la fréquence sont voisines de celles prévues avec le générateur.

5.1 - Identification dynamique du montage

L'identification dynamique du montage a pour but de mesurer les fréquences, les formes, les masses généralisées et les amortissements des premiers modes dans les plans vertical et horizontal. En roulis, seules les fréquences sont relevées.

La connaissance de ces grandeurs permet de construire le modèle mathématique décrivant le mouvement instantané de la maquette et de préciser les bandes de fréquence à éviter pour le fonctionnement du générateur de force afin de ne pas exciter un mode propre du montage. Il ne faut cependant pas oublier, pour cette expérience, que le support de la ligne de dards n'est pas le secteur porte-dards de la soufflerie et qu'une identification succincte est nécessaire au moment de l'entrée en veine.

L'excitation de la ligne de dards est faite à l'aide d'un pot électrodynamique équipé d'une bobine pouvant développer un effort maximal de 200 N.

Une première excitation est effectuée en bruit blanc dans une bande de fréquence 0 - 200 Hz de manière à relever les fréquences propres. Ces fréquences sont ensuite mesurées avec précision en excitant le montage par une force sinusoïdale et en recherchant la résonance de phase entre le courant d'excitation et la réponse d'un accéléromètre monté sur la maquette. Trois fréquences propres sont obtenues dans la bande de fréquence 0 - 100 Hz tant dans le plan vertical que dans le plan horizontal.

Les formes propres de chaque mode sont relevées avec un capteur de vitesse ; ce qui permet entre autres de déterminer le centre de rotation de la maquette dans chaque mode.

La mesure de l'amortissement est obtenue par la méthode des oscillations libres. Après un lâcher, le décrétement logarithmique de la réponse d'un accéléromètre de la maquette est mesuré sur les premières oscillations.

Les masses généralisées sont déterminées en utilisant la méthode des fréquences déplacées. Elles sont normées pour un déplacement angulaire de 1 radian au niveau de la maquette.

Le tableau ci-dessous présente les résultats obtenus dans le plan longitudinal :

N°	fréquences f (Hz)	Masses gén. μ (m ² kg)	amortiss ^t α %	Centre de rot. d (m)
1	7,42	1128	2,1	- 1,563
2	25,14	91,3	2,5	0,330
3	61,91	23,5	2,4	0,552

Pour l'excitation en roulis, deux pots électrodynamiques sont pilotés en opposition de phase.

5.2 - Validation de la méthode de dépouillement

La validation de la méthode d'essai comporte plusieurs phases. Il s'agit tout d'abord d'exciter la maquette avec une force sinusoïdale connue et de retrouver cette force par le dispositif de mesure mis en oeuvre. Ces mesures sont effectuées à différentes fréquences de manière à construire la fonction de transfert du dispositif. Ensuite le montage est excité par une force alternative ayant une forme plus proche des efforts développés par le générateur.

Pendant ces essais la méthode de calcul de l'attitude instantanée de la maquette est contrôlée grâce aux accéléromètres qui l'équipent.

5.2.1 - Excitation sinusoïdale

L'excitation en mode sinusoïdal se fait en tangage, en lacet, en roulis et ensuite en combinant les excitations de tangage et de lacet.

Le montage est excité par un pot électrodynamique à champ permanent qui permet de mesurer la force appliquée dans une bande de fréquence allant de 0 à 200 Hz. Avant l'essai, un tarage de cette force est effectué en mode statique en envoyant un courant permanent dans la bobine.

Une première série d'essais dans une bande de fréquence allant jusqu'à 200 Hz montre qu'au delà de 130 Hz les résultats obtenus sont nettement en dehors de la précision demandée. Les filtres analogiques passe-bas de la chaîne de mesure sont alors calés à 100 Hz et tous les essais sont effectués dans la bande de fréquence 0 - 100 Hz.

Pour le premier point de mesure effectué à une fréquence de 5 Hz tous les signaux (balance, accéléromètres, excitateur) sont en phase et les corrections d'inertie permettent de retrouver la force d'excitation d'une manière satisfaisante. Le second point est acquis à une fréquence de 7 Hz voisine de la première fréquence propre. Les figures 8 et 9 montrent les résultats en effort et en moment.

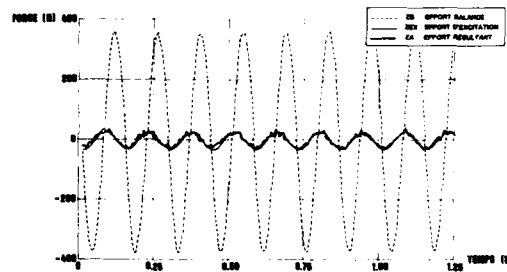


Fig. 8 - Excitation sinusoïdale en tangage, fréquence d'excitation : 7 Hz.

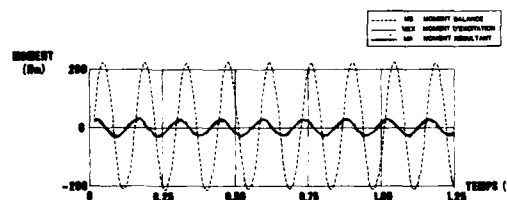


Fig. 9 - Excitation sinusoïdale en tangage, fréquence d'excitation : 7 Hz

La présentation de ces deux figures et des figures suivantes relatives à l'excitation forcée reste identique à savoir :

- l'excitation (ZEX, MEX) est en trait fin,
- la réponse balance (ZB, MB) est en trait pointillé,
- l'effort ou le moment résultant de l'exploitation (ZA, MA) est en trait fort.

L'expérience est satisfaisante lorsque la force d'excitation et l'effort résultant (combinaison de l'effort balance et des efforts d'inertie) se superposent.

Revenons aux figures 8 et 9. A proximité d'un mode, le niveau d'excitation est réduit de manière à limiter l'amplitude des mouvements de la maquette. L'amplitude de l'effort d'excitation (ZEX) est égale à 25 N alors que l'effort balance (ZB) a une am-

plitude de 350 N ce qui représente un coefficient de surtension ZB/ZEX égal à 14. De plus la réponse de la balance est pratiquement déphasée de 90° par rapport à l'excitation ce qui indique la proximité du mode propre. La correction de l'effort balance par les efforts d'inertie permet de retrouver l'effort d'excitation.

Au voisinage du premier mode propre, la méthode proposée donne d'excellents résultats.

Après la première fréquence propre, la réponse de la balance est en opposition de phase avec l'excitation, le niveau de la réponse balance étant inférieur au niveau d'excitation. Les figures 10 et 11 illustrent cette plage de fréquence ; la méthode proposée permet toujours de retrouver l'effort d'excitation avec une bonne précision.

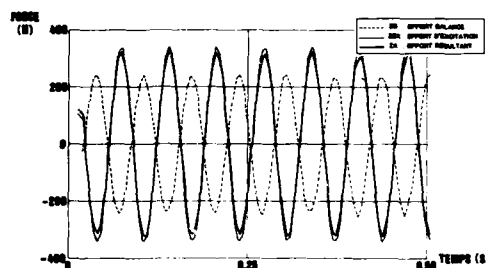


Fig. 10 - Excitation sinusoïdale en tangage, fréquence d'excitation : 15 Hz.

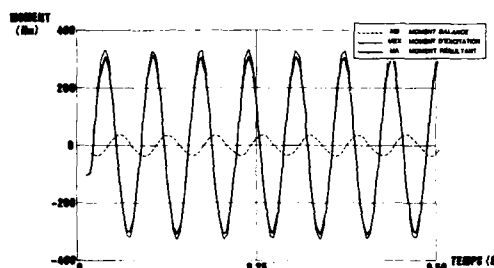


Fig. 11 - Excitation sinusoïdale en tangage, fréquence d'excitation : 15 Hz.

Au passage du deuxième mode vers 25 Hz, les écarts observés entre la force d'excitation et la force calculée sont plus importants (voir fig. 12 et 13). L'effort résultant n'a plus une forme de sinusoïde alors que l'effort imposé et l'effort balance sont toujours sinusoïdaux. Ce phénomène est moins accentué pour les moments (fig. 13) ; la correction d'inertie permet de retrouver le niveau du moment d'excitation mais il apparaît un déphasage d'environ 30° entre le moment d'excitation et le moment résultant.

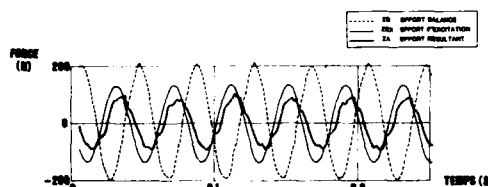


Fig. 12 - Excitation sinusoïdale en tangage, fréquence d'excitation : 25 Hz

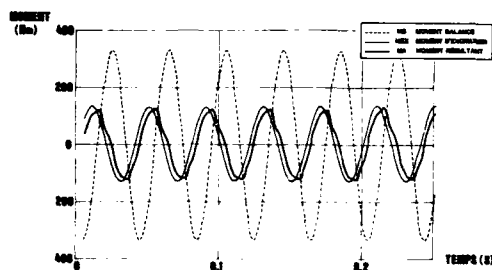


Fig. 13 - Excitation sinusoïdale en tangage, fréquence d'excitation : 25 Hz

Dès que la fréquence d'excitation est supérieure à la fréquence du deuxième mode, l'effort d'excitation et l'effort calculé sont à nouveau en phase ; il faut cependant noter pour certaines fréquences une perte de niveau pour l'effort calculé de 10 % par rapport à l'effort imposé. A 45 Hz, les résultats sont satisfaisants (voir fig. 14 et 15). La figure 15 montre que la réponse en moment de la balance est pratiquement nulle.

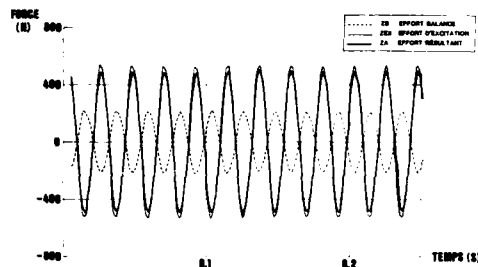


Fig. 14 - Excitation sinusoïdale en tangage, fréquence d'excitation : 45 Hz

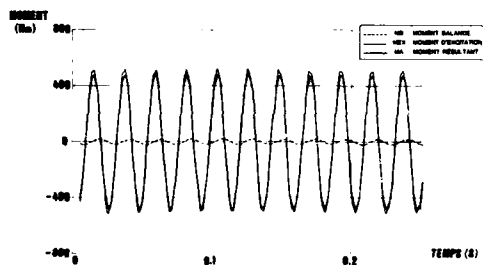


Fig. 15 - Excitation sinusoïdale en tangage, fréquence d'excitation : 45 Hz

D'une manière générale, ce constat est valable pour la plage de fréquence au-delà de 45 Hz. La réponse de la balance est quasi nulle, l'effort résultant provient essentiellement des mesures accélérométriques.

Les écarts observés au voisinage du troisième mode (60 Hz) sont accentués par rapport à ceux observés au passage du second mode. Au delà de 60 Hz, l'écart de phase entre l'effort d'excitation et l'effort calculé est de l'ordre de 10° et la perte de niveau de l'effort calculé de l'ordre de 30 %. Les figures 16 et 17 présentent les résultats obtenus à 90 Hz.

Tous ces points de mesure permettent d'établir la fonction de transfert de ce système en comparant les efforts et moments résultants aux efforts et moments imposés. La fonction de transfert des moments est présentée figure 18. Cette méthode de mesure permet dans le cadre de cet essai d'effectuer des mesures dynamiques avec la précision demandée ($\pm 10\%$) jusqu'à une fréquence de 60 Hz. Pour les fréquences supérieures jusqu'à 100 Hz, la méthode de mesure sous-estime les efforts et moments d'excitation.

AD-A202 496

AERODYNAMIC DATA ACCURACY AND QUALITY: REQUIREMENTS AND
CAPABILITIES IN WIND TUNNEL TESTING(U) ADVISORY GROUP
FOR AEROSPACE RESEARCH AND DEVELOPMENT NEUILLY

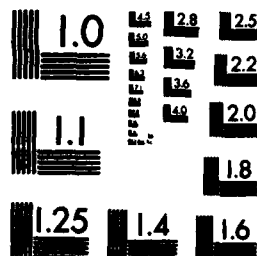
5/6

UNCLASSIFIED

JUL 88 AGARD-CP-429

F/G 1/1

NL



MICROCOPY RESOLUTION TEST CHART
NATIONAL BUREAU OF STANDARDS-1963-A

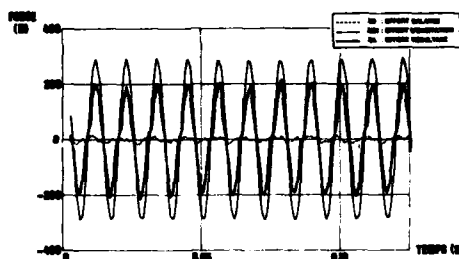


Fig. 16 - Excitation sinusoidale en tangage, fréquence d'excitation : 90 Hz

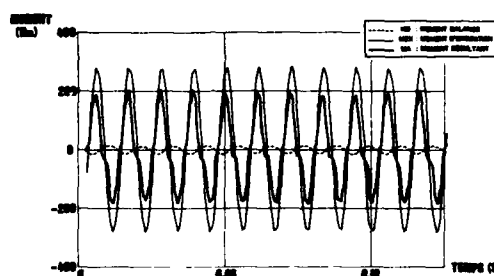


Fig. 17 - Excitation sinusoidale en tangage, fréquence d'excitation : 90 Hz

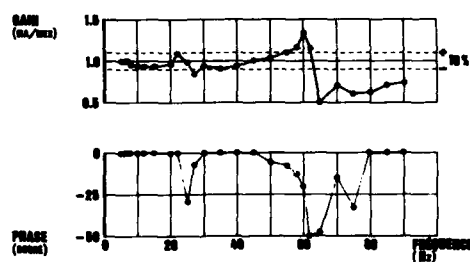


Fig. 18 - Fonction de transfert en tangage.

. Excitation en lacet

Il y a une symétrie parfaite entre le plan de tangage et le plan de lacet tant du point de vue des inerties de la maquette que des voies de mesure elles-mêmes. Les résultats sont comparables à ceux obtenus en tangage ; les fonctions de transfert sont identiques.

. Excitation en roulis

La première fréquence propre en roulis est à 90 Hz. Pour les basses fréquences, les corrections d'inertie sont faibles voire nulles ; à 10 Hz le moment d'excitation, le moment vu par la balance et le moment calculé sont pratiquement confondus (voir fig.19)

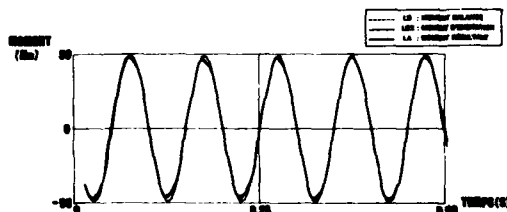


Fig. 19 - Excitation sinusoidale en roulis, fréquence d'excitation : 10 Hz.

Les résultats obtenus sont satisfaisants jusqu'à vers 60 Hz (voir fig. 20). A 70 Hz les résultats sont erronés, le rapport entre le moment résultant et le moment imposé (LA/LRX) est égal à 3. Des mesures accélérométriques faites en divers points de la maquette, notamment sur les gouvernes indiquent que celle-ci n'est plus indéformable ; le modèle utilisé est mis en défaut. Pour les fréquences plus élevées, les résultats redevennent corrects, comme le montre la figure 21 pour une excitation de 90 Hz. La fonction de transfert pour le moment de roulis est présentée figure 22.

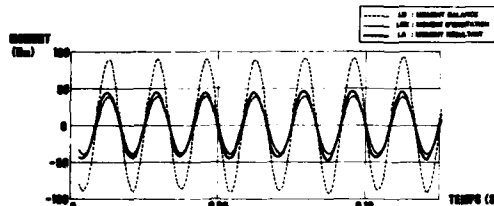


Fig. 20 - Excitation sinusoïdale en roulis, fréquence d'excitation : 60 Hz.

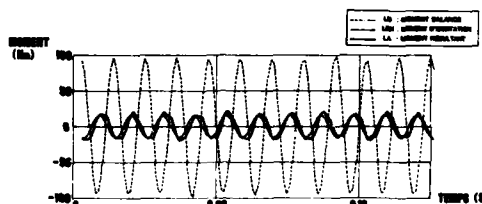


Fig. 21 - Excitation sinusoïdale en roulis, fréquence d'excitation : 90 Hz.

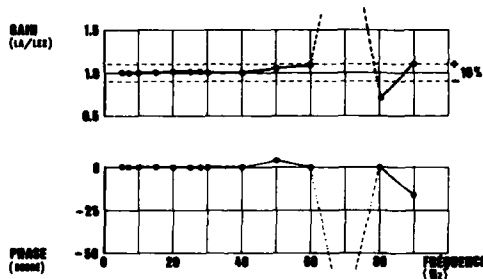


Fig. 22 - Fonction de transfert en roulis.

• Excitations simultanées en tangage et en lacet

Les essais préliminaires se sont poursuivis en excitant la maquette simultanément en tangage et en lacet de manière à s'assurer qu'une excitation dans un plan ne perturbe pas les résultats de l'autre plan et vice versa.

Dans le plan latéral, la maquette est excitée à deux fréquences 7,5 et 20 Hz. La fréquence de 7,5 Hz est choisie car elle correspond au premier mode propre en latéral. Pour chacune de ces excitations, un balayage en fréquence est effectué dans le plan longitudinal entre 5 et 50 Hz. Les figures 23 et 24 présentent les moments de tangage pour une excitation de 7,5 Hz en latéral et pour 20 puis 40 Hz dans le plan vertical. Les résultats sont satisfaisants, c'est-à-dire qu'ils sont tout à fait comparables à ceux obtenus lorsque l'excitation a lieu dans un seul plan.

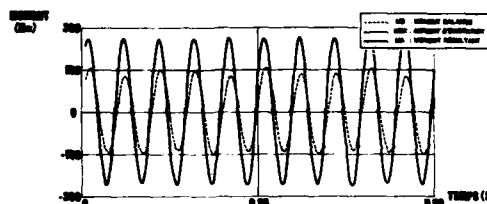


Fig. 23 - Excitation sinusoïdale simultanée; en tangage, fréquence d'excitation : 20 Hz, et en lacet, fréquence d'excitation : 7,5 Hz.

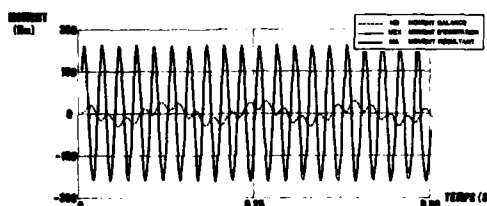


Fig. 24 - Excitation sinusoïdale simultanée; en tangage, fréquence d'excitation : 40 Hz, et en lacet, fréquence d'excitation : 7,5 Hz.

5.2.2 - Contrôle du calcul de l'attitude de la maquette

Pour contrôler l'attitude de la maquette, il faut une référence. Pendant les essais en mode sinusoïdal, les accélérations angulaires mesurées permettent d'obtenir cette référence.

La figure 25 regroupe l'accélération angulaire mesurée et la variation d'attitude de la maquette calculée par l'intégration des modes propres pour une excitation calée à 7 Hz. L'amplitude de l'accélération angulaire est de $0,5 \text{ rad/s}^2$ ce qui donne une amplitude de $2,6 \cdot 10^{-4} \text{ rad}$ pour la variation d'attitude. L'amplitude de la variation d'attitude calculée par l'intégration des modes propres est de $2,5 \cdot 10^{-4} \text{ rad}$. La figure 25 montre que le mouvement est bien en opposition de phase avec l'accélération.

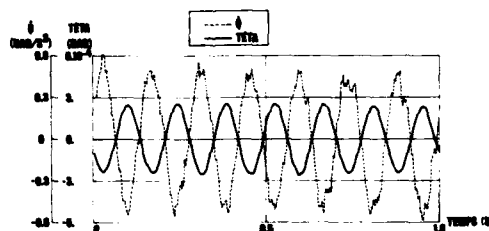


Fig. 25 - Excitation sinusoïdale en tangage, fréquence d'excitation : 7 Hz.

Cette méthode de calcul de l'attitude dépend évidemment des données telles que les masses généralisées, les fréquences propres, mais aussi de la qualité avec laquelle les efforts appliqués sont calculés. Pour les basses fréquences, les contrôles sont satisfaisants.

5.2.3 - Excitations périodiques en créneaux

Les efforts développés par le générateur ont des fronts de montée correspondant plus à un créneau qu'à une sinusoïde. Pour se rapprocher des conditions d'essai, des mesures sont effectuées avec une force excitatrice ayant la forme suivante (voir fig.26)

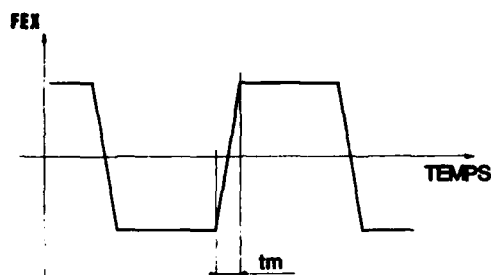
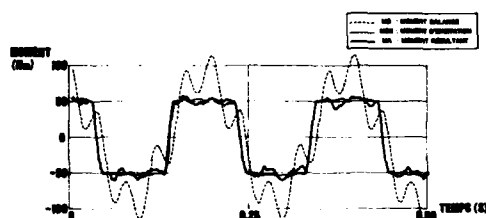
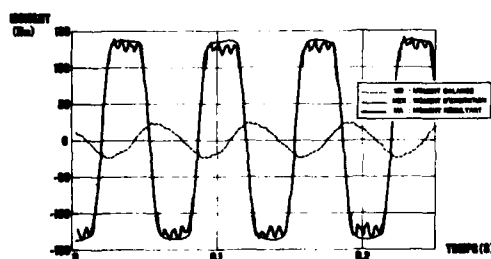
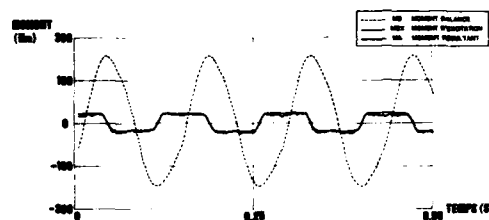
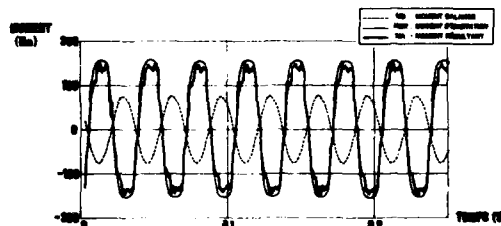


Fig. 26 - Excitation trapézoïdale.

Les essais sont réalisés en faisant varier le temps de montée t_m ($t_m = 10$ et 5 ms) et la fréquence d'excitation. Les figures 27 à 30 présentent les moments au centre balance pour 5, 7, 15 et 30 Hz. Selon les fréquences, la forme, l'amplitude et la phase, le moment balance diffère notablement du moment d'excitation. Les corrections d'inertie permettent de retrouver ce moment d'excitation d'une manière satisfaisante.

Fig. 27 - Excitation trapézoïdale en tangage,
fréquence d'excitation : 5 Hz.Fig. 28 - Excitation trapézoïdale en tangage,
fréquence d'excitation : 7 Hz.Fig. 29 - Excitation trapézoïdale en tangage,
fréquence d'excitation : 15 Hz.Fig. 30 - Excitation trapézoïdale en tangage,
fréquence d'excitation : 30 Hz.

Tous ces contrôles démontrent la faisabilité de l'essai du point de vue de la mesure ; il reste encore à vérifier que la ligne de dards peut supporter les efforts envisagés sans dommage.

5.3 - Excitation avec amplitude de force voisine de celle du générateur

Une excitation est réalisée avec un pot électrodynamique capable de fournir un effort voisin de celui développé par le générateur. Cette expérience montre que le montage peut supporter les sollicitations imposées par le générateur et aussi que la qualité des mesures ne dépend pas du niveau d'excitation (voir fig. 31 et 32).

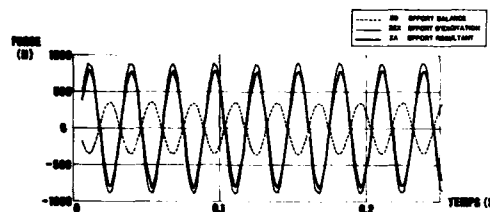


Fig. 31 - Excitation trapézoïdale en tangage, fréquence d'excitation : 35 Hz.

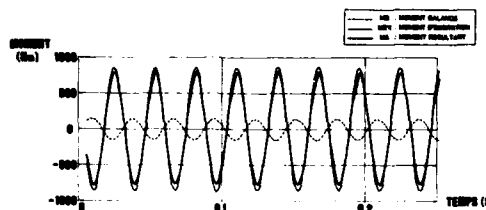


Fig. 32 - Excitation trapézoïdale en tangage, fréquence d'excitation : 35 Hz.

5.4 - Conclusions relatives à la phase préparatoire

Les conclusions de cette phase préparatoire sont les suivantes :

- La ligne de dards choisie doit supporter sans incident l'excitation du générateur de force ; une recommandation est faite au constructeur quant à la fréquence de pilotage du générateur de manière à éviter le second mode propre du montage.

- il est possible d'obtenir dans les plans de tangage et de lacet la partie fluctuante des efforts aérodynamiques avec une précision de l'ordre de 10 % dans une bande de fréquence allant de 0 à 55 Hz et avec une précision réduite entre 55 et 100 Hz.

- le roulis est obtenu avec une précision de l'ordre de 5 % jusqu'à une fréquence de 60 Hz.

Sous réserve des conditions énoncées ci-dessus l'ensemble des travaux préliminaires démontrent la faisabilité de l'essai envisagé. L'étape suivante consiste maintenant à effectuer un tir sans vent.

6 - TIR SANS VENT

La ligne de dards est fixée sur le secteur porte-dards de S2MA. Un essai de vibration succinct permet de relever les fréquences propres du montage et de vérifier toute la chaîne dynamique avant le tir ; tous ces contrôles sont effectués sur une maquette inerte. Par rapport aux essais préliminaires pendant lesquels la maquette était accrochée à un mur, il apparaît un glissement de fréquence de 25 à 21 Hz pour le deuxième mode et de 62 à 56 Hz pour le troisième mode.

Le générateur à poudre est alors monté dans la maquette et le premier tir peut être réalisé avec les ordres de manœuvre choisis et une fréquence correctement placée par rapport aux deux modes précédents.

Les figures 33 et 34 présentent l'évolution des ordres de commande du commutateur et les pressions mesurées en sortie des tuyères dans le plan vertical et dans le plan horizontal. Ces mesures indiquent que le générateur a bien fonctionné c'est-à-dire que les ordres de commande sont effectivement réalisés. En utilisant une échelle dilatée pour le temps, il est possible de mesurer le temps d'établissement des jets dans les tuyères. La figure 34 montre aussi qu'il y a eu un allas après quatre commutations dans le plan horizontal.

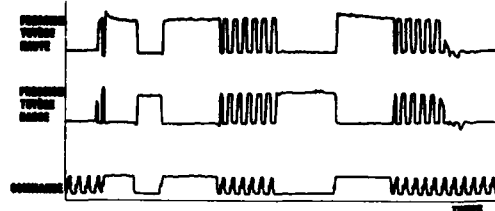
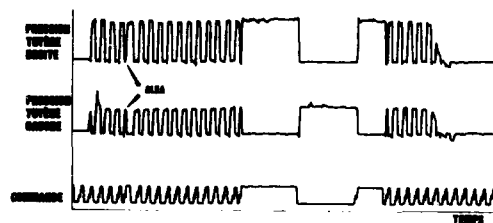


Fig. 33 - Tir sans vent, pressions tuyères, plan vertical.

Fig. 34 - Tir sans vent, pressions tuyères, plan horizontal.



L'analyse suivante consiste à observer les signaux des capteurs entrant dans le dépouillement du torseur appliqué à la maquette. Cette analyse met en évidence que les ponts de la balance et les accéléromètres sont surtout sollicités à la fréquence du premier mode propre comme le montrent les figures 35 et 36. Sur le pont M_2 de la balance, il apparaît une saturation du signal pendant quelques millisecondes qui n'empêche pas d'exploiter le tir.

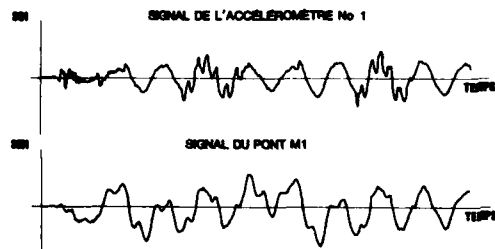


Fig. 35 - Tir sans vent.

Fig. 36 - Tir sans vent.

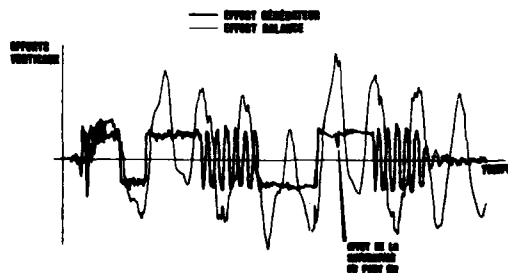
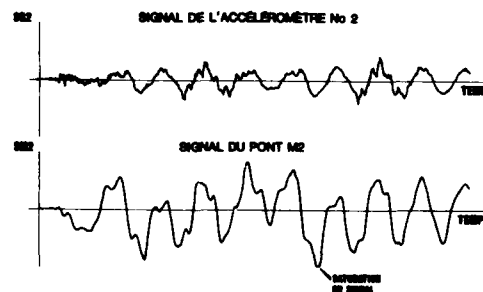


Fig. 37 - Tir sans vent.

A partir de ces signaux le programme de dépouillement calcule les efforts et les moments développés par le générateur. Les résultats sont présentés figures 37 à 40. Sur ces figures, les efforts et les moments mesurés par la balance sont tracés de manière à mettre en évidence les corrections d'inertie qui jouent un rôle prépondérant non seulement sur les amplitudes mais aussi sur la forme du torseur résultant.

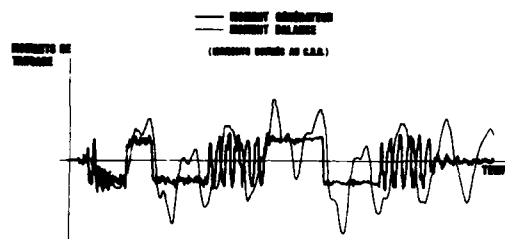


Fig. 38 - Tir sans vent.

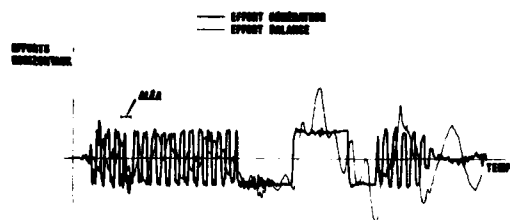


Fig. 39 - Tir sans vent.

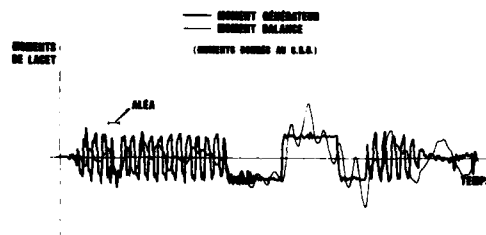


Fig. 40 - Tir sans vent.

Un premier examen qualitatif de ces résultats appelle les remarques suivantes:

- l'allure générale des efforts et des moments restitués par l'exploitation correspond bien aux cycles de commande du générateur.
- la perte de poussée pendant quelques millisecondes sur l'effort vertical (voir fig. 37) est un artefact de mesure ; elle est due à la saturation du signal du pont M_2 de la balance.
- dans le plan horizontal, l'aléa pendant la commande, est observé sur les efforts et les moments (voir fig. 39 et 40).
- après le tir, le système répond sur le premier mode. Alors que la force d'excitation est nulle, les efforts balance dans le plan vertical sont encore élevés (voir fig. 37). Les corrections d'inertie permettent de retrouver un effort quasi nul.
- des fluctuations d'effort apparaissent à une fréquence supérieure à 100 Hz bien que les signaux soient filtrés analogiquement à 100 Hz.

Cette dernière remarque a conduit à effectuer un filtrage numérique sur les signaux et à dépouiller à nouveau le tir. Le filtre numérique est calé à 60 Hz. Les figures 41 et 42 présentent les efforts obtenus dans les plans vertical et horizontal.

Pendant un ordre de commande maintenu la poussée est stabilisée. Ces résultats sont retenus pour effectuer les comparaisons avec les tirs avec vent.

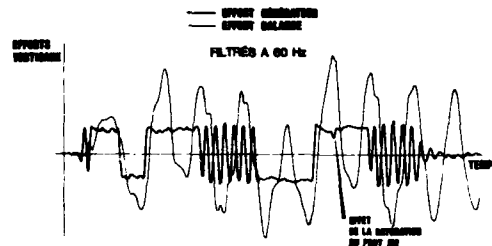


Fig. 41 - Tir sans vent.

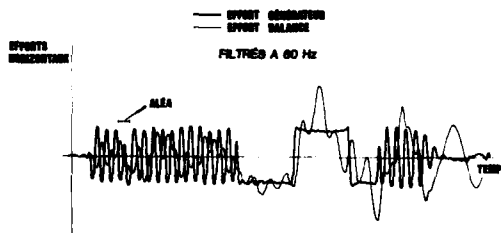


Fig. 42 - Tir sans vent.

7 - CONCLUSIONS

La mesure des efforts instantanés qui s'exercent sur une maquette soumise à des variations rapides de commande demande une préparation particulière avant les essais en soufflerie.

Un essai de ce type a été réalisé sur une maquette de l'AEROSPATIALE par la Direction des Grands Moyens d'Essais de l'ONERA au Centre de Modane-Avrieux. Il s'agissait de mesurer les efforts développés par un générateur de force en fonctionnement dynamique dans la veine supersonique de S2MA.

Cette préparation commence par une identification dynamique du montage de manière à préciser les plages de fréquence à éviter pour la commande du générateur de force et à définir un modèle mathématique pour le calcul des mouvements de la maquette.

Elle se poursuit par des excitations sinusoïdales du montage afin d'établir la fonction de transfert du dispositif de mesure. Le torseur appliqué à la maquette est mesuré avec une précision de $\pm 5\%$ en roulis et de $\pm 10\%$ en tangage et en lacet dans une plage de fréquence allant de 0 à 60 Hz. Des excitations sinusoïdales complémentaires montrent que la qualité de la restitution du torseur n'est altérée, ni par l'augmentation du niveau de l'effort appliqué, ni par des excitations simultanées en tangage et en lacet. Des excitations périodiques sont effectuées en appliquant des efforts alternés de forme trapézoïdale plus représentatifs de l'effort développé par le générateur. La coïncidence entre l'effort appliqué et l'effort résultant est satisfaisante.

La préparation se termine par un tir sans vent. Ce tir montre que le dispositif d'essai est opérationnel et que la méthode de mesure permet d'accéder aux efforts instantanés qui s'exercent sur la maquette.

8 - REFERENCES BIBLIOGRAPHIQUES

- [1] - E. CAIGNERET et G. HECKMAN
Nouvelles méthodes d'acquisition du buffeting
12ème colloque d'Aérodynamique Appliquée AAAF - novembre 75
- [2] - E. CAIGNERET et J. MOORELBEKE
Procédé de mesure des forces aérodynamiques en régime de tremblement
14ème colloque d'Aérodynamique Appliquée AAAF - novembre 77.

**BALANCE ACCURACY AND REPEATABILITY AS A LIMITING PARAMETER IN AIRCRAFT DEVELOPMENT
FORCE MEASUREMENTS IN CONVENTIONAL AND CRYOGENIC WIND TUNNELS**

by

Prof. Dipl.-Ing. B. Ewald
University of Darmstadt
Petersenstrasse 30
100 Darmstadt
Federal Republic of Germany

Summary

The success of a commercial transport development is heavily influenced by the accuracy of drag measurements during the aerodynamic development in the wind tunnel. It is shown, that the internal balance is one limiting factor of accuracy.

The accuracy standard of modern internal balances is compared to the accuracy and repeatability requirement of the aerodynamicist. The comparison with high precision single component load cells promises a large improvement potential in multi component balance design and calibration. The following fields of improvement are discussed in the paper:

- Balance design
- Balance material selection and treatment
- Calibration methods
- Calibration software
- Thermal effects

Perfect correction of the thermal effects is the key to the successful use of cryogenic tunnels. An approach for the crucial problem of balance body distortion due to temperature gradients is demonstrated.

1. Introduction

The call for Papers for this AGARD-Meeting suggested, that today the main source of uncertainties in wind tunnel testing is related to tunnel flowfield inaccuracies and simulation insufficiencies.

Nevertheless in force testing for transport performance the internal force balance is still far from being perfect. Even in conventional tunnels the balance limits the repeatability: in the future cryogenic tunnels the balance state of the art is even worse.

The basic principle of any internal force balance is the measurement of forces by a metallic spring equipped with strain gages. This basic principle allows an accuracy, which is at least one order of magnitude better than the accuracy of present six component balances. So a substantial improvement may be achieved. Such improvements are urgently required, if aerodynamicists like to derive any benefit from the perfect full scale flow field simulation of cryogenic tunnels.

2. Balance Accuracy Requirements

In wind tunnel testing the highest accuracy is required for transport aircraft cruise performance testing. In most cases the total improvement of an airplane design compared to its predecessor is achieved by a great number of minor detail improvements. So the wind tunnel experiment must be able to resolve very small drag increments from one test condition to the next. This resolution is limited by the repeatability of the balance.

Generally aerodynamicists agree that the repeatability from one wind tunnel run to the next run ("short term repeatability") should be much less than one Drag Count. The term "Drag Count" represents a drag coefficient increment of 0.0001.

The goal of a "long term repeatability" (repeatability from one test campaign to another test campaign) of one Drag Count is very difficult to achieve even in the best of conventional tunnels.

A technology improvement, which allows a short term repeatability of about 0.1 or 0.2 Drag Counts, would offer new possibilities in airplane optimisation work. To get the full benefit from the new technology of the cryogenic tunnel, such improvements in repeatability are urgently needed.

3. Present Accuracy Standard of Internal Balances

The drag of an airplane configuration is evaluated from the balance signals for Normal Force, Axial Force and Pitching Moment by a component transformation. An additional error is introduced during this process by unavoidable errors in angle of attack measurement. So a careful error analysis is necessary to convert the "One Drag Count Requirement" of the aerodynamicist into an accuracy requirement for the balance.

This analysis is done here using an actual test result of a transport cruise condition measurement done in the Transonic Tunnel HST of the NLR, see Fig. 1. Together with the dynamic pressure, reference area and mean aerodynamic chord of the model the force components of the balance were recomputed from the test results. These force components are given in fig. 2.: the weight of the model is already included in these values.

For the accuracy of internal six component balances no generally adopted definition exists. The error band of the balance may be estimated by a formula developed by DNW for the acceptance tests of new balances. Following this definition the tolerated error in the force or moment component "i" under the simultaneous impact of the other components F_n is:

$$\delta_{F_i} = \pm A \cdot F_{i\max} \cdot \left[a_i + \sum_{n=1}^{n=6} \frac{F_n}{F_{n\max}} \right]$$

$F_{i\max}$, $F_{n\max}$: Maximum Design Force

A: 0,001 for Absolute Accuracy

Ranges of Balance

0,00033 for Repeatability

a_i : 1,5 for Axial Force

1,5 for Rolling Moment

1,7 for Side Force

1,0 for Pitching Moment

1,3 for Normal Force

1,0 for Yawing Moment

This formula takes into account the variable influence of component interference. According to our experience with balances of different manufacturers the chosen magnitude of the factors "A" and "a" describes nearly the maximum which is achievable with the very best of modern balances.

The balance used for the measurement shown in Fig. 1 has the following ranges:

Axial Force	X = 930 N
Side Force	Y = 3530 N
Normal Force	Z = 9220 N
Rolling Moment	Mx = 235 Nm
Pitching Moment	My = 460 Nm
Yawing Moment	Mz = 265 Nm

Using the formula given above and the balance load data from Fig. 2 the balance errors may be calculated now. For the cruise condition ($C_d = 0,5$) the result is:

Component	Error	% of value	% of balance range
Normal force	$\pm 15.6 \text{ N}$	± 0.65	± 0.17
Axial Force	$\pm 1.92 \text{ N}$	± 2.36	± 0.21
Pitching Moment	$\pm 0.62 \text{ Nm}$	± 0.44	± 0.13

This table demonstrates two facts:

- A) With respect to the design load ranges of the balance the accuracy formula given above results in errors between $\pm 0.13 \%$ and $\pm 0.21 \%$ for this 3-component case.

A top class strain gage load cell (e.g. Schenck Master Load Cell) gives a maximum combined error of less than 0.01% of the design load range. This comparison demonstrates the large improvement potential of internal wind tunnel balances.

- B) With respect to the actual loads the errors are much higher (2.36% in Axial Force!). This demonstrates the unsatisfactory adaption of the balance to this actual test case. In fact careful adaption of the balance to the actual test condition is a most successful approach to better balance accuracy! Nevertheless this approach is limited. A certain reserve in design load capacity of the balance is necessary for dynamic overload (buffet), higher off design Mach numbers and on the other hand it is not possible to design the axial force load range to much less than 10% of the normal force range.

According to the law of propagation of error we can now compute the combined drag coefficient error from the errors in the balance components. In this computation it was assumed that the error of the angle of attack measurement is 0.01 degree. The drag coefficient error is shown in fig. 3. According to the balance accuracy specification the repeatability is about $1/3$ of the absolute accuracy: this repeatability is also shown in Fig. 3.

The goal of a drag measurement repeatability better than one Drag Count is hardly fulfilled by this test. A better adaption of the balance design ranges to the test condition may improve the situation.

Nevertheless the total accuracy of present-day internal strain gage balances is still far away from the real capabilities of force sensors based on the combination of metallic spring and strain gage. The improvement potential is hidden in nearly any detail of balance design, fabrication and calibration. Some of these aspects will be discussed in more detail.

4. Improvement of Conventional Balances

The main sources of balance inaccuracy and so the starting points for improvements are:

- Imperfect balance design philosophy
- Imperfect balance fabrication technique
- Imperfect calibration method
- Imperfect evaluation software
- Imperfect electronic readout equipment

4.1 Balance design and manufacture

Balance design and manufacture are covered by one chapter in this paper since they are closely coupled. It is an established fact that a first class multi-component balance must be fabricated from one piece of metal to avoid excess hysteresis. The standard fabrication process is spark erosion. So the geometric design of the balance is limited with regard to this fabrication process.

The method to assemble strain gage balances from several prefabricated parts by electron beam welding [7] eliminates these design limits. A considerable improvement of the stiffness especially of the axial force parallelogramme is possible by an interlocking design of the parallelogramme outrigger beams. Fig. 4 shows the parts of a balance prior to the welding process; the interlocking geometry of the outrigger beams is clearly visible. The increased stiffness greatly reduces axial force interference effects. Fig. 5 shows the balance body after the welding process and Fig. 6 shows the ready machined balance.

The repeatability depends very much on internal hysteresis effects of the balance material. Since internal wind tunnel balances are used through the positive load range and the negative range as well, the hysteresis behaviour also in the region of zero load is important. Fig. 7 shows Youngs Modulus of maraging steel 200 in the low stress range [16]. These effects produce scatter in the balance results. Apart from [16] this effect was not discussed elsewhere and up to now no provision is known to improve this effect.

The choice of material for a strain gage balance is still more black magic than science. Maraging steel (200, 250, 300 grade), PH 13-8 Mo, 17.4 PH are favorites of balance manufacturers. Nevertheless the knowledge of the reasons for internal hysteresis, the comparative qualities of the different materials and the influence of thermal treatment and preloading on these effects is very limited. A repetition of the work described in [16] using modern balance materials and more modern electronic and strain gage materials is urgently needed to clarify the effect of thermal treatment and mechanical treatment on the internal hysteresis.

Experience achieved so far indicate, that grain refinement by thermal treatment has a positive effect on internal hysteresis. Multiple loading of the balance to about 30 % more than the design loads in advance to calibration also improves the hysteresis behaviour. Nevertheless more scientific knowledge in this field is needed to get real improvements.

Another important balance design aspect is the design of the balance connections to sting and model. Friction and hysteresis in the connections quite easily produce scatter in the balance signals. Very careful design and manufacture is necessary to minimize these effects. Especially the manufacture of the frequently used cone connection is extremely critical. Cylindrical connections on the model side and flange connections to the sting are to be preferred. Effects can be minimized also by decoupling the measuring areas of the balance from the connections by a certain length of solid balance body.

Careful design of the axial force parallelogramme is necessary to avoid random non-linear behaviour which is caused by minor buckling effects in the structure. These effects mostly are caused by using very slim links and flexures in the design. So the designer runs into a conflict, because the fight against temperature effects leads to flexures with minimum stiffness. A useful tool for the optimized design is a computer programme for the balance body stress analysis, which allows the designer quick changes of all geometric dimensions in dialog with the computer. Using such a programme the balance designer soon acquires the experience how to optimize a balance design.

This computer programme can only be based on simple stress and strain calculations. Finite element methods are much too complicated for this optimization process; in the balance design business these methods can only be used to study basic design problems.

The most important balance design aspect is the design for low sensitivity against thermal effects. Because of the outstanding importance the thermal effects are discussed separately in chapter 5.

4.2 Balance Calibration Method

Present calibration methods are generally characterized by two common principles:

- Balances are calibrated by applying exactly known forces resp. moments exactly in the direction of one specific balance component. So one gets the calibration of this balance component and the interference of this component on the other components. In most cases this method is extended to the simultaneous application of two components, e. g. one force and one moment which is generated by asymmetric application of the force. Since the gravity field of earth is by far the most accurate instrument to generate known forces in a precisely defined direction, successful calibration methods respectively calibration rigs mostly use free hanging deadweights. Pulleys and levers should be avoided as far as possible.
- Result of the calibration is evaluated in form of a "Second Order Calibration". This means, that the signal of the strain gage bridge appointed to the component i is approximated by the equation:

$$R_i = \sum_{j=1}^6 a_{ij} X_j + \sum_{j=1}^6 \sum_{k=1}^6 b_{ijk} X_j X_k$$

A complete evaluation of these equations for all six components is only possible if any possible combination of two components is simultaneously used during the calibration. Normally only a part of these combinations is used during the calibration.

According to our experience all these calibration methods have two main disadvantages. The first disadvantage concerns the necessity to apply the calibration force (or moment) exactly at the right position in the right direction. Since the balance is deflected by the force, permanent realignments are necessary. The position of the force must be correct with respect to a reference point or reference planes which are defined relatively to reference surfaces of the balance.

During the calibration the balance is more or less hidden in the calibration sleeve; so the control of exact position and direction of the forces respectively moments is extremely difficult and time consuming. Since the calibration reacts very sensitively to errors in this respect, this problem is the main source of inaccuracy in the calibration. A totally different calibration method is necessary for a real improvement.

The second disadvantage mentioned above is the description of the signals by a second order polynomial. There are several physical reasons for a slightly nonlinear behaviour of a spring/strain gage sensor. Since a balance is designed symmetrically and is used and calibrated in negative and positive load direction, the nonlinear characteristic of such a balance should be symmetrical to zero as is shown in Fig. 8. This behaviour can be described only by a third order polynomial! So the evaluation method should give a third order approximation of the calibration data.

Nevertheless the square term should not be omitted. There are physical reasons for a slightly different sensitivity (linear term of the polynomial) in the positive and negative load direction. This can be described quite successfully by a second order term.

So the signal of the strain gage bridge appointed to the component "i" is described by the following equation:

$$R_i = \sum_{j=1}^6 a_{ij} X_j + \sum_{j=1}^6 \sum_{k=1}^6 b_{ijk} X_j X_k + \sum_{j=1}^6 c_{ij} X_j^3$$

Based on these considerations a new calibration method was invented at the Technical University of Darmstadt in cooperation with MBB Transport Division. The model end of the balance is attached to a very rigid mechanism, which is very similar to an external six component balance of high precision. The reference point and reference axis system of the balance to be calibrated is carefully adjusted to the reference system of this external balance. So the external balance measures all calibration load components applied to the internal balance.

The calibration loads are applied to the earth end of the examinee; normally combinations of two components are applied. No provision is made for distortion of the balance; so except the two calibration loads also the other components of the examinee will be slightly loaded. Since all these loads are measured correctly in the calibration axis system by the external balance, the loads may be applied by quite simple screw jacks. A comparison of this calibration principle with the conventional principle is given in Fig. 9. and Fig. 10.

Each data point gathered during this calibration process represents a mixed loading with one or two main components and slight interferences in the other components due to the distortion of the balance and the loading mechanism. So a numerical algorithm is needed to extract the third order calibration matrix from this data set. This algorithm was developed at the Technical University of Darmstadt; the nonlinear method evaluates the calibration matrix as a least square solution of the total calibration data set. The algorithm was written in a computer code and tested successfully. Computing time for the total calibration in a MicroVAX is about 15 minutes.

The new calibration methods allows the design of a fully automated calibration machine. This is of particular importance for cryogenic wind tunnels (see chapter 5).

Another balance software problem is the computation of the balance evaluation matrix. The calibration process delivers the calibration matrix; for evaluation of the signals given by the balance in the tunnel one needs the evaluation matrix which is the inverse function of the calibration matrix.

Of course the exact inverse function of a nonlinear system of equations does not exist. Ever since second order calibrations are used for internal balances, more or less crude approximations are used for this inverse function. The high speed of modern computers and the development of fast algorithms for the iterative solution of nonlinear systems of equations allows to do the job without the search for an inverse function. An iterative solution of the nonlinear calibration matrix equation system can be done so fast, that ON LINE solutions of the original calibration matrix can be used during the wind tunnel measurements.

4.3 Electronic Readout Equipment

Present standard in wind tunnel data systems for strain gage signal readout is the high precision D.C. amplifier with filter and digital voltmeter. Despite the extreme quality of such equipment errors of considerable magnitude are generated by thermoelectric voltage.

The accuracy requirements result in the need to resolve balance signals to fractions of a microvolt. Errors of several microvolts are generated already by small temperature differences in the lead wires and connectors.

This problem is eliminated by the use of A.C. excitation and readout equipment. The very best of this equipment is able to resolve strain gage signal to less than 0.1 μ V quite stable. The use of A.C. equipment is strongly recommended for high precision balance measurement.

5. Thermal Effects and Cryogenic Balances

5.1 Nature of Thermal Effects

Wind tunnel operation is always accompanied with temperature changes in the tunnel. Even when the tunnel is equipped with a sophisticated temperature control, overnight and weekend shutdowns result in a totally different temperature level in the tunnel and hence in the model and in the balance. So during tunnel operation the balance temperature changes and spatial temperature gradients occur in the balance body.

Thermal effects in the balance due to temperature changes presently are the most severe source of balance inaccuracies. In fact such thermal effects limit the accuracy and repeatability of internal balances in conventional tunnels already.

The cryogenic tunnel concept offers a dramatically improved full scale flow field simulation. Obviously this improved simulation is only profitable, if the balance gives at least the same accuracy as an excellent balance in a conventional tunnel. Since balance accuracy in conventional tunnels is already limited by thermal effects and the thermal environment in a cryogenic tunnel is so much severe, the required balance accuracy in a cryogenic tunnel is much more difficult to achieve.

In fact today we are still very far from the "1 Drag Count" accuracy goal in cryogenic tunnels. Unless dramatic improvements are achieved in thermal behaviour of internal balances, cryogenic tunnels like the NTF or ETW will give little benefit.

Balance errors due to thermal effects are caused by several different physical effects:

- Zero shift and sensitivity shift of a strain gage bridge due to uniform temperature change (no spatial temperature gradient!).

These effects are always combined by zero and k-factor shift of the gages and thermal expansion and Young's Modulus shift of the balance material.

- Zero shift due to different temperatures at the four gages of one bridge.
- False signals due to internal stresses in the balance body caused by spatial temperature gradients. This error looks like a zero shift, but since the gages really measure a strain distribution, this effect should not be classified as a zero shift.

5.1 Effects due to temperature level

The effects due to uniform temperature change can be minimized by "matching" of the four gages in one bridge and/or by conventional hardware compensation, see [14] for more details.

Residual effects of this type can be calibrated quite successfully against the temperature. After numerical correction for such residual effects a satisfying accuracy over the whole temperature range even for cryogenic tunnels can be achieved.

5.2 Effects of Bridge Temperature Differences

The second group of effects mentioned above is very difficult to eliminate. The only possibility is to avoid different temperatures at the gages of one bridge as far as possible. So the gages of one bridge should be arranged as close together as possible.

5.3 Balance Distortion due to Temperature Gradients

The most severe thermal effect is the distortion of the balance body due to spatial temperature gradients and especially the axial force measurement system is affected. It is this effect which prevents really accurate strain gage measurements in cryogenic tunnels up to now.

Fig. 11 demonstrates the distortion effect on the axial force system. It is assumed, that the left half of the upper outrigger beam is increased in length due to a temperature rise. The figure shows the resulting distortion of the complete system and demonstrates the origin of the false axial force signal. What can we do to correct, minimize or even avoid this effect?

- Prevention or minimization of the effect

One possibility is the prevention of any spatial temperature gradient. Some authors suggest to block off temperature gradients from the axial force system by controlled heating or cooling at the balance ends. Up to now this idea was not successful; the local heating introduces even steeper local temperature gradients into the balance body which worsen the situation. Furthermore it seems not possible to fully control the temperature gradients during temperature excursion of the tunnel. A long time is needed for stabilisation of the balance at the new temperature level.

Another possibility is to design an axial force element which is insensitive against temperature gradients. The only promising approach is to reduce the axial stiffness of the parallelogram flexures as far as possible. Unfortunately the flexures are very heavily stressed by side force and yawing moment, so the effort towards low flexure stiffness is closely limited. Nevertheless this demonstrates the extreme importance of a close match of the balance to the test case in the tunnel. If the use of the balance is strictly restrained on transport performance measurements, the balance can be designed for very low side components (side force, yawing and rolling moment). The design side component can be restricted to magnitudes which result from asymmetrical fabrication and alignment of the model. So very low flexure stiffness can be achieved with corresponding low sensitivity against temperature gradients. But in any case additional provisions are necessary.

A complete novel design of the axial force system which basically is not sensitive against temperature gradients, has not been invented or proposed up to now. This field is still open for creative engineers.

- Correction of temperature gradient effects

One possibility is to measure the temperature distribution in the balance body at a sufficient number of positions and to compute a correction of the false signal from this temperature distribution. Recent experience gathered at MBB Bremen demonstrated that big improvements can be achieved by this method [14]. Nevertheless a careful application of this method is very time consuming and the finally obtained accuracy is not sufficient for the large temperature gradients to be found in cryogenic balances.

A derivative of this method is to wire the temperature sensors (resistor sensors) directly into the axial force strain gage bridge. This simple method is less accurate than the computational method mentioned above and does not satisfy the accuracy requirement of transport performance measurements.

A more promising approach was developed at the Technical University of Darmstadt in cooperation with MBB. The idea is based on the fact, that the thermal distortion alone only produces an equilibrium of forces inside the balance body. Fig. 12 shows an axial force parallelogram system without the conventional bending beam sensor, which is distorted by a thermal expansion in the upper beam. The forces in the two flexure systems are of equal size and opposite direction. An axial force would produce equal deflections in the same direction in the flexures. So if a measuring element is integrated in both flexure systems, the sum of both signals is a measure of axial force and the difference of the signals represents the temperature effect.

This basic idea led to the design of three axial force systems with different sensing elements, see Fig. 13, 14 and 15. A complete six component balance was designed following the same design principle, see Fig. 16.

In a real system like this the separation of force effect and temperature effect will not be perfect due to tolerances in fabrication and gage application. Axial force will result in equal deflections of the front and aft system while temperature gradients will result in equal but opposite forces in both systems. So the simple sum of the front and aft signals will not exactly represent the net axial force effect. This problem can be solved by a special calibration procedure.

- Force calibration

With constant temperature the balance is calibrated by axial forces. Apart from the calibration this test gives the result, that the front element signal E_{1A} and the aft element signal E_{2A} always have the same ratio α , which is close to 1.

$$\frac{\epsilon_{1A}}{\epsilon_{2A}} = \alpha \quad (1)$$

- Temperature gradient calibration

In the unloaded balance a distortion like shown in Fig. 12 is generated by local heating of one beam. The result is, that signals generated by distortion always have the ratio

$$\frac{\epsilon_{1B}}{\epsilon_{2B}} = \beta \quad (2)$$

which is close to -1.

In operation the elements give the signals

$$\text{front end system} \quad \epsilon_1 = \epsilon_{1A} + \epsilon_{1B} \quad (3)$$

$$\text{aft end system} \quad \epsilon_2 = \epsilon_{2A} + \epsilon_{2B} \quad (4)$$

signal due to axial force 

The equations (1) to (4) form a linear system for the unknown values ϵ_{1A} , ϵ_{2A} , ϵ_{1B} and ϵ_{2B} .

By solving this set of equations one gets the net signals due to axial force

$$\epsilon_{1A} = \frac{\epsilon_1 - \beta \epsilon_2}{1 - \beta \alpha} \quad \epsilon_{2A} = \frac{\epsilon_2 - \beta \epsilon_1}{\alpha - \beta}$$

respectively the sum of the front and the aft end signal

$$\epsilon_{1A} + \epsilon_{2A} = \frac{(\epsilon_1 - \epsilon_2 \beta)(1 + \alpha)}{\alpha - \beta}$$

So the temperature effect is perfectly separated from the force measurement.

This concept was verified by a measurement with the axial force system shown in Fig. 13. The element was equipped with temperature sensors and heating elements as shown in Fig. 17. At different temperature levels from ambient temperature down to cryogenic temperature the element was locally heated to introduce temperature gradients into the structure.

Results of this test are plotted in Fig. 18. The signals of both bending beams (evaluated as micro-strains) are plotted against the difference of the mean values of temperature in the upper and in the lower beam. The result is a linear correlation between the signals and the mean temperature difference with a scatter of less than 0,04 microstrains through the whole temperature range. Approximation by a second order polynom results in a remaining scatter of about 0,02 microstrains.

The signals at zero temperature gradient show the apparent strain effect through the temperature range. Accidentally the gages on this element are closely matched, so the apparent strain effect is low.

The correlation of the signals to the mean temperature difference is also a function of the total temperature level. This is evident because parameters like thermal expansion coefficient, K-factor of gages and Young's modulus are functions of temperature.

The evaluation of front and aft signal ratio (see equation to above!) gives an even more accurate result than the correlation of the signals against mean temperature difference. The ratio is constant within a scatter of less than 0,01 microstrains, which is well below the accuracy requirements. Again this signal ratio is a function of the temperature level. The correlation can be described by simple mathematical functions, so the correction in the computer is possible.

These results promise an approach to a satisfying correction method for thermal effects in axial force systems. Considering the extremely high accuracy requirements and the unfavourable conditions in a cryogenic tunnel, a long distance is still to go for the final solution of force measurement in cryogenic wind tunnels.

6. Conclusion

Precise wind tunnel drag measurements are an urgent need in transport aircraft development. Present balance technology limits the accuracy and especially the repeatability of such measurements in conventional tunnels and much more in cryogenic tunnels.

Total accuracy of internal balances can be improved by a balance design, which is closely matched to the actual test case. Further improvements are possible by advanced calibration methods and calibration software as well as by advanced balance design methods.

Repeatability is mainly influenced by internal hysteresis of the balance material and by temperature effects. Hysteresis effects can be minimized by the selection of balance material and heat treatment. Further scientific work is needed in this field.

Temperature effects can be minimized and corrected by relatively simple methods except the effect of thermal distortion in the balance body due to temperature gradients. This effect up to now severely limits the accuracy of internal balances in cryogenic tunnel. The effect may be corrected with satisfying accuracy by a design with twin axial force elements and a special calibration procedure.

The development work on cryogenic balances done in cooperation of Technical University of Darmstadt and MBB Transport Division is funded by the German Ministry of Research and Technology.

Literature

- [1] Alice T. Ferris
Force Instrumentation For Cryogenic Wind
Tunnels Using One-Piece Strain-Gage Balances.
NASA TN 81845, Juni 1980
- [2] Judy Ferris
Cryogenic Wind Tunnel Force Instrumentation.
Symposium on Cryogenic Wind Tunnels
Southampton, April 1979
- [3] Richmond P. Boyden, William G. Johnson, Jr.
and Alice T. Ferris
Aerodynamic Force Measurements With a
Strain-Gage Balance in a Cryogenic Wind Tunnel.
NASA TP 2251, 1983
- [4] M. Bazin et M. Dubois
Balance and Sting Design for Cryogenic Wind Tunnels.
Symposium on Cryogenic Wind Tunnels.
Southampton, April 1979, TP ONERA 1979-40
- [5] Maurice Dubois
Six-component Strain-Gage Balances for
Large Wind Tunnels.
Experimental Mechanics, Vol. 21, Nr. 11,
401-407, Nov. 1981
- [6] Maurice Dubois
Feasibility Study on Strain-Gage Balances
for Cryogenic Wind Tunnels at ONERA.
Cryogenic Technology Review Meeting NLR,
Amsterdam, 15 - 17 September 1982
- [7] B. Ewald
"Development of Electron Beam Welded
Strain Gage Wind Tunnel Balances".
VFW-Fokker, Bremen.
AIAA-Paper 78-803
- [8] Alice T. Ferris
Cryogenic Strain Gage Techniques used in
Force Balance Design for the National
Transonic Facility.
NASA Technical Memorandum 87712, May 1986
- [9] Peter F. Jacobs, Alice T. Ferris
Testing Experience with unheated Strain-Gage
Balances in the NTF.
NASA Langley Research Center, Hampton,
Virginia.
Presentation at 66th Semiannual STA Meeting,
Albuquerque, New Mexico, October 1986
- [10] B. Ewald, G. Krenz
The Accuracy Problem of Airplane Development
Force Testing in Cryogenic Wind Tunnels.
Technical University of Darmstadt and
MBB Transport Division,
AIAA Paper 86-0776
- [11] B. Ewald
Grundsatzuntersuchung zum Temperaturverhalten
von DMS-Waagen-Axialkraftteilen.
University of Darmstadt,
Unpublished Report, June 1985
- [12] B. Ewald
Entwurf einer 6-Komponenten-DMS-Waage
zur Erprobung im KKK.
University of Darmstadt,
Unpublished Report, Febr. 1985
- [13] K. Hufnagel
Paarungsuntersuchungen an Dehnungs-
Meßstreifen.
University of Darmstadt,
Unpublished Report, March 1986
- [14] B. Ewald, E. Graewe
Development of Internal Strain
Gage Balances for Cryogenic Wind Tunnels.
ICIASF 1987, June 22 - 25, 1987,
Williamsburg
- [15] K. Hufnagel
Untersuchung von Axialkraftelementen.
University of Darmstadt
Unpublished Report, August 1987
- [16] P.-J. Weber
Einige Untersuchungen über die Grenzen
der Arbeitsbereiche metallischer Federwerkstoffe
für Windkanalanlagen mit Dehnungsmeßstreifensystemen
Deutsche Forschungs- und Versuchsanstalt für
Luft- und Raumfahrt
Forschungsbericht 73-81

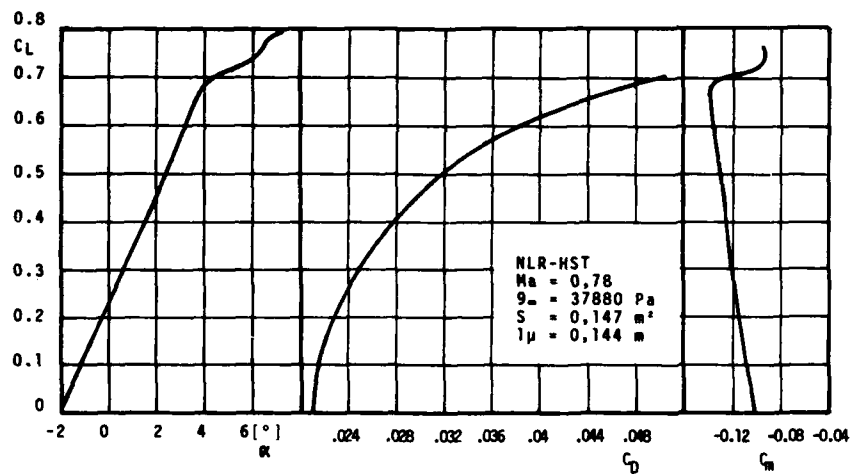


Fig 1 Example of Transonic Transport Measurement
(MBB Research Configuration)

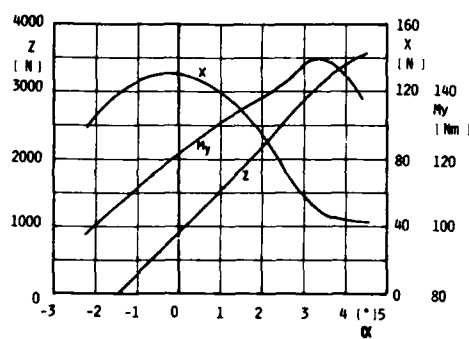


Fig 2 Balance Loads

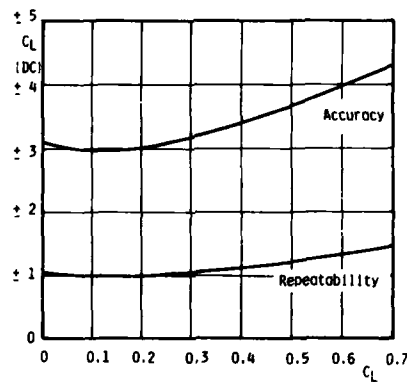


Fig. 3 Accuracy of Test Case

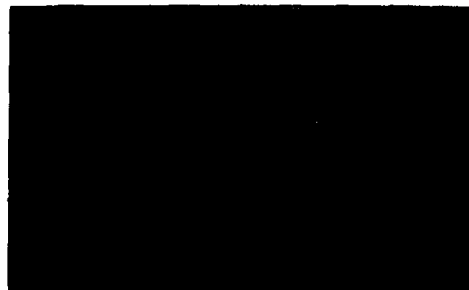


Fig. 4 Parts of balance W 607



Fig. 5 Balance W 607 after Welding

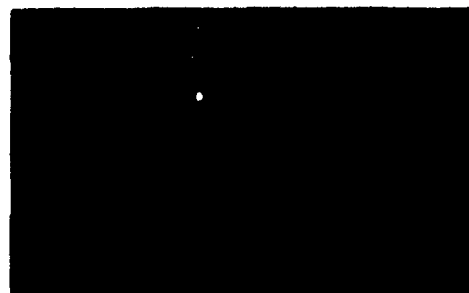


Fig. 6 Balance W 607 ready machined

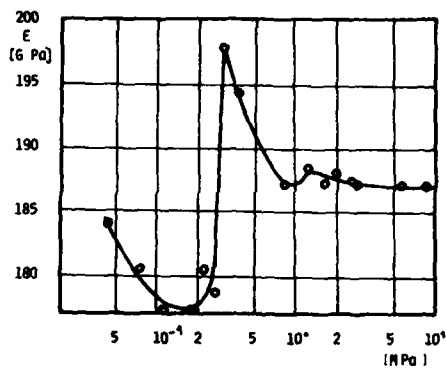


Fig. 7 Young's Modulus in the low stress region.
18 Ni 250 Maraging Steel

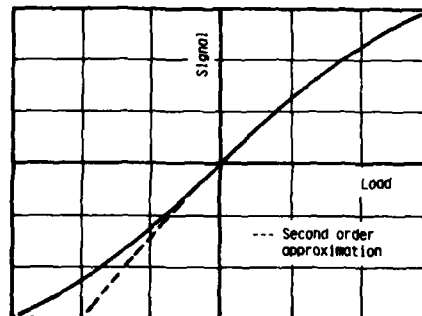


Fig. 8 Comparison of second order and third order approximation

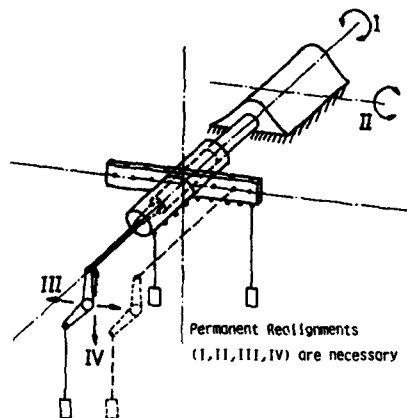


Fig. 9 Conventional Calibration Rig.

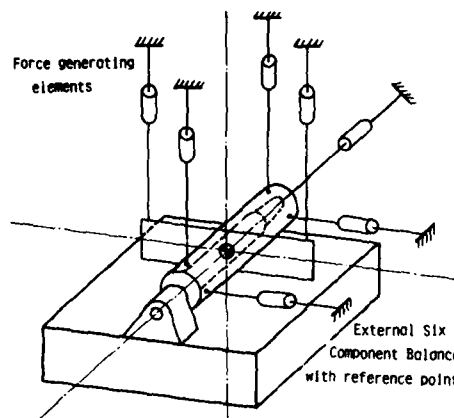


Fig. 10 Advanced Calibration Machine

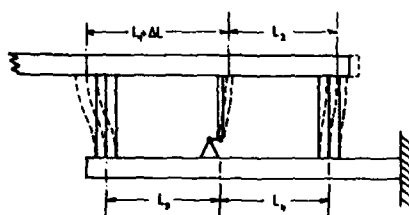


Fig. 11 Axial Force System Distorted by Temperature Gradient

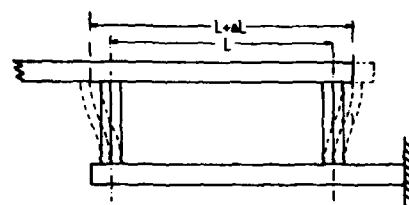


Fig. 12 Distorted Axial Force System



Fig. 13 Axial force element with decoupled bending beams



Fig. 14 Axial force element with coupled bending beams



Fig. 15 Axial force element with shear web elements

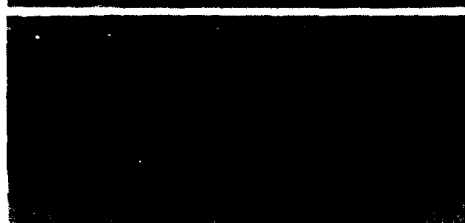
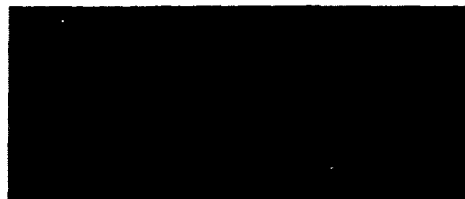
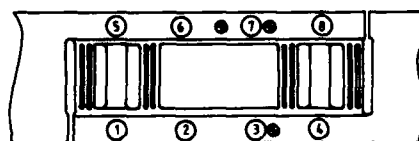


Fig. 16 Balance W 609



- : Position of Temperature Sensors
● : Position of Heating Elements

Fig. 17 Temperature Gradient Test Arrangement

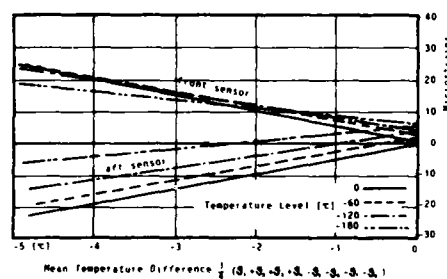


Fig. 18 Signals due to Temperature Gradients

CHARACTERIZATION OF HYPERSONIC WIND TUNNEL FLOW FIELDS FOR IMPROVED DATA ACCURACY

by
Albert H. Boudreau, Aerospace Engineer
Arnold Engineering Development Center
Arnold Air Force Station, Tennessee 37389-5000 USA

SUMMARY

Hypersonic test facilities produce flow fields which are difficult to characterize. In the past, many hypersonic facilities were reputed to produce test data of inferior quality when, in fact, it was poor characterization of the flow field principally at fault. With the renaissance in hypersonics at hand, experimentalists face anew the challenge of accurately characterizing flow fields. The U.S. Air Force's Arnold Engineering Development Center (AEDC) has faced these complex problems and developed techniques to accurately determine free-stream conditions. This paper highlights those "tools of characterization" and suggests a standard by which all hypersonic wind tunnels should be compared.

LIST OF SYMBOLS

C_a	Axial-Force Coefficient
C_n	Normal-Force Coefficient
C_p	Specific Heat at Constant Pressure
d^*	Wind Tunnel Throat Diameter
e_v	Energy of Molecular Vibration
h	Enthalpy
k	Constant
l	Model Length
M	Mach Number
P	Pressure
q	Heat Addition Term (Eq. (3))
R	Gas Constant
Re	Reynolds Number
r	Model Radius
s	Model Surface Distance
T	Temperature
U	Velocity
x_{CPN}	Axial Distance to Center of Pressure
x	Axial Distance
α	Angle of Attack
γ	Ratio of Specific Heats
ρ	Density
ϕ	Circumferential Angle on Model
σ	Shock Angle on Model

SUPERSCRIPIT

Conditions Behind a Normal Shock

SUBSCRIPTS

1	Conditions Before a Heat Addition Process
2	Conditions After a Heat Addition Process
b	Model Base
\bar{c}	Centerline
DP	Dew Point
FZ	Freezing
N	Nozzle Static
n	Model Nose
o	Reservoir Conditions
TR	Translational
V	Vibrational
w	Wall
∞	Free Stream

EXAMPLES OF CHARACTERIZATION PROBLEMS

In 1976 experimentalists working with AEDC's hypersonic wind tunnels discovered that the arc-driven hypersonic Tunnel F was operating at a lower Mach number than expected based on isentropic calculations. A task force was assembled to investigate errors as high as 25 percent in free-stream Mach number, and its findings serve as a basis for this paper.

Generally, improper characterization of hypersonic tunnel flow fields manifests itself as an error in Mach number. Although Tunnel F is an extreme case owing to its arc

heater, all hypersonic wind tunnels, regardless of type, appear to have some Mach number characterization problems. For example, AEDC's Tunnel C, heated by conventional clean-air heaters, exhibits a Mach error of as much as 1.5 percent compared to that predicted by isentropic flow using the ratio of free-stream pitot to reservoir pressure (see Fig. 1).

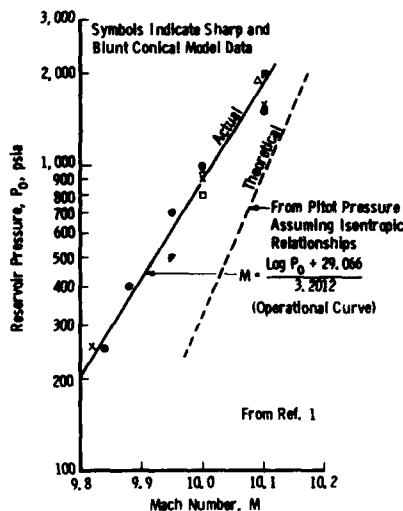


Fig. 1. AEDC Tunnel C Mach Number Adjustment.

shown in Fig. 2. Note that the vibrational state is excited beginning approximately at 1400°R which means that perfect-gas wind tunnels can experience the phenomenon when test section Mach numbers of six or more are produced. Duplication facilities (where true temperatures are produced in the test section) encounter excitation at test section Mach numbers above three. Generally, only arc-heated facilities where arc electron temperatures approach 25,000°R can excite the higher energy states. Once free of the arc column, the molecules recombine in the order of 10^{-6} seconds. The higher energy states thus decay to excited vibrational states which have relatively long relaxation times, such that a significant amount of the vibrational energy remains excited as it passes through the wind tunnel throat.

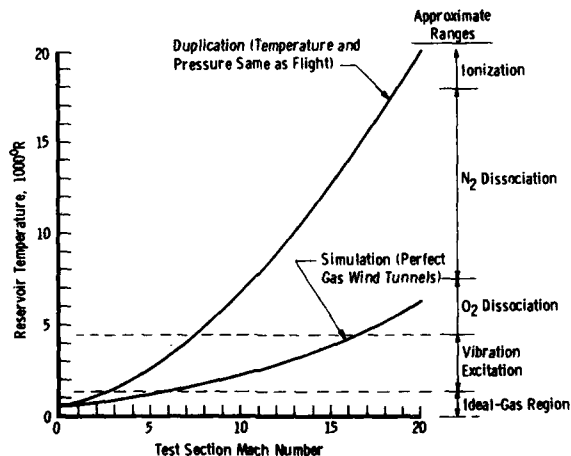


Fig. 2. Energetic Species in a Wind Tunnel Reservoir.

The vibrational freezing downstream of the throat is predictable based upon available N_2 relaxation rates. The subsequent relaxation (or de-excitation) hypothesis was tested in Tunnel C by measuring the vibrational temperature with various levels of water vapor using a Laser-Raman scattering technique. Mach number was experimentally determined from cone measurements.

These relatively small errors in Mach number can have large effects on the test article. Recently, A. Martellucci of Science Applications International reported (Ref. 2) that a 2-percent apparent Mach error produced a 20-percent error in static pressure measured on a model. Those tests were performed in a hypersonic wind tunnel at Mach 10.

The message distilled from these experiences is that any hypersonic wind tunnel operating at or above Mach 8 is likely to have flow-field characterization problems because of non-isentropic phenomena.

HYPOTHESIS OF NON-ISENTROPIC PROCESSES

The mechanism believed responsible for the Tunnel F problem (and also observed in Tunnel C) is vibrational excitation, followed by vibrational freezing just downstream of the nozzle throat, and subsequent rapid relaxation in the downstream section of the nozzle. The de-excitation phenomenon is apparently enhanced by the presence of water vapor. It is hypothesized that condensed water vapor (and other contaminants) act as third bodies. Collision of vibrationally excited air molecules with these third bodies allows de-excitation to take place.

The reservoir gas of most hypersonic wind tunnels is excited to various energetic states as

Figure 3 indicates the strong correlation between water vapor (dew point) and vibrational temperature, and the subsequent effects on measured Mach number. Figure 4 illustrates this process in the wind tunnels where the downstream portion of the contoured nozzle approximates a constant area duct. When a mechanism is present to raise the static temperature in a constant area, supersonic flow (for $M > 8$), the free-stream static pressure also rises significantly with $\Delta P_\infty / P_\infty \approx \Delta T_\infty / T_\infty$. However, velocity and density (hence pitot pressure) change very little.

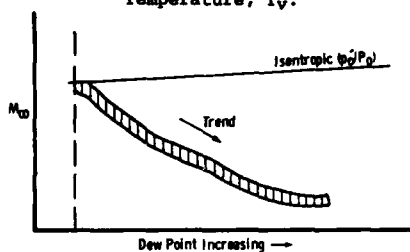
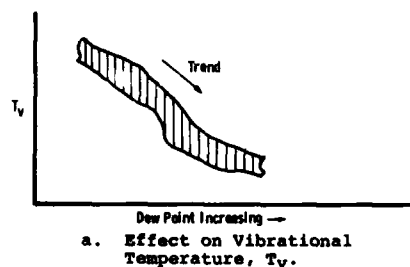


Fig. 3. Effect of Water Vapor on T_v and M_∞ .

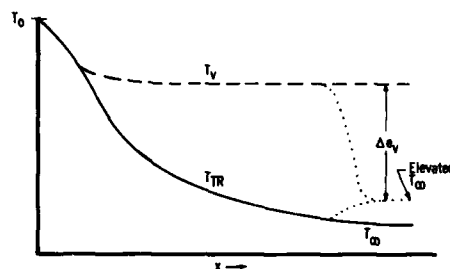
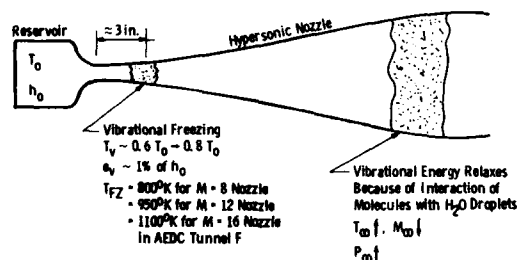


Fig. 4. Hypothesis of Cause.

This may be shown by considering a heat addition process in a constant area duct where condition "1" is prior to the addition and condition "2" is after it. The governing equations are

$$\rho_1 U_1 = \rho_2 U_2 \quad (1)$$

$$P_1 - P_2 = \rho_2 U_2^2 - \rho_1 U_1^2 \quad (2)$$

$$C_p T_1 + \frac{U_1^2}{2} + q = C_p T_2 + \frac{U_2^2}{2} \quad (3)$$

And rearranging Eq. (2),

$$\frac{\rho_2 U_2^2}{\rho_1 U_1^2} = \frac{P_1 - P_2}{\rho_1 U_1^2} + 1 = \frac{P_1 - P_2}{P_1 \gamma M_1^2} + 1 \quad (4)$$

since

$$\rho_1 U_1^2 \approx P_1 \gamma M_1^2 \quad (5)$$

Using the equations of state, continuity, and momentum,

$$\frac{P_2}{P_1} = \left[\frac{1 + \gamma M_1^2}{1 + \gamma M_2^2} \right] \quad (6)$$

and

$$\frac{\rho_2 U_2^2}{\rho_1 U_1^2} = \frac{1}{\gamma M_1^2} - \frac{P_2/P_1}{\gamma M_1^2} + 1 = \frac{1}{\gamma M_1^2} - \frac{1}{\gamma M_1^2} \left[\frac{1 + \gamma M_1^2}{1 + \gamma M_2^2} \right] + 1 \quad (7)$$

Simplifying,

$$\frac{\rho_2 U_2^2}{\rho_1 U_1^2} = \frac{M_2^2}{M_1^2} \left[\frac{1 + \gamma M_1^2}{1 + \gamma M_2^2} \right] \quad (8)$$

but

$$\rho U^2 = k P'_O \quad (9)$$

Therefore,

$$\frac{P'_{O2}}{P'_{O1}} = \frac{M_2^2}{M_1^2} \left[\frac{1 + \gamma M_1^2}{1 + \gamma M_2^2} \right] \quad (10)$$

A typical Mach change observed in Tunnel F was from $M_1 = 14$ to $M_2 = 12.5$. Solving for these values (assuming $\gamma = 1.4$), $P'_{O2}/P'_{O1} = 0.9991$, or for $M \gg 1$

$$\frac{P'_{O2}}{P'_{O1}} \approx 1 \quad (11)$$

With this relative insensitivity of pitot pressure to an entropy increase in the free-stream flow, it is obvious that measurement of pitot pressure alone cannot resolve even large changes in the upstream static temperature. Consequently, measurement of the ratio P'_O/P_O does not readily disclose the presence of real-gas effects that would lower M_∞ .

Since the static pressure, P , shows a large change, the simultaneous measurement of both P_∞ and P'_O is required to accurately determine free-stream conditions. The prediction of Mach number is, therefore, dependent upon precise determination of free-stream pressure.

The vibration de-excitation phenomenon noted here is strongly dependent upon both the species and concentration of impurities such as water vapor. Hence, it is extremely important to decrease these impurities to the lowest levels possible. Likewise, the rate of expansion is important in establishing the vibrational temperature at which that mode freezes. Contoured nozzles with high expansion rates are more prone to vibrational freezing problems than conical nozzles with lower rates.

While other processes could be present to produce non-isentropic flow, the vibrational relaxation phenomenon appears to be widespread. Regardless of the mechanism producing non-isentropic expansions, it is extremely important to experimentally determine free-stream pressure and Mach number to accurately characterize the flow.

EXAMPLE EXPERIMENTS

The AEDC Tunnel F investigation serves as an excellent example of flow-field characterization because of its depth of analysis and the wide variety of experimental techniques employed. In this section that investigation will be discussed as a practical example of the tools available for flow-field analysis.

It is important to note that the Tunnel F flow field had been characterized in the conventional style previous to the investigation described here. In fact, Tunnel F had operated for 15 years prior to these experiments. In addition to the standard pitot and heat-transfer surveys, sharp-cone models were used to demonstrate the validity of the calibrations. Figures 5 and 6 present some of those results which clearly leave the impression that no problems existed.

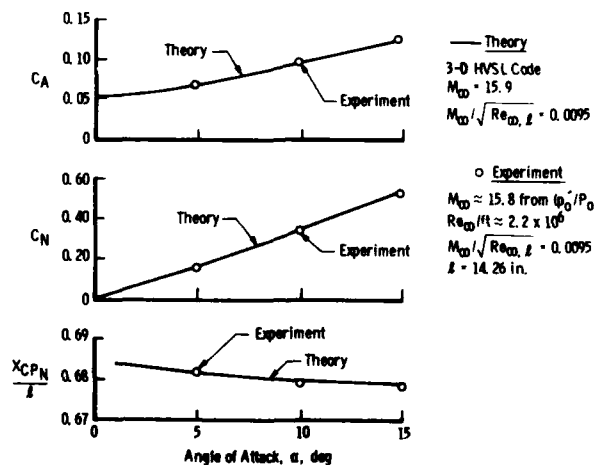


Fig. 5. Mach 16 Contoured Nozzle Force Results - 7-deg Half-Angle Sharp Cone.

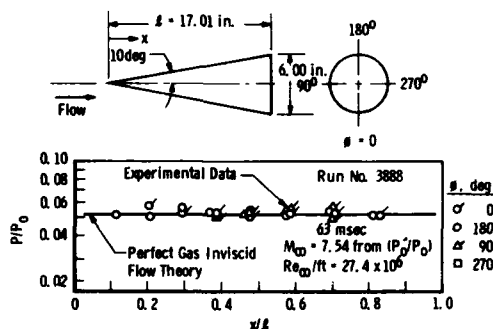


Fig. 6. Peripheral Pressure Measurements on a 10-deg Sharp Cone (Contoured Nozzle) in Tunnel F.

Figure 8 presents some solutions using the reliable Lubard Hypersonic Viscous Shock Layer (HVSL) Code. Experimental 5-deg cone measurements are compared to three of these solutions in Fig. 9. Note that the viscous contribution is relatively small at these Reynolds numbers. Hence the high sensitivity of wall pressure to Mach number makes this the best method of experimentally determining free-stream Mach number.

Sharp cones, however, are similar to pitot pressure measurements in that they are relatively insensitive to entropy changes in the free stream. Hence, the experimentalist obtains a false sense of well being.

Blunted, low-angle cones are aerodynamic configurations exhibiting extreme sensitivity to Mach number. Therefore, an $r_n/r_b = 0.168$, 5-deg half-angle cone was chosen for testing in Tunnel F. As noted in Fig. 7, the model was heavily instrumented with surface pressures and featured three nose pitot measurements for redundancy.

In order to interpret blunt-cone results, one must obtain high-quality predictions of surface pressure including the viscous-induced contribution. Figure

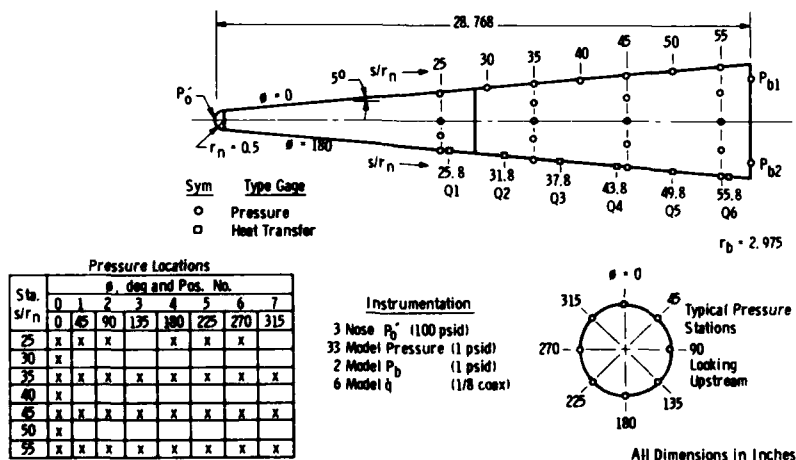


Fig. 7. 5-deg Cone Pressure Model.

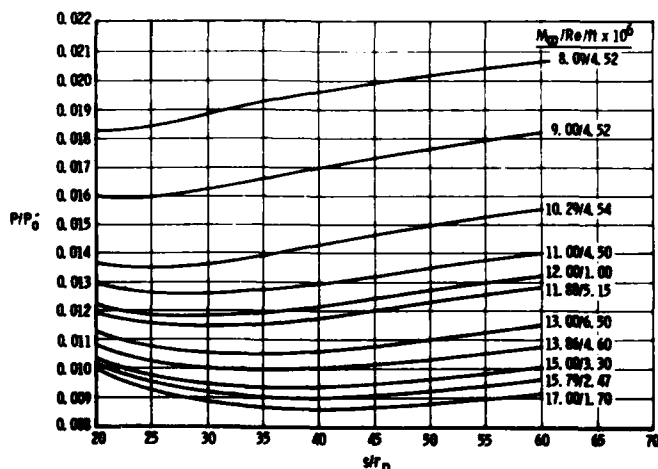


Fig. 8. Blunt 5-deg Cone Solutions Using the Lubard HVSL Code.

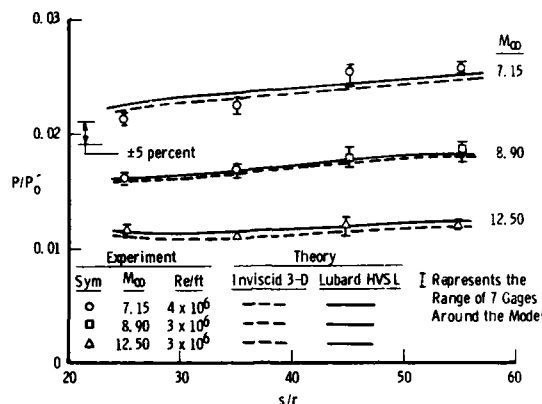


Fig. 9. 5-deg Blunt Cone Wall Pressure Measurements.

The high-quality cone results (Fig. 9) permitted a mapping of the Mach errors present in Tunnel F. Figure 10 compares Mach numbers derived from the cone measurements with those calculated from pitot pressure measurements assuming isentropic relationships. Note that the amount of water vapor in the reservoir clearly influences the Mach error, lending credence to the relaxation hypothesis raised in the previous section. Likewise, the use of a 4-deg half-angle conical nozzle with lower expansion rate also indicates less Mach error.

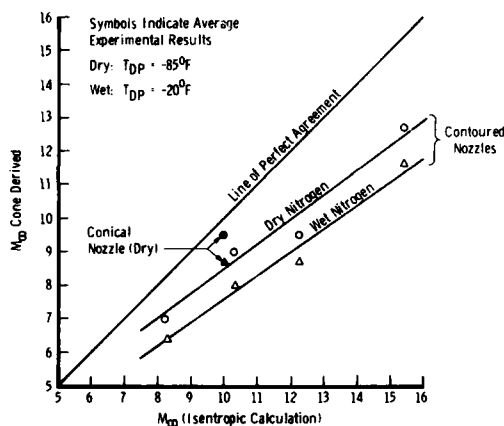


Fig. 10. Comparison of Mach Numbers for Tunnel F.

The rise in free-stream temperature affects Reynolds number as well as Mach number. Hence, the standard Mach-Reynolds number map of wind tunnel performance will show a marked decrease in simulation capabilities as indicated in Fig. 11. The degradation is most severe at higher Mach numbers where the reservoir gas must be heated higher to prevent liquefaction. The higher reservoir temperatures are hypothesized to put more energy into the vibrational mode, and hence more energy is available for the relaxation process.

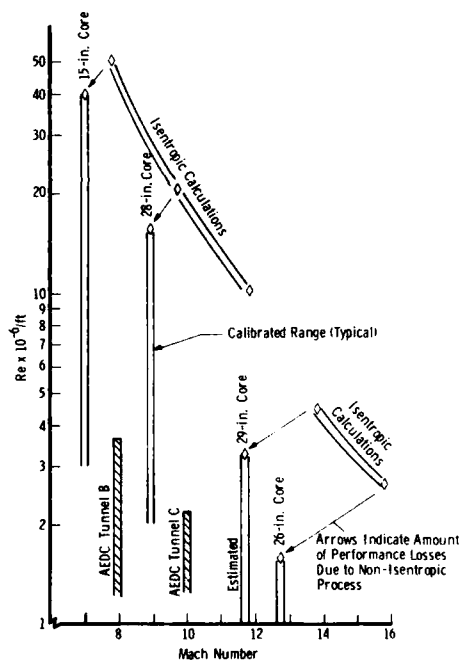


Fig. 11. Tunnel F Mach-Reynolds Number Map.

Of course, one cannot run a large 5-deg cone in the test section when other experiments are underway. Hence, the experimentalists at Tunnel F developed a correlation between measured nozzle static pressures (P_n) and Mach number determined from the blunt 5-deg cone. That correlation is illustrated graphically in Fig. 12. With a family of such correlations for each nozzle and throat, free-stream conditions could be accurately determined. This method was extremely successful, and Tunnel F subsequently produced data with accuracies comparable to those obtained in AEDC's continuous wind tunnels, i.e., ±5-percent uncertainty.

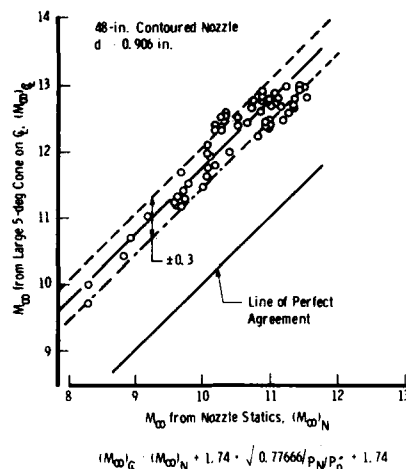


Fig. 12. Mach Number Correlation for Tunnel F.

which velocity is easily calculated. These measurements are compared with calculated velocity in Fig. 15. Note the excellent agreement. This agreement further reinforces the conclusion previously drawn: velocity and density are insensitive to a heat-addition process in the free-stream. The hypothesized relaxation of vibrational energy will be observed primarily as an increase in free-stream temperature and pressure, not a change in velocity.

This can be shown by considering the equation of state written as

$$P = \rho RT \text{ or } \rho = \frac{P}{RT} \quad (12)$$

But for the heat-addition process in a constant area duct previously discussed, Eq. (6) yields

$$\frac{P_2}{P_1} = \frac{1 + \gamma M_1^2}{1 + \gamma M_2^2} \Rightarrow 1.25 \quad (13)$$

for the case of $M_1 = 14$ and $M_2 = 12.5$.

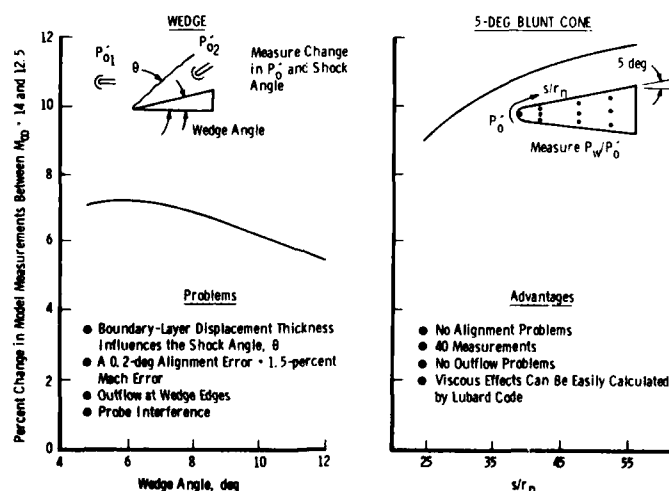


Fig. 13. Comparison of a Low-Angle Wedge and a 5-deg Blunt Cone for Determination of Mach Number.

OTHER EXPERIMENTAL METHODS

Wedges have been used often to check Mach number experimentally. While they may produce useful results, they are clearly inferior in sensitivity compared to a low-angle, blunted cone. Figure 13 compares the percentage change in measured pressure ratios between a wedge and the 5-deg cone used in the Tunnel F experiments. Not only is the blunted cone a factor of two more sensitive, but it eliminates many practical problems encountered with the wedge such as viscous sensitivity, alignment sensitivity, outflow problems, and probe interference problems. These can be critical considerations in hypersonic facilities since times are relatively short; hence, instrumentation accuracies are often inferior to those realized in continuous wind tunnels. In short, the factor of two increase in sensitivity may be required simply to make the measurements meaningful.

Free-stream velocity measurements were made in the course of the Tunnel F experiments. Figure 14 illustrates smear photography of free-stream density fluctuations as viewed through a narrow slit on the tunnel window. This extremely simple, yet highly accurate technique essentially produces a distance versus time plot on the film from

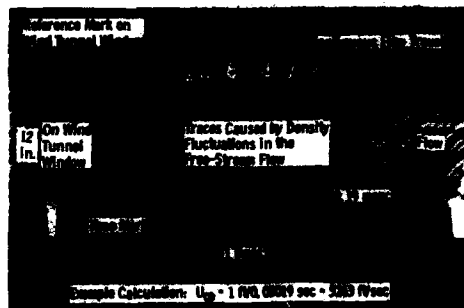


Fig. 14. Enlargement of a 16-mm Film Segment Used to Determine Free-Stream Velocity in Tunnel F.

Likewise,

$$\frac{T_2}{T_1} = \frac{M_2^2}{M_1^2} \left[\frac{1 + \gamma M_1^2}{1 + \gamma M_2^2} \right]^2 \rightarrow 1.25 \quad (14)$$

Hence,

$$\frac{\rho_2}{\rho_1} = \frac{P_1/RT_1}{P_2/RT_2} = \frac{P_1}{P_2} \frac{T_2}{T_1} = 1 \quad (15)$$

and considering the conservation of mass (Eq. (1)),

$$U_1 = U_2 \quad (16)$$

Vibrational temperature of the free-stream flow was measured using the Laser-Raman method in both AEDC's Tunnels C and F. The Tunnel C results are more complete and hence are presented here in Fig. 16. They clearly show the sensitivity of vibrational temperature to water vapor content of the free stream. Note that the measured Mach number closely follows the trend in vibrational temperature decay. The Tunnel F results were consistent with the Tunnel C measurements.

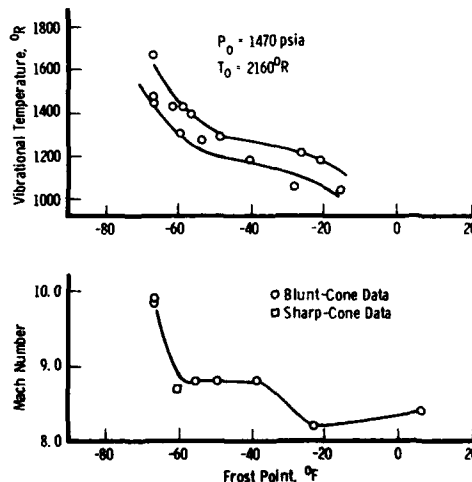


Fig. 16. The Effect of Water Vapor on Vibrational Temperature and M_∞ Measured in the Test Section of AEDC Tunnel C.

and pressure. This relaxation phenomenon is associated with impurities, such as water vapor, in the free-stream flow which act as third bodies.

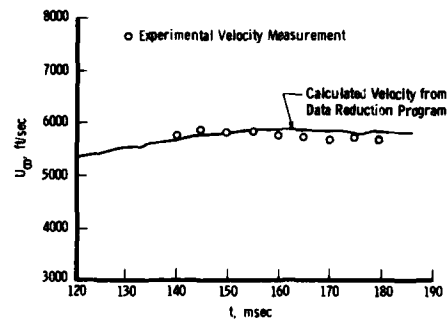


Fig. 15. Tunnel F Velocity Measurements at $M_\infty = 12.5$ (Run 5604).

In Tunnel F the free-stream flow contained, in addition to water vapor, vaporized copper and tungsten from the arc chamber. These impurities no doubt further exacerbate the situation. In general, one should expect non-isentropic processes to be enhanced in proportion to the amount of contamination present in the free stream. As reservoir temperatures increase to satisfy the requirements for hypersonic simulation, clean unadulterated flow will be increasingly more difficult to produce. Recognizing that perfectly clean flow is impossible to achieve in most hypersonic facilities, steps must be taken to account for the inevitable non-isentropic processes. Local test section measurements must be used to characterize free-stream test conditions.

CONCLUSIONS

1. Most hypersonic wind tunnels operating at or above Mach 8 appear to suffer a loss of free-stream Mach number because of non-isentropic processes occurring in the expansion nozzles.

2. It is hypothesized that the principal non-isentropic process consists of a rapid, non-equilibrium, vibrational relaxation which raises free-stream temperature and pressure.

3. Conventional methods of determining free-stream Mach number (i.e., pitot pressure measurements) are insensitive to such non-isentropic processes and hence are poor indicators of true Mach number. Blunt, low-angle cones, on the other hand, have been shown to be excellent indicators of free-stream Mach number.

RECOMMENDATION

The hypersonic wind tunnel testing community should adopt a standard Mach-sensitive model, such as a blunted 5-deg cone, by which all operating and newly calibrated hypersonic facilities can be compared.

REFERENCES

1. Boudreau, A. H., Arnold Engineering Development Center, "Performance and Operational Characteristics of AEDC/VKF Tunnels A, B, and C," AEDC-TR-80-48 (AD-A102614), July 1981.
2. Martellucci, A., Science Applications International, Private Communications, 4 September 1986.

PRÉCISION DES MESURES DE PORTANCE ET DE CENTRE DE POUSSÉE DE GOUVERNES DE MISSILE

par

J. Perinelle et M. Ribadeau Dumas
S.A. MATRA — Service Aérodynamique
B.P. No. 1
37 Avenue Louis Bréguet
78148 Vélizy-Villacoublay Cedex
France

Résumé

Au cours de l'étude de missiles pilotés par voie aérodynamique, il est nécessaire d'estimer les efforts et moments exercés sur les gouvernes.

Difficilement accessibles par le calcul numérique, ces études sont effectuées en soufflerie.

Après une première phase destinée à optimiser la position de l'axe et la forme en plan de la gouverne, il s'agit de mesurer les efforts et moments dans tout le domaine de vol.

Une connaissance aussi précise que possible des moments autour de l'axe gouverne (Moments de charnière) est nécessaire aux études de pilotage.

La communication proposée étudie l'effet de différents paramètres expérimentaux sur la qualité de telles mesures.

Abstract

During the study of aerodynamically piloted missiles it is necessary to estimate the forces and moments applied to the control surfaces.

These quantities are difficult to evaluate by numerical methods and the study is carried out in the wind tunnel experimentally.

After a first evaluation of an optimal position of the axis of rotation and of the planform, the efforts and moments are measured in the whole flight envelope.

An accurate knowledge of the moments about the axis (hinge moment) is required for guidance and control studies.

The proposed presentation assesses the influence of various experimental parameters on the accuracy of such measurements.

Description de l'étude effectuée

Dans le cadre de ce colloque sur la précision des essais en soufflerie, nous avons choisi de vous présenter une étude, effectuée il y a peu d'années, sur la meilleure façon d'obtenir une mesure précise et fiable de moment de charnière sur une gouverne de missile.

Nous verrons, tout au long de cette communication, que les moments de charnière, dans la mise au point du missile, sont certainement les coefficients les plus difficiles à mesurer dans de bonnes conditions.

Il y a très longtemps que l'optimisation de ces coefficients est un de nos soucis majeurs : cela tient à l'emploi systématique de servomoteurs électriques pour mouvoir nos gouvernes. Bien entendu, pour des problèmes d'encombrement, de puissance embarquée et malgré les progrès technologiques, il est toujours nécessaire de minimiser les moments de charnière. Ceci peut se faire en plaçant au mieux l'axe de la gouverne, compte-tenu du domaine de vol du missile. Mais c'est en général insuffisant et il faut étudier des formes spéciales qui permettent d'obtenir les résultats désirés en moment de charnière sans modifier l'équilibre général du missile.

Il y a deux genres d'optimisation :

- 1) Pour les missiles "tout Mach", le facteur le plus important est l'évolution du foyer en fonction du nombre de Mach, l'influence du braquage et de l'incidence étant réduite à un rôle secondaire qui n'est pas négligé pour autant.
- 2) Pour les missiles ayant une gamme de Mach de vol unique (sub ou supersonique), les facteurs prépondérants deviennent éventuellement le braquage et l'incidence. Les déplacements du foyer aérodynamique sont alors plus limités que dans le premier cas.

L'environnement aérodynamique dans lequel se débattent les gouvernes, est aussi très différent d'un missile à l'autre :

- écoulement sain pour des gouvernes "canard",
- écoulement très perturbé quand ce sont des gouvernes situées derrière des ailes. Là, elles sont soumises à la déflexion, au sillage et aussi, pour les ailes de très faible allongement, à l'écoulement tourbillonnaire.

Les difficultés se sont accrues, ces dernières années, à cause principalement de l'augmentation du domaine de vol en incidence de certains missiles, d'une compacité en envergure accrue, mais aussi d'un nouveau besoin de coefficient de moment de charnière qui commence à être introduit dans les lois de pilotage ; d'où une modélisation complète de ce coefficient au lieu de la détermination beaucoup plus simple de son enveloppe.

Pour toutes ces études, il n'est plus envisageable de faire appel aux essais en vol. L'époque où il était possible d'effectuer des séries de tirs de missile pour l'étude de l'aérodynamique, est révolue depuis longtemps et maintenant, à tout le mieux, un essai en vol peut donner un point de recalage. D'autre part, compte tenu de l'environnement aérodynamique des gouvernes, l'étude fine des moments de charnière n'est pas encore possible par le calcul : on peut seulement prépositionner l'axe.

Il reste donc l'utilisation de la soufflerie. Celle-ci peut intervenir à deux niveaux :

- 1) Pour étudier la forme de gouverne répondant au cahier des charges et optimiser la position de son axe : c'est l'aspect optimisation des moments de charnière.
- 2) Pour la détermination fine du moment de charnière en fonction de toutes les variables et en permettre la modélisation : c'est l'aspect identification qui suit logiquement la phase précédente.

On choisira de préférence dans le premier cas et pour des raisons économiques, des souffleries de taille moyenne à rafales qui permettent de nombreux changements de configurations en un temps minimum.

Les techniques employées sont alors :

- En recherche de formes en plan ou de position d'axe, une balance (éventuellement deux) est montée dans le corps du missile et sert de support à la gouverne ce qui, pour des missiles avec gouvernes à l'arrière, rend impossible le montage de la maquette sur un dard balance et sacrifie, dans ce cas, les pesées globales. La balance comporte généralement la mesure de trois composantes : portance, moment de charnière et moment d'encastrement. Les deux premières sont les principales. Elle est dimensionnée pour tenir aux efforts et avoir une grande rigidité, ce qui revient à dire que la plupart du temps, les moments de charnière - par définition de faible niveau - seront mesurés dans une zone ne concernant que quelques pour-cents de l'étendue de mesure de la balance.

Lors de l'exploitation des résultats, on suppose la balance indéformable. Elle est fixée au corps du missile. Les coefficients sont mesurés dans un système d'axes lié au missile. Avec trois composantes mesurées, on ne peut effectuer de changement de repère.

Les essais décrits dans la suite de cet exposé sont de ce type.

- Pour la détermination complète des moments de charnière, il est souhaitable de disposer d'une maquette importante dans une grande soufflerie mais, dans ce cas, il devient nécessaire de commander les braquages à distance et généralement, pour des missiles à gouvernes à l'arrière, d'intégrer les balances à l'intérieur même de la gouverne.

Les changements de configuration sont très peu nombreux, et il est alors intéressant d'utiliser une soufflerie à fonctionnement continu.

On peut être conduit à réduire à deux - voire à un - le nombre de composantes mesurées : moment de charnière et portance. La portance est mesurée suivant un axe perpendiculaire au plan de la gouverne.

La forme de la gouverne, la position de son axe étant figées, il y a tout intérêt à ce que les nouveaux résultats soient en bonne concordance avec les précédents.

Ayant constaté, sur deux configurations de missile :

- qu'il existait des différences non négligeables entre les résultats acquis dans deux souffleries, sur éventuellement une même maquette,
- que les essais en vol, au terme de leur dépouillement, mettaient en cause ces résultats

et pour essayer de répondre aux demandes de précision accrue, nous avons engagé une étude à caractère général. L'objectif fixé est la mise en évidence des principales sources d'erreur pouvant dégrader la précision des résultats et qui sont à relier soit à la maquette, soit à la balance, soit à la soufflerie.

Au-delà de cet objectif, il fallait définir les paramètres les plus influents et les tolérances à leur appliquer pour que le passage des coefficients de soufflerie au missile se fasse sans doute possible. Nous avons donc choisi trois configurations aérodynamiques très différentes de produits en développement pour lesquels les essais de moment de charnière étaient déjà faits, avec les résultats anciens à notre disposition.

- 1) Une configuration canard représentant l'avant d'une bombe guidée laser, à domaine de vol subsonique. Elle a fait, par le passé, l'objet de nombreux essais d'optimisation dans une seule soufflerie (S4 Saint-Cyr - I.A.T.) (figure 3).
- 2) Une configuration de missile aérobie à domaine de vol sub - trans - et supersonique dont les essais avaient été effectués à S2 et S3 Modane (figure 4).

3) Une configuration à ailes longues à domaine de vol sub - trans - et supersonique, dont les essais avaient été faits à S3 Modane et S4 Saint-Cyr, mais dans des conditions légèrement différentes (figure 6).

C'est pour les deux dernières configurations qu'un recalage avec un essai en vol était possible.

Nous allons rappeler brièvement les caractéristiques des deux souffleries où ont été faits les essais.

- La soufflerie S3 de l'ONERA à Modane est à rafales ; l'air est stocké sous pression dans des réservoirs et détendu à travers la veine à nos conditions d'essais (figure 1).

Les dimensions de la veine varient suivant les tuyères utilisées, mais sont de l'ordre de grandeur de : 0,76 m x 0,80 m en supersonique et 0,56 m x 0,4 à 0,78 m en transsonique. La pression génératrice peut varier dans un rapport 10 (0,4 à 4 bars) pour un même nombre de Mach, ce qui permet la variation du nombre de Reynolds. Les incidences vont de -2° à $+30^\circ$ pour le missile à ailes longues.

- La soufflerie S4 de l'Institut Aérotechnique de Saint-Cyr est également à rafales ; l'air est aspiré à travers un dessiccateur à billes d'alumine par des trompes à eau chaude situées au début du diffuseur, à l'aval de la veine d'essais (figure 2).

Les dimensions de la veine, à section carrée, sont de 0,85 m x 0,85 m. La pression génératrice est la pression atmosphérique. Il n'y a donc pas de variation possible de Reynolds pour un nombre de Mach donné.

Le nombre de Mach est réglable entre 0,4 et 2,5. Cette soufflerie a la réputation d'être très laminaire.

Il serait hors de propos de donner ici le détail des programmes effectués dans les deux souffleries, d'autant qu'ils tenaient compte de nombreux essais antérieurs : nous allons seulement exposer les différents paramètres étudiés.

1. Paramètres maquette

1.1. Evolution géométrique des gouvernes

Une étude attentive de la géométrie des gouvernes employées lors de différents essais concernant la même forme en plan de base, a montré que pour des raisons diverses : évolution du projet, fabrications hâtives sur le site, etc ..., les gouvernes étaient rarement identiques d'un essai à l'autre. Les variations portaient sur l'épaisseur relative, le profil, les rayons de bord d'attaque et de bord de fuite. Des recoupements ont donc été faits dans les deux souffleries avec les mêmes gouvernes dont on a fait varier le profil : lenticulaire, plaque plane biseautée au bord d'attaque, plaque biseautée au bord d'attaque et au bord de fuite pour une épaisseur relative identique (8 %). Pour un profil donné (double biseau), une variation de l'épaisseur relative a été effectuée : 12 %, 8 %, 7 % (figures 5 et 7).

A l'issue de ces essais, on peut dire que deux facteurs géométriques sont prépondérants :

- l'épaisseur relative,
- le biseau de bord de fuite (angle et longueur).

Entre les résultats extrêmes, les écarts moyens en portance sont de l'ordre de 30 % en incidence. C'est dans le cas du missile aérobie que nous avons effectué le plus d'essais de profils (schémas figure 8).

Sur les figures 8 et 9, nous avons tracé, à Mach = 0,9, pour différents angles de braquage de la gouverne, les valeurs obtenues pour la portance et le moment de charnière avec différents profils. La forme en plan est bien sûr inchangée. Les écarts atteignent 30 % en portance et sont très importants en moment de charnière. A Mach = 2, ces écarts se réduisent à 10 %, en portance, pour une incidence de 10° (figures 10 et 11).

Sur le missile à ailes longues, on obtient également des valeurs très dispersées pour la portance et le moment de charnière, les écarts, sur ce dernier coefficient, atteignent facilement 60 % (figures 12 et 13).

Les deux profils utilisés, numérotés 1 et 11, ont la même épaisseur relative, soit 7,2 %. Le premier est losangique, le deuxième lenticulaire. Le respect de la géométrie exacte du profil de la gouverne de vol, apparaît donc comme impératif pour l'obtention de mesures de moment de charnière, en soufflerie, comparables aux valeurs de vol. On surveillera, en particulier, les évolutions qui peuvent intervenir au cours du développement du missile. (Changement de procédé de fabrication, de structures affinées, ...). La fabrication des maquettes - épaisseurs des bords d'attaque et de fuite, dièdre, épaisseur - et leur mise en conformité, doivent être vérifiées avec soin. Les moments de charnière, et également l'équilibre général du missile, peuvent être modifiés par la géométrie du profil : son évolution remet en cause la position de l'axe de la gouverne.

1.2. Implantation de la balance

La balance étant interne, l'axe de la gouverne traverse la peau du missile. Un jeu doit être laissé afin d'interdire tout contact entre l'axe de la gouverne, pesé, et la peau du missile. Il doit être minimum pour éviter une interaction avec l'écoulement autour de la gouverne. D'autres essais ont montré que la perte de portance liée à un jeu trop important ne pouvait être négligée.

Il en est de même du jeu entre l'implanture de la gouverne et la peau du missile, qui est difficile à représenter à l'échelle en soufflerie du fait de la taille de la maquette.

1.3. Transition déclenchée

Des essais ont été réalisés, sur le missile aérobie et le missile à ailes longues, avec et sans déclenchement de la transition, à S3 Modane. Ce sont des grains de carborundum collés qui ont été utilisés à cet effet.

Il ne font apparaître aucun effet sensible sur la portance de la gouverne, l'écart maximum, soit 4 %, étant de l'ordre de grandeur de la précision de mesure. Il en est de même du moment de charnière, à l'exception du cas du missile à ailes longues, au-delà de 25° d'incidence (10 % d'écart), mais avec un écart correspondant à un faible déplacement du foyer de la gouverne.

2. Paramètres liés à la soufflerie

2.1. Fidélité des résultats

2.1.1. • Polaires aller et retour en incidence

A S3 Modane, les polaires sont effectuées avec une montée en incidence, suivie d'une descente, sans interruption de l'acquisition pendant cette deuxième phase.

Nous distinguons deux types d'écarts :

- des écarts liés à la précision de la mesure, presque négligeables en portance, mais plus sensibles en moment de charnière,
- des écarts plus importants, en portance et en moment de charnière, apparaissent à haute incidence. Ces phénomènes d'hystérésis se répètent pour tout nouvel essai de recouplement. Nous verrons, plus loin, que ces phénomènes semblent plus dus à un écart de nombre de Mach entre l'aller et le retour, qu'à un phénomène aérodynamique.

2.1.2. • Des polaires ont été répétées successivement, sans variation des paramètres d'essais

Ces recouplements sont de bonne qualité pour la portance, il y a quelques écarts sur les moments de charnière (figure 14).

Nous présentons un recouplement sur une polaire exécutée à trois reprises avec la maquette du missile aérobie, à Mach = 2. En portance, les courbes, presque confondues, ne sont pas présentées (écarts d'environ 3 %).

En moment, on voit une légère dispersion principalement à faible incidence. Compte-tenu des faibles niveaux mesurés, l'écart relatif est important (20 %).

2.2. Effet de Reynolds

Comme pour la transition déclenchée, l'utilisation de profils minces à bords d'attaque aigus rend faible l'influence du nombre de Reynolds, par variation de pression génératrice.

Sur le missile aérobie, entre $P_i = 1$ bar et $P_i = 3$ bars, il n'y a pas de modification sensible des niveaux de portance et de moment de charnière.

Sur le missile à ailes longues, les différences en incidence ne sont pas supérieures à la précision de la mesure.

Un effet de Reynolds plus important doit toutefois être envisagé entre le vol et la soufflerie, les variations de pression génératrice ne permettant pas d'atteindre les Reynolds élevés du vol réel.

2.3. Effet de Mach

En subsonique élevé, les obstructions de veine, aux grandes incidences, rendent difficile la stabilisation du nombre de Mach. Les temps de réponse des asservissements et de la soufflerie, font que le nombre de Mach dépend de l'historique de l'essai et il n'est pas le même selon qu'une situation est abordée en incidence croissante ou décroissante. Sur le missile à ailes longues, au cours d'une polaire en aller-retour à $M = 0,9$, nous avons pu remarquer qu'aux variations du nombre de Mach autour de sa valeur nominale entre les montées-descentes en incidence, correspondent des variations en portance et moment de charnière (figure 15). Les résultats d'un essai à incidence constante et variation continue en Mach, montrent que les écarts précédents s'expliquent par la seule évolution du nombre de Mach entre deux situations identiques par ailleurs.

Pour des comparaisons entre campagnes ou souffleries (temps de réponse à priori différents), le respect du nombre de Mach conditionne la qualité des recouplements.

2.4. Etalonnage de la balance

L'étalonnage d'une balance sur deux sites par des équipes différentes, ce qui suppose aussi des méthodes, des chaînes de mesure, des bancs de tarage, des pièces d'application de charges différentes, ne donne pas les mêmes coefficients.

Nous avons comparé les mêmes résultats dépouillés successivement avec les étalonnages obtenus dans les deux souffleries. En portance, l'écart est faible (2,5 %), mais atteint 10 % en moment de charnière, indépendamment du nombre de Mach : il est à peu près proportionnel à l'incidence, c'est-à-dire au chargement de la balance. D'où l'idée que les coefficients d'interaction portance-moment ne sont pas évalués au même niveau dans les deux étalonnages.

2.5. Montage en soufflerie

Nous avons effectué des mesures en tournant la maquette de 180° (maquette envers), avec le missile à ailes longues. On voit ainsi apparaître des différences supérieures à la précision de mesure allant jusqu'à 5 à 10 % sur le coefficient de portance et 20 % sur le coefficient de moment de tangage. Sur la position du foyer, cela se traduit par un écart voisin du millimètre (soit 2 % de la corde de la gouverne).

L'écart observé correspond en général à un décalage des courbes d'essais.

2.6. Influence de la soufflerie

De nombreux recoupements ont été faits, toutes choses égales par ailleurs, entre les souffleries $\Sigma 4$ de l'I.A.T. Saint-Cyr et S3 de l'ONERA Modane, pour les trois types d'engin, et avec plusieurs profils de gouvernes.

Pour le missile à ailes longues, les essais ont été réalisés avec les gouvernes à profil lenticulaire (N° 11) et prismatique (N° 1).

Dans les deux cas, c'est à $Mach = 0,9$ que les écarts sont les plus importants (figures 17 et 18).

En incidence, $\Sigma 4$ attribue une portance de gouverne plus élevée dans le cas de la gouverne n° 11 à profil lenticulaire.

En moment de charnière, les différences sont sensibles et sont supérieures à la dispersion normale (figure 19 et 20).

A $Mach = 2$, les écarts sont plus réduits (figures 21 et 22).

Rappelons qu'à $Mach = 0,9$, une légère variation du nombre de Mach introduit une importante variation des coefficients mesurés.

Pour le missile aérobie, les résultats à $Mach = 0,9$ ou $Mach = 2$, sont mieux regroupés. Une différence apparaît toutefois localement autour de l'incidence nulle à $Mach = 0,9$ (figures 23 et 24). Le profil, assez épais, est probablement à l'origine de ce comportement local différent, le type d'écoulement à faible incidence devant être différent dans les deux souffleries.

Dans le cas de l'engin canard, les recoupements entre les deux souffleries sont satisfaisants (figures 27 et 28). Comme le vol est subsonique, l'axe des gouvernes est positionné pour minimiser les moments de charnière à $Mach = 0,9$. Les écarts relatifs sur ce coefficient sont donc importants, bien que correspondant à de faibles variations de la position du foyer. Mais ce sont les moments de charnière pris en compte pour le positionnement de l'axe et la modélisation des moments de charnière : cette imprécision n'est pas négligeable pour la bonne réalisation de ces travaux.

En résumé, les recoupements sont satisfaisants pour l'engin aérobie et l'engin canard en portance. Il est à noter que ces engins n'évoluent que jusqu'à 13° d'incidence. Sur l'engin canard, avec positionnement de l'axe adapté à un vol subsonique, les essais, dans deux installations, mettent en évidence des différences relatives importantes sur le moment de charnière.

Dans le cas du missile à ailes longues, qui dépasse 30° d'incidence, les écarts entre les deux souffleries se creusent au-delà de 15° .

CONCLUSIONS

On peut obtenir, dans l'ensemble, une meilleure précision sur le coefficient de portance que sur le coefficient de moment de charnière. Ce résultat était attendu puisque l'axe est positionné de manière à minimiser les moments de charnière. Il est alors très délicat de mesurer simultanément des moments faibles et des portances élevées.

Parmi les différents paramètres étudiés, nous retiendrons :

- le déclenchement de transition, la variation du nombre de Reynolds (dans les limites permises par l'installation d'essai, qui reste éloignée du vol réel), sont sans effet important sur les pesées de gouverne, avec les profils utilisés,
- le bon respect du profil de la gouverne est essentiel ainsi que, d'une façon plus générale, la bonne réalisation de la maquette,
- les écarts observés entre deux souffleries ne sont pas de nature à remettre en cause le positionnement de l'axe de la gouverne optimisée pour les vol sub et supersoniques, où le déplacement du foyer entre le subsonique et le supersonique est prépondérant.

Dans le cas du vol uniquement subsonique, le paramètre Mach n'intervenant pas, le positionnement de l'axe de la gouverne pourrait être légèrement dépendant de la soufflerie.

Il en serait de même d'un engin entièrement supersonique.

La précision du nombre de Mach, la fidélité, le type de montage en soufflerie, font apparaître des écarts sensibles, en particulier sur le moment de charnière. Ils ne sont toutefois pas assez importants pour remettre en cause un réglage d'axe de gouverne. Mais il faut tenir compte, pour l'utilisation d'un modèle de moment de charnière dans les études de pilotage d'un missile, de l'imprécision sur la mesure de ce coefficient.

On apportera un soin tout particulier à l'étalonnage de la balance, en particulier dans le domaine intéressé, c'est-à-dire forte portance et moment faible. La bonne appréciation des coefficients d'interaction est essentielle pour réaliser des mesures de moment de charnière satisfaisantes.

Engin Effet de :	Mach	Missile Aérobie				Missile ailes longues				Engin canard				
		ΔC_z	$\frac{\Delta C_z}{C_z}$	ΔC_m	$\frac{\Delta C_m}{C_m}$	ΔC_z	$\frac{\Delta C_z}{C_z}$	ΔC_m	$\frac{\Delta C_m}{C_m}$	ΔC_z	$\frac{\Delta C_z}{C_z}$	ΔC_m	$\frac{\Delta C_m}{C_m}$	
Profil	0,9 2	0,14 0,04	0,31 0,11	0,05 0,018	3 0,6	0,2	0,16	0,04	0,6	0,02	0,05	0,005	0,3	Pl : 1,3b → 3,2b Mach 0,85 → 0,95 Mach 0,89 → 0,915 (Autour de $\alpha = 0^\circ$)
Fidélité : .AVR	0,9 2	NS	NS	0,002	0,1	0,01	0,01	0,02	0,3	0,01	0,025	0,001 0,001	NS NS	
Recoup.	0,9 2	0,005	0,03	0,004	0,2	0,001	0,01	0,004	0,2	0,01	0,025	0,003	NS	
Transit. Décl.	0,9 2	NS	NS	0,002	0,1	NS	NS	0,006	NS	0,01	0,05	0,003	NS	
Reynolds	0,9 2	0,015	0,03	0,013	0,2	0,04	0,044	0,02	0,5	0,01	0,05	0,003	NS	
Mach	0,2 0,9	0,008	0,026	0,002	0,1	0,02	0,066	0,008	0,4	0,01	0,05	0,003	NS	
Etalonn. bal.	0,9 2	0,01 0,01	0,025 0,025	0,005 0,005	0,1 0,1	0,04	0,1	0,02	0,5	0,01	0,05	0,003	NS	
Montage (Endroit/Env.)	0,9					0,02	0,05	0,008	0,2					
Montage (Dard tournant)	0,9					0,04	0,1	0,01	0,2					
Soufflerie	0,9 2	0,02 (0,04) 0,02	0,05 NS 0,1	0,012 (0,008) 0,005	0,2 (NS) 0,3	0,05 0,02	0,042	0,015	0,3	0,015	0,037	0,002		

NS : Non Significatif

FIGURE 1 : SOUFFLERIE S3 MODANE

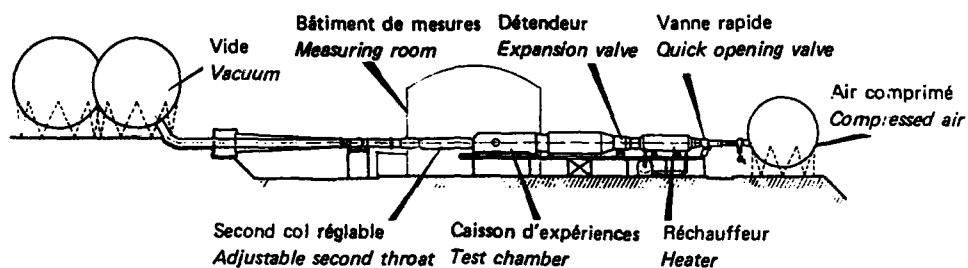


FIGURE 2 - COUPE SCHEMATIQUE REPRESENTANT LA SOUFFLERIE SIGMA 4

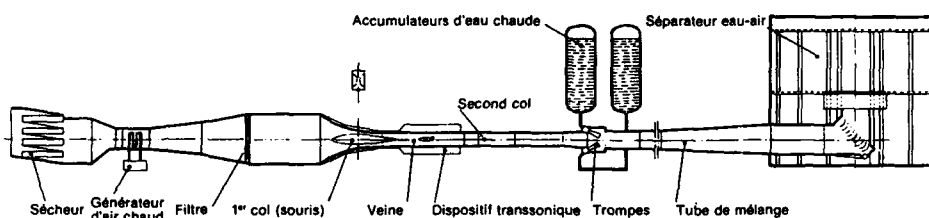
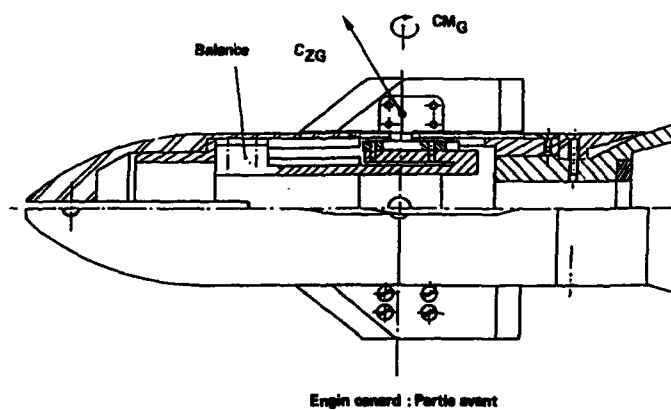


FIGURE 3



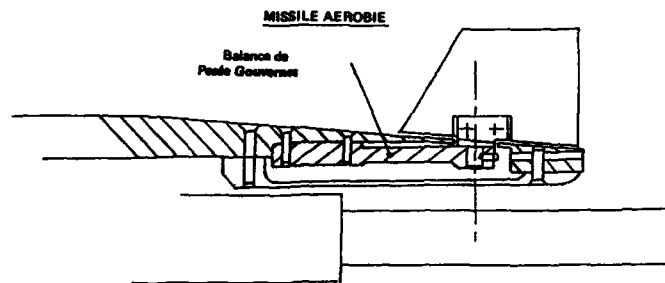


FIGURE 4

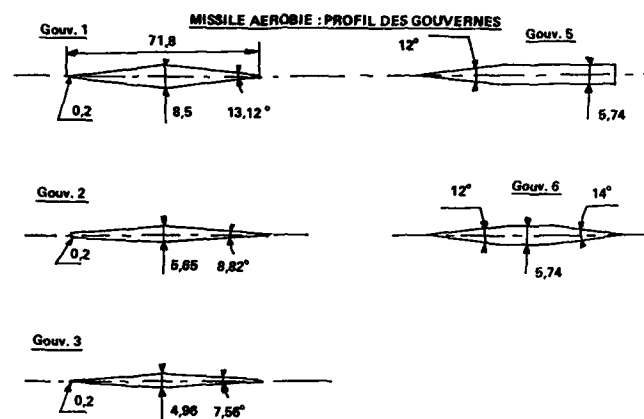
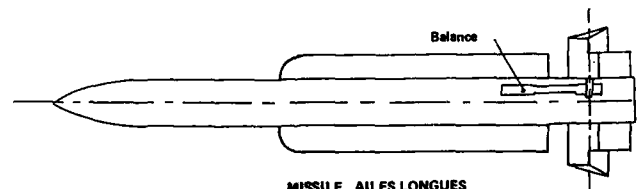


FIGURE 5



MISSILE AILES LONGUES

FIGURE 6

MISSILE AILES LONGUES : PROFIL DES GOUVERNES

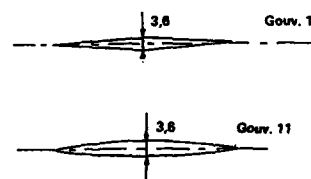


FIGURE 7

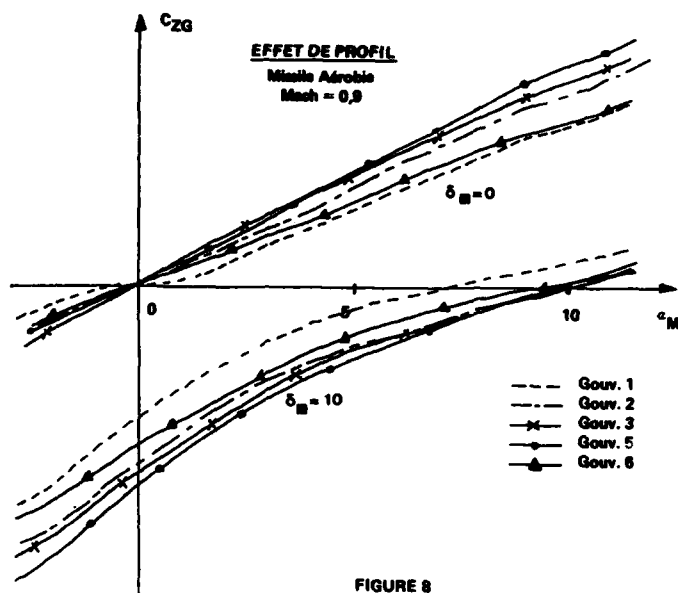


FIGURE 8

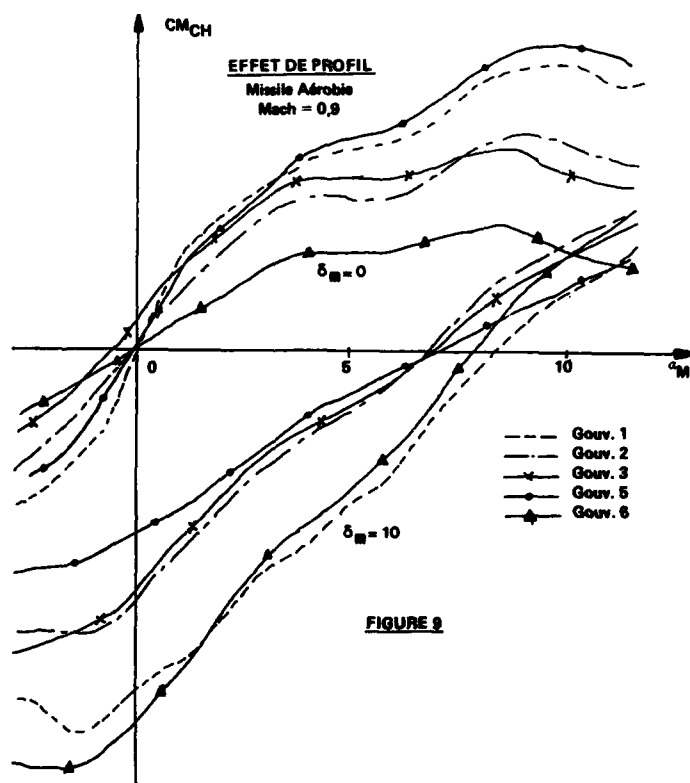


FIGURE 9

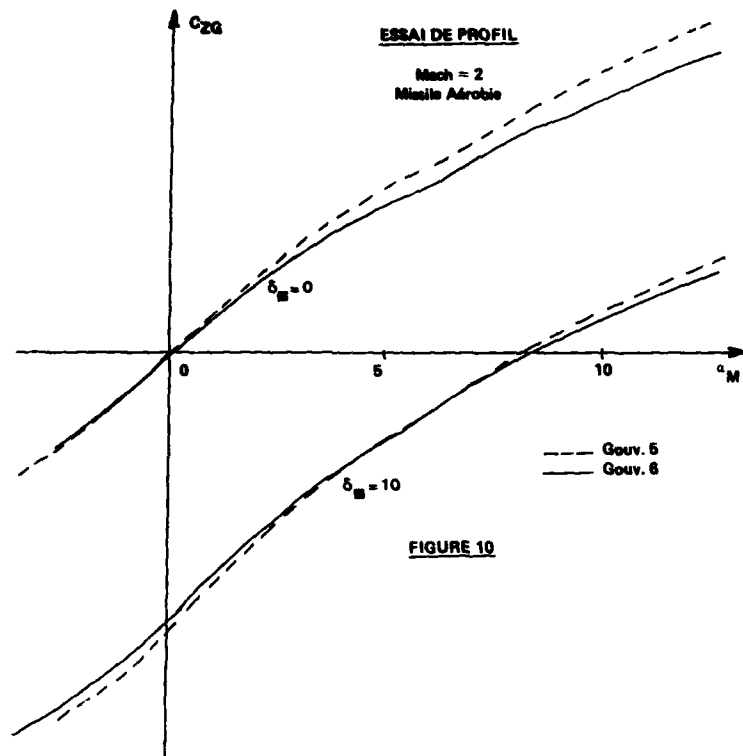


FIGURE 10

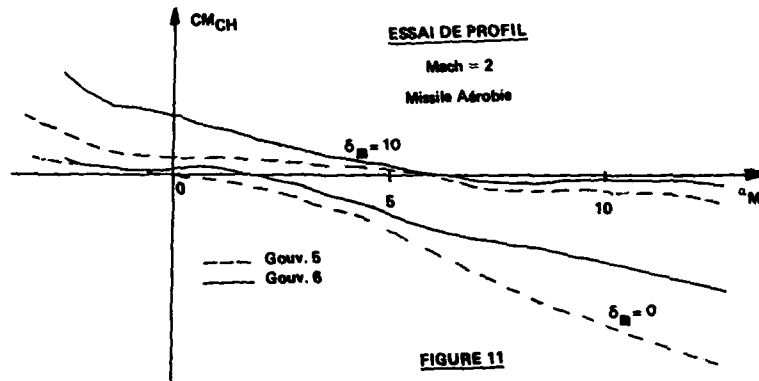


FIGURE 11

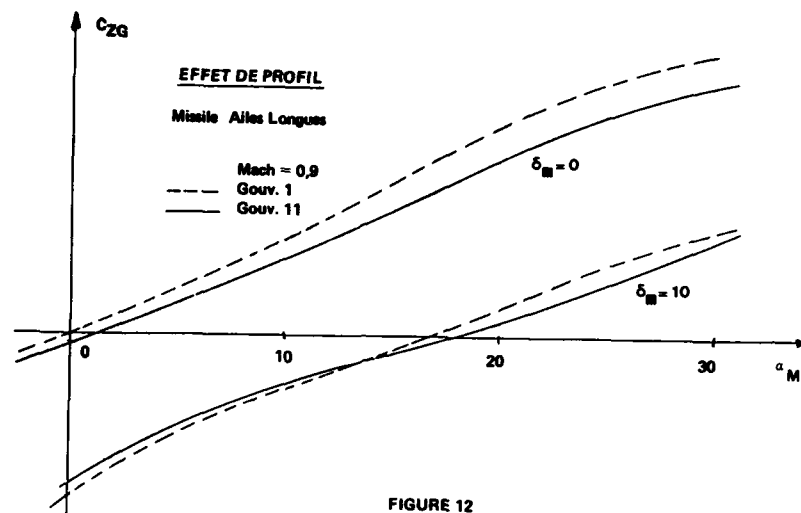


FIGURE 12

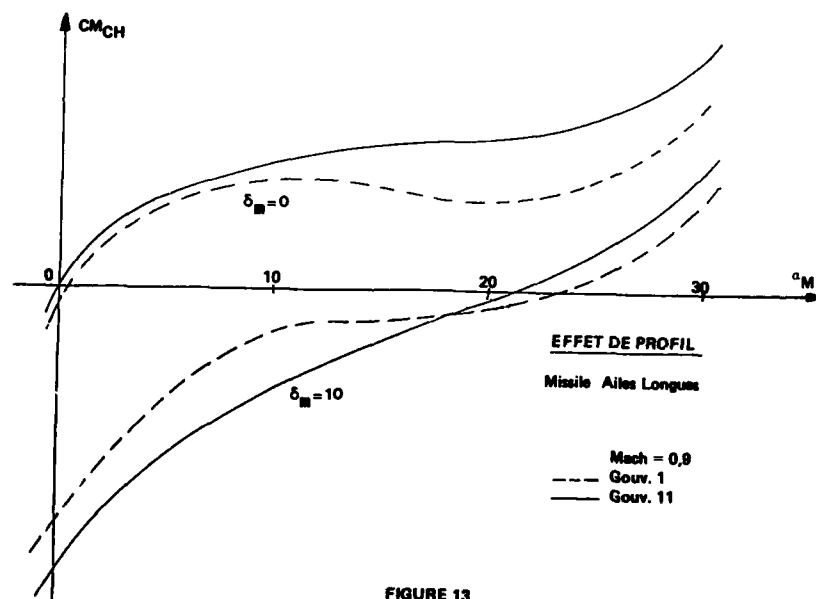
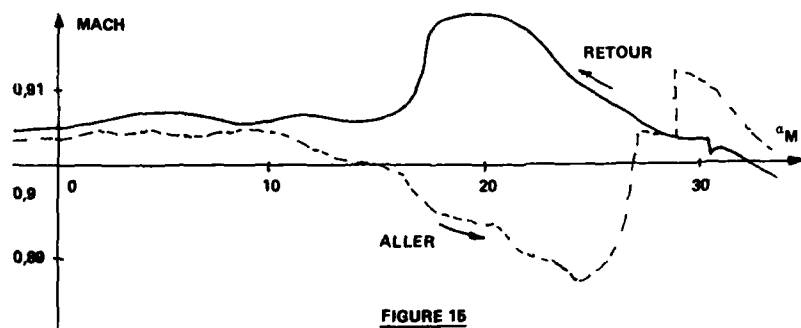
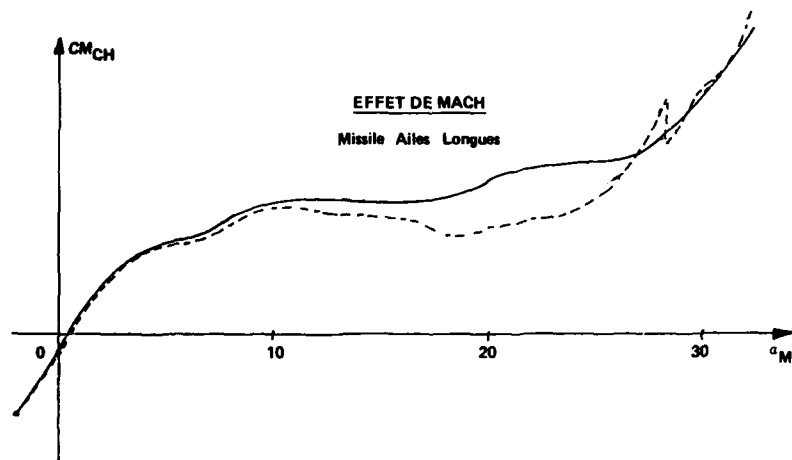
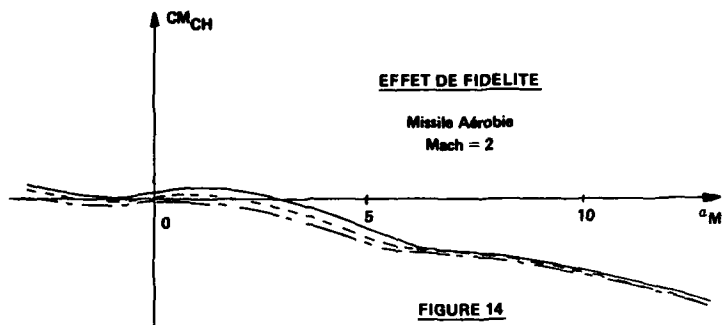
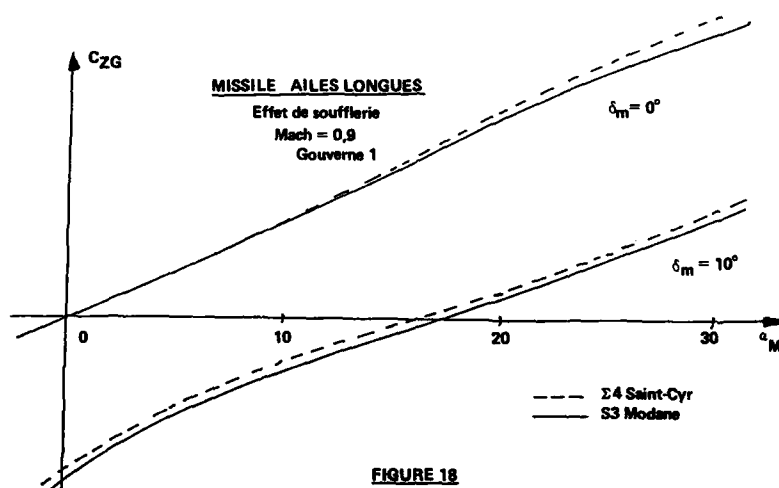
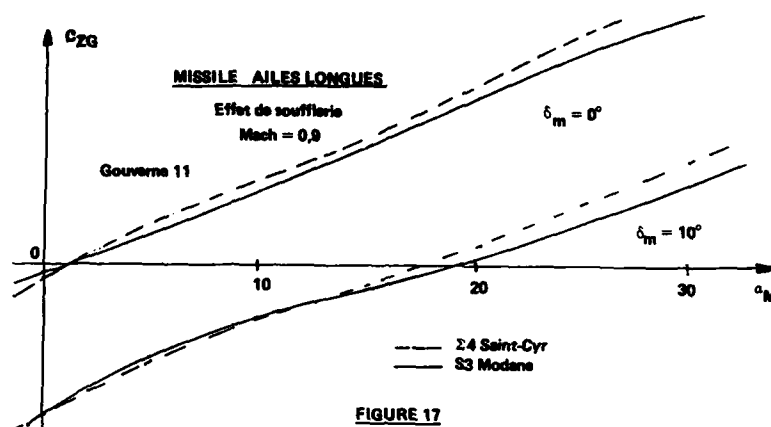


FIGURE 13





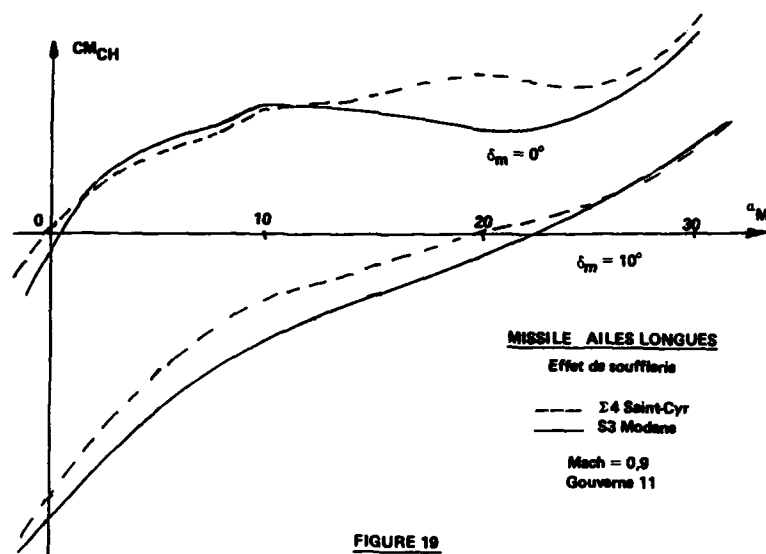


FIGURE 19

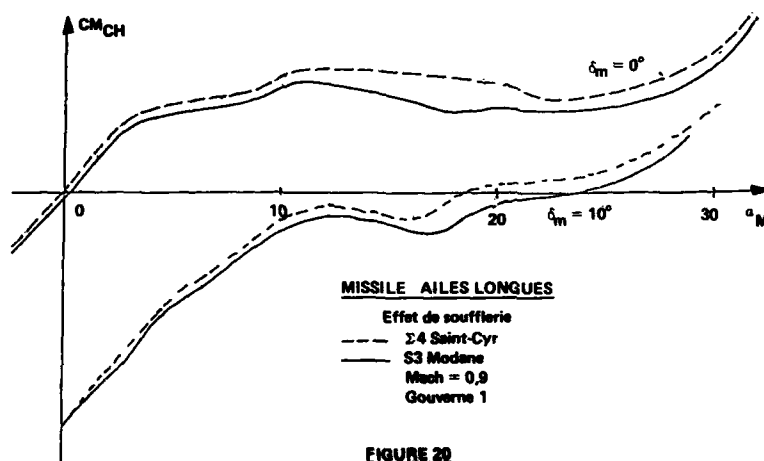


FIGURE 20

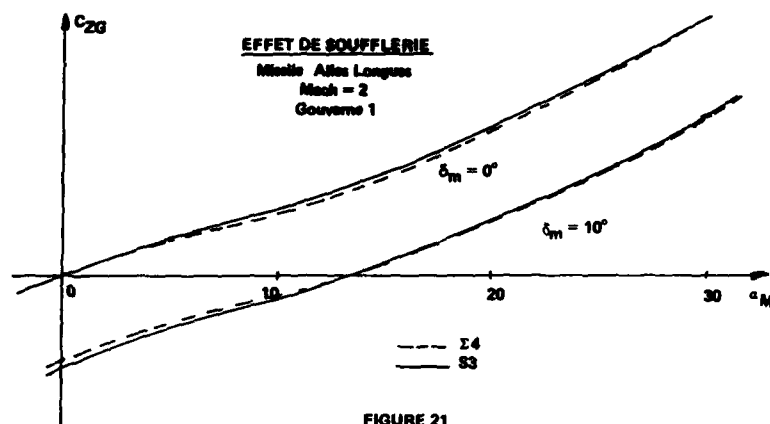


FIGURE 21

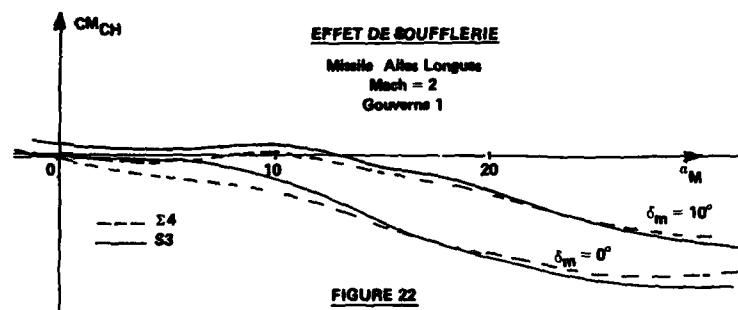


FIGURE 22

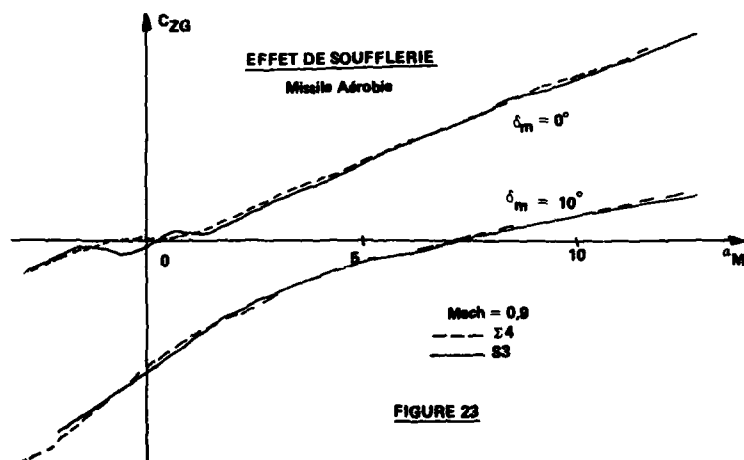


FIGURE 23

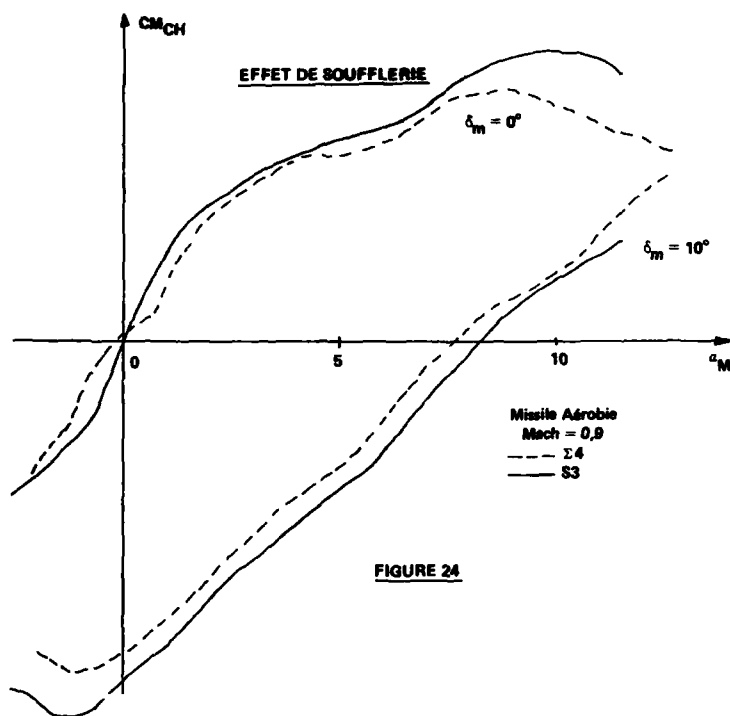


FIGURE 24

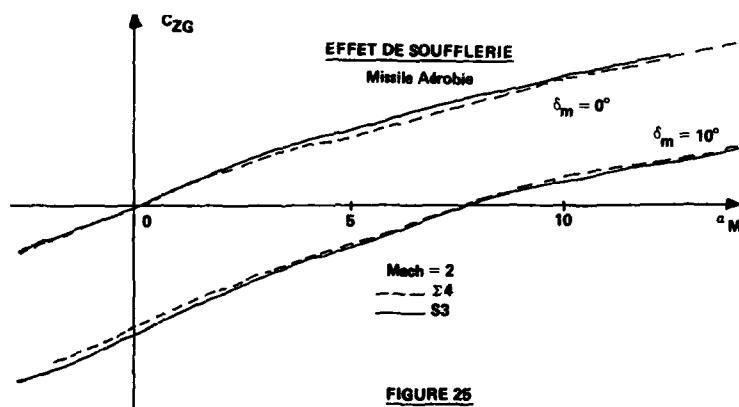


FIGURE 25

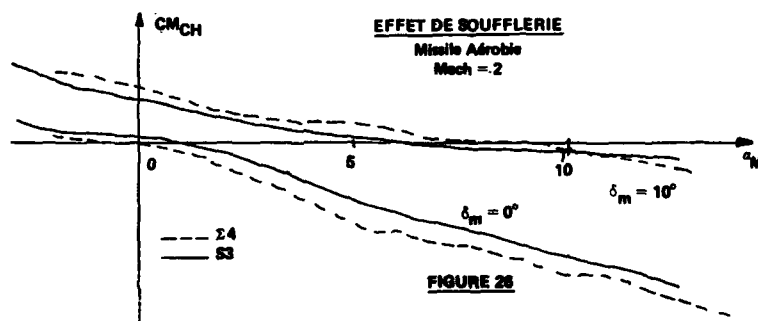
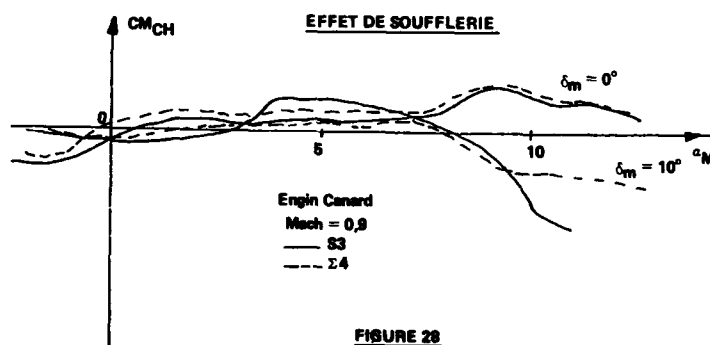
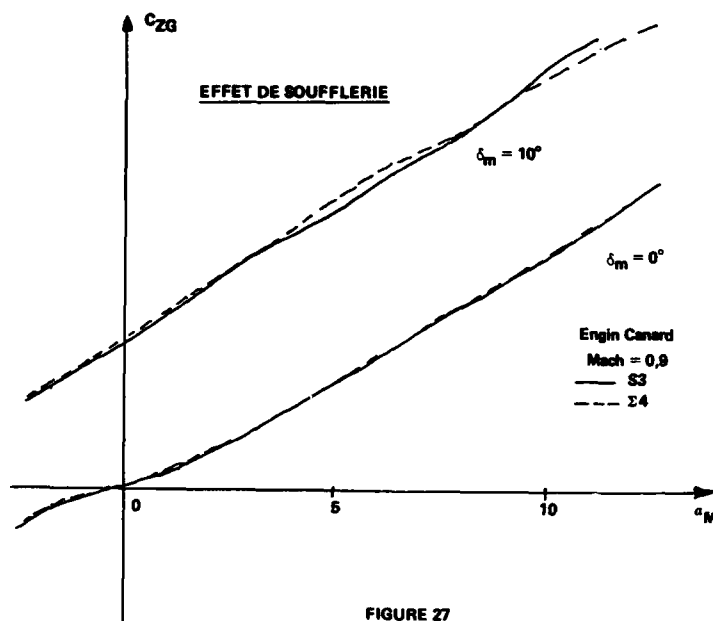


FIGURE 26



COMPUTERIZED THERMOGRAPHIC TECHNIQUE FOR THE DETECTION OF BOUNDARY LAYER SEPARATION

by

R. MONTI and G. ZUPPARDI

Institute of Aerodynamics "Umberto Nobile"
Faculty of Engineering of Naples
P.le V. Tecchio 80, 80125 Naples - Italy

SUMMARY

The computerized unsteady thermographic methodology has been used as a non-invasive technique to analyze the boundary layer development and to detect the transition lines and the separation regions on airfoils surface in wind tunnel. The method is based on the strong dependence of the heat transfer coefficient upon the flow field condition at the airfoil surface.

This non-invasive technique has proved to be very appropriate when studying the boundary layer behaviour at very low Reynolds numbers ($Re < 10^5$) in incompressible flow because at these conditions the boundary layer is very unstable and cannot tolerate any disturbance induced by intrusive techniques.

The experimental diagnostic equipment consists of a Thermograph (AGA 680), an A/D Conversion Unit (AVIORADIO DIGIMEM) and a Microcomputer (APPLE IIe).

The tests have been performed on an elliptic cylinder, on a WORTHMAN FX-63-137 and on a MILEY M06-13-128 airfoil.

The experimental results compare favourably with those obtained by other authors that utilized conventional techniques.

LIST OF SYMBOLS

c	Specific heat of the skin materials:	\dot{q}	Heat flux
C	Model chord:	Re	Reynolds number
c_f	Skin friction coefficients:	St	Stanton number
c_p	Specific heat at constant pressure:	t	Time
h	Convective heat transfer coefficient:	T	Temperature
k	Thermal conductivity:	U	Asymptotic velocity
N (I, J, t)	Thermograph signals:	x, y, z	Cartesian coordinates on TG map
Nu	Nusselt number:	X, Y, Z	Cartesian coordinates of the airfoil surface (see Fig.2)
p	Pressure:		
Pr	Prandtl number:		

Greek Letters

α	Angle of attack:	ν	Kinematic viscosity
δ	Thickness of the model skin:	ρ	Density
Δl	Curvilinear distance between two consecutive thermal pixels:	σ	Stephan-Boltzmann constant
Δt	Time between two thermographic acquisitions:	τ	Characteristic thermal time
ϵ	Emissivity of the observed surface:	τ_w	Wall shear stress
		ξ, η	Coordinates tangent to the airfoil surface

Subscripts and special symbols

a	Ambient or air:	LS	Laminar Separation
aw	Adiabatic walls:	o	Outer surface of the model skin
c	Convective:	r	Radiative
i	Inner surface of the model skin:	T	Transition
k	Conductive:	TR	Turbulent Reattachment
n	Normal to the model skin		

1. INTRODUCTION

One of the major difficulties in experimental aerodynamics is the evaluation of the interference effects induced by intrusive probes in the flow field. This problem, that is common in wind tunnel testings, becomes very critical when sampling the boundary layers at low Reynolds numbers.

Flow fields past aerodynamic bodies (airfoils, wings) at low Reynolds number ($Re < 10^5$) and in incompressible regimes are receiving today great attention for applications to Remotely Piloted Vehicles (RPV), sailplanes, turbine blades, inboard sections of helicopter rotors and so on.

Typical hysteresis loops appear in the lift and drag curves of airfoils and wings: i.e. the values of the lift and drag are different if measured when increasing or when decreasing the angle of attack. This phenomenon, caused by the boundary layer instability, makes all the aerodynamic measurements and their repeatability very difficult. The low Reynolds numbers flow fields are being studied today in wind tunnels

by several researchers (Refs.1-9) who have been performing mainly measurements of aerodynamic forces, flow visualization and pressure measurements. As pointed out by Mueller (Ref.3), the boundary layer at low Reynolds numbers is very sensitive to small, non-controllable disturbances as, for instance, free stream turbulence, acoustic waves and mechanical vibrations. These disturbances strongly depend on the test environments, test facilities, and surface conditions (roughness) of the aerodynamic models.

In particular:

- i) intrusive probes, as the hot wire anemometer, alter the flow field,
- ii) visualization techniques, as the smoke wire, are not accurate,
- iii) instrumented aerodynamic models, as the pressure tap models, may be inaccurate because of the finite number of sensors that can be located on the model surface.

The aim of the present paper is to show the feasibility of the thermographic technique as a non-intrusive method for the study of the boundary layer development and for the detection of the separation regions on the surface of airfoils at low Reynolds numbers, thus avoiding the drawbacks of the above mentioned methods.

The method relies on the fact that the distribution of the convective heat transfer coefficient (or its non dimensional value like the Nusselt or Stanton number) is related to the flow regimes, to the boundary layer characteristics and to the flow separation; the distribution of the Nusselt (or Stanton) number over the airfoil surface will then yield information on the boundary layer evolution.

The method has been already tested successfully by the first author (Refs.10, 11) that analyzed flow fields past non-lifting bodies (cylinder, sphere). In the present paper measurements are extended to aerodynamic models: 1) an elliptic model of aspect ratio 1:3 (test case), 2) a WORTMANN FX-63-137 airfoil (Ref.7) and 3) a MILEY M06-13-128 airfoil (Ref.4). These two belong to the class of airfoils specifically designed to operate at very low Reynolds numbers (say in a range $10^4 < Re < 10^5$).

2. THEORETICAL MODEL

The mathematical model needed to compute the Nusselt and Stanton number distribution is described in details in Refs.10, 11. The following discussion will therefore cover only the main aspects of the problem.

The unsteady 2-D heat balance equation for a thin skin airfoil model of thickness δ (Fig.1) that is exposed to heat fluxes at the outer and inner surface (\dot{q}_o , \dot{q}_i) reads, when integrating the equation across the model skin (Ref.10):

$$\dot{q}_o = \dot{q}_i - \rho c \delta \frac{\partial T_o}{\partial t} + k \delta \left(\frac{\partial^2 T_o}{\partial \xi^2} + \frac{\partial^2 T_o}{\partial \eta^2} \right) \quad (1)$$

where:

ρ , c , k are the skin thermophysical characteristics,
 T_o is the outer surface temperature of the model,
 δ is the thickness of the model skin,
 ξ , η are the coordinates in the plane tangent to the surface.

Apart the negligibility of the curvature effects, the main assumptions made in the derivation of Eq.1 are:

- i) the energy accumulation in the model (due to model heating or cooling) is approximated by:

$$\int_0^\delta c \frac{\partial T}{\partial t} dn = c \delta \frac{\partial T_o}{\partial t} \quad (2,a)$$

- ii) the heat conducted through the model skin is similarly approximated by:

$$\int_0^\delta k \left(\frac{\partial^2 T}{\partial \xi^2} + \frac{\partial^2 T}{\partial \eta^2} \right) dn = k \delta \left(\frac{\partial^2 T_o}{\partial \xi^2} + \frac{\partial^2 T_o}{\partial \eta^2} \right) \quad (2,b)$$

The above approximations are discussed in Refs.10, 11 where their validity is shown to depend on the thermal characteristics of the model and on the experimental thermographic observation times.

If only the convective heat transfer (\dot{q}_c) is of interest, then the overall heat flux between the model surface and ambient must be corrected by subtracting the radiative heat transfer (\dot{q}_{ro}):

$$\dot{q}_{co} = \dot{q}_o - \dot{q}_{ro}$$

The local convective heat transfer coefficient is then defined as:

$$h = \frac{\dot{q}_{co}}{(T_o - T_{\infty})}$$

and the Nusselt and Stanton numbers as:

$$Nu = \frac{hC}{k_a} \quad St = \frac{h}{\rho V c_{pa}} = \frac{Nu}{Re Pr}$$

where:

U is the asymptotic velocity,
 C is the body characteristic length (in the present case the chord of the airfoil),
 c_{pa} is the specific heat of air at constant pressure,
 k_a is the thermal conductivity of the air.
 With the above definitions, one may write:

$$Nu = Nu_c + Nu_k + Nu_r \quad (3,a)$$

where Nu_c , Nu_k , Nu_r are the contributions due to the heat capacity (unsteady term), to the conductive and to the radiative term, respectively;

$$Nu_c = - \frac{\rho c \delta}{(T_o - T_{aw})} \frac{\partial T_o}{\partial t} \frac{C}{k_a} \quad (3,b)$$

$$Nu_k = \frac{k \delta}{(T_o - T_{aw})} \left(\frac{\partial^2 T_o}{\partial \xi^2} + \frac{\partial^2 T_o}{\partial \eta^2} \right) \frac{C}{k_a} \quad (3,c)$$

$$Nu_r = - \frac{\epsilon \sigma (T_o^4 - T_a^4)}{(T_o - T_{aw})} \frac{C}{k_a} \quad (3,d)$$

Use of the computerized Thermographic System (TG) allows the outer surface temperature distribution to be measured in time $T_o(\xi, \eta, t)$ and therefore the Nu to be evaluated.

The knowledge of the heat transfer coefficient can release information on the boundary layer characteristics. In particular if the Reynolds analogy would apply ($St = c_f/2$) then one could immediately correlate the value of the velocity gradient at the surface with the measurement of the Stanton number:

$$\frac{\partial V}{\partial n} = \frac{V^2}{\nu} St = \frac{V}{C} \frac{Nu}{Pr}$$

So, in this case, the ratio Nu/Pr is a non dimensional value of the velocity gradient at the surface.

Several generalized forms of the Reynolds analogy are proposed in the literature to extend it to cases not considered in its classical formulation (i.e. $Pr = 1$, $dp/d\xi = 0$). In general for attached flows, the Stanton number profile is expected to be qualitatively similar to that of the skin friction coefficient.

Two typical formulas are reported here to substantiate the above statement.

The first one (Ref.12) is applicable to incompressible laminar flow past a wedge of angle $\beta\pi$ [rad]:

$$St = \frac{c_f}{2} Pr^{2/3} (6a^2)^{-1/3} (1 - \chi)^{-1/3} F_o \quad (4)$$

where:

$$\chi = (\xi_o/\xi)^{\frac{3}{4-2\beta}}$$

c_f is the skin friction coefficient,

a is the second order derivative of the Falkner-Skan velocity function on the body,

τ_w is the wall shear stress,

ξ_o is the curvilinear abscissa where the wall temperature has a discontinuity,

F_o is the dimensionless wall derivative of the temperature with respect to the coordinate normal to the surface.

The second formula (Ref.13) is for incompressible turbulent flows:

$$St = \frac{c_f F_1 F_2}{Pr} \quad (5)$$

where:

F_1 , F_2 are factors characterizing the deviation of the temperature field from the Reynolds analogy concept. In all the above cases one may relate the velocity gradient at the surface with St (or, more directly, with Nu).

3. NUMERICAL APPROXIMATIONS

A computer code has been developed on the basis of the Eqs. 3a-d. It processes the thermographic images to compute the Nusselt/Stanton number distribution on the surface of the airfoil.

The code has been arranged so that the three contributions to the Nusselt number are computed separately in order to evaluate their relative importance.

If Δt is the elapsed time between two thermographic images, the unsteady contribution is computed as:

$$Nu_c = \frac{\rho c \delta}{\Delta t} \frac{T_o(t + \Delta t) - T_o(t)}{\bar{T}_o - T_{aw}} \frac{C}{k_s} \quad (6)$$

where T_{aw} is the average value of the adiabatic wall temperature. It coincides with the average temperature of the observed surface, taken in adiabatic steady thermal condition.

T_o is the surface temperature at the intermediate time between t and $t + \Delta t$. This is numerically estimated as the arithmetic mean of the temperatures at the two times t and $t + \Delta t$:

$$\bar{T}_o = T_o(t + \frac{\Delta t}{2}) = \frac{T_o(t) + T_o(t + \Delta t)}{2} \quad (7)$$

In the case of incompressible flow ($T_{aw} = T_a$) the Nusselt number associated to the radiative contribution can be approximated by:

$$Nu_r = \frac{4 \sigma \epsilon T_a^3 C}{k_s} \quad (8)$$

This approximation is acceptable if the surface temperature (T_o) is not much higher than the ambient temperature (i.e. when $(T_o - T_a)/T_a \ll 1$).

The numerical evaluation of the conductive contribution to the Nusselt number (i.e. the second order derivatives of the surface temperature) takes into account the fact that the Thermograph detects the projection of the surface temperature over a plane orthogonal to the viewing axis; therefore it was necessary to develop an algorithm able to compute $\partial^2 T_o$ on curved surfaces taking into proper account the airfoil position with respect to the thermograph (i.e. the angle of attack).

In the present measurements the span axis of the airfoil is orthogonal to the viewing axis ($\eta = \chi$); therefore the correction refers only to the conductive heat flux along the chord direction.

The airfoil model is positioned with respect to the Thermograph so that the chord is aligned with the direction of the rows; the number of pixels available along the chord is 128 that is sufficient for the evaluation of $\partial^2 T_o / \partial \xi^2$ in Eq. 3c.

The numerical algorithm that evaluates the second order derivative, along a pre-selected row "I" and at the generic column point "J", relies on three pixels (not equally spaced) and reads:

$$\left(\frac{\partial^2 T_o}{\partial \xi^2} \right)_J = \frac{\frac{\bar{T}_o(i+2) - \bar{T}_o(j)}{\Delta l_{j+2} + \Delta l_{j+1}} - \frac{\bar{T}_o(j) - \bar{T}_o(i-2)}{\Delta l_j + \Delta l_{j-1}}}{\Delta l_{j+1} + \Delta l_j} \quad (9)$$

The geometrical computing scheme of the curvilinear distances $\Delta l_1, \Delta l_2, \dots, \Delta l_n$ between two consecutive thermographic pixels on the airfoil surface is shown in Fig. 2. The routine consists in evaluating:

i) a second order closed spline function (Ref. 14) interpolating the coordinates of a number m of assigned points of the airfoil surface ($X_i, Z_i, i=1, \dots, m$; typically $m=20$). The selected order of the spline is believed to be accurate enough for this computation. In fact the property of the spline function guarantees the continuity of the curve, its slope and curvature at each point of the surface. This is an iterative algorithm that computes both the curvilinear abscissas $\xi_i, i=1, \dots, m$ and the coefficients of the polynomial, parametric functions $X = X(\xi)$ and $Z = Z(\xi)$. At first step the coefficients of the functions $X^0 = X^0(\xi^0)$ and $Z^0 = Z^0(\xi^0)$ are evaluated using as curvilinear abscissas the distances measured along the polygon connecting the input points. A number (say 30-40) of subdivision points are then introduced in each interval. A new set of curvilinear abscissas ξ^1 is computed using the functions X^0, Z^0 and a new couple of $X^1 = X^1(\xi^1)$ and $Z^1 = Z^1(\xi^1)$ is then obtained. The computation is iterated until a convergence criterion, based on the percentage difference, at the generic iteration j : $(\xi_j^j - \xi_{j-1}^j) / \xi_{j-1}^j, i=1, \dots, m$, is fulfilled;

ii) the distance between two consecutive thermal pixels along the chord: $\Delta X = C / n$, $n = J_T - J_L$ where J_T and J_L are the pixel numbers identifying the trailing and the leading edge;

iii) the curvilinear abscissas $\xi_1, \xi_2, \dots, \xi_{n+1}$ of the points of the airfoil surface corresponding to the geometrical abscissa X_1, X_2, \dots, X_{n+1} , by means of the spline function;

iv) The curvilinear distances Δl_j ($j=1,2,\dots,n$) are finally obtained from $\xi_1, \xi_2, \dots, \xi_{n+1}$ by the approximative relationships:

$$\Delta l_j \approx \xi_j - \xi_{j-1} + (Z_{j-1} - Z_j) \sin \alpha \quad (10)$$

4. EXPERIMENTAL EQUIPMENT AND TEST PROCEDURE

4.1 Thermographic Equipment

The thermographic equipment implemented at the Institute of Aerodynamics "Umberto Nobile" consists of (Ref.10):

- 1) Thermograph AGA 680. This is a single detector, cryogenically cooled device. It uses two scanning mirrors (a rotating and an oscillating mirror) to map the temperature of a finite surface. The photons emitted by each point of the surface are focused on the detector at different times with a frequency which depends on the scanning time of the mirrors.
- 2) DIGIMEM AVIORADIO A/D Converter that acquires and digitizes the thermographic picture in a matrix of thermal pixels. The buffer RAM of this instrument can store simultaneously two digitized thermal images (or matrices) $N(t)$, $N(t + \Delta t)$ taken at a time interval Δt (that can be selected at will). Since the frequency is rather high, (the scanning time is shorter than the characteristic cooling time) a thermographic image is taken by averaging the pixel values over eight subsequent thermal images (one image every two seconds). Consequently the noise/signal ratio is substantially reduced and a more accurate surface temperature measurement is provided. The thermal accuracy is estimated to be about 0.1 centigrade.
- 3) Personal computer (APPLE IIe) where the two thermographic matrices are recorded. The microcomputer can store simultaneously two matrices of 68×128 pixels (8 bits) for subsequent elaboration.

4.2 Models

The geometry of the MILEY and the WORTMANN airfoil is shown in Fig.3. The dimensions (chord and span) of all the models are 0.1 [m] and 0.15 [m] respectively. These are dictated by the diameter of the wind tunnel test section. The wing span equals the exit diameter and two fences are located at the span ends in order to simulate a 2-D flow field. All the models are by a thin foil ($\delta = 0.5$ [mm]) of stainless steel (S304) whose thermophysical properties are:

Density (ρ)	= 7900	[Kg/m ³]
Specific heat (c)	= 500	[J/Kg/K]
Thermal conductivity (k)	= 14.6	[W/m/K]

This material was chosen for structural and thermophysical reasons:

- i) it was easily folded to fit the large curvature of the airfoil leading edge (due to the very small dimension of the chord) without wrinkling;
- ii) although the material foil is very thin, it is rigid enough to keep the shape of the airfoil;
- iii) the thermal conductivity and the foil thickness exhibits values that satisfy the assumptions made in the mathematical model (Eq.1).

In particular the temperature time derivative and the second order derivatives along the surface (Eqs.2a, b) are practically constant across the foil thickness. The rather high thermal conductivity may imply however a large contribution of the conductive term, in presence of non negligible surface temperature second order derivative along the tangential directions.

The external surface of the models was painted with black graphite powder in order to get a value of the surface emissivity close to one (and a TG signal only slightly dependent on the surrounding ambient conditions).

4.3. Experimental Procedure

The experimental procedure is the following one:

- i) establish a steady flow field past the airfoil model in a wind tunnel and measure by the TG system the surface temperature at one side (e.g. the upper side of the model). This temperature practically coincides with the adiabatic wall temperature (T_{aw});
- ii) heat up the airfoil model trying to obtain a temperature distribution as uniform as possible (to avoid large contribution of Nu_k);
- iii) shut-off the heat sources;
- iv) observe with the aid of the thermographic system the time evolution of the surface temperature of the model that is being cooled by the air flow: two thermographic images are taken at a time interval Δt ;
- v) by means of the Microcomputer, process the $N(t)$ and $N(t + \Delta t)$ signal matrices to obtain the Nusselt and/or the Stanton number distribution over the observed surface.

The experimental equipment is shown in Figs.4a,b.

4.4 Heating Systems

Two heating procedures will be described and the results compared. In the first procedure the heating of the model takes place when it is in the airflow; in the second procedure the heating is performed before the airflow is established over the model. The drawback of the first procedure is the disuniformity of the temperature profile along the chord (e.g. in correspondence of the leading edge due to the higher cooling rate).

Two different heating techniques have been used in connection with the first procedure:

- i) the first technique consists in blowing hot air ($\sim 300^\circ\text{C}$) into the hollow model by means of a blower connected to the model through a muff;
- ii) the second technique uses a "comb" of electric wires, positioned inside the model and running along the wing span, they radiate power onto the inner surface of the model.

With both the above techniques the first thermographic image is taken soon after the heating source is shut-off.

A typical profile of the first thermographic image, obtained for the WORTHMANN airfoil heated by the hot air, is shown in Fig.5a. One can notice the low temperatures at the leading edge because of the high local heat transfer to the air; low temperatures also occur at the trailing edge because of the reduced hot air mass flow rate in these regions.

The contribution of the conductive flux is therefore important and must be carefully evaluated.

When using electrical wires the value of \dot{q}_j , transmitted to the model wall by the wires (after the power source is shut-off), must be evaluated and included in Eq.1.

With the second procedure the heating of the model is accomplished with the tunnel airflow diverted away from the model by means of a baffle. With this procedure a third heating technique can be used: warm air ($\sim 60^\circ\text{C}$) is blown on the external model surface. The first thermographic image is taken 2-3 seconds after the baffle is removed and a steady flow field is created over the airfoil. This heating procedure may lead to an initial temperature distribution more uniform than the one achieved with the first procedure (Fig.5b).

The uniformity of the temperature may be appreciated by looking at the Thermograph Monitor; the experimenter can consequently blow warm air at the appropriate surface regions to achieve an almost constant surface temperature (this technique cannot be used in closed test chamber wind tunnels).

Most of the thermographic results, which will be shown in the next sections, have been obtained with this procedure.

4.5 Choice of Thermographic Measurement Sequence

The choice of the time interval Δt is a compromise among the following requirements:

- i) the numerical approximation of the time derivative (Eq.4) that calls for a small time interval;
- ii) the Thermograph sensitivity that would suggest long time intervals to achieve an accurate evaluation of the "difference" between the two temperature matrices $T(t + \Delta t) - T(t)$;
- iii) the validity of the assumptions (2a,b), that is best accomplished with a rather long time interval.

To estimate the value of Δt necessary to obtain a minimum temperature difference ΔT_m detectable by the Thermograph (as for requirement ii), one can write (Ref.10):

$$\Delta T_m = \Delta t (T_o - T_a) \quad (11)$$

where:

$T_o - T_a$ is the temperature increase of the model surface over the ambient temperature. By using the external heating technique: $T_o - T_a \approx 20^\circ\text{C}$ guarantees a sufficiently large value of ΔT_m .

In fact recalling the definition of the characteristic thermal time (τ):

$$\tau = \frac{\rho c \delta}{h} \quad (12)$$

and assuming for the Nusselt number an average value of 350, one obtains (from the definition of the Nusselt number): $h \approx 90 \text{ [W/m}^2\text{/K]}$. Eq.12 (by using the geometrical and thermophysical properties of the skin materials) gives $\tau \approx 20 \text{ [s]}$. To obtain sufficiently large values of ΔT_m , the value of Δt was therefore set at 4 [s] that implies average surface temperature differences of 4 [C] (measured with good accuracy by the TG System).

4.6 Calibration and Temperature Measurement

The success of the TG technique is based on the possibility of obtaining accurate temperature maps of the model surface. This involves a calibration procedure and a software for the transformation of the signal matrix $N(t)$ into a temperature matrix $T(t)$.

Calibration curves are constructed for the surface of interest at a given sensitivity and at constant ambient conditions by looking at a surface point where the temperature

can be changed at will (within the temperature range of interest) and where the temperature can be measured by a point sensor probe. The couple of values of T and N are recorded to construct a calibration curve to cover all the temperature range. The value of N that corresponds to the temperature T is however dependent on the window (or slot) position, chosen by the TG operator.

The calibration curve is built piecewise by patching together different legs, obtained at different window positions. At a window position "1" one records T_1 and N_1 at increased temperature values starting at temperature T_{\min} when the window range is covered (e.g. $\Delta T = 20^\circ\text{C}$) and the value of N corresponding to $T_{\max} = T_{\min} + \Delta T$ is at its maximum value (N_{\max}) then the window is shifted to position "2" so that the same T_{\max} corresponds to a smaller value of N (N_{\min}) (see Fig.6a where the calibration curves built for the elliptic model are shown). The patching of the two calibration curves is then performed by plotting the second curve shifted by $\Delta N = N_{\max} - N_{\min}$ (Fig.6b) (the maximum value of ΔN is the number of available bits/pixel of the A/D process, in the subject case $\Delta N = 203$).

A complete calibration curve is then obtained covering the temperature range of interest.

The measurement phase needs a reference temperature (T_r) in the field of view to recognize a point on the calibration curve. By reading the value of N_r corresponding to T_r , taken at the general window position (i), one is able to select the proper position of the calibration curve with respect to the N axis. In fact reading on the calibration curve the value of N_r corresponding to T_r allows to compute the value of the shift $\Delta N_r = N_r - N_{1r}$.

The point surface temperature corresponding to the value N is then found by computing the "corrected" signal N_c given by $N_c = N + \Delta N_r$, entering the calibration curve with this new value and reading $T(N_c)$.

4.7 Support Software

The Thermographic System is equipped (Ref.10, 11) with a number of routines written in machine language that allows: 1) the management of the thermographic images $N(I,J)$ (transfer from the Digimem to the Microcomputer, recording/reading on/from the Floppy Disk etc.), 2) the elaboration and 3) the visualization. These last routines consist in displaying and printing: i) the elements of the matrix $N(I,J)$, ii) the plot of the thermographic signals along an assigned row "I" (or column "J"), iii) the Thermograph signal on colour monitors.

Two graphic routines have been specifically developed: i) to plot the distribution of the Nusselt number along the preselected row "I" (e.g. along the airfoil chord) and ii) the Nusselt number footprint on the model surface. It is possible to choose the visualization and printing of the total Nusselt number or of one of its contributions (Nu_c , Nu_p).

5. RESULTS

5.1 Test Model

Experiments have been performed preliminarily to ensure that the thermographic measurements and the proposed procedure were correct. Due to the lack of any experimental and theoretical/numerical data about the Nusselt number distribution along the surface of the wing, it was necessary to get data for an elliptic cylinder of axis ratio 1:3 for which the Nusselt number distribution was available (Ref.15). The Nusselt number distributions, obtained for $\alpha = 0$, $Re = 7.92 \times 10^4$ and $\alpha = 15$, $Re = 7.93 \times 10^4$ are shown in Fig.7a and Fig.7b respectively.

The agreement between the TG results and the ones reported in Ref.15 are qualitatively good, thus the results that will be shown later can be believed to be reliable.

The discrepancy at the leading and trailing edges at $\alpha = 0$ is probably due to the fact that the local emissivity coefficient is different from the value adopted in the computation ($\epsilon = 1$); this may also be due to the effect of the curvature at the edges that alters the local view angle of the surface observed by the thermograph. This discrepancy is observed also in the middle part of the wing section (at large angles of attack). On the other hand the measurements made in Ref.15 (by the steady state method) do not seem to be very accurate because heat radiation from the model surface and heat conduction in the model skin have been neglected in the computations. Furthermore discrete temperature measurement points are taken. Finally the assumption of the uniform heat flux all over the surface (by Joule heating of the skin) seems to be too optimistic.

5.2 Boundary Layer Development Over Airfoils

The laminar separation bubble is the relevant phenomenon in boundary layer development past airfoils at low Reynolds numbers.

The separation bubble (Fig.8) is formed when the laminar boundary layer detaches from the airfoil surface. The bubble is formed by the combined effects of the adverse pressure gradient, downstream of the point of minimum pressure, and of the low value of the Reynolds number. The separated shear layer induces large velocity disturbances in the flow field, and typically the laminar/turbulent transition always occurs in the shear layer that subsequently reattaches to the surface (Refs.2, 9).

The laminar separation point is characterized by an abrupt decrease of the value of the Nusselt number. The opposite (increase of the Nusselt number) holds for the subsequent turbulent reattachment. A typical plot of the Nusselt number along the airfoil, for the

Miley airfoil at $\alpha = 0$ and $Re = 10^5$ is shown in Fig. 9; the Laminar Separation (LS), the Transition (T) and the Turbulent Reattachment (TR) points are indicated. The microvortices, inside the bubble, affect the heat transfer coefficient according to the flow regime in the separation shear layer. When the flow field in the shear layer is laminar, a decrease of the slope of the Nusselt number curve along the chord has to be expected, due to the increase of the boundary layer thickness. A heat transfer recovery occurs when the flow in the shear layer becomes turbulent. This is probably due to the fluid entrainment from the external stream into the bubble (Ref. 2). Therefore the minimum value of the Nusselt number can be taken as an indication of the laminar/turbulent transition in the shear layer.

Experimental tests have been made to check that the flow is laminar upstream of the abscissa $X/C = 0.25$ (otherwise no laminar bubble would exist at the conditions of Fig. 9). Turbulence was induced by means of a 1.5 mm diameter tripping wire (placed along the airfoil span at $X/C = 0.20$). The thermographic results (Fig. 10a) clearly show how the Nusselt number behaviour is similar to the one reported in Fig. 9 upstream of the wire and that it is totally different downstream of the wire. Similarly, to prove that the flow is turbulent in the downstream region, a wire is located at $X/C = 0.75$. The thermographic results (Fig. 10b) clearly show that the Nusselt number is similar to the one of Fig. 9 (the points of the plot that correspond to the wire location have no meaning).

The evaluation of the Nusselt/Stanton number distribution is performed along the airfoil (the row number is shown at the top of each plot generated by the computer); the plots shown refer to the centerline of the model (coinciding with the wind tunnel axis). The 2-D hypothesis of the thermofluidynamic flow field can be checked by analyzing Fig. 11 that shows the footprint of the Nusselt number of the MILEY airfoil upper surface at $\alpha = 0$ and $Re = 10^5$. The picture clearly shows that the Nusselt number profile is practically constant along the span (2-D flow). On the same picture the position of the row 31, along which the curves of Fig. 9 have been evaluated, is shown.

5.3 Discussion and Analysis

Systematic thermographic tests have been performed on the WORTMANN and MILEY airfoils according to the following conditions:

WORTMANN

$Re = 8 \times 10^4$; $\alpha = 0, 3, 6, 9, 12, 15, 18$

MILEY

$Re = 7 \times 10^4$; $\alpha = 0, 3, 7, 10, 13, 15, 17, 19, 21$

$Re = 10^5$; $\alpha = -9, -3, 0, 3, 7, 10, 13, 15, 17, 19, 23$

The position of the laminar separation, of the turbulent reattachment and of the transition in the shear layer are compared with those reported in Refs. 7 and 4 and are summarized in Figs. 12, 13, 14.

In general the agreement with previous results can be considered satisfactory, in view of the high instability of the boundary layer at low Reynolds numbers and to the fact that previous data have been obtained by intrusive techniques.

Results for the WORTMANN airfoil agree with other data particularly for the transition and the turbulent reattachment points. The only significant disagreements are found at $\alpha = 3$ and $\alpha = 12$ for the laminar separation points position.

Thermographic results for the MILEY airfoil show an agreement for the points of laminar separation. The comparison of the turbulent reattachment points is difficult because only few experimental data are reported in Ref. 4 (turbulent reattachments have been detected only at $\alpha = 21$, $Re = 7 \times 10^4$ and at $\alpha = -9, -3, 19$, $Re = 10^5$). On the contrary the Nusselt number plots seem to reveal the presence of a turbulent reattachment and also the existence of a laminar separation bubble at all the angles of attack.

The Nusselt number distributions at $\alpha = 21$, $Re = 7 \times 10^4$ (Fig. 15) clearly show a leading edge stall: the distribution of the Nusselt number is constant along the chord (this value is about the minimum value attained at different angles of attack at the same Reynolds number).

Non typical Nusselt number profiles at $\alpha = 17$ and $\alpha = 19$ for $Re = 7 \times 10^4$ are shown in Fig. 16a, b. They show a "pocket" (between $X/C = 0.20$ and $X/C = 0.45$), following the laminar separation bubble, that might prove the existence of a complex separation zone. This phenomenon does not appear in the Nusselt number profiles obtained for the same airfoil at the same Reynolds number and at smaller angles of attack (see Fig. 17 on which the Nusselt distribution at $\alpha = 15$ and $Re = 7 \times 10^4$ is shown).

6. CONCLUDING REMARKS

The high instability of the boundary layer at very low Reynolds number flow makes it very difficult to perform accurate and repeatable measurements by using conventional, intrusive methods.

The unsteady, computerized, thermographic method has proved to be a powerful, non-intrusive diagnostic technique able to measure local values of the Nusselt number over wings. The dependence of the convective heat transfer coefficient, (i.e. Nusselt/Stanton numbers) upon the flow regimes (laminar/turbulent) and upon the flow conditions (attached or separated flow) makes this technique able to analyze the boundary layer development in complex fluiddynamic conditions. In the present work the method has been specifically used to detect laminar separation bubbles (position and length) at low Reynolds number ($Re < 10^5$). A qualitative agreement was found with other

data reported in the literature obtained by other experimental techniques (pressure tap models, smoke wires). The position of the laminar separation, of the transition, and of the turbulent reattachment, obtained by the Nusselt number distribution analysis for the WORTMANN and for the MILEY airfoil suggest that the typical phenomenology takes place in the laminar separation bubble; by increasing the angle of attack the separation point shifts forward and the bubble length decreases. Further research activities on this subject will involve the analysis of the boundary layer in 3-D flow fields (finite wings), which still today is a critical matter in experimental aerodynamics, however the proposed method is immediately applicable to 3-D flows. Work is in progress to improve the heating technique in order to realize the desired temperature distribution and to operate in a closed test chamber wind tunnel.

7. REFERENCES

1. Mueller T.J., Jansen B. J.: "Aerodynamic Measurements at Low Reynolds Numbers"; AIAA 12th Aerodynamic Testing Conference, Williamsburg, March 1982
2. Mueller T.J., Batill S.M.: "Experimental Studies of Separation on a Two-Dimensional Airfoil at Low Reynolds Numbers"; AIAA J., Vol. 20, N. 4, 1982, pp. 457-463
3. Mueller T.J., Pohlen L.J. et al.: "The Influence of Free Stream Disturbances on Low Reynolds Numbers Airfoil Experiments"; Experiments in Fluids, Vol. 1, 1983, pp. 3-14
4. Pohlen L.J., Mueller T.J.: "Experimental Studies of Effect of Boundary Layer Transition on the Performance of the Miley Airfoil at Low Reynolds Numbers"; Final Report UNDAS 2036-FR-5, February 1983
5. Jansen B.J., Mueller T.J.: "Experimental Studies of the Boundary Layer on an Airfoil at Low Reynolds Numbers"; AIAA 16th Fluid and Plasma Dynamics Conference, Denver, July 1983
6. Mueller T.J.: "The Influence of Laminar Separation and Transition on Low Reynolds Number Airfoil Hysteresis"; J. Aircraft, Vol. 22, N. 9, 1985, pp. 763-770
7. Bastedo W.G., Mueller T.J.: "The Spanwise Variation of Laminar Separation Bubbles on Finite Wings at Low Reynolds Numbers"; AIAA 18th Fluid Dynamics, Plasmadynamics and Lasers Conference, Cincinnati, July 1985
8. Marchmann J.F., Abtahi A.A.: "Aerodynamics of an Aspect Ratio 8 Wing at Low Reynolds Numbers"; J. Aircraft, Vol. 22, N. 7, 1985, pp. 628-634
9. Marchmann J.F.: "Aerodynamic Testing at Low Reynolds Number"; J. Aircraft, Vol. 24, N. 2, 1987, pp. 107-114
10. Monti R.: "Measurement of the Local Heat Transfer Coefficient by Non-Invasive Techniques in Aerodynamics"; Proceedings of the 8th AIDAA Congress, Turin, September 1985
11. Monti R.: "Thermography"; "Flow Visualization and Digital Image Processing", L.S. 1986/9, Von Karman Institute for Fluid Dynamics, Rhode St. Genese, 9/13 June 1986
12. Chao B.T.: "An Improved Lighthill's Analysis of the Heat Transfer Through Boundary Layers"; Int. J. Heat and Mass Transfer, Vol. 15, 1972, pp. 907-920
13. Schulz Jander B.: "Heat Transfer Calculations in Turbulent Boundary Layers Using Integral Relations"; Acta Mechanica, Vol. 21, 1975, pp. 301-312
14. Napolitano L.G., Losito V.: "The Closed Spline Functions"; Computer Methods in Applied Mechanics and Engineering, Vol. 13, 1978, pp. 335-350
15. Terukazu Ota, Hideya Nishiyama et al.: "Heat Transfer and Flow Around an Elliptic Cylinder"; Int. J. Heat and Mass Transfer, Vol. 27, N. 10, 1984, pp. 1771-1779

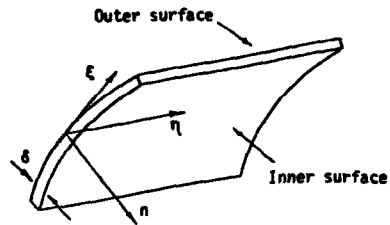


Fig. 1 - Model wall coordinate system

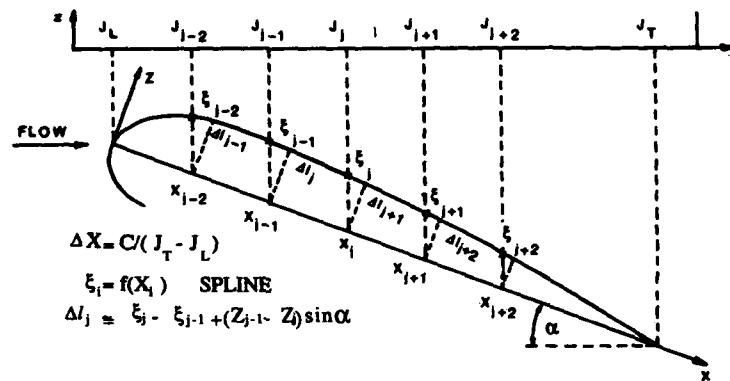
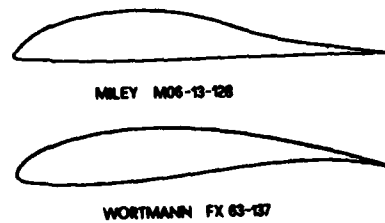
Fig. 2 - Geometrical scheme to compute the curvilinear distances Δl_j between two consecutive thermographic pixels

Fig. 3 - MILEY and WORTMANN airfoils



Fig. 4 - Experimental equipment

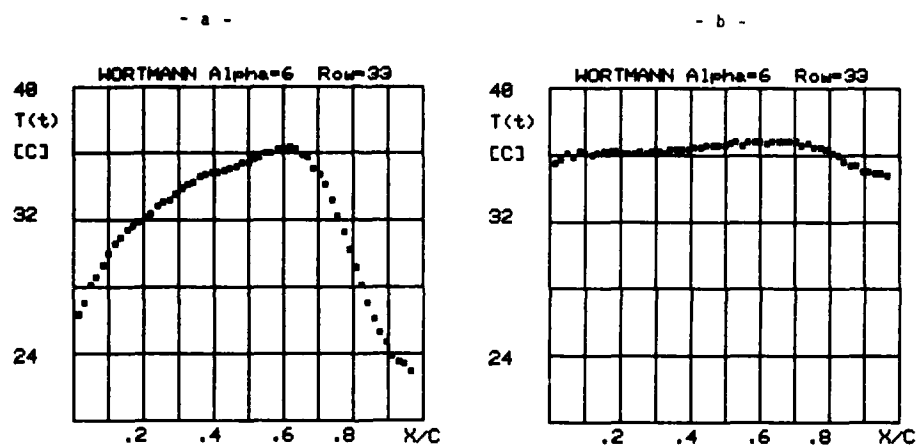


Fig. 5 - Initial profiles of the temperature along the airfoil upper surface obtained by blowing: a) hot air inside the model (first procedure) and b) warm air over the external surface of the model (second procedure)

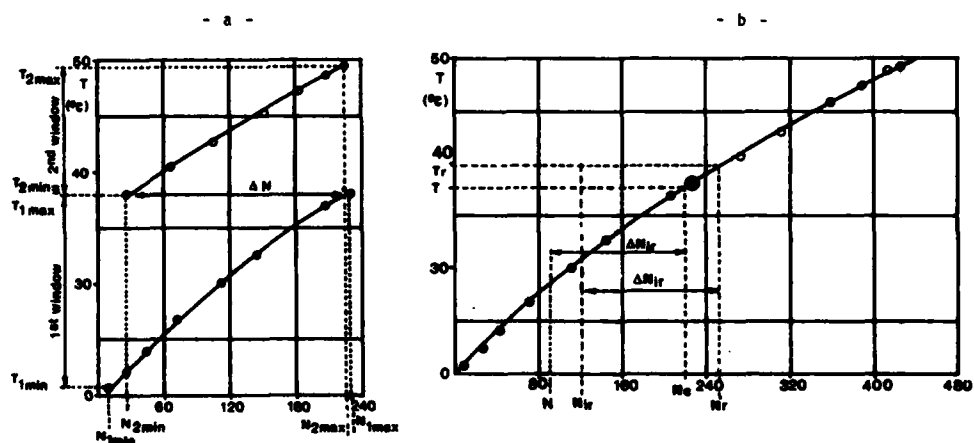


Fig. 6 - Construction of: a) an "ad hoc" calibration curve and b) measurement of the surface temperature by the calibration curve for the elliptic model

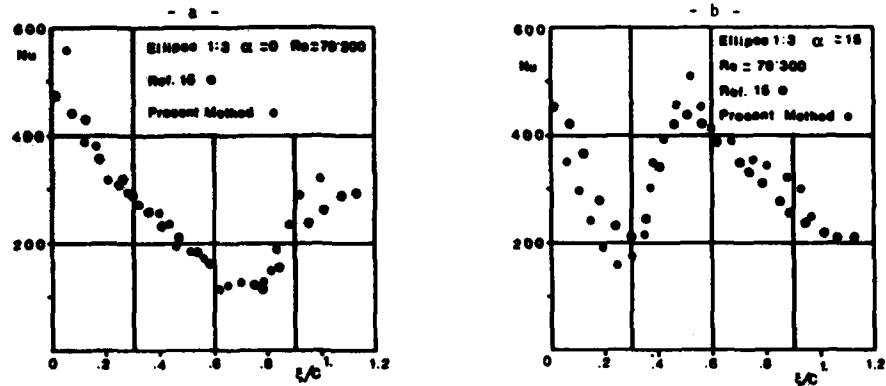


Fig. 7 - Comparison of the Nusselt number distribution for the elliptic model at: a) $\alpha = 0$, $Re = 79,200$ and b) $\alpha = 15$, $Re = 79,300$

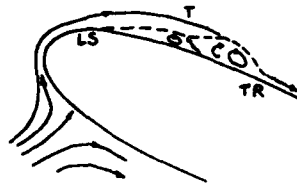


Fig. 8 - Schematic of the laminar separation bubble; LS Laminar Separation, T Transition, TR Turbulent Reattachment

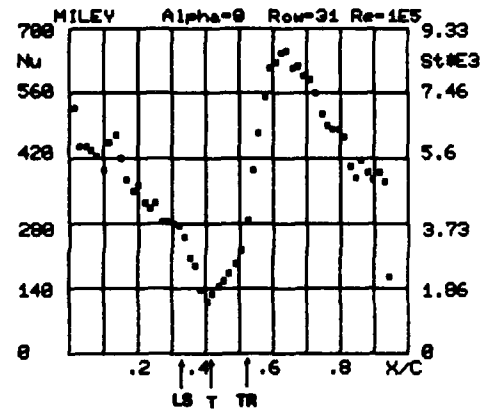


Fig. 9 - Typical output of the thermographic system for the Miley airfoil at $\alpha = 0$ and $Re = 10^5$

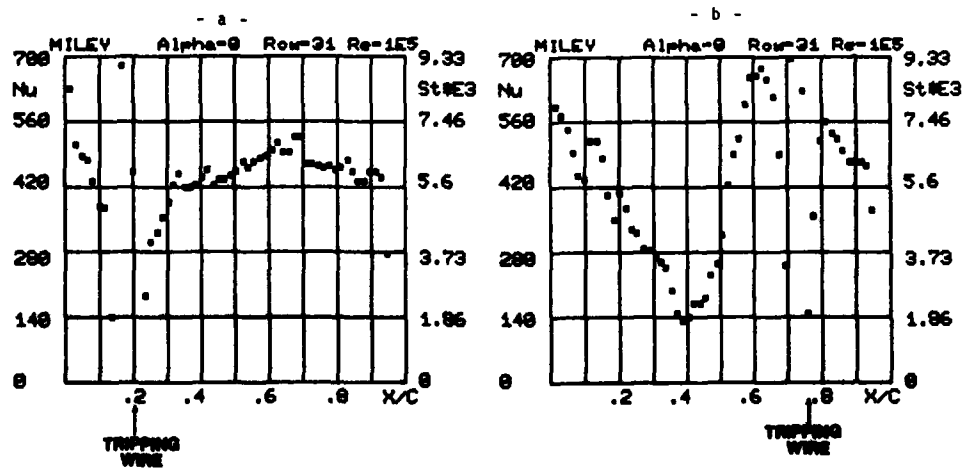


Fig. 10 - Effect of the tripping wire over the Miley airfoil

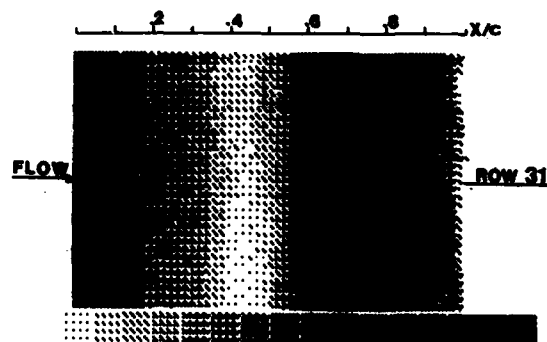


Fig. 11 - Footprint of the Nusselt number on the upper surface of the Miley airfoil at $\alpha = 0$ and $Re = 10^5$

○ Laminar Separ. □ Turbulent Reatt. Empty Symb. Ref. 7
 ▲ Transition ▼ Turbulent Separ. Full Symb. Pres. Met.

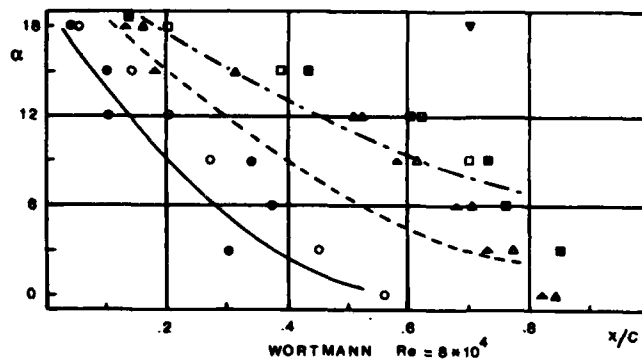


Fig. 12 - Comparison of the abscissas of the laminar separation, transition and turbulent reattachment points over the Wortmann airfoil at $Re = 8 \times 10^4$

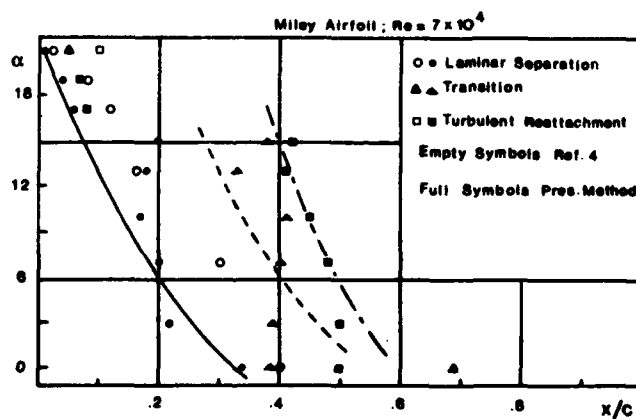


Fig. 13 - Comparison of the abscissas of the laminar separation, transition and turbulent reattachment points over the Miley airfoil at $Re = 7 \times 10^4$

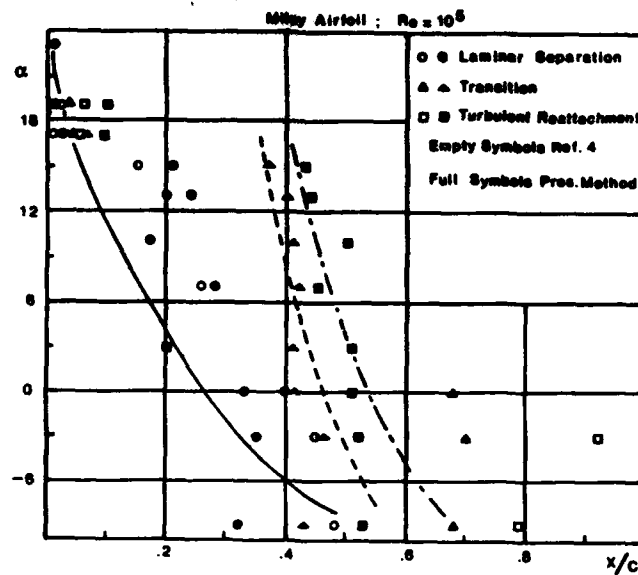


Fig. 14 - Comparison of the abscissas of the laminar separation, transition and turbulent reattachment points over the Miley airfoil at $Re = 10^5$

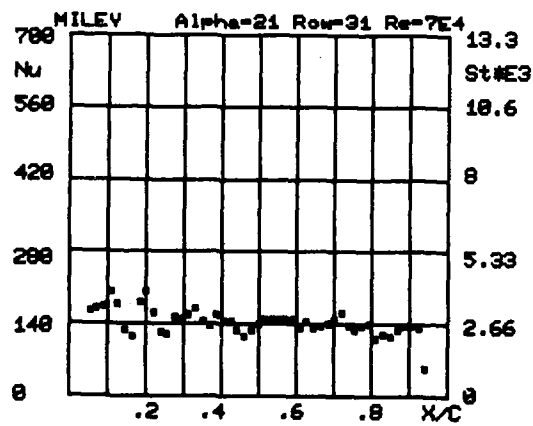


Fig. 15 - Nusselt number distribution over the Miley airfoil at $\alpha = 21$ and $Re = 7 \times 10^4$

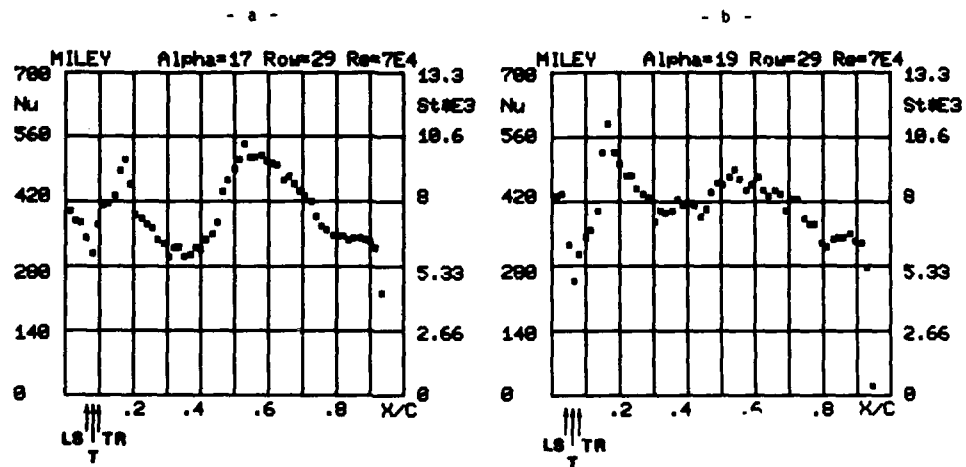


Fig. 16 - Nusselt number distribution over the Miley airfoil at $Re = 7 \times 10^4$ and:
a) $\alpha = 17$, b) $\alpha = 19$

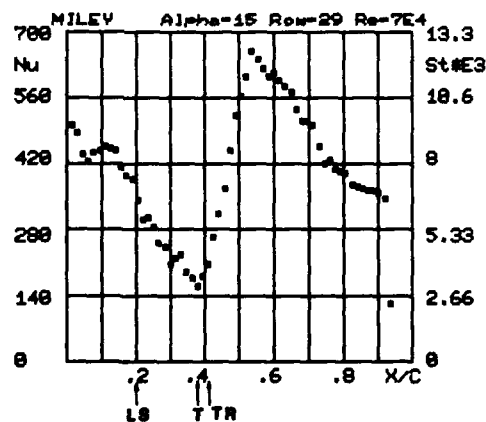


Fig. 17 - Nusselt number distribution over the Miley airfoil at $\alpha = 15$ and $Re = 7 \times 10^4$

ACCURACY PROBLEMS IN WIND TUNNELS DURING TRANSPORT AIRCRAFT DEVELOPMENT

by

Günter Krenz

Messerschmitt-Bölkow-Blohm GmbH
Unternehmensbereich Transport- und Verkehrsflugzeuge
D-2800 Bremen 1, FRG

SUMMARY

Wind tunnel test data accuracy requirements for transport aircraft are derived. Airline performance guarantees, model and tunnel test techniques available and the quality of prediction methods used form the concept for wind tunnel test programmes and set accuracy requirements for test data. The paper describes procedures we followed in high speed cruise and low speed take-off and landing. The accuracy of wind tunnel tests is limited by several parameters, the most important being flow quality, model and model suspension quality and balance accuracy. Problems which occurred during our tests with small models in the transonic regime led us to new test concepts presented in the present paper: The use of large models on a specific suspension with a range-limited balance and the improvement of small model test techniques in connection with the requirements for measurements in cryogenic facilities.

Low speed tests are ambitious and extensive due to the many configurations at take-off and landing. Furthermore, the work is complicated by the many details like closing plates and shutters, which can have a strong effects on the performance data. Some examples are presented in the report.

1. INTRODUCTION

The development of transport aircraft sets specific requirements for wind tunnels and therefore the design of such facilities must take into consideration fairly different test scenarios compared to those of fighter aircraft and missiles. Some differences regarding magnitude and variety of test requirements which users have for new wind tunnels are presented in FIG. 1. It contains an outline from test scenarios of a modern future transonic facility, the European Transonic Wind Tunnel (ETW). Its design began with dispute about size and shape of the test section: For tests of fighter aircraft models a large range of incidence is essential to measure extreme flight manoeuvres. Furthermore, as wing span is relatively small there is a demand for quadratic test sections or a vertical rectangle respectively. Transport airplanes, on the other hand, with large span wings are tested in a smaller range of incidence at cruise conditions and hence horizontal-rectangle test sections are required for model scale as large as possible to provide high Reynolds number measurements.

Typical differences between test programmes of transport and fighter aircraft can be specified.

Transport Airplanes: Very precise aerodynamic data of few aircraft configurations in a limited range of Mach number, angle of attack and sideslip.

Fighter Aircraft: Less precise data but for many configurations in a large range of M, α and β . Hence the main components of the test facility like model suspension and balance have to be designed for the specific test scenarios, i.e. for fighter aircraft to account for high flexibility with respect to model position in the tunnel and test range, for transport airplanes to design for limited positions and test range but higher data accuracy.

In a stiff competition of aircraft manufacturers the degree of test accuracy necessary for transports is dictated by increasing requirements of the airlines for performance guarantees. There is a demand for continuously improved aircraft performance standard connected with more and more closer tolerance limits for the guarantees. Regarding aerodynamics this process leads to a more and more advanced design of the wing, which dominates the performance level of the total transport aircraft. As performance prediction based on theory and experiment today can be done only with limited accuracy, improvements are needed to lower the development risk.

On the theoretical side rapid computer development is partially promoted by aerodynamic requirements i.e. solving Navier-Stokes equations in complex 3 D flow around aircraft shapes, but purely theoretical methods fail to supply the prediction accuracy required. The wind tunnel delivers the most accurate simulation of the flow field around an airliner and it is in the wind tunnel where the data basis for performance guarantee evaluation is produced. The main uncertainty for this task at present is the Reynolds number gap between wind tunnel and flight, this gap is being fairly closed by the cryogenic facilities. However, it is not to be expected that the pure occurrence of this new technology already delivers accurate full scale airplane performance data. Extensive experience which started with the NTF in the USA continuing in the ONERA T 2 (0.4 x 0.4 m², transonic) and in the DFVLR KKK (2.4 x 2.4 m², low speed) in Europe is necessary for successful utilization of the high Reynolds number capability of cryogenic tunnels.

One major problem is the balance accuracy which in those tunnels is connected with large temperature differences acting on the stranguages of the internal balance components. Another problem is the magnitude and variety of requirements due to different projects and testprogrammes. The experience in the Airbus Programmes led us to a model and test concept which includes the use of several European wind tunnels in a coordinated task. In the transonic regime these are: ARA Bedford (2.74 x 2.4 m²) and NLR-HST

($2.0 \times 1.6 \text{ m}^2$) for Reynolds numbers referred to MAC between 2.5 and 3.5 millions and ONERA S1 MA (8 m diameter) for Reynolds numbers between 5 and 8 millions.

Regarding future transonic facilities, cryogenic or others, the present experience with the tunnels is a basis for tunnel design. Moreover, a preview of future aircraft technology as well as model and test techniques is needed for successful operation of new wind tunnels. This demands close cooperation of users and tunnel operators as will be discussed in the present paper.

In the low speed regime $C_{L_{max}}$ for landing and L/D for take-off are the important performance data, and for twin engine aircraft second segment climb performance dominates the weight an airliner can lift from ground. High data accuracy is needed here, too, for performance guarantees and predictions as will be presented in chapter 3. One major problem occurs from the complexity of low speed models due to the many movable parts in different geometrical positions and from our experience, even small details like closing plates or shutters of slots and gaps can have a strong effect on aircraft performance data.

In low speed as in high speed the required test accuracy influences the main components of the facility like stings and balances to be designed and available for efficient tunnel operation. The use of suitable components like the right suspension and balance shortens the wind tunnel programme and saves time and money.

2. WIND TUNNEL TESTS IN THE TRANSONIC REGIME

2.1 Present status of testing commercial A/C-configurations

Aircraft development in wind tunnels is generally focussed on two project tasks:

- New aircraft design which for a family like Airbus normally concentrates on a new wing design
- Improvement of existing aircraft with respect to aerodynamic performance.

Both include two targets to be followed by aerodynamicists: Configuration improvement for best aircraft layout, which needs several steps of optimization and validation of aerodynamic data to determine the aircraft performance figures, mainly L/D and buffet onset.

For the first project task "New A/C Design" we use different methods to reach performance predictions as accurate as possible for the aircraft:

- A "Direct Scaling Method" based purely on wind tunnel tests with models of the new design.
- A "Reference Method" based on model tests of the new design and model tests of the "Reference Aircraft" (e.g. A 300 as reference for A 310 development) with the additional knowledge of the reference airplane flight test data.

Both methods together form the basis to predict aircraft performance as accurate as possible setting requirements for the accuracy of wind tunnel test results to be achieved. If we take into account the limits in data evaluation of the procedure, a repeatability better than 0.5 % of airplane cruise drag must be reached in the wind tunnel. This requirement stands for short term repeatability including operations like model dismounting and mounting again and for airplanes like Airbus means that the wind tunnel test data must fall inside a data band of 1 to 1.5 drag counts. For a complete aircraft test programme, in general extending over 3 to 4 years, the long term repeatability for reference tests in one tunnel with model disassembled and assembled again, should be in a band of 2 to 3 drag counts.

In the second project task "Aircraft Improvement" the design optimization is tested by model changes against the reference model. As the geometrical changes of the model and the corresponding drag improvements normally are small, short term repeatability should be in the range of 1 drag count and the balance must allow sufficient resolution inside this repeatability range. Moreover, Reynolds numbers as high as possible and strong requirements for model geometry precision are essential. This leads to a preference of large models.

Our experience is that in an airplane family programme even like Airbus with many new members product improvements cover a large part of the wind tunnel work and, as those tests set strongest requirements for repeatability of test results in the tunnel, they will be described in the next chapters.

One task was the modification of the A 300 trailing edge, sketched in FIG. 2. The inboard part of the wing behind the rear spar was affected including the allspeed aileron. Rear camber of the model was increased by deflecting the flap by 3° and the tap against the flap by further 2° . The aileron was deflected into mid position between inboard and outboard wing area to smoothen the surface. The effect of these changes on lift and drag curves is given in FIG. 3 and resulting buffet boundary as well as L/D -improvements are shown in FIG. 4. The modifications were introduced into A 300-600 and the performance gains were demonstrated during flight tests together with some other improvements resulting in 10 % more passengers and 15 % more range of the A 300-600 compared to the A 300.

For a more recent design the task was again to investigate the effect of t.e. modifications on performance data, and FIG. 5 shows sketches of the outboard wing model change. The most interesting effect on drag is presented in FIG. 6, once more a promising result. However, the very small geometrical change - on the model of 1.2 m span the deviation of the trailing edge was 0.8 mm - made a precise aerodynamic result questionable and indeed repeatability tests showed large scatter. FIG. 7 contains the results and a description of test repeating procedure. No conclusion can be drawn about the efficiency when outboard flap camber is increased. It is well known that the MLR-HST gives good repeatability, but the large scatter of data forced us to look for improved procedures for such verification tests. We went into two directions:

- Use of a big model with a special suspension in the ONERA S1 MA
- Improvement of small model test technique in the NLR-HST.

The latter task was important to provide model test techniques for the cryogenic facilities KKK (Kryo Kanal Kbin) and ETW (European Transonic Wind Tunnel), where models of similar small size will be tested which need even higher accuracy compared to models in conventional tunnels.

2.2 Large model tests in the transonic regime

After the experience with small model measurements we had to change and improve the test concept, and this we did using

- high Reynolds number testing in the wind tunnel to eliminate misleading flow effects as far as possible
- a large and very precise model which allows the realization of small configuration changes with high accuracy
- a precise balance with design load ranges harmonized with the important cruise test conditions
- a novel suspension system with minimum interference effects.

A visual impression of the resulting test arrangement is shown in FIG. 8, a big model in the wind tunnel ONERA S1 MA using a "false" fin as part of the rear sting mounting. FIG. 9 gives the major changes comparing the small model with the large model tests. The large model was carefully designed for long term accuracy with model dismounting and mounting again and was manufactured with high precision. Due to the large model scale special modification like the trailing edge droop could be manufactured very precisely and disturbances from the suspension - especially on the lower rear fuselage - were nearly eliminated. This area should be clean for correct tests of fuselage/tail interference. But also drag measurements of wing/fuselage configurations can be strongly effected by sting mounting as the rear part with its upsweep considerably contributes to the total drag. Of course, with the new model mounting, the test range was limited to zero or very small yaw angles and to lift conditions up to buffet onset only. The balance was adapted to this limited test range. Despite the low natural frequency of this model/sting arrangement of about 1 Hz the model behaviour was stable in the entire transonic test range. FIG. 10 presents the high quality of the test results. The repeatability was within 1 drag count including reference tests after one year. The model was tested in 1984, dismounted and mounted again in 1985 for a second test campaign. The trailing edge modification was tested two times without showing scatter of the test data and the results plotted in FIG. 7 for comparison demonstrated that this t.e. modification did not improve L/D at cruise conditions.

The example shows that user and operator of wind tunnels should work closely together to achieve better accuracy from specific tests. In our case main steps of the cooperation were:

• Definition of Accuracy Requirements and Test Programme - MBB Activity

This was based on guarantees required for the customers, experience about accuracy achievable with the test arrangement and failures connected with the method to predict aircraft drag from wind tunnel measurements.

• Model Design and Manufacture - MBB Activity

Methods for design and manufacture of the models were developed to guarantee for accurate repeated tests even after disassembly and reassembly of model parts. Accuracy control was performed on NC milling machines.

• Model Suspension Design and Manufacture - ONERA/MBB Joint Activity

A special suspension with low aerodynamic interference was designed and manufactured. The new concept required limitations in normal force and pitching moment to values up to buffet onset. Very small side forces were allowed.

• Balance Design and Manufacture - ONERA Activity

The balance was adapted to the limited test range which resulted in high sensitivity and accuracy in the cruise range

• Wind Tunnel Quality and Data Acquisition - ONERA Activity

Considerable improvements of flow quality and tunnel corrections were achieved in the S1 MA tunnel and a highly efficient data acquisition and data management system was introduced.

The successful cooperation encouraged us to transfer the proven techniques to wind tunnels of smaller test section.

2.3 Small model tests in the transonic regime

It is important to improve test accuracy in this field to reach more flexibility in wind tunnel programmes in existing tunnels and to gain experience for the cryogenic facilities. Therefore we initiated a combined action: Improve small scale model transonic testing in the NLR-HST and prepare tests in the KKK cryogenic low speed tunnel.

The Model

Working successfully now in his basic functions the KKK in Cologne after calibration tests are finished will be ready for transport aircraft measurements. We are preparing an Airbus A 310 model to be tested there in 1988. The size of the test section ($2.4 \times 2.4 \text{ m}^2$) limits the span of the model to 1.5 m.

The same model can be used later for the ETW. The NLR-HST allows only models up to 1.3 m span. This corresponds to an Airbus model scale of about 1 : 30 for the cryogenic tunnels and 1 : 35 for the NLR-HST. The experience described under 2.1 was that for this size the present model accuracy was not sufficient and for cryogenic models the requirements must be raised even more. FIG. 11 shows the actual status of model accuracy produced on NC machines and refinished if necessary. The accuracy control is done on Zeiss as well as on MBB measuring machines. This standard we aim to improve by a factor of 5 for surface roughness and by 2 for accuracy. A further prerequisite for precise testing is a suitable model design using the optimum material. For accurate drag measurements we have to manufacture a one piece model wing without pressure holes. The material for the cryogenic model will be maraging steel DIN WL 1.6359 comparable to US maraging steel 18 Ni 250. Provisions have to be made to control the actual shape of the model wing under loads and another improvement is the application of adaptive walls which allow larger models as well as more accurate flow field simulation. Both techniques are being provided by the NLR and the DFVLR.

Model Support

For more accurate drag measurements we have to learn from the experience made during the ONERA tests described under chapter 2.2. The NLR has designed and MBB manufactured the new suspension and tests with an MBB model are running and will be finished within this year. FIG. 12 shows the model/support arrangement using a "false" fin like the suspension in ONERA S1 MA. This type of sting designed in connection with special materials has the real fin root section profile and size but the taper is adverse compared to the actual aircraft fin. We assume it can be advantageous also in cryogenic wind tunnels. Of course, tests with yaw angles and in the regime of flow separation i.e. buffet measurements have to be made with a different suspension.

Balance

As in the ONERA S1 the balance in the NLR-HST was adapted for aircraft cruise range load conditions and, furthermore, was limited due to the suspension allowing only very small side slip angles of the model. In cryogenic facilities the balance must fulfill the most challenging requirements and therefore a strong limitation of the test range can be extremely helpful. MBB Transport Division and the Technical University of Darmstadt are working on a cryogenic balance for the ETW under government contract and it is intended to test the balance in the KKK during the MBB test campaign in autumn 1988. An extensive description of the work done so far on the balance is presented in Reference [1], [2].

3. WIND TUNNEL TESTS IN THE LOW SPEED REGIME

3.1 Requirements for accuracy of test data at take-off and landing

In low speed C_{Lmax} for landing and L/D for take-off are the dominant performance parameters. They have to be designed and evaluated precisely and high data accuracy is needed to validate and fulfill the performance targets like for take-off and landing field length.

One accuracy problem occurs from the complex low speed models with many movable parts in several geometrical positions, and although during aircraft development much emphasis is put on the high speed design, the low speed work like wing movable parts layout including engine interference effects is very ambitious and laborious.

The measure for test accuracy in high speed was the order of 1 drag count, as for planes like Airbus 2.5 to 3 counts correspond to 1 percent of aircraft drag. In low speed 10 to 20 counts correspond to 1 percent of drag at take-off depending on flap extension and take-off speed. As 1 % drag is equivalent to 1 % take-off field length respectively 0.5 % weight - in the case of A 310 corresponding to 7 passengers - the aerodynamic data in wind tunnels must be tested in a tolerance range of the order of 5 drag counts. Concerning repeatability this target is high because of the many wing shapes, well defined and representing different positions of movable surfaces, the effect of small fitting and closing parts on aerodynamic performance data is rather strong, generally for both, drag at take-off and lift at landing. Regarding the accuracy for C_{Lmax} tests 1 % is the order of $C_L = 0.03$ and expressed in aircraft landing performance values corresponds to about 0.5 % approach speed, which in case of Airbus is about 0.7 kts. Assuming that 1 to 2 kts difference in approach speed are less important deviations we have to make sure that prediction of C_{Lmax} data are correct inside a tolerance range of about ± 1.5 %. With the help of modern facilities like DNW, ONERA F1, RAE 5 m and Emmen Tunnel in Switzerland this target is not critical but the influence of small model details must be considered as described in the following chapter.

3.2 Effect of A/C component details on performance

During low speed wing development much work is being done to carefully design the flap and slat contours and all the gaps and slots, but when the wind tunnel model is manufactured some "minor details" are simplified or sometimes even forgotten.

FIG. 13 shows details around a slat track at the wing leading edge. A cut out was closed above all the twelve tracks for one test and for another one only the four tracks of the inboard slat were shuttered. The loss in C_{Lmax} is with 0.03 not penalizing, however, the increase in drag on the next FIG. 14 of about 20 counts at take-off conditions is not acceptable. On the next FIG. 15 the landing data are presented with considerable changes in maximum lift - a loss of $\Delta C_L = 0.27$ was measured - and corresponding changes in pitching moment. The reduction of nearly 10 % in C_{Lmax} has several impacts on the design work. At first the sensitive area has to be optimized, which generally is a laborious task between the aerodynamic and the structural design. Furthermore, during the aerodynamic design process the shutters must be defined extremely accurate to assure high repeatability from one model test to another as well as from test with different models. This is also important for cooperating work among partners in a shared

wind tunnel programme, where models with different tasks must deliver equal aerodynamic data for the same geometry specified. Often the discrepancy of test results with models of same specific geometry finds its reason in such details not being designed or attached carefully enough.

The effect of another detail is shown in FIG. 16 the area of slat/pylon interaction. The gap between inboard slat and pylon - 1 mm in model scale - was tested sealed and unsealed. The loss in maximum lift was small with $C_{Lmax} = 0.02$, but again the drag increment with 25 counts, which is equivalent to 2 % of aircraft drag at take-off, was unexpected high without sealing. The gap had to be on the aircraft and regarding the aerodynamic design and wind tunnel work we can conclude as in the example before: The models must be really comparable in the detail slat/pylon gap sealing.

A further experience can be taken from tests with Krüger leading edge devices, which replaced the slat at the inboard portion of the wing between pylon and fuselage. The sketch in FIG. 17 shows the small difference in Krüger flap connection to the clean wing leading edge resulting in a discrepancy of maximum lift of $\Delta C_L = 0.03$, which is 1 % of A/C maximum lift.

The last example is taken from experimental data we produced during trailing edge flap design, and C_{Lmax} depending on flap position is presented in FIG. 18. Parameters were the gap between fixed wing trailing edge and flap and the overlap. Best C_{Lmax} was found for negative overlap showing the flap in a position behind the shroud, and, as more the flap is shifted forward as lower drops the C_{Lmax} . On the other hand the higher C_{Lmax} is much stronger depending on the gap size between shroud and flap. In the case tested and shown here the reduction is 8 % C_{Lmax} between 2 % and 2.5 % gap. For positive overlap of + 1 % the reduction is shifted to values between 3 % and 3.5 % gap and counts for 3 %. We must consider that the flap on the aircraft is deformed under loads and even careful estimates of the real aircraft flap position with respect to gaps and overlaps results in tolerance range of the order of 1 %. Hence, a starting point for design might be a gap of 2 % with 0.5 % to 1 % overlap.

The complete low speed wing design is as the examples above show, a labourious work where the fundamental part is the layout of the flaps and slats. Designing an efficient aircraft flap system is an ambitious task with respect to theoretical methods being used and wind tunnel test programmes to be conducted. The aerodynamic team must do a creative design and seriously prove and confirm it in the wind tunnel. Furthermore, the team has to establish prediction methods to estimate the aircraft performance with a high degree of confidence. Both, the creative and efficient design of the aircraft components and a serious and precise prediction of their performance is of equal importance. Performance prediction in low speed looks difficult due to the complex configurations and due to strong effects of component details, as described above. Nevertheless, the methods we use (Reference [3]) - established during Airbus A 300, A 310, A 320 development and flight tests - allow predictions of high accuracy. One example for the A 310 is shown in FIG. 19. The L/D flight test results at take-off and landing are compared with drag estimates based on DNM and RAE 5 m wind tunnel measurements scaled for symmetrical drag with our method. The prediction was good for take-off and landing as well with the RAE results coming into a scatter band of ± 1 % of aircraft compared with the flight test results. The DNM results were generally more pessimistic for prediction of take-off performance.

4. REFERENCES

- [1] Krenz, G.
Ewald, B. The Accuracy Problem of Airplane Development Force Testing in Cryogenic Wind Tunnels.
AIAA 14th Aerodynamic Testing Conference, West Palm Beach, Florida, March 5-7, 1986
- [2] Ewald, B.
Graewe, E. Development of Internal Balances for Cryogenic Wind Tunnels. The 12th International Congress on Instrumentation in Aerospace Simulation Facilities
Williamsburg, Virginia, June 22. - 25. 1987
- [3] Haftmann, B. Drag Prediction Method for High Lift Configurations.
Churchill College, Cambridge, 16.12.1986

PARAMETER	TRANSPORTS	FIGHTER
Mach-No.-Range	0.2 ÷ 0.95	0.4 ÷ 1.3
Reynolds-No.-Range	max. at cruise ($M=0.8$) $Re = 40 \cdot 10^6$	max. at cruise and manoeuvre $Re = 40 \cdot 55 \cdot 10^6$
α - Range	$< 8^\circ$ at cruise	$> 20^\circ (M=0.8) - 10^\circ (M=2.0)$
β - Range	$< 5^\circ$	$> 10^\circ (M=0.8) - 5^\circ (M=2.0)$
Typical Test Program	few configurations ≈ 5 days	many configurations several weeks
Required Accuracy of Drag	order of 1 drag count	order of 5 drag counts

FIG. 1 ETW-Test Scenario for Transport- and Fighter Aircraft

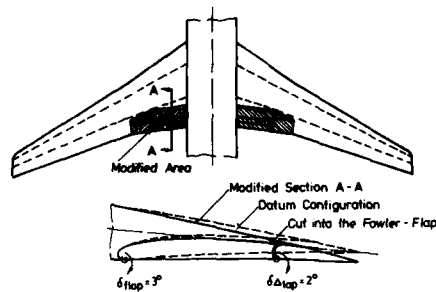


FIG. 2 Inboard Wing Modification

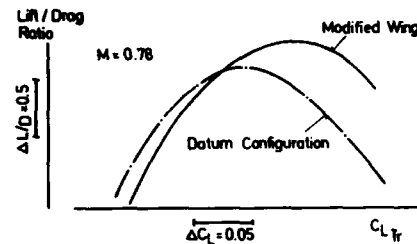
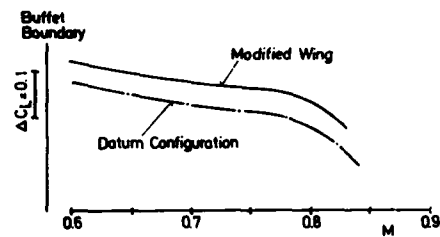


FIG. 4 Influence of Inboard Wing Modifications on Performance Boundaries

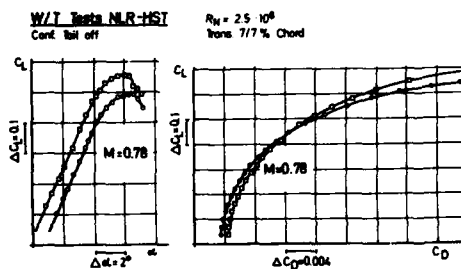


FIG. 3 Change of Lift and Drag Characteristics due to Inboard Wing Modification

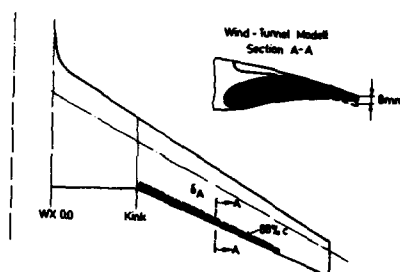


FIG. 5 Outboard-Wing Trailing Edge Modification

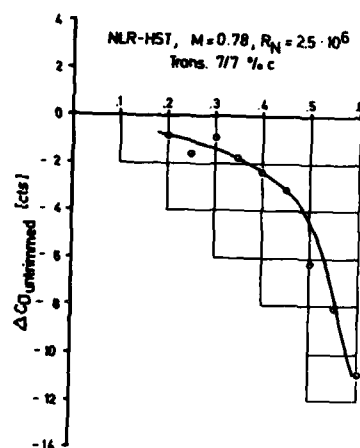


FIG. 6 Drag Reduction by Outboard Flap Camber

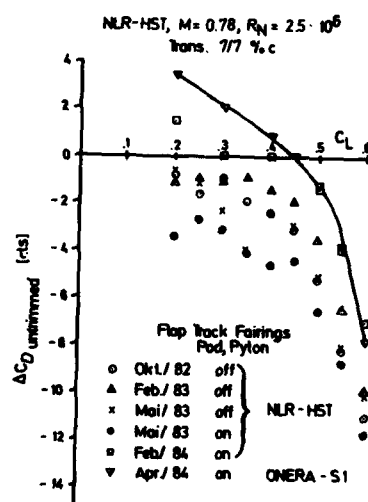


FIG. 7 Outboard Flap Camber Effect

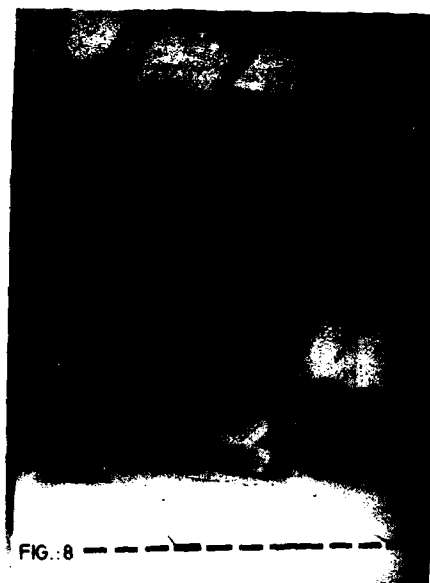


FIG. 8

MAIN CHANGES	NLR-HST	ONERA S1
Model Span / Mean Aer. Chord	115 / 20 cm	450 / 70 cm
T.E. Deviation	0.8 mm	3.1 mm
Reynolds Number M.A.C.	$3 \cdot 10^6$	$7 \cdot 10^6$
Model Suspension		
Test Range β	$\pm 5^\circ$	$\pm 2^\circ$
α	Force and Buffet Tests $0.3 \leq M \leq 0.95$	No Buffet Tests $0.6 \leq M \leq 0.84$
Balance	Normal Force Range Task 2 inch MK X1	Limited Force Range ONERA $\phi 180$ mm

FIG. 9 Increase of Model Size and Limitation of Test Range

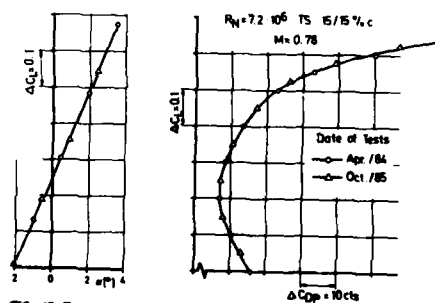


FIG. 10 Repeatability Tests in ONERA-S1 Wind-Tunnel

Typ of Model	Accuracy (μm)		Surface Roughness	Control	
	Geometry	Surface			
Low Speed up to 100 mm/min	± 0.2	± 0.07	1:250	5-8 μm	MBB Varel
Low Speed up to 100 mm/min	± 0.4	± 0.1	1:250	5-8 μm	MBB Varel
High Speed up to 500 mm/min	± 0.1	± 0.04	1:500	4-6 μm	Zeiss UHM 800
High Speed up to 500 mm/min	± 0.2	± 0.1	1:500	5-8 μm	MBB Varel
2-dim. Profile ($\pm 0.27 \mu\text{m}$)	± 0.1	± 0.02	1:750	2 μm	Zeiss UHM 800

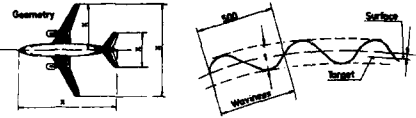


FIG.:11 Requirements for Model Accuracy and Surface Roughness

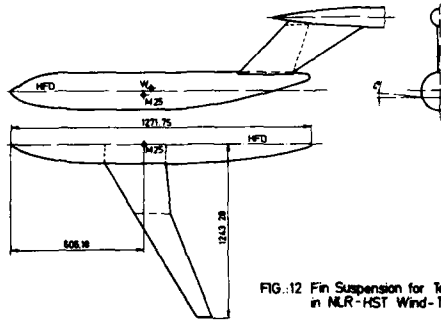


FIG. 12 Fin Suspension for Tests in NLR-HST Wind-Tunnel

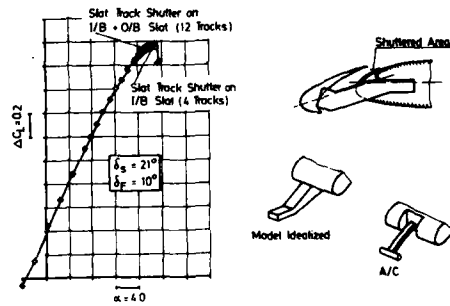


FIG. 13 Effect of Slat Track Shutter on T.O. Maximum Lift

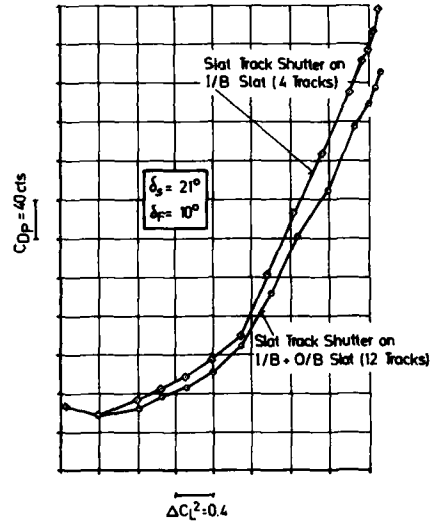


FIG.: 14 Effect of Slat Track Shutter
on T.O. - Drag

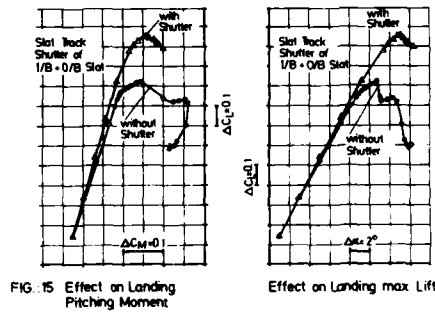


FIG. 15 Effect on Landing Pitching Moment

Effect on Landing max Lift

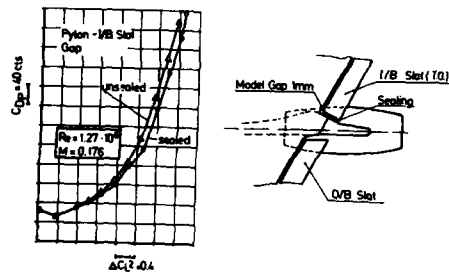


FIG.:16 Effect of Pylon-1/8 Slot Gap Sealing on T.O. Drag

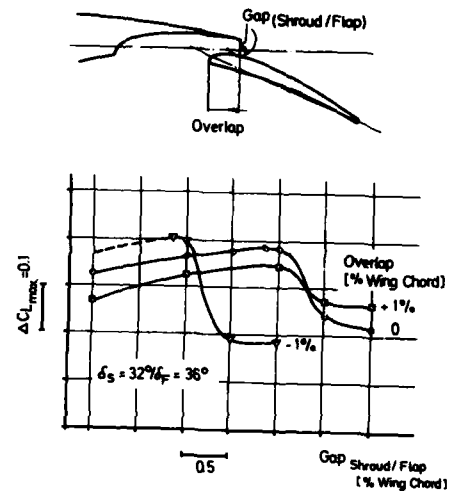


FIG.:18 Optimization of Fowler Flap Position

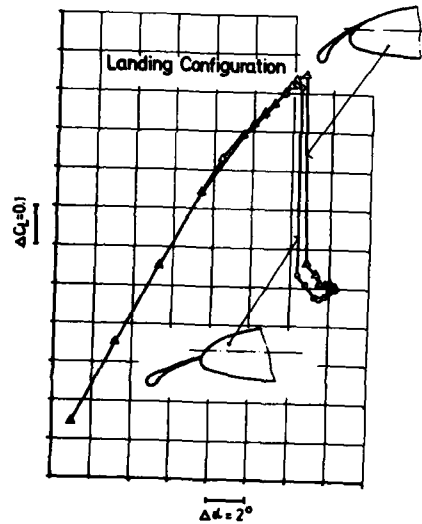


FIG.: 17 Effect of 1/8 Krüger Position on Landing max. Lift

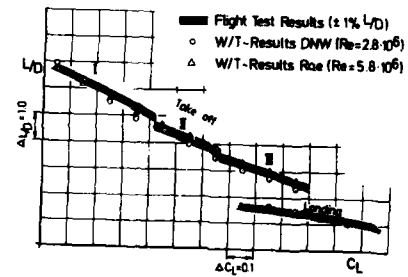


FIG.:19 A 300 Scaled W/T-Results Compared with F/T-Tests Results

REQUIREMENTS AND CAPABILITIES IN UNSTEADY WINDTUNNEL TESTING

by

R.D. den Boer*, R.Houwink**, R.J.Zwaan***
National Aerospace Laboratories
P.O. Box 90502, 1006 BM Amsterdam
The Netherlands

1. INTRODUCTION

Aeroelasticians are qualitate qua occupied in aerodynamics and unsteady aerodynamics in particular. Consequently the accuracy in unsteady windtunnel testing should be a matter of concern to them. This is the incentive for the present paper. The concern however is less evident to aerodynamicists who occupy themselves with steady flow problems, without an explanation of how the aeroelasticians make use of their aerodynamics. The subject of this paper is therefore twofold: first the accuracy required for aeroelastic applications concerning full-scale aircraft will be discussed, after which the accuracy in current unsteady windtunnel testing is considered.

2. AERODYNAMICS IN AEROELASTIC PROBLEMS

2.1 Survey of aeroelastic problems

The aerodynamics needed by the aeroelasticians is usually divided into the categories of steady and unsteady aerodynamics. The first category concerns the steady-state deflections of aircraft structures and is involved in problems like:

- * lifting surface divergence
- * control surface effectiveness,

while the second category concerns oscillatory and non-oscillatory motions of the complete aircraft or parts of it, and plays a role in problems like:

- * Aircraft stability
- * Flow-induced oscillations (flutter, vortex excitation, etc.)
- * buffeting
- * gust encounters
- * non-uniform inflow of rotors (helicopters, propellers)
- * Rapid deflections of control surfaces and spoilers.

The category of unsteady aerodynamics is the issue here and in the following all attention will be directed to it.

Considering modern computer methods to simulate the flow about the moving aircraft structure, impressive progress has been and is being made in predicting unsteady pressures and aerodynamic forces. Nevertheless, consensus of opinion exists that unsteady windtunnel testing remains necessary for quite some time, if not for all time. This testing is needed to improve the knowledge of the flow mechanism, to develop and validate computational and empirical methods, or simply to obtain experimental data for aircraft configurations and flow conditions which are too complicated to be simulated by computational methods with sufficient accuracy.

2.2 How do unsteady aerodynamics appear in aeroelastic problems?

The interest of the aeroelastician is directed mainly to the response of the aircraft structure to control surface deflections, gust encounters, etc. The question then is almost invariably what level of accelerations and dynamic loads in the vibrating aircraft structure will be attained, and whether this level will increase possibly due to a decreasing stability of the vibrations at higher flight speeds. How the unsteady aerodynamics come into the picture is explained here briefly by considering the equations of motion which describe in a general sense the aeroelastic phenomena mentioned before. The motion $\vec{r}(\vec{x}, t)$ is usually written as the summation of natural vibration modes $\vec{\phi}_i(\vec{x})$ of the aircraft structure, symbolized by: $\vec{r}(\vec{x}, t) = \sum_1 \vec{\phi}_i(\vec{x}) q_i(t)$, in which $q_i(t)$ is a generalised coordinate indicating the contribution of the

i -th vibration mode to the response. This procedure enables the formulation of an equation of motion for each vibration mode, which reflects the interaction of structural and aerodynamic forces involved in that mode. For the present discussion all equations of motion are combined in one matrix equation:

$$M\ddot{q} + C\dot{q} + Kq + A^N(q) = -A^D(t)$$

in which:

- M = inertial matrix
- C = damping matrix
- K = stiffness matrix
- A^N = motion-dependent aerodynamic matrix
- A^D = motion-independent aerodynamic matrix

The equations of motion are usually derived by applying some energy consideration, like Hamilton's principle or Lagrange's equation. This implies that each element by the matrix A^N , e.g. A^N_{ij} , represents the work performed by the aerodynamic load distribution generated by vibration mode j , \vec{p}_j , by a displacement in the direction of vibration mode i , both modes normalized to unit amplitude:

$$A^N_{ij} = \int_S \vec{p}_j \cdot \vec{n} \cdot \vec{\phi}_i dS,$$

in which \vec{n} is the unit normal of the aircraft surface.

- * Research Engineer
- ** Senior Research Engineer
- *** Head Aeroelasticity Department

The elements A_{ij}^D are defined in the same way:

$$A_{ij}^D = \int_S p_{ij}^D \cdot \frac{\partial}{\partial x_j} ds.$$

The explanation of these so-called generalized aerodynamic forces leads to some general conclusions on their accuracy. Reference is made to Fig. 1 where it is shown as an example how the generalized aerodynamic force A_{ij}^D for a swept wing in subsonic flow results from a bending-type vibration mode 1 and a torsion-type mode j . First: it is clear that the major contributions to A_{ij}^D originate from those parts of the wing where both the aerodynamic loads and the wing deflections are large. This makes e.g. the outer part of the wing to a sensitive area in most aeroelastic problems. Second: as drag forces and streamwise wing deflections are relatively small, their contribution is often neglected, which clarifies the relative indifference of aeroelasticians to drag forces!

2.3 Representation of unsteadiness

In the previous section it was discussed that the pressure distributions $p^M(t)$ and $p^D(t)$ depend on time, which means that they are influenced by the unsteadiness of the aircraft motion and the free-stream flow motions, respectively. Considering aircraft motions e.g. this unsteadiness may range from low frequencies, associated with aircraft stability and controllability, to moderate and high frequencies, associated with wing vibrations, control surface oscillations, etc. In unsteady windtunnel testing the unsteadiness is usually introduced by forcing the model into some harmonic oscillation, e.g. of the angle of attack:

$$\alpha = \alpha_0 + \Delta\alpha \cos \omega t,$$

in which α_0 is the mean angle of attack, $\Delta\alpha$ the vibration amplitude and ω the radial frequency. The aerodynamic reaction, e.g. the pressure in any point of the model surface, may be formulated in various ways:

$$\begin{aligned} p &= p_0 + (p'_0 \cos \omega t - p''_0 \sin \omega t) \Delta\alpha + \text{higher harmonics} \\ &= p_0 + |p'_0| \cos(\omega t + \varphi) \Delta\alpha + \text{higher harmonics,} \end{aligned}$$

or in usual complex notation:

$$p = p_0 + \operatorname{Re} \{ (p'_0 + i p''_0) e^{i\omega t} \} \Delta\alpha$$

The first term, p_0 , is the zeroth order harmonic and the second term the first order harmonic, which is explained in Fig. 2. Similar expressions can be given for lift and moment coefficients, etc. The unsteady aerodynamic parameter which governs the first order harmonic is the reduced frequency:

$$k = \omega l / U,$$

in which l is a reference length (e.g. semi-chord of a typical wing section) and U the free-stream velocity. The reduced frequency (and not the frequency ω itself) is an essential parameter which should be considered in unsteady windtunnel testing to guarantee a proper representation of time-dependency. The physical relevance of this parameter is typified by Fig. 3. The variation of bound vorticity at the wing induced by the incidence variations $\Delta\alpha$ are accompanied by wave-like variations of free vorticity in the wake. The parameter k is proportional to the ratio of semi-chord and wave length, l/L . For non-oscillatory motions the unsteadiness is given (again in the case of angle of attack variations) by combinations of α and $d\alpha/dt$.

2.4 Accuracy of full-scale unsteady aerodynamic forces in relation to other forces.

The accuracy of unsteady aerodynamic forces pursued in the prediction of full-scale aeroelastic characteristics, should be tuned to the intended employment of these forces. If used in full-scale predictions, they should be adjusted to the attainable accuracy of inertial, damping and stiffness forces as represented in the previous matrix equation of motion. Some light upon the required accuracy might be shed by the following table with - it should be granted - rather intuitive values.

Force	Order	Accuracy	Remarks
$M\ddot{q}, K\dot{q}$	1	$> \pm 0.05$	calculated, or measured in prototype GVT
$C\dot{q}$	0.05	$> \pm 0.01$	not known before prototype GVT
$A(q)$	0.20	?	depending on accuracy of aerodynamic loads and vibration modes

The numbers show that the required accuracy of the generalized aerodynamic loads is largely dictated by the attainable accuracy of inertial and stiffness forces, and that the error in aerodynamic forces might amount to ± 25 per cent.

To the steady aerodynamicist this required error estimate might look surprising large. He should realize however that the unsteady aerodynamic forces do not contribute to the aircraft performance characteristics, but that in many cases they are needed for demonstration that certain limits (flutter boundaries, load levels, etc.) are not exceeded. If predicted values are well away from these limits, the allowable errors may even be larger. If predictions point to critical situations, other measures (modify mass and/or stiffness distribution, add damping, etc.) may be preferred over a more accurate determination of the aerodynamic forces!

Although the accuracy margin given above looks very comfortable to live with in unsteady windtunnel testing, stern reality learns that the margin can be absorbed very easily by various simulation related inaccuracies like differences between model and full-scale effects concerning Reynolds number, vibration modes and static deformation.

When the aerodynamics are needed for aircraft stability and control derivatives, the situation is somewhat different. The steady derivatives can be obtained from steady windtunnel tests. Generally a rather high accuracy is required, which can also be provided, say ± 5 per cent error. The required accuracy of rate derivatives, however, is influenced by the accuracy of the aircraft moments of inertia, so that the error in these derivatives might be 20 per cent.

Without clinging too much to the numbers given above, it is recommendable to keep a balanced eye on the realisable accuracies during unsteady windtunnel testing.

3. ACCURACIES IN UNSTEADY WINDTUNNEL TESTING

3.1 Types of unsteady windtunnel tests

An excellent survey of unsteady windtunnel testing techniques was presented by Lambourn (Ref.1), from which figure 4 has been taken. Four categories of experimental systems are indicated which can be related to the following three distinctions:

- a. Fixed vs. moving model. The unsteady aerodynamic input may come from some controlled gust field which is imposed on the oncoming flow, from local unsteadiness as in buffeting, or from model motion, whether driven or not, as in flutter.
- b. Rigid vs. aeroelastic model. Rigid means always nominally rigid, as static and dynamic model deformations can never be excluded in practice.
- c. Aerodynamic (direct) vs. response (indirect) measurement. Measuring aerodynamic forces and pressures at given model motion is a direct way, measuring the response of the model and reducing it to aerodynamic quantities is an indirect way as the response results not only from aerodynamic forces, but also from inertial, stiffness and damping forces in the model structure. Typical examples of direct measurements are tests with aerodynamic pressures and loads models, while tests with a flutter model belong to the class of indirect measurements. With these three types of measurements the discussion will be continued in the next section. Figure 4 suggests the use of a full-span model, but often semispan models are being used to alleviate the problem of installing the support and excitation mechanism in the test section without too much interference with the flow.

3.2 Survey of major error sources

In figure 5 an attempt is made to summarize the major error sources in procedures to predict full-scale aircraft aeroelastic characteristics, which make use of dynamic windtunnel testing to a greater or less extent. In measurements with a pressures model (whether moving or not) pressures are measured and integrated numerically to obtain forces and moments. An improper choice of number and location of pressure orifices and failing of them are important error sources. This situation is essentially the same for steady tests but might be more serious in the unsteady case, as will be pointed out in a following section.

Concerning the flow, the Reynolds number is often not scaled properly, which might deteriorate a correct simulation of viscous effects on unsteady aerodynamic characteristics. Also unobserved static deflection might have a negative effect, although the vibration mode may have been measured correctly. Finally, existing correction methods for unsteady tunnel wall interference are only crude.

Sometimes the pressure measurement technique gives rise to lack of accuracy, mainly associated with failing of model instrumentation due to sensitivity to dynamic loading. Unsteady pressures and loads models may be scaled down from complete aircraft or from parts of them to more or less simplified geometries. The experimental data has to be combined then with calculations to enable full-scale predictions. In many cases this involves verification of the theoretical methods as an intermediate step after which the methods are used for full-scale predictions. In other cases the experimental data are applied in semi-empirical methods, which are essentially means for extrapolation of the data to full-scale.

In measurements with a loads model forces and moments are measured instead of pressures. In this case not only aerodynamic but also inertial forces are being measured so that a compensation procedure has to be applied during or after the measurement to extract the aerodynamic forces. As the inertial forces are usually dominating, it is clear that the accuracy of the aerodynamic quantities depends heavily on the precision of the compensation procedure. Application of this procedure is relatively simple if the model may be considered as rigid - like in stability derivative measurements - as then the compensation procedure involves only the subtraction of inertial contributions due to translatory and rotatory model motions. If an aeroelastic model is being used most effort has to be put into the proper design, fabrication and calibration of the model. The dynamic similarity of the model (scaling of natural frequencies, vibration modes, etc.) determines highly the quality of the full-scale prediction, and could form an important error source. The discussion of this subject is not considered to lie within the scope of this paper. The translation of measured responses into full-scale prediction should be relatively simple now. The error sources mentioned so far which have specific impact on unsteady windtunnel testing will be discussed later on in more detail. There are of course various other error sources, involved e.g. in the determination of vibrational characteristics of the aircraft structure and the extrapolation of windtunnel results to full-scale predictions. They are considered beyond the scope of this paper and their discussion is not pursued here any further. In addition to the above techniques, which are concerned directly with model surface loads, also flow visualisation and laser velocimetry techniques can be applied to determine other unsteady flow properties. The information obtained increases the understanding of unsteady flow, and is particularly valuable for computer code development and validation. However, because it is difficult to quantify the accuracy of these techniques and its influence on the accuracy of unsteady airload predictions, these techniques are not considered in the present paper.

3.3 Relation with accuracy in steady windtunnel testing

A fairly reliable indication about the accuracy of unsteady test results can be obtained from the accuracy of measured aerodynamic derivatives (pressures, forces), often defined by aeroelasticians as quasi-steady quantities. (Strictly speaking quasi-steady quantities are unsteady quantities for vanishing reduced frequency value, and differ from derivatives in case of nonlinear aerodynamic characteristics (see Ref.2). In figure 6 an example is presented of chordwise pressure distributions for the supercritical airfoil NLR 7301, given in reference 2, and derived from the investigations of Tijdeman (Ref.3) in which he consequently compared quasi-steady and unsteady data. Two observations are notable:

- a. The quasi-steady and unsteady pressure distributions are very similar;
- b. Both distributions show a strong peak at the shock position, the so-called shock peak, corresponding to the trajectory of the moving shock. The consequence is that a failing pressure point in the shock trajectory of steady lift and moment, but that this could be disastrous for the accuracy of quasi-steady and unsteady lift and moment. In the worst case the peak might remain unobserved.

3.4 Test setup

For the measurement of unsteady airloads two- and three-dimensional test setups are being used. In aeroelasticity the airloads on two-dimensional wings due to heaving and pitching oscillations are often

wanted as they have special significance in computer code validation and in applications to large aspect-ratio wings. Pitching oscillations in two-dimensional test rigs can be realized relatively easily. Airloads due to heaving can then be obtained from the difference between airloads corresponding to different pitching axis locations. The difference, however, is usually too small to result into airloads due to heaving with a sufficient accuracy. Realization of pure heaving oscillations requires a much more complicated test rig. An example is the NLR test rig used for the measurement of unsteady airfoil characteristics in transonic flow, which is presented in figures 7 and 8. Two pitching oscillation modes with axis positions at 20 and 45 per cent chord and a heaving oscillation mode could be realized (Ref.4). The maximum amplitude and frequency in the pitching modes were 1 degree and 200 Hz, and in the heaving mode 1.5 mm and 150 Hz. In three-dimensional tests both semi- and full-span wing models are used. The semi-span models enable tests at higher Reynolds numbers, like in steady tests, but permit in the unsteady case: a much easier driving mechanism. Mainly for the latter reason many three-dimensional tests are performed with semi-span models, accepting at the same time the drawbacks of the disturbing influence of the tunnel wall boundary layer at the wing root and the need of a labyrinth between model and tunnel wall if forces have to be measured. Several examples of semi-span wing models are given in this paper. An example of a full-span test setup is presented in figure 9, being used recently at NLR for low speed tests with a straked delta wing model oscillating in pitch (Ref.5). The complication of the many struts was necessary to guarantee a clean pitching motion in a wide range of incidences, pitching amplitudes and sideslip angles. To estimate the interference of the test rig with the flow a separate steady test was performed with the model suspended in wires to an overhead balance system.

3.5 Measuring techniques

To determine the time history of the position of the model surface, nowadays in most experiments only relative displacements are measured between parts of the construction which are close to each other, for instance:

- position of the root chord relative to the tunnel wall when it concerns a semi-span model
 - position of the flap relative to the wing when it concerns a model with oscillating flap.
- The accuracy of these measurements is better than 0.01 mm. On other places of interest, models are equipped with accelerometers, providing local amplitude of the motion by double integration of the signal. The accuracy of the amplitude obtained in this way will depend strongly on frequency. Optical systems, which enable the measurement of the position of a large number of points on the model surface with respect to (for instance) the tunnel walls, are under development, but still not available for routine applications. A big advantage of such a system would be the inclusion of the static deformation of the model.

When the model motion is known, the transfer function between motion and aerodynamic output can be established by measuring the overall loads and/or pressure distributions. As mentioned in section 3.2, the overall loads measured by a balance, must be corrected for inertia effects. Models for this kind of tests are therefore often made of special materials, like magnesium alloys, to improve the ratio between aerodynamics and inertia loads. At constant reduced frequency, the frequency of the model excitation will increase with windspeed, and inertia effects will become more pronounced. However, one should realize that not all components are affected by inertia loads: when the center of gravity is in the rotation axis of a pitching model, the unsteady normal force is not affected by inertia loads!

Pressure measurements provide detailed information about the flow, balance measurements do not. However, when the goal of these measurements is to obtain overall loads by integrating pressure distributions, one should realize that the accuracy might be limited by a too small number of pressures, steep pressure gradients and poor integration methods. Especially when transducers fail in the region with large pressure gradients (for instance at the shock position), a severe loss in accuracy may be expected (see Sections 3.2 and 3.3).

For the measurement of pressures on the model surface, two methods are mentioned here:

- * The first one uses a large number of identical pressure tubes, connected via scannivalves to a limited number of pressure transducers, outside the windtunnel (see Ref.3). The essential step in the data reduction procedure of this method is that the unsteady pressures measured with the transducers, (p) are reduced to the actual pressures at the model surface (p_s), with the use of the transfer functions of the pressure tubes. This procedure is schematically indicated in figure 10. By installing a limited number of miniature pressure transducers in the model, each of them positioned adjacent to some orifice, the tube transfer functions are measured during the windtunnel test. They can be applied to all other tubes. The tube transfer function depends on frequency, tube geometry, geometry of the tube entrance, steady pressure and velocity profile of the local boundary layer. The accuracy of pressure coefficients determined with this method is estimated to be better than 5% in amplitude and 3 deg in phase angle (see Ref.2 dataset 9 and Ref.3). The method is economic and does not deteriorate the model stiffness too much. However, not all pressures can be measured at the same time and extra postprocessing is needed as compared to the next method.
- * The second method uses a large number of miniature pressure transducers close to the model surface, leaving tubes of only very short length. The transducers are mounted in such a way that they are electronically insulated, free from model deformation and not influenced by accelerations. In this method the electronic output, in combination with the sensitivity of the transducer, yields directly the pressure signal at the model surface. In the range of test frequencies in aeroelastic applications (up to about 1 kHz), no correction for the transferfunction of the short tube and small volume between model surface and transducer is needed. This technique may be applied also with somewhat extended tubes, to enable measurements at places difficult to reach, like nose and trailing edge region. Failure of transducers occurs more frequently at places with a high acceleration level. By using a short tube, mounting of transducers at these places can be avoided. In this way, failure of transducers will be limited, resulting in a higher accuracy of the overall coefficients obtained by integration.

The technique is also suitable for the measurement of non-sinusoidal pressure signals and provides the possibility to measure all pressures simultaneously. In the last few years, miniature pressure transducers which are suitable for both static and dynamic pressure measurements have become available. In the past, in models equipped with a large number of miniature pressure transducers, also a large number of pressure tubes were installed to measure the static pressures. In this way, often a small stiffness of the model and consequently a large static deformation was obtained, which deteriorated the accuracy of the measurements.

The unsteady signals of motion and loads measuring instruments can be recorded directly on tape or disc for further analysis. For oscillatory motions, a large reduction of the amount of data can be obtained by transformation of the measured unsteady signals to a limited number of Fourier components. As a consequence, if the signal is far from harmonic, this may lead to errors due to neglect of higher harmonics. In case of wings in harmonic motion, such errors may become significant especially when the flow is strongly nonlinear e.g. close to moving shocks and at separated flow. Whether the higher harmonics are really serious in their contributions to the aeroelastic stability and responses of the aircraft depends on the vibrational characteristics of the structure.

3.6 Viscous effects

Like in steady aerodynamic investigations, viscous effects occurring during unsteady wind tunnel testing are an important matter of concern in the definition, measurement and analysis phases of the investigation. Depending on thickness and nature of the viscous layer, the effect of viscosity can vary from a small effect on magnitude and phase angle of the airloads relative to the airfoil motion, to a completely different behavior of the unsteady flow compared to the hypothetical inviscid case. As a consequence, results of unsteady wind tunnel tests cannot be used safely for full-scale flutter predictions, without a careful analysis of the possible effects of the difference between model and full-scale Reynolds number. In the following the major effects of viscosity on unsteady airloads are summarized, and consequences for the setup and analysis of unsteady flow experiments are discussed.

For a given model motion, the development of unsteady flow and airloads depends on Reynolds number in two ways (Ref.7):

1. By its influence on the initial or mean steady state flow field. This flow field determines the way in which unsteady flow perturbations propagate around the airfoil and contribute to the distribution of unsteady pressures on the model surface. This effect is most important at transonic flow conditions, where unsteady loading strongly depends on location and size of supersonic flow regions and shock waves.
2. By its influence on the unsteady change of the viscous region. For a given initial steady flow field, the unsteady changes of geometry and nature of the viscous region interact with the model motion and the inviscid part of the flow, and consequently affect the unsteady airloads.

The unsteady behavior of the viscous region can be classified as follows, in sequence of increasing effect on the unsteady airloads:

- (for fixed transition points) variation in time of attached laminar and turbulent parts of the viscous region
 - additional variation of the viscous region due to unsteady transition point displacement
 - motion-induced leading edge separation and vortex flow
 - motion-independent unsteady viscous-inviscid interaction, often characterized by strong periodicity.
- The above effects are important in many practical cases of unsteady loading and aeroelasticity, in particular involving control surface effectiveness, aeroelastic behavior of wings in attached transonic or natural laminar flow, transonic wing or aileron buzz and dynamic stall. Inaccurate simulation of viscous effects for the above cases, either by experiment or computation, leads inevitably to erroneous predictions of unsteady airloads and aeroelastic behavior.

A typical example of inadequate simulation of viscous effects in the windtunnel was reported in reference 8 which describes a flutter investigation of a supercritical wing semi-span model. In order to trace the flutter boundary sufficiently far in the transonic regime, the total pressure had to be reduced significantly. At the resulting low Reynolds number (LE06 based on representative wing chord) an unexpected stability boundary (Fig.11) was found, which could not be attributed to inviscid transonic effects or flow separation. After analysis of the transition strip effectiveness it was concluded that the strip had become ineffective, allowing an unsteady transition point motion. From various experimental studies of oscillating airfoils it is known, that such a motion has a strong influence on the unsteady loading, and in particular leads to a larger phase lag of unsteady airloads relative to the airfoil motion. In Fig. 12 this effect is illustrated by the unsteady lift coefficient measured on a supercritical (NLR7301) airfoil with oscillating flap, for various locations of a transition strip. This effect of a moving transition point explains the negative aerodynamic damping which leads to the observed low-Reynolds number instability.

Also here a useful means to detect the role of transition on unsteady airloads is quasi-steady analysis of available steady flow data. As an example, Fig. 13 shows the quasi-steady lift coefficient as function of angle of attack for a supercritical airfoil at its experimental design Mach number $M = 0.745$, for various locations of a transition strip. Fig. 13 also shows the motion $dx/d\alpha$ of the transition points on upper and lower surface measured during the tests with natural transition. Like in the previous example the lift is strongly affected by displacement of the transition point. The large peak can be correlated with a downstream motion of the transition point. Fixation of the transition point on a sufficient upstream location reduces this peak effectively.

If a wind tunnel investigation has to be carried out at a Reynolds number significantly different from full-scale, various measures can be taken to reduce the resulting error in unsteady flow simulation. These measures, which are also applicable to cope with wall interference effects, can be expected to yield qualitatively better unsteady airload predictions, of which the remaining quantitative error can be estimated and, to some extent, be corrected.

Analysis in advance of steady experimental and theoretical data, to define a test program at initial or mean steady flow conditions which correspond to full-scale by similarity in state of the viscous region and pressure distribution, rather than by similarity of angle of attack and Mach number. This measure helps to reduce inaccuracy of unsteady airloads due to misfit of full-scale and model initial flow field.

Both in unsteady pressure and flutter investigations, models should be equipped with steady pressure orifices in at least one characteristic section of the model, in order to be able to verify the assumed initial steady state flow field. This also is advisable if static model deformation and wall interference are expected to be significant.

Using the above steady flow data, the quasi-steady behavior of the transition line on model and at full-scale should be analyzed in advance (see the example discussed above). On the basis of this information an optimum location and size of transition strips can be chosen. This measure may eliminate anomalous behavior of unsteady airloads due to (at full-scale) unrealistic transition point motion. If the transition point at full-scale is expected to be strongly variable (e.g. on natural laminar flow airfoils), accurate simulation at wind tunnel conditions will be more difficult.

In the analysis phase the measured wind tunnel data can be applied to full-scale conditions, or used for code verification, on the basis of matching the initial steady flow fields. In transonic flow, this matching should be carried out on the basis of Mach number distribution and shock location. If pressure coefficients are used as basis for matching, a difference in free-stream Mach number must be corrected for in order to obtain similar local Mach number distributions.

An example of this matching is shown in Fig. 14, where experimental mean steady and unsteady pressure coefficients on a supercritical airfoil are compared with results of inviscid transonic small perturbation theory. The present case was selected from Ref. 2 and concerns the NLR7301 airfoil oscillating about its nearly shock-free design condition ($M = 0.748$, $\alpha = .85$ deg). The theoretical design point ($M = .721$, $\alpha = -.19$ deg) was used in the computation. Although the measured and computed mean steady pressure distributions are approximately shock-free, they do not match very well, and there is a considerable disagreement in unsteady pressure distributions on the upper surface (Fig. 14a). A better result is obtained, if the angle of attack in the computation is increased to improve the matching of the unsteady pressure distributions on the upper surface. To obtain similarity in Mach number distribution, first the experimental mean C_p values were corrected for the difference in free-stream Mach number. The resulting "target" pressure distribution was approximated in the computation by increasing the angle of attack by 0.5 deg (Fig. 14b). As a result, the computed unsteady pressures are in better agreement with the experimental results. Of course, the agreement is not yet satisfactory in particular due to the neglect of viscous effects. The present example shows, however, the importance of matching of the steady flow fields irrespective of the accuracy of the prediction of the unsteady perturbations of this field. A similar procedure can be followed if full-scale predictions are to be made on the basis of experimental results at lower Reynolds number.

The accuracy of the measured unsteady airloads for application at full scale can be estimated if both model and full scale steady flow data are available, by analysis of quasi-steady airloads at model and full-scale Reynolds number. For low reduced frequencies the unsteady airloads may be corrected for this difference, to improve the applicability at full scale conditions.

3.7 Tunnel wall interference

A constant source of concern to the wind tunnel experimentalist is unsteady tunnel wall interference. The effects as experienced by the model, originate from various causes:

- * deformation of the mean steady flow due to wall constraints
- * reflection of unsteady pressure disturbances at the walls
- * transverse tunnel resonance.

For a further discussion it is easiest to consider the flow about the oscillating model as a superposition of a steady flow governed by model geometry and mean incidence, and a perturbing unsteady flow generated by model motion or flow unsteadiness. The influence of the steady flow on the unsteady part may become very strong - as is well-known-under transonic conditions.

- a. Considering the effects of wall constraints it is now reasonable to accept that the correction methods and recommendations to avoid serious constraints effects, which are familiar in steady testing, are also applicable to the mean steady flow in unsteady testing. A rather common method to allow for this effect to some extent is to match the flow about the model in its mean position to the desired flow known e.g. from interference free steady tests. An example will be given later on. A similar matching is discussed in section 3.6 to account for Reynolds number.
- b. The second effect mentioned above is a typically unsteady one and effect is due to the pressure waves emitted from the oscillating model, which do not recede continually, but are reflected with the flow about the model. Correction methods are far from complete and show the tendency to follow ideas in the development of steady correction methods. A major problem in finding adequate theoretical correction methods is uncertainty about the unsteady boundary conditions at ventilated windtunnel walls. The most elaborated methods are based on integral equation formulations using the strongly simplified linear homogeneous boundary conditions. They are further restricted to uniform mean flow and therefore invalid in transonic flow. A recent survey has been given in reference 9. An alternative approach has been proposed which employs measured flow conditions at the walls (Ref. 10). This makes the method applicable to ventilated, especially slotted walls, but transonic flows remain excluded. Correction methods for more general cases, including three-dimensional models, transonic flow and/or ventilated tunnel walls, which have found some broader acceptance, are not known to the authors. Two examples will be given here to illustrate the concerns a 12% thick supercritical airfoil, pitching about 0.45 C (Ref. 4), in a transonic attached flow with a well-developed shock wave. Chord length was 0.18 m and tunnel height 0.55 m. Top and bottom floor were slotted walls with open-area ratio of 10%. In Fig. 15 the modulus and phase of the measured lift coefficient h_z is shown versus reduced frequency k , in comparison with calculated values of linear theory (Doublet-Lattice method) and small perturbation transonic theory (LTRAN2-NLR, Ref. 11). The following wall interference effects may be observed.

- At zero frequency the measured lift coefficient was corrected according to a standard procedure. The correction amounted into an increase of 31%. The corresponding corrected incidence was 2 deg.
 - The measured modulus values show a maximum at small reduced frequencies, while the phase lag is retarded.
 - The calculated transonic lift coefficients were obtained after matching the mean pressure distribution with the measured distribution, on the basis primarily of an equal shock location.
- The conclusion of comparing all these results is that the wall interference effects seem to be over at $k = 0.15$.

The second example concerns the so-called MORA wing, a harmonic oscillation semi-span model, which was tested in four different European wind tunnels (Ref. 12). The model planform is shown in figure 16. A comparison of the tunnel test sections involved is given in figure 17. Results of three wind tunnels are presented in figure 18. Result of the 82 tunnel were very similar to those of the EST and

have been left out. It can be observed in this rather securitive case that shock peaks occurred in the pressure distribution of the laye wind tunnel HST, which were almost suppressed in the smaller tunnels 1M and 3Ft, both in case of nominal comparison (NC) and in the case of pressure matched comparison (PC, i.e. best match of local Mach number distribution on the upper side). One of the conclusions of reference 12 is that the results of this comparative investigation tend to confirm the conventional practice in choosing model-to-tunnel size ratios to avoid large interference effects.

c. Under certain flow conditions the emitted and reflected pressure disturbance meet at the oscillating model surface in opposite phases, producing a pressure mode there. A standing wave pattern is generated which is the cause of transverse tunnel resonance. Usually the lowest resonance frequencies are of practical importance only in case of transonic test conditions. For the idealized case of two-dimensional uniform mean flow and either closed or open walls, simple formula's exist to calculate the resonance frequencies. Reference 9 explains that for homogeneous ventilated walls the resonance frequencies are in between. For more complicated cases, like three-dimensional models, lifting conditions and/or slotted walls. The mean flow becomes strongly nonhomogeneous so that the pressure waves experience substantial diffraction, refraction and scattering influenced also by the acoustic characteristics of the plenum chambers. Although tunnel resonance has been demonstrated experimentally to exist, it is doubtful in many tests whether this phenomenon should cause anxiety. The authors did not encounter it in any NLR unsteady windtunnel test.

4. AGARD SMP ACTIVITIES

In a discussion of the accuracy of unsteady windtunnel testing a reference may not be omitted to the "Compendium of Unsteady Aerodynamic Measurements" (Ref.2) of which the composing was sponsored by the AGARD Structures and Materials Panel. This document followed the earlier activity of the SMP to define the so-called AGARD Standard Configurations for Aeroelastic Application of Transonic Unsteady Aerodynamics. These configurations (both two- and three-dimensional) were intended as test cases in the evaluation of methods to predict transonic unsteady aerodynamics and aeroelastic response. The Compendium contributes to this evaluation with extensive sets of experimental data for most of the standard configurations. The reason of referring here to the Compendium is that in each data set the matter of data accuracy is raised explicitly. In an introductory chapter Lambourne, who edited the Compendium, indicates in what light the accuracy should be viewed. He remarks that the steady pressures, flow parameters, etc. are measured accurately enough, but that the unsteady pressures give rise to concern. He emphasizes that unsteady pressure measurements involve the separate measurement of small changes in pressure and small model displacements with instrumentation that is operating normally in a dynamic environment. Systematic measurement errors would therefore affect easily major parts of the data set. Lambourne concludes his review as follows:

"Whereas the resolution of the instrumentation or the day-to-day repeatability, both of which set limits to the accuracy, are fairly easy to determine, the overall accuracy of a measurement is extremely difficult to quantify. Usually the most that can be expected is a statement to the effect that the measurement of quantity A is no better than x percent. Such statements are usually made on personal, and to some extent intuitive, assessments based on the experience of the experimenter. To demand more would be unreasonable, for a thorough analysis of possible errors could easily entail as much work as the measurements themselves".

This situation makes presume a variety in quantitative error estimates. Figure 19 shows a summary of accuracies of unsteady pressure coefficients as stated by the contributing authors of the data sets. All included sets concern pitching type oscillations. The figure shows indeed that the error estimates are rather unequal, while estimates for data sets 1 and 4 could not be stated.

In view of all other error sources (see sect. 3.2) it is very difficult to feed these error estimates back to the requirements for full-scale aircraft given in section 2.4, in an attempt to enforce some opinion about their acceptability. All what can be said about these error estimates is probably that no strong argument exists to reject them.

Finally, an activity of the SMP should be mentioned which started Fall 1984, to compose a compendium concerning standard aeroelastic configurations for transonic aerodynamics and flutter research. The intention is to collect windtunnel data sets for validation of calculation methods for dynamic aeroelastic characteristics of two- and three-dimensional configurations. An initial choice of configurations has been made already. It is to be expected that the matter of accuracy will emerge in a similar way as for the compendium of unsteady aerodynamic measurements.

5. FINAL REMARKS

During the AGARD SMP meeting in Fall 1986 a workshop was organized on "Future research on transonic unsteady aerodynamics and its aeroelastic applications", chaired by Prof. H Foeraching. Various research needs were identified, from which the following subjects being relevant here are taken over:

- a. Theory
 - windtunnel wall effects
- b. Model testing
 - 2-D pitch/plunge flutter tests and measurement of related unsteady aero coefficients
 - Unsteady pressure measurements at high Reynolds No.
 - Analysis of model test results of low vs. high Re number facilities and vs. aircraft Re numbers
 - Windtunnel wall and resonance effects - how significant?

Further, as activities in a 5- to 6-year working program it was suggested (amongst others) to monitor these subjects by means of pilot papers, and to organize a FDP-SMP Symposium on transonic unsteady aerodynamics and its aeroelastic applications in 1990/91. Hopefully the present paper has contributed to stimulating such a future co-operation of both Panels.

6. REFERENCES

1. Lambourne, N.C. Experimental techniques in unsteady aerodynamics Chapter 10 of: Special course on unsteady aerodynamics, AGARD-R-679, 1980

2. Lambourne, N.C.
(Ed.) Compendium of unsteady aerodynamic measurements
AGARD-R-702, 1982, and AGARD-R-702 Addendum No. 1, 1985
3. Tijdeman, H. Investigations of the transonic flow around oscillating airfoils
NLR TR 77090 U, 1977
4. Horsten, J.J. Recent developments in unsteady pressure measurement techniques at NLR
Intern Symp. on Aeroelasticity, Nuremberg, W. Germany,
October 5-7, 1981, DGLR-Bericht 82-01, 1982
5. Den Boer, R.G.
Cunningham Jr., A.M. A windtunnel investigation at low speed of the flow about a straked delta
wing, oscillating in pitch
AIAA Paper 87-2493, presented at the AIAA Atmospheric Flight Mechanics
Conference, Monterey, CA,
August 17-19, 1987
6. Destuynder, R.
Tijdeman, H. An investigation of different techniques for unsteady pressure
measurements in compressible flow and comparison with lifting surface
theory
AGARD-R-617, 1974
7. Houwink, R. Some remarks on boundary layer effects on unsteady airloads
AGARD-CP-296, 1980
8. Houwink, R.
Kraan, A.N.
Zwaan, R.J. A wind tunnel study of the flutter characteristics of a supercritical wing
J. of Aircraft, Vol. 9,
No. 5, pp. 400-405, 1982
9. Mokry, M.
Chan, Y.Y.
Jones, D.J.
Ohman, L.H. (Ed.) Two-dimensional windtunnel wall interference
AGARD-AG-281, 1983
10. Sarvada, H. A new method of estimating windtunnel wall interference in the unsteady
two-dimensional flow
NAE-AN-9, 1983
11. Houwink, R.
Van de Vooren, J. Improved version of LTRAN2 for unsteady transonic flow computations
AIAA J., Vol. 18, No. 8, pp. 1008-1010, 1980
12. Lambourne, N.C.
Destuynder, R.
Kienappel, K.
Roos, R. Comparative measurements in four European wind tunnels of the unsteady
pressures on an oscillating model (the NORA experiments)
AGARD-R-673, 1980

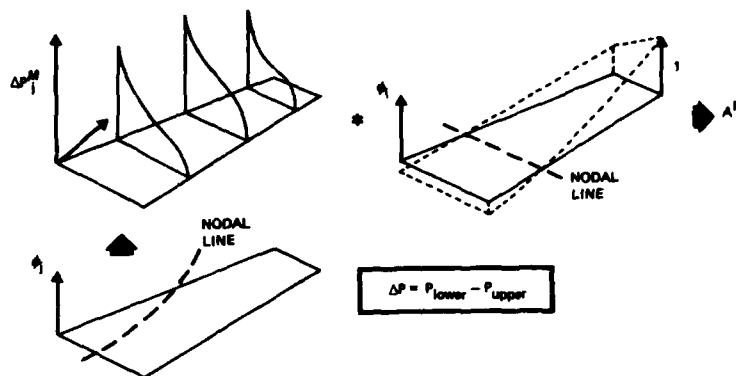


Fig. 1 Constitution of a generalized aerodynamic force

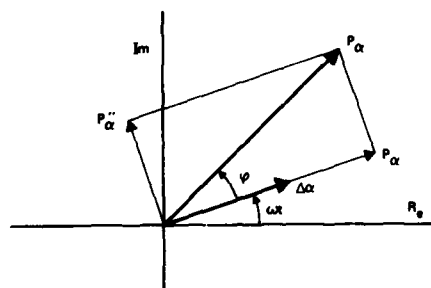
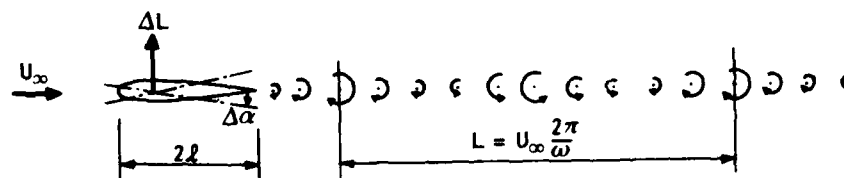


Fig. 2 Complex notation of unsteady aerodynamic pressure



VARIATION IN INCIDENCE : $\Delta\alpha \cos \omega t$

VARIATION IN LIFT : $\Delta L \cos (\omega t - \phi)$

MAIN PARAMETER : REDUCED FREQUENCY $k = \frac{\omega l}{U_\infty} = \pi \frac{2l}{L}$

Fig. 3 Flow about oscillating wing (Ref. 3)

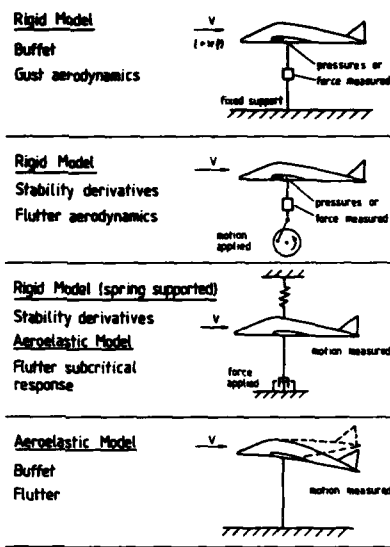


Fig. 4 Some experimental systems (Ref. 1)

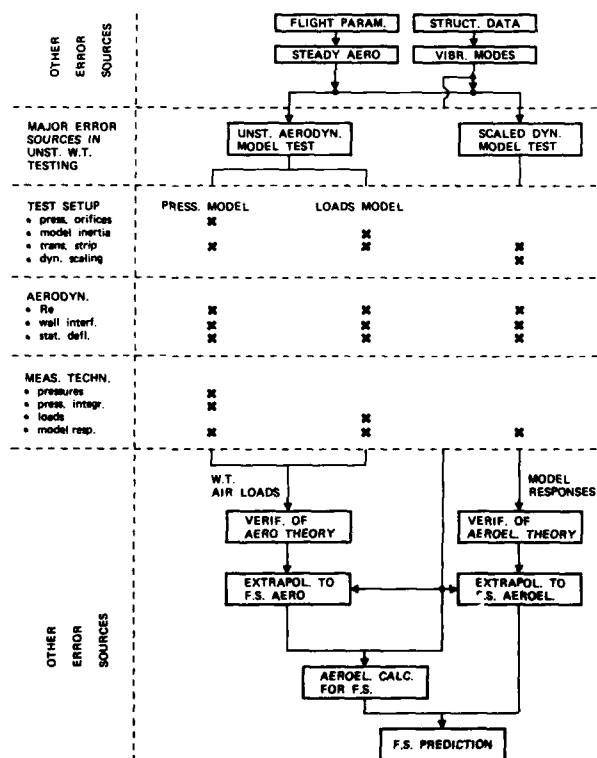


Fig. 5 Major error sources in unsteady windtunnel testing in view of prediction of full-scale aeroelastic characteristics

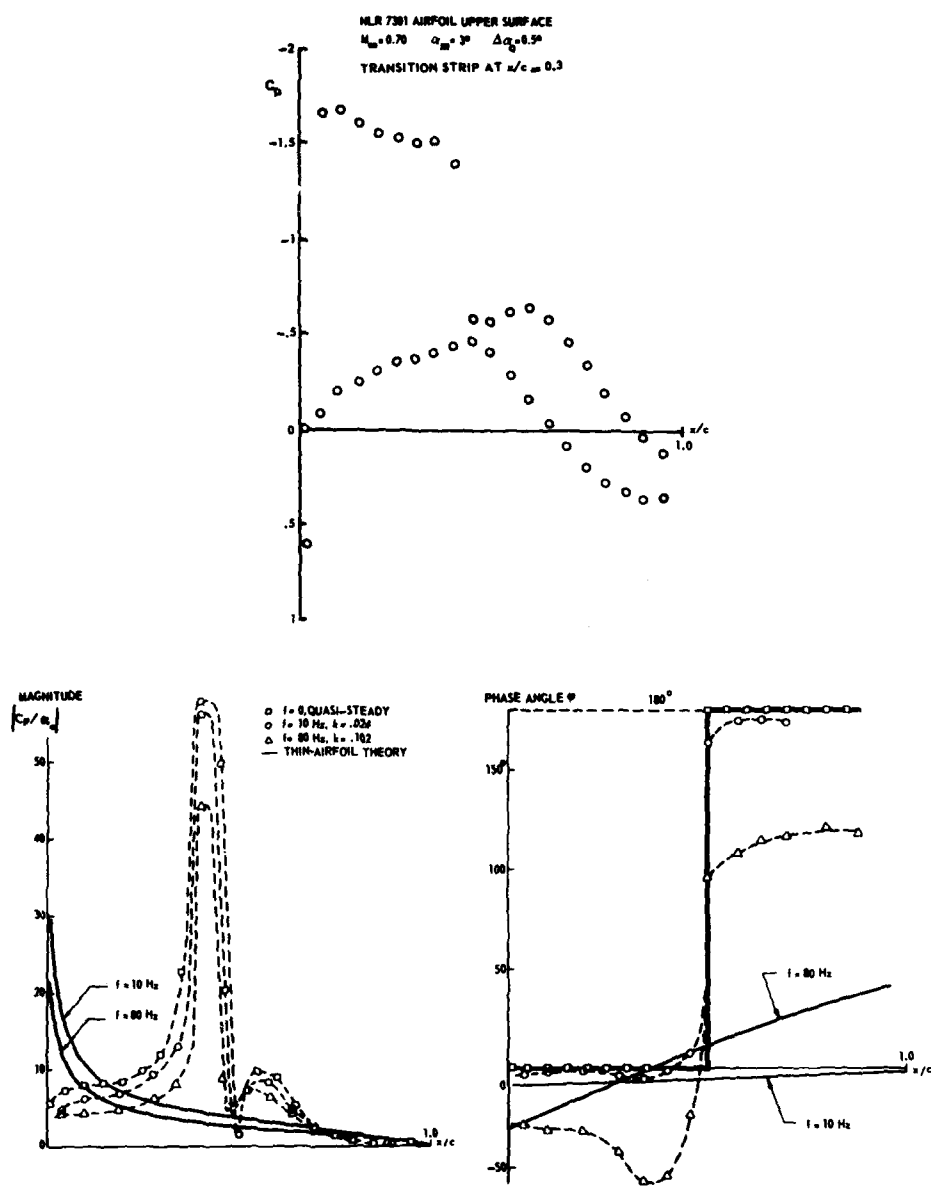


Fig. 6 Effect of shock wave on the unsteady pressure distributions; pitching oscillation (Ref 2)

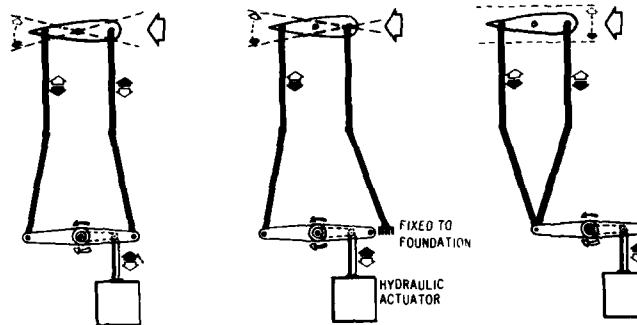


Fig. 7 Principle of the three vibration modes (Ref. 4)

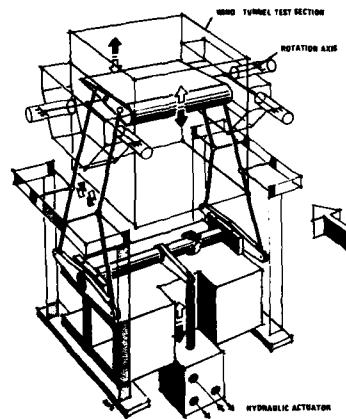


Fig. 8 Test set-up for the pitching motion around 0.45 C

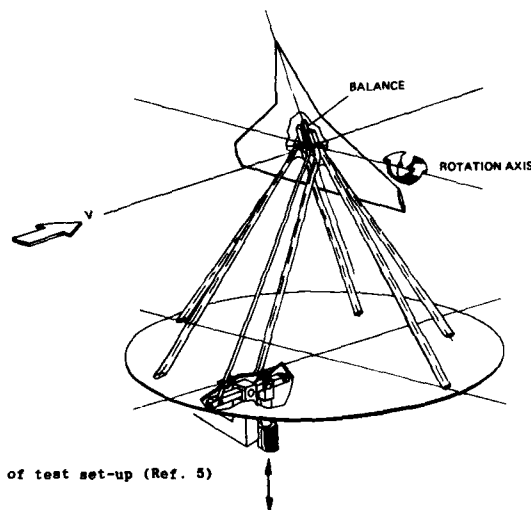


Fig. 9 Principle of test set-up (Ref. 5)

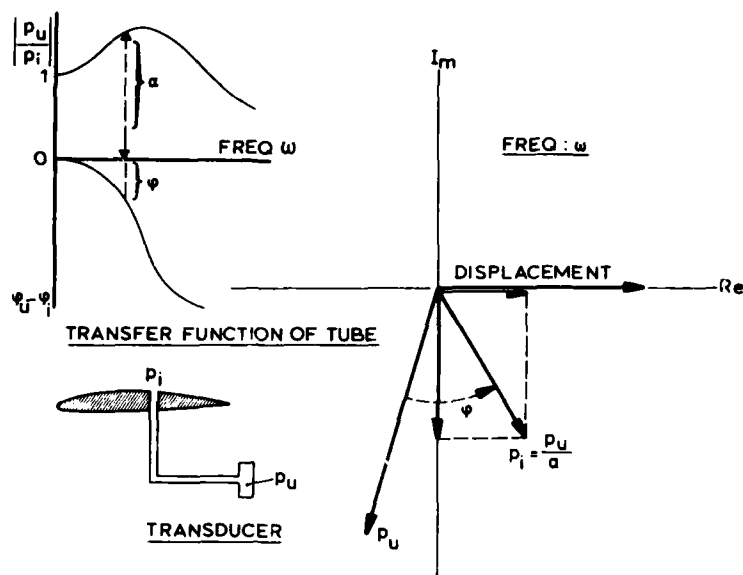
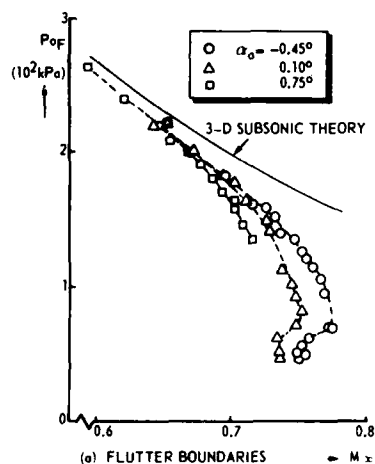
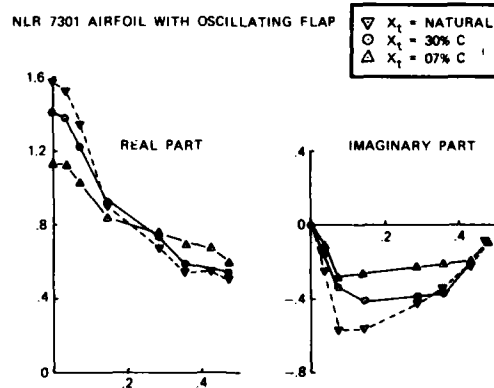


Fig. 10 Principle of data reduction procedure

Fig. 11 Flutter boundaries of supercritical wing semi-span windtunnel model showing anomalous behaviour at low total pressure (α_0 is mean incidence at wing root)Fig. 12 Unsteady lift coefficient on NLR 7301 airfoil with oscillating flap, showing the effect of transition point fixation (α_m is mean incidence)

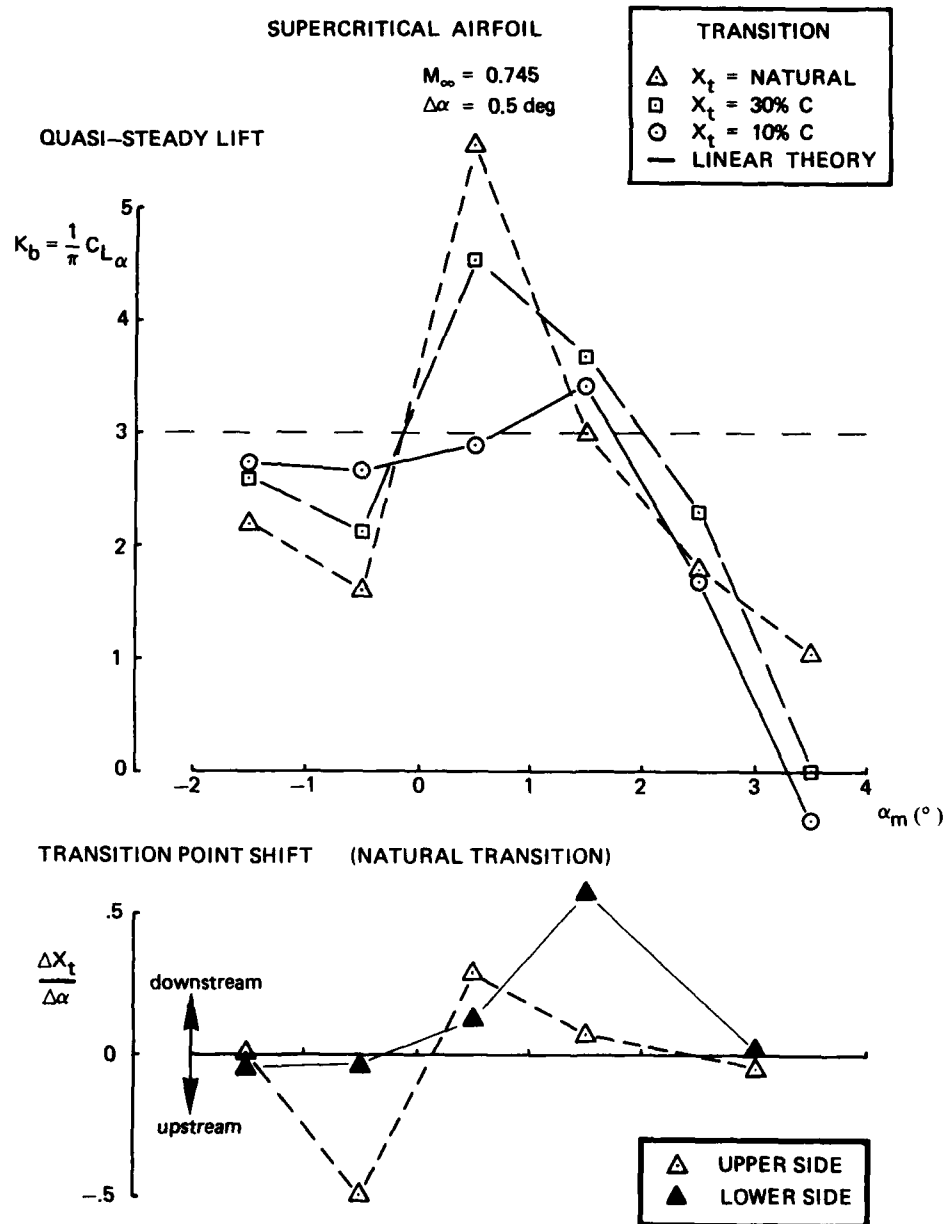


Fig. 13 Quasi-steady lift coefficient and transition point displacement, showing the effect of transition point fixation

NLR7301 AIRFOIL	— UPPER SIDE (MACH=.721, ALPHA=-.19 DEG)
	- - - LOWER SIDE (MACH=.721, ALPHA=-.19 DEG)
	- - - UPPER SIDE (MACH=.721, ALPHA=.31)
	- - - LOWER SIDE (MACH=.721, ALPHA=.31)
AMPL = 0.5 DEG	* UPPER SIDE (EXPT., MACH=.748, ALPHA=.85 DEG)
K = 0.068	o LOWER SIDE (EXPT., MACH=.748, ALPHA=.85 DEG)

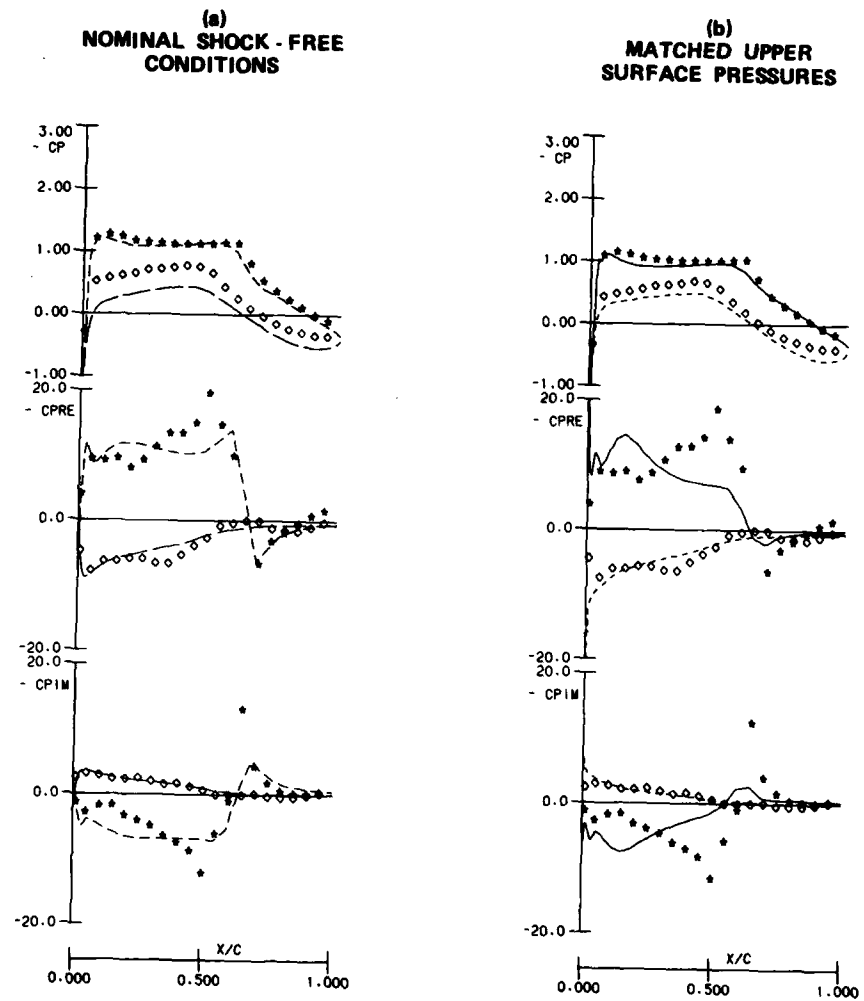


Fig. 14 Effect of matching of upper surface mean steady pressure distribution on computed unsteady pressures

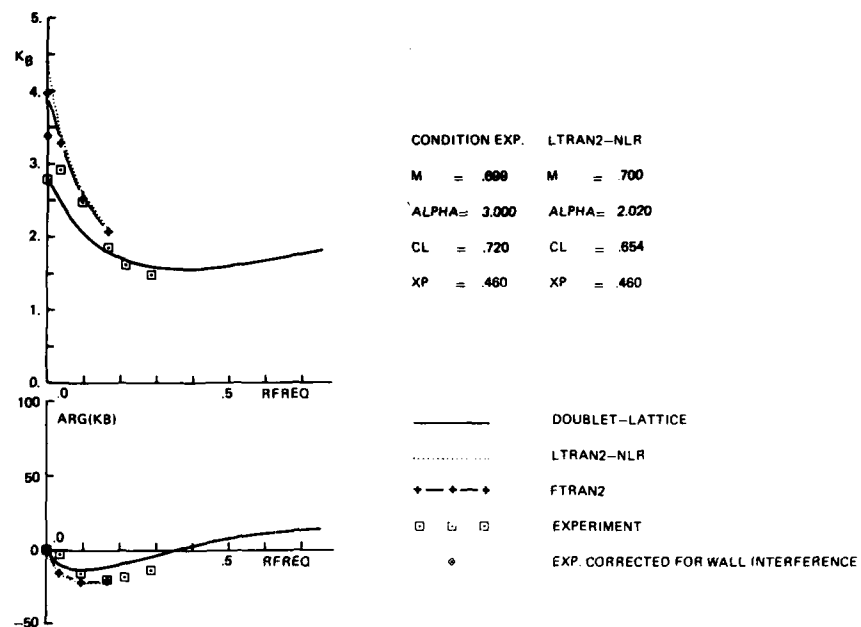


Fig. 15 Unsteady aerodynamic coefficients of a 12% thick supercritical airfoil oscillating in pitch about 0.45 C pitching motion

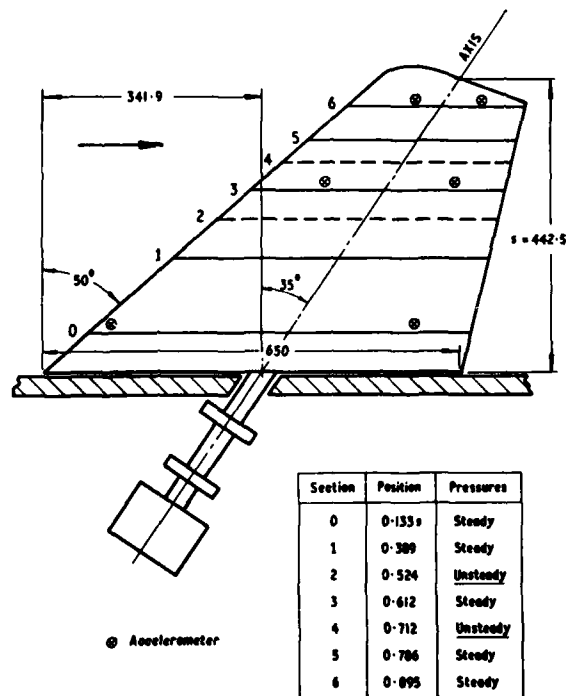


Fig. 16 NOBA model and rotary oscillator (dimensions in mm)

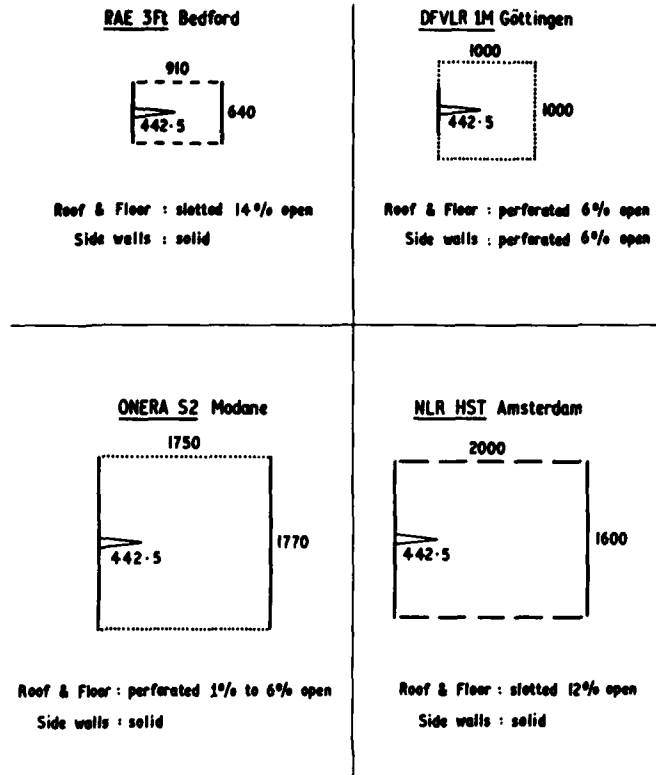


Fig. 17 Tunnelworking sections with NORA model (dimensions in mm)

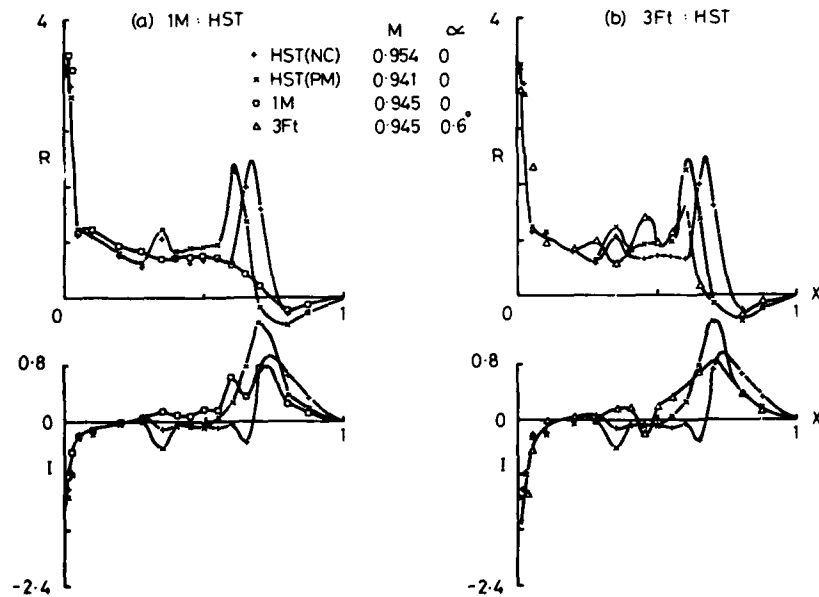


Fig. 18 Oscillatory pressures. (a) Comparison of 1M and HST
(b) Comparison of 3Ft and HST. $M = 0.95$, $\alpha = 0$, Section 2E, 40Hz

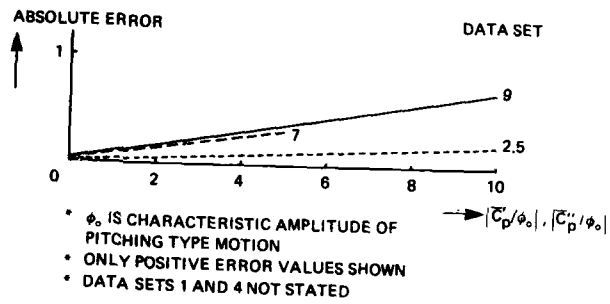


Fig. 19 Comparison of some accuracies of unsteady pressure coefficients stated in Ref. 2

**SPECIFICATIONS PARTICULIERES CONCERNANT LES RESULTATS
DES ESSAIS EN SOUFFLERIE POUR LA
MECANIQUE DU VOL**

par Marc PIANKO
avec la collaboration de Dominique TRISTRANT pour la 2ème partie
ONERA-IMFL - 5 boulevard Paul Painlevé - 59000 Lille, FRANCE

RESUME

L'objet de la présente communication est de cerner certains besoins et présenter des recommandations concernant la qualité et la précision des mesures en soufflerie analysés du point de vue de la Mécanique du Vol. A cet effet, dans une première partie l'auteur étudie quantitativement l'influence d'une imprécision relative à une caractéristique aérodynamique sur le comportement en vol de l'avion. Cette influence conduit à la notion de sensibilité attachée à chaque coefficient aérodynamique et à la possibilité d'un classement de ces coefficients en fonction du besoin de précision qui leur est attaché.

Dans une deuxième partie sont examinés les problèmes très particuliers que pose le vol aux grands angles (incidence et dérapage). Dans ce domaine, les effets aérodynamiques ne peuvent plus être considérés comme linéaires, le comportement de l'avion subit fortement l'action de phénomènes instationnaires et les perturbations (parois, supports, etc...) ont souvent une influence de très grande amplitude. De ce fait la principale difficulté dans ce domaine de vol aux grands angles n'est pas l'obtention d'une grande précision mais la possibilité même d'une caractérisation adéquate de l'avion.

Dans la dernière partie, par le biais d'une enquête effectuée auprès des principaux utilisateurs des souffleries, sont examinées les difficultés qui se présentent à l'utilisateur des souffleries au cours du développement d'un avion. On analyse également les améliorations qui sont demandées aux souffleries ainsi que les perspectives offertes aux souffleries à moyen terme.

INTRODUCTION

L'exposé qui suit est le résultat de l'invitation faite par le Panel FDP, organisateur du présent symposium, au Panel FMP de présenter sa contribution sur le sujet des qualités et caractéristiques des essais en souffleries.

Le titre en explicite l'objet : spécifications particulières concernant les résultats des essais en soufflerie pour la mécanique du vol.

Il serait souhaitable de commencer par éclairer et commenter l'objet, les objectifs et la notion du présent exposé. Tout d'abord qu'appelle-t-on "Mécanique du Vol" ? Et en quoi les besoins de la Mécanique du Vol se particularisent-ils par rapport aux autres besoins ?

a) L'objectif essentiel des études ayant trait à la Mécanique du Vol est la prévision du comportement dynamique de l'avion. Pour cela, il y a lieu de définir des "modèles de représentation et de prévision" du comportement de l'aéronef, pour ensuite les étudier et les exploiter : élaboration de lois de pilotage et du système de commandes de vol, calcul des performances, détermination des qualités de vol. Dans cette optique l'avion est un système intégré où l'aérodynamique et les structures interagissent. Alors que l'aérodynamicien s'intéressera plus à la notion de l'écoulement et à ses différentes caractéristiques, le mécanicien du vol sera plutôt intéressé par l'effet de celui-ci sur l'avion. Tous deux utiliseront bien sûr des supports expérimentaux et en particulier les essais en soufflerie, cependant les objectifs seront différents. Le premier effectuera des mesures souvent délicates : mesures de pression, visualisations instationnaires, pesées locales, etc... afin de connaître, de comprendre la structure intime des écoulements et afin d'en déduire les lois qui les régissent. Le second se préoccupera surtout de l'effet global du fluide sur le véhicule étudié et mesurera le torseur aérodynamique au moyen d'une balance spécifique.

Cela ne veut pas dire que le mécanicien du vol s'intéresse uniquement au torseur aérodynamique. Notre intérêt, en tant que mécanicien du vol, est concentré sur le comportement global du véhicule quand ce comportement peut être schématisé et globalisé bien que résultant d'interactions multiples. La figure 1 illustre ces interactions spécifiques de la Mécanique du Vol. Le problème de la précision sur la connaissance aérodynamique n'est qu'un sous-ensemble du problème général concernant la Mécanique du Vol.

Nous excluons de notre intérêt tous les essais d'éléments partiels tels que les essais d'entrée d'air ou de tuyère. Bien que de tels essais soient souvent effectués dans les souffleries nous avons estimé qu'ils ne seraient pas considérés comme essentiellement des essais pour la Mécanique du Vol.

b) Pour des raisons pratiques et de longueur de l'exposé, nous n'avons pas étudié les problèmes de tous les types de véhicules aériens qui font appel aux essais en soufflerie. Nous nous sommes limités aux avions de transport et avions de combat.

c) Enfin, nous nous sommes intéressés aux besoins des utilisateurs principaux des souffleries, qui sont les industriels aéronautiques. Néanmoins, les besoins pour les essais de recherche ont été également analysés dans la mesure où cette recherche est axée vers la Mécanique du Vol. Dans ce contexte notre souci a été de présenter une approche synthétique qui explicite les besoins et surtout les raisons des besoins des utilisateurs des souffleries. Notre exposé comprend trois parties :

1. Considérations sur la sensibilité des paramètres de la Mécanique du Vol
2. Problèmes particuliers de la Mécanique du Vol aux grands angles
3. Besoins généraux pour la Mécanique du Vol (actuels et perspectives)

1 - CONSIDERATIONS SUR LA SENSIBILITE DES PARAMETRES DE LA MECANIQUE DU VOL

L'objet de la Mécanique du Vol étant le comportement en vol de l'avion, il est évident que la précision dont a besoin le mécanicien du vol dépend de la manière dont est modifié le comportement de l'avion par suite d'une méconnaissance des caractéristiques aérodynamiques de l'avion. Dans le présent chapitre on se propose de quantifier la modification du comportement de l'avion résultant d'une erreur sur le modèle mathématique de l'avion, qui peut provenir par exemple d'essais en soufflerie.

Il nous semble utile au préalable de présenter les notations et les concepts dont nous allons parler. Ceci est fait sur les figures 2 à 5.

L'objet d'étude du mécanicien du vol, le comportement de l'avion, est décrit par le vecteur d'état X dont les composantes sont : $u, v, w, p, q, r, O, \Phi$.

Après linéarisation, l'équation du vecteur d'état X s'écrit :

$$(1) \quad \dot{X} = AX + BE(t)$$

où $E(t)$ est l'action sur les gouvernes, A et B sont des matrices fonction des coefficients C_i (C_{x_1}, C_{x_2}, \dots).

Si l'on se donne $E(t)$ l'action sur les gouvernes et des conditions initiales on peut intégrer l'équation et obtenir le vecteur d'état $X(t)$, c'est-à-dire ses composantes $x_i(t)$ (u, v, w, \dots).

Le problème que nous nous posons est le suivant : comment quantifier la distance entre le vecteur $X(t)$ calculé avec un jeu de coefficients C_1, \dots et le vecteur $X'(t)$ calculé avec les mêmes coefficients, sauf l'un d'entre eux, C_i , qui serait devenu $C_i + \Delta C_i$.

On calculera cette distance entre $X(t)$ (dont les composantes sont $x_i(t)$) et $X'(t)$ (de composantes $x_i(t) + \Delta x_i(t)$) par

$$\epsilon_i = \frac{1}{16} \sum_{j=1}^6 \frac{\int_0^T |\Delta x_{ij}(t)| dt}{\int_0^T |x_{ij}(t)| dt} + \frac{1}{16} \sum_{j=1}^6 \frac{\int_0^T |\Delta \dot{x}_{ij}(t)| dt}{\int_0^T |\dot{x}_{ij}(t)| dt}$$

T étant la durée du vol considéré.

A chaque coefficient C_i on peut faire correspondre ainsi une sensibilité S_i définie comme :

$$S_i = \frac{\epsilon_i}{\left| \frac{\Delta C_i}{C_i} \right|}$$

La signification de S_i est la suivante : un coefficient C_i dont la sensibilité S_i est grande doit être connu avec une grande précision car une faible erreur sur C_i va entraîner une grande erreur (S_i fois plus grande) sur le vecteur d'état $X(t)$ et sur le vecteur dérivé $\dot{X}(t)$. Inversement un coefficient dont la sensibilité S_i est très petite n'a pas besoin d'être connu avec une grande précision car l'erreur sur le vecteur d'état $X(t)$ sera très faible.

Pour calculer les S_i il faut se donner un modèle d'avion, c'est-à-dire les matrices A et B , se choisir une action sur les gouvernes $E(t)$ et des conditions de vol (conditions initiales, configuration de l'avion). Il faut ensuite intégrer l'équation (1) avec C_i puis avec $C_i + \Delta C_i$, et calculer S_i .

Il s'ensuit donc que la sensibilité S_i , c'est-à-dire la précision avec laquelle doit être connu un coefficient C_i , dépend en principe :

- du type d'avion,
- des conditions de vol (croisière, décollage, etc...),
- des actions ou des sollicitations sur les gouvernes.

Les calculs ([15]) ont été effectués pour deux types d'avion :

- un avion de transport,
- un avion d'armes à aile delta.

Pour chaque type d'avion plusieurs types de sollicitations de gouvernes ont été utilisés. Pour chaque coefficient S_i nous avons retenu la valeur de S_i qui est maximale parmi toutes les sollicitations. Les coefficients C_i ont été classés en trois groupes :

1er groupe : Les coefficients dont les sensibilités sont inférieures à 0,1. On peut admettre que ces coefficients peuvent être négligés.

2ème groupe : Les coefficients dont les sensibilités sont comprises entre 0,1 et 0,4. Ces coefficients ne peuvent être négligés mais on peut se satisfaire pour eux d'une précision relativement modeste.

3ème groupe : Les coefficients dont les sensibilités sont supérieures à 0,4. Ces coefficients doivent être connus avec une grande précision.

La figure 6 donne le résultat du classement. On peut faire à ce sujet les remarques suivantes :

a) Bien que, pour de nombreux coefficients, le groupe soit le même pour l'avion de transport et l'avion d'armes, on constate des différences. Ainsi $C_{y\delta}$ (efficacité de la direction pour la force latérale) peut être négligé pour l'avion de transport mais beaucoup moins pour l'avion d'armes. C_{δ} (efficacité des ailerons pour la force latérale), très important pour l'avion de transport, peut être négligé pour l'avion d'armes. L'influence du type d'avion est également visible sur $C_{\dot{\delta}}$, $C_{\dot{x}}$, $C_{\dot{\beta}}$.

b) Même pour des coefficients classés dans le même groupe il peut arriver que la valeur de la sensibilité diffère notablement. Ainsi le $C_{\dot{\delta}}$ classé dans le groupe 3 pour les deux types d'avion a une sensibilité de 1,23 pour l'avion d'armes et de 10,6 pour l'avion de transport.

c) La méthode de classement des coefficients, en retenant la valeur maximale de S_i , a effectué un filtrage qui a atténué fortement les influences de la trajectoire ou des sollicitations des gouvernes. Par exemple le $C_{\dot{\beta}}$ (influence du lacet sur le moment de roulis) est classé pour l'avion de transport dans le groupe 3 à cause de la sensibilité durant l'atterrissage. Mais cette sensibilité est divisée par trois pour la phase de vol de croisière.

d) On peut imaginer qu'il existe d'autres types de sollicitations non testés, qui feraient remonter l'importance de certains paramètres classés dans le groupe 1 ou le groupe 2. Il pourrait s'agir soit de sollicitations directes sur les gouvernes, soit de turbulences.

e) Le classement en trois groupes des coefficients C_i réduit beaucoup la finesse d'appréciation de la précision. Ainsi le coefficient $C_{\dot{\delta}}$ est classé dans le premier groupe (coefficient négligeable) avec une sensibilité égale à 0,07 alors que le C_{δ} est classé dans le groupe 2 (importance moyenne) avec une sensibilité très voisine (égale à 0,1).

f) Les valeurs des sensibilités qui ont conduit au tableau de classement proviennent d'un calcul complètement linéarisé (modèle d'avion et équations). Il est bien évident que cette simplification peut introduire des erreurs. De plus, comme on le verra dans la deuxième partie, la Mécanique du Vol aux grands angles ne peut certainement pas être linéarisée. Les besoins de précision pour la Mécanique du Vol aux grands angles doivent être traités à part.

g) Le paramètre choisi, ϵ , pour quantifier l'écart entre deux vecteurs d'état peut également être sujet à discussion. Le fait de prendre la somme de toutes les grandeurs d'état, y compris les dérivées, donne une certaine image de la sensibilité. Cette image pourrait être modifiée avec un autre paramètre (par exemple sans tenir compte du vecteur d'état dérivé).

La conclusion de ce qui précède peut être formulée comme suit : les coefficients du groupe 1 peuvent être connus de façon sommaire, voire négligés, ceux du groupe 2 doivent être connus avec une précision moyenne, et ceux du groupe 3 méritent d'être déterminés avec une grande précision.

Cependant, cette conclusion, qui doit déjà être atténuée à la lumière des remarques qui précèdent, risque d'être fortement mise en cause dans le cas d'un avion équipé d'un système de commandes de vol strictement électriques. En effet dans ce cas (cf [14]) le comportement en vol de l'avion dépend moins de ses caractéristiques aérodynamiques que des lois de contrôle introduites dans le système de commandes de vol. La précision avec laquelle on souhaite connaître les paramètres aérodynamiques est complètement modifiée. Quelques exemples seront fournis ultérieurement.

2 - PROBLEMES PARTICULIERS DE LA MECANIQUE DU VOL AUX GRANDS ANGLES

Phénomènes aérodynamiques associés aux grands angles

Le domaine de vol où les incidences sont élevées pose des problèmes divers dans la détermination du torseur aérodynamique à partir d'essais en soufflerie.

Le premier d'entre eux tient à la nature décollée de l'écoulement reproduit en soufflerie. Des phénomènes non linéaires, voire discontinus, apparaissent alors souvent, ils sont typiquement liés au domaine des grands angles. Nous pouvons en citer quelques uns :

- les dissymétries d'écoulements liées à l'apparition de vortex aux extrêmes pointes avant des fuselages ou des missiles,
- les éclatements tourbillonnaires sur les ailes en flèche ou ailes delta,
- les métastabilités des écoulements traduites par des effets d'hystérésis importants.

Ces caractéristiques aérodynamiques ont été étudiées depuis plusieurs années et un nombre considérable d'informations existe sur ces questions.

S'ils sont décrits, illustrés, voire expliqués dans la littérature, leurs impacts sur les paramètres de stabilité et sur les qualités de vol de l'avion n'en posent pas moins de sérieux problèmes.

Le problème pratique de leur prise en compte au travers du modèle aérodynamique de l'avion (ou du missile) est déjà délicat en soi, mais celui-ci est encore secondaire devant le problème de fond de la stabilité de ces écoulements tourbillonnaires et de leur sensibilité en regard de certains paramètres. L'influence du nombre de Reynolds sur les efforts latéraux d'une ogive ou pointe avant peut être prédominante et modifier à la fois l'incidence d'apparition de ces efforts latéraux et leurs intensités (figure 7). De même, l'état de surface de la maquette peut avoir un effet non négligeable sur l'effort latéral trouvé. Des mesures effectuées par Champigny sur une configuration ogive-cylindre ont montré que cet effort latéral dépendait étroitement du positionnement en roulis de la maquette même si celle-ci était symétrique de révolution et si son état de surface était réalisé avec une finition de l'ordre du micron (figure 8). Malgré une telle précision, l'hypothèse que l'effet de l'angle du roulis sur la dissymétrie d'écoulement soit dû à une micro-déformation géométrique semble confirmée. L'état de surface intervient également au niveau de la stabilité de l'écoulement. Champigny, ainsi que d'autres auteurs, ont montré qu'un état de surface rugueux pouvait conduire à des phénomènes aérodynamiques instables (figure 8). La répétabilité des essais est en effet bien moins bonne lorsque, en certains endroits bien localisés, la surface est rugueuse. On peut donc se poser la question de l'utilisation de ces données expérimentales pour le comportement de l'avion. Vu la complexité et la sensibilité de ces phénomènes, la transcription des résultats de la soufflerie au vol grandeur apparaît fort délicate. Comment utiliser correctement pour l'avion ces données provenant de la soufflerie ? Pourtant, celles-ci ne peuvent être négligées. Les efforts latéraux et couples induits par les phénomènes sont d'ailleurs souvent bien plus importants que ceux obtenus à l'aide des gouvernes, et il est clair que leur influence sur la stabilité de l'avion sera considérable. A ce titre on peut d'ailleurs signaler que de telles dissymétries aérodynamiques peuvent être la cause de vrilles parfois hyperstables. Il a été montré à l'IMPL, à partir d'essais sur maquette en soufflerie verticale, que l'existence d'un écoulement de pointe avant de nature dissymétrique conduisait à favoriser une vrille lente et privilégiait fortement un sens de rotation particulier [10]. Une étude spécifique effectuée sur une maquette d'avion d'armes typique a permis de reconnaître en vrille libre (soufflerie verticale) l'effet de différentes géométries de pointes avant. Celles-ci ont pu être classées en fonction de leur effet sur les vrilles et sur la récupération (figure 9). Le problème de la précision des mesures, et donc du modèle aérodynamique utilisé, apparaîtrait ici dérisoire en regard du problème de la qualité de la mesure et de la bonne représentativité du modèle aérodynamique. A ce titre, on peut signaler qu'à haute incidence la contribution de l'instationnaire sur la portance peut être de l'ordre de 50 % de sa portance maximale, voire beaucoup plus [12].

Phénomènes dynamiques en soufflerie

Jusqu'à présent nous avons évoqué les phénomènes aérodynamiques complexes associés aux grandes incidences, mais qui se produisaient sur un corps fixe en soufflerie, c'est-à-dire effectuant un simple mouvement de translation par rapport au vent infini amont. Or, la réalité à haute incidence est souvent très différente dans la mesure où dans la zone post-décrochée, les qualités en stabilité de l'avion se trouvent souvent dégradées. Ainsi les passages à haute incidence s'accompagnent-ils très souvent de mouvements dynamiques de l'avion. Ces phénomènes mécaniques peuvent présenter un caractère permanent ou oscillatoire comme par exemple les différents types de vrilles (plates ou piquées, calmes ou agitées), les autotonneaux, le wing rock, ou un caractère purement transitoire et instationnaire comme les pertes de contrôle, le décrochage dynamique, les mises en vrille ou les sorties de vrille.

Dans tous ces cas, les effets dynamiques deviennent importants et ne peuvent être négligés. Lors d'essais en soufflerie, les parois et structures du montage existant perturbent le champ aérodynamique de façon particulièrement sensible lorsque l'écoulement est décollé et instable. Ces effets peuvent être non négligeables en regard de ce qui se produirait sur un avion placé en atmosphère infinie. En dynamique ces effets sont encore souvent plus marqués. La complexité des écoulements aérodynamiques haute incidence se trouve encore accrue par le mouvement dynamique de l'avion et conduit les mécaniciens du vol et aérodynamiciens à concevoir des installations spécifiques où certains de ces effets peuvent être mesurés. Il s'agit en particulier des balances rotatives (figure 10) simulant des mouvements de rotation continue analogues à la vrille stationnaire ou au tonneau pur et les montages en oscillation (figure 11) permettant d'évaluer certaines caractéristiques instationnaires de l'écoulement sur le corps.

Cependant, ces différents montages posent des problèmes supplémentaires dans l'analyse et l'exploitation des mesures. Les problèmes évoqués précédemment en matière de conditions de similitude pour les écoulements décollés, se trouvent renforcés par ceux liés à la représentation des conditions limites lors de mouvements dynamiques. Les effets de parois se trouvent accentués par le mouvement du sillage de la maquette dans la soufflerie lors de mouvements tels que les oscillations ou rotations des maquettes. Les perturbations générées par les écoulements décollés se déplacent transversalement à l'axe de la soufflerie, atteignent les parois, se réfléchissent sur celles-ci et reviennent perturber le champ de la maquette après un certain délai Δt . Une interaction instationnaire maquette parois existe alors et celle-ci est caractérisée par un temps de retard Δt associé.

En plus des effets dit de parois proprement dits, d'autres induits par toutes les parties fixes du montage (supports, carénages de moteurs...) interviennent également. Ces surfaces ne sont pas entraînées en mouvement avec la maquette contrairement au sillage dynamique qui interagit périodiquement à chacun de ses passages et crée des causes supplémentaires d'erreurs d'estimation et d'instabilités de l'écoulement.

Les vortex générés par un avant-corps peuvent interagir avec le mât ou le dard supportant la maquette, en particulier aux très grands angles d'incidence lorsque ces vortex deviennent dissymétriques. Ainsi des écarts ont pu être relevés, même en statique (la maquette étant fixe dans la soufflerie), entre les mesures effectuées dans les mêmes conditions mais pour deux types différents de liaison maquette-montage. Malcolm et Schiff [3] ont pu comparer des mesures effectuées à grande incidence en montage arrière (par dard) avec celles réalisées en montage par l'extrados (mât sur le dessus du fuselage) pour deux angles de calage de la maquette. Des écarts notoires ont pu être relevés particulièrement sur le moment de lacet (figure 12). On comprend assez bien que l'interférence sur le bras support d'une paire de vortex dissymétriques sera importante pour la configuration montage par le dessus où le mât se trouve à proximité de l'écoulement tourbillonnaire sur l'extrados.

Les éclatements tourbillonnaires d'une aile en flèche peuvent être également fortement influencés par le type de support de la maquette. Des différences importantes peuvent alors être notées sur l'évolution des coefficients latéraux en fonction du dérapage (figure 13).

On comprend également que tous ces effets précités préoccupent beaucoup les mécaniciens du vol car ils ne sont pas négligeables qualitativement et quantitativement. Leur influence sur les calculs d'équilibre peut être de toute première grandeur et conduire à des fausses ou mauvaises conclusions quant au vol de l'avion. Pour un missile il a également été démontré qu'un montage par dard ou mât pouvait créer une interférence avec le sillage tourbillonnaire aux grands angles d'incidence et perturber très sensiblement la force normale mesurée en soufflerie.

De plus, le couplage entre le mouvement de l'aéronef et la structure de l'écoulement tourbillonnaire dissymétrique peut être très fort, bien plus fort encore qu'en statique. Le sillage de ces vortex peut également interagir à l'aval sur les parties arrière de l'avion (empennages, dérive) et induire des interférences sur ces surfaces fondamentales pour le contrôle et la stabilité de l'avion.

Préoccupations en terme de Mécanique du Vol haute incidence

Avant toutes choses il convient de séparer les préoccupations en deux classes bien différentes mais qui n'en sont pas moins importantes l'une et l'autre. Les préoccupations haute incidence de l'aviation de transport et de l'aviation générale sont à distinguer de celles liées aux avions de combat. Au cours de la vie d'un avion de transport les passages à haute incidence ne résultent que de circonstances accidentelles et très rares. La préoccupation principale est celle de la sécurité du vol et de l'avion. Ainsi, l'attention du mécanicien du vol sera-t-elle tournée vers les possibilités de retour à basse incidence lors de ces cas exceptionnels tels que les vrilles. Les principaux sujets d'intérêt seront donc la bonne connaissance des limites du domaine de vol piloté et contrôlé ainsi que la bonne connaissance des stabilités des vrilles et de l'efficacité des gouvernes pour obtenir le retour aux faibles incidences. Aussi des essais en soufflerie verticale sont-ils effectués sur maquette pour étudier les vrilles et les consignes à appliquer en cas de mise en vrille accidentelle. L'attention est alors tournée sur la validité et la bonne représentativité de ce type d'essais.

Or sur des configurations particulières d'avion légers, des cas de mauvaises corrélations vol-soufflerie ont pu être constatés en ce qui concerne le problème de la vrille. L'effet du nombre de Reynolds sur certaines géométries de profil à haute incidence apparaît une préoccupation importante des mécaniciens du vol car des discordances importantes sur les vrilles et les récupérations obtenues en vol et en soufflerie verticale ont été rapportées. Ce problème reste l'objet d'études aux U.S.A. et en France.

Pour l'avion de combat le problème est très différent dans la mesure où les grandes incidences font partie de son domaine de vol conventionnel. L'accent est alors mis plutôt sur les qualités de vol à haute incidence, sur la manoeuvrabilité en combat, sur le pilotage au voisinage et au-delà du décrochage.

A cet effet une correcte modélisation mathématique des efforts aérodynamiques dans tout un domaine de vol impliquant à la fois les grands angles (incidence et dérapage) et les mouvements dynamiques est nécessaire. Vu les problèmes évoqués précédemment en matière de caractérisation et mesure aérodynamiques en soufflerie, il est clair que cette tâche est rendue très ardue. Quand bien même les conditions de similitudes et conditions limites seraient-elles parfaitement respectées et maîtrisées, l'élaboration des modèles de comportement n'en demeurerait pas moins délicate. Même s'ils sont parfaitement reproduits en soufflerie, les écoulements décollés sont, pour les mécaniciens du vol, le siège de :

- fortes non linéarités vis-à-vis de l'incidence, du dérapage, des vitesses angulaires ou des braquages de gouvernes (figure 14),
- couplages entre les variables longitudinales et transversales (figure 15),
- forts effets instationnaires (tel le décrochage dynamique) qui se traduisent par une dépendance temporelle des coefficients liée à l'histoire du mouvement de l'avion (figure 16),
- effets d'hystérésis typiques du comportement non linéaire où l'on peut trouver plusieurs états d'équilibre de l'écoulement pour une même configuration de l'avion (figure 17),
- non linéarités en termes de dérivées dynamiques (figure 18).

Ces principales caractéristiques doivent être obtenues correctement en soufflerie. Or, hormis les problèmes liés au respect de conditions d'essais similaires à celles de l'avion, on peut constater qu'une bonne connaissance du domaine de vol exigera un grand nombre d'essais en soufflerie. En effet les moyens d'extrapolations des mesures à haute incidence sont très limités (méthodes de calcul ou lois de comportement) et les évolutions des caractéristiques aérodynamiques sont de plus à la fois fort non linéaires et dépendantes d'un grand nombre de variables.

La connaissance des efforts aérodynamiques nécessitera donc une profonde exploration du domaine de vol. Celle-ci devra être judicieusement choisie et accompagnée d'une analyse détaillée des mesures et des caractéristiques aérodynamiques.

Une illustration du problème spécifique de la précision à haute incidence est évoquée à présent à partir de simulations numériques de la vrille sur un avion de combat classique. A partir d'essais en soufflerie un modèle aérodynamique est construit. Celui-ci fournit les valeurs des coefficients aérodynamiques (différents de ceux décrits dans la première partie car le modèle ne peut être linéarisé) à partir des valeurs des variables aérodynamiques précitées : incidence, dérapage, vitesses angulaires et braquages de gouvernes. Ce modèle peut donc être introduit dans les équations du mouvement. Ces équations différentielles peuvent être intégrées, elles fournissent alors en fonction du temps les différentes caractéristiques du mouvement de l'avion, à savoir : les composantes de sa vitesse, les composantes des vitesses angulaires, les attitudes de l'avion par rapport au sol ou à la trajectoire. La simulation ainsi élaborée permet d'effectuer des prévisions sur le comportement avion en domaine décroché et permet d'en reconnaître les caractéristiques essentielles vis-à-vis des phénomènes "mécanique du vol" évoqués précédemment, en particulier les vrilles.

Un premier regard peut déjà être tourné vers l'effet des gouvernes en vrille. La vrille est un mouvement de l'avion caractérisé principalement par une incidence élevée, par une composante du taux de rotation non négligeable sur le vecteur vitesse, accompagnés d'une descente verticale de l'avion. Etant donné que ce mouvement est généralement très stable, on comprend qu'il est dangereux pour la sécurité du vol. Cette hyperstabilité peut à la limite conduire à l'impossibilité du retour à faible incidence à l'aide de commandes de vol.

Cependant, sur les avions certifiés il est possible d'en sortir à l'aide des gouvernes. Celles-ci, et en particulier le gauchissement, sont généralement efficaces vis-à-vis de la vrille et permettent d'obtenir la récupération.

Or, cet effet des gouvernes n'apparaît pas toujours de façon très nette à la simple vue des courbes provenant de la soufflerie. Les gouvernes ont une efficacité mesurée qui est plus réduite aux grandes incidences, dans le domaine de la vrille (figure 19). Pourtant cette efficacité est bien retrouvée en simulation en utilisant ces données de soufflerie. Cela démontre donc que le problème de la précision des mesures se pose de façon sensible puisqu'une caractéristique importante de la qualité de vol de l'avion à haute incidence (sortie de vrille) est trouvée à partir d'un effet mesuré en soufflerie qui est relativement faible.

On peut signaler également qu'un écart d'un point introduit dans le modèle sur le coefficient du moment de roulis ($\Delta C_l = .01$) peut modifier très sensiblement la tenue à la vrille étudiée en simulation. Ceci illustre l'impact que peut avoir une relativement faible imprécision sur les états d'équilibre retrouvés.

De plus, la précision relative de ces mesures à haute incidence est nettement dégradée puisque l'on constate à la fois une diminution du signal mesuré et une augmentation des bruits de mesures. Ceux-ci sont essentiellement d'origine aérodynamique ou structurale.

Or l'effet de la gouverne est déterminant pour prédire la consigne de sortie de vrille, d'où l'importance accordée par les mécaniciens du vol à la validité, à la qualité et à la précision des mesures aux grands angles en soufflerie.

3 - BESOINS GENERAUX POUR LA MECANIQUE DU VOL

Compte tenu des commentaires présentés dans l'introduction sur notre approche, nous avons estimé que la méthode la plus prometteuse pour obtenir les points de vue des principaux utilisateurs des essais en soufflerie serait de mener une enquête auprès de ces utilisateurs. A cet effet, un questionnaire a été bâti et distribué au sein des pays de l'AGARD par l'intermédiaire des membres du FMP. Vous trouverez ce questionnaire en annexe.

Bien que le nombre des réponses reçues soit relativement faible, la qualité et l'intérêt des réponses justifient a posteriori la méthode utilisée. Nous nous proposons de présenter une analyse des résultats de l'enquête. Il n'est pas dans notre intention d'examiner toutes les questions. Nous nous limiterons à quelques-unes, considérées comme les plus importantes et les plus significatives.

Une des caractéristiques des réponses obtenues est qu'elles sont très variées et même assez souvent contradictoires. Néanmoins, une unanimité tout à fait remarquable a été constatée sur l'utilité des essais en soufflerie. Pour tous, la soufflerie représente aujourd'hui un outil indispensable qui rend des services irremplaçables tant dans le domaine de l'étude des performances des avions que dans celui de l'étude des qualités de vol. Il est clair que les qualités des avions et les progrès que l'on peut encore y escompter reposent pour une grande part sur les essais en souffleries.

Les deux approches complémentaires des essais en soufflerie sont les essais en vol d'une part et les calculs théoriques d'autre part. L'un des aspects examinés était de comparer l'importance actuelle des essais en soufflerie par rapport au passé (20 à 30 ans). Comme il n'y a pas de critère objectif pour juger de cette importance les réponses données furent subjectives et de ce fait assez divergentes, voire contradictoires. Il y a ceux qui affirment que depuis 20-30 ans les calculs théoriques ont beaucoup progressé et donc que l'importance des essais en soufflerie a décroché. A l'opposé, il y a ceux qui affirment que les besoins en qualité des résultats, en précision, en réduction des délais, en affinement des performances, ont beaucoup augmenté sous la pression de la concurrence commerciale et industrielle, et que par conséquent l'importance des essais en soufflerie a crû. On ne peut donc que conclure que la question ne peut avoir aujourd'hui de réponse simple et définitive. Certains pourraient penser que sa nature est analogue à celle de la question de savoir qui existait d'abord de la poule et de l'oeuf. Cela dit, les raisons fondamentales pour utiliser les souffleries sont d'abord un besoin absolu technique car beaucoup de données aérodynamiques indispensables ne peuvent être aujourd'hui obtenues par calcul. Par ailleurs, pour ce qui est des essais en vol, ils sont considérés souvent comme trop chers pour la recherche et sont trop tardifs pour l'industriel. Au moment des essais en vol, la conception de l'avion, compte tenu des engagements sur les délais, doit être considérée comme figée. Seules des modifications mineures peuvent être raisonnablement envisagées. Dans certains cas les essais en soufflerie sont utilisés pour tester des configurations ou des conditions de vol pour lesquelles la sécurité du vol est jugée insuffisante. On peut citer à cet égard la certification d'un avion de transport ou les essais de vrille d'un avion d'armes. Une autre utilisation citée des essais en soufflerie est la création d'un modèle mathématique pour la conception du système de commandes de vol.

D'une façon très générale les essais en soufflerie sont essentiels durant la phase de conception et de développement d'un nouveau type d'avion, avec les objectifs suivants :

- optimiser la configuration de l'avion.
- satisfaire au cahier des charges.
- répondre aux exigences de la certification.
- recueillir les données aérodynamiques nécessaires à l'évaluation des performances et qualités de vol de l'avion.
- déterminer les caractéristiques principales de nombreux problèmes complexes : flottement, buffeting, décrochage, vrille...

Malgré l'importance reconnue aux souffleries et malgré la multiplicité des objectifs assignés aux essais qui y sont menés, il convient de noter qu'une des difficultés est liée à la nécessité d'appliquer des corrections aux résultats bruts obtenus. La qualité et la précision des résultats doivent énormément aux nombreuses précautions et corrections appliquées aux mesures. Les principaux phénomènes qui nécessitent des corrections sont :

- nombre de Reynolds : en général les corrections sont négligées si $Re > 5 \cdot 10^6$,
- influence des supports de la maquette,
- corrections de parois,
- corrections des imperfections de surface.

Les méthodes utilisées sont très variables, allant de simples ajustements inspirés par des manuels classiques aux calculs complexes, en passant par des corrections empiriques appliquées parce qu'elles donnent des résultats satisfaisants. En fait, chaque utilisateur possède son propre arsenal de méthodes de corrections, affinées au fil des années et validées soit pour certaines souffleries soit pour certains types d'avions. En général, les utilisateurs sont satisfaits des résultats corrigés par leurs méthodes, mais reconnaissent que leur mise en oeuvre nécessite beaucoup d'efforts et des précautions importantes. Des imperfections sont signalées pour la traînée en croisière et l'étude de l'effet de sol.

Un autre type de correction concerne non pas la soufflerie elle-même mais la maquette essayée. Il s'agit de corrections de déformations aéroélastiques qui affectent l'avion souple, mais non pas la maquette rigide. Certains négligent purement et simplement les effets aéroélastiques, d'autres en tiennent compte par calcul, d'autres enfin utilisent des méthodes semi-empiriques (plusieurs essais et interpolation théorique).

Parmi les nombreux problèmes techniques pour lesquels on fait appel aux essais en soufflerie, et reproduits sur la figure 20, les plus importants sont :

Performances

- Détermination de la polaire avec le système propulsif (en particulier l'hélice).
- Mesure de la traînée en croisière.
- Manoeuvrabilité d'un avion d'armes. Les mesures effectuées en soufflerie peuvent conduire à déterminer diverses caractéristiques telles que : taux de virage, vitesses angulaires, facteur de charge en fonction du domaine de vol.

Qualités de vol

- Détermination des coefficients aérodynamiques et de stabilité.
- Détermination des efficacités de gouvernes et dimensionnement des gouvernes.
- Détermination des forces et des moments de charnière sur les gouvernes.
- Détermination de la VMC.
- Comportement de l'avion au voisinage du décrochage et détection de l'autocabrage (pitch-up).

Il est important de rappeler que, pour un avion équipé d'un système de commandes de vol électriques, le besoin de précision sur certains coefficients aérodynamiques est fortement réduit. A titre d'exemple [14] on peut signaler le cas du Mirage 2000 sur lequel

- une erreur de 50 % sur le $C_{l\dot{\alpha}}$ (amortissement aérodynamique de roulis) ne change que de 10 % l'amortissement global de l'ensemble avion + commandes de vol sur ce même axe,

- une erreur de 100 % sur le coefficient croisé $C_{l\dot{\beta}}$ (lacet induit par la vitesse de roulis) modifie très peu le comportement de l'avion en manoeuvre de gauchissement (modification de quelques dixièmes de degrés du dérapage maximum atteint pendant la manoeuvre).

AD-A202 496

AERODYNAMIC DATA ACCURACY AND QUALITY: REQUIREMENTS AND
CAPABILITIES IN WIND TUNNEL TESTING (U) ADVISORY GROUP
FOR AEROSPACE RESEARCH AND DEVELOPMENT NEUILLY

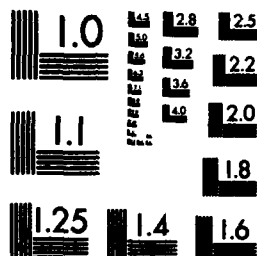
6/6

UNCLASSIFIED

JUL 88 AGARD-CP-429

F/G 1/1

NL



MICROCOPY RESOLUTION TEST CHART
NATIONAL BUREAU OF STANDARDS-1963-A

Cela ne veut pas dire qu'il n'est pas nécessaire d'effectuer une caractérisation aérodynamique complète d'un avion équipé de commandes de vol électriques et pourvu d'un contrôle actif. La définition du système de commandes de vol nécessite la connaissance de toutes les efficacités des gouvernes (directes et croisées). Par ailleurs, le bon fonctionnement d'un système de commandes suppose que ce système ne se trouve pas dans des conditions de saturation. Or, celles-ci étant liées au comportement aérodynamique de l'avion, on a également besoin de connaître tous les coefficients aérodynamiques généraux de l'avion d'une façon suffisamment précise.

D'une façon plus générale, la précision des mesures obtenues en soufflerie est considérée dans l'ensemble comme suffisante, bien que pour certains problèmes des exigences très sévères soient présentées. A titre d'exemple extrême on peut citer la mesure de la traînée d'un avion de transport en croisière, pour laquelle une précision de 0,5 "count" (10^{-4}) est demandée bien qu'on obtienne déjà 1 "count". Cette demande d'une précision extrêmement forte s'explique par la concurrence entre industriels qui cherchent l'optimum pour leur produit.

Pour l'avion d'armes une valeur typique de la précision pour la traînée en croisière est 2 "counts". Pour la traînée à basse vitesse et en manœuvre une précision de "5 counts" semble donner satisfaction.

Pour d'autres problèmes les exigences de précision sont moins grandes, et de plus très variables, les variations pouvant avoir plusieurs causes :

- nature du problème technique : on trouvera à cet égard des explications détaillées dans la 1ère partie de notre exposé,
- type d'avion : avion de transport ou avion d'armes,
- utilisateur : les exigences pour la recherche sont souvent différentes de celles pour l'industrie.

Enfin, contrairement à ce qu'on pourrait penser, il est souvent avancé que la précision obtenue en soufflerie est supérieure à celle obtenue lors d'essais en vol. D'une façon plus concrète on a souvent reproché aux résultats d'essais en vol d'être difficilement exploitables. A titre d'exemple on peut citer comme causes la connaissance insuffisante des masses, des déformées aéroélastiques, des inerties, de l'avion en vol et des conditions réelles de vol (vitesse, incidence, vent, etc...).

Contrairement aux exigences de précision qui sont, comme nous l'avons vu, très dispersées parmi les utilisateurs des souffleries, il y a un excellent accord sur les cas extrêmes d'utilisation des essais en soufflerie. Cet accord porte sur les points suivants :

- résultats très bons : $C_{x...}$ et portance en général,
- résultats satisfaisants : traînée, caractéristique aérodynamique à basse vitesse,
- résultats très mauvais : phénomène de buffeting et comportement près du décrochage.

Les causes des mauvais résultats imputables à la soufflerie peuvent être attribuées aux phénomènes suivants :

- a) Nombre de Reynolds, en particulier en transsonique et aux grandes incidences.
- b) Non représentation structurale de la maquette essayée en soufflerie.
- c) Dans la mesure où par mauvais résultats on entend désaccord entre résultats provenant des essais en vol et ceux en soufflerie, il arrive souvent qu'ils peuvent être attachés à une insuffisance d'analyse des essais en vol (méconnaissance des inerties par exemple).

Les figures 21 à 28 donnent quelques exemples de comparaisons entre essais en vol et en soufflerie.

Parmi les améliorations qui sont demandées aux souffleries, les plus importantes portent sur les points suivants :

a) Coût des essais

Le coût des essais doit rester une préoccupation permanente des souffleurs. Les différentes exigences et améliorations techniques doivent être jugées en regard des conséquences sur le coût des essais en soufflerie. A cet égard, on doit signaler que le coût des essais en soufflerie est inférieur aux coûts des calculs lorsqu'il s'agit d'identifier un avion donné, c'est-à-dire effectuer des essais avec un grand nombre de conditions d'essais. En revanche une optimisation d'un avion nécessitant la fabrication de plusieurs maquettes revient plus cher en soufflerie que par le calcul (quand celui-ci est possible).

b) Dimensions

Des dimensions plus grandes sont demandées pour pouvoir essayer des maquettes motorisées assez grandes, de façon qu'elles soient bien représentatives des conditions de décollement et d'atterrissage.

c) Techniques de mesures améliorées

Dans cette catégorie on peut citer deux exemples :

- techniques des mesures en dynamique,
- meilleure flexibilité des mesures par exemple mesures des pressions statiques par des moyens rapidement modifiables et non perturbateurs (éviter le percement des trous).

Comme on peut le constater dans le questionnaire nous avons essayé d'avoir l'avis des utilisateurs sur l'avenir des souffleries. De façon plus précise, la question posée était : "Pensez-vous que les progrès qui seront accomplis dans les méthodes et la puissance des calculs numériques modifieront l'utilité des souffleries d'ici 20-30 ans ?"

Cette question appelle encore une réponse de type subjectif puisqu'il n'est pas raisonnable d'avoir une prévision exacte de la façon dont évolueront les performances des calculs numériques. Néanmoins, on constate une très grande convergence parmi les utilisateurs de la soufflerie. L'opinion générale, bien que des exceptions existent, est que le rôle des souffleries dans l'avenir pourra être différent mais que leur importance ne sera pas diminuée. Les raisons avancées sont les suivantes :

Il est certain que les méthodes de calcul numérique feront de grands progrès, mais il est peu probable que dans un avenir prévisible on arrive à calculer des écoulements 3D, avec viscosité (surtout en transsonique) et dans des configurations géométriques très complexes (et dont la complexité risque de croître dans l'avenir). La figure 29 illustre la distance qu'il y a encore à franchir avant que les calculs ne puissent répondre à tous les besoins. Par ailleurs les souffleries progresseront également, et les progrès dans les calculs nécessiteront l'utilisation des souffleries pour valider ces calculs. Tout progrès dans les méthodes de calcul sera utilisé non pas pour réduire l'utilisation des souffleries mais pour en accroître la qualité et l'efficacité, pour optimiser les programmes d'essai. Enfin, comme on l'a déjà signalé, dans le cas où il n'y a pas lieu de fabriquer plusieurs maquettes le coût des essais en soufflerie restera vraisemblablement, comme il est aujourd'hui, inférieur au coût du calcul numérique.

CONCLUSIONS

1. Dans le domaine de vol classique (faibles angles) la précision des mesures en souffleries est une exigence importante. Les besoins de précision, qui peuvent être quantifiés aisément, dépendent de nombreux paramètres :

- type d'avion
- trajectoire,
- problème technique étudié.

2. Dans le domaine de vol aux grands angles les problèmes de précision de mesure passent au second plan devant l'importance et les difficultés de la mesure et de la caractérisation aérodynamique même de l'avion.

3. Les souffleries représentent aujourd'hui un outil indispensable et apprécié pour les besoins de la Mécanique du Vol.

4. Des améliorations sont néanmoins demandées et concernent, outre la précision dans certains cas :

- les coûts,
- les dimensions,
- l'influence du nombre de Reynolds,
- les phénomènes en transsonique,
- la flexibilité des mesures,
- la capacité d'effectuer des essais dynamiques.

5. De l'avis des utilisateurs l'avenir des souffleries n'est pas menacé par les progrès attendus dans les méthodes de calcul numérique. Bien au contraire, les souffleries bénéficieront de ces progrès pour améliorer la qualité et l'efficacité de leurs mesures.

L'auteur remercie Mlle Patricia COTON et M. Robert VERBRUGGE pour l'aide et les conseils qu'ils ont apportés lors de la préparation du présent exposé.

Lille, septembre 1987

REFERENCES

- [1] "Recent experience with techniques for prediction of spin characteristics of fighter aircraft"
J.R. CHAMBERS, J.S. BOWMAN - Nasa Langley
Journal of aircraft Vol 8 n°7 - July 1971
- [2] "Aerodynamic aspects of aircraft dynamics at high angle of attack".
K.J. ORLIK - RUCKEMAN - N.A.E. Ottawa Canada
AIAA 9th Atmospheric Flight Mechanics Conference
August 9 - 11 1982 - San Diego
- [3] "Recent developments in rotary balance testing of fighter aircraft configuration at Nasa Ames Research Center"
G.N. MALCOLM - L.B. SCHIFF
Agard CP386 - May 1985 Göttingen
- [4] "Reynolds Number effect on the aerodynamic characteristics of an ogive-cylinder at high angles of attack"
P. CHAMPIGNY - ONERA Chatillon France
2nd AIAA Applied Aerodynamics Conference
Seattle - 21-23 August 1984
- [5] "Stability of side forces on bodies at high angles of attack".
P. CHAMPIGNY - ONERA Chatillon France.
- [6] "Summary of sting interference effects for cone, missile and aircraft configurations as determined by dynamic and static measurements".
B.L. USETON - D.R. HABERMAN - Arnold AFS
AIAA 9th Atmospheric Flight Mechanics Conference
August 9-11 1982 - San Diego
- [7] "Unsteady flow concepts for Dynamic Stall analysis"
L.E. ERICSSON - J.P. REDING - Lockheed Missiles and space Company, Sunnyvale, California
Journal of aircraft - Vol 21 n°8 August 1984
- [8] "Reflections regarding recent rotary rig results"
L.E. ERICSSON - Lockheed Missiles and space Company
Journal of aircraft - Vol 24 n°1 January 1987
- [9] "Dynamic support interference in high-alpha testing"
L.E. ERICSSON - J.P. REDING - Lockheed Missiles and space Company.
Journal of aircraft - Vol 23 n°12 - December 1986
- [10] "Etat de l'art et perspectives nouvelles relatives à l'étude de la perte de contrôle et des vrilles".
M. VANMANSART - D. TRISTRANT - IMFL/ONERA France
N°16 Agard CP 319 - Florence 1981
- [11] "Enseignements tirés de la comparaison de vrilles sur maquettes en soufflerie et sur avions".
L. BEAURAIN - IMFL France
AAAF Lille - Novembre 1973
- [12] "The phenomenon dynamic-stall"
W.J. mac CROSKY - Nasa Ames
VKI Lecture series 1981-4 - Bruxelles March 1981
- [13] "Exploratory Investigation of vortex bursting on the high-angle of attack lateral directional stability characteristics of highly swept wings".
J.L. JOHNSON - S.B. GRAFTON - L.P. YIP
AIAA 88-0463 - March 1980
- [14] "Comportement à grande incidence d'un avion de combat : corrélation entre les prévisions et le vol".
P.L. MATHE / A.M.D-B.A. St Cloud France
Agard CP 339 n° 10 - Octobre 1982
- [15] "Modélisation en Mécanique du Vol - Identification de Paramètres"
P. COTON / IMFL Lille France
Rapport intérieur n° 84/38

MECANIQUE DU VOL

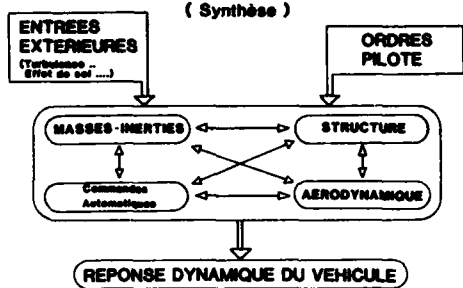
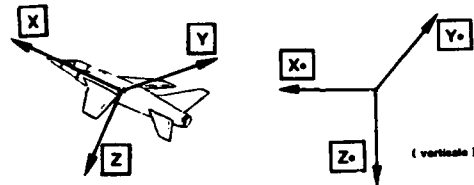


FIG. 1

POSITION DE L'AVION



AXES DE L'AVION $\langle \psi, \theta, \phi \rangle$ AXES FIXES

FIG. 2

MOUVEMENT DE L'AVION

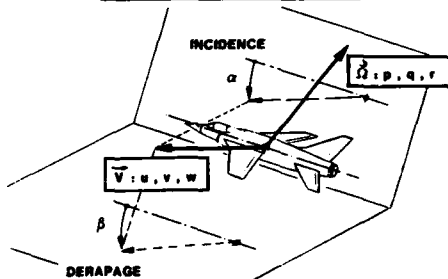
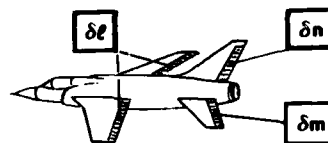


FIG. 3

GOUVERNES






Action sur les gouvernes

$$E(\underline{\delta \ell}, \underline{\delta m}, \underline{\delta n})$$

FIG. 4

SENSIBILITE DES COEFFICIENTS

-  Groupe 1. Négligeable
 Groupe 2. Moyennement sensible
 Groupe 3. Très sensible

TORSEUR AERODYNAMIQUE

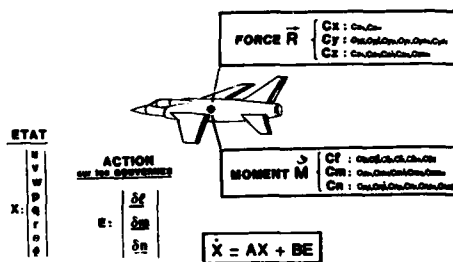


FIG. 5

		AVION DE TRANSPORT	AVION D'ARME
Coefficients Stationnaires	En		
	Co		
	Ca		
	Co		
Coefficients de Stabilité Statique	Ca		
	Ca		
	Ca		
	Ca		
Coefficients de Stabilité Dynamique	Ca		
	Ca		
	Ca		
	Ca		
Coefficients Inélastiques	Ca		
	Ca		
	Ca		
	Ca		
Effets des Gouvernes	Ca		
	Ca		
	Ca		
	Ca		

FIG. 6

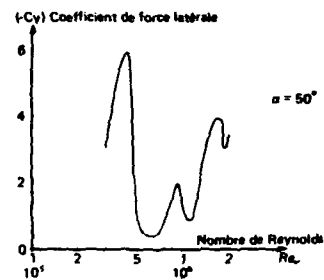
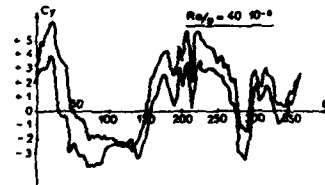


FIG. 1 : INFLUENCE DU NOMBRE DE REYNOLDS SUR LA FORCE LATÉRALE À $\alpha = 50^\circ$ D'UNE CONFIGURATION DELTA-CYLINDRE [5].



FIG. 2 :



EFFET DU POSITIONNEMENT DE θ SUR LA FORCE LATÉRALE À $\alpha = 50^\circ$ ET $Re = 0.28 \times 10^5$ ET EFFET DE L'ÉTAT DE SURFACE DE LA RACLETTE SUR LA REPÉTIVITÉ DES ESSAIS [8].

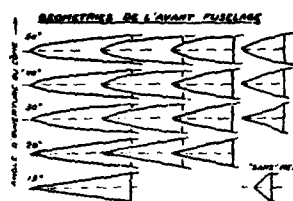
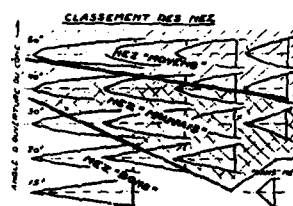


FIG. 3 :



CLASSEMENT DES MES MAGNETES PAR RAPPORT AUX ÉLÉMENTS DE VILLE LITRE [10].

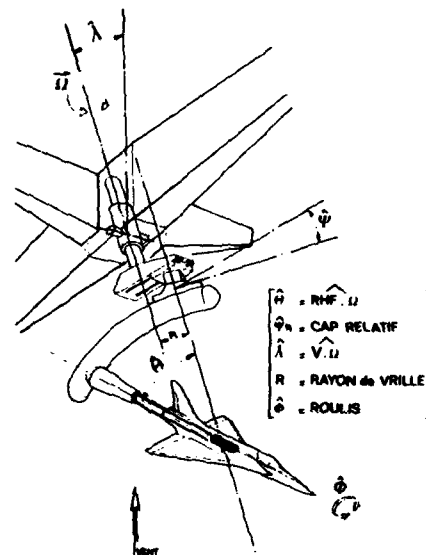


FIG. 10 : BALANCE ROTATIVE DE L'INFL.

BALANCE DYNAMIQUE MOUVEMENTS DE GRANDE AMPLITUDE

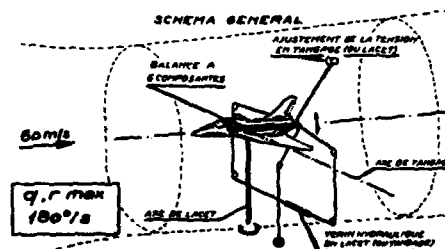
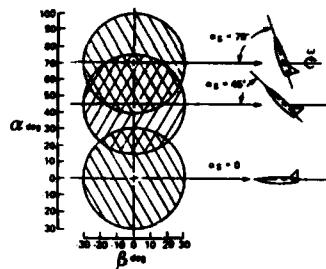


FIG. 11 : SCHEMA D'UN BALANCE DYNAMIQUE [10].



RECOURBEMENT DANS LE PLAN (β, α) OBTENU AVEC LES 3 TYPES DE MONTAGE.

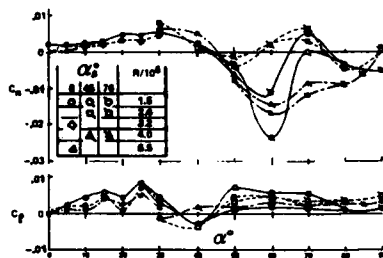


FIG. 12 :

EFFET DU TYPE DE MONTAGE (α_s) ET DU NOMBRE DE REYNOLDS SUR LES COEFFICIENTS LATÉRAUX D'UN AVION D'ARMES.

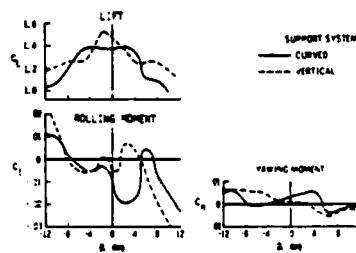
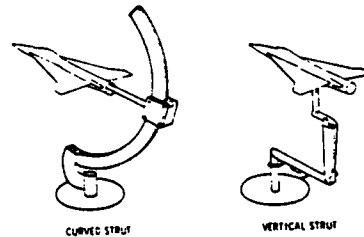


FIG. 13 :

EFFET DU SUPPORT DE LA MAQUETTE SUR LES CARACTÉRISTIQUES LATÉRALES À $\alpha = 35^\circ$ [12] [9]

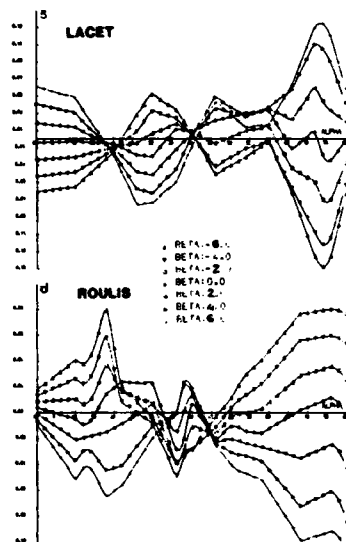


FIG. 14 :

EFFET DE L'INCIDENCE SUR LA SENSIBILITÉ AU DÉRAPAGE DES COEFFICIENTS LATÉRAUX DE LACET ET DE ROULIS (NON-LINÉARITÉ).

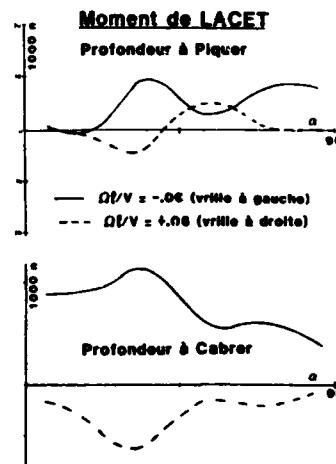


FIG. 15 : EFFET DE ROTATION CONTINUE, EN MANÈGE DE LA PORTANCE, SUR LE COEFFICIENT DE LACET, EN FONCTION DE L'INCIDENCE.

PORTANCE

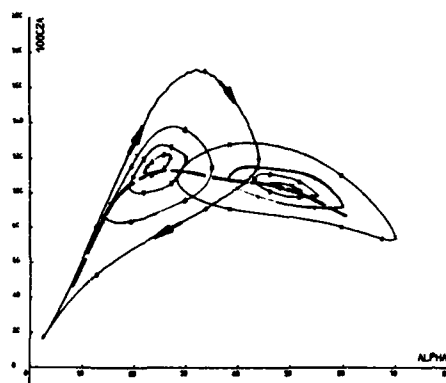


FIG. 16 : EVOLUTION DE LA PORTANCE AU COURS D'UN MOUVEMENT DE ROTATION DE L'INCIDENCE OSCILLE RAPIDEMENT. MISE EN EVIDENCE DU RECROQUEUR DYNAMIQUE.

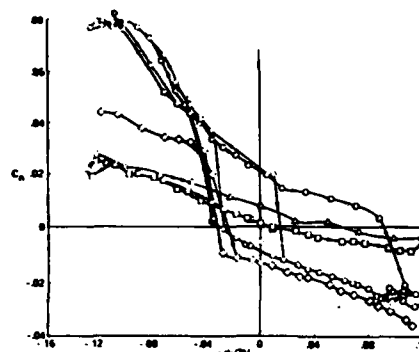


FIG. 17 : EFFET DU TAUX DE ROTATION SUR LE MOMENT DE LACET D'UN AVION D'ARMES [2]. EFFET D'HYSTERESIS.

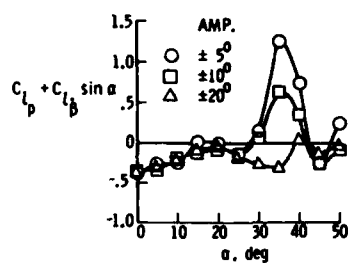


FIG. 18 : EFFET DE L'AMPLITUDE DE L'OSCILLATION SUR L'AMORTISSEMENT DE ROULIS [2].

FIG. 20

Problèmes de Mécanique du Vol
étudiés en Soufflerie

		AVION DE TRANSPORT	AVION D'ARME
P E R F O R M A N C E	Décollage monté	○	○
	Optimisation croisière	○	○
	Distance franchissable autonome	○	○
	Atterrissage	○	○
Q. de V.	Stabilité	○	○
	Manoeuvrabilité	○	○
	Extension domaine de vol	○	○
	Optimisation en turbulence	○	○

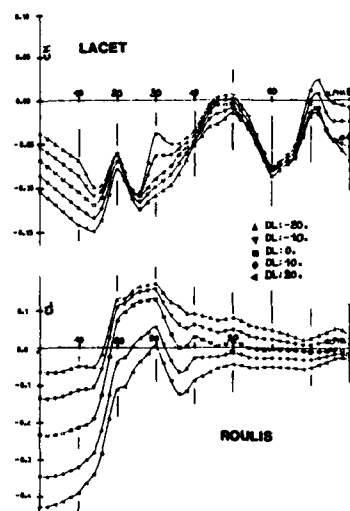


FIG. 19 : EFFET DE LA ROTATION CONTINUE DU MACHAGE DE LA GOUVERNE DE SAUTELAGE SUR LES COEFFICIENTS DE LACET ET DE ROULIS.

FIG. 21 LACET DÙ AU BRAGUAGE DIFFÉRENTIEL D'ÉLEVONS
YAWING MOMENT DUE TO DIFFERENTIAL ELEVON DEFLECTION

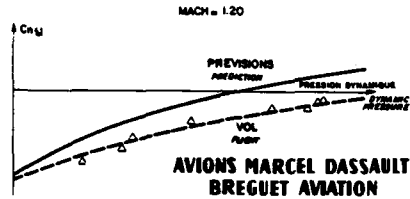


FIG. 23 ÉVOLUTION DU MOMENT DE TANGAGE EN TRANSSONIQUE
PITCHING MOMENT VS MACH IN TRANSSONIC FLIGHT REGIME

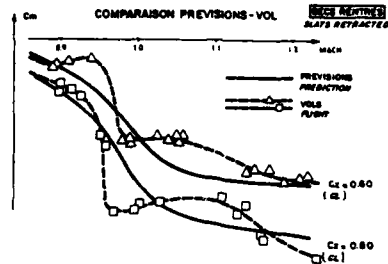


FIG. 22 STABILITE LONGITUDINALE A BASSE VITESSE
LONGITUDINAL STABILITY AT LOW SPEED

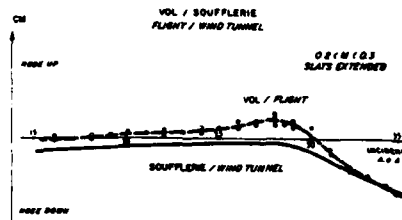


FIG. 24 MOMENTS DE ROULIS ET DE LACET A GRANDE INCIDENCE
ROLLING AND YAWING MOMENT AT HIGH ANGLE OF ATTACK

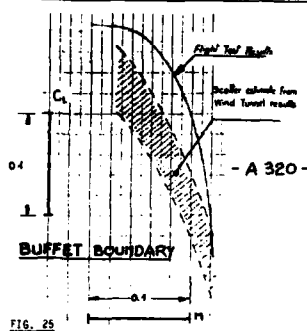
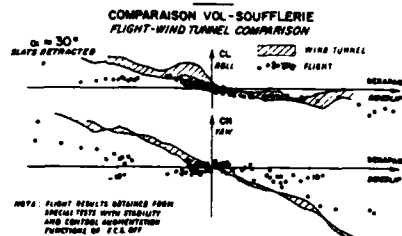


FIG. 25

FLIGHT - WIND TUNNEL comparison
FIG. 28

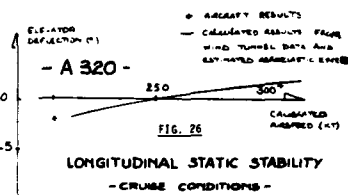
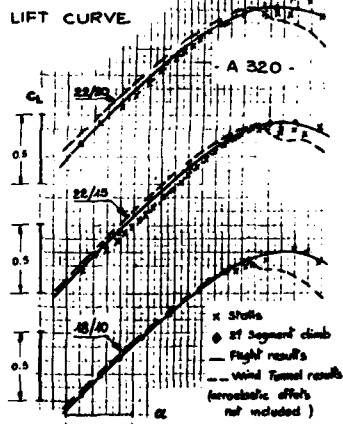


FIG. 26

LONGITUDINAL STATIC STABILITY
- CRUISE CONDITIONS -

aerospatiale

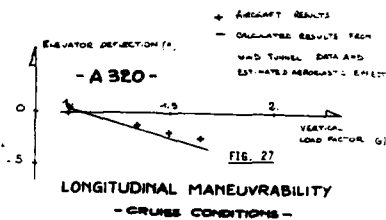


FIG. 27

LONGITUDINAL MANEUVRABILITY
- CRUISE CONDITIONS -

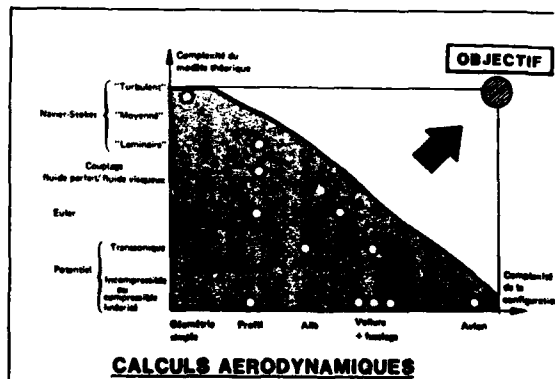


FIG. 29

A N N E X E

SURVEY ON

WIND TUNNEL REQUIREMENTS CONCERNING FLIGHT MECHANICS TEST RESULTS

GENERAL :

You are asked to add some general comments, when possible, to your answers. The issues to be addressed with your comments are presented here after. But this list is not exhaustive and may be completed according to your needs or wishes.

Please note that your comments are probably more important than the answers to the questions.

A - Reasons for using wind tunnels :

The use of wind tunnel testing during the development process of an aircraft is so large and so evident that questioning about this may appear unjustified. However the very reasons may be different from one technical problem to another. Among the various reasons one may distinguish the following :

- a) Reduce cost and time when compared to flight test,
- b) Reduce cost when compared to numerical computation (probably in a limited number of cases),
- c) Absolute technical or/and economical needs :
flight test too late and numerical computation impossible or not reliable,
- d) Reliability : to confirm the knowledge obtained by other ways,
- e) Any others.

B - Wind tunnel testing results qualities :

The basic question is : Are the wind tunnel test results in agreement with the real flight test results ? The comments may concern :

- a) the physical phenomena observed,
- b) the measurements accuracy.

In case of disagreement, please comment on suspected reasons (scales, wall corrections, ...).

C - Wind tunnel testing results requirements :

These comments should follow the previous ones when the agreement is not satisfactory. Again the requirements may concern :

- a) the physical phenomena observed,
- b) the measurements accuracy,
- c) any others.

D - The wind tunnel testing results utilization :

Some comments may be made such as :

- a) the use for aircraft identification,
- b) the use for aircraft design,
- c) any others.

QUESTIONNAIRE

- 1 - The wind tunnels testing are usefull and important rather for

	Transport aircraft	Fighter
Performance		
Handling qualities		
Both		

Please comment :

- 2 - What are the most important technical problems concerning the performance of the aircraft studied in the wind tunnel ?
- 3 - What accuracy do you obtain on the performance results ?
Please comment on the required accuracy (in particular for drag evaluation).
- 4 - What are the most important handling qualities problems studied in the wind tunnels ?

Please comment also the relative importance of aerodynamic stability coefficient and control surfaces efficiency in relation with the aircraft control system.
- 5 - Do you use wind tunnels for :
a) Study the unsteady phenomena ?
b) High angles (attack and yaw) behaviour ?
c) Spin ?
- 6 - How do you take into account the aeroelastic deformation of the aircraft studied on model in the wind tunnel ?
- 7 - What kind of corrections do you apply to the wind tunnel measurements (Reynolds number, power effects, ...) when applying to performance and flying quality evaluation ?

Could you indicate the methods used ?

Are you satisfied with the obtained data ?
- 8 - Could you comment on the methods used and the results obtained in the wind tunnels concerning the differences between the static phenomena and dynamic phenomena ?
- 9 - Could you comment on the use of wind tunnels for some particular problems such as :
a) Buffeting
b) Horizontal tail stall
c) Ground effect
d) Any others
- 10 - What are, according to your knowledge, the areas and the reasons where the agreement between the wind tunnels and the real flights tests are :
a) Very poor
b) Just acceptable
c) Very good
- 11 - What improvements are advisable or needed in the wind tunnels capabilities for the flight mechanics problems ?

12 - The importance and the usefulness of the wind tunnels, when compared to the 20-30 years ago situation, is : (accuracy, nature, ...)

a) Rather increased

b) Rather reduced

c) Identical

Please comment :

13 - Do you think that the improvements expected in the power and the reliability of numerical methods will reduce the usefulness of the wind tunnels or change the test purpose in the forthcoming 20 years ?

Please comment your answer.

WIND TUNNEL REQUIREMENTS FOR COMPUTATIONAL FLUID DYNAMICS CODE VERIFICATION

Joseph G. Marvin

NASA Ames Research Center
Moffett Field, California

SUMMARY

The role of experiment in the development of Computational Fluid Dynamics (CFD) for aerodynamic flow field prediction is discussed. Requirements for code verification from two sources that pace the development of CFD are described for: (1) development of adequate flow modeling, and (2) establishment of confidence in the use of CFD to predict complex flows. The types of data needed and their accuracy differs in detail and scope and leads to definite wind tunnel requirements. Examples of testing to assess and develop turbulence models, and to verify code development are used to establish future wind tunnel testing requirements. Versatility, appropriate scale and speed range, accessibility for nonintrusive instrumentation, computerized data systems, and dedicated use for verification were among the more important requirements identified.

1. INTRODUCTION

Computational fluid dynamics (CFD) is expected to play a prominent role, along with wind tunnel testing, in the design of aerospace vehicles.^{1,2} Such expectations and optimism are based on the premise that the continued development of CFD, coupled synergistically with the new developments in instrumentation and test techniques, will provide a clearer understanding of complex flow phenomena and lead to more efficient and more ambitious designs. However, the pace of CFD introduction in the design process, and the sophistication of its application, will depend largely on the designer's confidence in the computational method. Experiments that verify CFD are an essential part of the confidence-building process because mathematical approximations, limited computer capacity, and uncertainty in modeling various physical processes lead to compromised solutions to the complete set of governing equations.³

The topic of CFD verification is currently being debated. It is a relatively new concept that depends on closely coordinated planning between computational and experimental disciplines. Because the code applications are becoming more complex and the regions of interest are diverse and wide-ranging, it no longer suffices to use experimental data from integral or surface measurements alone to provide the required verification. Flow-physics, flow-field, and boundary-condition measurements emerge as critical information in this regard. Furthermore, measurement accuracy requirements must be examined from a new perspective.

As a consequence of this evolutionary status of code verification, before defining the wind tunnel requirements it is important to establish what we mean regarding the role of experiment in the development of CFD. The author and his colleagues have experience in this regard, as our experimental effort has for some time been closely allied with the CFD effort at Ames Research Center.

This paper, therefore, will begin by briefly describing the status, future direction, and pacing items of CFD technology development. Requirements for code verification from two sources that pace the development are then described. The first of these requirements involves experiments to establish phenomenological input for situations in which understanding of the flow physics is limited. The important problem of turbulence modeling for aerodynamic flows will be used as an illustration, but other examples (such as high-temperature, reacting-gas physics with simplifications to account for radiation and mass transfer, or vortex interactions within developing flow fields over aircraft at high incidence) also could have been used. The second requirement involves experiments that establish the confidence limits on CFD predictions of complex flows over parametric variations such as Mach and Reynolds number. Examples for external aerodynamic flows are used, but internal flows, rotating flows, or unsteady flows would also provide good illustrations. The wind tunnel and accuracy requirements naturally ally themselves with these verification requirements and they are discussed in the final sections of the paper.

2. STATUS AND FUTURE DIRECTION OF CFD

2.1 Status

CFD has experienced volatile growth and a measurable degree of maturity over the past decade. The point can be illustrated by referring to Fig. 1. In the mid 1970's, to predict the entry heating environment over the Space Shuttle at flight conditions (which could not be duplicated in the wind tunnel), it was necessary to reduce the problem to manageable proportions. This was done by approximating the complete configuration with simple geometries (Fig. 1a) that were amenable to computation. The choices were based on extensive wind tunnel test data from the complete configuration compared with inviscid computations over the simple configurations, coupled with boundary-layer solutions. Leaside, separated flow computations were not possible. Today (in contrast), calculations of the entire Shuttle flow field and surface heating, including the leaside, are being accomplished by solving the Reynolds-averaged, Navier-Stokes equations.^{4,5} A computer-generated surface geometry used for one such calculation is illustrated in Fig. 1b. Solutions of the time-dependent form of the equations are made in the subsonic regions, and

solutions of the parabolized thin-layer laminar form of the equations are used in supersonic regions. Equilibrium gas properties have been incorporated and the results compared with flight data.⁴ The main driving forces in the advancement were access to large, fast computers and significant advances in algorithm development.

2.2 Future Direction

The future direction of CFD is toward even more ambitious applications involving complex geometries and their attendant flow fields. For example, pathfinder computations employing Reynolds-averaged, Navier-Stokes equations will be obtained for a complete fighter aircraft,⁶ the flow around a hypersonic vehicle, the internal flow in the turn-around duct of the Shuttle main engine⁷ and the unsteady flow through a compressor stage.⁸ Such computations test the limits of CFD technology development and the spinoffs from the successes and failures of such computations are expected to spur new development. But the ultimate success of such technology development depends, to a large extent, on addressing and solving the important issues still pacing the development of CFD.

2.3 Pacing Issues

Some of the more important issues pacing the development of CFD are shown in Fig. 2. Solution methodology, grid generation, and computer power were discussed by Kutler.⁹ Flow modeling and code verification, which rely heavily on experiment, are two additional issues that establish the important link between computation and experiment. Flow modeling is required in instances in which the physics is poorly understood or is so complex as to make "brute-force" computation impractical. Important examples are turbulence models for closure of the Reynolds-averaged, Navier-Stokes equations^{10,11}; transition from laminar to turbulent flow; and high-temperature gas physics related to hypersonic flows. Code verification is required to establish the limits of accuracy of the computations, particularly as the complexity of the flow increases.

3. EXPERIMENTAL REQUIREMENTS

3.1 Role of Experiments

A framework for describing the important links between experiment and computation is shown in Fig. 3. Experiments are required at each stage of code development. Research codes refer to those in which the ability to predict a particular, and usually idealized, flow phenomena is first established. One or two researchers are involved in developing the code, and no documentation is available. At this stage, experiments that are referred to as "building blocks" are needed. These provide the phenomenological data required to understand the flow physics, to guide flow-modeling processes, and to ultimately verify the computational development for the particular problem at hand. Pilot codes refer to a more advanced stage. Documentation is more complete, the code may be operated by others besides the researchers involved in the original development, and the envelope of problem application is expanded. At this stage, benchmark experiments peculiar to the various applications are required to provide the parametric data that establish accuracy limits on the computations. Subsequently the code would advance to its ultimate development stage when it could be used alone (or even be combined with codes from other disciplines such as structures or propulsion) and applied confidently in the design process. Configurational data from wind tunnel experiments would be needed to verify performance.

The distinction between the various stages of development outlined here is idealized, and not always evident in practice, because of the dynamic nature of CFD and its wide-ranging possibilities for solving many different problems; but the framework depicts how experiment and computation, working together, could accelerate the pace of development at each stage and even between the various stages. Of course, the implication here is the need for close coordination between experimental and computational disciplines. For the remainder of this paper, the first two stages of development will be emphasized along with their wind tunnel requirements.

3.2 Measurement Requirements

Each experimental stage must provide specific information that will enable a critical assessment of computational capability and accuracy. Some examples of key measurement requirements are listed in Fig. 4. These measurements are only representative and are germane to the technological development for Reynolds-averaged, Navier-Stokes equations for fully developed turbulent flows.

Building-block experiments must document sufficient information on flow phenomena to provide 1) an understanding of the flow physics, 2) guidance for modeling the turbulence, and 3) a critical test of the code's ability to simulate the flow. Surface variables and flow variables, including turbulence information, are essential. Some phenomenological experiments that focus on new flow physics or basic understanding of turbulence may be performed at incompressible flow conditions, but measurements will be required ultimately at representative flight Mach numbers and Reynolds numbers if simulations of actual flow phenomena are to be tested.

Benchmark experiments must provide sufficient information to test the ability of codes to perform adequately over a range of flow conditions or for a variety of geometries. Detailed measurements on turbulence modeling physics are not essential, but parametric testing over as full a range of flight Mach numbers and Reynolds numbers as possible will be necessary to provide an accuracy assessment of the

computational methods. With the renewed emphasis on hypersonics, flight experiments may become essential elements of the process because ground based facilities may lack adequate flight simulation capability. Code failures at this benchmarking stage may suggest further need for building-block experiments and a synergistic evolutionary development may follow.

Design experiments at the final stage provide the optimal configuration data necessary for performance evaluation and the experiments should be carried out as close to flight conditions as practical. CFD is expected to expedite the execution of these experiments by eliminating the need for very fine increments in parametric variations and by helping resolve any anomalous data sets.

Careful measurements of free-stream and boundary conditions are required at all stages because they may influence the flow field around the test models. This is particularly important for transonic flow. Moreover, these measurements are often required to initiate computation or are approximated in the computation.

3.3 Instrumentation Trends

The outlook is promising for making the measurements required to guide and verify computations, such as those listed in Fig. 4, because impressive advances in instrumentation development and data acquisition have taken place over the past decade. Some examples of this development trend are shown in Fig. 5. Prior intrusive techniques are being replaced by nonintrusive ones and the laser has emerged as the device that makes such applications possible. Measurements, such as velocity and its fluctuations,¹² density,^{13,14} and temperature and its fluctuations,¹⁴ skin friction,¹⁵ and model position and attitude¹⁶ are now possible. These advances will have an impact on future wind tunnel requirements to be discussed later in this paper.

3.4 Building Blocks

An example of a building-block experiment is shown in Fig. 6. This experiment, in conjunction with CFD, was used to guide the development of an improved turbulence model for airfoils at transonic flow conditions where strong shock-wave boundary-layer interactions occur. The test model consisted of a cylindrical body, fitted with a circular-arc section. A transonic flow developed over the circular-arc section similar to that on an airfoil, and shock wave interactions of varying strengths were studied by varying free stream Mach numbers. The choice of an axisymmetric geometry and the long cylindrical section was made to eliminate three-dimensional effects and to develop a viscous interaction region of sufficient scale to allow detailed nonintrusive measurements. Mean flow and turbulence profiles, obtained with a Laser Doppler Anemometer System (LDA), and surface quantities such as pressure and oil-streak data were documented.¹⁷ The model was tested in two facilities, the Ames' 2-ft by 2-ft and 6-ft by 6-ft wind tunnels, to evaluate the influence of wind tunnel boundary conditions. (No significant influence occurred.)

Computations of the flow field from a Reynolds-averaged, Navier-Stokes code revealed deficiencies in the turbulence modeling. By using a model developed by Cebeci and Smith, primarily for attached boundary layers, the shock wave location was predicted incorrectly and consequently the pressure recovery was seriously overpredicted. The mean-and-turbulence-profile data from the LDA measurements were used to explain the differences and guide modeling improvement. The primary cause of the pressure recovery overprediction was the failure of the eddy viscosity model to adequately reflect the lag of turbulence adjustment through the shock wave and the resultant underprediction of the displacement thickness influence. By using modeling concepts in conjunction with the turbulence data, a significant model improvement was developed. In particular, the "history effects" of the turbulence changes through the shock wave were accounted for by prescribing and solving an ordinary differential equation for the maximum shear stress development.¹⁸ Modeling constants were determined using the turbulence data in conjunction with computations. The improved model results are shown in Fig. 6. The model has been introduced in two airfoil codes.^{19,20} Additional studies are under way to determine the range of applicability by making comparisons with other benchmark experimental airfoil data.

3.5 Benchmarks

An example of one of these benchmark experiments²¹ is illustrated in Fig. 7. The test model consisted of a supercritical airfoil section. It was mounted in a specially designed test section with solid walls. Boundary layer suction was applied ahead of the airfoil on the sidewalls to minimize interference; the upper and lower walls were contoured to stream-line shapes that were predetermined by computation to account for the presence of the model, which further minimized interference. Tests were performed at a Reynolds number of 6×10^6 , based on chord, and angle of attack and Mach number were varied over a range sufficient to produce transonic flows covering weak and strong shock-wave boundary-layer interaction and attendant displacement effects. The boundary layer was tripped on the upper and lower model surface to ensure turbulent flow beyond 7% chord. Model pressures, wall boundary pressures and shapes, total drag, lift, and flow field and wake velocities from an LDA system were documented. A data base of this type (with minimal interference from a tunnel with solid walls) provides an ideal basis for evaluating the development of codes for the transonic speed range because the codes can include the wall boundary conditions more precisely than interference corrections can be made to the data sets.

The data are being used to assess the influence of turbulence modeling on transonic airfoil computations and to verify the development of a transonic code.²⁰ At present the code does not include the solid tunnel wall boundary conditions, but a preliminary assessment using this benchmark data indicates that the

code provides very good simulation for the strong interaction cases when the Johnson-King turbulence model¹⁹ is employed. Results of the comparisons for one strong interaction case (where separation occurred at the trailing edge) are shown in Fig. 7. The airfoil pressures, flow field velocities at constant heights above the model, and a wake profile at the trailing edge are compared with computations using two different turbulence models, a two-equation (q-w) model,²⁰ and the Johnson-King (J-K) model.¹⁹ The comparison shows that the computations using the improved Johnson-King turbulence model simulates the measurements very well. It is important to emphasize that this conclusion could not have been drawn without the complete data set composed of total drag, lift, boundary conditions, and flow field surveys.

4. WIND TUNNEL REQUIREMENTS

The requirements for future wind tunnels used to verify CFD naturally result from our previous discussions on the role of experiment in the development of CFD. The most important of these requirements are: 1) versatility, along with well-defined test and boundary conditions; 2) appropriate scale and speed range; 3) accessibility of nonintrusive instrumentation; 4) provision for high-speed data systems; and 5) dedication of use to verification-experimentation. Some examples should help to develop these points further.

4.1 Versatility

As discussed previously, CFD applications are expected for a variety of aerodynamic flows over a wide speed range. Use of large, fast computers, which can timeshare among problem applications, means that the time needed to perform a variety of cost-effective computations will be far less than the time to design and perform companion experiments. Nevertheless, the computations still should be verified to ensure confidence in the results, and a limited number of well-thought-out, cost-effective experiments will be needed. Versatility must be kept in mind when considering facilities to accommodate these experiments. This is particularly true for the building-block studies in which phenomenological information will be required for a wide variety of flows and for the verification studies in which wind tunnel boundaries are critical (as in the transonic-speed regime) and may have to be modified from test to test.

The Ames High Reynolds Number Channel facilities provide an example of versatile design. These facilities, shown in Fig. 8, operate in a blow-down mode over a speed range from subsonic to supersonic (Mach = 3 maximum). Test section dimensions are 10 in. by 15 in. and 16 in. by 24 in. for channels I and II, respectively. In subsonic application, speed is varied through a downstream choking device. At supersonic speeds individual nozzles designed for the desired Mach numbers are used. Air from a large, high-pressure storage system provides the capability to operate at high Reynolds number, and run times are sufficient to collect the types of data required for modeling and benchmark experiments. The test sections are replaceable and are considered to be part of the test model. In this way, separate experiments dedicated to a particular test section can be interchanged without dismantling the entire setup, and reentry into the facility can be made to clarify or expand upon certain data sets. Savings in setup time, and the ability to perform several experiments in series, are the obvious advantages of such an arrangement.

Key building-block and verification experiments have been performed in these tunnels. Figure 9 shows geometries for some of the experiments performed in channel I, which can be equipped with either a rectangular or a circular stagnation chamber inlet. Some of these experiments were used by the international community at the 1981-2 Stanford Conference as test cases for evaluating the ability of codes to predict complex turbulent flows. Channel II is now configured for airfoil experiments. It uses shaped, solid, upper and lower walls and side-wall, boundary-layer removal as mentioned in the previously described benchmark experiment.

4.2 Appropriate Scale and Speed Range

Similitude is an important aspect of testing to validate CFD development. Applications of CFD will encompass internal as well as external aerodynamic flows, so the anticipated ranges of scale and speed in facilities employed for verification will be broad, indeed. An example of the Mach-number, Reynolds-number domain for external aerodynamic flow over an aerospace vehicle is shown in Fig. 10. A mean aerodynamic chord was used as the length scale in the Reynolds number. The hypersonic regime is typical of vehicle entry conditions. In this case it depicts the nominal Space Shuttle vehicle trajectory conditions. CFD applications and attendant verification studies are certain to arise over the speed regime from subsonic through hypersonic. A critical need for high Reynolds number capability occurs in the transonic and low supersonic regions, and in the hypersonic regions for exit trajectories associated within the latest aerospace plane concepts. It should also be noted that at hypersonic speeds the associated enthalpy and vehicle scale may preclude ground-based similitude, so flight verification experiments of important flow phenomena (such as reacting chemistry, radiation, and transition) may be necessary. Fortunately the viscous phenomena, important to vehicle stability and control, can usually be duplicated in ground-based verification experiments that test at the appropriate Mach and Reynolds numbers, in the absence of true enthalpy simulation.

Although scale is reflected in the test Reynolds number, actual model dimensions are also important because details of the viscous regions must be measured in some experiments. In this regard, model sizing must take account of the achievable resolution scale of the instruments to be employed. We have found that facilities with test section areas of 1 to 2 ft² have been quite satisfactory for use in building-block experiments. In our LDA applications, we achieved spatial resolution to within 0.01 in., which was

sufficient to provide viscous profile data. But in some of these experiments, the viscous region under study had to be developed along the tunnel walls to achieve adequate profile resolution. For verification in experiments of complex aerodynamic geometries, model dimensions of about 1 to 2 ft may be required to resolve viscous regions, so larger tunnels may be more appropriate.

4.3 Optical Access

Nonintrusive instrumentation will play an increasingly important role in experiments performed to verify CFD. Therefore another important requirement for facilities performing such experiments will be a provision for optical access. Furthermore, three-dimensional flows will comprise a majority of future studies, and accessibility for a wide range of viewing perspectives is desirable. Open-jet, test-section facilities provide the best access, but confined test sections are more conventional. Access requirements for the latter may present a formidable challenge, but successes have been achieved, as illustrated next.

The two-component laser velocimeter system,¹² which was used to measure the flow field velocities and turbulence quantities in the airfoil experiments performed in High Reynolds Number Channel II discussed previously, is shown in Fig. 11. The requirement was to provide nonintrusive test data in a high-Reynolds-number transonic test tunnel environment. The facility utilized a pressurized test cabin. The laser and its dual-beam-sending optics are mounted outside and on the top of the cabin, and a translating mechanism (equipped with inner optics and located inside the cabin) provides accurate, rapid, preprogrammed positioning. Fiber optics are used to collect the forward-scattered light from the focal volume in the test stream and to transmit it to the photomultiplier tubes located outside the cabin. Optical access into the test stream is provided by glass windows located in the model turntable and in the side walls downstream, in the vicinity of the model far wake. Experience to date with the system shows that stable optical alignment can be maintained during blowdown runs and from blowdown-to-blowdown.

It should be noted that there is a need for developing nonintrusive measuring devices with better spatial resolution, especially for three-dimensional applications.

4.4 Computerized Data System

The quantity and scope of the data needed for verification, the sophistication of new instrumentation, and the need for close coordination between experiment and computation all require that a computerized data system be provided. The system should provide control for tunnel and instrument functions, acquire data, perform arithmetic operations, and act as an interface between CFD users and the experimentalists. It should provide real-time data acquisition, especially if the time-dependent phenomena are encountered. Expert systems could be incorporated for faster and more accurate data acquisition.

An idealized system is depicted in Fig. 12. The kernel is a main computer with sufficient capacity and speed to perform multifunction tasks. For example, it would have command and control functions for smaller computers used to control and/or command tunnel and instrumentation operations; acquire low- and high-level data directly or indirectly; perform arithmetic operations to reduce the data to the desired form; direct data to storage or output devices; and make comparisons with computations. Importantly, it would interface with both the experimental fluid dynamics (EFD) and CFD user networks so that data comparisons and test decisions could be made in a synergistic fashion.

4.5 Dedication to Verification

Accurate, redundant (in some instances), and detailed measurements, often employing state-of-the-art instrumentation, are required in the experiments used to verify CFD. Inevitably, equipment breakdowns and data anomalies will arise so that retesting for clarification, and even further investigations using different instrumentation, may be needed. Sufficient time to conduct the comprehensive experiments will have to be provided. Therefore, dedicated equipment and test time, specifically for these experiments will have to be provided if timely developments are to occur.

5. DATA COMPLETENESS AND ACCURACY REQUIREMENT

Assessing the accuracy and predictability of CFD codes and their turbulence models requires special attention to data completeness and accuracy.

5.1 Completeness

The completeness requirements for a building-block experiment to study turbulence modeling of a supersonic shock-wave, boundary-layer interaction in the vicinity of a compression corner is shown in Figs. 13 and 14. In such flows unforced shock unsteadiness occurs,²² and laser velocimeter measurements of mean and fluctuating flow quantities must take account of the unsteadiness to avoid misleading interpretations regarding modeling.

A typical joint probability distribution function (JPDF) of velocities is shown in Fig. 13 (which is taken from Ref. 22). The geometry is an axisymmetric cylinder flare. The JPDF was obtained at a location in the outer boundary layer along the flare and downstream of the mean position of a separation shock wave. The bimodality of the distribution is particularly evident and is strongly indicative of unsteady shock wave motion. The two peaks, labeled s_1 and s_2 , are representative of velocity states upstream and downstream of the separation shock wave. With each of these states is associated a total probability of occurrence (p_1 and $p_2 = 1 - p_1$), mean velocities (u_1, u_2 and v_1, v_2), turbulent normal stresses, and

turbulence shear stresses. A straight-forward analysis reveals that the difference in mean values ($u_2 - u_1$) and ($v_2 - v_1$) for the two states contributes to the stresses. The shear stress contribution due to unsteadiness is $-p_1 p_2 (u_1 - u_2)(v_1 - v_2)$ and was measured to be 75% of the total shear stress. This contribution to the total Reynolds stresses is due to an organized or coherent motion of the shock rather than to incoherent or dissipative turbulence.

Figure 14 shows zero-drag particle paths in a plane of symmetry for a three-dimensional compression surface achieved geometrically by tilting the flare axis relative to the cylinder axis. Velocity measurements from an LBA were used to construct the paths by conditionally sampling the data on the basis of shock position (e.g., shock forward, shock back) and by using all data representing the long-time mean. These are compared with solutions from the Reynolds-averaged, Navier-Stokes equations which employ an eddy viscosity turbulence model. The separation location moves considerably, and even the long-time mean computer simulations do not compare favorably with the experiment. Turbulence data are also available so that flow unsteadiness can be separated from the random turbulence, and these data will be used to guide improvements in modeling.

5.2 ACCURACY

CFD validation will ultimately depend on a thorough understanding of the algorithm limitations, and the influence and physical basis of grid density. It will require experiments that verify the ability of the code to accurately model, for a range of practical parameters, the critical flow physics and its consequent flow behavior around aerodynamic shapes. The latter can occur only when the accuracy and limitations of the experimental data are known and thoroughly understood. We have already discussed the various types of experiments in our idealized scenario for development that are depicted in Fig. 3. Currently, the validation process is hampered somewhat by the lack of adequate instrumentation and ground-based facilities to cover the range of anticipated applications. Therefore, redundant measurement techniques, similar experiments performed in more than one facility, and careful substantiation and specification of experimental accuracy limits will be necessary. Such requirements make it essential that the computational and experimental disciplines be carefully coordinated.

6. CONCLUDING REMARKS

Experiments play a critical role in the development of CFD. They provide the phenomenological data to help in the process of flow modeling and they provide the verification necessary to instill confidence in the computations.

A synergistic approach, comprising closely coordinated experiments and computations at all levels of computational development, was described in order to set the groundwork necessary to develop requirements of facilities to be used to verify CFD. Building-block experiments, which address fundamental phenomenological questions, were described. Experiments of this type require more comprehensive sets of data. In these instances, more sophisticated instrumentation would be the norm rather than the exception. Benchmark experiments were described next. These experiments identify the accuracy and limits on our ability to compute complex flows. The types of data required differ from the more fundamental experiments in the sense that phenomenological issues are not investigated in detail sufficient to identify their causes. Data accuracy and completeness requirements were also noted.

The idealistic breakdown of the experiments and measurements described helped to identify the more important requirements for wind tunnels to be used to verify CFD. Versatility, appropriate scale and speed range, accessibility for nonintrusive instrumentation, computerized data systems, and dedicated use for verification were among the more important requirements identified.

REFERENCES

1. Chapman, D. R., "Computational Aerodynamics-Development and Outlook," AIAA J., Vol. 17, Dec. 1979, pp. 1293-1313.
2. Reinecke, G. "Forecasting the 80's," *Astronautics & Aeronautics*, Vol. 19, Jul/Aug. 1981, pp. 46-47.
3. Committee on Computational Aerodynamics Simulation Technology Developments, "The Influence of Computational Fluid Dynamics on Experimental Aerospace Facilities, A Fifteen Year Project," National Research Council, National Academy Press, Washington, D.C., 1983.
4. Prabhu, D. K., and Tannehill, J. C., "Numerical Solution of Space Shuttle Orbiter Flow Field Including Real Gas Effects," AIAA J. of Spacecraft and Rockets, 1987.
5. Rizk, Y., M., and Ben-Shmuel, S., "Computation of the Viscous Flow Around the Shuttle Orbiter at Low Supersonic Speeds," AIAA Paper 85-0168, Reno, NV, Jan. 1985.
6. Molst, T. L., Kaynak, U., Gundy, K. L., Thomas, S. D., Flores, J., and Chaderjian, M. M., "Numerical Solution of Transonic Wing Flows Using an Euler Navier-Stokes Zonal Approach," AIAA Paper 85-1640, Cincinnati, OH, Jul. 1985.

7. Chang, J. L. C., and Kwak, D., "A Three-Dimensional Incompressible Flow Simulation Method and Its Application to the Space Shuttle Main Engine, Part II - Turbulent Flow," AIAA Paper 85-1670, Reno, NV, Jan. 1984.
8. Rai, M. M., "Navier-Stokes Simulations of Rotor-Strator Interaction Using Patched and Overlaid Grids," AIAA Paper 85-1519-CP, Cincinnati, OH, Jul. 1985.
9. Kutler, P., "A Perspective of Theoretical and Applied Computational Fluid Dynamics (SP)," AIAA J., Vol. 23, No. 3, Mar. 1985, pp. 328-341.
10. Marvin, J. G., "Turbulence Modeling for Computational Aerodynamics," AIAA J., Vol. 21, No. 7, Jul. 1983, p. 941.
11. Lakshminarayana, B., "Turbulence Modelling for Complex Flows (Invited Paper), AIAA Paper 85-1652, Cincinnati, OH, Jul. 1985.
12. Seegmiller, H. L., Bader, J. B., Cooney, J. P., DeYoung, A., Donaldson, R. W., Jr., Gunter, W. D., and Harrison, D. R., "Development of a New Laser Doppler Velocimeter for the Ames High Reynolds Channel No. 11," ICASF '85 Record, IEEE Publication 85CH2210-3, Stanford Univ., CA, Aug. 1985.
13. Dunagan, S. E., and Brown, J. L., "A Holographic Interferometric Study of an Axisymmetric Shock-Wave/Boundary-Layer Strong Interaction Flow," AIAA Paper 85-1564, Cincinnati, OH, Jul. 1985.
14. Logan, P., and McKenzie, R. L., "Uncertainty in Hot-Wire Measurement of Compressible Turbulent Flows Implied by Comparison with Laser-Induced Fluorescence," AIAA Paper 86-0502, Reno, NV, Jan. 1986.
15. Monson, D. J., "A Laser Interferometer for Measuring Skin Friction in Three-Dimensional Flows," AIAA Paper 83-0385, Reno, NV, Jan. 1983; AIAA J., Vol. 22, No. 4, Apr. 1984, pp. 557-559.
16. Holmes, H. K., "Model Measurements in the Cryogenic National Transonic Facility - An Overview," ICASF '85 Record, IEEE Publication 85CH2210-3, Stanford Univ., CA, Aug. 1985.
17. Bachalo, W. D., and Johnson, D. A., "An Investigation of Transonic Turbulent Boundary Layer Separation Generated on an Axisymmetric Flow Model," AIAA Paper 79-1479, Williamsburg, VA, 1979.
18. Johnson, D. A., "Predictions of Transonic Separated Flow with an Eddy-Viscosity/Reynolds-Shear-Stress Closure Model," AIAA Paper 85-1683, Cincinnati, OH, Jul. 1985.
19. Johnson, D. A., and King, L. S., "Transonic Separated Flow Predictions Based on a Mathematically Simple, Nonequilibrium Turbulence Closure Model," IUTAM Symposium, Paris, France, NASA TM 86826, Oct. 1985.
20. Coakley, T. J., "Numerical Simulations of Viscous Transonic Airfoil Flows," AIAA Paper 87-0416, Reno, NV, Jan. 1987.
21. Mateer, G. G., Seegmiller, H. L., Coakley, T. J., and Hand, L. A., "An Experimental Investigation of a Supercritical Airfoil at Transonic Speeds," AIAA Paper 87-1241, Honolulu, HI, Jan. 1987.
22. Brown, J. L., Kussoy, M. I., Coakley, T. J., "Turbulent Properties of Axisymmetric Shock-Wave/Boundary-Layer Interaction Flows." In Turbulent Shear Layer/Shock Wave Interactions, Springer-Verlag, Berlin Heidelberg, 1986.

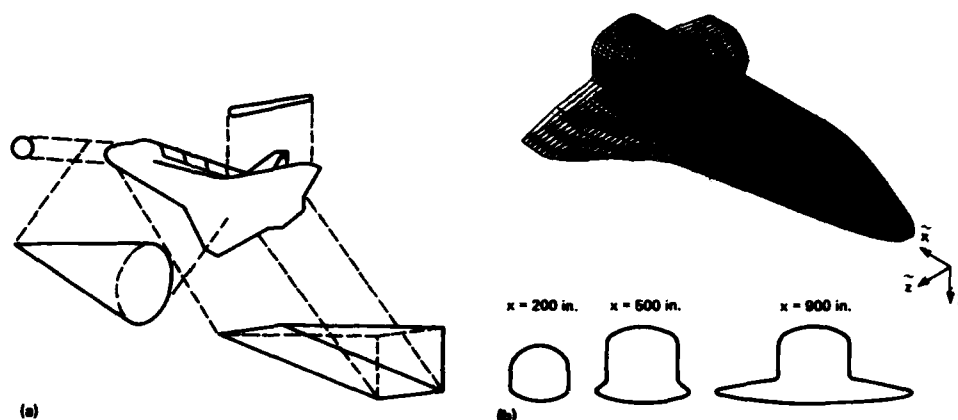


Figure 1. Maturation of CFD over the past decade for Space Shuttle Aerothermodynamics. a) Circa 1974: equivalent shapes and solutions from inviscid and boundary-layer equations. b) Present: complete geometry and solutions from Reynolds-averaged, Navier-Stokes equations.

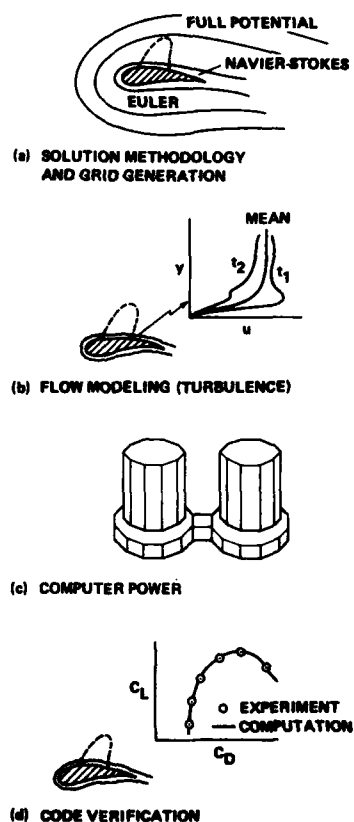


Figure 2. Issues pacing the development of CFD.

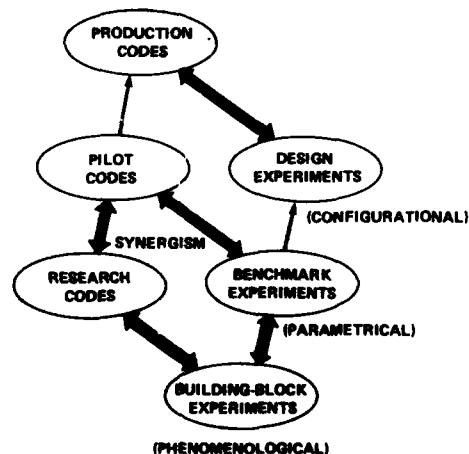


Figure 3. The role of experiment in the development of CFD.

EXPERIMENT	MEASUREMENTS (REPRESENTATIVE FOR TURBULENCE MODELING)	TEST CONDITIONS
BUILDING BLOCK (PHENOMENOLOGICAL)	SURFACE QUANTITIES FLOW FIELD QUANTITIES TURBULENCE INDIVIDUAL STRESSES CORRELATION LENGTHS STRUCTURE BOUNDARY CONDITIONS	REPRESENTATIVE FLIGHT M_{∞} , Re_{∞}
BENCHMARK (PARAMETRICAL)	SURFACE QUANTITIES FLOW FIELD QUANTITIES (SELECTED LOCATIONS) BOUNDARY CONDITIONS	VARY M_{∞} , Re_{∞} , α OVER FLIGHT RANGES
DESIGN (CONFIGURATIONAL)	DRAW, LIFT, MOMENTS, HEAT LOADS, SHEAR LOADS BOUNDARY CONDITIONS	AS CLOSE TO FLIGHT M_{∞} , Re_{∞} , α AS PRACTICAL

Figure 4. Key measurement requirements of experiments supporting development of Reynolds-averaged, Navier-Stokes codes for fully developed turbulent flows.

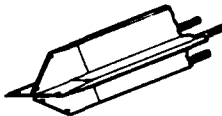
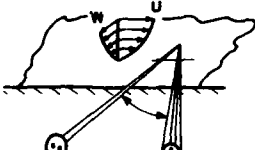


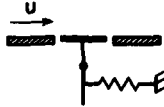
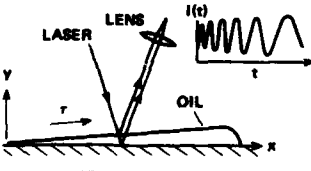
MEASUREMENT	CIRCA MID '70's	PRESENT (NONINTRUSIVE)
VELOCITY MEAN FLUCTUATING	 HOT WIRES PITOT-STATIC TUBES	 3-D LASER VELOCIMETER
TEMPERATURE MEAN FLUCTUATING	 HOT WIRES THERMOCOUPLES	 LASER-INDUCED FLUORESCENCE
LOCAL SKIN FRICTION	 BALANCES FENCES	 LASER-OIL INTERFEROMETER

Figure 5. Advances in instrumentation development over the past decade.

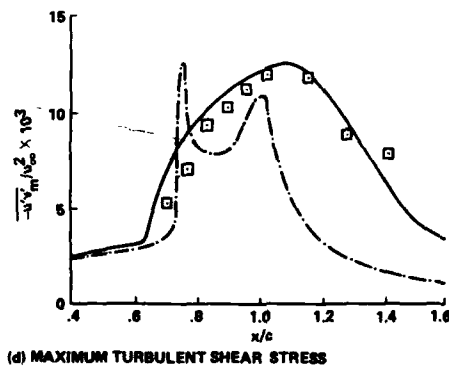
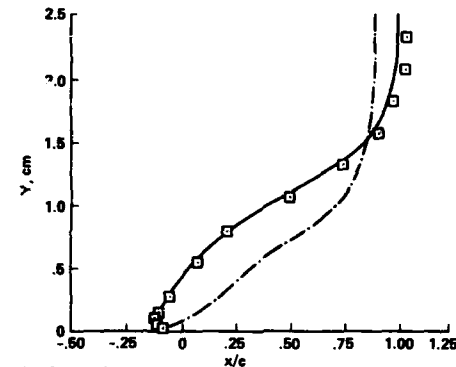
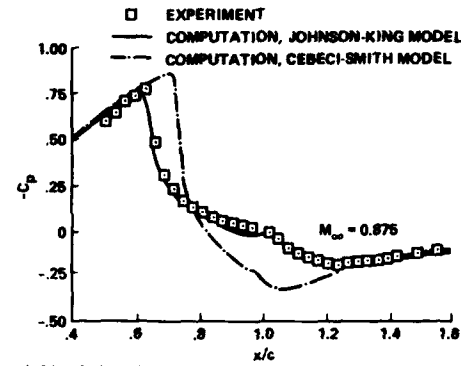
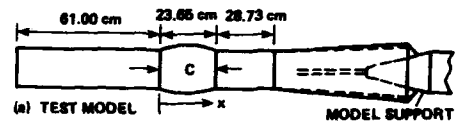


Figure 6. A building-block experiment used to develop an improved turbulence model.

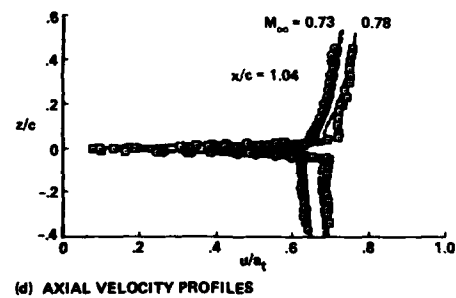
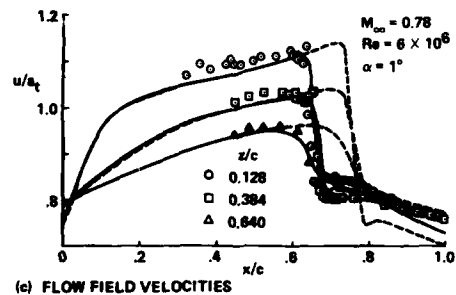
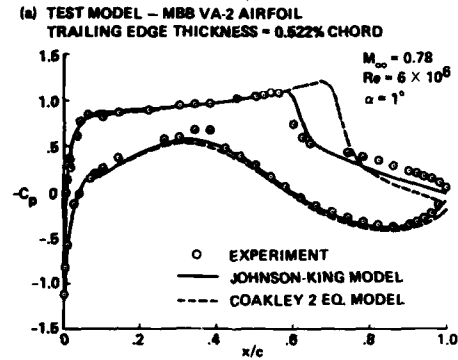
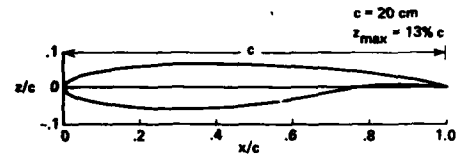


Figure 7. A benchmark airfoil experiment used to verify development of an improved turbulence model.



Figure 8. Ames High Reynolds Number Channels. a) Channel I. b) Channel II.

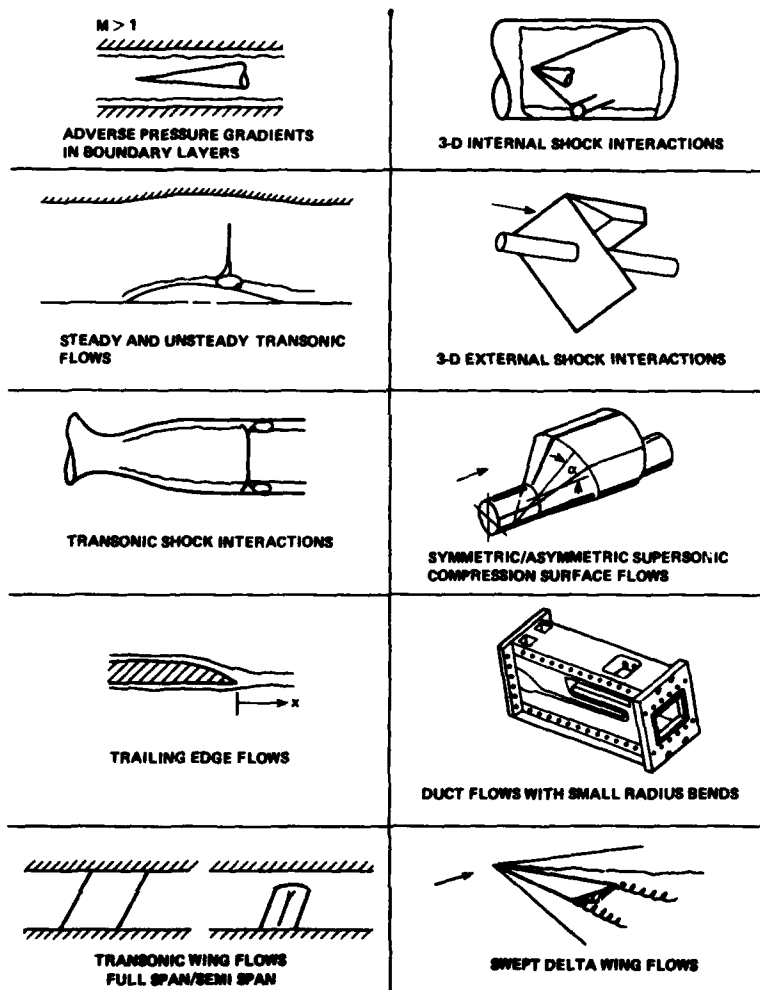


Figure 9. Experiments performed in a versatile wind tunnel.

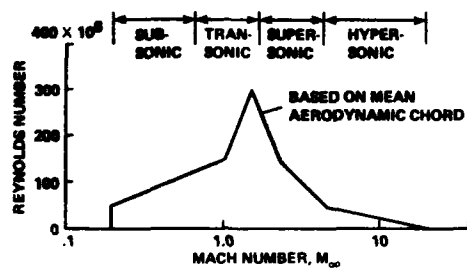


Figure 10. Mach-number, Reynolds-number domain for aerospace vehicles.

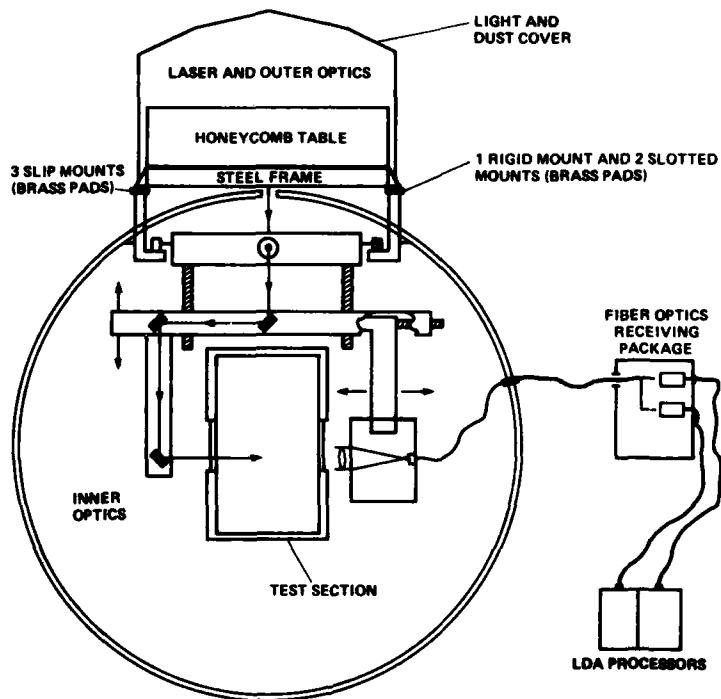


Figure 11. A dedicated laser anemometer system for the Ames High Reynolds Number Channel II.

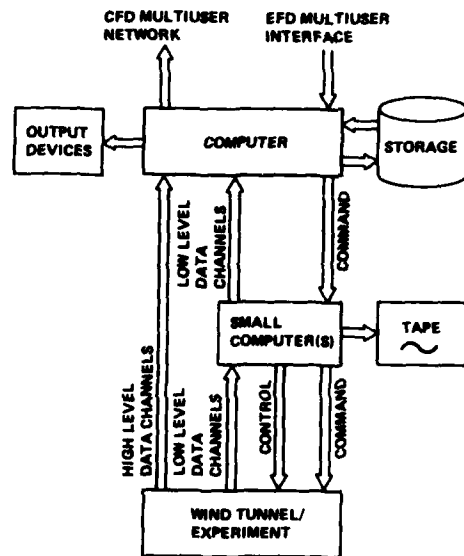
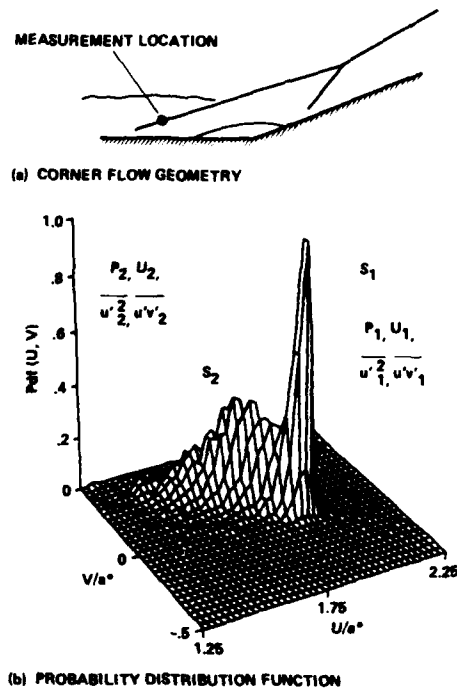
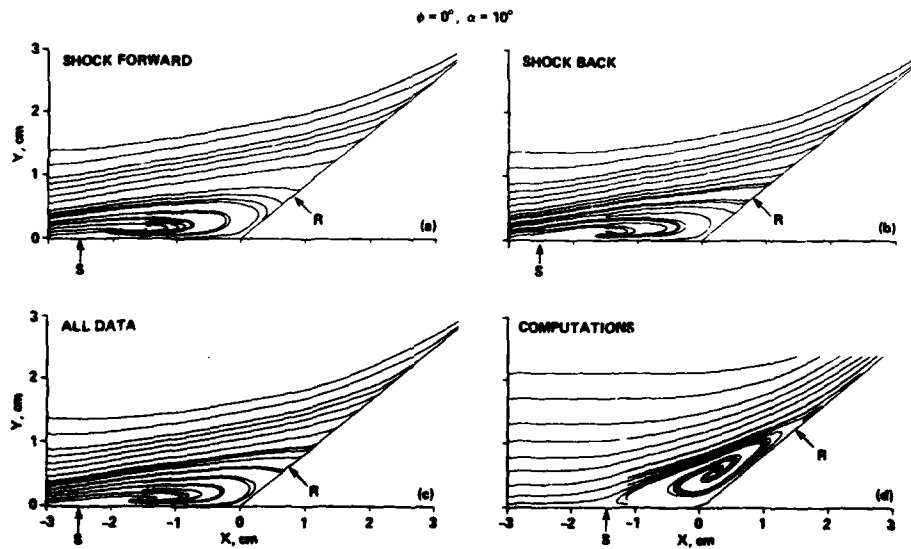


Figure 12. An ideal computerized data system.

Figure 13. Joint probability distribution function (JPDF) for u and v for a 30° axisymmetric compression corner.Figure 14. Particle paths over a skewed 30° axisymmetric compression corner from conditionally sampled laser velocimeter data and from a Reynolds-averaged, Navier-Stokes code computation.

AERODYNAMIC DATA ACCURACY AND QUALITY:
REQUIREMENTS AND CAPABILITIES IN WIND TUNNEL TESTING
Naples, Italy

28 September - 1 October 1967

ROUND TABLE DISCUSSION

Prof. Horenung

At the end of this Symposium we will have two things, first the report of the technical evaluator and then the discussion. The technical evaluator is T.E. Laater who will now speak about this Symposium and summarize his feeling of the presented talks.

Dr. Laater

It is always a problem to try to summarize such a variety of activities and papers that we have heard during a Symposium. At first I thought in terms of trying to give a rather extensive detailed account of a number of things here, but then I learned that our time is shorter than I expected. But there are some points that are worth bearing in mind with respect to this Symposium. The theme of the Symposium was very well stated in the brochure. There are basically three questions in there that are very well stated. In a minute I propose to go back and address those three questions and whether or not I think that this Symposium has addressed them or not.

There is one problem that permeated throughout the Symposium I noticed while listening to the papers which goes all the way from the title of the program to the content of some of the papers. That deals with terminology that we are using here in the windtunnel community. I am a part of that problem in that I had a hand in establishing the title of the Symposium itself. That word "accuracy" is the one that really throws me. Actually we have used several terms here somewhat interchangeably without thinking a lot about what we really mean. For example, the terms accuracy, error, absolute error, repeatability, uncertainty, bias, precision were used meaning the same and different things. You have heard all of these words and maybe there are a few more that I haven't thought of. The term accuracy has been used to represent many different things. It has been used to represent precision. It has been used to mean repeatability. I think that the two papers that we had from the PEP panel give us some guidance that might in the future be worthwhile. They have structured themselves in the propulsion world pretty well in that they are now talking in terms of uncertainty and using the terms bias and precision. Along with that they have developed, using the Abernathy approach, a method of calculating bias and precision. Something like this might be adopted by the windtunnel community. By far and large, though, the way the word "accuracy" is used is in terms of precision and repeatability, and more or less interchangeably. That is a little thing that has bothered me. I hope maybe in the future we can be a bit more precise about this.

The Symposium basically, dealt mostly with low speed and transonic flows. That was principally by design, although we had some reference to hypersonic flow. As time moves on there will be increasing interest in the supersonic and hypersonic regime. I think that the techniques that are used for designing vehicles are going to move from these so-called reference methods that Mr. Krenz mentioned this morning to the direct scaling techniques. In terms of uncertainty that means that you are going to have to design these new types of vehicles not just using data developed from precision measurements, but you are going to need to know more about bias effects in the data, because we don't have any reference data to use. That is going to make it more difficult in the high speed world to develop systems.

We heard throughout the Symposium a great deal about requirements for developing transport type aircraft, in particular we heard that we would like to have a repeatability or a precision in drag coefficient of about one count. Apparently that is achievable with current day technology in terms of balance design and so on. However, when we go into the cryogenic technology, it seems that this is not quite so easy a Prof. Ewald has pointed out to us. That raises a question. Is the uncertainty associated with making force measurements, in these cases where you have cryogenic windtunnel tests, is that uncertainty going to be more than what you would have if you were to take conventional windtunnel results and extrapolate them to the higher Reynolds number cases? I don't know the answer to that, but it is something to think about.

There was not a lot said about military aircraft and what the requirements are for their development with the exception of this morning. It was mentioned that a precision of the order of two drag counts was needed for cruise conditions and five drag counts for low speed. It would be nice if we could have heard more on that.

It seems to me that if we do think of "accuracy" in terms of meaning precision, then we are not doing too badly for the low speed and transonic flows in making force measurements. But bias is the problem in the windtunnels. Bias is basically related as much as anything to the differences that you might find between wind tunnels. Each windtunnel has its own unique bias made up of many factors and is different in each windtunnel. For example, wall interference is really a bias. So each tunnel has a different bias for wall interference. The same thing could be said for mounting interference and turbulence level, etc. Treating these things and knowing what they are and being able to reduce them is a goal that we should continue to work towards, especially if we are going to direct scaling type of designs.

Let me finish by commenting upon the three questions that we had put to us in our theme. The first question was, "what are the actual demands in terms of accuracy of data that the users have on facilities?". There were some explicit statements made along these lines, like measuring drag repeatability to 1% or one count. Mostly the question was treated implicitly and may have left us grasping a little bit. The second question was "what accuracy is achieved in modern facilities?". Here we had more response to the question, and it was dealt with reasonably well. The third question was "what measures can be taken to improve the situation?". Far and large the issues are identified pretty well; how to approach them is often a problem. Here I think we need to understand the various contributions of bias to wind tunnel data uncertainty. I don't have a suggestion that is based on something tangible, but one big problem the windtunnel community has, as I mentioned in the beginning, is the business of adopting a common basis of treating data uncertainty.

RTD-2

I believe that in terms of what we can do to help improve the situation in the future is to continue our research on improving things like correcting for wall interference and strut interference and being able to be a bit more controlled and rigid in the development of viscous simulation techniques. I might stop to say here that the Working Group 09 activity and the subsequent special course that is going to be presented, should be advertised well to our engineers in both Europe and the U.S. Anyway there is a lot of research that can continue to be done that is certainly going to help to reduce the bias part of the problem, and no doubt will do things to improve the precision as well.

Prof. Hornung

Thank you very much for those well taken points and also for your own views which you interspersed. We come now to a ritual which those of you who have attended AGARD meetings know about, a ritual in which we spend something like half an hour discussing the topic in an open discussion. I have very strong views about this kind of discussion. I believe that it only works in a sensible fashion if we really restrict ourselves to discussing questions in a brief manner and not allow any speeches. So I will not allow any speeches. I will cut short anybody who wants to give another presentation, and we will go about it in that manner.

Let me start out by saying how this started. It was the presentation that Bernard Monnerie made at the National Delegates Board Meeting where he, by presenting in this manner, got us support for the panel and these questions that appear on this slide were the ones that prompted him to start this Symposium. Maybe this is a good point at which to start the discussion.

Do you have any questions or any points that you want to discuss? Bernard Monnerie, do you want to start it off.

Mr. Ohmen

I'll start off from the back with Joe Marvin's paper, and I would like to address my question to the CFD people about code verification. Using the Reynolds averaged equation you can calculate the whole flow field. Now for a windtunnel man it is much easier just to do surface measurements, pressure and so on. If you want to go into field measurements you are talking of another order of magnitude of verification measurements. I would like to get some sort of feel for the rating from the CFD people of what is the most important for them. If you want to go into the field, I hope that surface measurements are still the most important, it certainly is for the aircraft designer. To what degree do you need field measurements? That can become an enormous task if you want to go into great detail.

Dr. Marvin

I think that the way to address that is as follows. If you look at the state of CFD as it currently exists, there isn't a sufficient data base to really indicate how accurately you are doing the Navier Stokes computations, which I have the most familiarity with. Without sufficient measurements, there may be ways of interpreting the surface data to make your comparisons look more accurate than they are. For example, one of the biggest mistakes has been to arrange angle of attack so that you match certain integral quantities such as lift or drag. In this approach you may miss the influence of wall interference effects which are significant transonically, for example. What I think should be done is to perform a small number of experiments initially on sample configurations, not on aircraft at this point. Those experiments would provide surface and flow field measurements that establish the generic aspects of your computations. Can you do a shock interaction problem, can you do a trailing edge problem? Once you have established that, then you can move on to the more complex cases. Following this approach when you do the more complex configuration type studies you probably will only have to perform a few selected flow field measurements. But you will have to know the precise boundary conditions of your tests and input those in your codes.

Mr. Eisenaar

I would just like to stress this point. I like the distinction very much between building-block experiments and benchmark experiments. It is very important for code validation to use benchmark experiments as well and to show how well CFD codes perform over a range of conditions. From that you can learn quite a lot I think and it is not done sufficiently. If you find large discrepancies, if there are unexplainable phenomena, if you don't catch properly certain physical phenomena, then I think it might be useful to go on with field measurements to find out, to answer real questions that come out of this comparison. Before that, rather compare basic things: lift, pressure distributions, pitching moments, drag for a range of conditions, and if that is satisfactory you don't have to go into field measurements at all.

Mr. Binion, AEDC

In doing CFD validation, you have to design the experiment to answer the questions that the code needs to have answered. If one is dealing with surface phenomena, then you may not need flow field measurements; but, if one is dealing, for example, with jet/free stream interactions, where you are trying to characterize the jet/free stream shear layer or the shock development in the jet, you have got to have flow field measurements. That is the only way that you can get the information you need. So, the experiments have to be designed explicitly to verify the code that you are trying to verify. One other point that I would like to reiterate that Joe made very well and that is: the codes that he is verifying are verified for the windtunnel conditions, he is using windtunnel measured boundary conditions. One can't properly verify a code using free air boundary conditions with experimental data having windtunnel boundary conditions. You have got to use the boundary conditions from which the experimental information was derived.

Prof. Hornung

Thank you. I think this is a very good point and perhaps one should also say that one should test that variable which is most sensitive.

I think that we have a question from our chairman who probably wants to want even more complicated experiments.

Mr. Sacher

I am not speaking as a Chairman now. I must say that I disagree to a large extent with Brom Elsenaar's statement from an experimental side of view. He claims that there is no need for flow field measurements at the present stage, or I misunderstood him. Let us say what have we done during the past. We have compared our theoretical results from different codes mainly potential flow codes corrected for viscous flow effects, of course, for the boundaries, for the geometry, for the surface, getting pressures, integrated loads and having forces and moments. We found a considerable amount of disagreement with the experimental results. Then we go to a higher hierarchy of equations, we come to Euler's and even Navier Stokes. We found the same basic disagreement and just to find the reason, we need much more detailed information from the experiment. That means in other words, we need the knowledge to measure the flow field, the flow field data, not only pressures but also velocities. Look at separated flow, we have done an exercise in the last two years. I would say that we need a complete new increased amount of experimental data including the whole flow field.

Prof. Hornung

At this point I think that we will stop the discussion on this topic, and we will change to one which leads maybe into the discussion of Working Group 09 results and that kind of work, by a prepared statement from Professor Van Ingen who will for a couple of minutes open the discussion on this field.

Prof. Van Ingen

Earlier this week after the presentation of Dr. Michel we were talking about the quality of windtunnels, and I then made a short statement in support of his views, that you might express the quality of a windtunnel in the N factor in the E^N method. Fig. 1 shows the result of the famous experiment by Schubauer and Skramstad on the transition Reynolds number of a flat plate in low speed flow as a function of turbulence level. The curve shows a kink at .1% turbulence level, and below this it was thought that turbulence would have no influence on transition any more. That resulted in the fact (only based on this single picture'), that everybody, building a low turbulence tunnel, was satisfied with .1% turbulence level. Only afterwards it was found out that at the lower turbulence level noise is determining transition. In more quiet tunnels you may find higher transition Reynolds numbers. Using linear stability theory one can calculate, as a function of the Reynolds number, UX/ν , the amplification factor N which is frequency dependent. This N is defined through $A/A_0 = e^N$ where A is the disturbance amplitude at some x and A_0 is the initial amplitude. Now it was found that for the flat plate, where transition at these low turbulence levels was between three and four million, but also for airfoils you get an N of about 9 and that method became known as the E^9 method. It is a bit strange that N would characterize transition because what is needed is really important is the actual amplitude $A = A_0 e^{N/9}$. However, since all of these low turbulence tunnels have been built more or less to the same recipe, you may expect that they have more or less the same initial amplitudes and so you can get away with N only in a first approximation. If you go to some more detail, you have to make this N a function of the turbulence characteristics in the tunnel. Of this the turbulence level is not the determining factor, as Dr. Michel pointed out already. One has to take into account that only part of the spectrum, containing the dangerous frequencies is important. If you do the linear stability calculations for the flat plate, you can convert the Reynolds number for transition, which varies with turbulence level, into a varying N factor. Plotting this N factor versus the turbulence level in percent on a log scale, a rather nice straight band is obtained (Fig. 2). The Schubauer and Skramstad result levels off at low turbulence, but other investigators (e.g., Wells) find points which are more or less in line with a linear extrapolation of the high turbulence results in Fig. 2. We use the linear relations shown in Fig. 2 to find an "effective turbulence level" after a comparison between the experimental transition region and calculated amplification has resulted in an N-factor. Either the N-factor or the "effective turbulence level" can be used as a quality number for the facility. For our low turbulence tunnel in Delft we get an N of 11, for gliders in flight we get about 15 and for older NACA measurements we get about 9. We are planning a project to do windtunnel and flight experiments with the same glider wing to calibrate the method for flight circumstances. (By the way we are looking for a sponsor'). If you want to calibrate the quality of a facility using the N factor or the effective turbulence level as a parameter, you have of course to keep in mind that the result may depend on model shape and wingspeed. You should not fool yourself, because the accuracy of finding the N factor depends of course on the shape of the pressure distribution. If you design the body such that N grows slowly with x, that is a good discrimination because the N factor does not change too much with the measured transition position. If you do it such that N grows rapidly near transition, it is very easy to claim a very high N factor by just measuring the transition position a little bit too late. So what I propose, in line with Dr. Michels paper, is that we should use the N factor as a kind of quality number for the facility.

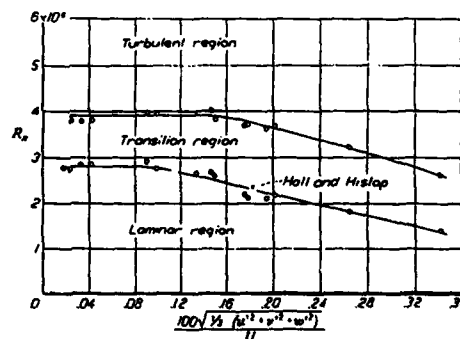


Fig. 1: Transition Reynolds number for a flat plate according to Schubauer and Skramstad (NACA Report 909).

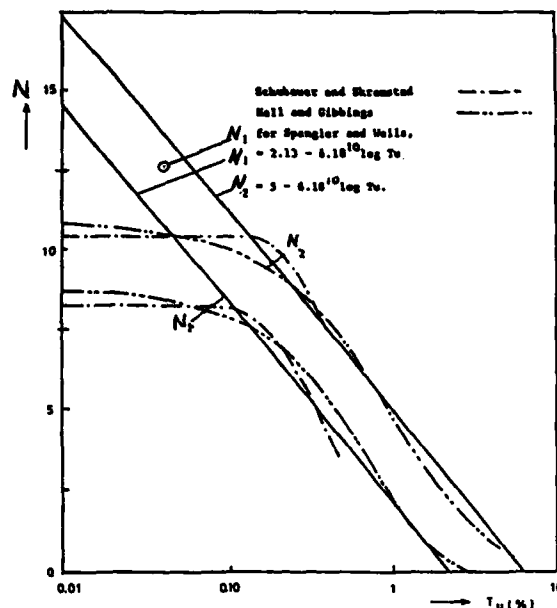


Fig. 2: The critical amplification factor N in the e^N method for transition prediction as a function of the 'effective turbulence level' Tu (%); N_1 = beginning of transition region; N_2 = end of transition region.

Prof. Hornung

This was also discussion by Dr. Michel. Maybe that is a theme that we should discuss in the view also of the people who did the WC 09. Is Eli Reshotko here? Would you like to say something?

Prof. Reshotko

Just with respect to the N factor. It is a useful technique but one must be cautioned that the value of N that correlates with transition is also dependent on the computational technique; how good the stability codes are that are being used. The N factors can vary depending on the degree of sophistication of the stability codes. As an aside, the e^N arguments have been carried into the transonic, supersonic and even are now getting close to hypersonic regimes through computations by Malik at NASA Langley. The number N of 10 to 11 holds up for the good quality flight experiments that have been analyzed as well as good quality tunnel experiments, provided that one carefully includes curvature, principally transverse curvature in the stability computations for cones. Also the correct relationship between flat plate and cone transition has in fact been duplicated when the transverse curvature is taken into account for cones. So the technique is a good one, but the computations have to be done carefully with good codes.

Prof. Giray

I think the tunnel environment is one of the subjects that has been raised frequently, recently. The tunnel environment is not merely composed of velocity fluctuations. Furthermore, turbulence of velocity field cannot be represented only by the so-called turbulence intensity or turbulence level. Other parameters such as scale of turbulence or power spectra are known to have their own input on boundary layer characteristics, development, transition, shocks, etc., therefore on windtunnel performance.

Another point to be added is that there does not seem to exist investigations on combined effect of various windtunnel environmental effects. Such studies like the combination of velocity fluctuations (represented by level, scale, spectra, etc.), pressure gradient, enthalpy fluctuations, noise, etc. Usually each of these parameters is investigated alone, such as the effect of turbulence level on boundary layer characteristics. In reality it is seldom that only one of these parameters is effective. Since the contribution of individual parameters is not simply additive, the combined effect should be separately investigated even if the result of the investigation shows that the individual contributions are additive. I think it is clear that the result of this kind of work is relevant to the subject of the Symposium.

Dr. Rodenker

I would like to stress the point of qualifying the windtunnel flow quality by the N factor. This is extremely important if you think on the next generation of aircraft having laminar wings. Nobody would like to go into a windtunnel having a small N factor. Thus, this value is needed for doing good research

work and experimental verification in a windtunnel when you deal with laminar flow on wings. So you must qualify your windtunnel in terms of N factor against free flight. This is very important.

Dr. Maier

I would like to refer to the paper presented by Dr. Michel. He demonstrated that his detailed turbulence measurements obtained in various wind tunnels can be correlated with transition measurements carried out on the DFVLR prolate spheroid in the same facilities. We just have started a proposal for the European Community to get some financial support for further transition and turbulence measurements in large European low speed and transonic wind tunnels. The purpose of these investigations is to compare wind tunnels with each other and to obtain meaningful experimental input for transition calculations like the N-factor mentioned by Prof. van Ingen. It would be very interesting of course to perform relevant free flight tests in addition. However, this should be the next step.

Mr. Eisenar

I would like to make one relative, maybe a little bit provocative remark about the windtunnel flow quality. Flow quality is very important for the transition location and in that respect it is very important for a number of flows like airfoils with laminar flow. For this case, flow quality is very important. Other aspects are very important as well. Surface quality is very important. We haven't talked at all about dirt in the windtunnels, but everybody who works with natural laminar flow testing in the windtunnels knows that dirt is a very serious problem. Heat transfer is very important, and I think about cryogenic tunnels. So for tests with free transition where the transition location depends very much on small effects like flow quality, surface finish, then you really have a problem in the windtunnel. For a lot of other flows where the transition location is determined by the pressure gradient or by the Reynolds number in the case of a wing, with wing sweep, and leading edge contamination, then flow quality is not important at all I think, at least when it is below a certain level. You can get away with present day windtunnels.

Prof. Hornung

A little bit of flow quality is always good, at all is excessive. This opens a new direction at the same time, I think that perhaps it is time for us to talk about the extreme pedantry that we have to practice in order to chase that last .1 of a drag count, let me exaggerate. The sort of thing that we heard this morning in Gunter Krenz' talk about having to watch the last little covered slot in order to make significant differences, I think that highlights the sort of extremes that we have to go to in order to be sufficiently accurate for what is needed for design. Perhaps we could have a bit of discussion about how far are we from really achieving the accuracy that is needed for design in more depth. I think that the paper this morning was a case in point. Perhaps Gunter would like to say something.

Mr. G. Krenz

I did show that one drag count we can achieve, but the amount of work and the expense of money is very high, so that in that sense I do not agree with the two sentences which Mr. Monnerie has written because they are connected. We can reach it, and we have done it in the S1 tunnel but the work is very laborious and very expensive. So the problem here, just talking transport aircraft and nothing else, is that we should find ways to do it less costly so that means the model must be manufactured accurately, with special methods, and so on. On the transport side we are satisfied regarding test accuracy, but not with the money.

Dr. Koerner

If you can have the drag in the windtunnel with one count accuracy, what is the accuracy of your extrapolation of the drag from windtunnel to flight? Do you have the same accuracy?

Mr. G. Krenz

That is the point, because it is not so easy. It is not the problem of looking for one drag count, we can do that, but the problem is how to translate, to transform the data from windtunnel tests to the full scale Reynolds number, to cover the gap between 12 million that we can reach in RAE with a half model and the full scale for Airbus for instance, of 40 million. That is the big problem, and when you go to design, which is ambitious, in that sense that the rear pressure gradient is steep and the flow near separation, you have to know how the flow develops over this distance of Reynolds number. That is not in our hands, neither in test facilities nor by theoretical methods, and I am wondering that researchers are working so much on new methods, numerical methods are sufficient, I think, as far as industry work is concerned, but a lot of research must be done in finding the effect of Reynolds number in this range.

Prof. Hornung

Perhaps Mr. Carter as an experimentalist would like to have a word on this.

Mr. Carter

The simple answer to your question is NO, I didn't want to have a word on this, but you called me so I will comment with a few words if you have time to give me. I think that the experimentalist's relationship with Gunter Krenz and Airbus is extremely good at the moment, so I don't want to rock that boat. I think he has not emphasized the point, which came out in his paper, that he wishes to relate intelligent testing at lower Reynolds numbers, to his flight data. He, in most respects, is looking at the effect of small "tweaks" of his design and minor modifications to relate them to changes in an absolute set of data which he has obtained from flight. So I think that it is possible to achieve final high accuracy conditions by using a flight reference condition. Dr. Koerner is quite right to ask the question, but we are not in the position where we have to make large extrapolation now because flight data is becoming more accurate and more project related and its value can be measured in terms of cost. Now the point I would like to take up with Mr. Krenz was the fact that he kept talking about cost. He often talks about cost, usually because it is too big, but somebody in one of the papers this week showed one of those typical large circular diagrams and the size of the width of the segment that was put on that diagram for the research costs was so minuscule that I would challenge his point about high research costs. Isn't it about time we realized the actual value of the research and make it a little tiny bit larger segment of this circle which is almost certainly composed of development costs and other costs which are more easily accepted. A factor of two in the research segment would make an enormous effect on

RTD-6

the research and virtually no effect on the size of the circle.

Mr. Chairman, may I raise a question that I would like to have asked Prof. Roshko on his various scale effect scenarios. Does he see a scenario where his WC 09 is going to come out with the conclusion that noisy transonic windtunnels with Reynolds numbers of 12 million and above are going to be useless because it is impossible to fix aft transition to represent the correct viscous boundary layer high Reynolds number conditions.

Mr. Roshko

The answer very simply is YES.

You are coming to a conclusion that expensive tunnels necessarily have poor flow quality. I think that there is a great sensitivity now to improving the flow quality in windtunnels, however expensive the tunnel. We can look forward to a much better situation. While I have the floor I think that I should mention that the fact that a tunnel reproduces full Reynolds numbers is no guarantee of flight quality results. The closer a windtunnel gets to achieving full Reynolds number the more it has to completely emulate the flight environment.

Prof. Hornung

We have now about 5 minutes of discussion left, I think that maybe we should let the number crunchers have a word too. Joop, you had your hand up before.

Mr. Slooff

Yes, but I am afraid that what I am going to say has nothing to do with number crunching. First of all I should say that due to the fact that we were having great difficulty in establishing the program for the next AGARD meeting which is on code validation, I witnessed only a few papers here, so the question may have been answered already. One of the papers I did witness was the one by Travis Binion, and I think support interference ranks high on his list of uncertainties. Obviously, number crunching comes in as one possibility for reducing the uncertainty in that respect, but I was wondering whether any progress has been made anywhere on non-intrusive suspension, such as magnetic suspension. Is this hardware solution being pursued anywhere or not?

Prof. Hornung

Certainly in this meeting there was no discussion of magnetic suspensions, and perhaps we should not go in depth in this field at this point, but I think that maybe in order to get the numerical world into the scene a bit, Wolfgang Schmidt should have a word.

Dr. Schmidt

I won't comment about CFD either. I am somewhat worried about the absolute accuracy of something like one drag count because of the fact that we are working with windtunnel models that are polished in surface, that are made of steel all the way through that have completely different bending and twist than actual aircraft and with completely different surfaces. So how can we actually relate the completely different shape and structure and quality of the model to what is happening in real flight?

Mr. Binion

Very simple, Wolfgang, you use the tools you have available to you. The power of CFD, I believe, is that one can take experimental data from a windtunnel and, if I may use the term, calibrate the CFD code with windtunnel boundary conditions, with windtunnel turbulence with windtunnel wall interference, with all the other factors that affect windtunnel data and then remove those factors in the CFD code and extrapolate the data to flight using flight boundary conditions, flight turbulence values, flight transition locations, etc. However, to do that we must develop an understanding of the physics in the windtunnel as well as in flight. I believe in the next decade that the only way we are going to solve the problem of trying to get precise flight predictions from a windtunnel because of all the factors involved. One other point before I give up the floor. I want to defend one of my favorite people, Dr. Osborne Reynolds. We tend to blame all of our ills on his number. There are 10's of factors that influence windtunnel data. We should not lose sight of that. We need to make sure that we are doing everything right and not just worrying about one parameter.

Dr. Schmidt

I am pleased that you gave the answer on the use of CFD that I had in mind. But still there is one point left and that is I would like to see the experimentalist who is willing to integrate his measured pressures to get drag. However, that is what people expect from all the CFD people. They take their computations, they integrate pressure over the surfaces and they say, "look, that is drag". Experimentalists will never do that because they all have balances.

Mr. Binion

We integrate pressures on nozzle afterbodies to get drag quite often. In doing comparisons between pressure integrations and balance measurements we found that the agreement between the two methods is very good if you do things correctly. Among other things, the pressure orifices must be distributed such that the regions of high gradients are well defined. For complicated three dimensional configurations that requires several thousand pressure orifices. Even on two-dimensional wings, the orifice density near the leading edge must be quite high just as does the grid spacing in the computations. Many times it is physically impossible to install enough orifices to adequately define the gradients. Then some other means must be employed. The computational and experimental people must work together to understand the limitations of each method so they can design computations and experiments that are mutually compatible.

Dr. McCroskey

I think that we really should be looking ahead to interactions between aerodynamics and the structures, propulsion, and other disciplines, and I hope that both CFD and the experimental work will move somewhat in that direction.

Prof. Hornung

While the electricity is flowing I should terminate the discussion because at this point the ritual is over and we hand over to the Chairman of the Panel who will round it off.

Mr. Sacher

Well gentlemen, after this high speed shoot out by Hans Hornung on our Symposium, it is up to the Chairman to make some final remarks, but before coming to those remarks, I will give General Grazioli, the National Delegate of Italy the opportunity to say something.

General Grazioli

Thank you Mr. Chairman. Ladies and Gentlemen. At the conclusion of this symposium, I note with great satisfaction the numerous participants and windtunnel specialists, and I want to thank particularly General Arpino who has welcomed us at the Italian Airforce Academy. General Bartolucci, President C.I.R.A. and the Director of C.I.R.A. who have helped us with the organization. Now, I will proceed with the distribution of souvenirs concerning the Symposium to the people who have particularly contributed to its wonderful success. Mr. Sacher, Chairman of the Panel, Mr. Monnerie, Co-Chairman of the Technical Committee, Mr. Ohman, Co-Chairman of the Technical Committee, Mr. Fischer, the Panel Executive, General Bartolucci, President of C.I.R.A. Mr. Abolloni, the Director General of C.I.R.A., Professor Napolitano, the National Panel Coordinator, Colonel Bertinaria, second in command, Lieutenant Colonel Cavallero, Local Coordinator. A special thank you to Mr. Sacher on behalf of the Italian delegation. This is Mr. Sacher's last meeting as Chairman of the Panel, and Mr. Peckham will replace him in October. I would like to thank also the authors of the technical papers and all the participants. I hope that Italy will have another opportunity to organize very soon another Symposium of the Fluid Dynamics Panel and in the meantime, thank you, good bye until the next time and have a good trip to your respective countries.

Mr. Sacher

Ladies and Gentlemen, as you have noticed that makes this an easy job this time to acknowledge all these important personalities who have contributed significantly to the success of this meeting. I just want, on behalf of the Fluid Dynamics Panel, to acknowledge General Grazioli, the National Delegate from Italy, for his tremendous effort for arranging this meeting and for providing us with the local connections to hold our meeting here in Naples. We thank very much the Italian National Delegation to AGARD. Please allow me to thank also the Italian Airforce Academy for providing all the local things, first of all of course, General Arpino and his staff. I want to add our personal thanks on behalf of the Panel to one of our oldest members, Professor Luigi Napolitano who has been with AGARD since 1960. Also, of course, his staff from the University, and on behalf of the Fluid Dynamics Panel I have to acknowledge specially the excellent preparation of our Ladies Programme which has been organized and sponsored by C.I.R.A.

Concluding I have to address our appreciation to the technical staff of this meeting. We have had again precise, excellent interpreters with us, and we thank very much Mrs. Borlat-Rossano, Mrs. Hicks and Mrs. Main for doing an excellent job during the whole week. Not to forget at the end of this meeting our thanks to the technicians, Mr. Dale Verly and Richard Adam who have provided all of these arrangements concerning the microphones and the projection system. Now I would like to thank our Executive Mike Fischer and his secretary Anne-Marie Rivault for providing again this excellent support throughout the whole week and her service from the administrative side. Before ending my acknowledgement, I want to thank all the participants of this meeting, not only for staying with us throughout all the meetings - four long days - but also for their active participation in the various discussions along with the presentations. Thank you for coming and allow me to express my hope that we will see as many of you as possible in one of our future activities.

Allow me to make some commercials. Our program for 1988 provides a spring meeting in Lisbon; it is CFD Code Validation which is very closely related to the subject of this past meeting. In the fall, the first half of October, we will have a second symposium in Turkey on the subject of Three-dimensional Turbulent Shear Flows and Transition. In addition, we are organizing two special courses in the next year; one in May on Aerodynamics of Hypersonic Vehicles which will be arranged in Brussels. The second one will be in April on Boundary Layer Simulation Methodology in Transonic Windtunnel Testing. This will also be a short course repeated at the University of Tennessee in the United States. I hope to see many of you in one of these future activities, and now I would like to say good bye and to wish everybody a good return.

REPORT DOCUMENTATION PAGE			
1. Recipient's Reference	2. Originator's Reference	3. Further Reference	4. Security Classification of Document
	AGARD-CP-429	ISBN 92-835-0469-0	UNCLASSIFIED
5. Originator	Advisory Group for Aerospace Research and Development North Atlantic Treaty Organization 7 rue Ancelle, 92200 Neuilly sur Seine, France		
6. Title	AERODYNAMIC DATA ACCURACY AND QUALITY: REQUIREMENTS AND CAPABILITIES IN WIND TUNNEL TESTING		
7. Presented at	the Symposium of the Fluid Dynamics Panel in Naples, Italy, 28 September—1 October 1987.		
8. Author(s)/Editor(s)	Various		9. Date July 1988
10. Author's/Editor's Address	Various		11. Pages 530
12. Distribution Statement	This document is distributed in accordance with AGARD policies and regulations, which are outlined on the Outside Back Covers of all AGARD publications.		
13. Keywords/Descriptors	<div style="display: flex; justify-content: space-between;"> <div> Wind tunnels Aerodynamics Accuracy </div> <div> Measurement Environments </div> </div>		
14. Abstract	<p>→ The wind tunnel continues to be the main instrument for providing experimental aerodynamic data to the aerospace industry and the aerodynamic researcher for the purpose of load and performance evaluation and for verification of theoretical results. In both cases it is imperative that the user has confidence in the quality of the results, which means that he must have information on what accuracy to attach to the data.</p> <p>• The quality of wind tunnel results depends upon both the accuracy of measurements and the imperfections provided by the wind tunnel environment. Great strides have been made in recent years on measurement accuracy and as a rule this need no longer be of much concern if properly attended to. However, imperfections provided by the wind tunnel environment are still with us and these are today the main sources affecting the quality and accuracy of aerodynamic data obtained in a wind tunnel.</p> <p>• It was the purpose of this symposium to try to define what accuracy has presently been achieved in modern facilities and to compare these achievements with the actual demands of the user.</p> <p><i>Session topics included:</i></p> <p style="text-align: center;">to p vii</p>		

<p>AGARD Conference Proceedings No.429 Advisory Group for Aerospace Research and Development, NATO AERODYNAMIC DATA ACCURACY AND QUALITY: REQUIREMENTS AND CAPABILITIES IN WIND TUNNEL TESTING Published July 1988 530 pages</p> <p>The wind tunnel continues to be the main instrument for providing experimental aerodynamic data to the aerospace industry and the aerodynamic researcher for the purpose of load and performance evaluation and for verification of theoretical results. In both cases it is imperative that the user has confidence in the quality of the results, which means that he must have information on what accuracy to attach to the data.</p> <p>P.T.O</p>	<p>AGARD-CP-429</p> <p>Wind tunnels Aerodynamics Accuracy Measurement Environments</p>	<p>AGARD Conference Proceedings No.429 Advisory Group for Aerospace Research and Development, NATO AERODYNAMIC DATA ACCURACY AND QUALITY: REQUIREMENTS AND CAPABILITIES IN WIND TUNNEL TESTING Published July 1988 530 pages</p> <p>The wind tunnel continues to be the main instrument for providing experimental aerodynamic data to the aerospace industry and the aerodynamic researcher for the purpose of load and performance evaluation and for verification of theoretical results. In both cases it is imperative that the user has confidence in the quality of the results, which means that he must have information on what accuracy to attach to the data.</p> <p>P.T.O</p>	<p>AGARD-CP-429</p> <p>Wind tunnels Aerodynamics Accuracy Measurement Environments</p>	<p>AGARD-CP-429</p> <p>Wind tunnels Aerodynamics Accuracy Measurement Environments</p>
<p>AGARD Conference Proceedings No.429 Advisory Group for Aerospace Research and Development, NATO AERODYNAMIC DATA ACCURACY AND QUALITY: REQUIREMENTS AND CAPABILITIES IN WIND TUNNEL TESTING Published July 1988 530 pages</p> <p>The wind tunnel continues to be the main instrument for providing experimental aerodynamic data to the aerospace industry and the aerodynamic researcher for the purpose of load and performance evaluation and for verification of theoretical results. In both cases it is imperative that the user has confidence in the quality of the results, which means that he must have information on what accuracy to attach to the data.</p> <p>P.T.O</p>	<p>AGARD-CP-429</p> <p>Wind tunnels Aerodynamics Accuracy Measurement Environments</p>	<p>AGARD Conference Proceedings No.429 Advisory Group for Aerospace Research and Development, NATO AERODYNAMIC DATA ACCURACY AND QUALITY: REQUIREMENTS AND CAPABILITIES IN WIND TUNNEL TESTING Published July 1988 530 pages</p> <p>The wind tunnel continues to be the main instrument for providing experimental aerodynamic data to the aerospace industry and the aerodynamic researcher for the purpose of load and performance evaluation and for verification of theoretical results. In both cases it is imperative that the user has confidence in the quality of the results, which means that he must have information on what accuracy to attach to the data.</p> <p>P.T.O</p>	<p>AGARD-CP-429</p> <p>Wind tunnels Aerodynamics Accuracy Measurement Environments</p>	<p>AGARD-CP-429</p> <p>Wind tunnels Aerodynamics Accuracy Measurement Environments</p>

<p>The quality of wind tunnel results depends upon both the accuracy of measurements and the imperfections provided by the wind tunnel environment. Great strides have been made in recent years on measurement accuracy and as a rule this need no longer be of much concern if properly attended to. However, imperfections provided by the wind tunnel environment are still with us and these are today the main sources affecting the quality and accuracy of aerodynamic data obtained in a wind tunnel.</p> <p>It was the purpose of this symposium to try to define what accuracy has presently been achieved in modern facilities and to compare these achievements with the actual demands of the user.</p> <p>Papers presented and discussions held at the Symposium of the Fluid Dynamics Panel in Naples, Italy, 28 September—1 October 1987.</p> <p>ISBN 92-835-0469-0</p>	<p>The quality of wind tunnel results depends upon both the accuracy of measurements and the imperfections provided by the wind tunnel environment. Great strides have been made in recent years on measurement accuracy and as a rule this need no longer be of much concern if properly attended to. However, imperfections provided by the wind tunnel environment are still with us and these are today the main sources affecting the quality and accuracy of aerodynamic data obtained in a wind tunnel.</p> <p>It was the purpose of this symposium to try to define what accuracy has presently been achieved in modern facilities and to compare these achievements with the actual demands of the user.</p> <p>Papers presented and discussions held at the Symposium of the Fluid Dynamics Panel in Naples, Italy, 28 September—1 October 1987.</p> <p>ISBN 92-835-0469-0</p>
<p>The quality of wind tunnel results depends upon both the accuracy of measurements and the imperfections provided by the wind tunnel environment. Great strides have been made in recent years on measurement accuracy and as a rule this need no longer be of much concern if properly attended to. However, imperfections provided by the wind tunnel environment are still with us and these are today the main sources affecting the quality and accuracy of aerodynamic data obtained in a wind tunnel.</p> <p>It was the purpose of this symposium to try to define what accuracy has presently been achieved in modern facilities and to compare these achievements with the actual demands of the user.</p> <p>Papers presented and discussions held at the Symposium of the Fluid Dynamics Panel in Naples, Italy, 28 September—1 October 1987.</p> <p>ISBN 92-835-0469-0</p>	<p>The quality of wind tunnel results depends upon both the accuracy of measurements and the imperfections provided by the wind tunnel environment. Great strides have been made in recent years on measurement accuracy and as a rule this need no longer be of much concern if properly attended to. However, imperfections provided by the wind tunnel environment are still with us and these are today the main sources affecting the quality and accuracy of aerodynamic data obtained in a wind tunnel.</p> <p>It was the purpose of this symposium to try to define what accuracy has presently been achieved in modern facilities and to compare these achievements with the actual demands of the user.</p> <p>Papers presented and discussions held at the Symposium of the Fluid Dynamics Panel in Naples, Italy, 28 September—1 October 1987.</p> <p>ISBN 92-835-0469-0</p>

88